International Association of Geodesy Symposia
Volume 135

Stelios P. Mertikas (Ed.)

Gravity, Geoid and Earth Observation

IAG Commission 2: Gravity Field, Chania, Crete, Greece, 23-27 June 2008

Springer

International Association of Geodesy Symposia

Michael G. Sideris, Series Editor

This International Symposium is sponsored by



International Association of Geodesy



Technical University of Crete, and Geodesy & Geomatics Engineering Lab



European Space Agency



Technical Chamber of Greece, Division of West Crete



The Hellenic National Cadastre



Chania Chamber of Commerce & Industry



Agro-Land, S.A.



National Aeronautics and Space Administration

The Holy Monastery of Agia Triada of Jagarolon, Chania, Crete, The Prefecture of Chania and the Greek National Tourism Organization have also subsidized this International Symposium.

For further volumes:
http://www.springer.com/series/1345

International Association of Geodesy Symposia

Michael G. Sideris, Series Editor

Symposium 101: Global and Regional Geodynamics
Symposium 102: Global Positioning System: An Overview
Symposium 103: Gravity, Gradiometry, and Gravimetry
Symposium 104: Sea SurfaceTopography and the Geoid
Symposium 105: Earth Rotation and Coordinate Reference Frames
Symposium 106: Determination of the Geoid: Present and Future
Symposium 107: Kinematic Systems in Geodesy, Surveying, and Remote Sensing
Symposium 108: Application of Geodesy to Engineering
Symposium 109: Permanent Satellite Tracking Networks for Geodesy and Geodynamics
Symposium 110: From Mars to Greenland: Charting Gravity with Space and Airborne Instruments
Symposium 111: Recent Geodetic and Gravimetric Research in Latin America
Symposium 112: Geodesy and Physics of the Earth: Geodetic Contributions to Geodynamics
Symposium 113: Gravity and Geoid
Symposium 114: Geodetic Theory Today
Symposium 115: GPS Trends in Precise Terrestrial, Airborne, and Spaceborne Applications
Symposium 116: Global Gravity Field and Its Temporal Variations
Symposium 117: Gravity, Geoid and Marine Geodesy
Symposium 118: Advances in Positioning and Reference Frames
Symposium 119: Geodesy on the Move
Symposium 120: Towards an Integrated Global Geodetic Observation System (IGGOS)
Symposium 121: Geodesy Beyond 2000: The Challenges of the First Decade
Symposium 122: IV Hotine-Marussi Symposium on Mathematical Geodesy
Symposium 123: Gravity, Geoid and Geodynamics 2000
Symposium 124: Vertical Reference Systems
Symposium 125: Vistas for Geodesy in the New Millennium
Symposium 126: Satellite Altimetry for Geodesy, Geophysics and Oceanography
Symposium 127: V Hotine Marussi Symposium on Mathematical Geodesy
Symposium 128: A Window on the Future of Geodesy
Symposium 129: Gravity, Geoid and Space Missions
Symposium 130: Dynamic Planet - Monitoring and Understanding
Symposium 131: Geodetic Deformation Monitoring: From Geophysical to Engineering Roles
Symposium 132: VI Hotine-Marussi Symposium on Theoretical and Computational Geodesy
Symposium 133: Observing our Changing Earth
Symposium 134: Geodetic Reference Frames
Symposium 135: Gravity, Geoid and Earth Observation

Gravity, Geoid and Earth Observation

IAG Commission 2: Gravity Field, Chania, Crete, Greece, 23–27 June 2008

Edited by

Stelios P. Mertikas

Springer

Editor
Stelios P. Mertikas
Technical University of Crete
Dept. Mineral Resources Engineering
Lab. Geodesy/Geomatics
University Campus
731 00 Chania, Crete
Greece
mertikas@mred.tuc.gr

ISBN 978-3-642-10633-0 e-ISBN 978-3-642-10634-7
DOI 10.1007/978-3-642-10634-7
Springer Heidelberg Dordrecht London New York

Library of Congress Control Number: 2010922542

© Springer-Verlag Berlin Heidelberg 2010
This work is subject to copyright. All rights are reserved, whether the whole or part of the material is concerned, specifically the rights of translation, reprinting, reuse of illustrations, recitation, broadcasting, reproduction on microfilm or in any other way, and storage in data banks. Duplication of this publication or parts thereof is permitted only under the provisions of the German Copyright Law of September 9, 1965, in its current version, and permission for use must always be obtained from Springer. Violations are liable to prosecution under the German Copyright Law.
The use of general descriptive names, registered names, trademarks, etc. in this publication does not imply, even in the absence of a specific statement, that such names are exempt from the relevant protective laws and regulations and therefore free for general use.

Cover design: Integra Software Services Pvt. Ltd., Pondicherry

Printed on acid-free paper

Springer is part of Springer Science+Business Media (www.springer.com)

Preface

These Proceedings include the written version of papers presented at the IAG International Symposium on "Gravity, Geoid and Earth Observation 2008". The Symposium was held in Chania, Crete, Greece, 23–27 June 2008 and organized by the Laboratory of Geodesy and Geomatics Engineering, Technical University of Crete, Greece. The meeting was arranged by the International Association of Geodesy and in particular by the IAG Commission 2: Gravity Field. It took place at the beautiful premises of the Venetian Arsenali, Centre of Mediterranean Architecture, right in the middle of the Venetian old harbor of the Chania city.

The symposium aimed at bringing together geodesists and geophysicists working in the general areas of gravity, geoid, geodynamics and Earth observation. Besides covering the traditional research areas, special attention was paid to the use of geodetic methods for: Earth observation, environmental monitoring, Global Geodetic Observing System (GGOS), Earth Gravity Models (e.g., EGM08), geodynamics studies, dedicated gravity satellite missions (i.e., GOCE), airborne gravity surveys, Geodesy and geodynamics in polar regions, and the integration of geodetic and geophysical information.

The meeting attracted more than 220 participants from Australia, Algeria, Argentina, Austria, Belgium, Brazil, Bulgaria, Canada, China, Croatia, Czech Republic, Denmark, Estonia, Finland, France, Germany, Greece, Hungary, Iran, Italy, Japan, Luxemburg, the Netherlands, Norway, Poland, Portugal, Russia, Slovakia, Korea, Spain, Sweden, Switzerland, Taiwan, Turkey, the United Stated of America and the United Kingdom.

The scientific program of the meeting was organized by the symposium conveners and the chairpersons of each Session. At the GGEO2008 Symposium, 91 oral presentations and more than 200 poster presentations were presented. The Symposium was organized into nine Sessions as follows:

- *Session 1: Gravimetry (terrestrial, shipborne, airborne) and gravity networks.*
- Chairs: Yoichi Fukuda (Japan), Leonid F. Vitushkin (France).
- *Session 2: Space-borne gravimetry: Present and Future.*
- Chairs: Roland Pail (Austria) and Pieter Visser (The Netherlands).
- *Session 3: Earth Observation by Satellite Altimetry and InSAR.*
- Chairs: Wolfgang Bosch (Germany), Masato Furuya (Japan), Roger Haagmans (ESA).
- *Session 4: Geoid modeling and vertical datums.*
- Chairs: Ambrus Kenyeres (Hungary) and William Kearsley (Australia).

- *Session 5: Regional gravity field modeling.*
- Chairs: Urs Marti (Switzerland) and Steve Kenyon (USA).
- *Session 6: Global gravity field modelling and EGM08.*
- Chairs: Nikos Pavlis (USA) and Jianliang Huang (Canada).
- *Session 7: Temporal gravity changes and geodynamics.*
- Chairs: Nico Sneeuw (Germany) and Juergen Kusche (Germany).
- *Session 8: Earth observation and the Global Geodetic Observing System (GGOS).*
- Chairs: Richard Gross (USA) and Hans-Peter Plag (USA), and
- *Session 9: Geodetic monitoring of natural hazards and a Changing Environment.*
- Chairs: Alexander Braun (Canada) and Rene Forsberg (Denmark).

Besides the Sessions and simultaneously with the meeting, five Working Group meetings also took place. These meetings were the IAG ICP 1.2: Vertical Reference Frames, the IAG Inter-Commission 2.1 Working Group on Absolute Gravimetry, the Sub-Commission 2.3: Dedicated Satellite Gravity Mapping Missions, the Joint IGFC/Commission-2 Working Group, and the IAG Study Group 2.2: High-Resolution Forward Gravity.

The symposium conveners and the session chairs decided on the acceptance of the submitted abstracts. The session chairs took an active role in the selection of papers for oral and poster presentations. In addition, they organized the review process for the papers presented in this Volume of Proceedings. The submitted papers were thoroughly reviewed by a panel of more than 65 international reviewers. This Volume contains a representative sample of 91 accepted papers from all sessions.

The scientific committee of this IAG International Symposium consisted of Michael G. Sideris (Canada), Yoichi Fukuda (Japan), Stelios P. Mertikas (Greece), Rene Forsberg, (Denmark), Pieter Visser (The Netherlands), Hermann Drewes (Germany), Leonid F. Vitushkin (France), Martin Vermeer (Finland), Roland Pail (Austria), Urs Marti (Switzerland), Nico Sneeuw (Germany), Jacques Hinderer (France), Juergen Kusche (Germany), Roger Haagmans (The Netherlands), and Steve C. Kenyon (USA).

The local organizing committee consisted of Stelios P. Mertikas (Symposium convener), Mrs. R. Papadaki (Secretary), Mrs. G. Tsiskaki (Public Relations) as well as Ach. Tripolitsiotis, X. Fratzis, Th. Papadopoulos, E. Ieronimidi, and P. Partsinevelos. We are also grateful to our graduate students D. Zacharaki, K. Manousaki, Z. Papadaki, F. Stathogianni and Ch. Apostolaki for their help and continuous support.

The IAG Executive Committee also approved several travel awards for students to attend the GGEO2008 Symposium under the direction of IAG Secretary General, Hermann Drewes.

Financial support and promotional support was given by a number of agencies. Special thanks go to the International Association of Geodesy, the Technical University of Crete, the European Space Agency, the Technical Chamber of Greece, Division of West Crete, the Hellenic National Cadastre (Ktimatologio, SA), the Chania Chamber of Commerce and Industry, Agro-Land, S.A. and the National Aeronautics and Space Administration, the Holy Monastery of Agia Triada of Jagarolon, Chania, Crete, the Prefecture of Chania and the Greek National Tourism Organization have also subsidized this International GGEO2008 Symposium.

To all individuals who have, in one way or another, been involved in the preparation of this International GGEO2008 Symposium and to all Organizations, Session

Chairs and Committees that have given their support, I extend sincere thanks. It is their hard work and support that laid the foundation for the success of this event. In addition to those cited above for their assistance, I am also grateful to the President of IAG, Michael G. Sideris, the IAG Secretary General, Hermann Drewes and the president of the University, Joachim Gryspolakis for their help and support.

A final word of thanks goes to Sessions Chairs who organized the review process of the submitted papers, the external reviewers and to Rania Papadaki who put many extra hours into checking the format of papers, collecting and organizing the revised manuscripts.

Chania, 23 July 2009 Stelios P. Mertikas

Contents

Part I Gravimetry (Terrestrial, Shipborne, Airborne) and Gravity Networks **1**

1 Preliminary Results of a GPS/INS Airborne Gravimetry Experiment Over the German Alps **3**
Ch. Gerlach, R. Dorobantu, Ch. Ackermann, N.S. Kjørsvik, and G. Boedecker

2 Co-seismic Gravity Changes Computed for a Spherical Earth Model Applicable to GRACE Data **11**
W. Sun, G. Fu, and Sh. Okubo

3 On Ambiguities in Definitions and Applications of Bouguer Gravity Anomaly **19**
P. Vajda, P. Vaníček, P. Novák, R. Tenzer, A. Ellmann, and B. Meurers

4 Harmonic Continuation and Gravimetric Inversion of Gravity in Areas of Negative Geodetic Heights **25**
P. Vajda, A. Ellmann, B. Meurers, P. Vaníček, P. Novák, and R. Tenzer

5 Results of the European Comparison of Absolute Gravimeters in Walferdange (Luxembourg) of November 2007 . . . **31**
O. Francis, T. van Dam, A. Germak, M. Amalvict, R. Bayer, M. Bilker-Koivula, M. Calvo, G.-C. D'Agostino, T. Dell'Acqua, A. Engfeldt, R. Faccia, R. Falk, O. Gitlein, Fernandez, J. Gjevestad, J. Hinderer, D. Jones, J. Kostelecky, N. Le Moigne, B. Luck, J. Mäkinen, D. Mclaughlin, T. Olszak, P. Olsson, A. Pachuta, V. Palinkas, B. Pettersen, R. Pujol, I. Prutkin, D. Quagliotti, R. Reudink, C. Rothleitner, D. Ruess, C. Shen, V. Smith, S. Svitlov, L. Timmen, C. Ulrich, M. Van Camp, J. Walo, L. Wang, H. Wilmes, and L. Xing

6 Aerogravity Survey of the German Bight (North Sea) **37**
I. Heyde

7 Results of the Seventh International Comparison of Absolute Gravimeters ICAG-2005 at the Bureau International des Poids et Mesures, Sèvres **47**
L. Vitushkin, Z. Jiang, L. Robertsson, M. Becker, O. Francis, A. Germak, G. D'Agostino,V. Palinkas, M. Amalvict, R. Bayer, M. Bilker-Koivula, S. Desogus, J. Faller, R. Falk, J. Hinderer, C. Gagnon, T. Jakob, E. Kalish, J. Kostelecky, Chiungwu Lee, J. Liard,Y. Lokshyn, B. Luck, J. Mäkinen, S. Mizushima, N. Le Moigne, V. Nalivaev, C. Origlia, E.R. Pujol, P. Richard, D. Ruess, D. Schmerge, Y. Stus, S. Svitlov, S. Thies, C. Ullrich, M. Van Camp, A. Vitushkin, and H. Wilmes

8 Post-Newtonian Covariant Formulation for Gravity Determination by Differential Chronometry **55**
P. Romero

9 Robust and Efficient Weighted Least Squares Adjustment of Relative Gravity Data **59**
F. Touati, S. Kahlouche, and M. Idres

10 Comparison Between GPS Sea Surface Heights, MSS Models and Satellite Altimetry Data in the Aegean Sea. Implications for Local Geoid Improvement **67**
I. Mintourakis and D. Delikaraoglou

11 First Experience with the Transportable MPG-2 Absolute Gravimeter **75**
S. Svitlov, C. Rothleitner, and L.J. Wang

12 Absolute Gravimetry at BIPM, Sèvres (France), at the Time of Dr. Akihiko Sakuma **83**
M. Amalvict

13 Correcting Strapdown GPS/INS Gravimetry Estimates with GPS Attitude Data **93**
B.A. Alberts, B.C. Gunter, A. Muis, Q.P. Chu, G. Giorgi, L. Huisman, P.J. Buist, C.C.J.M. Tiberius, and H. Lindenburg

14 Gravity Measurements in Panama with the IMGC-02 Transportable Absolute Gravimeter **101**
G. D'Agostino, A. Germak, D. Quagliotti, O. Pinzon, R. Batista, and L.A. Echevers

15 Comparison of Height Anomalies Determined from SLR, Absolute Gravimetry and GPS with High Frequency Borehole Data at Herstmonceux **107**
G. Appleby, V. Smith, M. Wilkinson, M. Ziebart, and S. Williams

16 Vibration Rejection on Atomic Gravimeter Signal Using a Seismometer **115**
S. Merlet, J. Le Gouët, Q. Bodart, A. Clairon, A. Landragin, F. Pereira Dos Santos, and P. Rouchon

17 Gravity vs Pseudo-Gravity: A Comparison Based on Magnetic and Gravity Gradient Measurements **123**
C. Jekeli, K. Erkan, and O. Huang

Part II Space-Borne Gravimetry: Present and Future **129**

18 Designing Earth Gravity Field Missions for the Future: A Case Study **131**
P.N.A.M. Visser

19 Regional Gravity Field Recovery from GRACE Using Position Optimized Radial Base Functions **139**
M. Weigelt, M. Antoni, and W. Keller

20 External Calibration of SGG Observations on Accelerometer Level **147**
R. Mayrhofer and R. Pail

21 Covariance Propagation of Latitude-Dependent Orbit Errors Within the Energy Integral Approach **155**
H. Goiginger and R. Pail

22 Future Mission Design Options for Spatio-Temporal Geopotential Recovery **163**
T. Reubelt, N. Sneeuw, and M.A. Sharifi

23 A Simulation Study Discussing the GRACE Baseline Accuracy . . . **171**
U. Meyer, F. Flechtner, R. Schmidt, and B. Frommknecht

24 GRACE Gravity Field Determination Using the Celestial Mechanics Approach – First Results **177**
A. Jäggi, G. Beutler, and L. Mervart

25 Fast Variance Component Estimation in GOCE Data Processing **185**
J.M. Brockmann and W.-D. Schuh

26 Analysis of the Covariance Structure of the GOCE Space-Wise Solution with Possible Applications **195**
L. Pertusini, M. Reguzzoni, and F. Sansò

Part III Earth Observation by Satellite Altimetry and InSAR **203**

27 Soil Surface Moisture From EnviSat RA-2: From Modelling Towards Implementation **205**
S.M.S. Bramer and P.A.M. Berry

28 An Enhanced Ocean and Coastal Zone Retracking Technique for Gravity Field Computation **213**
P.A.M. Berry, J.A. Freeman, and R.G. Smith

29 Measurement of Inland Surface Water from Multi-mission Satellite Radar Altimetry: Sustained Global Monitoring for Climate Change **221**
P.A.M. Berry and J. Benveniste

30 ACE2: The New Global Digital Elevation Model 231
P.A.M. Berry, R.G. Smith, and J. Benveniste

31 Ocean Dynamic Topography from GPS – Galathea-3 First Results 239
O.B. Andersen, A.V. Olesen, R. Forsberg, G. Strykowski, K.S. Cordua, and X. Zhang

32 Filtering of Altimetric Sea Surface Heights with a Global Approach 247
A. Albertella, X. Wang, and R. Rummel

33 Coastal Sea Surface Heights from Improved Altimeter Data in the Mediterranean Sea 253
L. Fenoglio-Marc, M. Fehlau, L. Ferri, M. Becker, Y. Gao, and S. Vignudelli

34 On Estimating the Dynamic Ocean Topography – A Profile Approach 263
W. Bosch and R. Savcenko

Part IV Geoid Modeling and Vertical Datums 271

35 Evaluation of the Topographic Effect using the Various Gravity Reduction Methods for Precise Geoid Model in Korea 273
S.B. Lee and D.H. Lee

36 Analysis of Recent Global Geopotential Models Over the Croatian Territory 283
M. Liker, M. Lučić, B. Barišić, M. Repanić, I. Grgić, and T. Bašić

37 On the Merging of Heterogeneous Height Data from SRTM, ICESat and Survey Control Monuments for Establishing Vertical Control in Greece: An Initial Assessment and Validation 289
D. Delikaraoglou and I. Mintourakis

38 Implementing a Dynamic Geoid as a Vertical Datum for Orthometric Heights in Canada 295
E. Rangelova, G. Fotopoulos, and M.G. Sideris

39 Evaluation of the Quasigeoid Models EGG97 and EGG07 with GPS/levelling Data for the Territory of Bulgaria 303
E. Peneva and I. Georgiev

40 Combination Schemes for Local Orthometric Height Determination from GPS Measurements and Gravity Data 309
A. Fotiou, V.N. Grigoriadis, C. Pikridas, D. Rossikopoulos, I.N. Tziavos, and G.S. Vergos

41 EUVN_DA: Realization of the European Continental GPS/leveling Network 315
A. Kenyeres, M. Sacher, J. Ihde, H. Denker, and U. Marti

42 Analysis of the Geopotential Anomalous Component at Brazilian Vertical Datum Region Based on the Imarui Lagoon System **321**
S.R.C. de Freitas, V.G. Ferreira, A.S. Palmeiro, J.L.B. de Carvalho, and L.F. da Silva

43 Preliminary Results of Spatial Modelling of GPS/Levelling Heights: A Local Quasi-Geoid/Geoid for the Lisbon Area **329**
A.P. Falcão, J. Matos, A. Gonçalves, J. Casaca, and J. Sousa

44 Physical Heights Determination Using Modified Second Boundary Value Problem **333**
M. Mojzes and M. Valko

Part V Regional Gravity Field Modeling **339**

45 Impact of the New GRACE-Derived Global Geopotential Model and SRTM Data on the Geoid Heights in Algeria **341**
S.A. Benahmed Daho

46 On Modelling the Regional Distortions of the European Gravimetric Geoid EGG97 in Romania **349**
R. Tenzer, I. Prutkin, R. Klees, T. Rus, and N. Avramiuc

47 Effect of the Long-Wavelength Topographical Correction on the Low-Degree Earth's Gravity Field **355**
R. Tenzer and P. Novák

48 A Comparison of Various Integration Methods for Solving Newton's Integral in Detailed Forward Modelling **361**
R. Tenzer, Z. Hamayun, and I. Prutkin

49 Further Improvements in the Determination of the Marine Geoid in Argentina by Employing Recent GGMs and Sea Surface Topography Models **369**
C. Tocho, G.S. Vergos, and M.G. Sideris

50 Comparison of Various Topographic-Isostatic Effects in Terms of Smoothing Gradiometric Observations **377**
J. Janák and F. Wild-Pfeiffer

51 Evaluation of Recent Global Geopotential Models in Argentina **383**
A. Pereira and M.C. Pacino

52 On the Determination of the Terrain Correction Using the Spherical Approach **389**
G. Kloch and J. Krynski

53 Smoothing Effect of the Topographical Correction on Various Types of the Gravity Anomalies **397**
Z. Hamayun, R. Tenzer, and I. Prutkin

54 Determination of a Gravimetric Geoid Model of Greece Using the Method of KTH **407**
I. Daras, H. Fan, K. Papazissi, and J.D. Fairhead

55 Method to Compute the Vertical Deflection Components **415**
E.A. Boyarsky, L.V. Afanasieva , and V.N. Koneshov

56 On Finite Element and Finite Volume Methods and Their Application in Regional Gravity Field Modeling **421**
Z. Fašková, R. Čunderlík, and K. Mikula

57 Quasi-Geoid of New Caledonia: Computation, Results and Analysis **427**
P. Valty and H. Duquenne

58 Assessment of a Numerical Method for Computing the Spherical Harmonic Coefficients of the Gravitational Potential of a Constant Density Polyhedron **437**
O. Jamet, J. Verdun, D. Tsoulis, and N. Gonindard

59 Improving Gravity Field Modelling in the German-Danish Border Region by Combining Airborne, Satellite and Terrestrial Gravity Data **445**
U. Schäfer, G. Liebsch, U. Schirmer, J. Ihde, A.V. Olesen, H. Skourup, R. Forsberg, and H. Pflug

60 An Inverse Gravimetric Problem with GOCE Data **451**
M. Reguzzoni and D. Sampietro

Part VI Global Gravity Field Modeling and EGMO8 . . . . . **457**

61 Assessment of the EGM2008 Gravity Field in Algeria Using Gravity and GPS/Levelling Data **459**
S.A. Benahmed Daho

62 On High-Resolution Global Gravity Field Modelling by Direct BEM Using DNSC08 . . . . . **467**
R. Čunderlík and K. Mikula

63 Is Australian Data Really Validating EGM2008, or Is EGM2008 Just in/Validating Australian Data? **473**
S.J. Claessens, W.E. Featherstone, and I.M. Anjasmara

64 Evaluation of EGM08 Using GPS and Leveling Heights in Greece **481**
C. Kotsakis, K. Katsambalos, D. Ampatzidis, and M. Gianniou

65 Validation of the New Earth Gravitational Model EGM08 Over the Baltic Countries **489**
A. Ellmann

66 Evaluation of EGM2008 by Comparison with Global and Local Gravity Solutions from CHAMP **497**
M. Weigelt, N. Sneeuw, and W. Keller

67 Testing EGM2008 on Leveling Data from Scandinavia, Adjacent Baltic Areas, and Greenland **505**
G. Strykowski and R. Forsberg

68 Least Squares, Galerkin and BVPs Applied to the Determination of Global Gravity Field Models 511
F. Sacerdote and F. Sansò

Part VII Temporal Gravity Changes and Geodynamics 519

69 Terrestrial Water Storage from GRACE and Satellite Altimetry in the Okavango Delta (Botswana) 521
O.B. Andersen, P.E. Krogh, P. Bauer-Gottwein, S. Leiriao, R. Smith, and P. Berry

70 Greenland Ice Sheet Mass Loss from GRACE Monthly Models . . . 527
L. Sandberg Sørensen and R. Forsberg

71 Water Level Temporal Variation Analysis at Solimões and Amazonas Rivers 533
D. Blitzkow, A.C.O.C. Matos, I.O. Campos, E.S. Fonseca, F.G.V. Almeida, and A.C.B. Barbosa

72 Spatiotemporal Analysis of the GRACE-Derived Mass Variations in North America by Means of Multi-Channel Singular Spectrum Analysis 539
E. Rangelova, W. van der Wal, M.G. Sideris, and P. Wu

73 Analysing Five Years of GRACE Equivalent Water Height Variations Using the Principal Component Analysis 547
I.M. Anjasmara and M. Kuhn

74 Observed Gravity Change at Syowa Station Induced by Antarctic Ice Sheet Mass Change 557
K. Doi, K. Shibuya, Y. Aoyama, H. Ikeda, and Y. Fukuda

75 Evaluation of GRACE and ICESat Mass Change Estimates Over Antarctica 563
B.C. Gunter, R.E.M. Riva, T. Urban, R. Harpold, B. Schutz, P. Nagel, and M. Helsen

76 Baltic Sea Mass Variations from GRACE: Comparison with In Situ and Modelled Sea Level Heights 571
J. Virtanen, J. Mäkinen, M. Bilker-Koivula, H. Virtanen, M. Nordman, A. Kangas, M. Johansson, C.K. Shum, H. Lee, L. Wang, and M. Thomas

77 Water Storage in Africa from the Optimised GRACE Monthly Models: Iterative Approach 579
E. Revtova, R. Klees, P. Ditmar, X. Liu, H.C. Winsemius, and H.H.G. Savenije

78 Estimating Sub-Monthly Global Mass Transport Signals Using GRACE, GPS and OBP Data Sets 587
M.J.F. Jansen, B.C. Gunter, R. Rietbroek, C. Dahle, J. Kusche, F. Flechtner, S.-E. Brunnabend, and J. Schröter

79 Regular Gravity Field Variations and Mass Transport in the Earth System from DEOS Models Based on GRACE Satellite Data 595
P. Ditmar, X. Liu, R. Klees, E. Revtova, B. Vermeersen, R. Riva, C. Siemes, and Q. Zhao

80 Estimating GRACE Monthly Water Storage Change Consistent with Hydrology by Assimilating Hydrological Information 603
B. Devaraju, N. Sneeuw, H. Kindt, and J. Riegger

81 Secular Geoid Rate from GRACE for Vertical Datum Modernization 611
W. van der Wal, E. Rangelova, M.G. Sideris, and P. Wu

82 Ten-Day Gravity Field Solutions Inferred from GRACE Data 619
J.M. Lemoine, S.L. Bruinsma, and R. Biancale

Part VIII Earth Observation and the Global Geodetic Observing System (GGOS) 625

83 GGP (Global Geodynamics Project): An International Network of Superconducting Gravimeters to Study Time-Variable Gravity 627
D. Crossley and J. Hinderer

84 Surface Mass Loading Estimates from GRACE and GPS 637
E.J.O. Schrama and B. Wouters

85 A Unified Approach to Modeling the Effects of Earthquakes on the Three Pillars of Geodesy 643
R.S. Gross and B.F. Chao

86 Modeling and Observation of Loading Contribution to Time-Variable GPS Sites Positions 651
P. Gegout, J.-P. Boy, J. Hinderer, and G. Ferhat

87 Investigating the Effects of Earthquakes Using HEPOS 661
M. Gianniou

88 Assessment of Degree-2 Zonal Gravitational Changes from GRACE, Earth Rotation, Climate Models, and Satellite Laser Ranging 669
J.L. Chen and C.R. Wilson

Part IX Geodetic Monitoring of Natural Hazards and a Changing Environment 677

89 PALSAR InSAR Observation and Modeling of Crustal Deformation Due to the 2007 Chuetsu-Oki Earthquake in Niigata, Japan 679
M. Furuya, Y. Takada, and Y. Aoki

90 On the Accuracy of LiDAR Derived Digital Surface Models 689
M. Al-Durgham, G. Fotopoulos, and C. Glennie

91 Multiscale Segmentation of Polarimetric SAR Data Using Pauli Analysis Images **697**
M. Dabboor, A. Braun, and V. Karathanassi

Contributors

Ch. Ackermann Institute for Astronomical and Physical Geodesy, Technische Universität München, München, Germany

L.V. Afanasieva Schmidt Institute for Physics of the Earth, Russian Academy of Sciences, Moscow 123995, Russian Federation

A. Albertella Institut für Astronomische und Physicalische Geodäsie, Technische Universität München, Munich, Germany, albertella@bv.tu-muenchen.de

B.A. Alberts Delft Institute of Earth Observation and Space Systems (DEOS), Delft University of Technology, GB Delft 2600, The Netherlands, B.A.Alberts@tudelft.nl

M. Al-Durgham Department of Civil Engineering, University of Toronto, Toronto, ON, Canada M5S 1A4, mohannad.al.durgham@utoronto.ca

F.G.V. Almeida Laboratory of Topography and Geodesy, Department of Transportation, University of São Paulo, EPUSP-PTR, São Paulo 61548, Brazil

M. Amalvict École et Observatoire des Sciences de la Terre (EOST), Strasbourg, France; Institut de Physique du Globe de Strasbourg/École et Observatoire des Sciences de la Terre (UMR 7516 CNRS-ULP), Strasbourg 67000, France, Martine.Amalvict@eost.u-strasbg.fr

D. Ampatzidis Department of Geodesy and Surveying, School of Engineering, Aristotle University of Thessaloniki, Thessaloniki 541 24, Greece, dimitrios_ampatzidis@yahoo.gr

O.B. Andersen DTU space – National Space Institute, Copenhagen DK-2100, Denmark, oa@space.dtu.dk

I.M. Anjasmara The Institute of Geoscience Research, Western Australian Centre for Geodesy, Curtin University of Technology, Perth, WA 6845, Australia; Department of Geomatics Engineering, Sepuluh Nopember Institute of Technology, Surabaya 6111, Indonesia, ira@geodesy.its.ac.id

M. Antoni Institute of Geodesy, Universität of Stuttgart, Stuttgart 70174, Germany, markus.antoni@gis.uni-stuttgart.de

Y. Aoki Earthquake Research Institute, The University of Tokyo, Tokyo 113-0032, Japan, yaoki@eri.u-tokyo.ac.jp

Y. Aoyama National Institute of Polar Research, Tachikawa-shi 190-8518, Tokyo

G. Appleby NERC Space Geodesy Facility, Herstmonceux Castle, Hailsham, East Sussex, BN27 1RN, UK, gapp@nerc.ac.uk

N. Avramiuc National Agency for Cadastre and Land Registration, Bucharest 060022, Romania, neculai.avramiuc@ancpi.ro

A.C.B. Barbosa Institute of Astronomy, Geophysics and Atmospheric Sciences, University of São Paulo, USP-IAG, São Paulo, Brazil

B. Barišić Croatian Geodetic Institute, Zagreb 10144, Croatia, bojan.barisic@cgi.hr

T. Bašić Croatian Geodetic Institute, Zagreb 10144, Croatia, tomislav.basic@cgi.hr

R. Batista CENAMEP AIP, Centro Nacional de Metrologìa de Panamà, Panamá, Repúbblica de Panamá

P. Bauer-Gottwein DTU Environment, Lyngby 2800, Denmark, pbg@er.dtu.dk

R. Bayer Dynamics of the Litosphere Laboratory CNRS/Montpellier University, Montpellier, France

M. Becker Institute of Physical Geodesy, Darmstadt University of Technology (IPGD), Darmstadt, Germany, becker@ipg.tu-darmstadt.de

S.A. Benahmed Daho Geodetic Laboratory, National Centre of Space Techniques, Arzew 31200, Algeria, d_benahmed@hotmail.com

J. Benveniste European Space Agency, Earth Observation Science, Applications and Future Technologies Dpt, Frascati (RM) I-00044, Italy, Jerome.Benveniste@esa.int

P.A.M. Berry E.A.P.R.S. Lab, Gateway House, De Montfort University, Leicester LE19BH, UK, pamb@dmu.ac.uk

G. Beutler Astronomical Institute, University of Bern, Bern CH-3012, Switzerland, gerhard.beutler@aiub.unibe.ch

R. Biancale CNES/GRGS, Toulouse Cedex 31401, France, richard.biancale@cnes.fr

M. Bilker-Koivula Finnish Geodetic Institute (FGI), Masala, Finland, mirjam.bilker@fgi.fi

D. Blitzkow Laboratory of Topography and Geodesy, Department of Transportation, University of São Paulo, EPUSP-PTR, São Paulo 61548, Brazil, dblitzko@usp.br

Q. Bodart LNE-SYRTE, UMR 8630 CNRS, Observatoire de Paris, UPMC, Paris 75014, France

G. Boedecker Bavarian Academy of Sciences and Humanity, Munich, Germany, boe@bek.badw-muenchen.de

W. Bosch Deutsches Geodätisches Forschungsinstitut (DGFI), München 80539, Germany, bosch@dgfi.badw.de

J.-P. Boy Institut de Physique du Globe de Strasbourg, Strasbourg 67084, France, JeanPaul.Boy@eost.u-strasbg.fr

E.A. Boyarsky Schmidt Institute for Physics of the Earth, Russian Academy of Sciences, Moscow 123995, Russian Federation, ernst@ifz.ru

S.M.S. Bramer EAPRS Lab, De Montfort University, Leicester LE1 9BH, UK, smsb@dmu.ac.uk

A. Braun Department of Geomatics Engineering, Schulich School of Engineering, University of Calgary, Calgary, AB, Canada T2N 1N4, braun@ucalgary.ca

J.M. Brockmann Department for Theoretical Geodesy, Institute of Geodesy and Geoinformation, University of Bonn, Bonn D-53115, Germany, brockmann@geod.uni-bonn.de

S.L. Bruinsma CNES/GRGS, Toulouse Cedex 31401, France, sean.bruinsma@cnes.fr

S.-E. Brunnabend Alfred-Wegener-Institut, Bremerhaven, Germany

P.J. Buist Delft Institute of Earth Observation and Space Systems (DEOS), Delft University of Technology, GB Delft 2600, The Netherlands, P.J.Buist@tudelft.nl

M. Calvo Space Geodesy Centre 'Giuseppe Colombo', 75100 Matera, Italy

I.O. Campos Laboratory of Topography and Geodesy, Department of Transportation, University of São Paulo, EPUSP-PTR, São Paulo 61548, Brazil

J. Casaca Laboratório Nacional de Engenharia Civil, Lisboa 1700-066, Portugal

Ben F. Chao College of Earth Sciences, National Central University, Chung-li, Taiwan, ROC, bfchao@ncu.edu.tw

J.L. Chen Center for Space Research, University of Texas, Austin, TX 78712, USA, chen@csr.utexas.edu

Q.P. Chu Control and Simulation, Faculty of Aerospace Engineering, Delft University of Technology, GB Delft 2600, The Netherlands, Q.P.Chu@lr.tudelft.nl

S.J. Claessens The Institute for Geoscience Research, Western Australian Centre for Geodesy, Curtin University of Technology, Perth, WA 6845, Australia, S.Claessens@curtin.edu.au

A. Clairon LNE-SYRTE, UMR 8630 CNRS, Observatoire de Paris, UPMC, Paris 75014, France

K.S. Cordua DTU space – National Space Institute, Copenhagen DK-2100, Denmark

D. Crossley Department of Earth and Atmospheric Sciences, Saint Louis University, St. Louis, MO 63108, USA, crossleydj@gmail.com

R. Čunderlík Department of Mathematics and Descriptive Geometry, Faculty of Civil Engineering, The Slovak University of Technology, Bratislava 813 68, Slovakia, cunderli@svf.stuba.sk

G. D'Agostino INRIM, Istituto Nazionale di Ricerca Metrologica, Torino IT-10135, Italia, g.dagostino@inrim.it

L.F. da Silva Oceanographic Laboratory, University of Itajai Valey, Itajai, Brazil

M. Dabboor Department of Geomatics Engineering, Schulich School of Engineering, University of Calgary, Calgary, AB, Canada T2N 1N4, mddabboo@ucalgary.ca

C. Dahle GeoforschungsZentrum Potsdam, Potsdam, Germany

I. Daras 54 Galatsiou Ave, Athens 11141, Greece, idaras@gmail.com

J.L.B. de Carvalho Oceanographic Laboratory, University of Itajai Valey, Itajai, Brazil

S.R.C. de Freitas Department of Geomatics, Federal University of Paraná, Centro Politécnico, Curitiba 81531-990, Brazil, sfreitas@ufpr.br

D. Delikaraoglou Department of Surveying Engineering, National Technical University of Athens, Zografos 15780, Greece, ddeli@mail.ntua.gr

T. Dell'Acqua Space Geodesy Centre 'Giuseppe Colombo', 75100 Matera, Italy

H. Denker Institut für Erdmessung, Leibniz Universität Hannover, Hannover, Germany, denker@ife.uni-hannover.de

S. Desogus National Institute of Metrological Research, Torino, Italy

B. Devaraju Institute of Geodesy, Universität Stuttgart, Stuttgart, Germany, devaraju@gis.uni-stuttgart.de

P. Ditmar Department of Earth Observations and Space Systems, Delft University of Technology, Delft, The Netherlands, P.G.Ditmar@tudelft.nl

K. Doi National Institute of Polar Research, Tachikawa-shi 190-8518, Tokyo, doi@nipr.ac.jp

R. Dorobantu Institute for Astronomical and Physical Geodesy, Technische Universität München, München, Germany

H. Duquenne IGN/LAREG, Champs sur Marne 77420, France

L.A. Echevers IGNTG, Instituto Geográfico Nacional "Tommy Guardia", Panamá, Repúbblica de Panamá

A. Ellmann Department of Civil Engineering, Tallinn University of Technology, Tallinn 19086, Estonia, artu.ellmann@ttu.ee

A. Engfeldt Lantmäteriet (The National Land Survey of Sweden)/Geodetic Research Division, 801 82 Gävle, Sweden

K. Erkan Division of Geodesy and Geospatial Science, School of Earth Sciences, The Ohio State University, Columbus, OH, 43210, USA

R. Faccia Space Geodesy Centre 'Giuseppe Colombo', 75100 Matera, Italy

J.D. Fairhead Department of Earth Sciences, GETECH-University of Leeds, Leeds LS2 9JT, UK

A.P. Falcão Departamento de Engenharia Civil e Arquitectura (DECivil), Instituto Superior Técnico, Universidade Técnica de Lisboa, Lisboa 1049-001, Portugal, afalcao@civil.ist.utl.pt

R. Falk Federal Agency of Cartography and Geodesy (BKG), Frankfurt/Main, Germany

J. Faller JILA, University of Colorado – National Institute of Standards and Technology (NIST), Boulder, CO, USA

H. Fan Department of Geodesy, School of Architecture and the Built Environment, Royal Institute of Technology (KTH), Stockholm SE-100 44, Sweden

Z. Fašková Department of Mathematics and Descriptive Geometry, Faculty of Civil Engineering, The Slovak University of Technology, Bratislava 813 68, Slovakia, faskova@math.sk

W.E. Featherstone The Institute for Geoscience Research, Western Australian Centre for Geodesy, Curtin University of Technology, Perth, WA 6845, Australia, W.Featherstone@curtin.edu.au

M. Fehlau Institute of Physical Geodesy, Technische Universität Darmstadt, Darmstadt, Germany

L. Fenoglio-Marc Institute of Physical Geodesy, Technische Universität Darmstadt, Darmstadt, Germany, fenoglio@ipg.tu-darmstadt.de

G. Ferhat Institut de Physique du Globe de Strasbourg, Strasbourg 67084, France; INSA de Strasbourg, Strasbourg 67084, France

M. Fernandez National Geographic Institute of Spain, Instituto Geográfico Nacional, 28003 MADRID, Spain

V.G. Ferreira Department of Geomatics, Federal University of Paraná, Centro Politécnico, Curitiba 81531-990, Brazil

L. Ferri Institute of Physical Geodesy, Technische Universität Darmstadt, Darmstadt, Germany

F. Flechtner Deutsches GeoForschungsZentrum (GFZ), Helmholtz Centre Potsdam, Wessling D-82234, Germany, flechtne@gfz-potsdam.de

E.S. Fonseca Laboratory of Topography and Geodesy, Department of Transportation, University of São Paulo, EPUSP-PTR, São Paulo 61548, Brazil

R. Forsberg Geodynamics Department, Danish National Space Center (DNSC), DTU, Copenhagen Oe DK-2100, Denmark, rf@space.dtu.dk

A. Fotiou Department of Geodesy and Surveying, Aristotle University of Thessaloniki, Thessaloniki 541 24, Greece

G. Fotopoulos Faculty of Applied Sciences and Engineering, Department of Civil Engineering, University of Toronto, Toronto, ON, Canada M5S 1A4, foto@civ.utoronto.ca

O. Francis Faculty of Sciences, Technology and Communication, University of Luxembourg and Centre Européen de Géodynamique et de Séismologie (ECGS), Luxembourg L-1359, Grand-Duchy of Luxembourg, olivier.francis@uni.lu

J.A. Freeman Earth and Planetary Remote Sensing Laboratory, De Monfort University, Leicester LE1 9BH, UK

B. Frommknecht Institut für Astronomische und Physikalische Geodäsie (IAPG), Technische Universität München, München 80333, Germany; ESA/ESRIN, Frascati 00044, Italy

G. Fu Earthquake Research Institute, The University of Tokyo, Tokyo 113-0032, Japan

Y. Fukuda Graduate School of Science, Kyoto University, Kyoto 606-8502, Japan, fukuda@kugi.kyoto-u.ac.jp

M. Furuya Department of Natural History Sciences, Hokkaido University, Sapporo 060-0810, Japan, furuya@mail.sci.hokudai.ac.jp

C. Gagnon Natural Resources Canada (NRCan), Ottawa, Canada

Y. Gao College of Environmental and Resources, Fuzhou University, Fuzhou, Fujian, China

P. Gegout Institut de Physique du Globe de Strasbourg, Strasbourg 67084, France, Pascal.Gegout@eost.u-strasbg.fr

I. Georgiev Central Laboratory of Geodesy, Bulgarian Academy of Science, Sofia, Bulgaria

Ch. Gerlach Department of Mathematical Sciences and Technology, Norwegian University of Environmental and Life Sciences, Norway, christian.gerlach@umb.no

A. Germak Mechanical Division, Istituto Nazionale di Ricerca Metrologica (INRiM), Torino I-10135, Italy, A.Germak@inrim.it

M. Gianniou Geodetic Department, Ktimatologio S.A. (Hellenic Cadastre), Athens 15231, Greece, mgianniu@ktimatologio.gr

G. Giorgi Delft Institute of Earth Observation and Space Systems (DEOS), Delft University of Technology, GB Delft 2600, The Netherlands

O. Gitlein Institute of Geodesy/Leibniz Universitat Hannover Institut für Erdmessung, Leibniz Universität Hannover, D-30167 Hannover, Germany

J. Gjevestad Department of Mathematical Sciences and Technology, University of Environmental and Life Sciences, N-1432 Ås, Norway

C. Glennie Terrapoint USA Inc, The Woodlands, TX 77380, USA

H. Goiginger Institute of Navigation and Satellite Geodesy, Graz University of Technology, Graz A8010, Austria, h.goiginger@tugraz.at

A. Gonçalves Departamento de Engenharia Civil e Arquitectura (DECivil), Instituto Superior Técnico, Universidade Técnica de Lisboa, Lisboa 1049-001, Portugal

N. Gonindard Ecole Nationale des Sciences Geographiques, Cedex 77455, France

I. Grgić Croatian Geodetic Institute, Zagreb 10144, Croatia

V.N. Grigoriadis Department of Geodesy and Surveying, Aristotle University of Thessaloniki, Thessaloniki 541 24, Greece

R.S. Gross Jet Propulsion Laboratory, California Institute of Technology, Pasadena, CA 91109-8099, USA, Richard.Gross@jpl.nasa.gov

B.C. Gunter Delft Institute of Earth Observation and Space Systems (DEOS), Delft University of Technology, Delft 2629HS, The Netherlands, b.c.gunter@tudelft.nl

Z. Hamayun Delft Institute of Earth Observation and Space Systems (DEOS), Delft University of Technology, Delft 2629 HS, The Netherlands

R. Harpold Center for Space Research (CSR), The University of Texas at Austin, Austin, TX 78759, USA

M. Helsen Institute for Marine and Atmospheric research Utrecht (IMAU), Utrecht University, Utrecht 3584CC, The Netherlands

I. Heyde Federal Institute for Geosciences and Natural Resources (BGR), Hannover 30655, Germany, ingo.heyde@bgr.de

J. Hinderer École et Observatoire des Sciences de la Terre (EOST), Strasbourg, 67084 France, Jacques.Hinderer@eost.u-strasbg.fr

O. Huang Division of Geodesy and Geospatial Science, School of Earth Sciences, The Ohio State University, Columbus, OH, 43210, USA

L. Huisman Delft Institute of Earth Observation and Space Systems (DEOS), Delft University of Technology, GB Delft 2600, The Netherlands

M. Idres Department of Geophysics, University of Science and Technology H.B., Algiers 16111, Algeria

J. Ihde Federal Agency for Cartography and Geodesy (BKG), Frankfurt am Main D-60598, Germany, johannes.ihde@bkg.bund.de

H. Ikeda Research Facility Center for Science and Technology Cryogenics Division, University of Tsukuba, Tsukuba 305-8577, Japan

A. Jäggi Astronomical Institute, University of Bern, Bern CH-3012, Switzerland, adrian.jaeggi@aiub.unibe.ch

T. Jakob Dynamics of the Litosphere Laboratory CNRS/Montpellier University, Montpellier, France, jacob@gm.univ-montp2.fr

O. Jamet Laboratoire de Recherche en Géodesie, Saint-Mandé 94160, France, Olivier.Jamet@ign.fr

J. Janák Department of Theoretical Geodesy, Slovak University of Technology, Bratislava 81368, Slovakia, juraj.janak@stuba.sk

M.J.F. Jansen Delft Institute of Earth Observation and Space Systems, TU Delft, The Netherlands, M.J.F.Jansen@tudelft.nl

C. Jekeli Division of Geodesy and Geospatial Science, School of Earth Sciences, The Ohio State University, Columbus, OH, 43210, USA, jekeli.1@osu.edu

Z. Jiang Bureau International des Poids et Mesures (BIPM), Sèvres, France, zjiang@bipm.org

M. Johansson Finnish Meteorological Institute, Helsinki FI-00101, Finland

D. Jones The Proudman Oceanographic Laboratory, L3 5DA Liverpool, UK

S. Kahlouche Geodetic Laboratory, Center of Space Techniques, Arzew 31200, Algeria

E. Kalish Institute for Automation and Electronics, Russian Academy of Sciences, Novosibirsk, Russian Federation

A. Kangas Finnish Meteorological Institute, Helsinki FI-00101, Finland

V. Karathanassi School of Rural and Surveying Engineering, National Technical University of Athens, Athens 15780, Greece

K. Katsambalos Department of Geodesy and Surveying, School of Engineering, Aristotle University of Thessaloniki, Thessaloniki 541 24, Greece

W. Keller Institute of Geodesy, Universität of Stuttgart, Stuttgart 70174, Germany, wolfgang.keller@gis.uni-stuttgart.de

A. Kenyeres FÖMI Satellite Geodetic Observatory, Budapest H-1592, Hungary, kenyeres@gnssnet.hu

H. Kindt Institute of Hydraulic Engineering, Universität Stuttgart, Stuttgart, Germany

N.S. Kjørsvik Terratec AS, Norway

R. Klees Department of Earth Observations and Space Systems, Delft Institute of Earth Observation and Space Systems (DEOS), Delft University of Technology, Delft 2629, The Netherlands, r.klees@tudelft.nl

G. Kloch Institute of Geodesy and Cartography, Warsaw PL 02-679, Poland, grazyna.kloch@igik.edu.pl

V.N. Koneshov Schmidt Institute for Physics of the Earth, Russian Academy of Sciences, Moscow 123995, Russian Federation, SLAVAKONESHOV@HOTMAIL.COM

J. Kostelecky Geodetic Observatory Pecny (GOP), Research Institute of Geodesy, Topography and Cartography, Ondrejov, Czech Republic

C. Kotsakis Department of Geodesy and Surveying, School of Engineering, Aristotle University of Thessaloniki, Thessaloniki 541 24, Greece, kotsaki@topo.auth.gr

P.E. Krogh DTU Space, Copenhagen 2100, Denmark, pernille@space.dtu.dk

J. Krynski Institute of Geodesy and Cartography, Warsaw PL 02-679, Poland, krynski@igik.edu.pl

M. Kuhn The Institute of Geoscience Research, Western Australian Centre for Geodesy, Curtin University of Technology, Perth, WA 6845, Australia, M.Kuhn@curtin.edu.au

J. Kusche GeoforschungsZentrum Potsdam, Potsdam, Germany, jkusche@gfz-potsdam.de

A. Landragin LNE-SYRTE, UMR 8630 CNRS, Observatoire de Paris, UPMC, Paris 75014, France

J. Le Gouët LNE-SYRTE, UMR 8630 CNRS, Observatoire de Paris, UPMC, Paris 75014, France

N. Le Moigne Dynamics of the Litosphere Laboratory CNRS/Montpellier University, Montpellier, France

Ch. Lee Center for Measurement Standards, Industrial Technology Research Institute (CMS/ITRI), Chinese Taipei, Hsinchu, Republic of China

S.B. Lee Department of Civil Engineering, Jinju National University, Jinju 660-758, Korea, sblee@jinju.ac.kr

D.H. Lee Department of Civil, Architectural and Environmental System Engineering, Sungkyunkwan University, Suwon 440-746, Korea, dhlee@geo.skku.ac.kr

H. Lee School of Earth Sciences, The Ohio State University, Columbus, OH 43210, USA

S. Leiriao DTU Environment, Lyngby 2800, Denmark, sleireio@gmail.com

J.M. Lemoine CNES/GRGS, Toulouse Cedex 31401, France, jean-michel.lemoine@cnes.fr

J. Liard Natural Resources Canada (NRCan), Ottawa, Canada

G. Liebsch Federal Agency for Cartography and Geodesy (BKG), Frankfurt am Main D-60598, Germany

M. Liker Croatian Geodetic Institute, Zagreb 10144, Croatia, mihajla.liker@cgi.hr

H. Lindenburg Delft Institute of Earth Observation and Space Systems (DEOS), Delft University of Technology, GB Delft 2600, The Netherlands

X. Liu Department of Earth Observations and Space Systems, Delft University of Technology, Delft, The Netherlands

Y. Lokshyn National Scientific Centre "Institute of Metrology", Kharkov, Ukraine

M. Lučić Croatian Geodetic Institute, Zagreb 10144, Croatia, maro.lucic@cgi.hr

B. Luck École et Observatoire des Sciences de la Terre (EOST), Strasbourg, France

J. Mäkinen Finnish Geodetic Institute (FGI), Masala, Finland, Jaakko.Makinen@fgi.fi

U. Marti Federal Office of Topography, Wabern, Switzerland, Urs.Marti@swisstopo.ch

J. Matos Departamento de Engenharia Civil e Arquitectura (DECivil), Instituto Superior Técnico, Universidade Técnica de Lisboa, Lisboa 1049-001, Portugal

A.C.O.C. Matos Laboratory of Topography and Geodesy, Department of Transportation, University of São Paulo, EPUSP-PTR, São Paulo 61548, Brazil

R. Mayrhofer Institute of Navigation and Satellite Geodesy, Graz University of Technology, Graz, Austria, reinhard.mayrhofer@tugraz.at

D. Mclaughlin Proudman Oceanographic Laboratory, Bidston, UK

S. Merlet LNE-SYRTE, Observatoire de Paris, 77 avenue Denfert Rochereau, Paris 75014, France, sebastien.merlet@obspm.fr

L. Mervart Institute of Advanced Geodesy, Czech Technical University, Prague 16629, Czech Republic

B. Meurers Institute of Meteorology and Geophysics, University of Vienna, Vienna 1090, Austria

U. Meyer Deutsches GeoForschungsZentrum (GFZ), Helmholtz Centre Potsdam, Wessling D-82234, Germany; Astronomical Institute, University of Bern, Bern 3012, Switzerland, meyeru@gfz-potsdam.de

K. Mikula Department of Mathematics and Descriptive Geometry, Faculty of Civil Engineering, The Slovak University of Technology, Bratislava 813 68, Slovakia

I. Mintourakis Department of Surveying Engineering, National Technical University of Athens, Zografos 15780, Greece, mintioan@survey.ntua.gr

S. Mizushima National Metrology Institute of Japan, National Institute for Advanced Industrial Sciences and Technology (NMIJ/AIST), Tsukuba, Japan

M. Mojzes Department of Theoretical Geodesy, Slovak University of Technology in Bratislava, Bratislava 813 68, Slovak Republic, marcel.mojzes@stuba.sk

A. Muis Control and Simulation, Faculty of Aerospace Engineering, Delft University of Technology, GB Delft 2600, The Netherlands

P. Nagel Center for Space Research (CSR), The University of Texas at Austin, Austin, TX 78759, USA

V. Nalivaev Bureau International des Poids et Mesures (BIPM), Sèvres, France

M. Nordman Finnish Geodetic Institute, Masala FI-02431, Finland

P. Novák Research Institute of Geodesy, Topography, and Cartography, Zdiby, Czech Republic; Department of Mathematics, University of West Bohemia, Pilsen, Czech Republic, pavel.novak@pecny.cz

Sh. Okubo Earthquake Research Institute, The University of Tokyo, Tokyo 113-0032, Japan

A.V. Olesen Geodynamics Department, DTU space – National Space Institute, Copenhagen DK-2100, Denmark, avo@space.dtu.dk

P. Olsson Lantmäteriet (The National Land Survey of Sweden)/Geodetic Research Division, 801 82 Gävle, Sweden

T. Olszak Institute of Geodesy and Geodetic Astronomy, Warsaw University of Technology, 00-661 Warsaw, Poland

C. Origlia National Institute of Metrological Research, Torino, Italy

A. Pachuta Institute of Geodesy and Geodetic Astronomy, Warsaw University of Technology, 00-661 Warsaw, Poland

M.C. Pacino Facultad de Ciencias Exactas, Ingeniería y Agrimensura de la Universidad Nacional de Rosario, Rosario 2000, Argentina-CONICET, mpacino@fceia.unr.edu.ar

R. Pail Institute of Navigation and Satellite Geodesy, Graz University of Technology, Graz A8010, Austria, pail@geomatics.tu-graz.ac.at

V. Palinkas Geodetic Observatory Pecny (GOP), Research Institute of Geodesy, Topography and Cartography, Ondrejov, Czech Republic, vojtech.palinkas@pecny.cz

A.S. Palmeiro Department of Geomatics, Federal University of Paraná, Centro Politécnico, Curitiba 81531-990, Brazil

K. Papazissi Department of Topography, School of Rural and Surveying Engineering, National Technical University of Athens (NTUA), Athens 15780, Greece, topoepy@central.ntua.gr

E. Peneva Faculty of Geodesy, Department of Geodesy, University of Architecture, Civil Engineering and Geodesy, Sofia, Bulgaria, penevae_fgs@uacg.bg

A. Pereira Facultad de Ciencias Exactas, Ingeniería y Agrimensura de la Universidad Nacional de Rosario, Rosario 2000, Argentina-CONICET, apereira@fceia.unr.edu.ar

F. Pereira Dos Santos LNE-SYRTE, UMR 8630 CNRS, Observatoire de Paris, UPMC, Paris 75014, France, franck.pereira@obspm.fr

L. Pertusini DIIAR, Politecnico di Milano, Polo Regionale di Como, Como 22100, Italy, lisa.pertusini@mail.polimi.it

B. Pettersen Department of Mathematical Sciences and Technology, University of Environmental and Life Sciences, N-1432 Ås, Norway

H. Pflug Department of Geodesy & Remote Sensing, GeoForschungsZentrum Potsdam (GFZ), Potsdam D-14473, Germany

Ch. Pikridas Department of Geodesy and Surveying, Aristotle University of Thessaloniki, Thessaloniki 541 24, Greece, cpik@topo.auth.gr

O. Pinzon CENAMEP AIP, Centro Nacional de Metrologìa de Panamà, Panamá, Repúbblica de Panamá

I. Prutkin Delft Institute of Earth Observation and Space Systems (DEOS), Delft University of Technology, Delft 2629, The Netherlands, I.Prutkin@tudelft.nl

E.R. Pujol Instituto Geográfico Nacional (IGN), Madrid, Spain

D. Quagliotti INRIM, Istituto Nazionale di Ricerca Metrologica, Torino IT-10135, Italia

E. Rangelova Department of Geomatics Engineering, Schulich School of Engineering, University of Calgary, Calgary, AB, Canada T2N 1N4, evrangel@ucalgary.ca

M. Reguzzoni Italian National Institute of Oceanography and Applied Geophysics (OGS), c/o Politecnico di Milano, Polo Regionale di Como, Como 22100, Italy, mirko@geomatica.como.polimi.it

M. Repanić Croatian Geodetic Institute, Zagreb 10144, Croatia, marija.repanic@cgi.hr

T. Reubelt Institute of Geodesy, Universität Stuttgart, Stuttgart D-70174, Germany, reubelt@gis.uni-stuttgart.de

R. Reudink Faculty of Aerospace Engineering, DEOS/PSG Technical University, Delft, The Netherlands

E. Revtova Department of Earth Observations and Space Systems, Delft University of Technology, Delft 2629, The Netherlands, e.Revtova@tudelft.nl

P. Richard Federal Office of Metrology (METAS), Bern-Wabern, Switzerland

J. Riegger Institute of Hydraulic Engineering, Universität Stuttgart, Stuttgart, Germany

R. Rietbroek GeoforschungsZentrum Potsdam, Potsdam, Germany, roelof@gfz-potsdam.de

R.E.M. Riva Delft Institute of Earth Observation and Space Systems (DEOS), Delft University of Technology, Delft 2629HS, The Netherlands, R.E.M.Riva@tudelft.nl

L. Robertsson Bureau International des Poids et Mesures (BIPM), Sèvres, France, LRoberts@bipm.org

P. Romero Instituto de Astronomía y Geodesia (UCM-CSIC), Facultad de Matemáticas, Universidad Complutense, Madrid E-28040, Spain, prp@mat.ucm.es

D. Rossikopoulos Department of Geodesy and Surveying, Aristotle University of Thessaloniki, Thessaloniki 541 24, Greece, rossi@topo.auth.gr

C. Rothleitner Max Planck Institute for the Science of Light, Erlangen 91058, Germany, crothleitner@optik.uni-erlangen.de

P. Rouchon Mines Paris Tech, Centre Automatique et Systèmes, Paris 75272, France

D. Ruess Federal Office of Metrology and Surveying (BEV), Vienna, Austria, diethard.ruess@bev.gv.at

R. Rummel Institut für Astronomische und Physicalische Geodäsie, Technische Universität München, Munich, Germany, rummel@bv.tum.de

T. Rus National Agency for Cadastre and Land Registration, Bucharest 060022, Romania

F. Sacerdote Dipartimento di Ingegneria Civile e Ambientale, Università di Firenze, Firenze 50139, Italy

M. Sacher Federal Agency for Geodesy and Cartography, Frankfurt, Germany

D. Sampietro DIIAR, Politecnico di Milano, Polo Regionale di Como, Como 22100, Italy, daniele.sampietro@polimi.it

L. Sandberg Sørensen Department of Geodynamics, National Space Institute, DTU-Space, Copenhagen Ø DK-2100, Denmark, slss@space.dtu.dk

F. Sansò DIIAR, Politecnico di Milano, Polo Regionale di Como, Como 22100, Italy, fernando.sanso@polimi.it

R. Savcenko Deutsches Geodätisches Forschungsinstitut (DGFI), München 80539, Germany, savcenko@dgfi.badw.de

H.H.G. Savenije Department of Water Management, Delft University of Technology, Delft, The Netherlands

U. Schäfer Federal Agency for Cartography and Geodesy (BKG), Frankfurt am Main D-60598, Germany, ufer@bkg.bund.de

U. Schirmer Federal Agency for Cartography and Geodesy (BKG), Frankfurt am Main D-60598, Germany

D. Schmerge United States Geological Survey, Longmont, CO, USA

R. Schmidt Deutsches GeoForschungsZentrum (GFZ), Helmholtz Centre Potsdam, Wessling D-82234, Germany; Astrium GmbH, München 81663, Germany, rschmidt@gfz-potsdam.de

E.J.O. Schrama Faculty of Aerospace Engineering, Astrodynamics and Satellite Systems, Delft University of Technology, HS Delft 2629, The Netherlands, e.j.o.schrama@udelft.nl

J. Schröter Alfred-Wegener-Institut, Bremerhaven, Germany

W.-D. Schuh Department for Theoretical Geodesy, Institute of Geodesy and Geoinformation, University of Bonn, Bonn D-53115, Germany, schuh@geod.uni-bonn.de

B. Schutz Center for Space Research (CSR), The University of Texas at Austin, Austin, TX 78759, USA

M.A. Sharifi Faculty of Engineering, Campus No. 2, Surveying and Geomatics Engineering Department, University of Tehran, Tehran, Iran, sharifi@ut.ac.ir

C. Shen Institute of Seismology, CSB, 430071 Wuhan, China

K. Shibuya National Institute of Polar Research, Tachikawa-shi 190-8518, Tokyo

C.K. Shum School of Earth Sciences, The Ohio State University, Columbus, OH 43210, USA, ckshum@osu.edu

M.G. Sideris Department of Geomatics Engineering, Schulich School of Engineering, University of Calgary, Calgary, AB, Canada T2N 1N4, sideris@ucalgary.ca

C. Siemes Delft Institute of Earth Observation and Space Systems (DEOS), Delft University of Technology, HS Delft 2629, The Netherlands, christian.siemes@uni-bonn.de

H. Skourup Geodynamics Department, Danish National Space Center (DNSC), DTU, Copenhagen Oe DK-2100, Denmark

V. Smith NERC Space Geodesy Facility, Herstmonceux Castle, Hailsham, BN27 1RN, UK, vism@nerc.ac.uk

R.G. Smith Earth and Planetary Remote Sensing Laboratory, De Monfort University, Leicester LE1 9BH, UK, rgs@dmu.ac.uk

N. Sneeuw Institute of Geodesy, Universität Stuttgart, Stuttgart D-70174, Germany, sneeuw@gis.uni-stuttgart.de

J. Sousa Departamento de Engenharia de Minas e Georrecursos (DEMG), Instituto Superior Técnico, Universidade Técnica de Lisboa, Lisboa 1049-001, Portugal

G. Strykowski DTU space – National Space Institute, Copenhagen DK-2100, Denmark, gs@space.dtu.dk

Y. Stus Institute for Automation and Electronics, Russian Academy of Sciences, Novosibirsk, Russian Federation

W. Sun Earthquake Research Institute, The University of Tokyo, Tokyo 113-0032, Japan, sunw@eri.u-tokyo.ac.jp

S. Svitlov Max Planck Institute for the Science of Light, Erlangen 91058, Germany, ssvitlov@optik.uni-erlangen.de

Y. Takada Department of Natural History Sciences, Hokkaido University, Sapporo 060-0810, Japan

R. Tenzer Faculty of Aerospace Engineering, Delft Institute of Earth Observation and Space Systems (DEOS), Delft University of Technology, Delft, The Netherlands, R.Tenzer@tudelft.nl

S. Thies Federal Office of Metrology (METAS), Bern-Wabern, Switzerland

M. Thomas GeoForschungsZentrum, Potsdam D-14473, Germany

C.C.J.M. Tiberius Delft Institute of Earth Observation and Space Systems (DEOS), Delft University of Technology, GB Delft 2600, The Netherlands

L. Timmen Institute of Geodesy, Institut für Erdmessung, Leibniz Universitat Hannover, D-30167 Hannover, Germany

C. Tocho Facultad de Ciencias Astronómicas y Geofísicas, La Plata, Argentina, ctocho@fcaglp.unlp.edu.ar

F. Touati Geodetic Laboratory, Center of Space Techniques, Arzew 31200, Algeria, fateh73@gmail.com

D. Tsoulis Department of Geodesy and Surveying, Aristotle University of Thessaloniki, Thessaloniki 541 24, Greece, tsoulis@topo.auth.gr

I.N. Tziavos Department of Geodesy and Surveying, Aristotle University of Thessaloniki, Thessaloniki 541 24, Greece, tziavos@topo.auth.gr

C. Ullrich Federal Office of Metrology and Surveying (BEV), Vienna, Austria

C. Ulrich Federal Office of Metrology and Surveying (BEV), Gruppe Eichwesen, 1160 Wien, Austria

T. Urban Center for Space Research (CSR), The University of Texas at Austin, Austin, TX 78759, USA

P. Vajda Geophysical Institute, Slovak Academy of Sciences, Bratislava 845 28, Slovak Republic, Peter.Vajda@savba.sk

M. Valko Department of Theoretical Geodesy, Slovak University of Technology in Bratislava, Bratislava 813 68, Slovak Republic

P. Valty IGN/LAREG, Champs sur Marne 77420, France, pierre.valty@ign.fr

M. Van Camp Royal Observatory of Belgium (ROB), Brussels, Belgium

T. van Dam Faculty of Sciences, Technology and Communication, University of Luxembourg, Luxembourg L-1359, Grand-Duchy of Luxembourg

W. van der Wal Department of Geomatics Engineering, University of Calgary, Calgary, AB, Canada T2N 1N4, wouter_van_der_wal@hotmail.com

P. Vaníček Department of Geodesy and Geomatics Engineering, University of New Brunswick, Fredericton, N.B., Canada E3B 5A3, vanicek@unb.ca

J. Verdun Laboratoire de Recherche en Géodesie, Saint-Mandé 94160, France; Ecole Nationale des Sciences Geographiques, Cedex 77455, France, Jerome.Verdun@ign.fr

G.S. Vergos Department of Geodesy and Surveying, Aristotle University of Thessaloniki, Thessaloniki 541 24, Greece, vergos@topo.auth.gr

B. Vermeersen Delft Institute of Earth Observation and Space Systems (DEOS), Delft University of Technology, HS Delft 2629, The Netherlands, b.vermeersen@lr.tudelft.nl

S. Vignudelli Consiglio Nazionale delle Ricerche, Istituto di Biofisica, CNR Pisa, Genova, Italy

J. Virtanen Finnish Geodetic Institute, Masala FI-02431, Finland, jenni.virtanen@fgi.fi

H. Virtanen Finnish Geodetic Institute, Masala FI-02431, Finland, heikki.virtanen@fgi.fi

P.N.A.M. Visser Faculty of Aerospace Engineering, Delft Institute of Earth Observation and Space Systems (DEOS), Delft University of Technology, Delft, The Netherlands, Pieter.Visser@lr.tudelft.nl

L. Vitushkin Bureau International des Poids et Mesures (BIPM), Sèvres, France, lvitushkin@bipm.org

A. Vitushkin AOSense, Inc., Sunnyvale, CA, USA

J. Walo Institute of Geodesy and Geodetic Astronomy, Warsaw University of Technology, 00-661 Warsaw, Poland

L.J. Wang Max Planck Institute for the Science of Light, Erlangen 91058, Germany, xinxing.wang@bv.tum.de

X. Wang Institut für Astronomische und Physicalische Geodäsie, Technische Universität München, Munich, Germany, xinxing.wang@bv.tum.de

L. Wang School of Earth Sciences, The Ohio State University, Columbus, OH 43210, USA

M. Weigelt Institute of Geodesy, Universität of Stuttgart, Stuttgart 70174, Germany, weigelt@gis.uni-stuttgart.de

F. Wild-Pfeiffer Institute of Navigation, University of Stuttgart, Stuttgart D-70174, Germany, franziska.wild-pfeiffer@nav.uni-stuttgart.de

M. Wilkinson NERC Space Geodesy Facility, Herstmonceux Castle, Hailsham, BN27 1RN, UK

S. Williams Proudman Oceanographic Laboratory, Liverpool, L3 5DA, UK

H. Wilmes Federal Agency of Cartography and Geodesy (BKG), Frankfurt/Main, Germany, herbert.wilmes@bkg.bund.de

C.R. Wilson Department of Geological Sciences, Jackson School of Geosciences University of Texas, Austin, TX 78712, USA, clarkw@maestro.geo.utexas.edu

H.C. Winsemius Department of Water Management, Delft University of Technology, Delft, The Netherlands, h.c.winsemius@tudelft.nl

B. Wouters Faculty of Aerospace Engineering, Astrodynamics and Satellite Systems, Delft University of Technology, HS Delft 2629, The Netherlands

P. Wu Department of Geoscience, University of Calgary, Calgary, AB, Canada T2N 1N4, ppwu@ucalgary.ca

L. Xing Institute of Seismology, CSB, 430071 Wuhan, China

X. Zhang School of Geodesy and Geomatics, Wuhan University, Wuhan, Hubei, China, xhzhang@sgg.whu.edu.cn

Q. Zhao GNSS Research and Engineering Centre, Wuhan University, Wuhan 430079, China

M. Ziebart University College London, London, WC1E 6BT, UK, marek@cege.ucl.ac.uk

Part I
Gravimetry (Terrestrial, Shipborne, Airborne) and Gravity Networks

Y. Fukuda and L. F. Vitushkin

Chapter 1

Preliminary Results of a GPS/INS Airborne Gravimetry Experiment Over the German Alps

Ch. Gerlach, R. Dorobantu, Ch. Ackermann, N.S. Kjørsvik, and G. Boedecker

Abstract Airborne gravimetry using a combination of GPS and a strapdown inertial measurement unit (IMU) is a well known method. We will present preliminary results of a flight campaign that was carried out in a Cessna 172 with a navigation grade IMU (iNAV-RQH) over a 20×20 km region in the German Alps. The experiment can be considered an extreme case with dense mapping of a very local area with rough gravity field in a very small aircraft. The recovered gravity disturbance along the trajectory is checked for internal consistency at crossover points. This indicates a precision of the solution in the range of 3 mgal for a spatial resolution for 2 km. Besides classical DGPS we also make use of absolute Precise Point Positioning (PPP), which is an useful alternative if it comes to post-processing solutions, especially for remote areas. The results indicate that the accuracy of the PPP solution is well suited for airborne gravimetry.

1.1 Introduction

Global and regional high resolution gravity field modelling is based on the combination of satellite and terrestrial observation techniques. In addition airborne methods are in use since many years to complement terrestrial methods over large and/or remote areas. Operational systems make use of a dedicated air/sea gravimeter on a stabilized platform (see, e.g., Olesen et al., 2002). The accuracy is usually in the range of 1.5–2 mgal for spatial resolutions of 5–6 km. Similar results can be achieved employing strapdown inertial navigation systems (INS), see, e.g., Wei and Schwarz (1994), Glennie (1999) or Kwon and Jekeli (2001). The basic observation equation for airborne gravimetry (here given in the inertial frame, see, e.g., Jekeli (2001)) reads

$$\boldsymbol{g}^i = \ddot{\boldsymbol{x}}^i - \boldsymbol{f}^i, \tag{1}$$

where the gravitational vector $\boldsymbol{g}$ is determined by subtracting the specific force $\boldsymbol{f}$ from kinematic accelerations $\ddot{\mathbf{x}}$. In case of a stabilized platform gravimeter the equation is restricted to the vertical component, while INS-based techniques allow to derive the full gravitational vector. The specific force is measured by the IMU, while the kinematic acceleration is derived from GPS observations.

Here the classical approach is to differentiate twice the positions determined by relativ GPS observations (in the sequel denoted by DGPS) between a stationary master and the rover receiver mounted on the aircraft. An alternative is the use of absolute GPS positioning based on precise orbit and clock information of the GPS satellites provided by the International GNSS Service(IGS, see Dow et al., 2005). This technique, also known as Precise Point Positioning (PPP), was first applied to static data by Zumberge et al. (1997) and further developed for kinematic applications (see, e.g., Kouba and Héroux, 2001 or Øvstedal, 2002). The advantage of PPP is that there is no need for a stationary master station, which is very convenient from the logistic point of view, especially for the survey of remote areas. In addition, problems arising from long baseline length in traditional DGPS can be avoided.

Ch. Gerlach (✉)
Department of Mathematical Sciences and Technology,
Norwegian University of Environmental and Life Sciences, ÅS, Norway
e-mail: christian.gerlach@umb.no

S.P. Mertikas (ed.), *Gravity, Geoid and Earth Observation*, International Association of Geodesy Symposia 135,
DOI 10.1007/978-3-642-10634-7_1, © Springer-Verlag Berlin Heidelberg 2010

It is one of the aims of the current projects to proof the applicability of PPP for airborne gravimetry. In our experiment we employed both techniques DGPS and PPP. The DGPS solution was computed using the GPS/INS navigation software KINGSPAD of the University of Calgary (Schwarz and El-Sheimy, 2000), while the software TerraPos (Kjørsvik, 2006), developed at the Norwegian company Terratec AS, was used to process the PPP solution. More details on PPP and the setup of the experiment are given in the following section.

1.2 Setup of the Airborne Experiment

1.2.1 Instrumentation

In the current experiment we made use of a navigation grade IMU of type iNAV-RQH and a 20 Hz L1/L2 Novatel GPS-receiver for positioning. The GPS antenna was mounted on the fuselage of the aircraft. The IMU was mounted almost directly below the GPS antenna inside the cockpit next to the pilot (the copilot seat was removed). The lever arm between the IMU reference point and the GPS antenna was determined by a total station.

The IMU contains three QA2000 accelerometers and three GG1320 ring laser gyroscopes arranged in two orthogonal triads. The main performance characteristics of both sensor types, as given by the manufacturer, are listed in Table 1.1. The performance of the accelerometers is well suited for gravimetric experiments aiming at a precision on the mgal level, which is the target for airborne gravimetry. In an earlier experiment with the same IMU Gerlach et al. (2005) have shown that the accuracy of the specific force vector measured with the IMU is in the range of 2 mgal (RMS of differences between the sensed magnitude of specific force and scalar gravity values determined with a Scintrex gravimeter during short static periods on ground).

Table 1.1 Performance characteristics of ring laser gyroscopes (RLG) and accelerometers (ACC) of the iNAV-RQH measurement unit

	RLG	ACC
Measurement range	$\pm 500°/s$	$\pm 2\,g$
Resolution	1.13 arcsec	$0.2\,\mu g$
Non-linearity	10 ppm	$15\,\mu g/g^2$
Scale factor error	10 ppm	70 ppm
Ang. random walk	$0.0018°/\sqrt{Hz}$	–
Acc. noise density	–	$8\,\mu g/\sqrt{Hz}$
Bias repeatability	0.002°/h	$< 15\mu g$

1.2.2 Test Area and Trajectory

The location selected for the experiment is a 20×20 km area of the German Alps close to the city of Garmisch-Partenkirchen. This area is used since several years by the Institute for Astronomical and Physical Geodesy of Technische Universität München as a gravity field test bed in a mountainous environment (for more details see Flury, 2002). The area is densely covered with terrestrial gravity values, which will be used for validation of the GPS/INS results. Since downward continuation of the GPS/INS results to ground level has not yet been performed, the current preliminary results will focus on internal precision, i.e. the fit of GPS/INS-derived gravity disturbances at crossover points. Free-air gravity anomalies in the area vary between about -60 and 90 mgal. Figure 1.1 shows the trajectory and the terrain of the area. The

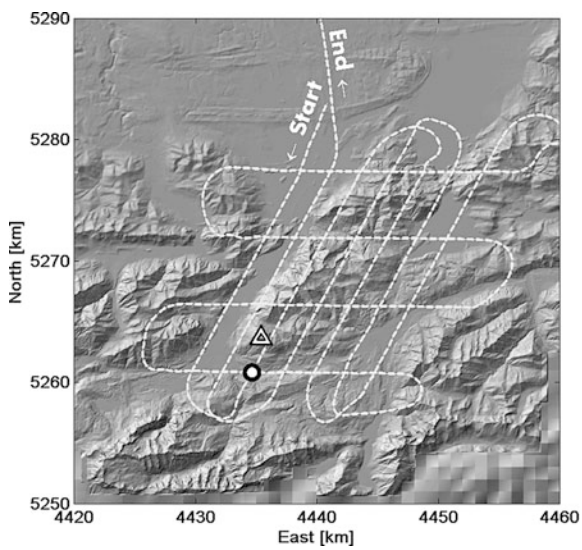


Fig. 1.1 Digital height model of the area and ground track of the flight trajectory. The *triangle* marks the SAPOS DGPS base station. The *circle* marks the crossover discussed in Sect. 1.5

heights below the trajectory vary between about 600 and 2,000 m, the flight altitude was 2,400 m. For the DGPS solution we made use of a reference station of the Satellite Positioning Service SAPOS of the German surveying authority. This station is located at an altitude of 1,846 m on mount Wank (marked with a triangle in Fig. 1.1). The maximum baseline length is around 25 km.

Compared to other airborne GPS/INS gravimetry campaigns, the current experiment is an extreme case, well suited for a detailed survey of a small area: (1) we have used a small aircraft (Cessna 172) going on low speed (about 50 m/s) in a relatively low altitude, (2) the gravity field over the mountainous area is quite rough and (3) the trajectory contains only relatively short (about 20 km) straight line sections (legs of about 6 min length).

1.2.3 Precise Point Positioning

Precise Point Positioning works very similar to the way a usual stand-alone GPS receiver determines its position. The main difference is that the broadcast ephemerides used in real-time applications are replaced by precise GPS satellite orbit and clock information. In addition special care must be taken for effects like ionospheric and tropospheric delays, phase center offsets and variations of both the satellite and the receiver antenna or satellite phase wind-up – many of which drop out in DGPS processing (especially over short baselines). While proper handling of these effects is essential to derive precise position estimates, the requirements for some of those effects is less stringent for the determination of accelerations for airborne gravimetry. This holds especially for long frequency components which have a much smaller impact on acceleration estimates as on the absolut positions themselves. A crucial point for a accurate PPP-solution is the length of the time span with continuous carrier phase observations (see Øvstedal et al., 2006). Since it is not possible to resolve the integer carrier phase ambiguities in absolute positioning (due to remaining satellite and receiver hardware biases) the outcome of the PPP processing is a float solution. Typical values for the accuracy of the vertical position in kinematic applications are 20, 5, and 4 cm for observation periods of 1, 6, and 24 h, respectively (Øvstedal et al., 2006). Observation periods of several hours can easily be achieved even for short campaigns by tracking data for some time before or after the actual survey. In the present experiment, the actual survey took only about 2 h (not counting the flight time of 15 min between airport and survey area), while data logging started nearly 3 h before take-off and continued through 45 min after landing. Therefore the overall GPS observation time sums up to about 6 h, allowing vertical position accuracies well below the decimeter.

1.3 Observational Model

GPS/INS airborne gravimetry is based on the so-called navigation equations (see, e.g., Jekeli, 2001). One can integrate them and implicitly determine the gravity disturbance as a component of the state vector in a Kalman-filter navigation solution. A more direct approach is to solve the navigation equations for the unknown gravity disturbance (as indicated by Eq. (1)). We will follow the second approach. In principle the combination of GPS and a strapdown IMU allows the derivation of all three components of the gravity vector. Given in a local level frame (referring to the ellipsoidal normal) this constitutes the scalar gravity as well as deflections of the vertical. For the preliminary results we have only focussed on the vertical component, i.e. scalar gravity. This approach is usually referred to as Strapdown Inertial Scalar Gravimetry (SISG). The computations were carried out in a local-level frame. Here the navigation equation (vertical component) solved for the gravity disturbance reads (see, e.g., Glennie, 1999)

$$\delta g = f_u - \dot{v}_u - \gamma + \left(\frac{v_e}{N+h} + 2\omega_e \cos\varphi\right) v_e + \frac{v_n^2}{M+h}, \tag{2}$$

where f_u is the vertical (up) component of the specific force vector sensed by the IMU, $\dot{v}_u$ is the derivative of the upward velocity and γ is the normal gravity. The terms in the second row of Eq. (2) constitute the vertical component of apparent forces in the local level frame and are usually referred to as Eötvös correction. They depend mainly on the horizontal velocities v_e and v_n . Furthermore ω_e is the Earth's rotational rate, φ and h are ellipsoidal latitude and height and M and N are

the radii of curvature along the meridian and the prime vertical.

1.4 Data Processing

In order to apply Eq. (2) one needs to derive (a) kinematic accelerations from GPS ($\dot{v}_u = \ddot{h}$), (b) estimates of the aircraft velocity in the local-level frame and (c) attitude information to allow the transformation of the specific force vector (originally referring to the IMU body frame) to the local level frame. The processing chain is illustrated in Fig. 1.2. In addition to the depicted steps, all GPS-derived quantities were corrected for lever-arm effects before linking them to IMU-derived quantities. The low-pass filtering and differentiation were performed using a FIR-filter (zero phase shift) and a FIR-differentiator, respectively (see, e.g., Bruton et al., 1999).

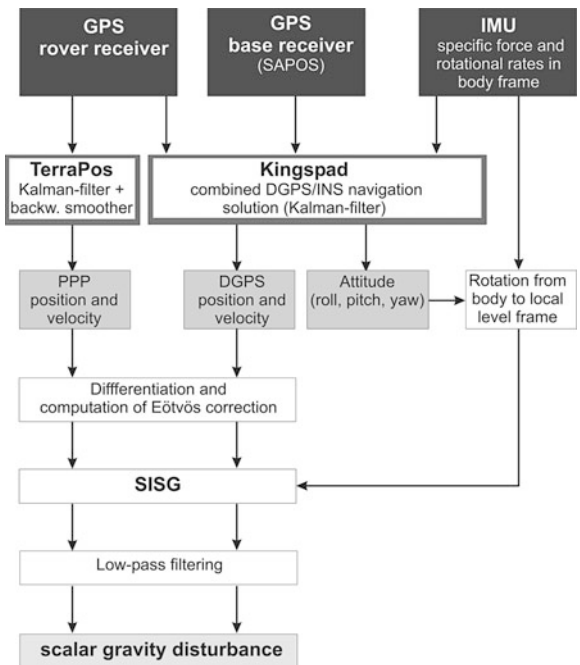


Fig. 1.2 Data processing flowchart. The two parallel chains of arrows leading from the GPS solutions via SISG down to the final gravity disturbances indicate that the same processing was applied to GPS results obtained from PPP and from DGPS

1.5 Preliminary Results

As already stated in the abstract, downward continuation of the gravity disturbances from flight altitude to ground level has not yet been performed. Therefore a final comparison with the reference values will not be presented. Instead the quality of the solution is described in terms of precision, i.e., internal consistency at crossover points of the trajectory. Figure 1.1 shows 7 legs in North–South and 4 in East–West direction. They intersect at 31 crossover points (including turns). Due to edge-effects the first leg had to be excluded from the solution, so there are 26 crossovers left to be analyzed. Figure 1.3 shows the gravity disturbance (SISG-results) along the trajectory which nicely follows the terrain. This can be expected because the terrain gives the strongest contribution to local signal variations. Figure 1.4 shows power spectral densities (PSD) of the same SISG-results. Even though the signal in flight altitude is somewhat smoother than on ground, the PSDs are compared to terrestrial gravity interpolated along the ground track. As can be expected, the SISG-results tend to have less power (since they are smoother) but in general the two curves show comparable signal characteristics in the range up to about $1.4 \cdot 10^{-4}$ Hz (corresponds to 70 s). For higher frequencies the signal power of the SISG-result rises considerably above the expected gravity signal, indicating high frequent noise. Therefore the results shown in Fig. 1.3 are low-pass filtered with filter length of 80 s. Considering the average speed of 50 m/s this corresponds to a spatial resolution (half wavelength) of 2 km.

As an indication of precision, gravity disturbances at crossovers are analyzed after low-pass filtering. The RMS of the misfit at all 26 crossovers is 5.1 mgal, with two extreme values of 15 and 13 mgal. In order to use this number as a measure of precision it must be considered, that full match of the values will never show up – except for very smooth gravity fields. This is due to the filtering along the trajectory which results in a non-isotropic signal. At the crossovers two such signals are compared, with one being filtered in East–West and one in North–South direction. Since the gravity field is quite rough in our case, the filtered values cannot match perfectly. This is illustrated in Figure 1.3. The dashed line connects the two epochs

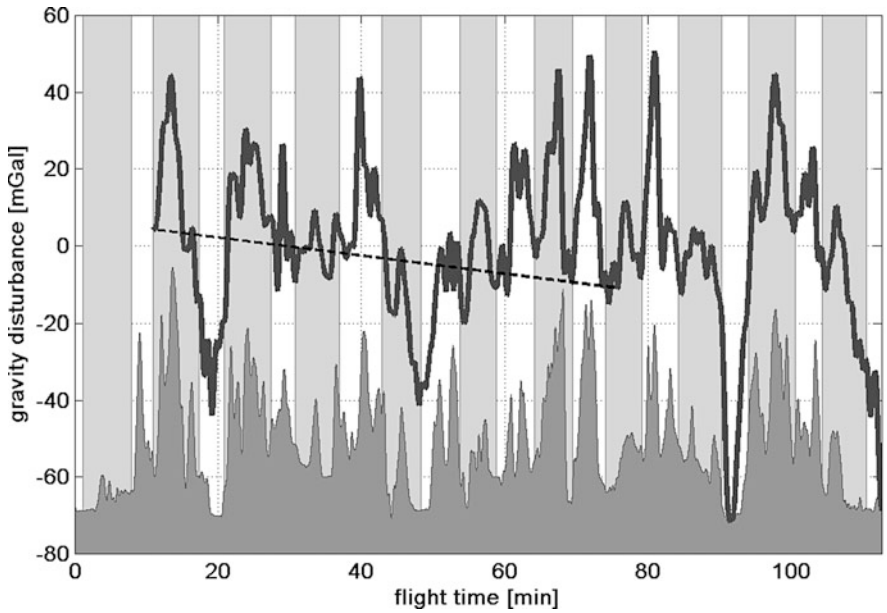


Fig. 1.3 Gravity disturbance from SISG at flight altitude and terrain heights along the ground track. The *dashed line* connects the two epochs of a crossover point with extrem misfit of 15 mgal. The periods marked in *light gray* indicate individual legs of the trajectory. Turns of the aircraft are in the *white spaces* between successive legs

corresponding to the crossover with extreme misfit. The same crossover is marked with a circle in Fig. 1.1. Obviously the West–East leg is almost parallel to a valley. Therefore the signal filtered *along* the valley represents the value at the crossover quite well. In contrast the signal filtered *across* the valley is affected by the mountains on both sides of the valley and is therefore a less good representation of the value at the crossover. The RMS misfit of 5.1 mgal must therefore be considered as a pessimistic measure for precision. A much better result can of course be expected from a regularized field, i.e., after reducing the SISG-results for topographic effects. This will be done in the future as a preprocessing step for downward-continuation. In order to derive a more realistic measure of precision without much computational effort, we have excluded the two crossovers with the largest misfit from the analysis. The RMS misfit at the remaining crossovers is

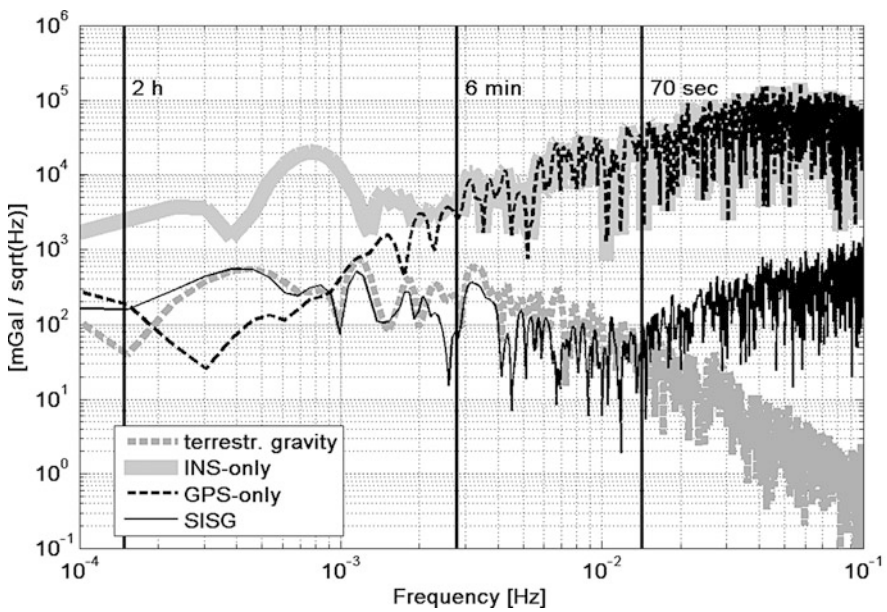


Fig. 1.4 Square root of power spectral densities (PSD): airborne gravimetry results (SIGS), terrestrial reference gravity along the ground track as well as vertical accelerations from GPS and INS

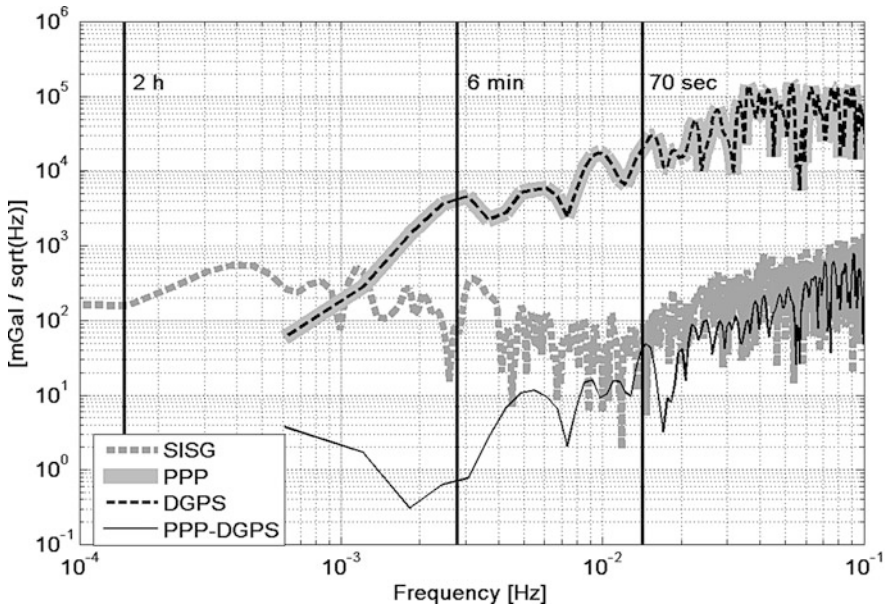


Fig. 1.5 Square root of power spectral densities (PSD): airborne gravimetry results (SISG), vertical kinematic accelerations from PPP and DGPS as well as the difference between both

3.3 mgal, which will be used as a measure for precision of the preliminary results.

Considering Fig. 1.4, it is also interesting to note, that a drift of the SISG-results, which would lead to increased signal power in the low frequencies, is not obvious. This indicates long-term stability of sensors and IMU performance. The obvious increase in signal strength of the specific force measurements (IMU-only) in the frequency band between about 4×10^{-4} and 1.3×10^{-3} Hz can be attributed to the apparent forces sensed by the IMU in the local-level frame (Eötvös correction).

The results shown in Figs. 1.3 and 1.4 are based on vertical accelerations from PPP. Figure 1.5 shows PSDs of vertical accelerations derived from PPP and DGPS and the respective difference. Even though the IMU-results are stable over long periods, the most interesting part of the spectrum is between 70 and 80 s (higher signal constituents are filter out) and 6 min, which is the average duration of the individual legs. Integrating over this frequency band one finds the differences between DGPS and PPP to have a standard deviation of 1.5 mgal, which is at the level of accuracy to be achieved by airborne gravimetry. The signal power does not rise if lower frequencies are included. This indicates, that PPP is also suited for applications in airborne gravimetry and can serve as a logistically conveniant alternative to classical DGPS. Strictly, one can draw this conclusion only for flights of similar type (geographic extension, altitude). But since high-quality PPP seems not to be affected by the length of the flight line, but rather by the requirement of at least about 6 h of continuous data, one can assume, that PPP is a viable alternative for DGPS also for geographically more extended surveys. A more detailed analysis of the results will be carried out as soon as the downward continued results are available for rigorous validation.

1.6 Summary and Outlook

The results achieved so far indicate, that (1) the precision of gravity disturbances derived in our experiment is at the level of about 3 mgal at a spatial resolution of 2 km and (2) PPP can be used as an alternative to traditional DGPS for airborne gravimetry. This can be of advantage for surveys of remote areas without reference stations. It must be considered, that the setup of the experiment is an extreme case because we use a small aircraft, the gravity field is very rough and the flight dynamics are relatively high (straight line segments of the trajectory are not longer than 20 km or 6 min). In a next step it will be necessary to regularize the field and to perform a downward continuation to the ground for rigorous validation against terrestrial gravity. This will also allow a more detailed analysis/validation of the differences between PPP and DGPS.

Acknowledgements Precise ephemerides and SAPOS data were provided by IGS and Bayerisches Landesamt für Vermessung und Geoinformation, respectively. Both are gratefully acknowledged. We are very grateful to our pilot Mr. Max Walch for the very pleasant and constructive cooperation and a perfect flight. The research was conducted under support from the Småforsk program of the Norwegian Government.

References

Bruton, A.M., C.L. Glennie, and K.P. Schwarz (1999). Differentiation for high-precision GPS velocity and acceleration determination. *GPS Solut.*, 2(4), 7–21.

Dow, J.M., R.E. Neilan, and G. Gendt (2005). The international GPS service (IGS): Celebrating the 10th anniversary and looking to the next decade. *Adv. Space Res.*, 36(3), 320–326, doi:10.1016/j.asr.2005.05.125.

Flury, J. (2002). Schwerefeldfunktionale im gebirge. DGK Reihe C, 557, Verlag der Bayerischen Akademie der Wissenschaften, München, Germany.

Gerlach, Ch., R. Dorobantu, and M. Rothacher (2005). Results of a combined INS/GPS experiment for geodetic application. *Navigation (Paris)*, 53(212), 31–47.

Glennie, C.L. (1999). An analysis of airborne gravity by strapdown INS/GPS. Report No. 20125 of the Department of Geomatics Engineering, University of Calgary, Canada.

Jekeli, Ch. (2001). Inertial navigation systems with geodetic applications. de Gruyter, Berlin/New York.

Kjørsvik, N.S. (2006). TerraPos – Users manual. Terratec AS, Norway.

Kouba, J. and P. Héroux (2001). Precise point positioning using IGS orbit and clock products. *GPS Solut.*, 5(2), 12–28.

Kwon, J.H. and Ch. Jekeli (2001). A new approach for airborne vector gravimetry using GPS/INS. *J.Geodesy*, 74, 690–700.

Olesen, A.V., R. Forsberg, K. Keller, and A.H.W. Kearsley (2002). Error sources in airborne gravimetry employing a spring-type gravimeter. In:Ádám, J. and K.P. Schwarz (eds), Vistas for Geodesy in the new millenium. IAG Symposia, Vol. 125, Springer.

Schwarz, K.P. and N. El-Sheimy (2000). KINGSPAD user manual, Version 3.0. Department of Geomatics Engineering, University of Calgary, Canada.

Wei, M. and K.P. Schwarz (1994). An error analysis of airborne vector gravimetry. In: Proc. Int. Symposium on kinematic systems in geodesy, geomatics and navigation (KIS94). Banff, Canada.

Zumberge, J., M. Heflin, D. Jefferson, M. Watkins, and F. Webb (1997). Precise point positioning for the efficient and robust analysis of GPS data from large networks. *J. Geophys. Res.*, 102(B3), 5005–5017.

Øvstedal, O. (2002). Absolute positioning with single frequency GPS Receivers. *GPS Solut.*, 5(4), 33–44.

Øvstedal, O., J.G.O. Gjevestad, and N.S. Kjørsvik (2006). Surveying using GPS precise point positioning. Paper presented at the XXIII. FIG Congress, Munich, Germany, October 8–13, 2006.

Chapter 2

Co-seismic Gravity Changes Computed for a Spherical Earth Model Applicable to GRACE Data

W. Sun, G. Fu, and Sh. Okubo

Abstract Dislocation theories were developed conventionally for a deformed earth surface because most traditional gravity measurements are performed on the terrain surface. However, through development of space geodetic techniques such as the satellite gravity missions, co-seismic gravity changes can be detected from space. In this case, the conventional dislocation theory cannot be applied directly to the observed data because the data do not include surface crustal deformation (the free air gravity change). Correspondingly, the contribution by the vertical displacement part must be removed from the traditional theory. This study presents the corresponding expressions applicable to space observations. In addition, a smoothing technique is necessary to damp the high-frequency contribution so that the theory can be applied reasonably. As examples, the Sumatra earthquakes (2004, 2007) are considered and discussed.

2.1 Introduction

Numerous studies have been undertaken by many scientists to study co-seismic deformation in a half-space Earth model, a spherical earth model, and even a 3D earth model. For a half-space earth model, Steketee (1958), Maruyama (1964), and Okada (1985), etc. presented analytical expressions for calculating the surface displacement, tilt, and strain resulting from various dislocations. Especially, Okada (1985) summarized previous studies and presented a complete set of analytical formulae for calculating these geodetic deformations. Okubo (1992) proposed closed-form expressions to describe potential and gravity changes resulting from dislocations. Because of their mathematical simplicity, these dislocation theories (e.g., Okada, 1985; Okubo, 1992) have been applied widely to study or invert seismic faults. However, the validity of these theories is strictly limited to a near field because Earth's curvature and radial heterogeneity are ignored. Modern geodesy can detect and observe far-field crustal deformation. Consequently, even a global so-seismic deformation, a dislocation theory for a more realistic Earth model, is demanded to interpret far-field deformation.

Efforts to develop formations for such a spherical Earth model have been advanced through numerous studies (e.g., Ben-Menahem and Singh, 1968; Smylie and Mansinha, 1971). Such studies have revealed that Earth's curvature effects are negligible for shallow events, although vertical layering might impart considerable effects on deformation fields. However, Sun and Okubo's (2002) study comparing discrepancies between a half-space and a homogeneous sphere and between a homogeneous sphere and a stratified sphere indicates that both curvature and vertical layering strongly affect co-seismic deformation.

Stratified spherical model such as the PREM model (Dziewonski and Anderson, 1981) is the most realistic: it reflects both sphericity and Earth's stratified structure. For such an Earth model, Pollitz (1992) solved the problem of regional displacement and strain fields induced by dislocation in a

W. Sun (✉)
Earthquake Research Institute, The University of Tokyo, Tokyo 113-0032, Japan
e-mail: sunw@eri.u-tokyo.ac.jp

S.P. Mertikas (ed.), *Gravity, Geoid and Earth Observation*, International Association of Geodesy Symposia 135,
DOI 10.1007/978-3-642-10634-7_2, © Springer-Verlag Berlin Heidelberg 2010

viscoelastic, non-gravitational model. Sun and Okubo (1993) presented methods to calculate co-seismic gravity changes in spherically symmetric Earth models. Piersanti et al. (1995) and Sabadini et al. (1995) studied displacement and its rates induced by dislocation in viscoelastic stratified Earth models, accounting for sphericity and self-gravitation using a self-consistent approach. Tanaka et al. (2006) computed co-seismic gravity changes for a visco-elastic earth model using an integrating technique to avoid intrinsic numerical difficulties. Fu and Sun (2008) presented a new theory for computing co-seismic gravity changes in a three-dimensional inhomogeneous earth model. In addition, Rundle (1982) studied deformations by a rectangular thrust fault in a gravitating model consisting of an elastic layer over a viscoelastic half-space.

All of the theories explained above were developed for a deformed earth surface because most traditional gravity measurements are performed on the earth surface. However, advances in modern geodetic techniques, such as GPS, InSAR, altimetry, and GRACE enable better detection of co-seismic deformations such as displacement, gravity change, and strain. For example, the co-seismic gravity change caused by the 2004 Sumatra earthquake was detected by GRACE (Gross and Chao, 2001; Sun and Okubo, 2004; Han et al., 2006). Han et al. (2006) calculated the gravity changes caused by the earthquake, and interpreted the gravity changes using a very simple method based on a half-space earth model. In this case, a more reasonable dislocation theory must be used instead. However, the conventional dislocation theory cannot be applied directly to the observed data because the theory includes contributions from the surface crustal deformation, although the GRACE data do not include it. Correspondingly, the contribution by the vertical displacement part must be removed from the traditional theory. For this purpose, in this study, we present the formulas applicable to the space observation. In addition, a smoothing technique, e.g., a Gaussian filter, is necessary to damp the high-frequency contribution, so that the theory can be applied reasonably. As an example, the 2004 Sumatra earthquake is considered and investigated. More case studies are made to observe whether or not the co-seismic gravity changes for a smaller earthquake (e.g., M8.0) are detectable from space.

2.2 Dislocation Theory Applicable in Satellite Data

If a dislocation is considered in a spherical Earth model (Fig. 2.1), such as a homogeneous sphere or a spherically symmetric, non-rotating, perfectly elastic and isotropic Earth (SNREI), the excited vertical displacement is represented as $u_r(a,\theta,\varphi)$ (radius, co-latitude and longitude) (Sun and Okubo, 1993). The co-seismic gravity change $\delta g(a,\theta,\varphi)$ on the deformed earth surface ($r = a + u$) is expressed as

$$\delta g(a,\theta,\varphi) = \Delta g(a,\theta,\varphi) - \beta u_r(a,\theta,\varphi) \qquad (1)$$

where the first term $\Delta g(a,\theta,\varphi)$ of the right-hand-side of (1) is the gravity change at a fixed-space point ($r = a$) and β is the free-air gravity gradient, which can be expressed as (Sun and Okubo, 1993) $\beta = 2\,g(a)/a$, where $g(a)$ is the mean gravity on the earth surface. The last term $-\beta u_r(a,\theta,\varphi)$ gives the free-air correction caused by the vertical displacement on the earth surface. This free-air correction is considered to convert the gravity change from the fixed-space point to the deformed earth surface. This correction is necessary if a theoretical co-seismic gravity change is computed to compare with the observed gravity change on the deformed earth surface. However, if one wants to study the co-seismic gravity change observed in space, such

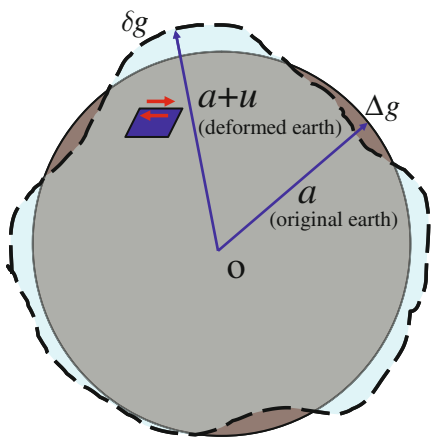


Fig. 2.1 Illustration of an original (un-deformed $r = a$) and a deformed ($r = a + u$) earth, and corresponding gravity changes

as by GRACE, Eq. (1) is not applicable, and the free-air correction term must be eliminated because the satellite gravity mission does not "see" this part.

We need only consider the first term on the right-hand-side in (1) to interpret the gravity change observed from space. This term $\Delta g(a,\theta,\varphi)$ is actually the gravity change at a fixed-space point on the undeformed earth (see level) surface $r = a$. The gravity change $\Delta g(a,\theta,\varphi)$ can be decomposed into two terms (Sun and Okubo, 1993) as

$$\Delta g(a,\theta,\varphi) = -\left.\frac{\partial \psi(r,\theta,\varphi)}{\partial r}\right|_{r=a} + 4\pi G\rho u_r(a,\theta,\varphi), \tag{2}$$

where $\psi(r,\theta,\varphi)$ is the co-seismic potential change caused by the mass redistribution of the whole earth, G is Newton's gravitational constant, and ρ is the density. The last term $4\pi G\rho u_r(a,\theta,\varphi)$ is the Bouguer gravity correction attributable to the deformation of the earth surface, i.e., the vertical displacement. It implies that the surface deformation is considered in $\Delta g(a,\theta,\varphi)$, but the free-air correction is eliminated. On the other hand, the first term on the right-hand-side in (2) also contains a Bouguer layer term, but it is opposite in sign.

$$-\left.\frac{\partial \psi}{\partial r}\right|_{r=a} = \frac{g}{a^3}\sum_{n,m}^{\infty}(n+1)\,k_{nm}^{ij}Y_n^m(\theta,\varphi) \cdot v_i n_j U dS - 4\pi G\rho u_r(a,\theta,\varphi) \tag{3}$$

As a result, the Bouguer terms related with the vertical displacement $u_r(a,\theta,\varphi)$ cancel each other. Finally, the gravity change $\Delta g(a,\theta,\varphi)$ is obtainable as

$$\Delta g(a,\theta,\varphi) = \frac{g}{a^3}\sum_{n,m}^{\infty}(n+1)\,k_{nm}^{ij}Y_n^m(\theta,\varphi) \cdot v_i n_j U dS, \tag{4}$$

where U denotes the dislocation slip, v_i, n_j respectively indicate the slip and normal components, and Y_n^m is the spherical function. The variable k_{nm}^{ij} is the dislocation Love number of the potential change. Its numerical computation can be made similarly to that in Sun and Okubo (1993).

2.3 Co-seismic Gravity Changes on the Deformed Earth Surface

The gravity changes on the deformed earth surface (1) and at a space-fixed point (4) are used respectively for surface and space measured gravity. They are different in distribution and opposite in sign. We consider the 2004 Sumatra earthquake to demonstrate the difference between the two gravity changes (Banerjee et al., 2005; Ammon et al., 2005). The seismic slip model (Fig. 2.2a) used in this study includes two seismic events: the Sumatra earthquake, which occurred on December 26, 2004; and the Nias earthquake, which occurred on March 28, 2005. Digital data are provided by Chen Ji and by Han et al. (2006).

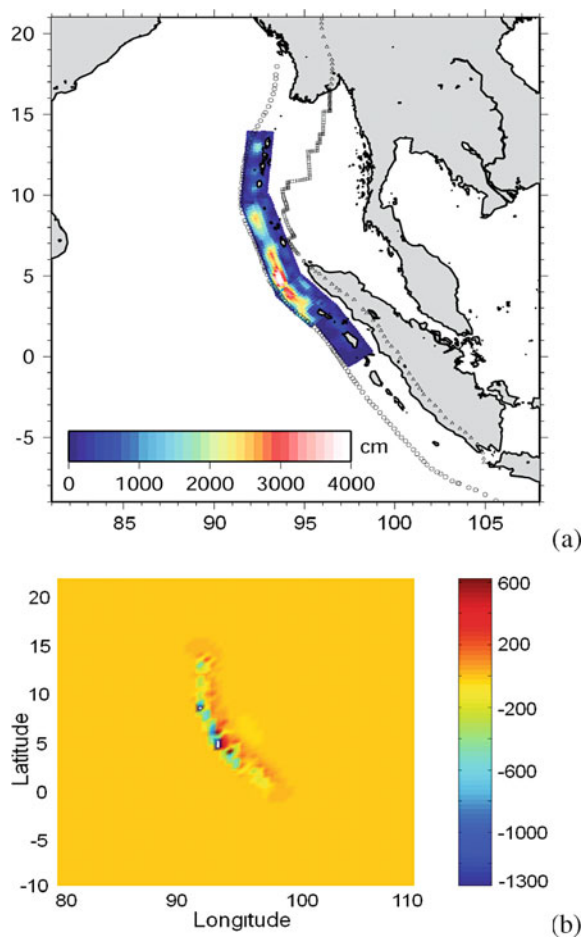


Fig. 2.2 (**a**) Fault slip distribution of the 2004 Sumatra earthquake, which includes seven fault planes (after Han et al., 2006). (**b**) Computed co-seismic gravity change (unit: μGal) on a deformed earth surface caused by the earthquake

Using the seismic fault model described above in Fig. 2.2a and Eq. (1), we calculate the co-seismic gravity changes $\delta g(a,\theta,\varphi)$ on the deformed earth surface and plot them in Fig. 2.2b. Results show that the co-seismic gravity changes vary from –1,250 μGal to +600 μGal. Generally, the gravity changes appear positive in the land side (northeast direction), and negative in the ocean side (the South-West direction) near the fault area. The distribution pattern appears positive and negative values mixed together and the positive-negative boundary is not clear. This phenomenon is attributable to the sparse computing points. The cell size of the computing points is about 50 × 50 km, i.e., the gravity change is calculated for 3,840 points in all in the plotted area shown in Fig. 2.2b. Actually, for a simple seismic slip model, e.g., one with few pieces of sub-tangential faults, these computing points are sufficiently dense to reflect the distribution of the gravity changes. However, because the Sumatra earthquake is a large event and the seismic slip distribution is complicated (Fig. 2.2a), the computing cell size of 50 × 50 km seems too large to visualize the phenomenon. This phenomenon is true not only for spherical dislocation theory but also for applying the half-space dislocation theory, such as Okubo (1992). In the following, we will make a computation for a smaller geometrical cell size to show the difference in distribution pattern. The rough results presented here were produced for two reasons: one is to illustrate that computation for large cells saves much computing time; the other is to clarify the following comparison.

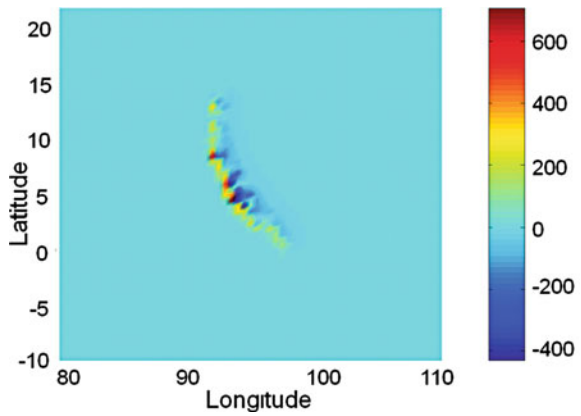


Fig. 2.3 Calculated co-seismic gravity changes (unit: μGal) at space-fixed point for the spherical earth model

2.4 Co-seismic Gravity Changes at Space-Fixed Point

We next compute the co-seismic gravity changes $\Delta g(a,\theta,\varphi)$ at the space-fixed point $r = a$ in the same computing scheme as $\delta g(a,\theta,\varphi)$, but using Eq. (4). Results of $\Delta g(a,\theta,\varphi)$ are depicted in Fig. 2.3. Comparing $\Delta g(a,\theta,\varphi)$ (Fig. 2.3) and $\delta g(a,\theta,\varphi)$ (Fig. 2.2b) reveals a great difference in amplitude and sign. The co-seismic gravity changes $\Delta g(a,\theta,\varphi)$ vary from –410 μGal to +640 μGal; they appear negative on the land side, and positive in ocean side. For comparison, we also calculate the gravity changes using the half-space dislocation theory (Okubo, 1992) with elimination of the free-air correction. Comparison of the results shows that, in the near field, the gravity changes calculated using spherical and half-space theories are fundamentally identical, but with some differences in detail and in the far field.

The satellite (GRACE) is known to observe only the low-frequency gravity change because of the attenuation of the signals; the accuracy of the high-frequency signals is low. In practical applications of satellite data, a filter is usually used for damping the error in the high-frequency part. For example, Han et al. (2006) adopted the Gaussian filter with smoothing radius of 300 km, which corresponds to the spherical harmonic degree of 60. The same filter is expected to be used in the theoretical computation to compare the observed gravity changes with theoretically predicted ones. In this case, the geometrical cell size of 50 × 50 km, as used above, is expected to be sufficiently small because the high-frequency contribution (less than 300 km) is expected to be filtered out. However, our investigation below shows that the geometrical cell size of 50 × 50 km is insufficient. We consider the more detailed geometrical cell size of 1 × 1 km to observe the effect of geometrical cell size on computing co-seismic gravity changes. The computed co-seismic gravity changes are depicted in Fig. 2.4. Comparison of the results in Figs. 2.3a and 2.4 shows that the gravity varies smoothly and the positive-negative boundary becomes clear and reasonable if the computing cells are sufficiently small. Results also show that the maximum amplitude of the gravity changes for small cells (1 × 1 km) size become larger than those of big cells (50 × 50 km).

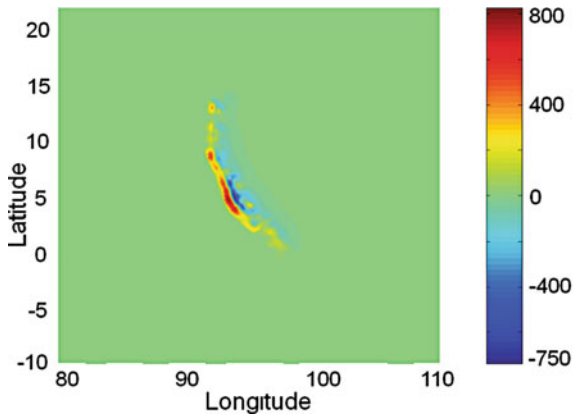


Fig. 2.4 The same as Fig. 2.3, but with small computing cell size of 1 × 1 km

2.5 Co-seismic Gravity Changes by Damping High-Frequency Part

As described above, to apply the theoretical prediction to satellite observed data, a filter must be used in computations. The smoothed gravity changes include only the low frequency part and become smaller in amplitude, as presented in Fig. 2.5, when the isotropic Gaussian filter ($R = 300$ km) is applied to the results shown above in Figs. 2.3a and 2.4. Figure 2.5a, b represent co-seismic gravity changes for a space-fixed point, but with cell size of 50 × 50 km and 1 × 1 km, respectively. They show different distribution patterns and amplitudes. The discrepancy is attributable entirely to the different computing cell sizes. The latter (Fig. 2.5b) looks reasonable and close to the GRACE observed one (Han et al., 2006). It implies that the computing cell size is sufficiently small to obtain reasonable results.

2.6 Are Co-seismic Gravity Changes Detectable for a M8.4 Earthquake?

As indicated by Han et al. (2006), GRACE can detect co-seismic gravity changes for a huge earthquake such as the 2004 Sumatra earthquake (M9.3). The magnitude of the gravity change is about ±15 μgal after the Gaussian filter (R=300 km) is used (Fig. 2.5b). In this section, we investigate co-seismic gravity changes caused by a smaller earthquake to see whether they are

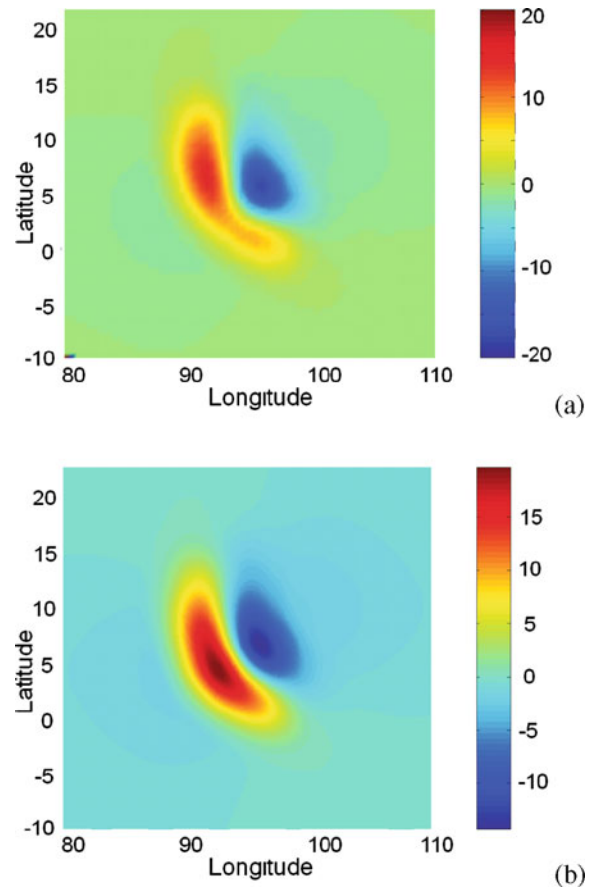


Fig. 2.5 Theoretical co-seismic gravity changes (unit: μGal) calculated for space-fixed point (Gaussian filter with R = 300 km): (**a**) for cell size of 50 × 50 km; (**b**) for cell size of 1 × 1 km

detectable by GRACE. For this purpose, we consider the 2007 Southern Sumatra earthquake. That earthquake includes several large shocks that occurred on September 12, 2007. Here we respectively consider the largest shock that occurred, with seismic magnitude of M8.4. The fault slip distribution is depicted in Fig. 2.6 (Chen, 2007). Then the co-seismic gravity changes caused by the earthquake are calculated. The results before the filter is used, as portrayed in Fig. 2.7a, show that the gravity changes were about –80 to +120 μGal. Finally, we apply the Gaussian filter with smoothing radius of R=300 km to the gravity changes in Fig. 2.7 and thereby obtain the smoothed gravity changes (Fig. 2.7b). The results show that the smoothed gravity changes become smooth but that the amplitude is smaller than that without a filter. However, the gravity changes still reach about –1.5 to

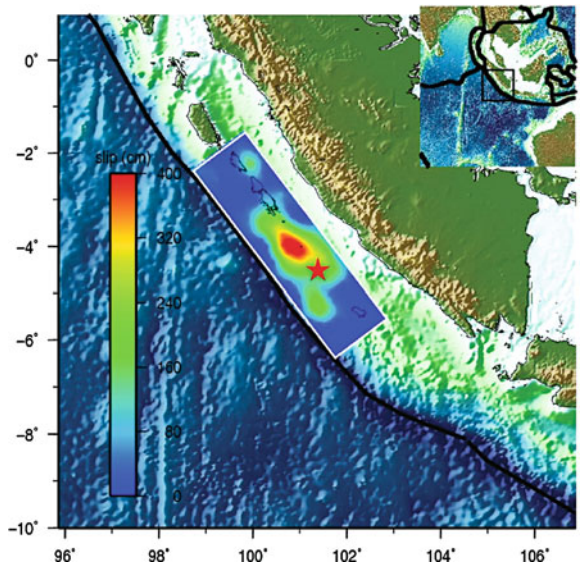


Fig. 2.6 Slip distribution on fault of the Southern Sumatra earthquake (2007, M8.4) (after Chen, 2007)

+2.5 μGal. According to the detection capability of GRACE (Sun and Okubo, 2004), the gravity changes are detectable. This conclusion is to be confirmed using actual GRACE data.

2.7 Summary

This study presented expressions of co-seismic gravity changes for a spherical earth model, applicable to satellite observed data. The difference between the co-seismic gravity changes for deformed earth surface and space-fixed point are compared and discussed. Results show that the two kinds of gravity changes are entirely different in both magnitude and sign. The effect of geometrical cell size on computation accuracy is investigated. Results show that to guarantee an accurate result of co-seismic gravity change, a small geometrical computing cell size is necessary. The co-seismic gravity change calculated by the present theory seems reasonable and coincides with the observed one. The gravity change for a smaller earthquake (M.8.4) is also investigated; the results show that they are detectable by GRACE.

Acknowledgements This research was supported financially by a JSPS Grant-in-Aid for Scientific Research (C16540377). The authors thank Dr. C. K. Shum and Mr. L. Wang very much for sharing their computing code of the Gaussian filter.

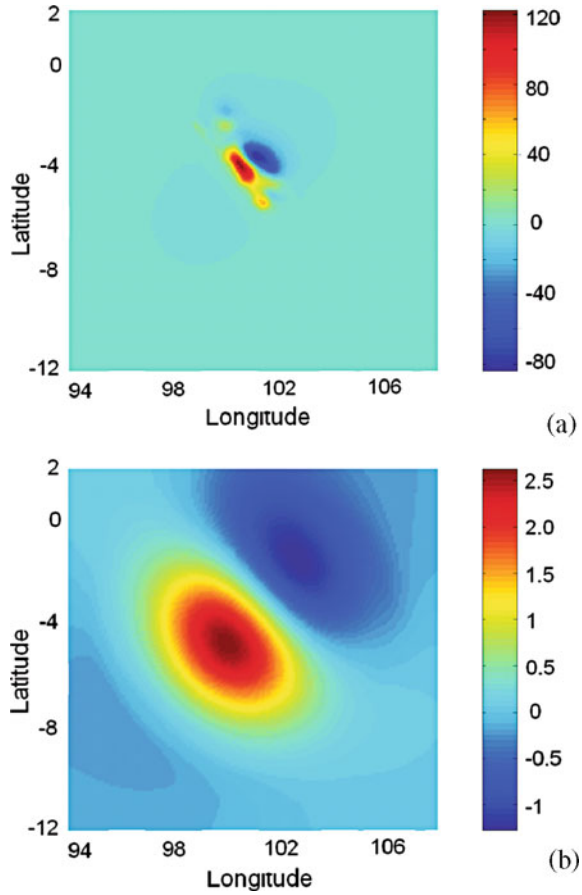


Fig. 2.7 Co-seismic gravity changes caused by the 2007 Sumatra earthquake (M8.4). (**a**) without filter; (**b**) with filter R=300 km (unit: μGal)

References

Ammon, C.J., J. Chen, and H. Thio, et al. (2005). Rupture process of the 2004 Sumatra-Andaman earthquake, *Science*, 308, 1133–1139.

Banerjee, P., F.F. Pollitz, and Burgmann (2005). The size and duration of the Sumatra-Andaman earthquake from far-field static offsets, *Science*, 308, 1769–1772.

Ben-Menahem, A. and S.J. Singh (1968). Eigenvector expansions of Green's dyads with applications to geophysical theory, *Geophys. J. R. Astron. Soc.*, 16, 417–452.

Chen, J. (2007). Preliminary result of the September 12, 2007 Sumatra earthquake, http://earthquake.usgs.gov/eqcenter/eqinthenews/

Dziewonski, A.M. and D.L. Anderson (1981). Preliminary reference earth model, *Phys. Earth Planet. Inter.*, 25, 297–356.

Fu, G. and W. Sun (2008). Surface co-seismic gravity changes caused by dislocations in a 3-D heterogeneous earth, *Geophys. J. Int.*, 172(2), 479–503.

Gross, R.S. and B.F. Chao (2001). The gravitational signature of earthquakes, in Gravity, Geoid, and Geodynamics 2000, 205–210, IAG Symposia 123, Springer-Verlag, New York.

Han, S.-C., C.K. Shum, M. Bevis, C. Ji, and C-Y. Kuo (2006). Crustal dilatation observed by GRACE after the 2004 Sumatra-Andaman earthquake, *Science*, 313, 658–662.

Maruyama, T. (1964). Static elastic dislocations in an infinite and semi-infinite medium, *Bull. Earthquake Res. Inst. Univ. Tokyo*, 42, 289–368.

Okada, Y. (1985). Surface deformation due to shear and tensile faults in a half-space, *Bull. Seism. Soc. Am.*, 75, 1135–1154.

Okubo, S. (1992). Potential gravity changes due to shear and tensile faults, *J. Geophys. Res.*, 97, 7137–7144.

Piersanti, A., G. Spada, R. Sabadini, and M. Bonafede (1995). Global post-seismic deformation, *Geophys. J. Int.*, 120, 544–566.

Pollitz, F.F. (1992). Postseismic relaxation theory on the spherical Earth, *Bull. Seismol. Soc. Am.*, 82, 422–453.

Rundle, J.B. (1982). Viscoelastic gravitational deformation by a rectangular thrust fault in a layered Earth, *J. Geophys. Res.*, 87, 7787–7796.

Sabadini, R., A. Piersanti, and G. Spada (1995). Toroidal-poloidal partitioning of global Post-seismic deformation, *Geophys. Res. Lett.*, 21, 985–988.

Smylie, D.S. and L. Mansinha (1971). The elasticity theory of dislocation in real Earth models and changes in the rotation of the earth, *Geophys. J. R. Astron. Soc.*, 23, 329–354.

Sun, W. and S. Okubo (1993). Surface potential and gravity changes due to internal dislocations in a spherical Earth – I. Theory for a point dislocation, *Geophys. J. Int.*, 114, 569–592.

Sun, W. and S. Okubo (2002). Effects of the earth's spherical curvature and radial heterogeneity in dislocation studies, *Geophys. R.L.*, 29(12), 46 (1–4).

Sun, W. and S. Okubo (2004). Co-seismic deformations detectable by satellite gravity missions, *J. Geophys. Res.,* 109, B4, B04405.

Steketee, J.A. (1958). On Volterra's dislocations in a semi-infinite elastic medium, *Can. J. Phys.*, 36, 192–205.

Tanaka, T., J. Okuno, and S. Okubo (2006). A new method for the computation of global viscoelastic post-seismic deformation in a realistic earth model (I), *Geophys. J. Int.*, 164, 273.

Chapter 3

On Ambiguities in Definitions and Applications of Bouguer Gravity Anomaly

P. Vajda, P. Vaníček, P. Novák, R. Tenzer, A. Ellmann, and B. Meurers

Abstract Over decades diverse definitions and use of the Bouguer gravity anomaly found place in geodetic and geophysical applications. We discuss three distinct Bouguer anomalies. Their definitions vary due to the presence or absence of various effects (corrections), such as the geophysical indirect effect and the secondary indirect effects. Here we discuss the significance and magnitude of these effects. We point out the different understanding of the Bouguer anomaly in geophysics compared to geodesy. We also address the diverse demands on the gravity data in geophysical and geodetic applications, such as the issue of the topographic density and the lower boundary in the volume integral for the topographic correction, as well as the need for the bathymetric correction. Recommendations are made to bring the definitions and terminology into accord with the potential theory.

3.1 Anomalous Gravity – Gravity Anomaly and Disturbance

Having the pairs *actual potential* and *actual gravity* (g), *normal potential* and *normal gravity* (γ), we would anticipate to encounter the pair *disturbing potential* (T) and *disturbing (anomalous) gravity*. In fact, two such anomalous quantities have been used, the *gravity anomaly* (Δg) and the *gravity disturbance* (δg). Both the *disturbance*, see Eq. (1), and the *anomaly*, see Eq. (2), can be defined either using *actual gravity*, cf. the left-hand sides of Eqs. (1) and (2), respectively – we refer to such a definition as "point-wise definition" – or using the *disturbing potential*, cf. the right-hand sides of Eqs. (1) and (2), respectively

$$\delta g(h,\Omega) \stackrel{\text{def}}{=} g(h,\Omega) - \gamma(h,\Omega) \cong -\frac{\partial}{\partial h} T(h,\Omega), \tag{1}$$

$$\Delta g(h,\Omega) \stackrel{\text{def}}{=} g(h,\Omega) - \gamma(h-Z,\Omega) \cong \left\{ -\frac{\partial}{\partial h} - \frac{2}{R} \right\} T(h,\Omega). \tag{2}$$

The definition of the gravity anomaly using the right-hand side of Eq. (2) is known as the *fundamental gravimetric equation* (in spherical approximation, R being the mean earth radius). We refer the positions of points in geodetic (Gauss-ellipsoidal) coordinates that are respective to a geocentric properly oriented equipotential reference ellipsoid (RE), such as GRS'80, where h is height above the RE, and Ω denotes the pair of latitude and longitude. The same RE plays the role of the normal ellipsoid generating normal gravity. Above, Z is the *vertical displacement*, i.e., the separation between the actual and the equivalent normal equipotential surfaces at (h, Ω), given by the *generalized Bruns equation* (e.g., Heiskanen and Moritz, 1967)

$$Z(h,\Omega) = T(h,\Omega)/\gamma(h,\Omega). \tag{3}$$

The two sets of definitions in Eqs. (1) and (2), the left-hand vs. right-hand sides, are not rigorously compatible. They differ by the *effect of the deflection of the vertical* at the order of 10 μgal (e.g., Vaníček et al., 1999, 2004), which is typically negligible in both

P. Vajda (✉)
Geophysical Institute, Slovak Academy of Sciences, Bratislava, 845 28, Slovak Republic
e-mail: Peter.Vajda@savba.sk

S.P. Mertikas (ed.), *Gravity, Geoid and Earth Observation*, International Association of Geodesy Symposia 135,
DOI 10.1007/978-3-642-10634-7_3, © Springer-Verlag Berlin Heidelberg 2010

geodetic and geophysical applications. Both sets define the disturbance or anomaly at the observation point located anywhere, not only on the geoid or the topo-surface. The "point-wise definition" is used to compile anomalous gravity from observed gravity, while the definition using the disturbing potential is used when modeling the observed gravity data synthetically based on density, or when computing other parameters of the gravity field based on disturbing potential. The approximate compatibility of the two sets of definitions for both the anomaly and disturbance is vital for both geodetic and geophysical applications in inverting or interpreting observed gravity and in computing the from potential derived parameters of the gravity field.

3.2 Topographically Corrected Anomalous Gravity

Let V^T be the gravitational potential of topographic masses globally enclosed between the relief (topo-surface, earth's surface) and the geoid/quasigeoid ("sea level" as vertical datum), and let A^T be the attraction (the vertical component of the gravitational attraction vector) of those masses. By removing the effect (potential and attraction) of topographic masses from the gravity disturbance and the gravity anomaly, in both the sets of their definitions presented in the previous section, we obtain (e.g., Vajda et al., 2007) the topographically corrected disturbance and anomaly

$$\delta g^T(h,\Omega) \stackrel{\text{def}}{=} \delta g(h,\Omega) - A^T(h,\Omega) \cong -\frac{\partial}{\partial h}[T(h,\Omega) - V^T(h,\Omega)], \tag{4}$$

$$\Delta g^T(h,\Omega) \stackrel{\text{def}}{=} \Delta g(h,\Omega) - A^T(h,\Omega) + SITE(h,\Omega) \cong \cong \left\{-\frac{\partial}{\partial h} - \frac{2}{R}\right\}[T(h,\Omega) - V^T(h,\Omega)], \tag{5}$$

where

$$A^T(h,\Omega) = -\frac{\partial}{\partial h} V^T(h,\Omega) \tag{6}$$

is the attraction of topography, and

$$SITE(h,\Omega) = \frac{2}{R} V^T(h,\Omega) \tag{7}$$

is the *secondary indirect topographic effect* on gravity anomaly (e.g., Vaníček et al., 2004). The two sets (Eqs. 4 and 5) define the topographically corrected gravity disturbances and anomalies, respectively, either based on actual gravity, or based on disturbing potential. Again the approximate compatibility of these two sets is vital for geodetic and geophysical applications, as it mediates the modeling or interpretation of observed topo-corrected anomalous gravity, or the computation of gravity field parameters derived from topo-corrected anomalous gravity data. Notice that the computation of the topo-corrected gravity anomaly (the so-called Bouguer anomaly) from observed gravity involves not only the removal of the attraction of the topography, but also the secondary indirect topographic effect (SITE). The SITE is a long-wavelength (trend-like) signal of the magnitude at the order of 100 mgal in mountainous regions. To illustrate it we show

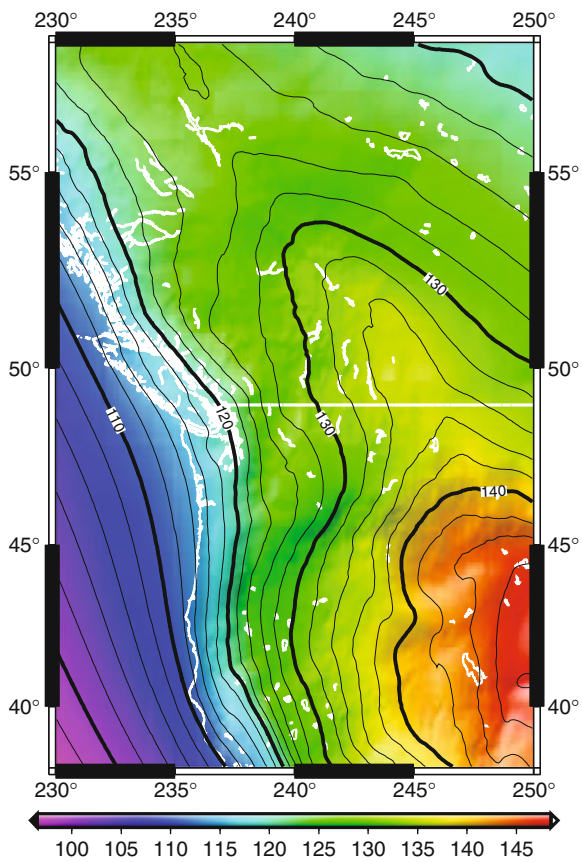


Fig. 3.1 The SITE in the Canadian rocky mountains (mgal). The contour interval is 2 mgal. The magnitude of SITE reaches 150 mgal

SITE computed for the region of Canadian Rockies in Fig. 3.1.

When SITE is not included in the topographic correction in the definition of the topo-corrected gravity anomaly based on actual gravity, then this definition will not be compatible with the definition of the topo-corrected gravity anomaly based on the topo-corrected disturbing potential (based on the fundamental gravimetric equation). In geophysical and geodetic applications the incompatibility will introduce a systematic error equal to the SITE.

To sum it up, when we remove the gravitational potential of topographic masses from disturbing potential, we have to remove from the gravity anomaly the effect of topographic masses, which consists of the attraction and secondary indirect effect of topographic masses. Similarly, if we were to remove from disturbing potential the gravitational potential of the bathymetric density contrast, or of the ice or sediments density contrast, we would have to remove from the gravity anomaly the complete effect of these density contrasts – not only the attraction of these density contrasts, but also the secondary indirect effects of these contrasts.

3.3 Bouguer Anomaly – Ambiguous Definitions

Under the name "Bouguer anomaly" there are currently at least three distinctly different quantities used in the geophysical and geodetic practice. We review and compare them below. For simplicity, we define them at stations $P \equiv [h_T(\Omega),\Omega]$ on the topo-surface. All the topo-corrections (evaluated at P) will be written in a general form, involving numerical integration of the Newtonian volume integrals over the entire globe. The numerical aspects of evaluating them, such as the truncation to a spherical cap (e.g., of the Hayford-Bowie radius, about 1.5 arcdeg), splitting into shell/cap and terrain ("roughness") terms, various approximations to the integral kernel, planar approximation, etc. are of no concern to us here.

The definition of the *Bouguer anomaly* in its *classical sense*, e.g., according to Heiskanen and Moritz (1967), denoted here by superscript "CB" (standing for "Classical Bouguer"), reads

$$\Delta g^{CB}(P) \stackrel{\text{def}}{=} g(P) - \gamma(P^*) - A^T(P), \qquad (8)$$

where the normal gravity is evaluated at the point (P^*) which is the vertical projection of the observation point P onto the telluroid, and where A^T is the attraction of the global topography, i.e., of masses contained between the sea level (geoid/quasigeoid) and the topo-surface. The *Bouguer anomaly* in its classical sense lacks the SITE (Fig. 3.1). Therefore, the Δg^{CB} is not a "topo-corrected gravity anomaly" in a rigorous sense. This anomaly is not well suited for geophysical interpretation of gravity data either, because normal gravity is not evaluated at the station P, and because the topo-masses in the topo-correction are defined with the geoid rather than RE as their lower boundary (cf. Vajda et al., 2006). When this gravity anomaly is used in geodetic applications, the SITE must be added to have a complete effect of the topo-masses (cf. Vaníček et al., 2004). The definition of the *Bouguer anomaly* in accord with the rigor, denoted here simply by superscript "B" (standing for "Bouguer"), reads (e.g., Vaníček et al., 2004, Eq. [53])

$$\Delta g^{B}(P) \stackrel{\text{def}}{=} g(P) - \gamma(P^*) - A^T(P) + SITE(P). \qquad (9)$$

Compared to the classical definition, it contains also the required SITE,

$$\Delta g^{B}(P) = \Delta g^{CB}(P) + SITE(P).$$

In literature the adjective "Bouguer" is sometimes replaced by synonyms "No Topography" ("NT") or "geoid-generated" and the superscript "B" by superscripts "NT" or "g", respectively. This "Bouguer anomaly" finds its practical use in geodesy, when solving the *boundary value problem* defined with sea level as the boundary, in computing the geoid, either via the "NT space" (e.g., Vaníček et al., 2004) or via the "Helmert space" (e.g., Vaníček et al., 1999), using the Stokes-Helmert scheme, where Bouguer anomalies are transformed into Helmert anomalies (ibid). The Bouguer anomaly defined by Eq. (9) is not suitable for geophysical applications for the same reasons as that defined by Eq. (8). It has been recognized (Hinze et al., 2005; Vajda et al., 2006; and references therein) that geophysical interpretation of gravity requires the normal gravity to be evaluated at the observation point (station) and the topographic masses to be defined (for the sake of the topo-correction) with the RE (replacing sea level) as their bottom boundary.

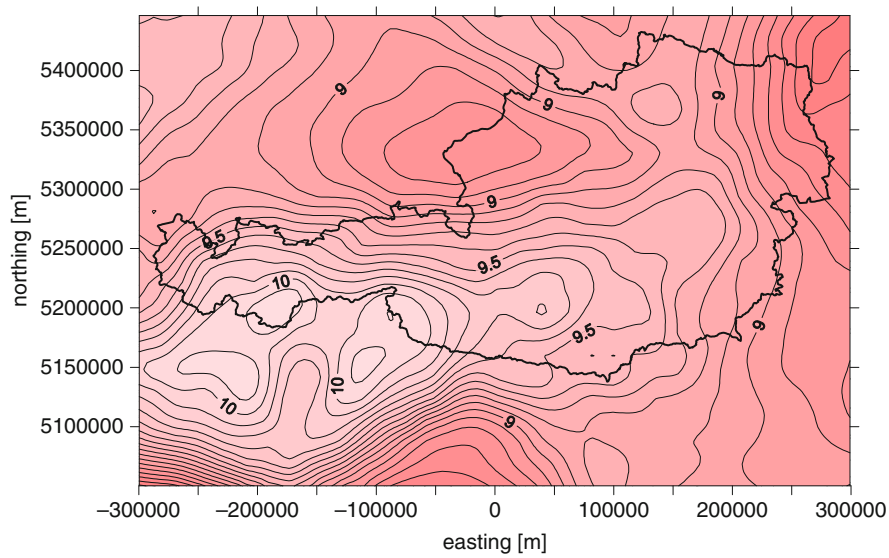


Fig. 3.2 The geophysical indirect effect (mgal) for the area of the Eastern Alps (Austria). It reaches the magnitude of 10 mgal. It is of long-wavelength ("regional trend") nature

Hinze et al. (2005) proposed a new definition of the "Bouguer anomaly" to meet the geophysical requirements. The definition of the *Bouguer anomaly* according to the newly proposed standards for gravity databases (Hinze et al., 2005), denoted here by superscript "NB" (standing for "New Bouguer"), while the new standards propose a term "Bouguer gravity anomaly", optionally to be preceded by the adjective "ellipsoidal", reads

$$\Delta g^{NB}(P) \stackrel{\text{def}}{=} g(P) - \gamma(P) - A^{ET}(P). \qquad (10)$$

This definition of "Bouguer anomaly" differs from the classical definition (Eq. (8)) in two aspects: (1) normal gravity is evaluated at the observation point (station), (2) the *reference ellipsoid* replaces the *sea level* as the lower boundary of topo-masses in the topo-correction, hence the superscript "ET" replacing "T". There is only one problem with this definition – that of terminology. The quantity defined by Eq. (10) is by the standards of the theory of the gravity field, which applies equally well to both geodesy and geophysics, the "topo-corrected gravity disturbance" (Vajda et al., 2006, 2007).

The difference between the "classical" and the "new" Bouguer anomalies amounts to the so-called *geophysical indirect effect* (GIE),

$$\Delta g^{NB}(P) = \Delta g^{CB}(P) + GIE(P),$$

which consists of two terms. One accounts for the difference between normal gravity at the topo-surface and that at the telluroid (between P and P^*). The other accounts for the attraction of masses globally enclosed between the RE and the geoid/quasigeoid (Vajda et al., 2006; and references therein). To illustrate the *geophysical indirect effect* we show it computed for the region of the Eastern Alps (Austria) in Fig. 3.2.

3.4 Gravity Data – Geophysical Versus Geodetic Applications

Just to illustrate that the demands on defining, compiling and using gravity data may differ between geophysical and geodetic applications, we compare (cf. Table 3.1) two examples: A geodetic application being represented by the boundary value problem (BVP) for geoid computation using the Stokes approach and the geoid as the boundary, and a geophysical application represented by interpretation or inversion of gravity.

The Stokes approach requires the use of a gravity anomaly, as opposed to the Hotine approach, which requires the gravity disturbance. The BVP requires harmonicity above the boundary, hence no topo-masses above the geoid. That implies the geoid as the lower boundary (bottom interface) of the topo-masses in the topo-correction and no need of a bathymetric

Table 3.1 Comparison between a geodetic and a geophysical application

Task (an example)	Geodetic application geoid computation, BVP based on geoid and Stokes approach	Geophysical application gravity interpretation or inversion (Vajda et al., 2006, 2008)
Anomalous gravity	Gravity *anomaly*	Gravity *disturbance*
Topographic correction	Attraction of topo-masses and SITE	Attraction of topo-masses
Lower boundary of topo-masses	Geoid/quasigeoid ("sea level")	Reference ellipsoid (RE)
Topographic density in topo-correction	Real	Reference (e.g., constant, average crustal) for solid topography onshore, that of water for liquid topography offshore
	NO need	YES, based on the RE

correction. The use of gravity anomaly implies that the topo-correction consist of two terms, the attraction of topo-masses and the SITE (cf. Sect. 3.2).

The geophysical interpretation or inversion of gravity data, by means of direct inversion, forward modeling, or pattern recognition, etc. (e.g., Blakely, 1995), requires that the gravity data exactly equal (match) the attraction of the anomalous masses being sought. It has been proved (Vajda et al., 2006, 2008) that such a requirement is satisfied by the bathymetrically and topographically corrected gravity disturbance (the so-called "BT disturbance"). In geophysical practice the "BT disturbance" has been and unfortunately remains to be called the "Bouguer anomaly" (Hinze et al., 2005).

3.5 Conclusion

The ambiguous terminology regarding the "Bouguer anomaly" could cause confusion when using the Bouguer gravity anomaly databases by geodesists and geophysicists, as the two groups would anticipate different quantities under the same name, as shown in Sects. 3.3 and 3.4. There is but one gravity field of the earth with its theory, and it is an inseparable part of the research and applications in both the geophysics and geodesy. These two disciplines overlap and therefore there is a great need not only for common standards but also for common terminology. We propose to refer to the "Bouguer anomaly" needed in geophysics, defined by Eq. (10), correctly as the *topographically corrected gravity disturbance*. When a bathymetric correction is applied in addition to the topographic correction, we propose to call it the *BT disturbance* (cf. Vajda et al., 2008).

Acknowledgements Peter Vajda acknowledges the partial support of the VEGA grant agency projects No. 2/3004/23 and 2/6019/26. Pavel Novák was supported by the Grant 205/08/1103 of the Czech Science Foundation.

References

Blakely, R.J. (1995). Potential theory in gravity and magnetic applications. Cambridge University Press, New York.

Heiskanen, W.A. and H. Moritz (1967). Physical geodesy. Freeman, San Francisco.

Hinze, W.J., C. Aiken, J. Brozena, B. Coakley, D. Dater, G. Flanagan, R. Forsberg, Th. Hildenbrand, G.R. Keller, J. Kellogg, R. Kucks, X. Li, A. Mainville, R. Morin, M. Pilkington, D. Plouff, D. Ravat, D. Roman, J. Urrutia-Fucugauchi, M. Véronneau, M. Webring, and D. Winester (2005). New standards for reducing gravity data: The North American gravity database. *Geophysics*, 70(4), J25–J32, doi: 10.1190/1.1988183.

Vajda, P., P. Vaníček, and B. Meurers (2006). A new physical foundation for anomalous gravity. *Stud. Geophys. Geod.,* 50(2), 189–216, doi: 10.1007/s11200-006-0012-1.

Vajda, P., P. Vaníček, P. Novák, R. Tenzer, and A. Ellmann (2007). Secondary indirect effects in gravity anomaly data inversion or interpretation. *J. Geophys. Res*., 112, B06411, doi: 10.1029/2006 JB004470.

Vajda, P., A. Ellmann, B. Meurers, P. Vaníček, P. Novák, and R. Tenzer (2008). Global ellipsoid-referenced topographic, bathymetric and stripping corrections to gravity disturbance. *Stud. Geophys. Geod.*, 52(1), 19–34, doi: 10.1007/s11200-008-00 03-5.

Vaníček, P., J. Huang, P. Novák, S. Pagiatakis, M. Véronneau, Z. Martinec, and W.E. Featherstone (1999). Determination of the boundary values for the Stokes-Helmert problem. *J. Geod.*, 73(4), 180–192, doi:10.1007/s001900050235.

Vaníček, P., R. Tenzer, L.E. Sjöberg, Z. Martinec, and W.E. Featherstone (2004). New views of the spherical Bouguer gravity anomaly. *Geoph. J. Int.*, 159(2), 460–472, doi: 10.1111/j.1365-246X.2004. 02435.x.

Chapter 4

Harmonic Continuation and Gravimetric Inversion of Gravity in Areas of Negative Geodetic Heights

P. Vajda, A. Ellmann, B. Meurers, P. Vaníček, P. Novák, and R. Tenzer

Abstract By the decomposition of the real earth's gravity potential it can be shown that the attraction of the anomalous mass density, which is sought as the unknown in gravimetric inversion (gravity data interpretation), matches exactly the gravity disturbance corrected for the attraction of topography and bathymetry (the BT disturbance), and eventually also for attractions of other known density contrasts, such as sediments, lakes, glaciers, isostatic roots, etc (the stripped BT disturbance). The involved (global) topographic correction requires the use of reference ellipsoid (RE) as the bottom interface of topographic masses. Topographic correction based on the RE introduces the attraction of "liquid topography" offshore, which is the attraction of sea water between the RE and sea level (geoid). The topo-correction onshore requires the use of reference (such as constant average crustal) topographic density for the "solid topography". The ultimate knowledge of real topo-density is avoided, since anomalous density relative to the reference topo-density is part of the interpretation (is sought). In areas of negative geodetic heights, both onshore (e.g., Dead Sea region) and offshore (negative geoidal heights), we run into the problem of evaluating the normal gravity and the problem of the legitimacy of the upward harmonic continuation of the gravity data to be interpreted (inverted). We propose to overcome these problems by a new approach based on the concept of the reference quasi-ellipsoid (RQE). The gravimetric inverse problem is first reformulated based on the RQE that replaces the RE in the decomposition of actual potential. The RQE approach enables for stations of negative heights the use of the international gravity formula (IGF) for computing normal gravity at the station, and facilitates the legitimacy of the harmonic continuation in regions of negative heights. Second, the gravity data (the RQE-based BT disturbances) are continued onto or above the RE. Third, the inverse problem is transformed back to be formulated with respect to the RE, and solved using classical known techniques.

P. Vajda (✉)
Geophysical Institute, Slovak Academy of Sciences, Bratislava 845 28, Slovak Republic
e-mail: Peter.Vajda@savba.sk

4.1 Gravity Data Inversion/Interpretation

Gravimetric inversion or gravity data interpretation, the objective of which is to find subsurface anomalous density distribution by inverting (or interpreting) anomalous gravity data compiled from observed gravity, is based on the fact that we can compile such an anomalous gravity quantity that matches the attraction (vertical component of the gravitational attraction vector) of the sought anomalous density. By the decomposition of earth's gravity potential it can be shown (Vajda et al., 2006, 2008a) that the anomalous gravity quantity that is exactly equal to the attraction δA of the unknown anomalous density distribution $\delta\rho$ globally enclosed onshore by the relief and offshore by sea bottom is but the bathymetrically and topographically corrected gravity disturbance, the so called "BT disturbance",

$$\delta g^{BT}(h,\Omega) = \delta A(h,\Omega), \tag{1}$$

S.P. Mertikas (ed.), *Gravity, Geoid and Earth Observation*, International Association of Geodesy Symposia 135,
DOI 10.1007/978-3-642-10634-7_4, © Springer-Verlag Berlin Heidelberg 2010

defined as follows:

$$\delta g^{BT}(h,\Omega) = g(h,\Omega) - \gamma(h,\Omega) - A^{ET}(h,\Omega) - \delta A^{EW}(h,\Omega), \quad (2)$$

where g is actual (observed) gravity, γ is normal gravity, $(-A^{ET})$ is the (global) topographic correction based on the *reference ellipsoid* (RE), and $(-\delta A^{EW})$ is the (global) bathymetric correction based on the RE. Both the corrections are computed at the observation point (station) using the Newtonian volume integral (Vajda et al., 2006, 2008a and references therein). Points are referred and positioned in geodetic (Gauss-ellipsoidal) coordinates, h is height above the RE, Ω is the pair of geodetic latitude and longitude. The RE is geocentric, properly oriented, biaxial (rotational), and equipotential (level), thus identical with the normal ellipsoid generating the normal gravity.

The gravity disturbance is defined based on normal gravity generated by the RE. Consequently, the decomposition of actual potential resulting in Eqs. (1) and (2) must be based on the RE, which implies that topographic and bathymetric corrections are defined based on the RE instead of geoid/quasigeoid ("sea level" as vertical datum). The use of the RE means that in terms of the topo-correction we have the attraction of the so called "reference solid topography" and the attraction of the so called "liquid topography". The "reference solid topography" is the reference rock density distribution $\rho_R(h,\Omega)$ (such as constant average crustal density ρ_0) globally enclosed onshore between the RE and the relief. The "liquid topography" is the (constant) density of sea water ρ_W enclosed between the RE and the geoid (positive above and negative below the RE), cf. Fig. 4.1. The bathymetric correction removes the attraction of the sea water density contrast $(\rho_w - \rho_0)$ offshore, globally enclosed between the sea bottom and the RE.

While in geodesy the normal density distribution of the normal ellipsoid (the RE) generating the normal potential and normal gravity may remain unspecified (normal potential is selected as a mathematical prescription) and even zero to some depth below the surface of the RE, in geophysics we must find a model normal density distribution $\rho_N(h,\Omega)$ (such as that of the Preliminary Reference Earth Model, PREM), cf. (Vajda et al., 2006, and references therein), which serves as the background density defining the (unknown and sought) density contrast $\delta\rho(h,\Omega)$ inside the RE (below the surface of the RE onshore and below the sea bottom offshore). Within the solid topography (between the RE and relief onshore), the sought $\delta\rho(h,\Omega)$ is defined relative to the ρ_0 background density.

Normal gravity in Eq. (2) is computed by the international gravity formula (IGF) which includes the height term (e.g., Heiskanen and Moritz, 1967).

The gravimetric inverse problem, formulated based on Eq. (1), is solved typically either by direct inversion or by forward modeling techniques, or eventually the gravity data are interpreted in terms of pattern recognition (e.g., Blakely, 1995). In either case the problem may be formulated for observation points at their natural positions (on relief, on sea surface, at flight trajectories, in boreholes, at sea bottom, etc.). However, in the case of forward modeling it is often required to have the gravity data on the surface of a half-space (planar approximation) or a sphere (spherical approximation), when the modeling software does not consider the relief of the earth. In such a case, the upward continuation of gravity data (BT gravity disturbances) to a reference surface is needed.

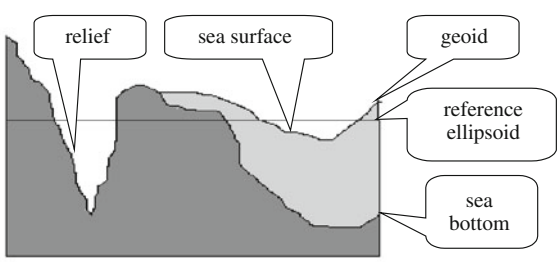


Fig. 4.1 Regions of negative geodetic heights

4.2 Regions of Negative Heights

Complications arise with the interpretation or inversion of gravity data in areas, where observation points have negative geodetic heights, such as in the Dead Sea region onshore, or offshore where geoidal heights are negative (Fig. 4.1). A point with negative height lies inside (below the surface of) the RE. The presence of a non-zero model normal density distribution $\rho_N(h,\Omega)$ there (1) violates the use of the IGF for normal

gravity computation (which must be there evaluated by the Newtonian volume integral over the ρ_N inside the RE), and (2) violates the harmonic continuation of the BT disturbance given by Eq. (2) in the "free-air" region between the relief (of negative geodetic heights) and the surface of the RE. Normal masses ρ_N are present in this "free-air" region, thus the δg^{BT} is not harmonic there.

We propose to overcome these two problems by means of the so called reference quasi-ellipsoid (RQE) approach, which makes use of a remove-restore technique for the upper layer of the model normal masses of the RE.

4.3 RQE Approach

The decomposition of the actual potential, which has lead to Eqs. (1) and (2) that are the basis for formulating the inverse problem (Vajda et al., 2006, 2008a), was performed based on the RE. Let us now replace the RE by the so called reference quasi-ellipsoid (RQE) in the decomposition of the actual potential, cf. Fig. 4.2.

The RQE is defined as the surface the depth of which h^* (reckoned along the ellipsoidal normal) below the surface of the RE is constant. As such, it is no longer an ellipsoidal surface, hence the name. The value of h^* is chosen so, that it is just greater than the maximum dip of the relief below the RE elsewhere over the entire globe, e.g., as 500 m. We let the RQE serve as both the lower boundary of the "topographic masses" and the upper boundary of the "normal masses". This implies that we have to define a

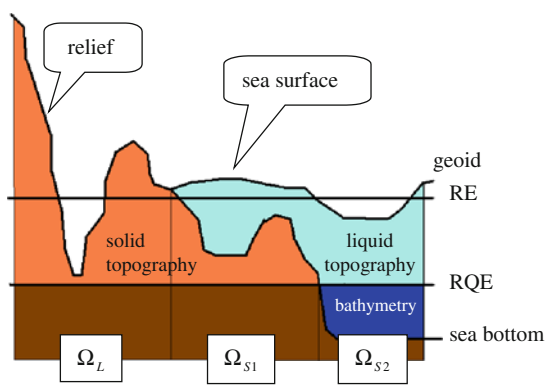


Fig. 4.2 The reference quasi-ellipsoid (RQE) approach

new model normal density distribution $\rho_N^*(h,\Omega)$ bound by the surface of the RQE, which generates the same normal potential and normal gravity in the exterior of the RE as is generated by $\rho_N(h,\Omega)$ bound by the surface of the RE. In our approach it is vital that the $\rho_N(h,\Omega)$ consists of an upper layer of constant density equal to ρ_0. We remove this upper layer of $\rho_N(h,\Omega)$ and restore it in an unspecified manner below the level of the deepest sea bottom to form an unspecified $\rho_N^*(h,\Omega)$. We do not require the $\rho_N^*(h,\Omega)$ to meet the geophysical constraints (cf. Vajda et al., 2008b, and references therein), and we even leave it unspecified. We only require that it generates the usual (IGF) normal gravity above the RE. In this approach the space between the surfaces of the RQE and of the RE is void of normal masses.

The decomposition based on the RQE leads to the following exact link (match) between the gravity and the attraction of anomalous density

$$\delta g^{BT*}(h,\Omega) = \delta A^*(h,\Omega), \tag{3}$$

where δA^* is the attraction of the sought anomalous density distribution $\delta\varrho^*(h,\Omega)$ now defined as follows: offshore below the sea bottom and onshore below the surface of the RQE relative to the background density distribution $\rho_N^*(h,\Omega)$ and onshore between the RQE and the relief relative to the average crustal density ρ_0, and where the BT disturbance is now defined with topographic and bathymetric corrections based on the RQE

$$\begin{aligned}\delta g^{BT*}(h,\Omega) = g(h,\Omega) - \gamma(h,\Omega) - \\ A^{QET}(h,\Omega) - \delta A^{QEW}(h,\Omega).\end{aligned} \tag{4}$$

Now the normal gravity in Eq. (4) can be computed using the IGF even at observation points of negative geodetic heights, because the space between the RQE and RE surfaces is void of normal masses. Also, now the new BT disturbance based on the RQE (in spherical approximation multiplied by geocentric distance), $(R+h)\delta g^{BT*}(h,\Omega)$, is harmonic (because even the space above the relief of negative heights is now free of any masses) and can be harmonically upward continued. The RQE approach resolves for observation points of negative heights both the problems: the problem of normal gravity computation and that of the legitimacy of harmonic continuation.

While the new normal density distribution $\rho_N^*(h,\Omega)$ inside the RQE, generating the normal gravity given

by the IGF, remains unspecified, the formulation of the gravimetric inverse problem based on the RQE and $\rho_N^*(h,\Omega)$ remains meaningless, because there is no use of a solved anomalous density defined relative to an unspecified background density. We do not intend to solve the inverse problem in the RQE approach. The RQE approach is used to resolve the problem of normal gravity computation and the upward continuation of the BT disturbance at stations of negative heights. The RQE approach is used only to compile the BT disturbance in such a way that the IGF may be used for computing normal gravity, and in order to harmonically upward continue the BT disturbance (based on RQE) onto or above the surface of the RE. Once we have the BT gravity disturbance (based on the RQE), δg^{BT*}, on or above the RE, we transform the formulation of the inverse problem back to being based on the RE and $\rho_N(h,\Omega)$, which is described in the next section.

4.4 Reverting from RQE to RE Approach

After harmonic upward continuation of the RQE-based BT gravity disturbance onto or above the RE, we have the inverse problem formulated based on the RQE, but for stations on or above the RE now

$$\forall h \geq 0\text{: } \delta g^{BT*}(h,\Omega) = \delta A^*(h,\Omega). \tag{5}$$

In the previous section we removed and restored the upper layer (between the RE and RQE surfaces) of the normal masses $\rho_N(h,\Omega)$, the upper layer being of constant density ρ_0. Now (already having all stations at which we interpret (invert) gravity data on or above the RE) we revert this step, which implies that we have to add the attraction (in spherical approximation) of this quasi-ellipsoidal layer of constant density ρ_0 and constant thickness h^*

$$A^{QELC}(h,\Omega) \approx 4\pi G\rho_0 h^*, \tag{6}$$

G being the gravitational constant, to both sides of Eq. (5). We realize that its left-hand side becomes

$$\forall h \geq 0\text{: } \delta g^{BT*}(h,\Omega) + A^{QELC}(h,\Omega) = \delta g^{BT}(h,\Omega),$$

because the addition of A^{QELC} transforms the sum of the RQE based topo– and bathymetric corrections to the sum of the RE-based topo– and bathymetric corrections, thus transforming the RQE-based BT disturbance δg^{BT*} into the RE-based BT disturbance δg^{BT}. We also realize that the right-hand side of Eq. (5) becomes

$$\forall h \geq 0\text{: } \delta A^*(h,\Omega) + A^{QELC}(h,\Omega) = \delta A(h,\Omega),$$

because $\rho_N^*(h,\Omega)$ becomes $\rho_N(h,\Omega)$ and $\delta\varrho^*(h,\Omega)$ becomes $\delta\varrho(h,\Omega)$. Consequently, Eq. (5) becomes

$$\forall h \geq 0\text{: } \delta g^{BT}(h,\Omega) = \delta A(h,\Omega). \tag{7}$$

and we have the inverse problem formulated based on the RE and $\rho_N(h,\Omega)$ using the RE-based BT gravity disturbances as observed gravity data to be interpreted or inverted.

4.5 Case Study

We have computed the RQE-based topographic and bathymetric corrections, as well as the RQE-based BT gravity disturbances in a test region comprising the NW part of North America including a portion of the Pacific. They are shown in Figs. 4.3, 4.4 and 4.5, respectively.

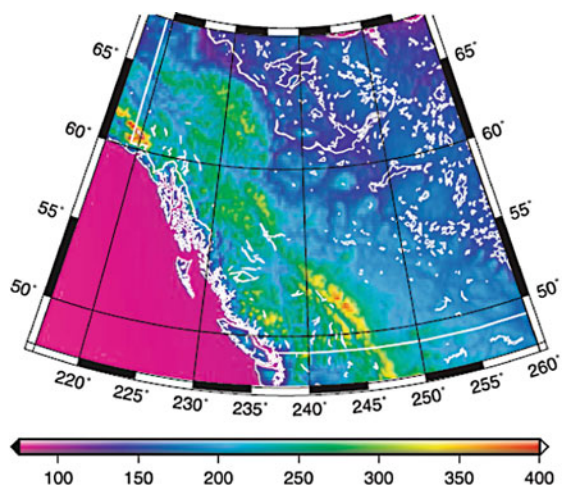


Fig. 4.3 The attraction (A^{QET}) of the RQE-based topography (both solid and liquid, cf. Fig. 4.2) evaluated on the topo-surface in our test region (mGal)

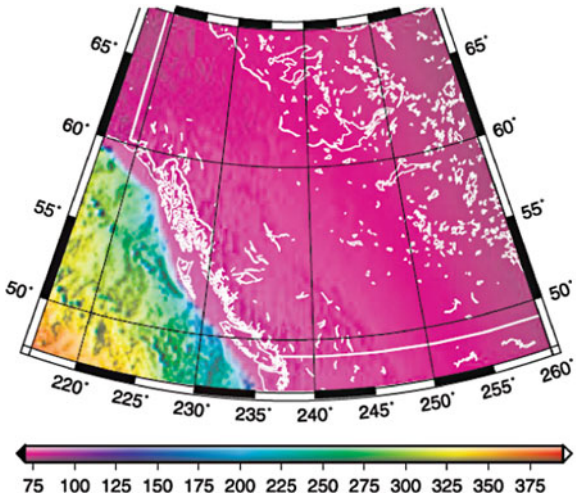


Fig. 4.4 The RQE-based bathymetric correction ($-\delta A^{QEW}$) in our test region computed on the topo-surface (mGal)

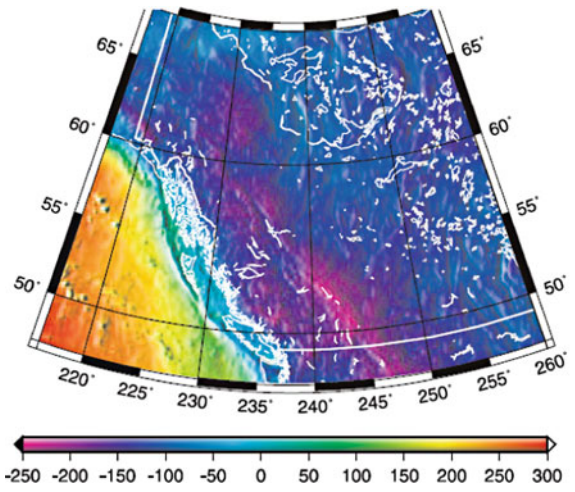


Fig. 4.5 The RQE-based BT gravity disturbance (δg^{BT*}) given on the topo-surface in our test region (mGal)

4.6 Conclusion

When the gravimetric inverse problem is formulated in terms of the attraction (vertical component of the gravitational attraction vector) of the sought unknown anomalous mass density distribution (the attraction being a Newtonian volume integral over the anomalous density distribution), the gravity data that match this attraction (Eq. (1)) and that must be compiled as input data entering the inversion or interpretation are the BT gravity disturbances (Eq. (2)). In areas of negative geodetic heights of gravity stations (observation points) the normal gravity in the definition of the BT disturbance (Eq. (2)) can no longer be computed using the IGF. Instead, it would have to be computed as inner normal gravity of the normal ellipsoid (the RE) using the Newtonian volume integral for attraction, over the normal density distribution of the RE. In "free air" areas between the topo-surface of negative geodetic heights and the surface of the RE, the BT disturbance (in spherical approximation multiplied by geocentric distance) is not harmonic due to the presence of normal masses below the surface of the RE. Consequently its harmonic continuation is not legitimate.

The above two problems complicate the compilation and inversion (interpretation) of gravity data (BT disturbances) at stations (in areas) of negative geodetic heights. They are tackled by our so called RQE approach that consists of four steps:

(1) The gravimetric inverse problem is formulated based on the RQE instead of based on the RE, as described in Sect. 4.3.
(2) The topographic and bathymetric corrections are computed and the BT disturbance compiled based on the RQE. In the RQE approach the normal gravity can be computed using the IGF even at stations of negative heights. In the RQE approach the BT disturbance (in spherical approximation multiplied by geocentric distance) is harmonic everywhere above the topo-surface even when the topo-surface is of negative heights.
(3) The RQE-based BT disturbances are harmonically upward continued onto or above the RE.
(4) The formulation of the inverse problem is now for all stations on or above the RE reverted to the RE approach and the BT disturbances are inverted or interpreted, cf. Sect. 4.4.

Acknowledgements Peter Vajda acknowledges the support of the VEGA grant agency projects No. 2/3004/23 and 2/6019/26. Pavel Novak was supported by the Grant 205/08/1103 of the Czech Science Foundation.

References

Blakely, R.J. (1995). Potential theory in gravity and magnetic applications. Cambridge University Press, New York.

Heiskanen, W.A. and H. Moritz (1967). Physical geodesy. Freeman, San Francisco.

Vajda, P., P. Vaníček, and B. Meurers (2006). A new physical foundation for anomalous gravity. *Stud. Geophys. Geod.*, 50(2), 189–216, doi:10.1007/s11200-006-0012-1.

Vajda, P., A. Ellmann, B. Meurers, P. Vaníček, P. Novák, and R. Tenzer (2008a). Global ellipsoid-referenced topographic, bathymetric and stripping corrections to gravity disturbance. *Stud. Geophys. Geod.*, 52(1), 19–34, doi: 10.1007/s11200-008-0003-5.

Vajda, P., A. Ellmann, B. Meurers, P. Vaníček, P. Novák, and R. Tenzer (2008b). Gravity disturbances in regions of negative heights: A reference quasi-ellipsoid approach. *Stud. Geophys. Geod.*, 52(1), 35–52, doi: 10.1007/s11200-008-0004-4.

Chapter 5

Results of the European Comparison of Absolute Gravimeters in Walferdange (Luxembourg) of November 2007

O. Francis, T. van Dam, A. Germak, M. Amalvict, R. Bayer, M. Bilker-Koivula, M. Calvo, G.-C. D'Agostino, T. Dell'Acqua, A. Engfeldt, R. Faccia, R. Falk, O. Gitlein, Fernandez, J. Gjevestad, J. Hinderer, D. Jones, J. Kostelecky, N. Le Moigne, B. Luck, J. Mäkinen, D. Mclaughlin, T. Olszak, P. Olsson, A. Pachuta, V. Palinkas, B. Pettersen, R. Pujol, I. Prutkin, D. Quagliotti, R. Reudink, C. Rothleitner, D. Ruess, C. Shen, V. Smith, S. Svitlov, L. Timmen, C. Ulrich, M. Van Camp, J. Walo, L. Wang, H. Wilmes, and L. Xing

Abstract The second international comparison of absolute gravimeters was held in Walferdange, Grand Duchy of Luxembourg, in November 2007, in which twenty absolute gravimeters took part. A short description of the data processing and adjustments will be presented here and will be followed by the presentation of the results. Two different methods were applied to estimate the relative offsets between the gravimeters. We show that the results are equivalent as the uncertainties of both adjustments overlap. The absolute gravity meters agree with one another with a standard deviation of 2 μgal (1 gal = 1 cm/s^2).

5.1 Introduction

On November 6th to November 14th 2007, Luxembourg's European Center for Geodynamics and Seismology (ECGS) hosted an international comparison of absolute gravimeters in the Underground Laboratory for Geodynamics in Walferdange (WULG). Twenty gravimeters from 15 countries (from Europe and 1 team from China) took part the comparison. Four different types of gravimeters were present: 17 FG5's, 1 Jilag, 1 IMGC and 1 prototype MPG#2 (Table 5.1).

O. Francis (✉)
Faculty of Sciences, Technology and Communication, University of Luxembourg, Luxembourg L-1359, Grand-Duchy of Luxembourg
e-mail: olivier.francis@uni.lu

In 1999, a laboratory (Fig. 5.1) dedicated to the comparison of absolute gravimeters was built within the WULG. The laboratory lies 100 m below the surface at a distance of 300 m from the entrance of the mine. The WULG is environmentally stable (i.e., constant temperature and humidity within the lab), and is extremely well isolated from anthropogenic noise. It has the power and space requirements to be able to accommodate up 16 instruments operating simultaneously.

Multiple absolute gravimeter comparisons are regularly carried out. Being absolute instruments, these gravimeters cannot really be calibrated. Only some of their components (such as the atomic clock and the laser) can be calibrated by comparison with known standards. The only way one currently has to verify their good working order is via a simultaneous comparison with other absolute gravimeters of the same and/or if possible even of a different model, to detect possible systematic errors.

During a comparison, we cannot estimate how accurate the meters are: in fact, as we have no way to know the true value of g, we can only investigate the relative offsets between instruments. This means that all instruments can suffer from the same unknown and undetectable systematic error. However, differences larger than the uncertainty of the measurements, is usually indicative of a possible systematic error.

For the second comparison in Walferdange, a few new procedures have been introduced. First, some of the participants accepted to take part in a European Association of National Metrology Institutes

S.P. Mertikas (ed.), *Gravity, Geoid and Earth Observation*, International Association of Geodesy Symposia 135,
DOI 10.1007/978-3-642-10634-7_5, © Springer-Verlag Berlin Heidelberg 2010

Table 5.1 Participants in the European comparison of absolute Gravimeters in Walferdange – November 2007

Country	Institution	Absolute gravimeter
Austria	Federal office of metrology and surveying (BEV)	JILAg#6
Luxembourg	University of Luxembourg/ECGS	FG5#216
Belgium	Royal observatory of Belgium	FG5#202
China	China earthquake administration (CEA)	FG5#232
Czech Republic	Geodetic observatory Pecny	FG5#215
Finland	Finnish geodetic institute	FG5#221
France	CNRS – Géosciences montpellier	FG5#228
	EOST, Strabourg	FG5#206
Germany	Leibniz Universität Hannover	FG5#220
	Bundesamt für Kartographie und Geodäsie	FG5#101
	University Erlangen-Nuremberg	MPG#2
Italy	Istituto Nazionale di Ricerca Metrologica (INRIM)	IMGC#02
	Italian space agency	FG5#218
Norway	University of environmental and life sciences	FG5#226
Poland	Institute of Geodesy and Geodetic – Warsaw University of Technology	FG5#230
Spain	National Geographic Institute of Spain	FG5#211
Sweden	National Land Survey of Sweden – Geodetic Research Division	FG5#233
The Netherlands	Faculty of Aerospace Engineering DEOS/PSG	FG5#234
United Kingdom	Proudman Oceanographic Laboratory	FG5#222
	Natural Environnement Research Council	FG5#229

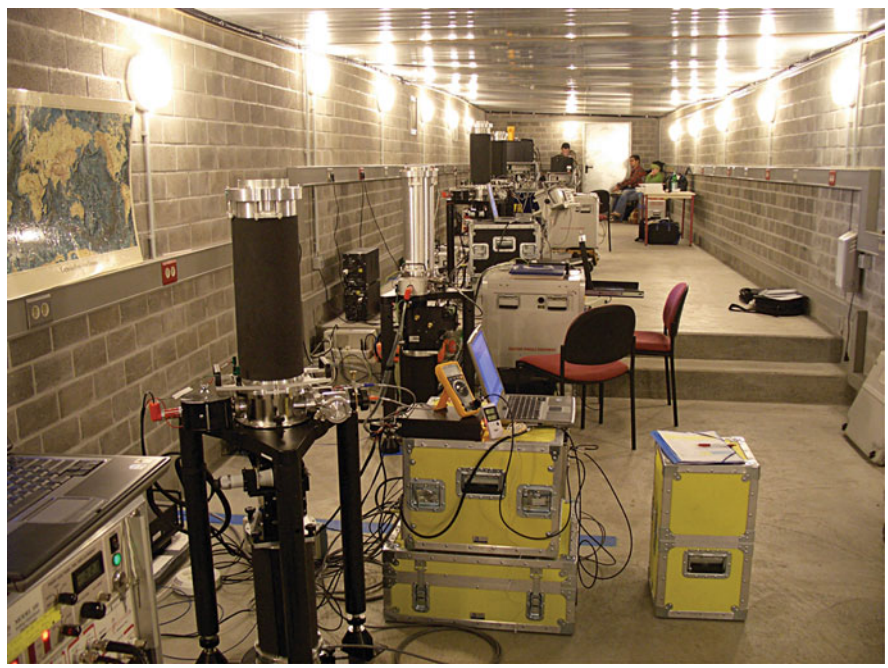


Fig. 5.1 Picture taken during the comparison of absolute gravimeters in the Underground Laboratory for Geodynamics in Walferdange

(EUROMET) Pilot Study in anticipation of the next key comparison at the BIPM in November 2009. This means that metrological rules of comparison were strictly followed. Secondly, it has been decided that the raw observations will not be processed by the same individual with the same software as in the past comparisons. Each operator had to process the data himself and present his results. This allows us to test the instruments as well as the data processing done by the operators. Third, for the first time during a



Fig. 5.2 Hourly record of the superconducting gravimeter CT40 in the WULG during the comparison corrected for tides and barometric effect pressure

comparison, a superconducting gravimeter was continuously recording the environmental gravity changes (Fig. 5.2).

The observed variation is about 1 μgal. At this stage, no correction based on this data set has been applied yet. Finally, due to the large number of instruments, the comparison was split in two sessions of 3 days each.

5.2 Protocol

Ideally to compare gravimeters, they should measure at the same site at the same time. Obviously, this is impossible for a practical point of view. Thus, the comparison was spread over 3 days. The first day, each instrument was installed at one of the 16 bench marks or sites. The second day, as the WULG is composed of three different platforms, all instruments moved to another site on a different platform and again on the third day. Overall, each instrument occupied at least 3 sites one on each platform. We also planned the observations in such a way, that two different instruments which occupied the same site did not measure at another common site again. This allows us to compare each instrument to as many other instruments possible.

5.3 Data Processing

Each operator provided the final g-values and their uncertainties for each station occupation. To process the data, they used the vertical gravity gradients and the observed tidal parameters obtained from the analysis of a 3-year record of the superconducting gravimeter in WULG. The atmospheric pressure effect was removed using a constant admittance and the polar motion effect using pole positions from IERS. The vertical gravity gradient was measured by three different operators (O. Francis, M. Van Camp and P. Richard) with two Scintrex CG3-Ms and one Scintrex CG5 before the 2003 comparison (Francis and T. van Dam, 2006). Gradients were remeasured in 2007 by O. Francis. As no significant variations have been observed, the same values as those used in 2003 have been applied. Comparisons between the rubidium clocks and the barometers were carried out by M. Van Camp and R. Falk. The results of these calibrations were communicated to the operators who were responsible for using these calibrations or not in the data processing. We did not have any laser calibrations as the WULG is not equipped for this.

5.4 Adjustment of the Data

Data from one instrument (MPG#2) were discarded as the instrument, being a prototype, had a significant offset that would have biased the final adjustment.

As each gravimeter measured at only 3 sites of the 16 sites, the g-values have to be adjusted to compare the results of all the gravimeters. Two different approaches for adjusting the data have been carried out.

In the first approach, O. Francis performed a least-square adjustment of the absolute gravimeters measurements using the following observation equation:

$$g_{ik} = g_k + \delta_i + \varepsilon_{ik}$$

with the condition

$$\sum_i \delta_i = 0$$

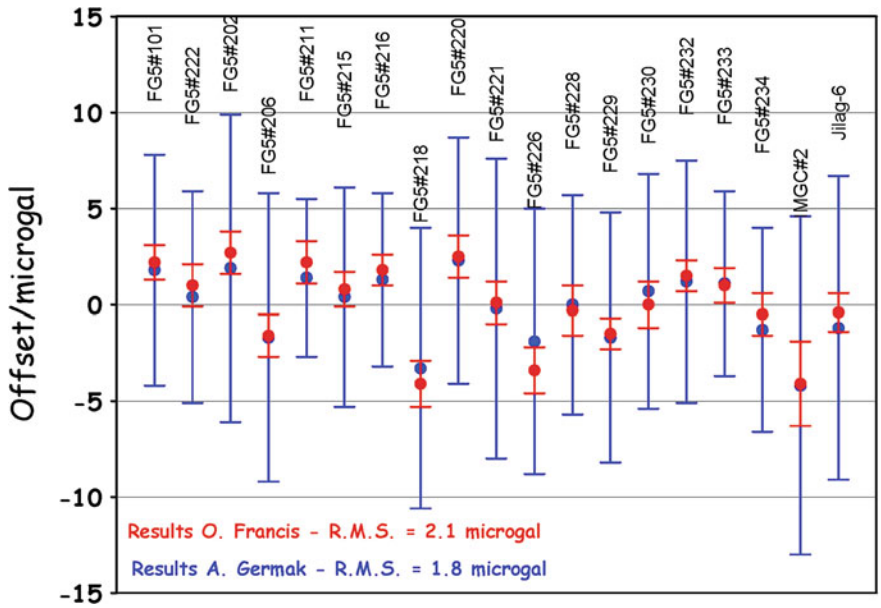


Fig. 5.3 Relative offsets between the gravimeters for two different methods of adjustment (O. Francis in red and A. Germak in blue) (for colors, see online version)

where g_{ik} is the gravity value at the site k given by the instrument i, g_k is the adjusted gravity value at the site k, δ_i the offset of gravimeter i and ϵik the stochastic error. The condition that the sum of the offsets should be zero is essential, otherwise the problem is ill-posed and numerically unstable. Without this condition, there is an infinite number of solutions: if one finds a solution (i.e., a set of the theoffsets of each instrument), on could find another solution simply by adding the same constant value to each offset. This expresses mathematically that one cannot estimate the true g value but only a reference value which is defined as the most likely value.

As a priori error, the mean set standard deviation as given by the operator plus a systematic error of 2 μgal has been implemented. The results are shown in

Table 5.2 Results of the adjustement of all the absolute gravity data expressed in microgal after subtstraction of the reference value 980,960,000 μgal for two different methods of adjustment (OF = O. Francis and AG = A. Germak)

Site	g value OF/μgal	g value AG/μgal	Difference
A1	4,227.4 ±1.0	4,228.2 ± 1.0	–0.8
A2	4,216.4 ± 1.0	4,216.4 ± 1.2	0.0
A3	4,206.6 ± 1.2	4,206.4 ± 3.1	0.2
A4	4,192.6 ± 1.1	4,193.4 ± 0.6	–0.8
A5	4,184.7 ± 1.1	4,184 ± 1.1	0.7
B1	4,079.3 ±1.2	4,080.6 ± 0.6	–1.3
B2	4,070.6 ± 2.1	4,067.2 ± 1.0	3.4
B3	4,069.0 ± 0.6	4,069.7 ± 0.6	–0.7
B4	4,064.5 ± 1.0	4,063.2 ± 0.8	1.3
B5	4,049.9 ± 1.0	4,050.8 ± 0.7	–0.9
C1	3,951.9 ± 0.9	3,951 ± 1.0	0.9
C2	3,949.3 ± 0.9	3,949.7 ± 1.1	–0.4
C3	3,949.3 ± 0.9	3,949.5 ± 1.0	–0.2
C4	3,946.5 ± 1.1	3,946.2 ± 1.6	0.3
C5	3,943.8 ± 1.0	3,944.8 ± 1.2	–1.0
C6	3,943.9 ± 1.0	3,944.5 ± 1.4	–0.6

Table 5.3 Relative offsets between the gravimeters for two different methods of adjustment (OF = O. Francis and AG = A. Germak)

Instrument	Offset OF/μgal	Offset AG/μgal	Difference
FG5#101	2.2 ± 0.9	1.8 ± 6.0	0.4
FG5#222	1.0 ± 1.1	0.4 ± 5.5	0.6
FG5#202	2.7 ± 1.1	1.9 ± 8.0	0.8
FG5#206	–1.6 ± 1.1	–1.7 ± 7.5	0.1
FG5#211	2.2 ± 1.1	1.4 ± 4.1	0.8
FG5#215	0.8 ± 0.9	0.4 ± 5.7	0.4
FG5#216	1.8 ± 0.8	1.3 ± 4.5	0.5
FG5#218	–4.1 ± 1.2	–3.3 ± 7.3	–0.8
FG5#220	2.5 ± 1.1	2.3 ± 6.4	0.2
FG5#221	0.1 ± 1.1	–0.2 ± 7.8	0.3
FG5#226	–3.4 ± 1.2	–1.9 ± 6.9	–1.5
FG5#228	–0.3 ± 1.3	0.0 ± 5.7	–0.3
FG5#229	–1.5 ± 0.8	–1.7 ± 6.5	0.2
FG5#230	0.0 ± 1.2	0.7 ± 6.1	–0.7
FG5#232	1.5 ± 0.8	1.2 ± 6.3	0.3
FG5#233	1.0 ± 0.9	1.1 ± 4.8	–0.1
FG5#234	–0.5 ± 1.1	–1.3 ± 5.3	0.8
IMGC#2	–4.1 ± 2.2	–4.2 ± 8.8	0.1
Jilag-6	–0.4 ± 1.0	–1.2 ± 7.9	0.8
RMS	2.1	1.8	

Fig. 5.3 and in Tables 5.2 and 5.3. The error bars are the a posteriori standard deviation resulting from the least-square fit.

In the second approach, A. Germak took the average value at each site and calculated the difference for each instrument with the average value. He obtained three values of the offset for each instrument corresponding to the three occupations. The mean value was then calculated as well as the standard deviation. The uncertainty assessment in this approach is much more elaborate than in the first approach. The operators were asked to provide as complete as possible a description of the stochastic and systematic errors affecting their gravimeters. The reported expanded uncertainty of measurement shown in Fig. 5.3 for the blue results is stated as the standard uncertainty of measurement multiplied by the coverage factor $k = 2$, which for a normal distribution corresponds to a coverage probability of approximately 95%.

Both approaches give equivalent results with differences less than 1 μgal except for the FG5#226. However, the estimated uncertainties are much bigger for the second approach. This could be explained partly by the coverage factor which is not applied in the first approach and by the more complete and detailed budget error used in the second approach.

5.5 Conclusions

The second international comparison of absolute gravimeters in Walferdange shows an overall agreement between the participating gravimeters of between 1.8 and 2.1 μgal depending on the method used for the final adjustment. The minimum and maximum offsets are –4.2 and 2.7 μgal.

This result demonstrates the importance of the comparison in particular if different gravimeters are used at different epochs at the same station for monitoring long term gravity variations with a precision of a few microgal. The instrumental offsets are not a limitation if they are properly monitored during comparisons.

References

Francis, O. and T. van Dam (2006). Analysis of results of the International Comparison of Absolute Gravimeters in Walferdange (Luxembourg) of November 2003, *Cahiers du Centre Européen de Géodynamique et de Séismologie*, 26, 1–23.

Chapter 6

Aerogravity Survey of the German Bight (North Sea)

I. Heyde

Abstract The Federal Institute of Geosciences and Natural Resources (BGR) is carrying out gravity surveys onboard marine research vessels since the 1960s. Since 1984 these measurements are performed with the KSS31 gravity meter system. This system has been modified and complemented during the last years to use it for aerogravity surveys as well.

In May 2007 the first aerogravity campaign was carried out with the complete system. Gravity data of the main part of the German exclusive economic zone in the North Sea were obtained. During 17 flights 32 northwest-southeast running profiles with a spacing of 5 km and 11 tie profiles with a spacing of 20 and 30 km respectively were surveyed. The total profile length added up to 10,500 km. The standard survey altitude was 1,000 ft. above sea level. Depending on the wind speed and direction the survey ground velocity ranged between 170 and 230 km/h.

In order to get the free air gravity anomalies several reductions to the measured gravity data have to be applied. For this purpose the flight trajectories were determined with high accuracy. Kinematic GPS data of 3 antennae were recorded and combined with the data of an inertial navigation system. One GPS base station was operated at the airfield. Additional base station data were obtained as necessary from the Land Survey Offices of Schleswig-Holstein and Niedersachsen.

The measured free-air gravity anomalies have an accuracy of about 4 mgal with a spatial resolution of 5 km half-wavelength. Comparative marine gravity measurements were carried out with the same gravity meter system during a BGR cruise with R/V FRANKLIN in June/July 2007. The agreement is satisfactory. The combined data sets result in a free-air gravity anomaly map of the German EEZ in the North Sea.

I. Heyde (✉)
Federal Institute for Geosciences and Natural Resources (BGR), Hannover 30655, Germany
e-mail: ingo.heyde@bgr.de

6.1 Introduction

A gravity sensor which is mounted on a moving platform measures the sum of the gravity and the inertial accelerations of the system motion. During aerogravity surveys the inertial accelerations can be 1,000 times higher than the gravity effect of different geological units. The inertial accelerations can be deduced from the movement of the aircraft. Therefore it is necessary to measure the flight trajectory with a non-inertial satellite navigation system like the GPS. The navigation data are also indispensable to calculate further corrections to determine the free-air gravity anomalies from the measured gravity sensor data.

Since 1984 marine gravity measurements at BGR are performed with the KSS31 gravity meter system manufactured by Bodenseewerk Geosystem GmbH. The KSS31 is considered to be the best sea gravity meter world wide. The system was updated to the KSS31M by Bodensee Gravitymeter Geosystem GmbH (BGGS), the successor company of the Bodenseewerke in 2001. This modified and complemented system can be used for aerogravity surveys. Due to the experiences of test flights in 2003 and 2005 (Heyde und Kewitsch, 2006) the system was improved concerning the recording of the platform movements

S.P. Mertikas (ed.), *Gravity, Geoid and Earth Observation*, International Association of Geodesy Symposia 135,
DOI 10.1007/978-3-642-10634-7_6, © Springer-Verlag Berlin Heidelberg 2010

and an INS system was added to enhance the quality of the GPS data and to record the flight attitude. In May 2007 the first major aerogravity campaign was carried out to test the performance of the updated system and its capability to deliver accurate data for mapping an area. Gravity data of the main part of the German exclusive economic zone in the North Sea were obtained.

6.2 The Aerogravity System

The complete aerogravity system consists of the gravity sensor, navigation system and data recording and processing unit. The system is shown in Fig. 6.1.

The gravimeter system KSS31M is a high performance instrument for marine gravity measurements, manufactured by the Bodenseewerk Geosystem GmbH. While the sensor is based on the Askania type GSS3 sea gravimeter designed by Prof. Graf in the 60ties, the development of the horizontal platform and the corresponding electronic devices took place at the Bodenseewerk Geosystem in the second half of the 70ties. The KSS31M system consists of two main assemblies: the gyro-stabilized platform with gravity sensor and the data handling subsystem. The system was modernized and modified in 2001 by BGGS. The modifications affected mainly the control electronics and the power supply and resulted in a considerable loss of volume and weight of the system. The sensor itself and the gyro-stabilized platform have not been changed up to now.

The gravity sensor consists of a tube-shaped mass that is suspended on a metal spring and guided frictionless by threads. It is non-astatized and particularly designed to be insensitive to horizontal accelerations. This is achieved by limiting the motion of the mass to the vertical direction. Thus it is a straight line gravity meter avoiding cross coupling effects of beam type gravity meters. The measuring range of the sensor amounts to 10,000 mgal with a drift rate of less than 1 mgal/month. The sensitivity is 0.01 mgal and the accuracy in static operation is ±0.02 mgal. In dynamic operation and without special data processing the accuracy ranges from ±0.5 mgal (vertical accelerations < 0.15 m/s^2) and ±2 mgal (vertical accelerations 0.8 – 2 m/s^2). The system can be operated during accelerations of up to 4 m/s^2. The leveling subsystem consists of a platform stabilized in two axes by a vertical electrically erected gyro. The stabilization during course changes can be improved by providing the



Fig. 6.1 Aerogravity system consisting of the KSS31M gravity meter (platform with sensor and electronics rack), GPS instrumentation, INS unit and laptop

system with online navigation data. This control works fine for shipborne measurements. For airborne surveys the platform errors are significant and have to be measured.

To obtain the best navigational results NovAtel OEM4 L1/L2 GPS receivers were used, both as base and as kinematic receivers. During the campaign a GPS base station on the airfield of Wilhelmshaven-Mariensiel was operated. Two rover receivers each with an own GPS antenna were run in the airplane. Additionally a NovAtel SPAN system was installed. It consists of a DL4Plus (OEM4 L1/L2) GPS receiver and an IMU-G2 inertial unit containing 3 accelerometers and 3 high precision ring laser gyros (Honeywell HG1700 AG58). The two components are integrated through receiver firmware that combines the GPS and inertial data to provide a joint solution (Kennedy et al., 2007). The evaluation of the navigation data was carried out by post-processing. Post-processing offers the advantage that further information concerning precise satellite ephemeris and above all one or more static reference stations can be considered. The DGPS software used was Inertial Explorer (version 7.70) from Waypoint Inc. It integrates rate data from six degrees of freedom IMU sensors with GPS data processed with an integrated GPS post-processor.

For the registration of analogue voltage signals a multimeter is used, which is controlled by a laptop. The software LabVIEW7.1 is used for data acquisition and processing. A second laptop was operated for flight guidance and management. Its display was duplicated to a second screen for the pilot.

6.3 System Installation

The flights were carried out with an Aero Commander 680 FL of Air Tempelhof Fluggesellschaft mbh & Co. KG (Fig. 6.2). The aircraft, usually used for aero photography, was very appropriate for the survey. The installation of the instruments in the cabin is shown in Fig. 6.2.

GPS aero antennas were installed on the hull above the gravity sensor, on the right wing and on the right of the horizontal tail. During post-processing it turned out that the GPS data of the 3rd antenna were throughout of lower quality than the other two. Mostly the number of satellites was reduced probably resulting from the shadowing effects of the empennage. Thus only the data of two rover receivers were considered for the data processing.

6.4 Aerogravity Survey of the German Bight

The flights were performed in May 2007 from the airfields Wilhelmshaven and Husum. During 17 flights 32 northwest-southeast running profiles with a spacing of 5 km and 11 tie profiles with a spacing of 20 and 30 km respectively were surveyed (Fig. 6.3). The total profile length added up to 10,500 km. Subtracting data during bad flight conditions and above all data after turns of the aircraft, data along a profile length of 9,000 km were useable.

The standard survey altitude was 1,000 ft. above sea level. Depending on the wind speed and direction the survey velocity ranged between 170 and 230 km/h. One GPS reference station was run in Wilhelmshaven. Additional reference data were bought after the campaign from the Land Survey Offices of Niedersachsen and Schleswig-Holstein.

6.5 Data Processing

To obtain the gravity variation, the following corrections have to be determined:

- Eoetvoes correction
- Correction of the inertial vertical accelerations
- Platform error or Harrison correction

The gravity variation in the flight altitude is the principal measured variable in an aerogravity survey. However, the preferable result for geophysical applications are free-air gravity anomalies. They are to be obtained by applying the following reductions to the gravity variation:

- Normal gravity reduction
- Free-air reduction

The Eoetvoes correction, the normal gravity and the free-air reduction can be calculated directly from

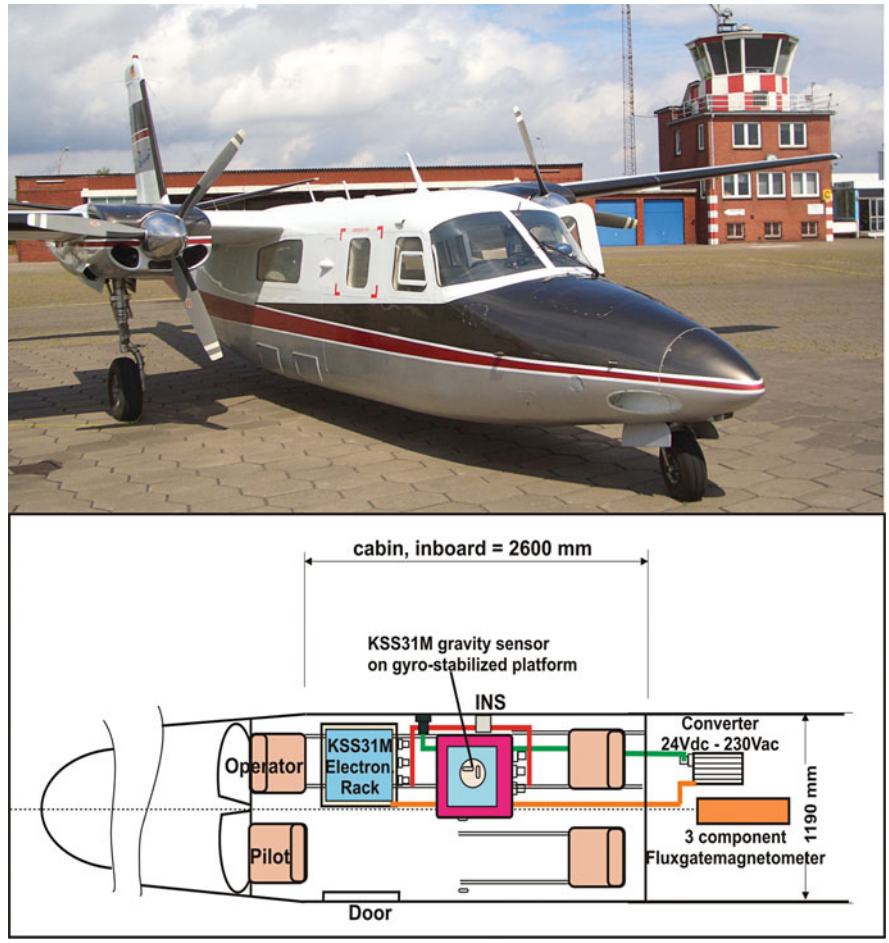


Fig. 6.2 Aero Commander 680 FL of Air Tempelhof (above). System installation in the aircraft cabin is shown below

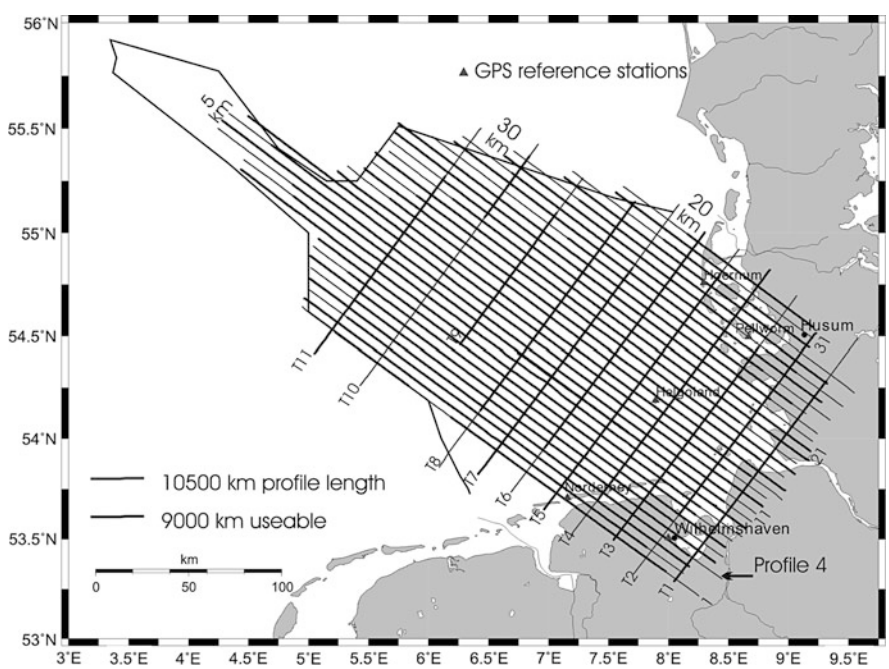


Fig. 6.3 Map of the profiles flown during the campaign

the positions and velocities, which were obtained by DGPS/INS post-processing. For the Eoetvoes correction formula the flight altitude is considered (Harlan, 1968). The normal gravity is calculated according to the GRS 1980 (Moritz, 1984). The inertial vertical acceleration is determined by gradient calculation of the vertical velocity. For the Harrison correction the error angles and the horizontal and vertical accelerations of the platform are used.

Before the values can be applied they have to be lowpass filtered with the so-called sensor copy filter describing the behaviour of the gravity sensor. Figure 6.4 shows exemplary the results along the 280 km long SE-NW running profile 4. The variation of the measured gravity and the vertical accelerations correlate directly with the variation of the flight altitude. The variation gets smaller with the reduced thermal above the sea than overland at the beginning of the profile. The amplitudes of up to ±6,000 mgal demonstrate the challenge to elaborate from the data geological anomalies with amplitudes of some mgal only.

Obviously the data have to be low-pass filtered. Good experiences were gained during the first system tests with Bessel filters (Heyde und Kewitsch, 2006). Figure 6.5 shows the results after filtering with a 3rd order Bessel filter with a corner frequency of 471 s. This ensures the presence of data with 200 s period and thus a spatial resolution of about 5 km half-wavelength considering the flight velocity. Whereas the differences of the further corrections and reductions are below 0.5 mgal using the 4 different navigation data sets, the differences of the vertical acceleration values are considerable higher. In the lower part of Fig. 6.5 the 4 vertical acceleration data calculated from the navigation data sets are shown together with the measured gravity including all corrections except for the vertical acceleration.

The differences between the data sets amount to less than 5 mgal on this profile. Along other profiles the differences are significant higher. Figure 6.6 shows the free-air gravity anomalies along profile 4 using the different DGPS/INS data sets for the corrections of the vertical accelerations.

Taking the quality of the DGPS/INS solution as decision support which free-air gravity data were favoured, for nearly all profiles the rover 7 with INS data were used. The antenna location and the smallest lever arm both to the gravity sensor and the INS unit resulted in the best navigation data.

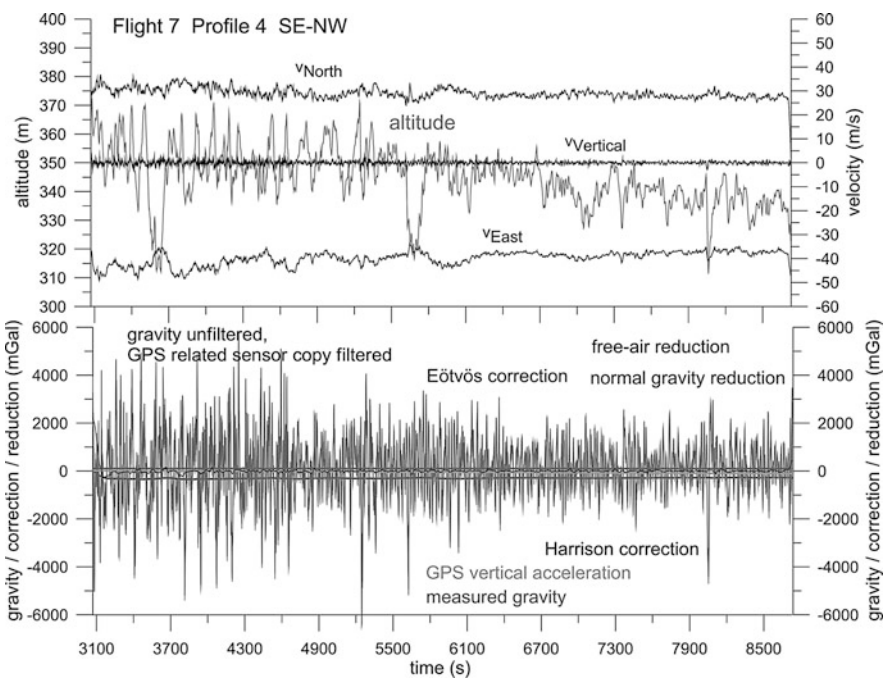


Fig. 6.4 Flight altitude and velocities along survey profile 4 (above). Measured gravity and calculated corrections and reductions along the profile are shown below

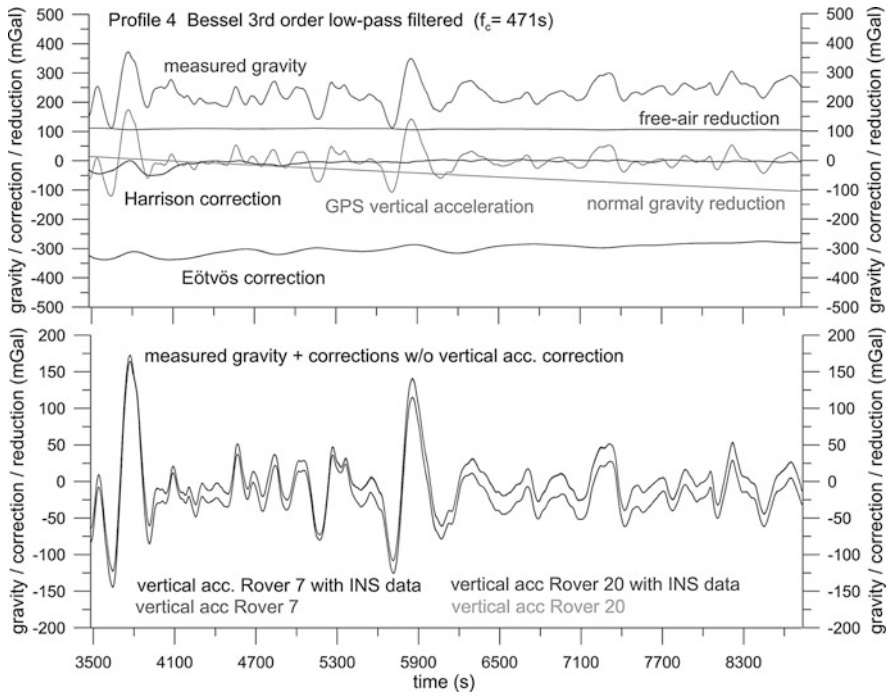


Fig. 6.5 Low-pass filtered values along profile 4 (above). Comparison of different DGPS/INS data sets used for the determination of vertical accelerations are shown below

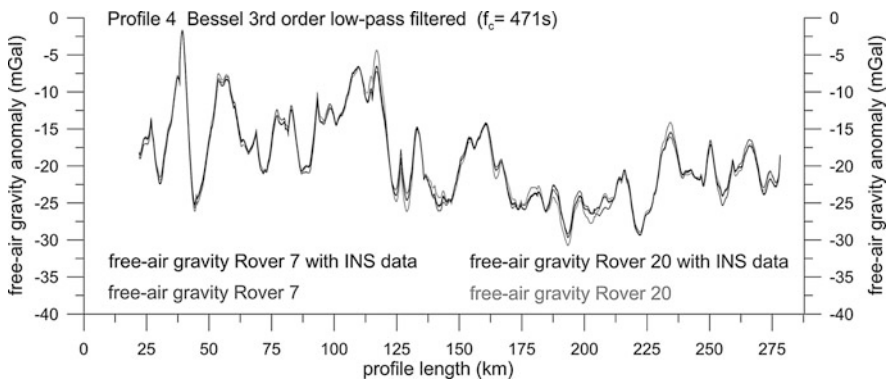


Fig. 6.6 Free-air gravity anomalies along profile 4 using different DGPS/INS data sets

6.6 Data Accuracy

To evaluate the accuracy of the free-air gravity data, the differences at these crossovers were examined. The map of the differences is shown in Fig. 6.7. There is no pronounced areal distribution and time dependence. Thus no adjustment was applied to the profile data. A histogram of the differences is shown in Fig. 6.8. The mean difference amounts to 3 mgal. This value represents the accuracy of the measurements after applying the mentioned low-pass filter guaranteeing a spatial resolution of 5 km half-wavelength. The value could be reduced by further or stronger low-pass filtering at the expense of reduced spatial resolution.

6.7 Map of the Free-Air Gravity Anomalies

Figure 6.9 shows the map of the free-air gravity anomalies based on the 43 profiles with a total length of 9,000 km. The anomalies range from –45 mgal in the North Sea Basin around Helgoland to +40 mgal northwest of Sylt.

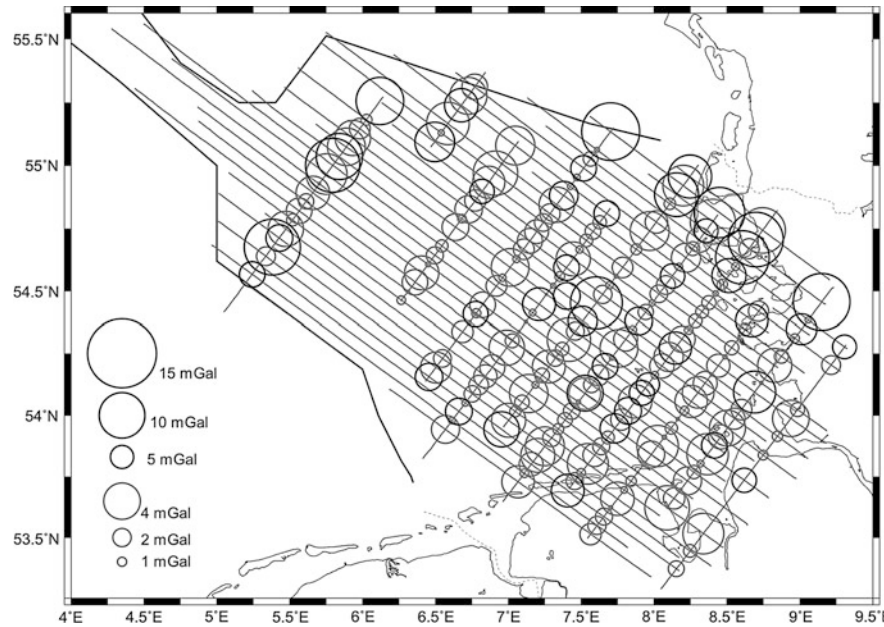


Fig. 6.7 Map of the value differences at profile crossovers

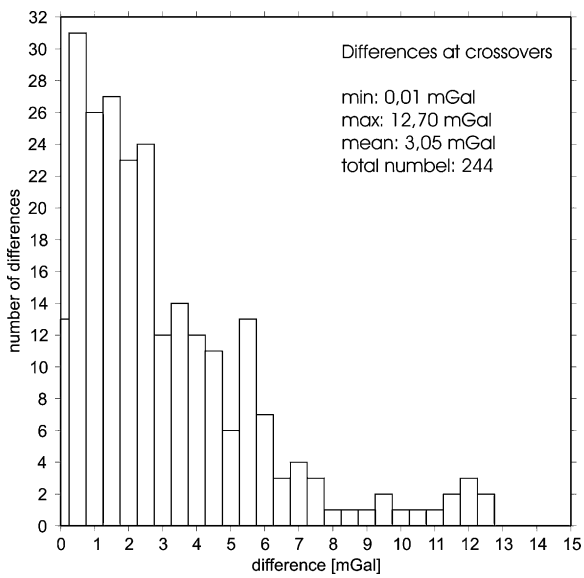


Fig. 6.8 Histogram of the value differences at the 244 profile crossovers

In June/July 2007 marine gravity measurements were carried out with the same gravity meter during cruise BGR07 with R/V FRANKLIN (Neben et al., 2007). The aim of the cruise was a detailed survey in the north westernmost area of the German EEZ (exclusive economic zone), the so-called "Entenschnabel". The marine gravity data were gathered both to compare the airborne measurements with ground truth data and to complete the data in the NW. The location of the marine profiles (blue) is shown together with the aero profiles (red) in Fig. 6.10. Along four lines there is in parts an agreement of the run of marine and aero profiles. Figure 6.11 shows the comparison of the free-air gravity data along two profiles. The consistence between the data is rather good, especially, if the aero profile data are additionally low-pass filtered. The marine data are not upward continued due to the low flight altitude. Considering the error of the marine data as insignificant the accuracy of the aero data amounts again to about 4 mgal.

The aero gravity data were combined with the BGR07 marine data and land gravity data of Northern Germany. The land gravity data from the Leibniz Institute for Applied Geosciences (GGA) in Hannover have for the most parts a spacing of 5–10 km. Figure 6.12 shows the free-air gravity anomaly map combining the 3 datasets. The aero gravity data were filtered again with a 10 km 2D low-pass median filter (Wessel and Smith, 1998). The broad gravity minimum in the middle corresponds to the southern North Sea basin. Further elongated minima reflect the runs of the Central Graben and the Horn Graben. The gravity maximum in between corresponds to a carboniferous/devonian basement high. This constitutes an extension of the Rynkøbing-Fyn high further east characterized by gravity maxima also.

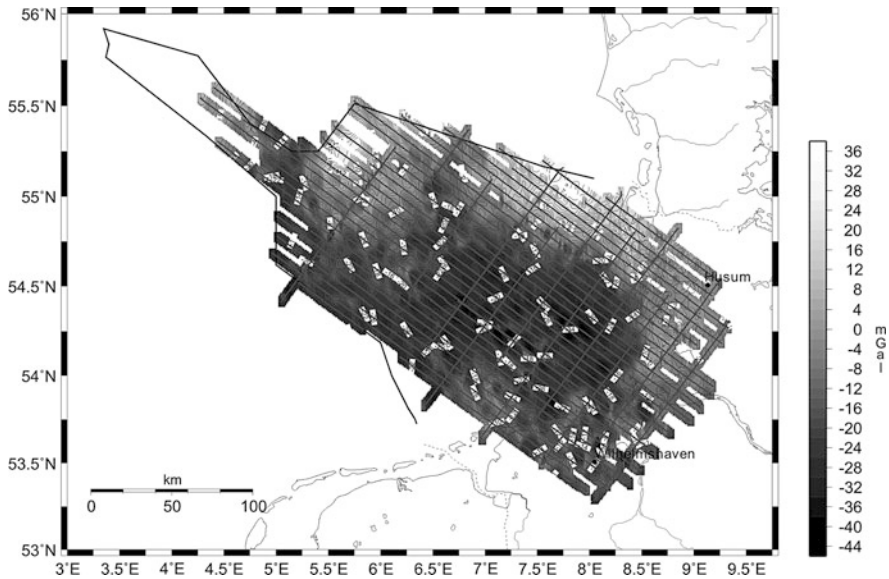


Fig. 6.9 Map of the free-air gravity anomalies in the survey area based on a 0.5 × 0.5 min grid. The map is drawn up to a distance of 3 (arc-) minutes from the lines

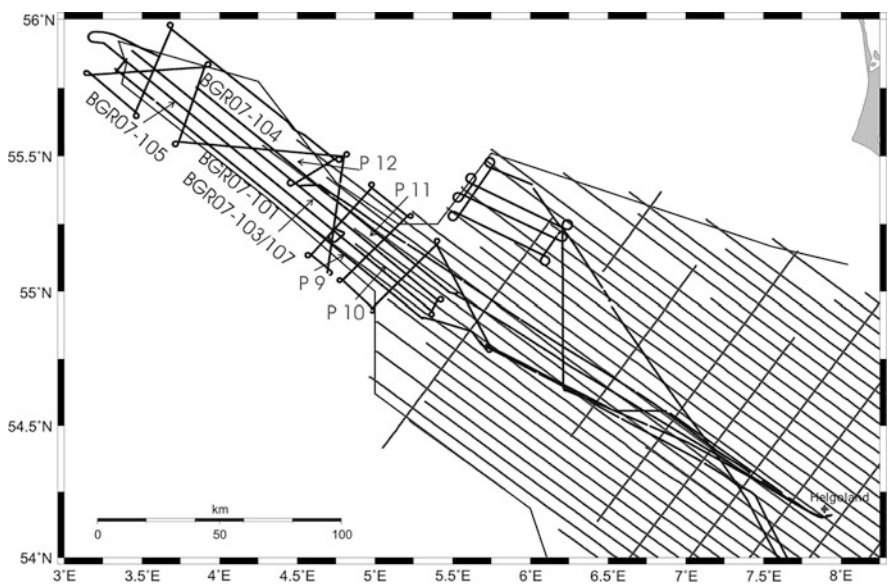


Fig. 6.10 Map of the marine (*blue*) and aero (*red*) profiles in the north western survey area. The nearly identically running profiles are marked (for colors, see online version)

6.8 Summary and Further Work

The survey in the German Bight showed that the KSS31M can be applied for aerogravity surveys. A new gravity data set for a large part of the German EEZ in the North Sea was acquired. With the KSS31M and the NovAtel GPS/INS equipment BGR has now a tested aerogravity system ready for operation. The accuracy of the free-air gravity data amounts to about 4 mgal with a spatial resolution of 5 km.

The behaviour of the sensor and particularly the platform have to be examined and optimized further to improve the accuracy of the data. Therefore it is indispensable to involve BGGS GmbH. With the aid of our experiences BGGS should revise the platform control, which is based on discrete analogue technology from the beginning of the 1980s. Additionally BGGS is working at the control circuit of the gravity sensor with the aim to reduce its response time.

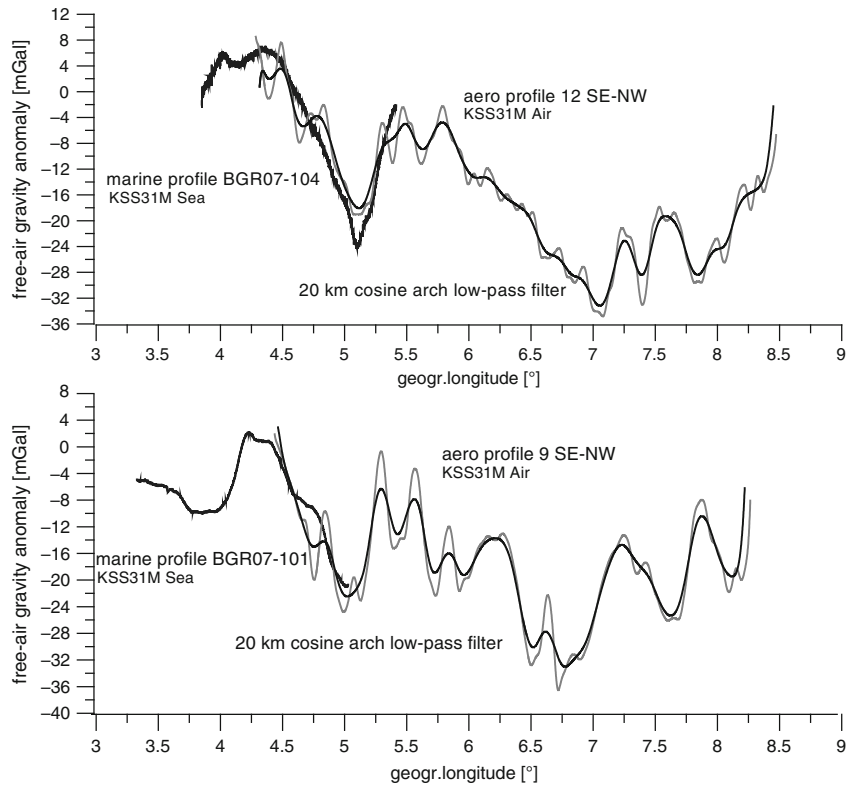


Fig. 6.11 Comparison of free-air gravity anomalies measured along nearly identical marine and aero profiles

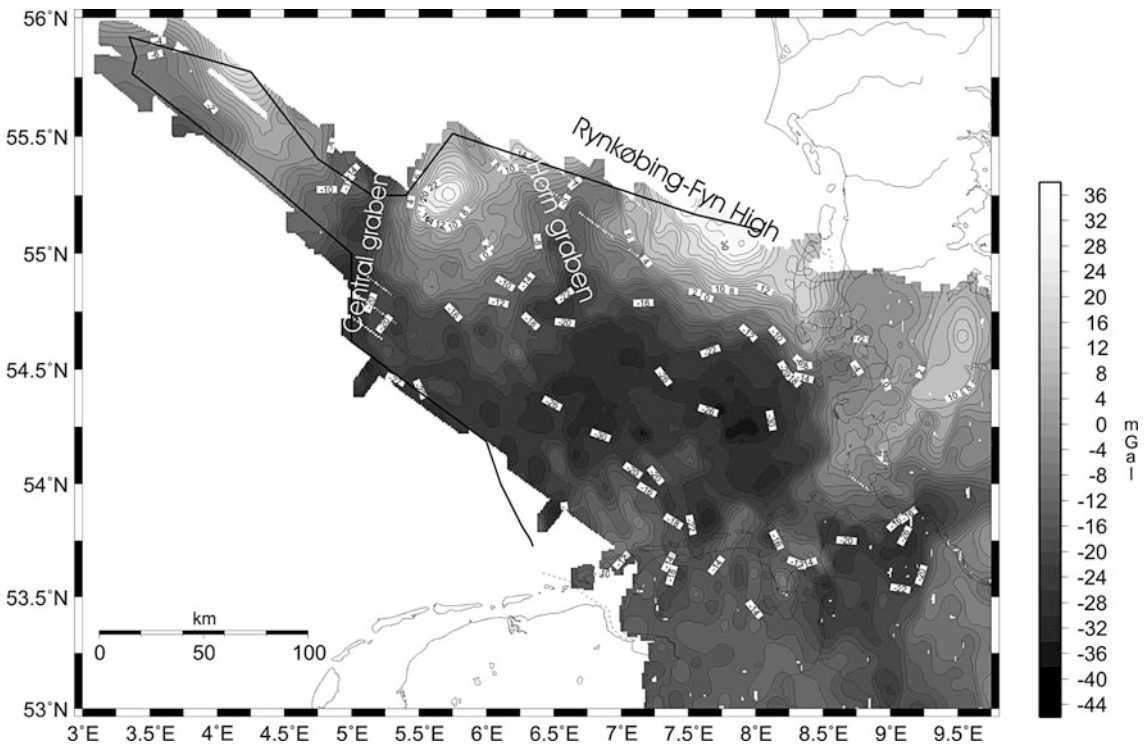


Fig. 6.12 Free-air gravity anomaly map combining the aero, BGR07 marine and land station gravity data. The map is drawn up to 3 (arc-) minutes from surveyed data

The pre-adjustment of the gravity sensor after profile changes should be applied routinely to reduce the actual settling time of 400 s.

However, the final accuracy is limited also by the accuracy of the DGPS/INS navigation data. The error of this data could be reduced by data of more satellites, which will be present if GALILEO becomes available.

References

Harlan, R.B. (1968). Eotvos corrections for airborne gravimetry. *J. Geophys. Res.*, 73(14), 4675–4679.

Heyde, I. und P. Kewitsch (2006). Neue flugergebnisse mit dem BGR-aerogravimetriesystem. – Vortrag: Tagungsband 66. Jahrestagung der Deutschen Geo-physikalischen Gesellschaft, S. 325–326, März 2006, Bremen.

Kennedy, S., D. Cosandier, and J. Hamilton (2007). GPS/INS Integration in Real-Time and Post-processing with NovAtel's SPAN System. International Global Navigation Satellite Systems Society Sym-posium 2007, Sydney.

Moritz, H. (1984). Geodetic reference system 1980. In: Tschernig, C.C. (ed), The geodesist's handbook 1984. *Bull. Geod.*, *58*, 388–398.

Neben, S., L. Reinhardt, and cruise participants (2007). BGR Cruise BGR07 FRANKLIN Leg 1: Geophysics Project: Nordsee. Cruise Report.

Wessel, P. and W. H. F. Smith (1998). New, improved version of generic mapping tools released. *EOS Trans. Am. Geophys. U.*, 79(47), 579.

Chapter 7

Results of the Seventh International Comparison of Absolute Gravimeters ICAG-2005 at the Bureau International des Poids et Mesures, Sèvres

L. Vitushkin, Z. Jiang, L. Robertsson, M. Becker, O. Francis, A. Germak, G. D'Agostino, V. Palinkas, M. Amalvict, R. Bayer, M. Bilker-Koivula, S. Desogus, J. Faller, R. Falk, J. Hinderer, C. Gagnon, T. Jakob, E. Kalish, J. Kostelecky, Chiungwu Lee, J. Liard, Y. Lokshyn, B. Luck, J. Mäkinen, S. Mizushima, N. Le Moigne, V. Nalivaev, C. Origlia, E.R. Pujol, P. Richard, D. Ruess, D. Schmerge, Y. Stus, S. Svitlov, S. Thies, C. Ullrich, M. Van Camp, A. Vitushkin, and H. Wilmes

Abstract The International Comparison of Absolute Gravimeters ICAG-2005 was held at the Bureau International des Poids et Mesures (BIPM), Sèvres, France in September 2005. The organization of ICAG-2005, measurement strategy, calculation and presentation of the results were described in a technical protocol pre-developed to the comparison. Nineteen absolute gravimeters carried out 96 series of measurements of free-fall acceleration g at the sites of the BIPM gravity network. The vertical gravity gradients were measured by relative gravimeters. For the first time the budgets of uncertainties were presented.

The g-values for the sites A and B of the BIPM gravity network at a height of 0.90 m are (980,925,702.2 $\pm$ 0.7) μGal and (980,928,018.5 $\pm$ 0.7) μGal, respectively. This result is in a good agreement with that obtained in ICAG-2001.

7.1 Introduction

The 7th from 1980 comparison ICAG-2005 at the BIPM was organized by the Working Group on Gravimetry of the Consultative Committee on Mass and Related Quantities, Study Group 2.1.1 on Comparison of Absolute Gravimetry of the International Association of Geodesy (IAG) and the BIPM.

Comparing the measurement results of absolute gravimeters of the highest metrological quality in the ICAGs at the BIPM as well as in the Regional Comparisons of Absolute Gravimeters (RCAG) (see, for example, Vitushkin et al., 2002; Boulanger et al., 1981; Francis et al., 2007) is currently the only way to test the uncertainty in absolute g-measurements and to determine the offsets of individual gravimeters with respect to Comparison Reference Values (CRV) (Vitushkin, 2008; Vitushkin et al. 2007). The CRVs in the ICAGs and RCAGs are the g-values obtained at one or more gravity stations at BIPM or at the sites of RCAGs.

The ICAGs and RCAGs may be organized as a key comparison (KC) or as a pilot study (Vitushkin et al., 2007; CIPM, 1999). The KCs are organized to establish the equivalence of national measurement standards. The pilot study is more flexible in the invitation of the participants which could be not only the National Metrology Institutes or designated laboratories responsible for the metrology in gravimetry but also other organizations, for example, geodetic, geophysical and geological institutes or services.

The ICAG-2005 was organized as a pilot study but according to the rules for KCs concerning the technical protocol which specified the organization, measurement strategy, data processing, calculation of the uncertainties and presentation of the results and reports.

L. Vitushkin (✉)
Bureau International des Poids et Mesures (BIPM), Sèvres, France
e-mail: lvitushkin@bipm.org

S.P. Mertikas (ed.), *Gravity, Geoid and Earth Observation*, International Association of Geodesy Symposia 135,
DOI 10.1007/978-3-642-10634-7_7, © Springer-Verlag Berlin Heidelberg 2010

7.2 Absolute Measurements

The gravity network of the BIPM consists of four sites with 13 gravity stations. The site in the Observatory building consists of two pillars located in one laboratory room with three gravity stations A, A0 and A1 at one pillar and the gravity station A2 at the other. There is also the site in Pavillon du Mail where seven gravity stations B and B1–B6 are located on the 80-tons basement installed on the special elastic pads. Two outdoor gravity stations C1 and C2 are in the garden of the BIPM. The *g*-difference between the sites C1 and C2, located on the hill, is about 9 mGal.

Ninety Six absolute measurements were carried out by 19 absolute gravimeters at 11 gravity stations of the BIPM gravity network mainly in the period from 3 to 24 September. The gravimeter FG5-108 belonging to the BIPM started the measurements on 5 August and subsequently measured on A2, A, A2, A, C2, B, C1, B, B3. The measurements were performed in the night during about 12 h and such measurement was considered as an individual result. Up to nine AGs occupied simultaneously the sites of the BIPM during the comparison.

From 3 to 24 September the FG5-108 occupied the B3 for the regular "in-the-night" measurements to monitor the stability of the gravity field. With the same goal, the FG5-202 was used at the gravity station A2 from 6 to 21 September.

In Table 7.1 all the AGs participated in the ICAG-2005 are presented. In addition this table lists those gravimeters which participated in ICAG-1997 and ICAG-2001. The gravimeter IMGC-2 (Germak et al., 2002) and TBG are that with rise-and-fall trajectory of free-moving test body. All other are of a free-fall type.

The BIPM verified the frequencies of all the lasers used in the laser displacement interferometers of AGs and the frequencies of Rb clocks or GPS receivers used as the reference for the time interval measurement systems of AGs. The atmospheric pressure was also measured continuously during the comparison. Prior to the absolute measurements, the vertical gravity gradients were measured using fifteen relative gravimeters.

Table 7.1 Participation of institutes and gravimeters in ICAG-2005

		Gravimeter		
	Country, institute	1997	2001	2005
1	Germany, BKG	FG5-101	FG5-101	FG5-101
2	BIPM	FG5-108	FG5-108	FG5-108
3	Belgium, ORB	FG5-202	FG5-202	FG5-202
4	France, EOST	FG5-206	FG5-206	FG5-206
5	Switzerland, METAS		FG5-209	FG5-209
6	Spain, IGN		FG5-211	FG5-211
7	Japan, AIST/NMIJ		FG5-213	FG5-213
8	Czech Republic, GOP			FG5-215
9	Luxemburg, UL/ECGS			FG5-216
10	Finland, FGI	JILAg-5	JILAg-5	FG5-221
11	Chinese Taipei, CMS/ITRI			FG5-224
12	France, DLL CNRS/MU			FG5-228
13	USA/USGS			A10-008
14	USA/JILA CU/NIST			FGC-1
15	Russia/IAE RAS	GABL-E		GABL-G
16	Italy/INRiM	IMGC	IMGC	IMGC-2
17	Austria/BEV	JILAg-6	JILAg-6	JILAg-6
18	Canada/NRCan	JILA-2	JILA-2	JILA-2
19	Ukraine/NSC IM			TBG

7.3 Results of ICAG-2005

The result of the ICAG is the CRV with its uncertainty. For the evaluation of the results of the ICAG the operators provided the results of *g*-measurements performed at all the sites occupied by their gravimeters and the uncertainties of these measurements.

The important work on the evaluation of uncertainties was done by the operators, pilot laboratory and Task Group on Technical Protocol and Budget of Uncertainties of the CCM WGG and IAG SG 2.1.1. Currently the participants in ICAG-2005 are agreed on the unified assignment of the instrumental uncertainty of 2.3 μGal for the FG5-type gravimeters, FGC-1 and JILA-2 and on the unified site-dependent uncertainty of 1.1 μGal for the FG5-108, -202, -209, -211, -213, -216, -221, -224, FGC-1, A10-008 and GABL-G.

Table 7.2 shows the estimated uncertainties of the AGs participated in ICAG-2005. The instrumental uncertainty of A10-008 was presented by the operator without the detailed budget of uncertainties.

The expanded uncertainty of each gravimeter in the absolute measurement of FFA was evaluated according to the ISO (International Standartization Organization) guide (ISO, 1993), sometimes referred to as the GUM. The evaluation of instrumental and site-dependent uncertainties was based on the current knowledge of the variability of input quantities, the results of verification of the laser and Rb clock frequencies, theoretical

Table 7.2 Estimations of the uncertainties of absolute gravimeters participated in ICAG-2005

Gravimeters	Instrumental uncertainty/μGal	Site-dependent uncertainty/μGal	Experimental standard deviation/μGal	Expanded uncertainty/μGal
FG5	2.3	1.1–1.3	0.2–0.7	4.8–5.6
FGC-1	2.3	1.1	1.2–2.2	5.6–6.6
A10-008	5.9	1.1	2.1–3.8	12.4–14.2
JILA	1.8–2.6	1.0–2.1	0.2–0.9	5.0–7.0
IMGC-2	3.8	1.5	1.1–1.3	8.6
GABL-G	5.1	1.1	1.1–1.5	11.6–11.8
TBG	10.0	8.7	7.0–15.0	29–40.0

models for the evaluation of geophysical effects (tides, ocean loading, etc.), manufacturer's specifications, etc.

An expanded uncertainty U is defined by the formula:

$$U = k_{\mathrm{p}}\, u_{\mathrm{c}}, \tag{1}$$

where u_{c} is the combined uncertainty and k_{p} is the coverage factor. An expanded uncertainty defines an interval of the values of the measurand FFA that has a specified coverage probability or level of confidence p. The usual value of 95% was chosen for such a probability in the case of ICAG-2005. The coverage factor k_{p} is used as a multiplier of the combined standard uncertainty in order to obtain an expanded uncertainty. The values of k_{p} were obtained under the assumption that the resultant probability distribution is a Student's one and with the evaluation of effective degrees of freedom from the Welch-Satterthwaite formula (ISO, 1993).

Combined uncertainty u_{c} is the square root of the sum of the squared instrumental uncertainty, site-depended uncertainty and experimental standard deviation. The expanded uncertainties are then used for the evaluation of the weight of each measurement result in the CRV calculation.

The comparison of absolute gravimeters is not somewhat similar to the comparison, for example, of the measurement of line scales in dimensional metrology when the measurement results of such a traveling standard by means of each of the laser interference comparator are compared. In the ICAGs the g-measurements at several gravity stations by means of several AGs are carried out and not all the stations are measured by all the AGs.

For this reason the adjustment of the results of gravity measurement in the gravity network was used to evaluate the CRV and its uncertainty (Vitushkin et al., 2002).

The CRVs of ICAG-2005 at the gravity stations A and B were calculated using the combined adjustment of all the absolute and relative data obtained in the comparison. The final results of ICAG-2005 are presented in Tables 7.3 and 7.4, and in Fig. 7.1. All the g-values are expressed in microgals after the subtraction of the integer value $g_{\mathrm{r}} = 980{,}920{,}000$ μGal. The standard uncertainties u_{av} of the adjusted CRVs are also expressed in microgals.

Table 7.3 presents the g-values at a height of 0.9 m above the mark of corresponding gravity station and Table 7.4 presents the offsets of all the AGs with respect to CRV at the station A for various selections of the results of the absolute and relative measurements to be adjusted. The results of the adjustments of the results of only absolute and only relative measurement as well as the results of the combined adjustment of all the absolute and relative data are presented in these tables. The adjustment results with only the absolute measurements are presented for both unweighted and weighted data.

The ICAG-2005 CRVs with the standard uncertainties of adjusted values at the gravity stations A and B are (980,925,702.2 ± 0.7) μGal and (980,980,018.5 ± 0.7) μGal, respectively. This result is in a good agreement (within 1 μGal) with the g-values obtained at A and B in the ICAG-2001 (Vitushkin et al., 2002). The results of ICAG-2001 at A and B are (980,925,701.2 ± 0.9) μGal and (980,928,018.8 ± 0.9) μGal, respectively (see Table 7.4 in (Vitushkin et al., 2002)). It should be remarked that the results of ICAG-2001 are obtained with the some omitted gravimeters.

The differences between the g-values at A and B obtained using the adjustments of various combinations of the measurement results (absolute, relative, absolute and relative, etc.) are not greater than 1.4 μGal and 0.8 μGal, respectively.

Table 7.3 Results of the adjustment of the results of the absolute and relative measurements carried out during ICAG-2005 for each gravity station (at 0.90 m above the mark) expressed in microgals after subtraction of the integer value $g_r = 980{,}920{,}000$ μGal. The standard uncertainty of adjusted values u_{av} is expressed in microgals

	Results of adjustment of only unweighted absolute data		Results of adjustment of only weighted absolute data		Results of adjustment of only relative data		Results of combined adjustment of all the absolute and relative data	
Gravity station	$g-g_r$	u_{av}	$g-g_r$	u_{av}	$g-g_r$	u_{av}	$g-g_r$	u_{av}
1	2	3	4	5	6	7	8	9
A	5,703.3	0.5	5,702.7	0.5	5,701.9	1.1	5,702.2	0.7
A1	5,690.0	0.9	5,689.7	0.8	5,690.7	1.1	5,690.9	0.8
A2	5,710.0	0.8	5,709.4	0.6	5,707.1	1.1	5,707.4	0.8
B	8,018.0	0.5	8,018.8	0.5	8,018.8	1.0	8,018.5	0.7
B1	8,012.3	0.8	8,012.3	0.6	8,013.3	1.0	8,012.9	0.7
B2	7,996.4	0.7	7,997.9	0.7	7,997.6	1.0	7,997.2	0.7
B3	8,002.3	0.9	8,002.4	0.6	8,001.7	1.0	8,001.4	0.7
B5	8,022.0	0.9	8,022.3	0.8	8,020.5	1.0	8,020.1	0.7
B6	8,000.0	0.8	7,998.4	0.9	7,997.8	1.0	7,997.4	0.7
C1	3,279.9	1.2	3,281.6	1.0	3,281.6	1.1	3,282.3	1.1
C2	12,040.4	1.5	12,040.4	1.0	12,040.3	1.1	12,039.1	1.3

Table 7.4 The offsets of each absolute gravimeter with respect to CRV at the gravity station A for various adjustments of the data of the absolute and relative measurements carried out during ICAG-2005 (expressed in microgals after subtraction of $g_r = 980{,}920{,}000$ μGal). The standard uncertainty of adjusted values u_{av} is in microgals (i = FG5-101, FG5-108, FG5-202...)

	Results of adjustment of only unweighted absolute data		Results of adjustment of only weighted absolute data		Results of adjustment of only relative data		Results of combined adjustment of all the absolute and relative data	
	$g_A-g_r = 5{,}703.3$		$g_A-g_r = 5{,}702.7$		$g_A-g_r = 5{,}701.9$		$g_A-g_r = 5{,}702.2$	
Gravimeter	g_i-g_r	u_{av}	g_i-g_r	u_{av}	g_i-g_r	u_{av}	g_i-g_r	u_{av}
1	2	3	4	5	6	7	8	9
FG5-101	2.4	0.9	2.4	1.2	2.7	1.8	2.5	1.5
FG5-108	−3.5	1.5	−3.5	1.2	−4.1	1.1	−4.3	1.1
FG5-202	−2.4	1.5	−2.7	1.2	−4.4	0.9	−4.2	1.1
FG5-206	−1.6	0.4	−0.8	0.9	−0.5	0.4	−0.7	0.1
FG5-209	7.5	1.0	7.7	0.4	6.8	0.5	6.7	0.8
FG5-211	−2.9	0.9	−2.7	0.9	−3.3	0.3	−3.4	0.3
FG5-213	1.4	0.4	1.2	1.0	0.7	1.1	0.5	1.1
FG5-215	−0.1	0.8	0.2	0.8	0.2	0.6	0.0	0.6
FG5-216	−2.2	1.9	−2.4	2.1	−1.9	2.6	−1.9	2.7
FG5-221	0.5	1.4	1.0	1.7	0.7	2.0	0.5	1.8
FG5-224	−0.8	0.3	0.0	1.3	−0.9	2.2	−1.1	1.9
FG5-228	3.3	0.2	3.0	0.1	3.1	1.0	3.0	0.7
JILA-2	1.3	1.6	2.1	1.2	2.3	1.5	1.9	1.5
JILAg-6	4.2	5.9	4.0	5.3	3.6	5.4	3.2	5.5
A10-008	−5.7	1.7	−6.1	2.7	−7.1	3.0	−7.2	3.3
IMGC-2	−0.1	0.1	0.1	0.8	−0.3	1.2	−0.3	0.9
FGC-1	7.0	3.3	6.4	2.3	5.0	2.8	4.6	2.8
GABL-G	−4.7	1.0	−4.8	1.6	−5.3	2.0	−5.2	1.7
TBG	−4.1	8.7	−3.9	>10.0	−4.4	>10.0	−4.6	>10.0

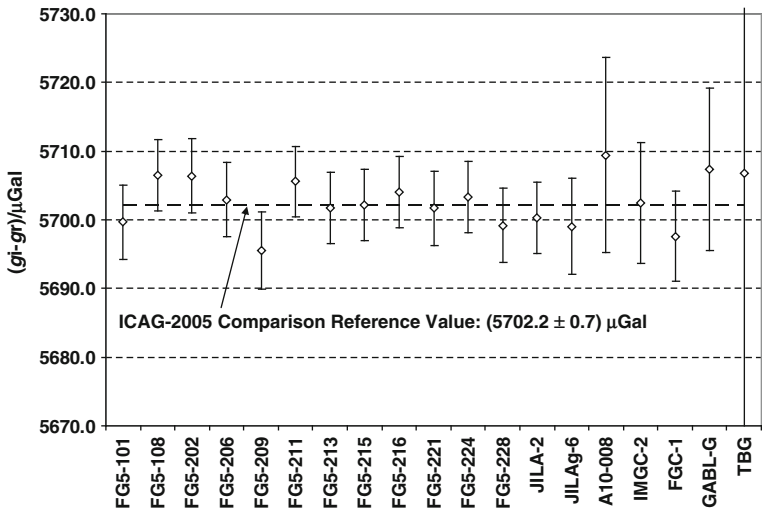


Fig. 7.1 Measurement results of the absolute gravimeters during ICAG-2005 with their expanded uncertainties. All the results transferred to site A (height of 0.90 m above the mark on the pillar). The results are expressed in microgals after subtraction of integer value g_r = 980,920,000 μGal

The offsets of the results of each gravimeter at all the gravity stations of the BIPM gravity network with respect to corresponding CRV are the same as that at A (at 0.90 m) in Table 7.4.

The results of the absolute measurements of each gravimeter in ICAG-2005 are presented in Fig. 7.1 with their expanded uncertainties U_i. For each gravimeter the maximum of all the expanded uncertainties obtained in measurements, is presented in Fig. 7.1. The variations of the expanded uncertainties of each gravimeter are related to the various experimental standard deviations obtained in each measurement at each site, i.e. these variations are statistical. It is seen from Fig. 7.1 that almost all the offsets of absolute gravimeters are within of their expanded uncertainties.

In Fig. 7.2 the CRVs at the station A obtained in the ICAG-2001 and ICAG-2005 and the result of ICAG-1997 are presented. The CRVs of ICAG-2001 and ICAG-2005 obtained using the combined adjustment of the absolute and relative data. The result of ICAG-1997 is the unweighted mean of all the absolute results transferred to A (Robertsson et al., 2001). The measurement results of FG5-108 obtained in three comparisons (Vitushkin et al., 2002, Robertsson et al., 2001) are also presented in Fig. 7.2 in confirmation of the gravity field stability at BIPM.

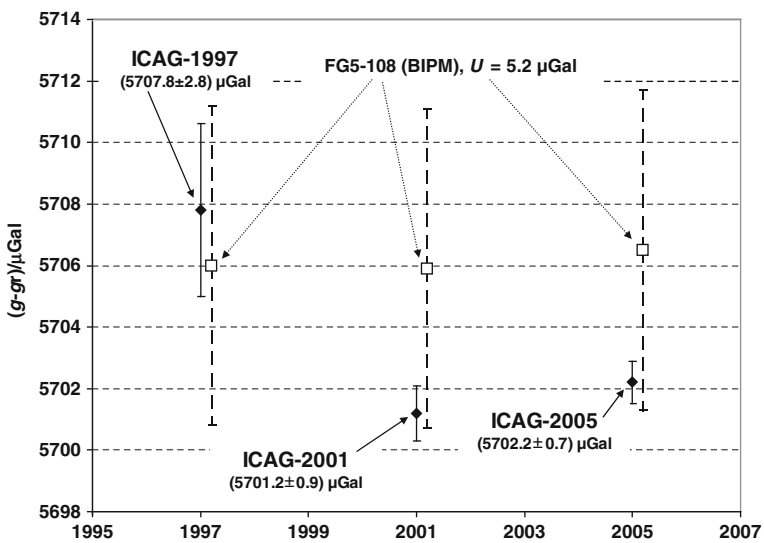


Fig. 7.2 The results of ICAG-1997, ICAG-2001, ICAG-2005 and the results of the gravimeter FG5-108 (BIPM) obtained in these comparisons

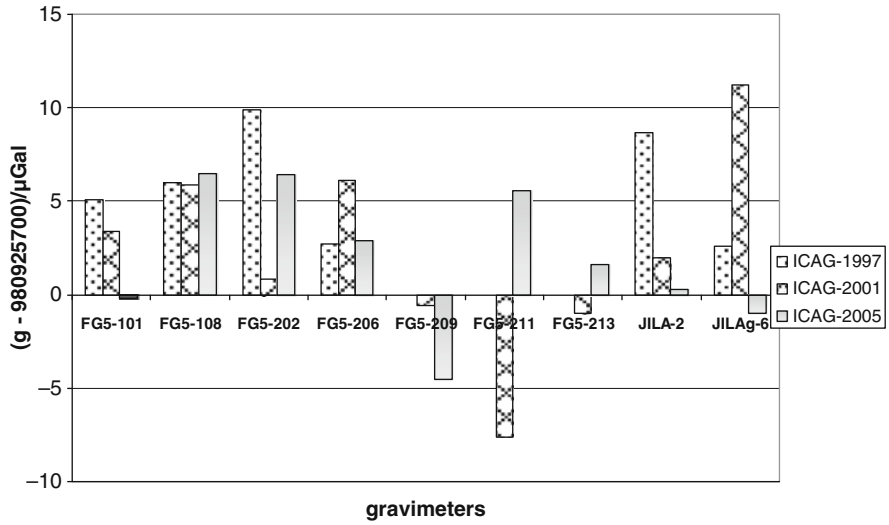


Fig. 7.3 Measurement results of the absolute gravimeters participated in the ICAG-1997, and in the ICAG-2001 and ICAG-2005 (CRVs at station A at 0.90 m)

The reproducibility (defined as a closeness of the agreement between the results of measurements of the same measurand carried out under changed conditions of measurement, as, for example, the location of measurement (VIM, 1993)) of the measurement results of AGs, participated in the ICAGs from 1997 to 2005, is illustrated by Fig. 7.3.

It is seen that for some gravimeters the discrepancy between their results in different comparisons is bigger than their expanded uncertainty.

The actual discrepancies between the results of the comparisons, illustrated by Fig. 7.2, and the discrepancies of individual AGs (Fig. 7.3) require further studies of the reproducibility of AGs which can be expressed quantitatively in terms of the dispersion characteristics of the results of measurement and included in the combined uncertainty of the AG. In the budgets of uncertainties applied in ICAG-2005 such uncertainty component was not included because of the lack of information on the reproducibility of the measurement results for each gravimeter. Such information may be obtained from the results of the next ICAGs at the BIPM and in the RICAGs with the participation of the same gravimeters.

Table 7.5 presents the polynomial coefficients of the second-order polynomials which describe the gravity field distribution $g(h)$ above the gravity stations measured during the ICAG-2005 by relative gravimeters.

Table 7.5 Polynomial coefficients for gravity field distributions above the gravity stations of the BIPM

Station	a	b	c
A	25,980.8	−315.37	6.417
A1	25,971.1	−321.73	11.583
A2	25,987.9	−319.80	9.000
B	28,287.2	−300.10	1.750
B1	28,276.0	−296.93	5.083
B2	28,254.4	−289.60	4.250
B3	28,274.3	−310.77	8.417
B5	28,287.0	−297.33	0.833
B6	28,263.0	−300.33	5.833
C1	23,282.3	−314.00	0.0
C2	32,039.1	−285.50	0.0

Such distributions are described by the formula:

$$g(h) = a + bh + ch^2, \tag{2}$$

where h is the height above the gravity station and a, b and c are the polynomial coefficients obtained by least-square minimization.

7.4 Conclusions

The CRVs (g-values obtained as a result of a combined adjustment of the weighted results of the absolute and relative measurements during ICAG-2005) at the

gravity stations A and B are (Table 7.3) at a height of 0.90 m above the mark are:

at A:980 925 702.2 μGal;

at B:980 928 018.5 μGal.

The standard uncertainty of adjusted values is 0.7 μGal. These results are in a good agreement with the results of the ICAG-2001.

The budgets of uncertainties were prepared by the operators except that of A10-008, for which only the instrumental uncertainty was declared.

For the first time unified instrumental uncertainties were agreed for gravimeters of similar type and the expanded uncertainties were evaluated for all the gravimeters. A big delay in achieving the evaluation of the results of ICAG-2005 was due to difficulties in the estimation of the uncertainties and in the harmonization of approaches.

Finally, almost all the offsets of the results of individual absolute gravimeters with respect to the CRV were within the expanded uncertainty of the corresponding gravimeters. For the first time it was demonstrated that the rise-and-fall gravimeter and free-fall gravimeters give the same result.

Nevertheless, some questions remain to be answered. One of them concerns the reproducibility of the absolute gravimeters. This question arises from the fact that for some gravimeters the differences between their results in subsequent ICAGs are bigger than their expanded uncertainties. Further investigations of the reproducibility of the AGs are required as well as their regular participation in the comparisons at the BIPM or in the regional comparisons of AGs.

The stability of the gravity field at the BIPM during the comparisons was confirmed in the continuous absolute gravity measurements with FG5-108 (in 2001 and 2005) and FG5-202 (in 2005). Their results were stable within 1 μGal.

The work on the technical protocol should be continued taking into account a possible and quite advisable participation in the future ICAGs of absolute gravimeters based on the use of different basic principles of operation (free motion of the massive test bodies or atom interferometry of free moving atoms) and different technical realizations. The important part of the work on the evaluation of the budgets of uncertainties made in the frame of the ICAG-2005 makes it possible to decrease significantly the period of preparation of the report on the future comparisons.

Nevertheless, the study of the sources of the uncertainties and of the evaluation procedure of the comparison results should be continued.

The study on linking of the ICAG results to the results of the RCAGs and the use of the CRVs in practical gravity measurements should be initiated.

Acknowledgements The authors wish to thank Dr R. Davis for many useful discussions and all staff members of BIPM for their invaluable support.

References

Boulanger, Yu., et al. (1981). Results of comparison of absolute gravimeters, Sèvres, 1981. *Bull. Inf. BGI*, 52, 99–124.

Francis, O., et al. (2007). Results of European comparison of absolute gravimeters in Walferdange (Luxembourg) in November 2007, ibidem.

Germak, A., S.Desogus, and C. Origlia (2002). Interferometer for the IMGC rise-and-fall absolute gravimeter. *Metrologia*, 39, 471–475.

Guide to expression of uncertainty in measurement, ISO, 1993.

International Vocabulary of Basic and General Terms in Metrology (VIM), ISO, 1993.

Mutual recognition of national measurement standards and of calibration and measurement certificates issued by national metrology institutes, CIPM, 1999, available from http://www.bipm.org

AugustRobertsson, L., et al. (2001). Results from the fifth international comparison of absolute gravimeters, ICAG-97. *Metrologia*, 38, 71–78.

Vitushkin, L. (2008). Measurement standards in gravimetry, Proceedings of the International Symposium "Terrestrial Gravimetry. Static and Mobile Measurements. TGSMM-2007", 20–23 August 2007, St Petersburg, Russia, SRC of Russia Electropribor, pp. 98–105.

Vitushkin, L., et al. (2002). Results of the sixth international comparison of absolute gravimeters, ICAG-2001. *Metrologia*, 39, 407–424.

Vitushkin, L., et al. (2007). The seventh international comparison of absolute gravimeters ICAG-2005 at the BIPM. Organization and preliminary results, Proceedings of the 1st International Symposium of the International Gravity Field Service "Gravity Field of the Earth", 28 August-1 September, 2006, Istanbul, Turkey, Ed. General Command of Mapping, June 2007. Special Issue:18, pp. 382–387.

Chapter 8

Post-Newtonian Covariant Formulation for Gravity Determination by Differential Chronometry

P. Romero

Abstract Following Synge's idea, a Post-Newtonian Covariant Formulation to estimate orders of magnitude in the design of experiments for the measurement by differential chronometry of the curvature of an observer world-line (g) and the curvature of space-time (R_{ijkm}) is discussed.

The local geometric model considered corresponds to local Fermi coordinates associated to an observer O and Fermi transported tetrads, and by using Synge's world-function the measurement formulation for the relative distance in terms of the O-proper time s_1, corresponding to the instant at which an electromagnetic signal is emitted from O, and the O-proper time s_2 at which the signal is received by O after a trip-time to complete a circuit is presented.

8.1 Introduction

In General Relativity (GR) the "observables", namely the physical quantities that we can predict and measure in real experiments, correspond to quantities that are invariant under coordinate transformations. The world-function (Synge, 1960), as a two point invariant in the sense that its value is unchanged if we transform independently the coordinate systems, is a useful tool to formulate geometric quantities in a covariant way. Furthermore, if local Fermi coordinates associated to an observer O and Fermi transported tetrads are used, a formulation in terms of measurable quantities with physical meaning corresponding directly with observations can be derived. With this procedure the necessity of constructing unambiguous and rigorous transformations between theoretical and measurable quantities is avoided. In this paper we try to present how to determine the Fermi distance in terms of a measurable quantity (the observer proper time s).

P. Romero (✉)
Instituto de Astronomía y Geodesia (UCM-CSIC), Facultad de Matemáticas, Universidad Complutense, Madrid E-28040, Spain
e-mail: prp@mat.ucm.es

8.2 Mathematical Definitions

8.2.1 The World Function

The world function Ω is a two point invariant scalar that characterizes the space-time. For a given space-time the world function has the same value independent of the metric-induced coordinates. It is defined for any two events P and Q as the integral

$$\Omega(P,Q) = \frac{1}{2}(u_2 - u_1)\int_{u_1}^{u_2} g_{ij}\frac{dx^i}{du}\frac{dx^i}{du}du \qquad (1)$$

taken along the geodesic Γ_{PQ} (with equations $x^i = x^i(u)$ where u is a special parameter between $[u_1\ u_2]$).

The value of the world function has a geometric meaning; it is one half the square of the space-time distance between points P and Q. Also, the covariant derivatives of it with respect to the coordinates of P or Q (these covariant derivatives will be simply denoted by subscripts) have a geometric interpretation appearing respectively as tangent vectors at P and Q with magnitude equal to the measure of the geodesic Γ_{PQ}.

S.P. Mertikas (ed.), *Gravity, Geoid and Earth Observation*, International Association of Geodesy Symposia 135,
DOI 10.1007/978-3-642-10634-7_8, © Springer-Verlag Berlin Heidelberg 2010

(We use Latin indices for the range of values 1, 2, 3, 4, with the usual summation convention, and Greek for the range values 1, 2, 3).

See, for example, Bahder (2001, 2003) for the use of the world function and its geometric interpretation to formulate a covariant theory of navigation in curved space-time.

8.2.2 Fermi Coordinates

Let O be a time like curve corresponding to an observer following a worldline and P some point chosen on it. Let A^i, B^i and b be respectively the unit tangent vector to O, its first unit normal and its first curvature. We consider an orthonormal tetrad $\lambda^i{}_{(\alpha)}$ carried along O by Fermi Walker transport with $\lambda^i{}_{(4)}$ tangent to O, so that

$$\begin{aligned} \frac{\delta \lambda^i_{(\alpha)}}{\delta_s} &= bA^i \lambda^j_{(\alpha)} B_j, \\ \lambda^i_{(4)} &= A^i, \end{aligned} \tag{2}$$

$\lambda^i{}_{(\alpha)}$ are orthogonal spacelike unit gyro axes that form the local spatial frame of the observer and $\lambda^i{}_{(4)}$ is the timelike unit vector that acts as its local temporal axis. Norm and inner product are preserved in this way.

The (FC) contravariant Fermi coordinates, $X^{(i)}$, relative to the baseline O are defined by

$$\begin{aligned} X^{(\alpha)} &= \sigma \mu^i \lambda^{(\alpha)}_i \\ X^{(4)} &= s \end{aligned} \tag{3}$$

where μ^i represents the unit tangent vector to the geodesic Γ_{PQ} cutting orthogonally O at P, and σ the distance PQ along this geodesic. The FC coordinates are the natural extension of Riemann normal coordinates which constitute an inertial system of coordinates at the event under consideration.

The FC coordinates are admissible in a finite cylindrical region about the worldline of O, where the space-time is locally flat at each event. In the vicinity of the Earth this hypothesis is realistic.

A relativistic description for the transformation under a change of baseline between Fermi coordinates using the world function can be found in Gambi et al. (2001).

8.3 Model Assumptions

The metric for the space-time in the vicinity of the Earth can be approximated by the sum of the Minkowski metric η_{ij} and the deviation h_{ij} from flatness tensor. In FC can be written (Synge, 1960, pp. 89) as:

$$\begin{aligned} g_{(\alpha\beta)} &= \delta_{\alpha\beta} + \frac{1}{2} S_{(\alpha\beta\gamma\delta)} X^{(\gamma)} X^{(\delta)}, \\ g_{(\alpha 4)} &= S_{(\alpha 4\gamma\delta)} X^{(\gamma)} X^{(\delta)} \\ g_{(44)} &= -1 - 2bB_\gamma X^{(\gamma)} + \frac{3}{2} S_{(44\gamma\delta)} X^{(\gamma)} X^{(\delta)} \end{aligned} \tag{4}$$

From the local point of view S_{ijkm} is the symmetrised Riemann tensor at the observer. At small scale, curvature tensor consists almost of nothing else but gravity gradients. As it happens to FC, the form of this metric is also valid for any space-time.

8.4 Measurement Formulation for the Relative Distance

We try to determine the Fermi distance, σ, in terms of the observer proper time, s.

A physical interpretation of this measurement formulation in General Relativity can be achieved with the locally inertial system along the worldline of the observer using the Fermi coordinates defined in (3) and the orthonormal tetrad frame propagated along its path according to (2).

As it has been said previously, the Fermi distance is the proper length of the spacelike geodesic joining P and Q. In terms of the world function defined in (1), the Fermi distance is given by:

$$\sigma = [\Omega_i(PQ)\Omega^i(PQ)]^{\frac{1}{2}} = [2\Omega(PQ)]^{\frac{1}{2}}. \tag{5}$$

It is useful recognize that being always the reference observer O at the spatial origin of Fermi coordinates, σ is equal to the radial Fermi coordinate of Q:

$$\sigma = \sqrt{\delta_{\alpha\,\beta} X^{(\alpha)} X^{(\beta)}}. \tag{6}$$

On the other hand, it must be pointed out that along the world line of the observer, the proper time τ may

be directly calculated from the invariant space line element as

$$\Delta\tau = \int \frac{ds}{c}. \tag{7}$$

Obviously, if gravitational units such that c=G=1 are used we have:

$$\Delta\tau = \Delta s. \tag{8}$$

From a local point of view, an observer is at rest in the rotating frame attached to him, and then the time given by the observer clock corresponds to its proper time (s being his fourth and unique non null Fermi coordinate).

A detailed description of the relativistic corrections needed for the synchronization of different clocks to obtain a global coordinate time can be found in Ashby (2003).

8.4.1 Procedure

(A) We use a Taylor series expansion of Ω up to s^2, needed to show GR effects to model local distance measurements (in other case GR could be avoided in this formulation).

$$\Omega(s) = \Omega + s\Omega_i A^i + \frac{1}{2}s^2(\Omega_i DA^i + \Omega_{ij}A^iA^j), \tag{9}$$

where as it has been noted previously, $\Omega = 1/2\ \sigma^2$, $\Omega_\iota = -\sigma\mu^\iota$, and the second covariant derivatives of the world-function (Synge pp.54) can be determined assuming that differ few from the metric tensor g_{ij}, i.e.,

$$\Omega_{ij} = [\Omega_{ij}] + \sigma\,\mu_i[\Omega_{ijk}] + \frac{1}{2}\sigma^2\,\mu^\alpha\,\mu^\beta[\Omega_{ij\alpha\beta}] \tag{10}$$

where for the coincidence limits (Q → P):

$$[\Omega_{ij}] = g_{ij}, [\Omega_{ijk}] = 0, [\Omega_{ij\alpha\beta}] = S_{ij\alpha\beta}. \tag{11}$$

Now, being $\mu_\iota\ A^i=0$, and taking into account Eqs. (10) and (11), Eq. (9) for Ω (s) reduces to:

$$\Omega(s) = \frac{1}{2}\sigma^2 + \frac{1}{2}s^2[-1 - \sigma\,\mu_i DA^i + \frac{1}{2}\sigma^2 S_{44\alpha\beta}\mu^\alpha\,\mu^\beta). \tag{12}$$

(B) We consider an electromagnetic signal emitted from O at a proper time s_1 and received at s_2 after a trip time. In this case the events of emission P_1 and reception P_2 cannot be chosen arbitrarily since P_1Q and QP_2 have to be null geodesics (Ω(s) = 0). Then, by imposing this condition in Eq. (12), we obtain:

$$\sigma^2 = s^2(1 + \sigma\,\mu_i DA^i - \frac{1}{2}\sigma^2 S_{44\alpha\beta}\mu^\alpha\,\mu^\beta). \tag{13}$$

From this Eq. (13), the Fermi distance in terms of the Fermi Coordinates of Q respect to the observer O results:

$$\pm\,\sigma = s(1 + \frac{1}{2}X_{(\alpha)}DA^\alpha - \frac{1}{4}S_{44\alpha\beta}X^{(\alpha)}X^{(\beta)}), \tag{14}$$

and using the Frenet-Serret formula $DA^\alpha = bB^\alpha$ we finally obtain for the trip P_1QP_2 :

$$\sigma = \frac{s_2 - s_1}{2}(1 + \frac{1}{2}bB^\alpha X_{(\alpha)} - \frac{1}{4}S_{44\alpha\beta}X^{(\alpha)}X^{(\beta)}). \tag{15}$$

It must be noted that for the special case of flat space, at Newtonian level, Eq. (15) reduces to the Euclidian distance obtained by classical two-way ranging:

$$\sigma = \mathrm{c}/2(t_2 - t_1). \tag{16}$$

8.5 Gravimetric Interpretation

We use Synge result (pp. 136–138) to point out that "the first curvature b of the world line is the gravity g" and following Moritz et al. (1993, pp. 256–264), that the Riemann tensor:

$$\begin{aligned} S_{ij\alpha\beta} &= -\frac{1}{3}(R_{ij\alpha\beta} + R_{i\beta j\alpha}), \\ S_{44\alpha\beta} &= \frac{2}{3}\mathrm{U}_{\alpha\beta} \end{aligned} \tag{17}$$

is connected to tidal forces ($U_{\alpha\beta}$ are the second order derivative of the gravitational potential). Then, by using (17), finally we can write Eq. (15) in the form:

$$\sigma = \frac{s_2 - S_2}{2}(1 + \frac{1}{2}gB^\alpha X_{(\alpha)} - \frac{1}{6}\mathrm{U}_{\alpha\beta}X^{(\alpha)}X^{(\beta)}). \tag{18}$$

A generalization of Michelson-Morley experiment by differential chronometry called The Five-Point Curvature Detector is described in Synge (1960, pp. 408–410). Equation (18) shows for this experiment how gravity and tidal forces affects the values of distance obtained with electromagnetic signals which go round circuits.

8.6 Conclusions

A covariant formulation, invariant under coordinate transformations, to determine the Fermi distance in terms of a measurable quantity (the observer proper time s) has been presented. To this end the world-function, and local Fermi coordinates associated to an observer O with Fermi transported tetrads have been used. To show General Relativity effects (gravity and tidal forces) in the model of local distance measurements, a Taylor series expansion up to s^2, has been needed. In other case, the formulation corresponds to the Euclidean distance.

Acknowledgements This research has been funded under projects CCG07-UCM/ESP-2411 and CGL 2007-65110.

References

Ashby, N. (2003). Relativity in the global positioning system. *Liv. Rev. Rel*., 1, 1–45.

Bahder, T.B. (2001). Navigation in curved space-time. *Am. J. Phys.*, 69, 315.

Bahder, T.B. (2003). Relativity of GPS measurements. *Phys. Rev. D*, 68, 063005.

Gambi, J.M., P. Romero, A. San Miguel, and F. Vicente (1991). Fermi coordinates transformation under baseline change in relativistic celestial mechanics. *Int. J. Theor. Phys.*, 30(11), 1097–1114.

Moritz, H. and B. Hofmann-Wellenhof (1993). Geometry, relativity, geodesy. Wichmann Karlsrure.

Synge J.L. (1960). Relativity: The general theory. North Holland, New York.

Chapter 9

Robust and Efficient Weighted Least Squares Adjustment of Relative Gravity Data

F. Touati, S. Kahlouche, and M. Idres

Abstract When gravimetric data observations have outliers, using standard least squares (LS) estimation will likely give poor accuracies and unreliable parameter estimates. One of the typical approaches to overcome this problem consists of using the robust estimation techniques. In this paper, we modified the robust estimator of Gervini and Yohai (2002) called REWLSE (Robust and Efficient Weighted Least Squares Estimator), which combines simultaneously high statistical efficiency and high breakdown point by replacing the weight function by a new weight function. This method allows reducing the outlier impacts and makes more use of the information provided by the data. In order to adapt this technique to the relative gravity data, weights are computed using the empirical distribution of the residuals obtained initially by the LTS (Least Trimmed Squares) estimator and by minimizing the mean distances relatively to the LS estimator without outliers. The robustness of the initial estimator is maintained by an adapted cut-off values as suggested by the REWLSE method which allows also a reasonable statistical efficiency. Hereafter we give the advantage and the pertinence of REWLSE procedure on real and semi-simulated gravity data by comparing it with conventional LS and other robust approaches like M and MM estimators.

F. Touati (✉)
Geodetic Laboratory, Center of Space Techniques, Arzew 31200, Algeria
e-mail: fateh73@gmail.com

9.1 Introduction

The typical approach of gravity data adjustment is the least squares method (LS), but LS estimation is sensitive to outliers, thus it will give unreliable results if the measurements are contaminated by outliers. There are various sources of errors: systematic errors, modeling errors of gravimetric signal, external effects, etc. In order to obtain a reliable parameter estimates, the outliers have to be appropriately handled.

The classical solution is to apply the outlier detection and identification procedure. This approach is based on statistical tests, like Baarda (1968) and Pope (1976) test which are usually used in geodesy and gravimetry, but when outliers appear in multiple observations, the task will not be easy because outliers are not correctly identified and the elimination of some observations may rise the problem of rank deficiency.

Robust estimation provides an alternative procedure. It allows best parameters estimation, without requiring any identification of specific observations as outliers or excluding them. Robust methods are basically developed by Huber's works (1964, 1981) and Hampel (1973). Use of them in geodesy was initiated by Carosio (1979) and Mäkinen (1981), Becker (1989) especially for gravimetric data. In statistic and geodesy literatures, different robust techniques are proposed. M-Estimators are largely used in geodesy and gravimetry (Wieser and Brunner, 2001; Yang et al., 2002; Csapo et al., 2003). Some other robust methods with high breakdown point are rarely used in geodesy due to their complexity and low statistical efficiency such as LMS (Least Median Squares), LTS (Least Trimmed Squares) and S-Estimator (e.g., Rousseeuw, 1984; Rousseeuw and Yohai, 1984; Ruppert, 1992;

S.P. Mertikas (ed.), *Gravity, Geoid and Earth Observation*, International Association of Geodesy Symposia 135,
DOI 10.1007/978-3-642-10634-7_9, © Springer-Verlag Berlin Heidelberg 2010

Hekimoglu, 2005; Rousseeuw and Van Dressen, 2006) for estimation with high efficiency and high breakdown point. However, tuning up these estimators for high efficiency leads to an increase in bias as an unpleasant side effect (Gervini and Yohai, 2002). Gervini and Yohai (2002) proposed a new class of estimators that simultaneously reach the maximum breakdown point and high efficiency under normal errors called REWLSE. We propose in this paper to modify this technique in order to adapt it to relative gravity measurements by replacing the weight function (with hard-rejection to outliers) by a new weight based on robust residuals obtained initially by LTS method and by minimizing the mean distances relatively to the LS estimator without outliers.

Given the availability of relative gravity data and by adding some simulated outliers, this paper aims at a comparative study between different methods of estimation (LS, M, MM and REWLSE) for parameter estimation with high reliability and efficiency. The paper starts with a presentation of model observation of relative gravity and LS estimation. After, summarizing briefly some robust methods and their principle, the REWLSE technique and its adaptation to relative gravity is discussed in detail. The paper ends with some results and discussion on robustness and efficiency performance of the considered methods and a special attention is given to REWLSE technique.

9.2 Least Squares Adjustment

Least squares estimation of unknown parameters is carried out in the Gauss-Markov model (Koch, 1987). The relative gravity observation equation is written as (Hwang et al., 2002):

$$\Delta \mathbf{L}_{i,j} + \mathbf{V}_{i,j} = \Delta \mathrm{F}(z_j) - \Delta \mathrm{F}(z_i) + \mathrm{D}(t_j) - \mathrm{D}(t_i) + \Delta \mathbf{G} \tag{1}$$

where

$\mathbf{V}_{i,j}$: residual of $\Delta \mathbf{L}_{i,j}$
$\Delta \mathbf{L}_{i,j}$: relative gravity observation between ith and jth stations
t_i, t_j: measurement times
$\Delta \mathrm{F}(z)$: unknown calibration function to correct scale factor
z: gravimeter reading in counter units (CU)
$\mathrm{D}(t)$: unknown drift of gravimeter
$\Delta \mathbf{G}$: unknown relative gravity between jth and ith station.

Assuming that there are m observations and n unknowns (gravity, drift and scale factor). If $\mathbf{W}(m\mathrm{x}m)$ is a weight matrix of $\mathbf{\Delta L}(m)$, the matrix representation of the observation equations become:

$$\Delta \mathbf{L} + \mathbf{V} = \mathbf{AX} \tag{2}$$

where A is the design matrix and X is a vector of n unknowns. The solution by least squares method is not possible without constraint because of rank deficit (Hwang et al., 2002). In order to obtain a unique solution in least squares sense, two methods can be used; gravimetric complementation and weighted constraints. The last one is selected to be used in this work and is given as follow:

$$\hat{\mathbf{X}} = \left(\mathbf{A}^{\mathrm{T}}\mathbf{WA} + \mathbf{A}_{\mathrm{g}}^{\mathrm{T}}\mathbf{W}_{\mathrm{g}}\mathbf{A}_{\mathrm{g}})\right)^{-1}\left(\mathbf{A}^{\mathrm{T}}\mathbf{W}\Delta\mathbf{L} + \mathbf{A}_{\mathrm{g}}^{\mathrm{T}}\mathbf{W}_{\mathrm{g}}\mathbf{L}_{\mathrm{g}}\right) \tag{3}$$

where $\mathrm{A_g}$, $\mathrm{L_g}$ and $\mathrm{W_g}$ are respectively, design matrix, absolute gravity vector and diagonal weight matrix of constraints and $\mathbf{A}_{\mathrm{g}}^{\mathrm{T}}\mathbf{W}_{\mathrm{g}}\mathbf{A}_{\mathrm{g}}$ is a diagonal matrix (Hwang et al., 2002).

9.3 Robust Estimates

Robust methods provide an alternative procedure, which do not require identifying specific observations as outliers or excluding them and make more use of the information provided by the data (Huber, 1981; Hampel et al., 1986; Rousseeuw and Leroy, 1987). They also should give the same result obtained by standard least squares method without outliers (Wicki, 2001).

Some robust methods are summarized as follow:

- M-Estimator is the generalized form of the maximum likelihood estimation introduced by Huber (1964). Instead of minimizing the sum squares of residuals, M-Estimator minimizes the sum of score function $\rho(v)$ of residuals.

$$\hat{\mathbf{X}}_{\mathrm{M}} = \underset{\mathbf{X}}{\operatorname{argmin}} \sum_{i=1}^{m} \rho\left(v(i)\right)$$

- Least Trimmed Squares (LTS) estimation is a high breakdown point method introduced by Rousseeuw (1984) and is defined as follow:

$$\hat{\mathbf{X}}_{\mathrm{LTS}} = \underset{\mathbf{X}}{\operatorname{argmin}} \sum_{i=1}^{h} v^2(i)$$

- $v^2(1) \leq v^2(2) \leq \ldots \leq v^2(m)$ are the ordered squared residuals and the default h is defined in the range:

$$\frac{m+n+2}{2} \leq h \leq m.$$

  The performance of this method was improved by the FAST-LTS algorithm of Rousseeuw and Van Driessen (2006).
- The MM-Estimators are introduced by Yohai (1987) and are based on the combination of high breakdown techniques as LTS and efficient techniques as M-estimator.
  The robust estimation of the scale factor is obtained by median method (Yang et al., 1999):

$$\hat{\sigma} = 1.4826\,\mathrm{med}\,\{|v_i|\}$$

- where med $\{|v_i|\}$ denotes the median of all $\{|v_i|\}$ and the value 1.4,826 allows to have a null bias in the estimation of σ with Gaussian distribution (Hampel et al., 1986).

9.4 Robust and Efficient Estimation

In order to maintain in the same time the robustness and statistical efficiency, the REWLSE technique is used in this work and adapted especially to relative gravity.

9.4.1 REWLSE Principle

Consider a pair of initial robust estimators of parameters and scale, $\hat{\mathbf{X}}_0$ and $\hat{\sigma}_0$ respectively. The standardized residuals are defined as:

$$\bar{v}_i = \frac{l_i - \mathbf{A}_i \hat{\mathbf{X}}_0^{\mathrm{T}}}{\hat{\sigma}_0} \tag{7}$$

A large value of $\bar{v}_i$ would suggest that the ith observation is an outlier.

In order to maintain the breakdown point value of the initial estimator and to have a high efficiency, Gervini and Yohai (2002) proposed the use of an adapted cut-off value as follow:

$$t_m = \min\left\{t{:}\mathrm{F}_m^+(t) \geq 1 - d_m\right\} \tag{8}$$

where F_m^+ is the empirical cumulative distribution function of the standardized absolute residuals and d_{m} is the measure of the proportion of the outliers in the sample given as follow:

$$d_m = \sup_{t \geq t_0} \left\{\Phi^+(t) - \mathrm{F}_m^+(t)\right\}^+ \tag{9}$$

Φ^+ denotes the normal cumulative distribution of the random errors, $t_0 = 2.5$ is the initial cut-off value and $\{\}^+$ denotes the positive part between $\Phi^+(t)$ and $\mathrm{F}_m^+(t)$.

Gervini and Yohai (2002) define the form of the weights W and the REWLS estimator T_m as follow:

$$\mathrm{T}_m = \begin{cases} (\mathbf{A}^{\mathrm{T}}\mathbf{W}\mathbf{A})^{-1}\mathbf{A}^{\mathrm{T}}\mathbf{W}\mathbf{L} & \text{if} \quad \hat{\sigma}_0 > 0 \\ \mathbf{X}_0 & \text{if} \quad \hat{\sigma}_0 = 0 \end{cases} \tag{10}$$

The weight function W is chosen in order to have a hard-rejection to outliers

$$w_i = \begin{cases} 1 & \text{if } |\bar{v}_i| < t_m \\ 0 & \text{if } |\bar{v}_i| \geq t_m \end{cases} \tag{11}$$

$$\mathbf{W} = \mathrm{diag}(w_1, w_2, \ldots, w_m) \tag{12}$$

Note that with this weight, T_m estimator maintains the same breakdown point value of the initial estimator $\hat{\mathbf{X}}_0$.

9.4.2 REWLSE Adaptation to Gravimetric Data

The adjustment model by weighted least squares as in Eq. (3) is modified in order to have a single design matrix (M) and single weight matrix (P):

$$\mathbf{A}^{\mathrm{T}}\mathbf{W}\mathbf{A} + \mathbf{A}_{\mathrm{g}}^{\mathrm{T}}\mathbf{W}_{\mathrm{g}}\mathbf{A}_{\mathrm{g}} = \mathbf{M}^{\mathrm{T}}\mathbf{P}\mathbf{M} \tag{13}$$

where

$$\mathbf{M} = \begin{bmatrix} \mathbf{A}^{\mathbf{T}} & \mathbf{A_g} \end{bmatrix} \quad \text{and} \quad \mathbf{P} = \begin{bmatrix} \mathbf{W} \\ \mathbf{W_g} \end{bmatrix}.$$

LS-estimator can be written then:

$$\mathbf{T} = (\mathbf{M}^{\mathrm{T}}\mathbf{P}\mathbf{M})^{-1}\mathbf{M}^{\mathrm{T}}\mathbf{P}\mathbf{L} = \mathbf{Q}\mathbf{P}\mathbf{L} \tag{14}$$

where $\mathbf{L} = \begin{bmatrix} \Delta\mathbf{L} \\ \mathbf{L_g} \end{bmatrix}$ and $\mathbf{Q}$ is a matrix of the same size as $\mathbf{M}^{\mathbf{T}}$.

By applying REWLSE method to gravity data differences using previous weight function, the normal equation matrix became singular. Thus, it is necessary to investigate an adaptable weight function for gravimetric data in order to obtain not only a unique solution of the problem, but also to ensure the efficiency and the robustness of the estimated parameters.

If the observations are contaminated by outliers $\mathbf{L}_\delta = \mathbf{L} + \delta$, Zhu (1986) has deduced that all robust estimates used in surveying adjustment can be written as:

$$\mathbf{T}_\delta = \left(\mathbf{M}^{\mathrm{T}}\mathbf{P}_\delta\mathbf{M}\right)^{-1}\mathbf{M}^{\mathrm{T}}\mathbf{P}_\delta\mathbf{L} = \mathbf{Q}\mathbf{P}_\delta\mathbf{L}_\delta \tag{15}$$

Here $\mathbf{P}_\delta$ is a function of v. Assuming that $\mathbf{Q}$ is approximately invariable, we obtain then:

$$\mathbf{T}_\delta = \mathbf{Q}\mathbf{P}_\delta\mathbf{L}_\delta \tag{16}$$

Taking difference between $\mathbf{T}_\delta$ and T*:*

$$\Delta = \mathbf{T} - \mathbf{T}_\delta = \mathbf{Q}(\mathbf{P}\mathbf{L} - \mathbf{P}_\delta\mathbf{L}_\delta) \tag{17}$$

The mean distances between the two estimators is: $Dm = \mathrm{E}(\Delta^{\mathrm{T}}\Delta)$. In order to make $\mathbf{P}_\delta$ optimal in robustness sense, Dm must be minimum, i.e.,

$$\frac{\mathrm{d}\,Dm}{\mathrm{d}\,p_\delta(i)} = 0 \tag{18}$$

The corresponding weight function under stochastic model (Zhu, 1996) will be:

$$p_\delta(i) = \begin{cases} p_i & \text{if } |v_i| \le k \\ \frac{p_i\sigma_i^2}{v_i^2/r_{ii}} & \text{if } |v_i| > k \end{cases} \tag{19}$$

σ_i^2 is the variance of the ith observation without outliers. Knowing that $p_i = 1/\sigma_i^2$ and opting to the adaptive cut-off value for k, we get:

$$p_\delta(i) = \begin{cases} p_i & \text{if } |\bar{v}_i| \le t_m \\ \frac{r_{ii}}{\hat{\sigma}_0\bar{v}_i^2} & \text{if } |\bar{v}_i| > t_m \end{cases} \tag{20}$$

r_{ii} is the local redundancy of the ith observation which can be determined from the so-called redundancy matrix R or the reliability matrix as in Eq. (21) where I is an identity matrix.

$$\mathbf{R} = \mathbf{I} - \mathbf{M}(\mathbf{M}^{\mathrm{T}}\mathbf{P}\mathbf{M})^{-1}\mathbf{M}^{\mathrm{T}}\mathbf{P} \tag{21}$$

9.5 Results and Comparison

The sample of data contains 56 relative gravity observations with standard errors around 0.03 mgal and 6 absolutes points with 0.002–0.003 mgal of accuracy.

In order to investigate the robustness of different estimators proposed above (LS, M, MM and REWLSE), firstly, we apply these estimators to the original real data, and then we simulate some outliers and add them to observations.

Figure 9.1 displays a Normal QQ-Plot for both robust and LS residuals. A normal QQ-plot (or quantile-quantile plot) consists of a plot of the ordered values of standardized residuals versus the corresponding quantiles of a *standard*normal distribution. From this figure it follows the effectiveness of the robust methods in outlier detection (5, 6, 22 and 24). The LS method does not detect any outlier. It should be pointed out that the detected errors are small and do not have significant impact on the estimated parameters; consequently, it is clear that the provided data is of good quality and can be set as a reference for comparison. Using now a large number of outliers by simulation, the Normal QQ-Plot in Fig. 9.2 and the standard errors of the adjusted parameters in Fig. 9.3 can be achieved. In fact, only two small errors are detected (36, 54) using standard LS estimation and the standard errors of the adjusted parameters are strongly affected by abnormal data which was well detected by most of robust techniques used in the present work. Furthermore, to show and compare the impact of outliers on the

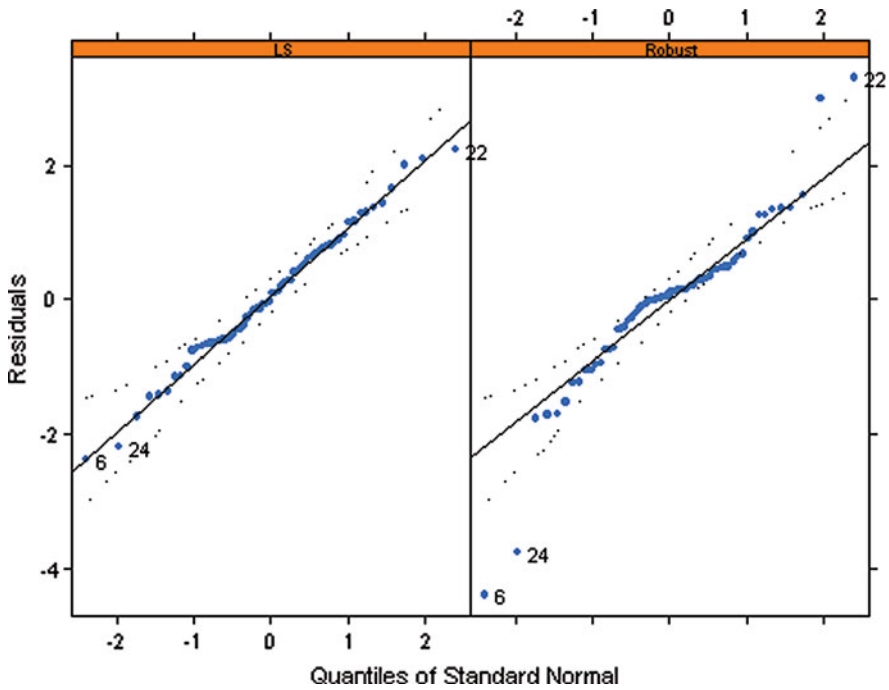


Fig. 9.1 Normal QQ-Plot of residuals for original data. x-axis: quantiles of normal distribution, y-axis: quantiles of empirical distribution represented by standardized LS residuals (*left*) and standardized robust residuals (*right*)

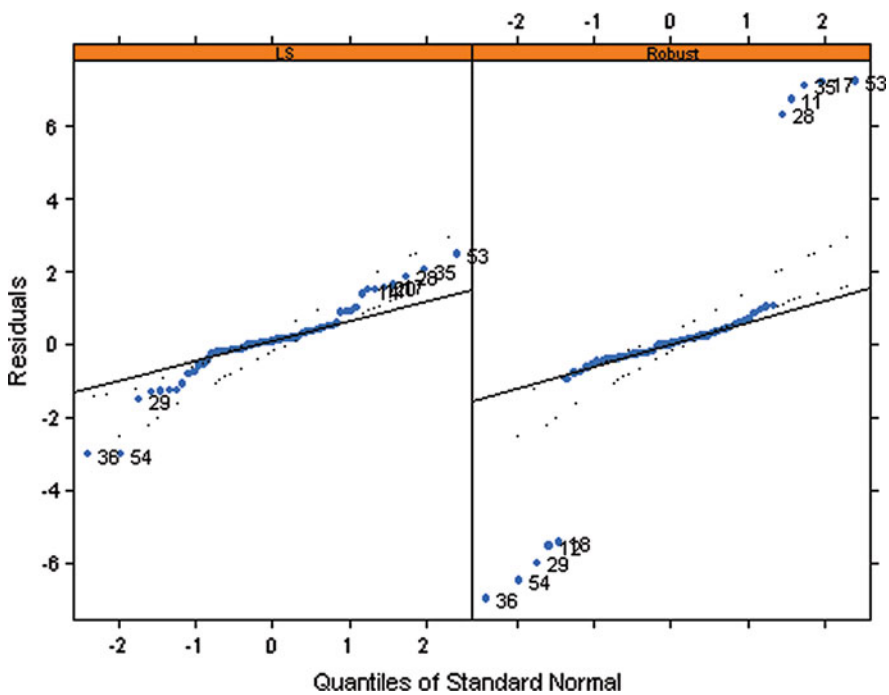


Fig. 9.2 Normal QQ-Plot of residuals with outliers. x-axis: quantiles of normal distribution, y-axis: quantiles of empirical distribution represented by standardized LS residuals (*left*) and standardized robust residuals (*right*)

standard errors of the parameters obtained by different robust methods, from Fig. 9.3, it is clearly shown that the REWLSE method has much better result and it gave the same results as in conventional LS without outliers. The MM-Estimator is relatively more robust than the M-Estimator.

In order to show the performance of REWLSE, 10 outliers are added to the observations and by increasing

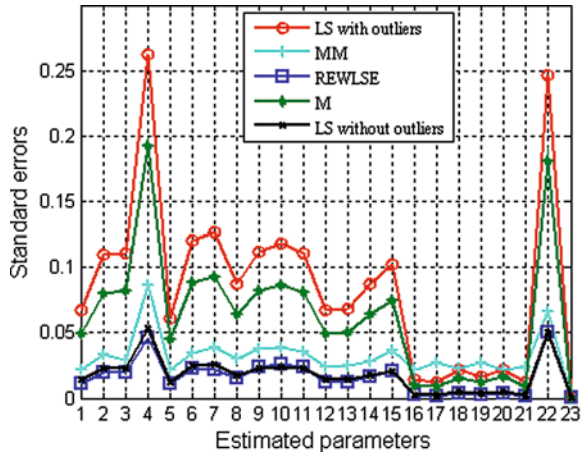


Fig. 9.3 Standard errors obtained from different estimators; x-axis: unknown parameters (1–21: gravity stations, 22: linear drift coefficient and 23: scale factor correction); y-axis: standard errors (in mgal)

the magnitude of outliers using the following formula: $L_\delta = L + k.\sigma$, k=1, 2, ... with $\sigma = 0.03$ mgal. Next we compute for each case (k=1, 2, and 3) the following statistics:

- Three estimators T1, T2 and T3:

  T1: Weighted LS without outliers
  T2: Weighted LS with outliers
  T3: REWLSE with outliers

- Two mean distances *Dm1* and *Dm2* according to $\mathbf{E}(\Delta^{\mathbf{T}}\Delta)$ given in Eq. (17):

  Dm1: between T1 and T2*;*
  Dm2: between T1 and T3

- Robust scale factor $\hat{\sigma}$ according to the Eq. (6) and standard error of each estimator.

The results are summarized in Tables 9.1, 9.2, and 9.3. The first values in bold *Dm1* and *Dm2* mean that the mean distances are computed as considering the completed vector of unknowns (the parameters of gravity vector and gravimeter) and the second values are referred to only parameters of gravity vector.

The robust scale factors are nearly the same for all cases (from 0.026 to 0.030 mgal), it reflects the accuracy of the gravimeter (LCR G838) used in data collecting. Since standard error is a good measure of statistical efficiency, consequently, we can conclude that the REWLSE method has a high efficiency.

Table 9. 1 Robustness and efficiency analysis of REWLSE with magnitude of outliers (***k*=1**)

Estimator	Standard error	$\hat{\sigma}$ [mgal]	*Dm1*	*Dm2*
T2	1.88			
T1	0.99	0.028	**0.008** /0.007	**0.008** /0.003
T3	1.02			

Initial cut-off value t_0= 2.5, adapted cut-off value t_m= 2.64 and % of detected outliers = 8/10.

Table 9. 2 Robustness and efficiency analysis of REWLSE with magnitude of outliers (***k*=2**)

Estimator	Standard error	$\hat{\sigma}$ [mgal]	*Dm1*	*Dm2*
T2	3.08			
T1	0.99	0.030	**0.031**/ 0.023	**0.015**/ 0.014
T3	1.00			

Initial cut-off value t_0 = 2.5, adapted cut-off value t_m= 5.48 and % of detected outliers = 10/10.

Table 9.3 Robustness and efficiency analysis of REWLSE with magnitude of outliers (***k*=3**)

Estimator	Standard error	$\hat{\sigma}$ [mgal]	*Dm1*	*Dm2*
T2	4.52			
T1	0.99	0.026	**0.078**/ 0.573	**0.003**/ 0.001
T3	0.97			

Initial cut-off value t_0= 2.5, adapted cut-off value t_m= 8.76 and % of detected outliers = 10/10.

By analyzing the values of the *Dm1* and *Dm2* in Tables 9.1, 9.2, and 9.3, it seems clearly the robustness of REWLSE notified by small values of *Dm2* which means that there is no significant difference between the estimated parameters by LS without outliers and REWLSE with outliers.

Other conclusions can be carried out from the tables, they concerns firstly the adapted cut-off values t_m which increase by increasing the magnitude of the outliers, and secondly, the percentage of outliers detected depends on the performance of the initial estimator (LTS in this case) which sometimes unable to detect small outliers. Finally, we can conclude that the obtained results show how well the high efficiency and robustness of REWLSE is.

9.6 Conclusions

In this paper, we have realized a comparative study on robustness and efficiency between different robust estimators such as (M, MM and REWLSE) in the case of

contaminated data. The conventional method (LS) is very sensitive to the outliers as it is shown by the normal QQ-Plot. The comparison between different robust estimators by adding simulating outliers allowed us to pick out some conclusions as follows: the outlier's effect is remarkable on standard errors computed by M-Estimator which do not tolerate a high percentage of errors in the observations, which is not the case with the MM-Estimator that has a high breakdown point value, but this gain in robustness has induced undesired effects on efficiency noticed by an increase in standard errors relatively to our proposed techniques (adapted REWLSE). In fact, the standard error values obtained by REWLSE method justifies the high efficiency of this estimator, and the use of an adapted cut-off values have allowed to keep the robustness of the initial estimator (LTS). In other part, the adapted weight function proposed in this paper has not only allowing to overcome the rank deficit problem but also to estimate the unknown of gravity vector and gravimeter parameters with high breakdown point. Finally, it is important to test the proposed approach in the future to other kind of gravimetric or geodetic data and especially to satellite gravity data such as SST and SGG measurements of the dedicated gravity field satellite missions GRACE and GOCE.

Acknowledgements The authors would like to first thank Prof C. Hwang from NCTU university of Taiwan for making available the data set used in this research. They also would like to thank Dr D. Gervini from university of Zurich for his help.

References

Baarda, W. (1968). A testing procedure for use in geodetic network. Netherlands Geodetic commission, Publications on geodesy, Vol. 2, Nphotogro. 5, delft, 97 pp.

Becker, M. (1989). Adjustment of microgravimetric measurements for detecting local and regional displacements. In: Rummel, R. and R.G. Hipkin (eds), Proceedings of IAG Symposium 103: Gravity, Gradiometry and Gravimetry. Springer-Verlag, Berlin, pp. 149–161.

Carosio, A. (1979). Robuste ausgleichung. Vermessung, photogrammetrie und kulturtechnik, 77, 293–297.

Csapo, G., M. Kis, and L. Völgyesi (2003). Different adjustment methods for the Hungarian part of the unified Gravity Network. XXIII General Assembly of the International Union of Geodesy and Geophysics. Sapporo, Japan.

Gervini, D., V.J. Yohai (2002). A class of robust and fully efficient regression estimators. *Ann. Stat.*, 30(2), 583–616.

Hampel, F. (1973). Robust estimation: A condensed partial survey. *Z. Wahrsch. Verw. Gebiete*, 27, 87–104.

Hampel, F., E.M. Ronchetti, P.J. Rosseeuw, and W.A. Stahel (1986). Robust statistics: The approach based on influence functions. Wiley, New York.

Hekimoglu, S (2005). Do robust methods identify outliers more reliably than conventional test for outlier, ZFV, 2005/3, 174–180.

Huber, P.J. (1964). Robust estimation of location parameter. *Ann. Math. Statist.*, 35, 73–101.

Huber, P.J. (1981). Robust statistics. Wiley, New York.

Hwang, C., C. Wang, L. Lee (2002). Adjustment of gravity measurements using weighted and datum-free constraints. *Comput. Geosci.*, 28, 1005–1015.

Koch, K.R. (1987). Parameter estimation and hypothesis testing in linear models. Edition Springer- Verlag.

Mäkinen, J. (1981). The treatment of outlying observations in the adjustment of the measurements on the Nordic land uplift gravity lines, unpublished manuscript, Helsinki.

Pope, A.J. (1976). The statistics of residuals and detection of outliers. Tech. Rep. NOS65 NGS1, Rockville, Md., 617 pp.

Rousseeuw, P.J. (1984). Least median of squares, regression. *J. Am. Stat. Assoc.*, 79, 871–881.

Rousseeuw, P.J. and V.J. Yohai (1984). Robust regression by means of S estimators. In: Franke, J., W. Härdle, and R.D. Martin (eds), Robust and Nonlinear Time Series Analysis, Lectures Notes in Statistics 26. Springer Verlag, New York, pp. 256–274.

Rousseeuw, P.J. and A.M. Leroy (1987). Robust regression and outlier detection. Wiley, New York.

Rousseeuw, P.J. and K. Van Dressen (2006). Computing LTS Regression for Large Data Sets. Data Mining and Knowledge Discovery, 12, 29–45, 2006, DOI: 10.1007/s10618-005-0024-4.

Ruppert, D. (1992). Computing S estimators for regression and multivariate location/dispersion. *J. Compt. Graph. Stat.*, 1, 253–270.

Wicki, F. (2001). Robust estimator for the adjustment of geodetic networks. Proceeding of the first international symposium on robust statistics and fuzzy techniques in geodesy and GIS. Report N0. 295, Institute of Geodesy and photogrammetry. ETH Zürich, pp. 53–60.

Wieser, A. and F.K. Brunner (2001). Robust estimation applied to correlated GPS phase observations. In: Carosio, A. and H. Kutterer (eds), Proceedings of the first international symposium on robust statistics and fuzzy techniques in Geodesy and GIS, ETH Zürich, pp. 193–198.

Yang, Y., M.K. Cheng, C.K. Shum, and B.D. Tapeley (1999). Robust estimation of systematic errors of satellite laser range. *J. Geod.* 73:345–349.

Yang, Y., L. Song, and T. Xu (2002). Robust estimator for correlated observations based on bifactor equivalent weights. *J. Geod.* 76, 353–358, doi: 10.1007/s00190-002-0256-7.

Yohai, V.J. (1987). High breakdown-point and high efficiency estimates for regression. *Ann. Stat.*, 15, 642–665.

Zhu, J. (1986). The unification of different criteria of estimation in adjustment. *Acta Geodetica et Cartographica Sinica*, 15(4).

Zhu, J. (1996). Robustness and the robust estimate. *J. Geod.* 70, 586–590.

Chapter 10

Comparison Between GPS Sea Surface Heights, MSS Models and Satellite Altimetry Data in the Aegean Sea. Implications for Local Geoid Improvement

I. Mintourakis and D. Delikaraoglou

Abstract We have conducted various experiments of sea surface height (SSH) measurements in Greece's Aegean Sea using on-board kinematic GPS recordings and the KMSS04 satellite altimetry-derived mean sea surface for comparison. This region is of particular interest because of strong crustal movements due to intense tectonic activity that create significant local geoid variations. In this paper, we report on the results of separate SSH surveys that were conducted in three test areas in the Aegean Sea. Ship borne GPS data were collected together with GPS data simultaneously collected at nearby mainland reference stations. These high rate data were processed in kinematic mode using scientific GPS software and related to SSH observations, thus allowing us to obtain maps of the instantaneous sea surface, which was estimated with a precision at the level of a few centimeters. Tidal recordings from nearby tidal stations provided us with the required tidal corrections for the reduction of the GPS-derived SSHs to mean sea level (MSL). Following a filtering process, a cross over adjustment and gridding of the pointwise SSH observations in each test area, local maps of the mean sea surface (MSS) were obtained, which can be compared with the available KMSS04 global solution for the MSS. To examine further the MSS-related results that we observed in these experiments, we compared both the GPS-derived and the KMSS04-related MSS with JASON-1 radar altimetry and ICEsat laser altimetry data over the same areas. We show that the SSHs derived from the GPS ship surveys, when carefully analyzed and applying suitable filtering techniques and necessary corrections for the Dynamic Ocean Topography (DOT) can provide enhanced shorter wavelength components of the local geoid. This is illustrated with additional comparisons with the EGM96 and EGM08 global geoid models, in order to reveal any significant differences, mainly in the short wavelength domain, when compared to the aforementioned local geoid models computed from purely GPS-derived SSH data.

I. Mintourakis (✉)
Department of Surveying Engineering, National Technical University of Athens, Zografos 15780, Greece
e-mail: mintioan@survey.ntua.gr

10.1 Introduction

The use of GPS receivers for collecting Sea Surface Height (SSH) data has been implemented mostly with the use of GPS equipped buoys for satellite radar altimetry calibrations (Born et al., 1994), while ship borne GPS SSH campaigns are quite rare, mainly because of the high costs associated with such sea trials.

The current project was motivated initially by the lack of regular SSH campaigns in Greece, so that when the opportunity presented itself it was decided to collect SSH data with a GPS receiver installed on the Hellenic Navy's Hydrographic Service vessel R/V NAUTILUS during some of its regular hydrographic surveys. Thus we have collected SSH data during three hydrographic cruises from May 2006 to September 2007, in the areas shown in Fig. 10.1. The GPS receivers used in the project were the Daussault Sercel SCORPIO 6002 (land survey) and AQUARIUS 5002 (marine survey) types. Both receivers are 12-channel, dual frequency instruments using DSNP NAP geodetic

S.P. Mertikas (ed.), *Gravity, Geoid and Earth Observation*, International Association of Geodesy Symposia 135,
DOI 10.1007/978-3-642-10634-7_10, © Springer-Verlag Berlin Heidelberg 2010

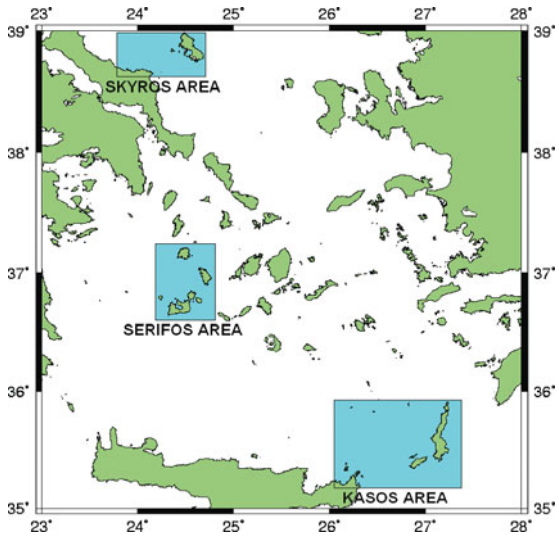


Fig. 10.1 Location of test areas

antennas and allowing code and phase observations on L1 and L2. Both systems are capable of LRK (long range kinematic) techniques and feature UHF coverage of up to 40 km, initialization time of a few seconds and 1–2 cm accuracy at 1-s sampling rate. The receivers operated at 1 Hz recording rate, thus offering a wealth of instantaneous SSH measurements with extremely high spatial resolution in the areas of operation.

Initial processing included the necessary reductions of the GPS SSH data to Mean Sea Level (MSL) using nearby tidal stations and a crossover adjustment. Subsequently, we made comparisons of the GPS-derived MSS results with the global mean sea surface model KMSS04 (Knudsen et al., 2005), which is the result of a combine solution of 9-year (1993–2001) repeated and averaged over time altimetry observations from multiple altimetry satellites (TOPEX/Poseidon, ERS-1 and -2, GEOSAT, and GFO).

From a preliminary inspection of the observed mean differences between the GPS-derived MSL and the KMSS04 MSS, ($MSL_{GPS} - MSS_{KMSS04}$), we concluded that there were some small biases present in the data, which ranged from –9 cm in the data collected in the region between Serifos, Sifnos, and Kimolos islands (hereby designated as *Serifos area*), to 23 cm in the region between Crete, Kasos and Karpathos islands (designated as *Kasos area*) and only 1 cm in the region between Skyros and Evia islands (designated as *Skyros area*). We first suspected that a likely influence for these biases had to do with the various tide systems used, i.e. the fact that the KMS04 MSS is given in the Mean tide system (MTS) whereas in the GPS processing (because of its inherently geometric positioning nature) the no tide system (NTS) is used. Typically, in marginal seas, this can give a latitudinal offset in the range of 10–20 cm. However, there is no evidence for this occurring in our test areas, considering also that the tides are particularly weak in these parts of the Aegean Sea. Instead, we feel that a large part of these biases can be attributed to unaccounted vessel vertical motion effects, which in our case were not possible to compensate for because of the lack of an onboard inertial navigation system (INS) and/or a heave-measuring sensor, which otherwise would help to correct for some of these effects during each cruise. In particular, the higher mean difference noted for the data collected in the Kasos area can be attributed to a lower precision (up to a few centimetres) of the antenna height measurement with respect to the vessels static waterline, and the changes in the vessel's payload during the specific survey trip, as well as the effect of the vessel's speed on the determination of the waterline (i.e. the influence of dynamic draft).

In order to alleviate these recognized weaknesses in our measuring process, it was decided to use the KMSS04 model as a reference surface for the data of each cruise. Therefore all GPS-derived SSHs were "leveled" to KMS04 by removing the observed bias for each of the three major cruises, thus reducing our data from the NTS to the MTS system. Subsequently, the strategy that was followed was to apply first an along-track time domain filter, followed by a reduction of the instantaneous SSH measurements to MSL with the use of mean monthly sea level anomalies from nearby tide gauges, and lastly, by performing a cross over adjustment of all kinematic GPS trajectories in order to minimize the sea height differences across the entire area of each experiment.

For each of these processing steps, we present in the sequel descriptive statistics of the corresponding comparisons with the KMSS04 mean sea surface in order to illustrate the amount of improvement in the results that was achieved at each step of this process. Most of our computations were done using the Generic Mapping Tools suite (GMT).

The major objective in this effort is to demonstrate the potential of shipborne GPS SSH measurements to produce accurate MSS maps inherently containing information about the short wavelength variations of

the local geoid in the areas of our tests. Hence, in order to validate further the results of these experiments, we made additional comparisons with the EGM96 (Lemoine et al., 1998) and EGM08 (Pavlis et al., 2008) global geoid models and the so-called Self-Consistent Synthetic Geoid regional model over Greece (SCSGGr) that has been produced and is distributed on a $5' \times 5'$ grid by the IAG Special Study Group SSG3.177 (2002).

10.2 Processing of GPS Derived SSH Data

10.2.1 Along Track Filtering

Our instantaneous GPS SSH measurements were contaminated (a) by high frequency noise mostly due to roll and pitch movements of the vessel while travelling in variable sea wave conditions, and (b) by the occasional difficulties to resolve the integer phase ambiguities of the kinematic GPS solutions.

In order to smooth the instantaneous SSH data we have applied different along track filters in the time domain. Initially we tried various options, such as, for example, the boxcar-, the cosine arch- and the Gaussian-type convolution filters, each with resolutions varying from 200 s to 1,200 s, and concluded that there were insignificant differences among these types of filters for the same resolutions. Therefore, it was decided to apply throughout a time domain Gaussian filter of 600 s resolution, which for an average vessel speed of 4 m/s corresponds to 2.4 km full wavelength (or 1.2 km spatial resolution). In addition, we applied a rejection criterion for any along-track data gaps exceeding 60 s duration.

The application of Gaussian filtering on the collected GPS SSH data, as compared with the KMSS04 model in a total of 10,20,711 points, resulted in a significant improvement. As shown in Table 10.1, this improvement is evident from the pre- and after-filtering minimum and maximum differences and their range by almost 50%, as well as the noticeable improvement in the corresponding standard deviations.

10.2.2 Reduction of GPS Sea Surface Heights to MSL

In order to reduce the filtered GPS sea surface heights to MSL we have used monthly tidal records from nearby tide gauge stations. This step required to bring each of the tidal datasets to an unbiased estimate of MSL at a common epoch, to express them all in a common datum, and to interpolate them into a continuous mean sea surface. These steps allowed us to produce a grid of sea level anomalies (SLA) using a tension surface algorithm. Although the SLAs are quite small in the Aegean Sea (ranging only to a few centimetres) special consideration was paid on the choice of the location of appropriate tide gauges that were used for this purpose. Subsequently, the reduction of each SSH measurement to MSL required an interpolation from the generated SLA grid to the location of each measurement point.

Diurnal sea level variations, which can also account for a few centimetres (i.e. not more than 10 cm, for most of the cases) were left to be treated through the subsequent cross over adjustment process. As shown in Table 10.2, the reduction to MSL, using monthly tidal records, brought the mean difference of the GPS-derived MSL and KMSS04 down to the millimetre level, also suggesting that the use of monthly tidal records was adequate for our purpose and there was little to be gained by using, for example, hourly or even daily SLA values.

Table 10.1 Statistics of the discrepancies between GPS-derived SSH and KMSS04 MSS as a result of along-track filtering

Mean (m)	Standard deviation (m)	Min (m)	Max (m)	Range (m)
Before along track filtering				
0.020	0.124	−1.482	1.485	2.967
After along track filtering				
0.020	0.112	−0.580	0.950	1.530

Table 10.2 Statistics of the discrepancies between GPS-derived MSL and KMSS04 MSS following SSH to MSL reductions

Mean (m)	Standard deviation (m)	Min (m)	Max (m)	Range (m)
Before reduction to MSL				
0.020	0.112	−0.580	0.950	1.530
After reduction to MSL				
−0.001	0.113	−0.633	0.928	1.561

10.2.3 Cross Over Adjustment

Cross over errors at the intersections of the vessel's GPS trajectories, in our case, can be attributed mostly to the difference, during the various legs of a cruise, in the vessel's draft caused by the change of its tonnage due to fuel usage and water consumption or any significant changes in the weight of its carried equipment (e.g. boat loading variances during the course of a survey). Considering the length of each cruise, in our case, it was considered adequate to implement a least squares cross over adjustment model consisting of a constant shift and a time drift.

For the implementation of the cross over adjustment methodology we divided our data to daily cruises and used the "x_over" module of GMT to perform the necessary computations (Wessel, 1989). Based on a total of 1,008 crossover points in all three test areas, the adjustment results showed a mean of the cross over differences of −0.011 m and a standard deviation of 0.111 m before adjustment, and after the adjustment these respective values fell to a mean of −0.001 m and a standard deviation of 0.059 m. The latter value should be interpreted as the internal accuracy of our dataset after the cross over adjustment. A slight improvement was noted in the statistics of the cross over adjustment-corrected GPS MSL dataset as compared to KMSS04. The improvement of the GPS-derived MSL dataset after the cross over adjustment becomes more evident in the first two test areas (i.e. the Serifos area and the Kasos area respectively) while there is a slight deterioration in the statistics for the Skyros area, as shown in Table 10.3, which needs to be examined further. The later could be attributed to the combination of very steep bathymetry near the shore and the fact that the major part of the comparison is held in a narrow zone very close to the coast where the KMSS04 satellite altimetry derived MSS possibly have a reduced quality.

Table 10.3 Statistics, per region of experiments, of the discrepancies between GPS-derived MSL and KMSS04 MSS following the cross over adjustment

Mean (m)	Standard deviation (m)	Min (m)	Max (m)	Range (m)
Serifos area before COA (4,66,705 SSH points)				
0.011	0.096	−0.280	0.298	0.578
Serifos area after COA				
0.003	0.065	−0.235	0.218	0.453
Kasos area before COA (3,21,498 SSH points)				
−0.025	0.129	−0.633	0.304	0.937
Kasos area after COA				
−0.006	0.112	−0.604	0.296	0.900
Skyros area before COA (2,19,156 SSH points)				
−0.009	0.115	−0.374	0.345	0.720
Skyros area after COA				
0.010	0.134	−0.383	0.437	0.821

10.2.4 Gridding and Smoothing of Datasets

As a final processing step, in order to produce the required MSS maps it was necessary to implement a gridding process on the cross over-adjusted GPS MSL data points, accompanied by a smoothing of the generated grid for each test area. For this purpose we used an adjustable tension continuous curvature surface algorithm, together with a Gaussian filter in the spatial domain with a 4 arcmin full wavelength, for the purpose of smoothing the final grids. The final MSS maps were computed with a resolution of 15 arcsec (i.e. grid spacing 450 m). These were then compared to KMSS04 for each region and the results are shown in Table 10.4. Due to the space limitations in this paper, we only show in Figs. 10.2 and 10.3 the respective maps for the Serifos area.

10.3 Comparisons with JASON-1 and ICESat Altimetry Data

In two of our test areas, we were able to make a further comparison of the final MSS, in each case, with the altimetry observations of the JASON-1 subtrack number 094 (cycles 70 through 205), which was crossing both areas. This subtrack descends from the Chalkidiki peninsula passing west of the island of

Table 10.4 Statistics of the discrepancies between the final GPS-derived MSS (gridded GPS-derived MSL) and KMSS04 MSS

Mean (m)	Standard deviation (m)	Min (m)	Max (m)	Range (m)
Serifos area MSS				
0.012	0.063	−0.141	0.187	0.328
Kasos area MSS				
−0.038	0.086	−0.286	0.166	0.451
Skyros area MSS				
0.043	0.111	−0.235	0.400	0.635

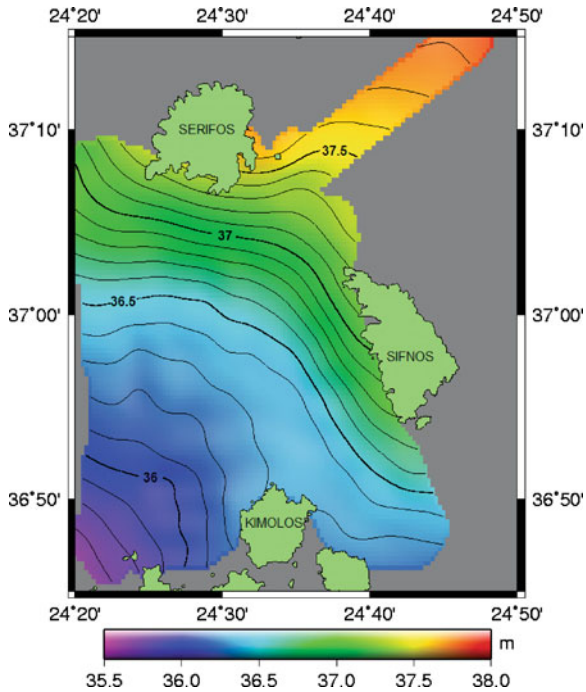


Fig. 10.2 Final GPS-derived MSS computed for the Serifos area

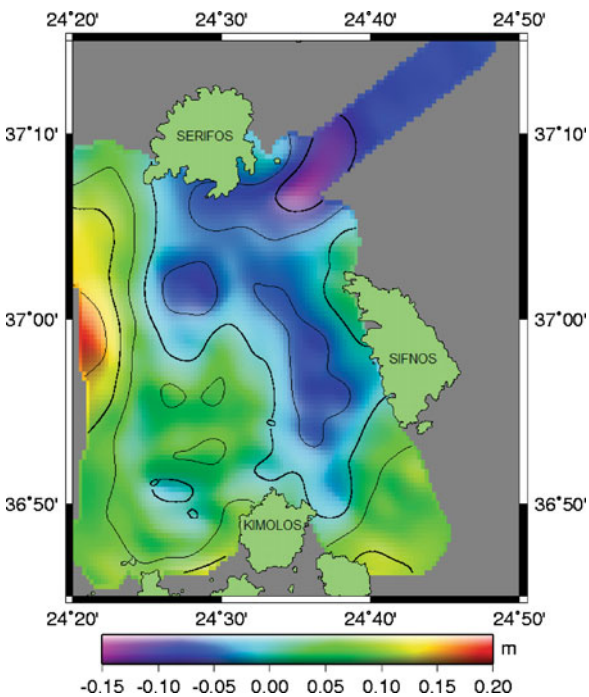


Fig. 10.3 Difference between the final MSS and KMSS04 for the Serifos area

Skyros and through the Kasos-Creta straight. For this purpose we use the data from the AVISO Geophysical Data Records (GDRs) and applied all the range corrections provided, namely: for the dry troposphere (model ECMWF) and the radiometer wet tropospheric correction on Ku-band, together with ionospheric and sea state bias corrections, as well as inverse barometer and tidal (FES99 model) corrections.

Similar comparisons were possible with the laser altimetry observations, covering all three areas of interest, from several subtracks of the Ice, Cloud, and land Elevation Satellite (ICESat) for the satellite's operational periods from 2003 till 2007. For these comparisons, we use pre-processed ICESat altimetry observations, without any additional reductions (e.g. stacking or cross over adjustments). In Tables 10.5 and 10.6 we present the statistics of the differences obtained between the altimetry observations from each of these satellites and the KMSS04 model. It should be noted that in both of these tables, the comparisons shown between the GPS-derived MSS smoothed grids and the KMSS04 are made on the locations of each altimetry footprint, and not for the entire grid as it was done for the similar comparisons shown in Table 10.4.

Table 10.5 Statistics of the discrepancies of pair combinations between the JASON-1 footprints, the GPS-derived MSS smoothed grids and the KMSS04

Delta	Mean (m)	Standard deviation (m)
JASON-*Kasos area* MSS	0.248	0.151
JASON-KMSS04	0.196	0.140
Kasos area MSS-KMSS04	−0.052	0.042
JASON-*Skyros area* MSS	0.142	0.137
JASON-KMSS04	0.191	0.138
Skyros area MSS-KMSS04	0.048	0.048

Table 10.6 Statistics of the discrepancies of pair combinations between the ICESat footprints, the GPS-derived MSS smoothed grids and KMSS04

Delta	Mean (m)	Standard deviation (m)
ICE-*Serifos area* MSS	−0.135	0.208
ICE-KMSS04	−0.121	0.213
Serifos area MSS-KMSS04	0.014	0.056
ICE-*Kasos area* MSS	0.028	0.251
ICE-KMSS04	0.006	0.254
Kasos area MSS-KMSS04	−0.022	0.066
ICE-*Skyros area* MSS	−0.164	0.218
ICE-KMSS04	−0.092	0.188
Skyros area MSS-KMSS04	0.072	0.124

From the results shown in Table 10.5, it is clearly seen that there are small differences, i.e. at the 5 cm level for the corresponding mean differences, and at the cm level for the Standard Deviations, for the comparisons of the JASON footprints and both the regional MSSs and KMSS04. It is also noticeable that the comparisons between KMSS04 and JASON-1 SSHs give almost identical results for both test areas.

Similarly, it is evident from Table 10.6, that there are no significant differences (i.e. at the 1–2 cm level for the corresponding mean differences, and at the sub-cm level for the Standard Deviations) in the comparisons between the ICEsat footprints data and both the regional MSSs and KMSS04 for the test areas of Serifos and Kasos islands. The corresponding results seem to be slightly worse for the area of Skyros Island (i.e. at more that 7 cm in the mean differences, and 3 cm in the Standard Deviations).

10.4 Comparisons with Global and Local Geoid Models

The MSS models generated from the GPS data contain both the geoid and the Dynamic Ocean Topography (DOT) signals. Therefore, in order to make meaningful comparisons with various geoid models it is necessary to remove the DOT signal from the estimated MSS. To do so, we used the DNSC08 MDT global model (Andersen and Knudsen, 2008) and made further comparisons of the resulting local marine geoid models with the EGM96 and EGM08 geopotential models and the existing SCSGGr geoid model. The results of these comparisons are shown in Table 10.7

To illustrate the differences of the new local geoid models versus EGM2008, the results for the Serifos area are depicted in Fig. 10.4, together with topography-bathymetry contours from the SRTM30 model. Although the SRTM30 is not accurate enough or even with the appropriate resolution, one can see the very close agreement between the major local topography-bathymetry variations described by the SRTM30 model and the corresponding variations described by the local geoid model in this area. It is clear that these local variations are strongly related to topography signal and that the new local geoid models that were derived purely from marine GPS measurements, are capable to depict short topography variations and have the potential to provide enhanced shorter wavelength components of the geoid.

Table 10.7 Statistics of the differences between the GPS-derived local marine geoid(s) and EGM96/08, SCSGGr geoid models

	Mean (m)	Standard deviation (m)
Serifos area geoid EGM08	0.267	0.087
Serifos area geoid EGM96	−0.133	0.158
Serifos area geoid SCSGGr	−0.654	0.072
Kasos area geoid EGM08	−0.240	0.124
Kasos area EGM96	−0.514	0.306
Kasos area SCSGGr	−1.341	0.119
Skyros area geoid EGM08	0.191	0.232
Skyros area geoid EGM96	−0.248	0.266
Skyros area geoid SCSGGr	−0.638	0.198

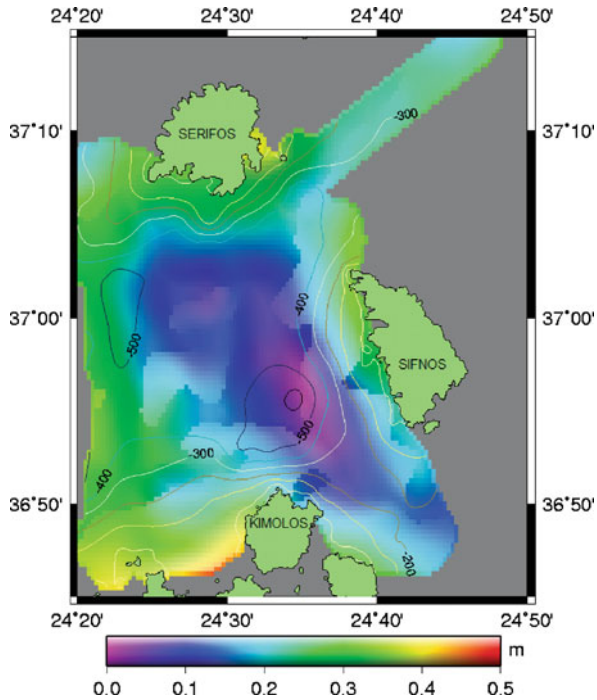


Fig. 10.4 Undulation differences between the local geoid model in the area of Serifos and the EGM2008 geoid. Topography-bathymetry contours are plotted at 200 m interval

10.5 Conclusions

Although these first results seem encouraging there are still a number of improvements possible in the methodology just outlined. Obviously, better results may be possible by using additional shipborne equipment in aid of the GPS receiver, such as an INS unit and a heave-draught correction sensor, which

could aid the compensation of many adverse effects of the vessel's motion, speed variations and sea wave conditions.

As this is a preliminary study, in our follow up investigations we plan to pursue a number of refinements, such as accounting for other contributions to sea level variations (e.g. seasonal heating and expansion of the sea surface), as well as further refinements in the GPS derived SSH data processing techniques (e.g. using daily or even hourly tidal corrections instead of monthly values) and experimenting with different crossover adjustment strategies (e.g. steady course vs. daily duration cruise legs).

References

Andersen, O.P. and P. Knudsen (2008). The DNSC08MDT mean dynamic topography. European Geosciences Union General Assembly, Vienna, Austria, April13–18.

Born, G.H., M.E. Parke, P. Axelrad, K.L. Gold, J. Johnson, K.W. Key, D.G. Kubitschek, and E.J. Christensen (1994). Calibration of the TOPEX altimeter using a GPS buoy. *J. Geophys. Res.*, *99*(C12), 24517–24526.

IAG Special Study Group SSG3.177 (2002). Synthetic modelling of the Earth's gravity field. Availabe at http://www.cage.curtin.edu.au/∼will/ssgres.html (Last accessed on June 18, 2008).

Knudsen, P., A.L. Vest, and O. Andersen (2005). Evaluating mean dynamic topography models within the GOCINA project. ESA SP–572, April.

Lemoine, F.G., S.C. Kenyon, J.K. Factor, R.G. Trimmer, N.K. Pavlis, D.S. Chinn, C.M. Cox, S.M. Klosko, S.B. Luthcke, M.H. Torrence, Y.M. Wang, R.G. Williamson, E.C. Pavlis, R.H. Rapp, and T.R. Olson (1998). The development of the joint NASA GSFC and the National Imagery and Mapping Agency (NIMA) geopotential model EGM96. *NASA Tech. Pub. 1998-206861*, Goddard Space Flight Center, Greenbelt, MD.

Pavlis, N.K., S.A. Holmes, S.C. Kenyon, and J.K. Factor (2008). An earth gravitational model to degree 2160: EGM2008. Presentation given at the 2008 European Geosciences Union General Assembly, Vienna, Austria, April1 3–18.

Wessel, P. (1989). XOVER: A cross-over error detector for track data. *Comput. Geosci.*, 15, 333–346.

Chapter 11

First Experience with the Transportable MPG-2 Absolute Gravimeter

S. Svitlov, C. Rothleitner, and L.J. Wang

Abstract We report on design details and first results obtained with the transportable absolute gravimeter MPG-2 ("Max-Planck-Gravimeter"). It is developed as an evolution of the stationary device MPG-1, completed in 2007. The MPG-2 is built on a common scheme where the position of a freely falling object is monitored. The setup consists of a ballistic block, an interferometer and the electronics. Free fall drops can be repeated every 10 s with the standard deviation close to 30 μgal. A one-day gravity observation gives a result with a standard deviation of the mean of less than 5 μgal. A prototype of the MPG-2 took part in the ECAG-2007. New measurements at the reference gravity station "Bad Homburg", Germany confirmed the declared combined standard uncertainty of 50 μgal.

11.1 Introduction

An absolute value of gravitational acceleration g is widely required in metrology, geodesy and geophysics. In an absolute gravimeter the position of a free falling test mass is monitored using an interferometer and highly precise length and time standards (Niebauer et al., 1995). The test mass contains one retro-reflector, while a second one is fixed to a pseudo-inertial reference frame. The freefall trajectory is given by timing the interference fringes generated during the test mass's motion. Afterwards, the g value is calculated by fitting a freefall motion model to the measured time-distance coordinates.

A comparison of different gravimeters helps to discover possible systematic errors. In this paper, we describe the MPG-2 absolute gravimeter and discuss first results obtained at different sites. The offset detected during the ECAG-2007 of (+515 ± 14) μgal was resolved by placing the ion pump about 0.3 m farther away from the ballistic block. In the specifications we introduce and explain the repeatability (5 μgal), reproducibility (25 μgal), and standard uncertainty (50 μgal). Such metrological components can be used separately, depending on a particular application, along with the reported result of measurement.

11.2 Setup

The classical freefall method is adopted for the instrument. It is developed as an evolution of the earlier completed stationary MPG-1 absolute gravimeter (Rothleitner, 2008). Figure 11.1 shows the setup of the MPG-2. It is a transportable apparatus, although still a prototype. It consists of the ballistic block with the falling body, motor and a lifting/releasing mechanism inside a vacuum chamber, plus the ion pump, a table, an interferometer, a notebook with a PCI extension, a laser, and a frequency standard (Rothleitner, 2008).

The interferometer is built following the modified Mach-Zehnder "in-line system" (Niebauer et al., 1995). It is mounted on top of the Superspring (Micro-g LaCoste), which is used as the vibration isolated reference retro-reflector. The actual MPG-2 vibration isolation system is still under construction. A frequency stabilized He-Ne laser with a wavelength

S. Svitlov (✉)
Max Planck Institute for the Science of Light, Erlangen 91058, Germany
e-mail: ssvitlov@optik.uni-erlangen.de

S.P. Mertikas (ed.), *Gravity, Geoid and Earth Observation*, International Association of Geodesy Symposia 135,
DOI 10.1007/978-3-642-10634-7_11, © Springer-Verlag Berlin Heidelberg 2010

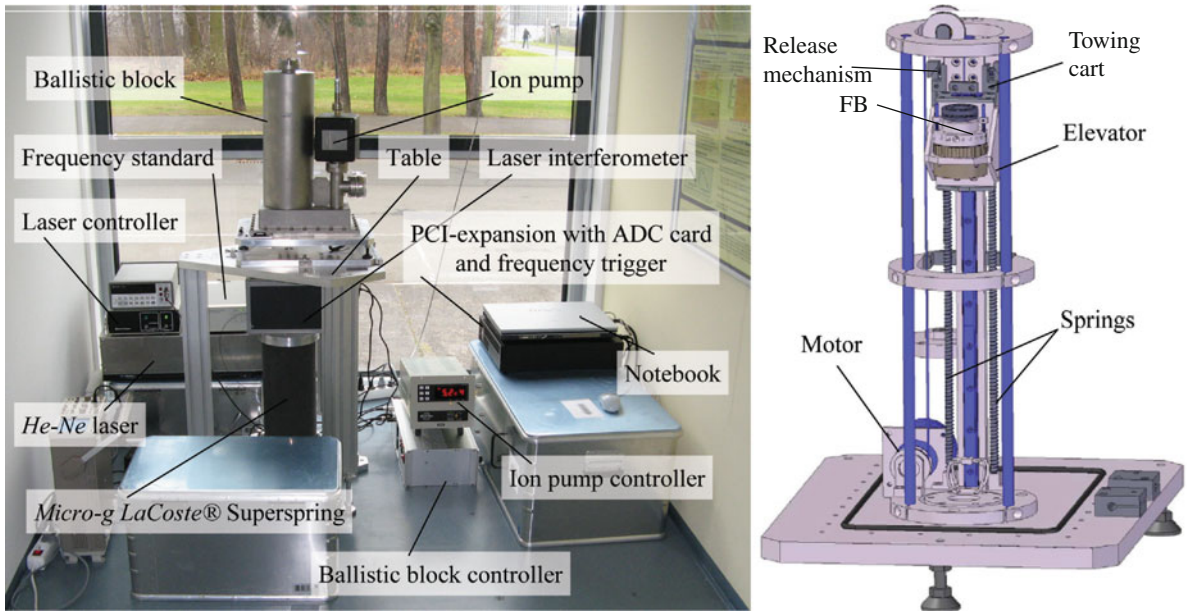


Fig. 11.1 Absolute gravimeter MPG-2: set-up and lifting/releasing mechanism

of 633 nm (Spectra Physics/Newport, 117A) is fiber-coupled to the interferometer. Its frequency was measured with a relative standard uncertainty of 3.7×10^{-10} in 2007, using the frequency comb (Menlo Systems, FC8004), referenced by a cesium tube clock (Agilent 5071A), which, in turn, is traceable to PTB, Germany. A specified long-term (24 h) stability of the laser frequency is $\pm6.3\times10^{-9}$; giving a standard uncertainty of g of 3.7 μgal. The fringe signal is detected with a high-speed DC to 200 MHz bandwidth photo-receiver (FEMTO Messtechnik GmbH, HCA-S-200 M-SI) with a built-in Si PIN photodiode.

The ballistic block is composed of a vacuum chamber containing the mechanics inside, plus the ion pump (Fig. 11.1). The vacuum compatible stepper motor (Phytron) is used only to lift the elevator with the falling body. The center of mass of the falling body is adjusted to the optical center of the retro-reflector in 3-D space to within 20 μm (Rothleitner et al., 2007). The elevator is guided by two ball bearings (THK) lubricated with vacuum grease. The elevator loads two springs, attached to its bottom, while it is lifted. At the top position the motor is stopped, and the elevator is released by a special mechanism. Then the elevator is accelerated down a little more than g by the stretched springs, and the falling body starts to fall freely. The spring length is adjusted in such a way as to catch the falling body gently close to the bottom. The free fall usually lasts 6 cm. Depending on the settings on the graphical user interface, several drops can be performed with a given repetition rate and then collected in series.

The acquisition electronics is accumulated in a 4-slot PCI-extension (Magma). To record the fringe signal, we use a digitizing 2-channel PCI card (Gage Applied, CS12400) with a sampling frequency of 100 MHz, phase-locked to an external 10 MHz rubidium frequency standard (SRS, FS725). The frequency of this standard was measured in 2007 using a cesium frequency standard (Symmetricom, 5071A), calibrated at PTB. The measured offset from the nominal value of (+4.7 ± 0.5) MHz agrees with that measured during the ECAG-2007 (+5.3 MHz). Converting to gravity, this gives a correction of +1.0 μgal with the standard uncertainty of 0.3 μgal (a specified aging in a range of up to 5×10^{-10} yearly is considered here). The card has an onboard memory of 512 MB, 10 bits of amplitude resolution (effective number), 200 MHz bandwidth, and sits in the PCI-extension, which is connected to a notebook (2 GB RAM, Intel®Core™ T7200 @ 2.00 GHz). The acquisition starts when a special trigger generates a pulse at 1 MHz ± 2.0 kHz of the fringe frequency, which corresponds to the initial height h_0 of (5±0.1) mm below the top position of the falling body.

The ballistic block controller contains a driver for the motor and the power supplies, and is placed in a separate 19 in. rack. The laser and the ion pump also have separate controllers (Fig. 11.1).

All the controlling, acquisition and processing codes are developed on the MATLAB® 7.0 platform. Since the entire fringe signal is digitized, different processing algorithms can be applied. In this paper we report only results calculated using the straightforward digital zero-crossing method.

A considered linear freefall motion model is a second-order (assumed vertical gravity gradient γ is equal to zero) or a fourth-order (with the known gravity gradient γ) polynomial (Timmen, 2003):

$$z(t) = z_0 + v_0 t + \frac{1}{2} g_0 t^2 + \gamma \left(\frac{1}{2} z_0 t^2 + \frac{1}{6} v_0 t^3 + \frac{1}{24} g_0 t^4 \right), \quad (1)$$

where z_0, v_0 and g_0 are the initial conditions at $t = 0$ and $z = 0$. In the MPG-2 data acquisition starts when the falling body fell about $h_0 = 5$ mm from the top position. The effect of the gradient in case of the second-order polynomial used is taken into account by referencing the least-squares solution for g to the effective height below the origin $z = 0$ (i.e., below the initial height h_0) (Timmen, 2003). Note that in both cases (the second order model with no gradient and the fourth order model with known gradient) the solutions for g are referenced to the same point in space, shifted by h_0 from the top position. One can transfer a g value to the top position with a correction of $-\gamma h_0$ (here γ is a positive number). For this, the initial height can be calculated as $h_0 \approx v_0^2/(2g_0)$, and the least squares solution for z_0 should not substitute h_0.

11.3 Experimental Results

11.3.1 Repeated Measurements

With the MPG-2, 10 drops are repeated every 10 s, giving an individual result with a standard deviation of the mean close to 10 μgal. Then the results are hourly collected in sets, providing the standard deviation of the mean value over one day of less than 5 μgal. Such a specific sampling rate with a low duty cycle is optimized to the current performance of the MPG-2. First, it allows to reach a permissible level of the statistical uncertainty (5 μgal) in the specified combined standard uncertainty (50 μgal), and second, it extends the life time of the instrument. An example of the one-day measurements in comparison with the theoretical tides, calculated using the TSoft program (Van Camp and Vauterin, 2005), is shown in Fig. 11.2. Here the mean value is corrected for the solid tides, polar motion, atmospheric pressure changes, the ocean loading effect, and includes an instrumental correction of +32.4 μgal. The standard deviation of the mean of 2.1 μgal (the repeatability) can be also treated as a resolution over one day at this particular site.

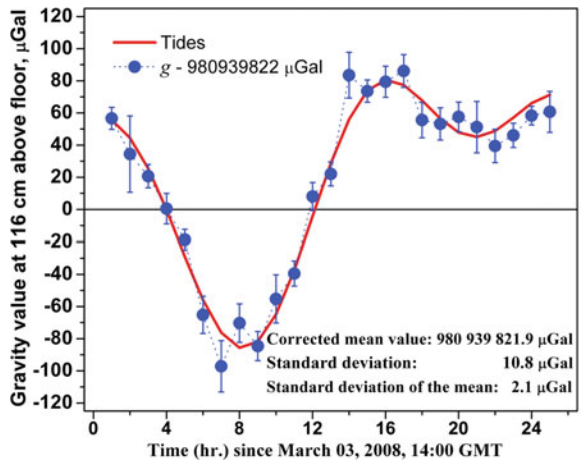


Fig. 11.2 One-day measurement results at the site "Erlangen"

11.3.2 Results of Comparisons

A prototype of the MPG-2 took part in the ECAG-2007, Luxembourg. At each of three visited sites the g value was measured with the repeatability of 5 μgal. However, an offset of (+515 ± 14) μgal was observed there. The reason for that was found to be the very close location of the ion pump with the strong permanent magnets to the ballistic block. The housing of the falling body is made of titanium, but also contains three supporting stainless steel balls. Because of the magnetic attraction downwards, the falling body was in addition accelerated. The problem was later resolved by placing the ion pump farther away by 0.3 m from the ballistic block. But, due to a possible remaining magnetization of the falling body, the standard uncertainty of 5.2 μgal is now associated

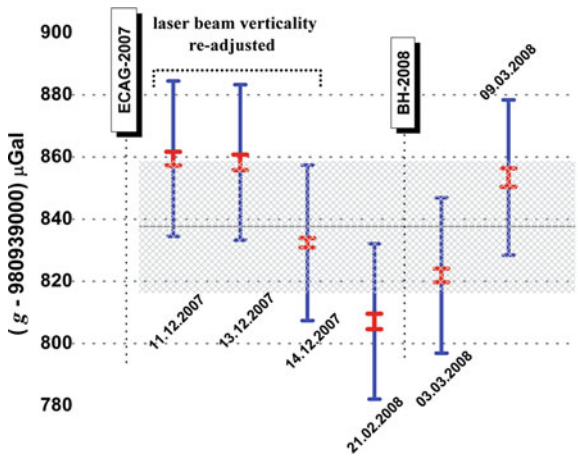


Fig. 11.3 Repeated measurements at the site "Erlangen"

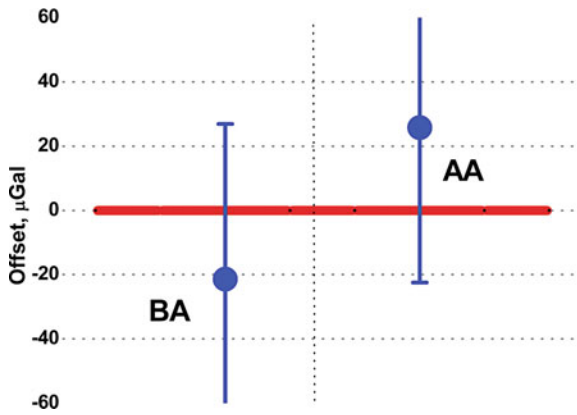


Fig. 11.4 Results of measurements at the site "Bad Homburg"

with the magnetic field effect (1% of the observed offset). Another construction of the falling body is under consideration.

With the improvements achieved, several measurements were repeated at the site "Erlangen". Fig. 11.3 reports its results at the height of 116 cm above the floor with all the corrections, mentioned in Sect. 11.3.1. The experimental repeatability for each particular set-up was up to 3 μgal (shown as the smaller error bars); however, the experimental reproducibility (the standard deviation of all the six results) was within ±22 μgal (shown as the shaded area around the mean value). To specify the reproducibility, a more conservative value of 25 μgal is used (shown as the larger error bars). Different set-ups of the instrument include results obtained with different alignments of the laser beam verticality and also before and after travelling (a closed loop "Erlangen – Bad Homburg – Erlangen" was performed). When the laser beam verticality was intentionally re-adjusted (the first three results in Fig. 11.3), the experimental standard deviation was 16 μgal; we attribute this to an overestimated value of the laser beam verticality effect.

In order to identify the detected offset and to prove the uncertainty budget, further measurements with new location of the ion pump were performed at the reference gravity station "Bad Homburg" in 2008. The results are reported in Fig. 11.4 with the calculated combined standard uncertainty of 48.3 μgal (error bars). The latest results overlap with the reference values known for two pillars at this station, which confirms the declared combined standard uncertainty of 50 μgal (Sect. 11.4).

11.3.3 Floor Recoil and Standard Uncertainty

This section discusses the major error source in the uncertainty budget, the floor recoil. With the MPG-2, we observed different recoil effects at the sites "Erlangen", "Walferdange" and "Bad Homburg", comparing the residuals between the calculated time-distance coordinates and the fitted freefall motion model (1). The floor recoil appears each time during start of a freefall. At this moment the stretched springs, being suddenly released, pull both the elevator down and the bottom of the chamber up. In addition, the mass of the instrument is quickly reduced by the mass of the falling body. A mechanical impulse, transmitted to the floor, originates resonant oscillations of the basement and excites internal modes of the spring-mass system in the Superspring (Rinker RLI, 1983). The amplitude of oscillations may also depend on a particular set-up of the instrument. The Superspring essentially damps the internal modes (Rinker RLI, 1983) and protects the reference reflector from oscillations of a basement; however, they still penetrate to other optical components and produce an effect also known as the air-gap modulation problem (Niebauer et al., 1995). Besides, some inclinations of the laser beam from its static vertical orientation are also possible due to the floor recoil. Ways to reduce the problem is minimizing the mass of the elevator, applying counterbalanced masses, building a rigid interferometer, and using the proper vibration absorbing pads. The possibility to remove this effect by the "system response correction" is restricted by the drop length (Charles and Hipkin,

1995), which in case of the MPG-2 is a constant of 80 ms.

In general, the standard deviation of g due to a sinusoidal displacement of the reference reflector in an absolute gravimeter with the data location equally spaced in distance is approximated as (Svetlov, 1997):

$$\sigma_z = \begin{cases} (2\pi f_0)^2 Z_0/\sqrt{2}, & f_0 < 0.7/T \\ \frac{30}{\pi T^3} \cdot \frac{Z_0}{f_0}, & f_0 \geq 0.7/T \end{cases}, \qquad (2)$$

where Z_0 is the amplitude, f_0 is the frequency of the displacement, and T is the total fitted falling time. This estimate is valid for a single drop, when an error in g takes any realization from a range of $\Delta g_z = \pm\sqrt{2}\sigma_z$ due to randomness of an initial phase. In a floor recoil effect, we assume that the initial phase of a sinusoid is fixed for a particular set-up of the instrument. This is equivalent to the systematic effect observed in the accumulated residuals over all the session of measurements. Thus, a mean value of the floor recoil effect is equal to the recoil effect in a single drop, and so the systematic error cannot be reduced statistically by the repeated measurements. Considering all the possible realizations of the fixed phase, a whole range of this systematic error either in one drop or over the whole set of measurements can be evaluated by the standard deviation (2).

An estimation (2) for the site "Erlangen", where $Z_0 = 1\,\text{nm}$, $f_0 = 50$ Hz, $T = 80$ ms, amounts to the standard deviation of $\sigma_Z = 37.3\,\mu\text{gal}$, which relates to the mean value of a one-day measurement result (Table 11.1). From (2) also follows that for a twice longer drop this error could be eight times less. In the current setup we do not apply any correction for the floor recoil. Instead, we included the full amount of this effect in the reported standard uncertainty, as was also proposed in (Lambert and Courtier, 1997). For example, at the different pillars BA and AA (Fig. 11.4) with the different recoils observed, systematic offsets are − 21.4 μgal and +25.8 μgal. However, these offsets are still within the standard uncertainty of ±37.3 μgal associated with the recoil effect (Table 11.1).

Table 11.1 Uncertainty budget of the one-day measurements result obtained with the MPG-2 absolute gravimeter

Influence parameter	Correction (μgal)	Uncertainty (μgal)
Instrumental:		
Time standard	+ 1.0	0.3
Length standard		3.7
Speed of light	– 7.5	0.2
Laser beam verticality	+ 11.0	15.6
Laser beam divergence	+ 22.0	1.8
Floor recoil		37.3
Air drag	+ 4.0	1.8
Magnetic field		5.2
Electronic phase shifts	+ 1.9	0.6
Others		0.9
Subtotal instrumental:	+ 32.4	41.0
Site-dependent corrections		0.7
Uncertainty of the measurand		Site-dependent
Repeatability		5.0
Reproducibility		25.0
Combined		48.3

11.4 Specifications and Terminology

Based on the results of investigations, we revised the original MPG-2 uncertainty budget (Rothleitner, 2008) in part of the laser beam verticality and the magnetic field effects (Table 11.1). Contribution of the instrumental parameters, listed in Table 11.1 as "Others", summarizes the reference height reduction, falling body rotation and the instrumental masses effect (it can be found in Rothleitner (2008) in full details). The eddy currents, the electrostatic field and the temperature effects are not evaluated in this report. The uncertainty due to the site-dependent corrections assumes that the reported one-day result is corrected (with some uncertainties) for the solid tides, polar motion, atmospheric pressure changes and the ocean loading effect (Rothleitner, 2008)]. An uncertainty of the measurand should be included, if the reported result will be used disregarding the actual time of measurement. This uncertainty must combine possible non-modeled gravity changes at the given site (in some cases, they are observable with the superconducting relative gravimeters) and the best knowledge about the measurand, say, in form of an uncertainty of the key comparison reference value (KCRV). The repeatability is given by the

Dynamic range	worldwide
Operating temperature range (ºC)	15–30
Set-up time (hr.)	1–2
Repeatability (μgal)	± 5.0
Reproducibility (μgal)	± 25.0
Standard uncertainty (μgal)	± 50.0
Overall dimensions (H×W×D, cm)	
Mechanics	130×70×70
Electronics	80×60×40
Total mass (kg)	70

experimental standard deviation of the mean over one day (statistical uncertainty), while the reproducibility comes from the Specifications and covers a possible range of the separately evaluated setup-dependent errors. As a result, the combined standard uncertainty amounts to 48.3 μgal.

The MPG-2 gravimeter is intended for various indoor and field applications. Assuming also other possible sources of errors, which are still under investigation in the prototype, in the Specifications we declare the combined standard uncertainty in a more conservative amount of 50 μgal:

According to the recommendations given in (BIPM, 1995), we avoid the terms "accuracy" and "precision". Instead, the *repeatability*, *reproducibility* and *standard uncertainty* are given here. This was also proposed at the GGEO-2008 Symposium, when the results of comparisons were discussed.

The "repeatability" is defined as the "closeness of the agreement between the results of successive measurements of the same measurand carried out under the same conditions of measurement" (BIPM, 1995). Such conditions include the same measurement procedure and the same instrument, used under the same conditions, the same observer, the same location and repetition over a short period of time [10]. With the MPG-2 we repeat g measurements every hour. Then the 1-h or the one-day repeatability for the site "Erlangen" is expressed in term of the standard deviation of the mean, which is 10.8 or 2.1 μgal (see Fig. 11.2). Hence, if a gravimeter occupies the same site, e.g., to evaluate the Earth crustal motions or to calibrate the superconducting gravimeter, the repeatability can be used to specify the standard uncertainty (resolution) of relative gravity measurements using an absolute gravimeter.

The "reproducibility" is defined as the "closeness of the agreement between the results of measurements of the same measurand carried out under the changed conditions of measurement" (BIPM, 1995). The changed conditions include the principle and/or method of measurement, observer, measuring instrument, location, condition of use, time. It follows that if a gravimeter is moved to another site, or if different instruments of the same type occupy the same site, or if different operators operate the same gravimeter, the "reproducibility" should be considered. The specified reproducibility of MPG-2 of 25 μgal covers the experimental setup-to-setup standard deviation of 22 μgal (Fig. 11.3).

A gravimeter could transfer ("reproduce") a known reference g value or that measured with the more accurate absolute gravimeter, to another location. In this case the instrumental correction should compensate the possible systematic offset. Then the combined uncertainty of that new g value is composed of the uncertainty of the reference value, repeatability (twice, at the reference site and at the new site), and the specified reproducibility. So far the reproducibility can be used for long-distance relative gravity measurements.

The "uncertainty of measurement" is the "parameter, associated with the result of measurement, that characterizes the dispersion of the values that could reasonably be attributed to the measurand" (BIPM, 1995). The specified uncertainty must be used if some application requires an absolute value of g at a given location (e.g., "the electronic realization of the kilogram" (Steiner et al., 2005)). This specified uncertainty should combine all the components listed in Table 11.1. To prove the rated operating conditions, various performance tests (climatic, mechanical, electrical) (OIML D11, 2004) might in addition be conducted. Here all the specified options of a gravimeter also needed to be tested, for example, a permitted range of variation of the time interval T in (2). Furthermore, the result of measurement with the declared uncertainty should be traceable to the KCRV or to the reference value of g, as it was demonstrated at the reference station "Bad Homburg" (Fig. 11.4). At the moment, we declare 50 μgal as the combined standard uncertainty of the one-day MPG-2 measurement result.

11.5 Conclusions

The new freefall absolute gravimeter MPG-2 was developed and tested during comparisons. The largest error sources, namely the magnetic field of the ion pump, floor recoil, and laser beam verticality were found and quantified. The first one was reduced by placing the ion pump farther from the ballistic block, the others are minimized and included in the declared standard uncertainty, which amounts to 50 μgal. Also we proposed to split the metrological features of the gravimeter into repeatability, reproducibility, and standard uncertainty.

With further improvements and modifications, we expect to construct a new transportable device (MPG-3) with better specifications for potential applications in geophysics, geodesy and metrology.

References

BIPM, IEC, IFCC, ISO, IUPAC, IUPAP and OIML (1995) Guide to the expression of uncertainty in measurements, 2nd edn (Geneva: ISO).

Charles, K. and R. Hipkin (1995). Vertical gradient and datum height corrections to absolute gravimeter data and the effect of structured fringe signals. *Metrologia*, 32, 193–200.

Lambert, A. and N. Courtier (1997). Toward realistic gravimeter error budgets. In: Proceedings of AGU Chapman Conference on Microgal Gravimetry: Instruments, Observations, and Applications, St. Augustine, Florida, USA, March 3–6: 8.

Niebauer, T.M., G.S. Sasagawa, J.E. Faller, R. Hilt, and F. Klopping (1995). A new generation of absolute gravimeters. *Metrologia*, 32, 159–180.

OIML D11 (2004). General requirements for electronic measuring instruments: 1–56.

Rinker, R.L.I. (1983). Super Spring – a new type of low-frequency vibration isolator. Ph.D. thesis, University of Colorado at Boulder.

Rothleitner, C. (2008). Ultra-high precision, absolute, earth gravity measurements. Ph.D. thesis, University Erlangen-Nuremberg: 138. http://www.opus.ub.uni-erlangen.de/opus/frontdoor.php?source_opus=994&la=de

Rothleitner, C., S. Svitlov, H. Mérimèche, and L.J. Wang (2007). A method for adjusting the centre of mass of a freely falling body in absolute gravimetry. *Metrologia*, 44, 234–241.

Steiner, R.L., D.B. Newell, E.R. Williams, R. Liu, and P. Gournay (2005). The NIST project for the electronic realization of the kilogram. *IEEE Trans. Instrum. Meas*., 54, 846–849.

Svetlov, S.M. (1997). An absolute gravimeter and vibration disturbances: a frequency responses method. In: Segawa, J., H. Fujimoto, and S. Okubo (eds), Proceedings of IAG Symposia 'Gravity, Geoid and Marine Geodesy', Vol. 117, Springer, Berlin, pp. 47–54.

Timmen, L. (2003). Precise definition of the effective measurement height of free-fall absolute gravimeters. *Metrologia*, 40, 62–65.

Van Camp, M. and P. Vauterin (2005). Tsoft: graphical and interactive software for the analysis of time series and Earth tides. *Comput. Geosci.*, 31(5): 631–640.

Chapter 12

Absolute Gravimetry at BIPM, Sèvres (France), at the Time of Dr. Akihiko Sakuma

M. Amalvict

Abstract The Bureau International des Poids et Mesures (BIPM) was created and established in 1875 at Sèvres, (France). The history of Absolute Gravity (AG) measurements at BIPM started soon after and can be divided into three periods. The 1st period went from 1886 to 1960, starting with the decision of CIPM to measure the gravity acceleration at BIPM. First AG measurements were made with a time device: i.e., a pendulum. But as soon as the end of World War I, Amédée Guillet considered monitoring the free fall of an object; a concept also adopted by Charles Volet and Åke Thulin who elaborated an in situ instrument. The second period started in February 1960, when Akihiko Sakuma arrived at BIPM. A. Sakuma was at that time a 29 year old scientist, coming from the National Laboratory of Metrology in Japan. He had already constructed an absolute gravimeter, observing the free fall of a divided line scale with a chronometer of his own invention. His first observation of the "g" value was obtained in 1959, at Tokyo. At BIPM Akihiko Sakuma started to develop a new gravimeter, based on the symmetrical free fall of a reflecting body. For that purpose, he designed new original parts: catapult, seismometer, ... and obtained his first result in October 1966, increasing by two orders of magnitude the precision of former measurements. Thanks to this precision, his observations led to the first observation of the solid earth tides with an absolute instrument. An improved copy of this instrument was installed at the International Latitude Observatory of Mizusawa (Japan), in order to establish new international reference absolute gravity acceleration stations, following the recommendations of the IAG. The BIPM gravimeter was a stationary one, and A. Sakuma worked continuously on the development of a transportable gravimeter. Between 1968 and 1975 he collaborated with the National Institute of Metrology in Turin (Italy), to finalize a transportable absolute gravimeter aiming to calibrate the European Gravity Network. Then between 1978 and 1983, A. Sakuma collaborated with the French Jaeger Co., to produce a transportable absolute gravimeter (GA-60), according to BIPM ideas. The BIPM copy of this instrument measured "g" to 10^{-9}, for the first time. It was also used to establish the 0th order network of the French Gravity Network. We enter then in the world of geophysics and geodesy to which A. Sakuma gave precise foundations. He retired from BIPM in 1996, and died in 2004, at the age 73. By that time, BIPM was in its third period of AG measurements, renouncing its efforts to develop AG instruments and acquiring in 1993 the commercial FG5#108. From then the instrument plays the role of a stationary instrument, monitoring the time variation of gravity at BIPM, and acting as a reference during the International Comparisons, every 4 years.

12.1 Introduction

The Bureau International des Poids et Mesures (BIPM), International Bureau of Weights and Measures was created on May 20 1875, at the last sitting of the "Conférence diplomatique du Mètre". The great achievement of the Conférence was the

M. Amalvict (✉)
Institut de Physique du Globe de Strasbourg / École et Observatoire des Sciences de la Terre (UMR 7516 CNRS-ULP), Strasbourg 67000, France
e-mail: Martine.Amalvict@eost.u-strasbg.fr

S.P. Mertikas (ed.), *Gravity, Geoid and Earth Observation*, International Association of Geodesy Symposia 135,
DOI 10.1007/978-3-642-10634-7_12, © Springer-Verlag Berlin Heidelberg 2010

signature by 17 countries of the so-called "Convention du Mètre", with the objective of the international unification and of the improvement of the Metric System. BIPM was created as a scientific body, supported by the Governments signatories and hosted by France, which was in charge to provide a location for the institution. BIPM is ruled by the "Conférence Générale des Poids et Mesures (CGPM)" and by the "Comité International des Poids et Mesures (CIPM)" which are respectively diplomatic and scientific bodies. The task of BIPM was to "establish new metric standards, maintain the international prototypes and perform the comparisons necessary to ensure the uniformity of measurements all over the world" (Moreau, 1975).

On April 22 1876, the French Government offered the free use of the Pavillon de Breteuil located at Sèvres, in the 25 153 m^2 domain of Parc Saint Cloud (Fig. 12.1).

Very soon, it became apparent to the CIPM (CIPM #1886) that to fulfil its task, BIPM should know precisely the gravity acceleration ("g") at Pavillon de Breteuil. It was already well known that because of the shape of the earth, and because of the heterogeneities of its internal structure (even very close to the surface), the value of "g" is highly variable from one point to another. The acceleration of gravity is indeed a part of the realisation of a number of other forces. The group measuring the barometric pressure was one of the most demanding working groups; it insisted on the necessity of a precise knowledge of "g" to define the so-called "normal atmosphere". The measurement of gravity acceleration was consequently organised soon after the request of CIPM.

12.2 Absolute Gravity Measurements at BIPM – First Stage: 1888–1960

Whatever the method used, the measurement of gravity acceleration requires the measurement of time and of a distance. The pendulum had been used to measure the gravity, since the seventeenth century. It was an absolute measurement and it was the only way to get the value of gravity. The number of oscillations in a given time of a pendulum of a given length, or the length of the pendulum having a given number of oscillations in a given time was observed. In both cases the length was the length of the pendulum.

12.2.1 Pendulum Measurements

During its meeting in 1886, the CIPM requested that French geodesists determine the value of the acceleration of gravity at the BIPM. This task has been entrusted to the Geographic Service of the War directed at that time by the famous General Perrier. Commandant Defforges, member of the Geodesy

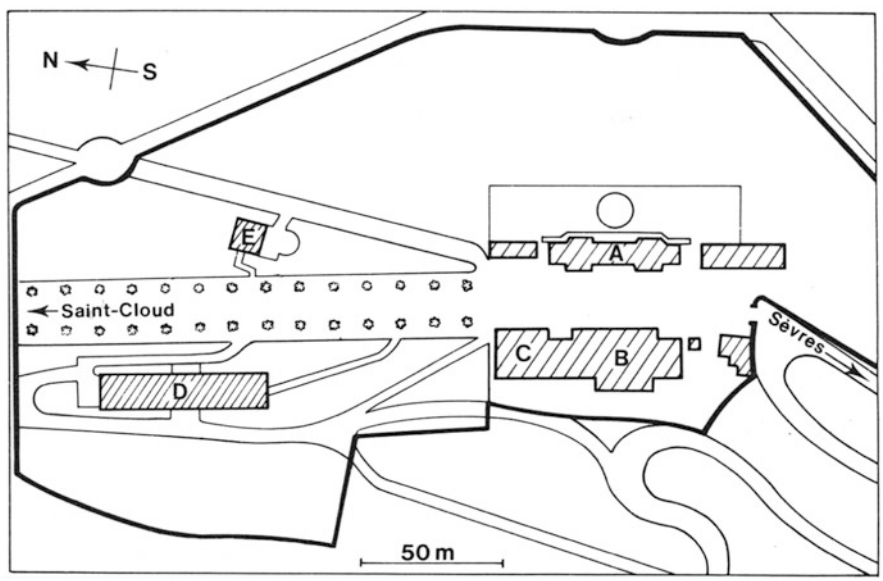


Fig. 12.1 BIPM and le Pavillon de Breteuil (A) (©"*Le Bureau International des Poids et Mesures 1875–1975*")

section, was in charge of the measurement. He used reversible pendulums that he ordered from the well-known firm of the Bruner brothers. The two pendulums (short and long) were used both in the vacuum and in the atmosphere. The measurements were taken in March–April 1888.

After a precise account of the effect of temperature, Defforges determined a final result, which seems to be the first value of absolute gravity at BIPM. It was given as: $g = 9.80991\ ms^{-2}$ with an estimated precision $\pm\ 5\ 10^{-5}\ ms^{-2}$ at the station located in the "room of the universal comparator" of the Pavillon de Breteuil, west longitude of Paris $0^{G},131$, North latitude $54^{G}.260$, altitude $70^{m}.4$ (CIPM, 1892).

12.2.2 Free Fall

Amédée Guillet (1917) compared the advantages and disadvantages of Galileo's pendulum and Newton's tube: the length of the drop is easier to measure than the length of the pendulum. Measurement of time seems to favour the pendulum but its construction is much more difficult and there are more corrections than for the tube (e.g., reaction of the support, effect of atmospheric pressure). He argued in favour of the free fall and mentions that he realised some conclusive tests with a Newton's tube in 1912, but does not present any detail or result. In a short Note to the French Academy of Science, Guillet (1938) described his instrument: a spherical body falls in the vacuum of a tube, along a divided scale. A camera falling in the same way takes pictures of the sphere along the scale. The scale is then reversed upside down for a new measurement, which can be repeated, on demand. The time is automatically taken at the beginning at the end of the drop. The tube is equipped with a thermometer and a barometer.

12.2.2.1 Charles Volet

The Swiss Charles Volet, as a member of the BIPM, improved the concept of Guillet's instrument: the falling object is the ruler itself, which is filmed during its drop (Volet, 1946). The expected duration and precision are respectively 0.5 s and 10^{-6}, which is comparable to the best observations with a pendulum. The scale drops in a vacuum of a few mmHg; there are 5 fixed marks on the scale; the ruler and a chronometric scale are photographed 20–25 times. The influence of the residual air in the tube can be as high as 4 mgal. He developed an improved instrument and obtained in 1952 the first value of gravity at BIPM observed with a falling object. His result, from 18drops of the ruler (409 observations), was: $g = 9.80916\ ms^{-2}$. The observation point is referred to as Sèvres, Point A; its coordinates are East longitude of Greenwich $2°13'14''$, latitude $48°49'45''$, altitude 65.93 m. But the result was compromised by systematic errors, mainly due to the remaining air in the tube.

12.2.2.2 Åke Thulin

The next step is due to Åke Thulin who got a position as assistant physicist in 1951 at BIPM where he remained until June 1959. Continuing the path open by Ch. Volet he developed an instrument the main features of which are detailed in his Doctorate thesis defended at the Paris University on June 9 1959, and published in 1961. The principle is to monitor the free fall of a graduated scale in a cylindrical chamber evacuated by a pump (Fig. 12.2). The falling ruler is 1.02 m

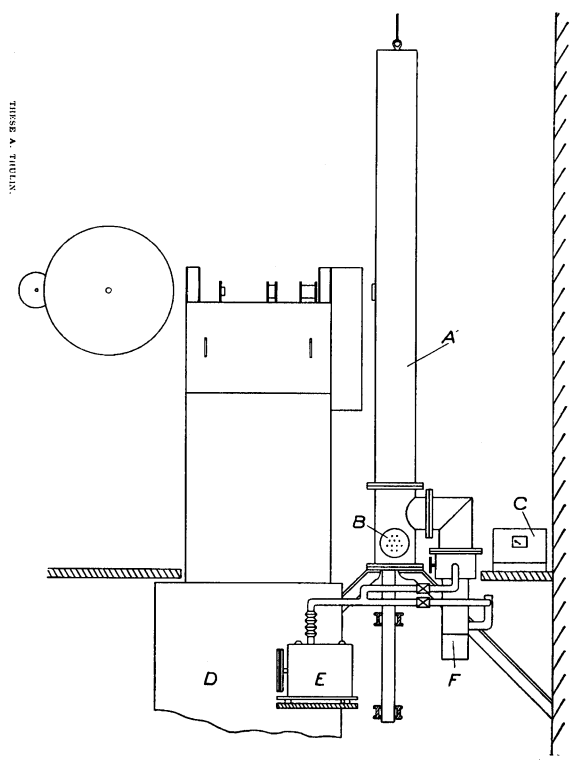


Fig. 12.2 Schematic of Å Thulin instrument, © Thulin, 1961

long and weights 3.6 kg; the cylinder is 2.7 m high, 250 mm diameter; the mean vacuum is $\sim 5 \times 10^{-8}$ mmHg; the photography of the scale is taken on a plane with reference line, using a flash-light; the vibrations are measured thanks to an electromagnetic pendulum with vertical motion.

The reference point is in room 1, station A at ground level.

Thulin detailed the budget error: actual length of the ruler, scaling of the divisions, temperature, applied corrections (temperature, height), and influence of residual atmosphere. He did not include the earth tide correction, since the amplitude of the earth tide (0.01 mgal) is negligible with respect to the precision of his result (~2 mgal).

He improved his preliminary result (Thulin, 1958) and obtains the final result for 20 drops between December 1957 and May 1958: $g = 9.809\ 272\ 5 \pm 2\ 10^{-5}$ ms^{-2}. Reducing his observation to the reference point Sèvres, Point A (vertical gradient $\gamma = 0.278$ mgal m^{-1}) he obtained: $g = 9.809\ 280$ ms^{-2}with an estimated error $\pm\ 2\ 10^{-5}$ ms^{-2}

The task of the instrument was oriented towards metrology.

12.3 Absolute Gravity at BIPM: Dr. Sakuma's Work 1960–1996

Dr. Akihiko Sakuma worked, at the Japanese National Laboratory of Metrology in Tokyo, at the determination of "g" and had developed an absolute gravimeter based on the free fall of an object, with which he obtained his first value in 1959. Akihiko Sakuma entered BIPM on February 4 1960, at the age of 29, as "Assistant" when Å. Thulin left BIPM to enter industry, (CIPM, 1960).

12.3.1 Instruments

Sakuma was in charge of developing an instrument for the absolute determination of gravity. In continuity with the previous attempts of Charles Volet and J. Terrien at BIPM and with his own work in Japan, he chose the free fall method. He constructed several instruments according to this principle.

12.3.1.1 Sèvres Stationary Instrument

The 1st instrument was to be settled in the Pavillon de Breteuil, at BIPM with the original task of the instrument was metrology.

The instrument (Fig. 12.3) had been developed from 1960, with the collaboration of other members of BIPM such as Jean-Marie Chartier for the laser. Let us quote the description of the apparatus, in Sakuma's own words: "A corner cube reflector forming one mirror of a Michelson interferometer is projected upwards and the four sets of white light fringes that are formed at two levels (distance 0.4 m) of the trajectory operate sub-nanosecond counters for timing the flight in vacuum ($\sim 10^{-5}$ Pa)" (Sakuma, 1974a).

A significant improvement was a stabilized table supporting the main parts of the interferometer (Fig. 12.4); as a protection against vibrations and ground motions (Sakuma obtained a patent for this table). The instrument was quite huge, the size of the box 2.8 m high, and weighted 850 kg. A laser later replaced the white light. Starting to develop the apparatus as soon as he arrived at BIPM, Sakuma obtained an accuracy $\Delta g / g = 7.3 \times 10^{-8}$, in 1962. The instrument was located in room 1, and the reference point at +1.02 height and 5.5 m in the West of "Sèvres Point A".

A similar instrument was installed in the 1970s at the International Latitude Observatory in Mizusawa (Japan) for the purpose of the polar motion studies and as one of the stations of the worldwide network. Mizusawa became the second permanent station.

12.3.1.2 Portable Instruments

Due to its large size, the BIPM gravimeter was a stationary one and Dr. Sakuma was aware of the need of numerous stations all over the world to improve the knowledge of the gravity variations and establish the International Gravity Standardization Net 1971 (IGSN71), Morelli et al., 1974. Very early, Dr Sakuma, as well as other institutions (Hammond, 1970) thought of developing a transportable to answer this task. In collaboration with the Istituto di Metrologia "G. Colonnetti" (IMGC) at Torino (Italy), he constructed between 1968 and 1974 a 1st prototype (Fig. 12.5a).

The principle was very similar to the stationary instrument of BIPM (symmetrical rise and fall); it was

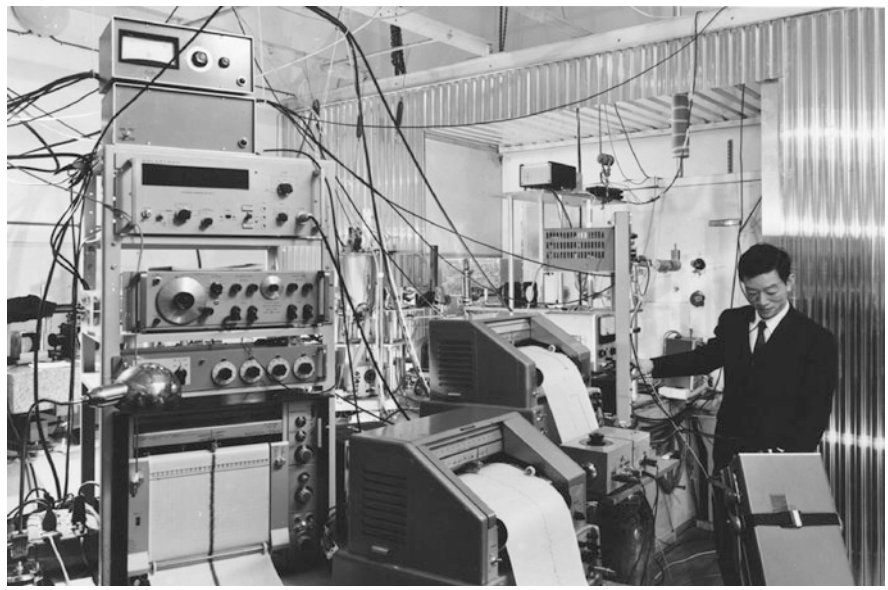


Fig. 12.3 A. Sakuma operating his stationary instrument, © BIPM, 1969

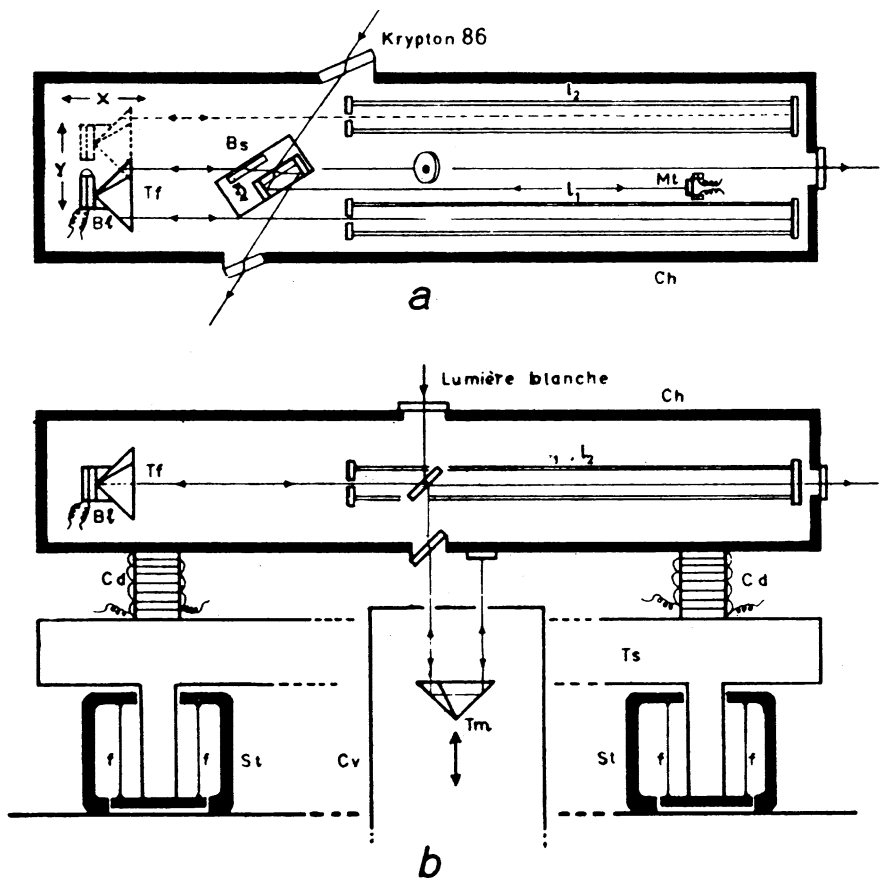


Fig. 12.4 Schematic of the interferometer and stabilized table, from Sakuma, 1966

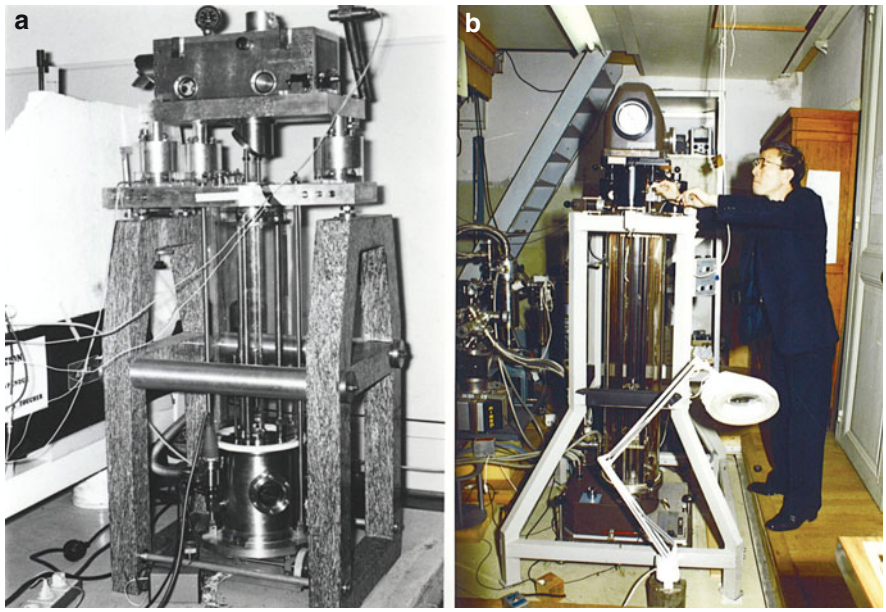


Fig. 12.5 **(a)** The 1st prototype of transportable IMGC-BIPM gravimeter in 1983, ©BIPM; **(b)** A. Sakuma operating the GA-60 instrument on 10 May 1985**,** ©BIPM

nevertheless much smaller. At 1.4 m high, and 0.5 × 0.5 section. It had two separable parts: (1) a Michelson interferometer in a pressure-tight case and (2) a catapult in a vacuum cylinder; the ensemble weighted ∼100 kg. Quoting again Sakuma's words, the three important differences are: (1) the determination of "g" is made in a low vacuum of about 0.1 Pa for which the secondary pump is not required, (2) instead of the end standard of length, a stabilised laser is employed with a reversible interferometric fringe counting position, and (3) the vibration effect is compensated automatically by an inertial reference corner reflector which itself forms the end mirror of the horizontal beam", Sakuma (1974a). This instrument measured at 52 stations in Europe, America and Asia between 1976 and 1981, for the unification of the worldwide gravimetric network (Alasia et al., 1982).

In the meantime, A. Sakuma was working on a second model of the transportable instrument, for the BIPM. Two samples of the so-called BIPM Jaeger GA-60 were manufactured in 1980–1981 by the French Jaeger Industries S.A.. One (#1) operated at the Geographical Survey Institute at Tsukuba (Japan) and #2 operated at BIPM (Fig. 12.5b) and at some stations in France. The tasks were both metrology and geophysics.

The main features are as follows: 1.95 m high, 0.9 × 0.9 section, total weight 400 kg, rise and fall, method of multiple stations ∼40 cm, catapult in vacuum cylinder (< 0.01 Pa), continuous ion pump, reflecting corner cube 70 g, iodine stabilised Helium – Neon laser, seismometer; 20 measurements of "g" with a semi-automatic procedure, over a period of 1 h, and accuracy $\Delta g/g = 1 \times 10^{-8}$.

A test comparison between the stationary gravimeter and the transportable gravimeter gave a difference of only ± 10 μgal (Alesia et al., 1982).

12.3.2 Scientific Achievements

12.3.2.1 Absolute Gravity Measurements at BIPM

Thanks to the efforts of Sakuma who had developed a stationary instrument of very high quality, BIPM became, in 1967, the 1st permanent gravity station, aimed at the study of the secular variation of gravity. This is the starting point of a long list of *firsts*, both in observations and results. Dr. Sakuma obtained the 1st measurement with relative accuracy 10^{-9}; jump of 2 orders of magnitude in the precision. Moreau who quotes Ch. Volet (1952): "it is very seldom in metrology, that the precision of a physical constant is multiplied by 100 in the time span of a few years".

The precision and accuracy made a decisive contribution to the revision of the Potsdam System, which had been in discussion for many years. For the first time, the perturbation of "g" due to the luni-solar influence was observed with an absolute instrument, in June 1967 (the maximum value of this perturbation in Paris is $\pm 1.6 \times 10^{-9}$ m/s^2). The luni-solar perturbation was then taken into account by a theoretical calculation of the tides. However, to get a better correction, Sakuma developed a relative gravimeter and establishes a gravimetric station at BIPM, to record and analyse Earth Tides (Sakuma, 1974b). This was, at that time, the only instrument of this type running in parallel with an absolute gravimeter.

With such an instrument, it became possible to extend its range of functions. A series of periodic measurements was taken for the study of stability of the site.

Sakuma presented, in 1973, the long term analysis 1966–1972 (Fig. 12.6) at the meeting "Earth's Gravitational Field & Secular Variations in Position". He notes significant discrepancies of 20∼40 μgal, which are unexplained. He found no correlation with the water table variations and made the hypothesis that the tidal wave of 18.61 year period, which was corrected for, could have a larger effect than derived from theory and could explain the trend in the series, Sakuma 1973.

Thus the stationary apparatus, originally designed for metrological purposes, achieved geodetic and geophysical results.

On the other hand, the transportable instruments were devoted to the building of the worldwide network of gravity and its variations. We have already mentioned that the Italian team from Torino, operating the IMGC instrument, obtained the first values of gravity in many stations from different continents. Sakuma operated, in the 1980s, the BIPM-Jaeger transportable instrument to measure the zeroth-order French gravimetric network. He measured five stations (Orléans, Dijon, Marseille, Nancy, Toulouse); his values were in good agreement with the FG5 observations done 20 yrs later (Amalvict et al., 2003). In 1983, he establishes a "satellite station" at Orléans, leading to the first calibration line (Sèvres – Orléans, BRGM). Sakuma measures for the last time with the BIPM-Jaeger instrument in 1994, at the foot and the top of the Puy-de-Dôme (1,464 m), France.

12.3.2.2 International Comparisons at BIPM

At the time of pendulum, BIPM was already a station for the comparison of pendulums measuring gravity at the end of nineteenth century. The 1st informal comparison of free fall gravimeters occurred in 1968 when

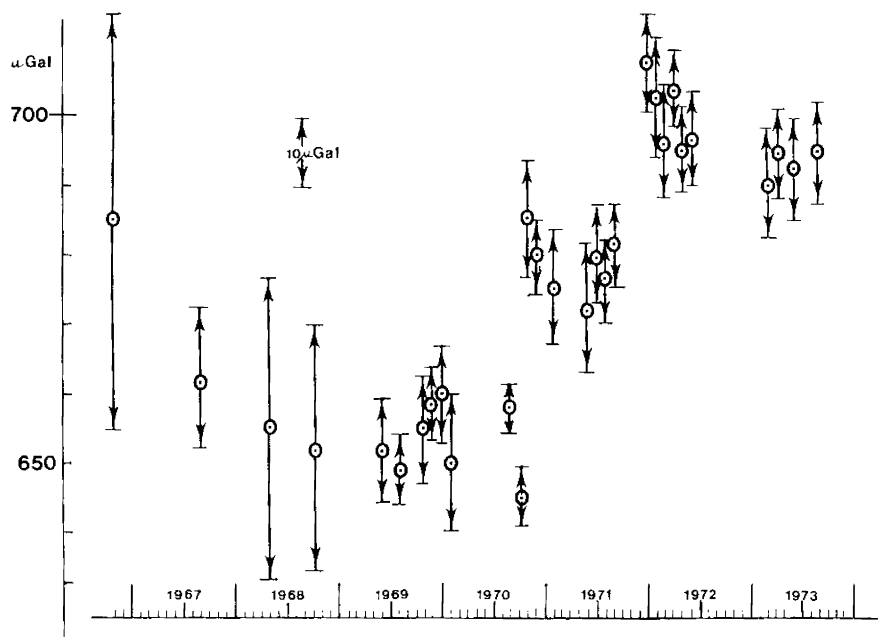


Fig. 12.6 "Monthly mean of absolute value of gravity with scatter of single measurement at Sèvres Point A2 (Apparatus site). BIPM: g_{A2} = 980,925,000 μgal + values on graph" Sakuma, 1973, original legend

Jim Faller measured at BIPM with his instrument; the agreement between Faller and BIPM instruments was of the order of 10 μgal. The organisation of International Comparison of gravity became a regular activity at BIPM since then. The BIPM-Jaeger transportable instrument is achieved for the International Comparison in 1981–1982. Comparisons take place every 4 years and, during Sakuma's activity, occurred in 1985, 1989, and 1993. Seven instruments (including BIPM) participated in the 1981–1982 international comparison; the best value of gravity at point A3 was given as: g = 980,925,914 ± 3.8 μgal (Boulanger et al., 1983). In 1985, six instruments (including BIPM) from five countries participated in the 1985 comparison (Boulanger et al., 1986).

12.4 Absolute Gravity at BIPM: Present and Future

Shortly before Dr Sakuma retired, BIPM acquired, in September 1993, the commercial FG5#108 (Axis Instrument) which continues to regularly measuring the gravity. After the departure of A. Sakuma who retired on 1 April 1996, BIPM stopped the development of original absolute gravimeters but L. Vitushkin (Sakuma's successor) works on some parts, such as a new laser, in collaboration with Russian teams (Vitushkin, personal communication). Gravimetry remains an important matter for BIPM, its name enters the appellation of one section: "Time, Frequency and Gravimetry Section" section.

International comparisons remain an important BIPM activity; they occurred in 1997, 2001, and 2005. In 2001, seventeen instruments (including BIPM), Fig. 12.7, participated with the final result, at site A (0.90 m): g = 980,925,701.2 ± 5.5 μgal (Vitushkin et al., 2002).

Nineteen absolute gravimeters participated in the ICAG2005, 11 sites were measured with 96 determinations of gravity. The final value, given at 0.90 m over the benchmark at point A is: g = 980,925,702.3 μgal ± 0.6 μgal. The next comparison will occur in 2009. The comparison of gravimeters aims for geophysical or geodetic tasks, but metrology becomes again an important goal and the 2009 ICAG will be a "key comparison" following the standards of metrologists. We should note also that the knowledge of the precise value of gravity is part of the Watt Balance developed (among others) by BIPM for the definition of the kilogram which is still defined by a material artefact.

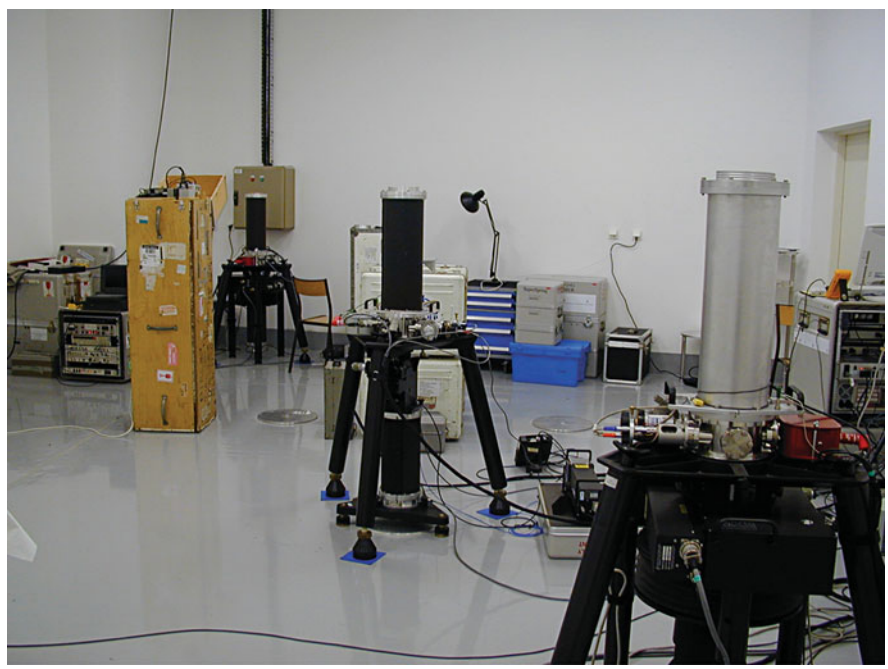


Fig. 12.7 FG5s participating in the ICAG-2001. The BIPM FG5#108 is on the right (photo MA)

Acknowledgments The author is very grateful to the BIPM, Felicitas Arias Head of the "Time, Frequency and Gravimetry Section" section, for her 2 weeks stay working on documents in the library with Daniele Le Coz, (librarian), and also to Leonid Vitushkin, Kazuo Shibuya, Jean Souchay, Magali Pierrat.

References

Alasia, F., L. Cannizzo, G. Cerutti, and I. Marson (1982). Absolute gravity acceleration measurements: experiences with a transportable gravimeter. *Metrologia*, 18, 221–229.

Amalvict, M., N. Debeglia, and J. Hinderer (2003). The absolute gravity measurements performed by Sakuma in France, revisited 20 years later. In: Tziavos (ed), Gravity and Geoid 2002 GG2002, Editions Ziti. pp. 76–83.

Boulanger, Y.D., et al. (1983). Results of comparison of absolute gravimeters, Sèvres, 1981. *Bull Info BGI*, 52, 99–124.

Boulanger, Y.D., et al. (1986). Results of the second international comparison of absolute gravimeters in Sèvres, 1985. *Bull Info BGI*, 59, 89–104.

CIPM, Procès-verbaux des séances du Comité International des Poids et Mesures, #1886, #1892, #1960

Guillet, M. (1917). Measurement of the intensity of gravity: Galileo's pendulum and Newton's tube. *C.R. Académie des Sci.*, 167, 1050–1052.

Guillet, M. (1938). Mesure précise de l'accélération g de la chute des corps dans le vide. *C.R. Académie des Sci.*, 207, 614–616.

Hammond, J.A. (1970), JILA Report No 103, University of Colorado.

Moreau, H. (1975). Introduction historique, in BIPM Centennial volume '*Le Bureau International des Poids et Mesures 1875–1975*'.

Morelli, C., et al. (1974). Public. Spec. No 4, Assoc. Int. Geod.

Sakuma, A. (1966). Mesure absolue de la pesanteur au Bureau International des Poids & Mesures, Bull. *Inf. BGI*, 14, 8–9.

Sakuma, A. (1973). A permanent station for the absolute determination of gravity approaching one micro-gal accuracy. In Proceeding of Symposium on Earth's gravitational field & secular variations in position, 674–684.

Sakuma, A. (1974a). Report on Absolute Measurements of Gravity, Report presented at the 7th International Gravity Commission, Paris 2–6 September 1974, Special Study Group 4.18 of th IAG.

Sakuma, A. (1974b). La station de mesure de la marée gravimétrique du B.I.P.M. – Installation et résultats préliminaires, exposé présenté par A. Sakuma le 29 janvier 1974, notes prises et rédigées par P. Carré.

Thulin, Å. (1958). Résultat d'une nouvelle détermination absolue de l'accélération due à la pesanteur, au Pavillon de Breteuil. *C.R. Académie des Sci.*, 246, 3322–3324.

Thulin, Å. (1961). Détermination absolue de l'accélération due à la pesanteur, Thèse, Université de Paris.

Vitushkin, L., et al. (2002). Results of the sixth international comparison of absolute gravimeters, ICAG-2001. *Metrologia*, 39, 407–424.

Volet, Ch. (1946). Sur la mesure absolue de la gravité. *C.R. Académie des Sci.*, 222, 373–375.

Volet, Ch. (1952). Mesure de l'accélération due à la pesanteur, au Pavillon de Breteuil. *C.R. Académie des Sci.* 235, 442–444.

Chapter 13

Correcting Strapdown GPS/INS Gravimetry Estimates with GPS Attitude Data

B.A. Alberts, B.C. Gunter, A. Muis, Q.P. Chu, G. Giorgi, L. Huisman, P.J. Buist, C.C.J.M. Tiberius, and H. Lindenburg

Abstract Gravity field estimation from differential GPS (DGPS) and strapdown inertial navigation system (SINS) measurements is based on differencing the observed accelerations from both systems. To rotate the specific force accelerations from the INS to the local level frame, accurate attitude information is required. In this study, we demonstrate how uncompensated errors in the gyroscope data from the INS can be corrected using GPS attitude estimates. A simulation study is carried out to investigate how gyro errors affect the gravity estimates, as well as what the accuracy requirements are for the GPS-derived attitude data in order to estimate gyroscope biases. Results show that the GPS attitude data obtained during a flight experiment are accurate enough to correct the gyro data and reduce the effect of attitude errors on gravity estimates to less than 1 mgal.

13.1 Introduction

In the past year, a new initiative has been started within the Faculty of Aerospace Engineering at the Delft University of Technology, called the Gravimetry using Airborne Inertial Navigation (GAIN) project. The project combines the expertise of several groups within the faculty, and has a range of facilities and equipment at its disposal, including an instrument plane for conducting flight experiments, commercial and custom built Inertial Navigation Systems (INS), and a new calibration table. The primary objective of this project is to improve upon existing GPS/INS gravimetry methods by exploring innovations in both hardware and processing methodologies.

One of the many features of the laboratory aircraft used by the project, a Cessna Citation II jointly operated with the Dutch National Aerospace Laboratory (NLR), is an array of built-in GPS antennae at the wing, nose and fuselage. Through the post-processing of the GPS signal phase differences, these antennae enable the accurate determination of the aircraft's attitude in time. This is useful in the context of airborne gravimetry because the gyroscopes (gyros) in any INS system usually exhibit some degree of drift or random walk, and such an independent measurement of aircraft attitudes can be used to reduce rotation errors, thereby improving the recovered gravity field.

The effect of INS errors on gravity estimates has been investigated by several authors. Wei and Schwarz (1994) performed an error analysis of airborne vector gravimetry using simulated data and Bruton (2000) provides a thorough description of strapdown INS (SINS) errors affecting scalar gravity using data obtained from various flight campaigns. Flight test results showed that with a SINS/DGPS gravity system an accuracy of 2–3 mgal at a half-wavelength resolution of 5 km is feasible and can be improved to 1.5 mgal at 2 km resolution, if errors are modelled correctly. The actual accuracy of airborne gravity from SINS, however, depends primarily on the error characteristics of the sensors used in the instrumentation.

The custom-built INS of the GAIN project makes use of a set of Fizoptika VG951 fiberoptic rate gyros. Generally, fiberoptic gyros have a lower bias

B.A. Alberts (✉)
Delft Institute of Earth Observation and Space Systems (DEOS), Delft University of Technology, GB Delft 2600, The Netherlands
e-mail: B.A.Alberts@tudelft.nl

S.P. Mertikas (ed.), *Gravity, Geoid and Earth Observation*, International Association of Geodesy Symposia 135,
DOI 10.1007/978-3-642-10634-7_13, © Springer-Verlag Berlin Heidelberg 2010

stability than ring-laser gyros, but their signal-to-noise ratio may be better. Uncompensated biases must therefore be estimated in order to obtain gravity estimates at the level of 1 mgal. In this paper we propose to correct gyro data using GPS attitude information. Results are shown for simulated data as well as for INS attitude data obtained during a flight experiment carried out in November 2007.

13.2 Methodology

13.2.1 Strapdown Inertial Gravimetry

The determination of gravity disturbances from strapdown inertial gravimetry is given in the local-level frame (l) as (e.g., Schwarz and Li (1997))

$$\delta \mathbf{g}^l = \dot{\mathbf{v}}^l - \mathbf{R}_b^l \mathbf{f}^b + (2\boldsymbol{\Omega}_{ie}^l + \boldsymbol{\Omega}_{el}^l)\mathbf{v}^l - \boldsymbol{\gamma}^l, \qquad (1)$$

where $\delta \mathbf{g}^l$ is the gravity disturbance vector, $\dot{\mathbf{v}}^l$ is the aircraft acceleration, $\mathbf{R}_b^l$ is the transformation matrix that rotates measured accelerations from the body frame (b) to the local-level frame, $\mathbf{f}^b$ is the specific force measured by the accelerometers, $\mathbf{v}^l$ is the aircraft velocity, $\boldsymbol{\Omega}_{ie}^l$ and $\boldsymbol{\Omega}_{el}^l$ contain the angular velocities due to Earth-rate and aircraft rate over the ellipsoid, and $\boldsymbol{\gamma}^l$ is the normal gravity vector.

The entries of $\mathbf{R}_b^l$ can be obtained by integrating the observed gyro rates as shown in the next section. Errors in these measurements obviously affect the gravity disturbance vector. Schwarz and Wei (1994) showed that effect of attitude errors on the scalar gravity estimates is given as

$$\mathrm{d}\delta g = f_n \epsilon_e - f_e \epsilon_n, \qquad (2)$$

where ϵ_e and ϵ_n are attitude errors due to initial misalignment and gyro measurement noise, and f_n and f_e are the north and east components of the specific force vector. Gyro errors such as biases and misalignments are usually determined by laboratory calibration. Nevertheless, changing flight conditions can have a non-negligible effect on the long-term stability of the gyros. The following sections show how these errors may be estimated using GPS attitude data. For a detailed discussion on other SINS errors affecting airborne gravimetry, the reader is referred to Bruton (2000).

13.2.2 Kinematic Model

Aircraft motion can be described by three sets of first-order differential equations for translational velocities, angular velocities and attitude angles. For the attitude angles, the rotational kinematic model is given as (e.g., Mulder et al. (1999)):

$$\begin{bmatrix} \dot{\phi} \\ \dot{\theta} \\ \dot{\psi} \end{bmatrix} = \begin{bmatrix} 1 & \sin\phi\tan\theta & \cos\phi\tan\theta \\ 0 & \cos\phi & -\sin\phi \\ 0 & \sin\phi\sec\theta & \cos\phi\sec\theta \end{bmatrix} \begin{bmatrix} p \\ q \\ r \end{bmatrix} \qquad (3)$$

where ϕ,θ,ψ are the roll, pitch and yaw angles, and p, q and r are the gyro rates. Equation (3) is valid for a flat and non-rotating Earth; several corrections must be applied for navigating on a rotating sphere. The model (3) may be interpreted as a dynamical system with state vector $\mathbf{x}$ and input vector $\mathbf{u}$ defined as

$$\begin{aligned} \mathbf{x} &= (\phi,\theta,\psi)^T \\ \mathbf{u} &= (p,q,r)^T. \end{aligned} \qquad (4)$$

The system state equation may be written as

$$\dot{\mathbf{x}} = f(\mathbf{x},\mathbf{u}). \qquad (5)$$

The rate gyros provide the components of the input vector $\mathbf{u}$. These measurements are corrupted with time-dependent errors. Here, it is assumed that the observed rates are contaminated with a constant bias and random errors, i.e., the error model is expressed as

$$\begin{aligned} p_m &= p + b_p + w_p \\ q_m &= q + b_q + w_q \\ r_m &= r + b_r + w_r \end{aligned} \qquad (6)$$

where b is the bias in the gyro rates and w is the measurement noise, which is assumed to be both white and uncorrelated. The observation model that relates measured variables to the state vector is here defined by the processed GPS attitudes:

$$\begin{aligned} \phi_m &= \phi + v_\phi \\ \theta_m &= \theta + v_\theta \\ \psi_m &= \psi + v_\psi \end{aligned} \qquad (7)$$

where v are the stochastic measurement errors, assumed to be uncorrelated.

The roll, pitch and yaw angles, and biases are estimated by applying an Extended Kalman Filter (EKF) in a joint parameter and state estimation, assuming that b is constant. As mentioned above, the rates serve as system input to the Kalman filter and the observation model is provided by GPS attitudes.

13.2.3 GPS Attitude Determination

Attitude information can be obtained from GPS phase measurements if two baselines are determined using three antennas placed on the fuselage and the wing of the aircraft. The approach used here is the same as described by Teunissen (2006) for the single baseline case (two antennas), referred to as the GNSS compass model. This model differs from the standard single GNSS baseline model in that the length of the baseline is assumed to be known. The standard GNSS baseline model is is given as

$$E\{\mathbf{y}\} = \mathbf{Aa} + \mathbf{Bb}, \qquad D\{\mathbf{y}\} = \mathbf{Q}_y \tag{8}$$

where $\mathbf{y}$ is the GNSS data vector containing double-difference (DD) phase observations accumulated over all observation epochs, $\mathbf{a}$ is a vector of unknown DD carrier phase ambiguities, $\mathbf{b}$ is a vector containing the remaining unknown parameters such as the baseline components (coordinates), and $\mathbf{A}$ and $\mathbf{B}$ are the design matrices relating the data vector to the unknown parameters. The solution of model (8) is obtained using the LAMBDA method (e.g., Teunissen (1993)). In case that the baseline lengths are assumed to be known, model (8) can be augmented by adding the length constraint of the baselines:

$$E\{\mathbf{y}\} = \mathbf{Aa} + \mathbf{Bb}, \qquad ||\mathbf{b}||_{I_3} = l \tag{9}$$

The solution to this model, which is described in detail in Teunissen (2006), is referred to as the constrained LAMBDA approach. For the experiment described in this study, the baselines are defined as (see Fig. 13.1):

b1: Main antenna (fuselage) – Nose antenna
b2: Main antenna (fuselage) – Wing antenna

Note that the necessary attitude information (roll, pitch and yaw angles) can only be recovered if both baselines are correctly fixed. The accuracy of GPS derived attitudes depends on the positioning accuracy (sub-cm level) and the length of the baseline. For the Cessna Citation II, the length of b1 is about 5 m, resulting in an expected accuracy of better than 0.1°. The second baseline (b2) is longer (about 7.5 m) and thus for this baseline the accuracy should be even better.

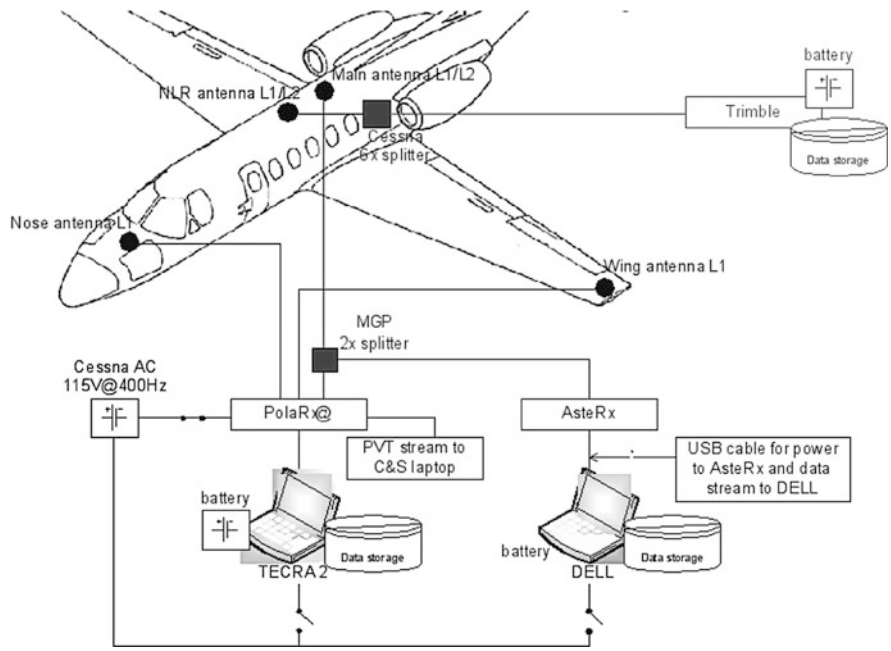


Fig. 13.1 Infrastructure and locations of the GPS antennas on the Cessna Citation II

A detailed analysis of the ambiguity fixing of baseline 1 for this configuration, using a data set collected in 2006, is given in Buist (2007).

13.3 Simulation Study

13.3.1 Data Simulation

To test the methodology described in the previous section, a simulation study was carried out to investigate how uncompensated gyro errors affect the gravity estimates, as well as how accurate the GPS-derived angles must be in order to estimate gyro biases. For this purpose, data were generated using flight simulation software that was designed to perform analysis and offline simulations with an aircraft model of the Cessna Citation 500. Using aerodynamic control inputs and thrust control inputs, the observation outputs are generated in real time. This way, realistic accelerometer and gyro data are obtained at a flight level of 1,500 m and at an air-speed of 65 m/s. The simulated rates and angles are shown in Fig. 13.2. The gyro rates are integrated within the Extended Kalman Filter to estimate angles, using the GPS attitudes as observations. Then, these angles are used to rotate body accelerations to the local level frame and compute gravity values from specific force and aircraft accelerations, according to Eq. (13.1). Errors are computed with respect to the true gravity values, which are computed within the simulator using a simple height-dependent gravity model.

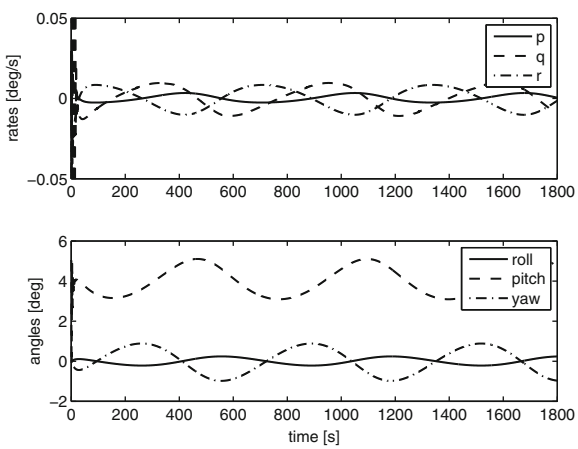


Fig. 13.2 Simulated gyro rates and aircraft attitude information

13.3.2 Results

Figure 13.3 shows the results for a bias of $0.1°h^{-1}$ added to the gyro data, which corresponds to the expected bias of the Fizoptika fiberoptic gyros to be used in the custom INS instrument mentioned earlier. Furthermore, we added white noise of $0.001°s^{-1}$ to the gyro rates. The GPS angles were initially corrupted by random noise of 0.1° RMS. When biases in p, q, and r are not estimated, the resulting drift in the angles is about $0.05°h^{-1}$. When the computed angles are used to rotate the noise-free accelerations to the local-level frame, the errors in the angles contribute to an gravity error of more than 5 mgal for a 30 min simulation. For longer time series, the estimated gravity values will, obviously, deviate even further from the true values.

When the state vector and biases are estimated simultaneously, the attitude errors have a RMS of 0.003°, which results in an error in the estimated gravity values of 0.2 mgal RMS after low-pass filtering (gray lines in Fig. 13.3). These errors are mainly caused by the white noise added to the rates and GPS angles. The same computation was repeated with GPS angles corrupted by random noise of 0.5° RMS. The resulting error in the estimated angles is 0.01° RMS and the corresponding gravity errors have a RMS of 1.0 mgal. Although these errors are much larger than for the previous case, the biases are still estimated correctly. The difference between added and estimated biases is less then $0.01°h^{-1}$ for all three gyros. This indicates that GPS attitude determination is a valid tool to correct the INS gyro data for uncompensated gyro biases. Future work will investigate the influence of colored noise in the data, as the white noise assumption made in this study is likely to be overly optimistic.

13.4 Test Flight

In November 2007 a test flight was carried out using a Honeywell INS strapped down to the aircraft. At the time of the flight, the new instrument was not available yet, so the developed methodology was

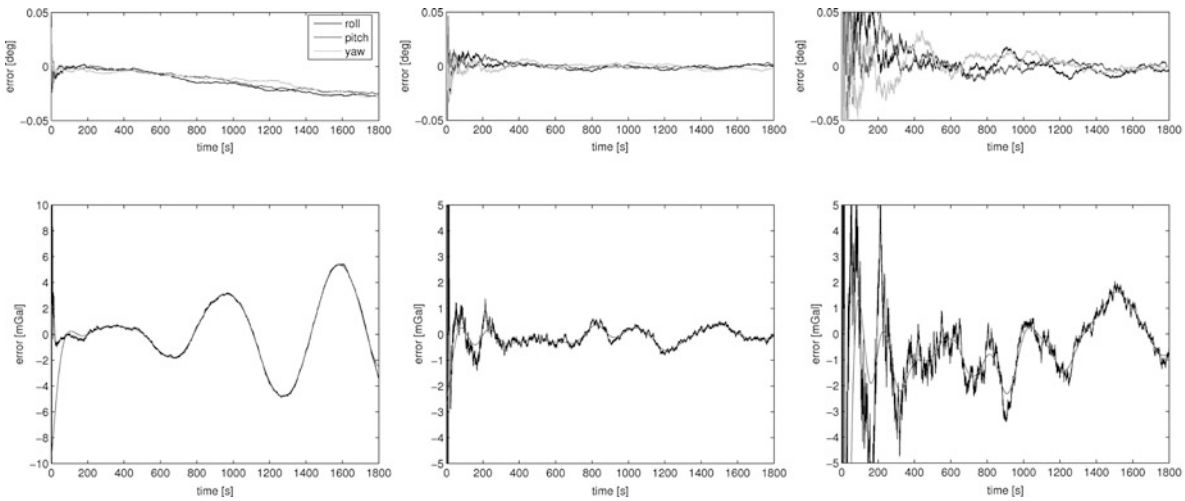


Fig. 13.3 The effect of attitude errors on gravity estimates. From left to right: biases are not estimated, GPS noise is 0.1°; biases are estimated, GPS noise is 0.1°; biases are estimated for increased GPS noise (0.5°)

applied to the Honeywell system, which contains ring-laser gyros. The flight trajectory was a single profile extending from the southern part of the Netherlands into Germany (see Fig. 13.4), with a total length of 125 km. The profile was flown six times; four times at a speed of 120 knots (60 m/s) and two times at 240 knots. The average flight level was 1,450 m above sea level. During the flight, conditions were very good with only minor turbulence on a few occasions. For accurate relative positioning, a GPS reference station was setup at the midpoint of the flight profile (point K). Some results of kinematic relative positioning using

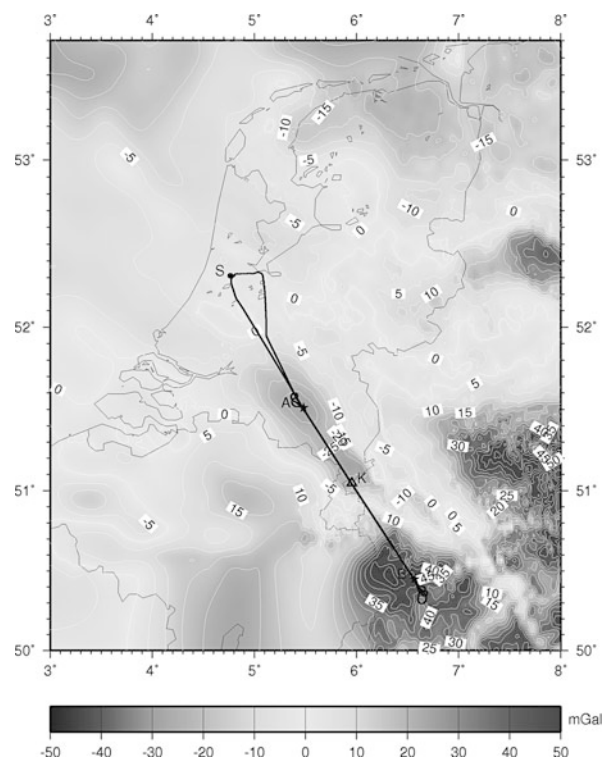


Fig. 13.4 Flight trajectory and gravity anomaly map

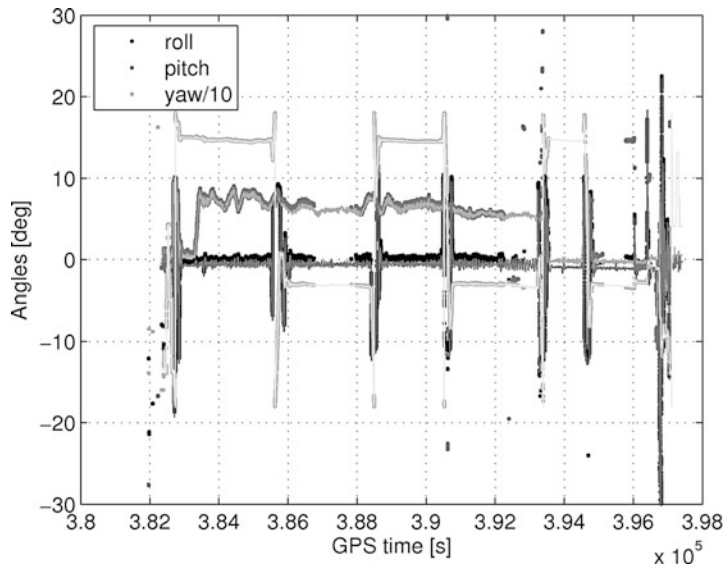


Fig. 13.5 Attitude information from the IRS (*solid lines*) and determined from GPS (*dots*)

the data collected in this experiment are described in Buist (2008).

Figure 13.5 shows the computed GPS attitudes and angles as obtained directly from the INS. The GPS attitude data were computed by applying the baseline constrained LAMBDA approach as described in Sect. 13.2. Angles are computed only when both baselines have been correctly fixed. For parts of the flight, no GPS solution was obtained due to multipath effects on the first baseline. The success rate for the whole flight was about 60% for the first baseline and about 90% for the second baseline. The GPS attitudes are generated at a rate of 10 Hz, whereas the INS attitudes are provided at a rate of 50 Hz. The estimated accuracy of the GPS attitude data is 0.1°, which is based on a comparison with the INS attitudes.

For the angular differences between INS and GPS data, a certain constant bias was observed over the whole time span: 0.66° for the roll angle, 0.20° for the pitch angle and 0.47° for the yaw angle. Nevertheless, the differences between the two solutions do not show a drift, indicating that the ring laser gyros of the Honeywell system are very stable. Therefore, the uncorrected raw gyro rates are used for the computations. The approach is tested for the third leg (approximately between 388,700 and 390,300 GPS seconds), which showed the best results for the GPS attitudes in terms of data gaps, i.e. both baselines were fixed correctly for the whole time span.

If no biases are estimated, the resulting angles show a large drift, as shown in Fig. 13.6. When biases are estimated, the resulting angles show a good agreement with the GPS attitudes, but naturally the EKF solution is much smoother. The estimated biases are shown in Fig. 13.7. From this figure, it is clear that the Kalman filter needs some time to stabilize, especially for the bias in the pitch rate. When looking at the differences between GPS and INS for the pitch angles, shown in Fig. 13.8, the differences are less constant than for the other two angles, especially for the first part of the profile. This may be attributed to the configuration of the antennae used in the experiment. For this kind of configuration, the yaw angle will be more accurate than the roll and pitch angles. The roll angle is mainly determined by the longer baseline b2 and therefore the expected accuracy of the roll angle is higher than the for the pitch angle, which is mainly determined by the shorter baseline. Furthermore, the first baseline showed more multipath effects, which affects the ambiguity fixing and thus the accuracy of the attitude estimation. In further research we will study how these large multipath effects occur and how they can be prevented.

13.5 Summary and Outlook

Tests with simulated data show that GPS attitude determination provides a valuable tool for correcting gyro data and thus increasing the accuracy of airborne gravity field estimates. The overall accuracy of the

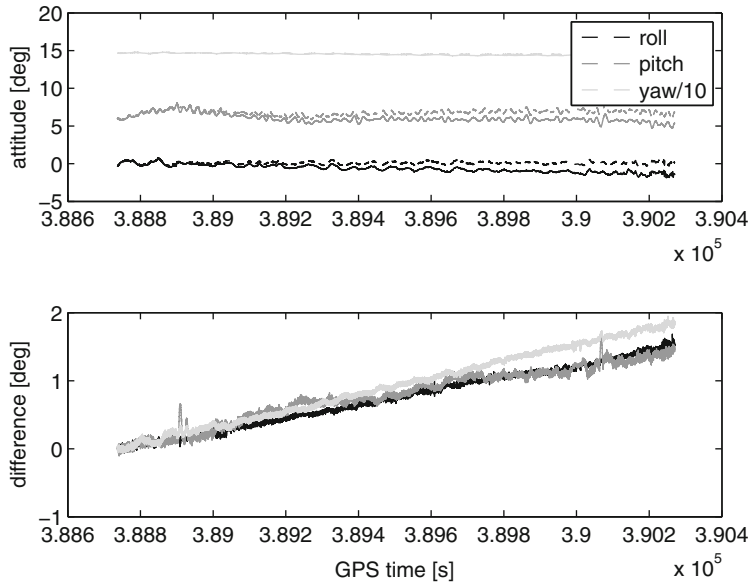


Fig. 13.6 The EKF solution (*solid lines*) compared to the GPS attitude solution (*dashed lines*) and their difference when a bias is not estimated

computed attitudes should be below 0.01° to obtain a gravity field accuracy of 1 mgal RMS, assuming small horizontal accelerations. To achieve this, gyro biases must be estimated with an accuracy better than $0.01°\mathrm{h}^{-1}$. For the simulations described in this paper, the data were assumed to be corrupted by white noise, which may be too optimistic. Future work will therefore investigate the influence of colored noise in the data.

The results from the test flight show that an uncompensated bias can be resolved using GPS attitudes in an Extended Kalman filtering scheme; however, uncertainties in the INS acceleration data prevented the calculation of accurate gravity field estimates. Nevertheless, the simulations showed that the estimated GPS attitudes from the test flight are accurate enough to correct gyro data. Further research will focus on the improvement of gravity field estimation from

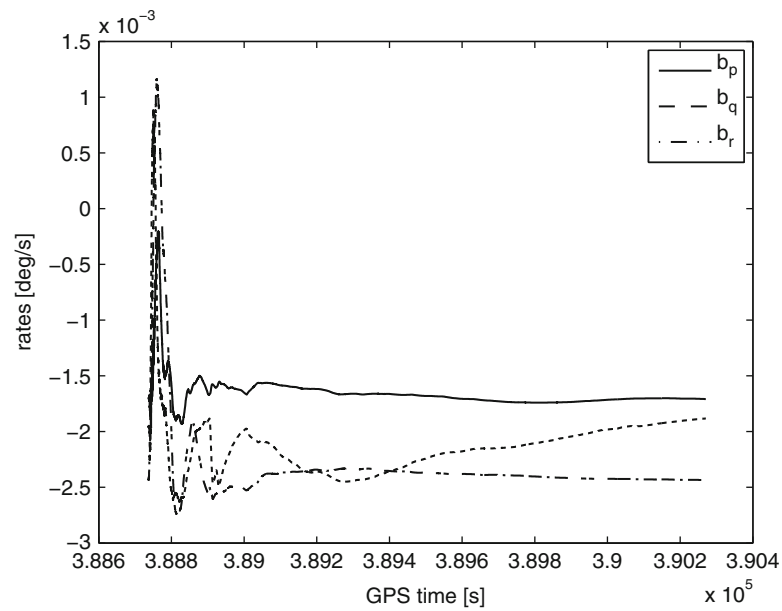


Fig. 13.7 Estimated biases for the gyro rates

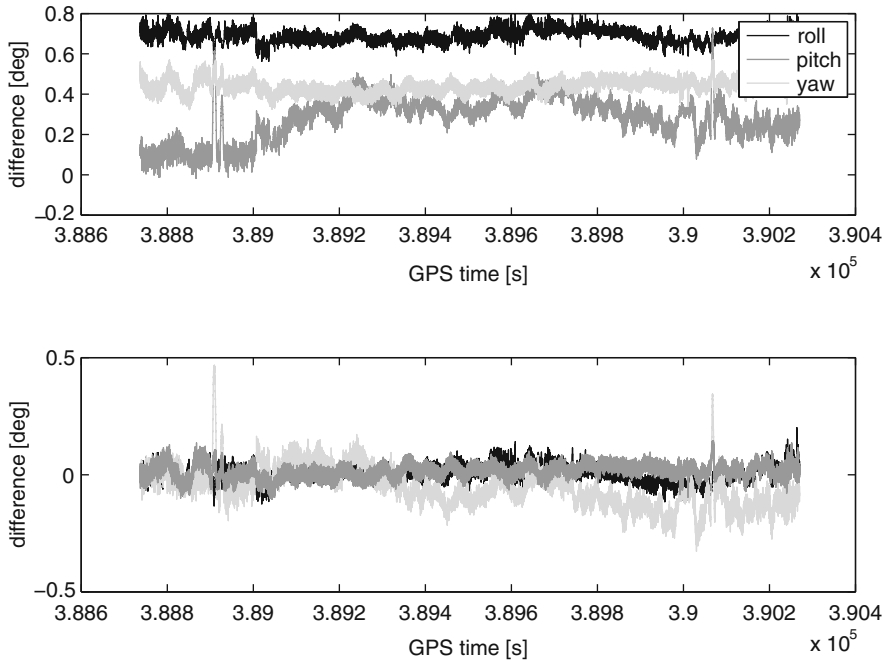


Fig. 13.8 *Top*: difference between the IRS angles and the GPS attitude solution. *Bottom*: difference between the EKF solution and GPS attitude solution when a bias is estimated

strapdown inertial gravimetry, using the new custom INS instrumentation.

References

Bruton, A.M. (2000). Improving the accuracy and resolution of SINS/DGPS airborne gravimetry. UCGE report # 20145, Calgary, Canada.

Buist, P.J. (2007). The baseline constrained LAMBDA method for single epoch, single frequency attitude determination applications. ION GNSS 2007 Proceedings, pp. 2962-2973. Fort Worth, Texas, USA, 25–28 September 2007.

Buist, P.J. (2008). GNSS kinematic relative positioning for spacecraft: data analysis of a dynamic testbed. 26th International symposium on space technology and science. Hamamatsu, Japan, 1–8 June 2008.

Mulder, J.A., Q.P. Chu, J.K. Sridhar, J.H. Breeman and M. Laban (1999). Non-linear aircraft flight path reconstruction review and new advances. *Prog. Aerospace Sci.*, 35, 673–726.

Teunissen, P.J.G (1993). Least-squares estimation of the integer GPS ambiguities. Invited lecture, section IV Theory and Methodology, IAG General Meeting, Beijing, China, 1993 (available on http://www.lr.tudelft.nl/mgp).

Teunissen, P.J.G (2006). The LAMBDA method for GNSS COMPASS. Artif. Satellites, 41(3), 89–103.

Schwarz, K.P. and Z. Li (1997). An introduction to airborne gravimetry and its boundary value problems. In: Sanso F. and R. Rummel (eds), Geodetic boundary value problems in view of the one centimeter geoid. Lecture notes in earth sciences. Springer, Berlin, Vol. 65, pp. 312–358.

Schwarz, K.P. and M. Wei (1994). Some unsolved problems in airborne gravimetry. In: Sünkel, and H.I. Marson (eds), Proc IAG Symposia 113, Gravity and geoid. Springer, Berlin, pp. 131–150.

Wei, M. and K.P. Schwarz (1994). An error analysis of airborne vector gravimetry. In: Proceedings of the International Symposium on Kinematic Systems in Geodesy, Geomatics and Navigation (KIS94), pp. 509–520.

Chapter 14

Gravity Measurements in Panama with the IMGC-02 Transportable Absolute Gravimeter

G. D'Agostino, A. Germak, D. Quagliotti, O. Pinzon, R. Batista, and L.A. Echevers

Abstract The work hereafter described was designed to determine the gravity datum at the Centro Nacional de Metrologìa de Panamà CENAMEP AIP through absolute measurement of the gravity acceleration, and settle a gravity network in Panama. Twelve gravity station points were settled. Gravity data were collected with the transportable absolute ballistic gravimeter IMGC-02, operated by a team of the Istituto Nazionale di Ricerca Metrologica INRIM, in cooperation with the CENAMEP AIP and the Instituto Geográfico Nacional "Tommy Guardia" IGNTG. Establishment of the gravity net in Panama, with the highest accuracy currently obtainable, will help in the realization of primary standards and in the definition of the geodetic reference level. Moreover the gravity net may serve as reference for further detailed surveys and detection of long-term, time-dependent gravity variations.

14.1 Introduction

The Centro Nacional de Metrologìa de Panamà CENAMEP AIP is responsible for developing, preserving and maintaining the national measurement standards in the country. Nowadays CENAMEP AIP performs calibrations concerning mechanical, thermal, time and electrical units. With respect to mechanical quantities, the knowledge of the local gravitational acceleration g is required for the realisation of the force unit and its derived units (e.g. pressure). Aiming at the lowest uncertainty nowadays possible, the CENAMEP AIP began searching for laboratories that could accurately measure the g value.

After examining the laboratories CENAMEP AIP contacted the Istituto Nazionale di Ricerca Metrologica INRIM, Italy, where, since the 1970s, it has been developed and tested a transportable absolute ballistic gravimeter, the present versions called IMGC-02.

Originally the project foresaw a single measurement station at the CENAMEP AIP, but, considering the opportunity to have the measuring equipment in Panama, the project was extended by adding other measurement points.

Therefore CENAMEP AIP contacted the Istituto Geografico Nacional "Tommy Guardia" IGNTG to advise on the location of the measurement points. IGNTG choose eleven points of a gravity network that will help also in a better definition of the Panama geoid.

Following the scheduled activity, in January and February 2008, twelve absolute gravity measurements were carried out in Panama with the IMGC-02. Subject of the paper is the results of the measurements.

14.2 The IMGC-02 Transportable Absolute Gravimeter

The present instrument, the IMGC-02, has been completely developed and tested at the INRIM laboratories, see D'Agostino (2005). A picture of the apparatus is

G. D'Agostino (✉)
INRIM, Istituto Nazionale di Ricerca Metrologica,
Torino IT-10135, Italia
e-mail: g.dagostino@inrim.it

S.P. Mertikas (ed.), *Gravity, Geoid and Earth Observation*, International Association of Geodesy Symposia 135,
DOI 10.1007/978-3-642-10634-7_14, © Springer-Verlag Berlin Heidelberg 2010



Fig. 14.1 Picture of the transportable gravimeter IMGC-02

shown in Fig. 14.1. As for the previous versions, it adopts the symmetrical rise-and-fall method, based on the reconstruction of the vertical trajectory followed by a test-body in its free rise-and-fall motion. In particular a launch pad, installed in a vacuum chamber, gives to the test-body the starting upwards-vertical velocity.

Laser interferometry is used to track the trajectory. The flying body acts as the moving reflector in a vertically oriented arm of a Michelson interferometer, whereas the reference reflector is fixed to the inertial mass of a vertical seismometer.

A iodine stabilized He-Ne laser is used to illuminate the interferometer. The optical fringes are converted to a voltage signal by a photodetector and acquired with a digital oscilloscope, whose frequency is driven by a rubidium clock.

Time values, correspondent to equally spaced positions of the test-body during its trajectory, are obtained by processing the acquired interference signal, see D'Agostino et al. (2005). A mathematical model, derived from the law of motion of a body subjected to a uniformacceleration, is fitted to the time-position coordinates in a least-squares algorithm. Among the model parameters there is the gravity acceleration g experienced by the testbody.

The apparatus, after the alignment of the interferometer and launch chamber, operates automatically by collecting the gravity data. The software package consists of two programs, custom developed in Labview platform: (i) GravisoftM is used to manage the instrument and collect the data, (ii) GravisoftPP is used for post-processing and computing the final g value (see Fig. 14.2).

At present the most important contributor to the data scattering is the vibration transferred from the ground floor to the reference reflector, despite the care taken to insulate it.

For this reason the measurement result is taken as the average of several individual launches forming a measurement session. In normal conditions the measurement session is performed during the night, when the disturbance of human noise is minimum. The instrument usually collects about 1,800 gravity data in 15 h of continuous working. Under the reasonable hypothesis of a Gaussian distribution for the ground vibrations, the experimental standard deviation of the mean value becomes negligible compared to the uncertainty contribution of other influencing parameters.

The measurement uncertainty ($p = 95\%$), under good experimental and environmental conditions, is valuated to be about 9×10^{-8} ms^{-2}. The most overriding factors are the retroreflector balance (instrumental) and the Coriolis acceleration (site-dependent), see Bich et al. (2008a, b).

The IMGC-02 participated to the last International Comparison of Absolute Gravimeter ICAG-05, organized by the Bureau International des Poids et Mesures BIPM. The results obtained were compatible with the Key Comparison Reference Value KCRV, within the declared uncertainty. Therefore the gravity data acquired in Panama with the IMGC-02 are consistent with the Calibration and Measurement Capabilities (CMCs) that are included in Appendix C of the Mutual Recognition Agreement MRA drawn up by the International Committee for Weights and Measures CIPM, see Vitushkin et al. (2008).

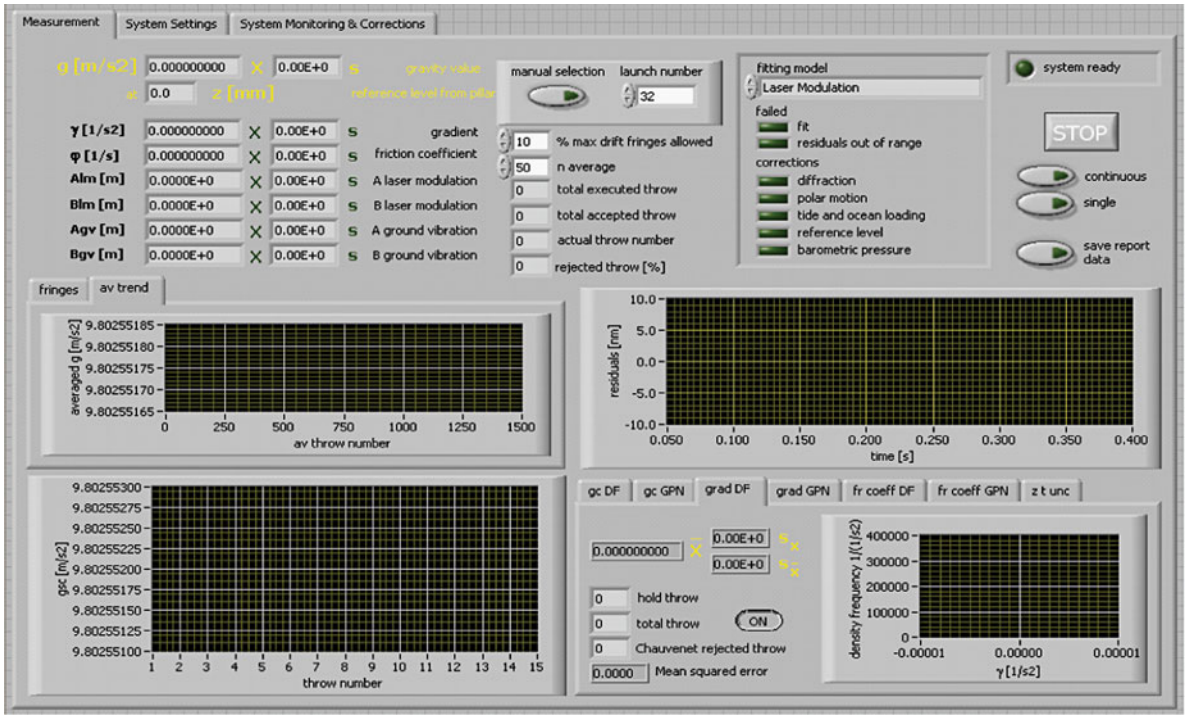


Fig. 14.2 Front panel of the program GravisoftPP

14.3 Logistics and Environmental Conditions

The first station was settled at the large mass laboratory of CENAMEP AIP. This allowed also training the CENAMEP AIP and IGNTG teams about the measurement procedure and planning the best solutions for possible instrumental and logistic problems. After establishing the twelve measurement points, we scheduled the itinerary for measurements. Based on this approach the following four points were carried on in sites relatively close to CENAMEP AIP, with easy access roads and buildings that have the minimum requirements of security and environmental stability needed for the good performance of the measuring equipment.

The relevant locations are: El Valle, Calobre, Tonosi and Colon. The remaining seven stations were settled far away from Panama City (except the station at IGNTG): Santa Fe, Yaviza, Panama City (IGNTG), Tolé, Changuinola, Boquete and the island of Coiba. A metal plate indicating the measurement point was fixed on the ground floor in each observation site (see Fig. 14.3).



Fig. 14.3 Picture of the metal plate fixed on the floor in Tonosi

The transportation of the measurement apparatus in the first eleven points was done by car while the last point in the island of Coiba was done by boat. Each observation site required at least two days. After the travel to the new location the instrument was assembled and the electronics devices switched on. After some hours of warming-up and the alignment of

the optical interferometer, the IMGC-02 collected the gravity data for all the night, and, if necessary, also for all the following day.

The measurement period was divided in two parts: the former from January, 19th to February 2nd, the latter from February, 7th to 22nd (the measurements stopped because of carnival festivities). Since Panama is located in a tropical zone, the above-reported period was chosen because it corresponds to the dry season. The absence of rain allowed good travelling conditions throughout the country.

The IMGC-02 performed about 25,000 launches correspondent to a total amount of 50 h of continuous working. Logistics and ambient conditions were a severe test for the apparatus that succeeded in measuring the free-fall acceleration in every observation site.

14.4 Results

Figure 14.4 gives the map of Panama with the stations where absolute measurements were carried on.

The instrument has been first operated at the large mass laboratory of the CENAMEP AIP, where the good environmental conditions allowed reaching the best measurement uncertainty.

Afterwards, following the time schedule, the IMGC-02 collected the gravity datum in all the remaining stations.

As we normally do in a survey, measurements were done by following a closed loop, namely they were started at our reference station at INRIM in Turin, then performed at the twelve planned stations in Panama, after which they were repeated at the same starting station in Turin, to check the results.

The difference between the results obtained in Turin immediately before and after the measurement survey in Panama was about 6×10^{-8} ms^{-2}, within the measurement reproducibility evaluated in Turin (8×10^{-8} ms^{-2}). This is a kind of warranty of the reliability of the individual results shown in Table 14.1, taking into account that the long-term stability of the free-fall acceleration in Turin is unknown. INRIM delivered to the CENAMEP AIP a measurement certificate for each observation site, reporting the results.

The measurement uncertainty gives an indication of the quality of the results. In particular the best was at CENAMEP AIP (Panama City) with un uncertainty of 9.2×10^{-8} ms^{-2} and the majority of the other measurement was about 10×10^{-8} ms^{-2}. Only in four points the uncertainty was higher than 12×10^{-8} ms^{-2} basically due to the ground noise and vibrations. The worst measurement with an uncertainty of 21×10^{-8} ms^{-2} was



Fig. 14.4 Map of Panama with the location of the measurement points indicated by the stars

Table 14.1 Measurement results in Panama

Station	Date	$g \pm U_{95\%}$ / $\times 10^{-8}$ ms^{-2}	h / mm	*lat., long.*	H *a.s.l.* / m
Panama city (CENAMEP AIP)	January 2008, 19–20	978,228,998.0 ± 9.2	521.9	9.00°, –79.58°	21
El Valle	January 2008, 26–27	978,026,661.2 ± 21.0	523.6	8.60°, –80.13°	586
Calobre	January 2008, 27–28	978,141,885.6 ± 10.4	524.2	8.32°, –80.84°	126
Tonosi	January 2008, 29–30	978,239,412.4 ± 10.1	522.6	7.41°, –80.43°	17
Colon	February 2008, 01–02	978,238,145.3 ± 14.4	526.7	9.35°, –79.91°	2
Santa Fe	February 2008, 07–08	978,232,805.5 ± 10.4	522.3	8.66°, –78.15°	19
Yaviza	February 2008, 08–10	978,174,139.1 ± 10.0	522.8	8.17°, –77.69°	64
Panama city (INGTG)	February 2008, 12–13	978,226,963.3 ± 12.1	523.5	8.98°, –79.53°	25
Tolé	February 2008, 13–15	978,114,936.1 ± 9.5	524.8	8.24°, –81.67°	315
Changuinola	February 2008, 16–17	978,183,389.9 ± 10.2	523.3	9.44°, –82.52°	8
Boquete	February 2008, 18–19	977,975,059.7 ± 9.4	525.1	8.77°, –82.43°	1,084
Coiba	February 2008, 21–22	978,234,461.7 ± 13.5	525.1	7.62°, –81.73°	2

carried out in a critical environmental conditions due to a strong wind that increased the experimental standard deviation. Even temperature conditions up to 38°C disturbed the good performances of the gravimeter.

Nevertheless all the results can be considered satisfactory for the purpose of the project.

It is evident from Table 14.1 that the measurement uncertainty in several sites exceed the IMGC-02 declared uncertainty (9×10^{-8} ms^{-2}).

This is because the best uncertainty (the declared one) is only reached under good experimental and environmental conditions, typically during the International Comparisons of Absolute Gravimeters.

14.5 Conclusion

The work done by the INRIM, CENAMEP AIP and IGNTG teams, concerning the determination of the gravitational acceleration carried on in twelve observation sites in Panama, was shown. The twelve absolute measurements carried out with the IMGC-02 are the first high-accuracy determination of a gravity network in Panama. The gravity station located in CENAMEP AIP will be used for metrology, in particular concerning the realization of measurement units requiring the knowledge of the free-fall acceleration. Moreover, this work is an initial step towards a detailed gravity surveys to provide useful data for geodetic and geophysical purposes.

References

D'Agostino, G. (2005). Development and Metrological Characterization of a New Transportable Absolute Gravimeter. *Ph.D. Thesis*, Polytechnic of Turin.

D'Agostino, G., A. Germak, S. Desogus, and G. Barbato (2005). A method to estimate the time-position coordinates of a free-falling test-mass in absolute gravimetry. *Metrologia*, 42(4), 222–228.

Bich, W., G. D'Agostino, A. Germak, and F. Pennecchi (2008a). Reconstruction of the free-falling body trajectory in a rise-and-fall absolute ballistic gravimeter. *Metrologia*, 45(3), 308–312.

Bich, W., G. D'Agostino, A. Germak, and F. Pennecchi (2008b). Evaluating measurement uncertainty in absolute gravimetry: an application of the monte carlo method. In: Proceedings of workshop advanced methods for uncertainty estimation in measurement. Trento, Italy, July 21–22, CDrom.

Vitushkin, L., J. Zhiheng, L. Robertsson, M. Becker, O. Francis, A. Germak, G. D'Agostino, and V. Palinkas (2008). Results of the seventh international comparison of absolute gravimeters ICAG-2005 at BIPM. In: Proceedings of International Symposium on "Gravity, Geoid and Earth Observation GGEO 2008", 23–27 June 2008, Chania, Crete, Greece, in press.

Chapter 15

Comparison of Height Anomalies Determined from SLR, Absolute Gravimetry and GPS with High Frequency Borehole Data at Herstmonceux

G. Appleby, V. Smith, M. Wilkinson, M. Ziebart, and S. Williams

Abstract The UK Space Geodesy Facility has operated a highly precise Satellite Laser Ranging station at Herstmonceux in southern England for over 25 years and the laser ranger is one of the ILRS core stations. It also operates two GNSS receivers contributing to IGS for over 14 years, and an Absolute Gravimeter (AG) which provides 24-h data weekly since November 2006. The facility has environmental monitoring in the form of a borehole, in close proximity to both the SLR and the gravimeter room, which provides automatic ground-water level measurements, and precise temperature, pressure and humidity devices. In this work we will investigate time series of site height variations determined by the independent techniques of SLR, AG and GPS since November 2006. The geodetic results suggest annual periodic vertical variations of amplitude about 15 mm and the absolute gravity values show systematic variations of order four microgals. We are particularly interested in the hydrological effects on the gravimeter data and will aim to use the space geodetic results to separate them from local vertical signals.

15.1 Introduction

In the era of the Global Geodetic Observing System, geodetic sites offering multi-technique capabilities are becoming increasingly important. Maintenance of the terrestrial reference frame, for example, benefits greatly from SLR, GNSS, DORIS and VLBI observations co-located and precisely linked via accurate site ties. Of prime importance is the generation of accurate, bias-free observations and a knowledge of the stability of the sites, since any local un-modeled deformation will directly influence the integrity of the global reference frame.

The Space Geodesy Facility at Herstmonceux, UK operates laser ranging, GNSS and absolute gravimetry systems, and is involved as an ILRS Analysis Centre in providing daily coordinate and Earth rotation solutions. A map is shown at Fig. 15.2.

Discussed in this paper are early efforts to quantify some local environmental effects on the gravity measurements, in particular the local wind speed and water table variations the influence of which are known to be difficult to model (see Van Camp et al., 2006). The space geodesy techniques are used to determine site vertical motion in order to remove that signal from the gravity data. The processed gravity data is then compared with local borehole measurements.

15.2 Site Description

The SGF building was built in the late 1940s, the first of the telescope domes to be built by the Royal Greenwich Observatory at Herstmonceux. Initially housing a solar telescope, the building was converted in the late 1970s for SLR use, at which time the basement of the facility was left superfluous. In 2004, with the decision to purchase a gravimeter, work began on the conversion of the basement into a workable area. Optically flat concrete benches which ran along its ninety foot length were stripped out and a gravimetry room was established at one end. The gravimetry room

G. Appleby (✉)
NERC Space Geodesy Facility, Herstmonceux Castle, Hailsham, East Sussex, BN27 1RN, UK
e-mail: gapp@nerc.ac.uk

S.P. Mertikas (ed.), *Gravity, Geoid and Earth Observation*, International Association of Geodesy Symposia 135,
DOI 10.1007/978-3-642-10634-7_15, © Springer-Verlag Berlin Heidelberg 2010

is 3 m under the ground level as measured at the borehole and has approximately 1 m of earth above it. The local soil type is known to be Weald clay (British Geological Survey website).

The SLR system is operated at a single-photon level of returns, giving a single-shot precision to the geodetic satellites of some 12 mm and enabling the computation of an accurate value to refer the observations to the centres of mass of the satellites (Appleby, et al., 1999). The system is in the process of being upgraded to a state-of-the-art solid state 2 kHz laser which further improves the precision of the range measurements (Gibbs et al., 2007).

The GNSS receivers both contribute RINEX data to IGS. HERS (Ashtech Z12) contributes thirty second data to IGS and HERT (Ashtech Z18 until 2007 December when it was replaced by a Leica GRX 1200) both contributes daily GPS and GLONASS data to the IGS and supports EUREF and IGS realtime projects via data streamed to the Internet.

As well as very precise meteorological equipment (temperature, pressure and humidity) the site also has a borehole situated less than 5 m from the laser telescope in which an underwater pressure sensor logs groundwater readings at 5 min intervals. The height of the groundwater is seen to fluctuate seasonally by around 2 m.

15.3 Gravimeter Installation

Installed in 2006, the FG-5 gravimeter (Niebauer et al., 1995) is permanently located in a room with stable temperature and humidity, at the south end of the basement. The room has four location studs denoting the available gravimeter locations, all of which have been surveyed and tied into the SGF local site map by the UK Ordnance Survey (Fane, C, Private communication, 2006).

Operationally the gravimeter is run in mid-GPS week for a period of 24 h (24 sets) each week, with 100 drops being used on each set. A data time series from November 2006 to May 2008 has been accumulated, with few interruptions in the time series. Some early data taken in June and July 2006 has been added to this time series, which is presented in Fig. 15.1. The early data clearly stands off from the rest of the series, but at this time there is no good reason to reject it.

The daily gravimetry measurements have been recorded using the Micro-g Lacoste program "G6" and then finally processed using the newer "G7" software, which, like "G6" corrects for parameters including the gravimeter's position, polar rotation (from the IERS), barometric pressure (internal barometer), ocean loading and earth tides (using ETGTAB). Both G6 and G7 use a "real time" analysis procedure to determine a best-fit trajectory of the test mass as it is dropped 20 cm in a vacuum and hence determine g for each drop. The precision of the gravity measurements (drop-to-drop scatter) discussed later in this paper is based upon the a-posteriori error estimate of the value of the local gravity acceleration determined from the model fit to the recorded time-distance pairs; see Niebauer (1995) or Van Camp et al. (2003).

The time series of gravity values presented here are weighted mean values over each 24 h period, and the drop-to-drop scatter is the standard deviation of measurements of 100 drops as processed by G7.

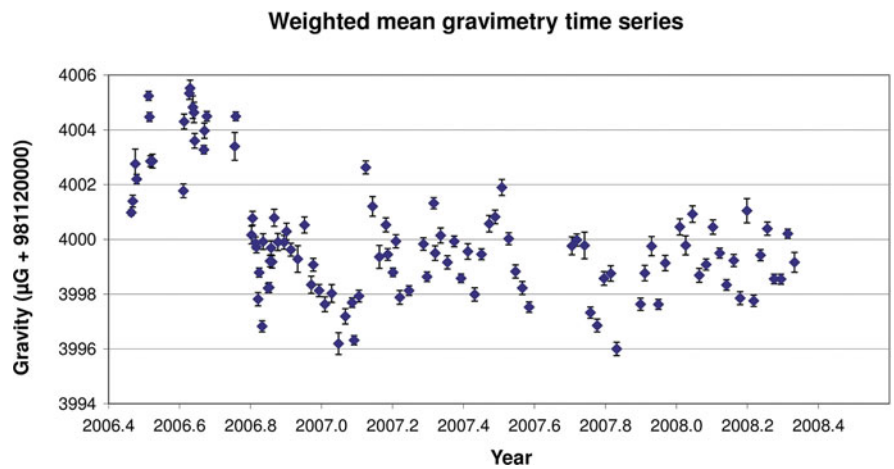


Fig. 15.1 Gravity time line of measurements from May 2006 to May 2008

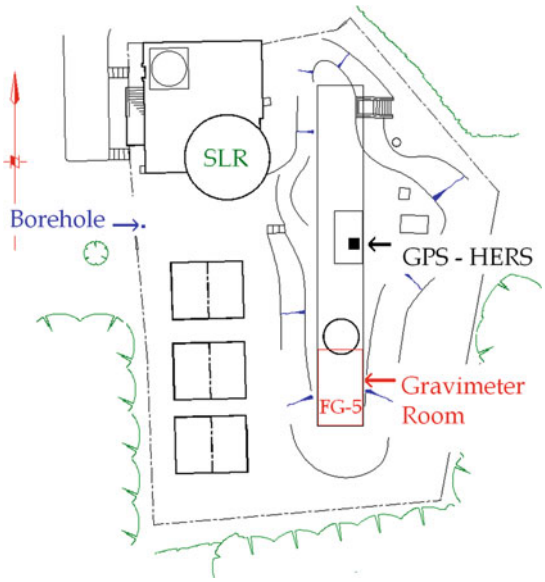


Fig 15.2 Herstmonceux SGF site layout

The gravimeter drop-to-drop scatter ranged from about 5 to 35 micro-gals (μgal) resulting in a set standard deviation of from one to seven μgal for each daily mean value of g.

All sets with a large drop-to-drop scatter considered to be due to an extreme event (e.g., an earthquake) have been excluded from this analysis. A least-squares solution for an annual variation in gravity found only a statistically-insignificant term of amplitude 0.4 μgal.

15.3.1 FG-5 Drop-to-Drop Scatter at Herstmonceux

Early in the operation of the gravimeter it was apparent that the drop-to-drop scatter was affected by local wind speed. Since the gravimetry room has trees in close proximity on three sides, any influence of wind on this scatter may be exacerbated by resultant local ground shaking (Fig. 15.2).

Hourly wind speed data (to nearest ms^{-1}) were obtained from a UK Met Office station, situated 3 km to the North East, for days on which the gravimeter was in operation from 2006 November up to 2008 April.

Data from two extremes of wind speed are shown in Fig. 15.3 where it can be seen that on a day where the wind speed is variable between 3 and 7 ms^{-1} the gravimeter drop-to-drop scatter lies between 18 and 32 μgal.

The following week, with wind speeds of less than 2 ms^{-1}, the drop-to-drop scatter improves to better than 12 μgal. Figure. 15.3 shows an example of the close relationship that the investigation has revealed.

To further quantify this relationship, drop-to-drop scatter values for the entire 2-year period were grouped and averaged according to the prevailing wind speed. These averages were plotted against wind speed (Fig. 15.4) and reveal a near-linear trend. It should be noted that the average wind speed values used here would tend to reduce the expected impact of gusts on set precision. Although the correlation cannot be said to be perfect, deviations may be due to effects such as micro-seismic noise generated by the non-linear

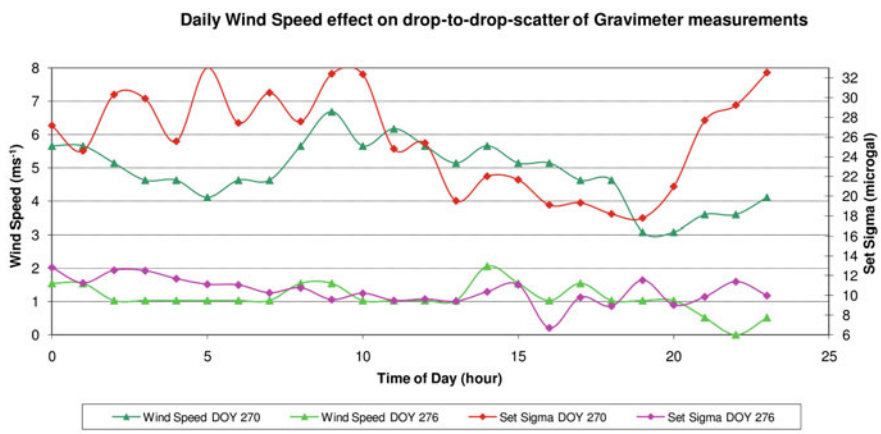


Fig. 15.3 Wind speed effect on gravimeter drop-to-drop scatter over 24 h on 2 days

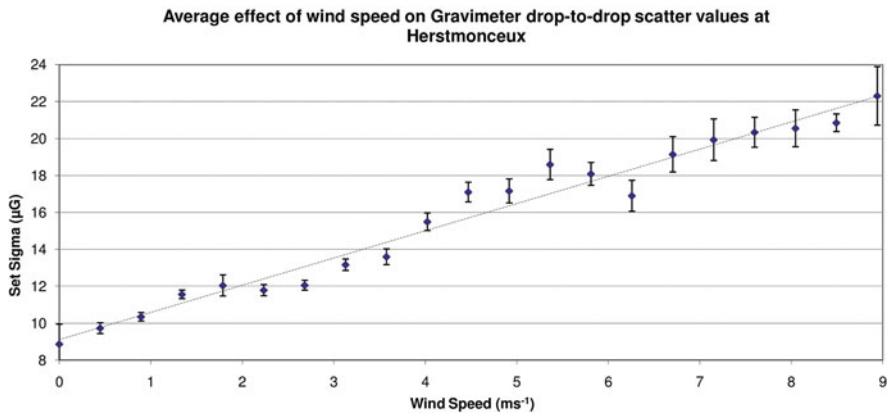


Fig. 15.4 Correlation between averaged wind speed and gravimeter drop-to-drop scatter from 2006 to 2008

response of the oceans to variable wind speed. This and other potential local and global effects are the subjects of ongoing work.

15.4 GPS and SLR Analysis

Daily 30-s GPS observations from a subset of some twenty globally-distributed stations, including HERS and HERT, of the large, well-distributed IGS network (Dow et al., 2005) have been obtained from the IGS data centres and processed for the 2-year period of this study. Daily, loosely-constrained, site coordinates were estimated using the GAMIT software, version 9.9 (King and Bock, 2004), IGS final solution orbits, satellite navigation files and USNO Earth rotation parameters. A-priori station positions were taken from the ITRF2005 (Altamimi et al., 2007), and no atmospheric loading was modeled. Daily coordinate solutions from GAMIT were combined using the associated Kalman filter package GLOBK (Herring et al., 2006) to form weekly site coordinates and error estimates, stabilised to the ITRF2005 by fixing the coordinates of some 20 globally-distributed sites to their ITRF2005 coordinates. From these solutions, weekly height series for HERS and HERT were extracted for the 2 years.

The ILRS network of some twenty-five operational stations (Pearlman et al., 2002) regularly obtains range measurements to the two LAGEOS and two ETALON geodetic satellites. The single-shot measurement precision varies by station from 5 to about 20 mm depending upon hardware and operational practice. The raw range measurements are compressed during post-processing into "normal points" and made available very rapidly through the two ILRS data Centres in Washington, DC and Munich, Germany. Normal points from the network for all four satellites during the period 2006 June–2008 May were processed using the in-house SGF analysis package SATAN (Sinclair and Appleby, 1986). Seven-day orbital arcs were fitted to the range observations for each satellite using orbital models conforming to IERS Conventions 2003 (McCarthy and Petit, 2004) and including the latest tropospheric zenith delay model and mapping function (Mendes and Pavlis, 2004), satellite centre-of-mass corrections (Otsubo and Appleby, 2003) and IERS tidal loading. Again, no atmospheric loading was modelled. A-priori station positions were taken from the SLRF2005, an ILRS Analysis Working Group combination of ITRF2000 and a re-scaled ITRF2005, available through the ILRS website.

The RMS of post-fit range residuals are typically about 10 mm. A final, all-satellite solution was performed to form weekly, unconstrained estimates of site coordinates and Earth orientation parameters. The geocentric site coordinates were converted to geodetic coordinates and their errors using the full covariance matrices.

15.5 Discussion

The time series of Herstmonceux height values with 1-sigma error bars, plotted with respect to each series' mean values are shown in Fig. 15.5. The HERS and HERT series are, as expected, very similar to each other and for clarity in the plot only the HERS series

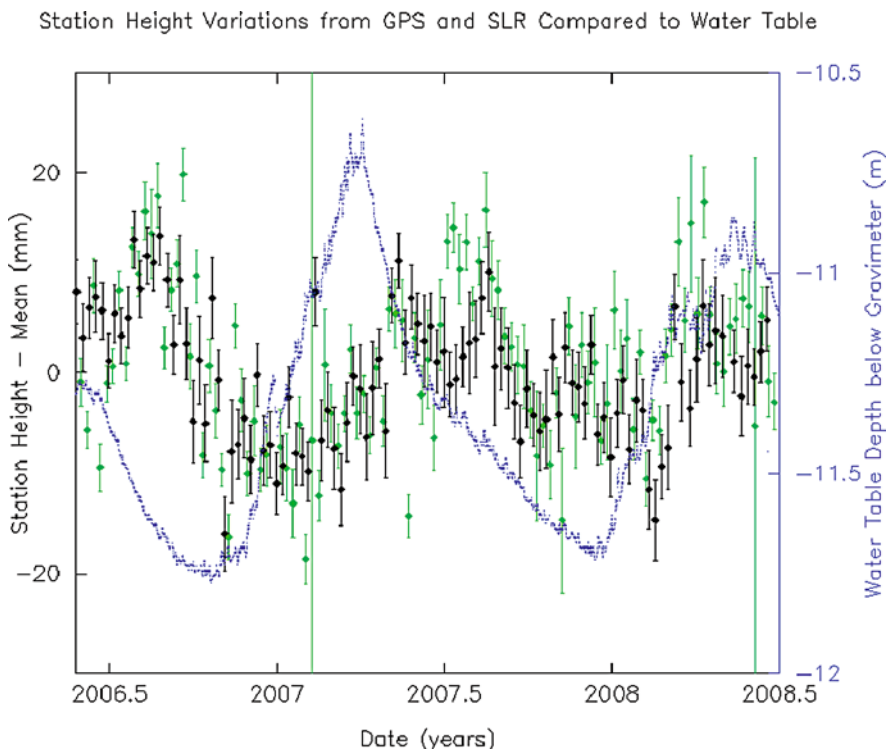


Fig 15.5 SLR (*Green*) and GPS (*Black*) time series of heights 2006–2008. In (*Blue*) is the water table level below the site (for colors, see online version)

is shown. Both GPS and SLR series have a few outlier points, but the general trends are similar and in particular both show a strong seasonal periodicity of semi-amplitude about 10 mm. Ongoing work with a longer time series of laser and GPS solutions (1996-present, e.g., Appleby et al. (abstract), 2008) has shown a clear empirical correlation of station height with local hydrology as determined from water table measurements. To illustrate this, shown in Fig. 15.5 are the daily values of the depth of the water table determined from measurements in the on-site borehole. During the period of this investigation the water table depth changed from a low of nearly –12 m to a high of –10.5 m, forced by seasonal rainfall, with a phase lag estimated at about 100 days. A comparison between the station heights and the water table depth shown in Fig. 15.5 strongly suggests that the site is subject to winter-time loading effects driven by hydrology, again with a phase-lag of 100 days or so.

The laser solutions are particularly sensitive to Earth centre of mass motion (Altamimi et al., 2007) and for that reason the SLR height series are used in the rest of this current investigation.

In order to begin an investigation into local environmental effects such as hydrology on the gravity results, the SLR height time series was used to remove the purely geometrical component, using a near-Bouguer conversion factor of 1 μgal equivalent to minus 4.8 mm. This conversion factor is an estimate only at this stage, which will be refined in future comparisons of height-change with gravity-change signatures, following Zerbini et al. (2007). The SLR-derived height time series was interpolated using a weak smoothing function in order to determine heights, relative to the overall mean value, at the central epoch of each of the gravity values. The resulting time series of height-corrected gravity values, shown in Fig. 15.6 relative to the mean for the 2-year data set, has a range of values of about ±5 μgal. Again, the water table depth series is plotted for comparison in the same Figure.

The final stage of this preliminary investigation is to estimate the expected gravitational potential change due to the change in water table depth in the clay. The standard Bouguer model is used, where the disturbing mass is assumed to be a sheet of thickness h meters and of infinite extent. The corresponding gravity change Δg_B is given by $\Delta g_B = 2\pi G\rho h = 0.0419\rho h$ μgal, where ρ is the density of the disturbing mass in kgm^{-3}. The maximum expected change in gravity forced by water table depth change is modelled

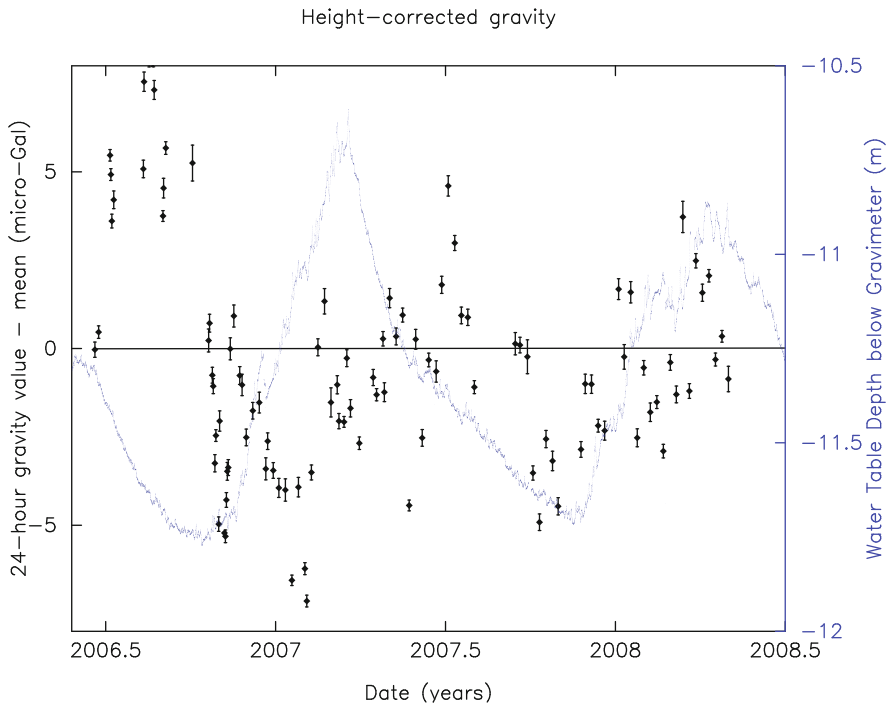


Fig 15.6 Borehole measurements (*blue*) and height-corrected gravity measurements (*black*) (for colors, see online version)

here by considering the *change* in Δg_B resulting from replacing 12 m of wet clay by 12 m of dry clay, against the corresponding effect for 10.5 m of clay. For each of these two situations, $\Delta g_B = 0.0419(\rho_{dry} - \rho_{wet})d$, where d is either 12 or 10.5 m. Estimates of densities ρ_{dry} and ρ_{wet} are taken as 1,070 and 1,600 kgm^{-3}. This leads to Δg_B values of –270 and –230 μgal respectively, giving a change in Δg_B of –40 μgal between a water table depth of –12 m and of –10.5 m. This theoretical change in gravity is greater by a factor of five from our observed range of gravity values, suggesting that the water table changes affect clay moisture changes in more complex ways than modelled by this simple treatment. It should also be remembered that the Bouguer model itself is a very simple infinite-slab approximation to the problem.

15.6 Conclusions

The result of the first 2 years of gravimetry data at Herstmonceux has facilitated these initial investigations which clearly emphasise the need to better understand the local environment. A linear relationship between gravimeter drop-to-drop scatter and local wind speed has been discovered, and a more detailed investigation is underway to look at micro-seismic effects including atmospheric influences on sea-state. Further, the acquisition of an on-site anemometer will improve the quality of future wind-speed data. The space geodetic height time series (SLR and GPS) have been used to remove vertical signals from the gravimeter results. A comparison of this height-corrected gravity time series with the local water table shows some intriguing signals but little correlation, and a simple, Bouguer-based computation of the magnitude of the water table effect overestimates the observed amplitude of the gravity variations by some five times. Future work will involve a more thorough investigation into the local geology including the use of soil-moisture probes to better quantify hydrological effects on local gravity. It will also be very important to measure the dry and wet densities of the local clay, as errors in the values assumed in this investigation will directly impact the modelled affect on gravity variation. This effort should improve the value of gravimetry in the interpretation of the SGF space geodetic results and have wider implications for similar multi-technique space geodetic facilities.

References

Appleby, G., M. Wilkinson, and V. Smith (2008). Analysis of vertical motion at herstmonceux from satellite geodesy and absolute gravity, Geophysical Research Abstracts, Vol. 10.

Altamimi, Z., X. Collilieux, J. Legrand, B. Garayt, and C. Boucher (2007). ITRF2005: A new release of the international terrestrial reference frame base on the time series of station positions and the earth orientation parameters. *J. Geophys. Res.*, 112, B09401, doi: 10.1029/2007JB004949.

Appleby, G., P. Gibbs, R.A. Sherwood, and R. Wood (1999). Achieving and maintaining sub-cm accuracy for the Herstmonceux single-photon SLR facility. Laser Radar Ranging and Atmospheric Lidar Techniques II, SPIE Vol 3865, 52–63.

Dow, J.M., R.E. Neilan, and G. Gendt (2005). The international GPS service (IGS): celebrating the 10th anniversary and looking to the next decade. *Adv. Space Res.*, 36(3), 320–326, doi: 10.1016/j.asr.2005.05.125.

Gibbs, P., G. Appleby, D. Benham, C. Potter, R. Sherwood, V. Smith, and M. Wilkinson (2007). Some early results of KiloHertz laser ranging at herstmonceux. In: Proceedings of the 15th International Laser Ranging Workshop, Canberra, Australia, pp. 250–258.

Herring, T., R.W. King, and S.C. McClusky (2006). Global Kalman filter VLBI and GPS analysis program, version 10.3, Mass. Inst. of Technol., Cambridge.

King, R. and Y. Bock (2004). Documentation for the GAMIT GPS analysis software, release 9.9, Mass. Inst. of Technol., Cambridge.

McCarthy, D.D. and G. Petit (2004) IERS CONVENTIONS (2003), IERS Technical Note No. 32, IERS Convention Centre.

Mendes, V. B. and E.C. Pavlis (2004). High-accuracy zenith delay prediciton at optical wavelengths. *Geophys. Res. Lett.*, 31, L14602, doi:10.1029/2004GL020308.

Niebauer, T., G. Sadagawa, J. Faller, and F. Klopping (1995). A new generation of absolute gravimeters. *Metrologia*, 32, 159–180.

Otsubo, T. and G. Appleby (2003). System-dependant centre of mass correction for spherical geodetic satellites. J. Geophys. Res., 108, B4, 2201, doi: 10.1029/2002JB002209.

Pearlman, M.R., J.J. Degnan, and J.M. Bosworth (2002). The international laser ranging service. *Adv. Space Res.*, 30(2), 135–143, July 2002, DOI:10.1016/S0273-1177(02)00277-6.

Sinclair, A. and G. Appleby (1986). SATAN – programs for the determination and analysis of satellite orbits from SLR data. *SLR Tech. Note*, 9, Royal Greenwich Observatory.

Van Camp, M., T. Camelbeck, and P. Richard (2003). The FG-5 absolute gravimeter: metrology and geophysics. Physicalia Magazine. *J. Belgian Phys. Soc.*, 25(3), 161–174.

Van Camp, M., M. Vanclooseter, O. Cormmen, T. Petermans, K. Verbeeck, B. Meurers, T. van Dam, and A. Dassarues (2006). Hydrogeological investigations at the Membach station, Belgium and application to correct long period gravity variations. *J. Geophys. Res.*, 111, B10403, doi:10.1029/2006JB004405.

Zerbini, S., B. Richter, F. Rocca, T. Van Dam, and F. Matonti (2007). A combination of space and terrestrial geodetic techniques to monitor land subsidence: case study, the south-eastern Po Plane, Italy. *J. Geophys. Res.*, 112, B05401, doi:10.1029/2006JB004338.

Chapter 16

Vibration Rejection on Atomic Gravimeter Signal Using a Seismometer

S. Merlet, J. Le Gouët, Q. Bodart, A. Clairon, A. Landragin, F. Pereira Dos Santos, and P. Rouchon

Abstract We use atom interferometry to perform an absolute measurement of the gravitational acceleration g.

The sensitivity of the interferometer is predominantly limited by vibration noise, even when drastically reduced by using a passive isolation platform. We present here an original correction scheme of the residual vibration induced interferometer phase fluctuations, based on the use of a low noise seismometer. In the best conditions, our instrument reaches an excellent sensitivity of $1.4 \times 10^{-8}\, g$ at 1 s, despite operating in an urban environment. But the method presented here allows reaching good performances even when operating without any vibration isolation. The sensitivity of our instrument at night is then as low as $5.5 \times 10^{-8}\, g$ at 1 s.

16.1 Introduction

Over the last 15 years, atom interferometry techniques have been used to develop novel inertial sensors, which now compete with state of the art "classical" instruments (Niebauer et al., 1995). After the first demonstration experiments in the early 1990s (Kasevich and Chu, 1991; Riehle et al., 1991), the performance of this technology has been pushed and highly sensitive instruments have been realized. A key feature of these instruments is to provide an absolute measurement with improved long term stability compared to other sensors, due to the stability of their intrinsic scale factor. Applications of this technology are growing, from the measurement of fundamental constants, such as the Newtonian gravitational constant G (Bertoldi et al., 2006; Fixler et al., 2007), to the development of transportable devices for navigation, gravity field mapping (Yu et al., 2006), detection of underground structures and finally for space missions, where ultimate performances can be met, because of the absence of gravity and a low vibration environment.

At LNE-SYRTE, we are currently developing a cold atom gravimeter based on atom interferometry, within the frame of the watt balance project, conducted by the Laboratoire National de Métrologie et d'Essais (LNE) (Genevès et al., 2005; Merlet et al., 2008b). In this project an absolute measurement of gravity with a targeted relative accuracy of 10^{-9} is needed to link the unit of mass to electrical units with relative accuracy of a few parts in 10^8 (Steiner et al., 2007; Robinson and Kibble, 2007).

In this article, we investigate the limits to the sensitivity of our atomic gravimeter, especially when operating without vibration isolation. We first describe our experimental setup and then introduce and compare two measurement schemes that allow operating the sensor in the presence of large vibration noise. In particular, we show how gravity measurements can be performed even though the interferometer phase noise amplitude exceeds 2π. These schemes use the independent measurement of vibration noise performed with a low noise seismometer. A technique based on the same principle has already been used with a "classical" corner cube gravimeter (Canuteson et al., 1997; Brown et al., 2001), and allowed improving its sensitivity by a factor 7 (Brown et al., 2001). Finally, the robustness of these measurement schemes versus large changes in

S. Merlet (✉)
LNE-SYRTE, Observatoire de Paris, 77 avenue Denfert Rochereau, Paris 75014, France
e-mail: sebastien.merlet@obspm.fr

S.P. Mertikas (ed.), *Gravity, Geoid and Earth Observation*, International Association of Geodesy Symposia 135,
DOI 10.1007/978-3-642-10634-7_16, © Springer-Verlag Berlin Heidelberg 2010

the vibration noise amplitude is illustrated by the capability of our instrument to operate and measure large ground accelerations induced by an earthquake.

16.2 Experimental Set Up

We use two-photon Raman transitions to manipulate the atomic waves and make them interfere. These transitions are induced by a pair of laser beams, both detuned from an electronic transition ($^5S_{1/2}$ to $^5P_{3/2}$ in our case), with a frequency difference that corresponds to the frequency of the hyperfine transition (6.834 GHz for ^{87}Rb). When an atom, initially in the $^5S_{1/2}$ $F=1$ hyperfine state, interacts with the two lasers, it first absorbs a photon in the laser beam 1, then reemits in a stimulated way a photon in the laser 2, ending up in the level $^5S_{1/2}$ $F=2$. When absorbing the photon 1, momentum conservation implies that the atom receives a momentum kick corresponding to the impulsion $\hbar k_1$ of the photon, and when reemitting a photon in the laser 2, a momentum $-\hbar k_2$. When the two lasers are counterpropagating, the net momentum change is $\hbar k_1 - \hbar k_2 = \hbar k_{eff}$, about twice the photon momentum, as $|k_1| \sim |k_2|$. This induces a velocity change of about 1 cm.s^{-1}.

This coherent coupling between the two hyperfine levels $F=1$ and $F=2$ allows preparing the atoms in a quantum superposition of the two states, with well controlled weights, by sending pulses of light onto the atoms (Fig. 16.1). Adjusting the duration of a Raman pulse, the atoms can be put in an equal weight superposition: this is a $\pi/2$ pulse. After this pulse, the two partial waves separate in space as they have different velocities: this $\pi/2$ pulse is analogous to a beam splitter in a light interferometer. With a subsequent pulse twice as long, the two wave-packets change electronic and momentum states, and are redirected towards each other. This π pulse acts as a mirror. Finally, a $\pi/2$ pulse allows recombining and having to interfere the two wave-packets. A matter wave interferometer of matter wave is thus created using a sequence of three pulses ($\pi/2 - \pi - \pi/2$), similar to the Mach-Zehnder interferometer in optics (Fig. 16.2).

In our case, the Raman lasers are oriented parallel to gravity chosen as z axis. During each atom-light interaction the phase difference $\phi = \phi_1 - \phi_2 = k_{eff} \cdot z$ of the laser beams is imprinted onto the atomic wave function. The difference in the phases accumulated along the two paths (*I* and *II* in Fig. 16.2) depends on the acceleration $\vec{g}$ experienced by the atoms. It can be written as (Kasevich and Chu, 1991):

$$\Delta\Phi = \phi(0) - 2\phi(T) + \phi(2T) = -\vec{k}_{eff}\,\vec{g}\,T^2 + \delta\phi \tag{1}$$

where $\phi(0, T, 2T)$ is the difference of the phases of the lasers, at the location of the center of the atomic wave-packets, for each of the three pulses (Bordé and Antoine, 2003) and T is the time interval between two consecutive pulses. The $\delta\phi$ indicates the presence of residual phase shifts in addition to the gravity phase shift, due to the acceleration of the atoms along the Raman beams. At the output of the interferometer, the transition probability from one hyperfine state to the other is given by the well-known relation for a two wave interferometer:

$$P = 1/2(1 + C\cos\Delta\Phi) \tag{2}$$

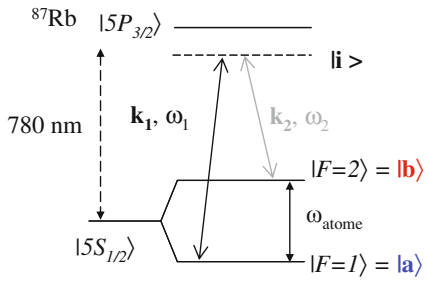


Fig. 16.1 ^{87}Rb energy levels relevant for the Raman transitions. Two laser beams allow to induce a coherent coupling between the two hyperfine levels of the ground state

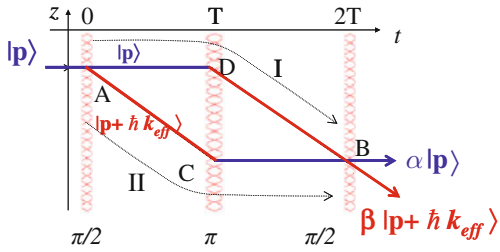


Fig. 16.2 Principle of the interferometer. The sequence of π/2 – π – π/2 pulses represents the atomic analog of a closed Mach-Zehnder type interferometer. Here, π/2 (π) pulse indicates that the atomic wave function is split into a superposition of ground and excited state with 50% (100%) population transfer

where C is the interferometer contrast. The population of each of the two states is measured by fluorescence (detection in Fig. 16.3), from which we derive the transition probability and finally the acceleration g.

As the phase of the interferometer increases quadratically with the interaction time, we use cold atoms in order to operate with large interaction times, reach large phase shifts, and thus good sensitivity. ^{87}Rb atoms from a room temperature vapor are first cooled by a 2D-MOT (Fig. 16.3), which generates an intense beam of slow atoms. From this beam, about 10^7 atoms are loaded within 50 ms into a 3D-MOT and then cooled in a far detuned (–25 Γ) optical molasses. The lasers are then switched off to release the atoms into free fall at a final temperature of 2.5 μK.

Before entering the Mach-Zehnder interferometer, atoms are selected in a narrow velocity distribution ($\sigma_\upsilon \leq \upsilon_r = 5.9\,\text{mm}\,\text{s}^{-1}$) in the $|F=1, m_F=0>$ state, using a combination of microwave and optical Raman pulses.

The 30 cm tall vacuum chamber is preserved from the external magnetic field fluctuations by a magnetic shield of 80 cm height and 60 cm diameter. The chamber is sustained with three legs clamped on an isolation platform in order to shield it against vibrations. Between the magnetic shields and the platform, we have placed a retro-reflecting mirror fixed onto a low noise broadband seismometer. The mirror retro-reflects upwards the laser beams that exit from a collimator attached at the top of the vacuum chamber.

The Raman light sources are two extended cavity diode lasers based on the design of (Baillard et al., 2006), which are amplified by two independent tapered amplifiers. Their frequency difference, which is phase locked onto a low phase noise microwave reference source, is swept according to $(\omega_2-\omega_1)(t)=(\omega_2-\omega_1)(0)+\alpha t$ in order to compensate for the gravity induced Doppler shift. This adds αT^2 to the interferometer phase shift (Eq. (1)), which cancels it for a perfect Doppler compensation, for which $\alpha_0 = \overrightarrow{k_{eff}} \cdot \vec{g}$. The measure of g is now obtained locking the frequency chirp of the Raman lasers so that this condition remains fulfilled. The seismometer is a Guralp CMG-40T (response option 30 s). The platform can be used ON or OFF. In the case where the platform is OFF, the spectrum is similar to the spectrum measured directly on the ground.

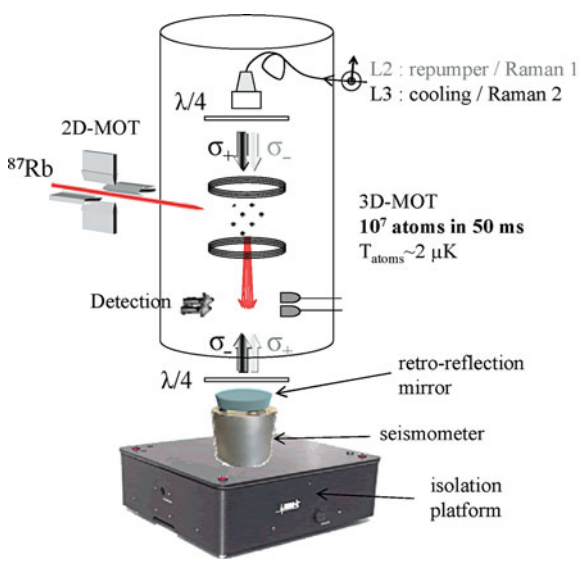


Fig. 16.3 Scheme of the experimental set-up. The distance between the first and the last pulse is 5 cm. A magnetic shield surrounds the chamber. The chamber is placed onto a vibration isolation platform

16.3 Vibration Correction

16.3.1 Correlation Between Atomic and Seismometer Signals

The phase shift of the interferometer due to residual vibrations can be determined by the seismometer by:

$$\phi^S_{vib} = k_{eff} K_s \int_T^{-T} g_s(t)\, U_s(t) dt \qquad (3)$$

where g_s is the sensitivity function (Cheinet et al., 2008), U_s the seismometer voltage output and K_s=400.2 V/(m.s^{-1}) is the velocity output sensitivity of the seismometer. For an interferometer time $2T$=*100 ms* in the two cases of platform ON and OFF, the measured transition probability is displayed on Fig. 16.4 as a function of ϕ^s_{vib}. The noise is low enough in the ON case for the interferometer to operate close to mid fringe, while in the OFF case, interferometer phase noise is larger than 2π, and the interferometer signal jumps from one fringe to another. It shows the good correlation between measured and calculated phase shifts. In the ON case, we find a correlation factor as high as 0.94. The seismometer can thus be

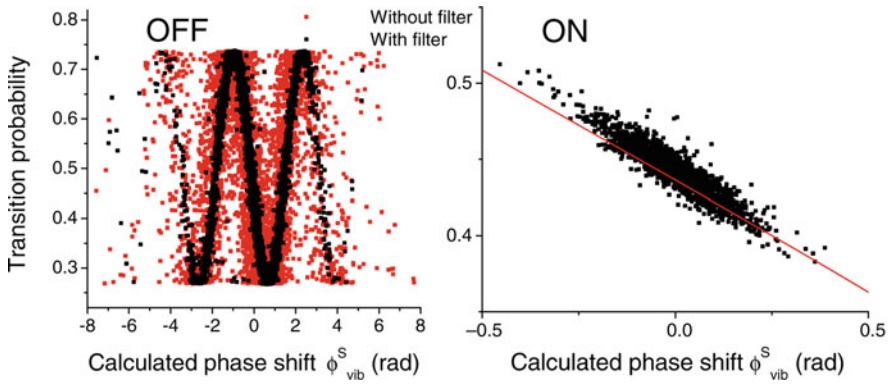


Fig. 16.4 Correlation between the transition probability of the interferometer and the phase shift calculated from the seismometer data

used to apply a post-correction on the transition probability measured at mid fringe. This correlation is not perfect though due to the response function of the seismometer that behaves as a low pass filter with a cut-off frequency of 50 Hz.

16.3.2 Digital Filtering and Cross Coupling

To compensate for the phase lag of the seismometer at intermediate frequencies, we implemented a numerical filtering of the seismometer signal. Its design is described in detail in (Le Gouët et al., 2008).

This digital filtering improves the rejection efficiency. Yet the gain on the sensitivity was limited to 25% due to excess noise of the seismometer arising from coupling between axes. In fact, recording simultaneously the seismometer outputs along the three directions, calculating three corrections, one along each axis (only the vertical correction was numerically filtered though) and fitting the transition probability measured at mid fringe with a linear combination of the three corrections showed couplings of 4% and 5% with the horizontal axes. Nevertheless, by night in the ON case, we obtained a sensitivity of $1.4 \times 10^{-8}\, g$ at 1 s.

16.4 Measurements Without Isolation

In order to operate the interferometer with large interrogation times despite excess noise, we propose two alternative measurement procedures. Both are based on the combination of measurements of the transition probability and of $\phi^{\mathrm{s}}{}_{\mathrm{vib}}$. Developed for the case of large vibration noise, these techniques can be extended to low vibration noise by adding a well controlled phase modulation.

16.4.1 Finge Fitting

The signal displayed in Fig. 16.4 calculated with the digital filter, can be fitted by the function:

$$P = a + b\cos\left(\sum_{j=x,y,z} \eta_j \phi^s_{vib,j} + \delta\phi\right) \qquad (4)$$

where a, b, η_j and $\delta\phi$ are free parameters and $\phi^s{}_{vib,j}$ is the phase shift calculated out of the filtered seismometer data along axis j. We operate the interferometer close to the central fringe, which corresponds to a small phase error $\delta\phi$. Every 20 points, we perform a fit of the signal and extract a value for the phase error $\delta\phi_m$. An additional and perfectly controlled phase modulation of $\pm\pi/2$ is applied in order to optimize the sensitivity of the interferometer to phase fluctuations.

16.4.2 Lock Procedure

The nonlinear feedback and estimation algorithms are more detailed in (Merlet et al., 2008a). We consider P_i the transition probability of the measurement i.

$$\begin{aligned} P_i &= a + b\cos((k_{eff}g - \alpha)T^2 + S_i) \\ &= a - b(\cos e \cos S_i - \sin e \sin S_i) \end{aligned} \tag{5}$$

where $e = (k_{eff}g - \alpha)T^2$ is the phase error varying slowly and S_i the phase shift induced by residual vibrations. Eliminating a and $\cos e$ from three consecutive measurements (P_{i-1}, P_i and P_{i+1}), gives

$$bB_i \sin e = A_i \tag{6}$$

with

$$\begin{aligned} A_i &= (\cos S_{i+1} - \cos S_i)(P_{i-1} - P_i) \\ &\quad - (\cos S_{i-1} - \cos S_i)(P_{i+1} - P_i) \\ B_i &= (\cos S_{i+1} - \cos S_i)(\sin S_{i-1} - \sin S_i) \\ &\quad - (\cos S_{i-1} - \cos S_i)(\sin S_{i+1} - \sin S_i) \end{aligned} \tag{7}$$

To stir the chirp rate onto the Doppler shift rate, an iterative correction is applied on α according to

$$\alpha_{i+2} = \alpha_{i+1} + K\frac{2B_i}{1 + B_i^2}A_i \tag{8}$$

where K is a positive gain and $2B_i/(1+B_i^2)$ is used as a pseudo inverse of bB_i.

As B_i is null in absence of vibration noise this scheme has to be modified: the pseudo inverse of B_i is finally change with $B_i/(\sigma_B{}^2+B^2+B_\iota{}^2)$and a 3-phases modulation $(-\pi/2, 0, \pi/2)$ is performed. σ_B is the standard deviation of the B_i's and B the mean. The modulation implies that the interferometer operates alternatively at the right and left sides of the central fringe and at the central fringe. In that case, B_i=1 for null vibration noise. The ultimate improvement is to first determine and servo the vibration phase coefficients η_j. We obtain P_i:

$$\begin{aligned} P_i &= a - b\cos\left(\delta\phi_i + \sum_{j=x,y,z}\eta_{j,i}\phi^s_{vib,j,i} + e + \sum_{j=x,y,z}\delta\eta_{j,i}\phi^s_{vib,j,i}\right) \\ &= a - b\left(\cos S_i - \left(e + \sum_{j=x,y,z}\delta\eta_{j,i}\phi^s_{vib,j,i}\right)\sin S_i\right) \end{aligned} \tag{9}$$

where $S_i = \delta\phi_i + \sum_{j=x,y,z}\eta_{j,i}\phi^s_{vib,j,i}$and $e+S_i+\delta\phi_i$ is the phase of the interferometer where $\delta\phi_i$ is the controlled additional phase shift $(-\pi/2, 0, \pi/2)$.

Finally,

$$b\left(B_i e + \sum_{j=x,y,z}C_{j,i}\delta\eta_{j,i}\right) = A_i \tag{10}$$

where

$$\begin{aligned} C_{j,i} &= (\cos S_{i+1} - \cos S_i)(\phi^s_{vib,j,i-1}\sin S_{i-1} \\ &\quad - \phi^s_{vib,j,i}\sin S_i) - (\cos S_{i-1} - \cos S_i) \\ &\quad (\phi^s_{vib,j,i+1}\sin S_{i+1} - \phi^s_{vib,j,i}\sin S_i) \end{aligned} \tag{11}$$

Chirp rates and vibration phase coefficients are then corrected with:

$$\begin{aligned} \alpha_{i+2} &= \alpha_{i+1} + K\frac{B_i}{\sigma_B^2 + B^2 + B_i^2}A_i \\ \eta_{j,i+2} &= \eta_{j,i+1} + L_j\frac{C_{j,i}}{\sigma_{C_j}^2 + C_{j,i}^2}A_i \end{aligned} \tag{12}$$

where L_j is the gain for direction j.

16.4.3 Results

The two techniques are compared on Figs. 16.5 and 16.6. On Fig. 16.5, we report the results of measurements performed during the day. The comparison between the techniques indicates that the fringe fitting procedure gives a better sensitivity than the lock one. The black line display the expected sensitivity, obtained by calculation out of the vibration spectrum, weighted by the transfer function of the interferometer, and corrected from the filtered signal of the seismometer. For larger $2T$, this line is below the sensitivity obtained with 1D signal processing, but good agreement with the experiment is found if seismometer signals along the three directions are used (3D). The vibration noise plotted as open triangles allow to show the gain of the vibration rejection with the different techniques, which is as high as 20 using long interrogation time (100 ms) and fringe fitting technique.

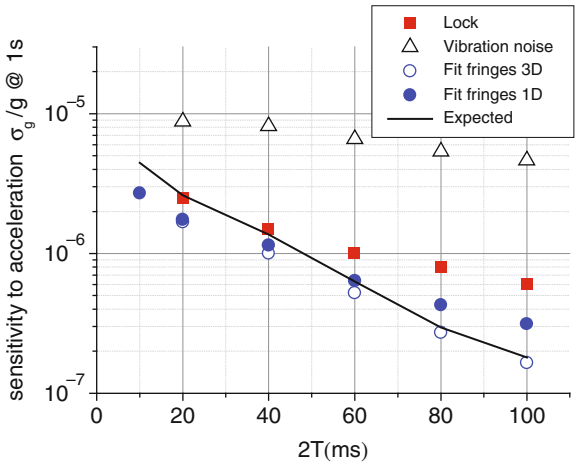


Fig. 16.5 Sensitivity to g at 1 s as a function of the interferometer duration $2T$. The measurements were performed during the day with the isolation platform OFF

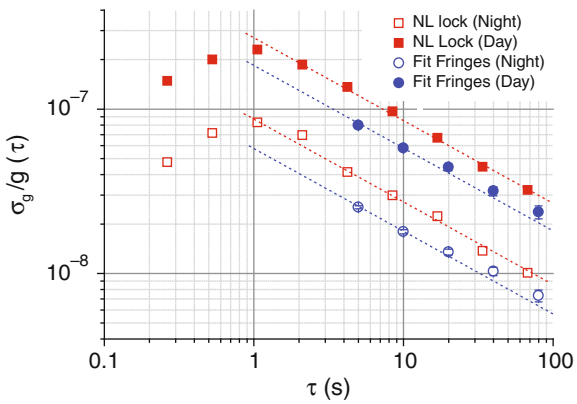


Fig. 16.6 Allan standard deviation of g fluctuations with the two techniques at day and night. Platform OFF

These results are confirmed on Fig. 16.6 where the Allan standard deviation of g fluctuations is plotted for $2T = 100$ ms. We obtain equivalent sensitivities at 1 s of 2.7×10^{-7} g (resp. 1.8×10^{-7} g) with the non-linear lock (resp. fringe fitting) technique during the day, and 8.5×10^{-8} g (resp. 5.5×10^{-8} g) during the night. The fit of the fringes is better than the lock technique, by about 50%. The best sensitivity achieved at night without vibration isolation ($5.5 \times 10^{-8}\, g$ at 1 s) is only 4 times worse than our best reported value with the platform floating (Le Gouët et al., 2008), and only twice larger than the sensitivity obtained in our laboratory with a commercial FG-5 corner cube gravimeter (Niebauer et al., 1995) in the same vibration noise conditions.

Finally, Fig. 16.7 displays the measurement realized during an earthquake of magnitude 7.7 (China, 20th of March 2008), which demonstrates the robustness of our system versus large excitations. It clearly shows that the gravimeter detects and samples efficiently seismic waves of period about 20 s. As the seismometer measures these waves with a large phase shift of 1 rad, they are not corrected by the lock algorithm, but appear as a well resolved signal in the gravimeter data. The use of a longer period seismometer and/or digital filtering to compensate for the transfer function at low frequency (high pass filter) would in principle allow removing efficiently these low frequency vibrations from the gravimeter data.

As explained in (Merlet et al., 2008a), numerical simulations indicate that none of the two techniques suffer from systematics. We confirmed experimentally this result performing differential measurements, alternating the standard integration technique described in (Merlet et al., 2008a) with the lock procedure, in the case where the platform was ON. The difference was $0.3\,\mu\text{gal} \pm 0.8\,\mu\text{gal}$, which is consistent with no bias. Moreover, the two techniques were compared together during the day with the platform OFF. The difference for a 6 h measurement was found to be $-5\,\mu\text{gal} \pm 10\,\mu\text{gal}$, which is also consistent with no bias.

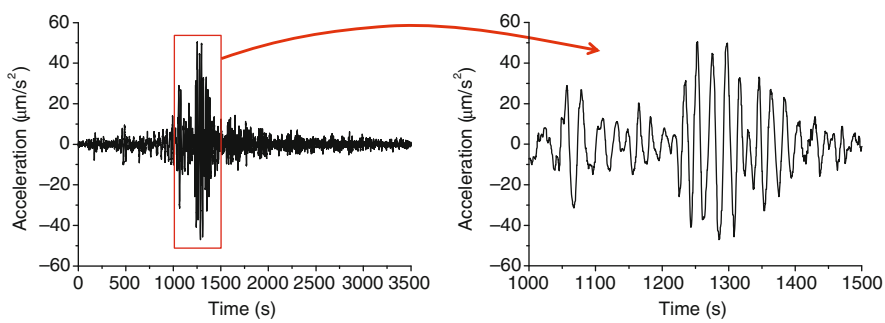


Fig. 16.7 Gravimeter signal during an earthquake of magnitude 7.7. Platform OFF

16.5 Conclusion

We show here that an atom interferometer reaches high sensitivities without any vibration isolation, when using an independent measurement of vibrations by a low noise seismometer. We introduced and compared here two measurement protocols that allow determining g, even when the interferometer phase noise amplitude exceeds 2π. In particular, fitting the fringes scanned by vibration noise allows reaching a sensitivity as low as $5.5 \times 10^{-8}\, g$ at 1 s during night measurements. This performance is obtained with a rather short interaction time ($2T = 100\ ms$), for which the vertical length of the interferometer corresponds to a few centimetres only. The techniques presented here are of interest for the realization of compact and portable atom gravimeters, with potential application to geophysics and gravity measurements in noisy environments.

References

Baillard, X., A. Gauguet, S. Bize, P. Lemond, Ph. Laurent, A. Clairon, and P. Rosenbusch (2006). Interference-filter-stabilized external-cavity diode lasers. *Opt. Commun.*, 266, 609–613,

Bertoldi, A., G. Lamporesi, L. Cacciapuoti, M. de Angelis, M. Fattori, T. Petelski, A. Peters, M. Prevedelli, J. Stuhler, and G.M. Tino (2006). *Eur. Phys. J. D*, 40, 271–279.

Bordé, C. and Ch. Antoine (2003). *Phys. Lett. A*, 306, 277.

Brown, J.M., T.M. Niebauer, and E. Klingele (2001). Towards a dynamic absolute gravity system, Gravity, Geoid, and Geodynamics 2000. *Int. Assoc. Geodesy*, 123, 223–228.

Canuteson, E., M. Zumberge, and J. Hanson (1997). An Absolute method of vertical seismometer calibration by reference to a falling mass with application to the measurement of the gain. *Bull. Seism. Soc. Am.*, 87, 484–493.

Cheinet, P., B. Canuel, F. Pereira Dos Santos, A. Gauguet, F. Leduc, and A. Landragin (2008). Measurement of the sensitivity function in a time-domain atomic interferometer. *IEEE Trans. Instrum. Meas.*, 57(6), 1141–1148.

Fixler, J. B., G. T. Foster, J. M. McGuirk, and M. A. Kasevich (2007). *Sci. Mag.*, 315(5808), 74–77.

Genevès, G. , P. Gournay, A. Gosset, M. Lecollinet, P. Pinot, P. Juncar, A. Clairon, A. Landragin, D. Holleville, F. Pereira Dos Santos, J. David, M. Besbes, F. Alves, L. Chassagne, and S. Topçu (2005). The BNM watt balance project. *IEEE Trans. Instrum. Meas.*, 54, 850–853.

Kasevich, M. and S. Chu. (1991). *Phys. Rev. Lett.*, 67, 181.

Le Gouët, J., T.E. Mehlstäubler, J. Kim, S. Merlet, A. Clairon, A. Landragin, and F. Pereira Dos Santos (2008). Limits to the sensitivity of a low noise compact atomic gravimeter. *Appl. Phys. B*, 92, 133–144.

Merlet, S., J. Le Gouët, Q. Bodart, P. Rouchon, A. Clairon, A. Landragin, and F. Pereira Dos Santos (2008a). Operating an atom interferometer beyong its linear range. *Metrologia*, 45, 265–274.

Merlet, S., A. Kopaev, M. Diament, G. Genevès, A. Landragin, and F. Pereira Dos Santos (2008b). Micro-gravity investigations for the LNE watt balance project. *Metrologia*, 45, 265–274.

Niebauer, T.M., G.S. Sasagawa, J.E. Faller, R. Hilt, and F. Klopping (1995). A new generation of absolute gravimeters. *Metrologia*, 32, 159.

Riehle, F., Th. Kisters, A. Witte, and J. Helmcke (1991). *Phys. Rev. Lett.*, 67, 177–180.

Robinson, I. and B.P. Kibble (2007). An initial measurement of Planck's constant using the NPL Mark II watt balance. *Metrologia*, 44, 427–440.

Steiner, R.L. , E. R. Williams, R. Liu, and D.B. Newell (2007). Uncertainty improvements of the NIST electronic kilogram. *IEEE Trans. Instrum. Meas.*, 56(2), 592–596.

Yu, N., J.M. Kohel, J.R. Kellogg, and L. Maleki (2006). *Appl. Phys. B*, 84, 647–652.

Chapter 17

Gravity vs Pseudo-Gravity: A Comparison Based on Magnetic and Gravity Gradient Measurements

C. Jekeli, K. Erkan, and O. Huang

Abstract Pseudo-gravity is a gravity-like acceleration implied by constant magnetization of material on the basis of Poisson's relationship. Pseudo-gravity anomalies from magnetic surveys, or pseudo-magnetic anomalies from observed (or computed) gravitational gradients can be used to enhance geologic interpretations of subsurface structures, such as their depth determination. We review the theory and fundamental assumptions behind Poisson's relationship. Then, using magnetic and gravity gradient measurements in the Parkfield, California, area, we demonstrate the validity of this relationship, as well as the non-validity of the assumptions in cases where the gravitational gradient and magnetic data do not correlate.

17.1 Introduction

The idea that gravitational gradients are intimately connected to the magnetization of the Earth's crust has motivated geologists to use more easily obtained magnetic data to make gravimetric-type interpretations (Fedi, 1989), and to combine (e.g., Dindi and Swain, 1988; Ates and Keary, 1995) or contrast (Briden et al., 1982) magnetic and gravimetric data for an improved characterization of subsurface geologic structures. The basic theory establishing the gravitation-magnetism connection was already known to Poisson (1826), was popularized by Baranov (1957), and was elaborated mathematically by Gunn (1975), Klingele et al. (1991), and others. While most previous investigations used gravimetric data to model the gravitational gradients, there now exist a number of gradiometric data sets that can be used directly to study the correlation between gravitation and magnetism. The purpose of this paper is to investigate this correlation and to demonstrate some of the issues that face users of the theory.

C. Jekeli (✉)
Division of Geodesy and Geospatial Science, School of Earth Sciences, The Ohio State University, Columbus, OH, 43210, USA
e-mail: jekeli.1@osu.edu

17.2 Basic Theory

For the gravitational potential, V, due to a mass-density distribution, $\rho(\boldsymbol{x}')$, over volume, v, we have the familiar formula (Heiskanen and Moritz, 1967):

$$V(\boldsymbol{x}) = G \int\int\int_v \frac{\rho(\boldsymbol{x}')}{|\boldsymbol{x}-\boldsymbol{x}'|} dv, \tag{1}$$

where G is Newton's gravitational constant. Analogously, for a distribution over the same volume with dipole magnetization, $M(\boldsymbol{x}')$ (a vector, with magnitude and direction), the magnetic potential is given by (Erkan, 2008)

$$A(\boldsymbol{x}) = -\frac{\mu_0}{4\pi} \int\int\int_v M(\boldsymbol{x}') \cdot \nabla \left(\frac{1}{|\boldsymbol{x}-\boldsymbol{x}'|} \right) dv, \tag{2}$$

where $\mu_0 = 4\pi \times 10^{-7}$ newt/amp^{2}is the magnetic permeability of free space. We assume that the evaluation point, $\boldsymbol{x}$, is outside the volume, v.

If the direction (unit vector, $\boldsymbol{\kappa}$) of the magnetization of the source is constant, $M(\boldsymbol{x}') = M(\boldsymbol{x}')\boldsymbol{\kappa}$, and if the

S.P. Mertikas (ed.), *Gravity, Geoid and Earth Observation*, International Association of Geodesy Symposia 135,
DOI 10.1007/978-3-642-10634-7_17, © Springer-Verlag Berlin Heidelberg 2010

mass-density is linearly related to the magnitude of the magnetization, $\rho(x') = c_0 M(x')$, then, Eq. (1) becomes

$$\tilde{V}(\boldsymbol{x}) = Gc_0 \int\limits_v \int\int \frac{M(\boldsymbol{x}')}{|\boldsymbol{x} - \boldsymbol{x}'|} dv, \tag{3}$$

which, after Baranov (1957), may be called the pseudo-gravity potential. The magnetization of the rocks of the crust may be induced at present by the main magnetic field of the Earth (which arises from the dynamo effect of its liquid outer core) and/or it may be remnant magnetization embedded during its formation or subsequent evolution. The ratio of remnant magnetization to induced magnetization, *the Koenigsberger ratio*, for most continental rocks (granites) is small. Considering only the induced magnetization, we may assume a linear relationship between the magnetization and the main magnetic field intensity, $\boldsymbol{H}_0$:

$$M(\boldsymbol{x}') = \chi H_0(\boldsymbol{x}'), \tag{4}$$

where χ is the magnetic susceptibility of the rock. Figure 17.1 shows the empirical relationship between mass-density and magnetic susceptibility, as compiled from data in Telford et al. (1990). Noting the logarithmically-scaled ordinate axis, this relationship is not linear, which means also that, since the main field is quite uniform in local regions, the magnetization and the mass-density, in fact, are not linearly related. Indeed, whereas the mass-density may change by a few percent over the range of materials within a volume, the magnetization may vary by an order of magnitude or more.

However, in some cases we may assume that the mass-density and the magnetization are both constant for the volume of interest. Then, with $\rho(\boldsymbol{x}') = \rho_0$, $M(\boldsymbol{x}') = M_0 \boldsymbol{\kappa}$, and $\boldsymbol{\kappa} \cdot \nabla = \partial/\partial\kappa$, we obtain

$$V(\boldsymbol{x}) = G\rho_0 \int\limits_v \int\int \frac{1}{|\boldsymbol{x} - \boldsymbol{x}'|} dv, \tag{5}$$

$$A(\boldsymbol{x}) = -\frac{\mu_0 M_0}{4\pi} \frac{\partial}{\partial\kappa} \int\limits_v \int\int \frac{1}{|\boldsymbol{x} - \boldsymbol{x}'|} dv. \tag{6}$$

The gradients of these potentials are the gravitational acceleration in case of V: $g = \nabla V$, and the magnetic field in case of A: $F = -\nabla A$; and, thus, Poisson's relation follows immediately:

$$F(\boldsymbol{x}) = \frac{\mu_0 M_0}{4\pi G\rho_0} \frac{\partial}{\partial\kappa} g(\boldsymbol{x}) \tag{7}$$

For applications of this relationship, we consider only the material of the upper crust where M_0 may be interpreted as the magnetization induced by the main field of the Earth (since in this regime the temperature is above the Curie point; Telford et al., 1990, p.72). Then, also the gravitational acceleration refers only to this material; that is, both F and g are anomalies relative to corresponding reference fields – the main magnetic field and the (approximately) ellipsoidal gravitational field of the Earth.

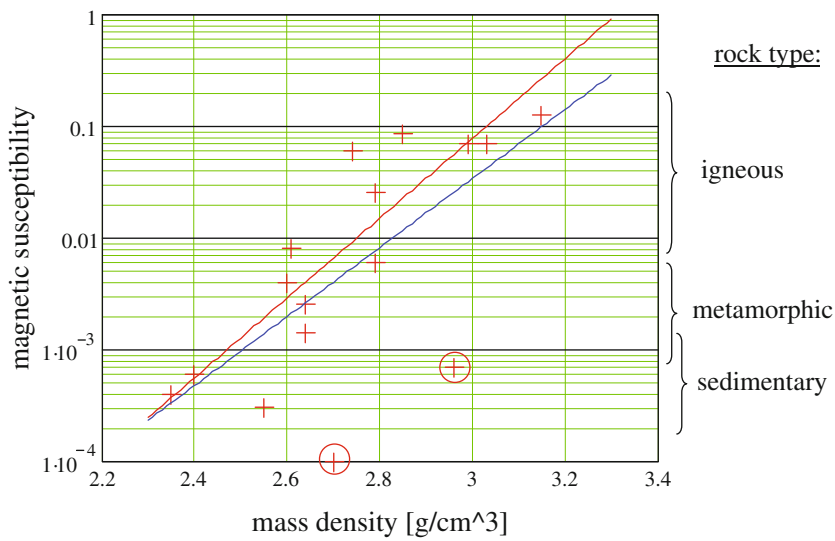


Fig. 17.1 Empirical relationship between mass-density and magnetic susceptibility of different rock types. The upper least-squares straight-line fit excludes the two circled outliers

The direction of magnetization can be written as

$$\boldsymbol{\kappa}_0 = (\cos\eta\cos\xi \quad \sin\eta\cos\xi \quad \sin\xi)^{\mathrm{T}}, \tag{8}$$

where ξ is the dip angle (inclination) with respect to the local horizon, and η is the strike angle (azimuth, or declination) with respect to local geodetic north. Let the (anomalous) gravitational gradient tensor in local Cartesian coordinates be

$$\Gamma = \nabla g^{\mathrm{T}} = \begin{pmatrix} \frac{\partial g_x}{\partial x} & \frac{\partial g_y}{\partial x} & \frac{\partial g_z}{\partial x} \\ \frac{\partial g_x}{\partial y} & \frac{\partial g_y}{\partial y} & \frac{\partial g_z}{\partial y} \\ \frac{\partial g_x}{\partial z} & \frac{\partial g_y}{\partial z} & \frac{\partial g_z}{\partial z} \end{pmatrix} = \begin{pmatrix} \Gamma_{xx} & \Gamma_{xy} & \Gamma_{xz} \\ \Gamma_{yx} & \Gamma_{yy} & \Gamma_{yz} \\ \Gamma_{zx} & \Gamma_{zy} & \Gamma_{zz} \end{pmatrix} \tag{9}$$

Then, we have

$$\frac{\partial g^{\mathrm{T}}}{\partial \kappa} = (\boldsymbol{\kappa}\cdot\nabla)g^{\mathrm{T}} = \boldsymbol{\kappa}^{\mathrm{T}}\nabla g^{\mathrm{T}} = \boldsymbol{\kappa}^{\mathrm{T}}\Gamma. \tag{10}$$

On the other hand, the quantity measured by a typical airborne (proton-precession) magnetometer is the magnitude of the total field, $\boldsymbol{B}$. The total field at any point is the vector sum of the main field, $B_0 = \mu_0 H_0$, and the magnetization of the material (induced plus remnant). The magnetic anomaly is defined as the difference in magnitudes of the total and main fields:

$$\Delta B = |B| - |B_0|. \tag{11}$$

It can be shown (Parasnis, 1986, p.23) that the magnetic anomaly is the field due to the magnetization in the direction, $\boldsymbol{\kappa}_0$, of the main field, provided $|F| \ll |B_0|$ (Fig. 17.2):

$$\Delta B(\boldsymbol{x}) = \boldsymbol{\kappa}_0 \ll F(\boldsymbol{x}). \tag{12}$$

Therefore, we have finally

$$\Delta B = \frac{\mu_0 M_0}{4\pi G\rho_0}\boldsymbol{\kappa}_0^{\mathrm{T}}\Gamma(\boldsymbol{x})\boldsymbol{\kappa}, \tag{13}$$

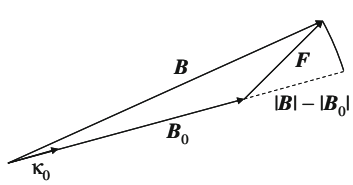


Fig. 17.2 The geometry of the magnetic field vectors

which directly relates magnetometry and gravity gradiometry. If there is no remnant magnetization in a direction different from $\boldsymbol{\kappa}_0$ (i.e., if $\boldsymbol{\kappa} = \boldsymbol{\kappa}_0$), then

$$\Delta B = \frac{\mu_0 M_0}{4\pi G\rho_0}\boldsymbol{\kappa}_0^{\mathrm{T}}\Gamma(\boldsymbol{x})\boldsymbol{\kappa}_0. \tag{14}$$

Furthermore, if the magnetization is due only to induction by the main magnetic field, B_0, values for its magnitude can be obtained from the magnetic susceptibility of the material, χ:$M_0 = \chi H_0 = \chi B_0/\mu_0$; see Eq. (4). For the continental U.S., $B_0 \approx 55{,}000\,\mathrm{nT}$ (nano-tesla); and for igneous rocks, $\chi \approx 0.05$. With $\rho_0 = 2{,}800\,\mathrm{kg/m^3}$ and $G = 6.67 \times 10^{-11}\,\mathrm{m^3/(kg\cdot s^2)}$, we find

$$\frac{\mu_0 M_0}{4\pi G\rho_0} = \frac{\chi B_0}{4\pi G\rho_0} \approx 1.2\frac{\mathrm{T}}{\mathrm{s}^{-2}} = 1.2\frac{\mathrm{nT}}{\mathrm{E}}. \tag{15}$$

Clearly, this proportionality factor depends on the (highly variable) magnetic susceptibility, χ. However, we see that magnetic anomalies, usually of the order of tens of nT, correspond roughly to anomalous gravitational gradients, usually of the order of tens of E (Eõtvõs).

17.3 Data Comparisons

Poisson's relationship is easily tested in areas containing both gravitational gradient and magnetic anomaly measurements. One such area is near Parkfield, California, where airborne gradiometer data were collected (Bell Geospace, 2004) and airborne magnetic data are available from the USGS[1]. Figure 17.3 shows the survey tracks for both data sets, which were flown at approximately the same altitude of about 300 m above the ground. The magnetic anomalies, on tracks separated by about 800 m, are given with respect to the International Geomagnetic Reference Field, IGRF80. The Bell Geospace data consists of the six gradients, Γ_{xx}, Γ_{xy}, Γ_{xz}, Γ_{yy}, Γ_{yz}, Γ_{zz}, smoothed using a 500-m filter and they refer to an arbitrary reference (mean value). The tracks of these data run in the NW-SE direction, are about 10 km in length, and are spaced at 200 m.

[1] http://pubs.usgs.gov/of/2002/ofr-02-361/State_html/CA.htm

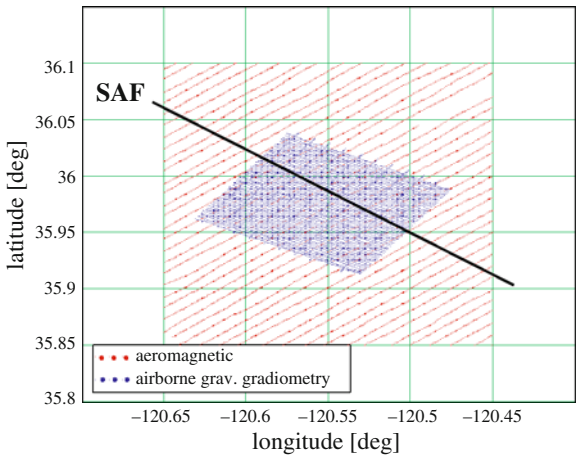


Fig. 17.3 Survey tracks of the aeromagnetic and airborne gravity gradiometric data sets in the Parkfield, CA, area. The San Andreas Fault is also indicated

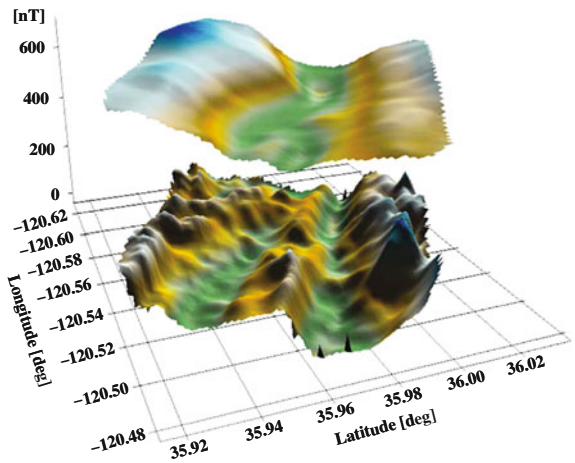


Fig. 17.4 Visual comparison of the observed magnetic anomaly (*top*, offset by 400 nT) and the pseudo-magnetic anomaly implied by measured gravitational gradients in the Parkfield, CA, area

Using the National Geophysical Data Center calculator[2], the values of the main field, B_0, and its inclination, ξ, and declination, η, according to the 10th International Geomagnetic Reference Field model (IGRF 10), are determined for the central part of the Bell Geospace survey area ($\lambda = -120.55°$, $\phi = 35.95°$) and for the approximate time of the aeromagnetic survey, 1986.0:

$$B_0 = 50000\,\text{nT},\ \xi = 60.45°,\ \eta = 15.10° \qquad (16)$$

To calculate the scaling coefficient in Eq. (13) we used a magnetic susceptibility, $\chi = 0.01$. All data were interpolated linearly onto a regular grid with spacing of about 170 m from a triangulation of the data.

Figure 17.4 offers a visual comparison between the observed magnetic anomaly (top) and the pseudo-magnetic anomaly (bottom) implied by the gravitational gradients (right side of Eq. (13)). The observed values are offset by 400 nT for better visualization. The SAF runs along the north side of the central maximum of the pseudo-magnetic anomaly. The apparent discrepancy in resolution of the data types (the magnetic data appear much smoother than the pseudo-magnetic anomalies) is most likely due to the much wider spacing between the magnetic survey lines. Since only a visual, and not a numerical comparison is made, we did not attempt to correct this discrepancy.

There is a clear positive correlation between these two anomalies, except in the central part of the survey area along the SAF. This discrepancy implies a gravity anomaly (density contrast) that is not magnetized. Indeed, such a structural characterization is verified in a recent geologic review of this area by McPhee et al. (2004). Figure 17.5, taken from this work, shows the geology of a cross-section perpendicular to the fault near the central part of the survey area. Non-magnetic granitic rock, southwest of the fault, is flanked on either side by magnetized rocks.

17.4 Conclusion

We have expounded on the mathematical and theoretical basis for the connection between gravitational gradients and the magnetization of the Earth's upper crust material, leading ultimately to a long-known proportionality known as Poisson's relationship. This connection is founded on strong but often reasonable assumptions of constant mass-density and constant magnetization (both magnitude and direction) of the source body. Recently available gravitational gradient measurements systematically collected over local areas offer simple tests of Poisson's relationship. We

[2] www.ngdc.noaa.gov/geomagmodels/struts/calcIGRFWMM

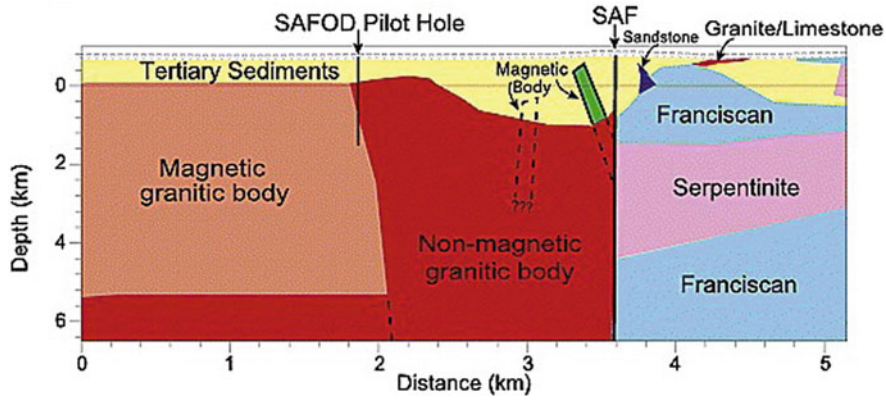


Fig. 17.5 Geologic cross-section perpendicular to the SAF; taken from Fig. 17.1 of McPhee et al. (2004). See the latter work for additional explanations

showed here one such comparison between observed magnetic anomalies and pseudo-magnetic anomalies derived from gravitational gradients. In a geologically well- studied area near Parkfield, CA, the two corresponding data sets exhibit strong correlation, except directly along the San Andreas Fault, where the rocks are characterized as non-magnetic. This is a beautiful example of both the potential benefits of combining gravimetric and magnetic data through Poisson's relationship to obtain an improved subsurface structural characterization, and of the potential pitfalls when the underlying assumptions do not hold.

References

Ates, A. and P. Keary (1995). A new method for determining magnetization direction from gravity and magnetic anomalies: application to the deep structure of the Worcester Graben. *J. Geol. Soc.*, 152, 561–566.

Baranov, V. (1957). A new method for interpretation of aeromagnetic maps: pseudo-gravimetric anomalies. *Geophysics*, 22, 359–383.

Bell Geospace (2004). Final report of acquisition and processing on Air-FTG survey in Parkfield earthquake experiment area, September 2004, Rice University, Houston, Texas.

Briden, J.C., R.A. Clark, and J.D. Fairhead (1982). Gravity and magnetic studies in the Channel Islands. *J. Geol. Soc.*, 139, 35–48.

Dindi, E.W. and C.J. Swain (1988). Joint three-dimensional inversion of gravity and magnetic data from Jombo Hill alkaline complex, Kenya. *J. Geol. Soc*., 145, 493–504.

Erkan, K. (2008). A comparative overview of geophysical methods. Report no. 488, Geodetic Science, Ohio State University, Columbus, Ohio; http://www.geology.osu.edu/~jekeli.1/OSUReports/reports/report_488.pdf.

Fedi, M. (1989). On the quantitative interpretation of magnetic anomalies by pseudo-gravimetric integration. *Terra Nova*, 1, 564–572.

Gunn, P.J. (1975). Linear transformations of gravity and magnetic fields. *Geophys. Prospect.*, 23, 300–312.

Heiskanen, W.A. and H. Moritz (1967). Physical geodesy. W. H. Freeman and Co., San Francisco.

Klingele, E.E., I. Marson, and H.-G. Kahle (1991). Automatic interpretation of gravity gradiometric data in two dimensions: vertical gradient. *Geophys. Prospect.*, 39, 407–434.

McPhee, D.K., R.C. Jachens, and C.M. Wentworth (2004). Crustal structure across the San Andreas Fault at the SAFOD site from potential field and geologic studies. *Geophys. Res. Lett.*, 32, L12S03.

Parasnis, D.S. (1986). Principles of applied geophysics. Chapman and Hall, London.

Poisson, S.D. (1826). Mémoire sur la théorie du magnétisme. *Mémoires de l'Académie Royale des Sciences de l'Institut de France*, 247–348.

Telford, W.M., L.P., Geldart, and R.E. Sheriff (1990). Applied geophysics, 2nd ed. Cambridge U. Press, Cambridge, U.K.

Part II
Space-Borne Gravimetry: Present and Future

R. Pail and P. Visser

Chapter 18

Designing Earth Gravity Field Missions for the Future: A Case Study

P.N.A.M. Visser

Abstract Gravity field changes due to mass changes in the Earth system have been observed successfully by the GRACE mission. Having a single tandem like GRACE limits the achievable resolution of observing such mass changes both in time and space. A simulation study was carried out to make a first assessment of the impact of different gravity satellite formations on the retrieval of temporal gravity, in this case caused by hydrology. These formations include polar formations of one, two and four GRACE-type tandems and a formation that includes one polar and one non-polar tandem. A comprehensive force modeling was used including gravity field changes due to ocean tides and hydrological, atmospheric, oceanographic, solid-earth and ice mass change processes. The impact of errors in these models in conjunction with observation errors by the space-borne gravity instruments was assessed. First results indicate that having more than one tandem helps to reduce the impact of errors in background models such as ocean tides, provided that instrument observation errors are sufficiently low.

18.1 Introduction

The current GRACE mission has successfully observed mass changes in the Earth system due to continental hydrology and Greenland ice mass losses, although great care has to be taken with interpreting the results since large uncertainties in observed mass change rates still exist (Schrama et al. 2007; Tapley et al., 2004; Velicogna and Wahr, 2006). In order to extract these mass changes from the GRACE observations, a comprehensive modeling is required that takes into account all sources of the Earth's gravity field that are within the sensitivity of the observing system. A distinction is made between sources that are to be observed and monitored, and sources that need to be included in the prior models (referred to as background models). Modeling errors are defined as errors of – or omissions in – the background models. For GRACE, examples are errors of ocean tide models, uncertainties in atmospheric mass change models, and gravity field omission errors such as unmodeled (known or unknown) mass changes and high spatial resolution parts of the gravity field. The point has been reached where the accuracy of mass changes observed by GRACE are not limited by instrument observation errors, but more by its spatio-temporal sampling and errors in the background models. Gravity field recovery errors typically show up as stripes in geographical representations of the solved for models (Schrama et al., 2007; Wahr et al., 2006).

There is strong support in the Earth sciences community for follow-on gravity satellite missions that will as a minimum continue the time series of gravity changes as currently observed by GRACE, but preferably enhances not only the precision, but also the spatial and temporal resolution with which such gravity changes can be observed (Koop and Rummel, 2008). Also, such missions might enhance the modeling of the high-resolution mean gravity field that will be provided by the upcoming GOCE mission.

P.N.A.M. Visser (✉)
Faculty of Aerospace Engineering, Delft Institute of Earth Observation and Space Systems (DEOS), Delft University of Technology, Delft, The Netherlands
e-mail: Pieter.Visser@lr.tudelft.nl

S.P. Mertikas (ed.), *Gravity, Geoid and Earth Observation*, International Association of Geodesy Symposia 135,
DOI 10.1007/978-3-642-10634-7_18, © Springer-Verlag Berlin Heidelberg 2010

This paper describes a case study to the effect of not only observation errors, but also modeling errors on the retrieval of mass changes due to hydrology. Different mission scenarios were taken into consideration, ranging from one pair of low-flying satellites in polar orbits to four pairs (Reubelt et al., 2009). In addition, a so-called Bender formation of two pairs, one in polar orbit and one with an inclination of 117.4° was considered (Bender et al., 2008). Observables that were taken into account include orbit perturbations (to be obtained from high–low satellite-to-satellite tracking – hl-SST) and low–low satellite-to-satellite tracking (ll-SST). It will be shown that Satellite Gravity Gradiometry (SGG) is probably not very suitable for observing temporal gravity.

Use was made of a detailed and comprehensive modeling of gravitational sources that was done by a consortium of institutes in the framework of a study sponsored by the European Space Agency (ESA). Gravity field sources that were taken into account include models for the mean gravity field, ocean tides, oceanographic and atmospheric mass changes, continental hydrology, and ice mass changes (Study Team, 2007).

After introducing the selected mission scenarios (Sect. 18.2), the simulation setup and results from gravity field retrieval experiments will be described (Sect. 18.3), followed by conclusions and an outlook (Sect. 18.4).

18.2 Mission Scenarios

The GRACE mission provides global coverage because of its polar orbit which is a requirement for observing for example mass changes in the (ant)arctic areas. The GRACE satellites are flying non-repeat orbits leading to a continuously changing ground track pattern that is one of the causes of changing quality of e.g., monthly gravity solutions. In addition, a geographical latitude dependency of such solutions can be anticipated due to the different density of the ground track pattern with latitude (e.g., confluence of tracks in the polar areas).

These effects can be overcome to a large extent by selecting satellite repeat orbits and by combining satellites that fly in orbits with different inclinations as proposed by e.g., Bender et al. (2008). The mission scenarios that were selected are presented in Table 18.1 and include purely polar satellite formations consisting of one (SC1), two (SC12) and four (SC14) pairs. Also a two-pair Bender-type formation was selected (BEN12). Satellite orbit repeat periods are equal to 8 days for the polar formations and 5/23 days for the pairs forming the Bender formation (see also Fig. 18.2 for the ground track patterns). It is not claimed that these formations are optimal, but they provide a good starting point for studying the sensitivity of temporal gravity field retrieval to different mission scenarios. In all cases, the inter-satellite distance α between satellites forming one pair is equal to 1.958° or about 230 km (comparable to the inter-satellite distance of the two GRACE satellites). It has to be noted that also this inter-satellite distance is a parameter that can be optimized in follow-on studies.

Table 18.1 Mission scenarios. The nominal single-tandem mission consists of pair 1 (indicated by SC1) and the Bender dual-tandem of pairs 2 and 3 (BEN12). In addition, two other formations are defined. The first consists of pair 1 plus another pair in identical orbits but interleaved by 4 days (SC12). The second consists of pair 1 plus three pairs in identical orbits but interleaved by 2, 4 and 6 days (SC1234). The inter-satellite distance is indicated by α

				Repeat period	
Pair	a (km)	i (deg)	α (deg)	days	rev.
1	6,746.3	90.0	1.958	8/7.98	125
2	6,696.4	90.0	1.958	5/4.99	79
3	6,784.8	117.4	1.958	23/23.17	360

A first assessment of the impact of different satellite formations on achievable gravity field recovery accuracy was based on the method of formal error predictions (Colombo, 1984; Visser, 1999). Typical noise levels are used for ll-SST observations (i.e., 1μm/s Gaussian noise at 1 Hz, Fig. 18.1). For comparison, the prediction for a gradiometer mission was included for an observation Gaussian noise level of just 0.001 E without bandwidth limitation (which is too optimistic, (ESA, 1999). It can be observed that for observing temporal gravity at spherical harmonic degrees up to degree 50, i.e., equivalent to a spatial resolution of about 400 km, the ll-SST concept is superior; SGG is especially suitable for observing static gravity at short wavelengths down to 100 km (Drinkwater et al., 2007). Therefore, no further investigations to SGG missions were conducted for this case study. It can be observed as well that the Bender formation leads to a more

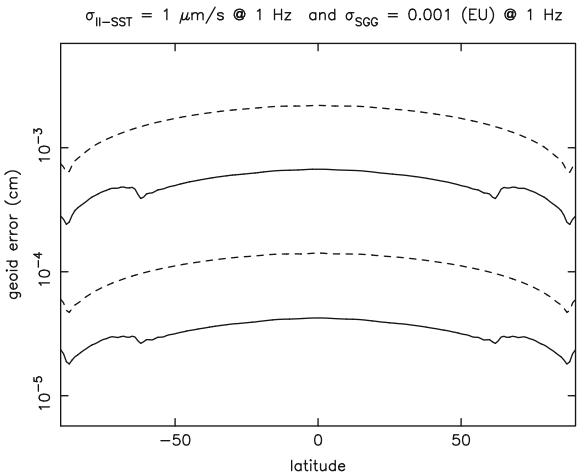


Fig. 18.1 Formal geoid error as a function of latitude for 50x50 gravity field estimation from ll-SST (*bottom pair of lines*) and SGG observations (*top pair of lines*). The *dashed* and *solid lines* hold for the nominal single-tandem (SC1) and Bender dual-tandem (BEN12) mission scenarios, respectively (Table 18.1, using one satellite for each pair in case of SGG). The observation precision is indicated above the plots. The formal errors are scaled to be consistent with a gravity field recovery for an 8-day period

homogeneous error pattern in the latitude direction (the formal errors are independent of the longitude for a repeat period): the error pattern is strongly correlated with the density of the ground tracks (Fig. 18.2). For example discontinuities can be observed at 62.6° latitude, which is equal to 180° minus the inclination for the second pair of the Bender formation (Table 18.1). The ratio between the geoid error at the equator and at the poles is about 4 for the single polar tandem mission, and less than 2 for the Bender-type mission.

18.3 Retrieval Experiments

Gravity field recovery simulation experiments were conducted for the period 1–8 January 1996 using a comprehensive force modeling (Table 18.2) and using a software infrastructure (Visser and Schrama, 2005) that was built around the NASA/GSFC GEODYN software package (Pavlis et al., 2006). All gravity field source models were provided with a time step of 6 h. Gravity field variations were modeled by connecting these 6-hourly fields piecewise linearly in time. As stated above, this paper contains first results. For future work, it is planned to extend the simulations to cover

Table 18.2 Definition of true world, reference and error models

Truth model	
Static gravity field:	GGM01S Tapley et al. (2002)
Ocean tides:	FES2004 Lyard et al. (2006)
Mass changes due to atmosphere, oceans, hydrology, ice and solid earth:	6-hourly piecewise linear fields Study Team (2007)
Choice of model errors	
Static gravity field:	GGM01S-clone[a]
Ice and solid-earth:	Switched-off
Atmosphere and oceans:	10% of signal
Atmosphere and oceans:	10% of signal
Ocean tides:	TPXO6.2 Egbert and Erofeeva (2002)
Observation errors (Gaussian)	
Low–low SST:	$\sigma = 1.0\mu$m/s @ 0.05 Hz
Orbit coordinates:	$\sigma(x,y,z) = 1$ cm @ 0.05 Hz
Accelerometer noise:	10^{-10}m/s^2 @ 0.05 Hz

[a]Using GGM01S 1σ coefficient error estimates.

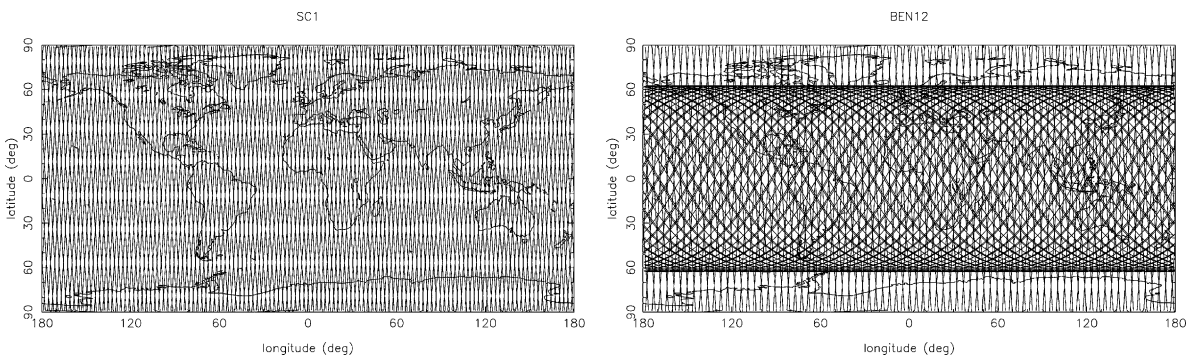


Fig. 18.2 Ground track for single-tandem polar mission (8-day period, left) and dual-tandem Bender mission (5-day period, right)

periods of at least 1 year (which will be demanding from a computational point of view).

18.3.1 Simulation Setup

The GEODYN package was used to simulate satellite orbits and ll-SST observations in the presence of a comprehensive force model (Table 18.2). Gravity field models were used complete to degree and order 50 (including the largest part of gravity field variations). It is assumed that the orbit perturbations are derived from GPS hl-SST observations. Therefore, the gravity field recovery will be based on the combination of time series of ll-SST observations and satellite position coordinates. A weighted least-squares estimation method was used where the weights are in accordance with the observation error levels indicated in Table 18.2. An observation time interval of 20 s was used. The observations were simulated by switching on the so-called true world (Table 18.2). The satellites complete an orbital arc of about 150 km in 20 s allowing sufficient sampling for a 50×50 spherical harmonic gravity field coefficient estimation. The observations are processed in daily batches, where for each day orbital parameters (start position and velocity for each satellite) are estimated together with spherical harmonic gravity field coefficients.

During the estimation process, hydrology was switched off in all cases such that observation residuals are caused by mass changes due to this hydrology. The aim was then to recover the hydrological signal (see Fig. 18.3: the hydrological signal is of the order of a few mm in terms of geoid relative to the yearly mean) in the presence of different combinations of error sources, including: error in the static gravity field model, ignoring contributions from mass changes due to solid-earth and ice processes, 10% model error of atmospheric and oceanographic mass changes, ocean tides, and observation errors (a rather conservative value of 1.0 μm/s at 1 Hz was used for ll-SST). It was possible to include accelerometer observation errors as well: it is assumed that the non-gravitational accelerations are observed by accelerometers (Table 18.2). For the simulations described in this paper, observation errors were assumed to be uncorrelated (Gaussian). It is planned to use more sophisticated and realistic

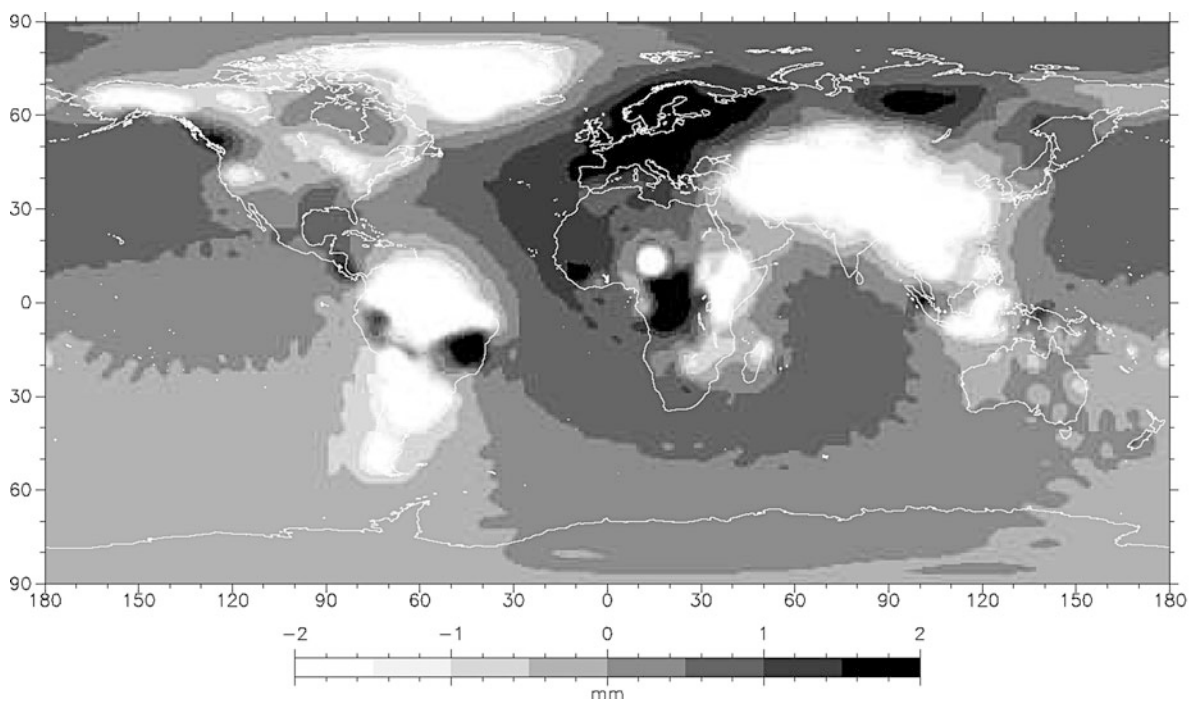


Fig. 18.3 Mean of hydrological signal for 1–5 January 1996 in terms of geoid (spherical harmonic degrees 2–50). The yearly mean was subtracted

observation error models in future simulations, but a first impression of how observation errors affect gravity field solutions can already be obtained by this approach.

18.3.2 Results

First, 5-day solutions (i.e., covering 1–5 January 1996) were obtained for the Bender formation in the presence of different error sources. Already in the absence of model and observation errors, retrieval errors can be observed (indicated by ERROR-FREE in Fig. 18.4), which can be explained by the fact that a 5-day averaged solution is produced whereas the input models have a temporal resolution of 6 h. It can be observed that the degree 1 terms are in fact not observable. It was found that the degree 1 terms are almost completely absorbed by the orbit parameters that are estimated together with the gravity field coefficients. The simulated observation errors lead to the largest gravity field retrieval errors (indicated by OBSERVATION NOISE Fig. 18.4), whereas the differences between the FES2004 and TPXO6.2 tide models lead to retrieval errors that are of the same order of magnitude at spherical harmonic degrees from 2 to 15 and at the higher degrees close to 50. It can thus be stated that with lower noise levels (at least an order of magnitude better, which can be anticipated for future missions), tide model errors will be dominant (assuming that tide model errors are at a level comparable to the differences between FES2004 and TPX06.2).

In the presence of tide model errors, the retrieval error in terms of geoid display the well-known stripes or "trackiness" (Fig. 18.5, top left). These stripes can be reduced by applying so-called Meissl smoothing operators (Meissl, 1971):

$$\beta_{l,\psi} = \frac{1}{1-\cos\psi}\frac{1}{2l+1}\left[\bar{P}_{l-1}(\cos\psi) - \bar{P}_{l+1}(\cos\psi)\right] \quad (1)$$

where $\beta_{l,\psi}$ represents the smoothing operator, ψ the spherical cap smoothing radius, and $\bar{P}_l$ the normalized Legendre polynomial of degree l. Each spherical harmonic coefficient of degree l is then multiplied by $\beta_{l,\psi}$. With $\psi = 20°$ the main hydrological features from Fig. 18.3 can then be clearly distinguished (Fig. 18.5, top right). In the presence of all error-sources (Table 18.2), the retrieval error already reaches the hydrological signal magnitude at degree 30 (i.e., at a spatial resolution of about 650 km). When using the full retrieved model complete to degree and order 50, the original hydrological signal (Fig. 18.3) can hardly be distinguished (Fig. 18.5, bottom left). An error pattern that is reflecting the ground track pattern (Fig. 18.2) can be observed. When again applying the Meissl operators with 20° radius, a significant part of the hydrological signal can be observed. Detailed analysis showed that a large part of the error pattern is due to the simulated error of the static gravity field model, which is of the order of 5 mm globally (2 mm when smoothed with a radius of 20°). Therefore, these

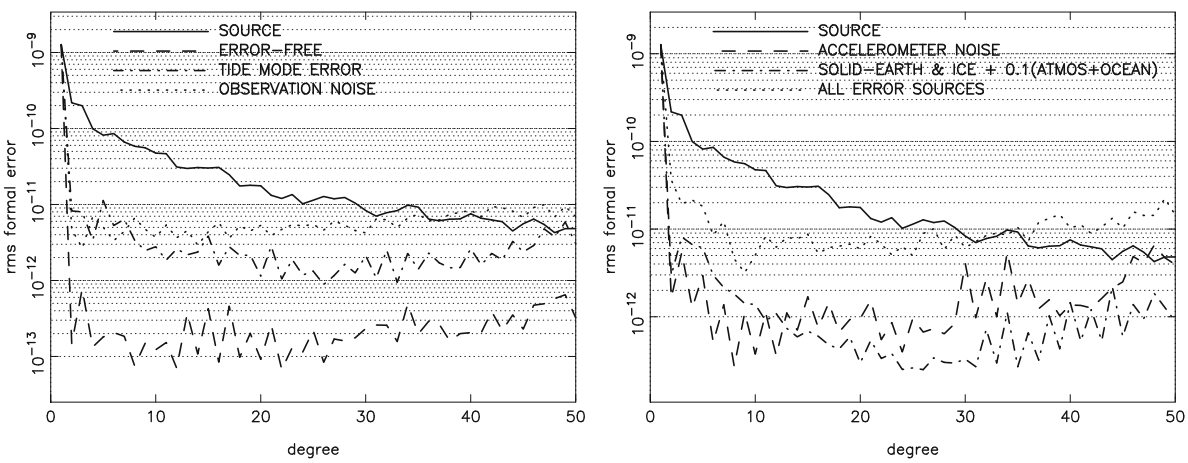


Fig. 18.4 RMS retrieval error as a function of spherical harmonic degree for 1–5 January 1996 for several error sources using the Bender formation. The *line* indicated by SOURCE holds for the 8-day average of the 6-hourly hydrological input models

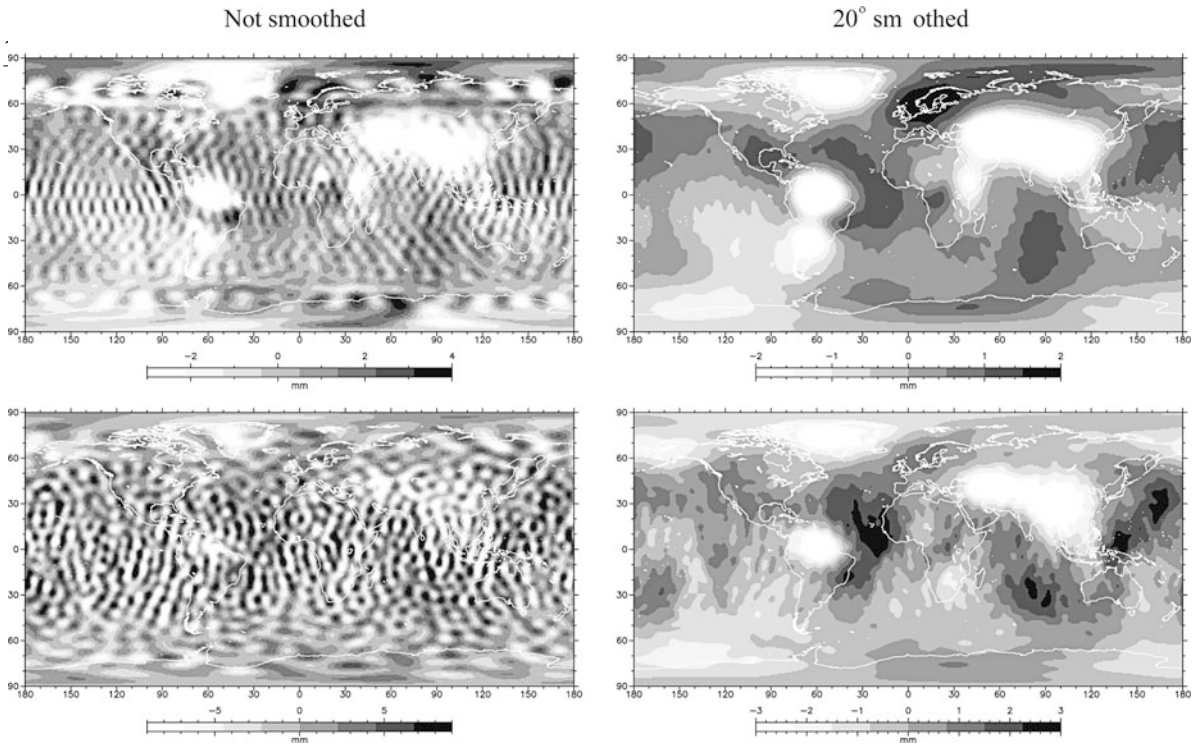


fig. 18.5 Retrieved gravity field for 1–5 January 1996 in terms of geoid (spherical harmonic degrees 2–50) with only tide model errors switched on (*top*) or with all error sources switched on (*right*). For the pictures at the *right*, a 20° spherical cap smoothing was applied (please note the different scales for the different pictures)

results can be considered pessimistic, since this error is systematic and it is fair to anticipate that at least part of this error will cancel when deriving changes in the gravity field from one period to the other. This will be investigated in more detail as well in future longer period simulations.

Gravity field retrievals were conducted as well for other mission scenarios in the presence of either tide model errors or with all error sources switched on: respectively 2-, 4- and 8-day retrievals were carried out for the one (SC1), two (SC12) and four (SC1234) polar tandems. Figure 18.6 (left) seems to

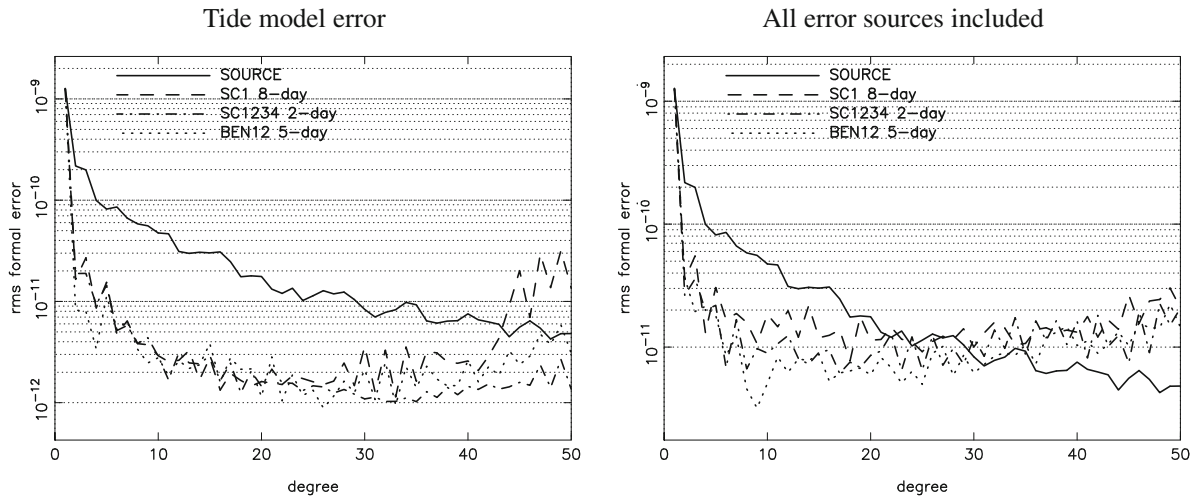


Fig. 18.6 RMS retrieval error as a function of spherical harmonic degree for 1–5 January 1996 for several error sources using different formations

suggest that the Bender and the multiple-tandem polar formations help to suppress the impact of tide model errors, but only at the higher degrees close to 50. It has to be assessed how results will change when the instrument noise levels are for example an order of magnitude lower, which can probably be achieved with future instruments. Also, it has to be assessed what will be the impact of flying more than one satellite tandem in the presence of such low sensor noise levels.

18.4 Conclusions and Outlook

A case study was conducted to assess the impact of dynamic force model and observation errors on the achievable gravity field recovery for different formations of satellites. First results indicate that instrument observation noise levels should be sufficiently low: for this study a rather conservative ll-SST noise level of $1\,\mu m/s^2$ @ 0.05 Hz (or equivalently $4.5\,\mu m/s^2$ @ 1 Hz) was used, which seemed to dominate other error sources. Model errors, e.g., those caused by ocean tides, can be reduced by for example flying a Bender formation, although the largest impact seems to be at spherical harmonic degrees above 40 (Fig. 18.4).

It has to be noted that results described in this paper should be considered preliminary, since the recovery simulation was done only for a limited period (covering 1–2, 1–4, 1–5 or 1–8 January 1996). It is planned to extend the simulations with lower instrument noise levels and also to extend the simulations to a period of at least 1 year allowing a more rigorous analysis of the impact of flying different mission scenarios on the mitigation of force model and observation errors. Also, it is planned to assess the possibilities for observing mass changes due to not only hydrology, but also oceanography and glaciology (Arctic and Antarctic) by longer period simulations. The question of how to separate such mass changes from space-borne gravimetric observations will be addressed as well.

Acknowledgments ESA provided the funding for a large part of the research described in this paper. An important part of the computations and simulations were done with the GEODYN software, kindly provided by NASA/GSFC, Greenbelt, Maryland.

References

Bender, P.L., S.N. Wiese, and R.S. Nerem (2008). A possible dual-GRACE mission with 90 degree and 63 degree inclination orbits. In: ESA (ed), 3rd International symposium on formation flying, missions and technologies, 23–25 April 2008, ESA/ESTEC. Noordwijk, The Netherlands, pp. 1–6.

Colombo, O.L. (1984). The global mapping of gravity with two satellites, vol. 7, no. 3, Netherlands Geodetic Commission, Publications on Geodesy, New Series.

Drinkwater, M., R. Haagmans, D. Muzzi, A. Popescu, R. Floberghagen, M. Kern, and M. Fehringer (2007). The GOCE gravity mission: ESA's first core explorer, in 3rd GOCE User Workshop, 6–8 November 2006, Frascati, Italy, pp. 1–7, ESA SP-627.

Egbert, G.D. and S.Y. Erofeeva (2002). Efficient inverse modeling of barotropic ocean tides. *J. Atmos. Ocean. Technol.*, 19, 183–204.

ESA (1999). Gravity field and steady-state ocean circulation mission. *Reports for mission selection, the four candidate earth explorer core missions, SP-1233(1)*, European Space Agency, July 1999.

Koop, R. and R. Rummel (Eds.) (2008). Report from the workshop on the future of satellite gravimetry. 12–13 April 2007, ESTEC, Noordwijk, The Netherlands, 1–21, TUM Institute for Advanced Study, January 2008.

Lyard, F., F. Lefevre, T. Letellier, and O. Francis (2006). Modelling the global ocean tides: modern insights from FES2004, *Ocean Dynamics*, 56(5–6), 394–415, doi: 10.1007/s10236–006–0086–x.

Meissl P. (1971). A study of covariance functions related to the earth's disturbing potential, Report no. 151, Department of Geodetic Science, OSU, Ohio, Columbus.

Pavlis, D.E., S. Poulouse, and J.J. McCarthy (2006). GEODYN operations manual. Contractor report. SGT Inc., Greenbelt, MD.

Reubelt, T., N. Sneeuw, and M.A. Sharifi (2009). Future mission design options for spatio-temporal geopotential recovery. In: IAG international symposium on gravity, geoid & earth observation 2008, this issue.

Schrama, E.J.O., B. Wouters, and D.D. Lavallée (2007). Signal and noise in gravity recovery and climate experiment (GRACE) observed surface mass observations. *J. Geophys. Res.*, 112(B08407), doi: 10.1029/2006JB004882.

Study Team[1] (2007). Mass Transport Study: Selection of models for the simulation study, ESA Contract 20403, Task 2 Report, RP-G-013SR/07, Issue 1, Revision 3.

[1] Utrecht Centre of Geosciences, Delft Institute of Earth Observation and Space Systems, Netherlands Institute for Space research (The Netherlands), Alfred-Wegener-Institut für Polar- und Meeresforschung, Institute of Astronomical and Physical Geodesy – Munich, Institute of Geodesy – Stuttgart (Germany),Bristol Glaciology Centre, School of Civil Engineering and Geosciences (Great-Britain), University of Luxembourg.

Tapley, B.D., D.P. Chambers, S. Bettadpur, and J.C. Ries (2003), Large scale ocean circulation from the GRACE GGM01 geoid. *Geophys. Res. Lett.*, 30(22), 2163, doi: 10.1029/2003GL018622.

Tapley, B.D., S. Bettadpur, J.C. Ries, P.F. Thompson, and M.M. Watkins (2004). GRACE measurements of mass variability in the earth system. *Science*, 305, 1503–1505.

Velicogna, I. and J. Wahr (2006). Acceleration of Greenland ice mass loss in spring 2004. *Nature*, 443, 329–331, doi: 10.1038/nature05168.

Visser, P.N.A.M. (1999). Gravity field determination with GOCE and GRACE, *Adv. Space Res.*, 23(4), 771–776.

Visser, P.N.A.M. and E.J.O. Schrama (2005). Space-borne gravimetry: how to decouple the different gravity field constituents? In: Jekeli, C., et al. (eds), *Gravity, geoid and space missions*, vol. 129 of *International Association of Geodesy Symposia*. pp. 6–11, Springer-Verlag, Berlin Heidelberg, pp. 6–11.

Wahr, J., S. Swenson, and I. Velicogna (2006), Accuracy of GRACE mass estimates, *Geophys. Res. Lett.*, 33(L06401), doi: 10.1029/2005GL025305.

Chapter 19

Regional Gravity Field Recovery from GRACE Using Position Optimized Radial Base Functions

M. Weigelt, M. Antoni, and W. Keller

Abstract Global gravity solutions are generally influenced by degenerating effects such as insufficient spatial sampling and background models among others. Local irregularities in data supply can only be overcome by splitting the solution in a global reference and a local residual part. This research aims at the creation of a framework for the derivation of a local and regional gravity field solution utilizing the so-called line-of-sight gradiometry in a GRACE-scenario connected to a set of rapidly decaying base functions. In the usual approach, the latter are centered on a regular grid and only the scale parameter is estimated. The resulting poor condition of the normal matrix is counteracted by regularization. By contrast, here the positions as well as the shape of the base functions are additionally subject to the estimation process. As a consequence, the number of base functions can be minimized. The analysis of the residual observations by local base functions enables the resolution of details in the gravity field which are not contained in the global spherical harmonic solution. The methodology is tested using simulated as well as real GRACE data.

19.1 Introduction

Local gravity field recovery has the advantage that the solutions can be tailored to the region of interest and can make better use of the available data. For example, global ocean tide models currently do not take into account the ice coverage in the winter months in some areas, e.g., in the Hudson Bay (Canada). Local and regional ocean tide models are available but cannot be applied due to the missing global support. Another example is the groundtrack pattern which defines the spatial sampling and the resolution of the gravity field model. A global solution is primarily governed by the data distribution at the equator which is sparser than in high-latitude areas, since the orbit converges towards the poles. As a consequence spurious signal is introduced and aliasing occurs. Maybe the most convincing motivation for regional analysis can be seen in Fig. 19.1. The top panel shows the comparison of the K-Band derived range rate vs. the relative velocity of the two GRACE satellites projected on the line of sight for an arc crossing the Himalayan mountains in August 2003. The relative velocities have been calculated by integrating a 6-min arc for each satellite using GGM02S until degree and order 110, which is the suggested maximum degree of this global GRACE-only model (Tapley et al., 2005). The bottom panel shows the profile of the topography along the groundtrack of the barycenter, defined as the arithmetic mean of the positions of the satellites. As the satellites cross the Himalayan mountain ridge, residual signal of $\delta\dot{\rho} \approx 2\mu\mathrm{m}/s$ is visible. Repeating the same procedure using GGM02C until degree and order 150, which incorporates also altimetric and terrestrial data, the topographic correlation is reduced. Consequently, a global spherical harmonic analysis using satellite data only makes not fully use of the available information and an improvement might be possible using local methods.

The idea of regional gravity field modeling from GRACE-data is not new. For example, Eicker (2008)

M. Weigelt (✉)
Institute of Geodesy, Universität of Stuttgart, Stuttgart 70174, Germany
e-mail: weigelt@gis.uni-stuttgart.de

S.P. Mertikas (ed.), *Gravity, Geoid and Earth Observation*, International Association of Geodesy Symposia 135,
DOI 10.1007/978-3-642-10634-7_19, © Springer-Verlag Berlin Heidelberg 2010

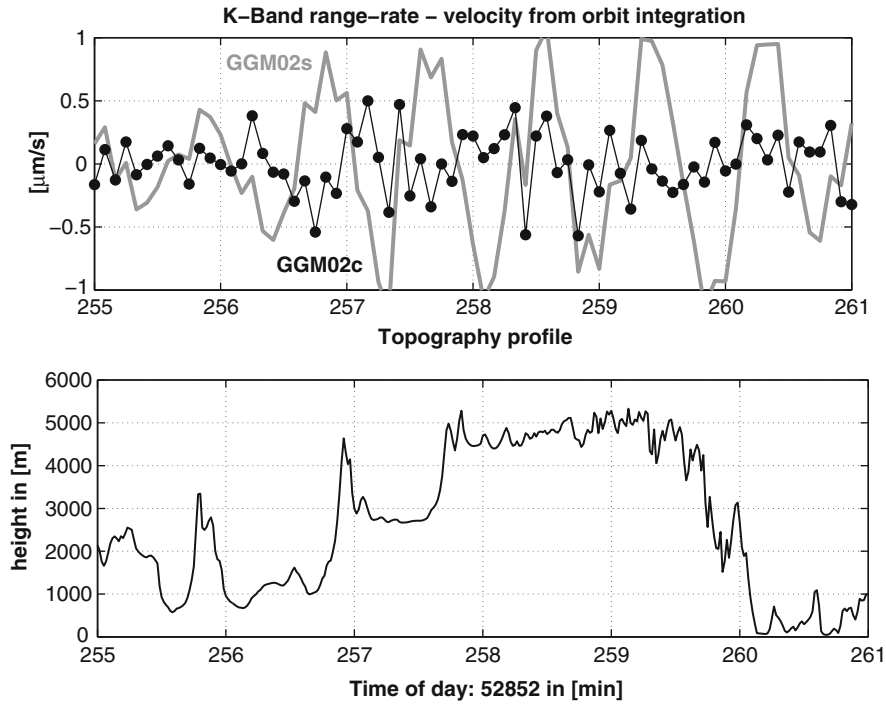


Fig. 19.1 K-band observation vs. velocity differences (*top*); profile of the topography for an arc crossing the Himalayan mountains in August 2003 (*bottom*)

adopts radial base functions on a spherical grid to refine the gravity solutions. The in-situ measurements are derived by the short-arc method developed by Mayer-Güerr (2006). Han and Simons (2008) utilize the energy balance approach and Slepian functions to detect the gravity change caused by the Sumatra-Andaman earthquake. Schmidt et al. (2007) applies multi-resolution analysis and spherical wavelets to the CHAMP and GRACE missions. All show that a regional refinement leads to improved solutions in the area of interest.

This paper will introduce an alternative approach for the estimation of local gravity field recovery which consists of two steps. First, in-situ observables will be derived by the line-of-sight (LOS) gradiometry (Keller and Sharifi, 2005). Second, the local recovery will also make use of radial base functions as in Eicker (2008) but beside the scale parameter also their position and their shape parameter are subject to an optimization process. The number of base functions is found in an iterative procedure which will avoid instabilities due to overparametrization and does not need regularization. However, the relation of the in-situ observable to the radial base functions requires to solve a non-linear least-squares problem resulting in a high computational effort.

The paper will start with the derivation of the basic equation for the calculation of the in-situ measurements in Sect. 19.2.1 followed by the introduction of the radial base functions in Sect. 19.2.2 and the optimization procedure in Sect. 19.2.3. Possible error sources are discussed in Sect. 19.2.4 before results using simulated and real GRACE-data are presented in Sect. 19.3 proving the applicability of approach.

19.2 Data Processing

The primary observables of the GRACE system are the K-band derived range rate and range acceleration between the two satellites. The basic geometry of the GRACE system has already been depicted in Rummel et al. (1978) and is shown in Fig. 19.2. The aim is to connect the measurements via the line-of-sight gradiometry to the radial base functions.

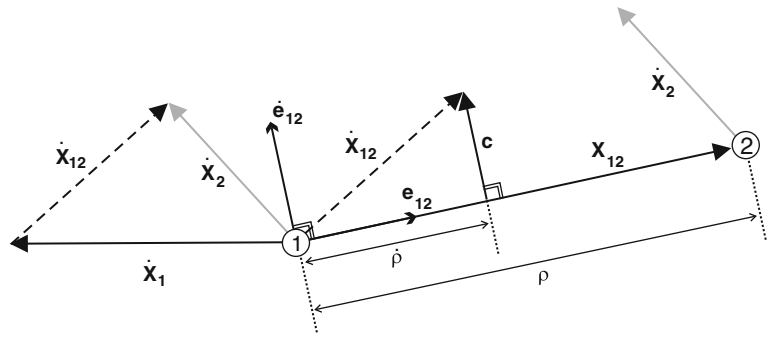


Fig. 19.2 Geometric setup of the GRACE-system (Rummel et al., 1978)

19.2.1 Line-of-Sight Gradiometry

The line-of-sight gradiometry relates the observables to the gravity tensor projected on the line of sight, which creates a direct link to the gravity field geometry, i.e., the curvature of the field in the evaluation point. At the cost of a slightly increased noise level due to differentiation, it yields an in-situ observation that is less affected by the orbital history and can be connected to the barycenter of the satellites. The range rate $\dot{\rho}$ is related to the relative velocity $\dot{\mathbf{X}}_{12}$ by projection on the line of sight which is expressed by the unit vector pointing from satellite 1 to 2:

$$\dot{\rho} = \dot{\mathbf{X}}_{12} \cdot \mathbf{e}_{12}. \tag{1}$$

Taking the derivative yields:

$$\ddot{\rho} = \ddot{\mathbf{X}}_{12} \cdot \mathbf{e}_{12} + \dot{\mathbf{X}}_{12} \cdot \dot{\mathbf{e}}_{12}. \tag{2}$$

The first term on the right hand side can be connected to the gradient of the potential at the position of each satellite. Reformulating the change of the line-of-sight vector $\dot{e}_{12}$ as a combination of the relative velocity vector and the range rate (Rummel et al., 1978) and rearranging the equation yields an expression which is generally referred to as the *differential gravimetry approach*:

$$(\nabla V_2 - \nabla V_1) \cdot \mathbf{e}_{12} = \ddot{\rho} + \frac{\dot{\rho}^2}{\rho} - \frac{\|\dot{\mathbf{X}}_{12}\|}{\rho}. \tag{3}$$

Dividing both sides by the range ρ, the left hand side contains the discretized first order differential of the gravity gradient and thus can be approximated by the projected gravity tensor $\mathbf{G}$:

$$\mathbf{e}_{12}^T \mathbf{G} \mathbf{e}_{12} + \mathcal{O}^2 = \frac{\ddot{\rho}}{\rho} + \frac{\dot{\rho}^2}{\rho^2} - \frac{\|\dot{\mathbf{X}}_{12}\|}{\rho^2}. \tag{4}$$

The left hand side contains the first order and the abbreviation for higher order terms $\mathcal{O}^2$. Keller and Scharifi (2005) demonstrated that the higher order terms cannot be neglected but the consideration of the linear term is sufficient if an adequate a priori field is subtracted and the observable is reduced to a residual quantity:

$$\mathbf{e}_{12}^T \mathbf{G} \mathbf{e}_{12} = \frac{\ddot{\rho}}{\rho} + \frac{\dot{\rho}^2}{\rho^2} - \frac{\|\dot{\mathbf{X}}_{12}\|}{\rho^2} - \frac{1}{\rho}\left(\nabla V_2^0 - \nabla V_1^0\right) \cdot \mathbf{e}_{12}. \tag{5}$$

Working on the residual signal is not a disadvantage for regional applications, since long-wavelength features have to be reduced anyway. The final step is to include all gravitational and non-gravitational disturbing forces $\mathbf{g}^i$ which need to be calculated or measured for each satellite separately. Their difference is also projected on the line of sight:

$$\begin{aligned} \mathbf{e}_{12}^T \mathbf{G} \mathbf{e}_{12} = \frac{\ddot{\rho}}{\rho} + \frac{\dot{\rho}^2}{\rho^2} - \frac{\|\dot{\mathbf{X}}_{12}\|}{\rho^2} - \frac{1}{\rho} \sum_i \mathbf{g}_{12}^i \cdot \mathbf{e}_{12} \\ - \frac{1}{\rho}\left(\nabla V_2^0 - \nabla V_1^0\right) \cdot \mathbf{e}_{12}. \end{aligned} \tag{6}$$

The equation contains quantities taken from the K-band ranging system as well as from GPS, namely the relative velocity of the two satellites. The poorer accuracy of the latter theoretically prevents the implementation but Keller and Sharifi (2005) showed also that practically they can be replaced by velocities derived using numerical integrated orbits derived from a known a priori gravity field. By Eq. (6) in-situ observations along the orbit can be calculated and can be connect to a function with local support, i.e., the radial base functions.

19.2.2 Radial Base Functions

The starting point is the description of the potential in terms of radial base functions Ψ_b:

$$V(\lambda,\vartheta,r) = \frac{GM}{R}\sum_{b=1}^{B}\eta_b\Psi_b(\lambda,\vartheta,r), \tag{7}$$

where η_b is the scale parameter. The aim of our approach is to keep B, i.e., the maximum number of base functions, as low as possible in order to avoid overparametrization. Every base function Ψ_b is given as:

$$\Psi_b(\lambda,\vartheta,r) = \sum_{n=0}^{N}\left(\frac{R}{r}\right)^{n+1}\sigma_b(n)\,P_n(\cos\varpi_b) \tag{8}$$

and has its individual and degree dependent shape parameter $\sigma_b(n)$. N denotes the maximum degree of development and ϖ_b is the spherical distance between the computational position (λ,ϑ) and the center of the base function (λ_b,ϑ_b). In order to connect the base functions to the line-of-sight gradiometry, the second derivative in the flight direction y has to be taken. According to Koop (1993):

$$\frac{\partial^2 V}{\partial y^2} = \frac{1}{a^2}\frac{\partial^2 V}{\partial u^2} + \frac{1}{a}\frac{\partial V}{\partial r}, \tag{9}$$

i.e., the derivative in the flight direction can be replaced by the second derivative towards the argument of latitude u and the first radial derivative in combination with the osculating (instantaneous) semi-major axis. Since in Eq. (7) only Ψ_b is dependent on r and u, it is sufficient to take the derivative of the base function itself:

$$\begin{aligned}\frac{\partial^2\Psi_b}{\partial^2} = \frac{1}{a^2}\sum_{n=0}^{N}\sigma_b(n)\left(\frac{R}{r}\right)^{n+1}\Bigg\{&\left(\frac{\partial\zeta_b}{\partial u}\right)^2 P_n''(\zeta_b)\\ &+\left(2\frac{-(n+1)e\sin E}{\sqrt{1-e^2}}\frac{\partial\zeta_b}{\partial u}-\zeta_b\right)P_n'(\zeta_b)\\ &+\left(\frac{(n+1)e^2\sin^2 E}{1-e^2}-\frac{re\cos E}{a(1-e^2)}-\frac{a}{r}\right)(n+1)\,P_n(\zeta_b)\Bigg\}\end{aligned} \tag{10}$$

where the abbreviation $\zeta_b := \cos\varpi_b$ is introduced. $P_n'(\zeta_b)$ and $P_n''(\zeta_b)$ denote the first and second derivatives of the Legendre-polynomials, E the eccentric anomaly and e the eccentricity of the orbit.

The final step is to connect the second derivative of the radial base function in flight direction to the linear term of the line-of-sight gradiometry. Thus, the model is applied to the residual field and model inconsistencies need to be considered.

$$\mathbf{e}_{12}^T\mathbf{G}\mathbf{e}_{12} = \frac{GM}{R}\sum_{b=1}^{B}\eta_b\frac{\partial^2\Psi_b}{\partial y^2} + \varepsilon \tag{11}$$

Equation (11) forms the basic observation equation for the subsequent optimization process.

19.2.3 Optimization of the Parameters

Commonly, the central position (λ_b,θ_b) of each base function is fixed on a regular grid and the shape parameter $\sigma_b(n)$ is derived from Kaula's rule (Kaula, 1966):

$$\sigma_b^2(n) = (2n+1)\,\frac{10^{-10}}{n^4} \tag{12}$$

Only the scale factors η_b are subject to an estimation process. The problem remains linear but numerous base functions might be necessary to achieve reasonable accuracies. It leads quickly to an overparametrization which needs to be counteracted by regularization (Eicker, 2008).

An alternative approach is to estimate all parameters of the radial base functions $(\lambda_b,\theta_b,\eta_b,\sigma_b(n))$ from the data directly. Thus, overparametrization is avoided by just using a minimal number of bases. Reviewing equation (10), it is evident that the optimization of the position and the shape parameter results in a non-linear least-squares adjustment, which needs to be solved iteratively.

Figure 19.3 shows the workflow of the iterative optimization process. Beginning with the preprocessed pseudo-observables of the line-of-sight gradiometry, a residual quantity is formed by subtracting the long wavelength part of the gravity field, cf. Eq. (6). The area of calculation has been chosen to be bigger than the area of interest in order to deal with edge effects later on. Empirically, we found that adding a frame of 3° is sufficient. The shape parameters are modeled by the exponential relationship

$$\sigma_b(n) = \sigma_b^n. \tag{13}$$

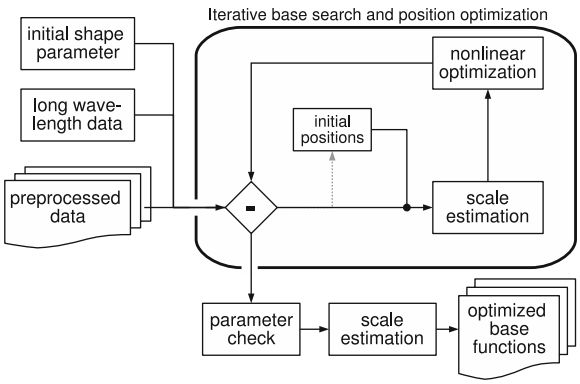


Fig. 19.3 Workflow of the algorithm

The localizing properties and the convergence of the base function is ensured if the σ is within the interval [0.9, 1]. Since we found in numerous test that most shape parameters converge to 1, we chose $\sigma = 0.97$ as the starting value in order to keep the number of iterations small.

Entering the iterative base search, initial values for the central positions of the base functions and the scale parameters η_b have to be estimated first. A reasonable choice for the positions are the minima and maxima of the residual field. By interpolating a copy of the data onto a 0.5° grid and smoothing it with a binomial filter, it is ensured that outliers are removed and the initial positions are not too close together. The scale parameters are estimated using a standard least-squares adjustment since they are linearly related according to Eq. (19.7).

These initial values are improved by a nonlinear least-squares solver, which is based on the Levenberg-Marquardt algorithm (Marquardt, 1963). Boundary restrictions ensure that the central positions do not change by more than 5° and the shape parameters remain in the aforementioned interval [0.9,1]. The scale parameters η_b are not restricted. In case of convergence, a synthesis of the estimated base functions is calculated and subtracted from the input field in order to get a new residual field.

$$\delta V_{i+1} = \delta V_i - \frac{GM}{R} \sum_{b=1}^{B_i} \eta_b \frac{\partial^2 \Psi_b}{\partial^2}. \qquad (14)$$

The procedure is repeatedly applied to increase the number of base functions but terminated if the center of the base functions get too close together, the scale factors become unreasonably small or the standard deviations are larger than the estimated value itself.

In the final steps of the procedure, the estimated parameters are tested for inconsistencies, e.g., base functions are located outside the area of interest. If base functions need to be rejected, the scale factors are readjusted. Finally, edge effects are minimized by removing the 3° frame and the user is provided with optimized parameters for the base functions.

19.2.4 Error Sources

In the local refinement, the residual signal consists of gravity signal, noise and spurious signal due to aliasing and modeling errors. Note that gravity is highly correlated with the topography whereas the correlation of all other components with the topography is generally minor.

1. Aliasing occurs due to an undersampling of a signal. If the temporal sampling along the orbit is not sufficient, signal or parts of it cannot be recovered from the data and will alias into other frequencies. The effect can be minimized by removing the signal using appropriate models. However, their accuracy is limited which is currently considered as one of the reason that GRACE does not match the expected baseline accuracy, e.g., Kanzow et al. (2005). Spatial aliasing takes place if the sampling in the spatial domain is insufficient. The solution becomes especially degraded if GRACE passes a repeat mode, e.g., Wagner et al. (2006).
2. Modeling errors are caused by an insufficient mathematical and/or stochastic representation of the signal. Considering our approach, the LOS gradiometry introduces a linearization error which can be minimized by the subtraction of an a priori field as already mentioned (Keller and Sharifi, 2005). Gravitational disturbing forces are considered but are limited by the accuracy of their underlying model, e.g., Han et al. (2004). Non-gravitational forces are measured by the accelerometers onboard but are biased and scaled due to instrument effects. Corrections have to be estimated from the data which in turn are also limited in their accuracy (Perosanz et al., 2005).

3. Any estimation process can be affected by under- or overparametrization which is here avoided due to the iterative search. However, the Levenberg-Marquardt algorithm does not necessarily find the global minimum and might converge to a local one instead (Ortega and Rheinboldt, 1970). This effect can be minimized by using the best available initial values.

19.3 Results

Having outlined the algorithm, the applicability of the approach can be tested. In a first step, simulated data is used to test for modeling errors. Subsequently, the method is applied to GRACE. Note that our primary intention is here to validate the methodology and its applicability to real data. Results using real GRACE data are preliminary and need to be cross-checked by e.g., GPS leveling.

19.3.1 Simulation

For the closed-loop simulation, 12 base functions were hidden in the area of the Mediterranean sea. The input signal ranges from -483 mE to 257 mE with a $RMS = 207.4$ mE and is two orders of magnitude stronger than the residual signal in the case of real data, which is desired here in order to reveal modeling errors. The left panel of Fig. 19.4 shows the difference between input and estimated signal, hereafter called approximation. Obviously, some type of "trackiness" remains which is likely related to the geometry of the system. Since the pseudo-observables represent the second derivative along the line of sight, leakage will primarily occur in the direction of travel which is practically in the north-south direction. For the quantification of the fit, we use the ratio of the standard deviation between the observed and the approximation in percent:

$$Q = \frac{STD(approximation)}{STD(signal)} \cdot 100, \qquad (15)$$

The field is recovered with a Q of 98% and a RMS of 37.9 mE. Since a full recovery is unlikely without the usage of numerous base functions, the fit can be considered as an excellent result. Interestingly, the algorithm used *12* base functions but the location of the estimated base functions (•) differs significantly from the original positions (♦), cf. the right panel of Fig. 19.4. Nevertheless, the input signal is represented almost as good by the new set of base functions as by the original one. This is a nice depiction of the inverse problem of geodesy and visualizes that a local minimum has been found in the adjustment.

19.3.2 Real GRACE Data

Generally, the residual signal of real GRACE data is noisy and contains, besides signal from the aforementioned error sources, a weak gravity component.

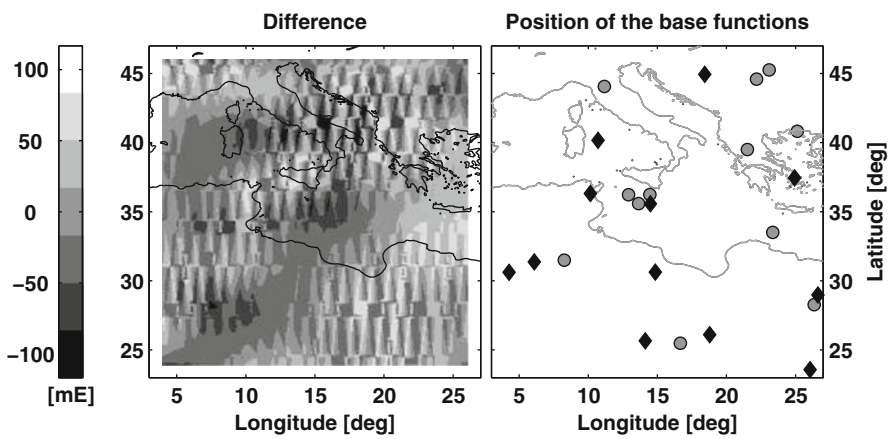


Fig. 19.4 Closed-loop simulation: difference between input and approximation (*left*), position of the base function (*right*)

In this test we are aiming at the recovery of the latter for an area in the Himalaya using level 1B GRACE data, which is provided by the Physical Oceanography Distributed Active Archive Center at the NASA Jet Propulsion Laboratory. The corresponding global gravity field solution for each month is provided by the GeoForschungsZentrum Potsdam (Rel. 4) (Schmidt et al. 2006).

Our first method of validation is to compare GGM02S and the local solution for 1 month, namely August 2003, with GGMC02C. Since the latter contains more gravitational signal and has less topographic correlation (cf. Fig. 19.1), it can be used as a reference. The comparison in Fig. 19.5 shows reduced and less regular variations for the local solution. The RMS reduces from 83.3 to 69.7 cm.

Next, the K-band range rate can again be compared to the relative velocity of the two satellites derived for the 6-min arc crossing the Himalayan mountain ridge. The fit can be quantified by differencing the crosscorrelation of GGM02C with the orbit arcs derived from GGM02S and from the local solution, respectively. Looking at the result in Fig. 19.6, the local model reduces the topographic correlation up to 50% peak to peak but is not able to remove it completely. We analysed all arcs crossing the area of interest in the year 2003 (cf. Table 19.1) and the local solutions show consistently an improvement up to 40% with the exception of a few spurious arcs. Note that the instrument data at the beginning of the mission is of less quality than e.g., since March 2003 (pers. com. Frank Flechtner).

Table 19.1 Statistics for arcs crossing the Himalayan area in 2003

		Improvement			
Period	# Arcs total	+	–	Max(%)	Mean(%)
Jan. – Mar.	138	120	18	39	11.1
Apr. – Jun.	138	135	3	29	15.0
Jul. – Sep.	135	131	4	38	13.7
Oct. – Dec.	142	142	0	33	12.9

Since the results show a reduced correlation with the topography and the contribution of the possible error sources are only poorly correlated with the latter, we can conclude that the solution must contain additional gravitational information. The data processing is not optimized yet and a topographic correlation is still visible. Background models are still based on

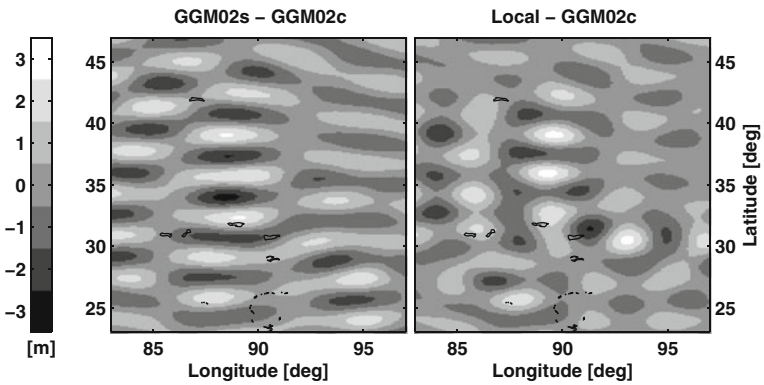


Fig. 19.5 Geoid height differences w.r.t. GGM02C in August 2003: GGM02S (*left*) and local solution (*right*)

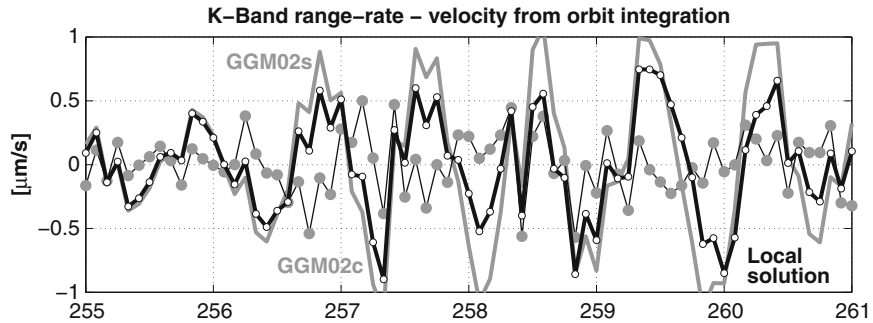


Fig. 19.6 K-band observation versus velocity difference

global data sets and the optimization process is based on empirical tests. It is expected that further improvements are possible and thus the results have to be considered preliminary.

19.4 Conclusions

In conclusion, a framework has been created in order to derive a refined model for the gravity field in local areas using the LOS gradiometry in combination with position optimized radial base functions. The approach promises to reveal further details in the level 1B data of the GRACE mission since the solutions can be tailored to local areas. The usage of the position optimized radial base functions avoids overparametrization and yields a stable system at the cost of a non-linear optimization problem. It has been shown with simulated and real data, that the approach can be successfully implemented. In further studies the trackiness and a refined background modeling need to be addressed.

Acknowledgments We like to thank Dr. Frank Flechtner for his helpful review and his hint that till March 2003 the data is of less quality. Also the detailed suggestions of one anonymous reviewer helped to improve this paper and are highly appreciated.

References

Eicker, A. (2008). Gravity field refinement by radial base functions from in-situ satellite data, Ph.D. thesis, Rheinische Friedrich-Wilhelms-Universität zu Bonn.

Han, S. and F. Simons (2008). Spatiospectral localization of global geopotenial fields from the Gravity Recovery and Climate Experiment (GRACE) reveals the coseismic gravity change owing to the 2004 Sumatra-Andaman earthquake. *J. Geophy. Res.*, 113, B01,405, doi: 10.1029/2007JB004927.

Han, S., C. Jekeli, and C. Shum (2004). Time-variable aliasing effects of ocean tides, atmosphere, and continental water mass on monthly mean GRACE gravity field. *J. Geophy. Res.*, 109, B04,403, doi: 10.1029/2003JB002501.

Kanzow, T., F. Flechtner, A. Chave, R. Schmidt, P. Schwintzer, and U. Send (2005). Seasonal variation of ocean bottom pressure derived from Gravity Recovery and Climate Experiment GRACE: Local validation and global patterns. *J. Geophy. Res.*, 110, C09,001.

Kaula, W. (1966). Theory of satellite geodesy. Blaisdell Publishing Company.

Keller, W. and M. Sharifi Wather (2005), Satellite gradiometry using a satellite pair. *J. Geod.*, 78, 544–557.

Koop, R. (1993). Global gravity field modelling using satellite gravity gradiometry, Ph.D. thesis, Technische Universiteit Delft, Delft, Netherlands.

Marquardt, D. (1963). An algorithm for least-squares estimation of nonlinear parameters. *J. Appl. Math.*, 11, 431–441.

Mayer-Gürr, T. (2006). Gravitationsfeldbestimmung aus der Analyse kurzer Bahnbögen am Beispiel der Satellitenmissionen CHAMP und GRACE, Ph.D. thesis, Rheinische Friedrich-Wilhelms-Universität zu Bonn.

Ortega, J. and W. Rheinboldt (1970). Iterative solution of nonlinear equations in several variables. Academic Press, NY.

Perosanz, F., R. Biancale, J. Lemoine, N. Vales, S. Loyer, and S. Bruinsma (2005). Evaluation of the CHAMP accelerometer on two years of mission. In: Reigber, C., H. Lühr, P. Schwintzer, and J. Wickert (eds), Earth Observation with CHAMP. Springer, NY, pp. 77–82.

Rummel, R., C. Reigber, and K. Ilk, (1978). The use of satellite-to-satellite tracking for gravity parameter recovery. In: Proceedings of the European Workshop on Space Oceanography, Navigation and Geodynamics (SONG).

Schmidt, R., F. Flechtner, U. Meyer, C. Reigber, F. Barthelmes, C. Förste, R. Stubenvoll, R. König, K.-H. Neumayer, and S. Zhu (2006). Static and time-variable gravity from GRACE mission data. In: Flury, J., R. Rummel, C. Reigber, M. Rothacher, G. Boedecker, and U. Schreiber (eds), Observation of the Earth System from Space, ISBN 3-540-29520-8. Springer, Berlin, pp. 115–129.

Schmidt, M., M. Fengler, T. Mayer-Gürr, A. Eicker, J. Kusche, L. Sánchez, and S. Han (2007). Reginonal gravity modeling in terms of spherical base functions. *J. Geod.*, 81, 17–38, doi: 10.1007/s00190-006-0101-5.

Tapley, B., J. Ries, S. Bettadpur, D. Chambers, M. Cheng, F. Condi, B. Gunter, Z. Kang, P. Nagel, R. Pastor, T. Pekker, S. Poole, and F. Wang (2005). GGM02 – An improved Earth gravity field model from GRACE. *J. Geod.*, 79, 467–478, doi: 10.1007/s00190-005-0480-z.

Wagner, C., D. McAdoo, J. Klokočník, and J. Kostelecký (2006). Degradation of geopotential recovery from short repeat-cycle orbits: application to GRACE monthly fields. *J. Geod.*, 80(2), 94–103.

Chapter 20

External Calibration of SGG Observations on Accelerometer Level

R. Mayrhofer and R. Pail

Abstract The satellite mission GOCE (Gravity Field and steady state Ocean Circulation Explorer) uses for the first time a gradiometer for the determination of the earth's global gravity field. The observations suffer stochastic and systematic errors. These errors are caused by rotations and shifts of the accelerometers with respect to their optimal alignments and positions. The main target of this study is to develop methods to deduce the inverse calibration matrix (ICM), which parameterizes these errors, by using least squares adjustment.

Beside signal filtering, weighting and rigorous noise analysis, a complete variance-covariance propagation chain is applied. For being able to comply with the given tasks, a simulation environment has been developed. With this environment it is possible to apply data synthesis, data analysis, filtering, calibration and variance-covariance propagation. In the frame of three external calibration approaches, methods for improving the calibration accuracy have been developed and implemented. For an as realistic as possible simulation study, the synthetic data has been defined according to the GOCE project error budget (Cesare et al., 2008).

The treatment of accelerometer measurement noise, angular acceleration noise and angular velocity noise is of great importance. By using an adequate bandpass filter, the overall noise level could be strongly reduced. Moreover, variance-covariance information corresponding to the stochastic noise models has been synthesized and introduced into the calibration system. By utilizing filtering and variance-covariance information, the maximal calibration error of the alignment parameters could be reduced to $<10^{-3}$.

Finally harmonic gravity field coefficients have been estimated from externally calibrated and uncalibrated data. It could be proven that an overall improvement of the signal quality could be achieved. Nevertheless, because of the maximal quality of only 10^{-3} of the deduced alignment parameters, larger deviations from the reference gravity field than in the ideal calibration case have to be expected.

20.1 Principles

A Three Axis Gradiometer consists of six accelerometers, which form three accelerometer pairs. In practice, it is not possible to perfectly align the accelerometers on their nominal positions. Thus, the measured quantities suffer erroneous variations. With the measured accelerations of an accelerometer pair *ij* common mode (CM) and differential mode (DM) accelerations can be formulated:

$$\underline{a}_c^{ij} = \frac{1}{2}\left(\underline{a}^i + \underline{a}^j\right) \tag{1a}$$

$$\underline{a}_d^{ij} = \frac{1}{2}\left(\underline{a}^i - \underline{a}^j\right) \tag{1b}$$

While the CM accelerations contain only non-conservative accelerations and thus cannot be synthesized with reasonable accuracy, the DM accelerations consist of gravitational accelerations and inertial accelerations. The main target of the external calibration

R. Mayrhofer (✉)
Institute of Navigation and Satellite Geodesy, Graz University of Technology, Graz, Austria
e-mail: reinhard.mayrhofer@tugraz.at

S.P. Mertikas (ed.), *Gravity, Geoid and Earth Observation*, International Association of Geodesy Symposia 135,
DOI 10.1007/978-3-642-10634-7_20, © Springer-Verlag Berlin Heidelberg 2010

method described in this study is to deduce calibration parameters from the measured CM and DM accelerations and synthetic DM accelerations. For this reason the model DM observations are synthesized by using an a priori gravity field model. The earth's gravity field is represented by the gravitational potential U, which is usually expressed by a spherical harmonic series expansion (Heiskanen and Moritz, 1967):

$$U(r,\theta,\lambda) = \frac{GM}{R} \cdot \sum_{l=0}^{\infty} \left(\frac{R}{r}\right)^{l+1} \cdot \sum_{m=0}^{l} (\overline{C}_{lm} \cos m\lambda + \overline{S}_{lm} \sin m\lambda) \cdot \overline{P}_{lm}(\cos\theta) \tag{2}$$

Here *r, θ and λ* are spherical coordinates, R is the earth's reference radius, GM the gravitational constant times mass of the earth, l and m are the degree and order of the fully normalized spherical coefficients $\overline{C}_{lm}$,$\overline{S}_{lm}$, and $\overline{P}_{lm}(\cos\theta)$ represents the fully normalized Legendre function.

Based on the gravity gradients computed from the second derivatives of Eq. (2), DM accelerations can be synthesized. If we assume that the accelerometer cage is stiffly connected to the satellite, and that there are no relative movements between the centre of the gradiometer and the centre of mass (COM) of the satellite, the accelerometer experiences the relative acceleration between its proof mass and the satellite. The complete detected acceleration of an accelerometer A_i is modeled by:

$$\underline{a}^i = -([U] - [\Omega]^2 - [\dot{\Omega}]) \cdot \underline{R}_i + 2[\Omega] \cdot \dot{\underline{R}}_i + \ddot{\underline{R}}_i + \underline{D} - \underline{S}_i - \underline{M}_i \tag{3}$$

Here, the gravity gradient tensor $[U]$ contains the second spatial derivatives of the gravity potential U. The angular velocity tensor and the angular acceleration tensor are defined by:

$$[\Omega] = \begin{bmatrix} 0 & -\omega_z & \omega_y \\ \omega_z & 0 & -\omega_x \\ -\omega_y & \omega_x & 0 \end{bmatrix}, [\dot{\Omega}] = \begin{bmatrix} 0 & -\dot{\omega}_z & \dot{\omega}_y \\ \dot{\omega}_z & 0 & -\dot{\omega}_x \\ -\dot{\omega}_y & \dot{\omega}_x & 0 \end{bmatrix} \tag{4}$$

$\underline{R}_i$ defines the position vector from the COM to the accelerometer A_i, while $\dot{\underline{R}}_i$ and $\ddot{\underline{R}}_i$ describe its first and second time derivative. Non-conservative forces like atmospheric drag, radiation pressure and thruster actions are summed up in $\underline{D}$, self-gravity of the satellite is described by $\underline{S}_i$, and the acceleration from magnetic coupling is $\underline{M}_i$. By combining Eq. (1b) with Eq. (3), the formula for synthesizing model DM accelerations can be found:

$$\underline{a}_d^{ij} = -([U] - [\Omega]^2 - [\dot{\Omega}]) \cdot \underline{A}_d^{ij} - \underline{S}_d^{ij} - \underline{M}_d^{ij} \tag{5}$$

Where the subscript d denotes the differential mode and the indices ij the involved accelerometers (Cesare et al., 2008)

20.2 The Inverse Calibration Matrix

Based on the synthetic DM accelerations, the inverse calibration matrix (ICM) can be deduced. The ICM contains the position and alignment parameters of the accelerometer pair. If we assume that the quadratic factors are zero, the relation between the measured and synthetic CM and DM accelerations is given by (Cesare et al., 2008):

$$\begin{bmatrix} \underline{a}_c \\ \underline{a}_d \end{bmatrix} = [K]^- \cdot \left(\begin{bmatrix} \underline{a}'_c \\ \underline{a}'_d \end{bmatrix} - \begin{bmatrix} \underline{b}_c \\ \underline{b}_d \end{bmatrix} \right) \tag{6}$$

$[K]^-$ denotes the ICM, while $\underline{b}_c$ and $\underline{b}_d$ are CM and DM related biases. The upper index ij has been omitted. The apostrophe indicates measured accelerations. The elements of the ICM are defined by:

$$[K]^- = \begin{bmatrix} [K_c] & [K_d] \\ [K_d] & [K_c] \end{bmatrix} - = \begin{bmatrix} C & D \\ D & C \end{bmatrix} \tag{7a}$$

$$C = \begin{bmatrix} c_{11} & c_{12} & c_{13} \\ c_{21} & c_{22} & c_{32} \\ c_{31} & c_{32} & c_{33} \end{bmatrix}, D = \begin{bmatrix} d_{11} & d_{12} & d_{13} \\ d_{21} & d_{22} & d_{23} \\ d_{31} & d_{32} & d_{33} \end{bmatrix} \tag{7b}$$

The CM and DM related calibration matrices $[K_c]$ and $[K_d]$ can be found by applying Eqs. (1a) and (1b). The elements c_{ij} and d_{ij} of the ICM consist of linear combinations of scale factors, rotation angles and shear factors of the accelerometer pair. These parameters can be deduced by applying linear combinations.

20.3 Functional Models

20.3.1 Estimation with Parameters Approach

Based on the fundamental relation shown in Eq. (6), the first least squares adjustment approach can be derived. The CM accelerations consist of non-conservative forces and thus can not be synthesized. The CM accelerations have to be omitted, leading to a linear model which consists only of the lower part of Eq. (6).

$$\underline{a}_d = [\,D\;C\,] \cdot \left(\begin{bmatrix} \underline{a'}_c \\ \underline{a'}_d \end{bmatrix} - \begin{bmatrix} \underline{b}_c \\ \underline{b}_d \end{bmatrix} \right) = \underline{K}^{-}_{low} \cdot \underline{a'}_{c,d} + \overline{\underline{b}}_{c,d} \tag{8}$$

Based on Eq. (8) the parameter vector, the design matrix and the observation vector of one epoch are defined by:

$$\underline{x} = [d_{11} \ldots d_{33}, c_{11} \ldots c_{33}, \overline{b}^x_{cd}, \overline{b}^y_{cd}, \overline{b}^z_{cd}]^T \tag{9a}$$

$$\underline{A} = \begin{bmatrix} a'^T_c & 0 & 0 & a'^T_d & 0 & 0 & 1\;0\;0 \\ 0 & a'^T_c & 0 & 0 & a'^T_d & 0 & 0\;1\;0 \\ 0 & 0 & a'^T_c & 0 & 0 & a'_{dT} & 0\;0\;1 \end{bmatrix} \tag{9b}$$

$$\underline{\ell} = [\,a^x_d\; a^y_d\; a^z_d\,]^T \tag{9c}$$

For having a solvable system, at least seven epochs are needed. The parameters are estimated by:

$$\hat{\underline{x}} = (\underline{A}^T \underline{P}_{\ell\ell} \underline{A})^{-} \underline{A}^T \underline{P}_{\ell\ell} \cdot \underline{\ell} \tag{10}$$

$\underline{P}_{\ell\ell}$ represents the weight matrix. It is defined as the inverse of the covariance matrix of the observation vector $\underline{P}_{\ell\ell} = \sigma^2_\ell \Sigma(\underline{\ell})^{-}$.

The main advantage of this approach is the possibility to easily assemble the normal equations epoch-wise, which makes it possible to use large data sets. Unfortunately, no variance-covariance information of the measured CM and DM accelerations can be introduced, because they are used to set up the deterministic design matrix. Thus, two other approaches have been developed, where it is possible to use complete variance-covariance information.

20.3.2 Estimation by Conditions Approach

Again, based on the fundamental relation shown in Eq. (6), the second least squares adjustment approach can be derived. In addition to the first approach, a condition vector $\underline{\beta}$ is introduced. It states that the difference between the synthetic DM accelerations and the calibrated DM observations should become zero. Thus, $\underline{\beta}$ is a vector containing only zeros. The fundamental equation for the estimation by conditions with parameters approach can be deduced from Eq. (8):

$$\underline{\beta} = -\underline{a}_d + \underline{K}^{-}_{low} \cdot \underline{a'}_{c,d} + \overline{\underline{b}}_{c,d} = 0 \tag{11}$$

Equation (12) can be reformulated and describes the functional f:

$$\underline{f}(\underline{\ell},\underline{v},\underline{x}) = \underline{B}^T \left(\underline{\ell} + \underline{v} \right) + \underline{A} \cdot \underline{x} = \underline{\beta} \tag{12}$$

Compared with the parameter approach (Eq. (9a)) the parameter vector $\underline{x}$ contains improvements to the a-priori Taylor vector which makes an iteration procedure necessary. While $\underline{v}$ describes the residuals, the conditions matrix B and the design matrix A can be found by applying Taylor linearization:

$$\underline{B}^T = \left. \frac{\partial \underline{f}}{\partial \underline{\ell}} \right|_{\substack{\underline{\ell}=\underline{\ell}_0 \\ \underline{x}=\underline{x}_0}} d\underline{\ell}, \quad \underline{A} = \left. \frac{\partial \underline{f}}{\partial \underline{x}} \right|_{\substack{\underline{\ell}=\underline{\ell}_0 \\ \underline{x}=\underline{x}_0}} d\underline{x} \tag{13}$$

While the design matrix and parameter vector are identical to the estimation with parameters approach, the conditions matrix and observation vector for one epoch are defined by:

$$\underline{B} = \begin{bmatrix} d^0_{11}\; d^0_{12}\; d^0_{13}\; c^0_{11}\; c^0_{12}\; c^0_{13}\; -1\; 0\;\; 0 \\ d^0_{21}\; d^0_{22}\; d^0_{23}\; c^0_{21}\; c^0_{22}\; c^0_{23}\; 0\;\; -1\; 0 \\ d^0_{31}\; d^0_{32}\; d^0_{33}\; c^0_{31}\; c^0_{32}\; c^0_{33}\; 0\;\; 0\;\; -1 \end{bmatrix}^T \tag{14a}$$

$$\underline{\ell} = [\,a'^x_c\; a'^y_c\; a'^z_c\; a'^x_d\; a'^y_d\; a'^z_d\; a^x_d\; a_{d^y}\; a_{d^z}\,]^T \tag{14b}$$

Besides the model DM accelerations, also the measured CM and DM accelerations are used as observations. The upper index of the elements c^0_{ij} and d^0_{ij} indicate that Taylor values have to be used for setting

up the conditions matrix. The estimated parameter vector can be found by:

$$\hat{\underline{x}} = -\underline{K}^T \underline{B}^T \underline{\ell} + \underline{K}^T \underline{\beta} \tag{15}$$

$\underline{K}$ denotes an element of the inverse normal equation matrix:

$$\begin{bmatrix} \underline{B}^T \underline{Q}_{\ell\ell} \underline{B} & \underline{A} \\ \underline{A}^T & 0 \end{bmatrix}^{-} = \begin{bmatrix} \underline{M} & \underline{K} \\ \underline{K}^T & \underline{L} \end{bmatrix} \tag{16}$$

The main advantage of this approach is the possibility to use complete covariance information $\Sigma\left(\underline{\ell}\right) = \underline{Q}_{\ell\ell}\sigma_\ell^2$ for the observation vector$\underline{\ell}$. Assuming that there are no correlations between CM and DM measurements and synthetic DM observations, the variance-covariance matrix of the observation vector can be split into two parts with block-diagonal structure.

20.3.3 Modified Conditions Approach

This approach was designed to combine the advantages of the parameter approach with those of the conditions approach. On the one hand, an epoch-wise assembling should become possible, and on the other hand variance-covariance information of the measured CM and DM accelerations should be introduced.

Therefore, the linear system of the parameter approach is changed by applying a linear transformation with the conditions matrix $\underline{B}^T$:

$$\underline{\ell}' = \underline{B}^T \underline{\ell}, \underline{v}' = \underline{B}^T \underline{v}, \sum(\underline{\ell}') = \underline{B}^T \cdot \sum(\underline{\ell}) \cdot \underline{B} \tag{17}$$

These linear transformed vectors and matrices are introduced into Eq. (12):

$$\underline{B}^T \underline{\ell} + \underline{B}^T \underline{v} - \underline{\beta} = (\underline{\ell}' - \underline{\beta}) + \underline{v}' = -\underline{A}\underline{x} \tag{18}$$

The solution of this system is identical to the solution of the parameter approach. Thus, the estimated parameters can be found by:

$$\hat{\underline{x}} = -(\underline{A}^T \sum(\underline{\ell}')^{-} \underline{A})^{-} \underline{A}^T \sum(\underline{\ell}')^{-} (\underline{\ell}' - \underline{\beta}) \tag{19}$$

It can be shown that by means of filtering the time-correlation of the input data can be substantially reduced (Mayrhofer, 2008). In this case, the whole system can be generalized by assuming that the time-wise correlation of the data can be neglected. If the data is not time-correlated, the variance-covariance matrix of the observations $\sum(\underline{\ell}')$ becomes block-diagonal, with remaining correlations only within one epoch. Thus, an epoch-wise assembling of this system can be introduced, which allows to process data sets of arbitrary length.

20.4 Calibration Results

For understanding how every single input element influences the stability of the system and the final calibration result, a complete variance-covariance chain has been additionally implemented. Thus, it was possible to analyse occurring correlations between the estimated calibration parameters.

20.4.1 Noise Analysis

Before some calibration simulations have been done, a rigorous noise analysis has been applied. For this purpose, GOCE E2E simulator data has been used (Catastini et al., 2003). Comparing the noise levels of accelerometer noise and angular information noise showed that at crucial frequencies within the measurement bandwidth (MBW) between 5 and 100 mHz, the effect of angular information noise is larger than the influence of the accelerometer measurement noise (cf. Fig. 20.1).

Two types of synthetic angular rates noise have been used for simulation: Noise corresponding to angular velocities and angular accelerations derived from star-tracker (STR) information only, and angular rates noise deduced from an enhanced product from a combination of star tracker and gradiometer data (IAQ).

A noise-free, closed-loop simulation has shown that it is possible to perfectly recover the parameters of the ICM. Based on this reference constellation, realistic noise has been added step-wise to every input component with all three approaches presented in Chap. 3 (Mayrhofer, 2008).

Table 20.1 shows the results of five calibration simulations. It can be seen that the calibration error caused by STR noise superposed on angular rates, which is used for synthesizing model DM acceleration, is quite

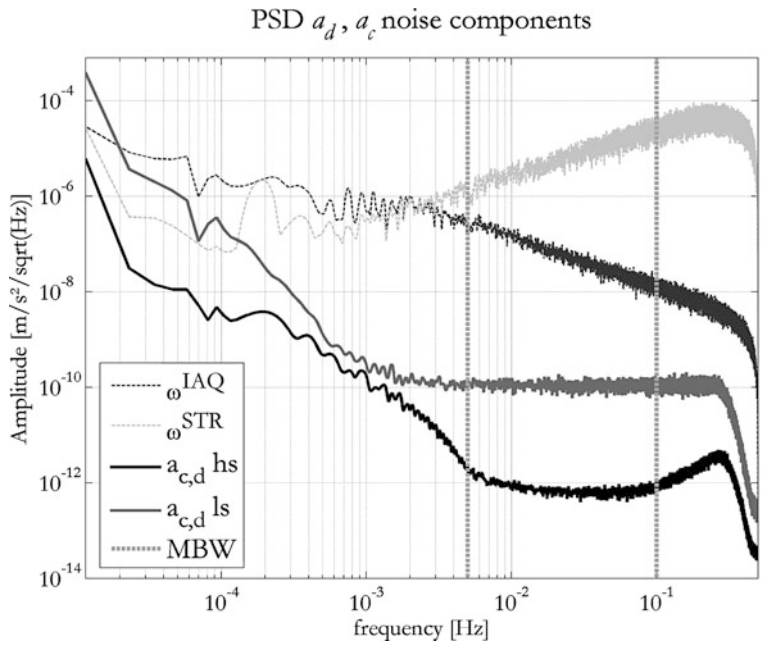


Fig. 20.1 Summary of noise PSD types represented in terms of accelerations by applying Eq. (6). Angular rates noise PSDs from IAQ (*dashed light grey*) and STR data (*dashed dark grey*), CM, DM acceleration noise PSD from gradiometer for ultra high-sensitive axis (*black solid*), CM, DM acceleration noise PSD from gradiometer for low-sensitive axis (*solid grey*), and MBW of the gradiometer (*horizontal dashed*). The angular acceleration noises have been omitted here

Table 20. 1 Comparison of calibration errors derived from different data-sets, 1,000 epochs and conditions approach used

Noise type	Med. error	Max. error
Noise-free	2×10^{-12}	1×10^{-11}
Noise on measured DM	5×10^{-3}	0.89
IAQ noise on angular rates	3×10^{-3}	0.07
STR noise on angular rates	5	30
Noise on meas. DM and IAQ noise on angular rates	1×10^{-2}	0.87

large, while the errors caused by the other noise types remain within a suitable level.

The properties deduced in Table 20.1 were calculated by using the difference between the real (a priori defined) ICM and the estimated ICM:

$$\text{Maximal error: } \max\left(abs(K_{real}^{-} - K_{est}^{-})\right) \tag{20a}$$

$$\text{Median error: } median(abs(K_{real}^{-} - K_{est}^{-})) \tag{20b}$$

20.4.2 Advanced Methods

Based on the noise PSD functions of all input time series, filters were designed, which cut-off or damp those frequencies where the noise level is largest (Mayrhofer, 2008). These filters were applied on the model DM accelerations and the observed CM and DM accelerations. By using this pre-processed data set and applying corresponding variance-covariance information, the calibration error could be reduced below 1×10^{-3} (7 days of data used). Moreover, the use of a high-pass filter strongly reduced the correlation of the estimated alignment parameters with the biases (cf. Fig. 20.2).

The correlation among the estimated ICM parameters is reduced, because low frequencies with high noise level were removed from the signal. A high-pass filter eliminates biases from a signal. Thus, the adjustment of biases is not possible if filtering is applied (Mayrhofer, 2008).

Based on the data derived from the calibration simulations, the three implemented calibration approaches could be compared. All three approaches delivered comparable results, whose quality mainly depends on the applied pre-processing methods. Nevertheless, the modified conditions approach is the preferable approach. It derived the most stable results (Mayrhofer,

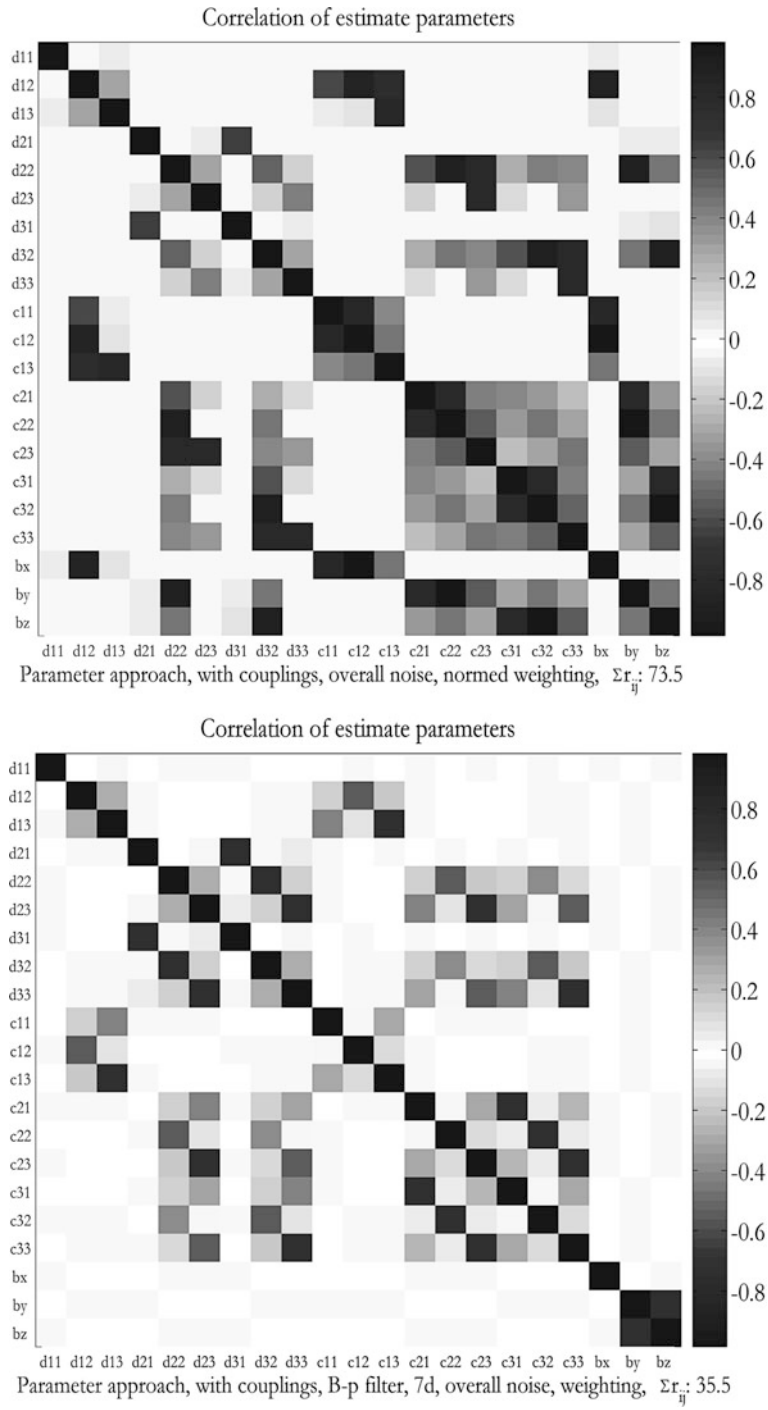


Fig. 20.2 Correlation matrix of estimated parameters computed from 7 days of noisy data (*upper*). After filtering the overall correlation could be strongly reduced (*lower*)

2008), CM and DM measurements variance-covariance information can be used and finally, it enables the use of large data-sets.

By using the GOCE QL-GFA software, which will be used in the operational GOCE processing for the generation of quick-look gravity field solutions (Pail et al., 2006), three gravity field models have been deduced. Figure 20.3 shows the degree median plot of the three error estimates. The grey line represents the error of the gravity field deduced from optimally

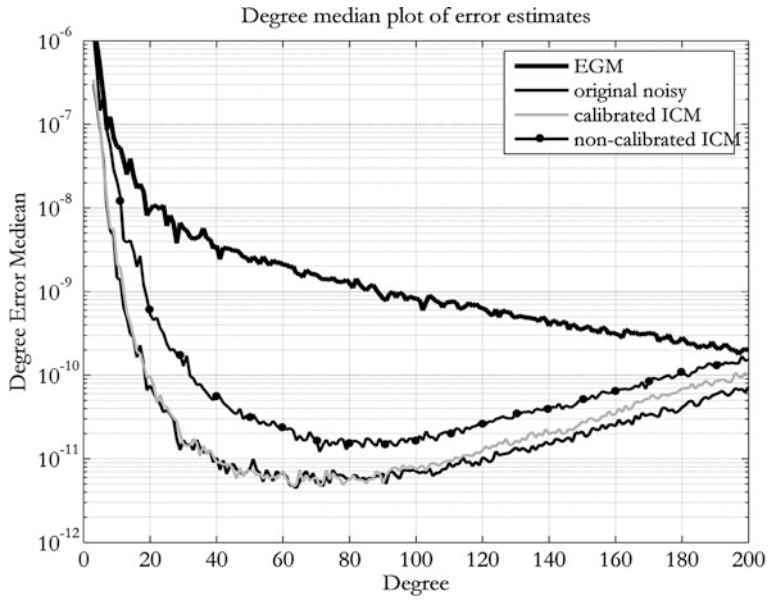


Fig. 20.3 Degree median plot of coefficients error estimates deduced from the ideally calibrated signal (*grey*), from the calibrated signal (*light grey*) and from the uncalibrated signal (*dotted*). The degree median of the EGM coefficients is drawn in black

calibrated data, which means that the calibration matrix is the unit matrix. The dotted line shows the error of the gravity field computed from non-calibrated data. For deducing this data, a calibration matrix ($\sim 10^{-3}$ magnitude of components) has been applied on the optimally calibrated data. Finally, the light grey line shows how the recovery error can be reduced by applying external calibration on the data (Mayrhofer, 2008).

The degree median is defined by:

$$Median_l = median_m(|\overline{R}_{lm}|), \overline{R}_{lm} = \{\overline{C}_{lm}, \overline{S}_{lm}\} \quad (20)$$

Figure 20.3 shows that especially at low degrees of 0–90 the errors of the recovered coefficients deduced from uncalibrated data could be reduced. Also at higher degrees of 91–200, the errors could be strongly reduced. This shows that the methods demonstrated in this study can become reliable tools for validation if appropriate pre-processing is applied to the observations.

20.5 Conclusions

In this study three approaches for external calibration of EGG satellite data on accelerometer level with an a-priori global gravity field model have been presented. The parameter approach cannot handle variance-covariance information of observed CM and DM accelerations. Additional variance-covariance information can be introduced in the conditions approach, but only shorter data sets compared to the parameter approach can be computed. The modified conditions approach combines both benefits, if it can be assumed that the observations are time-uncorrelated.

The influence of non-calibrated data on the quality of gravity field recovery is shown. It has been demonstrated that the overall estimated gravity field recovery error could be strongly reduced, by applying the external calibration methods presented in this paper.

In general, by applying efficient data pre-processing and consistent variance-covariance propagation, all calibration methods described in this study produced reliable results. The calibration error could be reduced below 10^{-3}. If angular rates with lower noise levels were available, the calibration quality could be further improved.

References

Catastini G., S. Cesare, S. De Sanctis, E. Detoma, M. Dumontel, R. Floberhagen, M. Parisch, G. Schi, and A. Anselmi (2003). The GOCE End-To-End System Simulator. Noordwijk, The Netherlands. *Geophys. Res. Abstr.*, 5, 02698, 200.

Heiskanen, W. and H. Moritz (1967). Physical Geodesy. W.H.Freeman & Co Ltd, ISBN-13 978-0716702337.

Koop R. and T. Gruber (2006). GOCE Level 2 Data Handbook, GO-MA-HPF-GS-0110, Issue 3.0.

Mayrhofer R. (2008). External Calibration of SGG observations. Master Thesis, Institutue of Navigation and Satellite Geodesy, Graz University of Technology.

Pail, R., B. Metzler, B. Lackner, T. Preimesberger, E. Höck, W.-D. Schuh, H. Alkathib, Ch. Boxhammer, Ch. Siemes, and M. Wermuth (2006). GOCE gravity field analysis in the framework of HPF: operational software system and simulation results. Proceedings 3rd GOCE User Workshop, Frascati, ESRIN, November 2006, SP-627, 249–256, European Space Agency.

Chapter 21

Covariance Propagation of Latitude-Dependent Orbit Errors Within the Energy Integral Approach

H. Goiginger and R. Pail

Abstract The satellite mission GOCE (Gravity and steady-state Ocean Circulation Explorer) has the demanding task to map the Earth's gravity field with unprecedented accuracy by using state-of-the-art observation technologies. The processing strategy of the orbit data is based on the energy integral approach to determine the long wavelength structure of the gravity field. The final product will consist of the gravity field model in terms of estimated spherical harmonic coefficients and the corresponding error description. The study about covariance propagation of latitude-dependent orbit errors is driven by the fact that the GPS receiver used for GOCE might not have full performance in the case of low-elevation GPS satellites, which might lead to a reduced number of observable satellites in higher latitudes. Therefore, the adjustment procedure is extended by a covariance propagation taking this fact into account. The studies have shown that the consistent error propagation can not significantly improve the coefficient solution itself but it rather provides a correct error description of the result.

21.1 Introduction

The scientific data processing of the GOCE mission (ESA, 1999) is performed by the "European GOCE Gravity Consortium" (EGG-C), a consortium of 10 European universities and research institutes, in the framework of the ESA-funded project "GOCE High-Level Processing Facility" (HPF; Rummel et al., 2004). In the frame of this contract, the "Subprocessing Facility (SPF) 6,000", a co-operation of TU Graz, Austrian Academy of Sciences, University of Bonn, and TU Munich, under the lead of TU Graz, is responsible for the processing of a spherical harmonic Earth's gravity field model and the corresponding full variance-covariance matrix from the precise GOCE orbit and from satellite gravity gradiometry (SGG) data.

The long wavelength part of the gravity field recovery is based on the energy integral approach (Jekeli, 1999; Visser et al., 2003) where the velocity of the satellite serves as basic input. Since the satellite velocity is not directly observed but derived from the measured satellite position, a suitable numerical differentiation technique should be applied. Results of the investigations on numerical differentiation applying the Taylor-MacLaurin and the Newton-Gregory method can be found in Goiginger and Pail (2006).

21.2 Mathematical Formulation

To derive the velocity of the satellite from the kinematic orbit positions, numerical differentiation methods can be applied. In the following, the Taylor-MacLaurin differentiator is introduced, which is based on a Taylor series expansion in each position. Let us consider a set of differentials Δ^j at a certain sampling point k,

$$\Delta_k^j = \frac{x_{k+j} - x_{k-j}}{2j\delta} \tag{1}$$

H. Goiginger (✉)
Institute of Navigation and Satellite Geodesy, Graz University of Technology, Graz A8010, Austria
e-mail: h.goiginger@tugraz.at

S.P. Mertikas (ed.), *Gravity, Geoid and Earth Observation*, International Association of Geodesy Symposia 135,
DOI 10.1007/978-3-642-10634-7_21, © Springer-Verlag Berlin Heidelberg 2010

where x indicates one of the three coordinates of the satellite 3D-position. The discrete function $x_k = x(t_k)$represents one of the three coordinates where

$$t_k = t_{k-1} + \delta \qquad k = 1,2,\ldots,n \tag{2}$$

and δ is a constant sampling interval. Inserting a Taylor series at position *(k–j)* and *(k+j)* in Eq. (1) yields

$$\Delta^j_k = x'_k + j^2\frac{1}{6}\delta^2 x'''_k + j^4\frac{1}{120}\delta^4 x^V_k + \ldots \tag{3}$$

To solve for the derivatives of the function x_k, the equation system according to Eq. (4) can be established. The vector containing the pseudo-observed differentials $\Delta^j{}_k$ is denoted as observation vector $\boldsymbol{l}$, whereas the vector $\boldsymbol{u}$ is composed of the unknown derivatives of the function x_k.

$$l = A \cdot u$$

$$\begin{bmatrix} \Delta^1_k \\ \Delta^2_k \\ \Delta^3_k \end{bmatrix} = \begin{bmatrix} 1 & \frac{1}{6} & \frac{1}{120} \\ 1 & \frac{4}{6} & \frac{16}{120} \\ 1 & \frac{9}{6} & \frac{81}{120} \end{bmatrix} \cdot \begin{bmatrix} x'_k \\ \delta^2 x'''_k \\ \delta^4 x^V_k \end{bmatrix} \tag{4}$$

The first element of the parameter vector represents the first derivative and, consequently, the satellite velocity. If the order of derivatives is smaller than the number of differences, an over-determined system can be established, which is solved by a standard least squares adjustment approach. Thus, it is suited to implement a covariance propagation by introducing a weight matrix. The weight of each observation $\Delta^j{}_k$ is related to its measurement accuracy. Since the observation vector $\boldsymbol{l}$, composed by the differentials $\Delta^j{}_k$, is not directly measured, but rather derived from the satellite positions, the variance$\sigma^2_{\Delta^j_k}$, and thus the weight, has to be computed from the known orbit errors. Therefore, a propagation of the orbit errors was performed. First, the basic observation equation Eq. (1) of the differentials is transformed into the matrix-vector notation.

$$y = B \cdot x$$

$$\begin{bmatrix} \Delta^1 \\ \Delta^2 \\ \Delta^3 \end{bmatrix} = \begin{bmatrix} 0 & 0 & -\frac{1}{2\delta} & 0 & \frac{1}{2\delta} & 0 & 0 \\ 0 & -\frac{1}{4\delta} & 0 & 0 & 0 & \frac{1}{4\delta} & 0 \\ -\frac{1}{6\delta} & 0 & 0 & 0 & 0 & 0 & \frac{1}{6\delta} \end{bmatrix} \begin{bmatrix} x_{-3} \\ x_{-2} \\ x_{-1} \\ x_0 \\ x_1 \\ x_2 \\ x_3 \end{bmatrix} \tag{5}$$

As an example, an equation system of a set of three differentials (*j=1,2,3*) at a certain epoch k has been established. Then the solution vector $\boldsymbol{y}$ is composed of the differentials, where vector $\boldsymbol{x}$ contains the known positions along one axis. Seven positions are required to compute three differentials. The transformation of vector $\boldsymbol{x}$ to vector $\boldsymbol{y}$ is charact-erized by the matrix $\boldsymbol{B}$.

The propagated errors of the solved differentials (which are subsequently the input of the adjustment process) can be determined by

$$\Sigma(\Delta^j) = B.\Sigma(x_i).B^T. \tag{6}$$

The quadratic and symmetric matrix $\Sigma(x_i)$ contains the information about the known orbit errors (cf. Eq. (7)). Note: it is assumed that there are no temporal correlations, i.e., $\sigma_{k+j,k-j} = 0$, as well as no correlation between the x-, y-, and z-direction of the satellite position.

$$\Sigma x_i = \begin{bmatrix} \sigma^2_{-3} & 0 & \cdots & 0 \\ 0 & \sigma^2_{-2} & \cdots & 0 \\ \vdots & \vdots & \ddots & \vdots \\ 0 & 0 & \cdots & \sigma^2_3 \end{bmatrix} \tag{7}$$

Due to the assumption stated above and the structure of the transformation matrix $\boldsymbol{B}$, the covariances of the differentials are zero. Thus the result of Eq. (6) is a diagonal matrix containing the variances of the differentials Δ^j.

Therefore, to simplify, the pythagorean sum of the basic observation equation (cf. Eq. (1)) can be formed to determine the propagated variance of the differentials:

$$\sigma^2_{\Delta^j_k} = \frac{1}{4j^2\delta^2}(\sigma^2_{k+j} + \sigma^2_{k-j}) \tag{8}$$

with $\sigma_{k\pm j}$as the standard deviation of the satellite position in each direction at a certain epoch ($k\pm j$).

Now, the weight of observation j at epoch k arises from the reciprocal of the inherent $\sigma^2_{\Delta^j_k}$, assuming the variance of the unit weight to be one.

$$P = \Sigma(\Delta^j_k)^{-1} = \begin{bmatrix} \frac{1}{\sigma^2_{\Delta^1_k}} & 0 & \cdots & 0 \\ 0 & \frac{1}{\sigma^2_{\Delta^2_k}} & \cdots & 0 \\ \vdots & \vdots & \ddots & \vdots \\ 0 & 0 & \cdots & \frac{1}{\sigma^2_{\Delta^n_k}} \end{bmatrix} \tag{9}$$

Expanding the equation system by the weight matrix $\boldsymbol{P}$ yields

$$\hat{u} = (A^T PA)^{-1} A^T Pl \tag{10}$$

The covariance matrix of the estimated parameters, i.e., of the derivatives, is obtained from

$$\Sigma(\hat{u}) = (A^T PA)^{-1} \tag{11}$$

Finally, the variance of the derived velocity can be found in element (1,1) of the covariance matrix.

The variance is used to set up a weight matrix for the least squares adjustment of the spherical harmonic coefficients in the energy integral software. Note: the assumption that the coordinates of each position are uncorrelated is in reality not true but feasible. Previous investigations (Jandrisevits, 2005) have shown that a full covariance propagation under consideration of correlations does not essentially improve the final result. Moreover, studies with real orbit data including covariances of the positions demonstrated that these covariances do not always describe the real correlations properly.

21.3 Test Data Sets

To evaluate the effect of latitude-dependent errors, the Astronomical Institute of the University of Bern (AIUB) performed studies with a GOCE-like orbit configuration (Bock et al., 2007). Based on this knowledge, the problem is investigated in a more general frame. Therefore, several case studies based on different noise scenarios have been processed. The test data set is composed of a noise-free orbit with GOCE characteristics, for a measurement period of 59 days, and with 1 s sampling. The orbit is based on the gravity field model OSU91a (Rapp et al., 1991) complete to degree/order 80. Three noise scenarios, which are listed in Table 21.1, shall be investigated.

In noise scenario [NM 1], a white noise time series with a standard deviation of $\sigma = 1$ cm is superposed to the x-, y-, and z-coordinate of the satellite position. Noise model [NM 2] is composed with the assumption that the position accuracy in all three coordinates decreases linearly in dependence of the geographical latitude, starting at $|\varphi| = 60°$ (cf. Fig. 21.1 top).

Table 21.1 Noise models

Acronym	Description
[NM 1]	White noise: std.dev. of orbit positions $\sigma = 1$ cm
[NM 2]	Uniformly increasing degradation towards the poles
[NM 3]	Approximation of error characteristics of a realistic noise scenario

[NM 3] is based on the case study performed by AIUB, where the latitude-dependent accuracy of the three coordinates behaves differently (cf. Fig. 21.1 bottom).

On the one hand the individual noise time series are superposed to the "true" orbit, and on the other hand the statistical characteristics of these noise models are introduced into the adjustment procedure to provide an appropriate error description of the final geopotential coefficient solution.

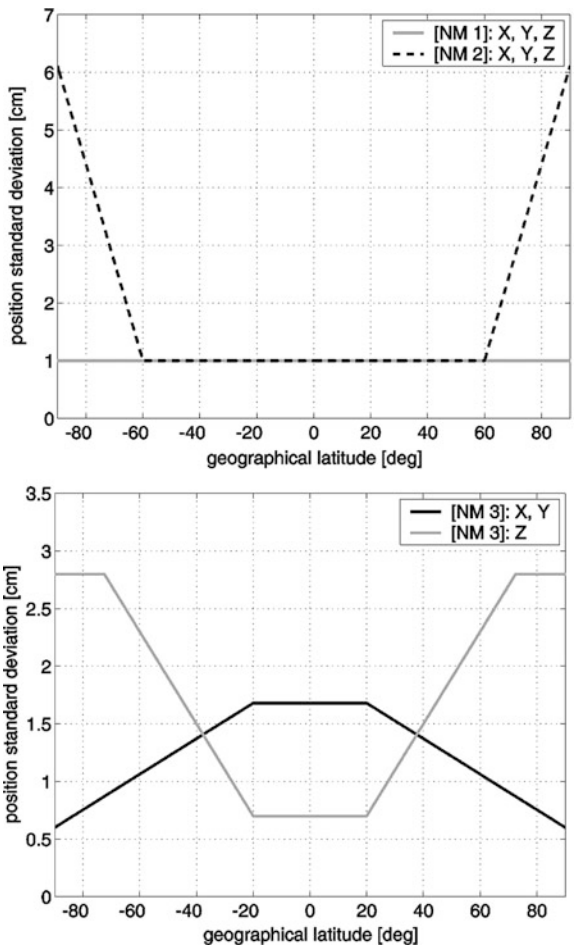


Fig. 21.1 Noise models for the three case study scenarios

21.4 Gravity Field Recovery

Generally, one of the basic assumptions in the processing of satellite-to-satellite tracking in high-low mode (SST-hl) orbit data is that the noise characteristics are (close to) white. In the present case studies [NM 2] and [NM 3], however, this is certainly not the case, but there is a significant dependence of the noise amplitude on the geographical latitude. Therefore, the case studies shall be processed applying two strategies:

- assumption of white noise, and
- assumption that the overall error characteristics of the orbit positions are known: In this case, a covariance propagation is performed, and the error information is used both in the numerical differentiation as well as for the set-up of a non-Euclidean metric in the frame of the gravity field processing.

21.4.1 Simulation Results with White Noise Assumption

Figure 21.2 shows the deviations of the recovered gravity field solutions from the reference gravity field model in terms of the degree error median.

The most obvious differences among the three curves appear in the lower degrees, where the scenario [NM 2] (black curve) yields the worst solution. To show the impact of the three test scenarios on the coefficient solutions more clearly, the cumulative geoid height errors are plotted in Fig. 21.4 (top). The solution based on kinematic orbit positions with the noise model [NM 1] superposed (Fig. 21.4 top left) shows larger geoid height errors around the equatorial region than at the polar areas. This is due to the denser data distribution in higher latitudes. Considering the scenario [NM 2], the situation is different. In addition to the geoid height errors at the equatorial region, the errors at higher latitudes (starting at $|\varphi| = 60°$) are larger because of the continuously degrading accuracy of the kinematic orbit positions towards the poles. The magnitude of the geoid height errors of the solution based on the [NM 3] orbit data is obviously in between of the geoid height errors based on the other two noise scenarios (cf. Table 21.2). The largest errors occur in the mid-latitude regions, which corresponds to the region of the crossing points of the latitude-dependent orbit errors (cf. Fig. 21.1 bot.).

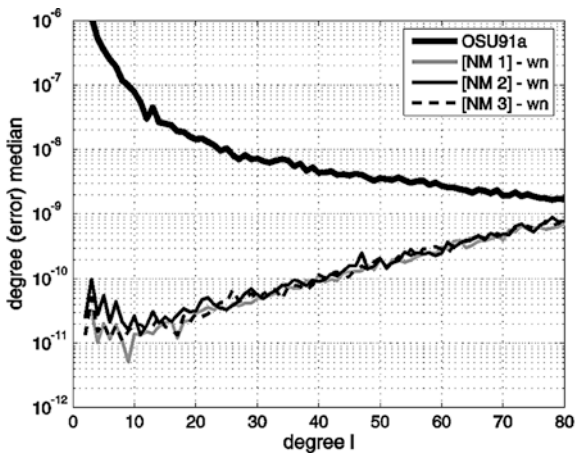


Fig. 21.2 Degree (error) median of SST-only gravity field solutions based on the different orbit noise scenarios

Table 21.2 Standard deviations of cumulative geoid height errors based on white noise assumption or on covariance propagation of the three noise models

	Geoid height errors [cm]	
Acronym	White noise assumption	Covariance propagation
[NM 1]	28.8	28.8
[NM 2]	35.9	33.9
[NM 3]	33.4	32.7

21.4.2 Simulation Results with Covariance Propagation

In contrast to the previous case studies, now the latitude-dependent error information is included as the metric of the system, by applying full covariance propagation based on the (known) error information of the orbit products. Figure 21.3 illustrates the deviations of the recovered gravity field solutions from the reference gravity field model in terms of the degree error median for [NM 2] and [NM 3], but now using full error propagation. In the case of [NM 1], the Euclidean metric is the correct error model, and thus there are no changes with respect to the previous simulation.

Evidently, the coefficient solution improves only slightly due to the use of the correct stochastic model.

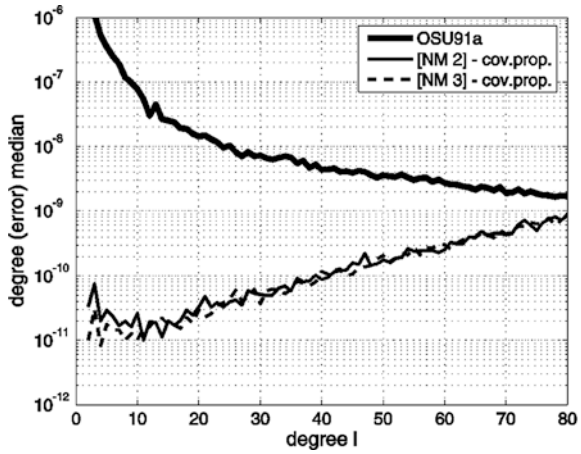


Fig. 21.3 Degree (error) median of SST-only gravity field solutions based on [NM 2] and [NM 3] with white noise assumption compared to covariance propagation

Thus, the computed geoid height errors are almost equivalent. That is the reason why it is also referred to Fig. 21.4 (top row), which shows the absolute coefficient deviations of the three noise models. The bottom row shows that the statistical error description reflects the geoid height errors in relation to the different noise models. The statistical error estimates of [NM 1] will apply for all three solutions, if the studies are based on the white noise assumption (as it was done in the previous section).

An overview of the standard deviations of these geoid height difference fields based on the Euclidean metric and on the full covariance propagation is provided in Table 21.2.

Evidently, there are only marginal improvements of the geoid height errors due to the application of the correct stochastic model, which is consistent with the conclusion drawn already from the comparison of the coefficient estimates.

In the case of [NM 1] of Fig. 21.4, the improved accuracy towards the poles is due to meridian convergence of the orbits, and thus a larger number of observations in near-polar regions with homogenous measurement accuracy. Concerning [NM 2], the degraded measurement accuracy towards the poles (cf. Fig. 21.1) leads to a reduced geoid height accuracy, which is reflected both in the geoid height deviations from the true reference (cf. Fig. 21.4 (top center)) and the geoid height standard deviations (bottom center). In the case of [NM 3], the spatial error bands in the mid-latitudes, which are also related to the initial orbit error model (cf. Fig. 21.1), are consistently reflected in the absolute deviations (top right) and the statistical error description (bottom right). The additionally

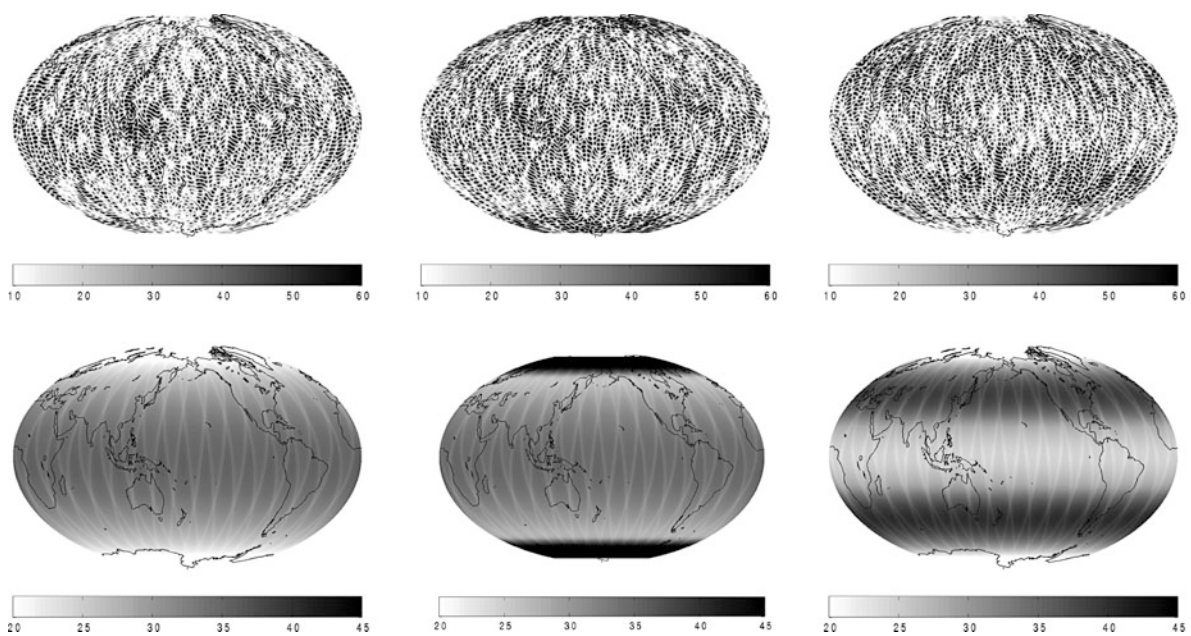


Fig. 21.4 Cumulative geoid height errors [cm] at degree/order 80 (*top*) and corresponding statistical error estimates [cm] (*bottom*) based on the three noise characteristics [NM 1] (*left*), [NM 2] (*center*) and [NM 3] (*right*)

visible orbit structure is due to the input data distribution, because the orbit data do not compose a perfect repeat cycle.

So far, the main conclusion could apparently be that the quality of the solution is quite insensitive to the metric applied in the normal equation system. In order to demonstrate that the use of a correct stochastic model is indeed important, Fig. 21.5 shows the standard deviation per geographical latitude from the geoid height differences, as well as a mean standard deviation per geographical latitude computed from the propagated geoid height standard deviations, for [NM 2]. In the case of the white noise assumption (Euclidean metric), the stochastic error estimate (dashed gray curve) corresponds to the one of [NM 1], and is inconsistent with the true geoid height errors per latitude (gray curve). If the correct stochastic model (in this case [NM 2]) is used and consistently propagated, the gravity field solution is only slightly improved (black curve). This fact has already been emphasized above.

However, the statistical error information (dashed black curve), which is obtained from covariance propagation, is now perfectly consistent, i.e., it describes the true error behaviour of the gravity field solution very well.

A similarly consistent picture is obtained when analyzing the results based on [NM 3], which are shown in Fig. 21.5 bottom. Here, only the results using the consistent stochastic model are included.

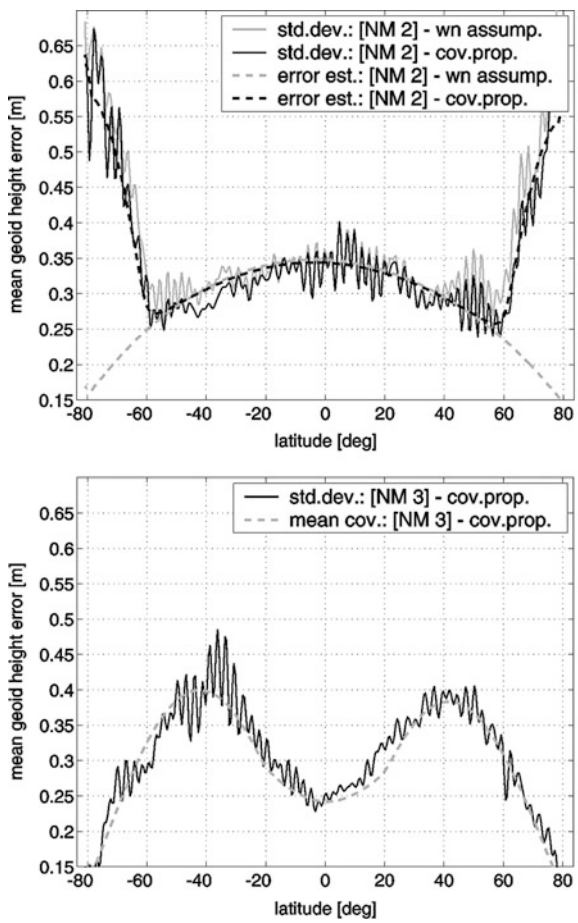


Fig. 21.5 Mean geoid height errors per degree: simulation based on [NM 2] (*top*) and [NM 3] (*bottom*)

21.5 Conclusion

It was demonstrated that the latitude-dependent orbit errors in the case of low GPS satellites are reflected in the final gravity field solutions in a characteristic way, leading to a modified spatial error structure. Based on several simulations it was shown, that the consistent propagation of latitude-dependent errors (assuming that these error characteristics are known a-priori) through the gravity field adjustment procedure, where they are used to modify the metrics of the normal equation systems, can not significantly improve the coefficient solution itself. However, the incorporation of the correct stochastic model leads to a consistent propagation to the variance-covariance information. A correct covariance information is important in the course of the combination with the SGG component, because a degraded accuracy of the SST gravity field component in a certain region, which is correctly reflected by the corresponding covariance information, will lead to a modified relative weighting of the SST and the SGG component. Therefore, if in reality there is indeed a significant spatial correlation of the orbit accuracy (due to the elevation cut-off or any other reason), it should be taken into consideration in the stochastic model.

References

Bock, H., A. Jäggi, D. Svehla, G. Beutler, U. Hugentobler, and P. Visser (2007). Precise orbit determination for the GOCE satellite using GPS. *Adv. Space Res.*, 39, 1638–1647.

ESA (1999). Gravity Field and Steady-State Ocean Circulation Explorer Mission. Reports for Mission Selection. The

Four Candidate Earth Explorer Core Missions, SP-1233(1), European Space Agency, Noordwijk, The Netherlands.

Goiginger, H. and R. Pail (2006). Investigation of velocities derived from satellite positions in the framework of the energy integral approach. In: Pro. *3rd GOCE User Workshop*, ESA SP-627, Frascati, European Space Agency, Noordwijk, The Netherlands, pp. 319–324.

Jandrisevits, C. (2005). Numerische Differentiationsverfahren mit voller Kovarianz-Information im Rahmen der GOCE-Erdschwerefeldlösung. *Master thesis*, Graz University of Technology.

Jekeli, C. (1999). The determination of gravitational potential differences from satellite-to-satellite tracking. *Celestial Mech. Dynamical Astron*., 75, 85_101.

Rapp, R.H., Y.M. Wang, and N.K. Pavlis (1991). The Ohio State 1991 geopotential and sea surface topography harmonic coefficient models. *Report*, The Ohio State University, Columbus, Ohio. no. 410.

Rummel, R., T. Gruber, and R. Koop (2004). High level processing facility for GOCE: Products and processing strategy. In: *Proc. Second International GOCE User Workshop "GOCE, The Geoid and Oceanography"*, ESA SP-569, Frascati, March 2004, European Space Agency, Noordwijk, The Netherlands.

Visser, P.N.A.M., N. Sneeuw, and C. Gerlach (2003). Energy integral method for gravity field determination from satellite orbit coordinates. *J. Geodesy*, 77, 207–216.

Chapter 22

Future Mission Design Options for Spatio-Temporal Geopotential Recovery

T. Reubelt, N. Sneeuw, and M.A. Sharifi

Abstract Sampling the Earth from single-satellite missions or single-orbit formations is necessarily limited by the mandatory balance between spatial and temporal resolution. A short repeat period leads to sparse ground-track spacing. Conversely, dense satellite coverage can only be attained at the cost of time resolution. For future gravity field missions, geoscience communities are pushing for ever higher resolution than GRACE, both in time and space. A logical consequence would be multi-satellite and/or multi-groundtrack configurations.

We investigate the basic parameters that determine space-time resolution. Under the assumption of a repeat orbit two basic rules for sampling the Earth from space are provided. The familiar Nyquist rule of thumb links the number of revolutions in a repeat period to the maximum spherical harmonic degree. A second sampling rule, expressing the balance between spatial and temporal resolution, is coined the Heisenberg rule.

Simulations demonstrate how future mission concepts might benefit from multi-satellite/multi-groundtrack configurations.

22.1 Introduction

With the GRACE mission, which was launched in spring 2002, for the first time global time-variable gravity fields could be recovered beyond the lowest degrees. The mission concept consists of a twin satellite leader-follower formation with an intersatellite distance of about 220 km, flying on a near-polar orbit. The K-band sensor, which provides range-rate with an accuracy of a few μm/s, allows for monthly time-variable geopotential recovery with a spatial resolution of about 1,000 km. The monthly GRACE solutions clearly show the continental scale hydrological (H) cycle (Tapley et al., 2004). Long-term GRACE time series also reveal trends in deglaciation in Antarctica or Greenland (Chen et al., 2006) as well as sea level rise.

Despite the huge progress in time-variable gravity research, the GRACE concept suffers from inherent deficiencies that lead to an erroneous North-South striping pattern (Schrama et al., 2007). Figure 22.1 attributes the error pattern to three sources:

i. The range-rate-observable in a leader-follower formation itself, which is an anisotropic functional, combined with the error structure due to North-South groundtracks and with a limited sensor accuracy.
ii. Aliasing due to temporal and spatial undersampling of the time-variable signals, combined with a time-variable groundtrack.
iii. Errors and aliasing due to limited dealiasing products used to correct the GRACE-measurements for high-frequency signals of the atmosphere and ocean and of the ocean tides.

The mitigation of these problems is the main task when designing a future mission for improved time-variable gravity determination (Sneeuw et al., 2004). Problem (*i*) is addressed on the one hand by a future laser-instrument, which can measure the range-rates

T. Reubelt (✉)
Institute of Geodesy, Universität Stuttgart, Stuttgart D-70174, Germany
e-mail: reubelt@gis.uni-stuttgart.de

S.P. Mertikas (ed.), *Gravity, Geoid and Earth Observation*, International Association of Geodesy Symposia 135,
DOI 10.1007/978-3-642-10634-7_22, © Springer-Verlag Berlin Heidelberg 2010

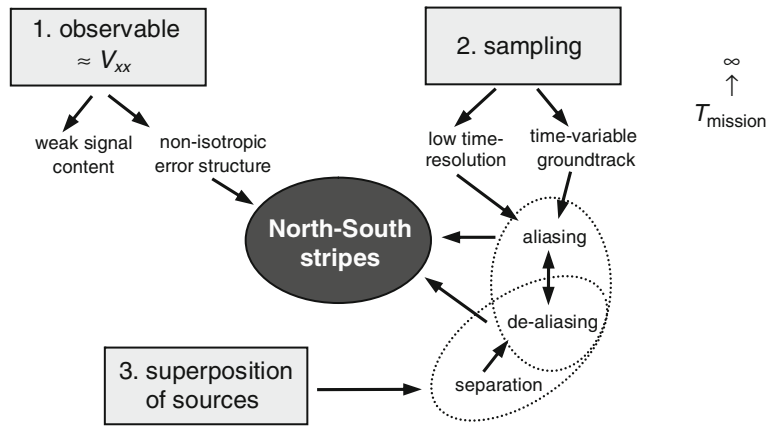


Fig. 22.1 Limitations of the GRACE-type mission concept

with an improved accuracy of 2–3 orders of magnitude compared to the GRACE K-band instrument (Bender et al., 2003). In addition, advanced satellite formations as the pendulum or the cartwheel produce signals with a much higher isotropy than a leader-follower formation (Sharifi et al., 2007; Sneeuw et al., 2008).

Problem (*ii*) can fundamentally only be solved by proper sampling, i.e., by a suitable configuration of satellites, which may improve both the spatial and temporal sampling of the time variable signals and thus reduces aliasing.

Problem (*iii*) may be reduced by improved atmosphere/ocean (A/O) and ocean tides (T) dealiasing products or co-estimation of A/O/T-parameters. Another option is the establishment of a satellite configuration, which is able to sample the time-variable effects of the A/O/T signals (or their errors after dealiasing) properly. Problems (*ii*) and (*iii*) are currently entangled through the dealiasing concept. With proper sampling from a suitable satellite configuration the so-called de-aliasing products may be used for separating the gravitational sources.

The treatment of the aliasing problem and the spatio-temporal sampling of a satellite mission and/or configuration is the main focus of this contribution.

22.2 Spatio-Temporal Sampling and the Heisenberg Sampling Rule

22.2.1 Single Sensor Missions

In order to reduce the aliasing effects due to time-variable groundtracks, only repeat orbits are considered. A satellite on a so-called β/α repeat orbit fulfils β revolutions in α nodal days, where β and α are relative primes. Thus, the repeat period of such a satellite is $T_{\text{rep}} = \alpha$ [nodal days] with a revolution time of $T_{\text{rev}} = \alpha/\beta$ [nodal days]. We take the equatorial track spacing as a representation measure of the spatial scale $D_{\text{space}} = 2\pi/\beta$ [rad]. For the temporial scale we simply use $D_{\text{time}} = \alpha$.

The product between the spatial sampling D_{space} and the temporal sampling D_{time} yields:

$$D_{\text{space}} \times D_{\text{time}} = 2\pi\alpha/\beta = 2\pi\, T_{\text{rev}} \tag{1}$$

Since the revolution time T_{rev} of a low-Earth orbiting satellite (LEO) is varying only marginally with the orbit height h, e.g., $T_{\text{rev}}(h = 300\text{ km}) \cong 90^{\text{m}}\ 22^{\text{s}}$, T_{rev} $(h = 500\text{ km}) \cong 94^{\text{m}}\ 28^{\text{s}}$), the product Eq. (1) can be regarded as a constant:

$$D_{\text{space}} \times D_{\text{time}} = const. \tag{2}$$

We call it the Heisenberg uncertainty principle of spatio-temporal sampling of a satellite because of the analogy to quantum physics. It means in other words, the better the temporal sampling is, the worse the spatial sampling becomes, and vice versa. The Heisenberg rule is demonstrated in Fig. 22.2.

Equation (2) is the equation of a hyperbola, on which any β/α repeat orbit is represented by a dot. Such a dot defines the space-time sampling space covered by the satellite mission (grey box, top right). Moving the dot to the left, i.e., improving the spatial resolution, automatically shifts the dot upwards, i.e., poorer time resolution.

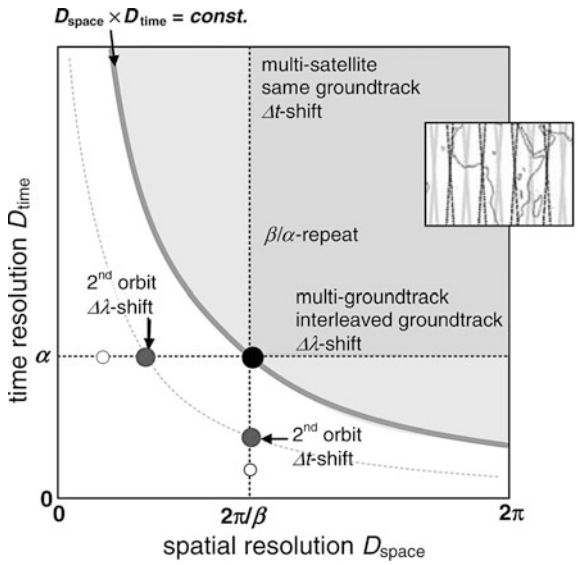


Fig. 22.2 Space-time sampling of satellite configurations

22.2.2 Multi-Sensor Missions

Within this paper, we consider a single satellite as well as a low–low SST (Satellite-to-Satellite-Tracking) formation, which both observe one gravitational functional, as a sensor.

Without compromising the time-resolution, the spatial sampling can only be improved by additional satellites on interleaved groundtracks with a $\Delta\lambda$-shift (longitudinal shift, multi-groundtrack configuration). In a similar vein, without changing the spatial sampling, the temporal sampling is improved by additional satellites on the same groundtrack with a Δt-shift (time-shift, multi-satellite configuration). Now, given a required space and time resolution, the number N of needed "sensors" is determined from the Heisenberg rule:

$$N \geq \left(\frac{2\pi T_{\text{rev}}[d]}{D_{\text{space}} \times D_{\text{time}}}\right) = \left(\frac{2\pi\alpha/\beta}{D_{\text{space}} \times D_{\text{time}}}\right) \quad (3)$$

Naturally, this number N represents a worst-case scenario, because also the aforementioned $D_{\text{space}} = 2\pi/\beta$ and $D_{\text{time}} = \alpha$ were worst-case numbers. In reality we have crossing arcs, groundtrack convergence towards the poles, sub-cycles, only approximate repeat orbits and so on, where the space and/or time sampling might be better. Nevertheless, we assert that any spatio-temporal sampling requirement can be fulfilled with different repeat modes β/α, if the Δt-shifts, $\Delta\lambda$-shifts and the number of sensors are selected adequately.

The maximum resolvable degree $L_{\max}$ of the spherical harmonics series expansion can be determined by the Nyquist rule of thumb from the number of revolutions β by

$$L_{\max} = \text{floor}(\beta/2). \quad (4)$$

Spatial patterns with $l > L_{\max}$ are undersampled and will alias into the solution (spatial sampling). The same holds for time-variable signals with periods $T < 2D_{\text{time}}$. They are temporally undersampled and will therefore alias into the results.

22.3 Simulations

In this section, the Heisenberg rule for the spatio-temporal sampling of satellites and its use in designing satellite configurations is demonstrated through a number of simulations. The simulation scenarios are based on CHAMP-like near polar (inclination $I = 87°$) and circular (eccentricity $e = 0$) satellite orbits at orbital heights of $h \cong 410$ km. A simple 31/2 repeat mode was chosen, which leads to a spatial sampling of $D_{\text{space}} = 360°/\beta = 11.61°$ ($\hat{=} L_{\max} = 15$) and temporal sampling of $\Delta T = D_{\text{time}} = \alpha = 2$ (nodal) days for a single satellite. As an observable, the time variable gravitational potential V was used. The simulated measurements are noise-free in order to investigate the pure aliasing effect.

The input for orbit and signal synthesis was a gravity field up to degree $L = 31$, composed of the static gravity field EGM96 (Lemoine et al., 1998) and 6-h time-variable gravity fields (linear interpolation in between). The latter were produced as GOCE-dealiasing products (Th. Gruber, IAPG, TU Munich, priv. comm.) and include the time variable effects of the ECMWF atmosphere (A), the OMCT ocean bottom pressure (O) and a GRACE seasonal correction up to $L = 20$ (H).

Within the gravity field analysis, 4-day solutions were estimated up to a spherical harmonic degree $L = 31$. The solutions were compared to the 4-day mean signal of the time-variable input-fields in order to investigate the aliasing effects due to spatial and temporal undersampling. The main time-variable signal within 4 days is produced by the short period A/O

signal, so that possible temporal aliasing effects should become clearly visible.

Several satellite configurations have been tested with additional satellites on Δt-shifts (same groundtracks) and $\Delta\lambda$-shift (interleaved groundtracks) to improve the temporal and spatial sampling:

(a) satellite 1: single satellite
(b) satellites 1+2: Δt-shift = 1 d
(c) satellites 1+3: $\Delta\lambda$-shift = $360°/(2\beta) = 5.8°$
(d) satellites 1+2+3+4: $\Delta\lambda$-shift = 5.8° and Δt-shift = 1 d
(e) satellites 1+2+7+8: Δt-shift = 1 d and $\Delta\Omega$-shift = $360°/(7.5{\cdot}\beta) = 87.1°$ on interleaved groundtrack ($\hat{=}\Delta\lambda = 5.8°$)
(f) satellites 1+2+3+4+5+6+9+10: Δt-shifts of 0.2581 d, 1 d and 1.2581 d (irregular due to the applied $\Delta\Omega$-shift), $\Delta\lambda$-shift = 5.8°, $\Delta\Omega$-shift = $360°/(8{\cdot}\beta) = 92.9°$ on same groundtracks

The resulting time and space resolutions are listed in Table 22.1. The inertial orbits and the initial positions at time t_0 of the used satellites as well as their resulting groundtracks on the surface of the Earth (spherical coordinates λ, ϕ) are displayed in Figs. 22.3 and 22.4. Satellites producing the same groundtrack as satellite 1 are coloured in dark grey while satellites following the interleaved groundtrack of satellite 3 are in light grey. As can be seen, satellites flying on the same inertial orbit plane do not necessarily produce the same groundtrack and vice versa. Thus the design of a suitable satellite configuration w.r.t. the inertial system is quite a complex task.

Besides the Δt- and the $\Delta\lambda$-shifts a third option was applied in scenarios (e) and (f): a $\Delta\Omega$-shift of the orbital plane. The $\Delta\Omega$-shift can be established in two ways. Either it shifts the new satellite again on the same groundtrack, so that it acts as a kind of

Table 22.1 Spatio-temporal sampling of configurations a–f and aliasing errors of a 4-day solution

Configurations	ΔT [d]	D_{space} [°]	min [mm]	max [mm]	RMS [mm]
a	2	11.6	−32.7	33.7	12.1
b	1	11.6	−4.9	4.8	1.3
c	2	5.8	−7.7	6.9	1.3
d	1	5.8	−1.4	1.8	0.4
e	1	5.8	−4.6	4.3	1.0
f	0.5	5.8	−0.9	0.9	0.1

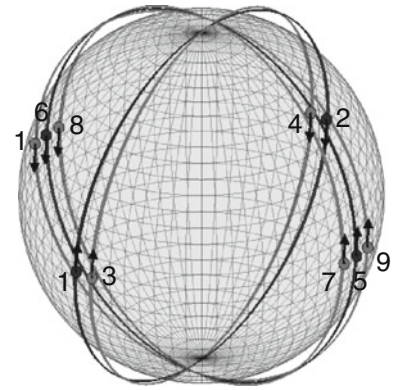


Fig. 22.3 Orbits in the inertial system; dark grey/light grey: satellites on same/interleaved groundtracks

Δt-shift, or the new satellite is shifted on an interleaved groundtrack so that it acts as $\Delta\lambda$-shift. The $\Delta\Omega$-shift, especially for $\Delta\Omega \cong 90°$, is regarded as an interesting option for reducing tidal aliasing. While one satellite is orbiting in the plane of a tidal maximum, the other samples the tidal minimum. Though tides are not considered here, this option is studied for completeness.

22.4 Results

The resulting aliasing errors of the 4-day-solutions for the satellite configurations (a–f) are displayed in Fig. 22.5 in terms of degree RMS (Root Mean Square). Figure 22.6a–f shows the spatial distribution of the aliasing errors in terms of geoid height in [mm]. For comparison, the variability of the 6 h-fields over the same 4-day period is illustrated in Fig. 22.7. Table 22.1 lists the minimum, the maximum and the global RMS value of the resulting aliasing error for the different tested satellite configurations.

Since it violates the Nyquist rule, the single sensor configuration (a) suffers significantly from the spatial and temporal undersampling. Thus very large aliasing errors occur with a global RMS of 12.1 mm and maximum distortions of 33.7 mm. Especially the coefficients $c_{31,31}$ and $s_{31,31}$ show large errors, such that they are omitted in Fig. 22.6a and Table 22.1. If a second satellite is added, the aliasing reduces significantly. Both configurations (b) and (c) are able to reduce the aliasing errors by a factor of about 10, if the

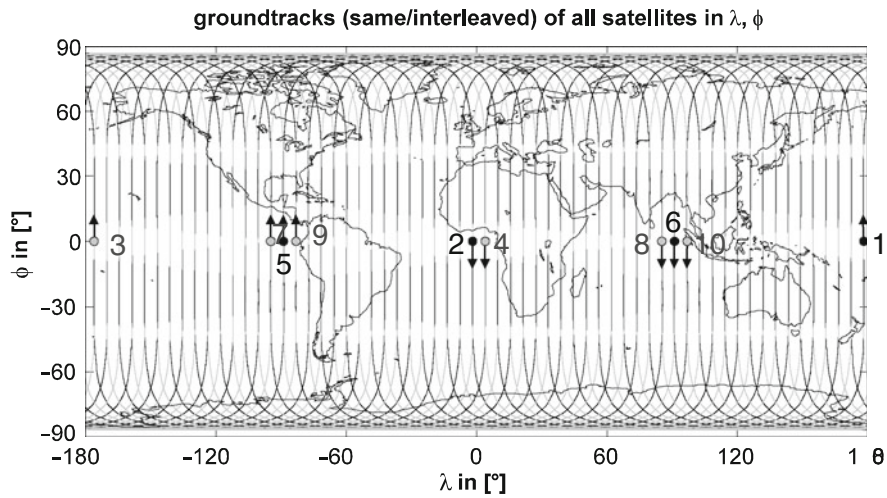


Fig. 22.4 Groundtracks (same/interleaved) of the satellites

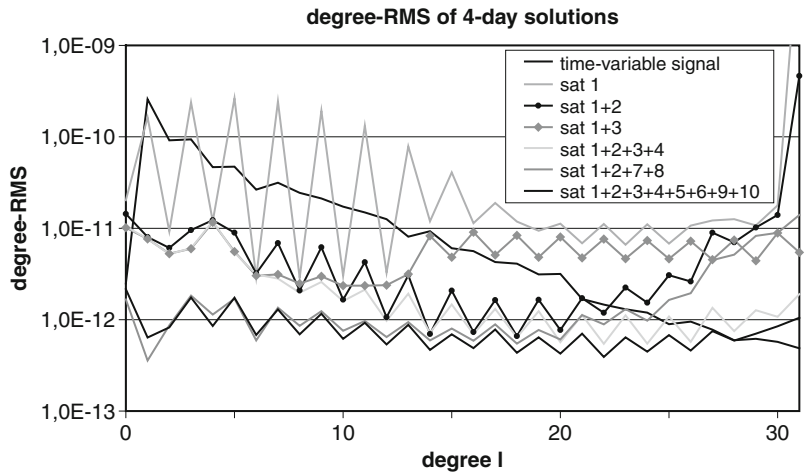


Fig. 22.5 Aliasing errors: degree RMS of 4-day solutions for different satellite configurations

global RMS value is regarded. Comparing Fig. 22.6b, c, though, reveals different aliasing behaviour between the two scenarios. Configuration (b), which has an improved temporal sampling, still suffers from spatial undersampling. According to the theory, this configuration is only able to sample signals up to the maximum degree $L_{\max} = 15$. But as it can be seen in Fig. 22.6b the degree RMS-curve rises not until degree $l = 25$ (rapid rise for $l > 25$), which demonstrates that the Nyquist rule is a rule of thumb. Again, the coefficients $c_{31,31}$ and $s_{31,31}$ are very poor so that we eliminate them in the results of Fig. 22.6b and Table 22.1. Due to the spatial undersampling (besides temporial undersampling), a significant North–South-striping pattern can be seen in Fig. 22.6b. In contrast scenario (c), which still has a reduced temporal sampling, offers an adequate spatial sampling which allows for the determination up to $L_{\max} = 31$ according to the theory. This can be seen by the degree RMS in Fig. 22.5, which doesn't exhibit a rapid increase for higher degrees. In addition, the spatial distribution of the aliasing errors (which should be mainly caused by temporal aliasing in this case) has a smoother signature.

The question where to put a potential second sensor in a 2-sensor configuration is difficult to answer. Based on the results of configurations (b) and (c), improving the temporal sampling seems to be more important. This is deduced, e.g., from Fig. 22.5, where the degree RMS curve of configuration (b) intersects the degree RMS curve of the 4-day-mean field at $l = 23$, while that of configuration (c) already intersects at $l = 15$. Furthermore the minimum and maximum values of the aliasing error are less for configuration (b). On the other hand, the striping pattern for configuration

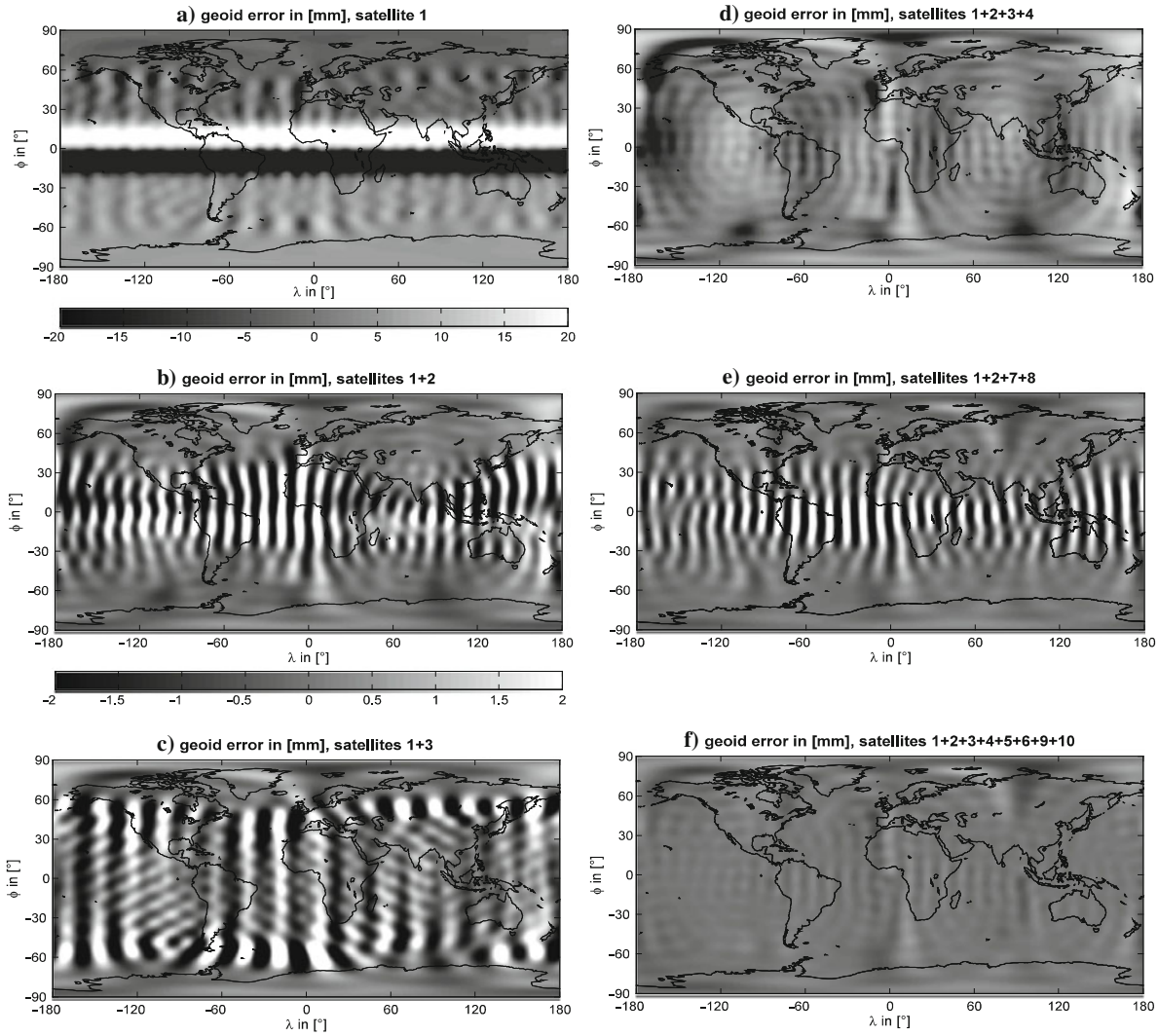


Fig. 22.6 **(a–f)** Aliasing errors of 4-day solutions for configurations (a–f); configurations (a and b) are displayed without $c_{31,31}$ and $s_{31,31}$; the colorbar of (b) is also valid for (c–f)

(b), which is also caused by spatial aliasing, is more distinct.

Figure 22.6d, e show the aliasing errors of the 4-satellite-configurations (d) and (e), which both should lead to an improvement of the spatial and temporal sampling of a factor 2 compared to configuration (a). Configuration (d), which is the extended combination of configurations (b) and (c) by application of the proper Δt- and $\Delta\lambda$-shifts is able to reduce the aliasing-effects in contrast to the 2-satellite-configurations by a factor of 3, as visible in Table 22.1 (RMS = 0.4 mm). The aliasing errors in Fig. 22.6d show now a less pronounced trackiness.

In contrast, the densification of the spatial sampling in configuration (e) by means of a $\Delta\Omega$-shift of satellites 7 and 8 didn't lead to a major reduction of the aliasing errors, as indicated by Table 22.1 (RMS = 1.0 mm). Furthermore, the pattern of the aliasing errors of configuration (e) in Fig. 22.6e looks quite similar as in Fig. 22.6b), which seems to lead to the concluson that the applied $\Delta\Omega$-shift does not improve the spatial sampling. A preliminary conclusion from Fig. 22.6d, e and Table 22.1 is that the direct $\Delta\lambda$-shift is much more powerful than the indirect $\Delta\lambda$-shift via the $\Delta\Omega$-shift.

On the other hand it is clear from the degree RMS in Fig. 22.5 that the $\Delta\Omega$-shift of configuration (e)

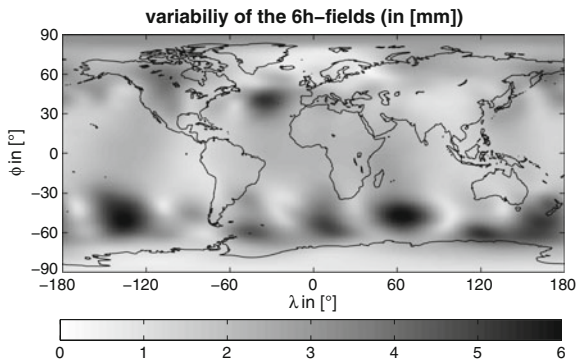


Fig. 22.7 Variability of the 6 h-fields over the applied 4-day period (RMS w.r.t. the 4-day mean)

improves the lower degrees ($l < 15$), while the $\Delta\lambda$-shift of configuration (d) mainly improves the higher degrees ($l > 15$). Taking this into account, the combination of both $\Delta\lambda$ and $\Delta\Omega$-shifts, i.e., a combination of configurations (d) and (e) might be of advantage. This was simulated in the 8-satellite-configuration (f), where configuration (d) was shifted additionally by a $\Delta\Omega$-shift. The $\Delta\Omega$-shift of the satellites (5,6) and (9,10) was applied so that these satellites fly on the same groundtracks as the satellites (1,2) and (3,4) respectively. By this, the $\Delta\Omega$-shift acts as a Δt-shift, which means that the temporal sampling is densified by a factor of 4 (with inconstant time shifts) and the spatial sampling is enlarged by a factor of 2 compared to configuration (a). As illustrated by Fig. 22.5, this combination indeed combines the advantages of configurations (d) and (e). The degree RMS-curve of configuration (f) now runs at the minimum of both configurations (d) and (e). The 8-sensor configuration is able to minimize the aliasing errors significantly, as illustrated by Fig. 22.6f and Table 22.1. The aliasing is again reduced by a factor of 3–4 (RMS = 0.1 mm) compared to the 4-sensor scenario (d).

22.5 Discussion

Since atmospheric and oceanographic dealiasing products may not be of adequate accuracy for future gravity field missions, the aliasing problem has to be solved through mission design. In this contribution we have investigated the issue of simultaneously improving the temporal and spatial resolution. The Heisenberg rule expresses that a single sensor mission like GRACE either enables a higher temporal resolution at the cost of spatial coverage or vice versa. Improving both time and space resolution can only be realized by a multi-sensor configuration.

Satellites placed on the same groundtrack with a time-shift (Δt-shift) improve the temporal sampling while satellites placed on an interleaved groundtrack by means of a $\Delta\lambda$-shift improve the spatial sampling. Simulations show that the aliasing effects can indeed be significantly reduced by means of such sensor configurations. The first results also seem to indicate that it is more important to reduce the temporal sampling rather than the spatial sampling. Temporal signals as the atmosphere and the ocean contain signals with daily or half-daily periods, which can only be sampled adequately by means of a temporal sampling of $\Delta t = 0.5$ d or $\Delta t = 0.25$ d respectively. The last simulation scenario, which already has a temporal sampling of $\Delta t \cong 0.5$ d, shows significantly reduced aliasing such that the solution shows marginal striping.

The results of this study encourages the investigation of suitable satellite configurations for the reduction of the aliasing problem. Extended simulations have to be performed in order to find the optimal configuration for future tasks. Different types of sensors and formations may request a different satellite configuration for the reduction of temporal and spatial aliasing, since there is an interaction between the measurement sensitivity and aliasing. In this contribution we have looked into configurations in which all satellites have the same parameters (α,β,I). That is not a necessity, though. Exploring a larger parameter search space for configuration design will be subject for future research.

Acknowledgement This study was performed within the contract 20403 "Monitoring and modelling individual sources of mass distribution and transport in the Earth system by means of satellites" of the European Space Agency. We thank ESA for the financial support and the project team for providing data and input to this study.

References

Bender, P.L., J.L. Hall, J. Ye, and W.M. Klipstein (2003). Satellite-satellite laser links for future gravity missions. *Space Sci. Rev.*, 108,377–384.

Chen, J.L., C.R. Wilson, and B.D. Tapley (2006). Satellite gravity measurements confirm accelerated melting of Greenland ice sheet. *Science* 313:1958–1960, DOI¯10.1126/science.1129007.

Lemoine, F., S.C. Kenyon, J.K. Factor, R.G. Trimmer, N.K. Pavlis, D.S. Chinn, C.M. Cox, S.M. Klosko, S.B. Luthcke, M.H. Torrence, Y.M. Wang, R.G. Williamson, E.C. Pavlis, R.H. Rapp, and T.R. Olson (1998). The development of the joint NASA Goddard Space Flight Center and the National Imagery and Mapping Agency (NIMA) geopotential Model EGM96, *NASA/TP-1998-206861*, Greenbelt, MD, USA.

Schrama, E.J.O., B. Wouters, and D.D. Lavallee (2007). Signal and noise in gravity recovery and climate experiment (GRACE) observed surface mass observations. *J. Geophys. Res*., 112 (B08407), doi: 10.1029/2006JB004882.

Sharifi, M., N. Sneeuw, and W. Keller (2007). Gravity recovery capability of four generic satellite formations. In: Kiliçoglu, A. and R. Forsberg (eds), Gravity field of the Earth. General Command of Mapping. ISSN 1300-5790 Special Issue 18:211–216.

Sneeuw, N., J. Flury, and R. Rummel (2004). Science requirements on future missions and simulated mission scenarios. *Earth Moon Planets*, 94(1–2), 113–142.

Sneeuw, N., M. Sharifi, and W. Keller (2008). Gravity recovery from formation flight missions. In: Xu, P.L., J.N. Liu, A. Dermanis (eds), VI hotine-marussi symposium on theoretical and computational geodesy. vol 132, Springer.

Tapley, B.D., S. Bettadpur, J.C. Ries, P.F. Thompson, and M.M Watkins (2004). GRACE measurements of mass variability in the Earth system. *Science*, 305, 503–505.

Chapter 23

A Simulation Study Discussing the GRACE Baseline Accuracy

U. Meyer, F. Flechtner, R. Schmidt, and B. Frommknecht

Abstract The twin GRACE-A and -B satellites are in orbit since more than 6 years and still perform well. They deliver gravity data of unprecedented accuracy, which enables hydrologists, oceanographers and geophysicists to study the temporal variations of the Earth's gravity field. But the baseline accuracy computed in a pre-launch simulation study (Kim, 2000) has not yet been reached by a factor of about 15. We therefore have to raise the question: are there improvements in the processing of GRACE data possible? To answer this question, a simulation study was performed, using the same software, processing strategy, background models and standards used at GFZ for the analysis of real GRACE data.

We present the results and analysis of this simulation study. Initially a closed loop simulation shows, that GFZ's EPOS software is numerically stable. The GRACE orbit geometry is sufficient and the sampling adequate to solve for monthly gravity fields at least up to degree and order 150. The estimation of instrument parameters as suggested by Kim (2000) does not absorb the gravity signal, but greatly reduces systematic effects in the observations. The accelerometer noise proved to be an important reason for not reaching the baseline accuracy with the processing strategy used so far. Additional accelerometer parameters do not really help, but the shortening of arcs gives promising results. Different background model errors were introduced and the ocean tide model turned out to be a probable error source, while atmospheric tides play a minor role.

U. Meyer (✉)
Deutsches GeoForschungsZentrum (GFZ),
Helmholtz Centre Potsdam, Wessling D-82234, Germany
e-mail: meyeru@gfz-potsdam.de

23.1 Introduction

The Gravity Recovery And Climate Experiment (GRACE, Tapley et al., 2004) satellites are approximately free falling test masses in the gravity field of the Earth. In addition to the determination of the satellite orbits by GPS-observations, which allows for a gravity field solution in spherical harmonics at least up to degree 70 (Prange et al., 2008), a K-Band inter-satellite link provides a differential range measurement between the satellites with micrometer-accuracy, which for the first time allows to calculate satellite-only monthly solutions up to degree and order 120 (Schmidt et al., 2007). Apart from the increased spatial resolution of the gravity field the low degree temporal variations can be observed as well, making the time series of monthly gravity fields suitable to study continental hydrological cycle (Schmidt et al., 2008), dynamic ocean topography (Flechtner et al., 2006b), polar ice mass changes and post glacial uplift (Barletta et al., 2008).

At GFZ Potsdam GRACE daily orbits and monthly as well as long time mean gravity fields are produced on a routine basis. The satellite orbits are computed with the orbit determination software EPOS-OC (Earth Parameter and Orbit System – Orbit Computation) using a dynamic approach and high–low (GPS code and phase) as well as low–low (K-Band range-rate) satellite tracking observables. The gravitational attraction of the Earth as well as of third bodies, direct and indirect tides and short-term atmospheric and oceanic mass variations (Flechtner et al., 2006a) are modelled. Non-gravitational forces acting on the satellites are measured by the onboard accelerometers. The satellites' equations of motion are solved by numerical

S.P. Mertikas (ed.), *Gravity, Geoid and Earth Observation*, International Association of Geodesy Symposia 135,
DOI 10.1007/978-3-642-10634-7_23, © Springer-Verlag Berlin Heidelberg 2010

integration of the aforementioned accelerations and the a priori values of GPS- and K-Band range-rate observations are calculated. From the terms "observed-computed", corrections to the model parameters, i.e., to the initial orbital elements and the background gravity field coefficients, as well as a number of instrument parameters (e.g., accelerometer biases and scales, K-band range-rate bias and periodic terms) are estimated by a least squares process. Details concerning orbit computation and parameter estimation are provided in Schmidt (2007).

The quality of the resulting gravity field is not easily assessed. A simulation study may help to quantify the impact of model errors and observation noise on the solutions. This study was stimulated by a sensor analysis performed at IAPG (Gerlach et al., 2004). Recent studies assess the role of geophysical background model errors (Schrama et al., 2007), omission and commission errors (Gunter et al., 2006), aliasing error from ocean tides (Seo et al., 2008), as well as the impact of ground track variability (Klokocník et al., 2008). The particularity of this simulation study is the use of the same software and processing environment that is also used for the routinely processing of real GRACE mission data at GFZ.

Simulated GPS and K-Band observations are calculated from orbits based on a gravity field model denoted as "true". The measured non-gravitational accelerations are replaced by modeled accelerations of atmospheric drag, solar radiation pressure and Earth albedo. The attitude angles roll, pitch and yaw along the orbits are assumed to be zero. Attitude, range, range-rate and modeled accelerometer observations are then transformed into the GRACE standard Level-1B format and realistic colored noise from the integrated sensor analysis at IAPG is added (Frommknecht, 2007; Thomas, 1999). White noise is added to the ionosphere-free zero difference GPS-observations (35 cm on code and 0.85 cm on carrier phase measurements, corresponding to values achieved in the GFZ routine analysis). The simulated observations then are used by EPOS-OC in a parameter estimation procedure to solve for gravity field coefficients (Fig. 23.1). The difference degree variances between the resulting gravity field and the initial gravity model used in the simulation step are a measure for the success of the gravity field recovery.

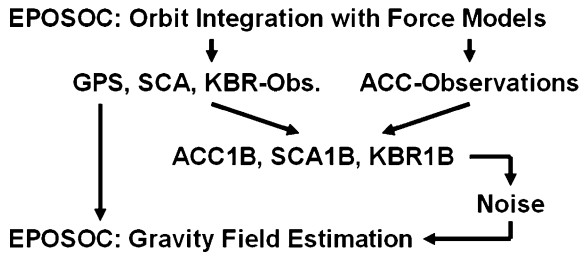


Fig. 23.1 Flowchart of the simulation of GRACE observations and subsequent gravity field recovery

23.2 Closed Loop Simulation

As a proof of concept, the EPOS-OC numeric and the format transformation tools were used in a closed loop simulation. In this step no noise was added to the simulated observations. EIGEN-CG03C (Förste et al., 2005) was assigned as the true model to simulate the observations, while GGM02C (Tapley et al., 2005) was taken as the a-priori model for the following parameter estimation step. The degree 1 terms and drift rates of low degree coefficients of both models were set to the same values to avoid differential once-per-rev accelerations. The a priori errors of the different observation types were chosen as 2 m for GPS code, 1 cm for GPS carrier phase and 0.1 μm/s for K-Band range-rate (default weighting). In a first step the 24 h-orbits were adjusted by estimation of arc specific parameters (only six initial conditions). After convergence the arc specific parameters were eliminated from the normal equations, the daily normal equations accumulated to monthly ones and in a last step the gravity field coefficients were estimated.

Figure 23.2 illustrates the results of the closed loop test. The square-roots of the difference degree variances between EIGEN-CG03C and GGM02C (orange line denoted as "introduced gravity error") roughly represent the current quality of the GRACE gravity fields (black line denoted as "achieved accuracy"). The targeted baseline accuracy (Kim, 2000) is about 15 times lower (brown line denoted as "GRACE baseline accuracy"). The remaining error between the estimated and the true gravity field represents the limits of machine accuracy using constant 5 s integration steps and double precision variables. The result is at least two orders of magnitude below the baseline when GPS

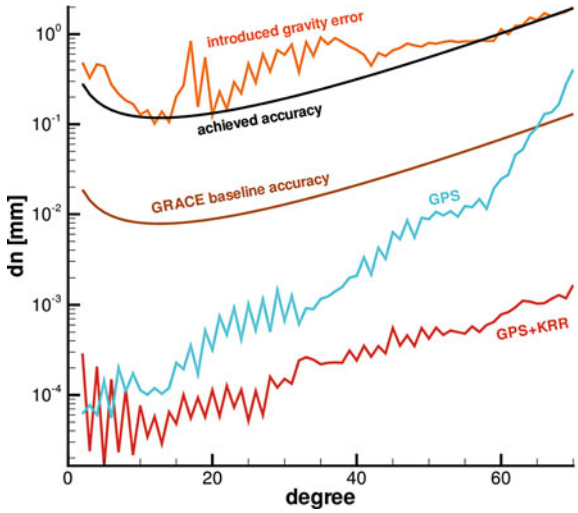


Fig. 23.2 Square-roots of the difference degree variances (in geoid heights) resulting from the closed loop simulation up to degree 70

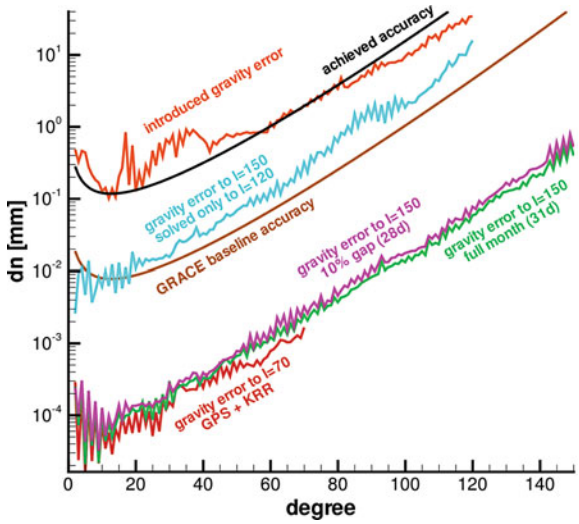


Fig. 23.3 Square-roots of the difference degree variances (in geoid heights) representing the influence of the orbit geometry, sampling rate and omission error. The notation "gravity error to $l = 150$" implies that a max. degree of 150 was used for the simulation and the a priori gravity field

and K-band range-rate observations are used (red line denoted as "GPS+KRR"). Even when using GPS only, the remaining errors (light blue line denoted as "GPS") stay below the baseline up to degree 60. The alternating errors between even and odd spherical harmonic coefficients at low degrees are a phenomenon often observed in simulation studies in the absence of observation noise and are attributed to the polar gap of the satellite orbits. As a result of the closed loop simulation we conclude that EPOS-OC is working properly.

Generally, in most simulation experiments the gravity field was only introduced and solved up to degree 70 to reduce computation time. Only once the full potential of the GRACE data up to degree 150 has been exploited to test the orbit geometry and observation sampling rate of 5 s. Figure 23.3 shows that from the numerical point of view it is no problem to estimate coefficients up to degree 150 from 1 month of simulated data with a non-repeat orbit geometry (green line denoted as "gravity error to $l = 150$, full month (31d)"). Even a 10% data gap of 3 days poses no problem (pink line denoted as "gravity error to $l = 150$, 10% gap (28d)"). However, the omission error immediately exceeds the baseline when a gravity field up to degree 150 is used for the simulation of observations but in the recovery step only coefficients up to degree 120 are solved for (light blue line denoted as "gravity error to $l = 150$, solved only to $l = 120$"). Therefore one has to set up enough coefficients to cover the full sensitivity of the GRACE observations.

A last experiment at the closed loop test series concerns the estimation of arc specific instrument parameters. They should absorb systematic observation effects like, e.g., drifts due to imperfections of the measurement instruments. These parameters include accelerometer biases in radial, along-track and cross-track and scale factors in along-track direction that are estimated twice per arc. The K-Band is parameterized with biases in range, range-rate and range-rate-drifts every 90 min as well as once per rev sine and cosine terms every 180 min (as proposed by Kim (2000)). GPS receiver clocks are estimated every 30 s, carrier phase ambiguities were neither simulated nor solved for. No instrument noise is introduced. The goal of the experiment is to show the correlation of the instrument parameters with the gravity field coefficients.

After the estimation of the new arc specific parameters the size of the residuals is reduced considerably. Surprisingly, this has little impact on the estimation of gravity field coefficients. In Fig. 23.4 the green, light blue and dark blue lines show the effect of accelerometer parameters, K-Band parameters, and a combination of both, on the estimation of gravity field coefficients. The additional estimation of GPS receiver clocks is accounted for in the pink line. The effect is still two orders of magnitude below baseline. We conclude, that the instrument parameters do not absorb gravity signal.

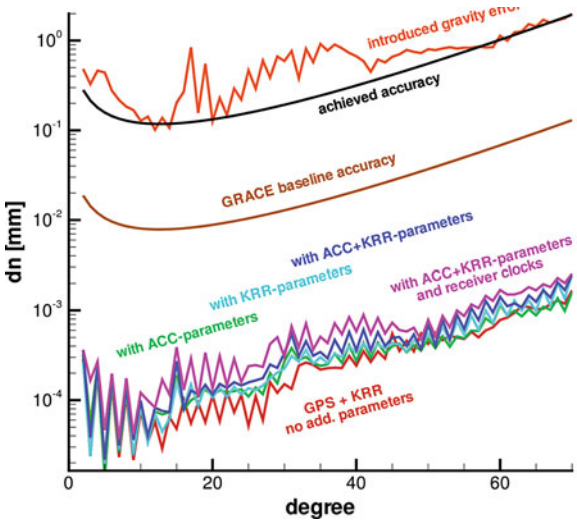


Fig. 23.4 Square-roots of the difference degree variances (in geoid heights) representing the effect of instrument parameters

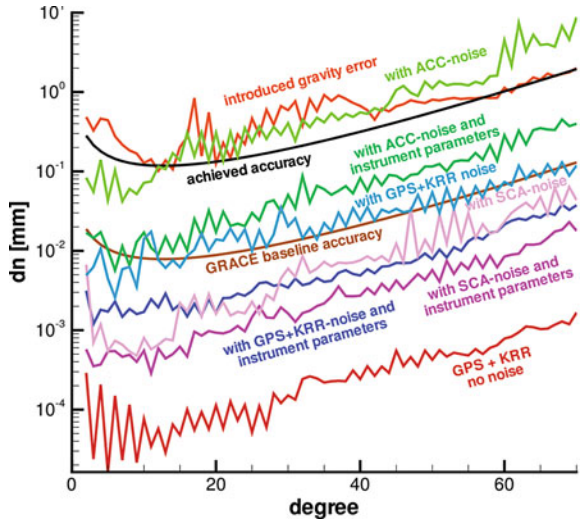


Fig. 23.5 Square-roots of the difference degree variances (in geoid heights) representing the effect of observation noise

23.3 Observation Noise

In order to be more realistic we introduce observation noise. While the effect of star camera and accelerometer noise is studied separately, K-Band range-rate noise and GPS code and phase noise have to be treated together since otherwise the gravity field would be fully defined by the noise-free observation type. From now on for every experiment the relative weighting between GPS code, carrier phase and K-Band range-rate observations has to be defined correctly. Starting from the values given in Sect. 23.2, pre fit residuals are computed and the relative weights are adjusted until the residuals do no longer change. In these experiments instrument parameters play a vital role.

For each type of observation noise two separate curves are given in Fig. 23.5, one representing a solution without, the other including instrument parameters. Star camera noise itself seems to be of little importance (light and dark pink line in Fig. 23.5, both well below baseline accuracy). The effect of mismodelled attitude on accelerometer observations is accounted for in the coloured accelerometer noise. K-band and GPS solutions touch the baseline as long as no instrument parameters are estimated (light blue line), but drop to insignificance as soon as empirical K-band parameters are introduced (dark blue line). Last but not least, accelerometer noise turns out to be a major problem. Without adequate instrument parameters (light green line) the gravity field coefficients of higher degrees cannot be improved and even with full instrument parameterization (dark green line) the effect stays well above the baseline. With the standard processing strategy applied at GFZ (see Sect. 23.2) the baseline therefore cannot be met.

Experiments with more accelerometer-related parameters (up to one bias and one scale parameter per component and per 6 h) and additional K-band once per rev range-rate parameters led to slight improvements in the simulation study. These results could not be confirmed with real data. The shortening of arcs from 24 to 6 h is more promising. This measure decreases the accumulation of accelerometer noise and yields a better fit of the resulting gravity fields to observed gravity anomalies and altimetry. Mayer-Gürr et al. (2006) successfully use a very short arc method.

23.4 Model Errors

Finally, the effect of errors in the background models was studied. These include ocean tides (FES2004, Lyard et al., 2006), atmospheric tides (Bode and Biancale, 2006) and short period atmosphere and

ocean mass variations as recorded by ECMWF meteorological data and the Ocean Model for Circulation and Tides (OMCT, Thomas et al., 2001) and routinely provided by GFZ as the AOD1B GRACE product (Flechtner, 2007). The error of these models is difficult to assess. Their effect on gravity field coefficients was studied by either completely omitting the model in the gravity recovery step (full effect) or by replacing it by a modified or more recent model (approximated effect of noise only).

A spectral analysis of time series of the low degree coefficients of weekly gravity field solutions spanning 4 years shows pronounced peaks at seasonal and 28d periods (GFZ internal investigation). While the seasonal signal can be attributed to a large extent to the hydrological cycle, the 28d signal indicates a problem in tide modeling. As no realistic noise estimates were available for ocean tides the amplitudes of the standard GRACE background model FES2004 were arbitrarily altered by up to 10%. The combined effect of observation noise and ocean tide errors on the gravity field coefficients is shown in Fig. 23.6 (pink line denoted "nom. obs. noise, 10% ocean tide error"). It is significantly larger than the effect of observation noise only (blue line, denoted as "nom. obs. noise (ACC, KRR, GPS, SCA)"). Tests with the tide model EOT08a, which includes corrections to FES2004 derived from altimeter data (Savcenko and Bosch, 2008) confirm the size of the effect (not shown). Hence, the ocean tide model seems to be an important error source.

In contrast, the effect of the atmospheric S2-tide is only visible in the very low degrees (green line). Even complete omission of this tidal signal has a smaller impact than the approximate ocean tide error. In comparison, the complete effect of the atmosphere ocean de-aliasing product (light blue line) reaches the current level of accuracy of the GRACE gravity field solutions. Further experiments with a realistic error measure of the AOD1B product are still pending.

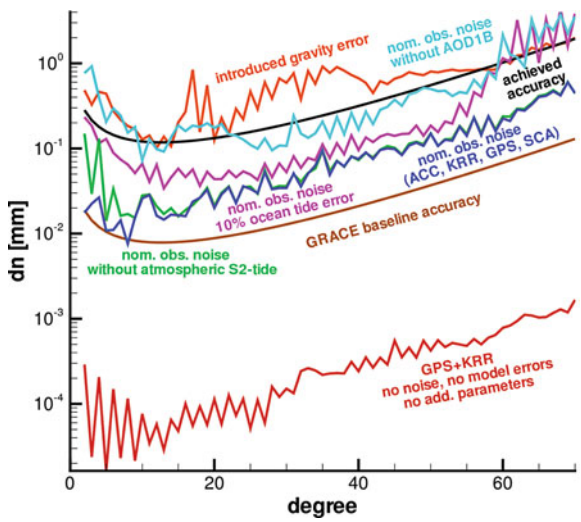


Fig. 23.6 Square-roots of the difference degree variances (in geoid heights) representing errors in tide models and atmosphere ocean de-aliasing

23.5 Conclusions

A closed loop simulation study has been performed at GFZ, in order to identify potential reasons why the GRACE baseline accuracy has not been reached. It turned out that the estimation of various instrument parameters does not absorb the gravity signal, but greatly reduces the systematic effects in the observations. While star camera and K-Band noise play a minor role, the accelerometer noise proved to be an important reason for not reaching the baseline accuracy with the processing strategy used so far. More accelerometer parameters do not really help, but the shortening of arcs gives promising results. Different background model errors were introduced and the ocean tide model turned out to be a probable error source, while atmospheric tides play a minor role. The short period mass variations of oceans and atmosphere have to be considered.

In the light of this simulation study the pre launch baseline accuracy seems to be somewhat optimistic. Some noisy features of the accelerometer data like twangs and spikes could not be foreseen and the effect of background model errors has not been considered sufficiently. The possibility to upgrade tide models using GRACE data is currently under investigation. On the other hand the processing of accelerometer data in 24 h arcs does not seem to be appropriate. The power of short arc methods has already been proven and should be applied.

Acknowledgements This study has been sponsored by the Geotechnologien programme of BMBF and DFG. The author wishes to thank two anonymous reviewers for their helpful comments.

References

Barletta, V.R., R. Sabadini, and A. Bordoni (2008). Isolating the PGR signal in the GRACE data: impact on mass balance estimates in Antarctica and Greenland. *Geophys. J. Int.*, 172,18–30, doi:10.1111/j.1365-246X.2007.03630.x.

Bode, A. and R. Biancale (2006). Mean annual and seasonal atmospheric tide models based on 3-hourly and 6-hourly ECMWF surface pressure data, Scientific Technical Report STR06/01, GeoForschungsZentrum Potsdam, Potsdam.

Flechtner, F. (2007). AOD1B product description document for product releases 01 to 04. GRACE Project Document, JPL 327-750, rev. 3.1, JPL Pasadena, Ca.

Flechtner, F., R. Schmidt, and U. Meyer (2006a). De-aliasing of short-term atmospheric and oceanic mass variations for GRACE. In: Flury, J., R. Rummel, C. Reigber, M. Rothacher, G., Boedecker, and U. Schreiber, U. (eds), Observation of the earth system from space, ISBN 3-540-29520-8, pp. 83–97, Springer, Berlin.

Flechtner, F., R. Schmidt, U. Meyer, T. Schoene, S. Esselborn, C. Foerste, R. Stubenvoll, R. Koenig, H. Neumayer, and M. Rothacher (2006b). The benefit of EIGEN gravity field models for altimetry and vice versa. Int. Symp. on 15 years of progress in Radar Altimetry proceedings, Venice.

Förste, C., F. Flechtner, R. Schmidt, U. Meyer, R. Stubenvoll, F. Barthelmes, R. König, K.H. Neumayer, M. Rothacher, Ch. Reigber, R. Biancale, S. Bruinsma, J.M. Lemoine, and J.C. Raimondo (2005). A new high resolution global gravity field model derived from combination of GRACE and CHAMP Mission and Altimetry/Gravimetry Surface Gravity Data, online available at http://www-app2.gfz-potsdam.de/pb1/op/grace/results.

Frommknecht, B. (2007). Integrated Sensor Analysis of the GRACE Mission. *PhD study*, Institute for Astronomical and Physical Geodesy, Technical University Munich, Germany, 206 pp.

Gerlach, C., J. Flury, B. Frommknecht, F. Flechtner, and R. Rummel (2004). GRACE performance study and sensor analysis. Proc. Joint CHAMP/GRACE Science Team Meeting Potsdam.

Gunter, B., J. Ries, S. Bettadpur, and B. Tapley (2006). A simulation study of the errors of omission and commission for GRACE RL01 gravity fields. *J. Geodesy*, *80*, 341–351, doi:10.1007/s00190-006-0083-3.

Kim, J. (2000). Simulation study of a low–low satellite-to-satellite tracking mission. *Technical Report*, University of Texas at Austin, TX, USA.

Klokocník, J., C.A. Wagner, J. Kostelecký, A. Bezdek, P. Novák, and D. McAdoo (2008). Variations in the accuracy of gravity recovery due to ground track variability: GRACE, CHAMP, and GOCE. *J. Geodesy*, 22–+, doi:10.1007/s00190-008-0222-0.

Lyard, F., F. Lefevre, T. Letellier, and O. Francis (2006) Modelling the global ocean tides: modern insights from FES2004. *Ocean Dyn.*, 56, 394–415, doi:10.1007/s10236-006-0086-x.

Mayer-Gürr, T., A. Eicker, and K.H. Ilk (2006). Gravity field recovery from GRACE-SST data of short arcs. In Flury, J., R. Rummel, C. Reigber, M. Rothacher, G. Boedecker, and U. Schreiber (eds), Observation of the earth system from space, ISBN 3-540-29520-8, Springer, Berlin, pp. 131–148.

Prange, L., A. Jäggi, G. Beutler, L. Mervart, and R. Dach (2008). Gravity field determination at the AIUB – the celestial mechanics approach. Article in this book.

Savcenko, R. and W. Bosch (2008). EOT08a – empirical ocean tide model from multi-mission satellite altimetry. Internal Report, No. 81, Deutsches Geodätisches Forschungsinstitut, München.

Schmidt, R. (2007). Zur Bestimmung des cm-Geoids und dessen zeitlicher Variationen mit GRACE. Scientific Technical Report STR07/04, GeoForschungsZentrum Potsdam, Potsdam.

Schmidt, R., F. Flechtner, R. König, U. Meyer, K.-H. Neumayer, Chr. Reigber, M. Rothacher, S. Petrovic, S.Y. Zhu, and A. Güntner (2007). GRACE time-variable gravity accuracy assessment. In: Tregoning, P. and Chr. Rizos (eds), Dynamic planet, IAG symposium 130, ISBN 3-540-49349-5, Springer, Berlin, pp. 237–243.

Schmidt, R., F. Flechtner, U. Meyer, K.-H. Neumayer, C. Dahle, R. König, and J. Kusche (2008). Hydrological signals observed by the GRACE satellites. *Surv. Geophys.*, 4–+, doi:10.1007/s10712-008-9033-3.

Schrama, E.J.O. and P.N.A.M. Visser (2007). Accuracy assessment of the monthly GRACE geoids based upon a simulation. *J. Geodesy*, 81, 67–80, doi:10.1007/s00190-006-0085-1.

Seo, K.W., C.R. Wilson, S.C. Han, and D.E. Waliser (2008). Gravity recovery and climate experiment (GRACE) alias error from ocean tides. *J. Geophys. Res. (Solid Earth)*, 113(B12), 3405–+, doi:10.1029/2006JB004747.

Tapley, B., S. Bettadpur, M. Watkins, and C. Reigber (2004). The gravity recovery and climate experiment: mission overview and early results. *Geophys. Res. Lett.*, 31, L09607.

Tapley, B., J. Ries, S. Bettadpur, D. Chambers, M. Cheng, F. Condi, B. Gunter, Z. Kang, P. Nagel, R. Pastor, T. Pekker, S. Poole, and F. Wang (2005). GGM02 – An improved earth gravity field model from GRACE. *J. Geodesy*, *79*, 467–478, doi:10.1007/s00190-005-0480-z.

Thomas, J. (1999). An analysis of the gravity field estimation based on dual-1-way intersatellite biased ranging. Technical Report, Jet Propulsion Laboratory, Pasadena, Ca, USA.

Thomas M., J. Sündermann, and E. Maier-Reimer (2001). Consideration of ocean tides in an OGCM and impacts on subseasonal to decadal polar motion excitation. *Geophys. Res. Lett.*, 12, 2457.

Chapter 24

GRACE Gravity Field Determination Using the Celestial Mechanics Approach – First Results

A. Jäggi, G. Beutler, and L. Mervart

Abstract We present the first gravity field model AIUB-GRACE01S, which has been generated using the Celestial Mechanics Approach in an extended version. Inter-satellite K-band range-rate observations and GPS-derived kinematic positions are used to solve for the Earth's gravity field parameters in a generalized orbit determination problem. Apart from the normalized spherical harmonic (SH) coefficients, arc-specific parameters like initial conditions and pseudo-stochastic pulses are set up as common parameters for all measurement types. Our first results based on 1 year of GRACE data demonstrate that the Earth's static gravity field can be recovered with a good quality, even using EGM96 as a priori model and without accelerometer data and sophisticated background models like short-term mass variations. The use of accelerometer data and sophisticated background models will be a prerequisite for the near future, however, to further improve the inferred gravity field solutions.

24.1 Introduction

The Gravity Recovery And Climate Experiment (GRACE) mission, launched on March 17, 2002, has significantly improved our knowledge of the Earth's gravity field both in terms of accuracy and resolution. For the first time the time-varying part of the Earth's gravity field has been inferred with unprecedented accuracy from space by analyzing GPS, accelerometer, and inter-satellite K-band observations (Tapley et al., 2004). Recent GRACE models report an accuracy of about 3 cm in terms of geoid heights for the long to medium wavelengths of the static field (Förste et al., 2008), which is an improvement by about one order of magnitude compared to the high-resolution model EGM96 (Lemoine et al., 1997). Apart from the official GRACE models derived by the Center for Space Research (CSR) of the University of Texas at Austin, the Jet Propulsion Laboratories (JPL), and the GeoForschungsZentrum Potsdam / Groupe de Recherche en Géodésie Spatiale (GFZ / GRGS), alternative state-of-the-art GRACE gravity field models have been computed, e.g., at the Institute of Theoretical Geodesy (ITG) of the University of Bonn (Mayer-Gürr, 2008).

Spaceborne gravity field recovery has recently been initiated also at the Astronomical Institute of the University of Bern (AIUB). The so-called Celestial Mechanics Approach for gravity field recovery has already been successfully applied to high-low satellite-to-satellite tracking (hl-SST) data of the GRACE and CHAMP missions (Jaeggi et al., 2008; Prange et al., 2008). This article focuses on extensions of the Celestial Mechanics Approach for gravity field recovery from a combined processing of GRACE hl-SST and low–low (ll) SST data of the K-band ranging system (Sect. 24.2). Simulated data are used to validate the concept of the extended Celestial Mechanics Approach to cope with additional ll-SST observations (Sect. 24.3). A first gravity field model AIUB-GRACE01S has been derived from real GRACE data of the year 2003 and is compared with official GRACE gravity field models (Sect. 24.4) and with terrestrial measurements (Sect. 24.5). We show what quality

A. Jäggi (✉)
Astronomical Institute, University of Bern, Bern CH-3012, Switzerland
e-mail: adrian.jaeggi@aiub.unibe.ch

S.P. Mertikas (ed.), *Gravity, Geoid and Earth Observation*, International Association of Geodesy Symposia 135,
DOI 10.1007/978-3-642-10634-7_24, © Springer-Verlag Berlin Heidelberg 2010

level can be achieved in GRACE gravity field estimation without making use of accelerometer data and advanced models like short-term mass variations and discuss their importance in view of planned refinements for the near future.

24.2 Celestial Mechanics Approach

GRACE gravity field determination using the Celestial Mechanics Approach is based on the analysis of Level 1B inter-satellite K-band measurements (Case et al., 2002) serving as observations and GPS-derived kinematic positions of both GRACE satellites (Jäggi et al., 2008) used as pseudo-observations (Sect. 24.2.1). The static part of the gravity field is modeled with a series of normalized spherical harmonic coefficients (Heiskanen and Moritz, 1967) from degree 2 up to the maximum degree of 120. Based on a priori orbits derived from the kinematic positions of both GRACE satellites (Sect. 24.2.2) normal equations for both types of (pseudo-) observations are set up on a daily basis for the unknown gravity field coefficients and for additional arc-specific parameters, i.e., two normal equation systems based on the kinematic positions of GRACE A and B (Sect. 24.2.3), and one normal equation system based on the ll-SST data of the K-band ranging system (Sect. 24.2.4). The resulting daily normal equations are then combined into one system for each daily arc. Finally, arc-specific parameters are pre-eliminated and the combined daily normal equations are accumulated into monthly and annual systems, which are eventually inverted to solve for the SH coefficients without applying any regularization. Details may be found in (Jäggi et al., 2008).

24.2.1 Observation Model

The stochastic properties of the observation errors are taken into account by epoch-wise weight matrices $\mathbf{P}_{hl}$ for the three components of the kinematic positions derived from hl-SST observations and a constant weight P_{ll} for the ll-SST observations:

$$\mathbf{P}_{hl} = \mathbf{Q}_{hl}^{-1} = \sigma_{0_{hl}}^2 \mathbf{C}_{hl}^{-1} \; and \; P_{ll} = \sigma_{0_{ll}}^2, \qquad (1)$$

where Q_{hl} and C_{hl} denote the epoch-wise cofactor and covariance matrices of the GPS-derived kinematic positions, respectively. Taking the cofactor matrices Q_{hl} into account, the weighting of the kinematic pseudo-observations is automatically linked to the a priori standard deviation $\sigma_{0_{hl}}$ of the GPS data processing (assumed to be 1 mm for the L1 and L2 carrier phase observable). The a priori standard deviations $\sigma_{0_{ll}}$ of the K-band observations are currently set to $1\,\mu m$ for range and $0.1\,\mu m/s$ for range-rate observations, yielding nominal weighting ratios $\sigma_{0_{hl}}^2 : \sigma_{0_{ll}}^2$ of $1{:}10^6$ and $1{:}10^8$, respectively.

24.2.2 A Priori Orbit Generation

The equation of motion of a low Earth orbiting satellite including all perturbations reads in the inertial frame as

$$\ddot{\mathbf{r}} = -GM\frac{\mathbf{r}}{r^3} + \mathbf{f}_1(t,\mathbf{r},\dot{\mathbf{r}},q_1,\ldots,q_d) \qquad (2)$$

with a set of initial conditions $\mathbf{r}^{(k)}(t_0) = \mathbf{r}^{(k)}(E_1,\ldots,E_6;t_0)$, $k = 0,1$ where $E_1,\ldots,E_6$ are the six initial osculating elements pertaining to epoch t_0. $q_1,\ldots,q_d$ denote d additional dynamical parameters considered as unknowns, e.g., arc-specific orbit parameters or global force model parameters which describe the perturbing acceleration $\mathbf{f}_1$ acting on the satellite.

A priori orbits are generated for the two GRACE satellites such that both trajectories $\mathbf{r}_{a0}(t)$ and $\mathbf{r}_{b0}(t)$ are particular solutions of the equation of motion (2). Based on a selected force model (given by an a priori gravity field model, ocean tide model, ...) the weighted kinematic positions of both satellites are approximated in the least-squares sense by numerically integrating the equation of motion (Beutler, 2005) and adjusting arc-specific orbit parameters. Apart from the initial osculating elements the adjusted parameters are three constant empirical accelerations acting over the entire arc in the radial, along-track, and cross-track directions, and pseudo-stochastic pulses (instantaneous velocity changes) with a spacing of 15 min acting in the same three directions (Jäggi et al., 2006). Currently K-band measurements are not used as observations for the generation of the a priori orbits.

24.2.3 Daily Normal Equations from Positions

Based on the a priori orbits $\mathbf{r}_{a0}(t)$ and $\mathbf{r}_{b0}(t)$ gravity field recovery from orbit positions may be set up as a generalized orbit improvement process for each GRACE satellite. The actual orbit $\mathbf{r}_a(t)$ of GRACE A, e.g., may be expressed as a truncated Taylor series with respect to the unknown orbit parameters p_{ai} and the unknown SH coefficients p_{ci} about the a priori orbit, which is represented by the a priori parameter values p_{ai0} and p_{ci0}:

$$\begin{aligned}\mathbf{r}_a(t) = \mathbf{r}_{a0}(t) &+ \sum_{i=1}^{n_a} \frac{\partial \mathbf{r}_{a0}(t)}{\partial p_{ai}} \cdot \Delta p_{ai} \\ &+ \sum_{i=1}^{n_c} \frac{\partial \mathbf{r}_{a0}(t)}{\partial p_{ci}} \cdot \Delta p_{ci}\end{aligned}, \tag{3}$$

where $\Delta p_{ai} \doteq p_{ai} - p_{ai0}$ denote the n_a corrections to be estimated for the arc-specific orbit parameters and $\Delta p_{ci} \doteq p_{ci} - p_{ci0}$ the n_c corrections for the SH coefficients. Efficient numerical integration techniques are applied to solve the so-called variational equations (Beutler, 2005) in order to obtain the partial derivatives of the a priori orbit $\mathbf{r}_{a0}(t)$ with respect to all parameters. These partials eventually allow it to set up the daily normal equations based on kinematic positions for all corrections according to standard least-squares adjustment.

24.2.4 Daily Normal Equations from ll-SST

Based on the a priori orbits $\mathbf{r}_{a0}(t)$ and $\mathbf{r}_{b0}(t)$ gravity field recovery from, e.g., K-band range measurements may be set up as a differential orbit improvement process. The actual orbit difference $\mathbf{r}_a(t) - \mathbf{r}_b(t)$ may be expressed as a truncated Taylor series with respect to the unknown parameters about the a priori orbit difference. Let us make the distinction between n_a parameters p_{ai} and n_b parameters p_{bi}, which are specific to GRACE A and B, respectively, and n_c parameters p_{ci}, which are common to both GRACE satellites (SH coefficients, K-band calibration parameters). The truncated Taylor series then reads as:

$$\begin{aligned}\mathbf{r}_a(t) - \mathbf{r}_b(t) = \mathbf{r}_{a0}(t) - \mathbf{r}_{b0}(t) &+ \sum_{i=1}^{n_a} \frac{\partial \mathbf{r}_{a0}(t)}{\partial p_{ai}} \cdot \Delta p_{ai} \\ &- \sum_{i=1}^{n_b} \frac{\partial \mathbf{r}_{b0}(t)}{\partial p_{bi}} \cdot \Delta p_{bi} \\ &+ \sum_{i=1}^{n_c} \left(\frac{\partial \mathbf{r}_{a0}(t)}{\partial p_{ci}} - \frac{\partial \mathbf{r}_{b0}(t)}{\partial p_{ci}} \right) \cdot \Delta p_{ci}\end{aligned}. \tag{4}$$

The same techniques as in Sect. 24.2.3 are applied to solve the variational equations separately for both GRACE satellites. K-band range observations contain, however, information about the line-of-sight orbit difference only. Depending on the parameter type, either the partial derivatives of the corresponding a priori orbits with respect to the satellite-specific parameters are therefore projected on the line-of-sight direction or the partial derivatives of the a priori orbit differences with respect to the common parameters are projected. These projected partials eventually allow it to set up the daily normal equations based on K-band range measurements for the corrections Δp_{ai}, Δp_{bi}, and Δp_{ci}. A similar but slightly more complicated procedure is applied when processing K-band range-rate observations. Note that the arc-specific parameters in Eq. (24.4) are set up for both GRACE satellites, which implies that the daily normal equation matrices would be singular if only K-band data were used.

24.3 Error-Free Simulation

Purely dynamic GRACE A and B orbits for 20 days in a true gravity field, defined by the gravity field model EIGEN-GL04C (Förste et al., 2008) up to degree 120, served as true orbits to generate GRACE A and B positions as well as inter-satellite range and range-rate observations. No random errors and no modeling errors were considered in the simulation in order to exploit the numerical limitations of the Celestial Mechanics approach.

Figure 24.1 shows the square-roots of the degree difference variances with respect to the true gravity field for two series of recoveries up to degree 120 based

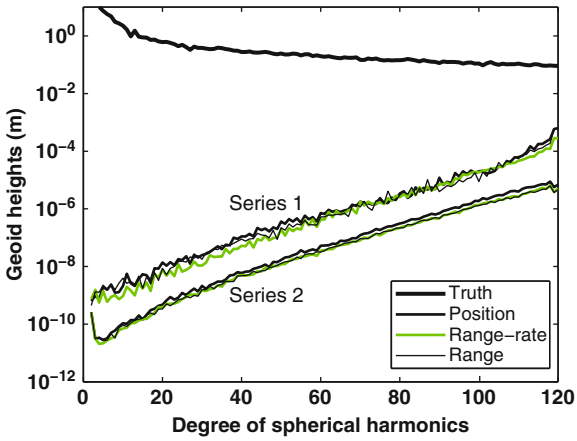


Fig. 24.1 Square-roots of degree difference variances of 20-day recoveries from simulated error-free data

on 20 days. The true gravity field model served for all solutions as a priori model to avoid commission errors. For solutions of the first series only initial conditions were set up as arc-specific parameters, whereas for solutions of the second series also constant empirical accelerations and pseudo-stochastic pulses with a spacing of 30 min were additionally set up as arc-specific parameters. Although the set up of the empirical parameters should not be necessary for a noise-free simulation, the deviations with respect to the true gravity field are further reduced for the solutions of the second series as shown in Fig. 24.1. This effect has to be attributed to the limitations of the numerical integration, which currently is restricted to about $0.2\,\mu m$ after 1 day. As a consequence, small random-walk-like errors are present in the GRACE satellite trajectories of the first series, which are mostly absorbed by the empirical parameters of the second series. The level of the degradation is, however, not yet critical for the processing of real data (Sect. 24.4).

For both series of 20-day solutions three different solutions are shown in in Fig. 24.1. Solutions labelled with "Position" indicate that only simulated positions of one satellite were used for the gravity field determination, whereas solutions labelled with "Range" and "Range-rate" indicate that the equally weighted normal equation contributions from both GRACE satellites as well as from the simulated K-band range and range-rate observations, respectively, were used for the gravity field recovery. Note that all three solutions of one series are of comparable quality with slightly better quality for the combined solutions as to be expected. Figure 24.1 demonstrates the ability of the current implementation of the Celestial Mechanics Approach to close the loop of a noise-free simulation on a comfortable numerical level. The statement holds for gravity field recovery based on orbit positions and for gravity field recovery based on additional inter-satellite range or range-rate observations.

24.4 Processing Real Data

The first gravity field model AIUB-GRACE01S has been derived from GRACE kinematic positions and K-band range-rate data of the entire year 2003 as described in Sect. 24.2. Using EGM96 as an a priori model up to degree 120, the AIUB-GRACE01S model was determined as a static field up to the same degree 120. A spacing of 15 min was selected for the pseudo-stochastic pulses in order to account for various model shortcomings. In order to assess the sensitivity of the current implementation of the Celestial Mechanics Approach on issues like data weighting (Sect. 24.4.1) and background modeling (Sect. 24.4.2), different versions of AIUB-GRACE01S have been generated, which are subsequently discussed and compared with respect to the superior gravity field model EIGEN-GL04C in terms of the square-roots of the degree difference variances or in terms of the square-root of the accumulated degree difference variances up to degree 120.

24.4.1 Data Weighting

According to Sect. 24.2.1 a nominal weighting ratio of $1{:}10^8$ and several experimental ratios between the GPS carrier phase and the K-band range-rate observations have been used for the determination of a gravity field model based on 1 year of data. Figures 24.2 and 24.3 show the square-roots of the degree difference variances with respect to EIGEN-GL04C and the square-roots of the formal degree error variances for the nominal weighting ratio and a ratio of $1{:}10^7$. Figure 24.2 shows that the agreement with respect to EIGEN-GL04C is slightly better for the the medium degrees if the experimental weighting ratio of $1{:}10^7$ is used. On the other hand, Fig. 24.3 clearly implies that

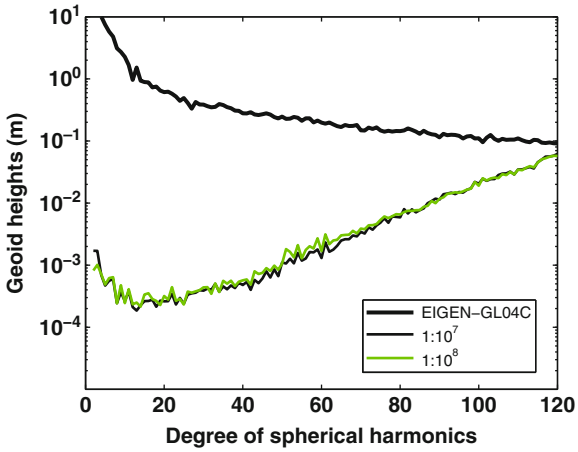


Fig. 24.2 Square-roots of degree difference variances of annual recoveries when using different weighting ratios

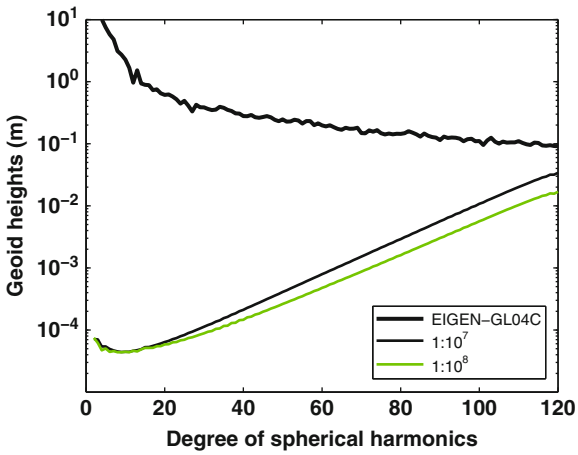


Fig. 24.3 Square-roots of degree error variances of annual recoveries when using different weighting ratios

the SH coefficients are formally better determined over the entire frequency range if the nominal weighting of $1{:}10^8$ is used. Despite this fact the weighting ratio of $1{:}10^7$ seems to be more realistic in view of the modeling level used here. A ratio of $1{:}10^7$ is thus selected for the following experiments.

24.4.2 Background Modeling

At present the implementation of the Celestial Mechanics approach is in progress. Eventually the impact of all relevant background models on gravity field recovery from GRACE will be studied. Currently non-tidal atmosphere and ocean short-term mass variations (Flechtner et al., 2006) are neglected in our processing. Also, we do not make use of the accelerometer data (Case et al. 2002) when analyzing the entire year 2003. Sections 24.4.2.1 and 24.4.2.2 thus assess the sensitivity of the current implementation of the Celestial Mechanics Approach concerning the modeling of the ocean tides and the use of a priori information of the Earth's static gravity field for the full time span of 1 year. The impact of accelerometer data is discussed in Sect.24.2.3 for a limited time span of 1 month.

24.4.2.1 Ocean Tides

A series of gravity field models based on 1 year of data has been determined by taking three different models into account for the description of the ocean tides, namely the model from Schwiderski up to degree 20 (CSR, 1995), the CSR 3.0 ocean tide model up to degree 30 (Eanes and Bettadpur, 1995), and the GOT00.2 ocean tide model up to degree 50 (Ray, 1999). Figure 24.4 shows the square-roots of the degree difference variances with respect to EIGEN-GL04C for the three versions of AIUB-GRACE01S. The gravity field recoveries are not yet very sensitive to the ocean tide modeling. The estimation of frequent pseudo-stochastic pulses is responsible for the differences to be small. The accumulated differences are

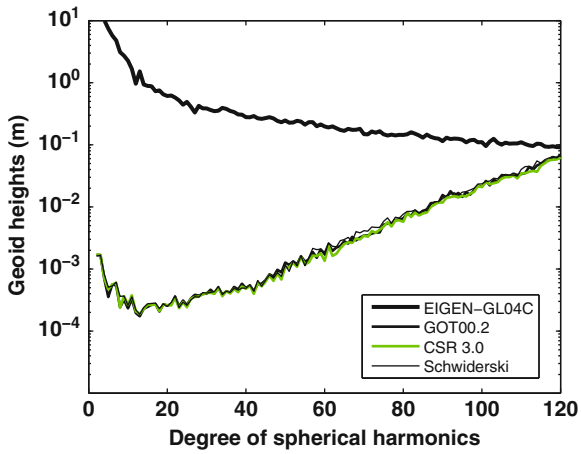


Fig. 24.4 Square-roots of degree difference variances of annual recoveries when using different ocean tide models

20.3, 18.9, and 21.4 cm. The CSR 3.0 ocean tide model was selected for the "final" gravity field determination.

In order to make better use of the ocean tide models a less frequent estimation of the pseudo-stochastic pulses would be required. Due to the current incompleteness of the relevant background models, however, the accumulated differences with respect to EIGEN-GL04C then generally increase, e.g., from 18.9 to 23.0 cm when using the CSR 3.0 model and a pulse spacing of 30 min. Therefore, a spacing of 15 min currently has to be selected, even if it might weaken the gravity field recovery.

24.4.2.2 A Priori Information

Although EGM96 was used as a priori model up to degree and order 120, no significant commission errors could be detected in the AIUB-GRACE01S solution. A complete iteration of the entire gravity field determination process improved the accumulated differences with respect to EIGEN-GL04C only marginally from 18.9 to 18.8 cm without changing the curves in Fig. 24.4. AIUB-GRACE01S can thus be considered as widely independent of the a priori gravity field model.

In order to assess the sensitivity of the current implementation of the Celestial Mechanics Approach to omission errors of the gravity field, a solution up to degree 120 based on 1 year of data has been determined by using EGM96 as a priori model up to degree 200 instead of 120. As the accumulated differences "only" changed from 18.9 to 18.0 cm, we conclude that the gravity field recoveries are not (yet) very sensitive to the neglected higher degree terms of the Earth's gravity field. No significant improvements are expected when solving gravity field coefficients up to degrees higher than 120, which might be different when processing longer data spans.

24.4.2.3 Non-gravitational Accelerations

Gravity field solutions based on 1 month of data have been derived by taking accelerometer data as non-gravitational accelerations into account, but without estimating additional scale factors. The time period selected covers GPS weeks 1235–1238, where the GRACE data were found to be of a continuously high quality. Compared to the corresponding solutions without accelerometer data from Sect. 24.4.2.1, the accumulated differences with respect to EIGEN-GL04C decrease from 56.3 to 50.2 cm and from 74.4 to 60.0 cm for a pulse spacing of 15 and 30 min, respectively. Similar to Sect. 24.4.2.1, a less frequent estimation of the pseudo-stochastic pulses is required to make better use of the quality of accelerometer data. At present, however, solutions based on 15 min pulses agree better with EIGEN-GL04C than solutions based on 30 min pulses, even if accelerometer data are taken into account. Further investigations, based on at least 1 year of data, are necessary to better quantify the impact of the accelerometer data.

24.5 Validation with External Data

Geoid heights based on different GPS-levelling data sets have been compared with geoid heights derived from AIUB-GRACE01S according to (Gruber 2004). The validation was performed by T. Gruber from the Institute for Astronomical and Physical Geodesy of the Technical University of Munich.

Table 24.1 RMS of differences (cm) between GPS-levelling and model geoid heights up to different maximum degrees

	AIUB-GRACE01S			ITG-GRACE02S		
GPS-levelling data	Degree 60	Degree 90	Degree 120	Degree 60	Degree 90	Degree 120
EUREF GPS	23.0	22.9	28.9	23.1	22.4	22.0
BRD EUVN	03.4	04.9	11.6	03.2	03.3	04.3
BRD GPS	03.6	05.5	11.2	03.5	04.1	05.0
Canada GPS 1998	19.6	20.0	24.2	19.8	19.9	19.9
Canada GPS 2007	14.5	14.7	21.4	14.7	14.7	15.3
Australia GPS	24.1	24.4	32.2	24.1	24.2	24.5
Japan GPS	11.6	11.0	21.0	11.6	10.0	10.0
USA GPS	33.3	33.3	37.9	33.3	33.2	33.4

Table 24.1 shows the RMS values of the differences around the mean values between the filtered GPS-levelling geoid heights and geoid heights from AIUB-GRACE01S up to different maximum degrees. For comparison the gravity field model ITG-GRACE02S (Mayer-Gürr, 2008) is included as well. It can be recognized that up to degree 60 the validation results are similar for the two satellite-only models. Deficiencies of AIUB-GRACE01S are not yet well visible and just show up in some of the high-quality data sets, e.g., in the BRD EUVN data set. Up to degrees 90 or 120, however, the limited quality of AIUB-GRACE01S compared to ITG-GRACE02S clearly shows up in most of the data sets. As ITG-GRACE02S is based on a higher resolution up to degree 170 and about three times more data, it will be mandatory to strive for a higher resolution based on more data for future AIUB-GRACE releases in order to achieve a quality level comparable to that of the ITG-GRACE releases.

24.6 Conclusions

We used the Celestial Mechanics Approach for gravity field determination with GPS-derived kinematic positions and K-band range-rate data to generate the static gravity field model AIUB-GRACE01S from GRACE data of the entire year 2003. We showed that the recovery can be based on EGM96 as a priori model and that the resulting field is of excellent quality in view of the currently limited modeling level. It is remarkable, on the one hand, that empirical parameters like pseudo-stochastic pulses are able to compensate to a large extent for model shortcomings, e.g., for the neglection of accelerometer data and short-term mass variations. The frequent estimation of pseudo-stochastic pulses most probably also weakens the quality of the gravity field solution.

The comparison with other GRACE models and the comparison with terrestrial measurements clearly revealed a great potential for improvements of the AIUB-GRACE01S model. The next step of sophistication of the Celestial Mechanics approach is in progress. Future releases of AIUB-GRACE models will be based on the available background models and on longer data spans, which hopefully will allow it to reduce the number of the empirical parameters and to solve SH coefficients up to higher degrees in order to improve the inferred gravity field solutions.

Acknowledgements The authors gratefully acknowledge the generous support provided by the Technical University of Munich's Institute for Advanced Study (IAS) in the frame of the project "Satellite Geodesy".

References

Beutler, G. (2005) Methods of celestial mechanics. Springer, Berlin, Heidelberg, New York.

Case, K., G. Kruizinga and S. Wu (2002). GRACE Level 1B Data Product User Handbook. D-22027, JPL Publication, Pasadena, California, USA.

CSR ocean tide model from Schwiderski (1995). ftp://ftp.csr.utexas.edu/pub/tide/oldfiles/spharm_schwid+

Eanes, R.J., and S.V. Bettadpur (1995). The CSR 3.0 global ocean tide model. Technical Memorandum 95-06, Center for Space Research, University of Texas, Austin.

Flechtner, F., R. Schmidt, and U. Meyer (2006). De-aliasing of short-term atmospheric and oceanic mass variations for GRACE. In: Flury, J., R. Rummel, C. Reigber, M. Rothacher, G. Boedecker, and U. Schreiber (eds), Observation of the earth system from space. Springer, Heidelberg, pp. 83–97.

Förste, C., R. Schmidt, R. Stubenvoll, F. Flechtner, U. Meyer, R. König, U. Meyer, H. Neumayer, R. Biancale, J.M. Lemoine, S. Bruinsma, S. Loyer, F. Barthelmes, and S. Esselborn (2008). The GeoForschungsZentrum Potsdam/Groupe de Recherche de Géodésie Spatiale satellite-only and combined gravity field models: EIGEN-GL04S1 and EIGEN-GL04C. *J. Geod.* 82, 331–346.

Gruber, T. (2004) Validation Concepts for Gravity Field Models from Satellite Missions. In: Proceedings of Second International GOCE User Workshop "GOCE, The Geoid and Oceanography", ESA-ESRIN, Frascati, Italy.

Heiskanen, W.A. and H. Moritz (1967). Physical Geodesy. Freeman.

Jäggi, A., U. Hugentobler and G. Beutler (2006). Pseudo-stochastic orbit modeling techniques for low-Earth orbiters. *J. Geod.*, 80, 47–60.

Jäggi, A., G. Beutler, L. Prange, R. Dach, and L. Mervart (2008). Assessment of GPS observables for Gravity Field Recovery from GRACE. In: Sideris, M.G. (ed), Observing our Changing Earth. Springer, Heidelberg, pp. 113–120.

Lemoine, F.G., D.E. Smith, L. Kunz, R. Smith, E.C. Pavlis, N.K. Pavlis, S.M. Klosko, D.S. Chinn, M.H. Torrence, R.G. Williamson, C.M. Cox, K.E. Rachlin, Y.M. Wang, S.C. Kenyon, R. Salman, R. Trimmer, R.H. Rapp, and R.S. Nerem (1997). The development of the NASA GSFC and NIMA joint geopotential model. In: Segawa, J., H. Fujimoto, and S. Okubo (eds), IAG Symposia: Gravity, Geoid and Marine Geodesy. Springer-Verlag, New York, pp. 461–469.

Mayer-Gürr, T. (2008). Gravitationsfeldbestimmung aus der Analyse kurzer Bahnbögen am Beispiel der Satellitenmissionen CHAMP und GRACE. Schriftenreihe

9, Institute for Geodesy and Geoinformation, University of Bonn, Germany.

Prange, L., A. Jäggi, G. Beutler, R. Dach, L. Mervart (2008). Gravity Field Determination at the AIUB – the Celestial Mechanics Approach. In: Sideris, M.G. (ed), Observing our Changing Earth. Springer, Heidelberg, pp. 353–360.

Ray, R.D. (1999). A global ocean tide model from TOPEX/Poseidon altimetry: GOT99.2. NASA Tech Memo 209478, Goddard Space Flight Center, Greenbelt.

Tapley, B.D., S. Bettadpur, J.C. Ries, P.F. Thompson, and M. Watkins (2004). GRACE measurements of mass variability in the Earth system. *Science*, 305(5683).

Chapter 25

Fast Variance Component Estimation in GOCE Data Processing

J.M. Brockmann and W.-D. Schuh

Abstract For the processing of GOCE (Gravity Field and steady-state Ocean Circulation Explorer) data the program system `pcgma` (Preconditioned Conjugate Gradient Multiple Adjustment) was designed as a tailored solution strategy for the determination of the Earth's gravity field in terms of a spherical harmonic analysis. Within GOCE-HPF (High Level Processing Facility) the `pcgma` algorithm works with the purpose of a tuning machine in that it is used to optimize the filter design and to determine optimal variance components with respect to the combination of satellite-to-satellite tracking (sst) data, satellite gravity gradiometry (sgg) data and additional prior information about the smoothness of the gravity field (the latter especially with regard to the polar regions). `pcgma` is based on an extended version of the iterative conjugate gradient (CG) algorithm, which allows for data combination in terms of observation and normal equations. A basic prerequisite for handling the nesting of the two iterative methods (variance component estimation (VCE) and parameter estimation using CG) is an efficient and fast implementation, because the VCE requires a repeated solution of the system. In this paper we will show how the nesting can be organized in an optimal way. We will concentrate on the reduction of CG iteration steps.

J.M. Brockmann (✉)
Department for Theoretical Geodesy, Institute of Geodesy and Geoinformation, University of Bonn, Bonn D-53115, Germany
e-mail: brockmann@geod.uni-bonn.de

25.1 Introduction

Starting from the linear normal equation system in terms of a least squares adjustment, the GOCE observations could be combined by summation of the normal equations of each observation group. Assuming the groups to be uncorrelated, the system reads

$$\begin{aligned}\left(\omega_{\mathrm{sgg}}\mathbf{A}_{\mathrm{sgg}}^{T}\mathbf{P}_{\mathrm{sgg}}\mathbf{A}_{\mathrm{sgg}}+\omega_{\mathrm{sst}}\mathbf{N}_{\mathrm{sst}}+\omega_{\mathrm{reg}}\mathbf{P}_{\mathrm{reg}}\right)\mathbf{x}=\\ \omega_{\mathrm{sgg}}\mathbf{A}_{\mathrm{sgg}}^{T}\mathbf{P}_{\mathrm{sgg}}\mathbf{l}_{\mathrm{sgg}}+\omega_{\mathrm{sst}}\mathbf{n}_{\mathrm{sst}}+\omega_{\mathrm{reg}}\mathbf{n}_{\mathrm{reg}}\end{aligned} \tag{1}$$

where

$\mathbf{A}_{\mathrm{sgg}}$ ... decorrelated design matrix (sgg group),
$\mathbf{l}_{\mathrm{sgg}}$ ... decorrelated observations (sgg group),
$\mathbf{P}_{\mathrm{sgg}}$ ... weight matrix (sgg group),
$\mathbf{N}_{\mathrm{sst}}$ ... normal equation matrix (sst group),
$\mathbf{n}_{\mathrm{sst}}$ ... right hand side (sst group),
$\mathbf{P}_{\mathrm{reg}}$ ... regularization matrix, inverse covariance matrix of prior information,
$\mathbf{n}_{\mathrm{reg}}$ ... prior information of parameter values,
ω_i ... unknown weight factor, $i \in$ {sgg,sst,reg} (inverse variance components),
$\mathbf{x}$ ... unknown parameters, $\{c_{lm}\ s_{lm}\}$.

The sgg observation equations are decorrelated by applying digital autoregressive-moving average filters (cf. Siemes, 2008; Schuh, 2003) estimated from the residuals. Since we estimate independent filters for the three tensor components V_{xx}, V_{yy} and V_{zz} correlations between the observations along on axes are modelled, but correlations between the three gradients are neglected. Then, after filtering the observation equations, $\mathbf{l}_{\mathrm{sgg}}$ and $\mathbf{A}_{\mathrm{sgg}}$ emerge as the decorrelated

S.P. Mertikas (ed.), *Gravity, Geoid and Earth Observation*, International Association of Geodesy Symposia 135,
DOI 10.1007/978-3-642-10634-7_25, © Springer-Verlag Berlin Heidelberg 2010

observation vector and design matrix, and $\mathbf{P}_{\mathrm{sgg}} = \mathbf{I}$. We did not compute the sst observation equations, but we used the sst normal equations as they have been preprocessed by the HPF. Mainly there are two alternative ways of solving Eq. (1),

1. Compute the joint normal equation matrix **N** as left hand side of Eq. (1) and solve $\mathbf{Nx} = \mathbf{n}$.
2. Avoid computing **N** (especially the large scaled product $\mathbf{A}_{\mathrm{sgg}}^T \mathbf{P}_{\mathrm{sgg}} \mathbf{A}_{\mathrm{sgg}}$), by using a tailored iterative solution strategy for Eq. (1) (in our case `pcgma`, Schuh, 1996).

The general equation to determine the variance components σ_i^2 for observation group i (e.g., Koch, 2007) can be written as

$$\sigma_i^2 = \frac{\Omega_i}{n_i - u_i} = \frac{\Omega_i}{r_i} = \frac{1}{\omega_i}, \tag{2}$$

where

n_i . . . # of observations in group i,
u_i . . . # of parameters determined by group i,
r_i . . . partial redundancy of observation group i,
ω_i . . . weight factor of observation group i.

Ω_i is weighted squared sum of residuals and equals

$$\Omega_i = \mathbf{v}_i^T \mathbf{P}_i \mathbf{v}_i \text{ or}$$
$$\Omega_i = \mathbf{x}^T \mathbf{N}_i \mathbf{x} - 2\mathbf{x}^T \mathrm{n_i} + \mathbf{l}_i^T \mathbf{P}_i \mathbf{l}_i$$

depending on whether the observation groups are available as observation or as normal equations (assuming the constant $\mathbf{l}_i^T \mathbf{P}_i \mathbf{l}_i$ to be known).

Starting with initial weights $\omega_i^{(0)}$, new weight factors $\omega_i^{(\iota)}$ could be determined as inverse variance components using the squared sum of residuals and the partial redundancy for each observation group $i \in$ {sgg,sst,reg} after parameter estimation. With these new weight factors Eq. (1) is then solved again using the iterative CG algorithm. Due to the nesting of a second iterative method in the processing chain and the fact that the normal equation matrix of the parameters is not explicitly computed, the algorithm for VCE must be modified. The whole strategy is briefly summarized by Fig. 25.1.

In this paper we will concentrate upon three parts:

1. Integration of a Monte-Carlo based trace estimator into the VCE algorithm (cf. Koch and Kusche, 2001) combined with iterative CG.
2. Quality requirement for weight factors ω_i to get an optimal solution (Brockmann, 2008).
3. Convergence of VCE, with regard to trace and squared sum of residuals in the iterative solver.

The paper is organized in the following way. Section 25.2 shows how the VCE suggested by Koch and Kusche (2001) is applied in an iterative parameter estimation procedure (Alkhatib, 2007). In Sect. 25.3 the effect of errors in the weight determination in the case of GOCE data processing is analyzed. In Sect. 25.4 numerical simulations are used to analyze the convergence of VCE. Using these results, we present an optimized nesting of the iterative methods with the goal of minimizing the number of CG steps necessary to obtain convergence of weights. This paper ends with a summary and an outlook in Sect. 25.5.

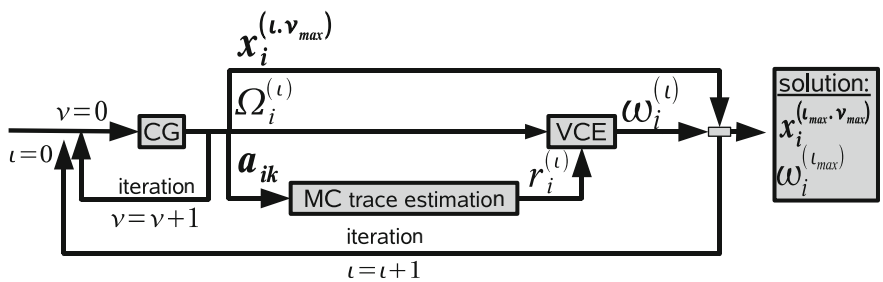


Fig. 25.1 Flowchart of the nested processing strategy

25.2 VCE as Part of an Iterative Solver

Starting from Eq. (2) to determine σ_i^2 and replacing the partial redundancy by (e.g., Alkhatib, 2007)

$$r_i = n_i - \frac{1}{\sigma_i^2}\text{trace}\left(\mathbf{A}_i^T\mathbf{P}_i\mathbf{A}_i\mathbf{N}^{-1}\right) \tag{3}$$

$$r_i = n_i - \frac{1}{\sigma_i^2}\text{trace}\left(\mathbf{N}_i\mathbf{N}^{-1}\right) \tag{4}$$

depending on whether the observation groups are available as observation or as normal equations, two facts become apparent: The procedure

(i) is iterative, because initial values for σ_i^2 are needed (cf. Eq. (3)), and the computation of σ_i^2 is based upon residuals, which change after parameter estimation with updated VCE (cf. Eq. (2)).
(ii) requires the combined normal equation matrix and $\mathbf{A}_i^T\mathbf{P}_i\mathbf{A}_i$, whose computation is avoided using CG.

Introducing the stochastic trace estimator for estimating the trace in Eqs. (3) and (4) as presented in Hutchinson (1990) and as suggested by Koch and Kusche (2001) in the context of GOCE data analysis, and noting the fact that the matrix in the trace term must be symmetric (cf. Hutchinson, 1990), we can reformulate the computation of the partial redundancy as

$$r_i = n_i - \frac{1}{\sigma_i^2}E\{\mathcal{P}_i^T\mathbf{R}_i\mathbf{A}_i\mathbf{N}^{-1}\mathbf{A}_i^T\mathbf{R}_i^T\mathcal{P}_i\} \tag{5}$$

$$r_i = n_i - \frac{1}{\sigma_i^2}E\{\mathcal{P}_i^T\mathbf{G}_i\mathbf{N}^{-1}\mathbf{G}_i^T\mathcal{P}\} \tag{6}$$

using the Cholesky decompositions $\mathbf{P}_i = \mathbf{R}_i^T\mathbf{R}_i$ and $\mathbf{N}_i = \mathbf{G}_i^T\mathbf{G}_i$ respectively. In these equations the random vectors $\mathcal{P}_i$ follow a discrete uniform distribution taking the values ± 1 with probability 0.5.

Replacing the random variable $\mathcal{P}_i$ with one of $k \in \{1 \ldots K\}$ realizations named as $\mathbf{p}_{ik}$, for each observation group i and each realization k, and introducing the transformed realizations of the random vector, $\bar{\mathbf{p}}_{ik} = \mathbf{A}_i^T\mathbf{R}_i^T\mathbf{p}_{ik}$ and $\bar{\mathbf{p}}_{ik} = \mathbf{G}_i^T\mathbf{p}_{ik}$ respectively, Eqs. (5) and (6) can be written for a single realization as

$$r_{ik} = n_i - \frac{1}{\sigma_i^2}\bar{\mathbf{p}}_{ik}^T\mathbf{N}^{-1}\bar{\mathbf{p}}_{ik}. \tag{7}$$

This equation can now be evaluated by applying the iterative solver `pcgma` to additional right hand sides $\bar{\mathbf{p}}_{ik}$ for each realization k of each observation group i. In other words, `pcgma` is used to solve the system of equations $\mathbf{N}\mathbf{a}_{ik} = \bar{\mathbf{p}}_{ik}$ to compute the product $\mathbf{a}_{ik} = \mathbf{N}^{-1}\bar{\mathbf{p}}_{ik}$. With the estimated parameters $\mathbf{a}_{ik}$ we are now able to compute the partial redundancy using the mean values of all realizations from each observation group by

$$r_i = n_i - \frac{1}{\sigma_i^2}\frac{1}{K}\sum_{k=1}^{K}\bar{\mathbf{p}}_{ik}^T\mathbf{a}_{ik}. \tag{8}$$

25.3 Effect of Inaccuracies in the Weights

When estimating new weight factors two elements could be erroneous, as we can see from Eq. (2). First, the partial redundancy due to a random error of the stochastic trace estimator and systematic error caused by insufficient CG convergence in the additional trace parameters; second, the squared sum of residuals due to insufficient CG convergence in the estimation of the primary parameters ($\{c_{lm}\ s_{lm}\}$).

25.3.1 Effect of a Trace Error on the Weights

Introducing an error into the trace estimation (number of parameters determined by group i) in Eq. (5) and (6), the erroneous weights follow to be (cf. (2))

$$\tilde{\omega}_i = \frac{n_i - (u_i + \Delta u_i)}{\Omega_i} = \frac{n_i - u_i}{\Omega_i} - \frac{\Delta u_i}{\Omega_i}$$
$$= \omega_i - \Delta\omega_i.$$

The relative weight error may then be written as a function of the relative error in the trace estimation,

$$\frac{\Delta\omega_i}{\omega_i} = \frac{\frac{\Delta u_i}{\Omega_i}}{\frac{n_i - u_i}{\Omega_i}} = \frac{\Delta u_i}{n_i - u_i} = \frac{1}{\frac{n_i}{u_i} - 1}\frac{\Delta u_i}{u_i}, \tag{9}$$

Table 25.1 Scaling factor of relative trace error on weights

i	n_i	u_i	a_i
sgg	$> 10^7$	$< 10^5$	$< 10^{-2}$
sst	$3 \cdot 10^6$	$< 10^4$	$< 3 \cdot 10^{-3}$
reg	$< 10^5$	$10^2 \ldots 10^5$	$10^{-3} \ldots 1$

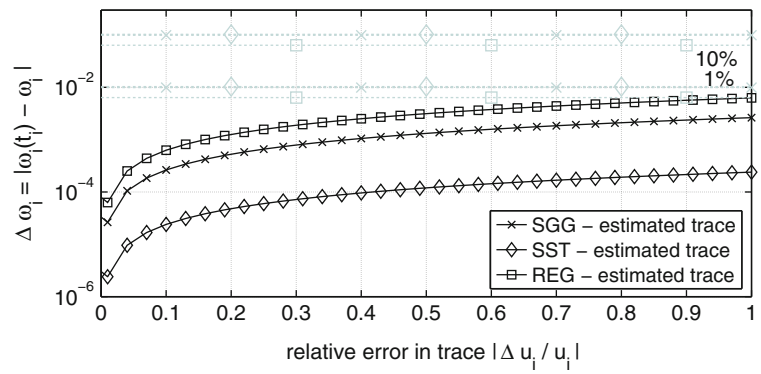
demonstrating a linear dependence (with factor $a_i = \frac{1}{\frac{n_i}{u_i} - 1}$) on the relative trace error. Evaluating the number of unknowns u_i and the number of observations u_i in the context of GOCE data processing (and taking into account the realistic resolutions), the factor a_i has the magnitude as shown in Table 25.1 for the different observation groups.

Realizing that we can always limit the trace error to 100% (replacing the trace estimation by the assumption $u_i = 0$) the resulting weight errors for sgg and sst are limited to less than 1%. The strict estimation of the trace turns out to be unnecessary for these two observation groups. By introducing additional assumptions (all low frequency parameters are determined by sst and all high frequency parameters are determined by sgg) about u_{sst} and u_{sgg}, the resulting error could be reduced to about 0.1%.

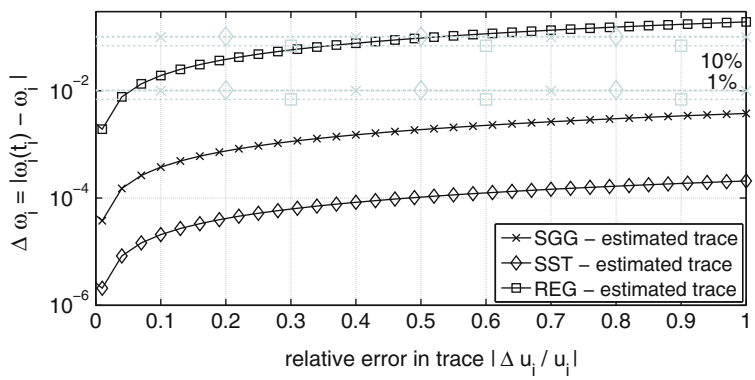
If we take a look at the regularization group, we see a generally greater influence up to $a_{\mathrm{reg}} = 1.0$. Inserting the optimal values for trace estimation and squared sum of residuals from a reference solution for two different resolutions (d/o 200 and d/o 270) we see the resulting weight error caused by a relative trace error in Fig. 25.2.

We may draw the following three conclusions:

1. The effect of a trace error is highly resolution dependent.
2. The effect of a trace error on sgg and sst is negligible for all realistic resolutions.
3. The quality in the trace estimation for the regularization group becomes more and more important with increasing resolution.



(a) For model up to d/o 200.



(b) For model upto d/o 270.

Fig. 25.2 Absolute weight error due to a relative trace error

25.3.2 Effect of Insufficiently Converged Residuals on the Weights

An error $\Delta\Omega_i$ in the squared sum of residuals caused for example by insufficient convergence of the CG algorithm for the primary parameter estimation, could be introduced as

$$\tilde{\omega}_i = \frac{n_i - u_i}{\Omega_i + \Delta\Omega_i}. \tag{10}$$

Linearization according to Taylor implies

$$\Delta\omega_i \approx -\frac{n_i - u_i}{\Omega_i^2}\Delta\Omega_i + \frac{n_i - u_i}{\Omega_i^3}\Delta\Omega_i^2 \mp \mathcal{O}\left(\Delta\Omega_i^3\right)$$

as an error in the weights. A relative weight error as a function of the relative error in Ω_i can be written as

$$\frac{\Delta\omega_i}{\omega_i} \approx -\frac{\Delta\Omega_i}{\Omega_i} + \left(\frac{\Delta\Omega_i}{\Omega_i}\right)^2 \mp \mathcal{O}\left(\left(\frac{\Delta\Omega_i}{\Omega_i}\right)^3\right). \tag{11}$$

As can be seen in Eq. (11) a relative error of insufficiently converged residuals in the first approximation causes an error scaled by 1 in the weights. In contrast to the trace estimator, the absolute error in $\Delta\Omega_i$ can be larger than Ω_i. Therefore, the relative error is not limited. But we have to keep in mind that an update of the weights has only a small influence on the parameters and therefore the iterative process (CG) can be restarted with more precise initial values. In addition we can take advantage of the typical behavior of the CG algorithm where the major part of the residuals is minimized in the first iteration steps.

25.3.3 Effect of Weight Errors on the Final Solution

As already mentioned in Sect. 25.3.1 and as will be seen in Fig. 25.5, the convergence of the weight for the regularization group is most critical. To investigate the behavior in detail we introduce an error in ω_{reg} to simulate the convergence of ω_{reg}. If convergence of the regularization group is reached we could assume that the sst and sgg weights have reached convergence up to higher digits. The error $\Delta\omega_{\text{reg}}$ is applied to the optimal estimation of ω_{reg}. With this weight and the optimal estimation of ω_{sst} and ω_{sgg} a complete CG iteration is performed to estimate an optimal solution for the potential coefficients $\mathbf{x}$ using the constant weight factors. Table 25.2 shows the results when a weight error of $\Delta\omega_{\text{reg}} = 0.1$ and 0.01, respectively, is added. With these errors the convergence of the weights up to the first and second digit is simulated. The differences are shown in terms of geoid heights with reference to the optimal solution for which all weights reached convergence (the model was resolved up to d/o 270).

Table 25.2 Effect of an error in ω_{reg} on geoid heights [m], as difference to solution with optimal weights

$\Delta\omega_{\text{reg}}$	Sector	Min/max	Mean	rms
0.1	±84°	−0.075/0.091	0.000	0.009
0.1	±90°	−0.127/0.112	0.000	0.012
0.01	±84°	−0.007/0.009	0.000	0.001
0.01	±90°	−0.012/0.014	0.000	0.001

Convergence of ω_{reg} up to the second digit (error $\approx 1.5\%$) causes a maximal error in terms of geoid heights with regard to the optimal solution of less than 1 cm, which is about one magnitude smaller than the mean error that the optimal solution of this test data set reaches with respect to the "true" model (ESA-AR3 data, EGM96 true model in closed loop simulation). As a conclusion we can say that the convergence of ω_{reg} up to the second digit leads to an insignificant error in the geoid, whereas the error caused by convergence up to the first digit ($\Delta\omega_{\text{reg}} = 0.1$) is one magnitude larger and thus exactly of the same magnitude as the outer accuracy, resulting in significant geoid errors.

25.4 Numerical Simulations

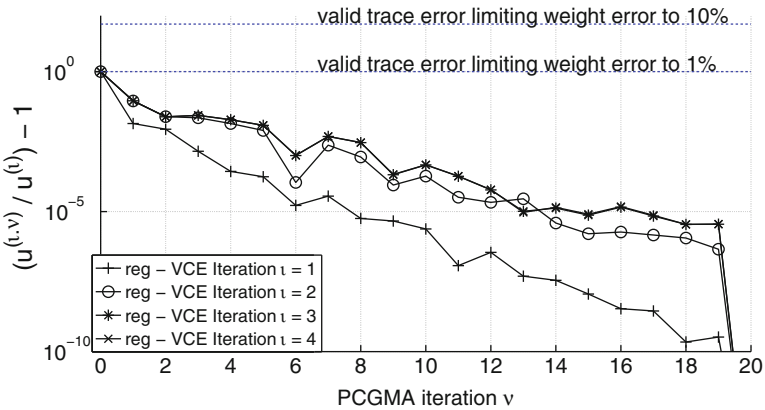
The following simulations are closed-loop simulations, i.e., the observations were created by using the EGM96 as input and adding a realistic GOCE noise; thus we have the advantage of knowing the true solution. We created a reference solution with simulated GOCE observations (60 days, 15,000,000 sgg observations, sst normal equation matrix up to d/o 90), where a sufficient number of CG iteration steps were performed within each VCE iteration. As the regularization model we used Kaula's rule of thumb, introducing stochastic prior information assuming the spherical harmonic coefficients to be zero with a variance given by Kaula's

rule ($\mathbf{P}_{\text{reg}}$). We computed the trace, squared sum of residuals and estimates for the weights within each CG iteration (step) ν of VCE iteration ι (named $\iota.\nu$) to see how the estimation performs. For this simulation $\nu_{\max}$ is fixed by 20 (d/o 200) and 10/20 (d/o 270) iterations for deriving a solution with 6–10 digits accuracy with respect to ω_i (see Fig. 25.5). The goal of this simulation is to determine where the main estimation effort takes place and to see where wasted CG iterations are done with respect to VCE. It will be seen that the main minimization in the CG algorithm is done in the first iterations. After this first steps, there is slow convergence to the optimal solution, which are wasted iterations in the context of VCE and for the parameter estimation, because the target function is, due to the non-optimal weights, wrong.

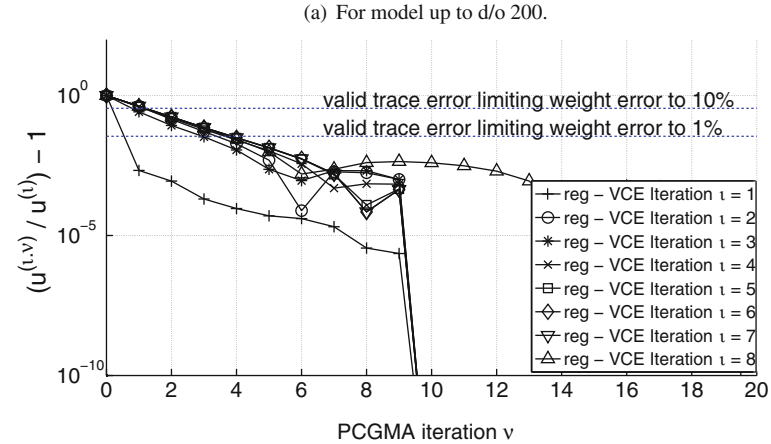
In a first simulation the model is resolved up to d/o 200, in a second up to d/o 270. The reference solution for the d/o 200 model consists of 4 VCE iterations with 20 CG iterations each. For the d/o 270 model, 8 VCE iterations with 10 CG iterations each were required (the last VCE iteration was performed with 20 CG iterations to make sure CG reached convergence). The initial weights were chosen so that $\omega_{\text{sst}} = \omega_{\text{sgg}} = 1.0$ and $\omega_{\text{reg}} = 10^{-12}$ (i.e., assuming no regularization is needed). The initial values for the parameters were set to $\mathbf{x} = \mathbf{0}$.

25.4.1 Convergence of the Trace Estimation

As explained in Sect. 25.3.1, the trace estimation for the regularization group is the most critical issue. We have shown in Sect. 25.3.3 that we have to make sure that an error in the weight estimation is limited to 1%. If we assume the last trace estimation in each VCE iteration to be optimal, Fig. 25.3 shows the remaining error after each CG iteration for both models.



(a) For model up to d/o 200.



(b) For model up to d/o 270.

Fig. 25.3 Remaining relative trace error regarding trace estimation $u^{(\iota)}$, the estimation at the last CG iteration of the ι-th VCE iteration

Using Eq. (9) we can calculate the trace error which limits the weight error to 1%. We see that in the lower resolution model this threshold is immediately reached, but regarding the higher resolution model we see that the trace estimation needs at least 4 CG iterations to ensure that the weight error is limited to 1% (in a strict sense the 1% line in Fig. 25.3 is only valid for the final VCE iteration step where the trace and Ω_i assume realistic values).

25.4.2 Convergency of Residuals

After applying the tailored preconditioner (cf. Boxhammer and Schuh, 2006; Boxhammer, 2006) the convergence of the CG algorithm is very fast. Assuming the Ω_i to be minimal after the final CG iteration step of the last VCE iteration Fig. 25.4 shows the remaining errors over all CG iteration steps.

We can notice two important facts: the convergence of residuals is highly dependent on the resolution, and the main advance in each VCE step occurs in the first few CG steps. Counting the steps where Ω_{reg} is significantly reduced we obtain for the d/o 200 model about 5–7 iterations and for the d/o 270 model about 35 iterations.

25.4.3 Overall Weight Convergence

Starting from the trace estimation and the squared sum of residuals, the weights $\omega^{(\iota.\nu)}$ may be computed in each CG step (without applying them to Eq. (1), which is why they will be called pseudo weights in the following figures). Assuming the ultimate weight estimation to be optimal, Fig. 25.5 shows the number of correct digits of weights in each CG step $\iota.\nu$.

Although sgg and sst weights start with accurate values, the first estimations lose in accuracy (as a consequence of large Ω_i), but reach the convergence of the second digit after at most 5 steps. The convergence of the regularization group is thus limiting the overall convergence rate. For the d/o 270 model the effect on trace estimation is strong (starting at iteration 5.10).

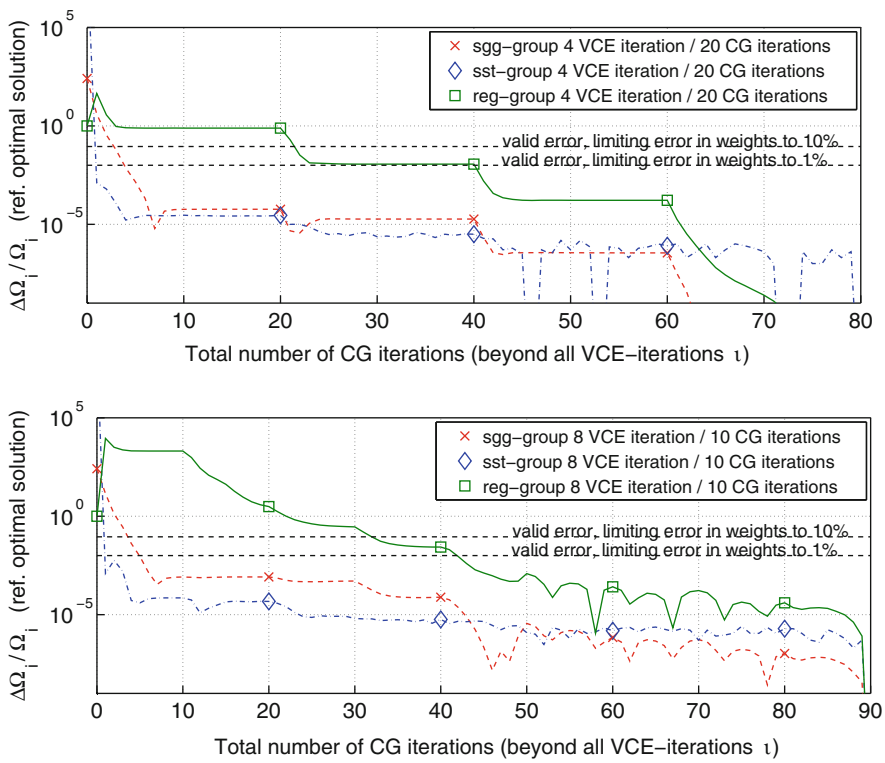
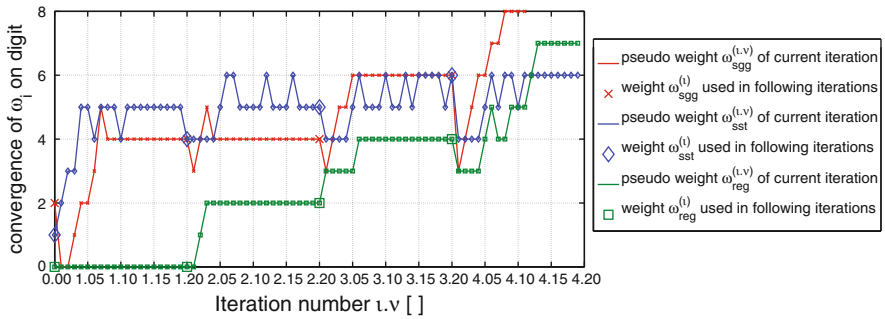
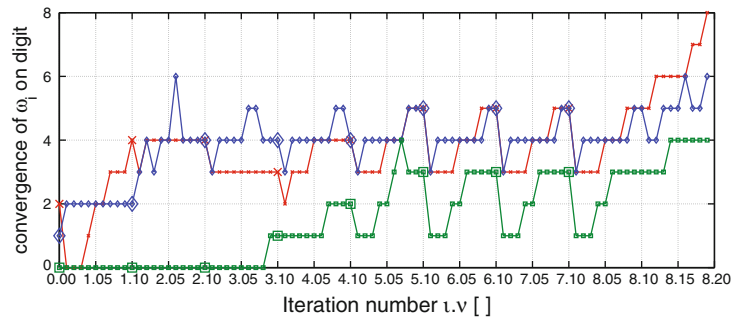


Fig. 25.4 Relative error in Ω_i with respect to the final value Ω_i of the last VCE iteration



(a) For model up to d/o 200.



(b) For model up to d/o 270.

Fig. 25.5 Number of correct weight digits in each CG iteration ν of every VCE iteration ι. Ref.: last estimation

Because the additional parameters start from zero at each VCE step, 4 CG steps are always required to reach the second correct digit, and 6 CG steps are required to reach the third digit.

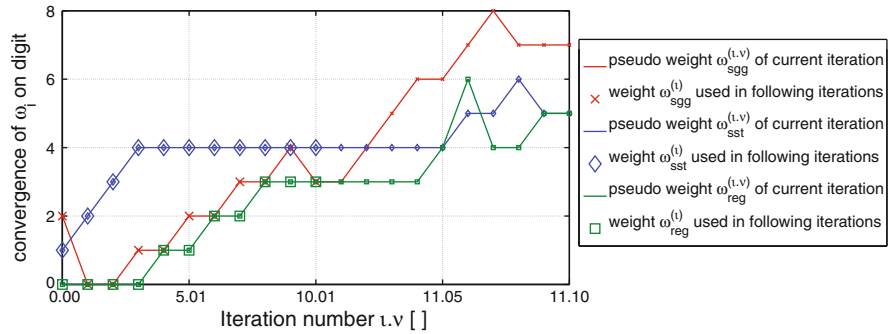
25.4.4 Optimized Solution Strategy

First of all, it is important to remark that for general parameter convergence it is not crucial how many CG iterations are done consecutively. The rate of convergence will not decrease if CG is restarted after only a few steps. It makes therefore sense to update the weights after as many CG steps the trace needs to be estimated correctly in each VCE iteration. This results in a sequence of 1 CG iteration in each VCE iteration for the d/o 200 model. Applying this strategy to the d/o 270 model 4 CG steps are necessary for the trace to converge. Figure 25.6 shows the number of correct digits of the weights computed in this optimized strategy using the same reference of Fig. 25.5.

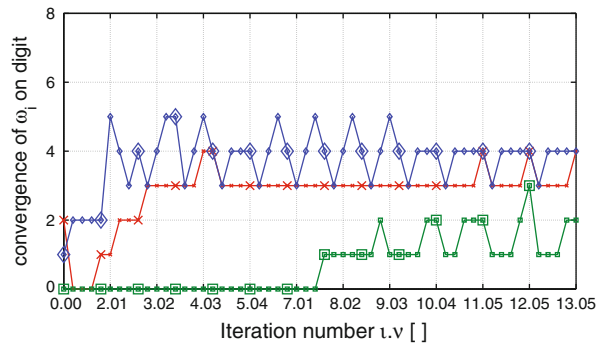
25.5 Summary and Outlook

In this paper we showed how VCE may be integrated into an iterative solution method for large scaled estimation problems. Starting from numerical simulations it was demonstrated how the VCE and especially the required trace estimation and the squared sum of residuals converge in two typical data sets of GOCE processing, limiting the expected resolution.

In this investigation we assumed the optimal decorrelation filter to be known. However, in the real GOCE data processing chain the iterative procedures considered in this paper are complemented by the iterative decorrelation filter estimation (Siemes, 2008). An interesting investigation would be how the filter estimation influences the VCE and vice versa. Another interesting investigation would be to integrate an additional data group, e.g. polar gap regularization (Metzler and Pail, 2005) or gridded surface gravity anomalies, and to analyse how this additional information influences the weight estimation.



(a) Model d/o 200, 1 CG iteration in each VCE iteration.



(b) Model d/o 270, 4 CG iteration in each VCE iteration.

Fig. 25.6 Number of correct weight digits in each CG iteration ν of every VCE iteration ι for the optimized strategy

Acknowledgments Part of this work was financially supported by the BMBF Geotechnologien program GOCE–GRAND II (Grant 03F0421B) and the GOCE High-level Processing Facility. Parts of the simulations were performed using JUMP at Jülich Supercomputing Center. The computing time was granted by the John von Neumann Institute for Computing (project 1827).

References

Alkhatib, H. (2007). On Monte Carlo methods with applications to the current satellite gravity missions. PhD thesis. Institute of Geodesy and Geoinformation. University of Bonn.

Boxhammer, C. (2006). Effiziente numerische Verfahren zur sphärischen harmonischen Analyse von Satellitendaten. PhD thesis. Institute of Geodesy and Geoinformation. University of Bonn.

Boxhammer, C. and W.-D. Schuh (2006). GOCE gravity field modeling: computational aspects – free kite numbering scheme. In: Flury, J., R. Rummel, C. Reigber, G. Boedecker M. Rothacher and U. Schreiber (eds), Observation of the earth system from space. Springer, New York, pp. 207–224.

Brockmann, J.M. (2008). Effiziente Varianzkomponenenten-schätzung ber iterative Techniken bei der GOCE–Daten Prozessierung. Diploma thesis. Institute of Geodesy and Geoinformation. University of Bonn.

Hutchinson, M.F. (1990). A stochastic estimator of the trace of the influence matrix for Laplacian smoothing splines. *Commun. Stat. Simula.*, 19(2), 433–450.

Koch, K.R. (2007). Introduction to bayesian statistics 2nd ed., Springer, Berlin, Heidelberg, New York.

Koch, K.R. und J. Kusche (2001). Regularization of geopotential determination from satellite data by variance components. *J. Geodesy*, 76(5), 641–652.

Metzler, B. and R. Pail (2005) GOCE data processing: the spherical cap regularization approach. *Stud. Geophys. Geod.*, 49, 441–462.

Schuh, W.-D. (1996). Tailored numerical solution strategies for the global determination of the earth's gravity field. Number 81 in Mitteilungen der Universität Graz.

Schuh, W.-D. (2003) The processing of band-limited measurements; filtering techniques in the least squares context and in the presence of data gaps. In: Beutler, G., M.R. Drinkwater, R. Rummel and R. v. Steiger (eds), Earth gravity field from space – from sensors to earth sciences, Band 108, Space Science Reviews, 67–78. ISSI Workshop, Bern.

Siemes, C. (2008). Digital Filtering Algorithms for Decorrelation within Large Least Square Problems. PhD thesis. Institute of Geodesy and Geoinformation. University of Bonn.

Chapter 26

Analysis of the Covariance Structure of the GOCE Space-Wise Solution with Possible Applications

L. Pertusini, M. Reguzzoni, and F. Sansò

Abstract The estimation of a global gravity model from a satellite mission like GOCE is a tough task from the numerical point of view and the computation of the error covariance structure of the solution is even tougher. This is due to the sophisticated treatment of the data and the large number of unknowns (e.g., 40,000) simultaneously processed.

However information on such a covariance matrix can be derived from the Monte Carlo method, basically propagating simulated input noise to derive the error vector of the spherical harmonic coefficients. The estimated covariance then is just the sample covariance of the output error. Since the number of samples can be much smaller than the number of unknowns, although the individual covariances are consistently estimated, the overall covariance structure cannot be caught by such a Monte Carlo estimate.

This fact is studied with some detail for the Monte Carlo covariance matrix of the GOCE space-wise solution, in order to confirm in the positive sense the conjecture that the solution organized by orders has a prevailing block diagonal structure.

Starting from this result, the problem of combining two sets of spherical harmonic coefficients is investigated. In particular this problem is studied in the framework of the space-wise approach that requires the combination between coefficients derived from a grid of potential and coefficients derived from a grid of second radial derivatives. Different combination strategies are considered, including one based on a Bayesian approach. All these strategies, however, lead to similar results in terms of accuracy of the final model.

L. Pertusini (✉)
DIIAR, Politecnico di Milano, Polo Regionale di Como, Como 22100, Italy
e-mail: lisa.pertusini@mail.polimi.it

26.1 Introduction

The space-wise approach (Migliaccio et al., 2004) to the analysis of GOCE (ESA, 1999) data is one of the possible solutions to estimate spherical harmonic coefficients of the gravitational potential and the corresponding error covariance matrix. It is a multi-step collocation (Reguzzoni and Tselfes, 2009): first the anomalous potential T along the orbit is estimated by applying the energy conservation method (Jekeli, 1999; Visser et al., 2003); then a spherical grid of potential T and of second radial derivatives T_{rr} at mean satellite altitude is predicted by collocation (Tscherning, 2005); finally two sets of coefficients are computed by harmonic analysis (Colombo, 1981) from T and T_{rr} grids respectively and these two solutions are combined by a weighted average.

The Monte Carlo method (Robert and Casella, 1999; Kusche, 2003; Alkhatib and Schuh, 2007) is used to estimate the error covariance matrix of the space-wise solution on the basis of simulated signal and noise samples (Migliaccio et al., 2009).

First, a study on the structure of the error covariance matrix is performed, investigating the conjecture that this matrix is prevailing block diagonal if the spherical harmonic coefficients are arranged by order. This is done both by applying a simple test on the linear correlation coefficients and by computing an index to "measure" the correlation between blocks of the error covariance matrix.

The result of this study has been applied in the frame of the space-wise approach for the determination of an optimal model combination (see Fig. 26.1). In fact the spherical harmonic coefficients derived from the potential grid and those derived from the

S.P. Mertikas (ed.), *Gravity, Geoid and Earth Observation*, International Association of Geodesy Symposia 135,
DOI 10.1007/978-3-642-10634-7_26, © Springer-Verlag Berlin Heidelberg 2010

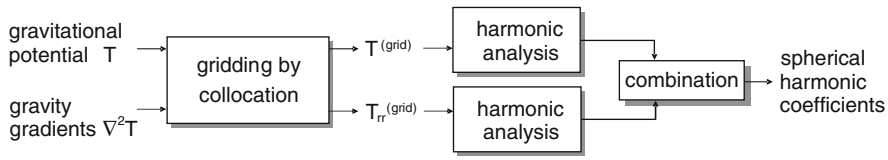


Fig. 26.1 Model combination for the GOCE space-wise solution

second radial derivative grid can be merged in different ways, in order to find an optimal combination of the two. At present a degree-by-degree combination is used, based on error degree variances. A coefficient-by-coefficient combination is studied by considering either only the error variances or the block diagonal error covariance matrix (order-by-order). Finally an optimal combination in a Bayesian sense is studied (Koch, 1990).

The computations presented in the paper are based on the End-To-End GOCE simulated data covering 2 months of observations, at a sampling rate of 1 s (Catastini et al., 2007). The gravity gradients are computed from the EGM96 model (Lemoine et al., 1998), up to degree and order 360, and are degraded with realistic noise. The GOCE orbit, including satellite position, velocity and attitude, is simulated again using EGM96, up to degree and order 200. The data set contains also other information, such as the common mode accelerations measured by the on-board gradiometer.

26.2 Study on the Structure of the Error Covariance Matrix

26.2.1 Correlation Between Single Coefficients

Regarding each pair of error coefficients, they can be considered as a double normal random variable

$$\begin{vmatrix} X \\ Y \end{vmatrix} \sim \mathrm{N}\left[\begin{vmatrix} \mu_X \\ \mu_Y \end{vmatrix}, \begin{vmatrix} \sigma_X^2 & \rho\sigma_X\sigma_Y \\ \rho\sigma_X\sigma_Y & \sigma_Y^2 \end{vmatrix} \right] \tag{1}$$

with mean values μ_X=μ_Y=0, variances $\sigma^2{}_X$ and $\sigma^2{}_Y$ and covariance σ_{XY}= $\rho\sigma_X\sigma_Y$.

If N samples of error coefficients are available by applying the Monte Carlo method, the corresponding sample statistics can be computed. Among these, we are interested in the sample variances $S^2{}_X$ and $S^2{}_Y$ and in the sample covariance S_{XY}, so that the sample linear correlation coefficient R results:

$$\mathrm{R} = \frac{S_{XY}}{S_X S_Y}, \tag{2}$$

The asymptotic distribution for a function of R, when N is a high number, is (Sachs, 1982):

$$\frac{1}{2}\log\frac{1+\mathrm{R}}{1-\mathrm{R}} \sim \mathrm{N}\left[\frac{1}{2}\log\frac{1+\rho}{1-\rho}, \frac{1}{\mathrm{N}-3}\right]. \tag{3}$$

The null hypothesis H_0: $\rho = \rho_0 = 0$ is accepted if

$$|\mathrm{R}| \leq \frac{e^{\frac{4}{\sqrt{N-3}}\cdot Z_\alpha} - e^{\frac{2}{\sqrt{N-3}}\cdot Z_\alpha}}{e^{\frac{4}{\sqrt{N-3}}\cdot Z_\alpha} + e^{\frac{2}{\sqrt{N-3}}\cdot Z_\alpha}} \tag{4}$$

where

$$p(|Z| > Z_\alpha) = \alpha \tag{5}$$

with Z a standard normal random variable and α the chosen significance level.

The test in Eq. (4) is applied to the error covariance matrix of the GOCE space-wise solution up to degree and order 200, with N = 150 samples. The percentage of rejected R values for pairs of error coefficients with different order is reported in Table 26.1. This percentage is consistent with the significance level α (also reported in Table 26.1), showing that the hypothesis of block diagonal covariance matrix is reasonable.

On the other hand, it has to be underlined that not all the error coefficients of the same order are correlated. An example of error correlation matrix for a fixed order (m = 10) is shown in Fig. 26.2.

Table 26.1 Percentage of rejected R values for different significance levels α. All the possible pairs of error coefficients with different order are tested

α (%)	0.1	1	5
Rejected R (%)	0.1	0.99	4.94

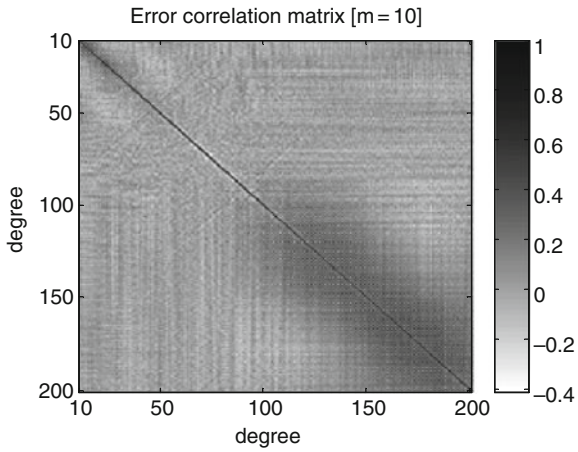


Fig. 26.2 Error correlation matrix for m = 10. It can be seen that only some coefficients near the diagonal are correlated

26.2.2 Correlation Between Blocks of Coefficients

The linear correlation coefficient expresses the correlation between single random variables. In this section a different index is used to evaluate the correlation between two sets of random variables. In particular we are interested in the correlation of error coefficients grouped by orders. Note that coefficients of the same order are further separated in four subgroups: even and odd degrees, sine and cosine coefficients. These subgroups are considered statistically uncorrelated among each other for symmetry reasons.

The theory on the block correlation index can be found in Wackernagel (1995) and it is summarized in the following. Having two random variable vectors $\underline{X}$ and $\underline{Y}$ the associated variance-covariance matrix can be obviously subdivided into four blocks:

$$\mathrm{cov}(\underline{X},\underline{Y}) = \begin{vmatrix} C_{XX} & C_{XY} \\ C_{YX} & C_{YY} \end{vmatrix}. \tag{6}$$

We consider now two linear functionals u and v, which are defined as follows:

$$u = \underline{a}^T \underline{X}, \quad v = \underline{b}^T \underline{Y} \tag{7}$$

where $\underline{a}$ and $\underline{b}$ are two generic vectors. Normalizing u and v, we get:

$$\sigma_u^2 = \sigma_v^2 = \underline{a}^T C_{XX} \underline{a} = \underline{b}^T C_{YY} \underline{b} = 1 \tag{8}$$

$$\mathrm{corr}(u,v) = \underline{a}^T C_{XY} \underline{b}. \tag{9}$$

We are searching for the two transformation vectors $\underline{a}$ and $\underline{b}$ satisfying the above normalization condition and making the correlation between the two functionals u and v maximum.

By considering

$$\begin{cases} C_{XX} = A^T A \\ C_{YY} = B^T B \end{cases} \quad \begin{cases} A\underline{a} = \underline{\alpha} \\ B\underline{b} = \underline{\beta} \end{cases} \tag{10}$$

the problem is reduced to the solution of the following equation:

$$\left(B^{-1}\right)^T C_{XY}^T C_{XX}^{-1} C_{XY} B^{-1} \underline{\beta} = \lambda^2 \underline{\beta} \tag{11}$$

so, the problem eventually results in the estimate of the eigenvalue λ^2_{MAX} of the matrix

$$M = \left(B^{-1}\right)^T C_{XY}^T C_{XX}^{-1} C_{XY} B^{-1} \tag{12}$$

because the maximum correlation between u and v is exactly equal to λ_{MAX}.

In the case under study, the vectors $\underline{X}$ and $\underline{Y}$ are composed by error coefficients of order m_1 and m_2 respectively ($m_1 \neq m_2$); the corresponding covariance matrices C_{XX}, C_{YY} and C_{XY} are extracted from the full error covariance matrix of the GOCE space-wise solution. Since this solution is complete up to degree and order 200, it is possible to compute the block correlation index λ_{MAX} for each pair of orders m_1 and m_2, with $m_1 = 1,2,\ldots,200$ and $m_2 = 0,1,\ldots,m_1{-}1$. The result of this computation is displayed in Figs. 26.3, 26.4, and 26.5, considering an increasing number of samples in the Monte Carlo covariance estimation.

Note that a numerical difficulty could arise in the inversion of the covariance matrix C_{XX}, because it is composed by error covariances with completely different orders of magnitude. This happens especially for low values of m, when the vector $\underline{X}$ includes error coefficients of both low and high degree. A possible solution is to replace the covariance matrices C_{XX}, C_{YY} and C_{XY} with the corresponding correlation matrices, without the need of changing the expression of matrix M (see Eq. (12)).

Furthermore, since the number of samples used for the Monte Carlo estimate of the covariance matrix is

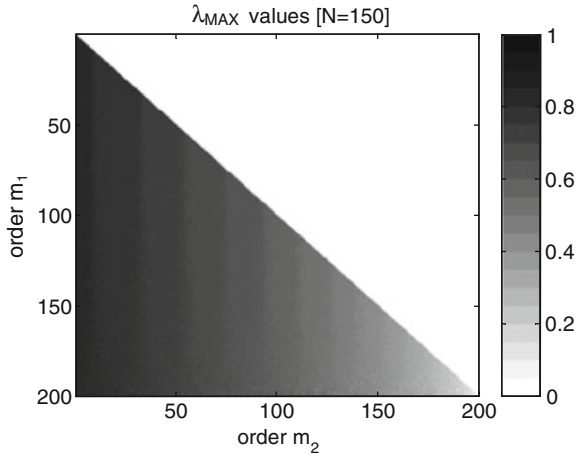


Fig. 26.3 Block correlation index (λ_{MAX}) values for an error covariance matrix derived from N = 150 samples

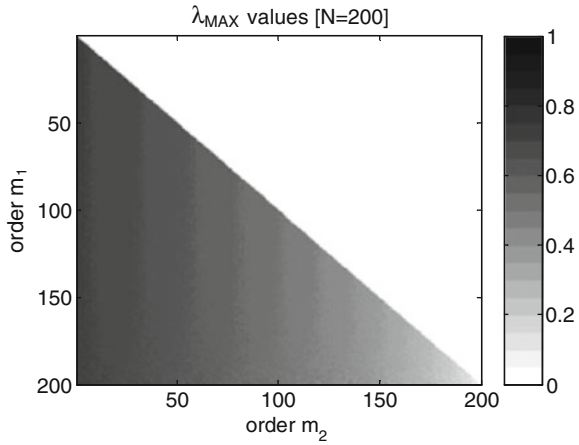


Fig. 26.4 Block correlation index (λ_{MAX}) values for an error covariance matrix derived from N = 200 samples

much smaller than the number of unknowns (about 40,000 for a maximum degree equal to 200), although the individual covariances are consistently estimated, the overall covariance structure of the space-wise solution cannot be fully caught. This is the reason why many λ_{MAX} values are close to 1 with N = 150 samples (see Fig. 26.3). However increasing the number N of Monte Carlo samples, the estimated λ_{MAX} values tend to decrease (compare Figs. 26.3, 26.4, and 26.5). We take this as an indication that the overall covariance matrix has a prevailing block diagonal structure.

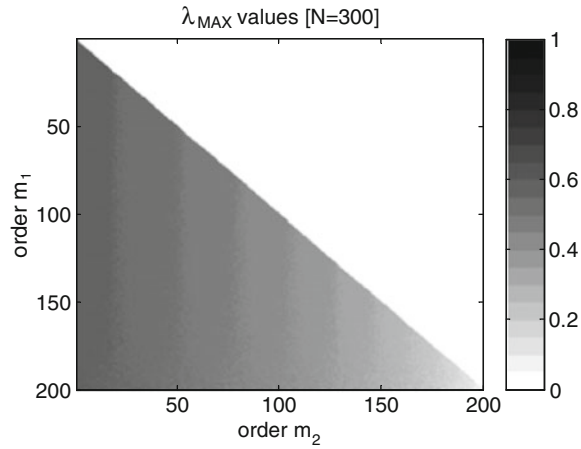


Fig. 26.5 Block correlation index (λ_{MAX}) values for an error covariance matrix derived from N = 300 samples. The downward trend of the values is evident

26.3 Study of Optimal Model Combinations

26.3.1 Combination Based on Error Degree Variances

Starting from the error variances of the spherical harmonic coefficients, derived by the Monte Carlo method, error degree variances are computed:

$$\hat{\sigma}^2_{n_A} = \frac{1}{2n+1} \sum_m \hat{\sigma}^2_{nmA} \tag{13}$$

$$\hat{\sigma}^2_{n_B} = \frac{1}{2n+1} \sum_m \hat{\sigma}^2_{nmB} \tag{14}$$

where A indicates the model derived from T grid and B the model derived from T_{rr} grid, in the frame of the space-wise approach. As one can see in Fig. 26.6 the low degree coefficients are better estimated from T, while the high degree information is better recovered from T_{rr}. This difference has to be exploited in the model combination. For this reason the weights for the combination are chosen to be inversely proportional to the error degree variances and they are computed as:

$$\beta_{n_A} = \frac{\frac{1}{\hat{\sigma}^2_{n_A}}}{\frac{1}{\hat{\sigma}^2_{n_A}} + \frac{1}{\hat{\sigma}^2_{n_B}}}, \quad \beta_{n_B} = \frac{\frac{1}{\hat{\sigma}^2_{n_B}}}{\frac{1}{\hat{\sigma}^2_{n_A}} + \frac{1}{\hat{\sigma}^2_{n_B}}}. \tag{15}$$

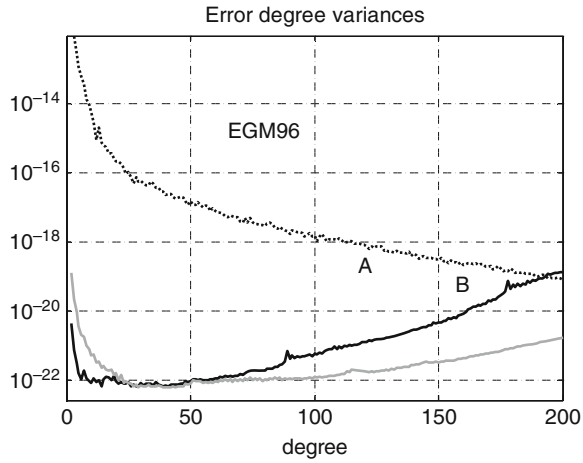


Fig. 26.6 Error degree variances for T (model A) and for T_{rr} (model B). Signal degree variances from EGM96

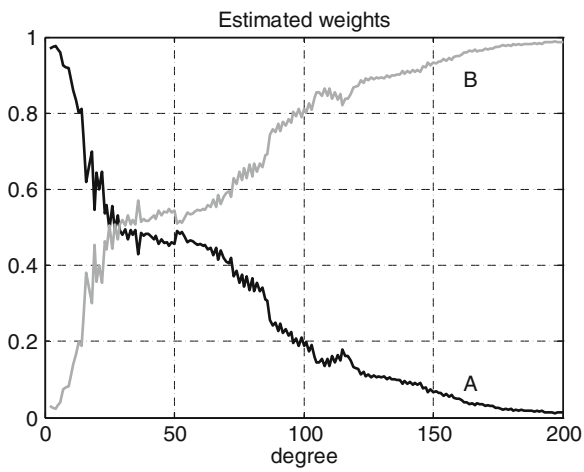


Fig. 26.7 Combination weights based on error degree variances for T (model A) and for T_{rr} (model B)

The weights in Eq. (15), which have a range from 0 to 1, are shown in Fig. 26.7; the corresponding combined model results:

$$T_{nm_C} = \beta_{n_A} T_{nm_A} + \beta_{n_B} T_{nm_B} \qquad (16)$$

where T_{nm} represents the spherical harmonic coefficient of degree n and order m.

Note that coefficients with the same degree are generally characterized by errors of similar magnitude (apart from the low order coefficients in the case of polar gaps). This is the reason why error degree variances represent a good index to evaluate the model accuracy. However the use of error degree variances to determine the combination weights between two models (as it is done in this section) completely disregards the correlations among the estimated coefficients, especially among coefficients of the same order. Therefore, this combination strategy is simplistic and definitely not optimal. The only advantages are that it is easy to be applied and the error degree variances are well estimated even with very few Monte Carlo samples (which is not the case for the full error covariance structure, as discussed in Sect. 26.2.2).

26.3.2 Combination Based on Error Variances of the Single Coefficients

In order to determine a different weight for each coefficient, single error variances are considered instead of error degree variances. This implies that the combination weights can be computed as follows:

$$\beta_{nm_A} = \frac{\frac{1}{\hat{\sigma}^2_{nm_A}}}{\frac{1}{\hat{\sigma}^2_{nm_A}} + \frac{1}{\hat{\sigma}^2_{nm_B}}}, \quad \beta_{nm_B} = \frac{\frac{1}{\hat{\sigma}^2_{nm_B}}}{\frac{1}{\hat{\sigma}^2_{nm_A}} + \frac{1}{\hat{\sigma}^2_{nm_B}}}. \qquad (17)$$

The resulting weights are shown in Figs. 26.8 and 26.9 and the combined model is given by:

$$T_{nm_C} = \beta_{nm_A} T_{nm_A} + \beta_{nm_B} T_{nm_B}. \qquad (18)$$

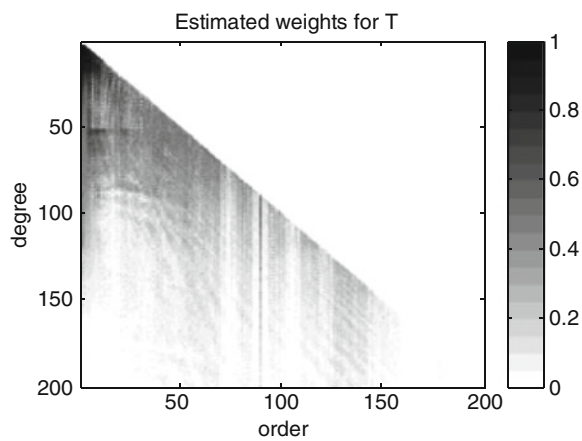


Fig. 26.8 Combination weights based on error variances for T (model A)

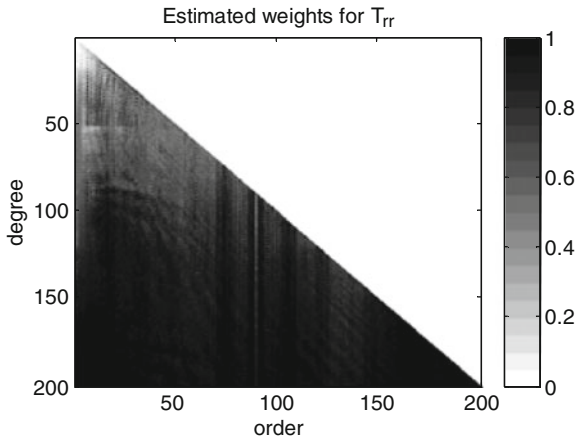


Fig. 26.9 Combination weights based on error variances for T_{rr} (model B)

Again, this approach does not take into account the correlations among the estimated coefficients and therefore it is not optimal. The advantage with respect to the solution based on error degree variances is that, for example, the low order coefficients that are affected by polar gaps are not weighted in the same way as the other coefficients of the same degree.

26.3.3 Combination Based on Block-Wise Error Covariances

A further step is to consider not only variances but also covariances, assuming a block diagonal covariance matrix, which is a reasonable hypothesis as discussed in Sect. 26.2. Therefore the combination can be done order by order.

The estimated coefficient vectors $\underline{T}_{m_A}$ and $\underline{T}_{m_B}$ for a fixed order m, derived from T grid and T_{rr} grid respectively, can be written as:

$$\begin{cases} \underline{T}_{m_A} = \underline{T}_m + \underline{\nu}_{m_A} \\ \underline{T}_{m_B} = \underline{T}_m + \underline{\nu}_{m_B} \end{cases} \tag{19}$$

where $\underline{T}_m$ represents the true coefficients, while $\underline{\nu}_{m_A}$ and $\underline{\nu}_{m_B}$ are the estimation error vectors.

By defining the vector

$$\underline{\xi} = \begin{vmatrix} \underline{\nu}_{m_A} \\ \underline{\nu}_{m_B} \end{vmatrix} \tag{20}$$

the corresponding covariance matrix is given by:

$$C_{\xi\xi} = \begin{vmatrix} C_{AA} & C_{AB} \\ C_{BA} & C_{BB} \end{vmatrix}. \tag{21}$$

The cross-covariance C_{AB} is neglected in the model combination. As a matter of fact the errors of the models A and B are fully correlated because they are computed starting from the same data. So neglecting C_{AB} is a strong approximation.

The optimal weights derived by a least-squares regression are then the following matrices:

$$W_{m_A} = (C_{AA}^{-1} + C_{BB}^{-1})^{-1} \cdot C_{AA}^{-1} \tag{22}$$

$$W_{m_B} = (C_{AA}^{-1} + C_{BB}^{-}) ^{-1} \cdot C_{BB}^{-1} \tag{23}$$

and the resulting combined model is:

$$\underline{T}_{m_C} = W_{m_A} \underline{T}_{m_A} + W_{m_B} \underline{T}_{m_B}. \tag{24}$$

A numerical problem arises from the bad conditioning of the matrices C_{AA} and C_{BB}, which is mainly related to the wide range of error variances for a fixed order m and varying the degree. A possible empirical solution is to perform the combination only for those coefficients having comparable error variances (for a fixed order m), as shown in Fig. 26.10.

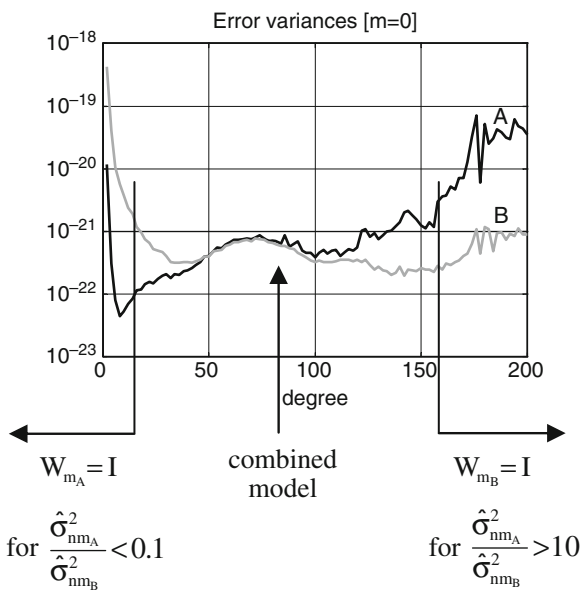


Fig. 26.10 Search for the window where the error variance ratio between the two models A and B is in the range from 0.1 to 10, in the case of m = 0

26.3.4 Optimal Combination in a Bayesian Sense

An alternative to the least-squares combination (which implies that the strong correlation between the models A and B is neglected) is represented by a Bayesian approach. In particular, we are searching for a combination

$$\underline{T}_{m_C} = \beta \underline{T}_{m_A} + (1-\beta)\underline{T}_{m_B} \tag{25}$$

where β is a number in the range from 0 to 1.

Assuming that the model errors $\underline{v}_{m_A}$ and $\underline{v}_{m_B}$ (see Eq. (20)) are normally distributed, the likelihood distribution can be written as:

$$\begin{aligned} &L(\underline{T}_{m_A},\underline{T}_{m_B}|\underline{T}_m,\beta) = \\ &= \frac{\beta}{(2\pi)^{b/2}\sqrt{\det C_{AA}}} e^{-\frac{1}{2}(\underline{T}_{m_A}-\underline{T}_m)^T C_{AA}^{-1}(\underline{T}_{m_A}-\underline{T}_m)} + \\ &+ \frac{1-\beta}{(2\pi)^{b/2}\sqrt{\det C_{BB}}} e^{-\frac{1}{2}(\underline{T}_{m_B}-\underline{T}_m)^T C_{BB}^{-1}(\underline{T}_{m_B}-\underline{T}_m)} \end{aligned} \tag{26}$$

where b is the number of spherical harmonic coefficients of order m, i.e.,

$$b = N_{max} - m + 1 \tag{27}$$

with N_{max} equal to 200.

Non informative prior distributions (NIP) (Box and Tiao, 1992) are considered for the parameters $\underline{T}_m$ and β:

$$p(\underline{T}_m,\beta) = p\left(\underline{T}_m\right) \cdot p(\beta) \tag{28}$$

$$p(\underline{T}_m) = \text{const in} R^b, \qquad p(\beta) = U[0,1]. \tag{29}$$

The marginal posterior distribution of the parameter $\underline{T}_m$ is given by:

$$\begin{aligned} &p(\underline{T}_m|\underline{T}_{m_A},\underline{T}_{m_B}) = \int p(\underline{T}_m,\beta|\underline{T}_{m_A},\underline{T}_{m_B})d\beta = \\ &= \frac{1}{2}\cdot\frac{1}{(2\pi)^{b/2}\sqrt{\det C_{AA}}} e^{-\frac{1}{2}(\underline{T}_m-\underline{T}_{m_A})^T} \\ &\quad C_{AA}^{-1}(\underline{T}_m-\underline{T}_{m_A}) + \\ &= \frac{1}{2}\cdot\frac{1}{(2\pi)^{b/2}\sqrt{\det C_{BB}}} e^{-\frac{1}{2}(\underline{T}_m-\underline{T}_{m_B})^T} \\ &\quad C_{BB}^{-1}(\underline{T}_m-\underline{T}_{m_B}) \end{aligned} \tag{30}$$

Therefore the maximum a posteriori (MAP) of this distribution with respect to $\underline{T}_m$ is obtained at the mean value of one of the two components, namely:

$$\underline{T}_{m_C} = \begin{cases} \underline{T}_{m_A} & \text{if} \frac{\det C_{BB}}{\det C_{AA}} > 1 \\ \underline{T}_{m_B} & \text{if} \frac{\det C_{AA}}{\det C_{BB}} > 1 \end{cases} \tag{31}$$

implying a "hard" combination.

Again the difficulty in the computation of the determinants is strongly influenced by the wide range of error variances. Moreover, the attempt to process all the degrees together for a fixed order m leads to systematically choose the coefficients of the T_{rr} model, even for the lowest degrees where the T model is evidently better. For this reasons the method is applied only for those coefficients with comparable error variances (see Fig. 26.10).

26.3.5 Accuracy of the Combined Models

The quality of the different combinations is evaluated by comparing the geoid error of the two initial models with those of the combined models, in the latitude interval $-83° < \phi < 83°$, at different maximum degree N_{max}. The results are reported in Table 26.2.

The combination that gives slightly better results is the one made by considering a block diagonal covariance matrix, despite the rough approximation of neglecting the cross-covariances between the two initial models.

Table 26.2 Geoid error by using different model combinations

Model	N_{max}=25	N_{max}=100	N_{max}=200
T only (cm)	0.61	1.17	23.6
T_{rr} only (cm)	0.81	1.17	2.89
Degree variances (cm)	0.58	1.10	2.91
Variances (cm)	0.59	1.09	2.93
Block covariances (cm)	0.57	1.05	2.83
Bayesian (cm)	0.60	1.12	2.89

26.4 Conclusions

The hypothesis that the GOCE error covariance matrix of the spherical harmonic coefficients estimated by the space-wise approach has a prevailing block diagonal structure, has been tested. It comes out that

cross-covariance blocks (outside the main block diagonal) have small entries, but can create strong correlations between linear functionals of sets of coefficients with different order. This phenomenon is attributed to the limited number of available Monte Carlo samples. In fact by increasing this number the phenomenon tends to attenuate, so as to convince us that the limit has a prevailing block diagonal structure.

This structure of the covariance matrix has been exploited, at different levels of approximation, to combine coefficients derived from different functionals, namely from T and T_{rr} in the case of GOCE. The conclusion is that all the proposed methods provide similar results; yet our preference goes to the Bayesian strategy, because it implies a smaller number of approximations in constructing the theoretical model.

Acknowledgement This work has been performed under ESA contract No.18308/04/NL/NM (GOCE High-level Processing Facility).

References

Alkhatib, H., and W.D. Schuh (2007). Integration of the Monte Carlo covariance estimation strategy into tailored solution procedures for large-scale least squares problems. *J. Geodesy*, 81, 53–66.

Box, G.E.P. and G.C. Tiao (1992). Bayesian inference in statistical analysis. Wiley, New York.

Catastini, G., S. Cesare, S. De Sanctis, M. Dumontel, M. Parisch, and G. Sechi (2007). Predictions of the GOCE in-flight performances with the end-to-end system simulator. In: Proceedings of the 3rd International GOCE User Workshop, 6–8 November 2006, Frascati, Rome, Italy, pp. 9–16.

Colombo, O.L. (1981). Numerical methods for harmonic analysis on the sphere. Report No. 310, Dept. of Geodetic Science and Surveying, Ohio State University, Columbus.

ESA (1999). Gravity Field and Steady-State Ocean Circulation Mission. ESA SP-1233 (1). ESA Publication Division, c/o ESTEC, Noordwijk, The Netherlands.

Jekeli, C. (1999). The determination of gravitational potential differences from satellite-to-satellite tracking. Celestial Mechanics and Dynamical Astronomy, 75, pp. 85–101.

Koch, K.R. (1990). Bayesian inference with geodetic applications. Lecture Notes in Earth Sciences, vol. 31. Springer, Berlin.

Kusche, J. (2003). A Monte Carlo technique for weight estimation in satellite geodesy.*J. Geodesy*, 76, 641–652.

Lemoine, F.G., S.C. Kenyon, J.K. Factor, R.G. Trimmer, N.K. Pavlis, D.S. Chinn, C.M. Cox, S.M. Klosko, S.B. Luthcke, M.H. Torrence, Y.M. Wang, R.G. Williamson, E.C. Pavlis, R.H. Rapp, and T.R. Olson (1998). The development of the joint NASA GSFC and NIMA geopotential model EGM96. NASA/TP-1998-206861, Goddard Space Flight Center, Greenbelt, Maryland.

Migliaccio, F., M. Reguzzoni, and F. Sansò (2004). Space-wise approach to satellite gravity field determination in the presence of coloured noise. *J. Geodesy*, 78, 304–313.

Migliaccio, F., M. Reguzzoni, F. Sansò, and N. Tselfes (2009). An error model for the GOCE space-wise solution by Monte Carlo methods. In: Sideris, M.G. (ed), IAG Symposia, 'Observing our Changing Earth', vol. 133, Springer-Verlag, Berlin, pp. 337–344.

Reguzzoni, M., and N. Tselfes (2009). Optimal multi-step collocation: application to the space-wise approach for GOCE data analysis. *J. Geodesy*, 83, 13–29.

Robert, C.P., and G. Casella (1999). Monte Carlo statistical methods. Springer-Verlag, New York.

Sachs, L. (1982). Applied statistics. A handbook of techniques. Springer-Verlag, New York.

Tscherning, C.C. (2005). Testing frame transformation, gridding and filtering of GOCE gradiometer data by Least-Squares Collocation using simulated data. In: Sansò, F. (ed), IAG Symposia, 'A window on the Future of Geodesy', vol. 128, Springer-Verlag, Berlin, pp. 277–282.

Visser, P.N.A.M., N. Sneeuw, and C. Gerlach (2003). Energy integral method for gravity field determination from satellite orbit coordinates. *J. Geodesy*, 77, 207–216.

Wackernagel, H. (1995). Multivariate geostatistics. Springer-Verlag, Berlin.

Part III
Earth Observation by Satellite Altimetry and InSAR

W. Bosch, M. Furuya, and R. Haagmans

Chapter 27

Soil Surface Moisture From EnviSat RA-2: From Modelling Towards Implementation

S.M.S. Bramer and P.A.M. Berry

Abstract This paper presents the current status of ongoing research into the extraction of soil surface moisture data from Radar Altimeter backscatter. One of the motivations for this work is to facilitate comparisons with GRACE data over specific targets such as the Okavango Delta.

Natural land targets for the monitoring of Radar Altimeter backscatter have previously been identified and modelled, utilising data provided by the ERS-1 Geodetic and 35-day Missions. These spatial models have been employed for cross-calibration between ERS-1/2 ice and ocean mode sigma0. The inherent variability of all but a few desert regions meant that the original techniques could not be used beyond these calibration zones.

A new automated technique has made it possible to develop models of wetter regions with the aim of taking these models as close to "dry earth" conditions as possible.

In parallel with this process a semi-empirical model of Radar Altimeter backscatter, which makes use of engineering and scientific parameters, has been developed and is undergoing final calibration.

The use of the spatial models in conjunction with the new semi-empirical backscatter model will enable predictions of soil surface moisture levels using values provided by EnviSat RA-2 backscatter.

27.1 Introduction

This paper discusses recent developments in the understanding of behaviour of overland radar altimeter sigma0 in response to surface moisture. The automated creation of spatial "dry earth" sigma0 models is discussed together with a new semi-empirical model. Synergistically, the two allow the creation of surface roughness maps together with prediction of sigma0 response to surface moisture.

27.2 Data

The radar altimeter data used in this study have been reprocessed using a rule-based expert system (Berry et al., 1997) to optimise the recovery of the range-to-surface. This works by selecting one of eleven retracking algorithms based on the waveform characteristics. The system has been under development for several years and has been tuned for ERS-1/2, Envisat, TOPEX and Jason-1.

The ERS-1 Geodetic Mission data-set has been used for the creation of spatial sigma0 models, together with data from the ERS-2 35-day mission (Capp, 2001). A number of cycles of Envisat 35-day data (Benveniste et al., 2002) have been used to illustrate global sigma0 variation.

27.3 Sigma0 Variation from Envisat Ku Band

As a first step in the illustration of the use of sigma0 in the recovery of soil moisture signals, Fig. 27.1

S.M.S. Bramer (✉)
EAPRS Lab, De Montfort University, Leicester LE1 9BH, UK
e-mail: smsb@dmu.ac.uk

S.P. Mertikas (ed.), *Gravity, Geoid and Earth Observation*, International Association of Geodesy Symposia 135,
DOI 10.1007/978-3-642-10634-7_27, © Springer-Verlag Berlin Heidelberg 2010

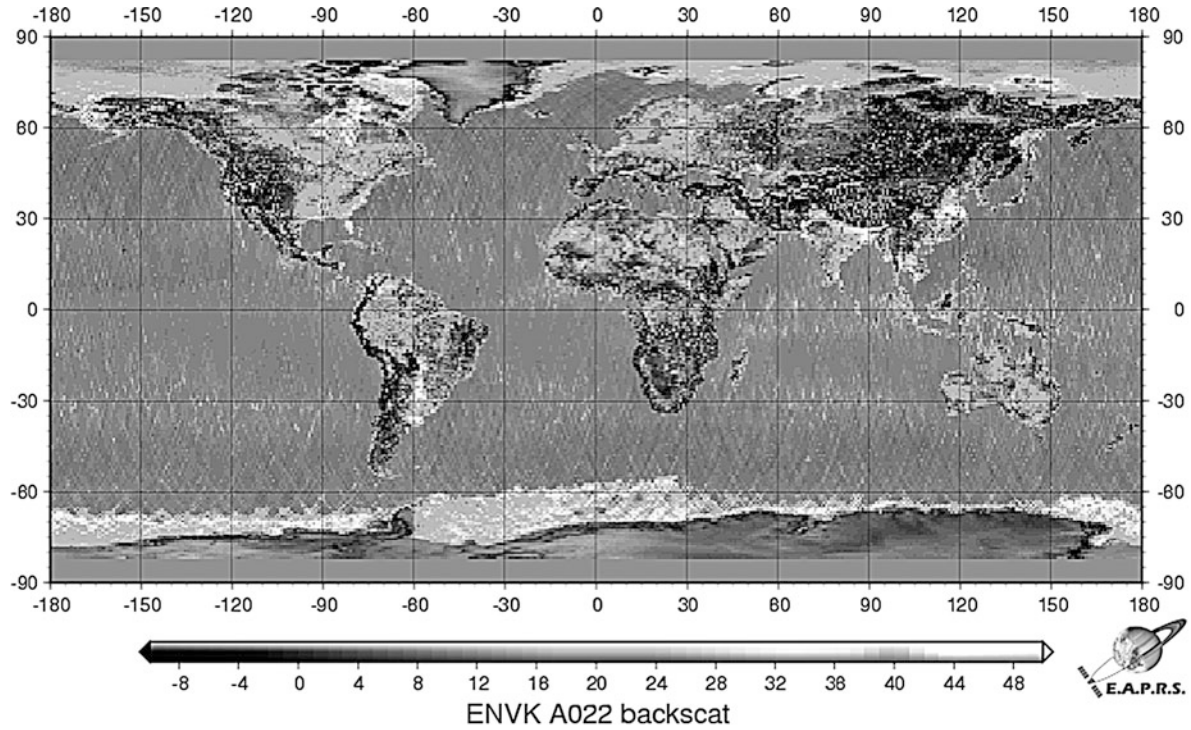


Fig. 27.1 Envisat sigma0 (dB) cycle 22 (December 2003)

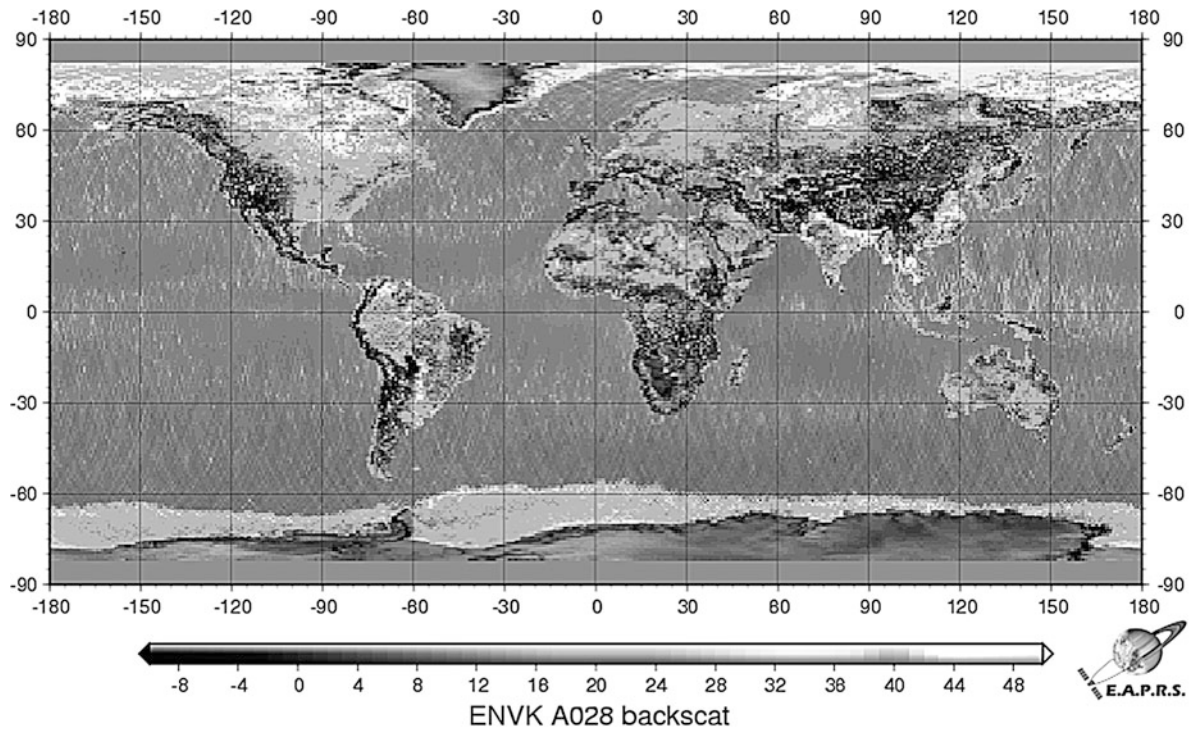


Fig. 27.2 Envisat sigma0 (dB) cycle 28 (June 2004)

shows the brightness of the Earth's surface in Ku band during the month of December 2003. In contrast, Fig. 27.2 reveals dramatic changes 6 months later when snow melt brightens much of the northern hemisphere. Sigma0 varies spatially on a fine scale, for example over the Kalahari region of Southern Africa, where the Okavango Delta is very bright, as are rivers and lakes, but saltpans are equally distinct, demonstrating that there is no simple relationship between moisture and sigma0. The plot of the Congo region (Fig. 27.4, discussed later) shows the land surface to have relatively low sigma0 values, despite the high moisture levels in the region.

In their 35-day missions, ERS-1 and 2 and Envisat cover the same ground track within a 2 km "dead band" every 35 days. Figure 27.3, showing Envisat Ku band sigma0 repeats over the central Simpson Desert illustrates both the variation due to cross track migration (similar features showing slightly offset in the lower traces), and raised sigma0 levels (the upper dark grey and part of the mid grey track) due to environmental contamination (resulting from rainfall).

The migration across track means that it is not possible to simply measure sigma0 values; a detailed model of the surface response must first be created. This was originally done manually, involving visual inspection of thousands of tracks. Any tracks showing the signature of environmental contamination were discarded entirely and the remainder reconciled to form models (Johnson, 2002). Clearly this labour intensive technique restricted models to a few carefully selected deserts. That technique allowed the successful cross calibration of ERS-1 and 2, both in ice and ocean modes (Johnson and Berry, 2002).

27.4 Creation of Empirical Sigma0 Models

The original, manual, method of empirical model creation could not be used to extend the number of modeled regions, both because of the huge numbers of data required for larger regions and because the need

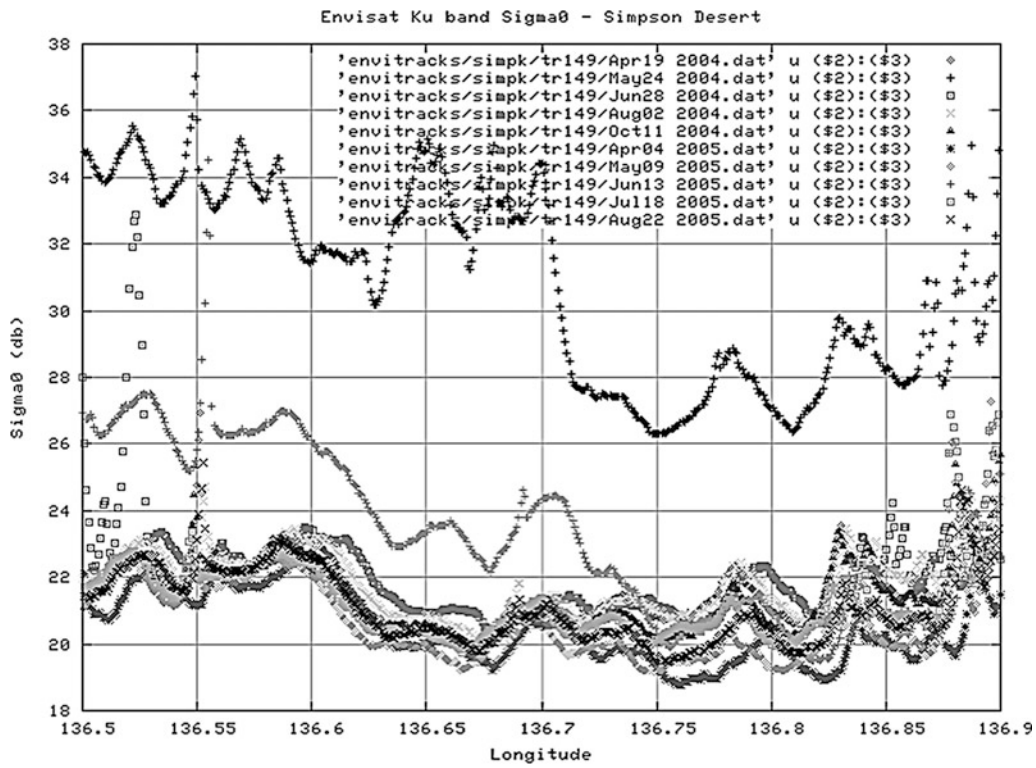


Fig. 27.3 Repeat passes of Envisat Ku band sigma0 over the simpson desert

to discard entire tracks if any part was contaminated left too little data to form models of any but the driest deserts. Accordingly, as part of a research programme designed to create accurate sigma0 models of selected desert areas for calibration/validation of multi-mission altimeter sigma0 (Bramer and Berry, 2006, Bramer et al., 2007) an automated method was used to remove environmental contamination from the processed sigma0 data. In all cases the lowest values at any point are chosen as most closely representing a "dry earth" value. Values from all tracks are reconciled in an iterative process, and the models are then created by use of triangulation and bilinear interpolation.

The technique was then tested by modelling progressively wetter regions, and proved extremely robust, to the extent of providing remarkable levels of detail even over wet terrain such as rainforests. This technique, admitting the identification and spatial extent estimation of inland water allows the possibility of comparison with GRACE data, Andersen et al. (2008) have already successfully combined radar altimeter and GRACE data.

27.5 The Simpson Desert 24-28S, 135-139E

The first region modelled by the automated technique was one of the original calibration zones. As a quantitative indicator of the internal consistency of the model, the sigma0 values at all locations where two altimeter tracks cross were calculated both before and after the track reconciliation and cleaning process. These statistics (Table 27.1) show good reduction in crossover difference even within this region, which was chosen, after a global crossover analysis, for its excellent stability.

27.6 The Congo 4S-4N, 16-26E

To investigate the performance of this technique in difficult circumstances, the entire Congo region was used as a test area. The technique used for modelling desert regions was applied to the data over this region. Whilst the environmental filter has screened out some data, a surprisingly high proportion of sigma0 data was retained, which allowed the successful calculation of a sigma0 model for the entire Congo region (Fig. 27.4). The paths of smaller tributaries within the Congo river network are clearly revealed in great detail Crossover differences (given in Table 27.2) do show that there is still a great deal of noise in the model, with standard deviations of crossover sigma0 differences in the region of 7dB. In contrast, typical values are in the region of 1–2dB over the central desert calibration zones. This does not, however, detract from the remarkable clarity of the mapping.

27.7 Understanding Sigma0

Any theoretical model for radar altimeter sigma0 must explain several facets of surface response:

Sigma0 is spatially very variable over land surfaces and some regions are much less variable temporally than others; these have been identified and used for calibration exercises.

Table 27.1 Crossover analysis for simpson desert model (24-28S, 135-139E)

	Mean sigma0 crossover difference (dB)	Standard deviation (dB)	Number of crossovers	Number of points
Simpson desert model				
GM prior to modification	0.080	3.264	908	140,349
35-day cycles crossed with GM prior to modification	−1.431	3.625	4606	399,239
GM rain cut	0.288	2.701	692	120,855
35-day rain cut	−1.542	3.469	4527	387,159
GM self adjusted and cleaned	0.000	1.949	692	120,855
35-day cycles cleaned and adjusted to GM	−0.000	2.971	4527	387,159

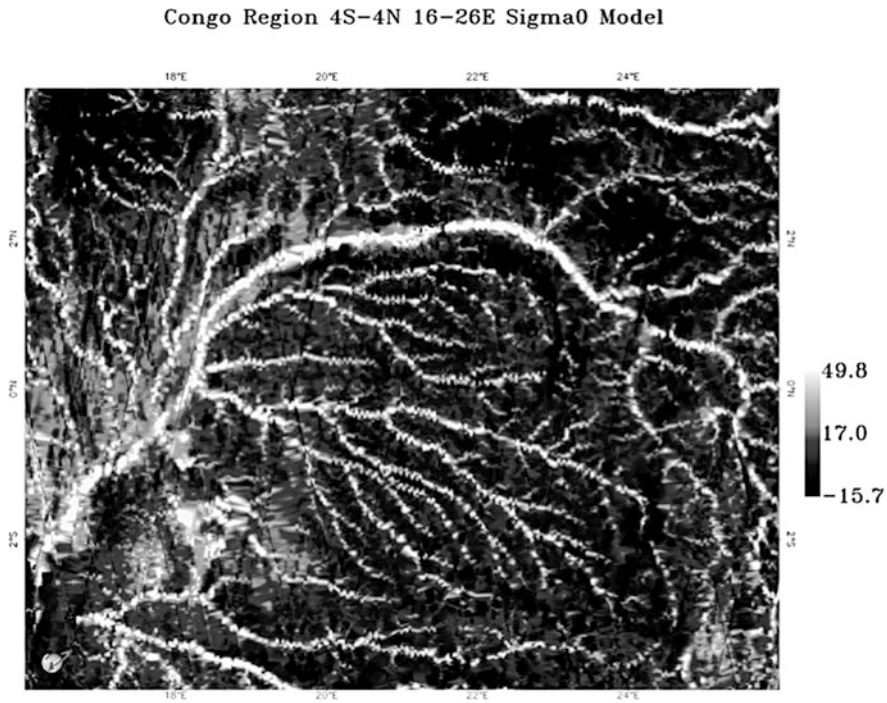


Fig. 27.4 Sigma0 (dB) model of Congo region (4S-4N 16-26E)

Table 27.2 Crossover analysis for Congo region model (4S-4N 16-26E)

Sigma0 crossover statistics	Standard deviation of crossover differences (dB)	Number of crossovers
GM prior to modification	7.465	484,490
35-day crossovers with GM prior to modification	7.947	733,574
GM after cleaning	5.992	430,955
35-day after cleaning	6.998	709,992

We also need to explain why moisture related increase occurs and quantify it.

Theoretical models exist for SAR (off nadir); these do not work for nadir looking Radar Altimeters. The first step is to understand that the surface response may be considered to be composed of a coherent "mirror like" return together with diffuse scatter from a rough surface. Off nadir SAR only receives the diffuse return, but both must be modelled if radar altimeter sigma0 is to be understood.

Further, sigma0 is dependent on surface roughness, constituents and moisture. Part of this dependence may be solved by correct inclusion of dielectric data, which is dependent on surface material and moisture content. Surface roughness and constituents change very slowly with time in semi arid regions, therefore rapid change must be due to changed moisture in the top few centimetres of the ground. It is clear therefore that any increase in sigma0 values between a "dry earth" model and actual data must be due to moisture. Resulting from extensive research, a semi-empirical model has now been developed and tuned for ERS-1 sigma0. This model provides predictions of sigma0 at varying surface roughness and moisture levels. Figure 27.5 shows predicted increase in Ku band sigma0 with moisture over sand for three small values of roughness. The result of the same process for five, much larger, roughness values is depicted in Fig. 27.6. As expected, there is a limit beyond which increase in roughness does not alter sigma0. This limit is reached sooner in drier conditions.

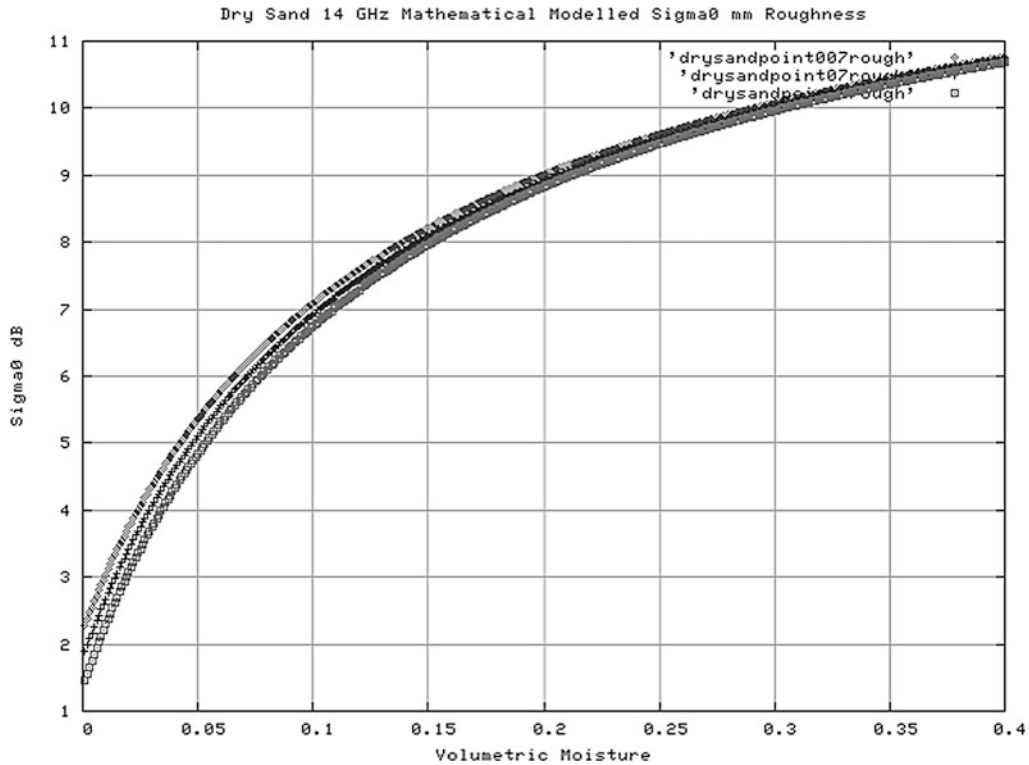


Fig. 27.5 Modelled backscatter (dB) from dry sand with moisture and roughness 0.007 m (*top curve*) 0.07 m (*middle*) 0.7 m (*bottom*)

27.8 Modelling Moisture Response for Western Australia (22-32S 116-128E)

Using the automated modelling techniques described earlier, a model of part of Western Australia has been created (Fig. 27.7). By combining this with data from the semi-empirical sigma0 model and assuming a sand/salt surface it proved possible to distinguish the salt pans in the region. These correspond closely with a geological map of part of the region (Geoscience Australia, 2004). With this information surface roughness was modelled; the dried rivers/salt pans of the region are clearly visible.

Finally, 8% volumetric moisture (chosen as literature (e.g., British Columbia Ministry of Agriculture 2002) generally gives this as the maximum holding capacity of sand) was added to the model, providing a prediction of the sigma0 response of the region when wet. The identified salt pans were excluded from this process as the dry sigma0 values are so high that no increase is expected to be apparent when wet (Fig. 27.8).

27.9 Discussion

The technique developed originally for modelling altimeter sigma0 in desert regions for calibration purposes has been shown to be very successful at modelling wetter regions. The modelling is now sufficiently advanced that we can predict the surface response to moisture in the top 5cms over a large region of Western Australia.

The next stage is to use these models with Envisat altimeter backscatter (recalculated using an expert system approach) and thus calculate the measured soil moisture.

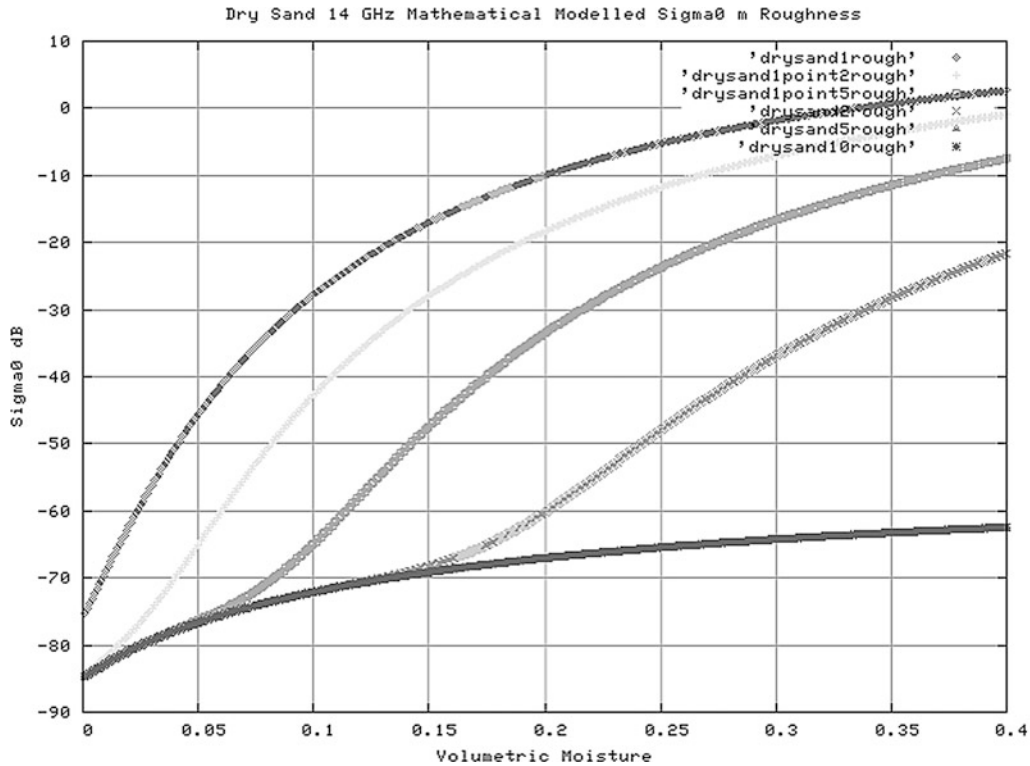


Fig. 27.6 Modelled backscatter (dB) from dry sand with moisture and roughness 1 m (*top curve*) descending through 1.2, 1.5, 2, 5, 10 m (*bottom curve*)

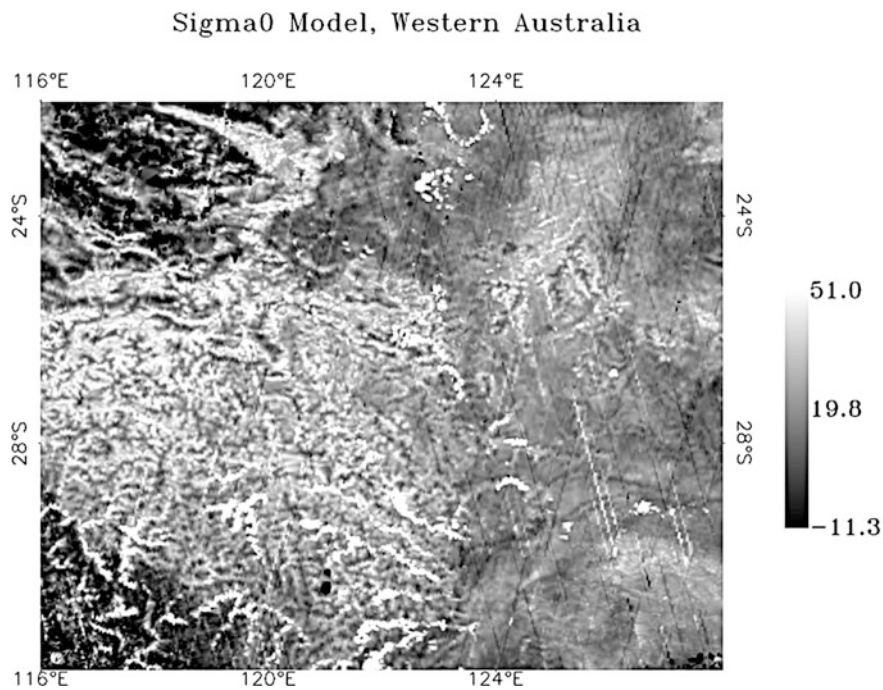


Fig. 27.7 Modelled sigma0 (dB), Western Australia (22-32S 116-128E)

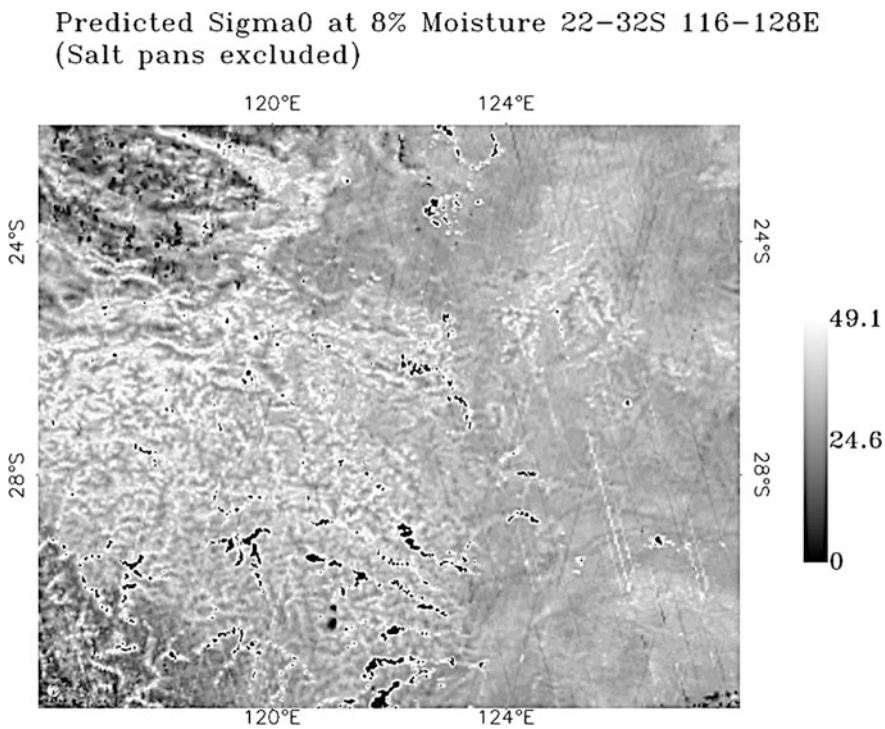


Fig. 27.8 Predicted sigma0 (dB) at 8% moisture for Western Australia, excluded salt pans in black (22-32S 116-128E)

These results will then be compared with the soil moisture calculated from in-situ rain gauge and other inputs from Australia. Empirical constants will be tuned to bring the estimates into agreement.

Acknowledgments The authors would like to thank the European Space Agency for providing the ERS and Envisat data used in this study.

References

Andersen, O.B., P. Berry, J. Freeman, F.G. Lemoine, S.C. Lutsckhe, F. Jascobsen, and M. Butts (2008). Satellite Altimetry and GRACE gravimetry for studies of annual water storage variations in Bangladesh. *Terr. Atm. Ocean Sci*., 19(1–2), 47–52.

Beneveniste, J. et al. (2002). ENVISAT RA-2/MWR Product Handbook, Issue 1.2 PO-TN-ERS-RA-0050, European Space Agency.

Berry, P.A.M., A. Jasper, and H. Bracke (1997). Retracking ERS-1 altimeter waveforms overland for topographic height determination: an expert system approach. *ESA Pub. SP414*, 1, 403–408.

Bramer, S.M.S. and P.A.M. Berry (2006). Cross Calibration of Multi-Mission Altimeter and TRMM PR Sigma0 Over Natural Land Targets. In: Proceedings of the Symposium on 15 Years Progress in Radar Altimetry, Venice, Italy, March 13–17.

Bramer, S.M.S., P.A.M. Berry, J.A. Freeman, and B. Rommen (2007). Global analysis of Envisat Ku and S Band Sigma0 over all Surfaces. In: Proceedings, ESA: ENVISAT Symposium, Montreux, Switzerland, April 23–27.

British Columbia Ministry of Agriculture, Food and Fisheries. (2002). Water Conservation Factsheet. Order No. 619.000-1.

Capp, P. (2001). Altimeter waveform product ALT>WAP compact user guide, Issue 4.0, PF-UG-NRL-AL-001, Infoterra Ltd.

Geoscience Australia (2004). Scanned 1:250 000 Geology Maps Commonwealth of Australia http://www.geoscience.gov.au

Johnson, C.P.D. (2002). Geodetic applications of satellite radar altimetry over land. PhD Thesis, De Montfort University, UK.

Johnson, C.P.D. and P.A.M. Berry (2002). Cross-calibration and validation of altimeter backscatter over natural land targets. In: Proceedings of European Geophysical Assembly, Nice, France, April 21–26.

Chapter 28

An Enhanced Ocean and Coastal Zone Retracking Technique for Gravity Field Computation

P.A.M. Berry, J.A. Freeman, and R.G. Smith

Abstract Satellite radar altimetry has been key to the improvement of geoid and gravity models. Of prime importance to this is obtaining stable and accurate height estimates over the ocean. This is especially difficult over coastal zones due to the non-Brown model nature of the waveforms.

Following a study of existing ocean retracking techniques and analysis of results from the Berry expert system, an enhanced retracking system has been developed which gives more consistent results compared with conventional techniques over both the open ocean and coastal zones. This paper presents results from retracked ERS-1, ERS-2 and Envisat data comparing these against existing methods and presenting details of enhancements made.

28.1 Introduction

Satellite radar altimetry has been used for many years to monitor the surface of the earth's oceans. Over the ocean, pre-processed data are available from the Space Agencies; these data have historically been utilised for oceanographic and geodetic applications. However, the processing chains which generate these data are configured for Brown model (Brown, 1977) waveform shapes and either reject or wrongly retrack other waveform shapes, producing erroneous range to surface values. Global analyses of waveform shapes from ERS1, ERS2, and EnviSat revealed that even over the open ocean, significant numbers of echoes have non-Brown model shapes. It was therefore decided to adapt the Berry Expert System (Berry et al., 1997, 2005), which was created to retrack the complex waveform shapes found over land and inland water, to re-process the ERS1 Geodetic Mission (GM) dataset over the ocean.

P.A.M. Berry (✉)
Earth and Planetary Remote Sensing Laboratory, De Monfort University, Leicester LE1 9BH, UK
e-mail: pamb@dmu.ac.uk

28.2 Waveform Shape Analysis

For this work, data from ERS1 (Capp, 2001), ERS2 (ibid) and EnviSat (Benveniste et al., 2002) were utilised. For ERS-2, improved orbit data were included (Scharroo et al., 2000). Analysing ERS1/2 and EnviSat waveform shapes over the ocean reveals complex patterns. Table 28.1 gives the waveform shape analysis for the ERS1 GM prior to retracking (note that the 75.6% of ocean-like echoes are not necessarily Brown model waveforms; those that fail the Brown model fit are retracked using a modified algorithm, more tolerant of noise). The largest group of other waveforms result from very calm sea, coastal zones and (seasonally) sea-ice. About 10% are extremely wide waveforms resulting from extreme sea states, seasonal sea-ice and coastal off-ranging to bright quasi-specular targets.

The distribution of accepted waveforms can be seen in Fig. 28.1; the primary cause of rejected echoes is the absence of a leading edge. The locations of complex waveforms, primarily associated with sea-ice (although a small percentage of these shapes also occur in coastal zones) are shown in Fig. 28.2. Figure 28.3 shows the global Brown model type echo distribution; note the lower counts over sea ice and in coastal zones.

S.P. Mertikas (ed.), *Gravity, Geoid and Earth Observation*, International Association of Geodesy Symposia 135,
DOI 10.1007/978-3-642-10634-7_28, © Springer-Verlag Berlin Heidelberg 2010

Table 28.1 Expert system waveform analysis results for ERS1 geodetic mission

Period of ERS1 data analysed	10/April/1994–21/March/1995	Geodetic mission
Total waveforms accepted	286,335,223	
Total waveforms rejected	38,361,593	
Total waveforms in file	324,696,816	
Waveform type	*Number of waveforms*	*Percentage accepted (%)*
Anomalous brown model type	10,097,972	3.53
Complex wide_1	50,917	0.02
Quasi-specular	82,026	0.03
Complex wide_2	54	0
Complex wide_3	418,792	0.15
Low sea state non_brown	37,376,493	13.05
Ocean and quasi-ocean -like	216,482,395	75.6
Extreme high power	1,002,865	0.35
SeaIce/anomalous brown rejected	20,823,709	7.27

The distribution of anomalous (non-Brown model) wide waveforms, with sea ice, storm events and coastal zone echoes as primary causative factors are shown in Fig. 28.4.

Following this global waveform classification, a specific study was undertaken into coastal zone waveforms, as it was clear that the proportion of non-Brown model waveforms rises sharply as the coast is approached. To do this, all echoes within 50 kms of any coast were identified and classified according to their distance from the coast. A global histogram was created for the entire ERS1 Geodetic Mission dataset; this gives the most comprehensive sampling of the coastal zone, as the ground tracks do not repeat.

The results (specifically excluding sea-ice regions in order to study the effect of the coastal zone on waveform shapes) are shown in Fig. 28.5, and very clearly demonstrate that within 10 km of the coast, a

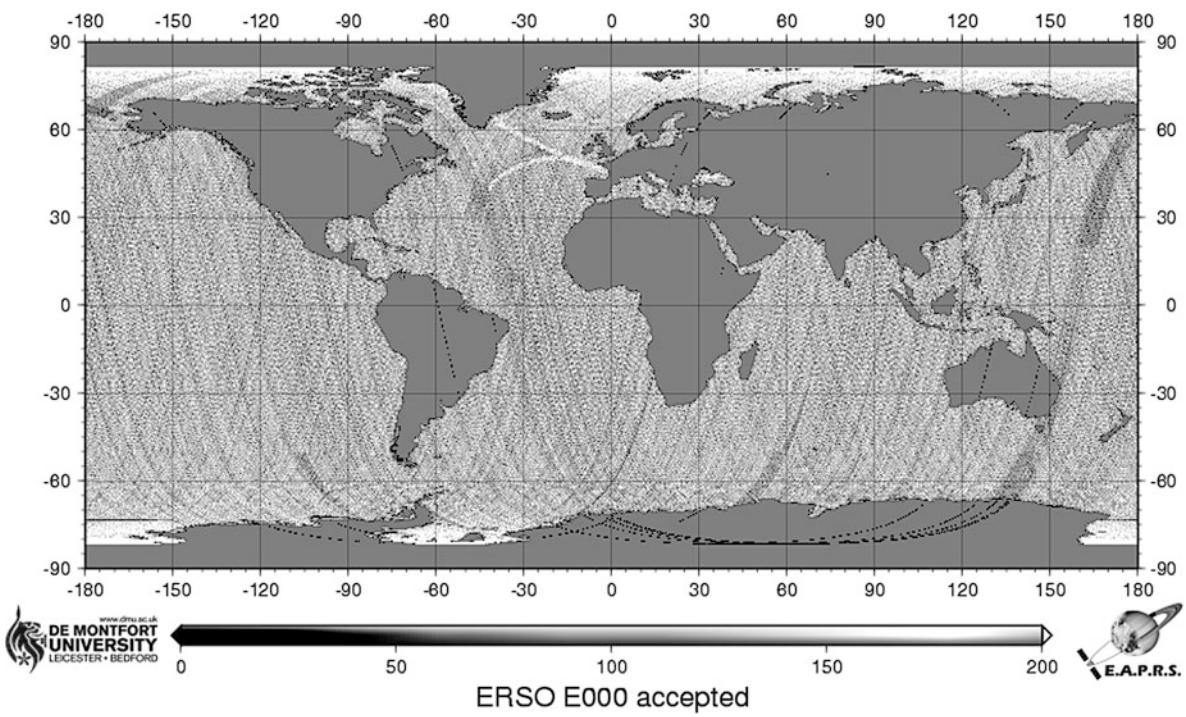


Fig. 28.1 Distribution of accepted waveforms from ERS1 GM

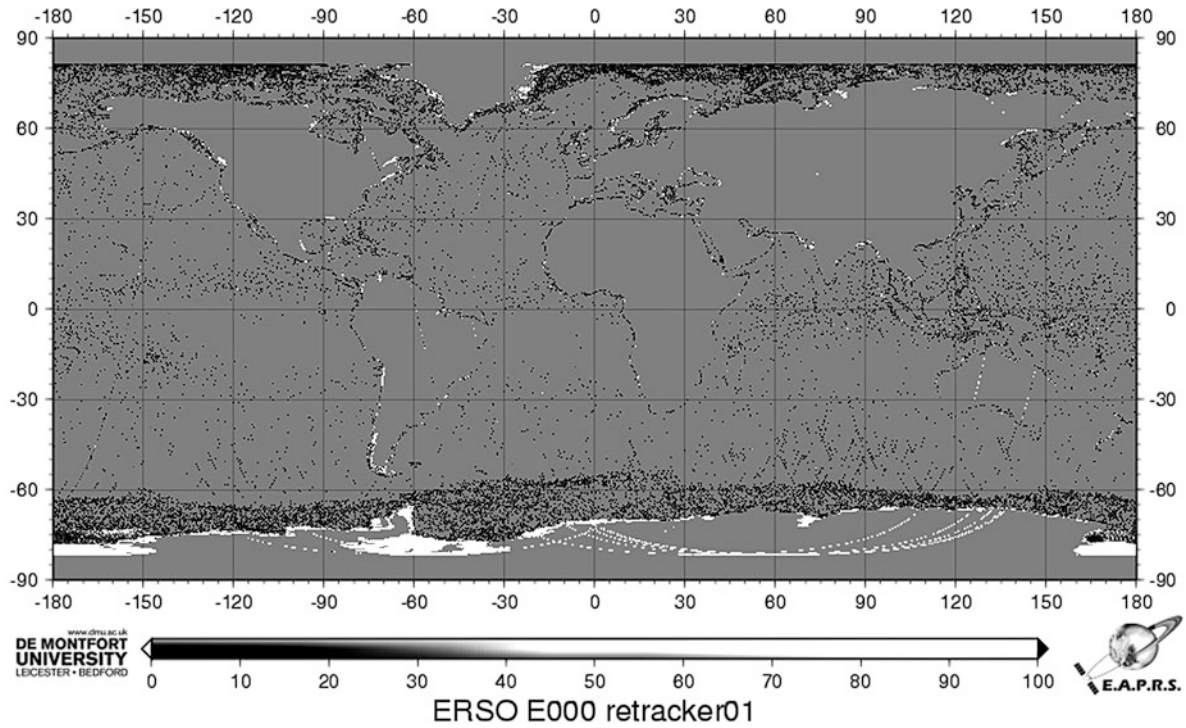


Fig. 28.2 Percentage of "anomalously wide" waveforms from the ERS1 GM

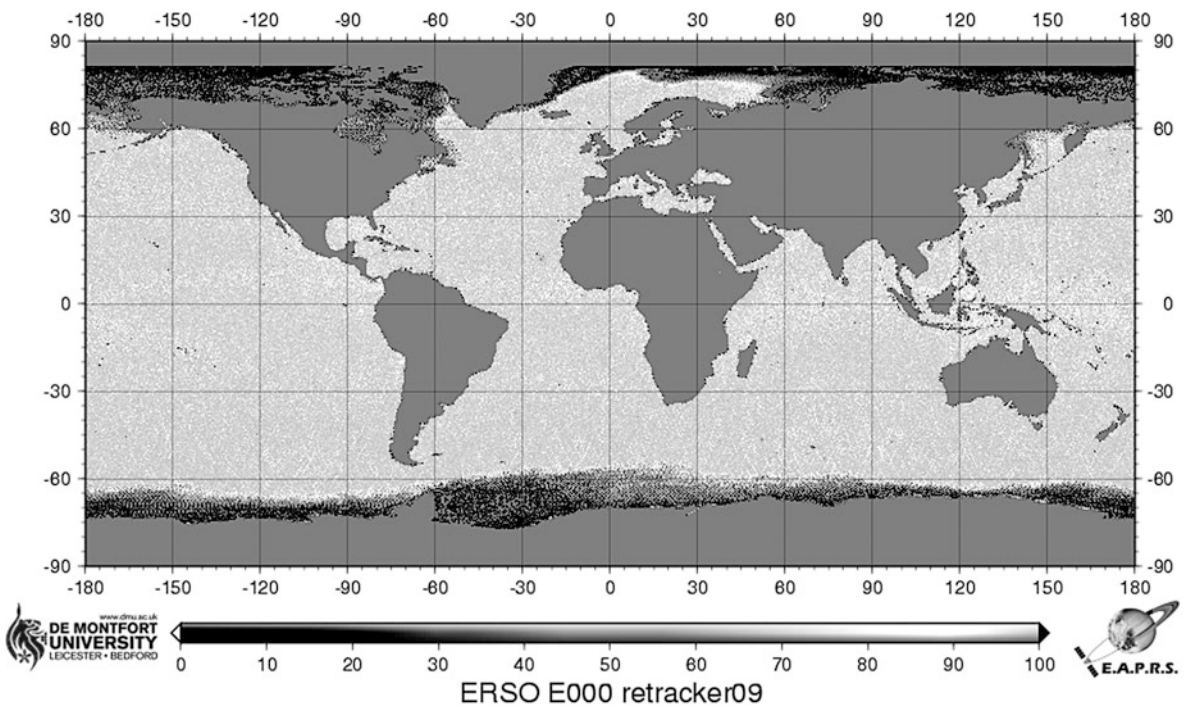


Fig. 28.3 Percentage occurrence of "ocean-like" waveforms from the ERS1 GM

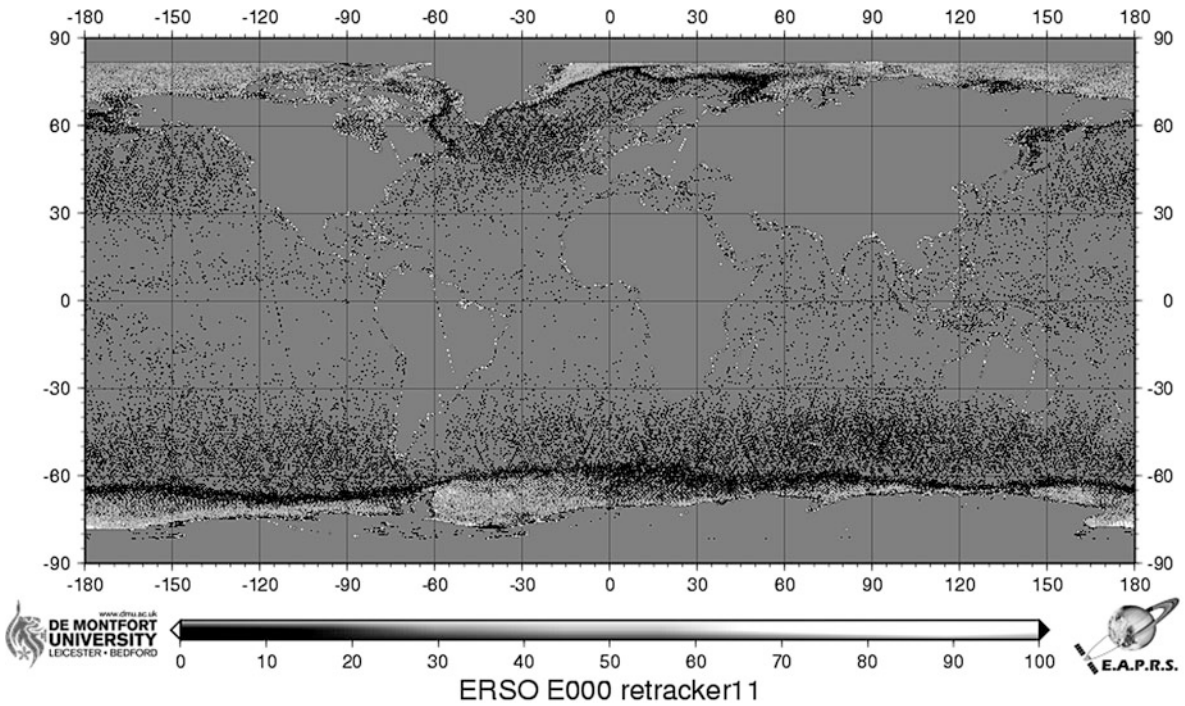


Fig. 28.4 Percentage occurrence of sea-ice/severely anomalous wide waveforms from the ERS1 GM

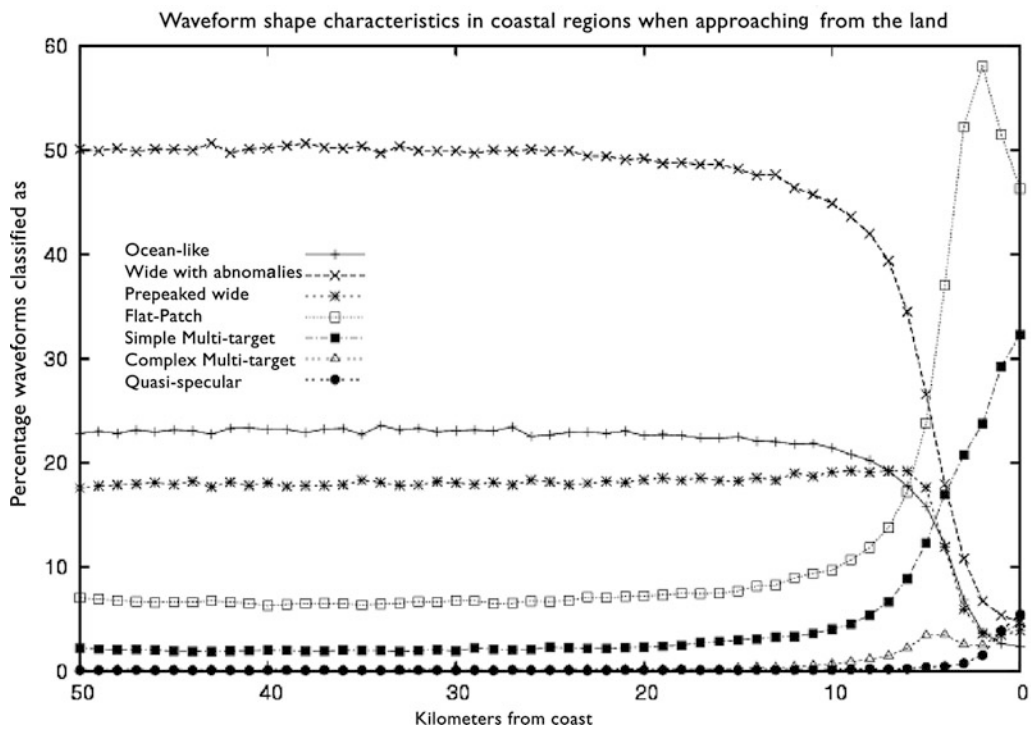


Fig. 28.5 Waveform shape distribution in global coastal zone (excluding sea-ice) from the ERS1 GM

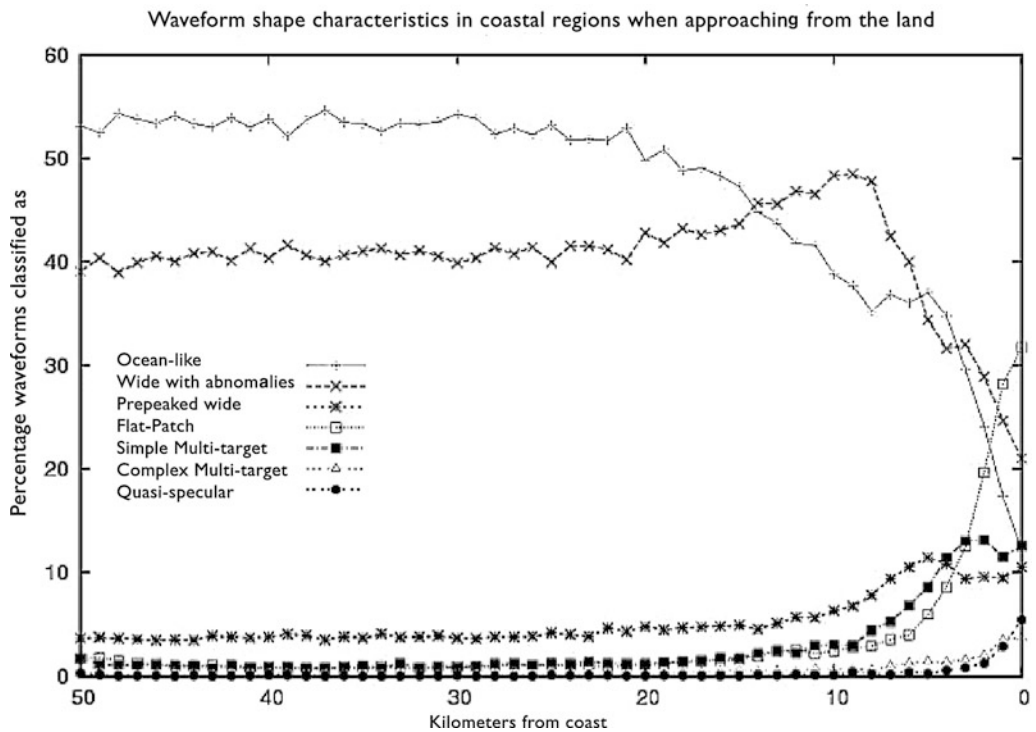


Fig. 28.6 Waveform shape distribution in global coastal zone (excluding sea-ice) from a representative cycle of EnviSat

rapid increase in non-Brown model waveforms is seen; within 5 km of the coast the majority of echoes are not Brown model in shape. A similar analysis was performed for one cycle of EnviSat RA-2 data (Fig. 28.6) for comparison.

28.3 Retracking

Having characterised the waveform shapes present over ocean in the ERS1 Geodetic Mission dataset, the next step was to retrack these waveforms. This was done using a version of the Berry Expert System (Berry et al., 1997) originally designed for land and inland water echoes. Because noise suppression on the ERS1/2 altimeter echoes means that the lowest part of the leading edge is missing, it is not possible to fit to sea surface skewness; a reduced Brown model fit (following the general approach of Challenor and Srokosz, 1989) was therefore utilised, with a second more tolerant quasi-Brown retracker processing those waveforms that failed the Brown model fit. The suite of 11 expert system retrackers was then tailored for the range of echo shapes identified in Fig. 28.5. The several classes of quasi-specular echoes were individually assessed; "clean" echoes were passed to a standard thresholding retracking algorithm (e.g., Laxon, 1994) whilst those echoes with minor anomalies in shape identified as contaminants were filtered and reconstructed before being passed to a second retracking algorithm. Echoes classed as "complex" were directed to the several retracking algorithms utilised for composite echoes; again, these echoes were reconstructed free of anomalies, and were then retracked. Error estimates were reconfirmed for all retrackers, and this information was recorded with each retracked height, in order that heights from complex echoes could be down-weighted in subsequent analyses. As with the original expert system, considerable time was expended in confirming that significant biases were not observed between echoes retracked using any of the suite of algorithms. This was done using along-track height analysis. One waveform class of quasi-specular echo was detected as showing a small height bias; the algorithm was re-tuned by adjusting the retrack threshold to return height values consistent with those from other retrackers. It should be stressed that this

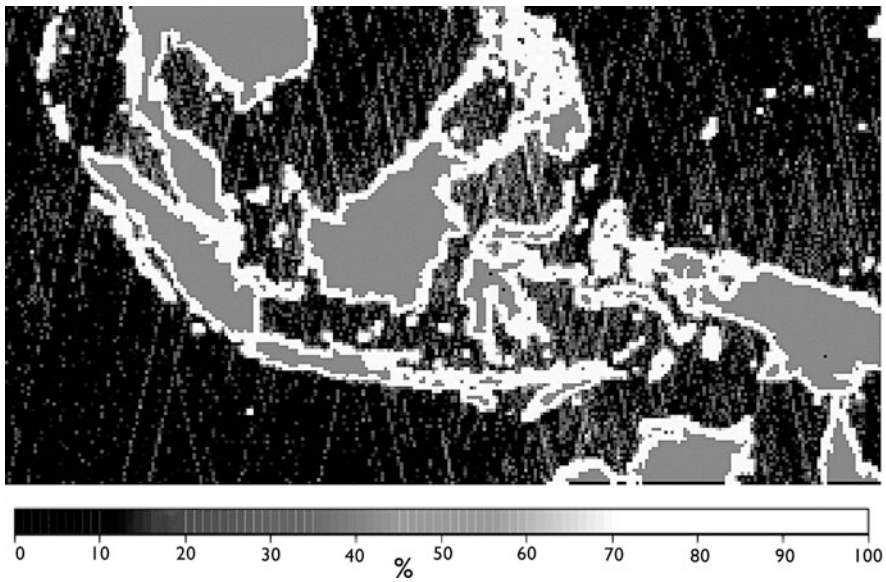


Fig. 28.7 Percentage of additional data retracked by the EAPRS system compared with that returned by RADS in region 15°S–15°N 105°E–135°E

analysis and rebalancing cannot be performed by putting echoes sequentially through each retracker in turn to assess bias between retrackers, since each retracking algorithm is configured for a particular class of waveform shape. To deal more effectively with the noise still apparent in the retracked heights from several of the retrackers, it was then decided to enhance the system further by using a "double retracking" technique; after an initial pass through the system, information from the first retracking was then utilised for each waveform to enhance the retracking on a second pass through the system. This was found to enhance the accuracy significantly, particularly in the case of Brown model waveforms, where it allowed the significant wave height to be constrained to vary only slowly, an approach consistent with that taken by other researchers (e.g., Sandwell and Smith, 2005). The next step was to perform more detailed assessments of data quantity and quality using this system, and a region was chosen which utilised the full range of retracking algorithms – the coastal zone.

28.4 Regional Study

As part of the global examination of waveforms in coastal zones, a special study was made of the Malay Archipelago. This complex group of islands presents a superb test region for coastal zone waveform analysis and retracking as the abundance of coastlines and sheltered extents of water means that many waveforms are not Brown model in shape. Retracking the ERS1 Geodetic Mission dataset produced viable data to within 1 km from the coast throughout this region. To assess the enhancement in the data recovery, the EAPRS expert system outputs were compared with the data in the RADS database (Naeije et al., 2006) and the percentage enhancement in data recovery was calulcated. The results are illustrated in Fig. 28.7. Note that to ensure a fair comparison, the RADS recommended flag settings referring to atmospheric corrections were disabled, so that a direct assessment could be made of the relative number of datapoints available to RADS and those generated by the EAPRS system. The EAPRS data were averaged to conform to the RADS along-track sampling rate.

In addition to coastal zones, areas with a high concentration of very low sea state are also flagged in RADS and more data are successfully recovered using the Berry system, as the Brown model fit can fail for low sea states.

28.5 Burst Echoes

The EnviSat RA-2 gives a unique opportunity to examine the effect of the Pulse Repetition Frequency (PRF)

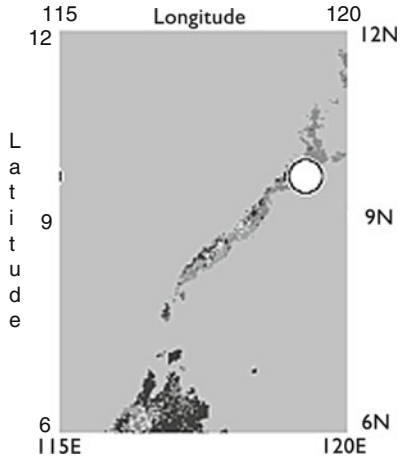
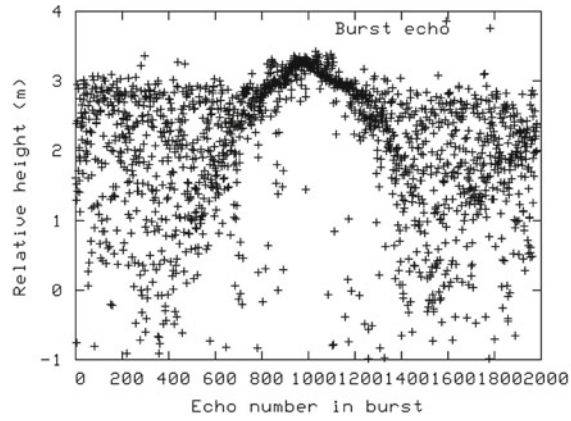


Fig. 28.8 Location of burst echoes on the Palawan coast (white circle) from EnviSat cycles 36.37.38

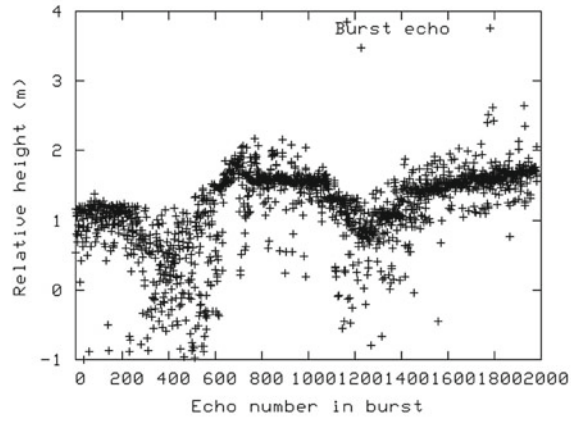
on coastal zone waveform recovery, as a small number of echoes are telemetered to ground at the full 1,800 Hz resolution in addition to the normal 18 Hz records (Berry et al., 2007). Although restricted to 1 s (about 7 km) every 2–3 min, the data are sampled in approximately the same locations in each cycle (ibid). Three sequences from the coast of Palawan in the Malay Archipelago (Fig. 28.8) are shown to illustrate the variable and complex surface response in the coastal zone, where the 18 Hz EnviSat averaged waveform characteristics are shown to change rapidly (Fig. 28.6); the echoes, from cycles 36 to 38 are (within orbit and onboard command timing limitations) from the same location. Analysing the waveform shapes using the Berry expert system gives the results in Table 28.2. Here, the noise on the echoes precludes a successful Brown model fit; note the significant changes in the relative proportions of quasi-specular and wider (low sea state) echoes from burst to burst, reflecting the changing coastal zone conditions. Retracking the echoes at the full 1800 Hz resolution gives the relative

Table 28.2 Waveform characterization for Palawan burst echoes

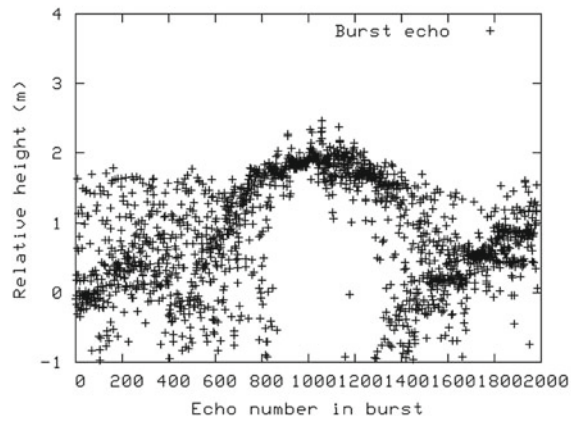
Echo shape	Cycle 36	Cycle 37	Cycle 38
Wide	77	6	64
Quasi-specular	802	1,069	879
Complex	192	186	180
Low sea state	913	722	861
Brown model ocean	0	0	0
Total accepted	1,984	1,983 (1 failed wfm)	1,984



a) cycle 36



b) cycle 37



c) cycle 38

Fig. 28.9 Cycles 36–38 bursts over Malay Archipelago coastal zone retracked using expert system

height changes along the bursts shown in Fig. 28.9 (note that tidal corrections have not been applied). Here, the central portion of each burst is over land. The profile height shape differences from cycle to cycle

show clearly how quickly the reflecting surface components change in the coastal zone. A higher PRF allows the different echo components to be separated out and gives the potential for more precise retracking from future altimeter missions in these complex environments.

28.6 Discussion

Traditionally, altimeter analyses over ocean have relied on the pre-retracked data available from the Space Agencies. However, significant amounts of data have been rejected during processing; this global analysis confirms that data are lost even over the open ocean. In sea-ice regions the majority of waveforms are not Brown model in shape; significantly, within 10 Km of the coast, a rapidly increasing percentage of echoes are not Brown model, and within 5 Km of the coast the majority of echoes cannot be successfully fitted by a Brown model retracker.

Utilising an expert system approach, with 11 retrackers specifically configured to recover the range to the nadir point from the variety of complex and varying echoes actually returned from the ocean, gives a significant enhancement in data even over the open ocean. In coastal zones the information content is transformed using this approach. However, analysis of Burst echoes close to coast also shows the significant further improvement in information recovery which would be possible with a higher PRF. The retracked ERS1 Geodetic Mission dataset has been used in DNSC08 (Andersen et al., 2007) and the global coastal zone dataset has significantly enhanced the EGM08 model.

Acknowledgements The authors would like to thank ESA for the ERS1-GM, ERS-2 and EnviSat datasets and TU Delft for the RADS dataset.

References

Andersen, O., P. Knudsen, P.A.M. Berry, J.A. Freeman, S. Kenyon, and R. Trimmer (2007). Refining global marine gravity prediction from satellite and ships, DNSC06 global marine gravity field and associated bathymetry. Envisat Symposium 2007, Montreux, Switzerland 23–27 April 2007, ESA Pub. SP-636 2007.

Benveniste, J., S. Baker, O. Bombaci, C. Zeli, P. Venditti, O.Z. Zanife, B. Soussi, J.P. Dumont, J.P. Stum, and M. Milagro-Perez (2002). ENVISAT RA-2/MWR Product Handbook, Issue 1.2, PO-TN-ESR-RA-0050, European Space Agency, Frascati, Italy.

Berry, P.A.M., A. Jasper, and H. Bracke (1997). Retracking ERS-1 altimeter waveforms over land for topographic height determination: an expert system approach. ESA Pub. SP-414, 1, 403–408.

Berry, P.A.M., J.D. Garlick, J.A. Freeman, and E.L. Mathers (2005). Global inland water monitoring from multi-mission altimetry. *Geophys. Res. Lett.*, 32(16), L16401, DOI: 10.1029/2005GL022814.

Berry, P.A.M., J.A. Freeman, C. Rogers, and J. Benveniste (2007). Global analysis of Envisat RA-2 burst mode echo sequences. *IEEE Geosci. Remote Sens.*, 45(9), 2869–2874, DOI: 10.1109/TGRS.2007.902280.

Brown, G.S. (1977). The average impulse response of a rough surface and its applications. *IEEE Trans. Antennas Propagation*, 25(1), 67–74.

Capp, P. (2001), Altimeter waveform product ALT.WAP compact user guide, Issue 4.0, PF-UG-NRL AL-0001, Infoterra Ltd., UK.

Challenor, P.G. and M.A. Srokosz (1989). The extraction of geophysical parameters from radar altimeter return from a nonlinear ocean surface. In: Brooks S.R. (ed), Mathematics in remote sensing. Institute of Mathematics and its Applications, Clarendon Press, pp. 257–268.

Laxon, S. (1994). Sea ice altimeter processing scheme at the EODC. *Int. J. Remote Sens*., 15(4), 915–924.

Naeije, M., E. Schrama, E. Doornbos, and R. Scharroo (2006). The role of RADS in building the 15-year altimeter record. Proceedings of Symposium on 15 years progress in RA, 13–18 March 2006, Venice Italy, ESA SP 614 July 2006.

Sandwell, D.T. and W.H.F. Smith (2005), Retracking ERS-1 altimeter waveforms for optimal gravity field recovery. *Geophys. J. Int.*, 163(1), 79–89.

Scharroo R., E. Schrama, M. Naeije, and J. Benveniste (2000). A recipe for upgrading ERS altimeter data, European Space Agency, (Special Publication) ESA SP, 461, pp. 1300–1309.

Chapter 29

Measurement of Inland Surface Water from Multi-mission Satellite Radar Altimetry: Sustained Global Monitoring for Climate Change

P.A.M. Berry and J. Benveniste

Abstract Multi-mission satellite radar altimetry makes a unique contribution to the monitoring of global inland surface water; existing datasets already allow derivation of decadal time-series over hundreds of targets worldwide. These data are utilised both for climate change research, to inform water resource management, and, in synergy with GRACE data, to examine time-varying gravity signatures from land surfaces and (potentially) measure sub-surface hydrological flow.

As the number of gauged catchments continues to fall, the importance of a global remote sensing measurement capability becomes ever more critical. The key to unlocking this potential is to retrack the complex waveforms returned from inland water targets, to identify and discard echo components returned from targets not directly beneath the satellite, and to discriminate successfully between wet land and inundated surface.

This paper presents a global assessment of current capabilities, showcases decadal time-series from past and current altimeters, and demonstrates the Near Real Time measurement capability now running for the ENVISAT RA-2 and soon for Jason-2 as an ESA pilot system, allowing users access to these data within 3 days of measurement. The enhancement of this unique capability anticipated from the series of proposed future missions (such as CryoSat-2 and Sentinel-3) is discussed, and the key contribution to global climate change monitoring is demonstrated.

P.A.M. Berry (✉)
E.A.P.R.S. Lab, Gateway House, De Montfort University, Leicester LE19BH, UK
e-mail: pamb@dmu.ac.uk

29.1 Introduction

Satellite radar altimetry has been used for more than a decade to measure inland water heights. From initial measurement of a few large lake targets (Guzkowska et al., 1990), the techniques have now been applied to many large water bodies (Berry, 2002; Maheu et al., 2003; Birkett et al.. 2002). A global evaluation of the current capability and future potential of this technique is clearly required.

29.2 Global Analysis

To assess the extent to which viable data have been collected over inland water by current and past altimeters, a global analysis has been performed for TOPEX (Algiers, 1993; Callahan, 1993), ERS2 (Capp, 2001), EnviSat RA-2 (Benveniste et al., 2002) and Jason-1 (Zanife et al., 2004). A mask was created to select only those waveforms likely to have returned from an inland water target, and each waveform was analysed and, if valid (i.e., contained significant signal and the leading edge was successfully captured) was retracked. Time series of successfully captured waveforms and their retracked heights were then generated. Statistics were generated for all missions for all inland water crossings where time series could be created successfully. Criteria for judging "success" included the requirement that valid waveforms be present for at least 90% of crossings. The results are summarised in Table 29.1 (note that for large lake targets several crossings can exist over the same target; thus these figures give the total number of independent time-series of measurements).

S.P. Mertikas (ed.), *Gravity, Geoid and Earth Observation*, International Association of Geodesy Symposia 135,
DOI 10.1007/978-3-642-10634-7_29, © Springer-Verlag Berlin Heidelberg 2010

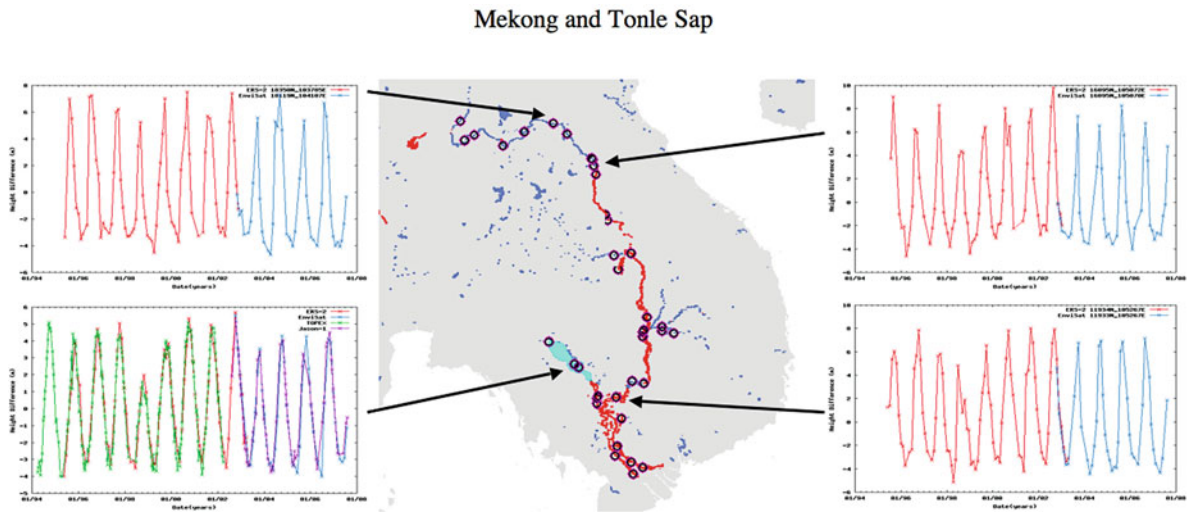


Fig. 29.1 Mekong river system monitoring from current and past altimeter missions showing ERS2 (*dark grey*), EnviSat (*light grey*)

Whilst only about 20% of these targets currently produce good time series, enhanced retracking is expected to increase this percentage to 40–60%. The increase from TOPEX to ERS-2 is evident, and is partly the effect of the different orbit repeat pattern. However, the majority of the enhancement is due to the ERS2 altimeter being configured with a wider range window over land. Whilst this restricted the vertical

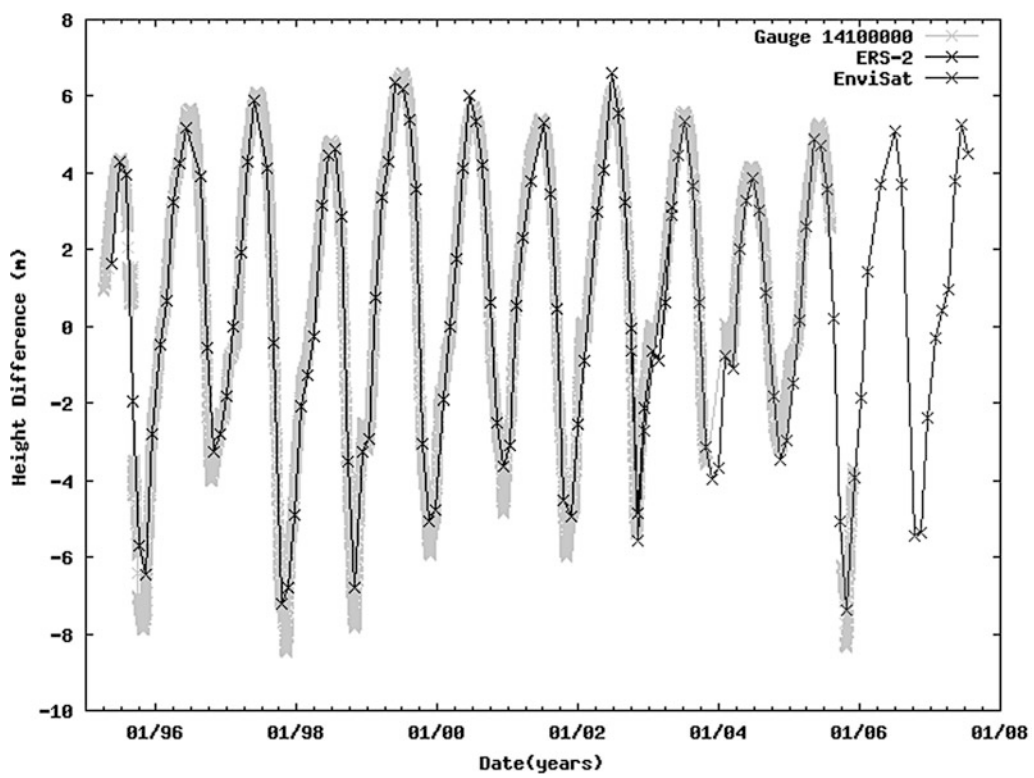


Fig. 29.2 Example time series against Amazon gauge measurements for ERS2 and EnviSat

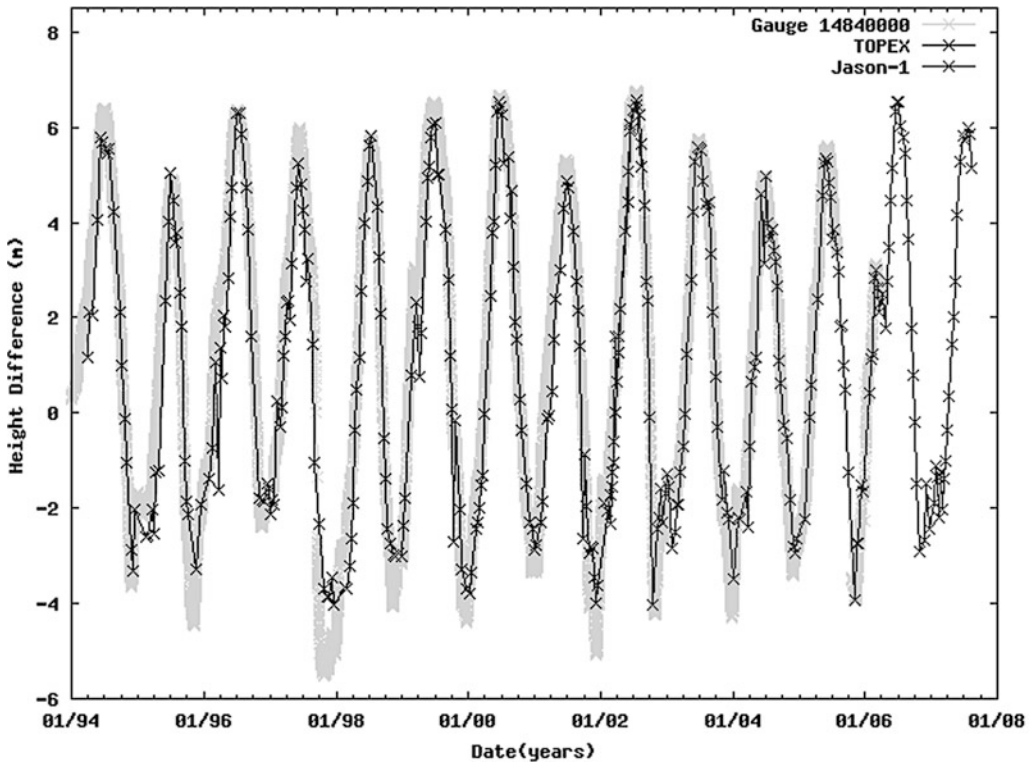


Fig. 29.3 Example time series against gauge from TOPEX and Jason-1

Table 29.1 Global waveform statistics for timeseries generation over inland water

Altimeter	Period of data	Total
ERS2	May1995–April 2003	22,224
EnviSat	Oct. 2002–Aug. 2007	25,636
TOPEX	Mar. 1994–Aug. 2002	8,124
Jason-1	Jan. 2002–Aug. 2007	7,329

precision of measurement, it greatly increases the number of targets successfully acquired. For EnviSat, even more targets are acquired, although the skewing of the instrument logic to favour ocean mode operation degrades the waveform capture over some inland water targets.

29.3 Example Systems and Analysis

29.3.1 Mekong River

Initially, time series of lake and river heights were only generated over a small number of large lake targets, and the Amazon basin, where pre-processed data from the Space Agencies could be utilized. In order to expand the measurement capabilities, it was necessary to "retrack" the inland water waveforms (analyse the complex composite echoes returned from land and inland water, isolate that part returned from an underlying water surface, and recalculate the range to that target). The change in measurement capability produced by both retracking the waveforms and utilising data from ESA's ERS2 and EnviSat altimeters, is shown in the example over the Mekong river system (Fig. 29.1). This provides a good illustration of both the historical context and the potential for future missions. Here, one of the first targets measured by satellite radar altimetry, Tonle Sap (successfully measured using SEASAT and GEOSAT data Guzkowska et al., 1990) is shown as monitored by ERS2, EnviSat, TOPEX and Jason-1. The ESA altimeters, configured to retrieve data over topographic surfaces, now successfully acquire good time series along the course of the Mekong river (every circle represents one derived time series and three examples are shown from ERS2 and EnviSat.

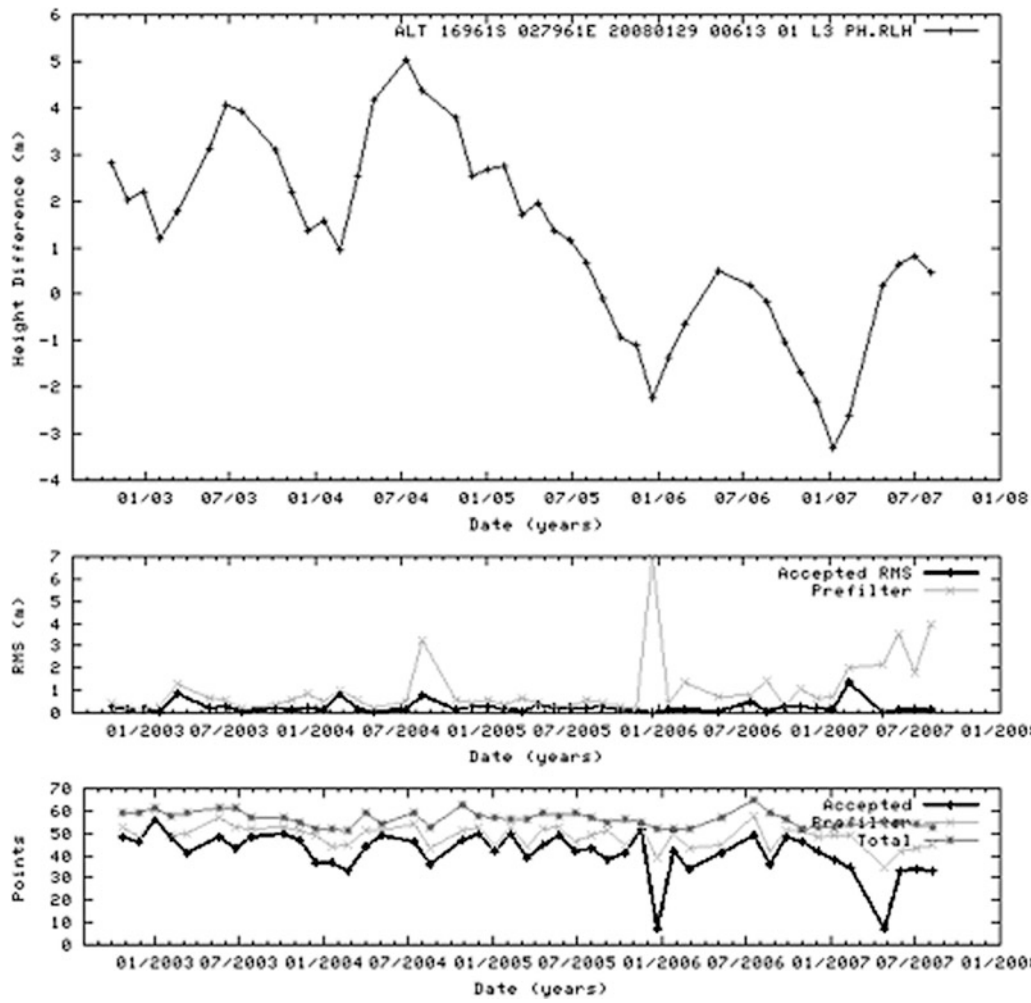


Fig. 29.4 Statistics for EnviSat time series over Lake Kariba

29.3.2 Amazon Basin Validation

A huge validation exercise has been undertaken in the Amazon basin, to assess the current accuracy of altimeter derived height time series using the network of available river gauge measurements. Typical examples are shown here for an ERS2/EnviSat crossing (Fig. 29.2) and a TOPEX/Jason-1 crossing (Fig. 29.3). It should be noted that small outliers in TOPEX and Jason-1 time-series contribute to the RMS against the gauge in Table 29.2; excluding these outliers significantly improves the statistics for TOPEX. EnviSat time series consistently present the lowest RMS against the gauges.

29.4 Near-Real-Time Measurements

The ESA River and Lake system currently retrieves data using the EnviSat RA-2, which allows generation of heights within 3 days of measurement for rivers and

Table 29.2 Statistics for example Amazon validation

	Satellite	RMS against gauge (m)	Correlation coefficient
Figure 29.2 stats	ERS-2	0.63	0.99
	EnviSat:	0.47	0.99
Figure 29.3 stats	TOPEX	1.84	0.86
	Jason-1	1.22	0.93

lakes globally (Berry, 2008). The next implementation will add data from Jason-2 over all targets that produce very consistent and reliable measurements. The system uses a global Near-Real-Time (NRT) mask to identify appropriate targets for inclusion within the system. This mask is set conservatively, and allows only data from the very "cleanest" targets to be retrieved.

29.4.1 Target Analysis

To illustrate the comparison in terms of targets acquired, historical data as used in Table 29.1 have been put through the NRT mask for EnviSat and Jason-1 over Africa, producing the comparison statistics shown in Table 29.3.

The EnviSat results are consistent over all continents, with about 20–30% of the targets retrieved by the research system retained in the NRT system. However, for Jason-1, this initial evaluation over Africa has produces a far greater differential between targets where waveforms are acquired and

Table 29.3 Comparison numbers of targets acquired from the full system and the initial NRT system for both EnviSat and Jason-1

Mission	Number of targets full mask	NRT mask
EnviSat	960	209
Jason-1	230	24

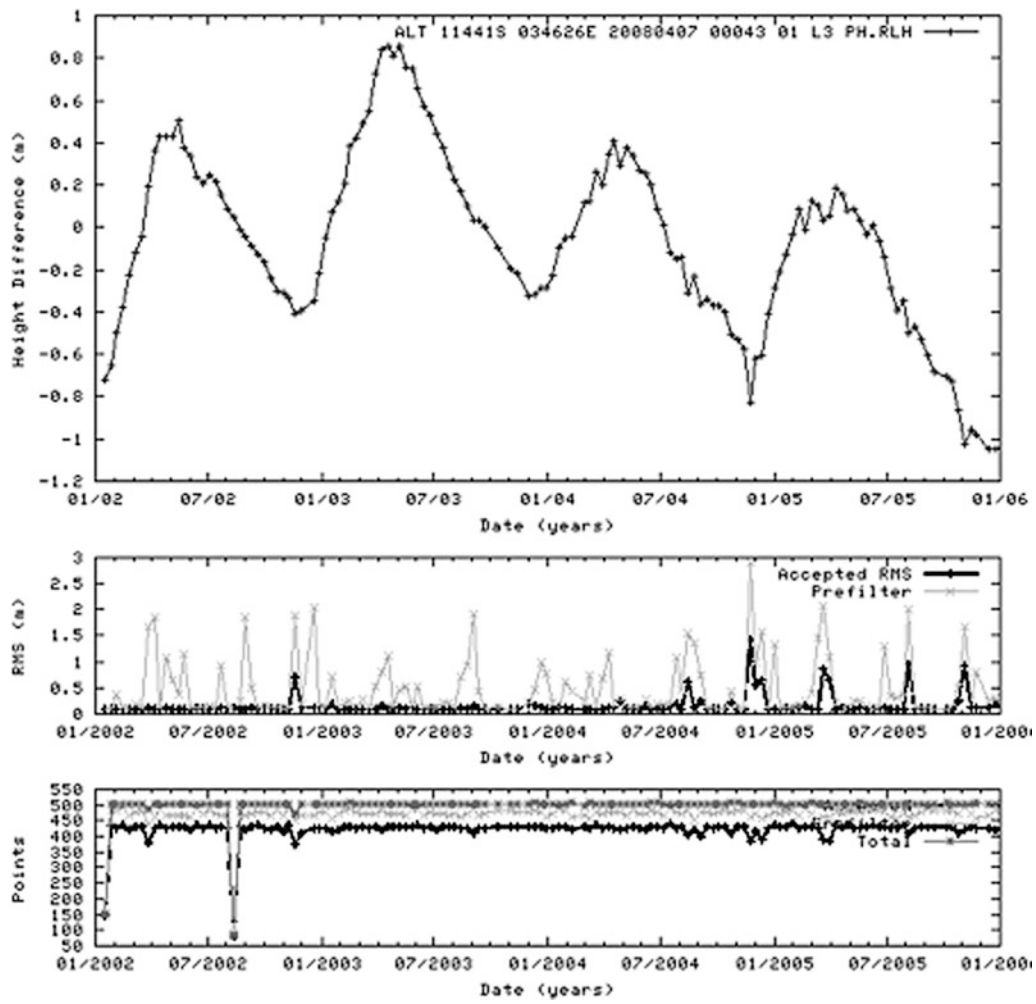


Fig. 29.5 Statistics for Jason-1 over Lake Malawi

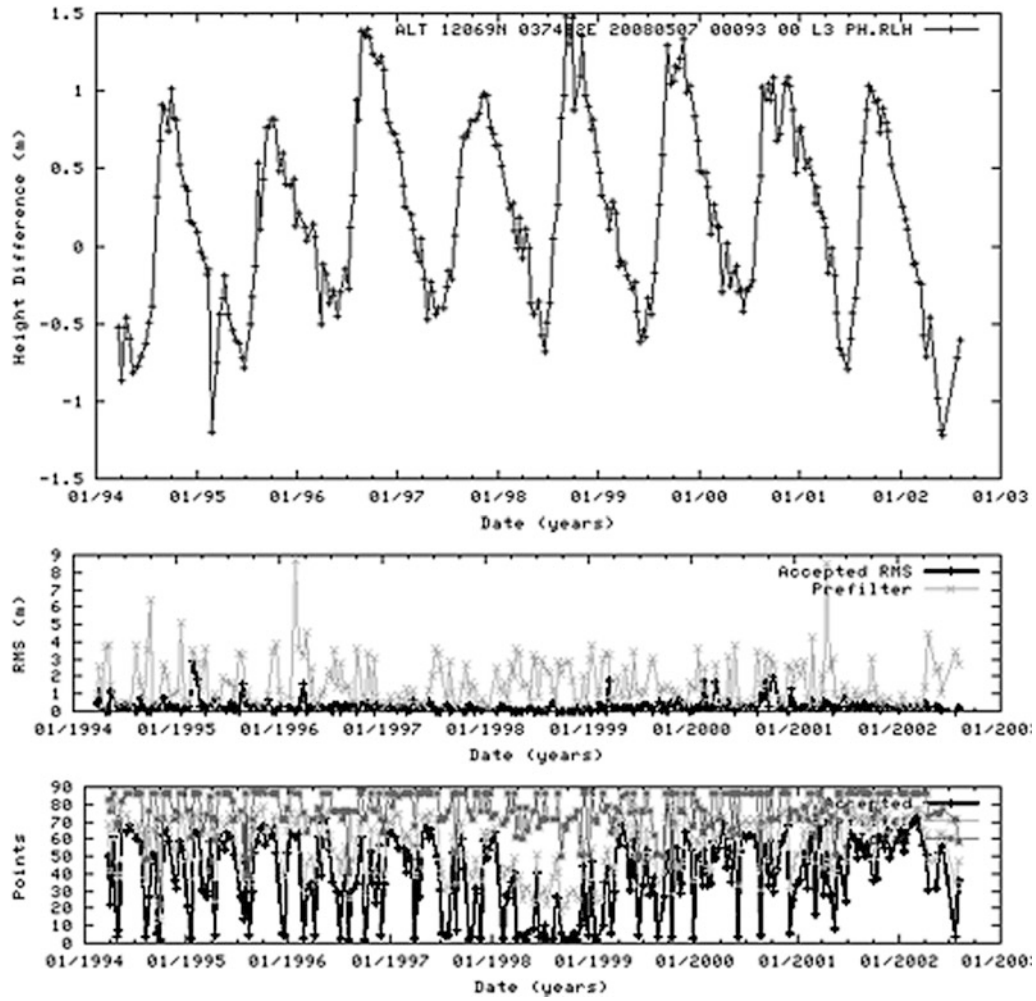


Fig. 29.6 Statistics for TOPEX over Lake Tana

targets whose measurements are sufficiently stable to be included in the NRT system.

29.4.2 Statistical Analysis

In order to investigate the widely varying performance of altimeters river inland water targets, and to evaluate the consistency of the expert system retracking, detailed examination of the waveforms and derived heights retrieved from current altimeters has been performed. To illustrate the typical outcome, four results are given here, one each from the four altimeters utilised in this study.

Fig 29.4 shows an EnviSat time series over Lake Kariba, with the time series of heights, the along-track RMS before and after full processing and filtering of each measurement shown (light grey before processing, dark grey as output). Also shown is the number of waveforms initially acquired (medium grey) then the number which passed the waveform analysis as being inland water (light grey) and the final number retained after retracking and filtering (dark grey). The improvement in the along-track RMS after full processing is clear, as is the variation in the number of waveforms retained.

A similar result for Jason-1 is shown for Lake Malawi in Fig. 29.5. Here, the very great improvement in the along-track RMS after full retracking and processing is evident; also clear is that the actual proportion of waveforms discarded is relatively low. Where Jason-1 does retrieve data, these data are often extremely good but the waveforms are very variably located with respect to the tracking point, and thus retracking is essential to recover an accurate range to surface.

The results of a TOPEX analysis for Lake Tana is shown in Fig. 29.6. Here, there is a dramatic improvement in the along-track RMS after full retracking and processing, but a significant number of waveforms have been rejected to produce the final retracked average height. This variable performance is often seen with Topex waveforms.

Finally, a time series for ERS2 from lake Nasser is shown in Fig. 29.7.

Overall, the statistical analysis revealed that over these targets, retracking the data using an expert system approach (Berry et al., 1997, 2005) has retained a high proportion of the data-points, but dramatically reduced the along-track RMS. This indicates that proper processing of the decadal time-series of waveforms already gathered by past and current altimeter missions has the potential to recover time-series of river and lake heights globally from a high proportion of the targets identified in Table 29.1.

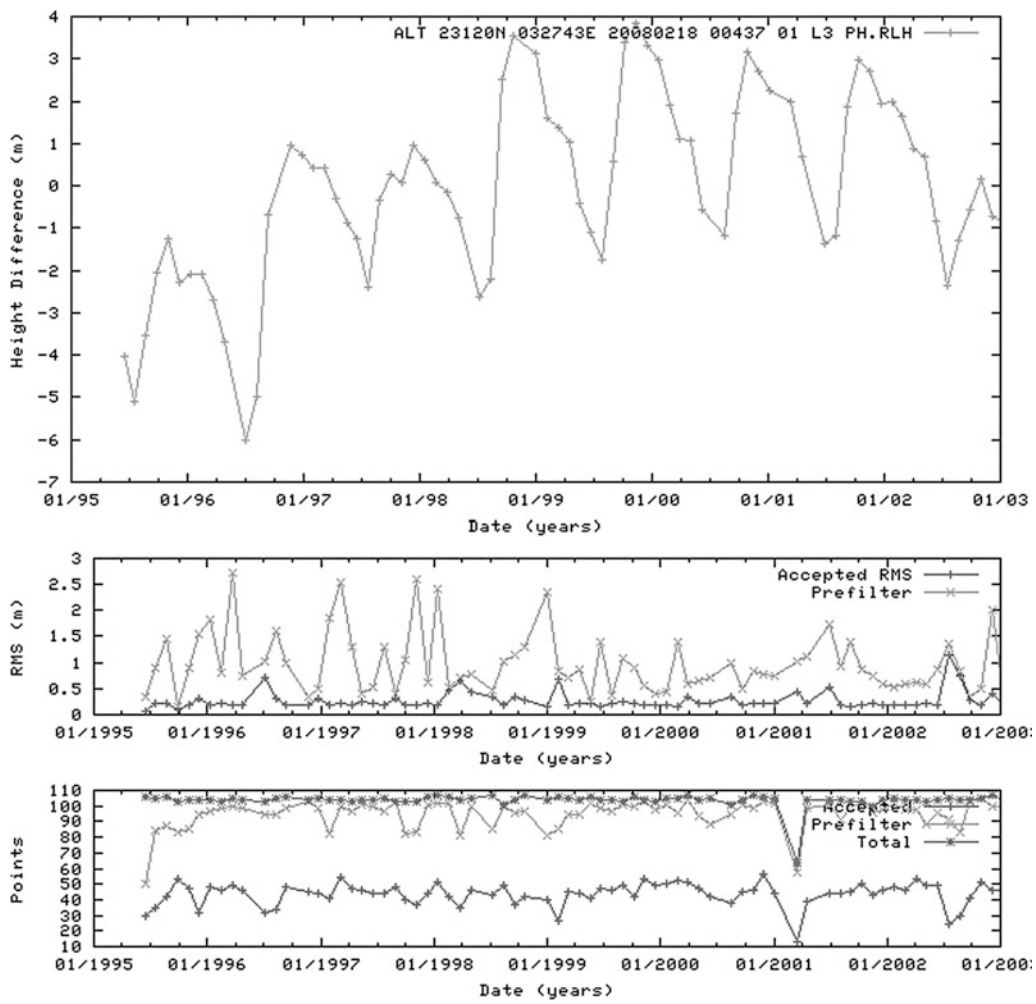


Fig. 29.7 Statistics for ERS2 over Lake Nasser

29.5 Burst Echoes

One critical limitation of current altimeters in recovery of inland water heights is the low along-track sampling rate. To gain an understanding of the potential for future missions to enhance inland water measurement by utilising a higher PRF, the EnviSat 1,800 Hz Individual Echoes, so-called burst echoes, have been analysed over inland water. The instrument returns these unique data approximately every 3 min, with 1 s of data returned at 1,800 Hz. This analysis (Berry et al., 2007) reveals complex surface reflectors, and a wealth of detailed information, clearly demonstrating the huge further monitoring potential from future missions with a higher PRF, compared to the usual 18 Hz compressed data rate. An example over the Congo River system is given in Fig. 29.8, showing multiple surface reflectors in the retracked 1,800 Hz heights.

29.6 Discussion

A huge amount of waveforms have already been gathered over inland water targets globally. Processing these complex echoes to retrieve decadal time-series of height changes has already recovered information over hundreds of targets worldwide. Information on ephemeral surface water can also be retrieved. Analysis of the 1,800 Hz burst echo data from EnviSat RA-2 reveals complex surface reflectors, and a wealth of detailed information, clearly demonstrating the huge further monitoring potential from future missions with a higher PRF, such as CryoSat-2 and Sentinel-3. With applications ranging from near-real-time monitoring for water resource management to decadal climate change indicators, and spatial scales which already allow correlations with GRACE data, the unique contribution of satellite radar altimetry to global inland

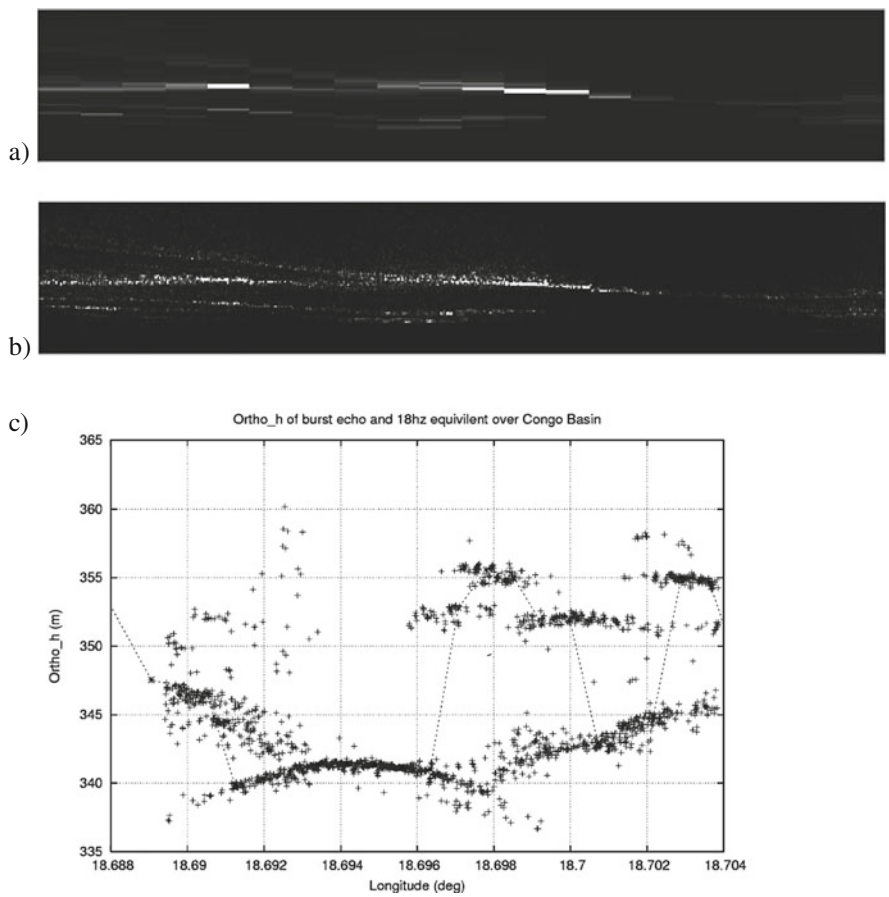


Fig. 29.8 Bust Echo example over Congo river system (**a**) 18 Hz waveforms (**b**) 1,800 Hz waveforms (**c**) Retracked heights at both resolutions

surface water monitoring and the importance of continued measurements is evident.

Acknowledgements The authors wish to thank CNES for supply of Jason-1 data, ESA for supply of EnviSat and ERS1/2 data, and JPL for supply of TOPEX waveform data.

References

Algiers, J. (1993). TOPEX ground system software interface specification, (SIS-2) altimeter sensor data record (SDR) – Alt SDR data (NASA). March, 1993, JPL D-8591 (Rev. C), TOPEX 633-751-23-001, Rev. C

Benveniste, J., S. Baker, O. Bombaci,C. Zeli, P. Venditti, O.Z. Zanife, B. Soussi, J.P. Dumont, J.P. Stum, and M. Milagro-Perez (2002). ENVISAT RA-2/MWR Product Handbook, Issue 1.2, PO-TN-ESR-RA-0050. European Space Agency, Frascati, Italy.

Berry, P.A.M. (2002). A new technique for global river and lake height monitoring using satellite altimeter data. Int. J. Hydropower Dams, 9(6), 52–54.

Berry, P.A.M. (2006). Two decades of inland water monitoring using satellite radar altimetry. In: Benveniste, J. and Y. Ménard (eds), Proceedings of the "15 Years of Progress in Radar Altimetry" Symposium, Venice, Italy, 13–18 March 2006, ESA Special Publication SP-614.

Berry, P.A.M., J.D. Garlick, J.A. Freeman, and E.L. Mathers (2005). Global inland water monitoring from multi-mission altimetry. *Geophys. Res. Lett.*, 32, L16401, doi:10.1029/2005GL022814.

Berry, P.A.M., A. Jasper, and H. Bracke (1997). Retracking ERS-1 altimeter waveforms over land for topographic height determination: an expert system approach. ESA Pub. SP-414, 1, 403–408.

Berry, P.A.M., J.A. Freeman, C. Rogers, and J. Benveniste (2007). Global analysis of Envisat RA-2 burst mode echo sequences. *IEEE Geosci. Remote Sens.*, 45(9), 2869–2874, DOI: 10.1109/TGRS.2007.902280.

Birkett, C.M., L.A.K. Mertes, T. Dunne, M. Costa, and J. Jasinski (2002). Altimetric remote sensing of the Amazon: application of satellite radar altimetry. *J. Geophys. Res.*, 107(D20), 8059, doi:10.1029/2001JD000609.

Callahan, P. (1993). TOPEX/POSEIDON Project GDR Users Handbook, JPL D-8944, Rev. A. Jet Propulsion Laboratory, Pasadena.

CA. Capp, P. (2001). Altimeter waveform product ALT.WAP compact user guide, Issue 4.0, PF-UG-NRL AL-0001, Infoterra Ltd., UK.

Guzkowska, M, C. Rapley, J. Ridley, W. Cudlip, C. Birkett, and R. Scott (1990). Developments in inland water and land altimetry. ESA Contract Report 7839/88/F/FL.

Maheu, C., A., Cazenave, and C.R. Mechoso (2003).Water level fluctuations in the Plata basin(South America) from Topex/Poseidon satellite altimetry. *Geophys. Res. Lett.*, 30, 3, 1143–1146.

Zanife, O.Z., J.P. Dumont, J. Stum, T. Guinle (2004). SSALTO products specifications – Volume 1: Jason-1 User Products, Issue 3.1, SMM-ST-M-EA-10879-CN, CLS/CNES, Toulouse, France.

Chapter 30

ACE2: The New Global Digital Elevation Model

P.A.M. Berry, R.G. Smith, and J. Benveniste

Abstract Detailed accurate Digital Elevation Model (DEM) data have historically not been available on other than a regional scale, and often have uncertainties in both vertical and horizontal precision.

This paper presents the results of a global assessment of the unique Shuttle Radar Topographic Mission (SRTM) DEM using more than 100 million height datapoints derived from ERS1, ERS2, Topex, EnviSat and Jason-1 radar altimeter data, retracked using an expert system approach. This paper outlines the retracking approach taken to derive heights from the altimeter waveforms and describes the methodology for fusion of these data with the SRTM dataset, correcting errors in the SRTM heights and providing accurate measurements beyond the SRTM latitude limit, to produce a full global DEM.

Of particular interest, the unique ability of radar altimeters to provide very precise vertical measurements has allowed the correction of vertical offsets to better than 1 m within ACE2, and has also allowed identification of horizontal misplacements. As part of this development, a detailed quality matrix is being generated, to give users information both on the data source of each pixel, and an assessment of the vertical precision of the measurement. It is this detailed global assessment of quality that makes the ACE2 development both unique and of special value for a range of geodetic applications.

The first full release of ACE2 is scheduled for later in 2008.

P.A.M. Berry (✉)
E.A.P.R.S. Lab, Gateway House, De Montfort University, Leicester LE19BH, UK
e-mail: pamb@dmu.ac.uk

30.1 Introduction

The ACE (Altimeter Corrected Elevations) Global Digital Elevation Model (GDEM) was created by fusing altimeter derived heights (produced using a system of multiple retrackers) with ground truth available from a range of publicly available datasets to create an enhanced GDEM (Berry, 2000; Berry et al., 2000; Hilton et al., 2003). However, this was curtailed in spatial resolution to 30″ (about 1 km at the equator) by the level of detail available in the ground truth, and the spatial distribution of the altimeter tracks from the ERS1 Geodetic Mission, which have an average across-track spacing of 4 km and an along-track sampling of about 350 m. The release of the SRTM dataset derived using interferometric SAR (Hensley et al., 2000) presents a 3″ dataset up to a latitude limit of 60°N and 54°S. This dataset represents a very substantial improvement in the quality and spatial resolution of the publicly available DEM data, with a global vertical accuracy estimate of ± 16 m (ibid). However, as both global and regional evaluations with ground truth have shown, there are regional differences in the estimate of accuracy of this dataset (Denker, 2004; Brown et al., 2005; Hall et al. 2005; Smith and Sandwell, 2003); crucially, these quality assessments are limited by the availability of ground truth. It was therefore decided to carry out a global assessment of the SRTM dataset by reprocessing the ERS1 Geodetic Mission altimeter dataset (Capp, 2001) using an augmented version of the original expert system (Berry, 2000) to optimise the height retrieval and hence determine whether enhancements could be made to the SRTM dataset by fusion with altimeter derived heights from multiple satellite altimeters.

S.P. Mertikas (ed.), *Gravity, Geoid and Earth Observation*, International Association of Geodesy Symposia 135,
DOI 10.1007/978-3-642-10634-7_30, © Springer-Verlag Berlin Heidelberg 2010

30.2 Topography

The expert system characterises each waveform according to shape, and then applies one of 12 retracking algorithms to obtain the best range to surface, by identifying the nadir return (Berry, 2000; Berry et al., 2000). Over flat terrain, this identification is fairly simple; however, most of the earth's land surface has varying topography and therefore the retracking process must identify and account for slope components in order to retrieve the nadir range. These data are fused with orbit data (Scharroo and Visser, 1998) and the EGM96 geoid model (Lemoine et al., 1997) is used to transform from ellipsoidal to orthometric heights.

A similar approach was taken to the retracking of ENVISAT RA-2 SGDR data (Benveniste et al., 2002). For TOPEX, the GDR dataset (Benada and Digby, 1997) was merged with the waveform data (Algiers, 1993). Again a tuned expert system was utilised to obtain optimal range to surface from each waveform. One year of Jason-1 data (Zanife et al., 2004) was also reprocessed. Statistics for the datasets are given in Table 30.1.

30.3 Global Comparison

The first requirement was to assess the geographic distribution of retracked ERS-1 data. Accordingly, all waveforms from the entire Geodetic Mission were analysed, and the proportion of rejected data was calculated (Fig. 30.1); each waveform was then retracked, and a series of combined plots made of the global distribution of the different categories of waveform shape. The first category, derived from three of the expert system retrackers (Berry, 2000) contained wide waveforms (Fig. 30.2) which are typically returned from desert surfaces, as is very clearly seen over Australia, or from snow. The second category, of narrow waveforms, return from wet land or inland water (Fig. 30.3); here, the Ganges in India and the Pantanal in Argentina are clearly seen. Finally, a composite category of "complex" waveforms' was created, as these waveforms generally return from complex topographic surfaces and sea ice (Fig. 30.4).

All waveforms were then retracked to yield height estimates, using the EGM96 geoid model (Lemoine et al., 1997) to convert to orthometric heights. The total percentage of waveforms which could be successfully retracked was then calculated as a percentage of the theoretical maximum for each 7.5′ pixel, and the results were sorted into one of three categories according to the percentage of the theoretical maximum waveform count successfully recovered. A global statistical analysis was then performed (Berry et al., 2007). For clarity, the global banding thresholds are given in Table 30.2, and the distribution is shown in Fig. 30.5.

The altimeter and SRTM datasets were then compared globally on a range of spatial and vertical scales, to obtain estimates of the precision of the SRTM heights. One of the most interesting results to emerge from this comprehensive global analysis was the existence of spatially correlated areas where the agreement between the altimeter derived heights and the SRTM was extremely high. There were also geographic regions where significant differences were found, the most substantial being over rainforest,

Table 30.2 Banding of ERS1 GM waveform recovery

Band	Range (percent)
3	>90
2	50–90
1	0–50

Table 30.1 Missions and datasets used for initial ACE2 analysis

Mission	Along-track sampling rate	Mode	Gate width	Time span used
Topex Ku band	10 Hz/594 m	320 MHz	0.47 m	March 1994–August 2002
ERS-1	20 Hz/332 m	320 MHz/80 MHz switching by mask	0.45 m/1.82 m	April 1994–March 1995
Envisat RA-2 Ku band	18 Hz/369 m	320 MHz/80 MHz/20 MHz autonomous selection	0.47 m/1.87 m/7.5 m	August 2002–July 2005
Jason-1 Ku band	20 Hz/297 m	320 MHz	0.47 m	August 2002–March 2004

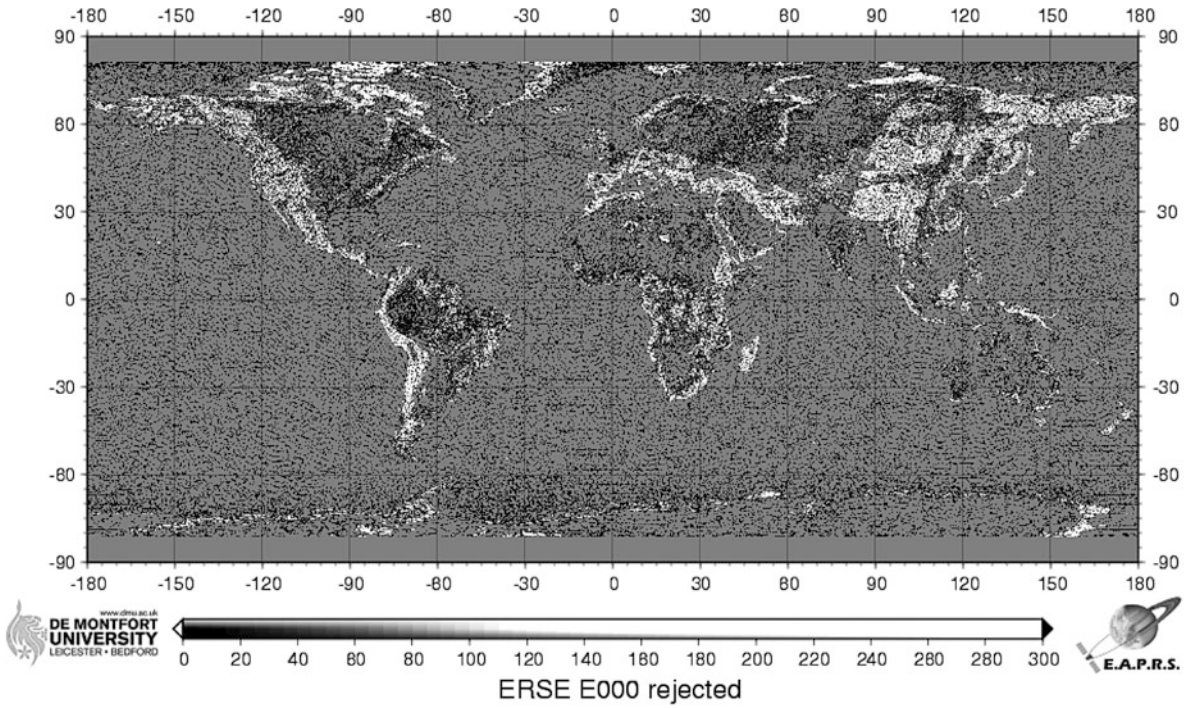


Fig. 30.1 Rejected waveforms from ERS1-GM

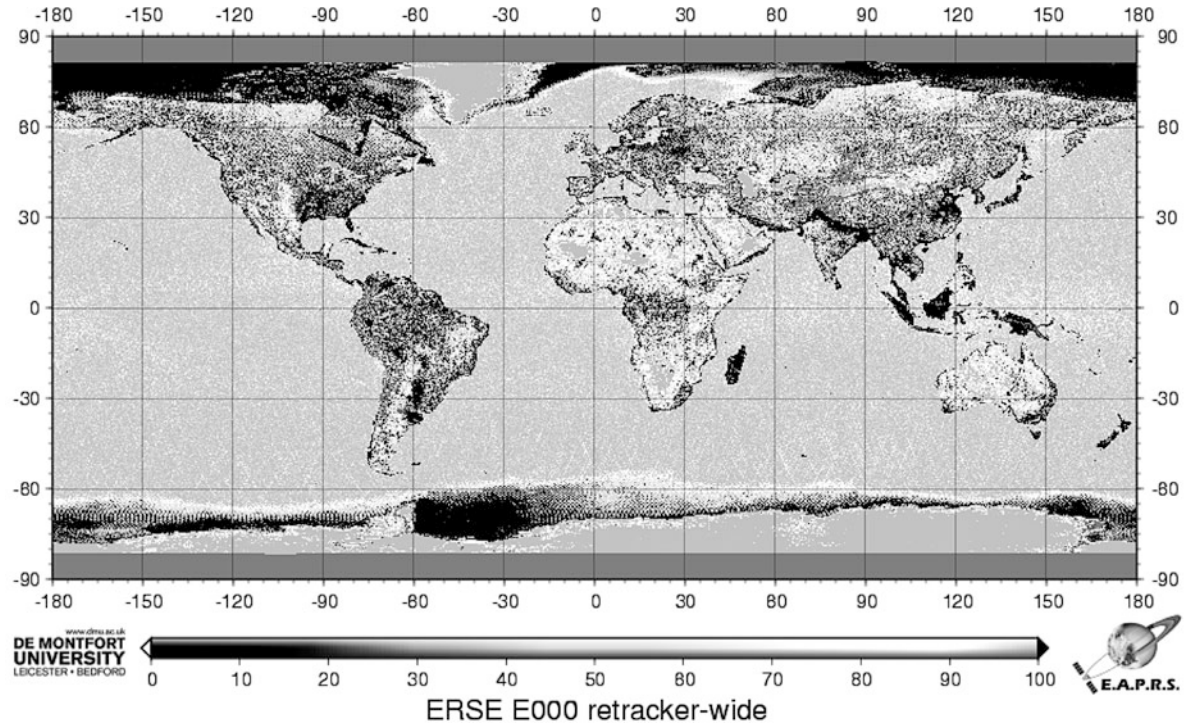


Fig. 30.2 Wide retracker distribution from ERS1-GM

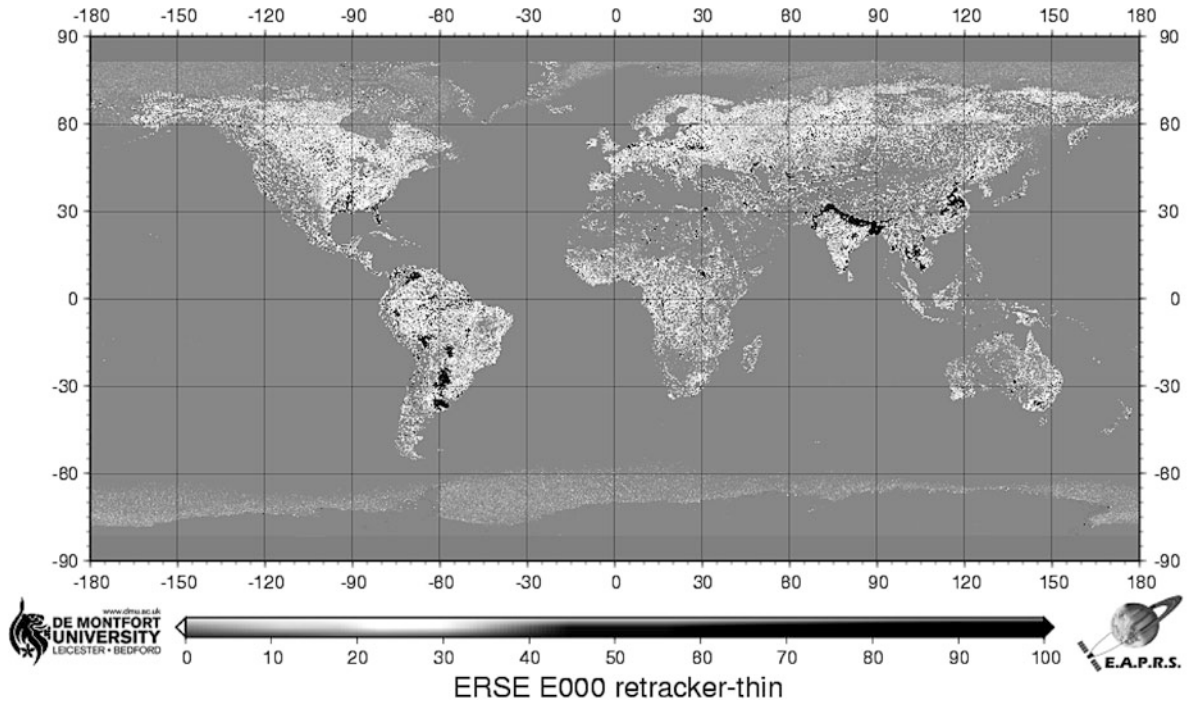


Fig. 30.3 Narrow retracker distribution from ERS1-GM

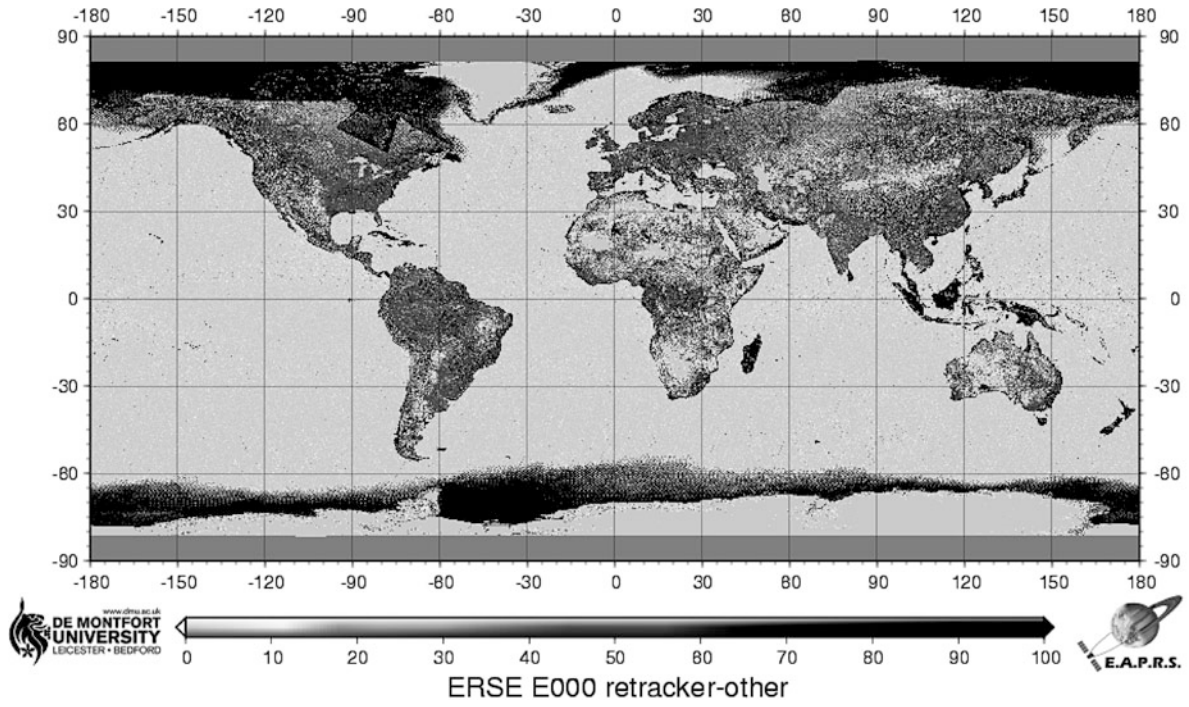


Fig. 30.4 Complex retracker distribution from ER1-GM

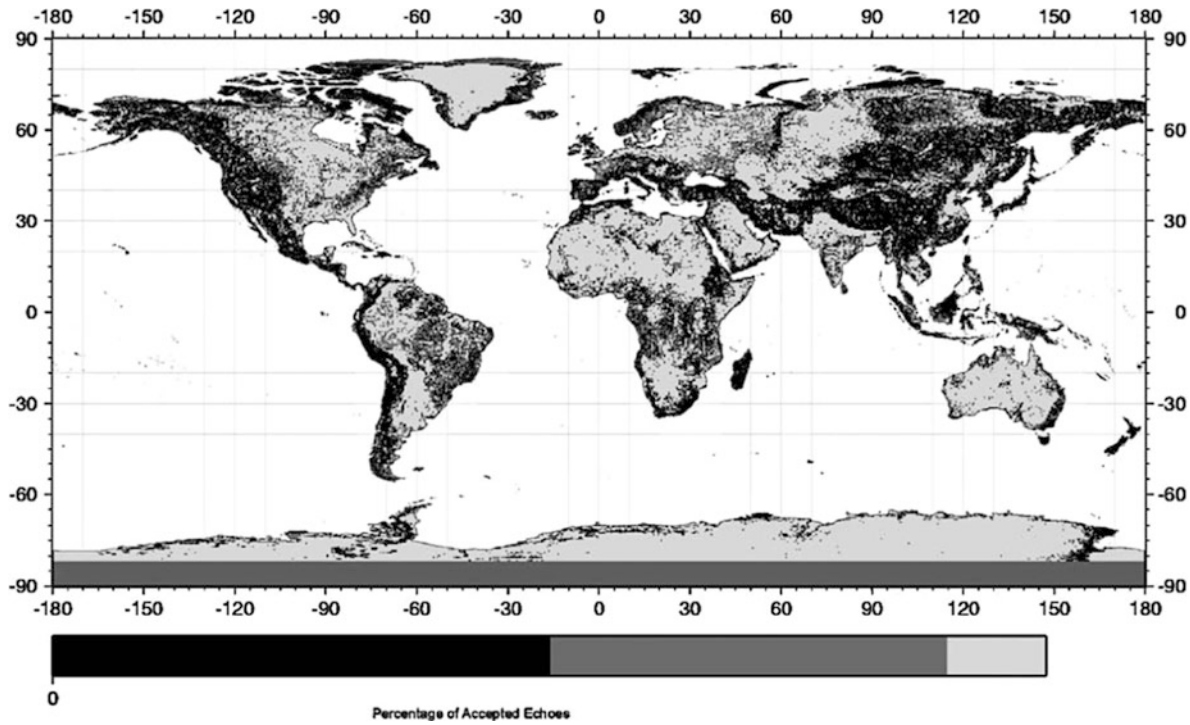


Fig. 30.5 Banding of ERS1-GM based upon percentage obtained of theoretical maximum number of waveform

where the SRTM return reflects from within the upper canopy (Kellndorfer et al., 2004). Over these regions, it was decided to utilise multi-mission satellite altimeter data, which returns from the underlying ground, to replace the SRTM pixels over rainforest areas. Beyond the SRTM latitude limits, multi-mission altimeter data would be fused with ground truth to generate the best topographic surface.

30.4 Data Fusion

For all areas categorised as Band 3, the ERS1 Geodetic Mission heights were used to warp the SRTM pixels according to a complex protocol. As an illustration, the results for changes within the SRTM stated accuracy are given in Table 30.1. Clearly, these small vertical changes are made in primarily flat areas. Those regions with larger geographically correlated differences due to rainforest cover (ibid) have been identified and replaced with an altimeter derived Digital Elevation Model; this has also enhanced the representation of river heights in these regions, where the SRTM values are contaminated by heights from the surrounding rainforest. A small number of other regions have been found where sustained differences exist, primarily over desert dune fields (ibid); the optimal solution for these regions is under development.

For areas classed as Band 2, all pixels with good altimeter values have been assessed, and where sufficient altimeter data exist, sustained vertical differences from the SRTM heights have been resolved by fusing the two datasets. At this stage of the ACE2 generation, the statistics obtained are given in Fig. 30.6.

A range of additional techniques is also being utilised, such as examining profiles of EnviSat RA-2 data over rougher terrain. Finally, over mountainous terrain (primarily the Himalayas) where the topography is so extreme that no altimeter mission has succeeded in maintaining lock, the SRTM data have been retained.

For regions outside the latitude bounds of the SRTM, all available altimeter data are being fused with existing ground truth to create the best possible topographic representation and extend the DEM to a full global model.

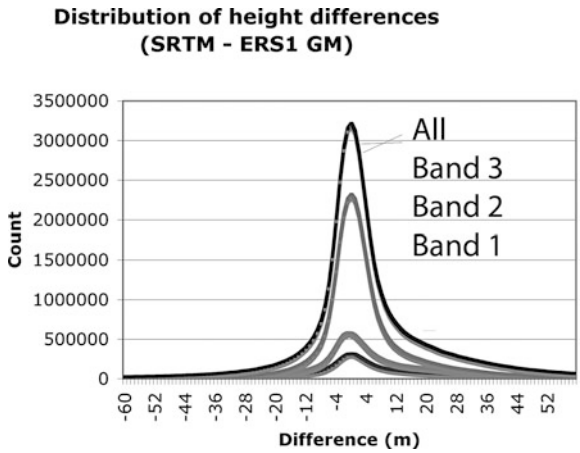


Fig. 30.6 Height differences sorted according to banding of ERS1-GM data

30.5 ACE2 Characteristics

Clearly, this complex analysis and fusion process has generated a wealth of information relevant for users of ACE2. In order to ensure that users will be fully informed, it has been decided to issue three additional matrices along with the actual height dataset. The first, a source matrix, summarises the source information for every pixel. Secondly, a quality matrix gives an assessment of the height accuracy. This is quite variable, as it depends on the extent to which the altimeter datasets have been able to assess the SRTM dataset. Finally, and critically, a confidence matrix is included, to give feedback on the certainty with which the error estimate has been made, again reflecting the variable extent to which independent confirmation of the height values has been obtained.

One specific topic currently under discussion is the possibility of adding a "water layer" to the ACE2 GDEM, to give enhanced heights and temporal change information for major water bodies worldwide. This is an enhancement already requested by users; currently an assessment is being made of the feasibility of developing this additional information for inclusion in the second generation of ACE2.

30.6 Discussion

The global assessment of the SRTM dataset shows that in many regions the heights are in good agreement with the altimeter derived global dataset but that fusing the SRTM 3″ heights with more than 60 million altimeter derived heights can produce a significantly improved GDEM. Much of this improvement is in correcting small vertical offsets detected in the SRTM DEM, and in replacing the canopy heights with a surface created from multi-mission satellite altimeter derived heights.

The first release of ACE2 is now being produced; key to the development of this model is the inclusion of quality and confidence information for each pixel.

ACE2 is scheduled for first release towards the end of 2008.

Acknowledgements The authors wish to acknowledge ESA, NASA, JPL and CNES for supply of data used in this development.

References

Algiers, J. (1993). TOPEX ground system software interface specification, (SIS-2) altimeter sensor data record (SDR) – Alt SDR data (NASA), March, 1993, JPL D-8591 (Rev. C), TOPEX 633-751-23-001, Rev. C.

Benada, R. and S. Digby (1997). TOPEX/POSEIDON altimeter merged geophysical data record generation B (NASA/PO.DAAC), JPL PO.DAAC 068.D002. Jet Propulsion Laboratory, Pasadena, CA.

Benveniste, J., S. Baker, O. Bombaci, C. Zeli, P. Venditti, O.Z. Zanife, B. Soussi, J.P. Dumont, J.P. Stum, and M. Milagro-Perez (2002). ENVISAT RA-2/MWR product handbook, Issue 1.2, PO-TN-ESR-RA-0050. European Space Agency, Frascati, Italy.

Berry, P.A.M. (2000). Topography from land radar altimeter data: possibilities and restrictions. *Phys. Chem. Earth(A)*, 25(1), 81–88.

Berry, P.A.M., J.E. Hoogerboord, and R.A. Pinnock (2000). Identification of common error signatures in global digital elevation models based on satellite altimeter reference data. *Phys. Chem. Earth(A)*, 25(1), 95–99.

Berry, P.A.M., J.D. Garlick, and R.G. Smith (2007). Near-global validation of the SRTM DEM using satellite radar altimetry. *Remote Sens. Environ.*, 106(1), 17–27, DOI: 10.1016/j.rse.2006.07.011.

Brown, C.G., Jr., K. Sarabandi, and L.E. Pierce (2005). "Validation of the shuttle radar topography mission height data," geoscience and remote sensing. *IEEE Trans.*, 43(8), 1707–1715, August 2005.

CA. Capp, P. (2001). Altimeter waveform product ALT.WAP compact user guide, Issue 4.0, PF-UG-NRL AL-0001, Infoterra Ltd., UK.

Denker, S. (2004). Evaluation of SRTM3 and GTOPO30 terrain data in Germany. In: Jekeli C. et al. (eds), International association of geodesy symposia, gravity, geoid and space missions, Vol 129. Springer Verlag, Berlin, pp. 218–223.

Hall, O., G. Falorni, and R.L. Bras (2005). Characterization and quantification of data voids in the shuttle Radar topography mission data. *Geosci. Remote Sens. Lett. IEEE*, 2(2), 177–181, April 2005.

Hensley, S., P. Rosen, and E. Gurrola (2000). "The SRTM topographic mapping processor," Geoscience and Remote Sensing Symposium, 2000. Proceedings. IGARSS 2000. *IEEE 2000 Int.*, 3, 1168–1170.

Hilton, R.D., W.E. Featherstone, P.A.M. Berry, C.P.D. Johnson, and J.F. Kirby (2003). Comparison of digital elevation models over Australia and external validation using ERS-1 satellite radar altimetry. *Aust. J. Earth Sci.*, 50(2), 157–168(12), April 2003, DOI:10.1046/j.1440-0952.2003.00982.x.

Kellndorfer, J.M., W.S. Walker, L.E. Pierce, M.C. Dobson, J.A. Fites, C. Hunsaker, et al. (2004). Vegetation height estimation from shuttle radar topography mission and national elevation datasets. *Remote Sens. Environ.*, 93, 339–358.

Lemoine, F.G., D.E. Smith, L. Kunz, R. Smith, E.C. Pavlis, N.K. Pavlis, S.M. Klosko, D.S. Chinn, M.H. Torrence, R.G. Williamson, C.M. Cox, K.E. Rachlin, Y.M. Wang, S.C. Kenyon, R. Salmon, R. Trimmer, R.H. Rapp, and R.S. Nerem (1997). The development of the NASA GSFC and NIMA joint geopotential model. In: Segawa, J. et al. (eds), International association of geodest symposia, gravity, geoid and marine geodesy, vol 117. Springer Verlag, Berlin, pp. 461–469.

Scharroo, R. and P.N.A.M. Visser (1998), Precise orbit determination and 459 gravity field improvement for the ERS satellites. *J.. Geophys. Res.*, 103(C4), 8113–8127.

Smith, B. and D. Sandwell (2003). Accuracy and resolution of Shuttle Radar 462 topography mission data. *Geophys. Res. Lett.*, 30(9), 1467.

Zanife, O.Z., J.P. Dumont, J. Stum, and T. Guinle (2004), SSALTO Products Specifications – Volume 1: Jason-1 User Products, Issue 3.1, SMM-ST-M-EA-10879-CN, CLS/CNES. Toulouse, France.

Chapter 31

Ocean Dynamic Topography from GPS – Galathea-3 First Results

O.B. Andersen, A.V. Olesen, R. Forsberg, G. Strykowski, K.S. Cordua, and X. Zhang

Abstract From August 14, 2006–April 24, 2007 the Danish expedition called Galathea-3 circumnavigated the globe. The Danish Technical University, DTU space, participated in the expedition with two experiments on-board. From Perth in Australia to Copenhagen Denmark measurements of the exact position and movements of the ship and also the sea surface height were carried out with high accuracy using a combination of GPS, INS, and laser.

The aim of this experiment was to measure the position of the GPS antenna on the ship to decimetre accuracy and try to transfer this height to estimates of the sea surface height as accurate as possible using lasers and INS, and to investigate the accuracy and feasibility of sea surface height observations in this way.

In this presentation the setup of the experiment will be described along with the first results in retrieving the mean dynamic topographic signal related to permanent currents in the ocean. Comparison with the DNSC08 mean dynamic topography derived from satellite altimetry across the Gulf Stream yields agreement on the 20 cm level, which is a very satisfactory preliminary result calling for further refinement of the technique.

31.1 Introduction

During the 9 months between August 14, 2006 and April 24, 2007 the Danish Galathea-3 expedition sailed more than 60.000 km and circumnavigated the globe from north to south and east to west following the route shown in Fig. 31.1 (web 1). Galathea-3 was the largest Danish natural science expedition for more than 50 years. The aim of the expedition was to strengthen Danish scientific research and also outreach in relation to the recruitment of the coming generations of research scientists.

The foundations of Galathea-3 and all the educational perspectives and dissemination of information-activities surrounding the expedition consist of the total of 71 research projects on board the navy surveillance vessel *Vaedderen* ("The Ram"). The ship had room for approximately 35 scientists. In addition to whom a dozen journalists, photographers, and TV crew members were on board, A 50-man crew from the royal navy, maintained the course, and performed the many tasks necessary onboard a ship (web1 reference).

The Danish Technical University DTU-Space participated in the Galathea-3 expedition on the ship's voyage from Perth to Copenhagen measuring gravity and the sea level to as high precision as possible. DTU-Space main tasks were the following:

1. Gravity anomaly observations. Gravity anomaly variations mainly reflect changes to the depth of the sea, and the depth remains relatively unknown in large parts of the oceans. At the same time, the purpose is to "cross-check" a number of old measurements of the Earth's gravity for which the reference level has often been uncertain, and which has rendered the measurements in-accurate.
2. Observing the hills and valleys of the ocean surface caused by variations in the earth gravity field and ocean currents and trying to estimate the accuracy with which the mean dynamic topography (difference between the mean sea surface and the geoid)

O.B. Andersen (✉)
DTU space – National Space Institute, Copenhagen, DK-2100, Denmark
e-mail: oa@space.dtu.dk

S.P. Mertikas (ed.), *Gravity, Geoid and Earth Observation*, International Association of Geodesy Symposia 135,
DOI 10.1007/978-3-642-10634-7_31, © Springer-Verlag Berlin Heidelberg 2010

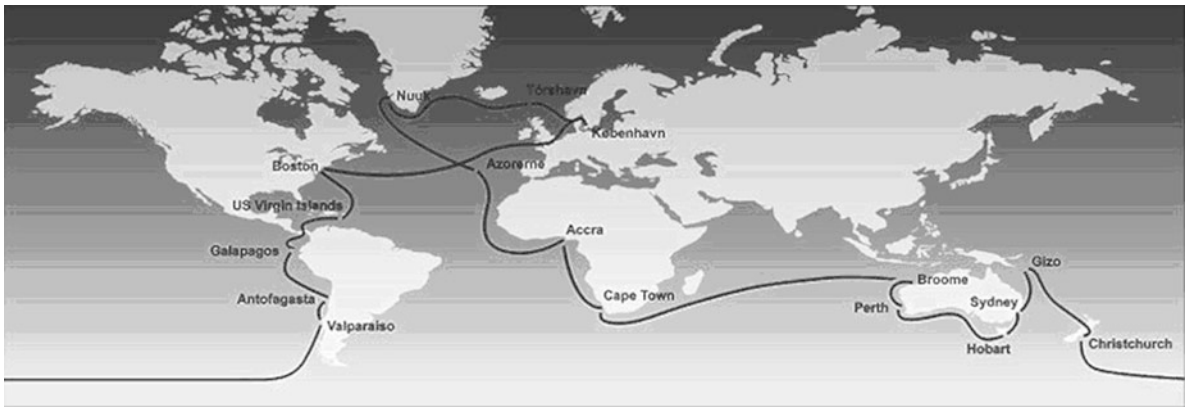


Fig. 31.1 The Galathea-3 route from Copenhagen and around the world

can be determined using GPS positioning of the ship. In this way direct measurement of the sea surface height could be made, and the height variations along the ship tracks could be related to variations in the Earth gravity field and to ocean dynamics.

The focus in this paper is to carry out a first evaluation of the GPS derived height of the ship and to estimate how accurate the sea surface topography can be retrieved using a combination of GPS, laser, and INS observations and to compare these with a mean sea surface (MSS) model derived from satellite altimetry.

31.2 GPS Observations of Ocean Dynamic Topography

The observed GPS height h is related to the ocean dynamic topography and the geoid height through

$$h(t) = N + L(t) + \xi(t) + e \qquad (1)$$

Where N is the geoid height above the reference ellipsoid, ξ is the ocean topography, L is the antenna height above the sea surface and e is the error. The setup is illustrated in Fig. 31.2. The ocean topography is made up of a mean dynamic topography ξ_{MDT} and a time variable dynamic topography $\xi_D(t)$ like $\xi(t) = \xi_{MDT} + \xi_D(t)$

The observation error e comprises direct observation errors by the GPS height observations along with contributions from errors in the geoid height, dynamic topography, GPS processing, and antenna height.

31.3 GPS Antenna Height Determination

The GPS antenna height is in principle a proxy for the instantaneous sea surface height, if the distance between the GPS antenna and the sea surface is known precisely. However, the situation is considerable more complex as one should account for the ship's own movements and changing weight.

In the Galathea-3 experiment two GPS antennas were mounted on the roof of the Bridge of the ship in order to have a redundant system. The GPS antennas were mounted to the portside and starside of the ship and placed such that no objects on the ship shade for the antennas (see Fig. 31.3 upper right figure, where the GPS antennas are indicated with arrows).

Mounting the antennas on the roof of the Bridge is roughly 13 m above sea-level and the distance between the antennas and the sea surface will depend on the speed and the weight of the ship along with the tilt and roll movements due to i.e., waves.

In order to measure the distance between the GPS antennas and the sea surface, a laser were mounted at the side of the Bridge of the ship as shown in the left figure of Fig. 31.3. The laser was a near infrared laser altimeter which was mounted so far from the sea surface so that saltwater would hopefully not damage the instrument in rough sea state conditions. The height

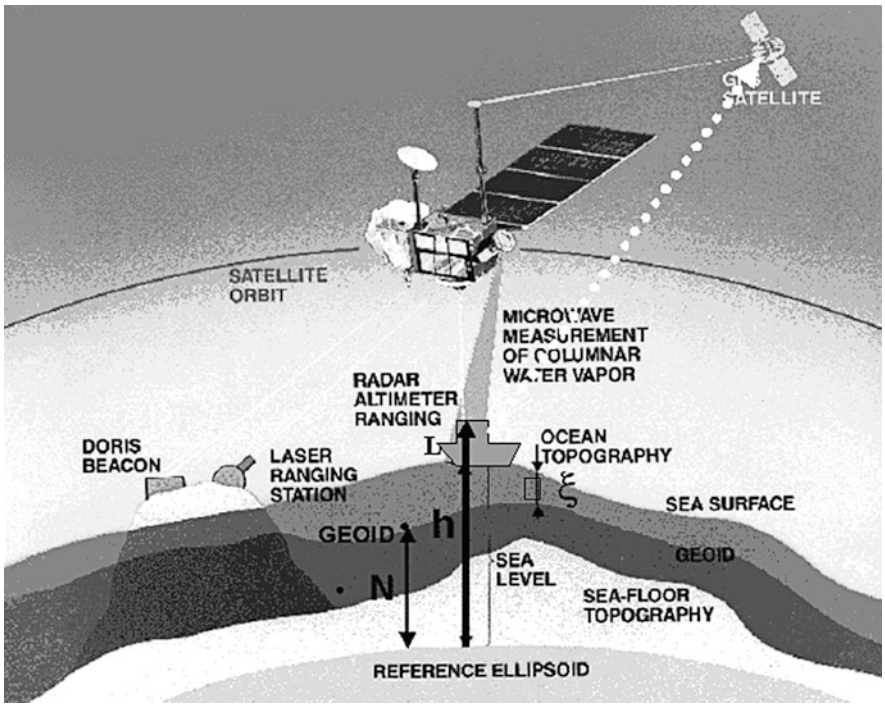


Fig. 31.2 Sea surface height from GPS on-board a ship compared with sea surface height from satellite. GPS measures the height h = N+L+ξ relative to the ellipsoid. (Illustration modified from AVISO)

of the GPS antenna $L_{GPS}(t)$ relative to the sea surface height can be described by

$$L_{GPS}(t) = H_{offset} + H_{laser}(t) \tag{2}$$

where H_{offset} is the fixed vertical distance between the GPS antenna and the laser. H_{offset} was measured to 2.1 m which is approximately valid for the antenna closest to the laser. The $H_{laser}(t)$ is the time-variable distance between the laser and the sea surface due to movements of the ship.

An example of the measured height above the sea surface $H_{laser}(t)$ is shown in Fig. 31.3 lower right. A sequence of 28 s in calm water in the western part of the Southern Pacific ocean is followed by a sequence of 42 s in stormy waters close to Antarctica.

The laser samples at 10 Hz and the barely visible light curve is a 10 s average. In calm water the 10 s averaged observations are relatively constant around 11.4 m with a scatter of less than 0.10 m. For the preliminary results presented in this paper (taken under calm conditions), 60 s averaging of the GPS data was performed and the antenna height above the sea level was fixed constant to 13.5 m (± 0.1 m).

In rough waters with higher waves, as shown in the right part of the lower right picture in Fig. 31.3, the height is considerably more difficult to determine accurately. If precise estimation of the antenna height is required, the movement of the ship was logged using the Inertial Navigation Unit on-board the ship. In this case one should account for the fact, that the height of the laser will be dependent on the speed and weight of the ship as well as the bow-wave created due to instantaneous wave-height and the tilt, roll, and yaw of the ship. A more detailed study following these lines will be pursued at a later stage.

31.4 Determining the Mean Dynamic Topography

In the current investigation the aim is to investigate how accurate it is possible to map the mean dynamic topography using GPS. The mean dynamic topography is related to the instantaneous GPS antenna height using the following equation.

$$\xi(t) = h(t) - L - N - \xi_D(t) \tag{3}$$

The continuous GPS observations collected on board Galathea-3 were post-processed using precise

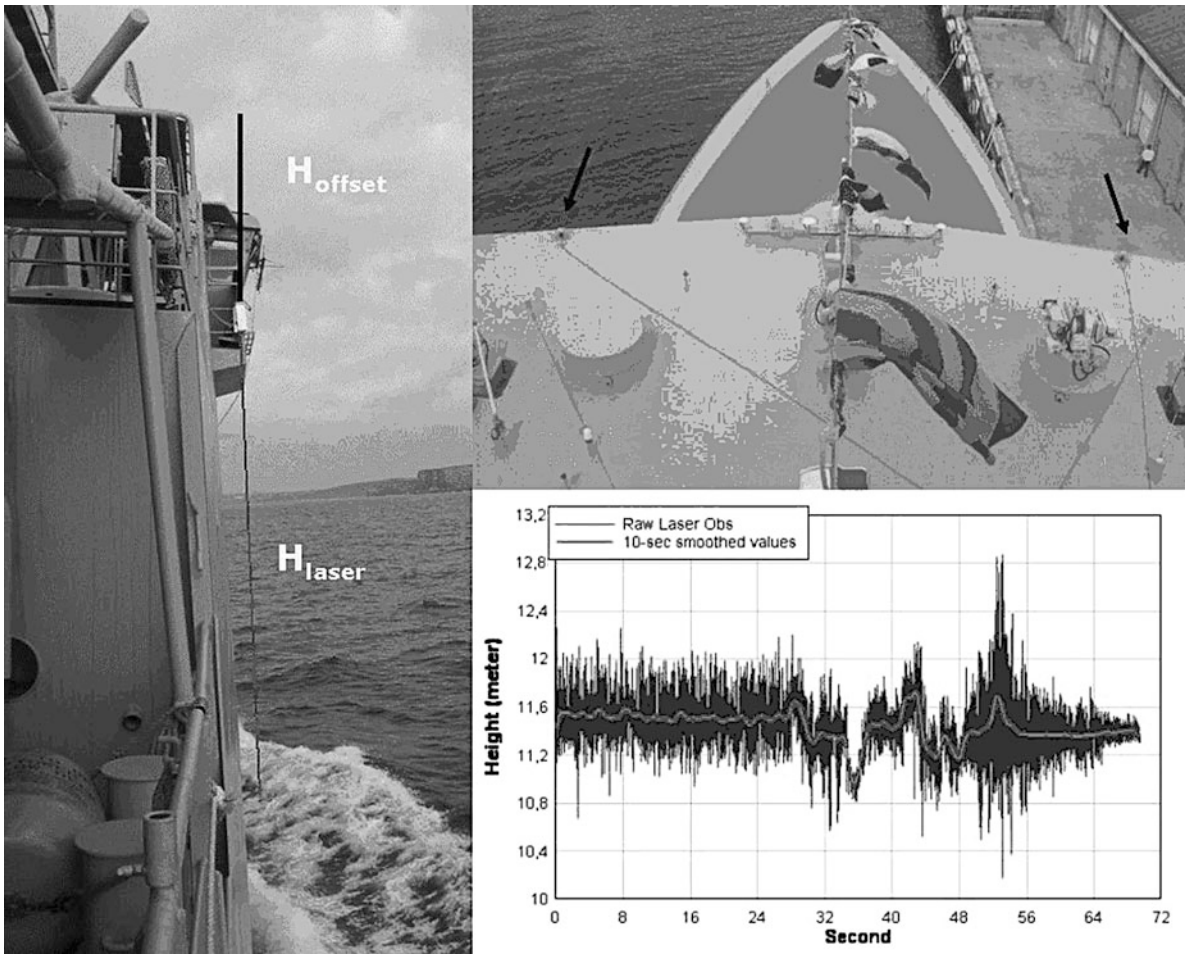


Fig. 31.3 Installation of the GPS and lasers on-board Galathea-3 in order to transfer the GPS antenna height to sea surface height observations. The Figure to the *left* shows the laser mounted on the side of the Bridge. The figure to the upper right shows the two GPS antennas on the roof of the Bridge (indicated with *black arrows*), and the lower *right* figure shows two periods of laser observations

point position (PPP) technology based on precise orbit and clock products from IGS. The "TriP" PPP software system was used (Zhang, 2005). This software has successfully been used to determine height variations of the Amery ice shelf for tidal studies (Zhang and Andersen, 2006).

It is important that the GPS data is processed in the same tidal system as was used for the derivation of the geoid. For the current investigation we used EGM2008 (Pavlis et al., 2008) given in the zero tide system. The GPS data are processed in the tide free system, and the difference was corrected for in order to get the data into the zero tide system.

The time-variable part of the ocean topography $\xi_D(t)$ comprises the ocean tide signal and the time-variable signal related to wind, waves, temperature, salinity, and pressure. Globally, the tides dominate the time variable dynamic ocean topography and analysis from altimetry (Fu and Cazenave, 2001) shows that globally, more than 70% of the dynamic topography variations are due to ocean tides.

It was, consequently, decided only to account for the ocean tides in this first investigation. The ocean tide model GOT4.7 (Ray, personal communication) is a improved version of the GOT 99 and GOT00.2 ocean tide model (Ray, 1999), and is believed to be

among the very best global ocean tide models presently available.

31.5 First Results

The north going transect between St. Croix on the Virgin Island and Boston on the US east coast, was used for this preliminary investigation (see Fig. 31.4). Sailing northwards towards Boston only the last part of the route marked with black arrows from around 28ºN and northwards were used. Around 38ºN the mean dynamic topography dips by around one meter as the ship crosses the Gulf Stream going from the warm water in the center of the Atlantic Ocean to the cooler water toward the coast of North America.

Figure 31.5 shows the ocean topography ξ observed with GPS on-board Galathea-3 as the ship sails from 28ºN towards Boston crossing the Gulf Stream. One minute mean GPS heights were used for the investigation.

The grey curve marks the GPS height only corrected for the EGM2008 geoid height, and the noisy black curve mark the height additionally corrected for ocean and loading tides using GOT 4.7 tide model. Applying the ocean tide correction reduces the magnitude of the height signal significantly. Between latitudes 32 and 35ºN the detided signal looks un-correlated with the ocean tide signal. However, there seems to be residual tide signal between 30 and 32ºN and 34.5–36.5ºN, which might indicate that GPS observations on-board the ship could potentially be used to improve or validate the ocean tide model in the future.

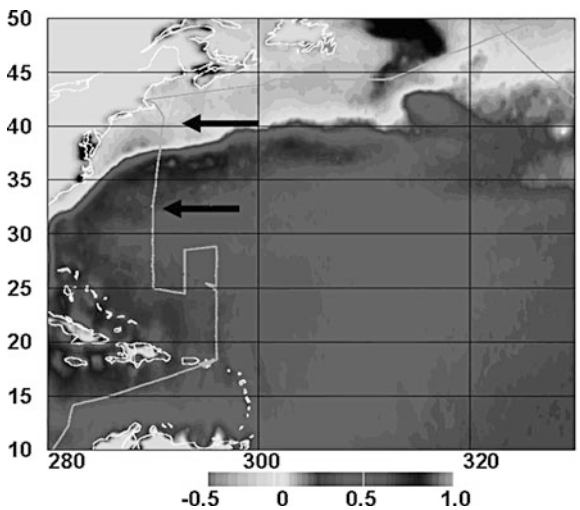


Fig. 31.4 The DNSC08 mean dynamic topography (in meters) and the ships route. The investigated part of the section between St. Croix on the Virgin Island to Boston crossing the Gulf Stream has been indicated with *arrows*

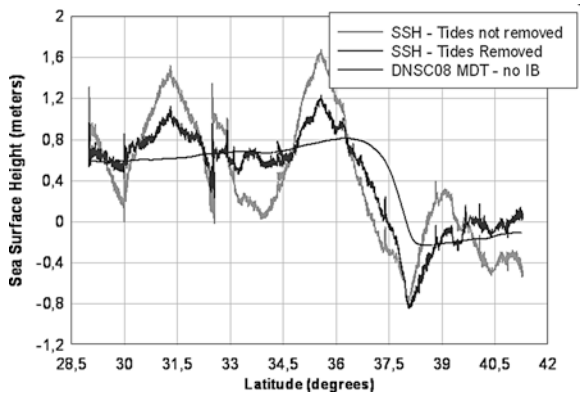


Fig. 31.5 The ocean dynamic topography observed with GPS on-board Galathea-3 as the ship sails from 28º N towards Boston crossing the Gulf Stream. Grey marks GPS heigh without correction for ocean tides. Noisy Black line marks the height corrected for ocean and loading tides using GOT 4.7 and Smooth black line represent the DNSC08 Mean Dynamic Topography (not corrected for Atmospheric Pressure using the Inverse Barometer correction)

The smooth black curve represents the altimetric mean dynamic topography called DNSC08MDT (Andersen and Knudsen, 2009). For this investigation the Mean Dynamic Topography uncorrected for inverse barometer pressure (no IB) was used. The DNSC08MDT has been derived from the difference between the DNSC08MSS Mean sea surface (Andersen et al., 2008) and the EGM2008 geoid (Pavlis et al., 2008). Most available MSS correct for the presence of the atmosphere using a hydrostatic approach to the inverse barometer correction, i.e., the CLS01 and GSFC00 (Hernandez and Shaeffer, 2000; Wang, 2000). However, the DNSC08MSS has been derived both as a true physical mean sea surface and mean sea surface corrected for the inverse barometer correction, and here the true physical mean sea surface uncorrected for the inverse barometer has been used here to derive the MDT.

The standard deviation of the difference between the GPS estimated MDT and the altimetric derived

DNSC08MDT is around 0.40 m before removing the tides and 0.20 m after removing the tides with a mean offset of only 0.05 m. This is believed to be very good under the present conditions and assumption of constant height of the GPS antennas above the sea surface.

It can be seen that during the Galathea-3 crossing the Gulf Stream meandered away from it mean location at 38ºN towards 37.5ºN and that this meandering contributes significantly to the difference. It is also obvious that the assumption to let time variable ocean topography $\xi(t)$ be approximated by the ocean tide correction is not valid here, and that the ocean dynamic topography is of an equal magnitude as the ocean tide signal.

Figure 31.6 shows the time variable ocean dynamic topography $\xi_D(t)$ from satellite altimetry combining data from several satellites on the 25 April, 2007 for the Gulf Stream region from SSALTO/DUACS (web 2). It clearly shows that the meandering of the Gulf Stream results in very large sea surface height variations. The altimetric sea level anomalies are derived from altimetric observations from multiple satellites within the week centred on the 25th April.2007.

It can be seen that the dynamic ocean topography (sea level anomalies) ranges up to roughly 0.70 m, which is around the same magnitude as the difference between the GPS observed height and the DNSC08MDT, which calls for further investigation.

Altimetric data are too sparse to be used for the correction for the time variable sea surface height signal,

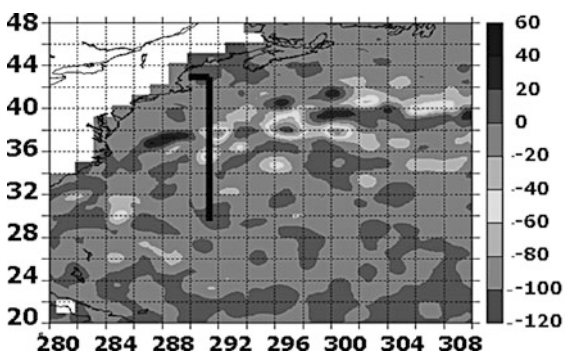


Fig. 31.6 Time-variable ocean dynamic topography from satellite altimetry on the 25 April, 2007 with the rough location of the route overlaid on the plot. The sea level anomalies are in cm and from SSAKTI/DUACT (web 2). The outlined profile was crossed within 2 days

and currently, investigations in the application of the MOG2D (Carrère and Lyard, 2003) is ongoing.

31.6 Outlook

The first results in trying to retrieve the Mean Dynamic Topography using GPS on-board the Galathea-3 expedition have been presented, and the setup of the experiment was described along with the very first results.

The standard deviation of the difference between the GPS estimated MDT and the altimetric derived DNSC08MDT is roughly 0.40 m before removing the tides and roughly 0.20 m after removing the tides with a mean offset of only 0.05 m, which is believed to be very good under the present conditions.

In these very first studies, several crude approximations were made. One was to fix the antenna height above the sea surface to be constant. The second was to ignore the oceanographic contribution to the time variable ocean dynamic topography. Such approximations will naturally limit the accuracy of our results and the comparison with the DNSC08MDT.

The results are so encouraging and calls for more accurate investigations. One improvement will be to use an improved definition of the antenna height. Another improvement will be to include the oceanographic contribution to the time variable sea surface height. This way we hope to see if we can obtain comparisons on the one decimeter level between the sea surface height observations using GPS on-board ships and satellite altimetric models.

References

Andersen, O.B. and P. Knudsen (2009). The DNSC08 mean sea surface and mean dynamic topography. *J. Geophys. Res.*, 114, C11001, doi:10.1029/2008JC005179.

Andersen, O.B., et al. (2008). The DNSC08 global Mean sea surface and Bathymetry. EGU-2008, Vienna, Austria, April.

Carrère, L. and F. Lyard (2003). Modeling the barotropic response of the global ocean to atmospheric wind and pressure forcing – Comparisons with observations. *Geophys. Res. Lett.*, 30(6), 1275.

Fu, L., and A. Cazenave (2001). Satellite altimetry and earth sciences. A handbook of techniques and applications, Academic Press, San Diego.

Hernandez, F. and P. Schaeffer (2000). Altimetric Mean Sea Surfaces and Gravity Anomaly maps inter-comparisons AVI-NT-011-5242-CLS, 48 pp. CLS Ramonville St Agne, France.

Pavlis, N.K, S. Holmes, S.C. Kenyon, and J.K. Factor (2008). An Earth Gravitational model to degree and order 2160: EGM2008, presented EGU GA, Vienna, April.

Ray, R.D. (1999). A global ocean tide model from Topex/Poseidon altimetry: GOT99, NASA Tech. Memo. 209478, Goddard Space Flight Center, 55 pp.

Wang, Y.M. (2000). GSFC00 mean sea surface, gravity anomaly, and vertical gravity gradient from satellite altimeter data. *J. Geophys. Res.*, 106, C12, 31167–31174.

Web 1: http://www.galathea3.dk/uk

Web 2: http://aviso.oceanobs.com

Zhang, X. (2005). Precise Point Positioning, Evaluation and Airborne Lidar Calibration, Danish National Space Center, Tech. Report 4. http://www.space.dtu.dk/upload/institutter/space/research/reports/technicalreports/tech_no_4.pdf

Zhang, X. and O. Andersen (2006). Surface ice flow velocity and tide retrieval of the amery ice shelf using precise point positioning. *J. Geodesy*, 80, 4.

Chapter 32

Filtering of Altimetric Sea Surface Heights with a Global Approach

A. Albertella, X. Wang, and R. Rummel

Abstract The geoid models from GRACE and soon GOCE in combination with sea surface geometry data from satellite altimetry allow to obtain a precise estimate of the absolute dynamic sea surface topography with rather high spatial resolution. However, this requires the combination of data with fundamentally different characteristics and different spatial resolutions. One of the central objectives must be to get altimetric data and the geoid spectrally consistent without loss of precision and/or resolution. Therefore it is necessary to find a representation common to the geoid model and to altimetry that allows to obtain spectral consistency by filtering the altimetric data. We try to design a filter for the altimetric data, using the spectral characteristics of the satellite gravimetric geoid, considering a "global" approach. It consists of the extension of the altimetric sea surface height so as to cover all of the Earth's surface and the representation of the data in terms of spherical harmonic functions. The effect of the extension of the data to the land areas is studied in detail.

32.1 Introduction

Accurate and high resolution knowledge of the geoid offers the possibility in combination with an altimetric ocean surface of a determination of the Dynamic Ocean Topography (DOT). The altimetric mean sea surface is computed using the profiles from different altimetric satellites. With the geoid models as produced by the gravimetric satellite missions GRACE and GOCE this possibility becomes reality.

In the studies by Ganachaud et al. (1997) and Wunsch and Gaposchkin (1980) in situ hydrographic data and a circulation model derived from altimetry and geoid information are combined to derive a global estimate of the absolute oceanic general circulation. Even though the limited spatial resolution and accuracy of the geoid models at that time limit the possibilities of DOT computation, the two estimates exhibit nicely large scale general circulation.

In constructing a geoid model, one truncates its spectrum at a certain maximum degree L. For all degrees less or equal to L one has the coefficients of the model together with their error (commission error). The signal for degrees greater than L is not modeled, but its expected average size is identified as omitted signal (omission error). In Losch et al. (2002) it is shown, based on an analysis in the Southern Ocean, that the introduction of the omission error in the geoid error model produces discrepancies in the solution. In particular, such effects are present on the long (well known) scales.

If the analysis is performed in a local region, the combination of the altimetric data and the geoid height could be inconsistent with the hydrographic estimate of the ocean circulation, also due to the inaccuracy of models like EGM96, see Losch and Schröter (2004). In order to allow a consistent assimilation of the geodetic and oceanographic sea surface topography, the accuracy of the heights of the geoid model must be around few centimeters and the band limitations must be taken into account.

A. Albertella (✉)
Institut für Astronomische und Physicalische Geodäsie, Technische Universität München, Munich, Germany
e-mail: albertella@bv.tu-muenchen.de

S.P. Mertikas (ed.), *Gravity, Geoid and Earth Observation*, International Association of Geodesy Symposia 135,
DOI 10.1007/978-3-642-10634-7_32, © Springer-Verlag Berlin Heidelberg 2010

The accuracy of the new geoid models, derived from dedicated satellite missions like GRACE and later GOCE, in particular for the long wavelengths, is better than all previous geoid models. The DOT could be determined with an accuracy of a few centimetres from these new geoid models in combination with a long-term time series of the sea surface height from multi-mission satellite altimetry. This should result in a profound improvement of the estimate of ocean circulation, Condi and Wunsch (2004).

The DOT ζ is the difference between the sea surface height (SSH) h relative to a reference ellipsoid (measured by satellite altimetry) and the geoid height N referred to the same ellipsoid:

$$\zeta = h - N$$

The two components h and N have different spatial and spectral resolutions. For the geoid the resolution is defined by the maximum degree of its spherical harmonic expansion. For the altimetric data the resolution is defined by the sample pattern in along-track and cross-track direction. We assume that the geoid resolution always be the limiting factor. For this reason we have to remove all small scales from the altimetric data that are beyond the resolution of the geoid. This synchronization of resolution is achieved by applying the same low-pass filter to the altimetric data and to geoid undulation. The concept of resolution is strictly related to the chosen representation of the data.

The geoid undulation is a *global* quantity and it is naturally represented by spherical harmonic functions, that are also *global*, while the SSH is defined only in ocean areas and its spectral content is much higher. To solve this spectral inconsistency, we propose here to expand the altimetric sea surface into the land areas. In this way the geoid and the sea surface have the same type of global spectral representation and they can be processed into a compatible form.

To remove the short wavelengths from the SSH, a low pass filter is needed. The accuracy of the filter can be studied by a simulation procedure which is shown in the following:

1. Construction of a simulated SSH, with known spectral content, using geoid heights synthesized from a gravity model to a certain maximum degree L;
2. Application of a filter (with threshold k_0) on this surface function obtaining a filtered surface with spectral content up to $k_0<L$;
3. Comparison between this filtered surface with the same surface obtained by spherical harmonic synthesis, using the same a-priori model up to k_0.

The differences between the estimated and the simulated surface give insight into the properties of the filtering procedure.

In the follow we use the EIGEN02s (computed from the data of the GRACE mission by GFZ Potsdam) model up to degree $L = 180$ to simulate the SSH on the oceans and we consider the threshold of the filter corresponding to $k_0 = 60$.

The results will be compared in a limited box. The chosen area (φ=[–45°, –65°], λ=[40W, 20E]) is approximately the Atlantic sector of the Antarctic Circumpolar Current (ACC). We decided to consider this area because the ACC is an important feature of the oceans deep circulation, it transports and exchanges deep and intermediate water between the Atlantic, Indian and Pacific Ocean, and it contributes to the deep circulation in all basins. This current is a fundamental component in the models for the global climate of the Earth.

32.2 Generation of a *Global* Surface

In order to be able to expand altimetric data into a series of spherical harmonics, all land areas (and ocean data gaps) have to be filled with data as well. The simplest way to achieve a *global* data coverage, is to complement the altimetric sea surface data by zero values on land. It is well known that the drawback will be very "unnatural" oscillations (Gibbs phenomenon) in the spherical harmonic representation along the borderline from altimetric data to zero values due to the sharp sea-to-land edge.

In order to reduce the strong discontinuity along the coastlines we fill the land with another geoid, namely EGM96, again up to degree L. We call this reconstructed global surface S_1. Of course, also in this case, a discontinuity along the coastlines is present but much smaller. It is necessary to reduce this discontinuity further, to make the input signal to spherical harmonic representation smooth enough.

32.2.1 Polynomial Interpolation

The general idea is to generate a "transition zone" along the coastlines, on the land side in which a smooth transition to the ocean and land function will be attempted. Through interpolation there will be mixed data in the interpolation zone based on both ocean and land data. The global data set will then be divided into three parts: the geoid heights from EIGEN model on the ocean representing the altimetric surface ($N^{180}{}_{\text{ocean}}$), the geoid heights from EGM96 on land ($N^{180}{}_{\text{land}}$) and the interpolated data in the transition zone. The transition zone is generated by expanding the coastline polynomial towards the land direction. The size of the transition zone is fixed here equal to 1.25°, but other choices may be considered as well.

The data on the ocean and on land will be used to interpolate the data in the transition zone and the values in the interpolation zone will be replaced by the predictions.

The prediction in the transition zone is made using a 2D cubic interpolator (standard Matlab routine), based on the Delauny triangulation of the data. With this method all the data points are connected with triangles in such way that all the data are located at the corners of each triangle. If the point to be predicted is inside a triangle, the values at the three corners are used to compute the prediction value. If it is not inside any triangle, it is linked to the nearest triangle and then linearly interpolated. We call the global surface reconstructed by polynomial interpolation S_2.

32.2.2 Iterative Approach

An alternative idea for the transition sea to land is proposed in Gruber (2000). We start using initially the geoid to degree and order 180 on land from the EGM96 model ($N^{180}{}_{\text{land}}$) and the EIGEN geoid to the same degree and order on ocean ($N^{180}{}_{\text{ocean}}$), the latter simulating the altimetric surface, without considering the transition zone.

Next we perform a global spherical harmonics analysis to get harmonic coefficients and then perform a synthesis to come back to geoid. After this process, we get a new "mixed surface" on the globe. We keep the original EIGEN geoid to degree and order 180 on ocean, but on land we replace the EGM96 geoid by the derived "mixed geoid". Then we repeat this process iteratively. Because this "mixed geoid" on land is also affected by data from ocean, it will combine the ocean and land data so that the discontinuity between land and ocean will become smaller and smaller. In this case, there is not a fixed transition zone like in the previous chapter. We call the surface obtained with this approach S_3.

32.3 Filtering

Summarizing we have now three global surfaces, see Table 32.1, that can be represented by a spherical harmonic expansion and then filtered up to the selected harmonic degree.

The filtering process in the spectral domain corresponds to a multiplication of the spherical harmonic coefficients with a spectral weight W_l:

$$\hat{N}(P) = R \sum_{l=2}^{L} \sum_{m=-l}^{l} W_l y_{lm} Y_{lm}(P) \tag{1}$$

The spherical harmonics coefficients are weighted by W_l, which can be calculated through

$$W_l = \int_0^{\pi} W(\alpha) P_l(\cos\alpha) \sin\alpha d\alpha \tag{2}$$

where $W(\alpha)$ is an isotropic weighting function on the sphere that is only dependent on the spherical distance α. To filter the high frequencies (from k_0+1 to L) of our surfaces we propose two alternative filters: the direct cut-off and the "Gauss" shape filter.

The direct cut-off filter up to k_0, or ideal low pass filter, consists in choosing as maximum degree L= k_0 in (1). An ideal low-pass filter completely eliminates all spectral content above the cut-off degree. The coefficients below will pass unchanged.

Table 32.1 Different considered *global* surfaces

Surface	Ocean	Transition zone	Land
S_1	EIGEN	–	EGM96
S_2	EIGEN	pol. interpolation	EGM96
S_3	EIGEN	–	"Mixed" geoid

Starting from a global surface S, by spherical harmonic analysis, it is possible to compute the corresponding spherical harmonic coefficients y_{lm} up to a certain harmonic degree related to the grid size. To obtain the surface containing the frequencies up to k_0, we consider:

$$\hat{N}^{k_0}(P) = R \sum_{l=2}^{k_0} \sum_{m=-l}^{l} y_{lm} Y_{lm}(P) \tag{3}$$

that corresponds to spectral weights

$$W_l = \begin{cases} 1 & l \le k_0 \\ 0 & l > k_0 \end{cases}$$

in (1).

An alternative is to consider a Gauss filter. The Gauss filter corresponds to a Gaussian function in both the space and spectral domain. It corresponds to a cap with a certain spherical radius α_r in the space domain. The formula for the weighting function W_l for the Gauss filter is defined in Jekeli (1981) and modifed by Wahr et al. (1998). It can be computed by recursive formulas:

$$W_0 = 1, \quad W_1 = \left[\frac{1+e^{-2b}}{1-e^{-2b}} - \frac{1}{b}\right], \quad \dots$$

$$W_l = -\frac{2l-1}{b} W_{l-1} + W_{l-2}$$

where

$$b = \frac{\ln(2)}{1 - \cos\alpha_r}$$

The radius α_r is empirically related to the degree k_0, as shown in Zenner (2006). The maximum degree 60 corresponds roughly to $\alpha_r = 250$ km.

32.4 Numerical Results

Following the scheme as described in the first chapter, we compare the differences between the simulated (N^{60}) and the filtered ($\hat{N}^{60}$) geoid undulations over all oceanic surfaces and in the chosen ocean box (φ=[–45°, –65°], λ= [40°W, 20°E]).

Figure 32.1 shows the results for the surface S_3, considering the direct cut off filter (upper panel) and the Gauss filter (lower panel).

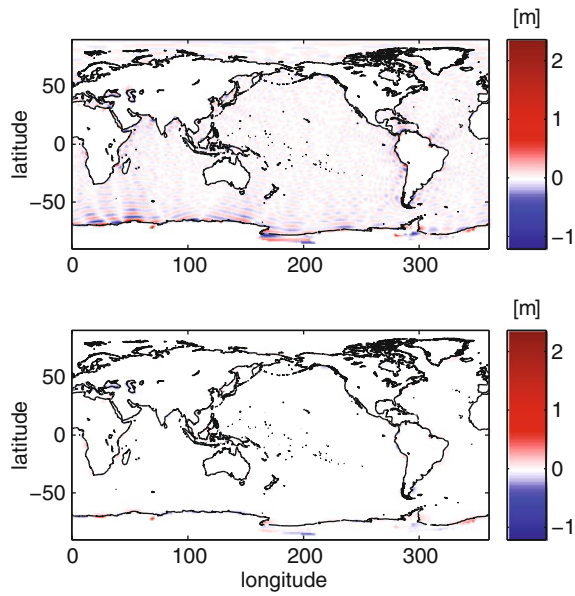


Fig. 32.1 Differences between simulated and filtered geoid undulations in all ocean area, for the surface S_3. *Upper panel*: direct cut-off filter; *lower panel*: Gauss filter. The units are meters

In both cases stronger effects occur near the coastlines. The direct cut-off filtering produces a clearer ringing effect as compared to the Gauss filter. The statistics of the differences over all the ocean areas are listed in Table 32.2.

As expected the results obtained with the Gauss filter are better than the results of the direct cut-off filtering. We can observe that the analysis using the surface S_1 is more accurate than the analysis using the surface S_2. As shown in Wang (2007) the simple polynomial interpolation in the transition zone is not able to reduce the discontinuities along the coastline and this can introduce further discontinuities instead of reducing them.

Table 32.2 Statistics of the differences between simulated (N^{60}) and filtered ($\hat{N}^{60}$) geoid undulations in all ocean areas. The units are meters

	Mean	St.dev.	Max	Min
S_1 cut-off	0.0260	0.1173	2.8681	–1.3279
S_2 cut-off	–0.1320	0.1380	2.4232	–2.2833
S_3 cut-off	$5.3\ 10^{-5}$	0.0865	2.3606	–1.2132
S_1 Gauss	0.0023	0.0476	1.2994	–0.7129
S_2 Gauss	0.0106	0.0684	1.0699	–1.1493
S_3 Gauss	$-6.6\ 10^{-5}$	0.0330	1.0444	–0.5798

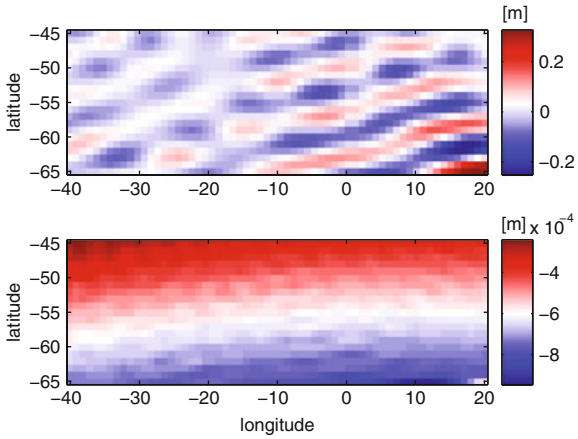


Fig. 32.2 Differences between simulated and filtered geoid undulations in the ocean box, for the surface S_3. *Upper panel*: direct cut-off filter; *lower panel*: Gauss filter. The units are meters

The smoothing of the discontinuities along the coastline made by the iterative procedure (surface S_3) allows a filtering procedure with a global accuracy of only 3 cm.

The selected ocean box (φ =[–45°, –65°], λ= [40°W, 20°E]) is sufficiently far from the coastlines. Thus here the results are better for both filtering procedures, as are shown in Fig. 32.2. In the upper panel (direct cut-off filtering) Gibbs effects are visible, while in the lower panel (Gauss filtering) they are successfully reduced. In Table 32.3 the statistics of these differences between simulated and filtered surfaces are shown considering only the points of the ocean box.

The iterative procedure (surface S_3) gives definitely better results compared to the interpolation and reaches high accuracy.

We can conclude that the global approach of the filtering gives excellent results in case of the Gauss filtering when a global surface is created using the proposed iterative procedure. In any case it must be observed that the results are good only at sufficient distance from the coastal areas.

Table 32.3 Statistics of the differences between simulated (N^{60}) and filtered ($\hat{N}^{60}$) geoid undulations in the ocean box. The units are meters

	Mean	St.dev.	Max	Min
S_1 cut-off	$9.7\ 10^{-3}$	0.0731	0.3515	–0.2746
S_2 cut-off	0.0200	0.0712	0.3940	–0.2560
S_3 cut-off	0.0013	0.0665	0.3275	–0.2525
S_1 Gauss	–0.0011	$8.6\ 10^{-4}$	$8.6\ 10^{-4}$	–0.0028
S_2 Gauss	0.0171	0.0020	0.0223	–0.0131
S_3 Gauss	$-5.6\ 10^{-4}$	$1.4\ 10^{-4}$	$2.4\ 10^{-4}$	$-9.4\ 10^{-4}$

32.5 Conclusions

A detailed analysis of the filtering procedure is necessary to take into account the different resolution of the geoid and the altimetric sea surface. To get altimetric data and geoid spectrally consistent by filtering the altimetric data, it is necessary to find a common representation.

Our approach consists of the extension of the altimetric sea surface height so as to cover all the Earth's surface and in the representation of the data by the spherical harmonic functions.

In order to be able to expand altimetric data into a series of spherical harmonics, all land areas (and ocean data gaps) have to be filled with a "synthetic" altimetric surface, e.g., a high resolution geoid model. We showed that the best results are obtained using a Gauss filter over a complete surface obtained with the "iterative procedure". In this case the accuracy of the filtering procedure is of the order of 3 cm over all ocean surfaces and less than 1 mm over our chosen ocean box.

A disadvantage of the Gauss filter is, that the cut-off degree k_0 is not defined "sharply".

In the future the dependency of the errors on the distance from the coastline must be investigated in details.

References

Condi, F. and C. Wunsch (2004). Measuring gravity field variability, the geoid, ocean bottom pressure fluctuations, and their dynamical implications. *J. Geophys. Res.*, 109, 10.1029/2002JC001727.

Ganachaud, A., C. Wunsch, M.C. Kim, and B. Tapley (1997). Combination of TOPEX/POSEIDON data with a hydrographic inversion for determination of the oceanic general circulation and its relation to geoid accuracy. *Geophys. J. Int.*, 128(3), 708–772.

Gruber, T., (2000). Hochauflösende schwerefeldbestimmung aus kombination von terrestrischen Messungen und Satellitendaten über Kugelfunktionen. *Scientific Technical Report STR00/16*, GeoForschungsZentrum Potsdam.

Jekeli, C. (1981). Alternative methods to smooth the earth's gravity field. *Rep.327, D. Sci. & Surv.*, Ohio State University, Columbus.

Losch, M. and J. Schröter (2004). Estimating the circulation from hydrography and satellite altimetry in the Southern Ocean: limitations imposed by the current geoid models. *Deep-Sea Res.*, 151, 1131–1143.

Losch, M., B.M. Sloyan, J. Schröter, and N. Sneeuw (2002). Box inverse models, altimetry and the geoid: Problems with the omission error. *J. Geophys. Res.*, 107, (C7) 10.1029/2001JC000855.

Wahr, J., F. Bryan, and M. Molenaar (1998). Time variability of the Earth's gravity field: Hydrological and oceanic effects and their possible detection using GRACE. *J. Geophys. Res.*, 103(B12), 30205–30229.

Wang, X. (2007). Global filtering of altimetric sea surface heights. Master Thesis on TU München, Institut für Astronomische und Physikalische Geodäsie.

Wunsch, C. and E.M. Gaposchkin (1980). On using satellite altimetry to determine the general circulation of the oceans with application to geoid improvement. *Rev. Geophys.*, 18, 725–745.

Zenner, L. (2006). Zeitliche schwerefeldvariationen aus GRACE und hydrologiemodellen. Diplomarbeit on TU München, Institut für Astronomische und Physikalische Geodäsie.

Chapter 33

Coastal Sea Surface Heights from Improved Altimeter Data in the Mediterranean Sea

L. Fenoglio-Marc, M. Fehlau, L. Ferri, M. Becker, Y. Gao, and S. Vignudelli

Abstract Standard and newly re-tracked altimeter data of the Topex/Poseidon and Envisat missions are analysed in the Mediterranean Sea in the proximity of selected coastlines.

Over-conservative selection criteria in standard level 2 products cause rejection of many data in coastal regions. Among the standard criteria, most critical for the data rejection are the checks on microwave radiometer wet tropospheric correction and on standard deviation of the 18 Hz ranges. Using a model tropospheric correction, Envisat performs better than Topex and is approaching the coast up to 5 km at sea-land transitions.

A further improvement in quality of coastal data is obtained using off-line retracked Topex-RGDR and Envisat data, these latter ones retracked with the β-5 and Improved Threshold empirical methods.

33.1 Introduction

There has been considerable interest recently in addressing the retrieval of altimeter data in coastal regions to monitor more accurately sea level change.

Data distributed by operational centers are not targeted to coastal areas. Standard altimeter products are therefore usually flagged as bad and removed. Moreover the signal to noise ratio is rapidly degraded as altimeter and radiometer are disturbed at 10 and 50 km to the coast respectively. In particular, due to the contamination of land surface in the measurements of brightness temperature made by the on-board microwave radiometer (MWR), the MWR derived wet tropospheric correction cannot be used at distances smaller than 50 km to the coast (Desportes et al., 2007).

New post-processing techniques recover additional coastal data and allow to detect smaller ocean dynamical processes (Roblou et al., 2007; Bouffard et al., 2008). In-situ sea level data at selected sites are used to assess the quality of the altimeter data (Fenoglio-Marc et al., 2007; Vignudelli et al., 2005).

New pre-processing of the altimeter waveforms, using non-standard waveform models in the attempt to recover the ocean surface parameters, improves the accuracy of altimeter ranges (Anzenhofer et al., 1999; Deng et al., 2002; Deng and Featherstone, 2006).

Purpose of this paper is to establish to what extent (1) standard criteria are applicable close to coast to both standard products and off-line re-tracked altimeter data, (2) non-uniform local conditions affect the altimeter retrievals on sea-land and land-sea along-track direction, (3) retracking methods improve the quality of data near coast. In Sect. 33.2 we describe data and methods. Results are presented in Sect. 33.3, conclusions in Sect. 33.4.

33.2 Data and Methods

The Mediterranean Sea region is analyzed using Topex and Envisat data. Both standard products and newly retracked data are used. For Topex, standard Level 2 Geophysical Data Records (GDR) at 1 Hz are extracted from the Radar Altimeter Database System (RADS) (Naejie et al., 2002). RADS data are provided at 1 Hz. Topex retracked data are the off-line retracked

L. Fenoglio-Marc (✉)
Institute of Physical Geodesy, Technische Universität Darmstadt, Darmstadt, Germany
e-mail: fenoglio@ipg.tu-darmstadt.de

S.P. Mertikas (ed.), *Gravity, Geoid and Earth Observation*, International Association of Geodesy Symposia 135,
DOI 10.1007/978-3-642-10634-7_33, © Springer-Verlag Berlin Heidelberg 2010

Geophysical Data Records (R-GDR) provided by the NASA-JPL Physical Oceanography Distributed Active Archive Center (PODAAC, P. Callahan, release 2.1). Two retracking products, corresponding to the least squares (RGDR1) and the maximum a posteriori estimation (RGDR2) algorithms, exist. Data at 1 and 10 Hz are available for about 2 years, between July 2000 and August 2002 (cycles 290–364 without 362). For Envisat, standard Level 2 data are extracted from the RADS database. In addition, the standard SGDR products (CLS, 2006) are used, with data at both 1 and 18 Hz. Envisat data are analysed over 1 year, between February 2006 and July 2007 (cycles 44–45, 47, 50, 52–59).

First the standard selection criteria (CLS 2006, AVISO 2006) are applied. Based on the data rejection analysis, criteria are slightly modified to compute sea level anomalies (SLA) (Sect, 33.3.2). For the comparison with tide gauges in Sect. 33.3.3 the altimetric SLA are computed without ocean and pole tide corrections and without accounting for the effect of atmospheric pressure on sea level (Fenoglio-Marc et al., 2004).

We assess the data quality of : (1) standard Envisat, (2) standard Topex products and (3) retracked Topex products by comparing the sea level variability measured from altimetry and tide gauges at the sites of Genova and Imperia. Hourly sea level measurements at the tide gauges are made available by the National Mareographic Service of the Agency for Environmental Protection and Technical Service (APAT). Bathymetry data available from the Italian navy and from the General Bathymetry Chart of the Ocean (GEBCO) (http://www.bodc.ac.uk).

We finally retrack the Envisat waveforms contained in the SGDR Level 2 products using four empirical retracking methods: the β-5 retracker (Martin et al., 1983), the Off-Center Of Gravity retracker (OCOG) (Wingham et al., 1986), the Threshold (Davis, 1995) and the Improved Threshold (Hwang et al., 2006). The quality of the retracked sea surface heights (SSHs) is evaluated from the improvement percentage (IMP) (Anzenhofer et al., 1999), defined by:

$$IMP = \frac{\delta_{raw} - \delta_{retracked}}{\delta_{raw}} \times 100 \qquad (1)$$

where δ_{raw} and $\delta_{retracked}$ are the standard deviations of the differences between raw SSHs and retracked SSHs and geoid heights (EGM2008), respectively.

33.3 Results

33.3.1 Distance Analysis

Four types of distances to the coast are considered: (1) distance to tide gauge, (2) distance to coast, (3) along-track distance at sea-land transition (sl) and (4) along-track distance at land-sea transition (ls). The minimum sampling of the last two is about 7 km for 1 Hz data and 400 m for the Envisat 18 Hz data, 700 m for the Topex 10 Hz data.

The histogram in Fig. 33.1 (top) shows that almost all passes have a minimum distance to coast smaller than 10 km.

Nearly 50% of Envisat and 45% of Topex passes have a minimum along-track distance in sea-land direction smaller than 7 km (Fig. 33.1, bottom). In land-sea direction only 15% of Envisat passes and none Topex pass have a minimum along-track distance smaller than 7 km (Fig. 33.1, middle).

The sea-land coastline crossing direction provides therefore more advantageous measurements conditions.

33.3.2 Analysis of Data Rejections

Standard selection criteria, including checks on the MWR land and the rain flags are used (Table 33.1). The wet tropospheric radiometer correction and the standard deviation of the 18 Hz ranges are the main causes of rejection, with 8% and 4% of data rejection (Fig. 33.2). The model wet tropospheric correction from ECMWF is used in Sect. 33.3.3. Outliers are eliminated by a 3-σ criteria, instead of spline fitting, with σ standard deviation of the data.

33.3.3 Sea Level Comparison at Tide Gauges

Atimetric and tide gauge sea level heights are compared near Genova and Imperia, in the N–W Mediterranean Sea. The differences between the local and GEBCO bathymetry are in the range of ± 200

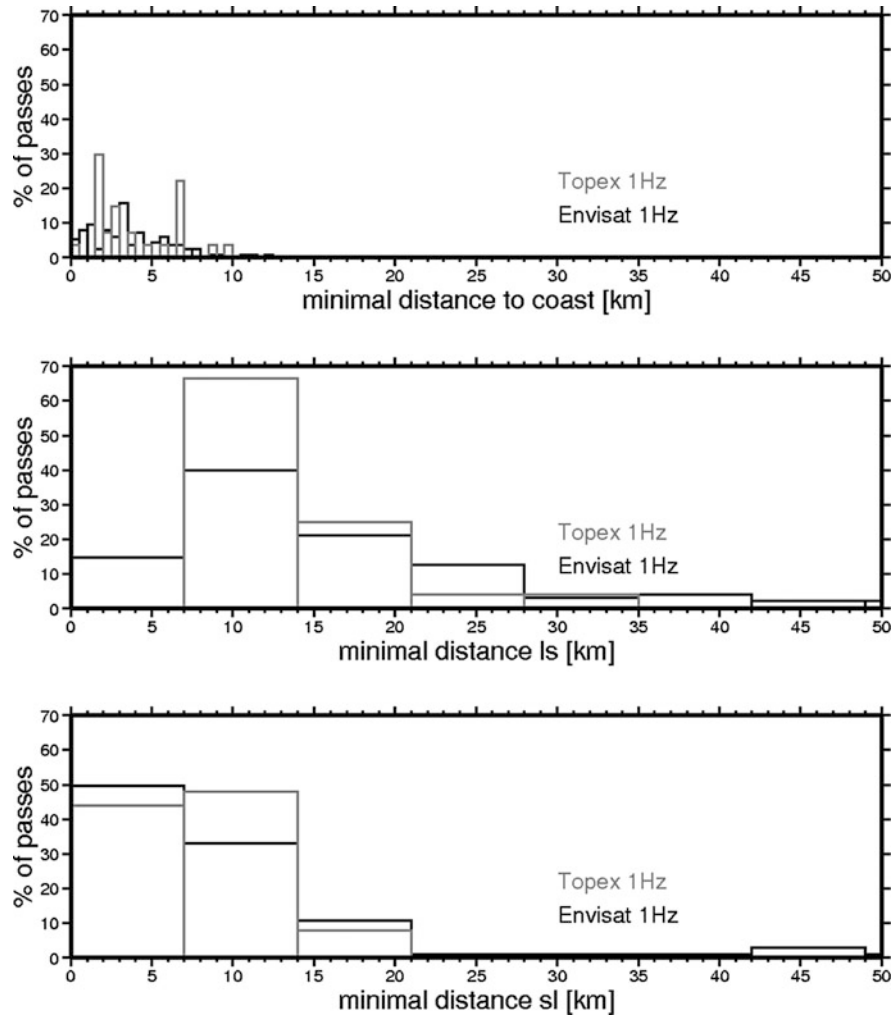


Fig. 33.1 Histogram of the percentage of passes for the three types of distance: distance to coast (*top*), minimum along-track distance land-sea (*center*) and sea-land (*bottom*) for Envisat (*dark*) and Topex (*grey*)

Table 33.1 Selection criteria for Topex (T) and Envisat (N1)

Criteria	N1 min	N1 max	T min	T max
N. obs	10	–	10	–
Std. range (m)	0.	0.25	0.	0.15
Off nadir (deg)	−0.2	0.16	–	–
Dry tropo (m)	−2.5	−1.9	−2.4	−2.1
Wet tropo (m)	−0.5	−0.001	−0.6	−0.001
Iono dual (m)	−0.4	0.04	−0.4	0.04
Inverse barom. (m)	−2.0	2.0	2.0	2.0
SWH (m)	0	11	0	11
Sea state bias (m)	−0.5	0.0	–	–
Backscatter (dB)	7	30	7	30
Wind speed (m/s)	0	30	0	30
Ocean tide (m)	−5	5	−5	5
Long per. Tide (m)	−0.5	−0.5	−0.5	−0.5
Earth tide	−1.0	1.0	−1.0	1.0
MWR land flag				
Rain flag				

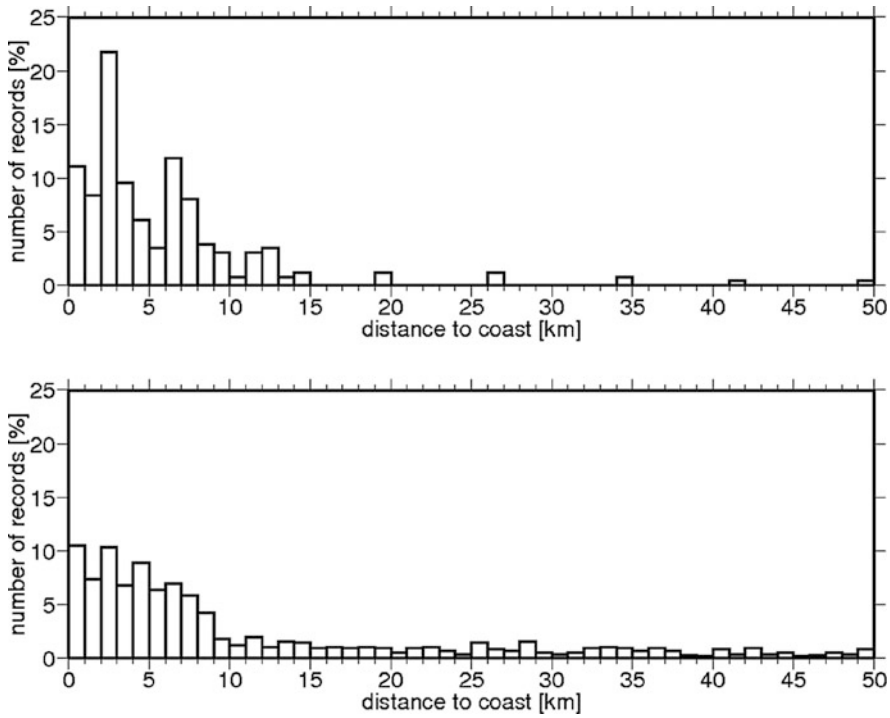


Fig. 33.2 Histogram of Envisat records rejected for the MWR wet tropospheric correction (*top*) and for the standard deviation of ranges (*bottom*)

m, there is a strong gradient in land and sea bottom topography (Figs. 33.3 and 33.4).

The altimeter data are interpolated at fixed locations, called Normal Points (NP) along the altimeter tracks. The relevant distances: (1) distance to tide gauge, (2) distance to coast and (3) along-track distance, as well as the type of transition, are shown for the first few NPs near to coast in Table 33.2.

Envisat has in Genova a sea-land transition, the first NP is at 6 km from coast for both RADS and SGDR data. The distance to the tide gauge is 18 km. Topex has in Genova a land-sea transition with the first NP at 15 and 24 km for the R-GDR and RADS data. The distances to tide gauge are 18 and 29 km.

Envisat has in Imperia a land-sea transition. The first NP of Envisat is at 8 km from coast for both RADS and SGDR data. The corresponding distance to the tide gauge is 29 km. Topex has in Imperia a sea-land transition with first NP at 6 and 22 km with R-GDR and RADS data respectively. The corresponding distances to the tide gauge are 31 and 53 km.

The time-series at each NP is compared to tide gauge sea level heights by analysing a set of parameters: (1) number of usable time-points, (2) correlation and Root Mean Square (RMS) difference of altimeter and tide gauge time series. The three parameters are shown in Figs. 33.5 and 33.6 (y-axis) for the first NPs against the distance from the tide gauge (x-axis). The total Topex cycles are 72, the Envisat cycles are 11. As the location approaches the coast, the number of observations at each Topex NP decreases quicker for RADS than for RGDR data.

In Genova the Topex data reduction reaches 85 and 60% of the 72 observations at 24 km to the coast for RADS and RGDR data (Fig. 33.5). The RGDR data show the best agreement, with correlation higher than 0.8 and RMS differences lower than 60 mm at all the NPs. Similar results are found with RGDR1,-2 retracked data. For Envisat, as the NP location approaches the coast, the decrease in the number of observations is slower. Both RADS and SGDR data agree with tide gauge data, correlation is higher than 0.9 and RMS differences smaller than 40 mm. Near Genova the correlation has a minimum

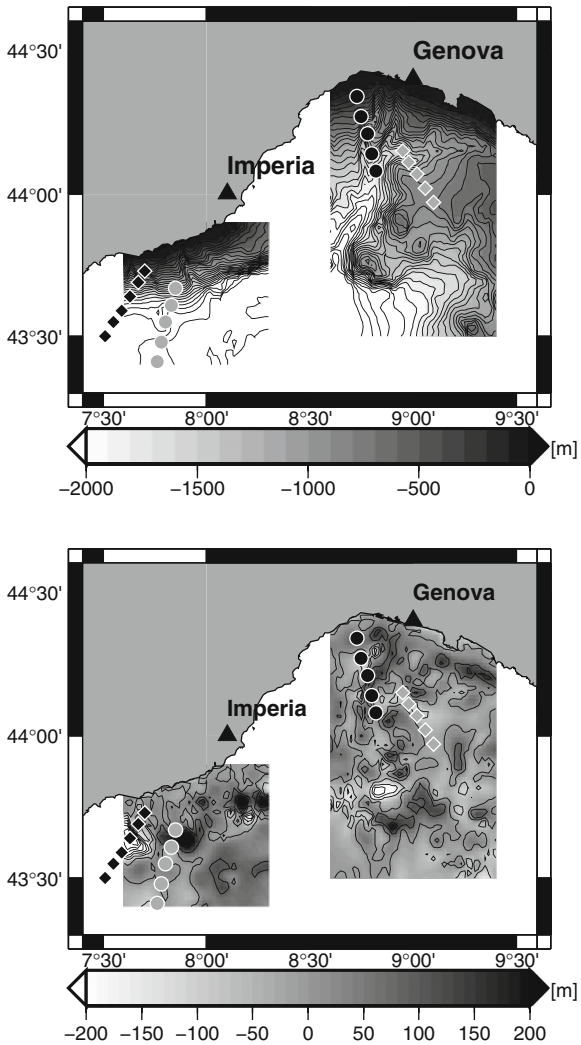


Fig. 33.3 Locations of Envisat (*circle*) and Topex (*diamond*) NPs near Genova and Imperia with local bathymetry (*top*) and difference between local and GEBCO (*bottom*)

at a distance of about 40 km from the tide gauge station.

In Imperia the Topex data reduction is smaller than in Genova, 50 and 20% of the observations for RGDR and RADS at 22 km from the coast (Fig. 33.6). The lower agreement between Topex and tide gauge is partially explained by the relative position of tracks and stations. Correlations are lower than 0.8 and standard deviation higher than 60 mm. Envisat has a better agreement (correlation bigger than 0.8, RMS smaller than 50 mm).

The agreement is higher for Envisat than for Topex, results are similar for Envisat RADS and SGDR. Topex retracked data are more near to coast than standard Level 2 products. The sea-land transition is the most advantageous.

33.3.4 Re-tracking

Figure 33.7 shows two example of land contamination from the Envisat RA-2 altimeter. Plotted are along-track distance to coast (x-axis), gate number (y-axis) and waveform amplitude in FFT filter units (scale).

Brown-like ocean waveforms are more near to land (5 km) in the sea-land transition (Genova) than in the land-sea transition (Imperia).

The Envisat waveform data are retracked using the four retracker methods: OCOG, β-5, Threshold and Improved Threshold retracker (Fig. 33.8). The performance of the retracked data is assessed by analyzing: (1) the two standard deviations of the differences between SSHs calculated from both raw and retracked ranges and geoid heights, (2) the improvement percentages (IMP). A negative improvement factor indicates that retracking deteriorates the SSHs.

Table 33.3 gives the statistics of the performance of the four retrackers for latitudes between 43.3 and 44.3 degrees of cycle 59 track 801 near Genova, The total number of waveforms is 307. The statistics for SSHs obtained from the SGDR ocean-1 range is given for comparison. The noise of the raw data is generally reduced in the retracked data. The β-5 and Improved Threshold methods produce retracked SSHs with less noise than the ocean-1 SGDR data. The success rate, i.e. the percentage of waveforms that could be retracked, is 87% for the β-5 method and 100% for the other methods.

33.4 Conclusions

Most of the Envisat data elimination near to the coast is due to the checks on the wet tropospheric correction (8%) and on the standard deviation of the 18 Hz

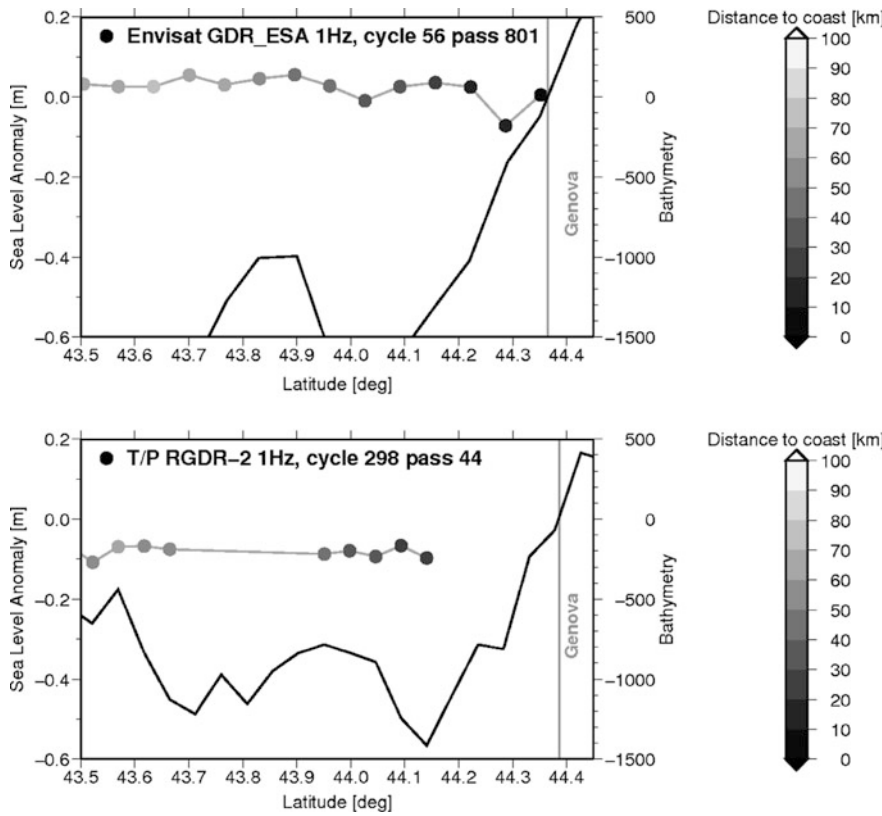


Fig. 33.4 Sea level anomalies (*circles*) in Genova relative to the CLS01 mean sea surface (CLS, 2006) along Envisat cycle 56, pass 801 (*top*) and Topex cycle 298, pass 44 (*bottom*). GEBCO bathymetry is shown (*bold line*)

Table 33.2 Minimum distance to coast for Genova and Imperia for Envisat (N1) and Topex/Poseidon (TP) at sea-land (s-l) and land-sea (l-s) transitions

Sat	Data	TG	Distance to coast (km)	Distance To TG (km)	Distance along-track (km)	Type
N1	SGDR	GEN	6.4	17.9	6.1	s-l
N1	RADS	GEN	6.2	18.2	5.9	s-l
N1	SGDR	IMP	8.9	28.7	10.1	l-s
N1	RADS	IMP	20.3	33.6	24.2	l-s
TP	RGDR	GEN	15.5	17.7	18.2	l-s
TP	RADS	GEN	24.2	28.8	32.2	l-s
TP	RGDR	IMP	6.0	30.8	6.9	s-l
TP	RADS	IMP	22.4	53.4	30.7	s-l

retracked ranges (4%). We therefore use the wet tropospheric model corrections from ECMWF to reduce the data rejection near coast.

Applying standard selection criteria to both satellites, Envisat data perform better in coastal regions with up to 15% more 1 Hz data available in the last 5 km. Envisat provides more usable data near to the coast independently from the crossing-land direction. In general, sea-land transitions perform better than land-sea transitions, with both satellites providing usable data closer than 15 km to the coastline for 90% of all passes in the Mediterranean Sea. In land-sea direction, Envisat provides data for the last 7 km offshore, while no Topex data are available in that distance range. The agreement between corrected altimetry and in-situ sea level is higher for Envisat than for Topex data in both correlation and RMS differences.

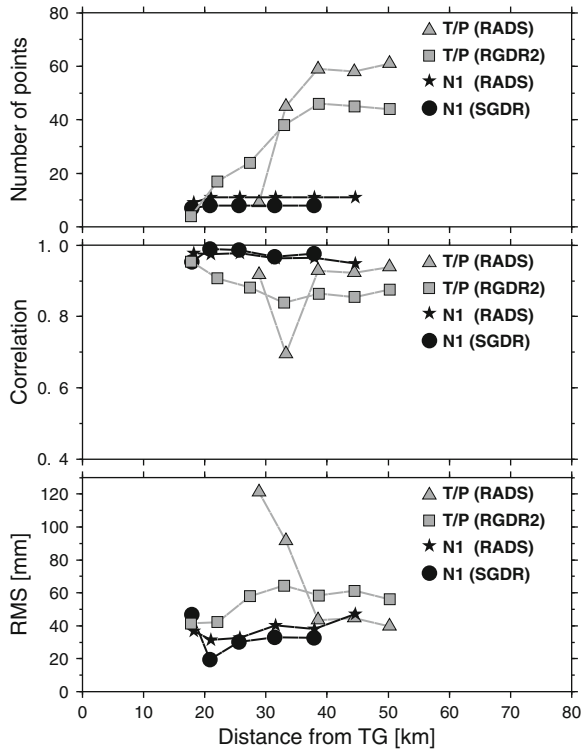


Fig. 33.5 Statistics for the normal points near Genova

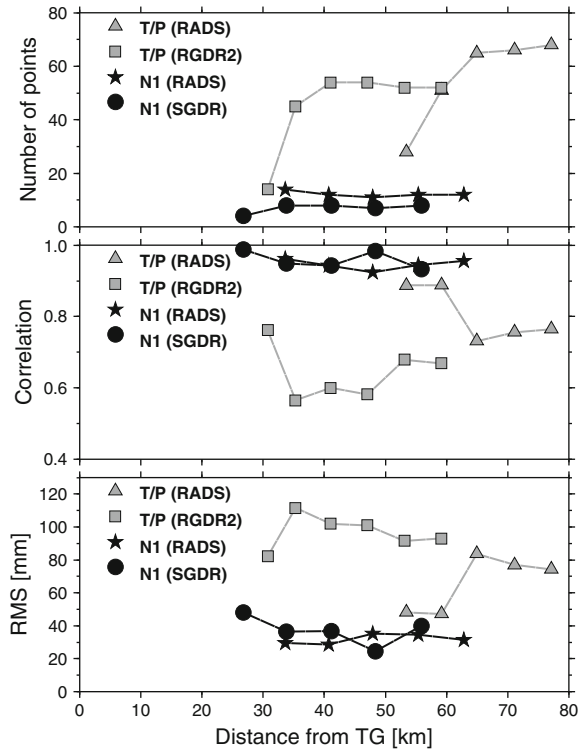


Fig. 33.6 Statistics for the normal points near Imperia

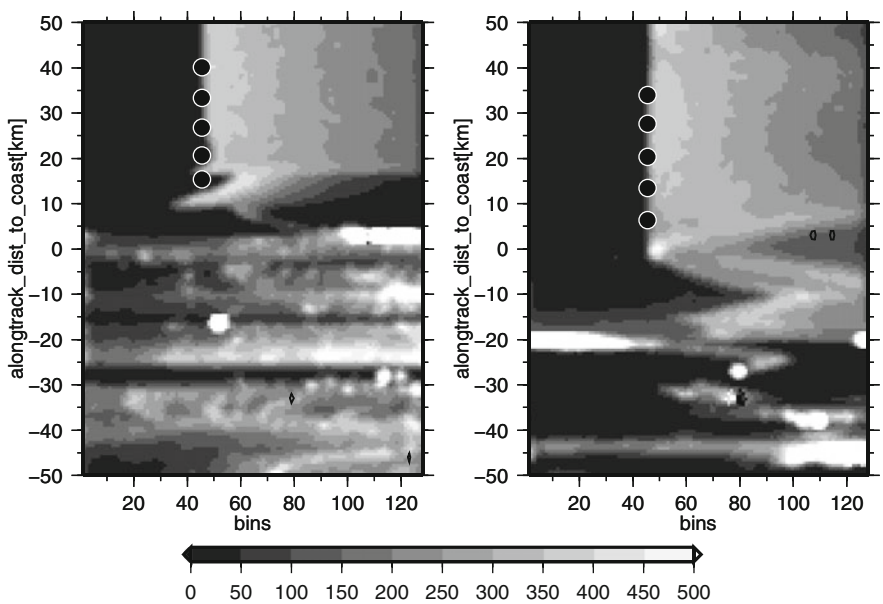


Fig. 33.7 Envisat waveforms at a sea-land (Genova, *left*) and a land-sea (Imperia, *right*) transition and Envisat 1 Hz NP (*circles*). Scale is waveform amplitude in FFT filter units

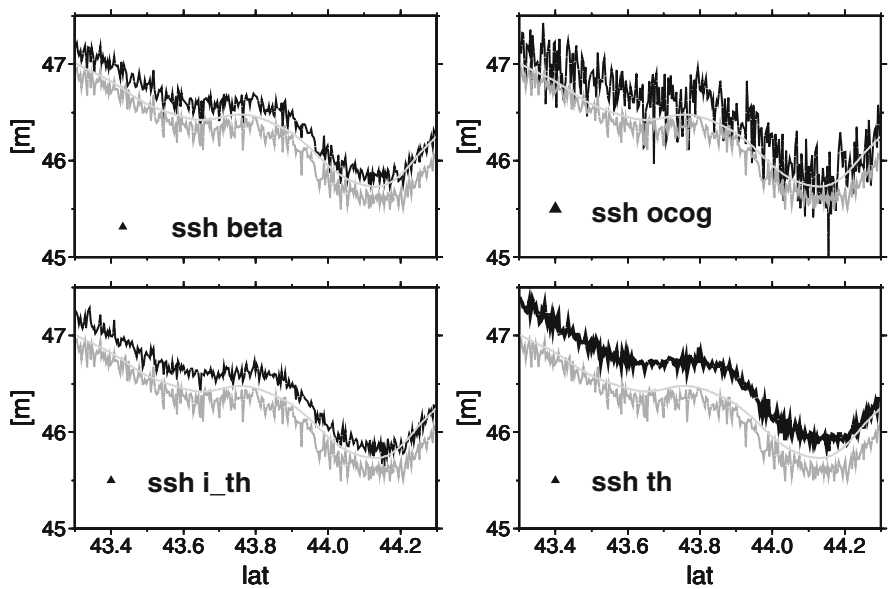


Fig. 33.8 SSH from β-5, OCOG, Improved threshold and threshold retrackers (*dark*) compared to GDR ocean (*grey*) SSH and EGM2008 (*light grey*) for Envisat cycle 59, pass 801 near Genova

Table 33.3 Statistics of Envisat retracking near Genova

Retracker	δ_{raw}	$\delta_{retracked}$	IMP[%]
β-5	0.209	0.084	59,8
OCOG	0.214	0.220	–2.8
Threshold	0.214	0.090	57.9
Imp. threshold	0.214	0.086	59.8
ocean1	0.214	0.088	58.9

The noise of the 18 Hz ranges is reduced by retracking the Envisat data with empirical retracker methods. The improved threshold and the β-5 retrackers are giving the best results.

References

Anzenhofer, M., C.K. Shum, and M. Rentsh (1999). Coastal altimetry and applications. In: Technical Report N. 464, Geodetic Science and Surveying. The Ohio State University Columbus, USA, pp. 1–40.

AVISO (2006). AVISO and PODAAC User Handbook, IGDR and GDR Jason Products, SMM-MU-M5-OP-13184-CN, 3.0, CNES.

Bouffard, J., S. Vignudelli, P. Cipollini, and Y. Menard (2008). Exploiting thepotential of an improved multimission altimetric data set over the coastal ocean. *Geophys. Res. Lett.,* 35, L10601, doi:10.1029/ 2008GL033488.

CLS (2006). Envisat RA-2 /MWR Level 2 User Manual, Issue 1.2, ESA.

Davis, CH. (1995). Growth of the Greenland ice sheet: a performance assessment of altimeter retracking algorithms. *IEEE Trans. Geosci. Remote Sens.*, 33(5), 1108–1116.

Deng, X., W. Featherstone, C. Hwang, and P.A.M. Berry (2002). Estimation of contamination of ERS-2 and Poseidon satellite radar altimetry close to the coasts of Australia. *Marine Geodesy*, 25, 249–271.

Deng, X. and W. Featherstone (2006). A coastal retracking system for satellite radar altimeter waveforms: application of ERS-2 around Australia. *J. Geophys. Res.*, 111, C06012.

Desportes, C., E. Obligis, and L. Eymard (2007). On the wet tropospheric correction for altimery in coastal regions. *IEEE Trans. Geosci. Remote Sens.*, 45(7), 2139–2149.

Fenoglio-Marc, L., E. Groten, and C. Dietz (2004). Vertical land motion in the mediterranean sea from altimetry and tide gauge stations. *Marine Geodesy*, 27, 683701.

Fenoglio-Marc, L., S. Vignudelli, A. Humbert, P. Cipollini, M. Fehlau, M. Becker (2007). An accessment of satellite altimetry in proximity of the Mediterranean coastline. In: 3rd ENVISAT Symposium Proceedings, SP-636, ESA Publications Division.

Hwang, C., J.Y. Guo, X.L. Deng, H.Y. Hsu, and Y.T. Liu (2006). Coastal gravity anomalies from retracked Geosat/GM altimetry: improvement, limitation and the role of airborne gravity data. *J. Geodesy*, 80, 204–216.

Martin, T.V., H.J. Zwally, A.C. Brenner, et al. (1983). Analysis and retracking of continental ice sheet radar altimeter waveforms. *J. Geophys. Res*., 88, 1608–1616.

Naejie M., E. Doornbos, L. Mathers, R. Scharroo, E. Schrama, and P. Visser (2002). Radar altimeter database system: exploitation and extension, final Rep. NUSP-2 02-06, Space Res. Organ. Neth., Utrecht, Netherlands.

Roblou, L., F. Lyard, M. Le Henaff, and C. Maraldi (2007). X-track, a new processing tool for altimetry in coastal ocean. In: 3rd ENVISAT Symposium Proceedings, SP-636, ESA Publications Division

Vignudelli, S., P. Cipollini, L. Roblou, F. Lyard, G.P. Gasparini, G. Manzella, and M. Astraldi (2005). Improved satellite altimetry in coastal systems: case study of the Corsica Channel (Mediterranean Sea). *Geophys. Res. Lett.*, 32, L07608.

Wingham, D.J., C.G. Rapley, and H. Griffiths (1986). New techniques in satellite tracking system. In: Proceedings of IGARSS' 88 symposium, Zurich, 1339–1344.

Chapter 34

On Estimating the Dynamic Ocean Topography – A Profile Approach

W. Bosch and R. Savcenko

Abstract Since the essential improvements of GRACE gravity field models reliable signatures of the dynamic ocean topography (DOT) can be obtained by subtracting geoid heights from the sea surface. The differences are usually performed after an initial data gridding of sea surface heights implying already an undesirable loss of signal. On the other hand, even the latest gravity field solutions from GRACE exhibit a meridional striping in the geoid and require a smoothing. In order to preserve the high along-track resolution of altimetry the present paper investigates a profile approach which (i) performs a spectral smoothing of the GRACE gravity field (ii) merges mean-tide geoid profiles to the along-track sea level measurements of satellite altimetry and (iii) performs a common low pass filtering of along-track differences in order to make filtered sea level and geoid heights spectrally consistent. The approach is performed with the latest GRACE-only gravity field models and the sea surface height profiles of TOPEX and Jason-1 and produces time varying profiles of the DOT. Globally, the profiles exhibit the expected topographic features which are compared with independent estimates of the DOT.

34.1 Introduction

To first order the sea level is in hydrostatic balance with gravity, that is the mean sea level is very close to an equipotential surface of the Earth gravity field. The geoid is defined as one of the equipotential surfaces, closest to the mean sea level and serving as global height reference surface.

The deviation between actual (mean) sea level and geoid is then defined as dynamic ocean topography (DOT). The magnitude of the DOT, caused by hydrodynamic processes, remains in the order of ± 1 – 2 m. The deviations are small but important: knowing the DOT is equivalent with knowledge on the ocean surface currents which in turn allows to infer the 3-dimensional mass and heat flow in the ocean, if additional data on water density is available.

There are different approaches to estimate the DOT. In ocean science numerical models of the ocean circulation are run and output the water level above a geoptotential surface as one of the prognostic variables. Combinations of such models and direct observations were published by Niiler et al. (2003) and Rio and Hernandez (2004). This paper focuses on the geodetic method, based on the basic relationship

$$\zeta = h - N \tag{1}$$

where ζ is the steady-state DOT, h is the altimetric height above an adopted reference ellipsoid (corrected for all short time variable effects such as tides) and N are the geoid heights referred to the same reference ellipsoid.

EGM96 (Lemoine et al., 1998) was the last gravity field model estimated in common with the dynamic ocean topography (DOT), the latter expressed in spherical harmonics. As eigenfunctions for the Laplace Differential Operator spherical harmonics are the most convenient base function for describing the global gravity field. However, spherical harmonics are less

W. Bosch (✉)
Deutsches Geodätisches Forschungsinstitut (DGFI),
München 80539, Germany
e-mail: bosch@dgfi.badw.de

S.P. Mertikas (ed.), *Gravity, Geoid and Earth Observation*, International Association of Geodesy Symposia 135,
DOI 10.1007/978-3-642-10634-7_34, © Springer-Verlag Berlin Heidelberg 2010

suited to represent the DOT defined over ocean area only.

The present paper addresses the general difficulty for the geodetic approach: while the geoid models are given globally altimetry profiles are limited to the oceans. Coastal areas are of particular importance for the understanding of ocean dynamics. Thus, the DOT estimate should avoid mathematical distortions at the ocean-land transition.

The profile approach introduced here takes care of both, the error characteristics of most recent gravity fields (discussed in Sect. 34.2) and the most precise information available through satellite altimetry (see Sect. 34.3). Section 34.4 describes the principle of the profile approach. The results are explained in Sects. 34.5 and 34.6 comparisons are performed with independent estimates of the DOT.

34.2 GRACE-Only Gravity Field Models

Since the realization of dedicated gravity field missions like CHAMP and GRACE (Tapley et al., 2004) the resolution and accuracy of the Earth gravity field has been dramatically improved. The accumulated geoid error is in the order of 2 cm for the harmonic coefficients up to degree and order 70 (ibid., Fig. 34.2). This justifies the geodetic approach, followed here.

However, even the latest GRACE-only gravity fields as, for example, EIGEN-GL04S or ITG03S exhibit a meridional striping, an artifact of GRACE processing which does not represent geophysical signal (see Fig. 34.1). The cause of these artifacts are not yet fully explained. The differences of GRACE gravity field solutions using different ocean tide models exhibit striping pattern similar to those shown in Fig. 34.1 (Wünsch et al., 2005). Most likely, the striping is

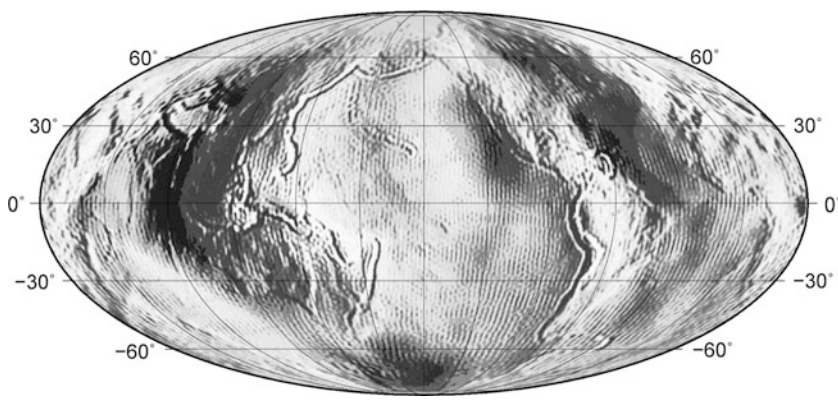


Fig. 34.1 Relief representation of the geoid, computed with the gravity field model ITG03S (Mayer-Gürr, 2007). The artificial illumination from left exhibits the meridional striping, still present in all GRACE based satellite-only gravity field models

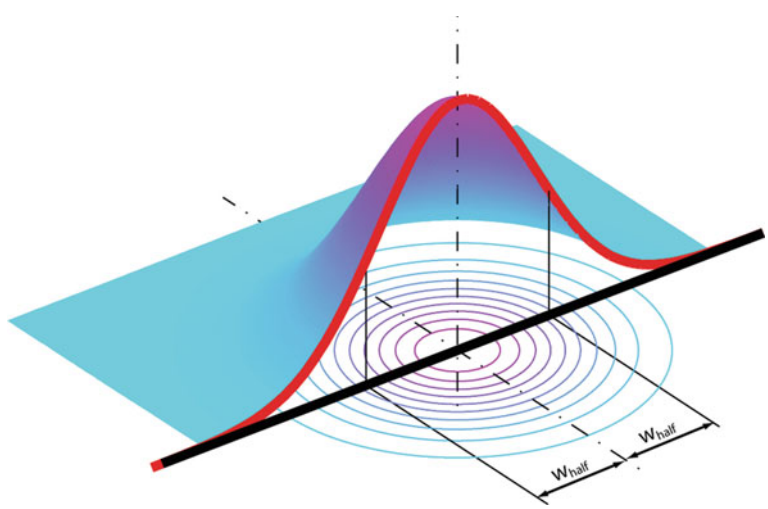


Fig. 34.2 The shape of the two dimensional, isotropic Gauss-type filter (*blue surface*) and the effective filter (*red curve*) if applied to one-dimensional profile data (for colors, see online version)

mainly caused by the fact that the inter satellite K-band range observation between the pair of GRACE satellites provide extreme precise along-track observations but omit any cross-track sensitivity.

Sophisticated un-isotropic de-correlation filter have been suggested by Kusche (2006) to remove the striping pattern. In this investigation the Gauss-type filter (Jekeli, 1981) has been used. The isotropic Gauss filter has si milar pattern in the spectral and the space domain and does not have any side lobes (see Fig. 34.2). The optimal filter length was found in an experimental way: comparing relief representations as shown in Fig. 34.1 it was found that a filter length of at least 200 km is sufficient to remove the striping pattern of the ITG03S geoid. On the other hand filter length above 200 km were not considered in order to keep as much geoid details as possible.

34.3 Satellite Altimetry – Profiling the Sea Surface

Radar altimetry performs observations along profiles: The basic pulse repetition frequency for the range measurements is about 1 kHz. Onboard software performs an averaging to 10 Hz (TOPEX) or 20 Hz (ESA missions) observations which are transmitted to the ground segment, where a further post-processing generates 1 s mean values for the altimeter ranges. The 1 Hz range values are taken for most follow-on processing (some high resolution application go back to the 10 or 20 Hz data).

According to their mean ground velocity altimeter satellites provide every 6.5–7 km a 1 s mean value of the range measurements. This along-track resolution is in contrast to the rather large spacing of neighbouring ground tracks. For TOPEX the equatorial distance of neighbouring ground tracks is more than 300 km; ESAs altimetry missions (ERS-2 and ENVISAT) have a ground track spacing of about 80 km. In both cases there are large unobserved diamond shaped areas in between the profiles.

In spite of these unfavourable sampling many applications perform an initial gridding by interpolating the observed data to values on the nodes of a regular equally spaced grid. For satellite altimetry this gridding is of particular difficulty: first, the interpolated values at grid nodes in the centre of any non-observed diamond shaped area will be a mean of all measurements available on the surrounding profiles. Second, the surrounding profiles are observed at different times such that the interpolated value is also a temporal mean. Thus gridded altimeter data is already smoothed in space *and* time and the degree of smoothing depends on the distance to the observed profiles and on the actual observation times of the surrounding profiles (in general, the latter is not at all taken into account). To circumvent this spatio-temporal fussiness the present investigation avoids any initial gridding, stays as long as possible on the profiles in order to perform necessary computations with the high resolution profile data. This is why the procedure is called "profile approach".

34.4 The Profile Approach

The Gauss filter proposed by Jekeli (1981) has been applied to remove the artificial striping of the GRACE-only gravity field model ITG03S (Mayer-Gürr, 2007). The filter, indicated by the operator $(\bullet)^{2D}$ is applied in the spectral domain and the filtered harmonic coefficients are taken to sample the geoid undulations N^{2D} at those points where altimetry provides a sea surface height h. The operation $(\bullet)^{2D}$ should now be consistently applied to both, the sea surface heights h and the Geoid undulations N.

$$\zeta = h - N = (h - N)^{2D} = h^{2D} - N^{2D} \qquad (2)$$

However, altimeter profiles are only available in the space domain. A spectral representation of the sea surface heights is not available and difficult to construct as sea surface heights are not defined over land. Thus, the equivalent spatial representation of the filter should be applied to the altimeter profiles in order to consistently filter both quantities, geoid and sea surface. The Gauss filter is isotropic and can be applied to data distributed only along the profiles. Thereby the two-dimensional filter $(\bullet)^{2D}$ reduces itself to a one-dimensional filter $(\bullet)^{1D}$ (cf. Fig. 34.2).

However, the 1D filtering of the altimetry profiles is not equivalent to a 2D filtering of laminar distributed data. Considering e.g. any mean sea surface in

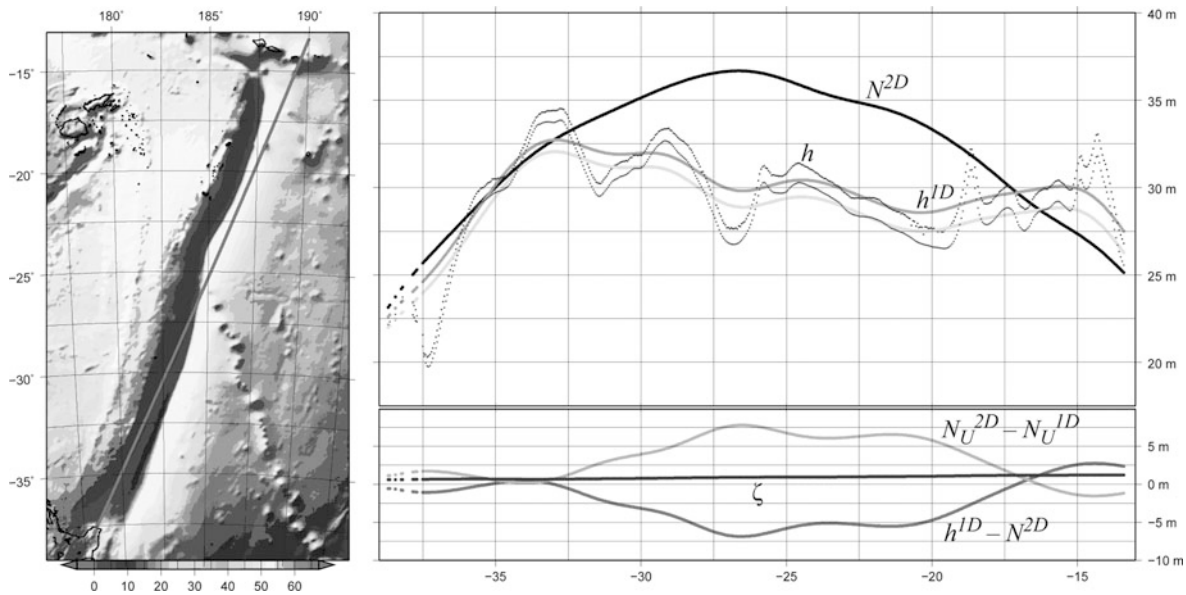


Fig. 34.3 Case study for the impact of 1D filtering of sea surface height profiles neighbouring a trench area. The *left* panel shows an ascending TOPEX-EM track close to the Kermadec and Tonga trenches North-East of New Zealand. The upper right panel shows the observed sea surface height profile (h, blue dotted line), the 1D filtered sea surface height profile h^{1D}, light blue solid line), and the geoid undulation N^{2D} (black solid line) computed from the spectrally smoothed GRACE-only model ITG03S. The *lower right* panel shows in red the differences $h^{1D} - N^{2D}$, in green the filter correction $N_U{}^{2D}$–$N_U{}^{1D}$ to be added, and in *blue* the final estimate $\zeta = h^{1D} - N^{2D} + (N_U{}^{2D} - N_U{}^{1D})$ of the DOT profile (for colors, see online version)

a neighbourhood of a trench (cf. Fig. 34.3), then the 2D filtering along a profile following this trench will raise the filtered sea surface heights due to the higher sea surface side wards of the trench while the 1D filtering along the profile preserves the low sea surface heights along the grounding line of the trench. Figure 34.3 illustrates these conditions in detail.

In order to compensate these systematic differences between a 2D filtering of laminar data and the 1D filtering of profile data a filter correction has been developed in the following way: The identity

$$h^{2D} = h^{1D} + (h^{2D} - h^{1D}) \tag{3}$$

provides a relationship between 2D and 1D filtering. The right hand term in round brackets can be considered as the necessary correction. This correction term can be approximated by filter operations applied to a global continuous surface with a similar spatial resolution as the sea surface. A high resolution geoid, represented by a spherical harmonic series, is such a proxy for the sea surface. It is first sampled along the altimeter profiles at those points where altimeter measurements are available. Then, the geoid is filtered twice: once along the profiles using the 1D spatial representation, giving N^{1D} and second by applying the same filter on the spherical harmonic representation of the geoid, giving N^{2D}. The difference

$$N_U{}^{2D} - N_U{}^{1D} \approx h^{2D} - h^{1D} \tag{4}$$

is a good proxy for the desired filter correction. Inserting (4) and (3) into Eq. (2) gives

$$\zeta = h^{2D} - N^{2D} \approx h^{1D} + (N_U{}^{2D} - N_U{}^{1D}) - N^{2D}, \tag{5}$$

the final recipe to estimate the DOT along altimeter profiles and to apply consistent filter operations for sea surface heights h and geoid undulations N.

34.5 Results

Initially, the EIGEN-GL04c, a hybrid degree 360 model, combining GRACE and Laser observations with high resolution surface gravity data (Förste et al., 2008), was used to derive the filter correction. With

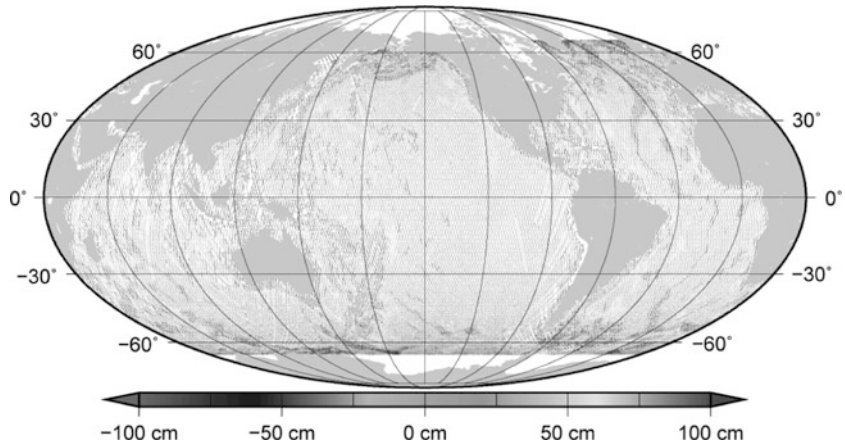


Fig. 34.4 The filter correction compensating the systematic differences between 1D filtering along profiles and 2D filtering in the spectral domain. The correction was derived with the ultra-high resolution gravity field EGM08 and is shown for the common 10-day ground track pattern of Jason-1 and TOPEX-EM (with shifted ground tracks)

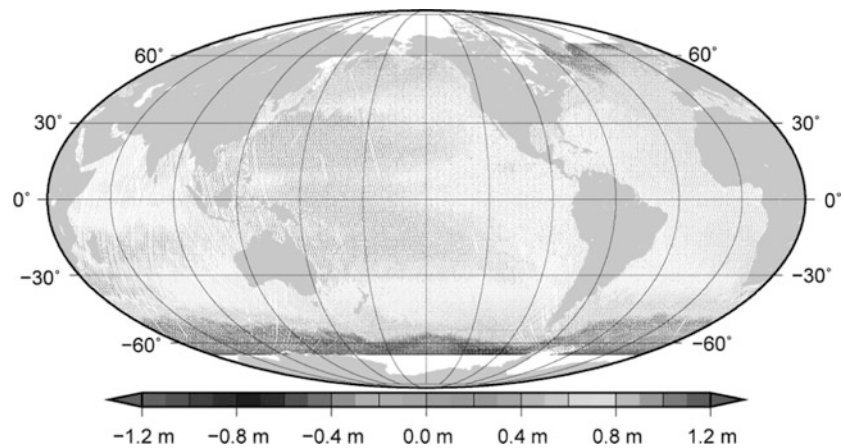


Fig. 34.5 Snapshot of DOT for a common 10-day cycle of TOPEX-EM and Jason-1, estimated with the "profile approach"

EGM08 (Pavlis et al., 2008) an ultra high resolution gravity field, developed up to degree and order 2,160, became available. Formally, EGM08 resolves spatial structures of 5′ extension which corresponds to 9 km on the Earth surface. Thus the spatial resolution of EGM08 is rather similar to the along-track resolution provided by the 1 Hz altimeter data. Therefore the latest version of the filter correction is based on EGM08. This was already indicated in the previous section by indexing the geoid terms N of the filter correction by "U" (ultra high resolution). Note, that the last term of Eq. (5), N^{2D}, is instead derived from the filtered GRACE-only model ITG03S. Figure 34.4 shows the global pattern of the filter correction, computed for the ground tracks of a common cycle of Jason1 and TOPEX-EM (shifted ground tracks). Figure 34.5 provides a snapshot of the DOT estimated with the profile approach. It is remarkable that already data from a 10 day period is able to recover those large scale pattern of the DOT that are to be expected from oceanographic results.

34.6 Validation

The profile approach was applied to the 36 cycles of TOPEX and Jason, observed in the year 2004. This mean annual DOT estimate was then compared to the independent estimates of Niiler et al. (2003) and Rio and Hernandez (2004). The geographic distribution of the differences between the 2004 DOT (this study) and Niiler's and Rio's DOT are shown in Fig. 34.6. In addition, the lateral means of the differences (a few cm only) are shown in the right panel. Note, the oceanographic estimates have offsets of about –115 cm (Rio) and +46 cm (Niiler) respectively. These offsets are most likely caused by the unclear reference level (in

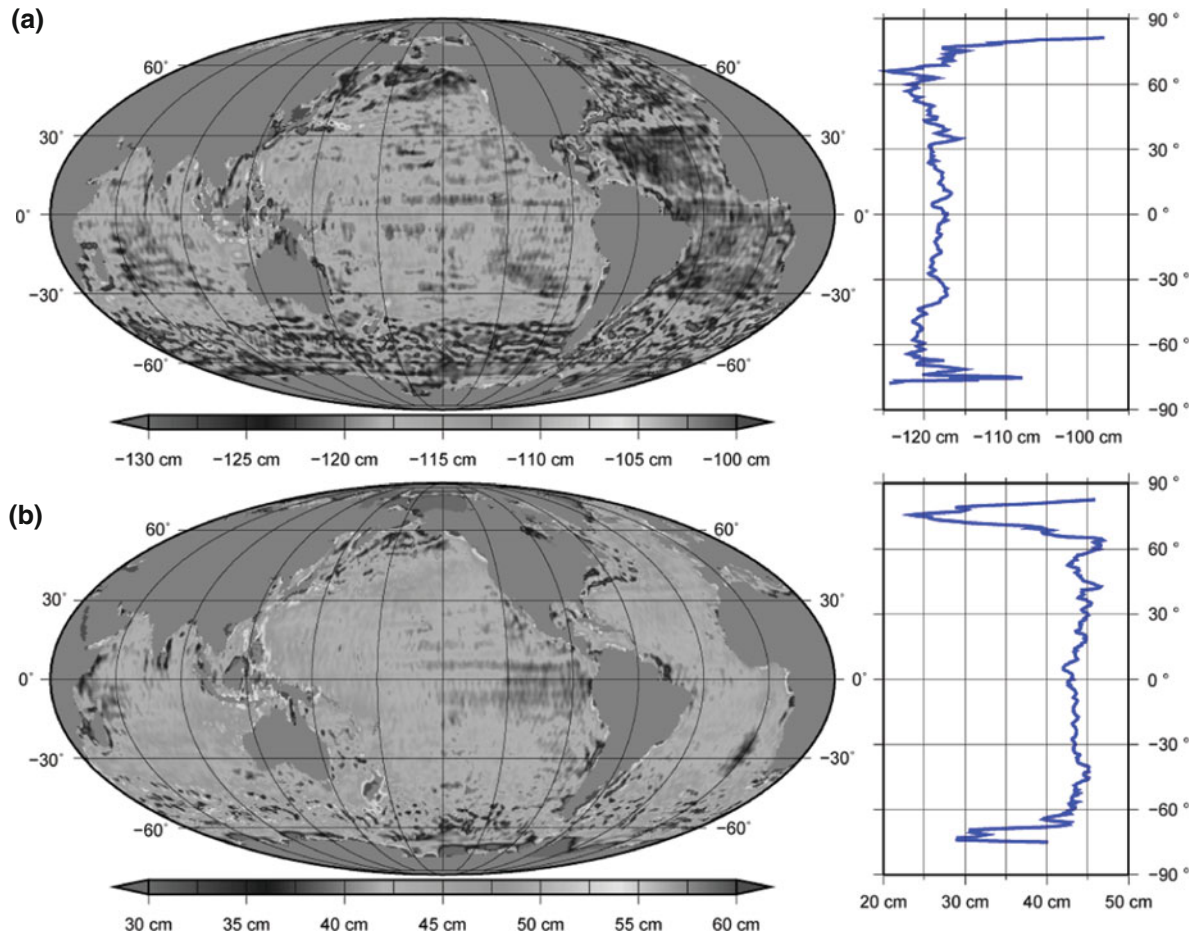


Fig. 34.6 Differences between the 2004 DOT (this study) and (**a**) the DOT estimate of Rio (*upper* panel) and (**b**) the DOT estimate of Maximenko & Niiler (*lower* panel). The lateral mean of the differences is shown in the panels on the right

terms of the level-of-no-motion) of the oceanographic estimates. Note also, that the geodetic DOT is a mean for the year 2004 only while the averaging periods of Rio's and Niiler's DOT are covering the period 1993–1999. Taking this into account, the overall agreement is rather satisfactory.

34.7 Conclusion

The profile approach performs (i) a spectral smoothing of satellite-only gravity fields (filtering as little as possible to keep as much structure of the geoid as possible), (ii) merges geoid profiles to the along track sea level measurements and (iii) applies the same low pass filter to the sea surface height profiles. The differences sea surface height minus geoid are then performed on the track without any initial gridding. This keeps the high resolution content of the altimeter profiles untouched. The systematic differences between the two-dimensional filtering and the one-dimensional filtering along the profiles is taken into account by a filter correction. The DOT profiles show rather good agreement with independent estimates of Rio and Niiler.

References

Förste, Ch., et al. (2008). The GeoForschungsZentrum Potsdam/Groupe de Recherche de Gèodésie Spatiale satellite-only and combined gravity field models: EIGEN-GL04S1 and EIGEN-GL04C. *J. Geodesy*, 82(6), 331–346(16), DOI: 10.1007/s00190-007-0183-8.

Jekeli, C. (1981). Alternative methods to smooth the earth gravity field. Rep. 327. Dept Geod Sci & Surv, Ohio State University, Columbus.

Kusche, J. (2006). Approximate decorrelation and non-isotropic smoothing of time-variable GRACE-type gravity fields. DEOS Delft University of Technology, Delft.

Lemoine, F.G., et al. (1998). The Developement of the Joint NASA GSFC and the National Imagery and Mapping Agency (NIMA Geopotential Model EGM96. NASA/TP-1998-206861, NASA Goddard Space Flight Center, Greenbelt, Maryland.

Niiler, P.P., N.A. Maximenko, and J.C. McWilliams (2003). Dynamically balanced absolute sea level of the global ocean derived from near-surface velocity observations. *Geophys. Res. Lett.*, 30(22), 2164, doi:10.1029/2003GL018628, 2003.

Pavlis, N.K., S.A. Holmes, S.C. Kenyon, and J.K. Factor (2008). An earth gravitational model to degree 2160: EGM2008, presented at the 2008 General Assembly of the European Geosciences Union, Vienna, Austria, April 13–18.

Rio, M.H. and F. Hernandez (2004). A mean dynamic topography computed over the world ocean from altimetry, in-situ measurements and a geoid model. *J. Geophys. Res.*, 109(12).

Tapley, B.D., S. Bettadpur, M.M. Watkins, and Ch. Reigber (2004). The gravity recovery and climate experiment: mission overview and early results. *Geophys. Res. Lett.*, 31, L09607, doi:10.1029/2004GL 019920, 2004.

Wünsch, J., P. Schwintzer, and S. Petrovic (2005). Comparison of two different ocean tide models especially with respect to the GRACE satellite mission, Scientific Technical Report STR05/08, Geoforschungszentrum Potsdam, Potsdam.

Part IV
Geoid Modeling and Vertical Datums

A. Kenyeres and W. Kearsley

Chapter 35

Evaluation of the Topographic Effect using the Various Gravity Reduction Methods for Precise Geoid Model in Korea

S.B. Lee and D.H. Lee

Abstract The topographic effect is a most important component in the solution of the geodetic boundary value problem (geodetic BVP) and should be considered properly for developing a precise geoid model. It is necessary to select a proper gravity reduction method in order to calculate the topographic effect precisely, especially in mountainous area. The selection of the gravity reduction method in context of precise geoid determination depends on the magnitude of its indirect effect, the smoothness and magnitude of the reduced gravity anomalies, and their related geophysical interpretation. In this paper, we studied gravimetric geoid solutions using various gravity reduction methods such as Helmert's second method of condensation, RTM method and Airy topographic-isostatic method and evaluated the usefulness of each method. In Korea, the gravimetric geoid model was determined by restoring the gravity anomalies (included TC) and the indirect effects was computed from various reduction methods on the EIGEN-CG03C reference field and the results were compared to geoid undulations at 503 GPS/levelling points after LSC fitting. According to the results, the RTM method is the most suitable for calculating topographic effect in the precise geoid determination in Korea.

S.B. Lee (✉)
Department of Civil Engineering, Jinju National University, Jinju 660-758, Korea
e-mail: sblee@jinju.ac.kr

35.1 Introduction

The topographic effect is one of the most important components in the solution of the geodetic boundary value problem. Therefore, the topographic effect should be treated properly for the precise determination of the geoid. The classical solution of the geodetic BVP using Stokes's formula for gravimetric geoid determination assumes that there are no masses outside the geoid. The gravity anomalies as input data should refer to the geoid, which requires the Earth's topography to be regularized in some way. Thus, the gravimetric reduction method plays an important role on precise (local or regional) gravimetric geoid determination (Bajracharya, 2003).

There are several reduction techniques, which all differ depending on how these topographical masses outside the geoid are dealt with. (Bajracharya, 2003). In theory, gravimetric solution for geoid determination using different mass reduction methods should give the same results, provided that the corresponding indirect effect is taken into account properly and consistently (Heiskanen and Moritz, 1967). However, the results from each reduction methods do differ slightly (Omang and Forsberg, 2000). Variation within each method also exist; e.g. Stokes' formula may be calculated using either summation over compartments or FFT, producing different results. One the reason for differences in the results is inability of the FFT method to handle data biases properly (Omang and Forsberg, 2000).

Therefore, the topographic effect should be considered properly, especially for the mountainous area like Korea. The selection of gravity reduction method

S.P. Mertikas (ed.), *Gravity, Geoid and Earth Observation*, International Association of Geodesy Symposia 135,
DOI 10.1007/978-3-642-10634-7_35, © Springer-Verlag Berlin Heidelberg 2010

depends on the magnitude of its indirect effect, the smoothness and magnitude of the reduced gravity anomalies, and their related geophysical interpretation (Heiskanen and Moritz, 1967).

In this paper, we studied gravimetric geoid solutions using three gravity reduction methods (Helmert's condensation method, RTM method and Airy-isostatic method) and evaluated the usefulness of each method in context of precise geoid. The gravimetric geoid model were determined by restoring the gravity anomalies (included TC) and the indirect effects was computed from various reduction methods on the EIGEN-CG03C reference field. The results were compared to geometric geoid undulation determined at 503 GPS/levelling points after LSC fitting. Through this study, it was found that the RTM method is the most effective method for calculating topographic effect in the precise geoid determination in Korea.

35.2 Gravimetric Reduction Method

35.2.1 Theory of Gravimetric Geoid Solution

In the remove-restore technique, the gravimetric geoidal height N is split into three parts

$$N = N_{GM} + N_{TC} + N_{res} \tag{1}$$

where N_{GM} is the low-frequency part of the geoid obtained from a geopotential model. For computation of the reference geoid undulation N_{GM}, we used the EIGEN-CG03C model (Förste et al., 2005) to degree 360 based on GRS80.

N_{res}, the medium-frequency part of the geoid, is the residual geoid computed from residual free-air anomalies (see, Fig. 35.1) using Stokes's integration,

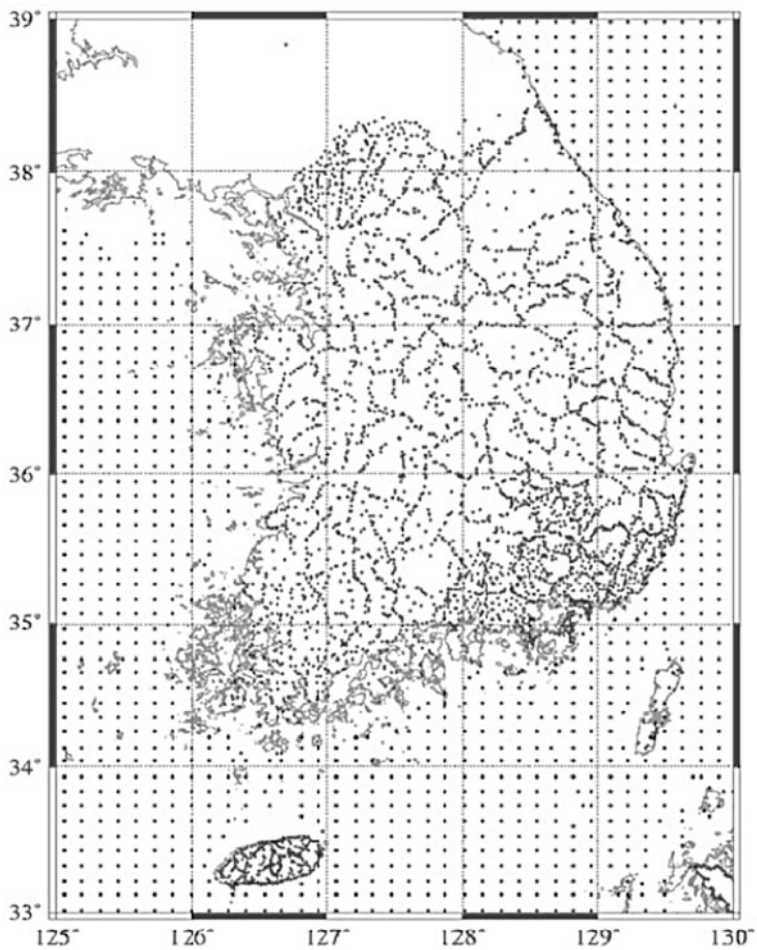


Fig. 35.1 Distribution of gravity data in Korea

extending, the integration in principle to cover the Earth. The residual free-air anomaly that remains in the gravity data after the contributions of the residual terrain effect (from reduction method) and the global field (from geopotential model) are subtracted.

To prevent the influence of local gravity on the longest wavelengths (Vanicek and Featherstone, 1998), we used the modified Stokes's kernel. The technique is the modified Wong-Gore method (Wong and Gore, 1969), in which the modified kernel $S_{\mathrm{mod}}(\psi)$ has the following expression.

$$S_{\mathrm{mod}}(\psi) = S(\psi) - \sum_{n=2}^{N_2} \alpha(n) \frac{2n+1}{n-1} P_n \cos(\psi) \quad (2)$$

where, the coefficients $\alpha(n)$ increase linearly from 0 to 1 between degrees N_1 and N_2 and can be determined under the following expression.

$$a(n) = \begin{cases} 1 & \text{for } 2 \le n \le N_1 \\ \frac{N_2 - n}{N_2 - N_1} & \text{for } N_1 \le n \le N_2, n = 2, ., N \\ 0 & \text{for } N_2 \le n \end{cases} \quad (3)$$

The coefficients N_1 and N_2 are determined by trial and error or by experience, and represent a trade-off between full use of the satellite fields and full use of the local gravity data. Geoidal heights derived from GPS-levelling data are typically used in the optimizations of N_1 and N_2 (Iliffe et al., 2003).

The residual gravity is transformed into the residual geoid by multi-band spherical FFT (Forsberg and Sideris, 1993), which provides a virtually exact implementation of Stokes's formula on a sphere and 100% zero padding is used in this study. For general details of the FFT methods, see Schwarz et al. (1990).

N_{RTM}, the high-frequency part of the geoid, is the terrain effect on the geoid generated by the gravimetric reduction methods using a DEM. For calculating the terrain effect by three reduction methods, we used a local DEM on a 100 m resolution grid, derived from an original DEM on a 30 m grid (Fig. 35.2). The original DEM was produced from digital topographic maps drawn on scale 1:25,000 and kindly provided by Environmental Geographic Information System (EGIS), Korea (see, http://egis.me.go.kr/).

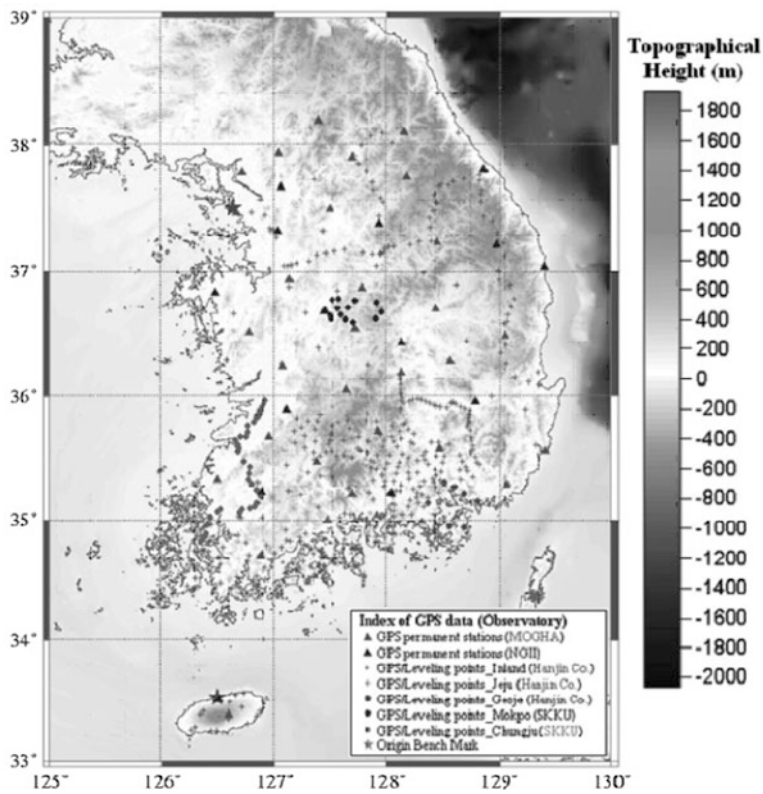


Fig. 35.2 Distribution of topographic height and GPS/Levelling data in Korea

35.2.2 Gravimetric Reduction Methods

Helmert's second method of condensation is one of the most common gravimetric reduction method used in practical geoid determination, where the topographical masses are condensed on the geoid surface as a surface layer. Helmert defined this condensation scheme in two ways depending on the location of this infinitesimally thin condensation layer. In his first method of condensation, the topographical masses are condensed on a surface parallel to the geoid located 21 km (this value represents the difference between semi-major axis and semi-minor axis of a reference ellipsoid) below the geoid, whereas these masses are condensed on the geoid surface in his second method (Heiskanen and Moritz, 1967; Heck, 2003). His first method has not been used in geoid determination and has been recently suggested by Heck (2003) (Fig. 35.3).

The Residual Terrain Model (RTM) scheme was introduced by Forsberg (1984). The RTM terrain reduction evaluates the gravitational effects of the mass anomalies relative to a mean elevation surface. The mean elevation surface is determined by moving-average filtering using local DEM data (Tscherning et al., 1994). The mean elevation surface corresponds in principle to the topographic signal already present in the spherical harmonic reference model. in Korea, the mean DEM surface of approx. 75 km ($42' \times 58'$) resolution was used (Fig. 35.4).

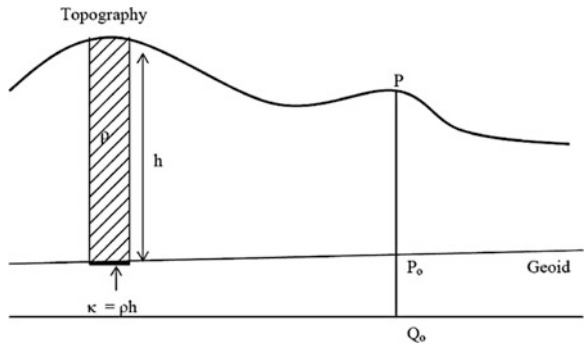


Fig. 35.3 Concept of Helmert reduction method

In the Airy-isostatic reduction method, the topographical masses are removed to fill roots of the

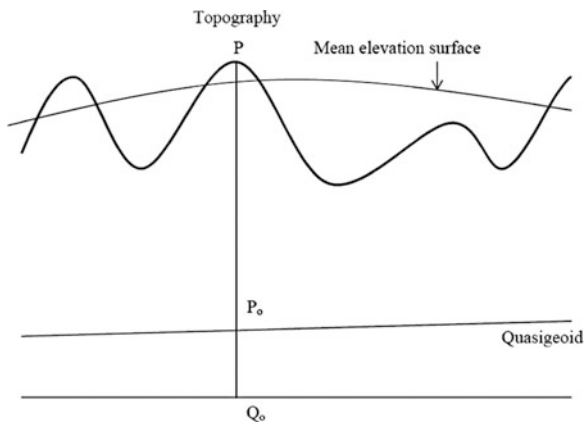


Fig. 35.4 Concept of RTM reduction method

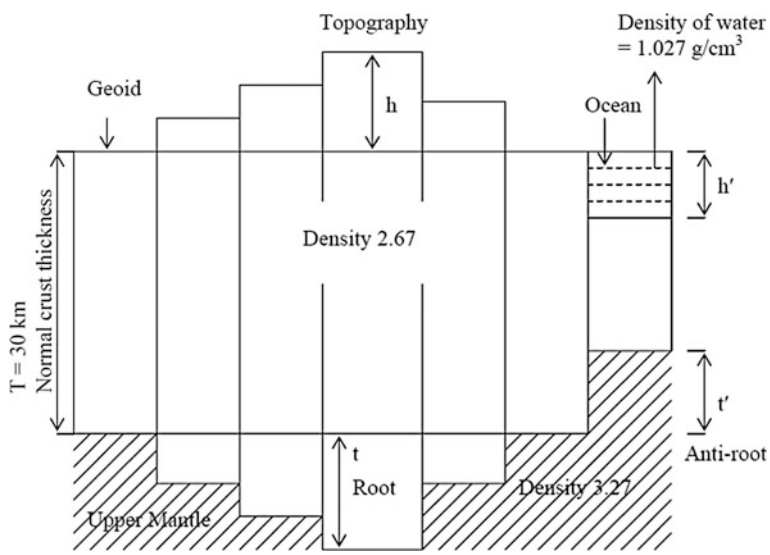


Fig. 35.5 Concept of Airy-isostatic reduction method

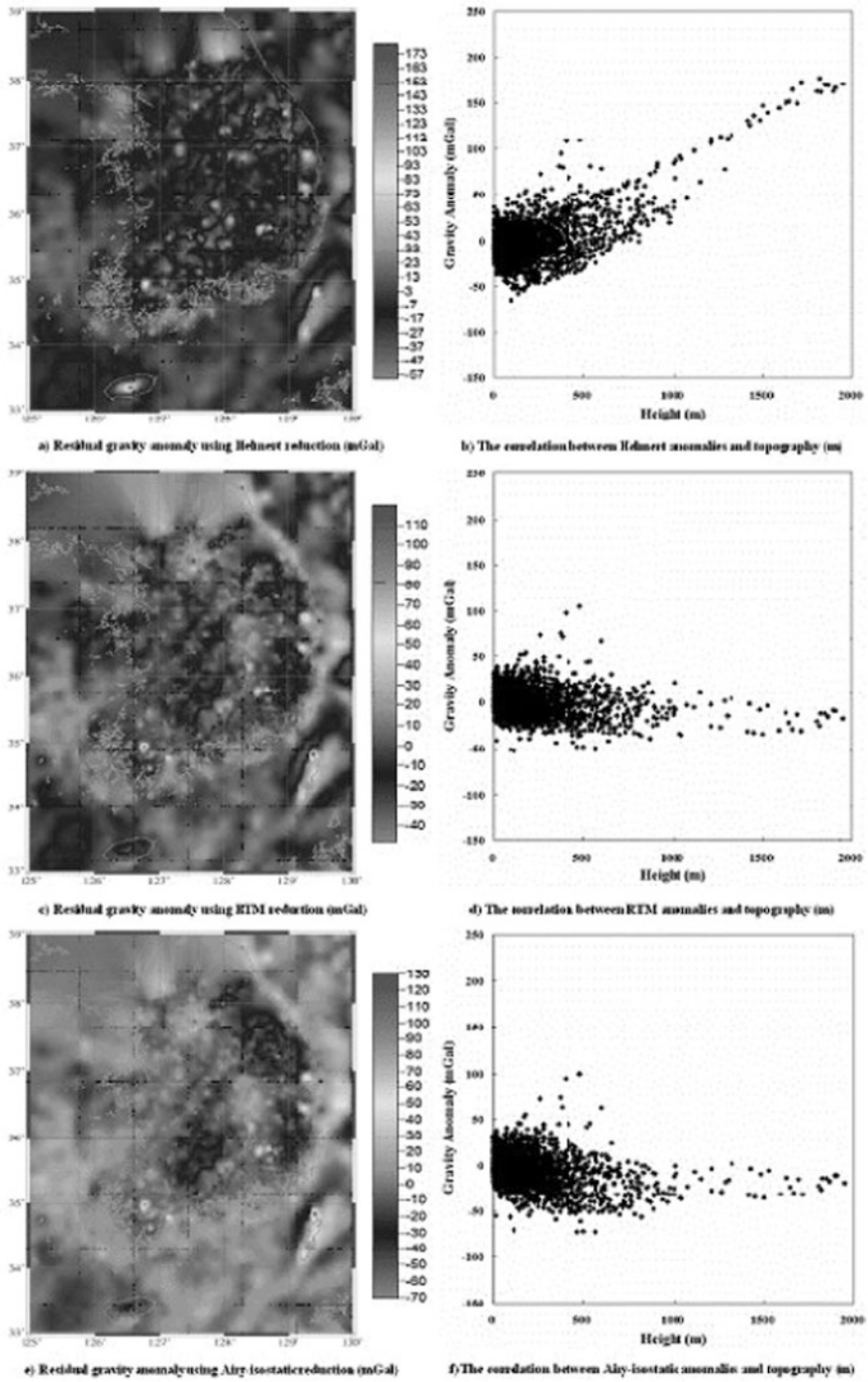


Fig. 35.6 Residual gravity anomalies (*left*: **a**, **c**, **e**) and correlation between anomalies and topography (*right*: **b**, **d**, **f**) from three reduction methods (from above, **a**, **b**: Helmert reduction method, **c**, **d**: RTM method, **e**, **f**: Airy-isostatic method)

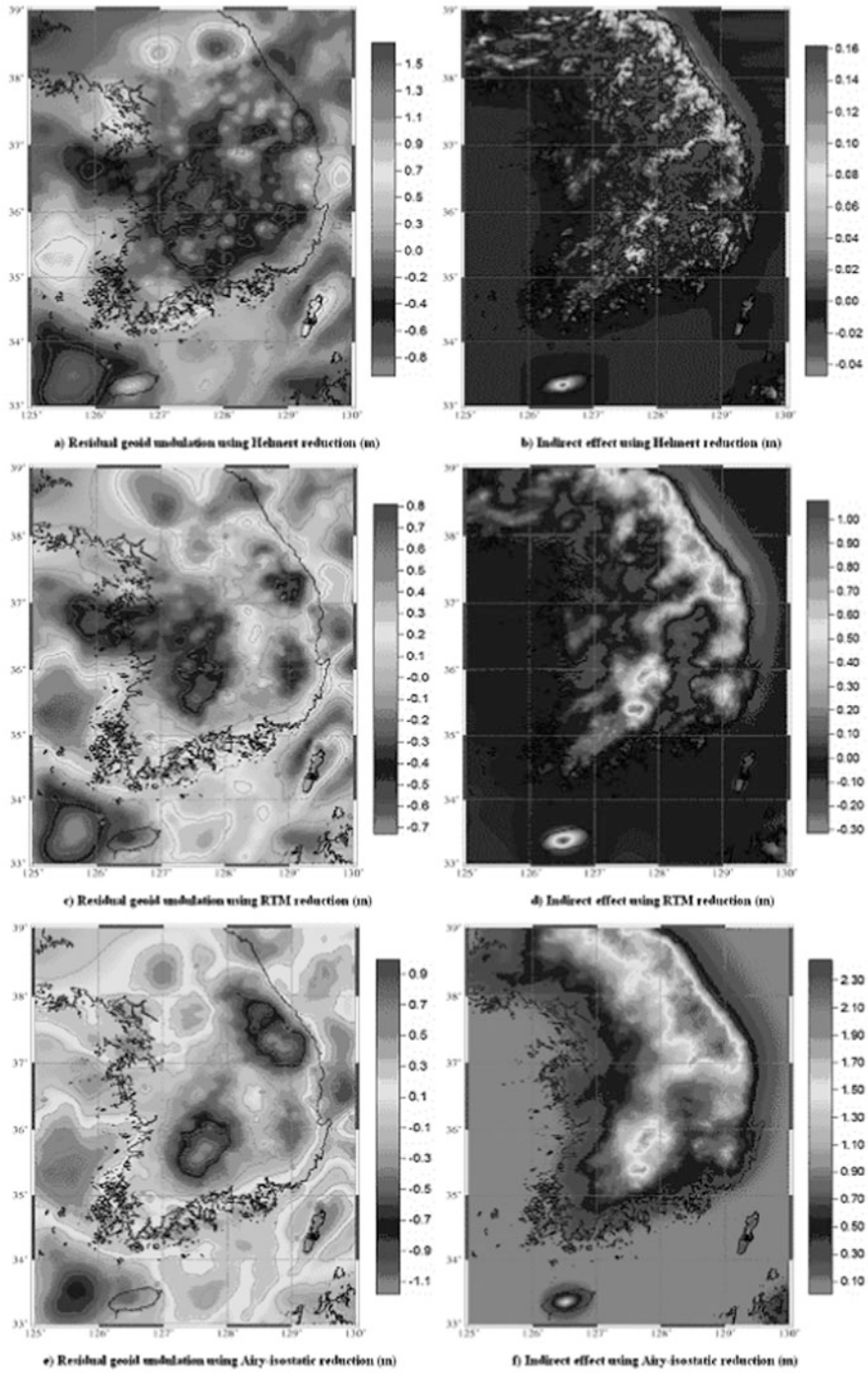


Fig. 35.7 Residual geoid undulations (*left*: **a**, **c**, **e**) and indirect effect (right: **b**, **d**, **f**) using the various reduction methods (from above, **a**, **b**: Helmert reduction method, **c**, **d**: RTM method, **e**, **f**: Airy-isostatic method)

Table 35.1 The statistic of residual anomalies from the each reduction methods (unit: mgal)

Reduction methods	Min	Max	Mean	STD
Height (m)	−0.6	1950.1	145.1	±201.2
Free-air	−26.05	176.10	25.49	±21.94
Helmert	−64.80	176.55	−4.74	±21.11
RTM	−52.87	104.49	0.66	±13.01
Airy	−72.42	99.43	−4.50	±15.22

Table 35.2 The statistic of residual and indirect effect on the geoid from reduction methods (unit: m)

Method	Geoid effect	Min	Max	Mean	STD
Helmert	Residual	−0.892	1.608	0.015	±0.278
	Indirect	−0.047	0.162	0.001	±0.013
RTM	Residual	−0.726	0.813	0.016	±0.236
	Indirect	−0.315	1.078	−0.004	±0.131
Airy	Residual	−1.181	0.994	0.028	±0.296
	Indirect	0.011	2.446	0.267	±0.439

continents bringing the density from its constant value to that of upper mantle. The masses above the geoid surface are removed together with their isostatic compensation according to the Airy's theory yielding a homogenous crust of constant density and constant normal crust thickness (Fig. 35.5).

According to the concepts of each reduction method, we calculated the residual gravity anomalies and indirect effects (Tables 35.1 and 35.2). The indirect effect is defined as the change in gravity and geoid due to the removal or shifting of masses underlying the gravity reduction (Fig. 35.6).

A well-suited reduction method should make small and smooth of the gravity anomalies and the indirect effect should be small (Omang and Forsberg, 2000) (Fig. 35.7).

35.3 Comparison and Results

35.3.1 Gravimetric Geoid in Korea

The gravimetric geoid in Korea was computed by the remove-restore method applying the two dimensional (2-D) multi-band spherical FFT transformation on the reduced gravity data followed by the restoration of the terrain effects and EIGEN-CG03C model effect. Data was gridded in the area 33–39°N, 124–131°E, at a basic grid spacing of $0.75' \times 1'$ in latitude and longitude.

The comparison of our results with the result of Yun (1999) indicated that the 2-D multi-band spherical FFT with 4-bands gave the best solution for Korea. The FFT was performed using 100% zero-padding to limit the periodicity effects. The 100% zero-padding puts zeros around the values of the original field (input matrix), practically doubling the dimensions (Yun, 1999). The final gravimetric geoid in Fig. 35.8a, c, e was computed by 2-D spherical FFT with 4-bands and Wong-Gore modification degree band 80∼90.

In order to select the optimal reduction method, we compared the accuracy of each gravimetric geoid with geoidal height from GPS/levelling data. Table 35.3 shows the statistics of the comparison.

35.3.2 Hybrid Geoid in Korea

The hybrid geoid of Korea was determined by fitting the geoid height from GPS/levelling data points. Using the geoid information from GPS/levelling, the long-wavelength geoid errors can be suppressed, and the inherent datum differences can be eliminated. Computing GPS geoid heights the levelling and GPS heights are error-free.

The fitting of a gravimetric geoid to a set of GPS geoid heights entails modelling of the difference and adding the modelled correction to the gravimetric geoid.

In this way a new geoid grid tuned to the levelling and GPS datum can be obtained. The method of least squares collocation is used for estimating the trend and modelling the residuals. For trend estimation, we used the 4-parameter model (Heiskanen and Moritz, 1967).

In the collocation process, a covariance function must be assumed for the residual geoid errors as a function of spherical distance.

We used the 2nd order Markov covariance function (Iliffe et al., 2003) for determination of hybrid geoid in Korea.

$$C(s) = C_0(1 + \alpha s)e^{-\alpha s} \tag{4}$$

Such a covariance function is characterized by the zero variance C_0 and correlation length $s_{1/2}$, which determines the fit and the smoothness of the interpolated geoid error. The constant α is the only quantity to be specified, with C_0 automatically adapted to the data. In the selection of the correlation length

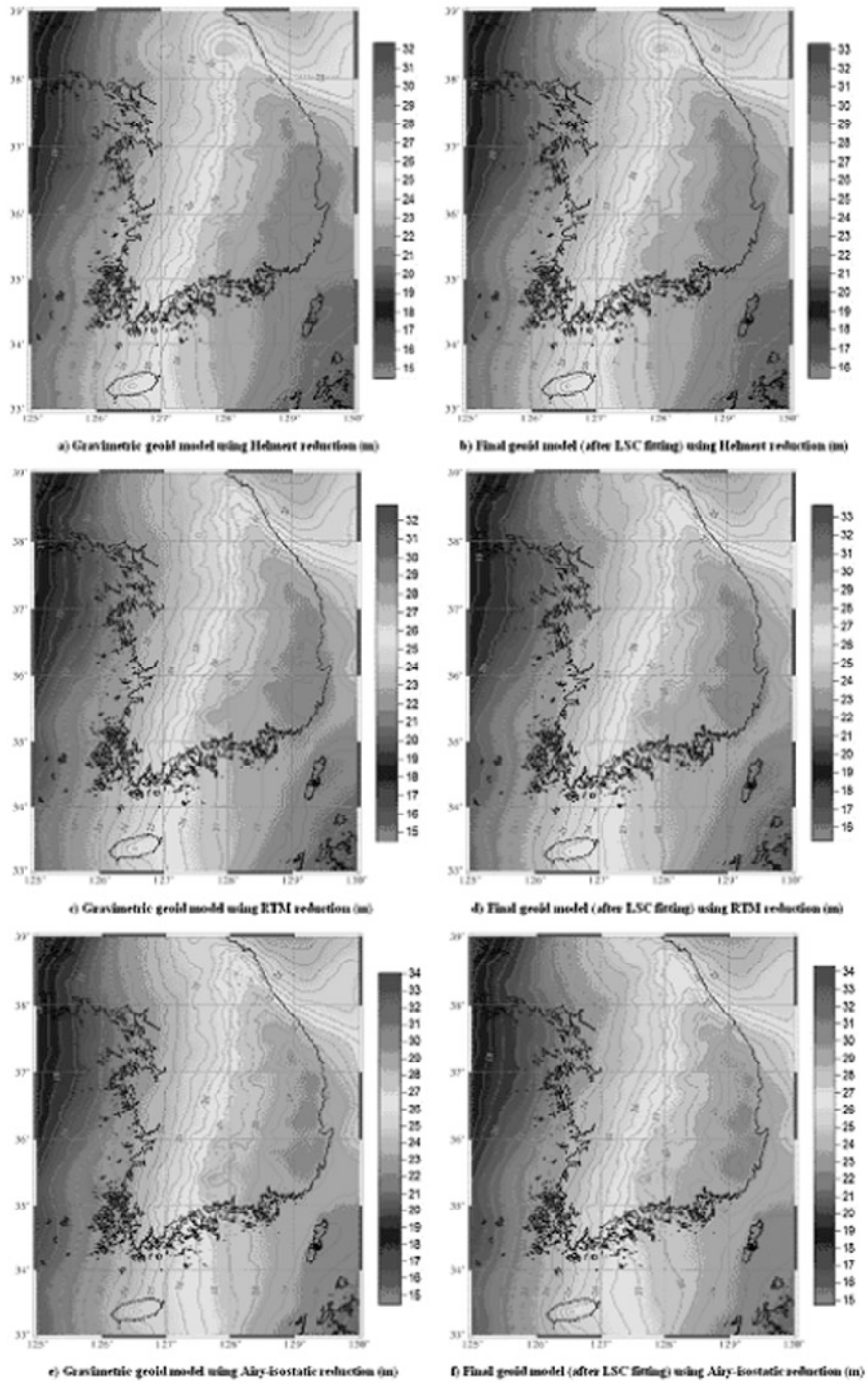


Fig. 35.8 Gravimetric geoid (*left*: **a**, **c**, **e**) and hybrid geoid (*right*: **b**, **d**, **f**) using the various reduction methods (from above, **a**, **b**: Helmert reduction method, **c**, **d**: RTM method, **e**, **f** : Airy-isostatic method)

Table 35.3 The statistics of accuracy of gravimetric and hybrid geoid to GPS/levelling data (unit : m)

Reduction method	Geoid model	Min	Max	Mean	STD
Helmert	Gravimetric	0.306	1.530	0.974	0.183
	Hybrid	−0.266	0.212	0.001	0.069
RTM	Gravimetric	0.426	1.158	0.808	0.129
	Hybrid	−0.268	0.203	0.001	0.053
Airy	Gravimetric	−0.292	0.952	0.272	0.246
Hybrid	-0.243	0.203	0.001	0.073	

and noise of observed errors, the user has a wide range of selection options.

We can use either a strong fit to the GPS data, or a more relaxed fit, which diminishes the impact of possible errors in the GPS data (Forsberg et al., 2003). We determined a correlation length of 40 km approximately to each gravimetric geoids and 1 cm a priori GPS noise was assumed.

Table 35.3 Shows the statistics of hybrid geoid compared with geoidal heights from GPS/levelling data.

35.4 Conclusions

In this paper, we studied and evaluated gravimetric geoid solutions using three gravity reduction methods (Helmert's condensation, RTM and Airy-isostatic). The selection of gravity reduction method depends on the magnitude of its indirect effect, the smoothness and magnitude of the reduced gravity anomalies, and their related geophysical interpretation.

For selection of the best reduction method, the Korean DEM with 100 m resolution was constructed and topographic effect was calculated by the three reduction methods. The corresponding gravimetric geoid models were determined by restoring the gravity anomalies (including TC) and the indirect effect was made from various reduction methods on the EIGEN-CG03C reference field. The results are compared to the geometric geoid undulation determined from 503 GPS/levelling points after LSC fitting.

The analysis of all computation methods shows that RTM reduction method is the optimal and the residual gravity anomaly and indirect effect are smaller and smoother than other methods. It also shows that the gravimetric and hybrid geoids from RTM reduction method are more accurate than the other methods proved by the analysis with GPS/levelling data.

We conclude that the RTM method is the most suitable for calculating topographic effect in the precise geoid determination of Korea.

Acknowledgments This research was supported by a grant(code 07KLSGC02) from Cutting-edge Urban Development – Korean Land Spatialization Research Project funded by Ministry of Land, Transport and Maritime Affairs of Korean government.

References

Bajracharya, S. (2003). Terrain effects on geoid determination, Ph.D. dissertation, University of Calgary, Canada.

Forsberg, R. (1984). Terrain corrections for gravity measurements, M.Sc. Thesis, Department of Surveying Engineering, University of Calgary, Calgary, Alberta, Canada.

Forsberg, R. and M.G. Sideris (1993). Geoid computation by the multi-band spherical FFT approach. *Manuscr. Geod.*, 18, 82–90.

Forsberg, R., C.C. Tscherning, and P. Kundsen (2003). An overview manual of the Gravsoft, Kort & Matrikelstyrelse.

Förste, C., F. Flechtner, R. Schmidt, U. Meyer, R. Stubenvoll, F. Barthelmes, R. König, K.H. Neumayer, M. Rothacher, C.H. Reigber, R. Biancale, S. Bruinsma, J.M.. Lemoine, and J.C. Raimondo (2005). A new high resolution global gravity field model derived from combination of GRACE and CHAMP mission and altimetry/gravimetry surface gravity data, EGU general assembly 2005, Vienna, Austria, pp. 24–29.

Heck, B. (2003) On Helmert's methods of condensation. *J. Geodesy*, 77(3–4), 155–170.

Heiskanen, W.A. and H. Moritz (1967). Physical geodesy. W.H. Freeman and Co., San Fransisco.

Iliffe, J.C., M. Ziebart, P.A. Cross, R. Forsberg, G.. Strykowski, and C.C. Tscherning (2003). OSGM02: a new model for converting GPS-derived heights to local height datums in Great Britain and Ireland. *Survey Rev.*, 37(290), 276–293.

Omang, O.C.D. and R. Forsberg (2000). How to handle topography in practical geoid determination: three examples. *Bull. Geod.*, 74, 458–466.

Schwarz, K.P. M.G. Sideris, and R. Forsberg (1990). Use of FFT methods in physical geodesy. *Geophys. J. Int.*, 100, 485–514.

Tscherning, C.C., P. Knudsen, and R. Forsberg (1994). Description of the GRAVSOFT package, Technical Report. Geophysical Institute, University of Copenhagen, Denmark.

Vanicek, P. and W.E. Featherstone (1998). Performance of the three types of Stokes's kernel in the combined solution for the geoid. *J. Geodesy*, 72(12), 684–697.

Wong, L. and R. Gore (1969). Accuracy of geoid heights from modified Stokes kernels. *Geophys. J. Royal Astron. Soc.*, 18, 81–91.

Yun, H.S. (1999). Precision geoid determination by spherical FFT in and around the Korean peninsula. *Earth Planets Space*, 51, 13–18.

Chapter 36

Analysis of Recent Global Geopotential Models Over the Croatian Territory

M. Liker, M. Lučić, B. Barišić, M. Repanić, I. Grgić, and T. Bašić

Abstract Independent quality control of the national geoid model HRG2000 was performed using 65 control points, obtained through the realization of EUVN and EUVN_DA projects and the Croatian fundamental gravity network. Ellipsoidal heights and positions of the control points are precisely determined by GNSS measurements while the geodetic heights are obtained by geometric levelling.

The latest geoid model HRG2000 is related to the old vertical system. The analysis indicated the need for a new improved national geoid model which has to be connected to the new vertical system HVRS71. As preparation, and as first step, an analysis of the global geopotential models was made, using eleven recent CHAMP and/or GRACE global models. The statistics of the differences between GNSS/levelling height anomalies (ζ_{HVRS71}) and corresponding anomalies obtained from global geopotential models (ζ_{MODEL}) shows that EGM2008 model is most suitable at this moment. Another interesting fact is that all global models are approximately 93 cm above the new Croatian vertical datum.

36.1 Introduction

In the Republic of Croatia there are two vertical systems currently in use. The older one is known as TRIESTE, and the more recent one is known as HVRS71. By 2010 Croatia should change the old vertical system to the new one. The national geoid model, HRG2000, is related to the old vertical system. This analysis is the preparation for the modelling of the national geoid model that will be connected to the new vertical system. The differences of height anomalies calculated from control GNSS/levelling points and those from global geopotential models are the indicator of which global geopotential model is the best for describing Earth's gravity field on our territory. Global geopotential models are usually used for the definition of long wavelength gravity field structures in geoid modelling.

The differences between height anomalies that were attained from three sources were used in the analysis.

- Height anomalies, calculated from GNSS/levelling data available at EUVN, EUVN_DA and FGN (Fundamental Gravimetric Network) points (h_{GNSS}-$H_{HVRS71} = \zeta_{HVRS71}$).
- Height anomalies, interpolated from the HRG2000 national geoid model ($\zeta_{HRG2000}$), and the
- Height anomalies obtained from eleven global geopotential models (ζ_{MODEL}).

36.2 Used Data

Altogether 65 EUVN, EUVN_DA and FGN control points were used in the analysis.

EUVN (EUropean Vertical Network) project in Croatia was realized in 1997. Eight EUVN points were defined; see Marjanović and Rašić (1998). The first analysis of geoid heights indicated two problematic points (HR05 Split and HR01 Bakar), see Kenyeres et al. (2002).

The problems were solved through EUVN Densification Action (EUVN_DA) project in 2005,

M. Liker (✉)
Croatian Geodetic Institute, Zagreb 10144, Croatia
e-mail: mihajla.liker@cgi.hr

S.P. Mertikas (ed.), *Gravity, Geoid and Earth Observation*, International Association of Geodesy Symposia 135,
DOI 10.1007/978-3-642-10634-7_36, © Springer-Verlag Berlin Heidelberg 2010

after the Croatian Geodetic Institute took the national coordination of the project. The number of EUVN sites has extended from 8 to 20. With the realization of the project, GNSS/levelling/ gravimetric points were determined in both new and old Croatian height systems.

The control points include twenty EUVN and EUVN_DA points and 45 points of the Croatian Fundamental Gravity Network (FGN). Ellipsoidal heights and positions are precisely defined by GNSS measurements while the geodetic heights are obtained by geometric levelling. The heights of all points are expressed in the old (TRIESTE) and new (HVRS71) national vertical systems.

The great value of these points is that they are all expressed in both height systems (normal-orthometric heights) and that all points have GNSS/levelling/ gravimetric data.

36.3 HVRS71 and TRIESTE Height Datum

In Croatia there are two vertical systems currently in use. The old one known as TRIESTE and the new one named HVRS71.

The old vertical system is defined for the epoch 1,875.0 by the averaging of 1-year tide gauge measurements in Trieste. The new vertical datum is based on zero-surface reference determined by the averaging of sea level data observed over 18.6 year period at five tide gauges along the Croatian (four) and Slovenian (one) part of the Adriatic coast and defined at the epoch 1,971.5. The extension of vertical datum to the continental part of Croatia has been realized through precise levelling using normal orthometric heights. On Fig. 36.1 one can see the height differences (H_{HVRS}-$H_{TRIESTE}$) of the two systems in discrete points when the shift of 22.7 cm is removed (the HVRS71 datum is for 22.7 cm higher then TRIESTE).

36.4 HRG2000 National Geoid Model

Croatia has a difficult shape for geoid determination. Furthermore, the Adriatic coast is extremely demanding for geoid modelling as very high mountain massif is raising fast from sea, causing high geoid gradients. In Croatia, the HRG2000 (HRvatski Geoid, 2000) national geoid model is currently in use, and it is fitted to the old Croatian height system TRIESTE.

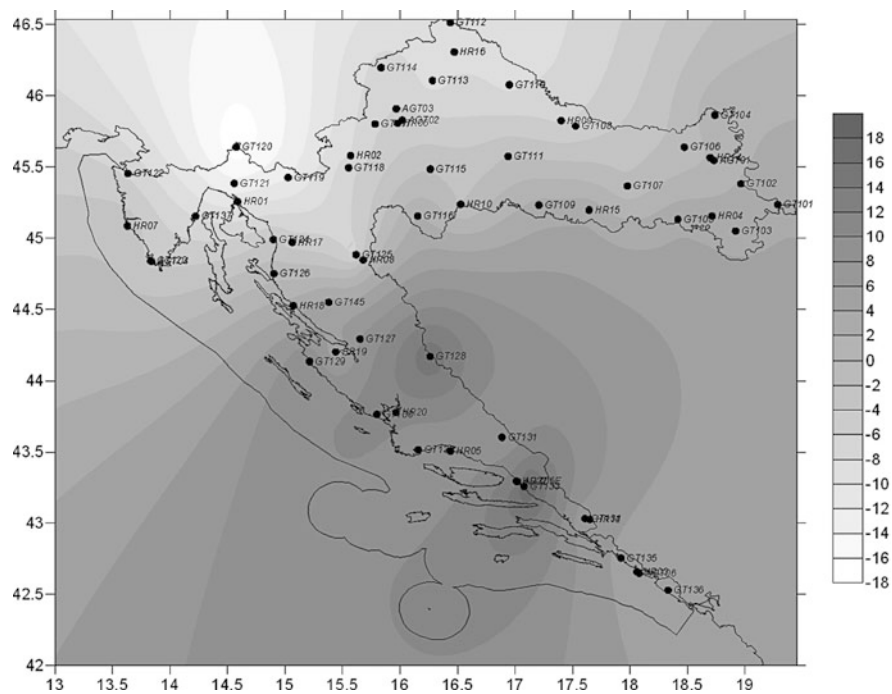


Fig. 36.1 Height differences between HVRS71 (new) and TRIESTE (old) vertical system (H_{HVRS}-$H_{TRIESTE}$)

The HRG2000 geoid model was developed at the Department for Geomatics at the Faculty of Geodesy, University of Zagreb, at 2000, see Bašić (2001). State Geodetic Administration proclaimed HRG2000 as the official geoid surface of the Republic of Croatia. This geoid model was calculated by least squares collocation. The following input data were used: global geopotential model EGM96, free-air gravity anomalies, height anomalies from GNSS/levelling data and high-resolution digital terrain models. For height anomaly interpolation a computer program was developed: IHRG2000. In IHRG2000 there are two interpolation options: bilinear and spline, see Bašić and Šljivarić (2003) and Bašić and Hećimović (2006). In this analysis bilinear interpolation was used.

Figure 36.2 shows height anomaly differences ($\zeta_{TRIESTE}$-$\zeta_{HRG2000}$), at discrete points between the old national vertical system TRIESTE and the national geoid model HRG2000. Statistical values are presented in Table 36.1.

Table 36.1 Statistical values of height anomaly differences ($\Delta\zeta$) at the control set

$\Delta\zeta$	AVERAGE [cm]	ST. DEV [cm]	MIN [cm]	MAX [cm]	RANGE [cm]
$\zeta_{TRIESTE}$-$\zeta_{HRG2000}$	0.47	11.0	–22.8	26.0	48.8

36.5 Global Geopotential Models

Height anomaly data, obtained from the International Centre for Global Earth Models (ICGEM) (URL1), were used in the analysis. The setting was: refsys – GRS80, functional – height anomaly, tide system – use unmodified model, gridstep – 0.01°, grid boundaries – 13° – 19.45° E, 42° – 46.54° N. The Surfer 8 software was used to perform bilinear interpolation of Z (ζ) value.

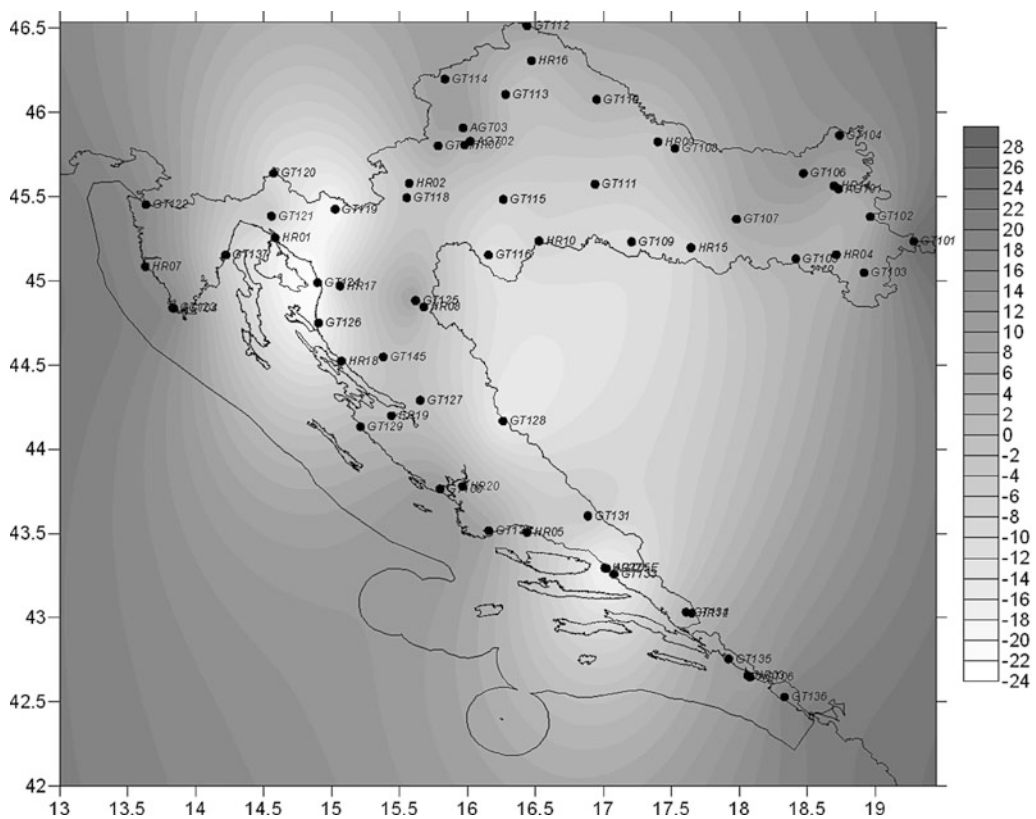


Fig. 36.2 Difference between height anomalies ($\zeta_{TRIESTE}$-$\zeta_{HRG2000}$), the unit is cm

Table 36.2 Global geopotential models that are used in this paper

MODEL	Max. degree	Year	Data[a]
EGM2008	2160×2159	2008	S(Grace),G,A
EGM2008(360)	360×360	2008	S(Grace),G,A
EGM96	360×360	1996	EGM96S,G,A
EIGEN-CGO1C	360×360	2004	S(Champ, Grace),G,A
EIGEN-GL04C	360×360	2006	S(Grace, Lageos),G,A

[a]S – satellite tracking data, G – gravity data, A – altimetry data.

Eleven models were analysed, but only the results of five models are presented in this article, see Table 36.2. These were chosen since they have better statistics in the height anomaly comparison. The following models were not included in the paper: EIGEN-CG03C, AIUMB-CHAMP01S, ITG-GRACE02S, GGM02C, EIGEN-CHAMP03S and ITG-GRACE03.

In winter 2008, National Geospatial-Intelligence Agency (NGA), EGM Development Team, has publicly released the new global geopotential model, EGM2008. EGM2008 model is complete to the degree and order 2,159, and contains additional spherical harmonic coefficients extending to degree 2,190 and order 2,159. Taking into consideration that the "old" models have been expanded to degree and order 360, the results are not so surprising. EGM2008 incorporates improved 5×5′ gravity anomalies and the latest GRACE based satellite solution (ITG-GRACE03S). EGM2008 also includes improved altimetry-derived gravity anomalies, estimated using PGM2007B model and its implied Dynamic Ocean Topography (DOT) model as reference, see Pavlis et al. (2008). The EGM2008 model is also available to degree and order 360 form (EGM2008(360)) (URL 2).

36.6 Results

Height anomalies obtained from three different sources were used in the analysis.

The first group in Table 36.3 represents height anomalies calculated from ground GNSS/levelling data at the EUVN, EUVN_DA and FGN (Fundamental Gravimetric Network) points (h_{GNSS}-H_{HVRS71}=ζ_{HVRS71}, h_{GNSS}-$H_{TRIESTE}$=$\zeta_{TRIESTE}$). The second and the third groups were acquired by interpolation from HRG2000 national geoid model ($\zeta_{HRG2000}$) and global geopotential models (ζ_{MODEL}).

Average in Table 36.3 is the arithmetic mean of height anomalies, calculated for discrete points, that refers to height reference surfaces of TRIESTE and HVRS71 vertical system, HRG2000 and five global geopotential models.

Table 36.4 presents the statistical values of height anomaly differences (ζ_{HVRS71}-ζ_{MODEL}) that were obtained by the subtraction of HVRS71 height anomalies from height anomalies interpolated from global geopotential models at discrete points. Reference values were height anomalies calculated from GPS/levelling data and expressed in the new

Table 36.3 Statistical values of height anomalies from three sources of data

Height ano-maly	AVERAGE [m]	ST. DEV. [m]	MIN. [m]	MAX. [m]	RANGE [m]
National vertical systems					
$\zeta_{TRIESTE}$	43.977	1.467	40.112	46.823	6.711
ζ_{HVRS71}	44.204	1.415	40.380	46.877	6.497
National geoid model HRG2000					
$\zeta_{HRG2000}$	43.972	1.493	39.920	46.930	7.010
Global geopotential models					
$\zeta_{EGM2008}$	45.103	1.369	41.483	47.603	6.120
$\zeta_{EGM2008(360)}$	45.095	1.389	41.275	47.162	5.888
ζ_{EGM96}	45.358	1.423	40.571	47.188	6.617
ζ_{CGO1C}	45.058	1.437	40.950	47.150	6.201
ζ_{GL04C}	45.078	1.453	40.783	47.011	6.228

Table 36.4 Statistical values of height anomaly differences between height anomalies refer to Croatian datum HVRS71 (ζ_{HVRS71}) and geopotential models (ζ_{MODEL})

HVRS71 datum (ζ_{HVRS71}-ζ_{MODEL})					
MODEL	AVERAGE [cm]	ST.DEV. [cm]	MIN [cm]	MAX [cm]	RANGE [cm]
HRG2000[a]	23.2	13.0	–10.0	52.4	62.4
EGM2008	–89.9	8.8	–113.5	–66.0	47.5
EGM2008 (360)	–89.1	21.1	–146.8	–28.6	118.2
EGM96	–115.4	29.7	–184.7	–19.1	165.7
EIGEN-CGO1C	–85.4	22.7	–137.3	–27.4	109.9
EIGEN-GL04C	–87.4	23.8	–143.6	–13.5	130.2

[a]National model HRG2000 referred to TRIESTE datum, the shift between two datum's of 23 cm in discrete points isn't removed.

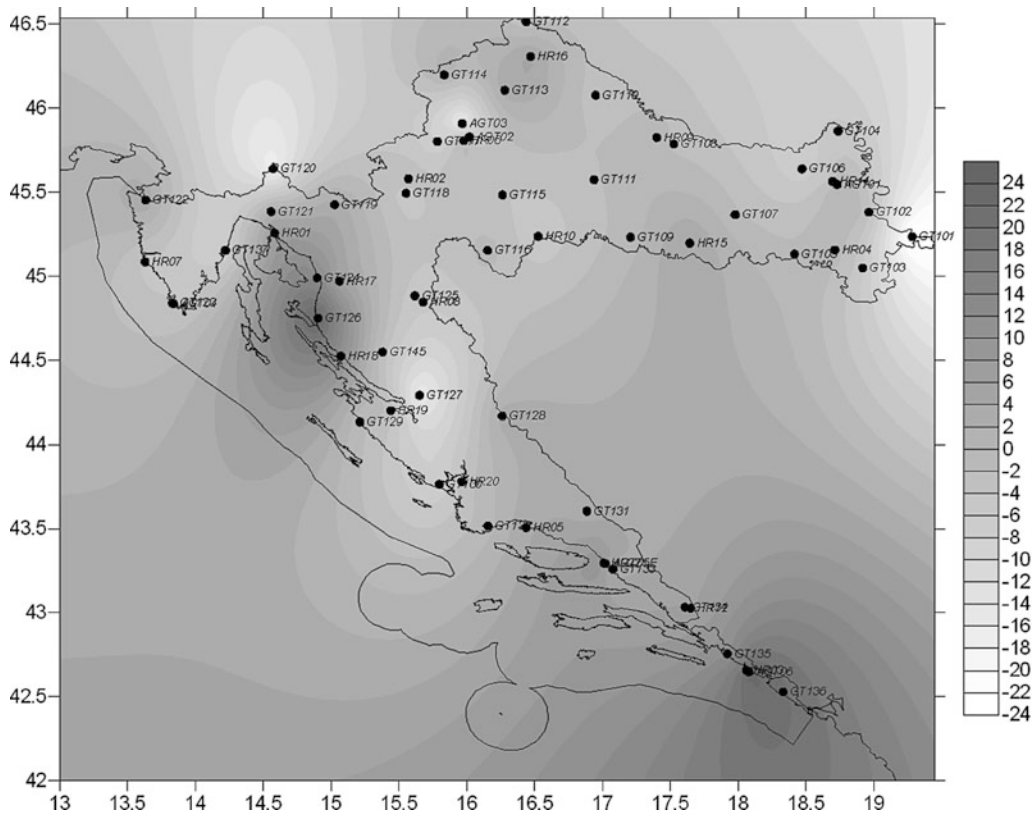


Fig. 36.3 Differences ζ_{HVRS71}-$\zeta_{EGM2008}$ when the shift of 89.9 cm is removed

Croatian vertical system HVRS71 ($\zeta_{HVRS71}=h_{GNSS}-H_{HVRS71}$). The vertical system HVRS71 is chosen as a reference because the purpose of this analysis was to contrive global geopotential model which will be used like as input model in the calculation of the new Croatian local geoid model that will refer to HVRS71 datum.

The statistical values (standard deviation) prove that EGM2008 fits best to the Earth's gravity field on the territory of Croatia. The EGM2008 model, up to degree and order 2160, has approximately three times better statistical values then other global models, see Table 36.4. In Fig. 36.3 it can be seen that maximum and minimum differences (–23.9 and 23.5 cm), when the shift of 89.9 cm is removed, pop up at points with greater normal-orthometric heights (mountains), in area near the national border and at points of great disproportion in height between sea surface and land (Dinaride mountain massif). GNSS/levelling data of the critical points need to be re-examined in the field and the sources of errors established. EGM2008 is 89.9 cm above HVRS71 datum and 112.6 cm above TRIESTE datum.

The global model EGM2008 (360), that is expanded to the degree and order 360, also has better statistical indicators than other models with the same expansion, see Table 36.4. Before the EGM2008 model was published, models EIGEN-CG01C and EIGEN-GL04C were the models with the best statistical values for Croatian territory. If all global models are taken into account, HVRS71 datum is approximately 93.2 cm below the referent surfaces of global geopotential models.

36.7 Conclusions

The purpose of the analysis of eleven global geopotential models was to find the most suitable Earth gravity model for Croatian territory. In this paper five models that give the best statistical results were presented. Without any doubt, the newest global model,

EGM2008, showed the best results. With EGM2008, a new era in geoid modelling started. As was already pointed out, the EGM2008, up to degree and order 2160, has three times better statistical indicators than other "old" global models, expanded "only" to the degree and order 360. It will be interesting to see the results of the modelling of new Croatian geoid model with the presumption that EGM2008 will be used for the definition of long-wavelength gravity structures in the calculation procedures.

References

Bašić, T. (2001). Detailed geoid model of the Republic of Croatia (in Croatian). Reports of the state geodetic administration on scientific and professional projects in the year 2000. Zagreb, Ed. Landek I., pp. 11–22.

Bašić, T. and M. Šljivarić (2003). Utility programs for using the data of the official croatian geoid and coordinate transformation between HDKS and ETRS. Reports of the State Geodetic Administration on Scientific and Professional Projects from the Year 2001. Zagreb, Ed. Landek I., pp. 21–32.

Bašić, T. and Ž. Hećimović (2006). Latest geoid determinations for the Republic of Croatia. *Newton's Bullet.*, 3. http://www.iges.polimi.it/index/pubbli/new_bulletins.htm.

Kenyeres, A., J. Ihde, et al. (2002). EUREF Action for the densification of the EUVN Network. Presented at the EUREF Symposium, Ponta Delgada.

Marjanović, M. and Lj. Rašić (1998). Results of the EUVN 1997 GPS Campaign in Croatia. Paper presented at the Second International Symposium Geodynamics of the Alps-Adria Area by means of Terrestrial and Satellite Methods, Dubrovnik.

Pavlis, N.K., S.A. Holmes, S.C. Kenyon, and J.K. Factor (2008). An earth gravitational model to degree 2160: EGM2008. *Geophys. Res. Abs.,* 10.

URL1 (2008), http://icgem.gfzpotsdam.de/ICGEM/ICGEM.html.

URL2 (2008), http://earth-info.nima.mil/GandG/wgs84/ gravitymod /egm2008/index.html/

Chapter 37

On the Merging of Heterogeneous Height Data from SRTM, ICESat and Survey Control Monuments for Establishing Vertical Control in Greece: An Initial Assessment and Validation

D. Delikaraoglou and I. Mintourakis

Abstract Earth surface elevations can be utilized in a variety of applications including e.g., terrain reductions for accurate geoid modeling, assessment of the vertical accuracy of Digital Elevation Models (DEMs), geodetic monitoring and characterization of urban areas. In this paper we are concerned with the rigorous merging of heterogeneous height data for providing vertical control in Greece. We assess and validate the accuracy of 3" $\times$3" SRTM grid elevations in Greece (a) by using a set of Survey Control Monuments (SCMs), used for geodynamic applications or for conventional ground geodetic control, and (b) by using an elevation dataset derived from the Geoscience Laser Altimeter System (GLAS) on the Ice, Cloud, and land Elevation Satellite (ICESat).

In order to conduct a consistent comparison of these data sets we studied various datum and calibration issues, and used geoid undulations derived from the spherical harmonic representations of EGM96 and EGM08. We also used various interpolation schemes to calculate the SRTM grid elevations at the irregularly spaced SCMs and the ICESat's footprint locations. Differences of the SRTM vis-à-vis SCM and ICESat elevations will be presented, together with a discussion of our findings regarding the various effects that influence any combination of these height data. The product may provide vertical georeferencing and associated height accuracy values which are deemed useful for numerous emerging applications such as environmental monitoring, remote sensing, lidar, and digital elevation modeling.

D. Delikaraoglou (✉)
Department of Surveying Engineering, National Technical University of Athens, Zografos 15780, Greece
e-mail: ddeli@mail.ntua.gr

37.1 Introduction

Assessing the quality of the DEM datasets is crucial in geoid determinations, where any errors in the digital elevation models will propagate into the geoid models, e.g., in interpolating free-air gravity anomalies.

The accuracy of a DEM depends on many factors e.g., the number of sampling points and their spatial distributions, the methods used for interpolating surface elevations and the propagated errors from the source data. Nowadays Synthetic Aperture Radar (SAR) data has become a useful source for generating accurate DEM datasets since it has high resolution, coverage and accuracy over large areas. The Shuttle Radar Topography Mission (SRTM) of the Space Shuttle Endeavour, in February 2000, has provided data with 3 arcsec resolution and $\pm$16 m absolute height errors (at 90% confidence level), cf. Rodriguez et al. (2005). In January 2003, a new spaceborne geodetic tool was placed into a 600 km, near polar Earth orbit on ICESat, the *Geoscience Laser Altimeter System* (GLAS) – a space-based LIDAR, was installed. GLAS was designed to generate high accuracy profiles of the polar ice sheets in order to enable detection of surface change (Zwally et al., 2002). ICESat provides global measurements of elevation, and repeats measurements along nearly-identical tracks which provide new surface elevation grids of the ice sheets and coastal areas, with greater latitudinal extent and fewer slope-related effects than radar altimetry.

S.P. Mertikas (ed.), *Gravity, Geoid and Earth Observation*, International Association of Geodesy Symposia 135,
DOI 10.1007/978-3-642-10634-7_37, © Springer-Verlag Berlin Heidelberg 2010

37.2 Study Area

The topography of Greece, because of its location at the meeting-point of three continents includes a multitude of high mountains, flat and rolling areas, coastal plains and bays and hundreds of kilometres of coastline. The study area covers Greece's entire territory that exhibits elevations ranging from 0 to 2,900 m above sea level and terrain slopes ranging on average from 0° to 20° and on extreme cases ranging up to 87°.

This study focuses on estimating the mean elevation error in the SRTM DEM using available ICESat data profiles over Greece, including the islands, as well as terrestrial discrete elevations at some 25,000 Survey Control Monuments (SCMs) which constitute the larger part of the national geodetic framework. The latter have been established over the last several decades using various geodetic techniques, including triangulation, Doppler Transit, mobile Satellite Laser Ranging, and GPS measurements. The network is therefore very diverse in terms of quality and spatial resolution. Their height above sea level has been determined using spirit and trigonometric leveling, as well as GPS leveling schemes.

37.3 SCM vs. SRTM Data Comparisons

The main goal of our SRTM vs. SCM elevation comparison was to answer the following questions pertaining to the SRTM performance over Greece:

1. Does absolute vertical accuracy of the 3″x3″ SRTM data exceed the nominal ±16 m value?
2. How do slope- and aspect-related effects influence the SRTM data accuracy?
3. Is it possible to increase the accuracy of the SRTM elevation predictions using slope and aspect information?

To address these questions, we examined the differences ($H_{SCM} - H_{SRTM}$) between the elevations from SRTM data interpolated at each SCM location and the corresponding available SCM elevations which we assumed to be accurate and, thus, used as reference values. The SRTM DEM refers to mean sea level realized by the EGM96 geoid model described by Lemoine et al. (1998).

For the interpolation we used various methods such as the *Near Neighbour* (NN), *the Inverse Distance squared Weighting* (ID^2W) and the Bilinear (BIL) schemes, which are computationally straightforward and relatively simple to implement. A small number of SCM points (less than 100 points overall) at SRTM voids (Hall et al., 2005) were excluded from any subsequent evaluation.

Visualization of the computed elevation differences did not reveal any uniform distribution of the discrepancies. Generally, greater discrepancies were associated with rugged terrain, while smaller discrepancies were noted at coastal and plain areas, suggesting that terrain characteristics (slope and slope direction) influence the SRTM data. These well known effects in the SRTM data have previously been reported and investigated, for example, by Miliaresis and Paraschou (2005). Our analysis showed that the observed differences at 8,397 points where the SRTM-derived slope values were greater than 10° exhibited almost twice of the mean difference and standard deviation compared to the corresponding values at the remaining 16,871 points where the slope values were $\leq 10°$.

Therefore we analyzed the magnitude of the absolute errors in the SRTM data with respect to slope and aspect characteristics of the landscape at each SCM point. "Slope" at a SCM point was computed from the SRTM grid data as the maximum rate of change in the elevation value from its eight neighboring cells. Specifically, we are interested in the angle of the slope defined by the so-called "rise" (vertical distance change) and "run" (horizontal distance change) values. The slope values were expressed in integer degrees between 0° and 90°. We are also interested in the so-called aspect effect, which related to the Space Shuttle's orbit characteristics and is mainly due to the view direction of the imaging radar at the time of the data acquisition and depends upon the imaging of each point on the Earth's surface from an ascending or descending orbit. The "Aspect" value at a point is defined as the down-slope direction of the maximum rate of change in the elevation value from the cell of the said point to its eight neighbors. The angle between the slope direction and North is expressed in integer degrees between 0° and 360°.

Following these pre-processing steps we estimated terrain elevations and checked whether the accuracy of predictions can be improved using available information regarding the slope and aspect characteristics of the landscape. For that purpose we used multiple regression models of the general form

$$H_{\text{pred}}^{\text{SRTM}} = \text{B}_0 + \text{B}_1{}^*\text{H}_{\text{SRTM}} + \text{B}_2{}^*\text{Slope} + \text{B}_3{}^*\text{Aspect} \quad (1)$$

to describe the relationship between the orthometric height of a point, used as the "predicted" (dependent) variable, and the interpolated H_{SRTM}, Slope and Aspect values used as "predictor" variables (independent) evaluated at each SCM point. We examined three sub-models: Model LR1, which contained only the first two terms on the right hand side of the general model (1), and models LR2 and LR3 each containing, in addition, the third and fourth terms. Table 37.1 shows statistics of the residual ΔH differences (i.e., $H_{\text{SCM}} - H_{\text{pred}}^{\text{SRTM}}$) coming from the regression models using the aforementioned interpolation schemes. In all analyses outlier data were rejected in terms of the ±3 rejection criterion applied on the standardized residuals from each model. From the SRTM elevation comparisons at all the SCM points, it is evident that the ID^2W and BIL interpolation schemes are identical and the respective mean differences agreed at the sub-cm level. The corresponding mean differences from the nearest neighbour interpolation were worse by about 9–11 cm. In all cases, among the three linear regression sub-models, the best performance was exhibited by the LR3 model, followed by the LR2 and LR1 model.

Analogous analyses revealed significant improvement in the ΔH differences when we compared only SCM points on terrain characterized by slope values $\leq 10°$. This was evident, for example, from the decrease in the mean differences by about 12–27 cm (e.g., –0.313 m vs. –0.587 m in the NN/LR1 case, and –0.262 m vs. –0.387 m in the ID^2W/ or BIL/LR3 cases). Improvement in the standard deviations (e.g., from 8.334 to 6.907 m in the NN/LR1 case, and from 7.78 m to 6.66 m in the ID^2W/ or BIL/LR3 cases) were also observed.

We also examined the Slope-Curve-Fitting (SCF) models of the general form:

$$H_{\text{pred}}^{\text{SRTM}} - \text{H}_{\text{SRTM}} = \text{C}_0 + \text{C}_1{}^*\text{Slope} + \text{C}_2{}^*\text{Slope}^2 + \text{C}_3{}^*\text{Slope}^3 \quad (2)$$

where the coefficients C_i were determined by fitting the SRTM-derived slope data to the observed $\text{H}_{\text{SCM}} - \text{H}_{\text{SRTM}}$ elevation differences. Three sub-models were tested: a linear model (i.e., containing only the C_0, and C_1 terms), and the quadratic and cubic models each containing, in addition, the C_2, and C_3 terms, respectively. The statistics (in terms of the noted mean differences and their standard deviations) of these models are shown in Table 37.2. The results are essentially the same (at the centimeter level) as the previously used linear regression models.

37.4 ICESat vs. SRTM Data Comparisons

In order to make comparable the ICESat- and the SRTM-derived elevations we referred both sets to the same vertical datum. Since the ICESat elevations

Table 37.1 Statistics of the ($H_{\text{SCM}} - H_{\text{pred}}^{\text{SRTM}}$) differences (in metres), using the regression models described by Eq. (1)

	All SCM points (regardless of Slope values)			Only points with slope values ≤ 10°		
	# Points	Mean	Std.D.	# Points	Mean	Std.D.
Interpolation/regression model						
NN/LR1	25,049	–0.587	8.334	16,752	–0.313	6.907
NN/LR2	25,059	–0.504	7.780	16,751	–0.314	6.667
NN/LR3	25,059	–0.504	7.780	16,751	–0.314	6.663
ID^2W/LR1	25,071	–0.496	8.619	16,772	–0.258	7.148
ID^2W/LR2	25,086	–0.410	7.584	16,763	–0.275	6.780
ID^2W/LR3	25,090	–0.404	7.586	16,762	–0.273	6.769
BIL/LR1	25,071	–0.492	8.462	16,778	–0.246	7.078
BIL/LR2	25,098	–0.394	7.440	16,768	–0.260	6.706
BIL/LR3	25,099	–0.387	7.431	16,767	–0.262	6.691

Table 37.2 Statistics of the ($H_{\mathrm{SCM}} - H_{\mathrm{pred}}^{\mathrm{SRTM}}$) differences (in metres), using the Slope Curve Fitting models

	All SCM points (regardless of Slope values)			Only points with slope values ≤ 10°		
	# Points	Mean	Std.D.	# Points	Mean	Std.D.
Interpolation/slope curve fit model						
NN/linear	25,060	–0.501	7.857	16,751	–0.316	6.754
NN/quadratic	25,060	–0.498	7.872	16,751	–0.316	6.744
NN/cubic	25,060	–0.498	7.884	16,751	–0.316	6.744
ID^2W/linear	25,086	–0.408	7.689	16,762	–0.274	6.914
ID^2W/quadratic	25,086	–0.407	7.691	16,762	–0.274	6.895
ID^2W/cubic	25,086	–0.408	7.712	16,762	–0.274	6.892
BIL/linear	25,092	–0.394	7.527	16,762	–0.267	6.836
BIL/quadratic	25,092	–0.393	7.530	16,762	–0.267	6.817
BIL/cubic	25,092	–0.394	7.552	16,762	–0.267	6.815

Table 37.3 Statistical results of the $Dh = h_{Icesat} - h_{SRTM}$ (filtered) differences observed over Greece

	Entire sample of data		Edited sample		
Threshold edit level a ($\mu_{\mathrm{Dh}} \pm a^* \sigma_{\mathrm{Dh}}$)	Total # of points	Points on land or on land and sea	# of filtered points (% accepted)	Mean difference (m)	Std deviation (m)
0.50	480,947	Land only	280,526 (58.3%)	0.102	1.596
0.75			346,482 (72.0%)	0.128	2.209
0.50	1,281,134	Land and sea	1,066,686 (83.3%)	–0.031	0.942
0.75			1,132,902 (88.4%)	–0.015	1.305

are expressed as geometric (ellipsoidal) heights with respect to the TOPEX ellipsoid, a constant value of 0.70 m was subtracted from all elevations in order to transform the ICESat data to the WGS84 ellipsoid. The SRTM orthometric elevations, referred to the EGM96 geoid, were interpolated from the SRTM grid to the ICESat footprint locations. These were transformed into ellipsoidal heights referenced to the WGS84 ellipsoid by adding the geoid undulations $\mathrm{N_{EGM96}}$ computed from the EGM96 spherical harmonic coefficients. A constant correction $\mathrm{dN_{EGM96}} = -0.53$ m was also added that enables the EGM96-derived undulations to refer to the WGS84 ellipsoid (Lemoine et al., 1998). We made statistical comparisons based on the differences $Dh = h_{Icesat} - h_{SRTM}$ from all the available ICESat data over Greece (for convenience we dropped the superscript WGS84, understanding that both ellipsoidal height data set now refer to WGS84). The Dh differences can be partially attributed to the different errors inherent in both data sets, such as unaccounted atmospheric effects on the GLAS data, tree canopy effects on the GLAS waveforms, vegetation and terrain slope effects on the SRTM elevations, ICESat and SRTM orbit accuracy, calibration errors etc. For the computed statistics shown in Table 37.3, we distinguish two data subsets: the first including ICESat footprints only on land, and the second on both land and sea. Extreme differences (outliers) were removed using the following "a*sigma" edit scheme according to the criterion $\mu_{\mathrm{Dh}} - a^* \sigma_{\mathrm{Dh}} \leq \mathrm{Dh} \leq \mu_{\mathrm{Dh}} + a^* \sigma_{\mathrm{Dh}}$, where a is a threshold edit factor (e.g., the lower the value of a, the more data is removed due to this editing), and μ_{Dh} and σ_{Dh} are the mean and standard deviation of the observed differences computed using ICESat elevations only available on land. The values $\mu_{\mathrm{Dh}} = -0.805$ m and $\sigma_{\mathrm{Dh}} = 6.234$ m were considered representative enough to be used for all points.

In order to more closely examine the ICESat and SRTM elevation datasets, we computed estimates of "geoid undulations" $N = h_{Icesat} - H_{SRTM}$ as the difference between the entire set of available ICESat ellipsoidal heights and SRTM orthometric heights interpolated at the corresponding ICESat footprint locations. We tested the observed differences $\mathrm{dN} = \mathrm{N} - \mathrm{N_{Reference}}$ on land and sea, using reference geoid undulations (a) the geoid computed (over land and sea) from the EGM96 and EGM08 (Pavlis et al., 2008) spherical

Table 37. 4 Statistics of the differences $dN = h_{ICESat} - H_{SRTM} - N_{Reference}$ over Greece

Thres-hold edit level a ($\mu_{DH} \pm a^* \sigma_{DH}$)	Along-track filter (s)	# Points	Land/sea	Ref. model	Min difference (m)	Max difference (m)	Mean difference (m)	Std. deviation (m)
0.75	8.00	283,981	L	EGM96	−3.522	1.620	−0.366	0.636
		1,072,432	L & S		−3.522	1.620	−0.507	0.475
		739,608	S		−2.716	1.0911	−0.551	0.380
		283,981	L	EGM08	−3.202	2.462	0.018	0.688
		1,072,432	L & S		−3.202	2.462	−0.094	0.481
		739,608	S		−1.926	1.521	−0.125	0.359
		739,608	S	KMSS04	−2.279	1.396	−0.069	0.260
	12.00	284,466	L	EGM96	−2.615	1.369	−0.395	0.595
		1,067,593	L & S		−2.615	1.369	−0.496	0.469
		734,530	S		−2.447	0.774	−0.521	0.398
		284,466	L	EGM08	−2.254	2.183	−0.013	0.654
		1,067,593	L & S		−2.254	2.183	−0.085	0.486
		734,530	S		−1.826	1.150	−0.096	0.393
		734,530	S	KMSS04	−2.145	1.298	−0.040	0.323
0.50	8.00	206,808	L	EGM96	−2.016	1.123	−0.389	0.488
		990,879	L & S		−2.677	1.123	−0.520	0.407
		741,375	S		−2.677	0.692	−0.550	0.371
		206,808	L	EGM08	−1.797	1.720	0.017	0.549
		990,879	L & S		−1.797	1.720	−0.100	0.406
		741,375	S		−1.779	1.111	−0.123	0.348
		741,375	S	KMSS04	−1.672	0.868	−0.066	0.245
	12.00	206,971	L	EGM96	−1.855	0.957	−0.422	0.472
		985,456	L & S		−2.411	0.957	−0.507	0.412
		735,131	S		−2.411	0.639	−0.520	0.387
		206,971	L	EGM08	−1.762	1.529	−0.019	0.537
		985,456	L & S		−1.762	1.529	−0.089	0.424
		735,131	S		−1.672	1.085	−0.094	0.379
		735,131	S	KMSS04	−1.650	1.299	−0.037	0.308

harmonic models, and (b) the KMSS04[1] global Mean Sea Surface model (over the sea). Table 37.4 summarizes the statistical results of these comparisons using (i) rejection criteria for noisy data corresponding to threshold edit levels with $a = 0.5$ and $a = 0.75$, and (ii) Gaussian smoothing filters with temporal windows set at 8 12 s, to reduce the sensitivity of the estimated differences dN to the noise of the ICESat and/or SRTM data. The chosen temporal windows correspond to a wavelength of approximately 60 and 90 km in the along track ICESat data respectively. We found that the mean differences from the combined ICESat/SRTM elevations and the EGM96 geoid undulations range from –36 cm up to –55 cm and from 2 cm up to –12 cm at the EGM08 comparisons. These values are comparable with the accuracy of the EGM96 and EGM08 gravity field models. Better agreement at the EGM08 comparisons is expected since ICESat and SRTM data have been included in the computation of this Earth Gravity Model. We also note that the comparisons of the ICESat/SRTM elevations with the KMSS04 solution for the points at sea yield better results, i.e., up to 50% improvement was observed in the mean differences vis-à-vis the respective EGM08 comparisons at the same points at sea.

37.5 Conclusions

We presented a national scale assessment of the accuracy of SRTM topographic data using the elevations from a large set of Survey Control Monuments (SCM),

[1] KMSS04 is a combined multi-satellite solution based on altimetry data from the Geosat, ERS-1 and -2, GFO and TOPEX/Poseidon satellites and is available from the Danish National Space Centre.

which are part of the national geodetic networks in Greece and from the available ICESat elevations over Greece and the surrounding seas. Linear regression analyses confirmed the strong correlation between the SCM elevations and the SRTM interpolated elevation values and demonstrated that a large part of the dominant random errors in the SRTM elevations, which exhibits geographic variability due to changes in the terrain surface slope and aspect (slope direction), can be recovered using one of the linear regression models we tested. The predictive value of SRTM data for estimating terrain elevations could be significantly improved using SRTM information regarding the slope and aspect characteristics of the lanscape at the points of interest. We demonstrated that the accuracy of the SRTM elevation predictions can exceed the mission goal of 16 m (at 90% confidence level) by a factor of two or more.

This study also examined the elevation values of the SRTM 90-m DEM and point wise elevations from ICESat laser altimetry in order to evaluate their combined use as source of information for regional geoid modeling. Using an optimal along-track filtering scheme to limit errors and time varying effects on the elevations of the ICESat footprints on land and/or in the seas surrounding Greece, it was shown that a good correlation exists between the computed ($h_{ICESat} - H_{SRTM}$) "geoid undulations" and the EGM96- and EGM08- derived geoid models, or the KMSS04 global mean sea surface.

Future investigations will focus on separating the study area into different morphology (hilly plains, mountainous areas, etc.) and land use covers (e.g., waters, wetlands, forests, bare grounds etc.), to identify dependency of the SRTM/ICESat uncertainties over different terrain surface types (e.g., areas of low/high relief and sparse/dense tree cover).

Acknowledgments The authors would like to thank the two anonymous reviewers of the initial manuscript for their useful comments and suggestions

References

Hall, O., G. Falorni, and R.L. Bras (2005). Characterization and quantification of data voids in the shuttle radar topography mission data. *IEEE Geosci. Remote Sens. Lett.*, 2(2), 177–181.

Lemoine, F.G., S.C. Kenyon, J.K. Factor, R.G. Trimmer, N.K. Pavlis, D.S. Chinn, C.M. Cox, S.M. Klosko, S.B. Luthcke, M.H. Torrence, Y.M. Wang, R.G. Williamson, E.C. Pavlis, R.H. Rapp, and T.R. Olson (1998). The development of the joint NASA GSFC and the national imagery and mapping agency (NIMA) geopotential model EGM96. NASA Tech. Pub. 1998-206861..Goddard Space Flight Center, Greenbelt, Maryland, USA.

Miliaresis, G.Ch. and C.V.E. Paraschou (2005). Vertical accuracy of the SRTM DTED level 1 of Crete. *Int. J. Appl. Earth Observation Geoinformation*, 7(1), 49–59.

Pavlis, N.K., S.A. Holmes, S.C. Kenyon, and J.K. Factor (2008). An earth gravitational model to degree 2160: EGM2008. Presented at the 2008 European Geosciences Union General Assembly. Vienna, Austria, April 13–18.

Rodriguez, E., C.S. Morris, J.E. Belz, E.C. Chapin, J.M. Martin, W. Daffer, and S. Hensley (2005). An assessment of the SRTM topographic products. Technical Report JPL D31639, Jet Propulsion Laboratory, Pasadena, California, 143 pp.

Zwally, H.J., B. Schutz, W. Abdalati, J. Abshire, C. Bentley, A. Brenner, J. Bufton, J. Dezio, D. Hancock, D. Harding, T. Herring, B. Minster, K. Quinn, S. Palm, J. Spinhirne, and R. Thomas (2002). ICESat's laser measurements of polar ice, atmosphere, ocean, and land. *J. Geodynamics*, 34(3–4), 405–445.

Chapter 38

Implementing a Dynamic Geoid as a Vertical Datum for Orthometric Heights in Canada

E. Rangelova, G. Fotopoulos, and M.G. Sideris

Abstract The geoid heights in Canada are subject to secular dynamic changes caused by the slow glacial isostatic adjustment of the viscoelastic Earth. As a result, the reference surface for orthometric heights changes with time at a level that is an order of magnitude smaller than the rate of change of heights. The objective of this paper is to provide a feasibility study on implementing the geoid as a dynamic vertical datum. For this purpose, the most accurate GPS ellipsoidal heights from the CBN (Canadian Base Network), orthometric heights from the most recent minimally constrained adjustment of the primary vertical control network and the latest geoid model for Canada are used. In this approach, the dynamic geoid is treated in the context of the combined adjustment of the ellipsoidal, orthometric and geoid heights.

In this paper, it is shown that the present-day accuracy of the three height components precludes the implementation of the dynamic vertical datum, and the accuracy of the orthometric heights appears to be the limiting factor. By means of a simulated example, we demonstrate that the dynamic vertical datum requires an accuracy of 1.0–1.5 cm for each of the three height components. Provided this level of accuracy is reached, the vertical reference surface must be adjusted for the secular geodynamic effect after 8–10 years have elapsed from the reference epoch. For comparison, vertical crustal motion can cause significant systematic discrepancies among the ellipsoidal, orthometric, and geoid heights over a 2-year time interval.

E. Rangelova (✉)
Department of Geomatics Engineering, Schulich School of Engineering, University of Calgary, Calgary, AB, Canada, T2N 1N4
e-mail: evrangel@ucalgary.ca

38.1 Introduction

Canada's official vertical datum (the reference surface for orthometric heights) is the Canadian Geodetic Vertical Datum of 1928 (CGVD28) constrained to the mean sea level of five tide gauges on the Pacific and Atlantic coasts (Véronneau, 2002). In addition to the large east-west tilt of the reference surface as a result of the imposed constraints, the datum is outdated, has limited coverage and large regional systematic errors of up to 1 m. Moreover, the glacial isostatic adjustment of the crust (e.g., Peltier, 2004) causes significant vertical crustal motion (uplift/subsidence) of benchmarks of the vertical control network. All of these effects led to the necessity for a new geoid-based vertical datum compatible with the GNSS positioning technique and easily accessible in the northern parts of Canada, where a vertical control network does not exist (Véronneau et al., 2006).

The geoid in North America, however, experiences large secular rise (1–2 mm/year) as a result of the mass transport beneath the uplifting crust. These significant dynamic variations and the continuously improving accuracy of the regional geoid model (see Huang et al., 2006) aiming towards a cm-level accuracy is the main motivation for investigating the effect of regional geodynamics on the geoid-based vertical datum.

Generally, the dynamic geoid height can be represented as a function of latitude φ and longtitude λ and the time epoch t as follows:

$$N(\varphi, \lambda, t) = N^{\text{stat}}(\varphi, \lambda) + \dot{N}(\varphi, \lambda)t + \overline{N}(\varphi, \lambda, t) \quad (1)$$

where $N^{\text{stat}}(\varphi,\lambda)$ is the static geoid height (also a mean geoid height over a sufficiently long period of time

S.P. Mertikas (ed.), *Gravity, Geoid and Earth Observation*, International Association of Geodesy Symposia 135,
DOI 10.1007/978-3-642-10634-7_38, © Springer-Verlag Berlin Heidelberg 2010

so that all periodic variations average out). $\dot{N}(\varphi, \lambda)$ is the estimated trend (rate of change) of the geoid height from, for example, the empirical models developed by Rangelova and Sideris (2008). The last term in Eq. (1), i.e., $\overline{N}(\varphi, \lambda, t)$, could represent semi-annual, annual, inter-annual and other non-periodic changes in the geoid height. The main periodic signal in North America is the annual cycle of snow mass accumulation and melting (e.g., Rangelova et al., 2008). Other temporal variations of interest are the decadal signal of mass loss in the Alaskan glaciers and Greenland ice sheet and the changes in the hydrological trends over the analyzed time period. The significance of the latter, will decreases as the GRACE time series increases.

The objective of this paper is to provide a feasibility study for incorporating the secular dynamic changes in the geoid height into the vertical datum in Canada. For this purpose, the most accurate GPS ellipsoidal heights from the Canadian Base Network (CBN), orthometric heights from the most recent minimally constrained adjustment of the primary vertical control network, and the latest regional geoid model CGG05 are used.

In the approach adopted herein, the dynamic geoid is treated in the context of the combined least-squares adjustment of the ellipsoidal, orthometric, and geoid heights. This approach provides a means for studying the effect of the secular dynamic component of the geoid height (as well as the crustal motion) and weighting this effect relative to the errors of the three height components.

38.2 Methodology

The observation equation for the combined adjustment of ellipsoidal, orthometric and geoid heights is given as follows:

$$\mathbf{l} = \mathbf{A}\mathbf{x} + \mathbf{v}, \mathbf{C}_v \tag{2}$$

where $\mathbf{l} = [l_1\, l_2 \cdots l_n]^{\mathrm{T}}$ is a vector of height misclosures $l = h - N - H$ (at n benchmarks of the vertical control network) computed with the three height components, i.e., the ellipsoidal height, h, geoid height, N, and orthometric height, H. $\mathbf{x} = [x_1\, x_2 \cdots x_k]^{\mathrm{T}}$ is a vector of k unknown parameters; $\mathbf{A}$ is the coefficient matrix of full column rank, $rank\, \mathbf{A} = k$, and vector rows $\mathbf{a}_i = [a_1\, a_2 \cdots a_k], i = 1, \ldots, n$; $\mathbf{v} = [v_1\, v_2 \cdots v_n]^{\mathrm{T}}$ is a vector of zero-mean residuals.

The covariance matrix $\mathbf{C}_v$ is defined as

$$\mathbf{C}_v = \mathbf{C}_h + \mathbf{C}_H + \mathbf{C}_N \tag{3}$$

where $\mathbf{C}_h$, $\mathbf{C}_H$, and $\mathbf{C}_N$ are the error covariance matrices for the ellipsoidal, orthometric and geoid heights, respectively.

Usually, the systematic component $\mathbf{A}\mathbf{x}$ is parameterized by means of a simple mathematical surface. Previous studies have shown that the classic four-parameter model given by Heiskanen and Moritz (1967) provides the best representation of the systematic errors among the GPS, orthometric, and geoid heights in Canada (e.g., Fotopoulos, 2003). Therefore, the systematic component at point (φ_i, λ_i) is represented as follows:

$$\mathbf{a}_i^{\mathrm{T}}\mathbf{x} = x_1 + x_2 \cos\varphi_i \cos\lambda_i + x_3 \cos\varphi_i \sin\lambda_i + x_4 \sin\varphi_i. \tag{4}$$

In the combined least-squares adjustment model in Eq. (2), $\mathbf{A}\mathbf{x}$ (theoretically) absorbs all distortions, long wavelength geoid errors, and datum inconsistencies among the ellipsoidal, orthometric, and geoid heights (Schwarz et al., 1987). It will also absorb the distortions caused by the different epochs of the levelling measurements in different parts of the vertical control network and the secular dynamic changes of the geoid height.

The accuracy of the estimated systematic component at point i is given by

$$\hat{\sigma}_i^a = \sqrt{\mathbf{a}_i^{\mathrm{T}} \mathbf{C}_{\hat{\mathbf{x}}} \mathbf{a}_i} \tag{5}$$

where the covariance matrix of the estimated parameters $\mathbf{C}_{\hat{\mathbf{x}}}$ is computed as

$$\mathbf{C}_{\hat{\mathbf{x}}} = (\mathbf{A}^{\mathrm{T}} \mathbf{C}_v^{-1} \mathbf{A})^{-1}. \tag{6}$$

Two cases for the covariance matrix $\mathbf{C}_v$ are of practical interest in the combined least-squares adjustment. In the first case, correlations between observations in each height component can be disregarded assuming diagonal matrices $\mathbf{C}_h$, $\mathbf{C}_H$, and $\mathbf{C}_N$. In the second case, the correlations are taken into account through the fully-populated matrices. As shown by Fotopoulos (2003 and 2005) for Canada, overly-optimistic (with

small variance factors) covariance matrices are estimated when the first approach is pursued. Conversely, more realistic error estimates are obtained if the fully-populated covariance matrices are used in the least-squares adjustment model (2).

To study the effect of the secular dynamic changes in the geoid height and crustal uplift, it is assumed that a levelling-based vertical datum is established at an arbitrary epoch t_o. For the same epoch, a static geoid model $N(\varphi,\lambda,t_o)$ is computed. The orthometric height at epoch $t$is computed by means of

$$H(\varphi,\lambda,t) = h(\varphi,\lambda,t) - N(\varphi,\lambda,t_o) - (\mathbf{a}^T\hat{\mathbf{x}})_t \qquad (7)$$

where the systematic component

$$(\mathbf{a}^T\hat{\mathbf{x}})_t = (\mathbf{a}^T\hat{\mathbf{x}})_o + \delta N + \delta H \qquad (8)$$

includes the static component $(\mathbf{a}^T\hat{\mathbf{x}})_o$, the temporal change in the geoid height, $\delta N = (t - t_o)\dot{N}$, and the change in the orthometric height, $\delta H = (t - t_o)\dot{H}$, for the time interval $(t - t_o)$. Ideally, the fundamental point of the vertical datum is assumed to be unaffected by vertical crustal motion, nor does the equipotential surface through the fundamental point change with time.

38.3 Description of Data

A set of 430 of the most accurate GPS-on-benchmark points in Canada (Fig. 38.1), used in the latest error calibration of the CGG05 geoid model (Huang et al., 2006), is provided by Geodetic Survey Division, Natural Resources, Canada. The ellipsoidal heights are determined from the campaign GPS surveys after 1994 in the ITRF1997 reference frame. Epoch rectification of the GPS ellipsoidal heights is currently undertaken (Fotopoulos et al., 2007). The orthometric heights are computed from the geopotential numbers obtained from the minimally constrained least-squares adjustment of the levelling measurements after 1981 with a single reference datum point in Rimouski (Véronneau, 2002). The vertical crustal motion is accounted for in the least-squares adjustment procedure. For all points, the height misclosures are computed together with the fully-populated co-factor matrices and the scale factors for the ellipsoidal, orthometric and geoid heights.

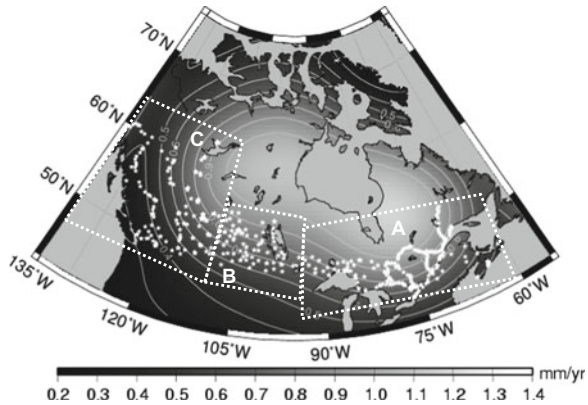


Fig. 38.1 Empirical rates of change of the geoid height and GPS on first order levelling points (*white stars*) for the three studied regions

The data points are divided into three regions, shown in Fig. 38.1, with respect to data coverage and distribution. Region A (206 points) is characterized by densely distributed points along the levelling lines with large data gaps. Region B (76 points) is relatively homogeneously covered, but the data points are sparsely distributed. Region C (148 points) has mixed data coverage.

Statistics of the three data sets is presented in Table 38.1. The accuracy of the orthometric heights degrades from region A to region C as a result of accumulated systematic errors in the vertical control network. The errors of the ellipsoidal heights range from a sub-centimetre level to two decimetres with mean values of 37 mm (for regions A and B) and 47 mm (for region C). The mean error of the geoid heights increases from 28 mm for region B (flat terrain) to 53 mm for region C (rocky terrain).

Figure 38.1 also shows the empirical model of the rate of change of the geoid height used in this study, which is computed by means of an optimal combination of CSR RL-04 GRACE data, vertical velocities

Table 38.1 Statistics of the standard deviation of the ellipsoidal, geoid, and orthometric heights (in mm) computed from the calibrated fully-populated covariance matrices

σ	Region A			Region B			Region C		
	Min	Mean	Max	Min	Mean	Max	Min	Mean	Max
h	6	33	92	9	37	80	5	44	96
H	31	83	142	143	158	169	161	181	208
N	28	34	59	25	28	32	22	53	169

from CBN, and absolute terrestrial gravity rates from the Canadian Gravity Standardization Net. A consistent model for crustal motion is also implemented herein. Details of the computational procedure are presented in Rangelova and Sideris (2008).

38.4 Analysis of Results

The accumulated over a decade effect of the secular dynamic changes of the geoid height and crustal displacement is compared with the calibrated errors of the ellipsoidal, geoid, and orthometric heights for each of the three regions. For this purpose, the following relative variables are defined:

$$\max\left(\frac{(\delta N)_i}{\hat{\sigma}_i^a}\right) \text{ and } \max\left(\frac{(\delta N+\delta H)_i}{\hat{\sigma}_i^a}\right) \qquad (9)$$

which are the maximum ratios of the temporal changes and the estimated error of the systematic component. Values larger than 1.0 (above the noise level) indicate that the secular dynamic effect should be accounted for.

$$\max\left(\frac{\overline{\sigma}_\vartheta}{\hat{\sigma}_i^a}\right), \vartheta = h, H, N \qquad (10)$$

is the maximum ratio of the mean standard deviation $\overline{\sigma}_\vartheta$ for each of the three height components and the estimated error of the systematic component.

38.4.1 Case Study with Calibrated Diagonal Error Covariance Matrices

The dynamic effect in the geoid height and the crustal displacement, computed by means of Eq. (9), is plotted in Fig. 38.2 as a linear increase for a 10-year time interval. Evidently, the change in the geoid height becomes significant (above 1.0 in the plot) after 4 years for region A and after 6 years for regions B and C. The densely distributed GPS-on-benchmarks points and the more accurate orthometric heights in region A result in a more accurately determined systematic component and, consequently, more significant dynamic geoid effect. The latter, however, is far below the mean error of the geoid, computed by means of Eq. (10).

The absolute crustal displacement far exceeds the accuracy of the systematic component for all of the three regions; however, for region A it becomes larger than the mean error of the geoid after 9 years. The rather optimistic accuracy of the orthometric and ellipsoidal heights obtained from the calibrated diagonal error covariance matrices leads to an unrealistically accurate systematic component and overestimated dynamic effect. Another consequence from the up-weighting of the ellipsoidal and orthometric heights is that the geoid errors may appear unrealistically large acting as a limiting factor for incorporating the dynamic effect into the vertical datum.

38.4.2 Case Study with Calibrated Fully-Populated Error Covariance Matrices

In all of the regions, the accumulated effect of the dynamic geoid changes is far below the estimated errors of the systematic component (see Fig. 38.3). The accumulated crustal displacement becomes significant after 5 years for region A and after 10 years for region B. However, it is much less than the mean error of the orthometric heights, which is the least accurate data set among the three height components. For comparison, the mean errors of the ellipsoidal and geoid heights are approximately equal for all of the regions.

The results obtained in this case study lead to some important conclusions. The contemporary accuracy of the three height components precludes the incorporation of the secular dynamic change in the geoid height as well as the crustal displacement in the vertical datum of Canada. Furthermore, the assessment of the contribution of the dynamic components clearly depends on the proper relative weighting of the ellipsoidal, orthometric and geoid heights.

The significance of the secular dynamics is assessed further through varying the variance factors of the ellipsoidal, orthometric, and geoid co-factor matrices in the combined least-squares adjustment for a simulated case study. From the GPS-on-benchmarks points in region A, a subset of the most accurate data points with a mean distance of 80–100 km is extracted. These GPS-on-benchmarks points provide a datum for

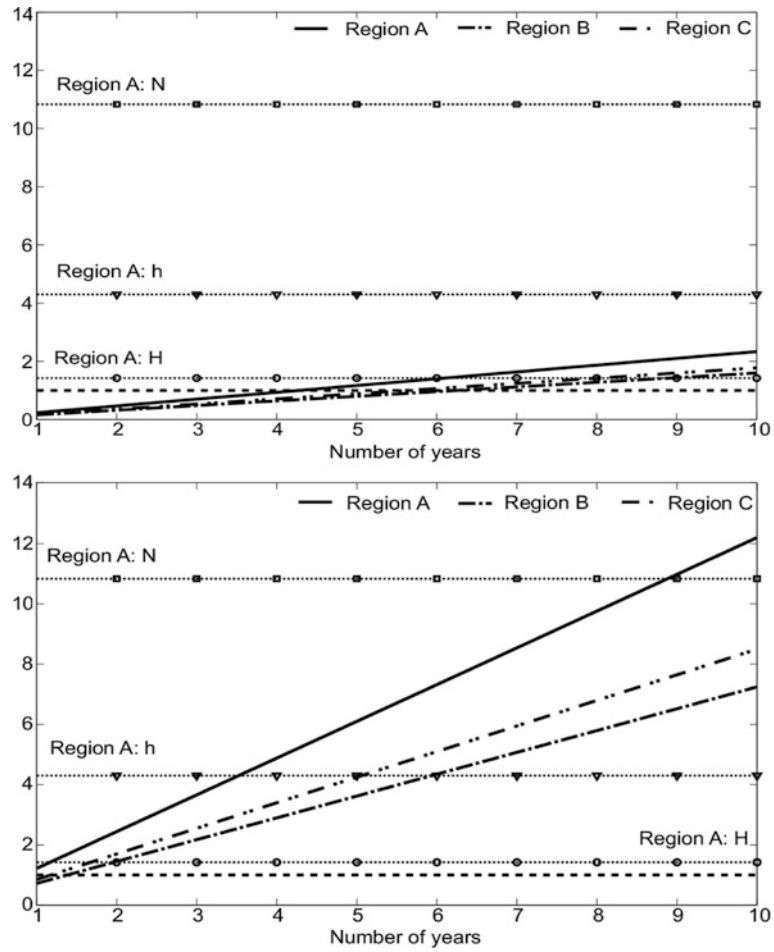


Fig. 38.2 Accumulated effect of the secular geoid changes (*above*) and crustal displacement (*below*) (in regions A: *solid*, B: *dash-dot*, and C: *dash-dot-dot line*) versus accuracy of the systematic and three height components for calibrated diagonal error covariance matrices. Vertical axis shows relative variables

GNSS/levelling in the test area, through which the orthometric heights can be obtained with respect to the mean sea level in Rimouski, Quebec (the fundamental datum point).

Ellipsoidal heights should be known with accuracy of at least 10 mm in order to incorporate the secular dynamic geoid changes in the vertical datum. The maximum errors of the geoid and orthometric heights should be 11 and 12 mm, respectively. At present, the orthometric heights, computed from the latest adjustment of the primary vertical control network of Canada, have accuracy at the decimetre level with respect to the equipotential surface through the fundamental datum point in Rimouski (Véronneau, 2002). The main challenge for improving the accuracy is the accumulation of systematic errors along the levelling lines of magnitude of 0.1 mm/km as well as undetected erroneous observations. The computational accuracy of the geoid can be improved further until it reaches the expected 1-cm level of after-GOCE geoid models. Provided that the errors of the three height components reach 10–15 mm, the geoid heights should be corrected for the dynamic effect every 8–10 years (Fig. 38.4), and the vertical crustal motion should be accounted for every 2 years.

38.5 Conclusions and Recommendations

Although the contemporary accuracy of the height data in Canada is below the standard accuracy requirements, it is desirable to provide recommendations (also summarized in Fig. 38.5) for establishing a dynamic geoid-based vertical datum. This is in lieu of the goal

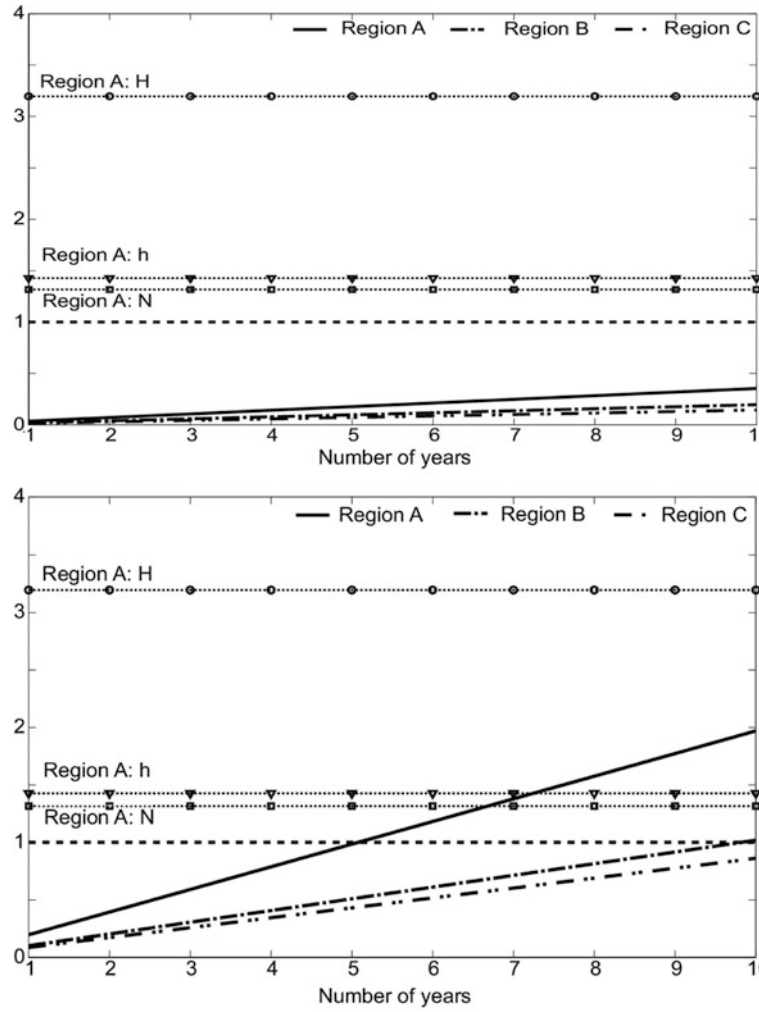


Fig. 38.3 Accumulated effect of the secular geoid changes (*above*) and crustal displacement (*below*) (in regions A: *solid*, B: *dash-dot*, and C: *dash-dot-dot line*) versus accuracy of the systematic and three height components for calibrated fully-populated error covariance matrices. Vertical axis shows relative variables

of achieving a one cm-level accurate regional geoid model.

- The vertical reference surface should be defined by a static geoid model computed for one reference epoch.
- Calibrated errors of the geoid model should be computed by means of a combined least-squares adjustment of ellipsoidal, orthometric and geoid heights. The geoid heights should be computed from the geoid model for the reference epoch, and the ellipsoidal and orthometric heights should be corrected for the vertical crustal displacement and referenced to the epoch of the geoid model. Note that even a geoid-based vertical datum will require some GPS-on-benchmarks points distributed in the region in order to periodically conduct validation and calibration studies.
- To obtain temporally homogeneous height data, consistent models of the rates of change of the geoid, orthometric, and ellipsoidal heights should be used.
- A criterion for *stability* of the vertical reference surface should be introduced in terms of the mean calibrated error of the static geoid model. The vertical reference surface should be assumed *stable* if the secular dynamic changes in the geoid height for the time elapsed from the reference epoch remain below the mean calibrated geoid error.
- The vertical reference surface should be corrected if the stability requirement is no longer met.

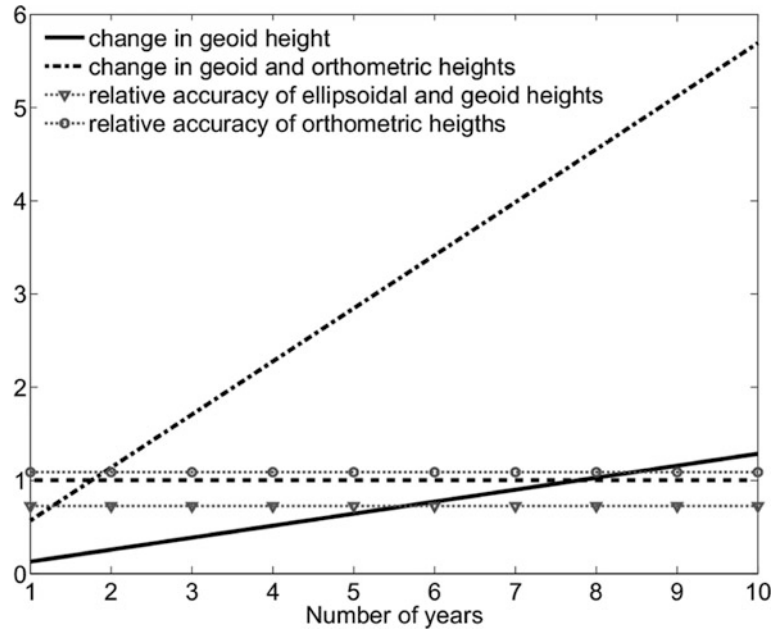


Fig. 38.4 Accumulated effect of the secular changes of the geoid and crustal displacement versus accuracy of the systematic component and height components for the simulated case study. Vertical axis shows relative variables

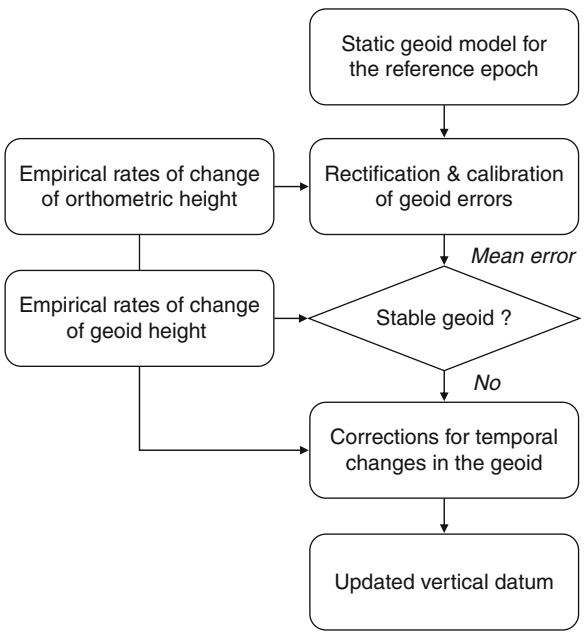


Fig. 38.5 Recommendations for establishing a dynamic geoid-based vertical datum

Acknowledgements The authors gratefully acknowledge Geodetic Survey Division, Natural Resources, Canada for providing the GPS ellipsoidal, orthometric and CGG05 geoid heights. The two anonymous reviewers are also acknowledged for their insightful and helpful comments. Financial support is provided by GEOIDE NCE and NSERC, Canada.

References

Fotopoulos, G. (2003). An analysis on the optimal combination of geoid, orthometric and ellipsoidal height data. PhD thesis, University of Calgary, Department of Geomatics Engineering, Report No 20185.

Fotopoulos, G. (2005). Calibration of geoid error models via a combined adjustment of ellipsoidal, orthometric and gravimetric geoid height data. *J. Geodesy*, 79, 111–123.

Fotopoulos, G., M. Craymer, and E. Lapelle (2007). Epoch rectification of GPS on benchmarks in Canada. IUGG2007, Perugia, Italy, July 2–13, 2007.

Heiskanen, H. and H. Moritz (1967). Physical Geodesy. Graz, Austria, (reprint 1999).

Huang, J., G. Fotopoulos, M.K. Cheng, M. Véronneau, and M.G. Sideris (2006). On the estimation of the regional geoid error in Canada. In: Tregoning, P. and C. Rizos C (eds), IAG Symposia, Vol. 130, Monitoring and Understanding a Dynamic Planet with Geodetic and Oceanographic Tools, Cairns, Australia, August, 22–26, 2005.

Peltier, W.R. (2004). Global glacial isostasy and the surface of the ice-age earth: The ICE-5G (VM2) model and GRACE. *Annu. Rev. Earth Planet. Sci*., 32, 111–149.

Rangelova, E. and M.G. Sideris (2008). Contributions of terrestrial and GRACE data to the study of the secular geoid changes in North America.*J. Geodyn.*, doi:10.1016/j.jog.2008.03.006.

Rangelova, E., W. Van der Wal, M.G. Sideris, and P. Wu (2008). Spatiotemporal analysis of the GRACE-derived mass variations in North America by means of multichannel singular spectrum analysis. In: IAG Symposia: Gravity, Geoid and Earth Observation 2008 (GGEO2008), Chania, Greece, 23–27, June.

Schwarz, K.P., M.G. Sideris, and R. Forsberg (1987). Orthometric heights without leveling. *J. Surv. Eng*., 113(1), 28–40.
Véronneau, M. (2002). The Canadian gravimetric geoid model of 2000 (CGG2000). Report, Geodetic Survey Division, Earth Sciences Sector, Natural Resources Canada, Canada.
Véronneau, M.,R. Duval, and J. Huang (2006). A gravimetric geoid model as a vertical datum for Canada. *Geomatica*, 60(2), 165–172.

Chapter 39

Evaluation of the Quasigeoid Models EGG97 and EGG07 with GPS/levelling Data for the Territory of Bulgaria

E. Peneva and I. Georgiev

Abstract The paper discusses the comparison of the quasigeoid models EGG97 and EGG07 for the territory of Bulgaria with GPS/levelling data. The models have been compared with precise GPS and levelling measurements from National Geodetic Network with regular distribution of stations. Height anomaly differences between the models and GPS/levelling are in the range of 0.693 m for EGG97 and 0.666 m for EGG07. The comparison is made with CMPGS program, developed by H. Denker. A bias as well as bias plus tilt fit are done. The rms of the unit weight after the fitting is ± 0.094 m.

39.1 Introduction

The European gravimetric quasigeoid model EGG97 was computed in 1997 at the Institut für Erdmessung (IfE), University of Hannover, Germany, operating as the computing centre of the International Association of Geodesy (IAG) Subcommission for the Geoid in Europe (Denker and Torge, 1997). EGG97 is based on the EGM96 geopotential model and gravity and terrain models. For western Europe gravity and terrain data with good coverage was used which made possible the realization of high-resolution undulations ($1.0' \times 1.5'$ grid). In the eastern part (25 N–77 N and 35 W–67 E) the quasigeoid undulations are with lower resolution $10' \times 15'$.

E. Peneva (✉)
Faculty of Geodesy, Department of Geodesy, University of Architecture, Civil Engineering and Geodesy, Sofia, Bulgaria
e-mail: penevae_fgs@uacg.bg

New improved global geopotential models became available based on the CHAMP and GRACE missions (Denker, 2005b). New national digital terrain data sets or improved old data, became available (Denker, 2005a). Improved techniques for processing of data and of geoid undulations were implemented too, these improvement lead to initiation of the European Gravity and Geoid Project (EGGP) in the IAG Commission 2. The project was planned for the period of 4 years – from 2003 to 2007 (Denker et al., 2005). The final product of the EGGP project is the new European quasigeoid model EGG07.

In EGG07 there was practically no gravimetric and GPS/levelling data for Bulgaria (Denker et al., 2008). In 2007 year in Bulgaria was started a project at the National Geodetic, Cartography and Cadastre Agency (NGCCA), to collect and analyze all available gravimetric data, which were provided for the EGGP project. The new National GPS network of Bulgaria enabled us to obtain a set of high precision GPS/levelling data, which was used to evaluate the EGG07 and EGG97 quasigeoid models for the territory of Bulgaria.

39.2 GPS/Levelling Data

The National GPS Network of Bulgaria was created in order to serve the renovation of the National Geodetic Network and is tied to the European Reference System. The National GPS Network includes 112 1st order and 353 2nd order points.

S.P. Mertikas (ed.), *Gravity, Geoid and Earth Observation*, International Association of Geodesy Symposia 135,
DOI 10.1007/978-3-642-10634-7_39, © Springer-Verlag Berlin Heidelberg 2010

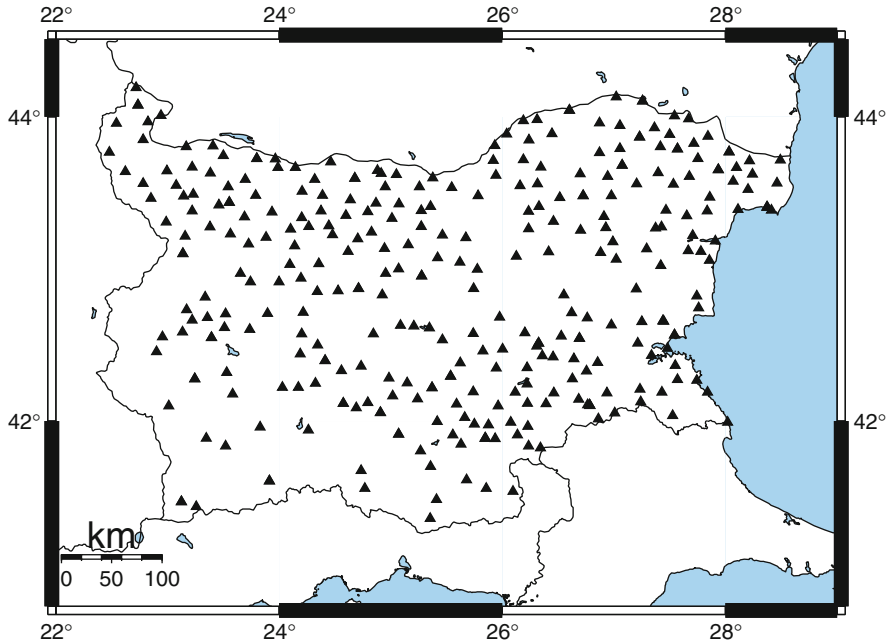


Fig. 39.1 GPS/levelling points

The 1st order National GPS Network has minimum distance of 30 kilometers between the points. It is created for realizing and maintaining the European Terrestrial Reference System 89 (ETRS89) on the territory of the country using the GPS technology. Besides practical activities, the 1st order network is also intended for research activities in the field of geodesy and Earth sciences –as monitoring tectonic motions.

The measurements of the 1st order points of the National GPS Network were performed in 2004 by the Military Geographic Service of the Bulgarian Army. The analysis of the measurements and obtaining the final coordinates were done at the Central Laboratory of Geodesy of the Bulgarian Academy of Sciences (CLG-BAS) in 2005/2006 (Georgiev et al., 2005, 2007). The accuracy of the obtained coordinates is within 5 mm and exceeds significantly the requirements, set by the technical task. We could state that the accuracy of the ellipsoidal heights is within 10 mm.

At 328 points of the National GPS Network precise levelling was performed by the Military Geographic Service to obtain normal heights. Normal heights are in Baltic system with accuracy within 5 mm. These points are used for the evaluation of EGG97 and EGG07 models. The GPS/levelling points are shown in Fig. 39.1. The points are covering almost evenly the country with exception of the highest mountain areas.

39.3 Comparisons

For the comparison of the height anomalies we use the CMPGPS program developed by Denker (1998). This program compares a set of interpolated quasi-geoid undulations, from EGG97 and EGG07, with GPS/levelling data. A bias, as well as a bias plus tilt are estimated. The bias plus tilt fit is based on three datum shift parameters. Considering the accuracy of GPS heights and normal heights we came to the conclusion that the accuracy of GPS/levelling should be approximately ± 0.015 m.

39.3.1 The Comparison Statistics

The final results are given in Table 39.1 for EGG97 and in Table 39.2 for EGG07.

Table 39.1 Statistics of differences between GPS/levelling and EGG97, [m]

	$\zeta_{GPS} - \zeta_{EGG97}$	ζ_{GPS} − after bias fit	ζ_{GPS} − after bias +tilt
No. of pts	328	328	328
RMS	± 0.279	± 0.114	± 0.112
Min.	– 0.122	– 0.377	– 0.385
Max.	+ 0.571	+ 0.316	+ 0.292
Adjusted bias	+ 0.255	±0.006	
Std. dev. of weight unit	± 0.113		

Table 39.2 Statistics of differences between GPS/levelling and EGG07, [m]

	$\zeta_{GPS} - \zeta_{EGG07}$	$\zeta_{GPS} - \zeta_{EGG07}$ after bias fit	$\zeta_{GPS} - \zeta_{EGG07}$ after bias +tilt
No. of pts	328	328	328
RMS	± 0.287	± 0.105	± 0.093
Min.	– 0.073	– 0.339	– 0.317
Max.	+ 0.593	+ 0.327	+ 0.261
Adjusted bias	+ 0.266	±0.006	
Std. dev. of weight unit	± 0.094		

Considering the number of points and standard deviation of unit weight in comparison of EGG97 and EGG07, we could state that the results are satisfying. Apparently from the statistics in Tables 39.1 and 39.2 the two models EGG97 and EGG07 are nearly at the same accuracy. The differences are mapped on Fig. 39.2 for EGG97 and Fig. 39.3 for EGG07. Both models are showing the same behaviour. This is due to the lack of gravimetric data in Bulgarian both models (Fig. 39.4).

In order to improve the quasigeoid model accuracy of Bulgaria more than 400 gravity points from the base gravity network of Bulgaria are handed over for the EGGP project. These data should be taken into account in the next realization of EGG model. The GPS/levelling data used here will be also delivered to EGGP project too.

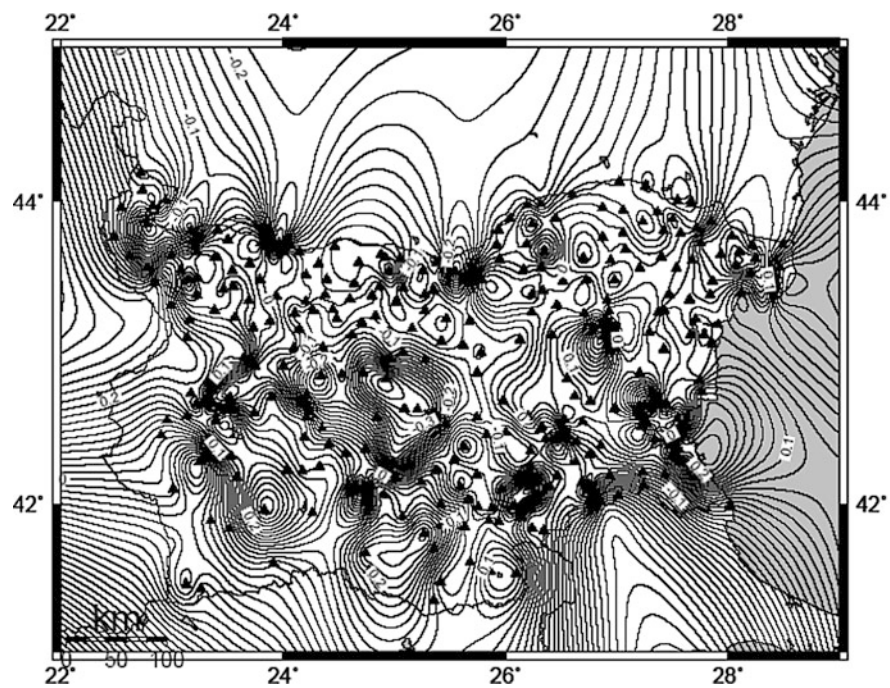


Fig. 39.2 Differences betweeen GPS/lev. pts and EGG97, [m]

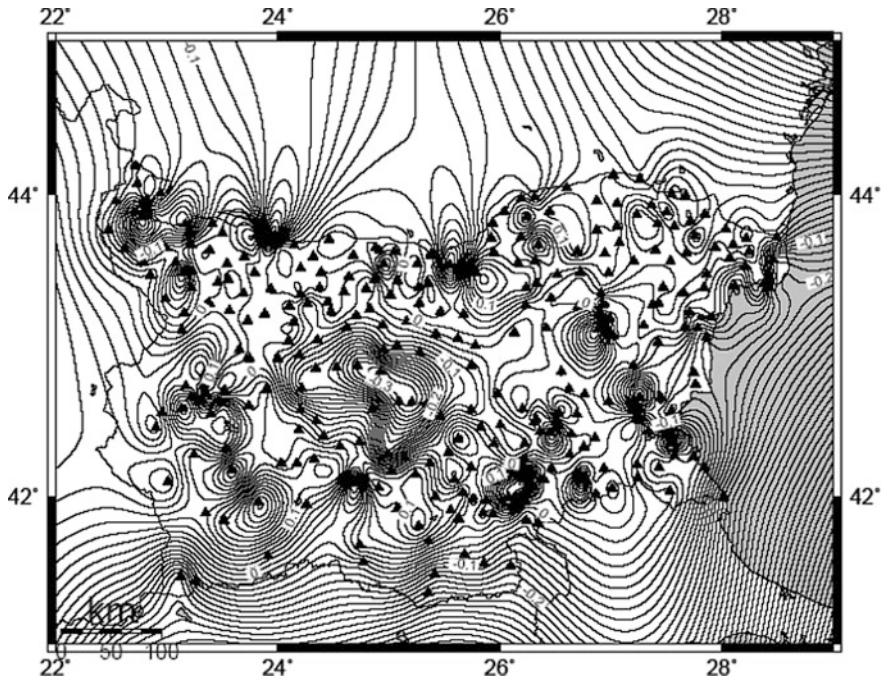


Fig. 39.3 Differences betweeen GPS/lev. pts and EGG07, [m]

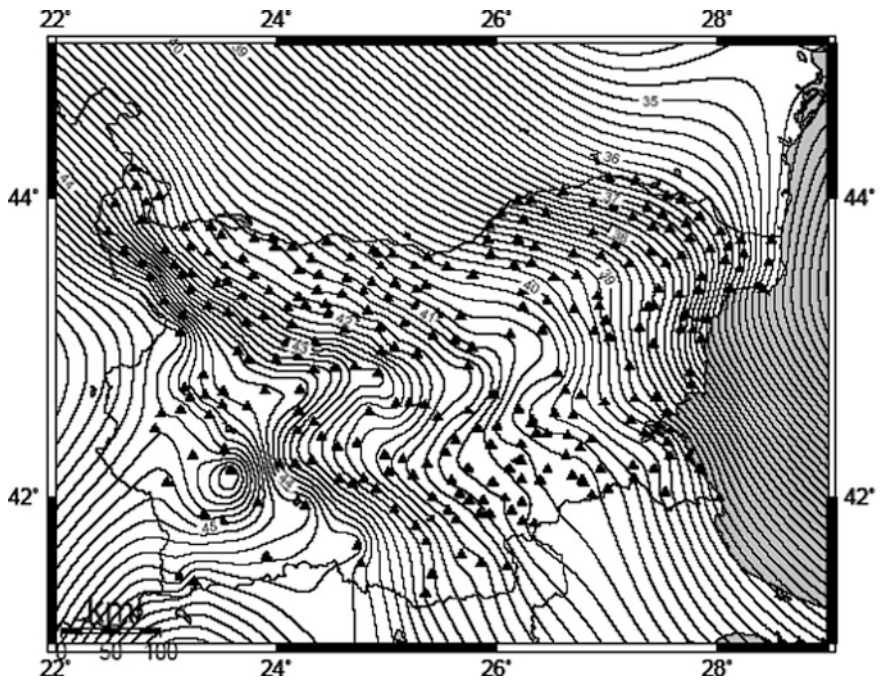


Fig. 39.4 Model EGG07 for Bulgaria, [m]

Acknowledgements The authors would like to thank for supplying with GPS/levelling data to the Bulgarian Military Geographic Service, for supplying gravity data to the National Geodetic, Cartographic and Cadastre Agency, and Heiner Denker for his assistance with software, data and recommendations.

References

Denker, H. (1998). Evaluation and improvement of the EGG97 quasigeoid model for Europe by GPS and levelling data. In: Reports of the Finish Geodetic Institutre, 98:4. Masala, pp. 53–61.

Denker, H. (2005a). Evaluation of SRTM3 and GTOPO30 terrain data in Germany. In: IAG Symposia. Springer Verlag, New York, pp. 218–223.

Denker, H. (2005b). Improved modeling of the geoid in Europe based on CHAMP and GRACE results. In: IAG Symp. Gravity, Geoid and Space Missions – GGSM2004, Porto, August 30–September 3, 2004, CD-ROM Proceed.

Denker, H. and W. Torge (1997). The European gravimetric quasigeoid EGG97. In: Proceed. IAG Symp. No. 119, Geodesy on the Move. Springer, Berlin, Heidelberg, New York, 1998, pp. 245–254.

Denker, H., J.-P. Barriot, R. Barzhagi, R. Forsberg, J. Ihde, A. Kenyeres, U. Marti, and I.N. Tziavos (2005). Status of the European Gravity and Geoid Project EGGP. In: Proceed. IAG Symposia No. 129. Springer Verlag, New York, pp. 125–130.

Denker, H., J.-P. Barriot, R. Barzhagi, D. Fairhead, R. Forsberg, J. Ihde, A. Kenyeres, U. Marti, M. Sarralih, and I.N. Tziavos (2008). The development of the European gravimetric model EGG07. In: Proceed. IAG Symposia No. 133. Springer Verlag, New York, pp. 177–185.

Georgiev, I., P. Gabenski, G. Gladkov, T. Tashkov, P. Danchev, and D. Dimitrov (2005). National GPS Network. Processing the observations of the main order. In: Geodesy, Vol. 18. Military Geographic Survey at Bulgarian Armed Force, Sofia, September 2005, p. 190.

Georgiev, I., P. Gabenski, G. Gladkov, T. Tashkov, P. Danchev, and D. Dimitrov (2007). National GPS Network. Processing the observations of the secondary order. In: Geodesy, Vol. 20. Military Geographic Survey at Bulgarian Armed Force, Sofia, January 2007, p. 190.

Chapter 40

Combination Schemes for Local Orthometric Height Determination from GPS Measurements and Gravity Data

A. Fotiou, V.N. Grigoriadis, C. Pikridas, D. Rossikopoulos, I.N. Tziavos, and G.S. Vergos

Abstract One of the most interesting and challenging tasks in the field of geodetic surveying is the accurate determination of orthometric heights from GPS measurements taking into account leveling data and additional gravity field information. This paper focuses on the presentation of the currently available various solution strategies which are then properly applied. The first method is based on the integrated geodetic model, where gravity field parameters are treated as signals. A second solution is based on a combination scheme employing least squares collocation as the optimal heterogeneous combination method for gravity and height data. Another method is the spectral domain equivalent of least squares collocation, namely the Multiple Input Multiple Output System Theory, where gravity and height data are treated as stochastic signals with full variance covariance information. The last method consists in a polynomial interpolation model of various orders expressing different geoid representations.

40.1 Introduction

The current availability of ever more accurate regional and local geoid models, the dramatic improvement in Global Geopotential Model (GGM) determination and the expected impact of the GOCE mission towards a cumulative geoid error of ± 1 cm to degree and order 200, make height combination schemes of major importance for a variety of applications in geodesy. The combination of various types of heights has been a topic of geodetic research for nearly 40 years, originating from the pioneering work of Krarup (1969), who first presented the integrated approach of geodetic data adjustment. From that idea stem the origins of the leading estimation principle in modern geodetic research, i.e., that of least squares collocation (LSC), which due to the use of many and various types of data and through the use of Fourier transforms (FT) introduced the use of system theory with geodetic data. These ideas are presented in this work in the frame of geoid height combination, when both gravimetric and GPS/Leveling geoid heights are available.

40.2 The Integrated Approach

Integrated geodesy has been introduced for the rigorous adjustment of observations with both geometric and gravimetric information using precise mathematical models. Furthermore, integrated geodesy is a method for the adjustment of observations depending not only on discrete parameters but also on unknown functions. Specific applications related to the estimation of orthometric heights from GPS baselines, leveling and gravity observations have been presented by Hein (1985), Hein et al. (1988), and Hatjidakis and Rossikopoulos (2002).

The observational data, considered in the integrated approach, can be GPS baselines and coordinates, orthometric heights, geoidal undulations, gravity anomalies, potential differences as well as data of any functional related to the Earth's gravity field. As

G.S. Vergos (✉)
Department of Geodesy and Surveying, Aristotle University of Thessaloniki, Thessaloniki 541 24, Greece
e-mail: vergos@topo.auth.gr

S.P. Mertikas (ed.), *Gravity, Geoid and Earth Observation*, International Association of Geodesy Symposia 135,
DOI 10.1007/978-3-642-10634-7_40, © Springer-Verlag Berlin Heidelberg 2010

more simply endorsed in the literature, we have the equations of geodetic heights h_i^{GPS}

$$h_i^{GPS} = H_i + N_i + v_i^h \tag{1}$$

which result from the analysis of GPS observations. In the same way, the equations of orthometric heights H_i^{LEV}

$$H_i^{LEV} = H_i + v_i^H \tag{2}$$

and geoid heights N_i^{GEO}

$$N_i^{GEO} = N_i + \delta N_i + v_i^\zeta \tag{3}$$

are determined. In Eq. (3), the parameter δN_i describes all possible datum inconsistencies and other systematic effects in the data sets (Table 40.1).

All observations, which can be different at every point, can be analyzed simultaneously with the general least squares collocation model

$$\mathbf{w} = \mathbf{A}\,\mathbf{x} + \mathbf{G}\,\mathbf{s} + \mathbf{v} \tag{4}$$

where $\boldsymbol{x}$ contains the orthometric heights ($x_i = H_i$, the deterministic parameters), $\boldsymbol{s}$ contains the geoid heights ($s_i = N_i = T_i/\gamma_i$, the stochastic parameters) and $\boldsymbol{v}$ are the observational errors. The adjustment problem is twofold, i.e., estimation with respect to $\boldsymbol{x}$ and prediction with respect to $\boldsymbol{s}$ and $\boldsymbol{v}$. For the stochastic parameters it is assumed that their means

$$E\{\mathbf{s}\} = \boldsymbol{\mu}, E\{\mathbf{v}\} = \mathbf{0} \tag{5}$$

and the covariance matrices are given as

$$E\{\mathbf{v}\mathbf{v}^T\} = \mathbf{C} = \begin{bmatrix} \sigma_h^2\mathbf{Q}_h & \mathbf{0} & \mathbf{0} \\ \mathbf{0} & \sigma_H^2\mathbf{Q}_H & \mathbf{0} \\ \mathbf{0} & \mathbf{0} & \sigma_N^2\mathbf{Q}_N \end{bmatrix}$$
$$E\{(\mathbf{s}-\boldsymbol{\mu})(\mathbf{s}-\boldsymbol{\mu})^T\} = \mathbf{K} \tag{6}$$

and $E\{(\mathbf{s}-\boldsymbol{\mu})\mathbf{v}^T\} = \mathbf{0}$. The covariance matrix of signals $\boldsymbol{K}$ is obtained from the covariance function *K(P,Q)* of the disturbing potential at two different points *P* and *Q*, by applying the law of covariance propagation to the functionals relating the signals with the disturbing potential. For example, the geoid height covariance function is given as

$$\mathbf{K}_N(P,Q) = \frac{1}{\gamma_P\gamma_Q}\mathbf{K}(P,Q) \tag{7}$$

Initially, an empirical covariance function is determined from the gravity anomalies. Local covariance models for the disturbing potential on the local plane extended to the subspace above it and the corresponding functions of the gravity anomaly are given in Table 40.2. The adjustment of observations is carried out by applying the least squares principle (Dermanis, 1987; Dermanis and Fotiou 1992)

$$\mathbf{v}^T\mathbf{C}^{-1}\mathbf{v} + \mathbf{s}^T\mathbf{K}^{-1}\mathbf{s} = \min \tag{8}$$

which leads to best linear unbiased estimates for the deterministic parameters $\boldsymbol{x}$ and best linear unbiased predictions for the stochastic ones $\boldsymbol{s}$,$\boldsymbol{v}$.

Table 40.1 The observations equations for orthometric height determination in the integrated adjustment approach

GPS coordinates $\mathbf{r}_i(X_i,Y_i,Z_i)$: $\mathbf{r}_i - \mathbf{r}_i^o + h_i^o\mathbf{m}_i = \mathbf{m}_i H_i + \mathbf{m}_i N_i$
or $\mathbf{r}_i - \mathbf{r}_i^o = \mathbf{m}_i\delta H_i + \mathbf{m}_i N_i$
where $\mathbf{m}_i = \begin{bmatrix} \cos\varphi_i\cos\lambda_i \\ \cos\varphi_i\sin\lambda_i \\ \sin\varphi_i \end{bmatrix}$ is the unit vector to the reference ellipsoid.
GPS baselines: $\mathbf{r}_{ij} - \mathbf{r}_{ij}^o = -\mathbf{m}_i\delta H_i + \mathbf{m}_j\delta H_j - \mathbf{m}_i N_i + \mathbf{m}_j N_j$
or $\mathbf{r}_{ij} - \mathbf{r}_{ij}^o - h_i^o\mathbf{m}_i + h_j^o\mathbf{m}_j = -\mathbf{m}_i H_i + \mathbf{m}_j H_j - \mathbf{m}_i N_i + \mathbf{m}_j N_j$
Geodetic heights: $h_i^{GPS} = H_i + N_i + v_i^h = H_i + \frac{1}{\gamma_i}T_i + v_i^h$
Orthometric height differences: $\Delta H_{ij} = H_j - H_i$
Gravity values: $g_i = \gamma_i^o + \mathbf{m}_i^T\mathbf{M}(\mathbf{r}_i - \mathbf{r}_i^o) + \mathbf{m}_i^T grad T_i$
or $g_i = \tilde{\gamma}_i^o + \mathbf{a}_g^T\mathbf{m}_i\delta H_i + \delta g_i - \frac{1}{\gamma_i^o}\mathbf{a}_g^T\mathbf{m}_i T_i$
where $\tilde{\gamma}_i^o = \gamma_i^o - N_i^o\mathbf{a}_g^T\mathbf{m}_i$ and the vector $\mathbf{a}_g$ depends on the Marussi matrix $\mathbf{M}$.
Geoid heights: $N_i^{GEO} = N_i + \delta N_i + v_i = \frac{1}{\gamma_i}T_i + \delta N_i + v_i$
Potential differences: $\Delta W_{ij} = -\gamma_i^o H_i + \gamma_j^o H_j + T_j - T_i + v_{ij}$

40.3 The Model Function Approach

Let us assume that geoid height data is not available in the region of a GPS network, but some orthometric heights are known. The observation equations for each point with known orthometric height are written

$$h_i^{GPS} = H_i + N_i + v_i^h$$

Table 40.2 Local covariance models

	For gravity anomaly $K_{\Delta g}(S)$	For disturbing potential K(S, z)
Exponential model	$\sigma_g^2 e^{-\frac{S^2}{2d^2}}$	$C_{\tilde{E}}(1,0)$
Reilly model	$\sigma_g^2\left(1-\frac{S^2}{2d^2}\right)e^{-\frac{S^2}{2d^2}}$	$C_R(1,0)$
Moritz model	$\sigma_g^2 d^3 \frac{2d^2-S^2}{2\sqrt{(S^2+d^2)^5}}$	$\sigma_g^2 \frac{d^3}{2\sqrt{S^2+(z+d)^2}}$
Poisson model	$\sigma_g^2 d^5 \frac{6d^2-9S^2}{2\sqrt{(S^2+d^2)^7}}$	$\sigma_g^2 \frac{(z+d)d^4}{6\sqrt{(S^2+(z+d)^2)^3}}$

where

$$C_E(q,m)=\sigma_g^2\left(\frac{d}{\sqrt{2}}\right)^{1-q}\frac{\rho^m}{m!}\sum_{k=0}^{l}\left\{\Gamma\left(\frac{m+q+k+1}{2}\right)_1 F_1\left(\frac{m+q+k+1}{2};m+1;-\rho^2\right)\frac{(-\zeta)^k}{k!}\right\}$$

$$C_R(q,m)=\frac{d^2}{2}C_E(q,m),\ \rho=\frac{S}{\sqrt{2}d},\ \zeta=\frac{(z_i+z_j)\sqrt{2}}{d}$$

$${}_1F_1(a;c;x)=1+\frac{a}{c}x+\frac{a(a+1)}{c(c+1)}\frac{x^2}{2!}+\ldots$$

$\Gamma(x)=(x-1)!$ when $x\succ 1\ \forall x\in Z$ or

$$\Gamma\left(x+\frac{1}{2}\right)=\frac{1\,3\,5\,\ldots\,(2x-1)}{2^x}\Gamma\left(\frac{1}{2}\right)$$

S is the horizontal distance between two signals, d the correlation length and z is the height from reference level of covariance function.

$$H_i^{LEV}=H_i+v_i^H,\quad i=1,2,\ldots,n \tag{9}$$

or in equivalence

$$u_i=h_i^{GPS}-H_i^{LEV}=N_i+v_i \tag{10}$$

where $v_i=v_i^h-v_i^H$ is the total error. The most usual method in surveying applications is based on the calculation of geoid heights using an analytic function in the form

$$N_i=\sum_{k=0}^{m}\sum_{l=0}^{m}\alpha_{kl}x_i^k y_i^l \tag{11}$$

The observation equation becomes

$$u_i=h_i^{GPS}-H_i^{LEV}=\sum_{k=0}^{m}\sum_{l=0}^{m}\alpha_{kl}x_i^k y_i^l+v_i \tag{12}$$

and for all the points in matrix notation it becomes $\mathbf{u}=\mathbf{Fa}+\mathbf{e}$, where we can use the principle $\mathbf{e}^T\mathbf{e}=$ min for the exact interpolation or, for the smoothing interpolation, $\mathbf{e}^T\mathbf{M}^{-1}\mathbf{e}=\min$, where $\mathbf{M}=\sigma_h^2\mathbf{Q}_h+\sigma_H^2\mathbf{Q}_H$. Therefore, in this case geoid heights are treated through a parametric surface.

40.4 A Hybrid Interpolation Approach

Let us assume, in contrast to the model presented in §3, that geoid heights are available for all GPS network benchmarks, and some orthometric heights are also known. For these points we have the three observation equations

$$h_i^{GPS}=H_i+N_i+v_i^h$$

$$H_i^{LEV}=H_i+v_i^H$$

$$N_i^{GEO}=N_i+\delta N_i+v_i^\xi \tag{13}$$

or in equivalence

$$h_i^{GPS}-H_i^{LEV}-N_i^{GEO}=\delta N_i+v_i \tag{14}$$

where $v_i=v_i^h-v_i^H-v_i^N$. The correction term δN_ican be decomposed in the form (Kotsakis and Sideris, 1999)

$$\delta N_i=\mathbf{f}_i^T\mathbf{a}+s_i \tag{15}$$

where $\mathbf{f}_i^T\mathbf{a}$ and s_i are the trend and signal components, and by using matrix notation in order to combine the points of the network with the triple information, we obtain

$$\mathbf{u}=\mathbf{Fa}+\mathbf{s}+\mathbf{v} \tag{16}$$

The adjustment is carried out by applying the least squares principle

$$\mathbf{v}^T\mathbf{M}^{-1}\mathbf{v}+\mathbf{s}^T\mathbf{K}^{-1}\mathbf{s}=\min \tag{17}$$

where $\mathbf{M}=\sigma_h^2\mathbf{Q}_h+\sigma_H^2\mathbf{Q}_H+\sigma_N^2\mathbf{Q}_N$. Then, the integrated adjustment model

$$h_i^{GPS}=H_i+N_i+v_i^h$$

$$H_i^{LEV}=H_i+v_i^H$$

$$\tilde{N}_i^{GEO} = N_i^{GEO} - \delta\hat{N}_i = N_i + v_i^{\zeta} \qquad (18)$$

can be used to the overall "observations" of the network for the estimation of orthometric and geoid heights, where the corrections $\delta\hat{N}_i = \mathbf{f}_i^T\hat{\mathbf{a}} + \hat{s}_i$ are calculated by using the values $\hat{\mathbf{a}}$ and $\hat{s}_i$.

40.5 System Theory in Gravity Field Modeling

In this section, combination schemes of heterogeneous data in the frequency domain are presented, while a specific example of gravimetric and GPS/Leveling geoid heights is given. Moreover, the similarities and differences between system theory and LSC are outlined, in order to show the physical relation between all methods presented in this work.

Spectral methods, and FT in particular, have been extensively used since the beginning of the 1970s for the solution of the classical boundary value problems of physical geodesy. The key concept for the utilization of FT in geodetic problems lies in the representation of well-known integral formulas (e.g., Stokes' and Vening-Meinesz integrals for the prediction of geoid heights from gravity anomalies and deflections of the vertical, respectively) as convolution integrals. Since in the spectral domain the convolution of some input signals is replaced by simple multiplication of their spectra, FT and Fast Fourier Transforms (FFT) have been used mainly due to the high-efficiency in terms of time that they offer compared to the usual integral methods of solving geodetic boundary value problems. Despite the gain in processing time, FFT methods carry some disadvantages, among which the main ones are: (a) the need for regularly spaced (i.e., gridded) data, (b) the inability to predict the estimation error for the output signal and (c) the prerequisite of having a single input and a single output signal. On the other hand, the leading estimation method in physical geodesy, i.e., LSC, which was previously discussed in the frame of height combination schemes, allows the use of multiple input signals and irregularly distributed data, while it provides an optimal, under the Wiener-Kolmogorov principle, estimate of the output signal with simultaneous estimation of the full variance-covariance matrix of the output signal error (Moritz, 1980).

Nevertheless, especially in modern day geodetic applications with the hundreds of thousands of altimetric, gravimetric and space borne gravity field related data, the application of LSC has become cumbersome. Therefore, a frequency domain equivalent to LSC has been developed employing system theory. The latter has been traditionally used in signal processing and signal transmission methods as well as in various applications of electrical engineering. The first, who proposed a solution of geodetic boundary value problems in the frequency domain employing system theory was Sideris (1996), who presented the general scheme for the use of a system with multiple input and multiple outputs (Multiple Input Multiple Output System Theory – MIMOST). Numerical solutions and examples of using MIMOST methods for the estimation of geoid heights, gravity anomalies, deflections of the vertical, the quasi-stationary sea surface topography from heterogeneous noisy data as well as in combined gravimetric and GPS geoid solutions have been presented in several papers (see, e.g., Andritsanos, 2000; Andritsanos et al., 2001, 2004; Andritsanos and Tziavos, 2002; Vergos et al., 2005).

A MIMOST system with two input signals and a single output is presented in Fig. 40.1, where

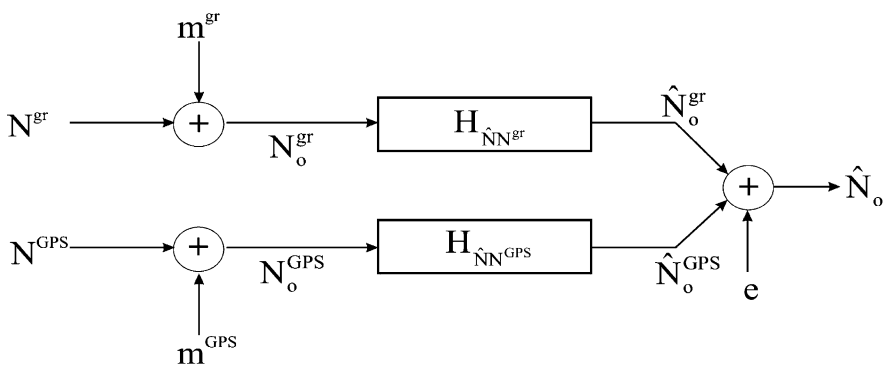


Fig. 40.1 A dual-input single output system for the prediction of geoid heights

an example of gravimetric and GPS/Leveling geoid heights combination is presented for the prediction of combined geoid heights. In many cases, since specific information for the input signal noise is not available, simulated noises are generated as input error under the assumption of white noise. It should be noted that as shown by Andritsanos et al. (2001) in the case of repeat altimetric missions an estimation of the input error Power Spectral Density (PSD) function can be directly evaluated using this successive information. The final solutions and the error PSD function of the MIMOST method are calculated according to the following equations:

$$\hat{\mathbf{N}}_o = \left[\mathbf{H}_{\hat{N}N^{gr}}\ \mathbf{H}_{\hat{N}N^{GPS}}\right]\left(\begin{bmatrix}\mathbf{P}_{N_o^{gr}N_o^{gr}} & \mathbf{P}_{N_o^{gr}N_o^{GPS}}\\ \mathbf{P}_{N_{oa}N_o^{gr}} & \mathbf{P}_{N_o^{GPS}N_o^{GPS}}\end{bmatrix} - \begin{bmatrix}\mathbf{P}_{m^{gr}m^{gr}} & 0\\ 0 & \mathbf{P}_{m^{GPS}m^{GPS}}\end{bmatrix}\right) \begin{bmatrix}\mathbf{P}_{N_o^{gr}N_o^{gr}} & \mathbf{P}_{N_o^{gr}N_o^{GPS}}\\ \mathbf{P}_{N_{oa}N_o^{gr}} & \mathbf{P}_{N_o^{GPS}N_o^{GPS}}\end{bmatrix}^{-1}\begin{bmatrix}\mathbf{N}_o^{gr}\\ \mathbf{N}_o^{GPS}\end{bmatrix} \tag{19}$$

$$\begin{aligned}\mathbf{P}_{\hat{e}\hat{e}} = \{&\left[\mathbf{H}_{\hat{N}N^{gr}}\ \mathbf{H}_{\hat{N}N^{GPS}}\right]\\ &\left(\begin{bmatrix}\mathbf{P}_{N_o^{gr}N_o^{gr}} & \mathbf{P}_{N_o^{gr}N_o^{GPS}}\\ \mathbf{P}_{N_{oa}N_o^{gr}} & \mathbf{P}_{N_o^{GPS}N_o^{GPS}}\end{bmatrix} - \begin{bmatrix}\mathbf{P}_{m^{gr}m^{gr}} & 0\\ 0 & \mathbf{P}_{m^{GPS}m^{GPS}}\end{bmatrix}\right) -\\ &- \left[\hat{\mathbf{H}}_{\hat{N}_oN_o^{gr}}\ \hat{\mathbf{H}}_{\hat{N}_oN_o^{GPS}}\right]\begin{bmatrix}\mathbf{P}_{N_o^{gr}N_o^{gr}} & \mathbf{P}_{N_o^{gr}N_o^{GPS}}\\ \mathbf{P}_{N_{oa}N_o^{gr}} & \mathbf{P}_{N_o^{GPS}N_o^{GPS}}\end{bmatrix}\\ &\left(\begin{bmatrix}\mathbf{H}^*_{\hat{N}N^{gr}}\\ \mathbf{H}^*_{\hat{N}N^{GPS}}\end{bmatrix} - \begin{bmatrix}\hat{\mathbf{H}}^*_{\hat{N}_oN_o^{gr}}\\ \hat{\mathbf{H}}^*_{\hat{N}_oN_o^{GPS}}\end{bmatrix}\right)\left[\hat{H}_{\hat{N}_oN_o^{gr}}\ \hat{H}_{\hat{N}_oN_o^{GPS}}\right]\\ &\begin{bmatrix}\mathbf{P}_{m^{gr}m^{gr}} & 0\\ 0 & \mathbf{P}_{m^{GPS}m^{GPS}}\end{bmatrix}\begin{bmatrix}\mathbf{H}^*_{\hat{N}N^{gr}}\\ \mathbf{H}^*_{\hat{N}N^{GPS}}\end{bmatrix}\end{aligned} \tag{20}$$

where $\hat{\mathbf{N}}_o$ is the combined geoid estimation, $\boldsymbol{N}^{gr}$ and $\boldsymbol{N}^{GPS}$ are the pure gravimetric and GPS/Leveling signals respectively, $\boldsymbol{N_o}^{gr}$ and $\boldsymbol{N_o}^{GPS}$ are the gravimetric and GPS/Leveling observations, m^{gr} and m^{GPS} are the input noises, $\boldsymbol{H}_{xy}$ is the theoretical operator that connects the pure input and output signals, $\hat{\mathbf{H}}_{x_oy_o}$ is the optimum frequency impulse response function, $\mathbf{P}_{\hat{e}\hat{e}}$ is the error PSD function, $e$is the noise of the output signal and the * denotes complex conjugate of the matrix under consideration.

If we substitute the vector of observation and estimation signals with

$$\mathbf{Y}_o = \begin{bmatrix}N_o^{gr}\\ N_o^{GPS}\end{bmatrix};\quad \mathbf{X}_o = [N_o], \tag{21}$$

then Eqs. (19) and (20) can be written in matrix notation as

$$\begin{aligned}\hat{\mathbf{X}}_o &= \hat{\mathbf{H}}_{X_oY_o}\mathbf{Y}_o = \mathbf{P}_{XY}\mathbf{P}^{-1}_{Y_oY_o}\mathbf{Y}_o =\\ &= \mathbf{H}_{XY}\left(\mathbf{P}_{Y_oY_o} - \mathbf{P}_{mm}\right)\mathbf{P}^{-1}_{Y_oY_o}\mathbf{Y}_o\end{aligned} \tag{22}$$

$$\begin{aligned}\mathbf{P}_{\hat{e}\hat{e}} = &\left[\mathbf{H}_{XY}\left(\mathbf{P}_{Y_oY_o} - \mathbf{P}_{mm}\right) -\right.\\ &\left. - \hat{\mathbf{H}}_{X_oY_o}\mathbf{P}_{Y_oY_o}\right]\left(\mathbf{H}^{*T}_{XY} - \hat{\mathbf{H}}^{*T}_{X_oY_o}\right) +\\ &+ \hat{\mathbf{H}}_{X_oY_o}\mathbf{P}_{mm}\hat{\mathbf{H}}^{*T}_{XY}\end{aligned} \tag{23}$$

where and the theoretical operator impulse response function is

$$\mathbf{H}_{XY} = \mathbf{P}_{XY}\mathbf{P}^{-1}_{YY} \tag{24}$$

In order to see the equivalence with space domain least squares collocation, lets assume that we have a stationary, isotropic random input signal described by the vector

$$\mathbf{y} = \begin{bmatrix}N^{gr}\\ N^{GPS}\end{bmatrix} \tag{25}$$

and that there exists a linear estimator ***h(x,y)*** (represented by ***h*** for simplicity) which relates the input signal ***y***with the output signal ***x***, i.e.,

$$\mathbf{x} = \mathbf{h}\mathbf{y} \tag{26}$$

If we denote the error vector by ***e*** then its covariance matrix will be given as:

$$\begin{aligned}\mathbf{C}_{\hat{e}\hat{e}} = E\{\mathbf{e}\mathbf{e}^{\mathrm{T}}\} = \mathbf{h}E\{\mathbf{Y}\,\mathbf{Y}^{\mathrm{T}}\}\mathbf{h}^{\mathrm{T}} - E\{\mathbf{X}\,\mathbf{Y}^{\mathrm{T}}\}\mathbf{h}^{\mathrm{T}} -\\ - \mathbf{h}E\{\mathbf{Y}\,\mathbf{X}^{\mathrm{T}}\} + E\{\mathbf{X}\mathbf{X}^{\mathrm{T}}\}\end{aligned} \tag{27}$$

where $E\{\}$denotes expectation. From Eq. (27), taking into account that all our signals are centered ($E\{\boldsymbol{.}\}=0$) and that $\boldsymbol{C}_{(\cdot)(\cdot)}=E\{(\cdot)(\cdot)^T\}$, after some simple

substitutions we arrive at the following expression for the error covariance matrix of the output signal

$$\mathbf{C}_{\hat{e}\hat{e}} = \mathbf{C}_{XX} - \mathbf{C}_{XY}\mathbf{C}_{YY}^{-1}\mathbf{C}_{YX} + \\ + \left(\mathbf{h} - \mathbf{C}_{XY}\mathbf{C}_{YY}^{-1}\right)\mathbf{C}_{YY}\left(\mathbf{h} - \mathbf{C}_{XY}\mathbf{C}_{YY}^{-1}\right)^{T} \quad (28)$$

Equation (28) shows that the error covariance matrix of the predicted signal is composed by two parts, one that depends on the linear operator $\boldsymbol{h}$ (lets denote it as $\mathbf{A}_2 = \left(\mathbf{h} - \mathbf{C}_{XY}\mathbf{C}_{YY}^{-1}\right)\mathbf{C}_{YY}\left(\mathbf{h} - \mathbf{C}_{XY}\mathbf{C}_{YY}^{-1}\right)^{T}$) and another one that is independent of $\boldsymbol{H}$ (we denote it as $\mathbf{A}_1 = \mathbf{C}_{XX} - \mathbf{C}_{XY}\mathbf{C}_{YY}^{-1}\mathbf{C}_{YX}$). The latter means that matrix $\boldsymbol{A_1}$does not change for every possible linear prediction and every possible linear operator $\boldsymbol{h}$. According to Moritz (1980) in order to achieve the best unbiased minimum variance linear estimation of signal $\boldsymbol{X}$from $\boldsymbol{Y}$, matrix $\boldsymbol{A_2}$ should be equal to zero, which holds if our linear operator is given as

$$\mathbf{h} = \mathbf{C}_{XY}\mathbf{C}_{YY}^{-1} \quad (29)$$

Comparing Eqs. (24) and (29) we can easily verify that they are in fact the same with $\boldsymbol{h}(\mathrm{x,y}) \xrightarrow{\mathrm{F}} \boldsymbol{H}_{\mathrm{xy}}$, i.e., that $\boldsymbol{h}$ and $\boldsymbol{H}_{XY}$ form a FT pair. Given that, and comparing Eqs. (23) and (28) we can easily deduce the similarity between MIMOST and LSC. An extensive comparison between the two methods is given in Sansò and Sideris (1997).

40.6 Conclusions

A complete overview of the basic concepts in height adjustment has been presented, starting from the concept of the integrated approach in geodesy, least squares collocation, multiple input multiple output system theory and a hybrid approach treating both deterministic and stochastic errors, the first representing datum inconsistencies and the later random errors in the height data to be combined. Moreover, a comparison between least squares collocation and its frequency-domain equivalent of multiple-input multiple-output system theory has been presented showing that the two methods are practically identical.

References

Andritsanos, V.D. (2000). Optimum combination of terrestrial and satellite data with the use of spectral techniques for applications in geodesy and oceanography. PhD dissertation, Aristotle University of Thessaloniki, Department of Geodesy and Surveying.

Andritsanos, V.D. and I.N. Tziavos (2002). Estimation of gravity field parameters by a multiple input/output system. *Phys. Chem. Earth A*, 25(1), 39–46.

Andritsanos, V.D., M.G. Sideris, and I.N. Tziavos (2001). Quasi-stationery Sea Surface topography estimation by the multiple Input-Output method. *J. Geodesy*, 75, 216–226.

Andritsanos, V.D., G. Fotopoulos, A. Fotiou, C. Pikridas, D. Rossikopoulos, and I.N. Tziavos (2004). New local geoid model for Northern Greece. Proceedings of INGEO 2004 – 3rd Inter Conf on Eng Surv, FIG Regional Central and Eastern European Conference, Bratislava, Slovakia.

Dermanis, A. (1987). Geodetic applications of interpolation and prediction. Int. School of Geodesy A. Marussi, Erice, Italy, 15–25 June.

Dermanis, A. and A. Fotiou (1992). Methods and applications of observation adjustment. Editions Ziti (in Greek).

Hatjidakis, N. and D. Rossikopoulos (2002). Orthometric heights from GPS: the integrated approach. In Tziavos (ed), 3rd Meeting of the International Gravity and Geoid Commission (IGGC), Gravity and Geoid, pp. 401–406.

Hein, G.W. (1985). Orthometric height determination using GPS observations and the integrated geodesy adjustment model. NOAA Technical Report NOS 110 NGS 32, Rockville, MD.

Hein, G.W., A. Leick, and S. Lambert (1988). Orthometric height determination using GPS and gravity field data. GPS'88 Conference on Engineering. Applications of GPS Satellite Surveying Technology, May 11–14, 1988, Nashville, TN.

Kotsakis, C. and M.G. Sideris (1999). On the adjustment of combined GPS/levelling/geoid networks. *J. Geodesy*, 73, 412–421.

Krarup, T. (1969). A contribution to the mathematical foundation of physical geodesy. Rep no 44, Danish Geodetic Institute.

Moritz, H. (1980). Advanced physical geodesy. 2nd ed, Wichmann, Karlsruhe.

Sansò, F. and M.G. Sideris (1997). On the similarities and differences between systems theory and least-squares collocation in physical geodesy. *Boll di Geodesia e Scienze Affini*, 2, 174–206.

Sideris, M.G. (1996). On the use of heterogeneous noisy data in spectral gravity field modeling methods. *J. Geodesy*, 70: 470–479.

Vergos, G.S., I.N. Tziavos, and V.D. Andritsanos (2005). On the determination of marine geoid models by least-squares collocation and spectral methods using heterogeneous data. In: Sansó F (ed), A window on the future of geodesy, Inter Assoc of Geod Symposia, Vol. 128, Springer – Verlag, Berlin, Heidelberg, pp. 332–337.

Chapter 41

EUVN_DA: Realization of the European Continental GPS/leveling Network

A. Kenyeres, M. Sacher, J. Ihde, H. Denker, and U. Marti

Abstract EUREF, the Sub-commission for the European Reference Frame within IAG Commission 1, in cooperation with the European Geoid and Gravity Project (EGGP), is developing a homogeneous continental GPS/leveling database. EUVN_DA, the Densification Action of the EUVN (European Unified Vertical Reference Network) project is designed to support the development of the new European geoid solutions and to contribute to the realization of an accurate continental height reference surface. The cm-accuracy GPS/leveling database could also be used for the realization of the European Vertical Reference System (EVRS) and for the analysis of the national height networks.

The establishment of the EUVN_DA network was started in 2003. The database now consists of about 1,500 high quality GPS/leveling points contributed from 25 countries. The GPS coordinates refer to the realizations of the ETRS89 and the leveling data to EVRS2007. Most of the EUVN_DA benchmarks are integrated into the UELN (United European Leveling Network) to assure the long term homogeneity and consistency of the height information. The GPS database mostly relies on existing measurements which fulfilled pre-defined quality requirements. The main phase of the project terminates by the end of 2008, but the periodic maintenance of the database is planned on long term.

This paper summarizes the activities within the EUVN_DA project, gives an overview on the actual status and presents the results on the analysis of the continental geoid solutions.

A. Kenyeres (✉)
FÖMI Satellite Geodetic Observatory, Budapest H-1592, Hungary
e-mail: kenyeres@gnssnet.hu

41.1 Introduction

The large scale GPS/leveling networks may have multiple functions in geodesy, as they may be used for height datum definition, serve as control points for continental geoid solutions and global geopotential models and may be used for the creation of height reference surfaces in the application of GPS heighting.

The skeleton of such a network in Europe was the EUVN, established in 1997, and involves 196 points covering the continent and the larger islands. The network incorporated selected leveling nodal points (54), permanent EUREF (66) and national (13) GPS stations and tide gauges (63). Details about EUVN can be found in Ihde et al. (2000).

The EUVN points were associated with high quality cm-accuracy 3D coordinates in ETRS89 (ETRF96 epoch 1997.4) and geopotential numbers related to EVRS2000 zero level, which were used to derive normal heights. However the joint analysis was difficult, because the network was relatively sparse and the continental geoid available, EGG97 (Denker and Torge, 1997) had quality problems with both the gravity data and geopotential models.

In order to distinguish, identify and/or eliminate the data inconsistencies, and to improve the separation of the various error components a more accurate continental geoid solution and a denser GPS/leveling network were essential.

The last decade brought substantial improvement at the geoid modeling thanks to the satellite missions

S.P. Mertikas (ed.), *Gravity, Geoid and Earth Observation*, International Association of Geodesy Symposia 135,
DOI 10.1007/978-3-642-10634-7_41, © Springer-Verlag Berlin Heidelberg 2010

(GRACE, CHAMP) and the updated marine and terrestrial gravimetric databases. Additionally the re-adjustment of leveling networks using homogenized standards and reductions made better opportunities in the combined geoid-GPS/leveling analysis.

41.2 EUVN_DA: Densification of EUVN

In 2003 the former IAG European Sub-commission IGGC (International Gravity and Geoid Commission) in cooperation with EUREF initiated an action to densify the EUVN network. A parallel development was started targeting the establishment of a homogeneous, cm-accuracy continental GPS/leveling database and a new improved European geoid solution.

The institutions and national mapping agencies were asked to provide a set of benchmarks with high quality GPS derived coordinates and leveling data. The planned site separation was 50–100 km to keep the data preparation costs at a reasonable level. Due to the large number of the expected sites a single continental GPS campaign could not be designed, the site selection and the (existing or new) measurements–corresponding to pre-defined quality standards, remained the responsibility of the contributing countries. In order to get the one-cm accuracy for the ellipsoidal heights, optimally 24 h of GPS measurements, processed by a scientific software package (e.g., Bernese) were preferred. Most of the countries could meet these requirements; if not, a denser dataset was provided (e.g., UK, Italy, France, Spain, Portugal).

The reference system of the GPS coordinates is ETRS89 and for the leveling data it is EVRS2007. The geopotential differences submitted should directly refer to an UELN marker. Those benchmarks are integrated into UELN to assure long term homogeneity. When a direct connection was not available, the heights submitted were transformed to EVRS2007 with existing transformation parameters. The leveling data validation and the sequential UELN adjustments were done at the UELN/EUVN Data Centre in Leipzig. The timing of the project was perfect as several countries (Finland, Lithuania, Norway, Sweden, Poland, Portugal, Slovakia,) had just completed the re-leveling of their networks.

The definition and the standards of the European Vertical Reference System (EVRS) have been changed in 2008 from EVRS2000 to EVRS2007 (Sacher et al., 2008). Beyond the datum definition, the main change was the consistent handling of the permanent tidal effect as described by Ekman (1989), which means that all height information has to be transformed to the zero tidal system. The new UELN adjustment was done accordingly, the European geoid solutions are already available in the zero tidal system and we had to transform of the GPS-derived ellipsoidal heights from the tide-free to the zero tidal system using the following formula (Sacher et al., 2008):

$$h^{\text{zero}} = h^{\text{tide free}} - 0.179 \sin^2 \varphi - 0.0019 \sin^4 \varphi + 0.0603$$

The transformation is only latitude-dependent and introduces about 0.1 m N–S "tilt" on a continental scale. The GPS coordinates submitted were still referred to the tide-free system, so subsequently we had to apply this transformation on the ellipsoidal heights.

In theory, the reference epoch of the ellipsoidal and leveled heights is 2000.0, but practically the data refer to the epoch of the observations. In particular the age of the leveling data is very variable, ranging from 0 to 50 years. The oldest leveling data is from Spain, but a re-leveling there will be completed by 2009.

The weak point of the EUVN_DA database is that measurement epoch varies country by country, and therefore the validity of the height information homogeneity relies on the assumption of the long term site stability. The Nordic countries are exceptional, where due to the well known glacial-isostatic adjustment (GIA) the heights were transformed to epoch 2000.0 using the latest GIA model NKG2005LU (Ågren and Svensson, 2006).

The EUVN_DA database now consists of about 1500 benchmarks contributed from 25 countries.

The available GPS and leveling data was transformed to the common reference frames, then it was submitted to a detailed internal consistency check and external comparisons. The latter was done in cooperation with EGGP. Both, EUREF and EGGP benefitted from the cooperation. The European geoid may be used for identifying outliers in the GPS/leveling data and EUVN_DA is used for the validation of the new European geoid solutions (Fig. 41.1).



Fig. 41.1 Distribution of the EUVN and EUVN_DA benchmarks (*gray* and *black dots*) as of August 2008

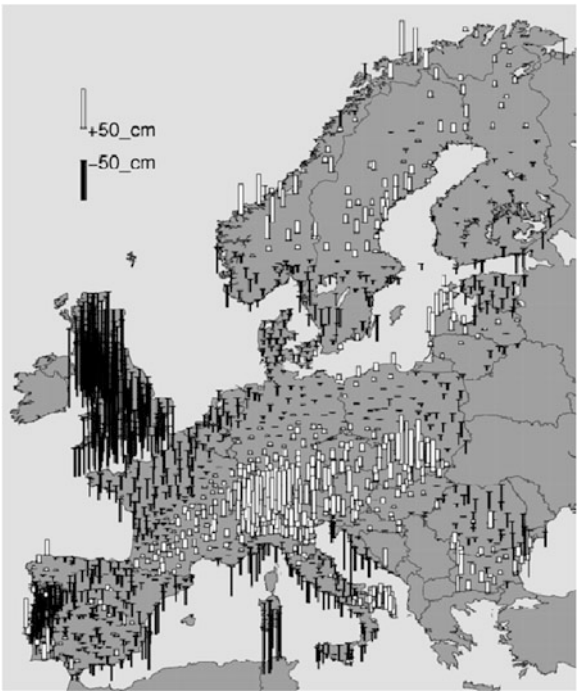


Fig. 41.2 Height anomaly differences of EUVN_DA and EGG97

41.3 Analysis of the GPS/Leveling Data

The comparison of GPS/leveling derived height anomalies and independent gravimetric quasigeoid solutions is useful to check the data consistency of both data sources. In this connection, leveling datum misalignments and gross errors can be easily identified by geoid comparisons. This is especially important in our case, where the databases are built up from separate national records. In order to easily manage the comparisons, a uniform MS Excel worksheet has been developed, which includes all GPS leveling information, geoid tests and the derived statistics.

As a general test we compared EUVN_DA GPS/leveling data with the EGG97 and EGG07 height anomalies (see Figs. 41.2 and 41.3.).

Figure 41.2 is more or less the real densification of the main long wavelength structures we already observed at the EUVN-EGG97 comparison (Ihde et al., 2000) but here they show up more clearly. The long wavelength continental scale structures are mainly due to the shortcomings of the geopotential model

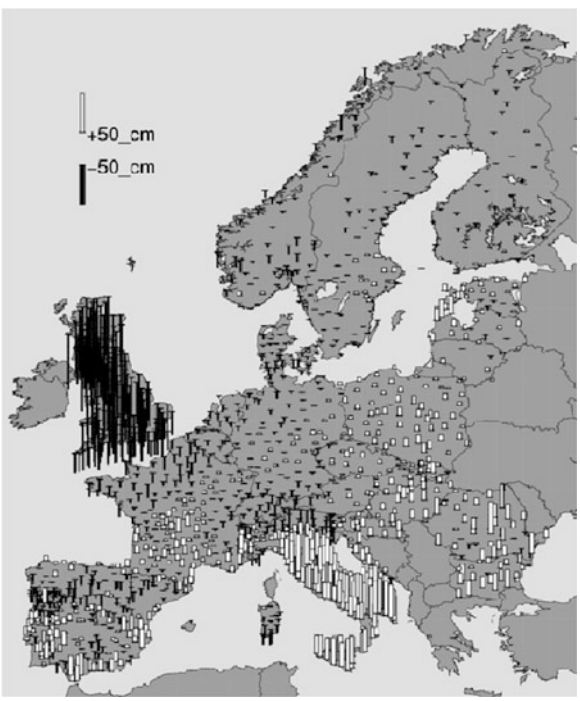


Fig. 41.3 Height anomaly differences of EUVN_DA and EGG07

(EGM96) used for EGG97 (e.g., Alpine region) and the marine/terrestrial gravity database (e.g., High Tatras). A more detailed comparison, also with some intermediate EGG solutions can be found in Kenyeres et al. (2006).

If we compare Figs. 41.2 and 41.3 we clearly observe the huge improvement which took place during the last decade, but we also find remaining and newly apparent discrepancies of the datasets.

The Spanish data shows higher scatter in both cases, because here we could only use the old leveling dataset. The complete re-leveling of the Spanish network will be finished by 2009 and lead to a much more uniform picture.

The large, negative and tilting differences in the British Isles is due to the tilt of the UK leveling network (Edge, 1959); we can only model this, when the height reference surface is computed.

Similar, but smaller N-S tilt is seen for France on both maps, which was also proved by new 1st order leveling measurements (Rebischung et al., 2008).

The most critical component of EUVN_DA is Italy. The EGG97 comparison has shown reasonable results, although we observed negative, systematic differences along the Mediterranean coastline. This fact may be explained by marine gravity data problems. In contrast, in the EGG07 comparison we found about 0.3 m positive systematic difference between EUVN_DA and EGG07, which we cannot explain at the moment. Both the GPS/leveling and the geoid input data seem to be correct. The explanation and later modeling of this bias need further investigations.

If we check the statistics of the comparisons (samples are shown in Table 41.1) we observe a significant improvement all over Europe; the rms of the EGG97 and EGG07 geoid – GPS/leveling differences dropped about 50%!

Countries with moderate topography and/or fairly good gravity data coverage (e.g., FI, SE and HU) show excellent agreement, and Slovakia exhibits a huge improvement when the geoid input data of High Tatras has been corrected. The Alpine countries (AT and CH) have slightly higher rms, and this is no wonder due to the difficult topography. The statistics of GB are weaker with small improvement due to the tilt in the leveling network (Edge, 1959), but after the tilt removal the residual rms drops to 2 cm! The situation is similar in France, where the tilt in the French leveling network contaminates the statistics. We observe moderate improvement at the Romanian sites, and this is probably due to the sparse gravity data available for the European geoid computation. The most difficult case is Italy, where for both comparisons, but for different reasons we got larger discrepancies with negligible improvement. The complete dataset from the gravity database to the leveling data must be re-visited, and carefully checked in order to find the source of the discrepancies. The investigations done so far did not provide any explanations for this.

Table 41.1 Comparison statistics of EUVN_DA and the EGG solution differences for some countries

Nat. code	No. of pts	RMS [cm]		MAX-MIN range[cm]	
		EGG97	EGG07	EGG97	EGG07
AT	17	11	6	33	20
CH	20	10	5	31	16
DE	75	10	4	46	17
FI	50	11	2	51	8
FR	168	12	8	70	36
GB	189	19	14	74	54
HR	20	20	6	80	27
HU	20	9	3	40	11
IT	*195*	*23*	*20*	*116*	*77*
RO	43	15	12	83	69
SE	87	12	3	85	15
SK	28	17	3	57	16

41.4 Towards the Combined European Height Reference Surface

The statistical values in Table 41.1 clearly show the huge improvement in the geoid modeling achieved during the last decade. The RMS values indicate that the latest EGG solution already has the potential to serve as an accurate continental height reference surface, especially in areas with a good coverage and quality of the input data. However due to the problems observed in the current comparisons, described in the above section, the realization of a European *combined* height reference surface is postponed until clear explanation or improvement is found. Only preliminary test computations have been conducted to demonstrate and quantify the efforts we need and gains we achieve towards realizing such a future product.

There are two groups of methods offered in the literature to combine gravity data/gravimetric geoid and GPS/leveling data: one proposes a common analysis (e.g., LSC) and the other suggests a post-fit of the geoid surface to the GPS/leveling points (from the simple polynomial fit to sophisticated fitting techniques).

As the European geoid is computed using the FFT technique with the spectral combination method which does not yet include the option for the joint adjustment, we use one of the post-fit solutions to combine gravimetric geoid surface and the GPS/leveling information. We are searching for techniques offering robust (less dependence on single data outliers) smooth solutions with some filtering capability to eliminate local, non-representative features.

At the *demonstration* phase we tested several methods like "minimum curvature", kriging and numerous variations of the polynomial fitting offered by the SURFER software package (Golden Software Inc.). Our target was to find a kind of corrector surface, which is as simple and smooth as possible, therefore does not provide a perfect fit, but well represents the large scale differences of the gravimetric geoid and the GPS/leveling database.

Without describing the details of the comparisons, we selected the local polynomial fitting solution, where each grid knots has been determined with a 2nd order polynomial fit using neighboring points. This method was robust enough to disregard outliers (free from "bull's eyes") and provide a solution, where only the large scale effects are present (see Fig. 41.4). At this stage the Italian data was not included.

The method selected was able to fulfill the basic requirements and using this simple corrector surface we achieved at this early stage 3 cm overall residual RMS! For the greatest part of the continent the RMS is around 2 cm, there being only two exceptions; the Iberian peninsula and Romania, where we observe higher residual scatter and a more "disturbed" fitted surface. This also reflects the data quality problems noted earlier. As a further example we mention UK, where the fit eliminated the 0.5 m tilt and the residuals were then at the 2 cm level. We also observe about 0.1 m discrepancy between the geoid model and the GPS/leveling data at the Alpine region, which needs further study to understand.

This preliminary study has demonstrated that using the current European geoid model and EUVN_DA data the accurate continental height reference surface can easily be realized. As this surface is very much dependent on the mathematical tool used for the computations further careful investigations and tests are needed to find the mathematically robust approach which provides a realistic solution for the height reference surface.

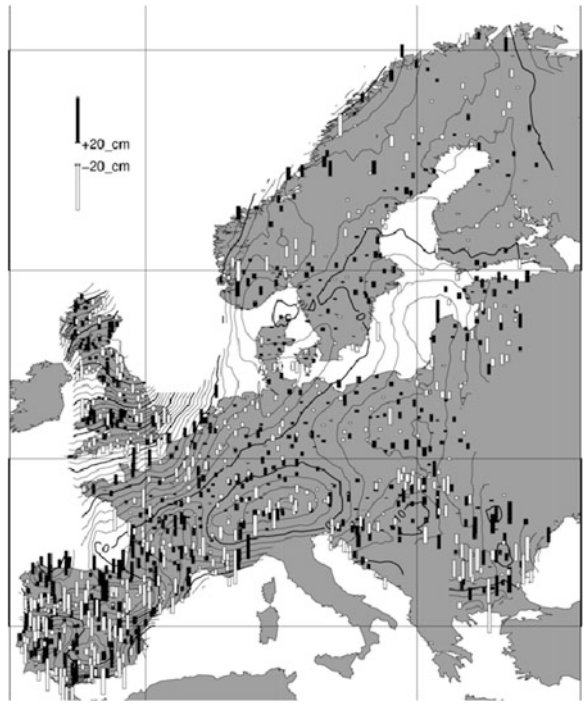


Fig. 41.4 The modeled differences of the EGG07-EUVN_DA data, where the fit residuals are also indicated (Denker et al., 2007)

41.5 Summary and Outlook

In cooperation of EUREF and EGGP, and with the support of the European mapping agencies, the creation of a regional GPS/leveling database is in progress. The EUVN_DA database includes about 1500 GPS/leveling benchmarks, where existing and new data which fulfilled pre-defined quality requirements, were collected. The submitted data was carefully tested and transformed to common reference systems (ETRS89/GRS80 for the GPS and EVRS2007/UELN for the leveling data). The uniform and homogeneous database is of great value for practical GPS-leveling applications. The first version of the database is being completed by the end of 2008

and will be available for the data providers and later for scientific, non-commercial users. The maintenance of the EUVN_DA database will be planned on long term, new releases are created when new data will be available.

The EUVN_DA web pages also have been created, (crs.bkg.bund.de/evrs/euvn_da/EUVN_DAmain) where a summary, preliminary results and a metadatabase is available.

An important product of the EUREF/EGGP cooperation could be the computation of a combined gravimetric-GPS/leveling geoid solution serving as a realization of a uniform and accurate European height reference surface. In this paper we gave a general overview of the project and we successfully demonstrated our potential for geoid testing at the cm level as well as to realize the accurate continental height reference surface.

Acknowledgments The authors are expressing their thanks to all institutions, mapping agencies and persons who made measurements and provided GPS and leveling data to EUVN_DA. Without their extensive support, the project could not be run successfully. The plots have been created using the GMT software tools (Wessel and Smith, 1998).

References

Ågren, J. and R. Svensson (2006). Land uplift model and system definition used for the RH2000 adjustment of the Baltic Levelling Ring. Pres. Paper, 15th General Meeting of the Nordic Geodetic Comm., Copenhagen, May 29–June 2, 2006.

Denker, H. and W. Torge (1997). The European gravimetric quasigeoid EGG97 – An IAG supported continental enterprise. In: IAG Symposium Proceedings IAG Scient. Assembly Rio de Janeiro, 1997. Springer Verlag, New York.

Denker, H., J.P. Barriot, –R. Barzaghi, –D. Fairhead, R. Forsberg, –J. Ihde, –A. Kenyeres, –U. Marti, –M. Sarrailh, and –I.N. Tziavos (2007). Development of the European Gravimetric Geoid Model EGG07. Paper presented at the IUGG XXIV General Assembly, 2–13 July, 2007, Perugia, Italy.

Edge, R.C.A. (1959). Some considerations arising from the results of the Second and Third Geodetic Levelings of England and Wales. Bulletin Geodesique, No.52, pp.28–36.

Ekman, M. (1989). Impacts of geodynamic phenomena on systems of height and gravity. *Bull. Geod.*, 63, 281–296.

Ihde, J., J. Ádám, W. Gurtner, B.G. Harsson, M. Sacher, W. Schlüter, and G. Wöppelman (2000). The EUVN height solution – Report of the EUVN working group. Proceedings of the EUREF2000 Symposium, Tromsø, Norway, 22–24 June, 2000. Veröffentlichungen der Bayerischen Kommission für die Internationale Erdmessung der BAW, Heft Nr. 61, pp. 132–145.

Kenyeres, A., M. Sacher, J. Ihde, H. Denker, and U. Marti (2006). Establishment of the European continental GPS/leveling network. Proceedings of the 1st Int. Symposium of the IGFS, 28 August–01 September, 2006, Istanbul, Turkey, pp. 124–129.

Rebischung, P., F. Duquenne, and H. Duquenne (2008). The new French zero-order leveling network – First global results and possible consequences for the UELN. Paper presented at the EUREF2008 symposium, 18–20 June, 2008, Brussels, Belgium.

Sacher, M., J. Ihde, G. Liebsch, and J. Makinen (2008). EVRF07 as Realization of the European vertical reference System. Paper presented at the EUREF2008 symposium, 18–20 June, 2008, Brussels, Belgium.

Wessel, P. and W.H.F. Smith (1998). New, improved version of Generic Mappig Tools released. *EOS Trans. AGU*, 79(47), 579.

Chapter 42

Analysis of the Geopotential Anomalous Component at Brazilian Vertical Datum Region Based on the Imarui Lagoon System

S.R.C. de Freitas, V.G. Ferreira, A.S. Palmeiro, J.L.B. de Carvalho, and L.F. da Silva

Abstract The region contiguous to the Brazilian Vertical Datum (BVD) lacks of observations and data required for realizing its connection with other vertical networks in the world as required for a Global Vertical Reference System (GVRS). A consistent positional and gravity data base in the region is a fundamental condition for realizing the future Vertical Datum SIRGAS (Sistema de Referência Geocêntrico para as Américas) – DVSIRGAS (Drewes et al., Vertical Reference System, IAG Symposia Series, Springer, Berlin. vol. 124, pp. 297–301, 2002). In the BVD region, placed in the Imbituba harbor, South Brazil, several benchmarks (BM's) have been lost. In order to improve the distribution of data in this region, we conducted a study on the behavior of the system of three linked lagoons under influence of the ocean dynamics in the region. They cover about 20 × 30 km with a 140 km perimeter in the contiguous region of the BVD. The purpose was to use its mean level as an indicator of a natural equipotential surface close to the geoid (or quasi-geoid). A local geodetic network with about 200 points was established. In this network gravity and precise position with Global Positioning System (GPS) were observed. Some of these points are existing BM's connected to the BVD. Three tide gauges that recorded the heights of the water level in the lagoons over a period of approximately 3 months were also employed. In this lagoon system, it was possible to determine an approximate equipotential surface from the mean lagoon level (MLL). Then, we determined the shift between the geopotential in the BVD and the lagoon system. Estimations coming from a global geopotential model allowed determination of a provisional value for the Sea Surface Topography (SST) in the BVD.

S.R.C. de Freitas (✉)
Department of Geomatics, Federal University of Paraná, Centro Politécnico, Curitiba 81531-990, Brazil
e-mail: sfreitas@ufpr.br

42.1 Introduction

Most of the Brazilian vertical network (BVN) composed of around 65,000 Bench Marks (BMs), over 180,000 km of leveling lines, was built in the last 60 years without associated gravity observation. Only in the last 20 years the standard of spirit leveling associated with gravity observations was established. The BVD is placed near the southern extremity of the country. It was established by observing 9 years of sea level around the central epoch 1953. There was then more than 20 years without sea level records. The Brazilian coast is about 8,000 km long. Such an extent is not consistent with placing a vertical datum in the south part of the country. In the beginning of 2000 four tide-gauge geodetic control nets in Brazil were placed. However, the temporal and geographic heterogeneities of the BVN by themselves insert several problems relating to the question: How best to use date from the new control tide gauge net? It is obvious that these problems are similar to that of DVSIRGAS: How to link the BVN with other nets in the South American continent? It is evident that the only way to face the problems is to establish one only control based on a global equipotential surface and give physical meaning for the heights in the BVN.

Since 1995, a research group from Federal University of Paraná and the IBGE (Brazilian Institute of Geography and Statistics) have been developing

S.P. Mertikas (ed.), *Gravity, Geoid and Earth Observation*, International Association of Geodesy Symposia 135,
DOI 10.1007/978-3-642-10634-7_42, © Springer-Verlag Berlin Heidelberg 2010

strategies related to the BVN improving and BVD redefinition (Freitas et al., 2002; Luz et al., 2007; Dalazoana et al., 2007). Some achievements have already been obtained as: historical reference level recovered at BVD allowing the link with new sensors; determine the geocentric position of the BVD which is continuously monitored nowadays; monitoring the eustatic movements allowing us to determine the Mean Sea Level (MSL) trend at the BVD by an approach based on satellite altimetry. Analysis of the BVN, considering its evolution and possible strategies to give physical meaning for heights in the whole network and introducing some external control were recently defined. These aspects are reported by Luz (2008). The fusion of continental and ocean gravity data are now under consideration for the BVD region. This approach is directed at solving the local geodetic reference inconsistencies and aim to link the BVD with a Global Vertical Height System by determining the local SST. One estimation of SST is reported here.

42.2 A General View of Vertical Datums Connection

Heck and Rummel (1990) proposed four strategies to determine the SST as basis for connecting different vertical datums by integrating land and ocean observations:

i. *Oceanographic approach*: In this approach the SST is considered consequence of oceanic currents, meteorological effects and spatial variation of temperature and salinity; it would be determined only by analysis of oceanographic phenomena. Then the SST can be determined by steric and geostrophic leveling. The main problems in this approach are (1) the complexity and (2) the lack of resolution of these techniques in shore regions, were the tide gauges are generally placed.
ii. *Satellite altimetry associated to geostrophic leveling*: The SST in open ocean areas is derived from satellite altimetry and extrapolated to the tide gauge by geostrophic leveling. The main problem is the lack of resolution of geostrophic leveling in coastal shallow basins. Dalazoana et al. (2007) developed strategies to overcome this problem by using a model based on the correlation of the ocean behavior in satellite altimeter bins and in tide gauge sites at the Brazilian coast.
iii. *Gravity associated to satellite positioning*: In this approach, the 3D geometrical position by satellite positioning of vertical datum is used as additional information to compute the offset of SST and the gravity anomalies bias by a least square collocation adjustment. Data fusion procedures are now under investigation for the BVD.
iv. *Geodetic boundary-value problem approach (GBVP)*: In this approach, the vertical datum is considered as part of the framework of GBVP. Advanced solutions of this problem are proposed by Lehmann (2000), considering free vertical datum in the altimetry-gravimetry problems.

Nowadays, the possibilities are expanded because of the potential use of data coming from spatial platforms. In general the SST can be associated with local disturbances related to the geopotential. The densification of gravity information around the Datum must enable the determination of the local disturbances. For this, it is necessary to integrate the contribution coming from anomalous continental mass as well as that from the ocean.

42.3 A Test Approach for SST Determination at the BVD

The lagoon system of Imarui is formed by three linked lagoons affected by the ocean tides. Because smoothed meteorological effects on it, this system is an excellent basis for studying physical aspects related to the gravity field in the region of the BVD. By analyzing of its dynamics in one local height system it is possible to determine one equipotential surface from the mean lagoon levels (MLL) in the form:

$$\mathrm{MLL} = \text{equipotential surface} + \varepsilon \qquad (1)$$

where the term ε refers to the influence of several common ocean processes on the lagoons. According with Mesquita (1997), the most important among these effects are the near offshore ocean streams, density heterogeneities, surrounding mass attracting effects, meteorological disturbances, local basin resonances

and un-modeled tidal driving forces with seasonal effects.

In the present context, the levels of the lagoons are measured with respect to a realized and controlled local height system based on geopotential differences. The determination of normal heights over the points around the lagoons allows us to refer this system to the quasi-geoid. Because the lack of a sufficient number of BMs in the region of the BVD, this local height system was also linked to the BVN and the heights were also expressed as Helmert-orthometric and Dynamic ones.

The lagoon system has a mean height close to the local MSL. Then, the connection of the local network related to the lagoon system with the BVD was based in the propagation of geopotential differences based on height anomalies from several points to the Datum. The SST is given by difference of the mean value of geopotential propagated between the Datum W_{BVD} and a global reference value W_0 in the form:

$$\mathrm{SST} = \frac{W_{\mathrm{BVD}} - W_0}{\gamma_{\mathrm{BVD}}} \tag{2}$$

where γ_{BVD} is the normal gravity value at the BVD. The details of the approach are in the next sections.

42.4 Mean Lagoon Level (MLL)

The water levels were measured continuously at three tide gauge stations (TG-01, TG02 and TG03) in the three lagoons. The distribution of stations is shown in the Fig. 42.1.

From the lagoon water levels it is possible to investigate if the MLL can be considered a good reference for materialize one equipotential surface, and consequently, if it is a reasonable basis for studying the local geopotential anomaly related to a global reference coming from one global geopotential model. The geometry of the proposed study is shown in the Fig. 42.2.

From Fig. 42.2 we note that the equipotential surface determined from the MLL has no constant orthometric height or normal height, but its dynamic height is constant because:

$$H^{\mathrm{D}} = \frac{W_{\mathrm{BVD}} - W_{\mathrm{MLL}}}{\gamma_{45^\circ}} \tag{3}$$

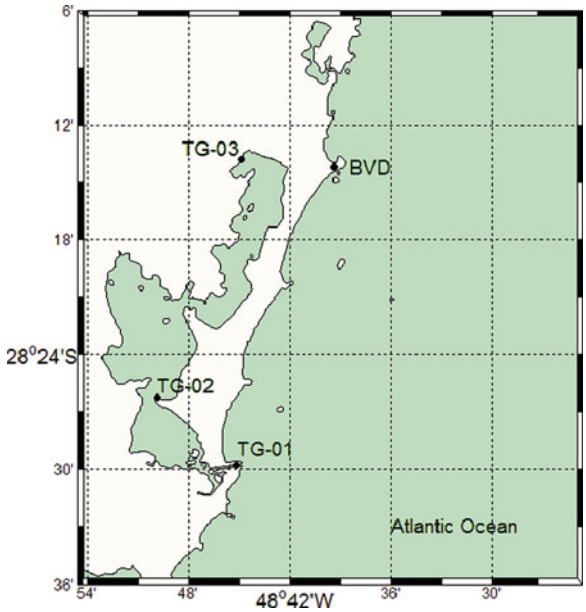


Fig. 42.1 Imarui lagoon system and Brazilian vertical datum

being its geopotential number related to the BVD:

$$C_{(\mathrm{MLL})(\mathrm{BVD})} = W_{\mathrm{BVD}} - W_{\mathrm{MLL}}. \tag{4}$$

The link of the TG stations to the BVD was done by spirit leveling from some nearby BMs and also by differential GPS positioning if limitations for spirit leveling existed. From several leveled points around the lagoons we also determined the water level by GPS/RTK. From the analysis of hourly water level in the TG stations and the water level in the other points it was possible to estimate the values of ε related to a spatial distribution of local shifts of the MLL from an

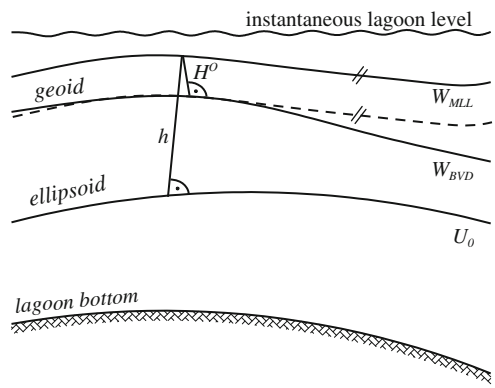


Fig. 42.2 Geometry for studying the MLL

equipotential surface. These shifts were initially associated with variations in the obtained height anomaly values.

The observed water levels in shallow waters are mainly affected by slopes determined by interaction with the wind. A level difference in the direction of the wind occurs. It is function of the depth and horizontal dimensions of the lagoons, and wind velocity. When the driving forces disappear the water mass tends to recover the equilibrium state in an oscillatory process (*seiche*). The *seiche* can be classified as a function of the nodal points where there is no oscillatory movements. It is more common to experience one-nodal *seiche* and less frequent to have bi-nodal ones.

The tidal analysis for the three stations allowed us to determine a residual tide for each station, in according with Pugh (1987, pp. 186). The residual tides must contain local effects not predicted in the harmonic analysis like *seiches*, bottom high frequency resonances, and meteorological effects. From the harmonic tide analysis it is also possible to obtain secular tendencies but it is limited by the data window. In the present work the time series in each tide gauge has only 107 days. For this reason the analysis of secular trends is limited. The spectral analysis was considered as an important tool because it reveals red noise in the residual tide.

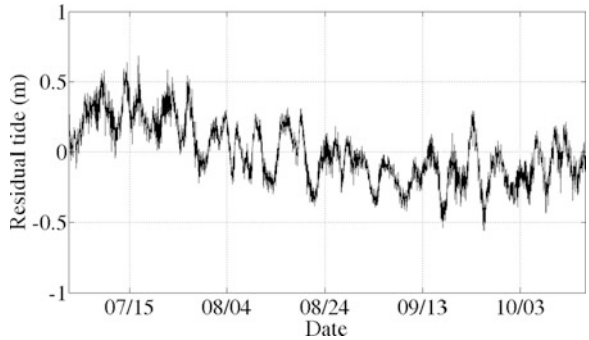


Fig. 42.3 Residual tide in TG-01 station

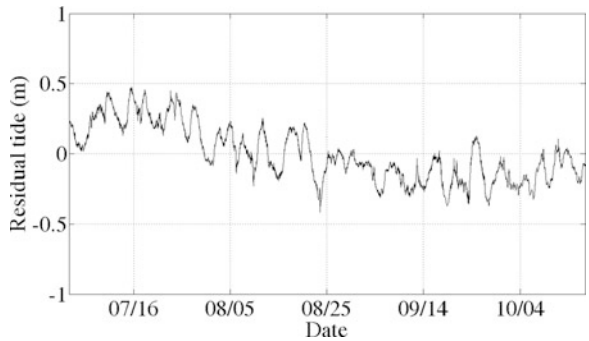


Fig. 42.4 Residual tide TG-02 station

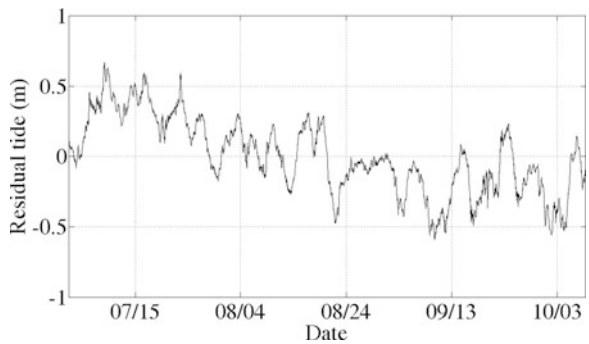


Fig. 42.5 Residual tide TG-03 station

42.5 Data Analysis

42.5.1 Tidal Analysis

The phase-lag of M2 wave (the most significant wave in the region) is 4.29 h in the EM-01, 10.3 h for EM-02 and 15.5 h for EM-03. The phase lag in the EM-01 is close to the value predicted for the BVD region by De Freitas (1993) as 64° (4.26 h). These results had shown the delays for the tide propagation in the lagoon system. The mean level related to the GRS80 at each of TG was 1.56 m (TG-01), 1.48 m (TG-02) and 1.45 (TG-03). We can see a very similar form for residual tides at each TG stations (Figs. 42.3, 42.4, and 42.5). The residuals at each TG station have shown a long period trend of decreasing level of about 50 cm.

The correlation analysis of the residuals from the TG stations, considering the phase lag between them is shown in the Table 42.1. The residuals show a high

Table 42.1 Residuals correlation among TG stations

TG stations	Corr. Coef. R	Phase Lag (h)
01 and 02	0.89	3.33
01 and 03	0.91	7.33
02 and 03	0.89	4.00

correlation between the remaining signals at the TG stations.

For the dimensions of the lagoon system, it is possible to determine that for the direction of predominant winds in the region, the extension of the water nap is 30 km long with a mean depth of 13.5 m. These values related to a *seiche* period of 1.43 h or 16.1 CPD (cycles per day). The power spectrum densities of residual tides did not had shown expressive energy for frequencies over 8 CPD at the three TG stations. Consequently, the spectral analysis is considered only less than 8 CPD. The spectral analysis for each TG station is done considering two frequency intervals for the power spectrum densities: 0.02 CPD to 0.5 CPD (Figs. 42.6, 42.7, and 42.8); and 0.5 CPD to 8 CPD (Figs. 42.9, 42.10, and 42.11).

A long period level variation as well as periodic signal under 0.5 CPD is common in all three TG stations. In some frequencies the amplitudes can reach decimeters. They do not introduce error in reductions

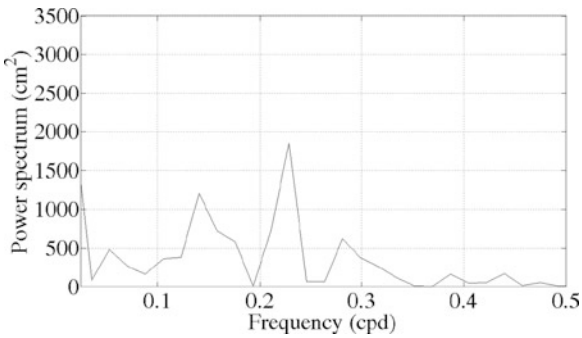


Fig. 42.6 Residual tide power spectrum density in the TG-01 (0.02–0.5 CPD)

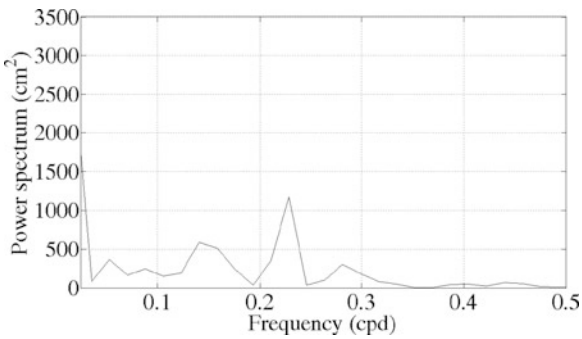


Fig. 42.7 Residual tide power spectrum density in the TG-02 (0.02–0.5 CPD)

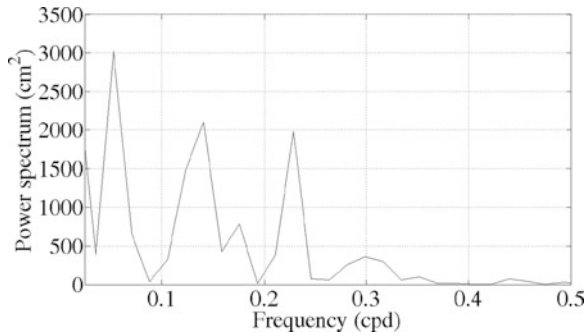


Fig. 42.8 Residual tide power spectrum density in the TG-03 (0.02–0.5 CPD)

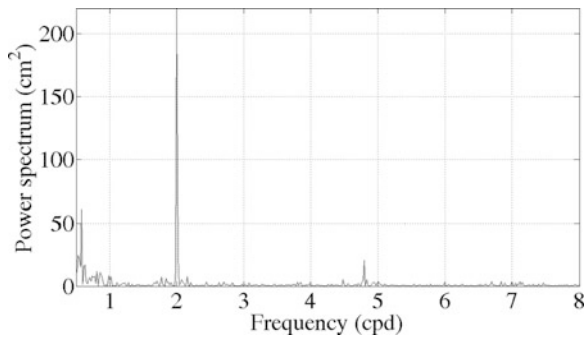


Fig. 42.9 Residual tide power spectrum density in the TG-01 (0.5–8 CPD)

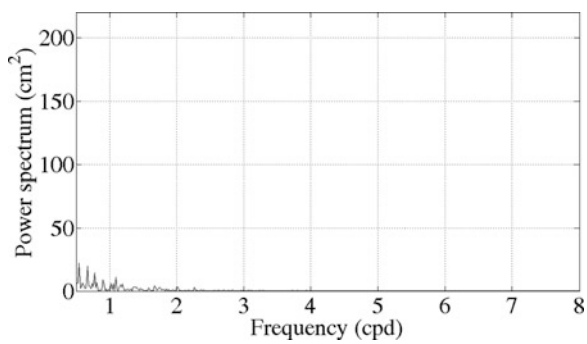


Fig. 42.10 Residual tide power spectrum density in the TG-02 (0.5–8 CPD)

of the MLL with basis in points around the lagoon system. This is because the interpolation at the intermediary points is based on the signal recorded at each TG station.

It can be considered that for the frequencies between 0.5 CPD and 8 CPD, only at TG-01 does a strong

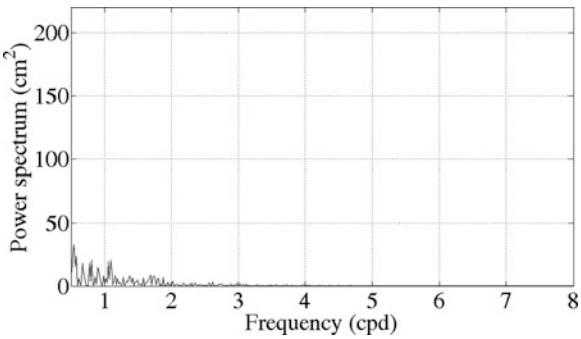


Fig. 42.11 Residual tide power spectrum density in the TG-03 (0.5–8 CPD)

residual energy at 2 CPD exist. This corresponds to the amplitude of about 14.6 cm which can explain the discrepancy of the mean level height in this station when compared with the two other. It is indeed that this component happens as consequence of semi-diurnal meteorological effect in the station close to the shore region and tide contamination from the ocean tide.

42.5.2 Geopotential Numbers and Heights

The derivation of geopotential numbers for the points around the lagoon system related to the BVD was based in leveling associated with gravimetry. The observed water level by GPS/RTK from the points of the local leveling network around the lagoon system was corrected using the synthetic tides interpolated for each site. In this process we considered the phase delays estimated from the relative position between the two nearest TG stations.

We computed the heights for the local network in the normal, Helmert-orthometric and dynamic systems. Table 42.2 shows the values for the geopotential numbers C, normal heights H^N, Helmert-orthometric heights H^H and dynamic heights for the three TG stations. Their geopotential numbers were computed using the EGM96 model (degree and order 360). Geopotential differences were determined from the TG stations to four existing BMs around the lagoon system. The mean value of geopotential differences at each BM was considered and propagated to BMs near the BVD. As a close height reference related to the BVD, BM 4X-IBGE was chosen. Its propagated geopotential number was $C_{4X} = 84.62\,\mathrm{m^2 s^{-2}}$.

Table 42.2 Geopotential numbers and heights for the TG

Tidal gauge	$C(\mathrm{m^2 s^{-2}})$	H^N(m)	H^H(m)	H^D(m)
TG-01	0.75	0.08	0.08	0.08
TG-02	–0.10	–0.01	–0.01	–0.01
TG-03	–0.22	–0.02	–0.02	–0.02

The equipotential surface associated with the MLL was determined as having $C_{(MLL)(BVD)} = 0.14\ \mathrm{m^2\ s^{-2}}$. It is realized as having the dynamic height $H^D = 0.01$ m. The intersection of this surface with the terrain can be established by its height difference measured from the local network around the lagoon system. That was the basis for determining the geopotential difference of BVD as related to a global reference value.

It was then, possible to propagate the geopotential value from the lagoon system to the BVD as W_{IMB}=62636855.45 $\mathrm{m^2\ s^{-2}} \pm 0.1\ \mathrm{m^2\ s^{-2}}$. If it is considered the reference value for a global geoid as W_0= 62636853.3 $\mathrm{m^2\ s^{-2}}$ (Sánchez, 2008), then it is indeed an SST of – 22 cm ± 0.01 m (EGM96), – 29 cm ± 0.01 m (EGM2008 up to 360) and – 30 cm ± 0.01 m (EGM2008 up to 2190) related to the global reference value.

42.6 Final Remarks

In the contiguous region of the BVD there is no sufficient geodetic reference related to heights or gravity to use a classical approach for determining the anomalous potential. Most of BMs in the region were destroyed or affected by movements. In order to minimize these problems and the local difficulties for establishing geodetic control with a sufficient density, the existing lagoon system was used. The relationship of its mean surface to an equipotential surface was determined. A local leveling network was linked to this mean surface. This allowed us to determine its geopotential number and obtained several controls for offsets related to the EGM96 model. From the mean value of these residuals it was possible to determine a geopotential value for the BVD.

Acknowledgements The authors would like to thank by the financial support from CNPq (Brazilian Council of Research) Process 134943/2006-6, 550830/2002-2, and 140084/2004-5. The following institutions must be acknowledged for their fundamental support: the IBGE; and Imbituba Harbor Administration.

References

Dalazoana, R., S.R.C. de Freitas, J.C. Baez, and R.T. Luz (2007). Brazilian. Vertical datum monitoring – vertical land movements and sea level variations. In: Dynamic planet, IAG symposia series, Springer, Berlin, Vol. 130: pp. 71–74.

De Freitas, S.R.C. (1993). Marés Gravimétricas: Implicações para a Placa Sul-Americana. Tese (Doutorado em Geofísica)– Instituto Astronômico e Geofísico, Universidade de São Paulo, São Paulo. 264 pp.

De Freitas, S.R.C., S.H.S. Schwab, E., Marone, A. Pires, and R. Dalazoana (2002). Local effects in the Brazilian vertical datum. In: Vistas for geodesy in the new millennium. IAG symposia series. Springer, Berlin, Vol. 125: pp. 102–107.

Heck, B. and R. Rummel (1990). Strategies for solving the vertical datum problem using terrestrial and satellite data. In: Sea surface topography and the geoid. Springer-Verlag, Berlin. pp. 116–128.

Lehmann, R. (2000). Altimetry-gravimetry problems with free vertical datum. *J. Geodesy*, 74, 327–334.

Luz, R.T. (2008). Estratégias para a Modernização da componente vertical do sistema Geodésico Brasileiro e Sua Integração ao SIRGAS. Curitiba. Tese (Doutorado em Ciências Geodésicas) – Setor de Ciências da Terra, Universidade Federal do Paraná. 179 pp.

Luz, R.T., R. Dalazoana, S.R.C. de Freitas, J.C. Baez, and A.S. Palmeiro (2007). Tests on integrating gravity and leveling to realized SIRGAS vertical reference system in Brazil. In: Dynamic planet, IAG symposia series, Springer, Berlin, Vol. 130, pp. 646–652.

Mesquita, A.R. (1997). Marés, circulação e nível do mar na costa sudeste do Brasil. Instituto Oceanográfico – USP, Report. São Paulo. <http://www.mares.io.usp.br/sudeste/-sudeste.html> Access 10 June 2007.

Pugh, D.T. (1987). Tides, surges and mean sea-level. John Wiley e Sons, Chichester.

Sánchez, L. and W. Martínez (2008). Avances en el procesamiento unificado de las redes verticales involucradas en sirgas. In: SIRGAS Meeting May 28–29, 2008 Montevideo, Uruguay.

Chapter 43

Preliminary Results of Spatial Modelling of GPS/Levelling Heights: A Local Quasi-Geoid/Geoid for the Lisbon Area

A.P. Falcão, J. Matos, A. Gonçalves, J. Casaca, and J. Sousa

Abstract Taking GPS-measured ellipsoidal heights with in situ measured gravity values, levelling-measured heights, and knowing the difference between normal gravity potential and geoidal potential, the calculation of normal heights is possible. The difference between normal and ellipsoidal heights allows the computation of gravity anomalies and geoid undulation, and thus the calculation of quasi-geoid and geoid surfaces, to serve practical applications such as large scale map production and engineering applications.

In this work an evaluation of the spatial interpolation techniques used in the quasi-geoid/ geoid local calculation methods is presented. Deterministic interpolators (Inverse Power of Distance – IPD and Radial Basis Functions– RBF), and probabilistic interpolators (Ordinary Kriging – OrdK and Kriging with External Drift – KED) were tested. The sample used in this study is from a 34 km × 28 km area including Lisbon, which includes 25 levelling heights and gravity values measured by the Instituto Geográfico Português, and the related ellipsoidal heights, measured with a LEICA AX1200 double-frequency GPS receiver.

43.1 Introduction

The definition of a common height reference system in the European space has deserved attention in latest EUREF promoted symposia. Resolution no. 3 of the 2007 London symposium describes the definition and realization of the EVRS (European Vertical Reference System) as a priority. The height systems are traditionally based on tide gauge observations, which differ from the geoid due to ocean currents, temperature, pressure, salinity and other local conditions (Fotopoulos, 2003).

The definition and choice of the reference surface for height representation is not consensual and has been widely discussed in the geodetic community, with several authors to address this problem (Hannah, 2001; NOAA, 1998; Featherstone and Kuhn, 2006). As an alternative to the geoid, many countries use the quasi-geoid as reference. According to the official data published by EUREF, several height reference systems coexist, using normal, orthometric and normal-orthometric heights (Jekeli, 2000). In the Portuguese mainland, the official height system is relative to the tide gauge in Cascais, fixed in 1938, and therefore official heights are geopotential related (Casaca, 2007).

The objective of this work is to present a preliminary quasi-geoid for the Lisbon area, obtained by several interpolation functions and to compare their results.

The test area is 34 km × 28 km, and includes Lisbon, where 19 benchmarks (obtained by levelling) and 6 geodetic marks of the geodetic network (for which the orthometric height and gravity values are known) were identified. Ellipsoidal heights, for the whole sample, were obtained using a double-frequency GPS receiver and a LEICA AX1200 antenna. For each point, at least 360 positions were recorded with a frequency of 5 s. The next step was transformed ellipsoidal coordinates to the ETRS89 system, according to Boucher and Altamimi (2007).

A.P. Falcão (✉)
Departamento de Engenharia Civil e Arquitectura (DECivil), Instituto Superior Técnico, Universidade Técnica de Lisboa, Lisboa 1049-001, Portugal
e-mail: afalcao@civil.ist.utl.pt

S.P. Mertikas (ed.), *Gravity, Geoid and Earth Observation*, International Association of Geodesy Symposia 135,
DOI 10.1007/978-3-642-10634-7_43, © Springer-Verlag Berlin Heidelberg 2010



Fig. 43.1 Spatial distribution of the sample

Figure 43.1 illustrates the location and spatial distribution of the sample.

43.2 Normal Heights and Height Anomalies

We describe in this section the process of normal height determination.

The first step involves setting up the normal height, as the distance between the ellipsoid and the telluroid. The telluroid surface is defined by points where normal gravity potential equals the gravity potential at earth surface, that is:

$$U(Q) = W(P). \tag{1}$$

The difference between the telluroid and earth surface is the height anomaly (AA).

Normal heights were first introduced by Molodensky around 1960 (Heiskanen and Moritz, 1967) based on the theory of normal gravity potential, and are conceptually similar to orthometric heights. The quasi-geoid surface results from the addition of the height anomaly to the ellipsoid. Symbolically, the normal height is represented by:

$$H_N(P) = S(Q) \approx h(Q) \tag{2}$$

The normal height is calculated by dividing the normal potential gravity difference by the medium normal gravity in point Q, according to the following expression (Casaca et al., 2007):

$$H_N(P) = \frac{U_0 - U(Q)}{\bar{\gamma}(Q)} \tag{3}$$

or

$$H_N(P) = \frac{\bar{g}(P)H(P) + U_0 - W_0}{\bar{\gamma}(Q)} \tag{4}$$

For small values of the ellipsoidal height, mean normal gravity can be approximated by the following expression:

$$\bar{\gamma}(\phi,h) = \gamma(\phi)\left(1 - \psi(\phi)\frac{h}{a} + \left(\frac{h}{a}\right)^2\right) \tag{5}$$

where

$$\psi(\phi) = 1 + m + f(1 - 2\sin^2\phi) \tag{6}$$

and

$$m = \frac{\omega^2 a^2 b}{GM} \tag{7}$$

where a, b mean, respectively, the semi-major and semi-minor axes of the GRS80 ellipsoid, GM is the gravitational constant value and ω represents angular velocity.

The ellipsoidal height, h(P), relates to the normal height, $H_N(P)$, and the height anomaly AA(P), according to:

$$h(P) = H_N(P) + AA(P) \tag{8}$$

Using this formula, for each point in the sample normal height and the corresponding height anomalies were calculated.

43.3 Interpolation Techniques

Several local quasi-geoid surfaces were obtained by applying distinct interpolation techniques. The purpose was to allow the evaluation of interpolator results. Deterministic functions (Inverse Power of Distance – IPD and Radial Basis Functions – RBF) and probabilistic methods (Ordinary Kriging – OrdK and Kriging with External Drift – KED) were used.

In order to evaluate and validate the results, the sample was divided into two data sets:

- One set for training (corresponding to 80% of the sample – 21 square points on Fig. 43.1); and
- One set for test (corresponding to 20% of data – 4 triangle points on Fig. 43.1).

Two types of validation were executed: a statistical cross validation for training data and an independent validation with the test data set. Figures in the following section illustrate the distinct quasi-geoid surfaces obtained by the interpolators.

43.3.1 Inverse Power of Distance

Inverse Power of Distance (IPD) is an interpolation method that estimates cell values by averaging the values of sample data points in the neighbourhood of each processing cell. The closer a point is to the centre of the cell being estimated, the more influence. In this case, the value of the power was 2, with a variable search radius with 4 as the minimum number of elements. Figure 43.2 shows the quasi-geoid result when this interpolator was used.

43.3.2 Radial Basis Functions

This method belongs to the group of deterministic exact interpolators, that is, the surface must predict exactly each sample value. A completely regularized spline method was chosen. Figure 43.3 shows the quasi-geoid result when this radial basis function was used.

43.3.3 Ordinary Kriging

The Ordinary Kriging (OrdK) method is a probabilistic interpolator. A spherical model was used as a probabilistic model, and an isotropic behaviour for the variable was assumed. Figure 43.4 shows the quasi-geoid result.

43.3.4 Kriging with External Drift

Finally, kriging with external drift (KED) was used. The auxiliary variable was elevation (a DEM grid).

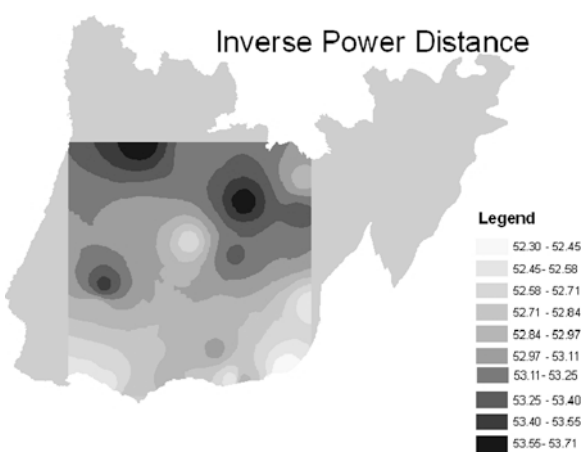


Fig. 43.2 Quasi-geoid result by inverse power of distance interpolation technique

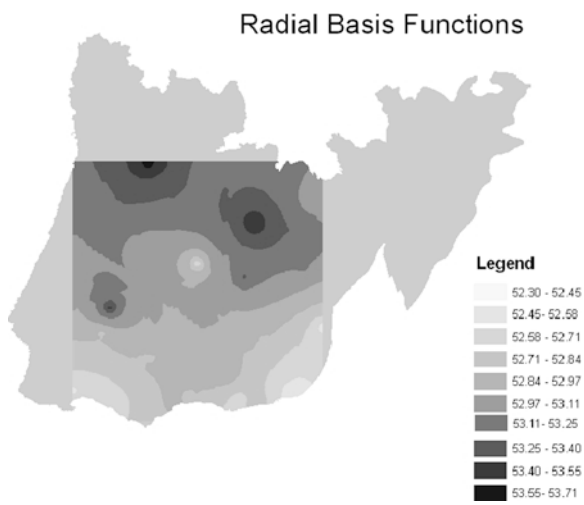


Fig. 43.3 Quasi-geoid result by radial basis function interpolation technique

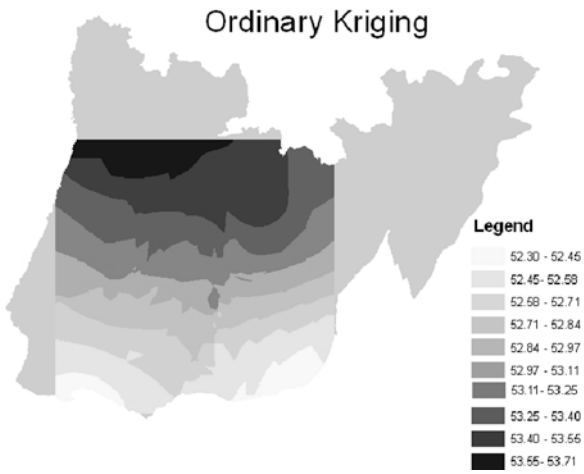


Fig. 43.4 Quasi-geoid result by Ordinary Kriging interpolation technique

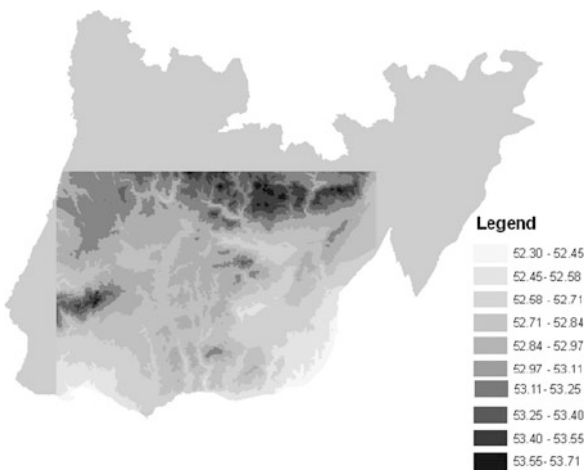


Fig. 43.5 Quasi-geoid result by Kriging with external drift interpolation technique

The justification for the use of KED in the set of methods under analysis relies on the high value for the correlation coefficient between height anomaly and orthometric height (~0.75). The same assumptions made for the previous interpolation methods or models were made in this case. Figure 43.5 shows the results.

43.4 Analysis and Conclusions

An assessment of the performance for the results of the interpolators was made using the test data set in an independent way. As such, for all points in the test data set, the true values of height anomaly were compared with the outcome of the interpolation technique. Root mean square and range values were calculated. The results are presented in Table 43.1.

Table 43.1 Comparison of interpolator results

Interpolator	RMS (m)	Range (m)
IPD	0.16	0.50
RBF	0.17	0.42
OrdK	0.07	0.13
KED	0.09	0.19

In each interpolator group (deterministic or probabilistic) the results are very similar. As expected, the best results were obtained with the probabilistic interpolators, in this case with a small advantage of OrdK on RMS result, despite of the KDE result, which appears to be more realistic.

Acknowledgments Authors would like to thank Instituto Geográfico Português for data availability.

References

Boucher, C. and Z. Altamimi (2007). Specifications for reference frame fixing in the analysis of a EUREF GPS campaign. Technical Note.

Casaca, J. and A.P. Falcão (2007). A gravidade normal e as altitudes normais. In: Actas da V Conferência Nacional de Cartografia e Geodesia. Lisboa, Portugal, April 19–20.

Featherstone, W. and M. Kuhn (2006). Height systems and vertical datums: a review in the Australian context. *J. Spatial Sci.*, 51(1):21–42.

Featherstone, W.E., M.C. Dentith, and J.F. Kirby (1998). Strategies for the accurate determination of orthometric heights from GPS. Survey Review, No 34, 267.

Fotopoulos, G. (2003). An analysis on the optimal combination of geoid, orthometric and ellipsoidal height data, PHD thesis, Department of Geomatics Engineering. University of Calgary, Alberta. Canada.

Hannah, J. (2001). An assessement of New Zealand's height systems and options for a futures height datum. Prepared for the Surveyor General land Information New Zealand. University of Otago.

Heiskanen, W. and H. Moritz (1967). Physical geodesy. W. H. Freeman and Company, San Francisco, USA.

Jekeli, C. (2000). Heights, the geopotential, and vertical datums. Technical Report 459. Ohio Sea Grant Development Program, NOAA.

NOAA (1998). National height modernization study. Executive summary of a report to congress available from the National Geodetic Survey.

Chapter 44

Physical Heights Determination Using Modified Second Boundary Value Problem

M. Mojzes and M. Valko

Abstract The realization of the physical height system involves information related to a certain positioning system, a vertical datum, and a gravity reference system. The reference systems reflect the accuracy of a specified epoch characterized by the measurement techniques and by the adopted models of disrupting influences. If we use able to find a solution where the need for at least one reference system disappears, then the accuracy of the estimated function will naturally increase. In this paper, we would like to point out that it is possible to realize the physical heights based on the solution to the modified *second* geodetic boundary value problem, using only the Earth Gravity Model (EGM), the Global Navigation Satellite System (GNSS) and gravity measurements. The solution does not require any information about the local physical heights and it is therefore independent of a local vertical datum. The theoretical principle of such a solution and its practical application in Slovakia is presented.

44.1 Introduction

A theoretical model to realize the world height system has undergone a significant development. Development of the measurement techniques using the artificial Earth satellites has brought a significant contribution to the realization of the World Height System (WHS). Several reputable authors, for example Heck and Rummel (1989), Rummel (2000), Burša et al. (2000), Kouba (2001), Ihde (2007), have formulated the theoretical axioms of the WHS realization. Basically four methods of creating the WHS exist. They are theoretically described by Heck and Rummel (1989) and Rummel (2000). In this paper, we would like to point out that it is possible to realize the WHS by solution to the *second* geodetic boundary value problem, using only the EGM, GNSS and gravity measurements. This solution does not require any information about the local physical heights and it is therefore independent of the local vertical datum. The theoretical principle of the solution and its practical application in Slovakia is presented below.

M. Mojzes (✉)
Department of Theoretical Geodesy, Slovak University of Technology in Bratislava, Bratislava 813 68, Slovak Republic
e-mail: marcel.mojzes@stuba.sk

44.2 Mathematical Formulations

We start with modified formula for normal height determination

$$H_P^n = \frac{W_0 - W_P}{\bar{\gamma}}, \tag{1}$$

where W_0 is the gravity potential on the geoid, W_P is the gravity potential at the point P on the Earth surface and $\bar{\gamma}$ is the mean value of the normal gravity acceleration between the equipotential ellipsoid and the point P and can be determined from the following formula

$$\bar{\gamma} = \frac{1}{h_P} \int_{ellipsoid}^{P} \gamma \, dh, \tag{2}$$

where h_P is the ellipsoidal height of P. The geometry of Eq. (1) is shown in Fig. 44.1. The maximum differences between formula (1) and classical Molodensky

S.P. Mertikas (ed.), *Gravity, Geoid and Earth Observation*, International Association of Geodesy Symposia 135,
DOI 10.1007/978-3-642-10634-7_44, © Springer-Verlag Berlin Heidelberg 2010

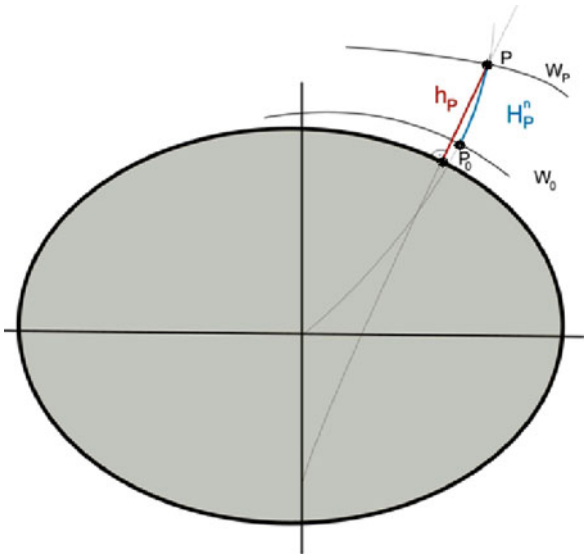


Fig. 44.1 Normal height

formula (Molodensky et al., 1962) in Himalayas is 17 cm.

As it has been shown, (see Burša et al., 1998), it is possible to derive the value of the gravity potential on the geoid using the satellite altimetry measurements. The gravity potential at the point P we can determine by formula

$$W_P = W_{EGM,P} + \delta W_{RES,P}, \tag{3}$$

where $W_{EGM,P}$ is the global part of the Earth gravity potential and $\delta W_{RES,P}$ is the residual part of the Earth gravity potential at the point P.

The global part of the gravity potential can be calculated from the formula

$$W_{EGM,P} = \frac{GM}{r_P} + \frac{GM}{r_P}\sum_{n=2}^{n_{\max}}\left(\frac{a}{r_P}\right)^n \cdot \left[\sum_{k=0}^{n}\left(\bar{C}_{n,k}\cos(k\lambda_P) + \bar{S}_{n,k}\sin(k\lambda_P)\right)\bar{P}_{n,k}(\sin\bar{\varphi}_P)\right] + \frac{1}{2}\omega^2\left(X_P^2 + Y_P^2\right), \tag{4}$$

where $GM, a, \omega, \bar{C}_{2,0}$ are the basic parameters of the Earth, $\bar{C}_{n,k}, \bar{S}_{n,k}$ are the fully normalized spherical harmonic coefficients of a particular EGM, $\bar{P}_{n,k}$ represents the normalized Legendre function, $r_P, \bar{\varphi}_P, \lambda_P$ are the spherical coordinates of the point P and X_P, Y_P are the Cartesian coordinates of the same point P.

The residual part of the Earth gravity potential at the point P is given by the formula

$$\delta W_{RES,P} = \delta W^0_{RES,P} + \delta W^1_{RES,P}, \tag{5}$$

where

$$\delta W^0_{RES,P} = \frac{R}{4\pi}\iint_{\sigma=100\,km}\delta g_{RES}H(\psi)d\sigma,$$
$$\delta W^1_{RES,P} = \frac{R}{4\pi}\cdot \iint_{\sigma=100\,km}\left(\delta g_{RES} - \frac{\partial \delta g_{RES}}{\partial h}(h-h_p)\right)H(\psi)d\sigma, \tag{6}$$

where R is the mean radius of the Earth, approximating the reference ellipsoid when dealing with the second boundary value problem, $H(\psi)$ is the spherical approximation of the Hotine function (Hofmann-Wellenhof and Moritz, 2005)

$$H(\psi) = \frac{1}{\sin(\psi/2)} - \ln\left(1 + \frac{1}{\sin(\psi/2)}\right), \tag{7}$$

ψ is the spherical distance and δg_{RES} is the residual gravity disturbance given by

$$\delta g_{RES} = \delta g_{mer,P} - \delta g_{EGM,P}. \tag{8}$$

In Eq. (8), $\delta g_{mer,P} = g_P - \gamma_P$ is the measured gravity disturbance, g_P is the measured gravity acceleration in certain gravity reference system, γ_P is the normal gravity acceleration based on the accepted standard Earth reference parameters GM,a,ω,$\bar{C}_{2,0}$ computed according to formula (Hofmann-Wellenhof and Moritz, 2005)

$$\gamma_P = \sqrt{\gamma^2_{u,P} + \gamma^2_{\beta,P}},$$
$$\gamma_{u,P} = \left(\frac{1}{w}\frac{\partial U}{\partial u}\right)_P, \gamma_{\beta,P} = \left(\frac{1}{w\sqrt{u^2+E^2}}\frac{\partial U}{\partial \beta}\right)_P. \tag{9}$$

The last term in Eq. (8) can be computed by the following formula

$$\begin{aligned}\delta g_{EGM,P} &= \frac{GM}{r_P^2}. \\ &\cdot \sum_{n=2}^{n_{\max}} (n+1) \left(\frac{a}{r_P}\right). \\ &\cdot \sum_{k=0}^{n} \left[\Delta \bar{C}_{n,k} \cos(k\lambda_P) + \Delta \bar{S}_{n,k} \sin(k\lambda_P)\right]. \\ &\cdot \bar{P}_{n.k}(\sin \bar{\varphi}_P),\end{aligned} \tag{10}$$

where

$$\begin{aligned}\Delta \bar{C}_{n,k} &= \bar{C}_{n,k} - \bar{C}^n_{n,k} \text{ for } k = 0, \\ \Delta \bar{C}_{n,k} &= \bar{C}_{n,k} \text{ for } k \neq 0, \\ \Delta \bar{S}_{n,k} &= \bar{S}_{n,k} \text{ for } k \neq 0,\end{aligned} \tag{11}$$

and $\bar{C}^n_{n,k}$ are fully normalized spherical harmonic coefficients accepted for chosen equipotential ellipsoid.

44.3 Practical Solutions

The practical solution has been carried out using the tide free reference model. Calculation of normal gravity acceleration, global potential and global gravity disturbance has been performed using the GRAFIM (Gravity Field Modelling) software developed at the Department of Theoretical Geodesy, see (Janák and Šprlák, 2006) and (Vaľko et al., 2008). The EGM96 global Earth model parameters (Lemoine et al., 1998) have been used, where

$$\begin{aligned}\text{GM} &= 398\,60\,441.5 \times 10^6 \text{ m}^3.\text{s}^{-2} \\ \omega &= 7292\,115\ 10^{-11} \text{ rad.s}^{-1}, \\ \bar{C}_{2,0} &= 484\,65.371\,736 \times 10^{-9}\end{aligned}$$

with geopotential coefficients up to degree and order 360. The value of the gravity potential on the geoid has been adopted (Burša et al., 2000)

$$W_0 = 62\,636\,856.0 \text{ m}^2.\text{s}^{-2}.$$

This value is based on TOPEX/POSIDON altimetric satellite measurements.

Detailed gravity measurements at approximately 200,000 points with the average density of 4–6 points/km^2, have been used for computation of gravity disturbances. The measured gravity values have been transformed into the Gravimetric Reference System 1995 of Slovak Republic (Klobušiak and Pecár, 2004). The position of the points, initially exported from the topographic maps 1:25,000, has been transformed into the reference system ETRS89 using a 2D transformation model (Mojzeš, 1997).

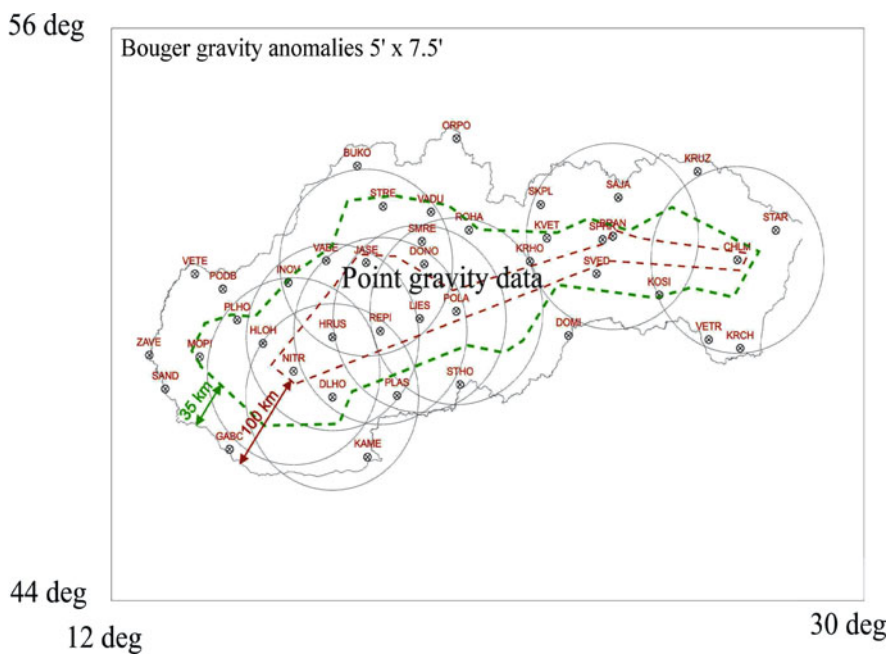
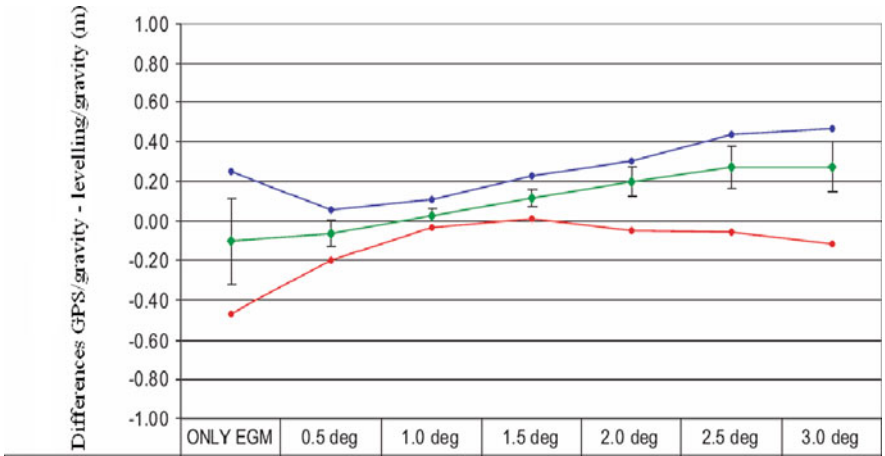


Fig. 44.2 Location of gravity disturbance boundaries and points of SLOVGERENET95

The Bouguer gravity anomalies covering the area 44°N–56°N and 12°E–30°E to boundary of Slovakia with grid spacing 5′ × 7.5′ were transformed to gravity disturbances (Fig. 44.2). The ellipsoidal height of all points has been derived from normal heights and heights anomalies. The height anomalies were interpolated from quasigeoid model EGG97 (Denker and Torge, 1998).

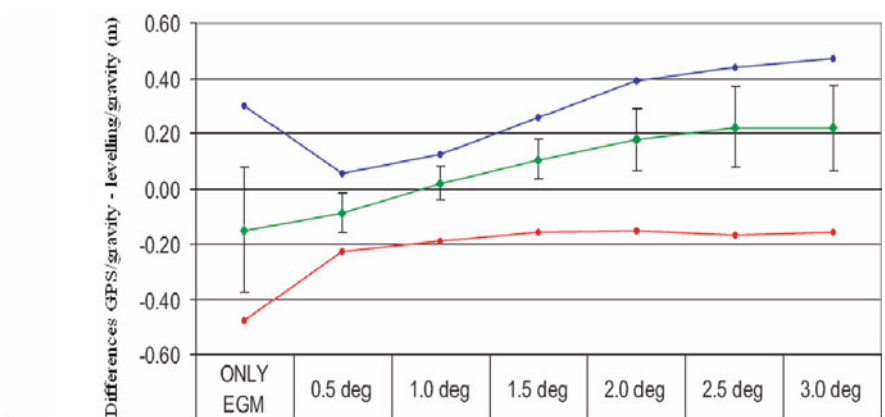
According to the above mentioned theory, the normal heights of the 42 GPS sites of SLOVGERENET95 network (Fig. 44.2) have been computed and tested with classical normal heights determined by leveling/gravity method.

The computation of normal height was tested for different radii of spherical caps (0.5°, 1.0°, 1.5°, 2.0°, 2.5° and 3.0°) on all SLOVGERENET95 points. The numerical values of differences between GPS/gravity and leveling/gravity heights are presented on Fig. 44.3 using all points, Fig. 44.4 using 25 points located 35 km from boundary of Slovakia and Fig. 44.5 using 9 points located 100 km from boundary of Slovakia.



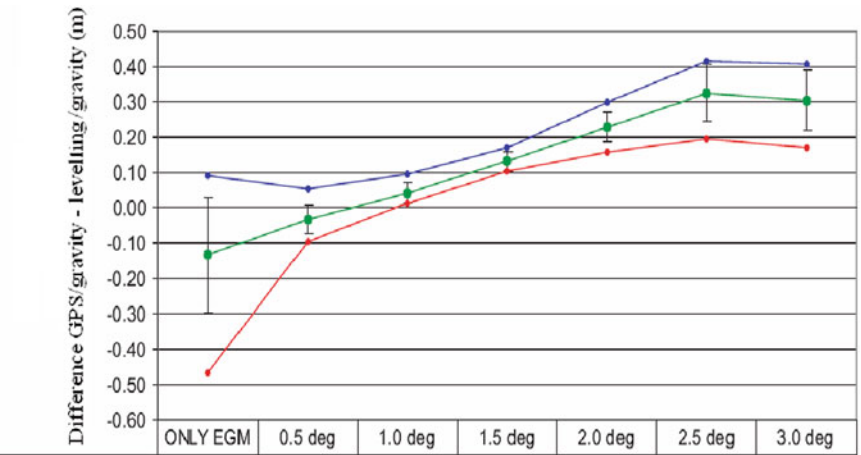
	ONLY EGM	0.5 deg	1.0 deg	1.5 deg	2.0 deg	2.5 deg	3.0 deg
MEAN (m)	-0.1028	-0.0672	0.0298	0.1144	0.1999	0.2725	0.2735
MIN (m)	-0.4664	-0.2005	-0.0356	0.0139	-0.0472	-0.0592	-0.1198
MAX (m)	0.2506	0.0551	0.1095	0.2277	0.3036	0.4388	0.4709
STAND. DEV (m)	0.2156	0.0673	0.0364	0.0468	0.0767	0.1076	0.1296

Fig. 44.3 Differences between normal heights determined by GPS/gravity and leveling/gravity on the all points of SLOVGERENET95



	ONLY EGM	0.5 deg	1.0 deg	1.5 deg	2.0 deg	2.5 deg	3.0 deg
MEAN (m)	-0.1499	-0.0857	0.0207	0.1052	0.1775	0.2223	0.2209
MIN (m)	-0.4797	-0.2278	-0.1904	-0.1585	-0.1517	-0.1700	-0.1558
MAX (m)	0.3006	0.0551	0.1245	0.2562	0.3926	0.4388	0.4709
STAND. DEV (m)	0.2272	0.0730	0.0614	0.0715	0.1121	0.1474	0.1565

Fig. 44.4 Differences between normal heights determined by GPS/gravity and leveling/gravity on 25 points of SLOVGERENET95 located 35 km from boundary of Slovakia



	ONLY EGM	0.5 deg	1.0 deg	1.5 deg	2.0 deg	2.5 deg	3.0 deg
MEAN (m)	-0.1349	-0.0327	0.0416	0.1317	0.2287	0.3259	0.3059
MIN (m)	-0.4664	-0.0972	0.0119	0.1055	0.1566	0.1938	0.1689
MAX (m)	0.0922	0.0550	0.0958	0.1728	0.2992	0.4158	0.4076
STAND. DEV (m)	0.1625	0.0417	0.0296	0.0274	0.0421	0.0806	0.0850

Fig. 44.5 Differences between normal heights determined by GPS/gravity and leveling/gravity on 9 points of SLOVGERENET95 located 100 km from boundary of Slovakia

44.4 Conclusion

The preliminary results have been presented for normal height determination using Earth Geopotential Model, GPS and gravity measurements without leveling. The results of the experiment are very promising for future investigation because the normal heights determined by thi method have a global significance. For future application the unification of all input parameters, especially position and gravity data transformed to a zero-tide reference model as the geodetic standard are strongly recommended. The simultaneous measurements of position by GNSS and of gravity are very useful. Gravity data exchanged between neighboring countries is necessary, or perhaps by establishing of Consortium for exchanging of Gravity Data between all European Countries.

Acknowledgements This study was funded by the Commission of Slovak Grant Agency, Registration number 1/0882/08. We gratefully thank to Commission of Slovak Grant Agency for financial supporting of the Project.

References

Burša, M., J. Kouba, K. Raděj, S.A. True, V. Vatrt, and M. Vojtíšková (1998). Monitoring geoidal potential on the basis of TOPEX/POSEIDON altimeter data and EGM96. Presented at the 5th Common Seminar PfP. Torun, September, 21–23.

Burša, M., J. Kouba, K. Raděj, V. Vatrt, and M. Vojtíšková (2000). Geopotential at tide guage stations usedf for specifying a Word Height System. In: The contributions of participants to the workshop "The way forward to come to an improved World Height System". Geographic Service of the Czech Armed Foces. Prague, November 8–9.

Denker, H. and W. Torge (1998). The European gravimetric quasigeoid EGG97. In: Proceedings of International Association of Geodesy Symposia "Geodesy in the Move". Springer, Berlin, pp. 249–254.

Heck, B. and R. Rummel (1989). Strategies for Solving the Vertical Datum Problem Using Terrestrial and Satelite Geodetic Data. In: Proceedings of International Association of Geodesy Symposia "Sea Surface Topography and the Geoid". International Association of Geodesy Symposia 104. Springer-Verlag, New York.

Hofmann-Wellenhof, B. and H. Moritz (2005). Physical geodesy. Springer, Wien, New York.

Ihde, J. (2007). IAG In: Inter-Commission Project "Conventions for the Definition and Realization of a Conventional Vertical Refrence System", Draft 3.0.

Janák, J. and M. Šprlák (2006). A new software for gravity field modelling using spherical harmonics. *Geodetický a kartografický obzor*, 52(94), 1–8 (in Slovak).

Klobušiak, M. and J. Pecár (2004). Model and algorithm of efective processing of gravity measurement realized with a group of both absolute and relative gravimeters. *Geodetický a kartografický obzor*, 50(92), 99–110 (in Slovak).

Kouba, J. (2001). International GPS service (IGS) and world height system. Acta geodaetica 1/2001. Geographic Service of the Army of the Czech Republic.

Lemoine, F.G., et al. (1998). The development of the joint NASA GSFC and the national imagery and mapping agency (NIMA) Geopotential Model EGM96 NASA/TP-1998-206861, 575 p. Goddard Space Flight Center, NASA Greenbelt Maryland 20771, USA.

Mojzeš, M. (1997). Transformation of coordinate system by multiregresion polynomials. *Kartografické listy*, 5, 12–15 (in Slovak).

Molodensky, M.S., V.F. Eremeev, and M.I. Yurkina (1962). Methods for study of the external gravity field and figure of the earth. Israel Program of Scientific Translations, Jerusalem (Russian original 1960).

Rummel, R. (2000). Global unification of height systems and GOCE. In: International Association of Geodesy Symposia "Gravity, Geoid and Geodynamics 2000" 123. Springer-Verlag, New York, pp. 13–20.

Vaľko, M., M. Mojzeš, J. Janák, and J. Papčo (2008). Comparison of two different solutions to Molodensky's G1 term. *Studia Geophysica et Geodaetica,*52, 71–86.

Part V
Regional Gravity Field Modeling

U. Marti and S. Kenyon

Chapter 45

Impact of the New GRACE-Derived Global Geopotential Model and SRTM Data on the Geoid Heights in Algeria

S.A. Benahmed Daho

Abstract In Algeria and since 2000, two geoid models have been published by the Geodetic Laboratory of the National Centre of Space Techniques using different data sets and techniques. Although these results were satisfactory and internally consistent they do not have the required accuracy to transform a GPS ellipsoidal height to an orthometric height. Recently, the quantity and quality of terrestrial gravity data slightly increased, and especially several new GGM from the recent satellite missions were released. At the same time, the new high resolution SRTM (Shuttle Radar Topography Mission) global DEM was constructed. Logically, these new data represent improvements that must be included in a new geoid for Algeria. The main purpose of this paper is to study the impact of the above new data on the geoid heights in Algeria. For this reason, a new gravimetric geoid determination has been carried out including these new data. The method used in the computation of the geoid has been the Stokes integral in convolution form. This solution was based on the land gravity data supplied by the BGI (Bureau Gravimétrique International), Digital Elevation Model derived from SRTM for topographic correction and the optimal Grace-derived GGM EIGEN-GL04C. This gravimetric geoid and previous geoids existing for this area, are compared to the geoid undulations corresponding to 62 GPS/levelling points located in northern part of Algeria. The study shows that the new gravimetric geoid model agrees considerably better with GPS/levelling than any other local geoid models. Its standard deviations are 27 and 25 cm before and after fitting using a four-parameters model as corrector surface. The new geoid model will be used in low accuracy scientific applications and in low-order levelling network densification with regard to the national levelling network coverage considered as good in the north and becomes poor in the south and West of the country. The availability and accuracy of the land gravity data remain insufficient to agree with GPS/levelling at the sub-centimeter level.

S.A.B. Daho (✉)
Geodetic Laboratory, National Centre of Space Techniques, Arzew 31200, Algeria
e-mail: d_benahmed@hotmail.com

45.1 Introduction

The determination and availability of a high-resolution and more-precise geoid model is a necessity in several geosciences. Nowadays geoid determination is getting more crucial, due to the development of the Global Navigation Satellite Systems (GNSS). The combination of GPS heights with geoid undulations ones can to provide an efficient alternative to derive orthometric heights. This fact makes the study of Geoid and GPS/levelling differences necessary for both practical surveying and scientific applications. To this extend many studies have been performed in different places all over the world and as examples we mention (Forsberg and Madsen, 1990; Fotopoulos et al., 1999b; Kearsley et al., 1993) among others.

In this context, a number of geoid models for Algeria have been produced in recent years to support Levelling by GPS. In particular $5' \times 5'$ geoid models were generated in 2000 (Benahmed Daho, 2000) and in 2004 (Benahmed Daho and Fairhead, 2004), using different data sets and techniques. The comparisons of these local geoid models with a set of

S.P. Mertikas (ed.), *Gravity, Geoid and Earth Observation*, International Association of Geodesy Symposia 135,
DOI 10.1007/978-3-642-10634-7_45, © Springer-Verlag Berlin Heidelberg 2010

the GPS/levelling data available only in the northern part of Algeria have shown that these models do not have the required accuracy to be able to transform a GPS ellipsoidal height to an orthometric height. During the same time and with the recent satellite missions CHAMP and GRACE several new GGM were released. Furthermore, the SRTM has improved tremendously our knowledge of the topography of the Earth's land surface and consequently, the new high resolution SRTM global DEM was generated. The main objective of this work is to study the impact of these new data on the geoid heights in Algeria. In this context, a new geoid model was computed by Fast Fourier Transformation from the land gravity data supplied by the BGI, SRTM based DEM for computation of the effects of the topography, and the optimal global geopotential model EIGEN-GL04C complete to degree and order 360 in terms of spherical harmonic coefficients.

The results of this computation and from the previous geoid solutions over Algeria are compared to GPS/levelling data collected from the international TYRGEONET (TYRhenian GEOdynamical NETwork) project and the local GPS/levelling surveys covering the northern of Algerian and extending from $31° \leq \varphi \leq 37°$ in Latitude and $-2° \leq \lambda \leq 9°$ in Longitude.

45.2 The Used Data

45.2.1 Gravity Anomalies

Gravity anomalies used in this work composed of 12,472 land data covering the territory of Algeria, were supplied by the BGI. The accuracy of these measurements ranges from 0.1 to 0.2 mgal. The data set is referred to the IGSN71 gravity datum and reduced using the GRS80 gravity formula. Figure 45.1 shows the geographical distribution of the available gravity data. All data have been validated and duplicate points removed in a consistent manner. A validation procedure has been applied using Least Squares Collocation method (LSC). The error ratio we have detected using this method was about 4.7% and remains high with regard to the number of measures used (Benahmed Daho and Kahlouche, 1999).

45.2.2 Global Geopotential Model

The problem of choosing a geopotential model which best fits the gravity field in Algeria has not solved definitely. So and in order to obtain an optimal determination of the new Algerian gravimetric geoid

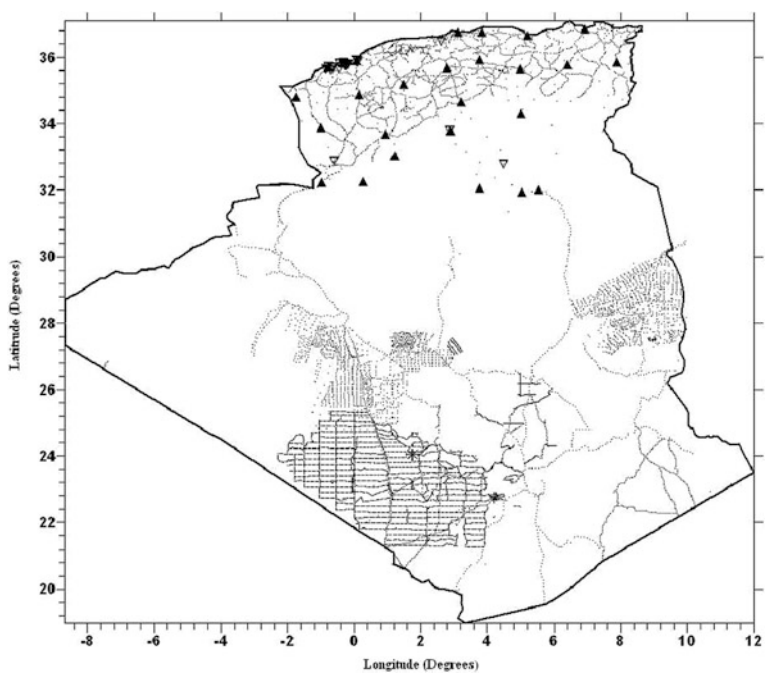


Fig. 45.1 Geographical distribution of BGI gravity measurements and GPS/levelling stations in Algeria (▲: Benchmark point, ∇: Control point)

to support Levelling by GPS, an analysis was carried out to define the geopotential model, which fits best the local gravity field in Algeria. Six global geopotential models have been used in this study: The new GRACE satellite-only and combined models EIGEN-GRACE02S and GGM02C, the combined CHAMP and GRACE model EIGEN-CG01C, the combined GRACE and LAGEOS model EIGEN-GL04C, OSU91A and EGM96. The test of the fitting of these high order geopotential models to the gravity field in Algeria was based on the gravity data supplied by the BGI. and GETECH, and some of the precise GPS data collected from the TYRGEONET and ALGEONET (*ALGerian GEOdynamical NETwork*) projects.

The study has shown that the newly released combined model (EIGEN-GL04C) is consistently superior to other models in the Algerian region (Benahmed Daho et al., 2008). This model was adopted as reference in order to remove and restore the long wavelength components of the gravity and the geoid respectively.

45.2.3 Algerian Digital Elevation Model Based on SRTM Data

The recently available SRTM digital elevation data set opens new perspectives for the regional or local determination of the gravity field. Due to the lack of any high resolution photogrammetric based DEM in the Algeria, a new DEM model was constructed with a resolution of 15″ by use of recent 3″ (∼100 m) high resolution SRTM. The output grid size is limited to $15° \leq \varphi \leq 40°$ and $-15° \leq \lambda \leq 15°$. Small gaps in land and marine areas were patched and filled by an interpolation procedure using information from the new version of GTOPO DEM with a resolution of $30'' \times 30''$. This DEM is used for the interpolation of free-air anomalies and to compute topographic correction in the new geoid model.

A first test of the suitability of the constructed DEM for this purpose was preformed by comparing it to the heights of the BGI gravity data points. The last ones are also compared to GTOPO DEM used in previous gravimetric geoid computations in Algeria. The minimum, maximum, mean and standard deviation of BGI heights are 1, 2,538, 499.2 and 268.8 m, respectively. Table 45.1 shows the statistics in meters of the differences between the constructed DEM and BGI heights data. In most points and for both tested DEM, the differences are smaller than 10 m. According the accuracy of SRTM data, 83.7% (82.9% respectively for GTOPO) of the covered area is in agreement with BGI heights data better than ±16 m (the given SRTM vertical accuracy on the 90% level). There are very few stations where really large differences occur. Usually they are located in areas where there is a SRTM data lack nearby or in south of country.

Table 45.1 Statistics of the differences between BGI heights and tested DEM (Unit: [m])

Differences	Min.	Max.	Mean	σ
SRTM	–320.844	474.712	–0.079	21.726
GTOPO	–324.233	495.921	–0.242	22.060

In conclusion, the comparisons of the different DEM with the BGI heights show that the constructed DEM based on SRTM data agrees considerably better than the GTOPO one. Nevertheless, further comparisons remain necessary to test the quality of SRTM in Algeria.

45.2.4 GPS/Levelling Data

There are several GPS/levelling points distributed over some regions of Algeria principally in the north part of the country. The distribution is fairly good but the total number of GPS stations is too small in relation to north part of Algerian's area. For this investigation, 62 precise GPS levelled points have been used for the evaluation and validation of the new gravimetric geoid of which 45 are benchmarks of the first order levelling network, and the others belong to the second order levelling network. All of these points are located in the north of Algeria territory between $31° \leq \varphi \leq 37°$ and $-2° \leq \lambda \leq 9°$ (see Fig. 45.1). The GPS observations were performed using ASHTECH Z-12 dual frequency receivers with a observation periods between 3 and 12 h and were processed with the Bernese GPS software version 4.2 using the precise ephemerides supplied by IGS. The computed ellipsoidal heights were referred to WGS84 system and their standard deviations do not exceed 3 cm. All GPS stations have been connected by traditional levelling to the national levelling network, which consists of orthometric heights.

45.3 Overview on the Gravimetric Geoid Models of Algeria

Before to compute a new geoid model for Algeria, we present firstly a review of the available gravimetric geoid solutions in Algeria. The first determination of a preliminary geoid over the Algeria named BGI solution was done in 2000 using the Fast Collocation method and with the GRAVSOFT package (Tscherning et al., 1992). This solution is based on a set of 12,183 validated free air gravity anomalies supplied by the BGI, and two elevation grids; 1 km × 1 km digital terrain model for the north of Algeria and the ETOPO5 for the rest of the area, and furthermore the tailored global geopotential model OSU91A complete to degree and order 360. The final result is a gravimetric geoid on a $5' \times 5'$ grid in the area bounded by the limits $20° \leq \varphi \leq 37°$ and $-7° \leq \lambda \leq 10°$ (Benahmed Daho, 2000).

In 2002, an improved geoid was computed for the whole Algeria based on spectral combination techniques in connection with the remove-restore procedure. For this computation, the pre-processed $5' \times 5'$ grid of the free air anomalies from GETECH (Geophysical Exploration Technology Ltd) database covering the area bounded by the limits $16° \leq \varphi \leq 40°$ and $-10° \leq \lambda \leq 14°$, derived by merging terrestrial gravity data and satellite altimetry data, has been used. The computation of the effects of the topography according to the RTM reduction modelling method is based on the global topographic model GLOBE of $30'' \times 30''$. However, for long wavelength gravity field information, the global geopotential model OSU91A complete to degree and order 360 was used. The final result is a gravimetric geoid on a $5' \times 5'$ grid in the area bounded by the limits $16° \leq \varphi \leq 40°$ and $-10° \leq \lambda \leq 14°$. The major contributions to the final geoid are coming from the global geopotential model OSU91A (Benahmed Daho and Fairhead, 2004).

45.4 High-Resolution Geoid Computation

The present gravimetric quasigeoid solution is build up in the usual "remove-restore" technique by three terms

$$\zeta = \zeta_{\mathrm{GM}} + \zeta_{\mathrm{RTM}} + \zeta_{\mathrm{r}} \qquad (1)$$

where ζ_{GM} is the contribution of the geopotential model, while ζ_{r} is the contribution of residual gravity anomalies with the effect of the geopotential model and the terrain removed. ζ_{RTM} is the indirect effect of the terrain reduction.

The computations were done using the GRAVSOFT package, developed during a number of years at the National Survey and Cadastre of the Copenhagen University. For the actual solution, the Fast Fourier Transformation (FFT) was used to compute the quasigeoid. In order to smooth the gravity field, the validated BGI gravity data must be reduced with global geopotential model and the effect of the topography. The global geopotential model EIGEN-GL04C complete to degree and order 360 has been used to remove the long wavelength components of the Earth Gravity Field. The computation of the effects of the topography according to the RTM reduction modelling method is based on previous $15'' \times 15''$ digital terrain model from SRTM which was used up to a distance of 200 km. The reference surface of $30' \times 30'$ needed for the RTM reduction has been obtained by means of a moving average applied to the detailed one. Table 45.2 below shows the statistics in mgal of the reduced gravity data for the new geoid model and for the BGI solution described above in which the same land gravity data supplied by BGI, was used in their determinations but with different reference gravity field and Digital Elevation Model for RTM terrain effect (The statistics given in bold refer to the previous BGI solution). We can see that, for the new solution, the residuals after reduction are significantly smoother than the original data and the corresponding ones from BGI solution. These achievements show clearly the effect of the new global geopotential model EIGEN-GL04C and the SRTM data for the local geoid determination in Algeria.

Table 45.2 Statistics of the reduced gravity data in the computation area (mgal)

Anomalies	Min	Max	Mean	σ
Δg_{Obs}	–82.59	136.99	0.36	23.79
Δg_{GL04C}	–85.44	97.85	1.43	23.07
Δg_{RTM}	–39.57	78.54	–1.16	4.87
Δg_{Obs}-Δg_{GL04C}	–99.36	62.86	–1.07	9.67
	(–67.75)	**(123.46)**	**(0.12)**	**(12.31)**
Δg_r(Re *sidual*)	–73.40	55.16	0.09	9.44
	(–34.17)	**(110.38)**	**(3.09)**	**(13.00)**

Table 45.3 Quasigeoid heights statistics

Unit: Meter	Min	Max	Mean	σ
ζ_r	–1.872	2.483	0.202	0.418
ζ_{GM}	23.090	57.040	35.490	8.320
ζ_{RTM}	–0.634	0.799	0.000	0.060
Final quasigeoid	22.640	56.610	35.150	8.420

The gridding of Δg_r to produce a $5' \times 5'$ grid of residual gravity anomalies between the limits $18° \leq \varphi \leq 38°$ and $-9° \leq \lambda \leq 11°$, was done with the GEOGRID program using a fast quadrant-search collocation algorithm. The gridded residual gravity anomalies have subsequently been converted to heights anomalies by using 1DFFT method. The FFT was carried out on a grid of 241 × 241 points with zero-padding. The Fortran program FFTGEOID of the GRAVSOFT package written by Sideris was used (Tscherning et al. 1992). The final quasigeoid was obtained by adding the geopotential model and the residual terrain effect on the $5' \times 5'$ residual quasi-geoid grid. The statistics of the total quasigeoid values are summarised in Table 45.3. The major contributions to the final quasigeoid are coming from the EIGEN-GL04C. Figure 45.2 shows the final quasigeoid surface referred to the GRS80 ellipsoid. However, the Algerian height system is based on orthometric heights, so the gravimetrically determined quasigeoid has been transformed to a geoid model.

45.5 Comparison of All Gravimetric Geoid Models with GPS/Levelling Data

For our study and in order to conduct comparative evaluation, the different gravimetric geoid undulation solutions (new geoid, BGI and GETECH) are compared with 62 observed GPS/levelling geoid undulations. To minimize the datum inconsistencies between the available height data, long-wavelength geoid errors and GPS and Levelling errors included in the ellipsoidal and orthometric heights, we have tested a four and a seven-parameters transformation models. The four-parameters model is the most commonly used in such adjustments and is given by the following formula (Heiskanen and Moritz, 1967):

$$N_i^{GPS} - N_i = \cos\Phi_i \cos\lambda_i . x_1 + \cos\Phi_i \sin\lambda_i . x_2 + \sin\Phi_i . x_3 + x_4 + v_i \quad (2)$$

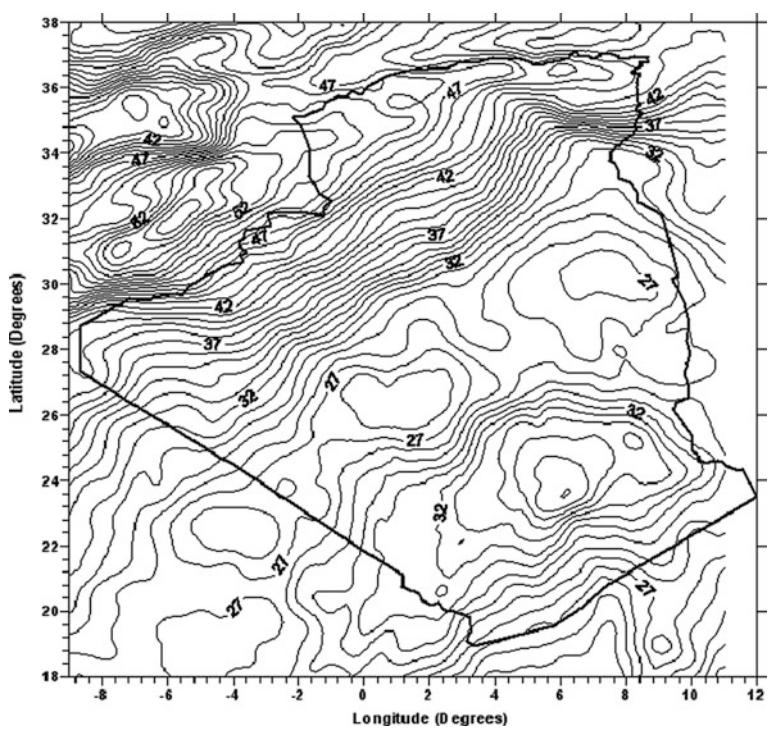


Fig. 45.2 Quasigeoid solution in Algeria (Unit: [m])

where (N) is interpolated geoid undulation at a network of GPS benchmarks, (N^{GPS}) is the corresponding GPS/levelling-derived geoid height, x_4 is the shift parameter between the vertical datum implied by the GPS/levelling data and the gravimetric datum, x_1, x_2 and x_3 are the shift parameters between two "parallel" datums and $\mathbf{v_i}$ denotes a residual random noise term.

The seven-parameters model is a more complicated form of the differential similarity transformation model. It was developed and tested in the Canadian region. It is given by the following formula (Kotsakis et al., 2001):

$$N_i^{GPS} - N_i = \cos\Phi_i \cos\lambda_i . x_1 + \cos\Phi_i \sin\lambda_i . x_2 + \sin\Phi_i . x_3 + \frac{\cos\Phi_i \sin\Phi_i \cos\lambda_i}{W_i} x_4 + \frac{\cos\Phi_i \sin\Phi_i \sin\lambda_i}{W_i} x_5 + \frac{\sin^2\Phi_i}{W_i} . x_6 + x_7 + v_i \quad (3)$$

with Φ_i and λ_i are the horizontal geodetic coordinates of the network and $w_i = \sqrt{1 - e^2 \sin^2 \Phi_i}$ where **e** is the eccentricity of a common datum ellipsoid.

In practice, the most common method used to assess the performance of the selected parametric model is to compute the statistics for the adjusted residuals after fit. The model that results in the smallest set of residuals is considered to be the most appropriate one ("optimal" fit). In fact, these values give an assessment of the precision of the model as they indicate how well the data sets fit each other.

Among these 62 GPS levelled stations, only 27 well distributed GPS points are used as benchmarks in a least-squares adjustment. The 35 uniformly distributed remaining points are excluded from the least-square computation and used as control points in order to make a comparison with the interpolated ones. Several tests using the previous parametric models were conducted to find the adequate functional representation of the correction which should be applied to the gravimetric geoid models that can describe more effectively the general trend of the discrepancies between the GPS/levelling and the gravimetric geoid. The statistics of the differences at benchmarks before and after fitting out the systematic biases and tilts between the gravimetric geoid models and the GPS/levelling data are summarised in Table 45.4 (the statistics given in bold refer to the values of the residuals obtained after fitting using the seven-parameters model). We can see that the best agreement (new geoid model) is at the ± 27 cm level in terms of the standard deviation of the differences, before the application of the transformation. It is at ± 55 cm and ± 45 cm for the BGI and GETECH solutions respectively. This can be mainly attributed to the more accurate long-wavelength information contained in EIGEN-GL04C in comparison to OSU91A used in all previous Algerian geoid computations. After the transformation, a good fit between the tested gravimetric geoid models and GPS/levelling has been reached when the seven-parameters model was used as surface corrector. The fit improvement is almost up to 2.4 cm level for the new geoid model, 23.1 and 18.4 cm for the BGI and GETECH solutions respectively. In addition, we can see that the results from this model are very close to those given by the four-parameters model in terms of standard deviation. The differences range from a few mm to 1.9 cm. The improvement by GETECH solution is negligible. Based on the data sets used in the present work, the new geoid model is consistently superior to others local gravimetric geoid models.

Table 45.4 Comparison of all gravimetric geoid undulations with GPS/levelling heights in benchmarks before and after the bias and tilt fitting (Unit: [m])

	Geoid models	Min	Max	Mean	RMS
Before	New geoid	–0.213	1.097	0.428	***0.274***
	BGI	–3.698	–0.505	–1.933	0.550
	GETECH	–2.244	–0.249	–0.811	0.451
After	New geoid	–0.490	0.411	0.000	0.255
		–0.478	**0.396**	**0.000**	***0.250***
	BGI	–0.645	0.466	0.000	0.338
		–0.582	**0.475**	**0.000**	**0.319**
	GETECH	–0.402	0.574	0.000	0.267
		–0.364	**0.569**	**0.000**	**0.267**

However, the previous RMS value is not the real accuracy of the determined geoid, this provides the proof that the combined adjustment can optimally fit the gravity geoid to the GPS/levelling points. So and in order to assess the real accuracy of the adjustment, the observed orthometric heights in the excluded control points (35) have been compared with the corresponding adjusted ones derived from the combination of ellipsoidal heights and the corrected undulations of the geoid computed using the known parameters for each parametric model. The statistics of the differences obtained with different models are summarized in Table 45.5. We can see that the combination of the new

Table 45.5 Comparison of all gravimetric geoid models with GPS/levelling heights in control points after the bias and tilt fitting (Unit: [m])

Geoid models	Min	Max	Mean	RMS
New geoid	–0.190	0.388	0.020	0.133
	–0.105	**0.453**	**0.084**	**0.160**
BGI	–0.973	0.328	–0.120	0.246
	–0.855	**0.405**	**–0.053**	**0.230**
GETECH	–0.638	0.378	–0.032	0.216
	–0.660	**0.280**	**–0.111**	**0.227**

geoid model with GPS/levelling gives the best results when the four-parameters model is used as corrector surface. The standard deviation of the discrepancies between these two representations at control points is about ± 13.3 cm after fitting. This fact confirms the improvement of the new geoid solution comparatively to other gravimetric geoid. From these results, we may conclude that the four-parameters model used as corrector surface is able to minimize the residuals so that an extended version is not necessary. Of course, we must not neglect that a few millimetre improvement will be important if we are after the centimetre level fit between our data set. However and with regard the present level of agreement, such a constraint is not considered to be necessary.

45.6 Conclusion

The main purpose of this work is to study the impact of the new GRACE-derived global geopotential model and SRTM data on the geoid undulations in Algeria. In this context, a new gravimetric geoid model was computed by Fast Fourier Transformation from the land gravity data supplied by the BGI, Digital Elevation Model derived from SRTM for topographic correction and the optimal Grace-derived GGM EIGEN-GL04C. In order to assess the performances of the new geoid model, homogenous GPS/levelling data (only in the north part of Algeria) were used. We can note that in general this new geoid model is an improvement over other tested gravimetric geoid models. According to our numerical results, the new geoid model fits better the observed GPS/levelling values. The comparisons of the new geoid with GPS/levelling data provide, after fitting, an RMS of about ± 25.0 cm for the north part of Algeria. That remains not sufficient for GPS/levelling purpose but it can be used in low accuracy scientific applications. The biggest weakness in this model is the lack of data in a large part of the country. A significant improvement in the quality of the model will only be realised once these gaps have been filled.

References

Benahmed Daho, S.A. (2000). The new gravimetric geoid in Algeria. Bulletin No 10 of the IGeS, pp. 78–84.

Benahmed Daho, S.A. and S. Kahlouche (1999). Gravimetry data validation in Algeria. *Bolletino Di Geofisica Teorica Ed Applicata*, 40(3–4), 205–210.

Benahmed Daho, S.A. and J.D. Fairhead (2004). A new quasi-geoid computation from gravity and GPS data in Algeria. Newton's Bulletin No. 2, pp. 52–59.

Benahmed Daho, S.A., J.D. Fairhead, A. Zeggai, B. Ghezali, A. Derkaoui, B. Gourine, and S. Khelifa (2008). A new investigation on the choice of the tailored geopotential model in Algeria. *J. Geodynamics*, 45(2–3),154–162.

Forsberg, R. and F. Madsen (1990). High precision geoid heights for GPS leveling. Proceedings of the 2rd international symposium on precise positioning with the global positioning system, September 2–7, Ottawa, Canada, pp. 1060–1074.

Fotopoulos, G., C. Kotsakis, and M.G. Sideris (1999). Evaluation of geoid models and their use in combined GPS/Leveling/Geoid height network adjustment. Technical reports of the Department of Geodesy and Geoinformatics, Universität Stuttgart, Report Nr. 1999.4.

Heiskanen, W.A. and H. Moritz (1967). Physical geodesy. Freeman & Co., San Francisco.

Kearsley, A.H.W., Z. Ahmad, and A. Chan (1993). National height datums, leveling, GPS heights and geoids. *Aust. J. Geod. Photogram. Surv*.59, 53–88.

Kotsakis, C., G. Fotopoulos, and M.G. Sideris (2001). Optimal fitting of gravimetric geoid undulations to GPS/levelling data using an extended similarity transformation model. Presented at the Annual Scientific Meeting of the Canadian Geophysical Union, Ottawa, Canada, May 14–17.

Tscherning, C.C., R. Forsberg, and P. Knudsen (1992). Description of the GRAVSOFT package for geoid determination, Proceedings of First Continental Workshop on the Geoid in Europe, Prague, pp. 327–334.

Chapter 46

On Modelling the Regional Distortions of the European Gravimetric Geoid EGG97 in Romania

R. Tenzer, I. Prutkin, R. Klees, T. Rus, and N. Avramiuc

Abstract We analyze and model the regional distortions of the European Gravimetric Geoid 1997 (EGG97) in Romania using GPS-levelling data. A comparison of the EGG97 gravimetric quasi-geoid with the GPS-levelling data indicates the presence of significant regional distortions in particular areas along the border of the country. To model the regional distortions, we apply two methods: (i) the recently proposed innovation function approach by Prutkin and Klees (J. Geod. 82(3), 147–156, 2007), which is based on a mathematical formulation of the differences between gravimetric quasi-geoid and GPS-levelling data in terms of a Cauchy boundary-value problem for the Laplace equation. (ii) the conventional approach of a low-degree polynomial correction surface. The results reveal that the innovation function approach gives more options to model a more complex trend of the regional gravimetric quasi-geoid distortions than the correction surface approach.

46.1 Introduction

The height reference surface (quasi-geoid) in Romania is realized by the European Gravimetric Geoid 1997 (Denker and Torge 1998). The remove-restore technique was used for computing the EGG97, and data were combined according to the least-squares spectral combination approach (cf. Wenzel, 1982). About 3 million gravity data and 700 million terrain data were used for compiling EGG97. The spatial resolution of the gravity data set was at least 10 km for the entire European continental area, and the digital terrain models had different resolutions varying from about 30 m to a few km. Furthermore, altimetry data were added in marine areas and combined with shipborne gravity.

The comparison of the gravimetric geoid model EGG97 with the geometric geoid at GPS-levelling points revealed the existence of long-wavelength geoid errors with a magnitude of 0.1–1.0 ppm, while over shorter distances up to 100 km the agreement was at the level of 1–2 cm (Torge and Denker, 1999). The existing long-wavelength discrepancies were mainly attributed to corresponding errors in the underlying global geopotential model and the terrestrial gravity data. The systematic deformations of gravimetric geoid/quasi-geoid are commonly modelled either using the empirical correction surface computed by the least-squares collocation method using the signal and trend components (correction surface approach) or by the combined least-squares adjustment of gravimetric and GPS-levelling data using point masses (combined point mass approach). These methods were implemented for further improvement of the EGG97 in particular counties. Denker (1998) and Denker et al. (2000) used the smooth empirical correction surface to compute a height reference surface with cm accuracy in France and Germany. Later, Liebsch et al. (2006) used the combined point mass approach for computing the German Combined (Quasi) Geoid 2005 (GCG2005).

R. Tenzer (✉)
Delft Institute of Earth Observation and Space Systems (DEOS), Delft University of Technology, Delft 2629, The Netherlands
e-mail: R.Tenzer@tudelft.nl

S.P. Mertikas (ed.), *Gravity, Geoid and Earth Observation*, International Association of Geodesy Symposia 135,
DOI 10.1007/978-3-642-10634-7_46, © Springer-Verlag Berlin Heidelberg 2010

The problem of modelling the observed height anomaly differences by a correction surface is that the algebraic polynomial is not the trace of a harmonic function, i.e., it is not compatible with the gravity data (cf. Klees and Prutkin 2008a,b). An alternative method for combining the gravity and GPS-levelling data was recently formulated analytically by Prutkin and Klees (2007). They formulate a Cauchy boundary-value problem for the Laplace equation and solve this problem numerically treating the observed height anomaly differences as boundary data. The result is the innovation function which has to be added to the gravimetric height anomalies in order to obtain the final quasi-geoid. The advantage of the innovation function is that it has the particular property of being compatible with the gravity data, because it is the trace of a harmonic function. Moreover, there is no need to select a priori a proper parameterization as any correction surface requires. Hence, this approach can be used easily for different areas and data sources. Recently, we implemented the innovation function approach for improving the Dutch height reference surface (Klees et al., 2008). In Tenzer et al. (2008), we made a comparison of this approach with the correction surface approach and the combined point mass approach using the gravity and GPS-levelling data sets in a small region in Germany; the main conclusion was that all these methods provide very similar results if the differences between gravimetric quasi-geoid and GPS-levelling data are very smooth. In this study, we apply the innovation function approach to model the regional distortions of the EGG97 in Romania. The results of the innovation function approach are compared with the results of a simplified correction surface approach.

46.2 Numerical Realization

46.2.1 Input Data

Input data are the gravimetric quasi-geoid model EGG97 and 38 GPS-levelling points in Romania. The observed height-anomaly differences at the remaining 38 GPS-levelling points (Fig. 46.1) form the boundary data to compute the innovation function. The distortions range from –36 to 24 cm, the standard deviation is 12.8 cm and the mean –3.5 cm.

46.2.2 Innovation Function Approach

The innovation function can represent a broad range of functions including non-smooth ones. In the presence of data noise, this may lead to over-fit if no precautions are taken. Therefore, the smoothness of the innovation function is chosen appropriately depending on the expected standard deviation of the geometric height anomalies at the GPS-levelling points. The current implementation foresees only one parameter to

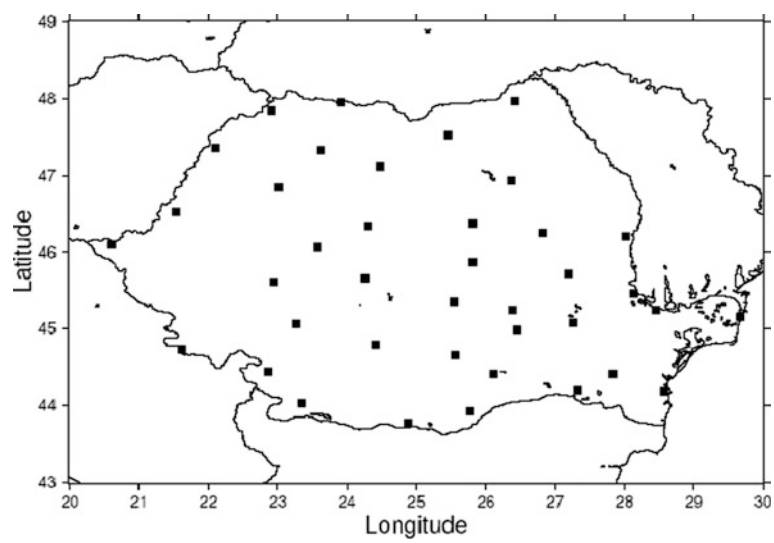


Fig. 46.1 The initial configuration of the 38 GPS-levelling points

describe the standard deviation. In reality, the accuracy may be quite inhomogeneous, varying from point to point. We prefer to choose this parameter equal to the average standard deviation of geometric height anomalies at the GPS-levelling points. This provides the best average fit over the target area, with overfit at GPS-levelling points of lower accuracy and underfit at GPS-levelling points of higher accuracy.

In order to demonstrate how the choice of this parameter affects the innovation function, we did the computations for five different levels of accuracy ranging from 2 to 6 cm. The corresponding innovation functions are shown in Fig. 46.2. The histograms for the height anomaly residuals are shown in Fig. 46.3, and the statistics are summarized in Table 46.1.

Figure 46.2 shows that the chosen standard deviation has a direct influence on the smoothness of the innovation function. When choosing smaller values, the innovation function represents local details. Then, isolated GPS-levelling points may change the shape of the function in the vicinity of these points, which can be seen as an indicator of higher noise at these particular points. This is clearly visible in the innovation functions associated with a standard deviation of 2 and 3 cm (Fig. 46.2a,b). Increasing the standard deviation to 4 cm or higher gives smoother solutions,

Table 46.1 The innovation functions computed for the five different RMS of the height anomaly residuals at the GPS-levelling points

RMS (cm)	Min (cm)	Max (cm)	Mean (cm)
2.0	–4.0	4.8	–0.1
3.0	–4.5	8.4	–0.1
4.0	–7.1	10.9	0.0
5.0	–9.8	12.5	0.0
6.0	–11.7	13.1	0.0

but increases the risk of loss of information. Based on the information we got from the national authorities, we decided to use the innovation function with a RMS fit of 4 cm to correct the gravimetric height anomalies of EGG97. We are aware of the fact that this level of accuracy may be too optimistic for some GPS-levelling points and that the innovation function may pick up some noise at these points. However, without complete information about the standard deviations of the geometric height anomalies at the GPS-levelling points and due to the current limitation of the innovation function approach to account for spatially varying standard deviations, this is the optimal result. Recently, Klees and Prutkin (2008a) have extended the innovation

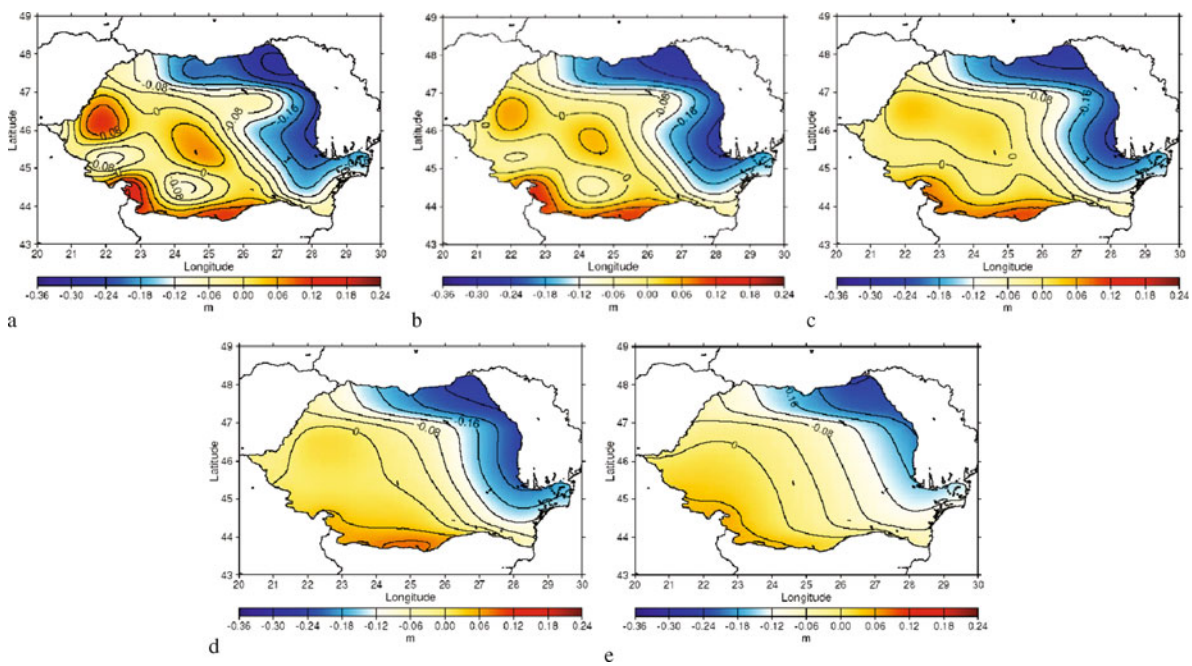


Fig. 46.2 Innovation functions. The RMS fit to the observed height-anomaly differences at the 38 GPS-levelling points is: (**a**) 2 cm, (**b**) 3 cm, (**c**) 4 cm, (**d**) 5 cm, (**e**) 6 cm

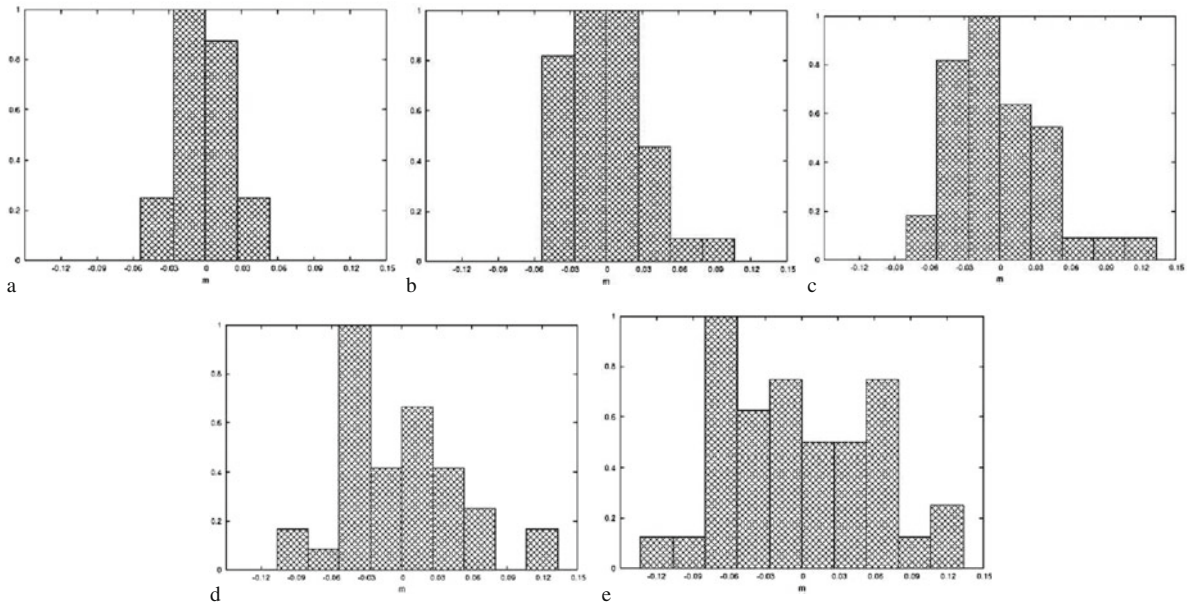


Fig. 46.3 Histograms of the height anomaly residuals at the 38 GPS-levelling points after applying the innovation functions (shown in Fig. 46.2) with the RMS fit: (**a**) 2 cm, (**b**) 3 cm, (**c**) 4 cm, (**d**) 5 cm, (**e**) 6 cm

function approach to account for full variance-covariance information, which allows us to account for spatially varying standard deviations.

46.2.3 Correction Surface Approach

For comparison of the results obtained from the innovation function approach, we approximated the observed height-anomaly differences by the polynomial correction surfaces of degree 2–6. The best approximation in terms of the residual RMS was obtained from the 2nd and 4th degree correction surfaces, while the 5th and 6th degree correction surfaces provided very large residuals. Fig. 46.4 shows the 2nd degree correction surface and the histogram of the height anomaly residuals at the GPS-levelling points. The height anomaly residuals range from –11.3 to

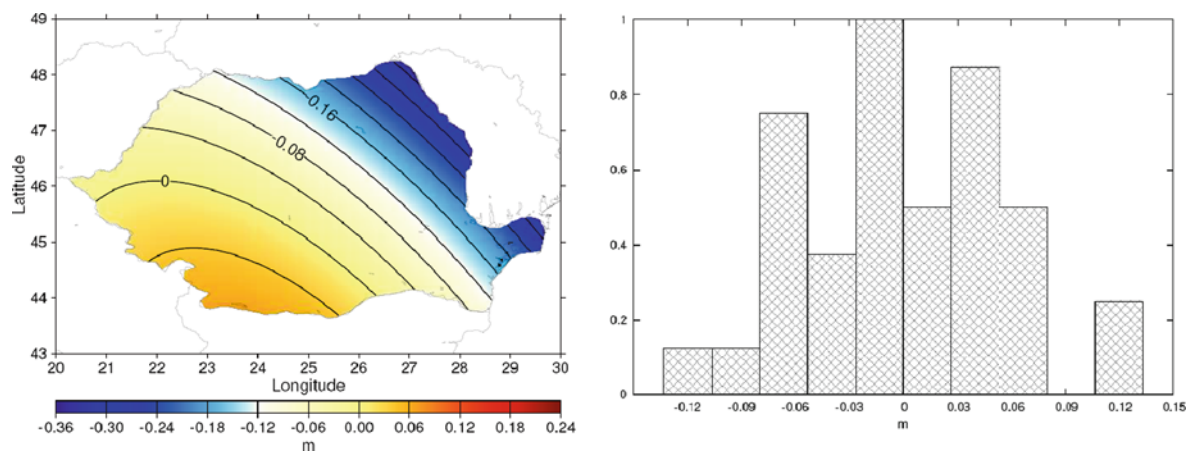


Fig. 46.4 The 2nd degree correction surface and the histogram of the height anomaly residuals after applying the 2nd degree correction surface

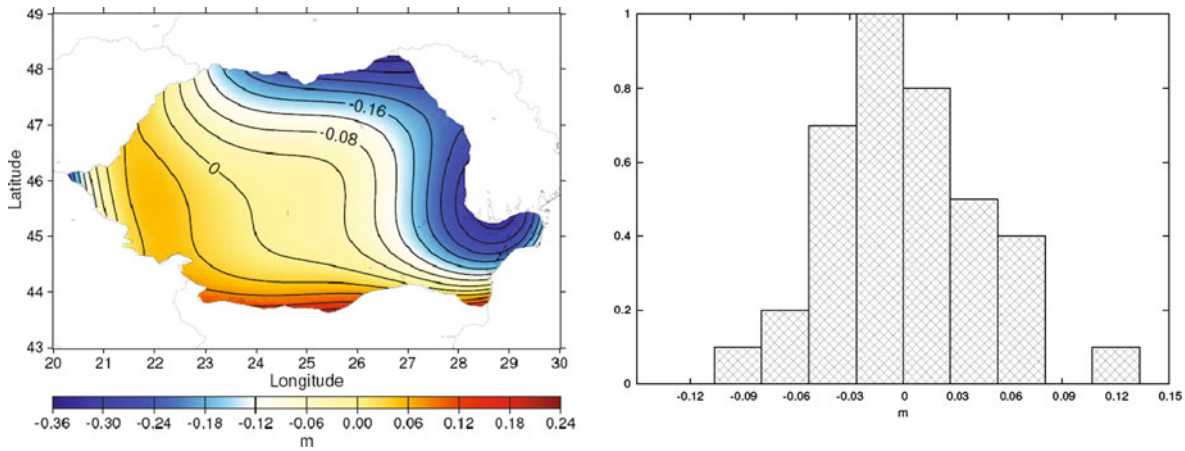


Fig. 46.5 The 4th degree correction surface and the histogram of the height anomaly residuals after applying the 4th degree correction surface

12.7 cm, and the RMS of the residuals is 6.3 cm. When applying the 4th degree correction surface, the RMS of height anomaly residuals further decreased to 4.4 cm (cf. Fig. 46.5); the residuals range from –8.1 to 12.1 cm. The statistics for the correction surface approach are summarized in Table 46.2.

The selected innovation function and the 4th degree correction surface have about the same RMS of the residuals. They have a similar trend (cf. Figs. 46.1c and 46.4). Nevertheless, the innovation function approach offers more options for modelling the observed height-anomaly residuals and thus has a better approximation property than the correction surface approach.

Table 46.2 The correction surface of degree 2 and 4

Degree	RMS (cm)	Min (cm)	Max (cm)	Mean (cm)
2nd	6.3	–11.3	12.7	0.1
4th	4.4	–8.1	12.1	–0.1

46.3 Summary and Conclusions

The innovation function approach was applied to combine the EGG97 gravimetric quasi-geoid with GPS-levelling data in Romania. The combination showed the presence of regional distortions of the EGG97, in particular along the border of the country. The reason may be due to inconsistencies between the Romanian gravity data set and gravity data sets from the neighbouring countries of Bulgaria, Moldova and Ukraine. The distortions range from –36 to 24 cm. The combination of GPS-levelling data and EGG97 reduces the differences to a range from –7 to 11 cm; the RMS difference at the GPS-levelling points is 4 cm. The low spatial density of the GPS-levelling points, their irregular distribution, and the lack of GPS-levelling data along the border of Romania, where the largest distortions are documented, require further investigation once better GPS-levelling data have become available.

The comparison of the innovation function approach with the simplified correction surface approach revealed a better approximation property of the innovation function in the presence of more complex regional distortions. The innovation function can approximate the observed height-anomaly differences for any RMS fit chosen according to the accuracy of the gravimetric geoid/quasi-geoid and GPS-levelling data. On the other hand, the approximation of the observed height-anomaly differences with a more complex trend by the algebraic polynomials is restricted to some level of the accuracy.

References

Denker, H. (1998). Evaluation and Improvement of the EGG97 Quasigeoid Model for Europe by GPS and Leveling Data. Proceed. Second Continental Workshop on the Geoid in Europe, Budapest, Hungary, March 10–14, Reports of the Finnish Geodetic Institute 98(4), 53–61, Masala.

Denker, H., W. Torge (1998). The European gravimetric quasigeoid EGG97 – An IAG Supported Continental Enterprise.

In: Forsberg R, M. Feissel, and R. Dietrich (eds), Geodesy on the Move – Gravity, Geoid, Geodynamics and Antarctica. IAG Symp, Vol. 119, pp. 249–254, Springer Verlag, Berlin, Heidelberg, New York.

Denker, H., W. Torge, G. Wenzel, J. Ihde, and U. Schirmer (2000). Investigation of different methods for the combination of gravity and GPS/levelling data. In: Schwarz, K.P. (ed.), Geodesy Beyond 2000 – The Challenges of the First Decade. IAG Symposia, Vol. 121, pp. 137–142, Springer Verlag, Berlin, Heidelberg.

Klees, R., R. Tenzer, I. Prutkin, and T. Wittwer (2008). A data-driven approach to local gravity field modeling using spherical radial basis functions. *J. Geod*., DOI 10.1007/s00190-007-0196-3.

Liebsch, G., U. Schirmer, J. Ihde, H. Denker, and J. Müller (2006). Quasigeoidbestimmung für Deutschland. DVW Schriftenreihe, Band 49.

Prutkin, I. and R. Klees (2007). On the non-uniqueness of local quasi-geoids computed from terrestrial gravity anomalies. *J. Geod.* 82(3), 147–156, DOI: 10.1007/s00190-007-0161-1.

Klees, R. and I. Prutkin (2008a). On the combination of gravimetric quasi-geoids and GPS/levelling data. Sideris, M.G. (ed.), Observing our Changing Earth, International Association of Geodesy Symposia 133, Springer-Verlag Berlin Heidelberg, pp. 237–244.

Klees, R. and I Prutkin (2008b). The combination of gravimetric quasi-geoid and GPS-levelling data in the presence of noise. Paper presented at GGEO 2008, June 23–27, Chania, Greece.

Tenzer, R., R. Klees, I. Prutkin, T. Wittwer, B. Alberts, U. Schirmer, J. Ihde, G. Liebsch, and U. Schäfer (2008). Comparison of techniques for the computation of a height reference surface from gravity and GPS/levelling data. Sideris, M.G. (ed.), Observing Our Changing Earth, International Association of Geodesy Symposia 133, Springer-Verlag Berlin Heidelberg, pp 263–273.

Torge, W. and H. Denker (1999). Zur Verwendung des Europäischen Gravimetrischen Quasigeoids EGG97 in Deutschland. Z.f.Verm. wesen 124, pp. 154–166.

Wenzel, H.-G. (1982). Geoid computation by least squares spectral combination using integral kernels. Proceedings IAG General Meeting, 438–453, Tokyo.

Chapter 47

Effect of the Long-Wavelength Topographical Correction on the Low-Degree Earth's Gravity Field

R. Tenzer and P. Novák

Abstract In the context of the regional gravity field modelling, the smoothing effect of the topographical correction on the high-frequency part of the gravity signal is well documented. In this study, the effect of the long-wavelength topographic correction on the low-degree Earth's gravity potential and attraction is investigated. For this purpose, the Earth's gravity field and the topography-corrected gravity field are compared for various spectral resolutions. The topography-corrected gravity field is obtained from the low-degree Earth's gravity field after subtracting the long-wavelength gravitational field generated by the topography. The Earth's gravity field is computed from a global geopotential model (GGM). The gravitational field generated by the topography is modelled from a global elevation model (GEM), adopting the constant topographical mass-density distribution.

47.1 Long-Wavelength Gravitational Field Generated by the Topography

To model the long-wavelength gravitational field generated by the topography in terms of spherical height functions $\mathrm{H_n}(\Omega)$, the actual topographical density is approximated by the mean value ρ_o. After applying the analytical upward continuation, the gravitational potential V^t reads

$$V^t(r,\Omega) = V^t(\mathrm{R},\Omega) + \sum_{k=1}^{\infty} \frac{(r-\mathrm{R})^k}{k!} \left. \frac{\partial^{\mathrm{k}} V^t(r,\Omega)}{\partial\, r^{\mathrm{k}}} \right|_{r=\mathrm{R}}. \tag{1}$$

Similarly, the gravitational attraction g^t is given by

$$g^t(r,\Omega) = g^t(\mathrm{R},\Omega) + \sum_{k=1}^{\infty} \frac{(r-\mathrm{R})^k}{k!} \left. \frac{\partial^{\mathrm{k+1}} V^t(r,\Omega)}{\partial\, r^{\mathrm{k+1}}} \right|_{r=\mathrm{R}}. \tag{2}$$

The 3-D position is defined in a frame of the geocentric spherical coordinates r, ϕ,λ; r is the geocentric radius, ϕ and λ are the spherical latitude and longitude, $\Omega = (\phi,\lambda)$. The geocentric radius of the geoid is approximated by the mean radius of the Earth R. The substitution from Eqs. (12, Appendix) to (1), yields

$$\begin{aligned} V^t(r,\Omega) \cong\, & V^t(\mathrm{R},\Omega) + 2\pi \mathrm{G}\,\rho_{\mathrm{o}} \frac{H(\Omega)}{\mathrm{R}} \times \sum_{n=1}^{N} \frac{n}{2n+1} \\ & \sum_{\mathrm{m}=-\mathrm{n}}^{\mathrm{n}} \left[2\mathrm{R}\,\mathrm{H_{n,m}} + (1-n)\,\mathrm{H_{n,m}^2}\right] \mathrm{Y_{n,m}}(\Omega) \\ & + \pi \mathrm{G}\,\rho_{\mathrm{o}} \frac{H(\Omega)^2}{\mathrm{R}^2} \times \sum_{n=2}^{N} \frac{n(n-1)}{2n+1} \\ & \sum_{\mathrm{m}=-\mathrm{n}}^{\mathrm{n}} \left[2\mathrm{R}\,\mathrm{H_{n,m}} + (1-n)\,\mathrm{H_{n,m}^2}\right] \mathrm{Y_{n,m}}(\Omega) \end{aligned} \tag{3}$$

R. Tenzer (✉)
Delft Institute of Earth Observation and Space Systems (DEOS), Delft University of Technology, Delft 2629 HS, The Netherlands
e-mail: R.Tenzer@tudelft.nl

S.P. Mertikas (ed.), *Gravity, Geoid and Earth Observation*, International Association of Geodesy Symposia 135,
DOI 10.1007/978-3-642-10634-7_47, © Springer-Verlag Berlin Heidelberg 2010

The potential V^t, evaluated on the geoid, results in

$$V^t(\mathrm{R},\Omega) = 2\pi \mathrm{G}\,\rho_o \sum_{n=0}^{N} \frac{1}{2n+1} \times \sum_{\mathrm{m}=-\mathrm{n}}^{\mathrm{n}} \left[2\mathrm{R}\,\mathrm{H}_{\mathrm{n,m}} + (1-n)\mathrm{H}^2_{\mathrm{n,m}}\right] \mathrm{Y}_{\mathrm{n,m}}(\Omega), \tag{4}$$

where N is the upper summation index for $\mathrm{H_n}(\Omega)$, G is Newton's gravitational constant, and H the orthometric height. $\mathrm{H_{n,m}}$ and $\mathrm{H^2_{n,m}}$ are the GEM coefficients, and $\mathrm{Y_{n,m}}(\Omega)$ the surface spherical functions (see e.g. Heiskanen and Moritz, 1967). The second constituent on the right-hand side of Eq. (3) represents the linear change of the potential V^t with the height. It can be readily shown that the third constituent sufficiently approximates its non-linear changes. Accordingly, terms of higher than second degree (i.e. $k > 2$) in Eq. (2) are omitted. The substitution from Eqs. (12) to (2) yields

$$g^t(r,\Omega) \cong g^t(\mathrm{R},\Omega) + 2\pi \mathrm{G}\,\rho_o \frac{H(\Omega)}{\mathrm{R}^2} \times \sum_{n=2}^{N} \frac{n(n-1)}{2n+1} \sum_{\mathrm{m}=-\mathrm{n}}^{\mathrm{n}} \left[2\mathrm{R}\,\mathrm{H}_{\mathrm{n,m}} + (1-n)\mathrm{H}^2_{\mathrm{n,m}}\right] \mathrm{Y}_{\mathrm{n,m}}(\Omega) + \pi \mathrm{G}\,\rho_o \frac{H(\Omega)^2}{\mathrm{R}^3} \sum_{n=3}^{N} \frac{n(n-1)(n-2)}{2n+1} \times \sum_{\mathrm{m}=-\mathrm{n}}^{\mathrm{n}} \left[2\mathrm{R}\,\mathrm{H}_{\mathrm{n,m}} + (1-n)\,\mathrm{H}^2_{\mathrm{n,m}}\right] \mathrm{Y}_{\mathrm{n,m}}(\Omega). \tag{5}$$

The gravitational attraction g^t, evaluated on the geoid, results in

$$g^t(\mathrm{R},\Omega) = 2\pi \mathrm{G}\,\rho_o \frac{1}{\mathrm{R}} \sum_{n=1}^{N} \frac{n}{2n+1} \times \sum_{\mathrm{m}=-\mathrm{n}}^{\mathrm{n}} \left[2\mathrm{R}\,\mathrm{H}_{\mathrm{n,m}} + (1-n)\mathrm{H}^2_{\mathrm{n,m}}\right] \mathrm{Y}_{\mathrm{n,m}}(\Omega). \tag{6}$$

47.2 Numerical Experiment

The global digital terrain model ETOPO5 (provided by the NOAA's National Geophysical Data Centre) is used to generate the GEM coefficients. The long-wavelength topographical gravitational potential and attraction are then computed from the GEM coefficients for 5 different levels of the spectral resolution up to degree $N = 20, 60, 100, 140, 180$. Terms of lower than third degree are not taken into account. The mean topographical density 2,670 kg m^{-3} is adopted. The computation is realized at the 5×5 arc-min geographical grid of the points at the Earth's surface. Over the area of study in the Canadian Rocky Mountains (bounded by the parallels of 42 and 67 arc-degree Northern latitude and the meridians of 205 and 270 arc-degree Eastern longitude), the orthometric heights reach 5,449 m. The results over the area of study are summarized in Tables 47.1 and 47.2.

Table 47.1 Statistics of the long-wavelength topography-generated gravitational potential

Spectrum	Min (m^2s^{-2})	Max (m^2s^{-2})	Mean (m^2s^{-2})	STD (m^2s^{-2})
$3 \le n \le 20$	–97	203	39	50
$3 \le n \le 60$	–216	1,685	408	351
$3 \le n \le 100$	–196	1,787	409	348
$3 \le n \le 140$	–196	1,799	409	348
$3 \le n \le 180$	–197	1,808	409	348

Table 47.2 Statistics of the long-wavelength topography-generated gravitational attraction

Spectrum	Min (mgal)	Max (mgal)	Mean (mgal)	STD (mgal)
$3 \le n \le 20$	–4.8	18.5	8.1	4.7
$3 \le n \le 60$	–47.1	181.8	28.0	43.6
$3 \le n \le 100$	–61.0	217.8	28.1	46.7
$3 \le n \le 140$	–67.6	262.1	28.2	47.8
$3 \le n \le 180$	–56.7	296.9	28.2	48.5

The Earth's gravity field and the topography-corrected gravity field are computed for 5 different levels of the spectral resolution up to degree $N = 20, 60, 100, 140, 180$. Terms of lower than third degree (i.e. parameters of the Clairaut spheroid) are not taken into account, i.e. $3 \le n \le N$. The GGM coefficients of the EGM96 (Lemoine et al., 1998) are used. The results over the area of study are shown in Figs. 47.1, 47.2, 47.3 and 47.4, the statistics are summarized in Tables 47.3, 47.4, 47.5 and 47.6.

47.3 Conclusions

The spectral resolution of the topography-generated gravitational potential up to degree 100 represents

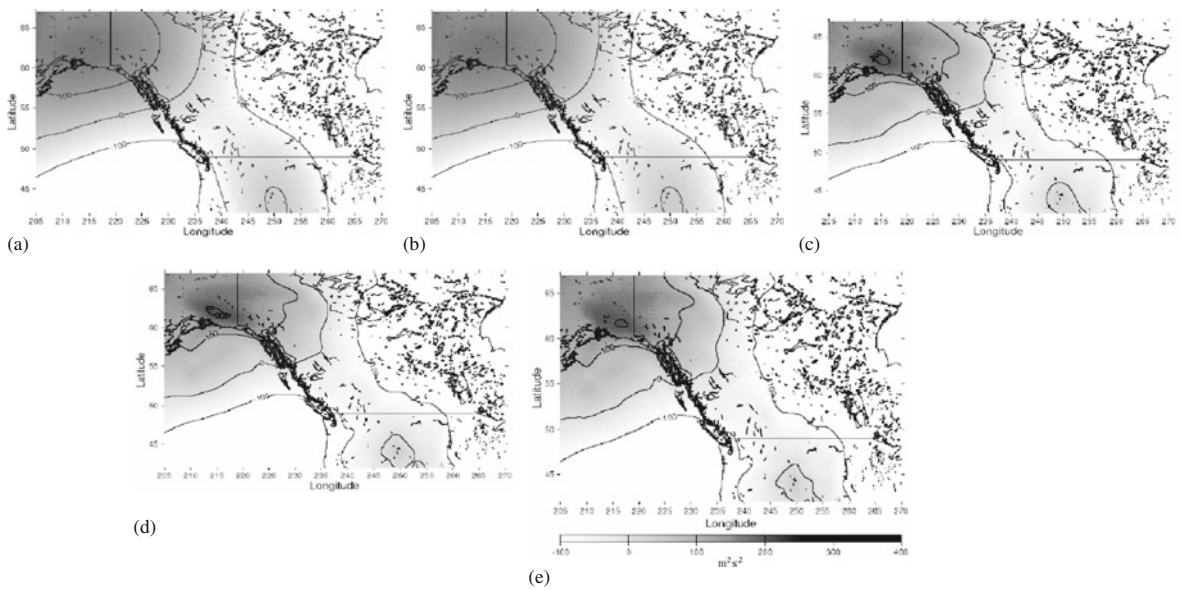


Fig. 47.1 Earth's gravity potential computed with the spectral resolutions: (**a**) $3 \leq n \leq 20$, (**b**) $3 \leq n \leq 60$, (**c**) $3 \leq n \leq 100$, (**d**) $3 \leq n \leq 140$, (**e**) $3 \leq n \leq 180$

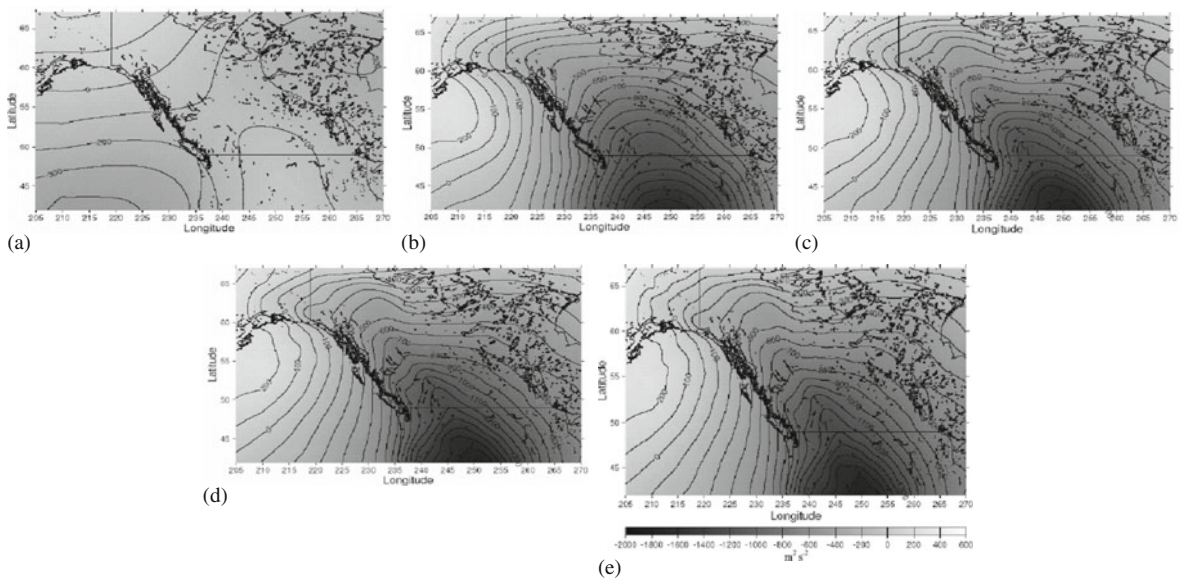


Fig. 47.2 Topography-corrected gravity potential computed with the spectral resolutions: (**a**) $3 \leq n \leq 20$, (**b**) $3 \leq n \leq 60$, (**c**) $3 \leq n \leq 100$, (**d**) $3 \leq n \leq 140$, (**e**) $3 \leq n \leq 180$

most of the signal (cf. Table 47.1). Results of the numerical investigation not presented in this study revealed that the topographical potential computed according to Eq. (3) up to degree 100 differs less than 5% comparing with the results obtained from the 5×5 arc-min detailed digital terrain model. The spectral resolution of the topography-generated gravitational attraction depends significantly on the maximum spectral resolution of GEM (cf. Table 47.2). The reason is a strong correlation of the topography-generated

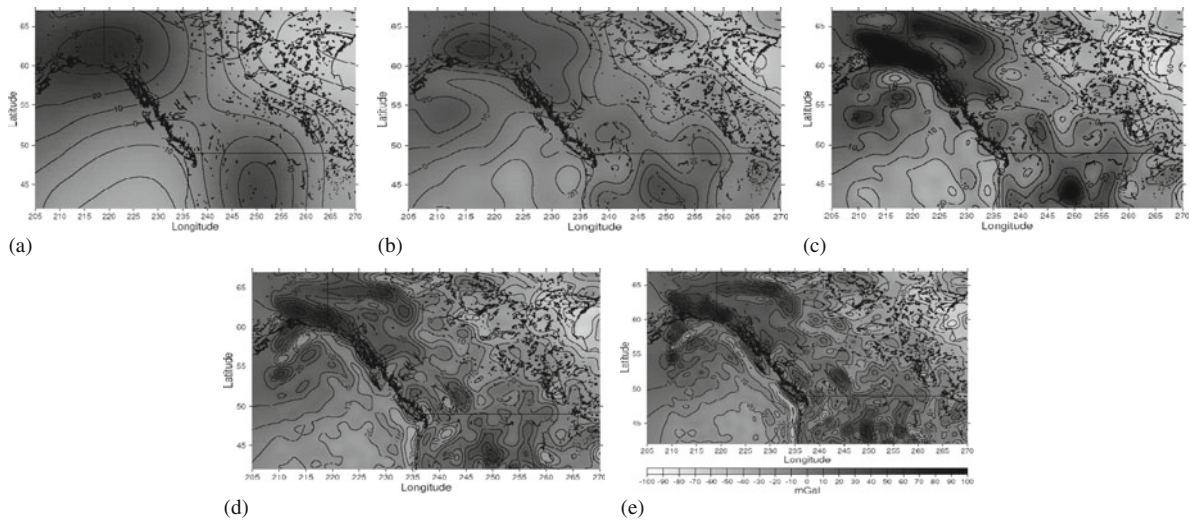


Fig. 47.3 Earth's gravity attraction computed with the spectral resolutions: (**a**) $3 \leq n \leq 20$, (**b**) $3 \leq n \leq 60$, (**c**) $3 \leq n \leq 100$, (**d**) $3 \leq n \leq 140$, (**e**) $3 \leq n \leq 180$

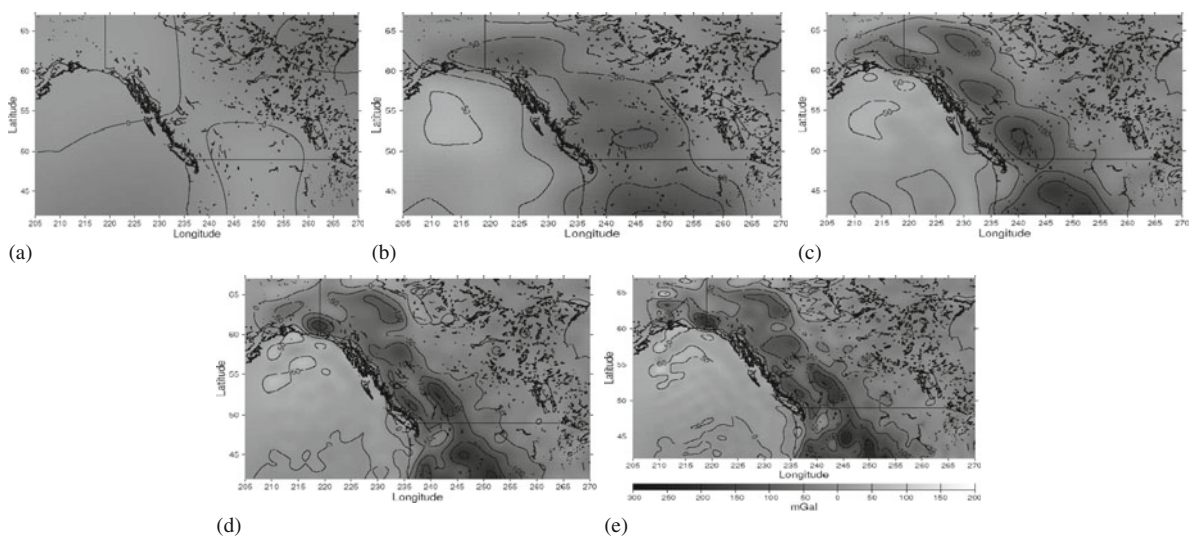


Fig. 47.4 Topography-corrected gravity attraction computed with the spectral resolutions: (**a**) $3 \leq n \leq 20$, (**b**) $3 \leq n \leq 60$, (**c**) $3 \leq n \leq 100$, (**d**) $3 \leq n \leq 140$, (**e**) $3 \leq n \leq 180$

gravitational attraction with the local topography. In mountainous regions, the contribution of the terms above degree 180 can reach several hundred miligals.

As can be seen in Figs. 47.1, 47.2, 47.3 and 47.4, the topography-corrected gravity field from degree 20–180 of spherical harmonics is rougher than the corresponding Earth's gravity field. It is due to the fact that the long-wavelength part of the gravitational field generated by the topography is isostatically compensated in the Canadian Rocky Mountains to a large extent.

The main conclusion is that the smoothing effect of the topographical correction is only on the high-frequency part of the gravity signal.

Table 47.3 Statistics of the low-degree Earth's gravity potential

Spectrum	Min (m^2s^{-2})	Max (m^2s^{-2})	Mean (m^2s^{-2})	STD (m^2s^{-2})
$3 \le n \le 20$	–370	164	–101	111
$3 \le n \le 60$	–387	196	–99	109
$3 \le n \le 100$	–389	204	–99	109
$3 \le n \le 140$	–390	204	–99	109
$3 \le n \le 180$	–391	203	–99	109

Table 47.4 Statistics of the low-degree topography-corrected gravity potential

Spectrum	Min (m^2s^{-2})	Max (m^2s^{-2})	Mean (m^2s^{-2})	STD (m^2s^{-2})
$3 \le n \le 20$	–433	217	–141	103
$3 \le n \le 60$	–1,679	263	–507	351
$3 \le n \le 100$	–1,782	257	–508	348
$3 \le n \le 140$	–1,797	227	–508	348
$3 \le n \le 180$	–1,801	276	–508	348

Table 47.5 Statistics of the low-degree Earth's gravity attraction

Spectrum	Min (mgal)	Max (mgal)	Mean (mgal)	STD (mgal)
$3 \le n \le 20$	–51.9	34.6	–4.0	17.9
$3 \le n \le 60$	–62.3	55.3	–3.2	17.9
$3 \le n \le 100$	–67.1	72.7	–3.3	18.4
$3 \le n \le 140$	–69.7	79.8	–3.3	18.9
$3 \le n \le 180$	–75.1	83.6	–3.3	19.3

Table 47.6 Statistics of the low-degree topography-corrected gravity attraction

Spectrum	Min (mgal)	Max (mgal)	Mean (mgal)	STD (mgal)
$3 \le n \le 20$	–58.2	16.3	–12.1	17.3
$3 \le n \le 60$	–168.9	63.2	–31.4	32.5
$3 \le n \le 100$	–198.8	59.03	–31.4	35.2
$3 \le n \le 140$	–217.5	77.1	–31.5	36.3
$3 \le n \le 180$	–235.1	99.8	–31.5	36.9

Appendix: Generic Expression for the Radial Derivatives of the Gravitational Potential V^t in Terms of the Spherical Height Functions

Adopting the constant topographical mass-density distribution and applying the spherical approximation of the geoid, the radial derivatives of the gravitational potential $\{\partial^k V^t/\partial r^k : k = 1,2,\ldots\}$ in Eqs. (1) and (2) are defined by

$$\left.\frac{\partial^k V^t(r,\Omega)}{\partial r^k}\right|_{r=R} = G\rho_o \times \iint_{\Omega'\epsilon\Omega_O} \int_R^{R+H(\Omega')} \left.\frac{\partial^k \ell^{-1}(r,\psi,r')}{\partial r^k}\right|_{r=R} r'^2 dr' d\Omega', \tag{7}$$

where ℓ is the Euclidean spatial distance of two points (r,Ω) and (r',Ω'), $d\Omega' = \cos\phi' d\phi' d\lambda'$ is the infinitesimal surface element on the unit sphere, and Ω_O denotes the full solid angle. The radial derivatives of ℓ^{-1} for $r < r'$ read

$$\frac{\partial^k \ell^{-1}(r,\psi,r')}{\partial r^k} = \frac{k!}{r'^{k+1}} \sum_{n=k}^{\infty} \left(\frac{r}{r'}\right)^{n-k} \binom{n}{k} P_n(\cos\psi), \tag{8}$$

where P_n is the Legendre polynomial of degree n for the argument of cosine of the spherical distance ψ. The substitution from Eqs. (8) to (7) yields

$$\left.\frac{\partial^k V^t(r,\Omega)}{\partial r^k}\right|_{r=R} = G\rho_o \sum_{n=k}^{\infty} \frac{1}{R^{k-1}} \frac{n!}{(n-k)!} \times \iint_{\Omega'\epsilon\Omega_o} \int_o^{H(\Omega')} \left(1 + \frac{H'}{R}\right)^{1-n} dH' P_n(\cos\psi) d\Omega', \tag{9}$$

where $H' = r' - R$. The application of the binomial theorem to $(1 + H'/R)^{1-n}$ and integration of Eq. (9) with respect to H' results in

$$\int_0^{H(\Omega')} \left(1 + \frac{H'}{R}\right)^{1-n} dH' \cong R \sum_{i=0}^{\infty} \binom{1-n}{i} \left(\frac{H(\Omega')}{R}\right)^{i+1} \frac{1}{i+1}. \tag{10}$$

Disregarding terms higher than the second degree in Eqs. (10), (9) becomes

$$\begin{aligned}\left.\frac{\partial^{\mathrm{k}} V^{t}(r,\Omega)}{\partial\, r^{\mathrm{k}}}\right|_{r=\mathrm{R}} &\cong \mathrm{G}\,\rho_{\mathrm{o}} \sum_{n=k}^{\infty} \frac{1}{\mathrm{R}^{k-1}} \frac{n!}{(n-k)!} \\ &\times \iint_{\Omega' \epsilon \Omega_{\mathrm{O}}} H(\Omega')\mathrm{P}_{\mathrm{n}}(\cos\psi) d\Omega' \\ &+ \frac{\mathrm{G}\rho_{\mathrm{o}}}{2} \sum_{n=k}^{\infty} \frac{1-n}{\mathrm{R}^{k}} \frac{n!}{(n-k)!} \\ &\times \iint_{\Omega' \epsilon \Omega_{\mathrm{O}}} H(\Omega')^2 \mathrm{P}_{\mathrm{n}}(\cos\psi) d\Omega'.\end{aligned} \tag{11}$$

From Eq. (11), the generic expression for the radial derivatives of the gravitational potential in terms of surface spherical height functions is introduced. It reads

$$\begin{aligned}\left.\frac{\partial^{\mathrm{k}} V^{t}(r,\Omega)}{\partial\, r^{\mathrm{k}}}\right|_{r=\mathrm{R}} &= 4\pi \mathrm{G}\,\rho_{\mathrm{o}} \sum_{n=k}^{\infty} \frac{1}{\mathrm{R}^{k-1}} \frac{n!}{(n-k)!} \\ &\times \frac{1}{2n+1} \sum_{\mathrm{m}=-\mathrm{n}}^{\mathrm{n}} \mathrm{H}_{\mathrm{n,m}} \mathrm{Y}_{\mathrm{n,m}}(\Omega) \\ &+ 2\pi \mathrm{G}\,\rho_{o} \sum_{n=k}^{\infty} \frac{1}{\mathrm{R}^{k}} \frac{n!}{(n-k)!} \\ &\times \frac{1-n}{2n+1} \sum_{\mathrm{m}=-\mathrm{n}}^{\mathrm{n}} \mathrm{H}^{2}_{\mathrm{n,m}}\, \mathrm{Y}_{\mathrm{n,m}}(\Omega) \\ &= 2\pi \mathrm{G}\,\rho_{o} \sum_{n=k}^{\infty} \frac{1}{\mathrm{R}^{k}} \frac{n!}{(n-k)!} \frac{1}{2n+1} \\ &\times \sum_{\mathrm{m}=-\mathrm{n}}^{\mathrm{n}} \left[2\mathrm{R}\,\mathrm{H}_{\mathrm{n,m}} + (1-n)\mathrm{H}^{2}_{\mathrm{n,m}}\right] \mathrm{Y}_{\mathrm{n,m}}(\Omega).\end{aligned} \tag{12}$$

The surface spherical height functions $\mathrm{H_n}(\Omega)$, and the surface spherical squared height functions $\mathrm{H^2_n}(\Omega)$ in Eq. (12) are defined as follows

$$\begin{aligned}\mathrm{H_n}(\Omega) &= \frac{2n+1}{4\pi} \iint_{\Omega' \epsilon \Omega_{\mathrm{o}}} H(\Omega')\mathrm{P_n}(\cos\psi) d\Omega' \\ &= \sum_{\mathrm{m}=-\mathrm{n}}^{\mathrm{n}} \mathrm{H_{n,m}} \mathrm{Y_{n,m}}(\Omega),\end{aligned} \tag{13}$$

and

$$\begin{aligned}\mathrm{H^2_n}(\Omega) &= \frac{2n+1}{4\pi} \iint_{\Omega' \epsilon \Omega_{\mathrm{o}}} H(\Omega')^2\, \mathrm{P_n}(\cos\psi) d\Omega' \\ &= \sum_{\mathrm{m}=-\mathrm{n}}^{\mathrm{n}} \mathrm{H^2_{n,m}} \mathrm{Y_{n,m}}(\Omega).\end{aligned} \tag{14}$$

An alternative expression for computing the topographical potential in terms of the spherical height functions was derived in Vaníček et al. (1995). A different method was introduced by Novák and Grafarend (2006). They treat the topographical effects separately for a contribution of the spherical Bouguer shell and the spherical terrain correction expressed in terms of spherical height functions.

References

Heiskanen, W.H. and H. Moritz (1967). Physical geodesy. WH Freeman and Co, San Francisco.

Lemoine, F.G., S.C. Kenyon, J.K. Factor, R.G. Trimmer, N.K. Pavlis, D.S. Chinn, C.M. Cox, S.M. Klosko, S.B. Luthcke, M.H. Torrence, Y.M. Wang, R.G. Williamson, E.C. Pavlis, R.H. Rapp, and T.R. Olson (1998). The development of the joint NASA GSFC and the National Imagery and Mapping Agency (NIMA) geopotential model EGM96. NASA Technical Publication TP-1998-206861, NASA GSFC.

Novák, P. and E.W. Grafarend (2006). The effect of topographical and atmospheric masses on spaceborne gravimetric and gradiometric data. *Stud. Geoph. Geod.*, 50(4), 549–582; doi: 10.1007/s11200-006-0035-7.

Vaníček, P., M. Najafi, Z. Martinec, L. Harrie, and L.E. Sjöberg (1995). Higher-degree reference field in the generalised Stokes-Helmert scheme for geoid computation. *J. Geod.*, 70, 176–182.

Chapter 48

A Comparison of Various Integration Methods for Solving Newton's Integral in Detailed Forward Modelling

R. Tenzer, Z. Hamayun, and I. Prutkin

Abstract We compare the numerical precision and the time efficiency of various integration methods for solving Newton's integral, namely the rectangular prism and the line integral analytical approaches, the linear vertical mass and the Gauss cubature semi-analytical approaches, and the point-mass numerical approach. The relative precision of the semi-analytical and numerical integration methods with respect to the rectangular prism approach is analyzed at the vicinity of the computation point up to one arc-min of spherical distance. The results of the numerical experiment reveal that the Gauss cubature approach is more precise than the linear vertical mass and the point-mass approaches. The time efficiency of integration methods is compared, showing that the point-mass approach is the most time-efficient while the line integral approach is the most time-consuming.

48.1 Introduction

Number of authors analyzed various methods for solving Newton's integral. The comparison of methods for computing terrain corrections can be found for instance in Li and Sideris (1994), and Tsoulis (2003). Heck and Seitz (2007) compared the numerical precision and the time efficiency of the tesseroid, rectangular prism and point-mass approaches. In this study, a similar comparison is done for five different integration methods commonly used in detailed gravity field modelling at the vicinity of the computation point.

R. Tenzer (✉)
Delft Institute of Earth Observation and Space Systems (DEOS), Delft University of Technology, Delft 2629 HS, The Netherlands
e-mail: R.Tenzer@tudelft.nl

48.2 Integration Methods

The gravitational potential V at the computation point $\mathbf{r}$ generated by a rectangular parallelepiped (prism) of homogeneous density ρ is defined by

$$V(\mathbf{r}) = \mathrm{G}\,\rho \int_{z'_1}^{z'_2}\int_{y'_1}^{y'_2}\int_{x'_1}^{x'_2} |\boldsymbol{\ell}|^{-1}\,\mathrm{d}x'\mathrm{d}y'\mathrm{d}z', \qquad (1)$$

and the vertical component of the gravitational attraction vector g_z reads

$$g_z(\mathbf{r}) = -\frac{\partial V(\mathbf{r})}{\partial z} = -\mathrm{G}\,\rho \int_{z'_1}^{z'_2}\int_{y'_1}^{y'_2}\int_{x'_1}^{x'_2} \frac{(z-z')}{|\boldsymbol{\ell}|^3}\,\mathrm{d}x'\mathrm{d}y'\mathrm{d}z', \qquad (2)$$

where G is the gravitational constant, and $|\boldsymbol{\ell}| = |\mathbf{r}' - \mathbf{r}|$ the Euclidean distance between the computation point $\mathbf{r}$ and the running integration point $\mathbf{r}'$. The position vectors $\mathbf{r} = (x,y,z)$ and $\mathbf{r}' = (x',y',z')$ are defined in the topocentric Cartesian coordinate system. Due to the curvature of the Earth, the topocentric Cartesian coordinate systems of the computation and integration points are not parallel. The transformation formulae between (x,y,z) and (x',y',z') is given by Heck (2003).

To solve the integrals in Eqs. (1) and (2), we apply: (i) the analytical rectangular prism approach (e.g. Nagy et al., 2000), (ii) the analytical line integral approach (e.g. Pohánka, 1988), (iii) the semi-analytical

S.P. Mertikas (ed.), *Gravity, Geoid and Earth Observation*, International Association of Geodesy Symposia 135,
DOI 10.1007/978-3-642-10634-7_48, © Springer-Verlag Berlin Heidelberg 2010

linear vertical mass approach (e.g. Martinec, 1998), (iv) the semi-analytical Gauss cubature approach, and (v) the numerical point-mass approach (e.g. Barthelmes et al., 1991).

48.2.1 Rectangular Prism Approach

The gravitational potential generated by the rectangular prism of homogeneous density is defined analytically (e.g. Nagy et al., 2000)

$$V(\mathbf{r}) = -\,\mathrm{G}\,\rho \left|\left|\left| XY \ln(z+|\boldsymbol{\ell}|) + XZ \ln(Y+|\boldsymbol{\ell}|) + YZ \ln(X+|\boldsymbol{\ell}|) - \frac{X^2}{2}\mathrm{atan}\frac{YZ}{X|\boldsymbol{\ell}|} - \frac{Y^2}{2}\mathrm{atan}\frac{XZ}{Y|\boldsymbol{\ell}|} - \frac{Z^2}{2}\mathrm{atan}\frac{XY}{Z|\boldsymbol{\ell}|} \right|_{x_1'}^{x_2'}\right|_{y_1'}^{y_2'}\Bigg|_{z_1'}^{z_2'}, \tag{3}$$

where $X = x - x'$, $Y = y - y'$, $Z = z - z'$; and $|\boldsymbol{\ell}| = \sqrt{X^2+Y^2+Z^2}$. Similarly, the vertical component of the gravitational attraction vector reads (*ibid*)

$$g_z(\mathbf{r}) = -\,\mathrm{G}\,\rho \left|\left|\left| X \ln(Y+|\boldsymbol{\ell}|) + Y \ln(X+|\boldsymbol{\ell}|) - Z\,\mathrm{atan}\frac{XY}{Z|\boldsymbol{\ell}|} \right|_{x_1'}^{x_2'}\right|_{y_1'}^{y_2'}\Bigg|_{z_1'}^{z_2'}. \tag{4}$$

48.2.2 Line Integral Approach

The analytical expression in terms of line integrals for the gravitational potential generated by an arbitrary polyhedral body (in this case the rectangular prism) of homogeneous density reads

$$V(\mathbf{r}) = \frac{\mathrm{G}\rho}{2} \sum_{\mathrm{k}=1}^{\mathrm{K}} \sum_{\mathrm{q}=1}^{\mathrm{Q_k}} \mathbf{n}_\mathrm{k} \cdot (\mathbf{a}_{\mathrm{k}1} - \mathbf{r}) \Phi(u_{\mathrm{kq}}, v_{\mathrm{kq}}, w_{\mathrm{kq}}, z_\mathrm{k}, \varepsilon), \tag{5}$$

where K is the number of prism sides (i.e. K = 6), and $\mathrm{Q_k}$ is the number of polygon segments which form the prism side k {$\mathrm{Q_k}$= 4: k = 1,2, .., K}. Pohánka (1988) defines the line integral kernel function ϕ as follows

$$\Phi(u,v,w,z,\varepsilon) = w\,L_\varepsilon + 2z\,A_\varepsilon, \tag{6}$$

where ε is the small positive parameter to decrease numerical errors if $|\boldsymbol{\ell}|$is large, and

$$\begin{aligned}
&\mathrm{sign}(u) = \mathrm{sign}(v): \quad L_\varepsilon = \mathrm{sign}(v) \ln \frac{V_\varepsilon + |v|}{U_\varepsilon + |u|},\\
&\mathrm{sign}(u) \neq \mathrm{sign}(v): \quad L_\varepsilon = \ln \frac{(V_\varepsilon + |v|)\,(U_\varepsilon + |u|)}{W_\varepsilon^2},\\
&A_\varepsilon = -\mathrm{atan}\frac{2wd}{(T_\varepsilon + d)|T_\varepsilon - d| + 2T_\varepsilon z_\varepsilon},\\
&z_\varepsilon = z + \varepsilon,\ W^2 = w^2 + z^2,\ W_\varepsilon^2 = w^2 + z_\varepsilon^2,\ d = v - u,\\
&U_\varepsilon = \sqrt{u^2 + W_\varepsilon^2},\ V_\varepsilon = \sqrt{v^2 + W_\varepsilon^2},\ T_\varepsilon = U_\varepsilon + V_\varepsilon.
\end{aligned} \tag{7}$$

The quantities in Eq. (7) are computed from the given values u, v ($v = u + d$, $d > 0$), w, $z(z \geq 0)$, which are defined for each polygon segment kq: $u_{\mathrm{kq}} = \boldsymbol{\mu}_{\mathrm{kq}} \cdot (\mathbf{a}_{\mathrm{kq}} - \mathbf{r})$, $v_{\mathrm{kq}} = u_{\mathrm{kq}} + d_{\mathrm{kq}}$, $w_{\mathrm{kq}} = \boldsymbol{\nu}_{\mathrm{kq}} \cdot (\mathbf{a}_{\mathrm{kq}} - \mathbf{r})$, $z_\mathrm{k} = |\mathbf{n}_k \cdot (\mathbf{a}_{\mathrm{k}1} - \mathbf{r})|$; where $\mathbf{n}_\mathrm{k}$is the outwards unit normal vector of the prism side k; $\boldsymbol{\mu}_{\mathrm{kq}}$ the unit vector of the polygon segment kq; $\boldsymbol{\nu}_{\mathrm{kq}}$ the outwards unit vector perpendicular to the polygon segment kq and lying in the plane of the prism side k; $\mathbf{a}_{\mathrm{kq}}$ and $\mathbf{a}_{\mathrm{kq}+1}$ are the vertex position vectors of the polygon segment kq; and $d_{\mathrm{kq}} = |\mathbf{a}_{\mathrm{kq}+1} - \mathbf{a}_{\mathrm{kq}}|$ is the length of the polygon segment kq. By analogy with Eq. (5), the vertical component of the gravitational attraction vector is given by (cf. Pohánka, 1988)

$$g_z(\mathbf{r}) = -\mathrm{G}\rho \sum_{\mathrm{k}=1}^{\mathrm{K}} \sum_{\mathrm{q}=1}^{\mathrm{Q_k}} \mathbf{n}_\mathrm{k} \cdot \Phi(u_{\mathrm{kq}}, v_{\mathrm{kq}}, w_{\mathrm{kq}}, z_\mathrm{k}, \varepsilon). \tag{8}$$

Alternative expressions for the gravitational field generated by arbitrary polyhedral bodies of homogenous density can be found for instance in Holstein et al. (1999) and Petrović (1996).

48.2.3 Gauss Cubature Approach

Integrating Eq. (1) with respect to z'we get

$$V(\mathbf{r}) = -\mathrm{G}\,\rho \int_{y_2'}^{y_2'} \int_{x_2'}^{x_2'} \Big| \ln[(z - z') + |\boldsymbol{\ell}|]\Big|_{z_1'}^{z_2'} \mathrm{d}x'\,\mathrm{d}y'. \tag{9}$$

After applying the Gauss cubature discretisation in Eq. (9), the expression for the gravitational potential generated by the rectangular prism of homogeneous density is

$$V(\mathbf{r}) = -\frac{1}{4}\mathrm{G}\,\rho\,(x_2'-x_1')\,(y_2'-y_1')\,\big|\,f_V(x_A',y_A') + f_V(x_B',y_B') + f_V(x_A',y_B') + f_V(x_B',y_A')\,\big|_{z_1'}^{z_2'}, \tag{10}$$

where the function $f_v = \ln[(z-z') + |\boldsymbol{\ell}|]$ is computed for the Gauss nodes:

$$x_A' = \tfrac{x_1'+x_2'}{2} + \tfrac{1}{\sqrt{3}}\tfrac{x_2'-x_1'}{2}, y_A' = \tfrac{y_1'+y_2'}{2} + \tfrac{1}{\sqrt{3}}\tfrac{y_2'-y_1'}{2},$$

$$X_B' = \tfrac{x_1'+x_2'}{2} - \tfrac{1}{\sqrt{3}}\tfrac{x_2'-x_1'}{2}, y_B' = \tfrac{y_1'+y_2'}{2} - \tfrac{1}{\sqrt{3}}\tfrac{y_2'-y_1'}{2}.$$

The expression for the vertical component of the gravitational attraction vector reads

$$g_z(\mathbf{r}) = -\mathrm{G}\,\rho \int_{y_1'}^{y_2'}\int_{x_1'}^{x_2'} \big||\boldsymbol{\ell}|^{-1}\big|_{z_1'}^{z_2'}\,\mathrm{d}x'\mathrm{d}y' = -\frac{1}{4}\mathrm{G}\,\rho(x_2'-x_1')(y_2'-y_1')\,\big|f_{g_z}(x_A',y_A') + f_{g_z}(x_B',y_B') + f_{g_z}(x_A',y_B') + f_{g_z}(x_B',y_A')\,\big|_{z_1'}^{z_2'}, \tag{11}$$

where $f_{g_z} = |\boldsymbol{\ell}|^{-1}$.

48.2.4 Linear Vertical Mass Approach

We define the linear vertical mass approach in a frame of the geocentric spherical coordinates (r,ϕ,λ). The gravitational potential and the vertical component of the gravitational attraction vector generated by the tesseroid of homogeneous density read (cf. Martinec, 1998)

$$V(\mathbf{r}) = \mathrm{G}\,\rho\Delta\phi'\Delta\lambda'\cos\phi'\left|\frac{1}{2}(|\mathbf{r}'|+3|\mathbf{r}|\cos\psi)|\boldsymbol{\ell}| + \frac{1}{2}|\mathbf{r}|^2(3\cos^2\psi-1)\ln\big||\mathbf{r}'|-|\mathbf{r}|\cos\psi+|\boldsymbol{\ell}|\big|\right|_{r_1'}^{r_2'}, \tag{12}$$

and

$$g_z(\mathbf{r}) = -\mathrm{G}\,\rho\,\Delta\phi'\Delta\lambda'\cos\phi'\,\big||\boldsymbol{\ell}|^{-1}\big(|\mathbf{r}'|^2+3|\mathbf{r}|^2\big)\cos\psi + |\boldsymbol{\ell}|^{-1}(1-6\cos^2\psi)|\mathbf{r}||\mathbf{r}'| + |\mathbf{r}|(3\cos^2\psi-1)\ln\big||\mathbf{r}'|-|\mathbf{r}|\cos\psi+|\boldsymbol{\ell}|\big|\big|_{r_1'}^{r_2'}, \tag{13}$$

where ψ is the spherical angle between $\mathbf{r}$ and $\mathbf{r}'$, $\cos\psi = \sin\phi'\sin\phi + \cos\phi'\cos\phi\cos(\lambda'-\lambda)$; and the Euclidean distance is computed from: $|\boldsymbol{\ell}| = \sqrt{|\mathbf{r}^2| + |\mathbf{r}'|^2 - 2|\mathbf{r}||\mathbf{r}'|\cos\psi}$. We consider: $x_2'-x_1' = r_1'\Delta\phi'$, $y_2'-y_1' = r_1'\Delta\lambda'\cos\phi'$, $z_2'-z_1' = r_2'-r_1'$; where $\Delta\phi' = \phi_2'-\phi_1'$ and $\Delta\lambda = \lambda_2'-\lambda_1'$. We note here that the application of the one-point cubature formula instead of the Gauss cubature discretisation in Eqs. (9) and (11) yields the expressions for the linear vertical mass approach in a frame of the topocentric Cartesian coordinates.

48.2.5 Point-Mass Approach

A simple numerical integration is applied to compute V and g_z (e.g. Barthelmes et al., 1991);

$$V(\mathbf{r}) = \mathrm{G}\,\rho\,|\bar{\boldsymbol{\ell}}|^{-1}(x_2'-x_1')(y_2'-y_1')(z_2'-z_1'), \tag{14}$$

$$g_z(\mathbf{r}) = -\mathrm{G}\,\rho\frac{z-\bar{z}'}{|\bar{\boldsymbol{\ell}}|^3}(x_2'-x_1')(y_2'-y_1')(z_2'-z_1'), \tag{15}$$

where $|\bar{\boldsymbol{\ell}}| = |\mathbf{r}-\bar{\mathbf{r}}|$ is the Euclidean distance between the computation point $\mathbf{r}$ and the geometrical centre of the rectangular prism $\bar{\mathbf{r}}' = (\bar{x}',\bar{y}',\bar{z}')$, $\bar{x}' = (x_2'-x_1')/2$, $\bar{y}' = (y_2'-y_1')/2$, $\bar{z}' = (z_2'-z_1')/2$. Heck and Seitz (2007, Eqs. 29 and 36) define the point-mass approach (for the tesseroid) in a frame of the geocentric spherical coordinates.

48.3 Numerical Experiment

The numerical experiment was conducted for five different base areas of the rectangular prism, corresponding to 1×1, 2×2, 3×3, 5×5, and 10×10 arc-sec geographical resolution of the digital terrain model. The constant height 100 m of the rectangular prisms was adopted. Consequently, five different heights of the 1×1 arc-sec rectangular prism were chosen, namely 100, 200, 500, 1,000, and 2,000 m. The rectangular prism approach was used to compute the gravitational potential and attraction generated by the rectangular prisms (Figs. 48.1 and 48.2). The same results were obtained using the line integral approach.

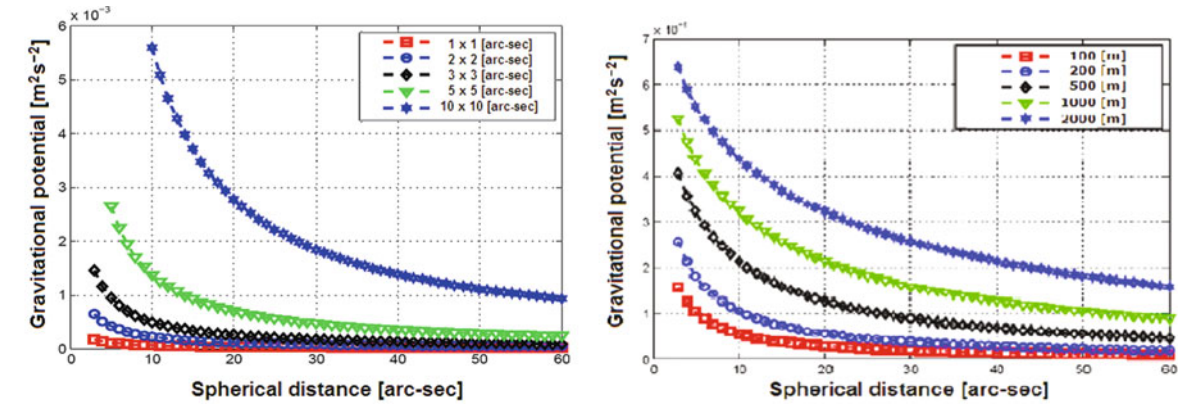


Fig. 48.1 Results of the rectangular prism approach. The gravitational potential generated by: (**a**) the rectangular prisms of the constant height 100 m, and the base areas 1 × 1, 2 × 2, 3 × 3, 5 × 5 and 10 × 10 arc-sec, and (**b**) the rectangular prisms of the constant base area 1 × 1 arc-sec, and the heights 100, 200, 500, 1,000 and 2,000 m

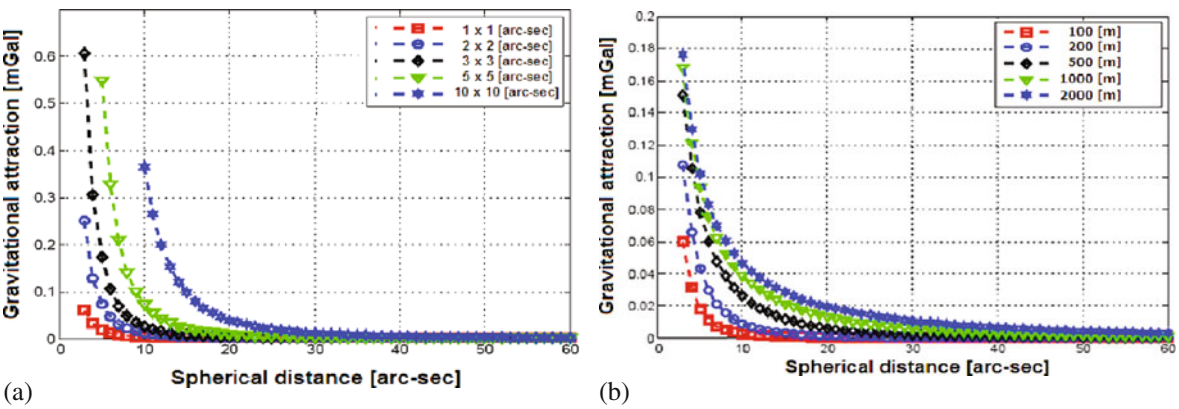


Fig. 48.2 Results of the rectangular prism approach. The gravitational attraction generated by: (**a**) the rectangular prisms of the constant height 100 m, and the base areas 1 × 1, 2 × 2, 3 × 3, 5 × 5, and 10 × 10 arc-sec, and (**b**) the rectangular prisms of the constant base area 1 × 1 arc-sec, and the heights 100, 200, 500, 1,000 and 2,000 m

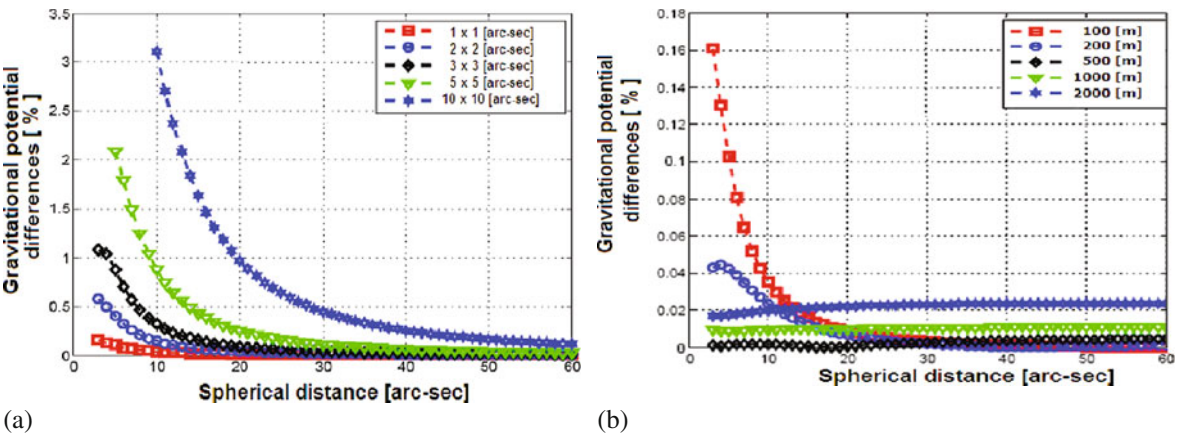


Fig. 48.3 The relative precision of the linear vertical mass approach. The gravitational potential generated by: (**a**) the tesseroids of the constant height 100 m, and the base areas 1 × 1, 2 × 2, 3 × 3, 5 × 5 and 10 × 10 arc-sec, and (**b**) the tesseroids of the constant base area 1 × 1 arc-sec, and the heights 100, 200, 500, 1,000 and 2,000 m

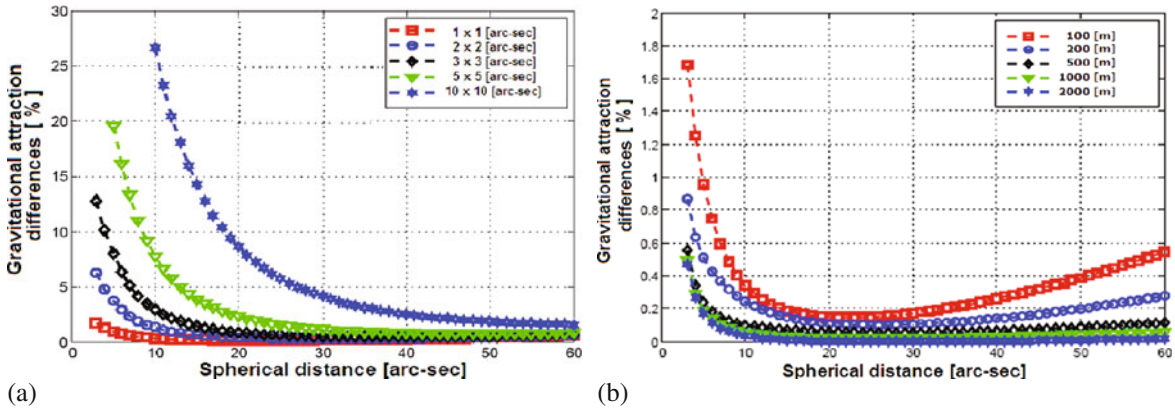


Fig. 48.4 The relative precision of the linear vertical mass approach. The gravitational attraction generated by: (**a**) the tesseroids of the constant height 100 m, and the base areas 1×1, 2×2, 3×3, 5×5 and 10×10 arc-sec, and (**b**) the tesseroids of the constant base area 1×1 arc-sec, and the heights 100, 200, 500, 1,000 and 2,000 m

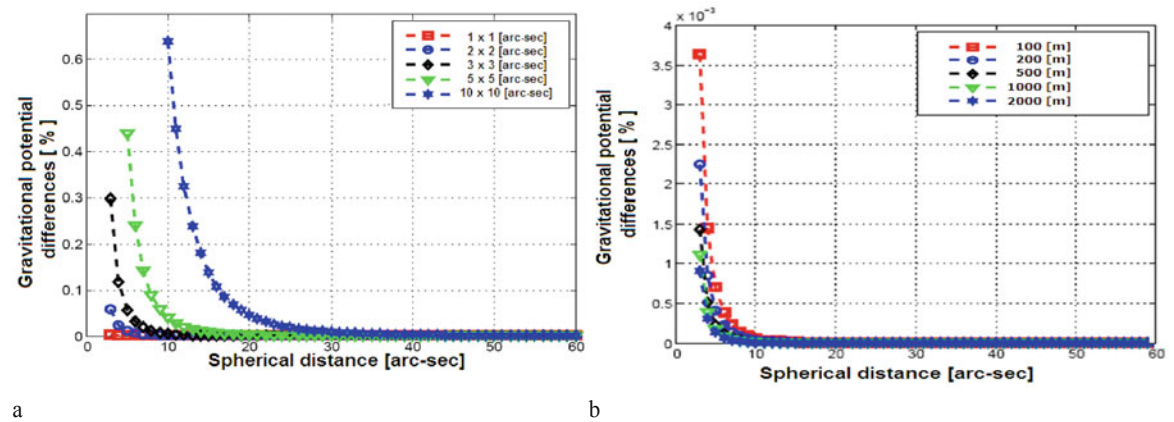


Fig. 48.5 The relative precision of the Gauss cubature approach. The gravitational potential generated by: (**a**) the rectangular prisms of the constant height 100 m, and the base areas 1×1, 2×2, 3×3, 5×5 and 10×10 arc-sec, and (**b**) the rectangular prisms of the constant base area 1×1 arc-sec, and the heights 100, 200, 500, 1,000 and 2,000 m

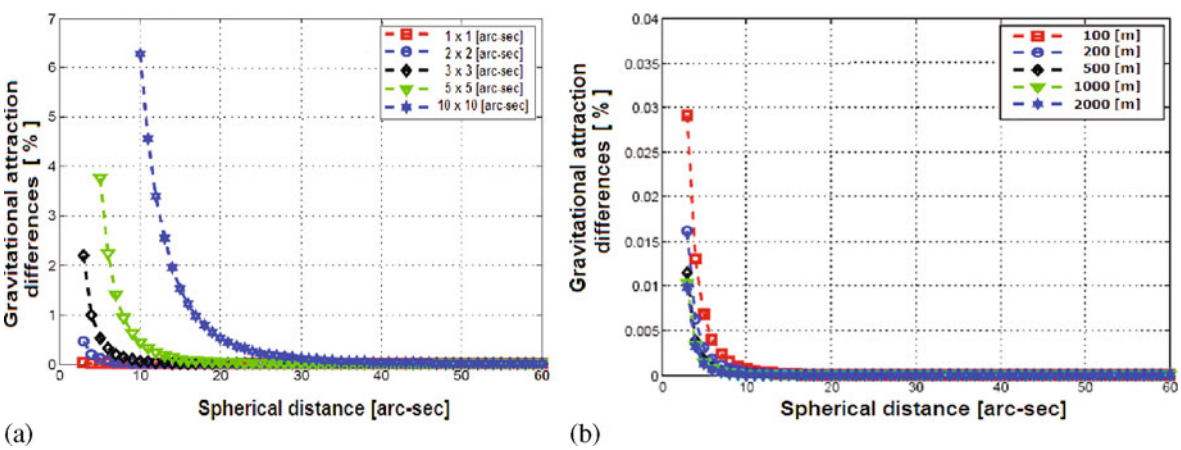


Fig. 48.6 The relative precision of the Gauss cubature approach. The gravitational attraction generated by: (**a**) the rectangular prisms of the constant height 100 m, and the base areas 1×1, 2×2, 3×3, 5×5 and 10×10 arc-sec, and (**b**) the rectangular prisms of the constant base area 1×1 arc-sec, and the heights 100, 200, 500, 1,000 and 2,000 m

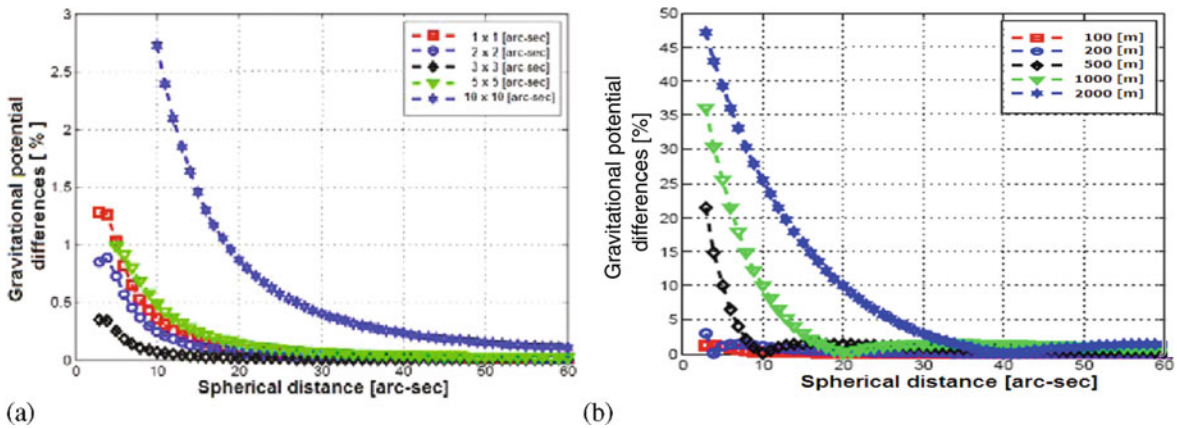


Fig. 48.7 The relative precision of the point-mass approach. The gravitational potential generated by: (**a**) the rectangular prisms of the constant height 100 m, and the base areas 1×1, 2×2, 3×3, 5×5 and 10×10 arc-sec, and (**b**) the rectangular prisms of the constant base area 1×1 arc-sec, and the heights 100, 200, 500, 1,000 and 2,000 m

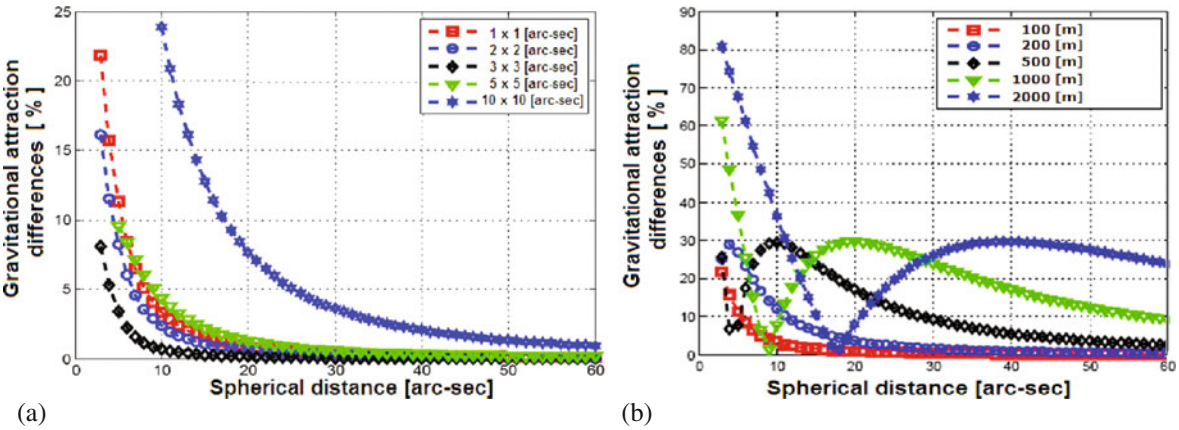


Fig. 48.8 The relative precision of the point-mass approach. The gravitational attraction generated by: (**a**) the rectangular prisms of the constant height 100 m, and the base areas 1×1, 2×2, 3×3, 5×5 and 10×10 arc-sec, and (**b**) the rectangular prisms of the constant base area 1×1 arc-sec, and the heights 100, 200, 500, 1,000 and 2,000 m

The relative precision of the linear vertical mass and the Gauss cubature approaches with respect to the rectangular prism approach at the vicinity of the computation point up to 1 arc-min of the spherical distance is shown in Figs. 48.3, 48.4, 48.5 and 48.6. The corresponding relative precision of the point-mass approach is shown in Figs. 48.7 and 48.8.

The comparison of the time-efficiency of the analytical, semi-analytical and numerical methods applied for computing the gravitational potential and attraction is given in Fig. 48.9. The time-efficiency is provided in terms of the relative computation time.

48.4 Conclusions

Precision: The Gauss cubature approach provides a higher relative precision with respect to the rectangular prism approach than the linear vertical mass and the point-mass approaches. The relative precision of computing the potential and attraction better than 99.9 and 99% respectively can be achieved outside the inner zone of $\psi > 20$ arc-sec, provided that the geographical resolution of input data is higher than 10×10 arc-sec (see Figs. 48.5 and 48.6). The relative precision of computing the potential better than 99% can be

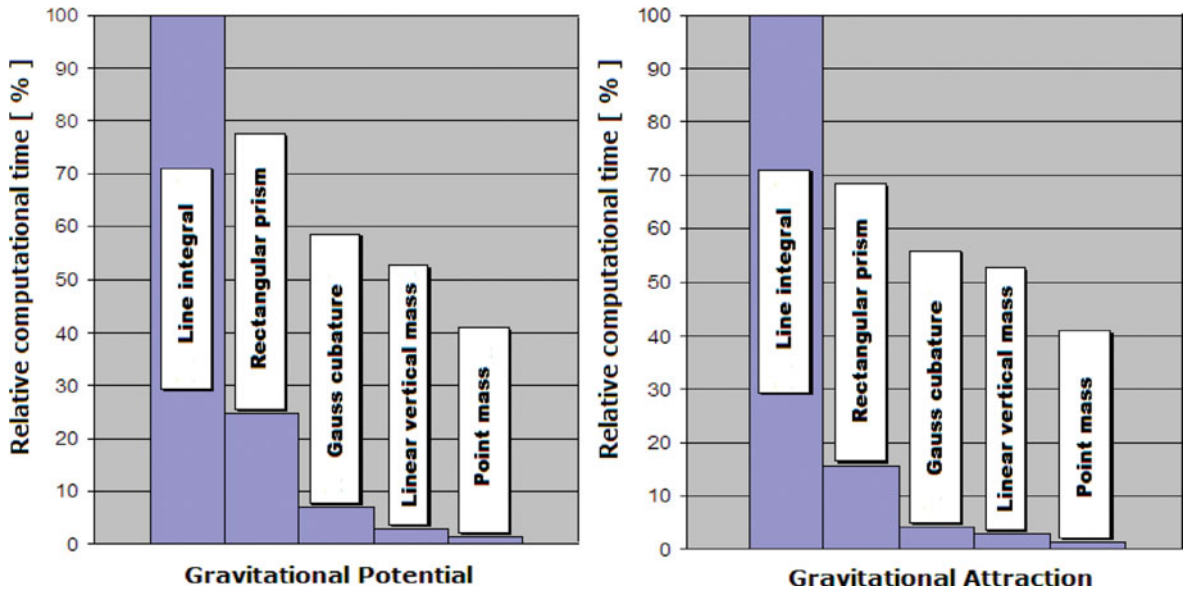


Fig. 48.9 The time-efficiency of integration methods for computing the potential and attraction

achieved by the linear vertical mass approach if $\psi >$ 20 arc-sec and the geographical resolution of input data is 10×10 arc-sec or higher (cf. Fig. 48.3). The same relative precision of computing the attraction by the linear vertical mass approach is, however, guarantied only if 1×1 arc-sec geographical resolution of input data is used for the semi-analytical integration (cf. Fig. 48.4). Comparing with the attraction, the investigated semi-analytical and numerical methods provide almost ten times higher relative precision of the potential. We note that a more refined version of the linear vertical mass approach (so-called the tesseroid approach) was proposed by Heck and Seitz (2007). Within the vicinity of the computation point up to 1 arc-min of the spherical distance, the use of the numerical point-mass approach is inadequate. It introduces large errors, especially in computing the attraction.

Time efficiency: The line integral approach is the most time-consuming. The rectangular prism approach is less time-consuming; it requires 25% of the total time otherwise needed for computing the potential by the line integral approach, and less than 15% for computing the attraction. The time efficiency of the semi-analytical methods is similar, reducing the computer calculation time by order of magnitude comparing with the line integral approach. The point-mass approach is the most time-efficient. Comparing with the line integral approach, it reduces the computer calculation time almost by two orders of magnitude.

References

Barthelmes, F., R. Dietrich, and R. Lehmann (1991). Use of point masses on optimised positions for the approximation of the gravity field. In: Rapp, R.H. and F. Sanso (eds), Determination of the Geoid, Springer, Berlin, pp. 484–493.

Heck, B. (2003). Rechenverfahren und Aswertemodelle der Landesvermessung. Klassische und moderne Methoden. 3rd ed, Wichmann, Heidelberg.

Heck, B. and K. Seitz (2007) A comparison of the tesseroid, prism and point-mass approaches for mass reductions in gravity field modelling. *J. Geod.*, 81, 12–136.

Holstein, H., P. Schürholz, A.J. Starr, M. Chakraborty (1999). Comparison of gravimetric formulas for uniform polyhedra. *Geophysics*. 64(5), 1434–1446.

Li, Y.C. and M.G. Sideris (1994). Improved gravimetric terrain corrections. *Geophys. J. Int.*, 119, 740–752.

Martinec, Z (1998). Boundary value problems for gravimetric determination of a precise geoid. Lecture Notes in Earth Sciences, Vol 73, Springer Verlag, Berlin, Heidelberg, New York.

Nagy, D., G. Papp, and J. Benedek (2000). The gravitational potential and its derivatives for the prism. *J. Geod.*, 74, 552–560

Nagy, D., G. Papp, and J. Benedek (2002). Erratum: Corrections through "The gravitational potential and its derivatives for the prism". *J. Geod*., 76(8), 475–475.

Petrović, S. (1996). Determination of the potential of homogeneous polyhedral bodies using line integrals. *J. Geod*., 71, 44–52.

Pohánka, V. (1988). Optimum expression for computation of the gravity field of a homogeneous polyhedral body. *Geophys. Prospecting*, 36, 733–751.

Tsoulis, D. (2003). Numerical investigations in the analytical and semi-analytical computation of gravimetric terrain effects. *Studia Geophysica et Geodaetica*, 47(3), 481–494.

Chapter 49

Further Improvements in the Determination of the Marine Geoid in Argentina by Employing Recent GGMs and Sea Surface Topography Models

C. Tocho, G.S. Vergos, and M.G. Sideris

Abstract During the last 6 years, extensive efforts have been put for the determination of the marine geoid in the Atlantic coastal area of Argentina. Up until recently, the main focus has been directed in the development of combined solutions through heterogeneous data, such as gravity anomalies, altimetric sea surface heights and bathymetric information employing both space and frequency domain methods. With the advent of the gravity-field dedicated satellite missions of CHAMP and GRACE and the development of more accurate satellite-only and combined global gravity models (GGMs), improved solutions have been acquired. Nevertheless, one point that still needed attention was the incorporation of proper, in terms of accuracy, sea surface topography models for the reduction of altimetric sea surface heights to the geoid. With that in mind, and the fact that 2008 is a benchmark year for GGMs due to the presentation of the new NGA GGM (EGM08), additional efforts have been carried out for the determination of new improved solutions for the marine geoid in Argentina.

This work focuses on the determination of combined solutions through the combination of all available gravity and satellite altimetry data for the area under study, while digital bathymetric data are used to compute topographic effects and reduce the data in the usual remove-compute-restore scheme. Finally, the new improved Combined Mean Dynamic Topography (CMDT) model by Rio for the area under study is used to reduce the altimetric data to the geoid. All these are carried out using the latest GGMs employing CHAMP and GRACE data, i.e., EIGEN-GL04C, EIGEN-CG01C, EIGEN-CG03C and GGM02C, together with the new EGM08. Combination methods such as Input Output System Theory (IOST) is investigated, while purely altimetric, gravimetric and combined marine geoid models are determined as well. The quality of the estimated new marine geoid solutions is assessed through comparisons with previous solutions, stacked Topex/Poseidon (T/P) sea surface heights, Jason-1 and Envisat data.

C. Tocho (✉)
Facultad de Ciencias Astronómicas y Geofísicas,
La Plata, Argentina
e-mail: ctocho@fcaglp.unlp.edu.ar

49.1 Introduction

The main objective of this paper is to investigate the possibility of improving the accuracy of the marine geoid models available offshore Argentina employing the new Global Gravitational Model EGM2008 (Pavlis et al., 2008) and the Rio Combined Mean Dynamic Topography Model (Rio and Hernandez, 2004).

EGM2008 has been recently release to public by the US Geospatial-Intelligence Agency (NGA) EGM Development Team. It is developed up to degree and order 2,159, and contains additional spherical harmonics coefficients extending to degree 2,190 and order 2,159.

Sea Surface Heights (SSHs) refer to the Mean Sea Surface (MSS), therefore in order to estimate geoid heights from altimetry data we need to reduce the SSHs to the geoid using a Mean Dynamic Topography Model (MDT). This is an important step in altimetric geoid and/or gravity field determination and can be viewed as an equivalent to the free-air reduction of surface and marine gravity anomalies to the geoid.

S.P. Mertikas (ed.), *Gravity, Geoid and Earth Observation*, International Association of Geodesy Symposia 135,
DOI 10.1007/978-3-642-10634-7_49, © Springer-Verlag Berlin Heidelberg 2010

Neglecting that reduction will result in the determination of the MSS and not the geoid. Since the MDT varies between –2.2 m and 70 cm with a standard deviation of ±62 cm in a global scale (Koblinsky et al., 1999) it becomes apparent that such considerations are mandatory and not optional (Vergos et al., 2005a, b). Assuming that the geoid is stationary, we can compute altimetric geoid heights as:

$$\mathrm{GEOID} = \mathrm{SSHs} - \mathrm{MDT} \quad (1)$$

In the frame of this work, pure gravimetric and altimetric geoid models as well as a combined solution using the Multiple Input Multiple Output System Theory (MIMOST) (Sideris, 1996; Andritsanos et al., 2000, 2001) have been determined. The area under study is located in the Atlantic Coastal region of Argentina, bounded between 34°S to 55°S in latitude and 56°W (304°E)–70°W (290° E) in longitude.

Both the purely gravimetric and altimetric solutions were computed using the following reference Global Gravity Models: EGM96 (Lemoine et al., 1998), the models based on CHAMP and GRACE satellite mission data: EIGEN-CG01C (Reigber et al., 2004), EIGEN-CG03C (Förste et al., 2005), EIGEN-GL04C (Förste et al., 2008), GGM02C (Tapley et al., 2005) and EGM2008 up to maximum degree 2,190 (Pavlis et al., 2008).

The quality of the estimated new marine geoid solutions is assessed through comparisons with older geoid solutions computed by the authors (Tocho et al., 2005a, b), stacked Topex/Poseidon (T/P) Sea Surface Heights, JASON1 data and ENVISAT altimetric observations.

49.2 Computation Strategy and Results

As Global Gravity Models (GGMs) play an important role in the remove-compute-restore technique the first test was to validate the new EGM2008 model in the area under study. Table 49.1 shows the statistics of the differences between EGM2008 and the other Global Gravity models; the difference between EGM2008 and EGM96 is depicted in Fig. 49.1. The differences are mainly over the Argentinean mainland. From a comparison with the differences between EGM96 and GGM02C, these differences seem to come mostly from GRACE data. From Table 49.1 it is also worth mentioning that the differences between the latest NGA combination GGM and the latest GFZ models (namely EIGEN-CG03C and EIGEN-GL04C) are at the ±20 and ±19 cm level while the range reaches the 5.26 and 4.9 m respectively.

In the frame of the present work, nineteen geoid models have been computed in the area under study. These include six purely gravimetric solutions, 12 purely altimetric solutions and 1 combined solution. All the solutions were estimated using the remove-restore technique. The processing sequence for the estimations is extensively outlined in (Tocho et al., 2005a, b).

The purely altimetric solutions have been computed using 70510 ERS1-GM SSHs corresponding to all cycles from November 28th, 1994 to March 21st, 1995. These raw SSHs have been corrected from all instrumental errors and geophysical effects that affect altimetric measurements, obtaining in this way Corrected Sea Surface Heights (CSSHs) (AVISO, 1998). These heights refer to the mean sea surface, so they have to be reduced to the geoid by removing the contribution of the MDT. The EGM96 Dynamic Ocean Topography (EGM96.DOT) (Lemoine et al., 1998), complete to degree and order 20 and the Rio Combined Mean Dynamic Topography (Rio and Hernandez, 2004) were used to take into account the MDT. Both models are presented in Figs. 49.2 and 49.3 respectively, where it is evident that the EGM96 MDT model presents a very simplistic and smooth version of the sea surface topography and of the circulation of the area compared to the Rio model. Of course this is normal, given that

Table 49.1 Statistics of the differences between geoid heights computed from the new EGM2008 and the other GGMs. Values in parenthesis refer to oceanic regions. Unit: (m)

	Min	Max	Mean	σ
$N^{EGM2008}$-N^{EGM96}	–4.13 (–1.83)	2.60 (1.38)	0.013 (–0.06)	0.58 (0.31)
$N^{EGM2008}$-$N^{EIGEN\text{-}CG01C}$	–1.75 (–1.30)	3.30 (1.15)	–0.008 (0.005)	0.25 (0.20)
$N^{EGM2008}$-$N^{EIGEN\text{-}CG03C}$	–1.63 (–1.15)	3.63 (1.03)	–0.012 (–0.013)	0.25 (0.20)
$N^{EGM2008}$-$N^{EIGEN\text{-}GL04C}$	–1.73 (–1.39)	3.17 (1.25)	0.002 (0.002)	0.24 (0.19)
$N^{EGM2008}$-N^{GGM02C}	–2.06 (–1.66)	2.99 (2.01)	0.001 (0.007)	0.34 (0.32)
N^{EGM96}-N^{GGM02C}	–2.39 (–1.54)	2.99 (1.86)	–0.012 (0.076)	0.62 (0.38)

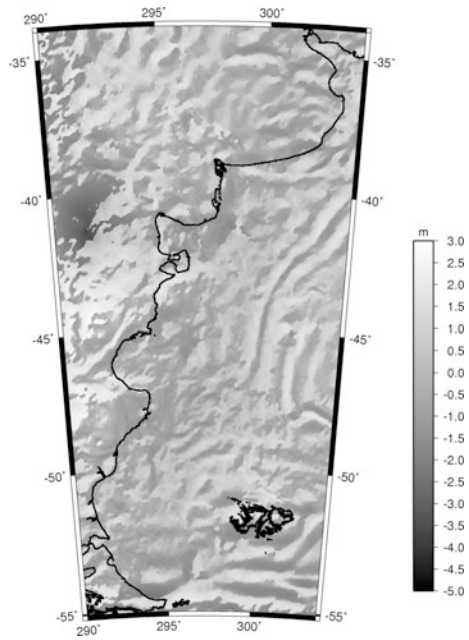


Fig. 49.1 Differences between EGM2008 and EGM96 geoid heights

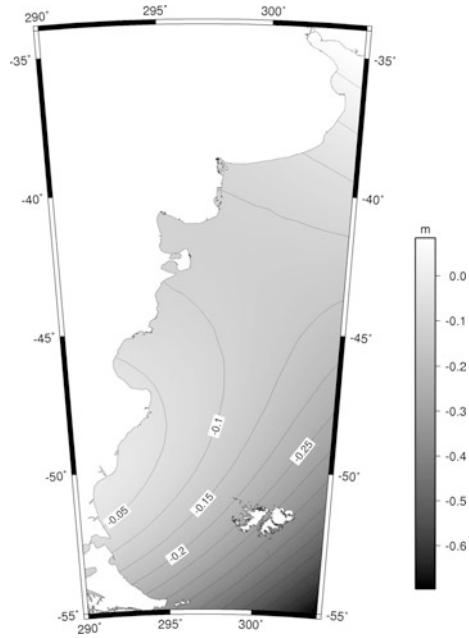


Fig. 49.3 EGM96.DOT

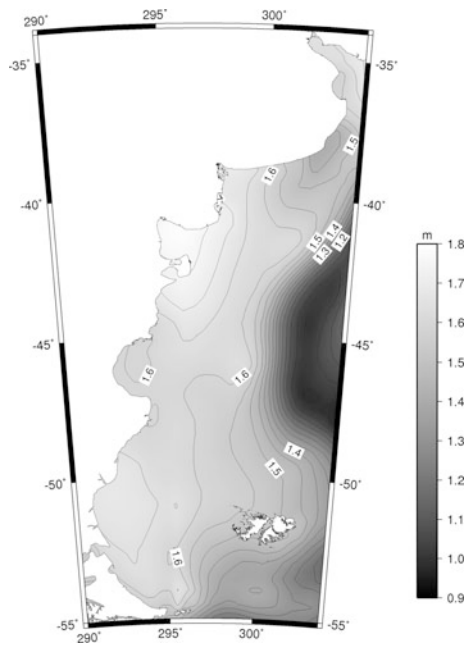


Fig. 49.2 Rio CMDT

the EGM96.DOT model has been computed 15 years ago and incorporates fewer data than the Rio model. In any case, the availability of the Rio MDT model allows for a more rigorous treatment of the sea surface topography contribution in geoid modeling.

Then, following the remove-restore method, the contribution of the six global geopotential models and the contribution of the bathymetry, using the Sandwell and Smith model (1997) were removed from the corrected SSHs, obtaining residual geoid heights. From these residual geoid heights a 3 rms test was performed in order to detect blunders and then they were interpolated on a $3' \times 3'$grid. A low-pass filter was applied to the residual grid to reduce the high sea surface variability in the area under study. Finally, the contribution of the bathymetry and the geopotential models were restored yielding the final geoid solutions. The statistics of the final models, reduced with the Rio CMDT and the EGM96.DOT are presented in Tables 49.2 and 49.3 respectively.

The gravimetric geoid solution were based on terrestrial and satellite altimetry-derived gravity anomalies, while they were computed using the remove-compute-restore technique, employing the 1D-FFT spherical Stokes's convolution formula (Haagmans et al., 1993) for the prediction of residual geoid heights. Before the prediction of the residual geoid, the free-air gravity anomalies have to be reduced by a geopotential model during the remove step.

Table 49.2 Statistics of the final altimetric geoid solutions computed with the Rio CMDT. Unit: (m)

	Min	Max	Mean	σ
N^{ERS1}(EGM2008)	0.691	19.260	11.221	±2.933
N^{ERS1}(EGM96)	0.423	19.276	11.235	±2.939
N^{ERS1}(EIGENCG-01C)	0.583	18.889	11.143	±2.935
N^{ERS1}(EIGENCG-03C)	0.495	18.922	11.208	±2.933
N^{ERS1}(EIGENGL-04C)	0.669	18.853	11.166	±2.932
N^{ERS1}(GGM02C)	0.706	18.993	11.202	±2.933

Table 49.3 Statistics of the final altimetric geoid solutions computed with the EGM96.DOT. Unit: (m)

	Min	Max	Mean	σ
N^{ERS1}(EGM2008)	0.580	19.379	11.184	±3.065
N^{ERS1}(EGM96)	0.346	19.387	11.206	±3.071
N^{ERS1}(EIGENCG-01C)	0.545	19.138	11.236	±3.054
N^{ERS1}(EIGENCG-03C)	0.458	19.209	11.300	±3.052
N^{ERS1}(EIGENGL-04C)	0.631	19.144	11.258	±3.057
N^{ERS1}(GGM02C)	0.669	19.169	11.294	±3.052

Table 49.4 Statistics of final gravimetric geoid solutions (m)

	Min	Max	Mean	σ
N^{GRAV}(EGM2008)	1.032	19.526	11.833	±3.103
N^{GRAV}(EGM96)	1.034	20.017	11.809	±3.083
N^{GRAV}(EIGENCG-01C)	1.118	19.631	11.849	±3.103
N^{GRAV}(EIGENCG-03C)	1.150	19.599	11.848	±3.115
N^{GRAV}(EIGENGL-04C)	1.055	19.616	11.836	±3.112
N^{GRAV}(GGM02C)	1.054	20.411	11.875	±3.127

Furthermore, the effect of the topography/bathymetry was taken into account through a topographic reduction. In this study, Helmert's second method of condensation was used to account for the terrain effects. The final gravimetric geoid is obtained in the restore step adding back the effect of the topography and the geopotential model. Six different gravimetric geoid models were obtained; each one was referenced to a different GGM, while the statistics of final models are summarized in Table 49.4.

49.3 Geoid Model Validation

For the validation of the estimated geoid solutions, stacked T/P, JASON1 and ENVISAT SSHs were used. Table 49.5 shows the statistics of geoid height differences between EGM2008 and EGM96 with T/P, ENVISAT and JASON1 SSHs reduced with the CMDT model (m). In all the cases, the differences between the geoid solutions from these Global Gravity Models and the mentioned SSHs were computed and minimized using a four parameter similarity

Table 49.5 Geoid heights differences between EGM2008 & EGM96 and T/P, JASON1 and ENVISAT SSHs after bias and tilt fit. Unit: (m)

	Min	Max	Mean	σ
$N^{EGM2008}$-$N^{T/P}$	–1.140	0.700	0.000	±0.180
N^{EGM96}-$N^{T/P}$	–1.160	1.460	0.000	±0.293
$N^{EGM2008}$-$N^{ENVISAT}$	–0.650	0.510	0.000	±0.140
N^{EGM96}-$N^{ENVISAT}$	–1.230	1.620	0.000	±0.271
$N^{EGM2008}$-N^{JASON1}	–0.460	0.590	0.000	±0.160
N^{EGM96}-N^{JASON1}	–1.050	1.500	0.000	±0.296

Table 49.6 Statistics of geoid height differences between T/P, ENVISAT and JASON1 SSHs and the estimated altimetric geoid solutions using Rio CMDT & EGM96.DOT. Unit: (m)

	Rio CMDT (σ)	EGM96 DOT
	σ	
$\Delta N^{T/P\text{-}ERS1}$ (EGM2008)	±0.188	±0.189
$\Delta N^{T/P\text{-}ERS1}$ (EGM96)	±0.189	±0.194
$\Delta N^{T/P\text{-}ERS1}$ (EIGENCG-01C)	±0.194	±0.191
$\Delta N^{T/P\text{-}ERS1}$ (EIGENCG-03C)	±0.191	±0.190
$\Delta N^{T/P\text{-}ERS1}$ (EIGENGL-04C)	±0.190	±0.189
$\Delta N^{T/P\text{-}ERS1}$ (GGM02C)	±0.189	±0.191
$\Delta N^{JASON1\text{-}ERS1}$ (EGM2008)	±0.164	±0.166
$\Delta N^{JASON1\text{-}ERS1}$ (EGM96)	±0.166	±0.169
$\Delta N^{JASON1\text{-}ERS1}$ (EIGENCG-01C)	±0.169	±0.166
$\Delta N^{JASON1\text{-}ERS1}$ (EIGENCG-03C)	±0.166	±0.164
$\Delta N^{JASON1\text{-}ERS1}$ (EIGENGL-04C)	±0.164	±0.171
$\Delta N^{JASON1\text{-}ERS1}$ (GGM02C)	±0.171	±0.166
$\Delta N^{ENVISAT\text{-}ERS1}$ (EGM2008)	±0.143	±0.140
$\Delta N^{ENVISAT\text{-}ERS1}$ (EGM96)	±0.140	±0.150
$\Delta N^{ENVISAT\text{-}ERS1}$ (EIGENCG-01C)	±0.150	±0.145
$\Delta N^{ENVISAT\text{-}ERS1}$ (EIGENCG-03C)	±0.145	±0.146
$\Delta N^{ENVISAT\text{-}ERS1}$ (EIGENGL-04C)	±0.146	±0.144
$\Delta N^{ENVISAT\text{-}ERS1}$ (GGM02C)	±0.144	±0.145

transformation model. From Table 49.5 it is evident that EGM08 brings significant improvement in the determination of the Earth's gravity field, since it outperforms EGM96, in all cases, by 11–14 cm. Moreover, and with respect to the different altimetric data used, it can be concluded that ENVISAT SSHs are superior to T/P ones by ±4 cm and by ±2 cm compared to JASON1. Furthermore, JASON-1 SSHs present a ±2 cm improvement in terms of the std of the differences, compared to T/P. The latter is in line with the conclusions drawn in Tocho et al. (2007) and Vergos et al. (2007) where a validation of T/P, ENVISAT and JASON-1 SSHs has been performed.

The T/P, JASON1 and ENVISAT SSHs were corrected with the EGM96.DOT and the Rio CMDT. The statistics of the differences between the T/P, JASON1 and ENVISAT SSHs and the pure altimetric geoid solutions can be seen in Table 49.6 and with the gravimetric solutions in Table 49.7.

Table 49.7 Statistics of geoid height differences between T/P, ENVISAT and JASON1 SSHs and the estimated gravimetric geoid solutions. Unit: (m)

	Rio CMDT (σ)
$\Delta N^{T/P\text{-}GRAV}$ (EGM2008)	±0.263
$\Delta N^{T/P\text{-}GRAV}$ (EGM96)	±0.275
$\Delta N^{T/P\text{-}GRAV}$ (EIGENCG-01C)	±0.283
$\Delta N^{T/P\text{-}GRAV}$ (EIGENCG-03C)	±0.291
$\Delta N^{T/P\text{-}GRAV}$ (EIGENGL-04C)	±0.295
$\Delta N^{T/P\text{-}GRAV}$ (GGM02C)	±0.319
$\Delta N^{JASON1\text{-}GRAV}$ (EGM2008)	±0.242
$\Delta N^{JASON1\text{-}GRAV}$ (EGM96)	±0.261
$\Delta N^{JASON1\text{-}GRAV}$ (EIGENCG-01C)	±0.271
$\Delta N^{JASON1\text{-}GRAV}$ (EIGENCG-03C)	±0.281
$\Delta N^{JASON1\text{-}GRAV}$ (EIGENGL-04C)	±0.282
$\Delta N^{JASON1\text{-}GRAV}$ (GGM02C)	±0.306
$\Delta N^{ENVISAT\text{-}GRAV}$ (EGM2008)	±0.206
$\Delta N^{ENVISAT\text{-}GRAV}$ (EGM96)	±0.214
$\Delta N^{ENVISAT\text{-}GRAV}$ (EIGENCG-01C)	±0.223
$\Delta N^{ENVISAT\text{-}GRAV}$ (EIGENCG-03C)	±0.234
$\Delta N^{ENVISAT\text{-}GRAV}$ (EIGENGL-04C)	±0.235
$\Delta N^{ENVISAT\text{-}GRAV}$ (GGM02C)	±0.266

49.4 Combined Solution

The combined geoid model was determined with the FFT-based Multiple Input–Multiple Output System Theory. MIMOST theory with double input and single output combined solution was based on the formulas given by Sideris (1996) and Andritsanos et al. (2001). The combined geoid solution was estimated in a smaller area between 40°S–50°S in latitude and 56°W (304°E)–66°W (294° E) in longitude. The inputs of MIMOST were residual gravimetric geoid heights and residual altimetric geoid heights with the contribution of the EGM2008 model removed in order to avoid long wavelength errors and with the altimetric data reduced with EGM96.DOT.

The input noises for each dataset were generated using the standard deviation of the differences between ENVISAT SSHs and the gravimetric geoid (±13.5 cm) and between ENVISAT SSHs and the altimetric geoid (±14 cm). The statistics of the solutions in the small area can be seen in Table 49.8 and in Table 49.9 their validation with ENVISAT data. Figure 49.4 depicts the MIMOST combined solution for the area under study.

The results presented in Table 49.6 lead to some important outcomes. For all comparisons the superiority of EGM08 over all other models is evident. EGM08 provides smaller std of the differences, by 1 cm compared to EGM96 and by 4–6 cm compared to the CHAMP and GRACE combination models. Comparing the results presented in Table 49.7 with those from Table 49.6, the superiority of the altimetric models over the gravimetric ones is evident, since in all cases the std of the differences of the former is smaller by about 6–10 cm over the latter.

Table 49.8 Statistics of the geoid models in the inner area (m)

	Min	Max	Mean	σ
N^{ERS1}	0.579	15.281	10.078	3.306
N^{GRAV}	1.077	16.153	10.847	3.433
$N^{EGM2008}$	0.960	14.755	10.124	3.068
N^{COMB}	1.061	16.140	10.845	3.437

Table 49.9 Statistics of the differences between ENVISAT SSHs and the gravimetric, altimetric and combined solutions (EGM08 as reference). (After bias and trend removed). The ENVISAT SSHs reduced with EGM96.DOT. Unit:[m]

	Min	Max	Mean	σ
N^{ERS1}-ENVISAT	–1.270	0.870	0.000	±0.142
N^{GRAV}-ENVISAT	–0.500	0.730	0.000	±0.134
$N^{EGM2008}$-ENVISAT	–0.710	0.530	0.000	±0.181
N^{COMB}-ENVISAT	–0.520	0.700	0.000	±0.136

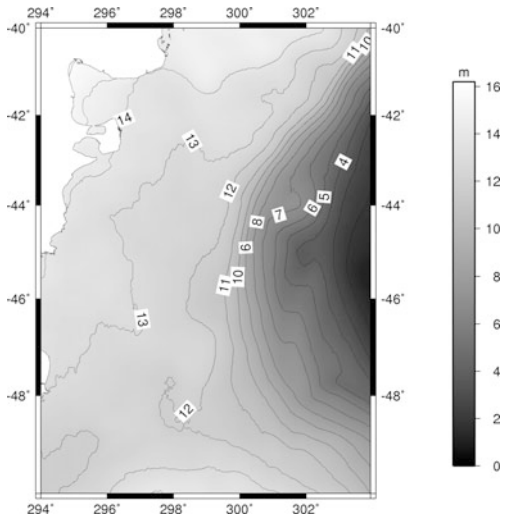


Fig. 49.4 MIMOST solution

From the results presented in Table 49.9, it becomes evident that the combined model improves the gravimetric geoid model in purely marine areas and the altimetric one close to the coastline.

49.5 Conclusions-Future Plans

The new NGA GGM EGM2008 was evaluated. When compared to EGM96 it provides a 11–13 cm improvement and an improvement of ~4–6 cm compared to CHAMP/GRACE GGMs. The Rio CMDT and EGM96.DOT were investigated for the reduction of altimetric sea surface heights to the geoid, and it became evident that it provides a much more realistic representation of the MDT in the area.

ENVISAT data provide higher accuracy compared to T/P and JASON1. The differences between ENVISAT SSHs and the gravimetric and altimetric geoid models, both referenced to EGM2008, dropped to ± 14.5 and ± 14 cm, respectively, in terms of the std (1σ). The combination improves the altimetric solution close to the coastline and the gravimetric one in the open ocean.

Other bathymetry models need to be evaluated, since an in-accurate model reduced the accuracy of the final solution and a detailed analysis of the combination of land and marine gravity data on the coastline should be carried out. The altimetric geoid models are ~2–8 cm better than the gravimetric.

The marine gravity data are probably not free-air reduced hence the large differences when using the Rio CMDT. The effect of the EGM96.DOT is removed with the bias and tilt fit. The new marine gravity Field DNSC08-GRA has to be evaluated to improve the accuracy of the gravimetric geoid.

References

Andritsanos, V.D., M.G. Sideris, and I.N. Tziavos (2000). A survey of gravity filed modeling applications of the Input-Output system Theory (IOST). *Int. Geoid. Serv. Bull.*, 10, 1–17.

Andritsanos, V.D., M.G. Sideris, and I.N. Tziavos (2001). Quasi-stationery Sea Surface topography estimation by the multiple input-output method. *J. Geod.*, 75, 216–226.

AVISO User Handbook (1998). Corrected Sea Surface Heights (CORSSHs) AVI-NT-011-311-CN Edition 31.

Förste C., F. Flechtner, R. Schmidt, U. Meyer, R Stubenvoll, F. Barthelmes, R. König, K.H. Neumayer, M. Rothacher, Ch. Reigber, R. Biancale, S. Bruinsma, J.M. Lemoine, and J.C. Raimondo (2005). A New High Resolution Global Gravity Field Model Derived from Combination of GRACE and CHAMP Mission and Altimetry/Gravimetry Surface Gravity Data, Poster presented at EGU General Assembly 2005, Vienna, Austria, 24–29, April 2005.

Förste, C., R. Schmidt R. Stubenvoll F. Flechtner U. Meyer R. König H. Neumayer R. Biancale S. Lemoine J-M, Bruinsma Loyer S, Barthelmes F, and Esselborn S (2008) The GeoForschungsZentrum Potsdam/Groupe de Recherche de Geodesie Spatiale satellite-only and combined gravity field models: EIGEN-GL04S1 and EIGEN-GL04C. *J. Geod.*, 82(6), 331–346, doi:10.1007/s00190-007-0183-8.

Haagmans, R., E. de Min, and M. van Gelderen (1993). Fast evaluation of convolution integrals on the sphere using 1D FFT and a comparison with existing methods for Stokes' integral. *Manuscripta Geodaetica*, 18, 227–241.

Koblinsky, C.J., R. Ray, B.D. Beckley, Y.M. Wang, L. Tsaoussi, A. Brenner, and R. Williamson (1999). NASA Ocean Altimeter Pathfinder Project, Report 1: Data Processing Handbook, NASA/TM-1998-208605.

Lemoine, F.G., S.C. Kenyon, J.K. Factor, R.G. Trimmer, N.K. Pavlis, D.S. Chinn, C. Cox, S.M. Klosko, S.B. Luthcke, M.H. Torrence, Y.M. Wang, R.G. Williamson, E.C. Pavlis, R.H. Rapp, and T.R. Olson (1998). The development of the join NASA GSFC and NIMA geopotential model EGM96, NASA Technical Paper, 1998–206861.

Pavlis, N.K., S.A. Holmes, S.C. Kenyon, and J.K. Factor (2008). An earth gravitational model to degree 2160: EGM2008, presented at the 2008 General Assembly of the European Geosciences Union, Vienna, Austria, April 13–18, 2008.

Reigber, Ch., P. Schwintzer, R. Stubenvoll, R. Schmidt, F. Flechtner, U. Meyer, R. König, H. Neumayer, Ch. Förste, F. Barthelmes, S.Y. Zhu, G. Balmino, R. Biancale,

J. Lemoine, H. Meixner, and J.C. Raimondo (2004). A high resolution global gravity field model combining CHAMP and GRACE satellite mission and surface gravity data: EIGEN-CG01C, Science Tech Report GFZ Potsdam STR 06/07.

Rio, M.H. and F. Hernandez (2004). A mean dynamic topography computed over the world ocean from altimetry, in-situ measurements and a geoid model. *J. Geophys. Res.*, 109(12), C12032.

Sideris, M.G. (1996). On the use of heterogeneous noisy data in spectral gravity field modelling methods. *J. Geod.*, 70(8), 470–479.

Smith, W.H.F. and D.T. Sandwell (1997) Global sea floor topography from satellite altimetry and ship depth soundings. *Sci. Mag.*, 277(5334), 1956–1962.

Tapley, B., J. Ries, S. Bettadpur, D. Chambers, M. Cheng, F. Condi, B. Gunter, Z. Kang, P. Nagel, R. Pastor, T. Pekker, S. Poole, and F. Wang (2005). GGM02 - An improved Earth gravity field model from GRACE. *J. Geod.*, 79(8), 467–478, doi 10.1007/s00190-005-0480-z.

Tocho, C., G.S. Vergos, and M.G. Sideris (2005a). Optimal marine geoid determination in the Atlantic coastal region of Argentina. In: Sanso, F. (ed.), A window on the future of Geodesy. International Association of Geodesy Symposia, vol. 128, Springer–Verlag, Berlin, Heidelberg, pp. 380–385.

Tocho, C., G.S. Vergos, and M.G. Sideris (2005b) A new marine geoid model for Argentina combining altimetry, ship-borne gravity data and CHAMP/GRACE-type EGMs. *Geod. Cartogr.*, 54(4), 177–189.

Tocho, C., G.S. Vergos, and M.G. Sideris (2007). Estimation of a New High-Accuracy Marine Geoid Model Offshore Argentina Using CHAMP- and GRACE-derived Geopotential Models. Presented at the XXIV General Assembly of the IUGG (IUGG2007), July 2–13, Perugia, Italy.

Vergos, G.S., V. Grigoriadis, I.N. Tziavos, and M.G. Sideris (2007). Combination of multi-satellite altimetry data with CHAMP and GRACE EGMs for geoid and sea surface topography determination. In: Tregoning, P. and C. Rizos (eds), Dynamic planet 2005 – monitoring and understanding a dynamic planet with geodetic and oceanographic tools. International Association of Geodesy Symposia, vol.130, Springer-Verlag, Berlin, Heidelberg, pp. 244–250.

Vergos, G.S., I.N. Tziavos, and V.D. Andritsanos (2005a). On the determination of marine geoid models by least-squares collocation and spectral methods using heterogeneous data. In: Sansó, F. (ed.), A window on the future of geodesy. International Association of Geodesy Symposia, vol. 128, Springer-Verlag, Berlin, Heidelberg, pp. 332–337.

Vergos, G.S., I.N. Tziavos, and V.D. Andritsanos (2005b). Gravity data base generation and geoid model estimation using heterogeneous data. In: Jekeli, C., L. Bastos, and J. Fernandes (eds), Gravity geoid and space missions 2004. International Association of Geodesy Symposia, vol. 129, Springer-Verlag, Berlin, Heidelberg, pp. 155–160.

Chapter 50

Comparison of Various Topographic-Isostatic Effects in Terms of Smoothing Gradiometric Observations

J. Janák and F. Wild-Pfeiffer

Abstract The main intention of the contribution is the computation and the comparison of five different topographic-isostatic effects and the analysis of the influence on all components of the disturbing gravity tensor. Based on the five different isostatic models, the topographic-isostatic effects are generated and their influence is analyzed for a GOCE-like satellite orbit. In particular the models of Airy-Heiskanen (A-H) and Pratt-Hayford (P-H), the combination of the Airy-Heiskanen model (land area) and the Pratt-Hayford model (ocean area) and the first (H1) and the second (H2) condensation model of Helmert, are considered. As it has been widely known, the reduction of the topographic-isostatic effect can significantly smooth the gravity signal, especially in or above the mountains. The benefit of this natural phenomenon is appreciated by the geodetic and geophysical community. Geodesists use the smoothed data, e.g. the refined Bouguer gravity anomalies, for interpolation and block-mean value computation, while geophysicists analyze the anomalous density distribution. A similar smoothing effect and advantageous use can also be expected in case of the gravity tensor components. A possibility to use the smoothing of measured satellite gradiometric data for regularization of the gradiometric inverse problem is discussed. The results can be applied on satellite gradiometry data in general; of course the primary interest is the application on the expected data of the ESA gradiometric mission GOCE.

J. Janák (✉)
Department of Theoretical Geodesy, Slovak University of Technology, Bratislava 81368, Slovakia
e-mail: juraj.janak@stuba.sk

50.1 Introduction

The downward continuation of gravimetric or gradiometric data either using an inverse of Abel-Poisson's integral or an inverse of the derivatives of Pizzetti's integral leads – from a mathematical point of view – to a problem of solving the Fredholm integral equation of the first kind. It is known that the mathematical properties of these equations make it difficult to obtain useful solutions by straightforward methods (see Aster et al., 2005). After discretization the above mentioned problem of gravimetric or gradiometric downward continuation can be expressed as a system of linear equations. There are two major difficulties: the system of linear equations is usually large and it is ill posed (see ibid.). In this paper the focus is put on the stability and quality of the solution, the size of the system is ignored.

The linear system of equations is

$$\mathbf{y} = \mathbf{A}\mathbf{x} + \boldsymbol{\varepsilon}, \tag{1}$$

where $\mathbf{y}$ is an n-dimensional vector of observations, $\mathbf{x}$ is a t-dimensional vector of unknowns ($t < n$), $\mathbf{A}$ is an $(n \times t)$ design matrix and $\boldsymbol{\epsilon}$ is the observation error vector. If the linear system (Eq. 1) is based on the Fredholm integral equation of the first kind, the matrix $\mathbf{A}$ is often ill conditioned, i.e. the condition number, defined as the ratio of the biggest and smallest singular values, is very large. Then the normal equation matrix $\mathbf{N} = \mathbf{A}^{\mathrm{T}}\mathbf{P}\mathbf{A}$, whereas $\mathbf{P}$ is the weight matrix of the observations, is also ill conditioned. Therefore the least squares solution is unstable in such a way that even a very small turbulence in observations can be magnified above all limits in the vector of unknowns.

S.P. Mertikas (ed.), *Gravity, Geoid and Earth Observation*, International Association of Geodesy Symposia 135,
DOI 10.1007/978-3-642-10634-7_50, © Springer-Verlag Berlin Heidelberg 2010

The elements a_{ij} of the matrix **A** are computed from known expression of the discretized integration kernel and depend only on the geometry of discretization and on the type of the problem to be solved. There have been several methods and many modifications suggested in mathematical, geophysical and geodetic literature on how to improve the stability of the solution by modifying the matrix **A** or the normal matrix **N**. Among these methods the truncated singular value decomposition (TSVD) method (see e.g. Xu, 1998) and the ridge regression method (RR) (see e.g. Xu, 1992; Xu and Rummel, 1994) are mentioned and used in the numerical experiment (see Chap. 4). Indeed, one or another method modifying the normal matrix is inevitable to be used while seeking for a reasonable quality of the solution. On the other hand, these methods have limitations too. Further improvement of the solution can be achieved modifying the vector of observations.

The modification of the observations can be understood as a supplementary method of regularization of inverse problems. As an example a band-limitation of airborne gravity data is used which has a positive impact on the downward continuation in significant stabilization of its numerical evaluation (see Novák and Heck, 2002). In this paper five different topographic-isostatic effects (A-H, P-H, A-H/P-H, H1, H2) are subtracted from the gradiometric data. The impact on smoothing the data and improvement of the quality of the solution after downward continuation is studied.

50.2 Topographic-Isostatic Effect

The effect of the topographic and isostatic masses can be described in the frequency or in the space domain. This paper will focus on the modelling in the space domain. A comparison between both computation methods is described e.g. in Wild-Pfeiffer and Heck (2007).

The potential of the topographic and isostatic masses can be described by Newton's integral in spherical coordinates which is in general

$$V(Q) = G \cdot \iint_{\sigma} \left[\int_{\xi=\xi_1}^{\xi=\xi_2} \rho \cdot \frac{\xi^2}{l} \cdot d\xi \right] \cdot d\sigma, \qquad (2)$$

$$\ell = \sqrt{r^2 + \xi^2 - 2r\xi \cdot \cos\psi},$$

$$\cos\psi = \sin\varphi \cdot \sin\varphi' + \cos\varphi \cdot \cos\varphi' \cdot \cos(\lambda - \lambda') \qquad (3)$$

The spherical coordinates, related to a terrestrial reference frame, of the computation point and the variable integration point are denoted by (r, ϕ, λ) and (ξ, ϕ′, λ′). G is the gravitational constant, ρ the local mass density and $d\Omega = \xi^2 \cdot d\xi\, d\sigma$ the volume element (dσ: surface element of the unit sphere).

To model the topographic and isostatic masses a segmentation into volume elements Ω_i is made where the density ρ_i is assumed to be constant:

$$V(Q) = G \cdot \sum_i \rho i \iiint_{\Omega_i} \frac{d\Omega}{\ell}. \qquad (4)$$

The triple integral can be approximated by prisms, point masses, mass lines, mass layers and tesseroids. Integral in Eq. (4) is analytically solvable for the prism and its approximation by the point mass, the mass line and the mass layer. In case of the tesseroid – bounded by geographical grid lines and surfaces of constant height (see Heck and Seitz, 2007) – no analytical solution exists in general. One possibility to solve the triple integral is its evaluation by purely numerical methods, e.g. the Gauss-Legendre cubature (3D), sees Wild-Pfeiffer (2008). A second alternative is provided by a Taylor series expansion of the integrand, where the term of zero order is equivalent to the point mass expression. Another possibility to compute the volume integral is its decomposition into a one-dimensional integral over the radial parameter ξ for which an analytical solution exists, and a two-dimensional spherical integral which is solved by quadrature methods, especially the Gauss-Legendre cubature (2D). The approximation of the tesseroids by prisms, postulating mass conservation, also provides an option for the solution of the triple integral; this procedure requires a transformation of the coordinate system of the prism into the local coordinate system at the computation point. A comparison between these mass elements and computation methods concerning accuracy and computation time is described in detail in Wild-Pfeiffer (2007) and Wild-Pfeiffer (2008).

50.3 Downward Continuation

A downward continuation of satellite gravity gradiometry (SGG) data can be performed in several ways. In this paper the approach based on the inverse solution of second derivatives of the Pizzetti integral formula in spherical coordinates is used, see Kern and Haagmans (2005) and Janák et al. (2008). Here the SGG data are continued downward and transformed into the free-air gravity anomalies. Each of six different components of disturbing gravity tensor ($T_{\phi\phi}$, $T_{\phi\phi}$, $T_{\phi r}$, $T_{\lambda\lambda}$, $T_{\lambda r}$, T_{rr}), observed or simulated at the satellite orbit level, are transformed into the free-air gravity anomalies Δg on or above the surface of the Earth inverting the equations

$$
\begin{aligned}
T_{\varphi\varphi}(r,\varphi,\lambda) &= \frac{R}{4\pi r^2}\cdot\int_{\sigma}\Delta g(R,\varphi',\lambda')\cdot S_{\varphi\varphi}(t,\psi,\alpha)\cdot d\sigma,\\
T_{\varphi\lambda}(r,\varphi,\lambda) &= \frac{R}{4\pi r^2}\cdot\int_{\sigma}\Delta g(R,\varphi',\lambda')\cdot S_{\varphi\lambda}(t,\psi,\alpha,\varphi)\cdot d\sigma,\\
T_{\varphi r}(r,\varphi,\lambda) &= \frac{R}{4\pi r^2}\cdot\int_{\sigma}\Delta g(R,\varphi',\lambda')\cdot S_{\varphi r}(t,\psi,\alpha)\cdot d\sigma,\\
T_{\varphi\lambda}(r,\varphi,\lambda) &= \frac{R}{4\pi r^2}\cdot\int_{\sigma}\Delta g(R,\varphi',\lambda')\cdot S_{\lambda\lambda}(t,\psi,\alpha,\varphi)\cdot d\sigma,\\
T_{\varphi r}(r,\varphi,\lambda) &= \frac{R}{4\pi r^2}\cdot\int_{\sigma}\Delta g(R,\varphi',\lambda')\cdot S_{\lambda r}(t,\psi,\alpha,\varphi)\cdot d\sigma,\\
T_{rr}(r,\varphi,\lambda) &= \frac{R}{4\pi r^2}\cdot\int_{\sigma}\Delta g(R,\varphi',\lambda')\cdot S_{rr}(t,\psi)\cdot d\sigma,
\end{aligned}
\tag{5}
$$

where $t = R/r$, ψ is the angular distance between the point of computation and the particular integration element and α stands for the spherical azimuth. The formulae for the integration kernels $S_{\phi\phi}$, $S_{\phi\lambda}$, $S_{\phi r}$, $S_{\lambda\lambda}$, $S_{\lambda r}$, S_{rr} can be found in Janák et al. (2008). After discretization, Eq. (5) can be written in form of Eq. (1).

50.4 Results

The different topographic-isostatic effects in terms of second derivatives of the gravity potential have been computed on a regular geographical grid with a resolution of $30' \times 30'$ on GOCE-type flight level of 260 km in the area ($41° \times 41°$), surrounded by parallels 15° and 56° and by meridians 116° and 157°. The tesseroid approach using the Taylor series expansion has been applied for the calculation of the topographic effect, the Airy-Heiskanen and Pratt-Hayford isostatic components and the combined Airy-Heiskanen and Pratt-Hayford model. In case of the two Helmert's models, the surface integral is evaluated by the 2D Gauss-Legendre product formula with $2 \times 2 = 4$ nodes per element.

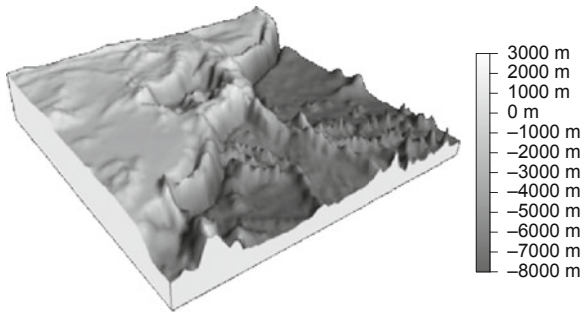


Fig. 50.1 The terrain and the sea bottom relief from the ETOPO2v2c model in the target area

For the simulation the following standard numerical values of the respective parameters have been used: $R = 6371008.7714$ m, $G = 6.673 \cdot 10^{-11}\,m^3 \cdot kg^{-1} \cdot s^{-2}$, $h_Q = r–R = 260$ km (satellite height), $\rho_0 = 2{,}670\ kg \cdot m^{-3}$, $\Delta\rho = 600\,kg \cdot m^{-3}$, T = 25 km (A-H), d = 21 km (H1) or d = 0 (H2). Furthermore, the digital terrain model ETOPO2v2c (NOAA, 2006) with a resolution of $10' \times 10'$ has been used (see Fig. 50.1).

The components of the disturbing gravity tensor have been generated from the EGM2008 (Pavlis et al., 2008) model ($n_{max} = 360$) at the same altitude and grid. The particular topographic-isostatic effects have been subtracted from the corresponding disturbing gravity tensor components; the smoothing effect has been investigated in terms of range and standard deviation. One parallel section ($\phi = 35.75°$) is plotted exemplarily in Appendix; the average improvement in range and standard deviation for the whole area is shown in Table 50.1.

For the downward continuation experiment the area ($22° \times 22°$), surrounded by parallels 24° and 46° and by meridians 126° and 148°, has been chosen. The area is smaller then the area where the topographic-isostatic effects have been computed because of the computer memory and computation time limitations.

Table 50.1 Smoothing the disturbing gravity tensor components by applying the topographic-isostatic effects in terms of range and standard deviation (in percentage). The best result for every component is in bold

		A-H	P-H	A-H/P-H	H1	H2
$T_{\phi\phi}$	Range	**24**	21	21	19	0
	Std	**19**	10	12	19	0
$T_{\phi\lambda}$	Range	26	**30**	30	24	0
	Std	17	14	16	**18**	0
$T_{\phi r}$	Range	19	**19**	19	19	0
	Std	19	11	13	**19**	0
$T_{\lambda\lambda}$	Range	23	**29**	29	22	0
	Std	**21**	19	19	20	0
$T_{\lambda r}$	Range	**26**	25	25	23	0
	Std	13	12	13	**13**	0
T_{rr}	Range	25	34	**35**	25	0
	Std	19	15	16	**19**	0

The experiment has been designed as follows (see also Fig. 50.2):

- The free-air gravity anomalies have been generated from the EGM2008 model ($n_{max} = 360$) in 10 km altitude in regular $30' \times 30'$ grid. The values are denoted by A;
- The particular topographic-isostatic effects on the gravity using A-H, P-H, A-H/P-H and H1 models in 10 km altitude have been subtracted from set A, obtaining the sets B, C, D, and E. This yields to 5 sets of free-air gravity anomalies in 10 km altitude: set A (uncorrected), set B (corrected for A-H), set C (corrected for P-H), set D (corrected for A-H/P-H) and set E (corrected for H1). The H2 method has not been applied in this experiment because it does not smooth the gravity data (see Table 50.1);
- From every set (A, B, C, D, E) the disturbing gravity tensor in spherical coordinates on 260 km altitude in regular $12' \times 12'$ grid has been computed using the derivatives of the discretized Pizzetti formula (see Eq. 5). The new sets are denoted by TA, TB, TC, TD, TE. Each of these sets consists of 6 subsets corresponding to particular gravity tensor components (e.g. $TA_{\phi\phi}$, $TA_{\phi\lambda}$, $TA_{\phi r}$, $TA_{\lambda\lambda}$, $TA_{\lambda r}$, TA_{rr});
- A Gaussian noise with the standard deviation of 0.005 ns^{-2} has been applied to every set (TA, TB, TC, TD, TE) obtaining the new sets TAN, TBN, TCN, TDN, TEN (N stands for noise);
- The downward continuation of sets TAN, TBN, TCN, TDN, TEN (5 sets, 30 subsets) has been performed using the TSVD and RR stabilization methods obtaining the 5×2 sets (30×2 subsets) of free-air gravity anomalies on 10 km altitude in regular $30' \times 30'$ grid. The sets are: AT, BT, CT, DT, ET (T stands for TSVD) and AR, BR, CR, DR, ER (R stands for ridge regression);
- The comparison of the downward continued sets with the sets of exact free-air gravity anomalies A, B, C, D, E has been performed obtaining the 5×2 sets (30×2 subsets) of differences, denoted as DAT = AT-A, DBT = BT-B, DCT = CT-C, DDT = DT-D, DET = ET-E and DAR = AR-A, DBR = BR-B, DCR = CR-C, DDR = DR-D, DER = ER-E;

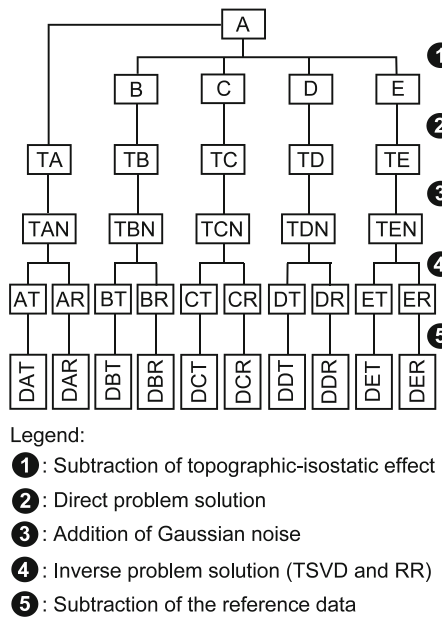


Fig. 50.2 Block diagram of the experiment

Table 50.2 Mean standard deviations σ_m of differences of Δg computed from 200 repetitions (in mgal)

		DA	DB	DC	DD	DE
$\sigma_{m(\phi\phi)}$	T	14.937	12.270	12.266	**12.214**	12.597
	R	14.487	12.097	**12.029**	12.085	12.435
$\sigma_{m(\phi\lambda)}$	T	12.163	**10.299**	10.749	10.899	10.628
	R	11.748	**9.808**	10.192	10.340	10.094
$\sigma_{m(\phi r)}$	T	11.270	**9.628**	10.125	10.261	9.921
	R	10.882	**9.258**	9.667	9.735	9.492
$\sigma_{m(\lambda\lambda)}$	T	10.051	8.359	8.661	8.766	**8.314**
	R	9.657	8.104	8.426	8.492	**8.076**
$\sigma_{m(\lambda r)}$	T	8.999	7.522	7.985	7.971	**7.486**
	R	8.544	**7.307**	7.783	7.779	7.324
$\sigma_{m(rr)}$	T	8.169	**7.112**	7.556	7.613	7.153
	R	7.867	**6.849**	7.323	7.362	6.920

DA – uncorrected data, DB – A-H corrected data, DC – P-H corrected data, DD – A-H/P-H corrected data, DE – H1 corrected data, T – TSVD and R – RR regularization. The best result for every component is in bold.

- The mean standard deviations (from 200 repetitions) of differences DAT, DBT, DCT, DDT, DET and DAR, DBR, DCR, DDR, DER have been computed and are presented in Table 50.2.

50.5 Conclusions

The numerical results show that the application of the topographic-isostatic effect in downward continuation of SGG data (from 260 to 10 km altitude) improves the quality of the solution by about 15% in terms of standard deviation. The particular inverse problems behave differently and have different degree of instability. Therefore the results shown in Table 50.2 differ.

The smoothing of simulated SGG data is in detail:

- The H1 method provides the best smoothing in terms of standard deviation (best for 4 components and second best for 2 components after A-H method).
- PH method seems to provide the best smoothing in terms of range or amplitudes (best for 3 components, second best for 1 component after A-H/P-H method, third best for 2 components after A-H and A-H/P-H methods). Here it should be mentioned that about 70% of the area of investigation is in the ocean.
- The A-H and H1 methods usually give similar results (see also Appendix). For the components $T_{\phi\phi}$, $T_{\phi\lambda}$, and $T_{\phi r}$ the A-H method gives slightly better smoothing in terms of range.
- The P-H and A-H/P-H methods give similar results because most of the area of interest is in the ocean.
- The improvement in smoothing in terms of standard deviation varies from 13 to 21% for particular components.
- The improvement in smoothing in terms of range varies from 19 to 35% for particular components.
- The H2 method does not provide any smoothing of the SGG data.

Concerning the downward continuation experiment, the results show that the best results have been achieved for 5 disturbing gravity tensor components using the A-H or H1 corrected data and only for 1 component the best results have been obtained using the P-H or A-H/P-H corrected data. Based on the presented results and assuming the effectiveness of computation the H1 method can be recommended to apply for regional gravity field modeling when using the SGG data. The A-H method also works well, sometimes even slightly better, but it is more laborious.

Acknowledgements The authors thank Prof. Dr. A. Kleusberg and two anonymous reviewers for their valuable comments. Part of presented research has been supported by Slovak national projects VEGA 1/0775/08 and APVV-0351-07.

References

Aster, R.C., B. Borchers, and C.H. Thurber (2005). Parameter estimation and inverse problems. Elsevier, Amsterdam.

Heck, B. and K. Seitz (2007). A comparison of the tesseroid, prism and point-mass approaches for mass reductions in gravity field modelling. *J. Geod.*, 81, 121–136, doi: 10.1007/s00190-006-0094-0.

Janák, J., P.L. Xu, and Y. Fukuda (2008). Application of GOCE data for regional gravity field modeling, submitted to EPS

Kern, M. and R. Haagmans (2005). Determination of gravity gradients from terrestrial gravity data for calibration and validation of gradiometric GOCE data. In: Jekeli C., L. Bastos, and J. Fernandes (eds), Gravity, geoid and space missions. Springer, Berlin, pp. 95–100.

NOAA (2006). 2-minute gridded global relief data ETOPO2v2. National Geophysical Data Center, US Department of Commerce.

Novák, P. and B. Heck (2002). Downward continuation and geoid determination based on band-limited airborne gravity data. *J. Geod*., 76, 269–278.

Pavlis, N.K., S.A. Holmes, S.C. Kenyon, and J.K. Factor (2008). An earth gravitational model to degree 2160 EGM2008. Geophysical Research Abstracts EGU 2008.

Wild-Pfeiffer, F. (2007). Auswirkungen topographisch-isostatischer Massen auf die Satellitengradiometrie. Deutsche Geodätische Kommission, Reihe C, Heft Nr 604, München.

Wild-Pfeiffer, F. (2008). A comparison of different mass elements for use in gravity gradiometry. *J. Geod.*, 82, 637–653, doi: 10.1007/s00190-008-0219-8.

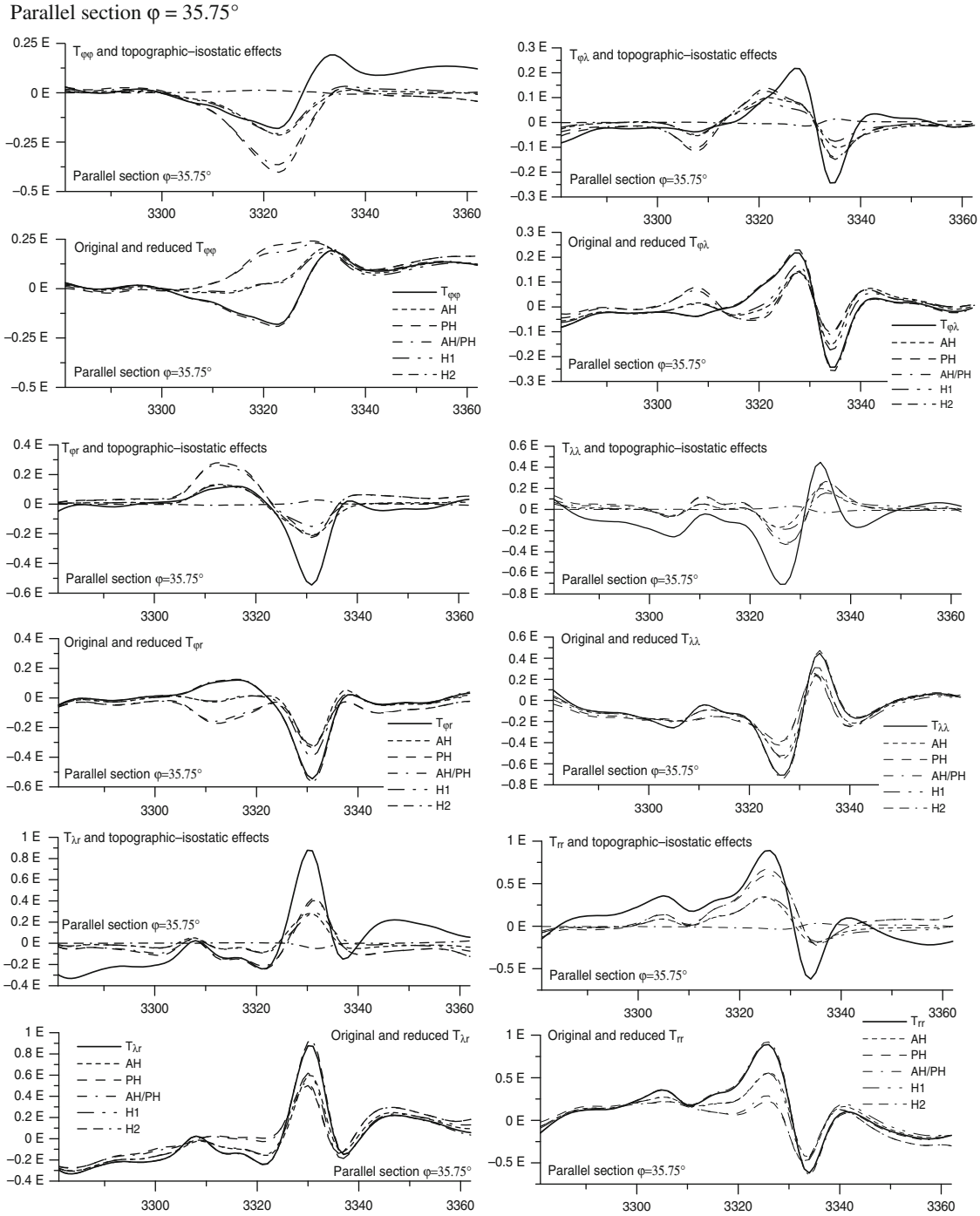
Wild-Pfeiffer, F. and B. Heck (2007). Comparison of the modelling of topographic and isostatic masses in the space and the frequency domain for use in satellite gravity gradiometry. Proceedings of the 1st International Symposium of the International Gravity Field Service: Gravity Field of the Earth, Istanbul, August 28-September 1, Harita Dergisi – Special Issue 18 (2007), ISSN 1300-5790, S. 312-317.

Xu, P.L. (1992). Determination of surface gravity anomalies using gradiometric observables. *Geophys. J. Int.*, 110, 321–332.

Xu, P.L. (1998). Truncated SVD methods for discrete linear ill-posed problems. *Geophys. J. Int*., 135, 505–514.

Xu, P.L. and R. Rummel (1994). Generalized ridge regression with applications in determination of potential fields. *Manuscripta Geodaetica*, 20, 8–20.

Appendix


Parallel section φ = 35.75°
Tφφ and topographic–isostatic effects
Parallel section φ=35.75°
Original and reduced Tφφ
Tφφ
AH
PH
AH/PH
H1
H2
Tφλ and topographic–isostatic effects
Original and reduced Tφλ
Tφr and topographic–isostatic effects
Original and reduced Tφr
Tλλ and topographic–isostatic effects
Original and reduced Tλλ
Tλr and topographic–isostatic effects
Original and reduced Tλr
Trr and topographic–isostatic effects
Original and reduced Trr
3300
3320
3340
3360

Chapter 51

Evaluation of Recent Global Geopotential Models in Argentina

A. Pereira and M.C. Pacino

Abstract Recent Earth Geopotential Models (EGMs) represent a great improvement to several applications related to gravity field modeling. These models offer higher accuracy and better resolution of the gravity field.

In this research, the most recent models' behavior like EIGENs, EGM2008 as well as the classic EGM96, are analyzed and compared in Argentina, aiming to know which one suits better in the country.

This investigation also studies the differences between EGMs and geoid undulation values (calculated with height data from GPS and spirit leveling) and gravity anomalies (obtained from terrestrial gravimetric campaigns).

In principle, a great difference is detected with the satellite-only geopotential models. The EGMs that perform better results are those that include satellite altimetry and terrestrial information in their calculation.

The comparison between local data and the results of seven global models is shown with the residual statistic.

51.1 1 Introduction

The practical use of theories for studying the Earth – built a century ago – was only possible since the advance of satellite technology and computing tools. In practical specific applications, having a geoid model allows us to use an algorithm from which ellipsoidal heights can be transformed into orthometric heights.

Many countries, including Argentina, are encouraging the investigation and computing of Geoid Models, mainly due to the increasing use of GNSS technology. In addition, a lot of geological and geophysical applications demand the knowledge of the terrestrial gravity field. Basically, this demand is concentrated in engineering, mining and petroleum companies.

In the determination of the third coordinate that locates the point in its spatial position with respect to the sea level, the entailment between the geodetic systems and the knowledge of the geoid undulation value is essential. Therefore, the local and regional geoid determination is fundamental when GPS is used in a three dimensional survey.

Until the launching of the gravity satellite missions, the Earth gravity field models arose from the combination of different space and ground data that has been collected during the last decades. This data included information obtained from space tracking stations (like SLR, Doris, PRARE, and GPS), conventional terrestrial gravimetry and satellite altimetry over the oceans. The gravity models precision was limited due to the heterogeneity of the quality and origin of the data and the lack of a global coverage with a uniform precision.

Recent gravity satellite campaigns represent a great improvement to several gravity field modeling – related applications; moreover, they provide valuable information about our planet's geodynamic behavior since they offer the temporal variations of the gravity field.

A. Pereira (✉)
Facultad de Ciencias Exactas, Ingeniería y Agrimensura de la Universidad Nacional de Rosario, Rosario 2000, Argentina-CONICET
e-mail: apereira@fceia.unr.edu.ar

S.P. Mertikas (ed.), *Gravity, Geoid and Earth Observation*, International Association of Geodesy Symposia 135,
DOI 10.1007/978-3-642-10634-7_51, © Springer-Verlag Berlin Heidelberg 2010

51.2 Study Area

Argentina is the second biggest country in South America and is located between 20° and 56° South Latitude and 53° and 74° West Longitude. It has several geological and physiographical areas, presenting mainly plains at the Eastern region, hills in the center and mountains at the West. The country is bounded in its western extreme by the Andes Mountain Chain.

The continental territory includes four big geological regions: the Patagonian massif (a Precambrian basement); the Andes System (caused by the Andean bending); the Brazilian massif (Precambrian basement); and the Pampa Plain (originated from marine and volcanic sediments) (Gentili et al., 1980).

51.3 Data Description

51.3.1 Terrestrial Data

The evaluation was carried out using two different kinds of ground information: GPS/leveling data and surface gravity data.

Regarding the terrestrial information available in Argentina, the undulation coverage is very heterogeneous. The height data comes from different sources: universities, provincial geodetic networks, national geographic institutes, etc. The ellipsoidal heights were mainly obtained from the GPS provincial networks that were developed for cadastral purposes. All the information is in the official reference frame of Argentina (POSGAR94) which is based on the WGS84 system.

The gravity anomaly information has better coverage in the country and was retrieved from the gravity anomaly maps of Argentina (Pacino et al., 2007).

The gravimetric activity in Argentina was initiated in 1906 with the Buenos Aires – Potsdam link. In 1952, the gravity fundamental Datum was built and 2 years later it was linked to Bad Harzburg (Germany) with a cuadripendular Askania instrument.

The gravity stations in Argentina that formed part of the IGSN-71 network were measured in 1971 and in 1988–1991. In 2002 "Instituto Geográfico Militar" (IGM) finished the tasks related to the altimetric national network measurements, coincident with the first order national gravity network. It consists of 370 leveling lines containing 16,320 benchmarks and 225 network nodes. The geopotential correction of the leveling benchmarks has not been performed yet. Thus, the heights above the sea level are just the result of spirit leveling plus the adjustment correction. The reference height for leveling was established in 1945 at the Mar del Plata tide gauge.

At the same time, academic and research institutions performed an important amount of gravity measurements. Most of this information has been added to the data base, after a careful verification process. This has been achieved by the coordinated work from Universities of Sao Paulo, Rosario, Leeds and IGM.

The complete data base is then composed of about 170,000 data points acquired from different sources: IGM, Universidad Nacional de La Plata, Universidad Nacional de Buenos Aires, Universidad Nacional de Tucumán, Instituto Antártico Argentino, Institut für Geologische Wissenschafte (Frei Universitat of Berlin), YPF. All gravity data has been connected to the IGSN71 Network. The mean accuracy of the data was estimated to be of the order of 0.5 mgal.

Standard expression for the free-air correction calculation have been used, depending on height H (leveled height, in meters) and latitude ϕ.

For the Bouguer correction calculation, the infinite horizontal slab expression has been used with a crust density of 2.67 g cm^{-3} for land stations. Curvature correction to the Bouguer correction was applied using Cordell et al. (1982) expression.

The WGS84 gravity formula was used to define the normal gravity for each station. Terrain corrections have been also added according to Pacino et al. (2007).

51.3.2 Geopotential Models

In accordance with Heiskanen and Moritz (1967), among other authors, a form of representation of the geoidal heights is a series of spherical harmonic functions.

The values of the coefficients of that series, up to a certain degree and order, represent a *geopotential model*.

The analysis of the satellites orbital perturbations revolutionized the knowledge of the subject since the publication of the first value for the coefficient of dynamic flattering C_{20} (Buchar, 1958).

Since then, different specialized centers released several geopotential models. It could be mentioned the

GEM10A, GEM10B and GEM10C models, complete to degree and order 30, 36 and 180 respectively (Lerch et al., 1977, 1981); the GRIM1 models, complete to degree and order 22 (Balmino et al., 1976); GRIM3, to degree and order 36 (Reigber et al., 1983); the OSU86, OSU89 and OSU91 models (Rapp, 1989, 1992); the JGM models, complete to degree and order 70 (Nerem et al., 1994) and the EGM96 model (Lemoine et al., 1998).

From the evaluation of Blitzkow (1998) for South America it can be concluded that the EGM96 is better than previous models in terms of comparison with gravimetric anomalies. At present, the EGM2008 model represents an important improvement on the knowledge of the gravitational potential in the region (Blitzkow and De Matos, 2009).

Before this new gravity satellite missions era, the long wavelength of the Earth gravity field was obtained from the tracking measurement of satellites orbiting our planet. These measurements had a heterogeneous quality and quantity coverage, and had a low geographical coverage density. Therefore, the accuracy and precision of the gravity models that had come up this way was limited, and only the important geophysical features of the Earth's structure could be detected. As a result, the development of Earth's gravity models in medium and short wavelengths arose with the measurements of terrestrial and marine gravity, which came from different times and also had diverse quality and geographical coverage.

But in the last few years, this scenario has changed and a great advance has been developed concerning the knowledge of the terrestrial gravity field, thanks to the combined use of GPS receivers, accelerometers and gradiometers.

The successful launching of CHAMP (CHAllenging Mini-satellite Payload) in 2001 and GRACE (Gravity Recovery And Climate Experiment) in 2002 marked the beginning of a new age in satellite gravimetry (Wahr et al., 1998; Beutler, 2004).

51.4 Models Evaluation

The combined high-resolution gravity models are essential in those applications where an accurate knowledge of the static gravity field potential (and their short and long wavelengths gradients) is necessary.

In the present investigation, seven EGMs were compared and analyzed, to finally determine which one suits Argentina better.

These EGMs have differences between them, the main one is the source of data used for their computing; therefore there will be satellite-only models as well as those including terrestrial and/or satellite altimetry information. This first categorization determines the maximum degree and order of the spherical harmonic coefficients, which will derive in short and long wavelength models, with resolutions from 9 to 141 km.

One model considered for the analysis was the EGM96 (Lemoine et al., 1998), which is the most used in geodetic surveys and geoid calculation in Argentina. This geopotential model is defined by spherical harmonic coefficients complete to degree and order 360; it is based on satellite data (from the EGM96S model), gravity ground surveys data and satellite altimetry information provided by TOPEX/POSEIDON, ERS-1 and GEOSAT missions, among others.

In this evaluation, the recent EGM2008 (Pavlis et al., 2008) was included. This geopotential model was developed by the NGA and released in April 2008, it is complete to degree and order 2,159 and contains additional spherical harmonic coefficients extending to degree 2,190 and order 2,159. This model is based on GRACE mission data and terrestrial gravity and satellite altimetry information.

In addition to these EGMs, four models from the EIGEN series with information coming from different sources were considered in this research.

One of them is the EIGEN-CG03C, computed in 2005 by the GFZ Potsdam and the GRGS Toulouse (Groupe de Recherche de Geodesia Spatiale, France). This model is based on GRACE and CHAMPS satellite missions and also includes terrestrial gravity and satellite altimetry data; it is complete to degree and order 360 in terms of spherical harmonics. The second model is the EIGEN-GL04C (Förste et al., 2006), calculated in 2006 by the centers mentioned before, but in this case the data was provided by GRACE and LAGEOS campaigns. This model is also complete to degree and order 360.

Another models used for the analysis were the EGMs satellite-only data. From EIGEN series, one of the models chosen was the EIGEN-GL04S1 (Förste et al., 2006), computed in 2006 by the GFZ Potsdam and the GRGS Toulouse, and that represents the

Table 51.1 Principal characteristics of the EGMs used in this investigation

Model	Year	Degree/order	Resol.
EGM96	1996	360	30′
EIGEN-CHAMP03S	2004	140	1°17′
EIGEN-CG03C	2005	360	30′
EIGEN-GL04C	2006	360	30′
EIGEN-GL04S1	2006	150	1°12′
ITG-GRACE03	2007	180	1°00′
EGM2008	2008	2190/2159	5′

satellite part of the EIGEN-GL04C. This model is the result of GRACE and LAGEOS data to degree and order 150. Also, the EIGEN-CHAMP03S (Gerlach et al., 2003; Reigber et al., 2005) was included in this study; it is complete to degree and order 140 and was developed in 2004 for the same centers previously mentioned. This last model was computed from satellite-only data of CHAMP mission.

Finally, the ITG-GRACE03S (Mayer-Guerr, 2007) was considered; it was computed in 2007 by the ITG (Institute of Theoretical Geodesy of Bonn) from GRACE satellite-only data and it is complete to degree and order 180 (Table 51.1).

The methodology applied in this work includes several stages: analysis and evaluation of the geopotential models, inclusion of geodetic data, and computing and analysis of the residuals.

In the first stage, after the study area was delimited, the geopotential models to be analyzed were chosen. In order to do this, the latest EGMs were selected taking into account several aspects, such as the diversity in the origin of the data of each model and the scientific centers that carry out their calculation. Furthermore, satellite-only models and EGMs obtained with data from others sources were included.

The geopotential models were downloaded from the ICGEM site (International Centre for Global Earth Models), that depends on the International Gravity Field Service of the International Association of Geodesy. For each model a $0.25° \times 0.25°$ grid was downloaded from the site to evaluate geoid undulations and gravity anomaly functions. The reference system used in all the calculations was the GRS80 that has similar parameters than the WGS84. Mean tide system was considered and zero and first degree terms have been assumed.

The next step was the collection, compilation and analysis of the available geodetic data of Argentina: 1,927 points having ellipsoidal and orthometric heights and 124,898 gravity station values (obtained from ground gravimetric campaigns) were used.

The comparison of the geopotential models was performed with two different set of points data: on one side, the EGMs' geoid undulations were compared with the 1,927 GPS/leveling points; and on the other side, the differences between the EGMs' gravity anomalies and the 124,898 gravity values were analyzed.

Then, the geoid undulation and gravity anomalies residuals were computed in the points of observation using Kriging interpolation method; and finally, the residual statistics were obtained.

51.5 Conclusions

It can be concluded from the analysis of gravity anomalies and undulation residuals, that the EGMs that present better results in Argentina are those calculated with terrestrial gravity data and satellite gravimetry data. A greater difference with the geopotential models arisen from satellite-only data is detected.

From the statistics of the gravity anomalies and geoid undulation residuals of the combined models, the best agreement was obtained with the EGM2008, in terms of average and standard deviations. Instead, the one showing the minimum mean and range was the EGM96. Analyzing the gravity anomaly maps, it can be said that the EGM2008, EGM96, EIGEN-GL04C and the EIGEN-CG03C show a similar distribution of the residuals. Also, most of the extreme residual values for all the EGMs could be seen in the northern part of the Andes Mountain Chain.

Comparing the satellite-only models statistics, the EIGEN-CHAMP03S is the one that shows the maximum mean and standard deviations. Furthermore, it could be seen in the gravity anomaly maps that the EIGEN-GL04S1 and the ITG-GRACE03 present a heterogeneous distribution with stripes along the North-East side of the country.

Finally, it can be concluded that the EGM2008 is the best model for Argentina in terms of statistics (Fig. 51.1 and Tables 51.2 and 51.3).

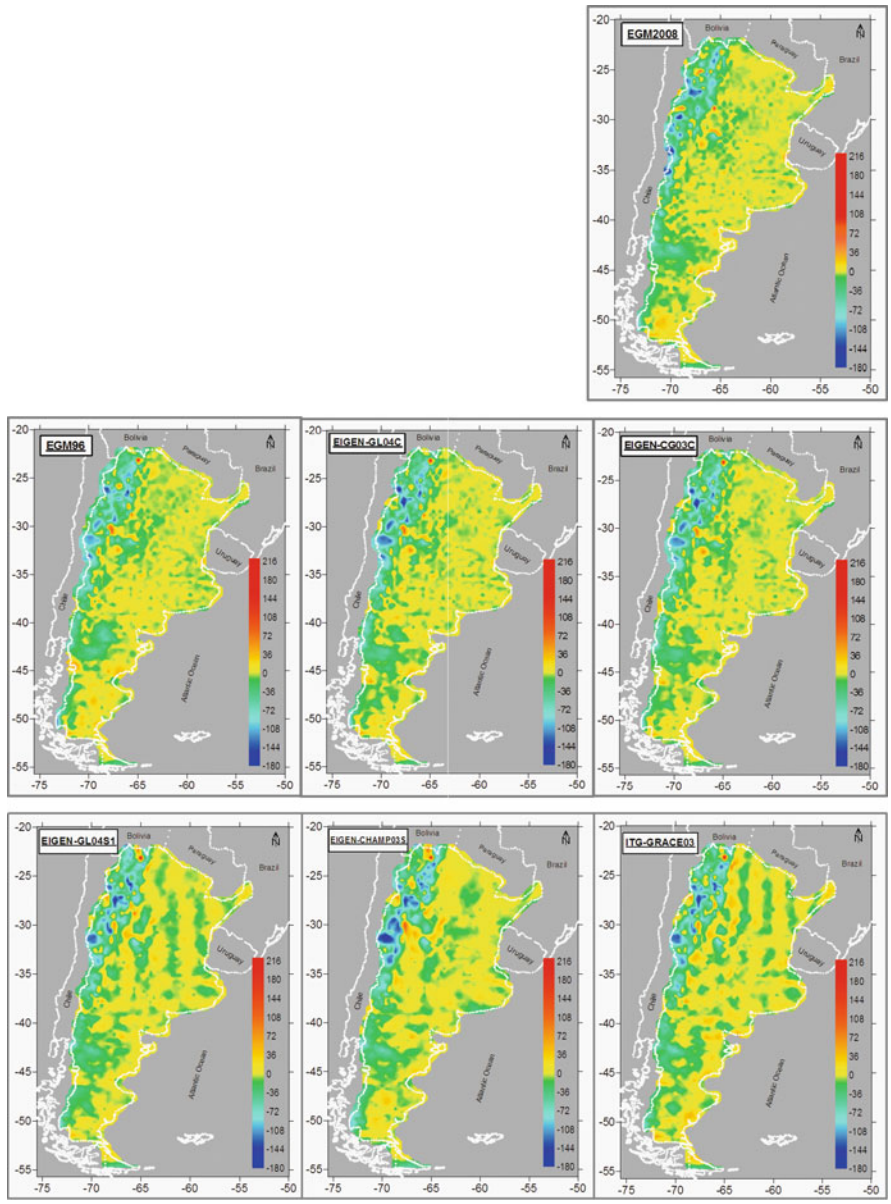


Fig. 51.1 Residual maps of gravity anomalies in Argentina (mgal) for each model (ground gravity anomalies vs. EGMs gravity anomalies)

Table 51.2 Undulation residuals statistics for each model in Argentina in meters (undulation from ellipsoidal and spirit leveling data vs. undulation from EGMs)

Model	Min	Max	Mean	σ
EGM2008	–2.287	3.004	–0.044	0.340
EGM96	–1.977	4.345	0.005	0.470
EIGEN-CG03C	–2.343	2.866	–0.132	0.402
EIGEN-GL04C	–2.153	2.766	–0.117	0.367
EIGEN-GL04S1	–5.092	4.805	–0.182	0.704
ITG-GRACE03	–4.622	4.170	–0.150	0.675
EIGEN-CHAMP03S	–5.625	2.923	–0.443	1.192

Table 51.3 Gravity anomaly residuals statistics for each model in Argentina in mgal (gravity anomaly from ground gravimetric campaigns vs. gravity anomaly from EGMs)

Model	Min	Max	Mean	σ
EGM2008	–227.662	195.688	–3.601	16.254
EGM96	–197.575	222.184	–3.288	19.606
EIGEN-CG03C	–216.267	220.303	–4.822	20.583
EIGEN-GL04C	–206.261	220.421	–4.167	20.689
EIGEN-GL04S1	–184.577	240.560	–7.946	27.245
ITG-GRACE03	–195.494	238.220	–5.830	27.569
EIGEN-CHAMP03S	–186.425	250.354	–9.059	28.734

Acknowledgements The authors want to express their acknowledgement to the institutions, universities and colleagues that provide data for this research, especially to: Agrim. Rubén Rodríguez, Ing. Geog. Eduardo Lauría (Instituto Geográfico Militar), Agrim. Daniel Luengo, Dr. Daniel Del Cogliano, Lic. Raúl Perdomo and Dra. Claudia Tocho (Fac. de Cs. Astronómicas y Geofísicas de la Universidad Nacional de La Plata).

This work was partially supported by the "Agencia Nacional de Promoción Científica y Técnica" (PICT 01590).

References

Balmino, G., C. Reigber, and B. Moynot (1976). A geopotential model determined from recent satellite observing campaigns (GRIM1). *Manuscripta Geodetica*, 1(1), 41–69.

Beutler, G. (2004). Revolution in geodesy and surveying. *FIG Article*, July 2004, p. 19.

Blitzkow, D. (1998). NASA (GSFC)/NIMA Model Evaluation. International Geoidal Service. *Bull. 6,*71–81.

Blitzkow, D. and A. De Matos (2009). EGM2008 and PGM2007A evaluation for South America, No. 4, Newton's Bulletin 79–89.

Buchar, E. (1958). Motion of the nodal line of the second Russian Earth satellite and flattening of the Earth. *Nature*, 182, 198–199.

Cordell, L., G.F. Keller, and T.G. Hildenbrand (1982). Bouguer gravity map of the Rio Grande Rift, Colorado, New Mexico and Texas. Map GP-949 USGS 1:1,000,000 series.

Förste, C., F. Flechtner, R. Schmidt, R. König, U. Meyer, R. Stubenvoll, M. Rothacher, F. Barthelmes, K.H. Neumayer, R. Biancale, S. Bruinsma, J.-M. Lemoine, and S. Loyer (2006). A mean global gravity field model from the combination of satellite mission and altimetry/gravimetry surface gravity data -EIGEN-GL04C. *Geophys Res Abstr*, 8, 03462.

Gentili C., H. Rimoldi, J. Di Gregorio, M. Ullana, E. González Díaz, F. Nullo, A. Riccordi, E. Rolleri, A. Russo, M. Fabres, H. Di Benedetto, P. Stepancic, E. Methol, R. Caminos, P. Leste, R. Perello, and W. Theabli (1980). Geología Regional Argentina. Vol I-II. Academia Nacional de Ciencias.

Gerlach, C., L. Földvary, D. Svehla, T. Gruber, M. Wermuth, N. Sneeuw, B. Frommknecht, H. Oberndorfer, T. Peters, M. Rothacher, R. Rummel, and P. Steigenberger (2003). A CHAMP-only gravity field model from kinematics orbits using the energy integral. *Geophys. Res. Lett.*, 30(20), 2037, doi: 10.1029/2003GL018025.

Heiskanen, W.A. and H. Moritz (1967). Physical Geodesy. W. H. Freeman and Co., San Francisco and London, p. 364.

Lemoine, F.G., S.C. Kenyon, J.K. Factor, R.G. Trimmer, N.K. Pavlis, D.S. Chinn, C.M. Cox, S.M. Klosko, S.B. Luthcke, M.H. Torrence, Y.M. Wang, R. Williamson, E.C. Pavlis, R.H. Rapp,. and T.R. Olson (1998). The Development of the Joint NASA GSFC and the National Imagery and Mapping Agency (NIMA) Geopotential Model EGM96. *Goddard Space Flight Center Report*.

Lerch, F.J., S.M. Klosko, R.E. Laubscher, and C.A. Wagner (1977). Gravity model improvement using GEOS-3 (GEM9 and GEM10). *Goddard Space Flight Center. Report* X-921-77-246. Greenbelt.

Lerch, F.J., B.H. Putney, C.A. Wagner, and S.M. Klosko (1981). Goddard earth model for oceanographic applications (GEM10B and GEM10C). *Mar Geod*, 5(2), 145–187.

Mayer-Guerr, T. (2007). ITG-Grace03s: The latest GRACE gravity field solution computed in Bonn. In: GSTM+SPP, 15–17 Oct 2007, Potsdam.

Nerem, R.S., F.J. Lerch, J.A. Marshall, E.C. Pavlis, B. Putney, B.D. Tapley, and R.J. Eanes (1994). Gravity model development for TOPEX/POSEIDON: Joint gravity models 1 and 2. *J. Geophys. Res*., 99 (C12), 24421–24447.

Pacino, M.C., E.A. Lauría, D. Blitzkow, and J.D. Fairhead (2007). New gravity anomaly maps for argentina: MAGARG2007 (in press).

Pavlis, N.K., S.A. Holmes, S.C. Kenyon, and J.K. Factor (2008). An Earth gravitational model to degree 2160: EGM2008. In: General Assembly of the European Geosciences Union, Vienna, Austria, April 13–18.

Rapp, R.H. (1989). Combination of satellite, altimetric and terrestrial gravity data in theory of satellite geodesy and gravity field determination. Lecture Notes in *Earth Sciences* No 25, Springer-Verlag.

Rapp, R.H. (1992). Computation and accuracy of global geoid undulation models. In: Proc. Of the Sixth International Geodetic Symposium of Satellite Positioning, DMA.

Reigber, C., G. Balmino, B. Moynot, and H. Mueller (1983). The GRIM3 Earth Gravity field model. *Manuscripta Geodaetica*, 8, 93–138.

Reigber, C., H. Jochmann, J. Wünsch, S. Petrovic, P. Schwintzer, F. Barthelmes, K.-H. Neumayer, R. König, Ch. Förste, G. Balmino, R. Biancale, J.-M. Lemoine, S. Loyer, and F. Perosanz (2005). Earth gravity field and seasonal variability from CHAMP. In: Reigber, Ch., H. Lühr, P. Schwintzer, and J. Wickert (eds.), 2004. Earth observation with CHAMP – Results from three years in orbit, Springer, Berlin, pp. 25–30.

Wahr, J., M. Molenaar, and F. Bryan (1998). Time-variability of the earth's gravity field: Hydrological and oceanic effects and their possible detection using GRACE. *J. Geophys. Res*., 103, 30205–30230.

Chapter 52

On the Determination of the Terrain Correction Using the Spherical Approach

G. Kloch and J. Krynski

Abstract In the classical approach of planar representation of the Bouguer plate the terrain correction including all its components is always positive and quickly converges with growing radius of integration of topography heights referred to the Bouguer plate. When, however, the Bouguer plate is considered spherical, some components of the terrain correction as well as the resultant terrain correction may become negative. The terrain correction determined using spherical approach does not exhibit the evidence of convergence in distant zones with growing radius of integration. It makes thus difficult to determine the limitation for the area of integration of topography to compute the terrain correction of the required accuracy.

The paper presents the results of research concerning the occurrence of negative components of the terrain correction and their contribution to the resultant terrain correction considering different range of roughness of topography. The convergence of the terrain correction with growing integration radius was investigated in both planar and spherical approach and the differences between the solutions obtained using those approaches were discussed. Special attention was paid to both analytical and empirical investigations of the convergence of the terrain correction when using spherical approach. Numerical tests were performed with the use of DTMs and of real data in a few test areas of Poland that are representative in terms of the variety of topography as well as with the use of simple artificial terrain models.

G. Kloch (✉)
Institute of Geodesy and Cartography, Warsaw, PL 02-679, Poland
e-mail: grazyna.kloch@igik.edu.pl

52.1 Introduction

One of the components of gravity anomalies that are appropriate for modelling precise geoid with the use of Stokes formula is the terrain correction c that represents the deviation of the actual topography from the Bouguer plate of a gravity station P in terms of gravitational attraction (Heiskanen and Moritz, 1967). Computation of terrain corrections is one of the most laborious tasks in precise geoid modelling. It requires the knowledge of the height H of a gravity station P above the geoid, the characteristics of heights of the terrain within a certain radius from P as well as the density ρ of the upper crust of the Earth. Particularly important is a very good knowledge of topography around the gravity station P (Sideris, 1984).

The extensive research on methodology of terrain corrections computation was conducted in the framework of the project on modelling centimetre geoid in Poland in 2002–2005 led by the Institute of Geodesy and Cartography, Warsaw, (Krynski and Lyszkowicz, 2006; Krynski, 2007). Most of numerical experiments with computing the terrain corrections were performed using the classical rectangular prism method. The results obtained illustrated the relation between the mean dispersion of heights $\Delta H = 50$ m in the area of integration, the radius d of integration of prisms and a required accuracy of the solution (Grzyb et al., 2006). They were referred to the case when the Bouguer plate is considered planar. The developed strategy for computing terrain corrections was used for the determination of terrain corrections at all 1 078 046 gravity stations from the gravity database in Poland.

Both theoretical as well as practical aspects of the determination of terrain corrections as well as their

S.P. Mertikas (ed.), *Gravity, Geoid and Earth Observation*, International Association of Geodesy Symposia 135,
DOI 10.1007/978-3-642-10634-7_52, © Springer-Verlag Berlin Heidelberg 2010

accuracy estimate are quite complex. Parameterisation of the terrain correction computing algorithm depends on the accuracy requirements, computational strategy used, data available and designation of terrain corrections, e.g. geoid modelling or geophysical prospecting. In particular, the choice between planar and spherical approach must be taken. Growing requirements concerning the precision of terrain correction, accessibility to DTMs of higher resolution and accuracy as well as possibility of enlarging the area of integration of prisms indicate the need for optimising the strategy of determination of terrain corrections but also address new problems that must be solved, e.g. negative components of the terrain correction, convergence of the process of terrain correction determination with growing radius of area of integration, effect of numerical errors with growing DTM's resolution, etc. The paper discusses the complexity of problems related to the use of spherical approach of the terrain correction computation.

52.2 Problem of Negative Terrain Correction in Spherical Approach

In the classical planar approach (Fig. 52.1a) all components of the terrain correction are always positive (Heiskanen and Moritz, 1967). Both deficiency and surplus of mass with respect to the Bouguer plate generate in that case negative gravitational effect that is balanced by a positive terrain correction. When, however, the Bouguer plate is considered spherical, the components of the terrain correction become both positive and negative (Fig. 52.1b). Masses above spherical Bouguer plate that are below the top of planar Bouguer plate generate, however, negative contribution to the terrain correction.

Using local Cartesian coordinate system of the origin $P_m(x_m, y_m, z_m)$, the relation between the component of the terrain correction generated by a single prism of the size dx, dy, dz situated in distance d from P_m, calculated using planar (Δc_{pl}) and spherical (Δc_{sp}) approach is as follows

$$\Delta c_{sp} = \Delta c_{pl}\left(1 - \frac{d^2}{dz \cdot R_E}\right) \tag{1}$$

where R_E is the mean radius of the Earth. Since Δc_{pl} is always positive, the component Δc_{sp} of the terrain correction will become negative when

$$d > \sqrt{dz \cdot R_E} \tag{2}$$

Zones of positive and negative components of the terrain correction from a single prism of height dz situated in a distance d from the computational point are shown in Fig. 52.2.

In contrast to planar approach when equivalent surplus and deficiency of masses with respect to the Bouguer plate generate identical terrain correction, in spherical approach their contributions in total terrain correction differ.

The behaviour of the component of the terrain correction Δc caused by a single prism of 3" × 3" and different height H, distant from the computation point by 100–300 km is illustrated in Fig. 52.3.

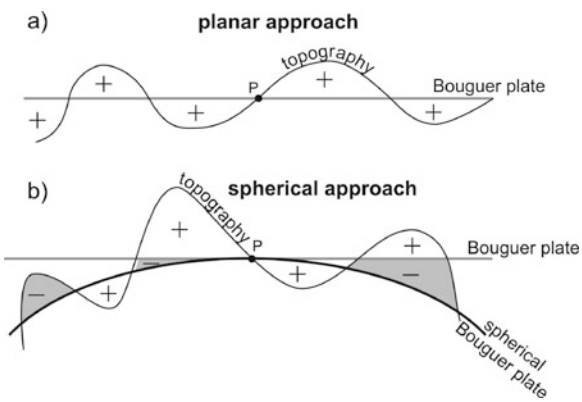


Fig. 52.1 Illustration of positive and negative contribution of topographic masses to the terrain correction

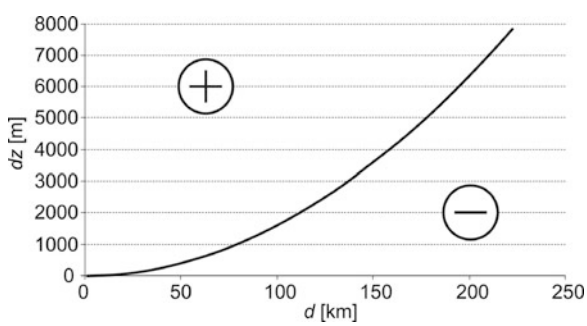


Fig. 52.2 Zones of positive and negative components of the terrain correction from a single prism of height dz situated in a distance d

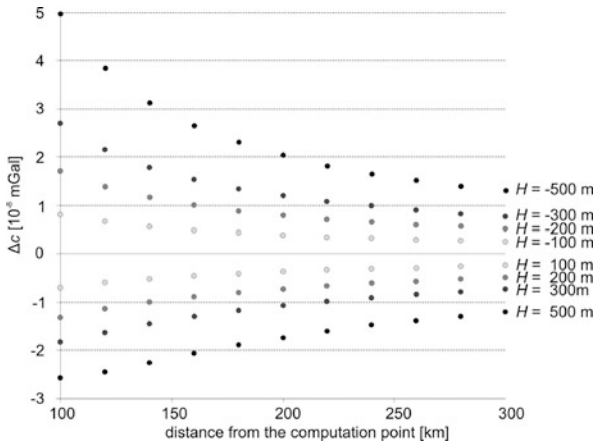


Fig. 52.3 The component of the terrain correction caused by a single prism of 3" × 3" of the height H, distant from the computation point by 100–300 km

The effect of the terrain correction due to distant zones may thus practically cancel when both surplus and deficiency of mass takes place there. When, however, a significant majority of the components of the terrain correction due to distant zones are of the same sign the effect of those zones will not be negligible.

Five test areas (Table 52.1) of different roughness of topography and different locations in Poland were selected for numerical experiments.

Components of terrain corrections corresponding to the attraction of topography of concentric rings of the widths of 10 km each, were calculated for all points of each test area (Table 52.1) using both planar and spherical approach.

First the components of terrain corrections were analysed in terms of the occurrence of negative components and statistics for each zone and for the entire terrain correction.

In test area 2 of lowest mean elevation and smallest roughness negative components of terrain correction occur already due to the attraction of the ring of 10–20 km radii. The mean terrain correction in that test area becomes negative starting from the ring of 40–50 km radii. Test area 2 is the only one out of 5 test areas investigated in which the mean total terrain correction computed within the radius of 200 km from the gravity point is negative.

In test areas 3 and 4 of medium mean elevation and medium roughness negative components of terrain correction occur starting from the ring of 30–40 km radii while in test area 5 of the largest mean elevation and largest roughness – from the ring of 50–60 km.

In test area 1 no negative components of terrain correction occur. Total terrain correction computed within the radius of 200 km from the gravity point is always positive in test areas 1 and 5. It should be noted that the terrain of test area 1 is clearly convex with respect to the topography of distant zones.

Further analysis concerned the discrepancy between terrain correction computed using spherical and planar approach. Statistics of the differences between terrain corrections computed within the radius of 200 km with the use of spherical and planar approach at gravity points of 5 test areas are given in Table 52.2.

Maximum difference between the solutions in the test area 5 equals to 1.4 mgal. Typical difference, however, that is represented by the standard deviation is in that area at the level of 0.3 mgal. Terrain corrections obtained using spherical approach are statistically larger than the respective ones obtained using planar approach. Difference between spherical and planar

Table 52.1 Statistics of heights H of gravity points in test areas [m]

Test area	No of points	Min	Max	Mean	Std dev.
1	2,107	112.91	307.04	195.75	27.53
2	6,055	29.96	173.19	73.49	17.51
3	14,622	240.00	490.99	345.93	50.86
4	9,374	130.00	938.87	274.66	118.70
5	15,591	204.95	1296.03	502.09	191.98

Table 52.2 Statistics of the differences between terrain corrections computed within the radius of 200 km with the use of spherical and planar approach [mgal]

Test area	Min	Max	Mean	Std dev.
1	0.076	0.398	0.213	0.045
2	−0.091	0.146	−0.029	0.026
3	−0.149	0.270	0.041	0.076
4	−0.193	1.106	−0.019	0.175
5	−0.288	1.458	0.141	0.301

solutions of terrain corrections grows with increasing terrain correction obtained using planar approach.

52.3 Convergence of the Terrain Correction with Growing Distance from the Computation Point

When computing terrain corrections their convergence with growing distance from the computation point must be clear and the maximum distance of integration must be determined. Analyses of terrain corrections calculated using planar approach indicated that they converge much faster in flat than in hilly areas and that the maximum radius of integration depends on required accuracy (Grzyb et al., 2006). Moreover, independently on the elevation of the gravity point and topography the terrain correction computed using planar approach converges to zero with growing distance from that point.

An idea on the convergence of the terrain correction with growing distance d from the gravity point, computed using spherical approach, can be given by analysing the attraction of a single prism ($dx = dy =$ 30 m, $dz = -1$ m) of a constant density $\rho = 2.67$ g/cm^3.

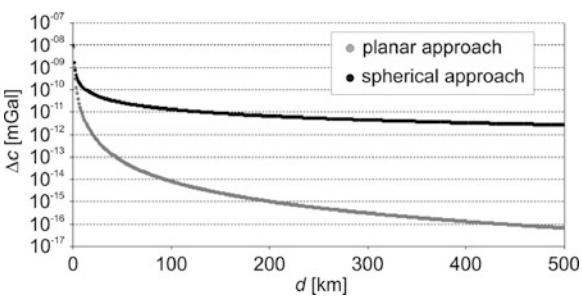


Fig. 52.4 Dependence of the component of the terrain correction from a single prism of 30 × 30 × −1 m on the distance d from the computation point

The results obtained using both planar and spherical approach of the terrain correction are shown in Fig. 52.4.

Figure 52.5 shows that starting from the distance of 50 km the components of the terrain correction calculated using spherical approach become of 3–4 orders of magnitude larger than the respective ones obtained when neglecting the spherical shape of the Earth. In planar approach of terrain correction computation the extension of distance from 100 to 200 km results in decrease of the attraction of a single prism by an order of magnitude. In spherical approach such a decrease takes place only when extending the distance from 100 to 500 km. Thus taking into account the spherical shape of the Earth when computing the terrain correction substantially slows down its convergence with growing distance from the computation point.

Two simple terrain models (Fig. 52.5) of equal surplus and deficiency of mass with respect to the Bouguer plate were used for further investigation of the convergence of the process of terrain correction determination using spherical approach.

The components $\Delta c_{20i,20(i+1)}$ ($i = 1, 2, \ldots, 14$) of the terrain correction corresponding to the attraction of topography of sectors of 20 km widths from 20 up to 300 km were calculated for both models with the use of both planar and spherical approach. The results obtained are shown in Fig. 52.6.

As expected, both terrain models provide identical terrain corrections when using planar approach. In that case the terrain correction converges to zero with growing radius of integration and the maximum radius of integration can be determined (lowest graph of Fig. 52.6). This is, however, not the case when spherical approach is applied. Starting from certain radius that depends on the height H of the terrain model the components $\Delta c_{20i,20(i+1)}$ are proportional to H and for each height H they practically do not decrease with growing distance from the computation point (two upper graphs of Fig. 52.6). It seems that for large radii

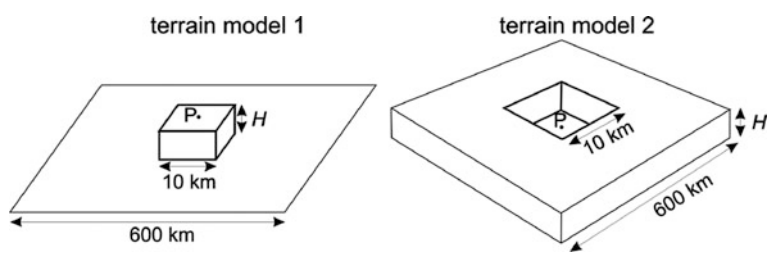


Fig. 52.5 Simple terrain models

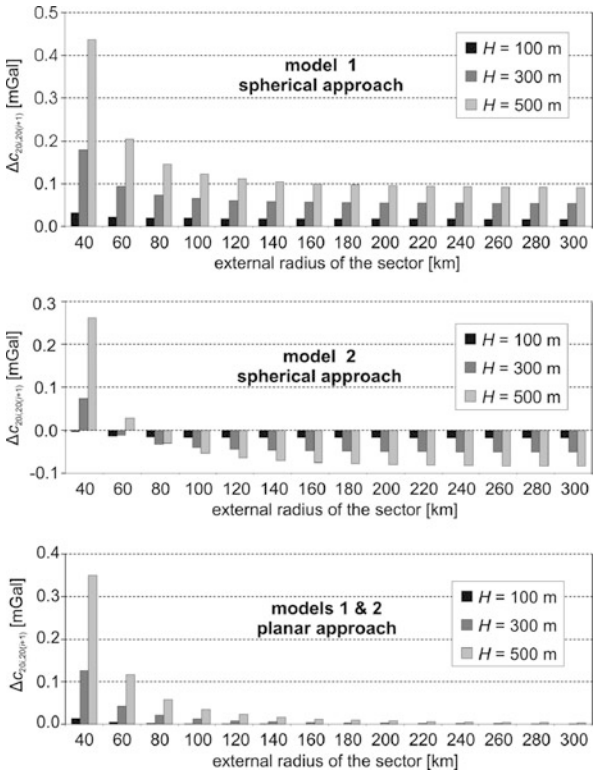


Fig. 52.6 Components $\Delta c_{20i,20(i+1)}$ ($i = 1, 2, \ldots, 14$) of the terrain correction calculated for both models with the use of both planar and spherical approach

of integration the summed up consecutive components $\Delta c_{20i,20(i+1)}$ may apparently result in a very large total terrain correction.

The effect of distant zones on the terrain correction computed applying spherical approach was also investigated applying analytical formulae that can easily be derived using Fig. 52.7.

When mass element dm is on the height h above the surface spherical Earth the vertical component of its attraction on point P can be calculated as

$$dg = G\frac{\sin\beta}{r^2}dm \tag{3}$$

The attraction of a spherical ring can be calculated as

$$dg = 2\Pi G\rho R^2\overline{h}\,(\cos\psi_2 - \cos\psi_1)\,\overline{E} \tag{4}$$

where

G – gravitational constant,
ρ – crustal density,

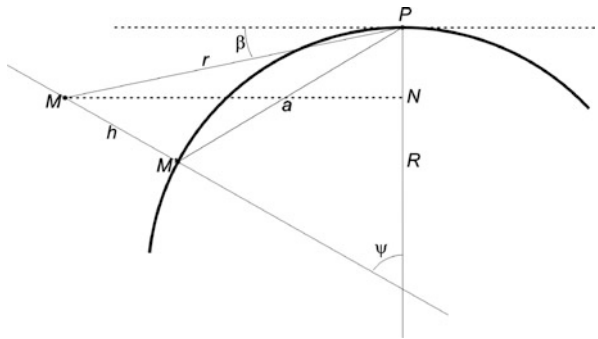


Fig. 52.7 Concept of calculating a distant zone component of the terrain correction considering spherical shape of the Earth

R – mean radius of the Earth,
$\overline{h}$ – mean height in the ring,
ψ_1, ψ_2 – spherical angles of the ring,
$\overline{E}$ – mean value of the function $E(\overline{h}, \psi_1, \psi_2)$

$$E\,(h,\psi) = \frac{\frac{a^2}{2R-h\cos\psi}}{\left[a^2+h^2+2ah\sin\left(\frac{\psi}{2}\right)\right]^{3/2}} \tag{5}$$

The attraction of spherical rings of 1° width and mass deficiency of 100 m height (Fig. 52.8) converges to zero when the spherical distance of the attracting ring reaches 180°. That convergence is practically not noticeable for spherical distance shorter than 1,500 km. Total terrain correction corresponding to a sum of components shown in Fig. 52.8 equals 11.079 mgal. With the use of the same model for 1,000 m height of mass deficiency total terrain correction would reach over 110 mgal. It corresponds to the results of far-zone terrain correction investigation

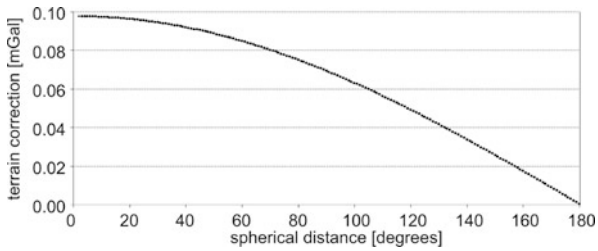


Fig. 52.8 Components of the terrain correction due to the attraction of spherical rings of 1° width and of 100 m mass deficiency, calculated using spherical approach

taking into account spherical shape of the Earth (Novak et al., 2001).

Convergence of the terrain correction with growing distance from the gravity point, computed using spherical approach was further investigated using real topography. Planar and spherical solutions for terrain corrections were investigated and mutually compared on the test profile along 49.55º parallel between the meridians 20ºE–21ºE, situated in most rough terrain in Poland (Fig. 52.9).

Both types of terrain corrections were calculated using DTED2 within 22.5 km radius and SRTM in the outer zone, up to 100, 200 and 600 km. The extension of the integration radius from 200 to 600 km results in increase of terrain corrections calculated using spherical approach up to 3.5 mgal at the elevation 1,200 m (Fig. 52.10) while it is negligibly small when using planar approach.

The increase of terrain correction $\Delta c_{R_{\max}-R_{100}}$ calculated using spherical approach due to the extension of the maximum radius of integration $R_{\max}$ from 100 km is strongly correlated with height H of the gravity station. For the gravity station of height H in the profile investigated the increase of terrain correction calculated using spherical approach due to the extension of the maximum radius of integration $R_{\max}$ from 100 is practically linear

$$\Delta c_{R_{\max}-R_{100}} = -0.126897 - 0.002578(R_{\max} - R_{100}) + \left[0.000235 + 9.13 \times 10^{-6}(R_{\max} - R_{100})\right] H \tag{6}$$

The results of the analysis of the behaviour of the components of terrain corrections due to the attraction of topography in zones from 100 to 600 km in the profile investigated fully correspond to those obtained with the use of artificial models.

The results of numerical tests performed show that starting from certain radius of integration the components of the terrain correction practically do not decrease with growing distance from the computation point. When using spherical approach there is no optimum radius of integration beyond which the components of terrain corrections due to the attraction of topography can be considered negligibly small.

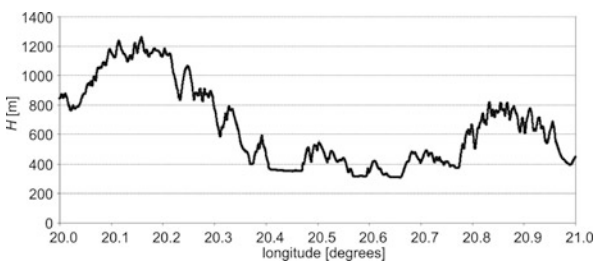


Fig. 52.9 Heights along the test profile

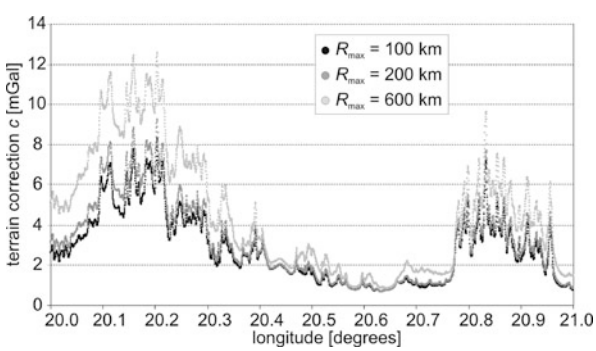


Fig. 52.10 Spherical solutions for terrain corrections along the test profile obtained using different maximum radii of integration

52.4 Conclusions

The use of spherical approach instead of planar approach provides new quality of terrain corrections. The main novelty concern the occurrence of negative terrain corrections as well as much slower convergence of terrain corrections with growing distance from the computation point. When using spherical approach there is no optimum radius of integration beyond which the components of terrain corrections due to the attraction of topography can be considered negligibly small.

Although spherical approach of the determination of terrain corrections certainly seems more adequate then the planar one its use requires carefulness. The terrain correction due to the attraction of far-zone calculated taking into account spherical shape of the Earth may become quite large; even they may exceed the maximum free-air anomaly.

Numerical tests conducted using real topography indicated that terrain corrections calculated within the radius of 200 km with the use of planar and spherical approach are practically equivalent in terms of their use for modelling geoid with centimetre accuracy.

If, one considered the differences between the planar and spherical approach solutions as the measure of uncertainty of terrain corrections calculated, such

uncertainty would be quite acceptable. Errors in the position of gravity station as well as errors of the DTM in the mountains can easily result in Poland in an error of calculated terrain correction at the level of a few mgal.

Acknowledgement The work was supported by the Polish Ministry of Education grant No N526 006 32/1079.

References

Grzyb M., J. Krynski, and M. Mank (2006). The effect of topography and quality of a digital terrain model on the accuracy of terrain corrections for centimetre quasigeoid modelling. *Geod Cartogr*, 55(1), 23–46.

Heiskanen W.A. and H. Moritz (1967). Physical Geodesy. W.H. Freeman & Co., San Francisco.

Krynski J. (2007). Precise quasigeoid modelling in Poland – results and accuracy estimation (in Polish), Monographic series of the Institute of Geodesy and Cartography, Warsaw, Nr 13 (p. 266).

Krynski J. and A. Lyszkowicz (2006). Centimetre quasigeoid modelling in Poland using heterogeneous data, IAG Proceedings of the 1st International Symposium of the International Gravity Field Service (IGFS) "Gravity Field of the Earth", 28 August – 1 September 2006, Istanbul, Turkey, pp. 37–42.

Novak P., P. Vaníček, Z. Martinec, and M. Véronneau (2001). Effects of the spherical terrain on gravity and the geoid. *J. Geod.,* 75, 491–504.

Sideris M.G. (1984). Computation of Gravimetric Terrain Corrections Using Fast Fourier Transform Techniques, UCSE Reports, No 20007, The University of Calgary, Division of Surveying Engineering (p. 114).

Chapter 53

Smoothing Effect of the Topographical Correction on Various Types of the Gravity Anomalies

Z. Hamayun, R. Tenzer, and I. Prutkin

Abstract We investigate the smoothing effect of the topographical correction applied to various types of the gravity anomalies commonly used in gravimetric geoid modelling. In particular, we compare the correlation of gravity anomalies with respect to the elevation of observation points, and the contribution of the local and regional topography on the roughness of gravity anomalies. The numerical experiment is conducted using the observed free-air gravity anomalies over the regional area of study which comprises a rough part of the American Rocky Mountains. The comparison is done for various types of the Bouguer gravity anomalies and the no-topography gravity anomalies. Results reveal that the smoothing effect of the topographical corrections on the high-frequency signal of gravity anomalies is very similar, despite the magnitudes of the topographical corrections vary significantly.

53.1 Introduction

Various types of the Bouguer gravity anomalies have been used in gravimetric interpretations. Traditionally, the Bouguer gravity anomaly is computed so that the topography-generated gravitation attraction (i.e. the direct topographical effect) is subtracted from the free-air gravity anomaly. In Vaníček et al. (2004), the new concept for a definition of the gravity anomalies harmonic above the geoid was formulated. According to this concept, the no-topography gravity anomaly is introduced, provided that the complete effect of the topography on the gravity anomalies comprises not only the direct topographical effect but also the secondary indirect topographical effect (i.e. the topography-generated gravitational potential multiplied by $2r^{-1}$; where r is the geocentric radius of the observation point). The application of topographic corrections to gravity anomalies and gravity disturbances, and their use in formulating and solving the gravimetric inverse problem were further analyzed by Vajda et al. (2007). They showed that the gravity anomaly, whose definition is based on the disturbing potential by means of the fundamental gravimetric equation, rather than by the vertical derivative of the disturbing potential, differs from the gravity disturbance, which also has implications to the application of the topographic correction. As a consequence, the application of the topographic correction to the gravity anomaly gives origin to the secondary indirect topographic effect. In this study, we compare the no-topography gravity anomalies with various types of the Bouguer gravity anomalies and investigate the smoothing effect of the terrain corrections applied to the gravity anomalies.

53.2 Numerical Experiment

The numerical realization is done over the regional area of study bounded by the parallels of 36 and 44 arc-degree northern geodetic latitudes, and the meridians of 251 and 259 arc-degree eastern geodetic longitudes. This area comprises the rough part of the American Rocky Mountains and surrounding

Z. Hamayun (✉)
Delft Institute of Earth Observation and Space Systems (DEOS), Delft University of Technology, Delft HS 2629, The Netherlands

S.P. Mertikas (ed.), *Gravity, Geoid and Earth Observation*, International Association of Geodesy Symposia 135,
DOI 10.1007/978-3-642-10634-7_53, © Springer-Verlag Berlin Heidelberg 2010

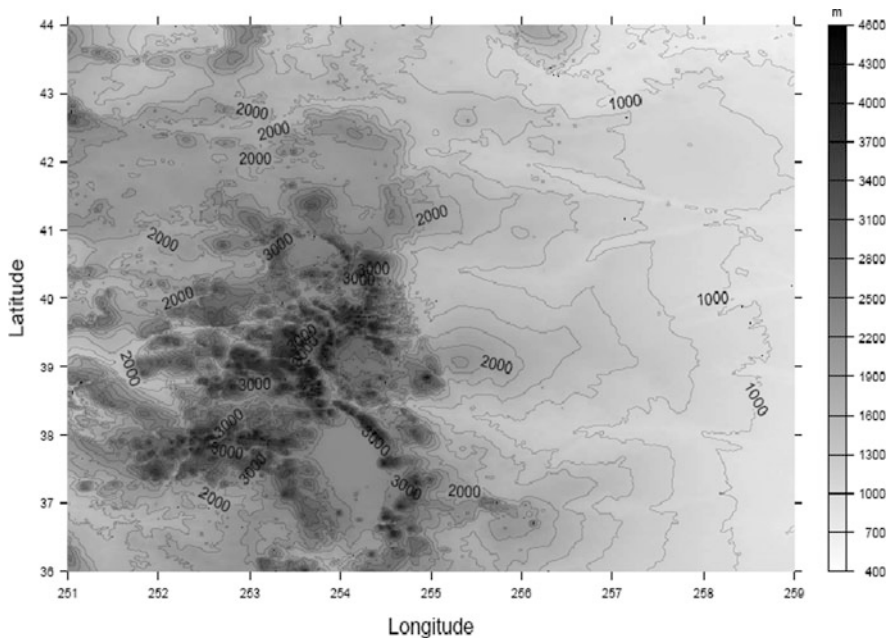


Fig. 53.1 Topography over the regional study area

flat regions (Fig. 53.1). The orthometric heights range from 409 to 4,392 m.

For modelling the gravitational field generated by the topography, the mean value 2,670 kg m^{-3} of the topographical mass-density distribution was adopted. Three different resolutions of the DTM were used, subdividing the surface integration domain into the near zone, the middle zone, and the far zone. For the near zone of the size 2 × 2 arc-degree and centred at the observation point, we used the detailed 30 × 30 arc-sec digital terrain model GTOPO30 developed by the US Geological Survey. The averaged heights for the geographical grid cells of 5 × 5 arc-min were used over the middle zone (of the size 6 × 6 arc-degree), and complemented over the far-zone by the global elevation model with the 1 × 1 arc-degree spatial resolution. The semi-analytical linear vertical mass approach was used for the integration, utilizing the Newton-Cotes numerical integration for the surface component of Newton's integral, while the vertical component was defined analytically according to Gradshteyn and Ryzhik (1980), see also Martinec (1998). To reduce the numerical inaccuracy of the semi-analytical integration approach, the rectangular prism approach (see Nagy et al., 2000) was used for the analytical integration at the vicinity of the observation point (i.e. over the inner zone of the size 4.5 × 4.5 arc-min and centred at the observation point).

The numerical results of the complete topographical effect and its components (i.e. the direct and secondary indirect topographical effects) within the regional area of study are shown through Figs. 53.2, 53.3 and 53.4, and statistics summarized in Table 53.1. The computation was realized for the points at the Earth's surface. The strong correlation of the direct topographical effect with the local topography is evident from Fig. 53.2. On the other hand, the secondary indirect topographical effect is mostly correlated with the regional topography. The magnitude of a high-frequency signal of the direct topographical effect reaches several hundred miligals, whereas the magnitude of a high-frequency signal of the secondary indirect topographical effect is less than a few miligals (cf. Fig. 53.3). Comparing with the direct topographical effect, the complete topographical effect over the flat regions is smaller, while a presence of the high-frequency signal remains almost unchanged in mountainous regions (cf. Fig. 53.4). The secondary indirect effect thus partly reduces the long-wavelength contribution when combined with the direct topographical effect.

The correlation between the elevation of observation points and the components of the complete topographical effect at the Earth's surface is demonstrated in Fig. 53.5. The magnitude of the direct topographical effect varies with the elevation of observation

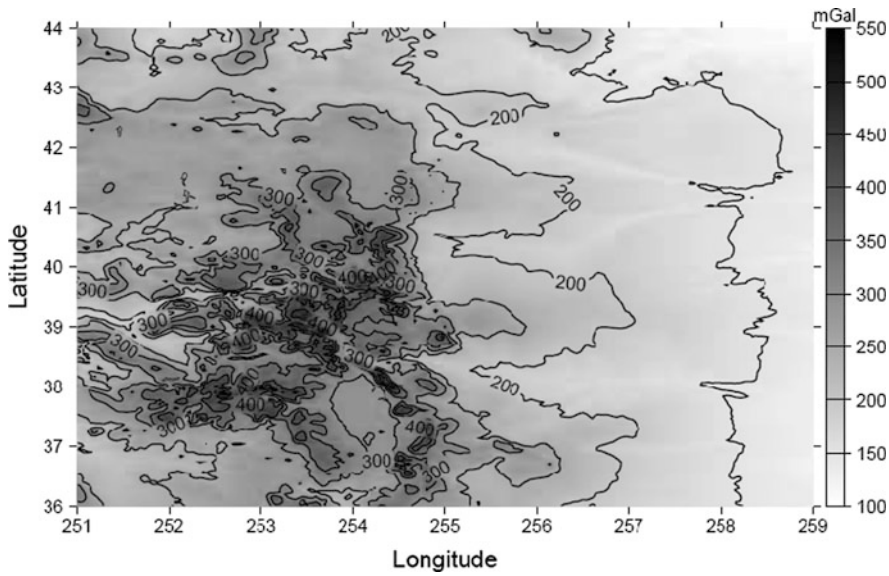


Fig. 53.2 The direct topographical effect computed at the Earth's surface

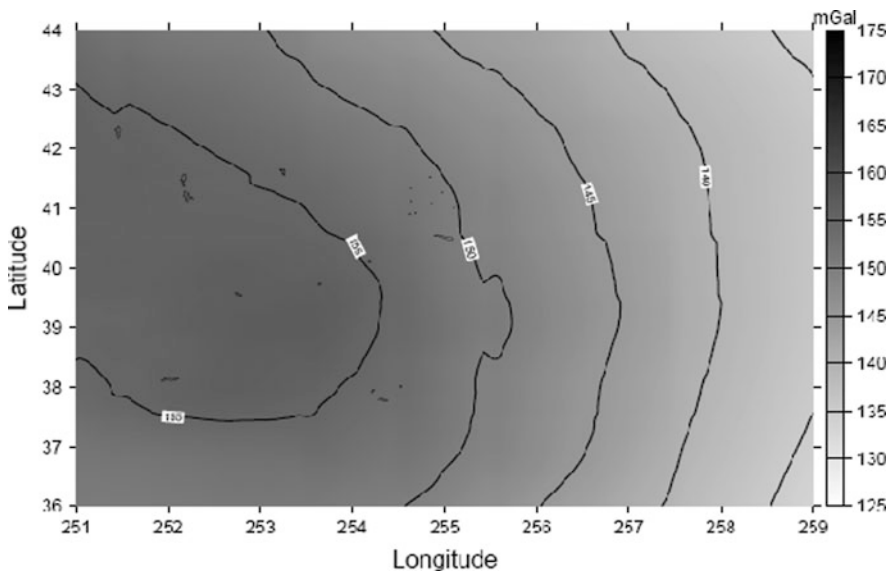


Fig. 53.3 The secondary indirect topographical effect computed at the Earth's surface

points , and this variation has almost a linear trend. Moreover, the dispersion of the direct topographical effect due to a contribution of the local topography increases with the elevation of computation points (cf. Fig. 53.5a). After removing the linear variation of the direct topographical effect with the elevation, the standard deviation of residual values reaches about 20 mgal for the elevations larger than 4,000 m, while it is smaller than 4 mgal at the elevations bellow 1,100 m. The variation of the secondary indirect topographical effect with the elevation of observation points is very small, due to the fact that this effect is mostly correlated with a contribution from the regional topography. In our numerical example, the standard deviation of the secondary indirect topographical effect is 6.6 mgal, and the largest dispersions are presented within the elevations from 1,300 to 2,100 m (cf. Fig. 53.5b).

Various types of the Bouguer gravity anomalies were computed over the regional area of study and compared with the no-topography gravity anomalies. The results are shown through Figs. 53.6, 53.7,

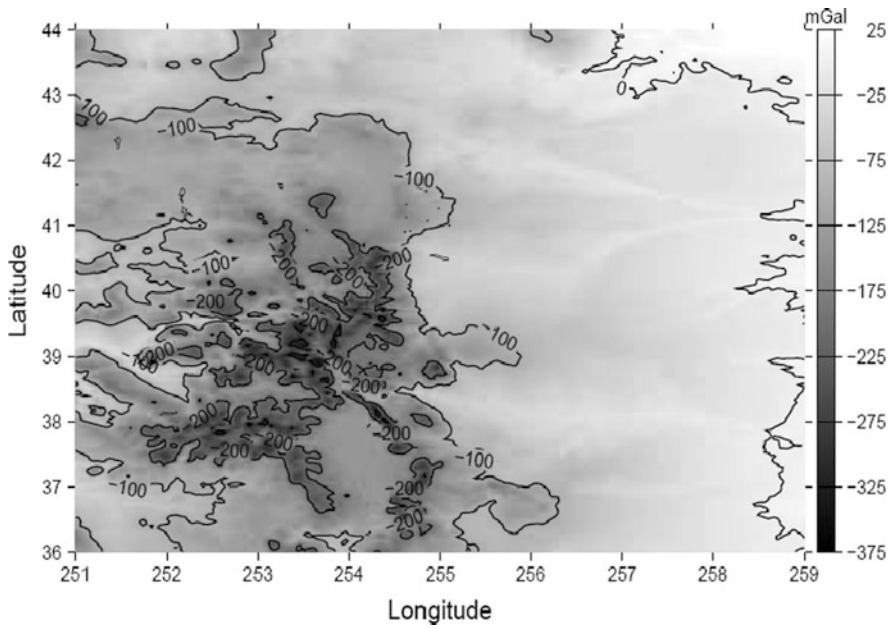
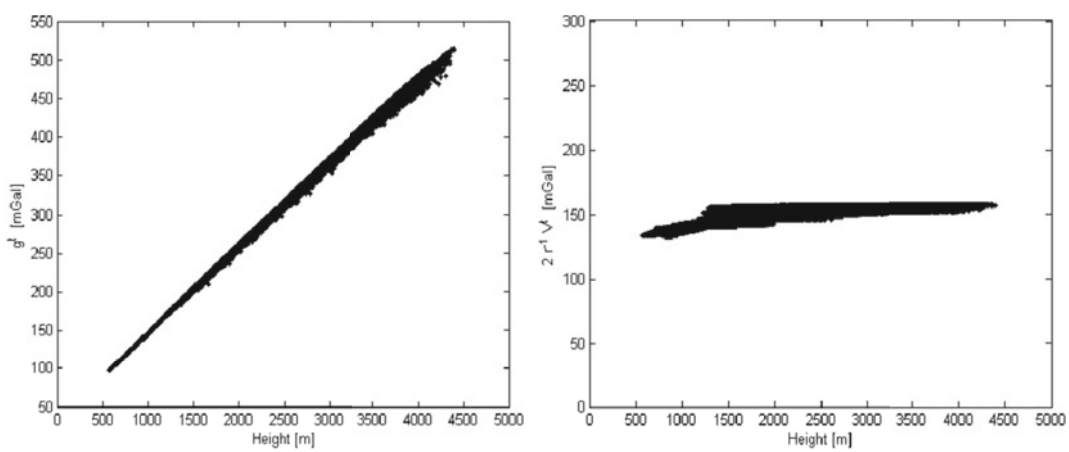


Fig. 53.4 Negative of the complete topographical effect computed at the Earth's surface

Table 53.1 Statistics of the complete topographical effect and its components

Topographical effect	Min [mgal]	Max [mgal]	Mean [mgal]	STD [mgal]
Direct	97.1	514.4	233.3	71.8
Secondary indirect	133.3	157.6	148.3	6.6
Complete	37.0	375.7	85.0	66.3



a b

Fig. 53.5 The correlation between the elevation of observation points and the components of the complete topographical effect: (**a**) the direct topographical effect, (**b**) the secondary indirect topographical effect

53.8, 53.9 and 53.10, and statistics summarized in Table 53.2. The simple planar Bouguer gravity anomalies (see Fig. 53.7) were obtained from the observed free-air gravity anomalies (Fig. 53.6) after subtracting the gravitational attraction generated by the Bouguer plate. The complete planar Bouguer gravity anomalies (see Fig. 53.8) were obtained from the simple planar Bouguer gravity anomalies after

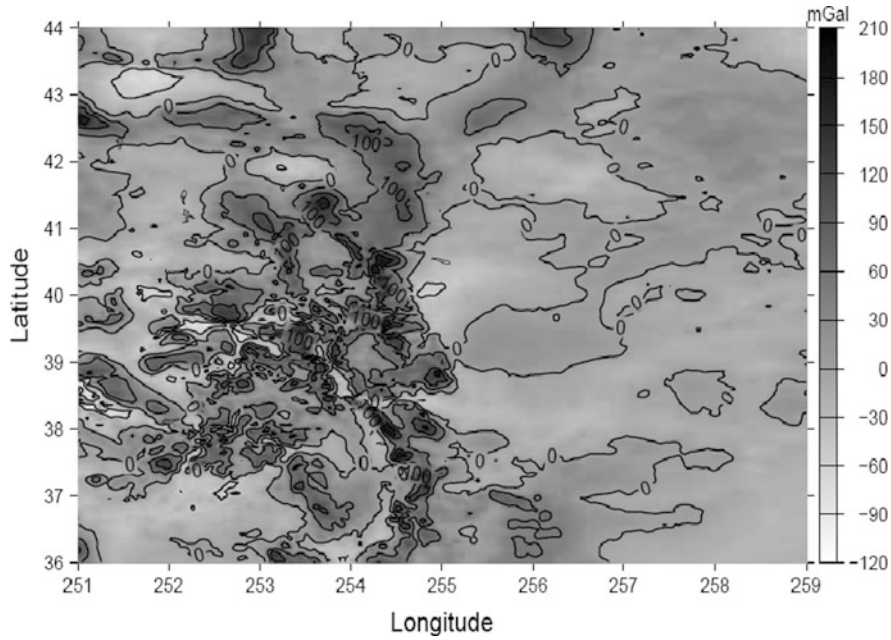


Fig. 53.6 The free-air gravity anomalies observed at the Earth's surface

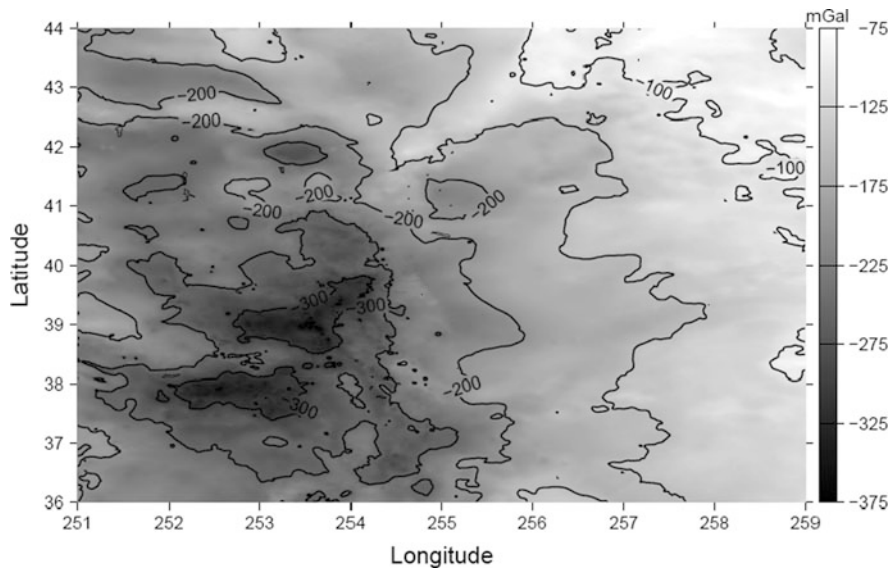


Fig. 53.7 The simple planar Bouguer gravity anomalies computed at the Earth's surface

applying the planar terrain correction. Note that within the regional area of study, the planar terrain correction varies from 0.0 to 38.5 mgal (the mean value is 0.9 mgal, and the standard deviation 1.6 mgal). The complete spherical Bouguer gravity anomalies (see Fig. 53.9) and the no-topography gravity anomalies (see Fig. 53.10) were obtained from the observed free-air gravity anomalies after adding the direct topographical effect and the complete topographical effect respectively.

The differences between the no-topography gravity anomalies and the complete spherical Bouguer gravity anomalies are given by the secondary indirect topographical effect. These differences thus range from

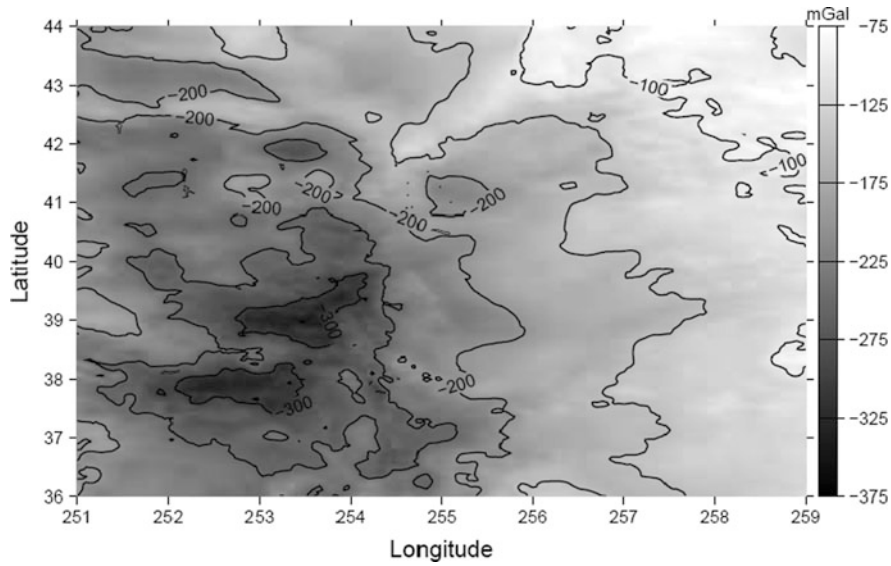


Fig. 53.8 The complete planar Bouguer gravity anomalies computed at the Earth's surface

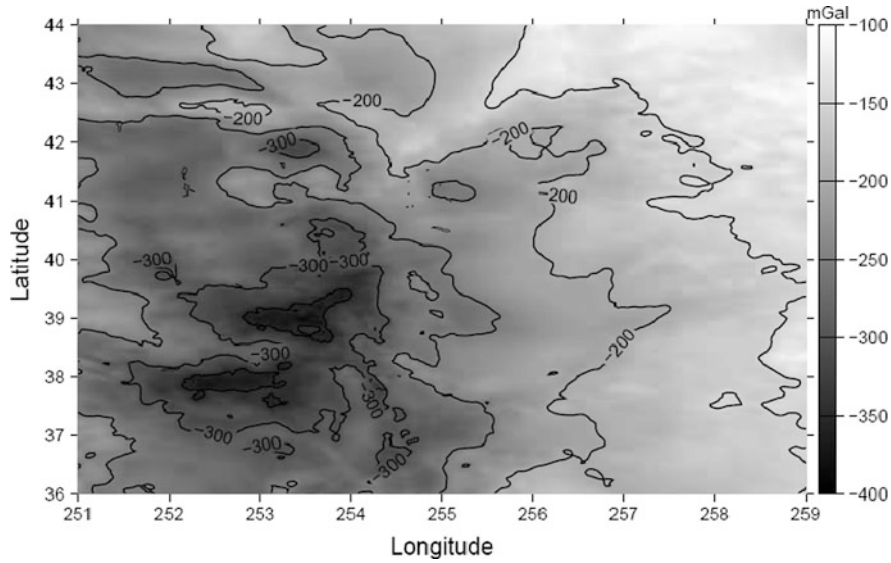


Fig. 53.9 The complete spherical Bouguer gravity anomalies computed at the Earth's surface

133.3 to 157.6 mgal (the mean value is 148.3 mgal, and the standard deviation 6.6 mgal). In addition, we compared the no-topography gravity anomalies with the planar simple and complete Bouguer gravity anomalies. Results are shown in Figs. 53.11 and 53.12. The differences between the no-topography gravity anomalies and the simple planar Bouguer gravity anomalies range from 100.2 to 158.3 mgal (the mean value 112.4 mgal, and the standard deviation is 6.0 mgal). The differences between the no-topography gravity anomalies and the complete planar Bouguer gravity anomalies are smaller and range from 100.2 to 121.9 mgal (the mean value is 111.8 mgal, and the standard deviation 5.2 mgal). In both cases, the main contribution to the differences is again due to the secondary indirect topographical effect.

The correlation between the gravity anomalies and the elevation of computation points is investigated in Fig. 53.13. The free-air gravity anomalies increase with the elevation (cf. Fig. 53.13a). As seen from Fig. 53.13b–e, the Bouguer gravity anomalies as well as the no-topography gravity anomalies decrease (due to the absence of the topographical masses and the possible presence of the isostatic compensation). The

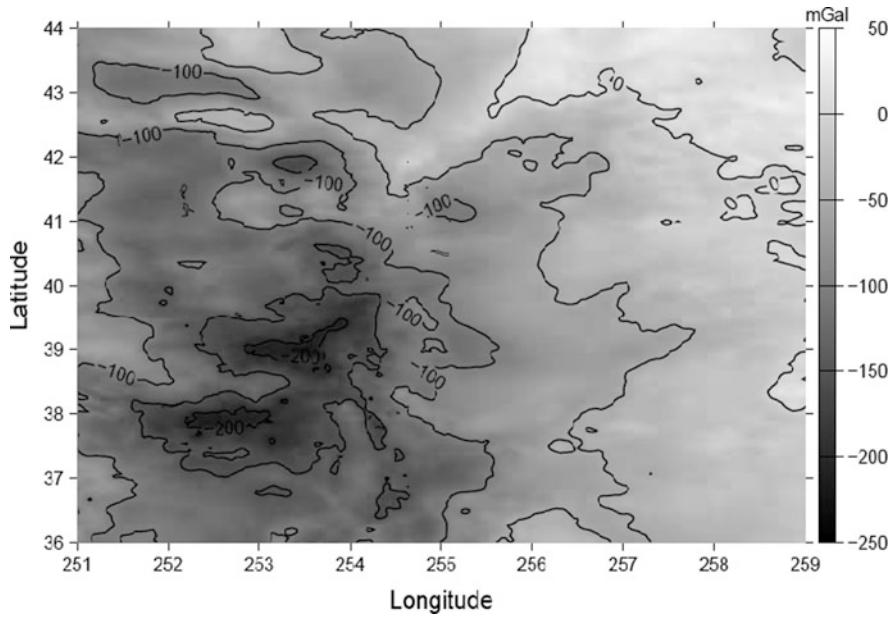


Fig. 53.10 The no-topography gravity anomalies computed at the Earth's surface

Table 53.2 Statistics of the gravity anomalies

Gravity anomaly	Min [mgal]	Max [mgal]	Mean [mgal]	STD [mgal]
Free-air	–112.4	203.8	11.4	34.5
Simp. pl. Bouguer	–364.2	–67.5	–186.0	58.4
Comp. pl. Bouguer	–354.5	–67.5	–185.3	57.5
Comp. sp. Bouguer	–390.4	–101.7	–221.8	58.7
No-topography	–233.4	35.9	–73.6	52.9

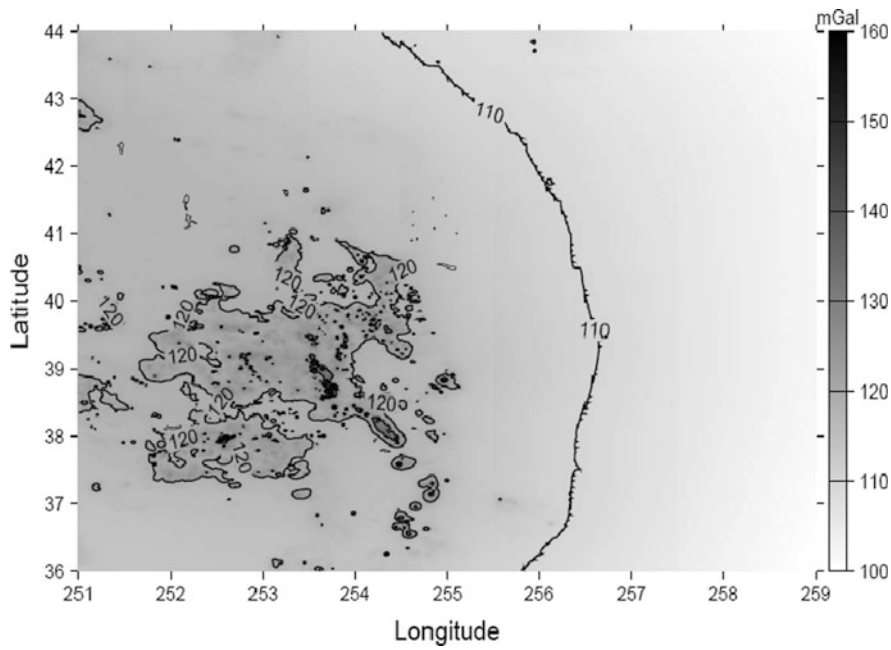


Fig. 53.11 Difference between the no-topography gravity anomalies (Fig. 53.10) and the simple planar Bouguer gravity anomalies (Fig. 53.7)

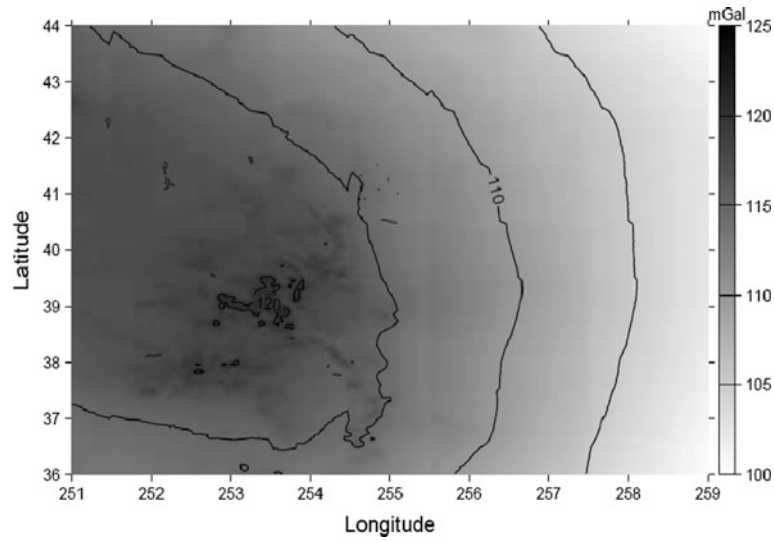


Fig. 53.12 Difference between the no-topography gravity anomalies (Fig. 53.10) and the complete planar Bouguer gravity anomalies (Fig. 53.8)

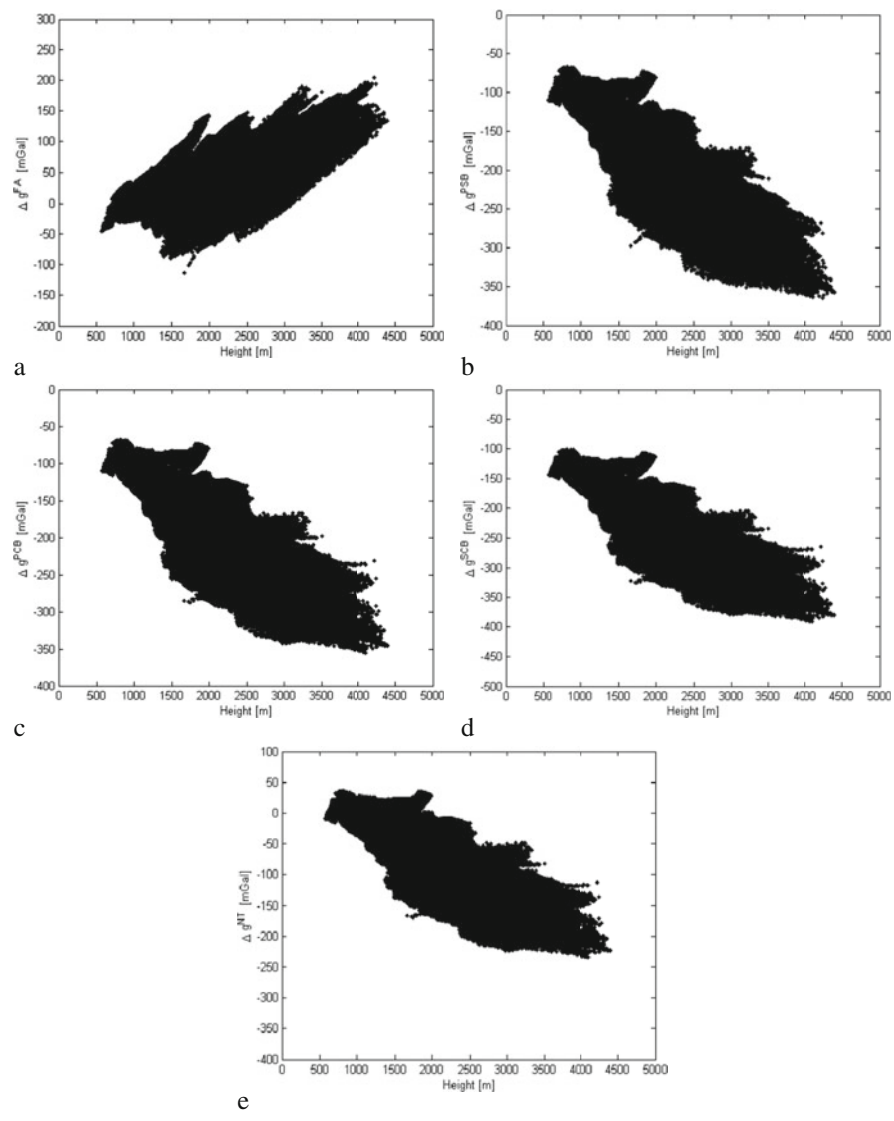


Fig. 53.13 The correlation between the elevation of observation points and the various types of the gravity anomalies: (**a**) the free-air gravity anomalies, (**b**) the simple planar Bouguer gravity anomalies, (**c**) the complete planar Bouguer gravity anomalies, (**d**) the complete spherical Bouguer gravity anomalies, (**e**) the no-topography gravity anomalies

smoothing effect of various types of the topographical correction on the high-frequency gravity anomaly signal is similar. The same conclusion also holds for the smoothing effect of the complete topographical effect on the high-frequency gravity anomaly signal applied in computing the no-topography gravity anomalies. The reason is that the secondary indirect effect has mainly a long-wavelength character

53.3 Conclusions

The direct topographical effect computed at the Earth's surface is strongly correlated with the local topography. The secondary indirect topographical effect is mainly correlated with the regional topography. Since the high-frequency variations of the secondary indirect topographical effect are much smaller in mountainous regions, the high-frequency variations of the complete topographical effect and of the direct topographical effect are very similar.

The free-air gravity anomalies increase with the elevation of observation points, while the Bouguer and no-topography gravity anomalies decrease. For the points with the same elevations, the dispersions of all types of the investigated Bouguer gravity anomalies as well as the no-topography gravity anomalies have a similar magnitude.

The main conclusion is thus that the smoothing effect of the topographical corrections on the high-frequency gravity anomaly signal is very similar despite the magnitudes of the topographical corrections vary significantly depending on the type of the gravity anomaly for which the particular topographical correction was applied.

References

Gradshteyn, I.S. and I.M. Ryzhik (1980). Tables of integrals, series and products. Translated by Jeffrey A, Academic Press, New York.

Martinec, Z. (1998). Boundary value problems for gravimetric determination of a precise geoid. Lecture Notes in Earth Sciences, Vol 73, Springer Verlag, Berlin, Heidelberg, New York.

Nagy, D., G. Papp, and J. Benedek (2000). The gravitational potential and its derivatives for the prism. *J. Geod.,* 74, 552–560.

Vajda, P., P. Vaníček, P. Novák, R. Tenzer, and A. Ellmann (2007). Secondary indirect effects in gravity anomaly data inversion or interpretation. *J. Geophys. Res.,* 112, B06411, doi:10.1029/2006JB004470.

Vaníček, P., R. Tenzer, L.E. Sjöberg, Z. Martinec, and W.E. Featherstone (2004). New views of the spherical Bouguer gravity anomaly. *J. Geoph. Int.*, 159(2), 460–472.

Chapter 54

Determination of a Gravimetric Geoid Model of Greece Using the Method of KTH

I. Daras, H. Fan, K. Papazissi, and J.D. Fairhead

Abstract The main purpose of this study is to compute a gravimetric geoid model of Greece using the least squares modification method developed at KTH. In regional gravimetric geoid determination, the modified Stokes' formula that combines local terrestrial data with a global geopotential model is often used nowadays. In this study, the optimum modification of Stokes' formula, introduced by Sjöberg (2003), is employed so that the expected mean square error (MSE) of the combined geoid height is minimized. According to this stochastic method, the geoid height is first computed from modified Stokes' formula using surface gravity data and a global geopotential model (GGM). The precise geoid height is then obtained by adding the topographic, downward continuation, atmospheric and ellipsoidal corrections to the approximate geoid height. In this study the downward continuation correction was not considered for the precise geoid height computations due to a limited DEM. The dataset used for the computations, consisted of terrestrial gravimetric measurements, a DEM model and GPS/Levelling data for the Greek region. Three global geopotential models (EGM96, EIGEN-GRACE02S, EIGEN-GL04C) were tested for choosing the best GGM to be combined into the final solution. Regarding the evaluation and refinement of the terrestrial gravity measurements, the cross-validation technique has been used for detection of outliers. The new Greek gravimetric geoid model was evaluated with 18 GPS/Levelling points of the Greek geodetic network. After using a 7-parameter model to fit the geoid model to the GPS/Levelling data, the agreement between the absolute geoid heights derived from the gravimetric method and the GPS/Levelling data, was estimated to 27 cm while the agreement for the relative geoid heights after the fitting, to 0.9 ppm. In an optimal case study, considering the accuracies of the ellipsoidal and orthometric heights as $\sigma_h \approx \pm 10$ cm and $\sigma_H \approx \pm 20$ cm respectively, the RMS fit of the model with the GPS/Levelling data was estimated to $\sigma_N \approx \pm 15$ cm. The geoid model computed in this study was also compared with some previous Greek geoid models, yielding better external accuracy than them.

54.1 Introduction

Nowadays, the most common way for precise regional gravimetric geoid determination is to combine regional gravity data with a global geopotential model (GGM) using a modified form of Stokes' formula, originally proposed by Molodenskii in 1958. Over the last decades, two distinct groups of modification approaches have been proposed in geodetic literature, the deterministic and the stochastic modification methods. Their most significant difference is that the deterministic approaches aim only at reducing the truncation bias while the stochastic approaches attempt also to reduce the error stemming from the terrestrial gravity and the GGM data. The stochastic methods by Sjöberg (1984, 1991, 2003), aim at reducing the GGM and terrestrial data errors, as well as the

I. Daras (✉)
National Technical University of Athens, Rural and Surveying Engineering Dept., Athens, Greece
e-mail: idaras@gmail.com

S.P. Mertikas (ed.), *Gravity, Geoid and Earth Observation*, International Association of Geodesy Symposia 135,
DOI 10.1007/978-3-642-10634-7_54, © Springer-Verlag Berlin Heidelberg 2010

truncation error, by matching all three error sources in the LS sense.

In this study (Daras, 2008), the optimum modification of Stokes' formula, introduced by Sjöberg (2003), is employed so that the expected mean square error (MSE) of the combined geoid height is minimized.

54.2 Geoid Determination Based on the Least-Squares Modification of Stokes' Formula

54.2.1 Modification of Stokes' Formula

The computational scheme for estimating the geoid height $\hat{N}$ in the KTH approach can be summarized by the following formula:

$$\hat{N} = \tilde{N} + \delta N_{comb}^{Topo} + \delta N_{DWC} + \delta N_{comb}^{a} + \delta N_{e}, \quad (1)$$

where $\tilde{N}$ stands for the approximate geoid height and the rest are the additive corrections of the KTH approach which will be described in Sect. 53.2.3. Assuming a cap σ_o with spherical radius ψ_o of integration around the computation point, Sjöberg (2003) presented a simple and general modification model for Stokes' formula for computing the approximate geoid height $\tilde{N}$, by defining two sets of arbitrary modification parameters (s_n and b_n) as follows:

$$\tilde{N} = \frac{c}{2\pi} \iint_{\sigma_o} S^L(\psi) \Delta g d\sigma + c \sum_{n=2}^{M} b_n \Delta g_n^{EGM}, \quad (2)$$

where $S^L(\psi)$ is the modified Stokes' function which can be expressed as:

$$S^L(\psi) = S(\psi) - \sum_{n=2}^{L} \frac{2n+1}{2} s_n P_n(\cos\psi), \quad (3)$$

and $S(\psi)$ is the original Stokes' function which can be expressed as a series of Legendre polynomials:

$$S(\psi) = \sum_{n=2}^{\infty} \frac{2n+1}{n-1} P_n(\cos\psi), \quad (4)$$

The modification parameters (s_n and b_n) can be calculated by:

$$b_n = \left(Q_n^L + s_n^*\right) \frac{c_n}{c_n + dc_n} \quad for \quad 2 \le n \le M,$$
$$s_n^* = \begin{cases} s_n & if \quad 2 \le n \le L \\ 0 & otherwise \end{cases}, \quad (5)$$

where $c = R/2\gamma$ and Δg_n^{EGM} is the gravity anomaly Laplace harmonics of degree n calculated from an EGM (Heiskanen and Moritz, 1967).

$$\Delta g_n^{EGM} = \frac{GM}{a^2} \left(\frac{a}{r}\right)^{n+2} (n-1) \sum_{m=-n}^{n} C_{nm} Y_{nm}, \quad (6)$$

where a is the equatorial radius of the reference ellipsoid, r is the geocentric radius of the computation point, GM is the adopted geocentric gravitational constant, the coefficients C_{nm} are the fully normalized spherical harmonic coefficients of the disturbing potential provided by the GGM, and Y_{nm} are the fully normalized spherical harmonics (Heiskanen and Moritz, 1967). The truncation coefficients Q_n^L in Eq. (5) can be calculated as:

$$Q_n^L = Q_n - \sum_{k=2}^{L} \frac{2k+1}{2} s_k e_{nk}, \quad (7)$$

where Q_n are the Molodenskii's truncation coefficients (Heiskanen and Moritz, 1967), and e_{nk} are functions of ψ_o called Paul's coefficients.

Generally the upper bound of the harmonics to be modified in Stokes's function L, is arbitrary and not necessarily equal to the GGMs' upper limit M. Based on the spectral form of the "true" geoidal undulation N (Heiskanen and Moritz, 1967), the expected global MSE of the geoid estimator $\tilde{N}$ can be written:

$$m_{\tilde{N}}^2 = E\left\{\frac{1}{4\pi} \iint_{\sigma} \left(\tilde{N} - N\right)^2 d\sigma\right\}$$
$$= c^2 \sum_{n=2}^{M} \left(b_n^2 dc_n\right) + c^2 \sum_{n=2}^{\infty} \left[b_n^* - Q_n^L(\psi_0) - s_n^*\right]^2 c_n$$
$$+ c^2 \sum_{n=2}^{\infty} \left[\frac{2}{n-1} - Q_n^L(\psi_0) - s_n^*\right]^2 \sigma_n^2, \quad (8)$$

where $E\{\}$ is the statistical expectation operator, c_n are the *gravity anomaly degree variances,* σ_n^2 are the terrestrial gravity anomaly *error degree variances*, dc_n are the *GGM derived* gravity anomaly *error degree variances* and

$$b_n^* = \begin{cases} b_n & if \quad 2 \le n \le L \\ 0 & otherwise \end{cases} \tag{9}$$

For the purposes of this study, a specially designed Matlab program made by Ellmann (2005) was used to obtain the LS parameters s_n, b_n of the optimum LS modification method by Sjöberg (2003). After that, the parameters were used as input to Matlab programs that were designed for the scope of this study, to derive the approximate geoidal height $\tilde{N}$.

54.2.2 Models for Signal and Noise Degree Variances

The degree variance c_n can be obtained by using coefficients C_{nm} and S_{nm} of disturbing potential and fundamental constants (gravity mass constant *GM* and equatorial radius (*a*) of the used GGM as follows:

$$c_n = \frac{(GM)^2}{a^4}(n-1)^2 \sum_{m=0}^{n} \left(C_{nm}^2 + S_{nm}^2\right) \tag{10}$$

In practice the infinite sum in Eq. (10), must be truncated at some upper limit of expansion; $n_{\max} = 2000$ for our study. The higher signal degree variances can be generated synthetically. The Tscherning and Rapp model (Tscherning and Rapp, 1974) was used to account for the highest degrees of gravity anomaly degree variance, which are defined by:

$$c_n = A' t^{n+2} \frac{(n-1)}{(n-2)\,(n+24)}, \tag{11}$$

where the coefficients $A' = 425.28 mGal^2$ and $t = 0.999617$. The *error (noise) anomaly degree variance* (dc_n) of the erroneous potential coefficients is derived from the GGMs with standard errors d_{Cnm} and d_{Snm} (cf. Rapp and Pavlis, 1990):

$$dc_n = \frac{(GM)^2}{a^4}(n-1)^2 \sum_{m=0}^{n} \left(d_{Cnm}^2 + d_{Snm}^2\right) \tag{12}$$

The error degree variances for the terrestrial gravity anomalies were estimated by using a reciprocal distance model which according to Moritz (1980) can be estimated from the simple relation:

$$\sigma_n^2 = c_T(1-\mu)\mu^n, \quad 0 < \mu < 1, \tag{13}$$

where the constants c_T and μ can be estimated from the knowledge of an isotropic error degree covariance function $C(\psi)$ presented in closed form (Moritz, 1980):

$$C(\psi) = c_T \{ \frac{1-\mu}{\sqrt{1-2\mu\cos\psi+\mu^2}} - (1-\mu) - (1-\mu)\mu\cos\psi \} \tag{14}$$

Equation (14) is just a rough model for computing σ_n^2 and it is utilized for determining the constant μ. For $\psi = 0$ the variance by Eq. (13) becomes:

$$C(0) = c_T \mu^2 \tag{15}$$

and thus it follows that:

$$C(\psi_0) = \frac{1}{2} c_T \mu^2 \tag{16}$$

The solution with μ=0.99899012912 (associated with $\psi_0 = 0.1^\circ$) is used in the software used for the computations. The constant μ is found from trivial iterations; see Eqs. (14) and (16). Inserting μ into Eq. (15) c_T is completely determined and σ_n^2 is then calculated. Pre-defined quantity $C(0)$ must be chosen from the user, as the accuracy of the gridded gravity anomalies. In our study we chose C(0) = 9mGals^2.

To obtain the Least-Squares Modification (LSM) parameters, Eq. (8) is differentiated with respect to s_n, i.e., $\partial m_{\tilde{N}}^2 / \partial s_n$. The modification parameters s_n are thus solved in the least-squares sense from the linear system of equations (Sjöberg, 2003):

$$\sum_{r=2}^{L} a_{kr} s_r = h_k, \quad k = 2,3,\ldots..,L, \tag{18}$$

54.2.3 Additive Corrections in the KTH Approach

As mentioned before, Eq. (2) is the formula for computing the precise geoid height by adding the corrective terms to the approximate geoid height. The *combined topographic effect* $\left(\delta N_{comb}^{Topo}\right)$ is the sum of the direct and indirect effects, and can be added directly to the approximate geoidal height values as (Sjöberg, 2000, 2001):

$$\delta N_{comb}^{Topo} = \delta N_{dir} + \delta N_{indir} \approx -\frac{2\pi G\rho}{\gamma} H^2 \qquad (19)$$

where $\rho = 2.67\,\mathrm{g/cm^3}$ is the mean topographic mass density and H is the orthometric height. In this study the *downward continuation correction* (δN_{DWC}) was not considered for the precise geoid height computations due to a limited DEM. In the KTH scheme, the *combined atmospheric effect* δN_{comb}^{a} can be approximated to order H by (Sjöberg and Nahavandchi, 2000):

$$\delta N_{comb}^{a}(P) = -\frac{2\pi R\rho_0}{\gamma}\sum_{n=2}^{M}\left(\frac{2}{n-1} - s_n - Q_n^L\right)H_n(P) - \frac{2\pi R\rho_0}{\gamma}\sum_{n=M+1}^{\infty}\left(\frac{2}{n-1} - \frac{n+2}{2n+1}Q_n^L\right)H_n(P), \qquad (20)$$

where ρ_0 is the result of the density at sea level $\rho^0 = 1.23\times10^{-3}\,\mathrm{g\,cm^{-3}}$ multiplied by the gravitational constant G, γ is the mean normal gravity at sea level, and H_n is the Laplace harmonic of degree n for the topographic height which can be expressed by the formula:

$$H^v(\varphi,\lambda) = \sum_{m=0}^{\infty}\sum_{m=-n}^{n} H_{nm}^v Y_{nm}(\varphi,\lambda), \qquad (21)$$

The normalized spherical harmonic coefficients $\left(H_{nm}^v\right)$ used in this study, were given by Fan (1998) and they were computed to degree and order 360.

The *ellipsoidal correction* (δN_e) was estimated approximately by a simple formula (Sjöberg, 2004):

$$\delta N_e \approx \psi_0^o\left[\left(0.12 - 0.38\cos^2\theta\right)\Delta g + 0.17\tilde{N}\sin^2\theta\right]_{mm}, \qquad (22)$$

where ψ_0° is the cap size (in units of degree of arc), θ is geocentric co-latitude, Δg is given in mgal and $\tilde{N}$ in m.

54.3 Geoid Computation

The gravity anomaly database of Greece (GETECH, 2007) contained 9,335 points of raw observed gravity, free air gravity anomalies and Bouguer gravity anomalies. Regarding the evaluation and refinement of the terrestrial gravity measurements, the cross-validation method was used for detection of outliers using the Bouguer gravity anomalies. 87 points with interpolation error $\varepsilon > 35$ mGals were omitted from the computations. The Molodesnkii's gravity anomalies were then computed for the outlier-free point data.

For the construction of the gravity anomaly grid, a grid of $5' \times 5'$ resolution was chosen, according to the density of the gravity data. The South-West corner of the target area grid had $\varphi = 34°.50$ *and* $\lambda = 19°.50$ while the North-East had $\varphi = 42°.00$ *and* $\lambda = 28°.25$. The gravity anomaly value in each block was given by extrapolation of the Molodenskii's gravity anomalies of the point data, using the Kriging gridding algorithm with the Linear variogram model (slope=1, anisotropy: ratio=1, angle=0). For the scope of this study, the grid was extended beyond the target area in an offset of 3°, as the integration for each computation point was truncated at the fixed spherical distance $\psi_o = 3°$. A "moving" spherical cap of that size, with the computation point at its center, was used. Blocks with no gravity information, were given free-air gravity anomalies from EGM96 model. A DEM of 250×250 m resolution, necessary for the computations of some of the additive corrections, was provided by the NTUA in the extent of the region $18°.6 \le \lambda \le 29°.5$ *and* $34° \le \varphi \le 42°$.

For the choice of the best GGM in the combined solution of the LSMS (Least Squares Modification of Stokes) formula, three GGMs have been tested: The EGM96, EIGEN-GRACE02S (satellite only) and EIGEN-GL04C models. The selection of the upper limit of the geopotential model, M, and the upper limit of the harmonics to be modified in Stokes's function, L, are of crucial importance in the geoid modeling. The choice of the upper limit M of the GGM is directly

related to the quality of the GGM to be used. In practice, due to restricted access to terrestrial data the integration radius ψ_0 is often limited to a few hundred kilometres. This implies that a relative high M should counterbalance this limitation. On the other hand, the GGM error grows with increasing degree, so there must be a compromise between those two aspects for choosing the best value for M. In this study, the optimum (Sjöberg, 2003) LS modification method is implemented, which assumes that the upper bound of the harmonics to be modified in Stokes's function, L, is $L \geq M$. In our case it is $L = M$. Table 54.1 summarizes he parameters chosen for computing s_n and b_n parameters with *LScoeff.m* program by Ellmann (2005).

After testing the GGM models, the EIGEN-GRACE02S model seemed to minimize the truncation bias in a better way than the other models and to have a better fit with the GPS/Levelling data used in a next step for evaluating the geoid model (Table 54.2). Thus the EIGEN-GRACE02S model was the GGM model chosen for the computations (Fig. 54.1).

Table 54.1 Input parameters chosen for computing the s_n and b_n LS parameters with *LScoeff. m* program

	EIGEN-GRACEO2S	EGM96	EIGEN-GL04C
M=L	120	360	360
ψ_0	3°	3°	3°
$\sigma_{\Delta g}$	9 mgal	9 mgal	9 mgal

Table 54.2 Gravimetric geoid height and GPS/Levelling data agreement, before and after the seven parameter fitting, for the three GGM models tested

	EIGEN-GRACEO2S	EIGEN-GL04C	EGM96
	St.dev (m)	St.dev (m)	St.dev (m)
Before fitting	0.370	0.351	0.441
After fitting	0.241	0.248	0.257

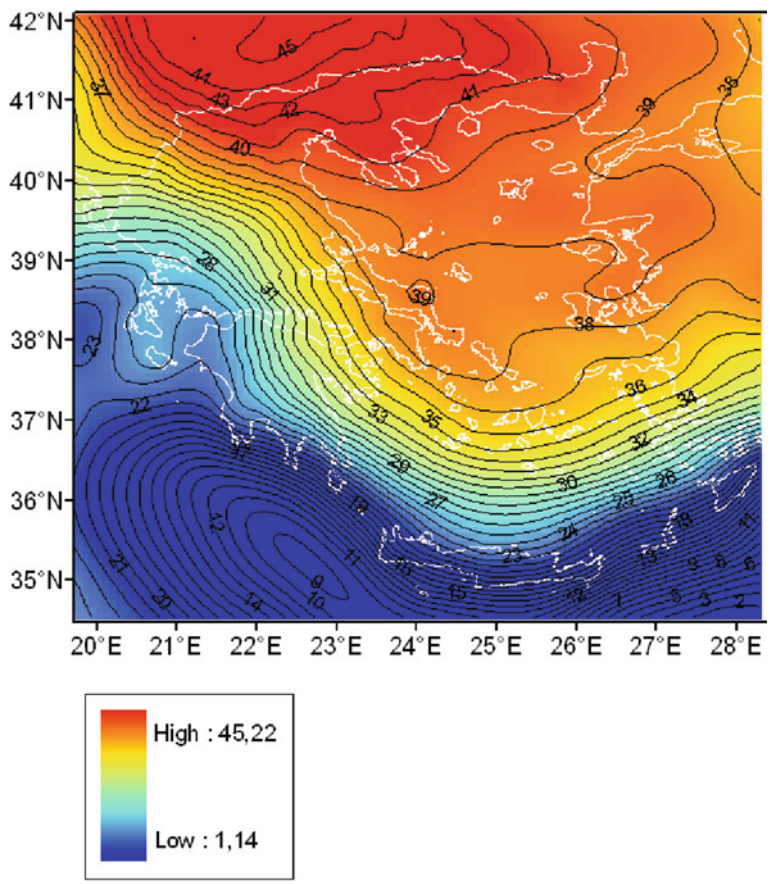


Fig. 54.1 The new Greek gravimetric geoid in GRS80. Unit: (m)

54.4 Evaluation of the Gravimetric Geoid Model

The real potential of the gravimetric geoid is nowadays estimated when comparing its result with the externally derived geoid height from GPS/levelling measurements. 18 GPS/Levelling points of the Greek geodetic network, provided from the NTUA, were used to externally evaluate the geoid model. In practice, because of the presence of different random and systematic errors in the values of *h, H* and *N* the simple model $h \approx H + N$ doesn't work properly.

In order to reduce the effect of the systematic errors in evaluation of geoid models, several systematic parameter models can be used in order to fit the quasi-geoid to a set of GPS levelling points through an integrated least squares adjustment. After testing several models, the seven parameter model (Kotsakis and Sideris, 1999) gave the best fitting in all selected GGM and the new gravimetric geoid model, thus it was chosen for implementation. Table 54.2 shows the agreement between the absolute approximate geoid heights from the gravimetric geoid model and the GPS/Levelling data, before and after the seven parameter fitting, for the three GGM tested in this study. The same agreement for the corrected/precise geoid heights was estimated to 0.266 m for the EIGEN-GRACE02S model which was chosen for the computations.

It seems that the standard deviation after the fitting for the precise geoid heights has a bit larger value than the corresponding standard deviation of the approximate geoid height. This can be partially explained by the fact that the DWC correction was not considered in the computation of the precise geoid heights. In an optimal case study, considering the accuracies of the ellipsoidal and orthometric heights as $\sigma_h \approx \pm 10$ cm and $\sigma_H \approx \pm 20$ cm respectively and their errors to be uncorrelated, the RMS fit of the model with the GPS/Levelling data was estimated to $\sigma_N \approx \pm 15$ cm.

Because of the presence of different systematic errors and adjustment of the GPS/levelling and gravity

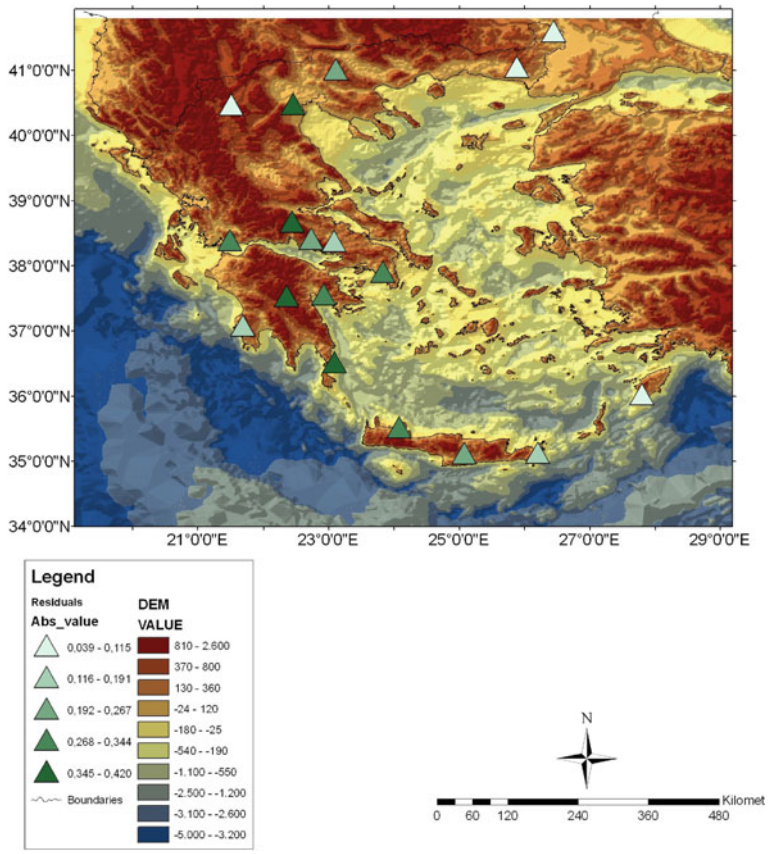


Fig. 54.2 Distribution of the GPS/levelling points inside the Greek region. The absolute value of the residuals ε_i with the geoid model after the 7-parameter fitting is visualized with the difference in the color scale (for colors, see online version)

data, the estimation of the agreement of the absolute geoid heights stemming from the GPS/Levelling data and the gravimetric geoid model, usually can not show the real potential of the geoid model. It is well known, that GPS and levelling observations have very good accuracies in the relative sense, because most of the systematic errors are cancelled or eliminated through the differencing of the observations. The agreement between the relative geoid heights, after the seven parameter fitting, was estimated to 0.9 ppm (Fig. 54.2)

54.5 Concluding Remarks

The new Greek gravimetric geoid model was compared with two existing geoid models of Greece. The new model seems to have a better external accuracy (± 27 cm) than the FINGRAV-GPSOLAC model (Hellenic Military Geographical Service, 2005) estimated to ± 29 cm and the geoid by (Tziavos, 1984) estimated to ± 53 cm. Some recommendations for further work could be the use of a more compact gravity dataset including gravity data from the neighbouring countries and altimetric data from the sea region combined in the solution. The DWC correction should also be considered into the final solution, thus an extended DEM is essential for the computations. A research should also be conducted about the choice of a decent GPS/Levelling dataset for an explicit evaluation of the model.

References

Daras, I. (2008). Determination of a gravimetric geoid model of Greece using the method of KTH. Master of science thesis in Geodesy No.3102, ISSN 1653-5227, Royal Institute of Technology, Stockholm.

Ellmann, A. (2005). Computation of three stochastic modifications of Stokes's formula for regional geoid determination. *Comput. Geosci.*, 31/6, 742–755.

Fan, H. (1998). On an Earth ellipsoid best-fitted to the Earth surface. *J. Geod*, 72(3), 154–160.

GETECH (2007). Gravity point data for Greece, Geophysical Exploration Technology (GETECH), University of Leeds.

Heiskanen, W.A. and H. Moritz (1967). Physical Geodesy. W H Freeman and Co., New York, London and San Francisco.

Hellenic Military Geographical Service, Mylona (2005). The geoid model of Greece in WGS84, combined by GPS and gravity measurements. Vol. 152, Publication 2003–2005.

Kotsakis, C. and M.G. Sideris (1999). On the adjustment of combined GPS/levelling/geoid networks. *J. Geod.*, 73(8), 412–421.

Moritz, H. (1980). Advanced physical geodesy, Herbert Wichmann Verlag, Karlsruhe.

Rapp, R.H. and N.K. Pavlis (1990). The development and analysis of geopotential coefficients models to spherical harmonic degree 360. *J. Geophys. Res.*, 95(B13), 21885–21911.

Sjöberg, L.E. (1984). Least squares modification of Stokes' and Vening Meinesz' formulas by accounting for truncation and potential coefficient errors. *Manuscripta Geodaetica*, 9, 209–229.

Sjöberg, L.E. (1991). Refined least squares modification of Stokes' formula. *Manuscripta Geodaetica*, 16, 367–375.

Sjöberg, L.E. (2000). On the topographic effects by the Stokes-Helmert method of geoid and quasi-geoid determinations. *J. Geod.,* 74(2), 255–268.

Sjöberg, L.E. (2001). Topographic and atmospheric corrections of gravimetric geoid determination with special emphasis on the effects of degree zero and one. *J. Geod.,* 75, 283–290.

Sjöberg, L.E. (2003). A general model of modifying Stokes' formula and its least squares solution. *J. Geod.,* 77, 459–464.

Sjöberg, L.E. (2004). A spherical harmonic representation of the ellipsoidal correction to the modified Stokes formula. *J. Geod.,* 78(3), 1432–1394.

Sjöberg, L.E. and H. Nahavandchi (2000). The atmospheric geoid effects in Stokes' formula. *Geophys. J. Int.,* 140, 95–100.

Tscherning, C. and R. Rapp (1974). Closed covariance expressions for gravity anomalies, geoid undulations and deflections of the vertical implied by anomaly degree variance models. Report No. 208, Department of Geodetic Science, Ohio State University, Columbus, OH.

Tziavos, I.N. (1984). A study of optimum combination of heterogeneous data for the determination of the geoid: A case study of Greece (PhD Dissertation). Thessaloniki, Greece.

Chapter 55

Method to Compute the Vertical Deflection Components

E.A. Boyarsky, L.V. Afanasieva , and V.N. Koneshov

Abstract To make a more exact mathematical model of the global atmosphere circulation and to improve the weather forecast one needs to take into account the Vertical Deflection Components (VDCs). The required accuracy for these tasks is 1–2″ now and 0.4–1.0″ in future. The VDCs were calculated by integration of the free air gravity anomalies (taken from the Internet site of Scripps Institute of Oceanography) on the grid of $2' \times 2'$, an integration radius $R = 4{,}000$ or 5,000 km. Also the approaches to calculate the far zone contribution are discussed. As the first test the results are compared with the VDCs obtained from the global spherical harmonics expansion of the order of 1,800. For the Mariana trench area, where the variation of *W*–*E* component exceeds 50″, the standard deviation from Wenzel's model is of 2″. The other region for testing with a more dense grid $1' \times 1'$ is the Kane fracture zone; standard deviations are about 0.6″.

55.1 Introduction

Meteorologists usually express the tangential components of the gravity Δg_φ and Δg_λ in the physical unit m/s^2. Below we shall mainly use the term the vertical deflection components (VDCs) as geodesists traditionally do:

$$\xi = -\frac{\Delta g_\varphi \rho''}{\mathrm{g}} \text{ and } \eta = -\frac{\Delta g_\lambda \rho''}{\mathrm{g}}. \qquad (1)$$

E.A. Boyarsky (✉)
Schmidt Institute for Physics of the Earth, Russian Academy of Sciences, Moscow, 123995, Russian Federation
e-mail: ernst@ifz.ru

The VDCs are significant in solving (or modeling of) a number of geophysical problems. Among them are the modeling of the atmospheric general circulation (AGCM) and improvement of short-term (48 h) weather forecasts. In 1987 IUGG XIX General Assembly included the AGCM in the list of the most important geophysical problems.

The gravity vector g is always considered in the basic equations of meteorology. Traditionally, however, only a normal gravity field, (i.e. the gravitational attraction of the Earth ellipsoid plus the centrifugal acceleration) has so far been taken into account in the mathematical models of the Earth atmosphere. The recent studies (Makosko and Panin, 2002, Makosko et al., 2007) have shown that it was reasonable to take the influence of the anomalous gravity field upon the Earth atmosphere dynamics into consideration. There are other factors (mass variations of the atmosphere, tidal effects, changes of the Earth rotation velocity, displacement of the Earth center, elastic deformations of the Earth crust, seasonal changes of the Ocean level, geodynamical events) that induce temporal variations of the vector $\boldsymbol{g}$ but these variations are at least one hundred times weaker than anomalies of the gravity. Therefore, the vector g can be reckoned to be constant in the case.

It was found in the cited publications:

- The encouraging results were obtained when the tangential components were included into mathematical models. The calculated values of the kinetic energy in the lower atmosphere and the zonal distribution of monsoon precipitation in the AGCM came nearer to the standard. Thus, the improvements of the 48-h weather forecasts calculated with a regional hydrodynamic model were statistically

S.P. Mertikas (ed.), *Gravity, Geoid and Earth Observation*, International Association of Geodesy Symposia 135,
DOI 10.1007/978-3-642-10634-7_55, © Springer-Verlag Berlin Heidelberg 2010

significant in most cases. However, the influence of the anomalous vertical component

$$\Delta g_R = \frac{-\partial T}{\partial R}$$

(where T is the anomalous potential) turned out insignificant. The tangential components Δg_φ and Δg_λ are twice smaller than Δg_R (which does not exceed 0.07% of the gravity g), but they are present only in a model with the anomalous gravity field, and this fact seems to be the cause of this phenomenon.

- The size of grid for the tangential components has to correspond to that of meteorological data in an AGCM. For example, if a regional weather forecast model has a step of 50 km, the anomalous gravity field should be averaged at about $30' \times 30'$. In this connection and with a perspective to reduce the step in the regional model to 20–25 km now and 10–12 km later on, it is desirable to get tangential components at the grid of $12' \times 12'$ or $6' \times 6'$ with the uncertainty less than 0.4–1.0″.

55.2 Getting the VDCs

By now we cannot make direct measurements of the VDCs all over the Earth in sufficient number. Measurements with high-precision digital zenith camera are not yet possible at sea, swamp etc. However, the VDCs can be computed by using the free air gravity anomalies either via a preliminary calculation of the spherical harmonics expansion of the gravitational potential or by the direct integration of anomalies. Contemporary gravimeters give the vector g magnitude with the uncertainty of 0.1 mgal even on shipboard. The measurements aboard an aircraft and the satellite data supply the bulk of information as well. Thus, a detailed anomalous gravity field is known. Even at places, where the vertical deflections are external, change of the measured vector g by its magnitude gives a bias within the bounds of the same 0.1 mgal.

There are three ways to compute the VDCs from the gravity anomalies:

- to approximate the anomalous gravity potential with the surface spherical harmonics;
- to approximate the real anomalies with the attraction of fictitious masses;
- to integrate directly ("outer Neumann problem").

Each method has its advantages and disadvantages discussed briefly below.

55.2.1 Spherical Harmonics (Legendre Polynomials)

Some sets of Legendre polynomial coefficients C_{mn} and S_{mn} are now available for the Earth as a whole. We have dealt with two geopotential models: Pz90 of 360th order (Parameters, 1991) and Wenzel's GPM98A of 1800th order (Wenzel, 1998). Both models have been obtained using the satellite data together with the direct gravity measurements. The satellite method yields valuable information for hard-to-reach areas and more accurate information for global-scale anomalies (hundreds or more kilometers long). On the other hand, surface measurements reveal the local details of the field (dozens or less kilometers long). There are models of higher order but they are aimed only at some chosen regions. Furthermore, the calculated gravity values in poorly studied areas often contradict the reliable real measurements, if these measurements have not been included in calculation of the high-order model.

In addition, the spherical harmonics inevitably represent a smoothed anomalous gravity field. However, it is local anomalies that can strongly affect the dynamics of processes in atmosphere, because almost the whole atmospheric mass concentrates in the lowermost layer with the thickness of several kilometers.

55.2.2 Attraction of Fictitious Masses

The anomalies can be described with the attraction of either a set of points, or single/double layers, or both of them. This is a typical geophysical inverse problem where the choice of the origins has an approximate feature; and as a rule, its appropriate solution cannot be obtained without additional geophysical information. In the case concerned, the number of unknown quantities amounts to tens of thousands. The more unknown quantities are in calculations the nearer the

gravitational effect of each of them on the uncertainties of the initial values. As a result, the solution becomes unsteady.

55.2.3 Direct Integrating of Gravity Anomalies

The required VDCs at a point $(\varphi_0, \lambda_0, h_0)$ is represented by the integrals over the surface σ of an ellipsoid, where the gravity anomalies $\Delta g\,(\varphi, \lambda, h)$ are given:

$$\xi\,(\varphi_0, \lambda_0, h_0) = \frac{\rho''}{2\pi\gamma_0} \times \int\int_{\sigma} \frac{\Delta g(\varphi,\lambda,h) \sin\nu \cos A}{D^2} d\varphi\, d\lambda$$

and

$$\eta\,(\varphi_0, \lambda_0, h_0) = \frac{\rho''}{2\pi\gamma_0} \times \int\int_{\sigma} \frac{\Delta g(\varphi,\lambda,h) \sin\nu \sin A}{D^2} d\varphi\, d\lambda \quad (2)$$

where γ_0 is a normal gravity in computation point, D is the distance from the computation point $(\varphi_0,\lambda_0,h_0)$ to a current integration point (φ,λ,h), ν is the angle between the vertical at the point $(\varphi_0,\lambda_0,h_0)$ and the direction in the line of a point (φ,λ,h), A is the azimuth of this direction at the horizontal plane in the computation point.

The input anomalies Δg_0 on the latitude interval of $\pm 72^{\circ}$ were taken from the site of Scripps Institute of Oceanography (Sandwell and Smith, 1997). Our repeated comparisons of real measurements with those data confirm that they are quite appropriate to compute the VDCs by (2). The effect of the polar areas was taken from Legendre polynomials expansion of the anomalous potential at the grid $2' \times 2'$.

The trouble was that the total number of initial values exceeds 5×10^7 and the number of computation points is more than 2.5×10^5 for rather widely spaced grid $30' \times 30'$. That made the task too bulky even for single height h. Therefore, in our preliminary tests (Makosko et al., 2007) the anomalies at the grid $2' \times 2'$ were averaged to the grid $6' \times 6'$ using modified Crain's algorithm (Crain and Bhattacharyya, 1967; Swain, 1976). The integrating radius was $R = 50\,h$ but not less than 1,000 km. These tests were made for a flat Earth and with the neglect of the "far zones" (all the rest Earth) contribution. The tangential components were calculated for the heights from 0 to 30 km, step 1 km. The results were obtained at the grid $30' \times 30'$. In later experiments we increased the radius R up to 4,000 km and minimized the number of heights to 11 as a standard in the meteorological modeling.

Equations (2) represent a modified formula of Vening Meinesz (1928, Eq. 5), who emphasized that the influence of an anomaly $\Delta g\,(\varphi, \lambda, h)$ decreases with the distance D in this formula more rapidly than in Stokes' formula. Equations (2) are based upon the assumption that anomalous masses are located at the given points on the ellipsoid surface and are proportional to the gravity anomalies at the points. The analogous assumption is being accepted in many algorithms that use the free air anomalies. The formulas should give more accurate results, if we insert the individual height h of the anomaly $\Delta g\,(\varphi, \lambda, h)$ for each integration point, but this approach requires extra data and/or new assumptions.

The computation of D and ν takes a long time, but it can be greatly accelerated when the output and input grids are in the integer-valued ratio. In this case, the computation of 2D arrays of D and ν as functions of $\varphi_0 - \varphi$ and $|\lambda_0 - \lambda|$, within the limits of integrating, should precede the computation of VDCs by (2) for each row relating to the same latitude φ_0.

The length D of the vector, its inclination angle ν and the azimuth A can be obtained for either a sphere or an ellipsoid. Our computed results were practically the same. So, at the grid $30' \times 30'$ in the Northern hemisphere with the 0º–120º longitude interval the tangential components η obtained in those two ways had the maximum difference of $0.2''$ at a standard deviation of $0.02''$. The component η varies from $-50''$ to $+40''$ within the mentioned area. The differences were evidently less than the representation error, so we made the subsequent computation exclusively for the sphere.

55.2.4 The Contribution of Far Zones

The contribution of far zones can be estimated in three ways:

- To calculate it by means of Legendre polynomials. The model is determined all over the Earth; while within the near zone all the anomalies have been zeroed beforehand in order to avoid the double counting. As the far zones contribution is small and it smoothly varies from point to point, a comparatively low order of expansion would be sufficient (say, 36th or 72[d]). In that kind of a model some outbursts can arise near the borders, where true anomalies are replaced with zeros, but these outbursts would not affect the calculated far zones contribution because the borders are 4,000 km or more apart from a computation point.
- To compute the far zones contribution by the same formula (2) taking initial data much more widely spaced: at the grid 1º×1º or 2º×2º.

  In both methods described above it is possible to save the computation time by setting a border of the near zone not separately for each computation point but for a joint fragment in the area of interest. Then, the calculation of the contribution of far zones would be restricted to a few points of a fragment (say, its center and four corners) with the following interpolation for each point to be computed.
- To "fix" the component ξ computed by (2) to the value ξ_a from a spherical model. Here again a small order of model would be sufficient. The correction to a computed value is

$$\Delta = A_0 + A_\varphi \delta\varphi + A_\lambda \delta\lambda + \\ + A_{\varphi\varphi}(\delta\varphi)^2 + A_{\lambda\lambda}(\delta\lambda)^2 + A_{\varphi\lambda}\delta\varphi\delta\lambda$$

- where $\delta\varphi = \varphi - \varphi'$ and $\delta\lambda = \lambda - \lambda'$; φ' and λ' represent a chosen point of origin, for example, the averages of ϕ and λ.

The coefficients A are estimated by the least squares method under the condition

$$\sum (\xi + \Delta - \xi_a)^2 = \min . \qquad (4)$$

Depending on the size of the near zone and the complicity of the gravity field one might take only the constant or linear part from (3). Besides, any term in (3) should be excluded if its value is statistically insignificant.

As for component η, the far zones contribution is added to the computed values as mentioned above for ξ.

55.3 Test Results

The computed results were compared with the VDCs from the gravity anomalous potential models of 360th and 1800th order all over the Earth at the grid $30' \times 30'$. The model of 360th order turned out to be unsound and was rejected as could be expected. The far zones contribution was included by the third method (to "fix") after the computations by (2).

A rather interesting example is the Mariana trench area, where the *S–N* component is small and the variation of *W–E* component exceeds $50''$ (Fig. 55.1a). The standard deviations the model are $1.0''$ and $2.0''$, respectively. However, it is only with some extra data that one can distinguish for certain which result corresponds to the real gravity field more adequately.

Computations with a more dense grid $1' \times 1'$ were made for the small Kane fracture zone (Fig. 55.1b). Sandwell's anomalies together with the gravity survey data obtained in R/V "XVII S'ezd Profsoyuzov" cruise served as the initial data. Both components have r.m.s. deviations about $0.6''$.

These comparisons relate to the sea. At the next stage a comparison must involve measurements with a zenith camera to estimate more adequately the accuracy and resolution of the method.

The described choices of the VDCs computation are now under tests aimed at finding proper parameters (the near zone dimensions, the density of the input grid for near and far zones, the model order etc), and to achieve the accuracy of 0.2–$0.4''$ in VDC.

55.4 Conclusions

- The proposed method allows to compute the VDCs for a grid of any density, provided it is backed up with sufficient number and density of source free-air anomalies in the near zone. The method is suitable at sea and in other areas where measurements with a zenith camera are not possible yet. A global model of ξ and η computed by this method can improve modeling the atmosphere general circulation and the regional hydrodynamic weather forecasts.
- An attempt to take into account the computed ξ and η for the weather forecast was fairy encouraging (Makosko et al., 2007), in spite of the fact that the VDCs vary too abruptly from nod to nod of the grid

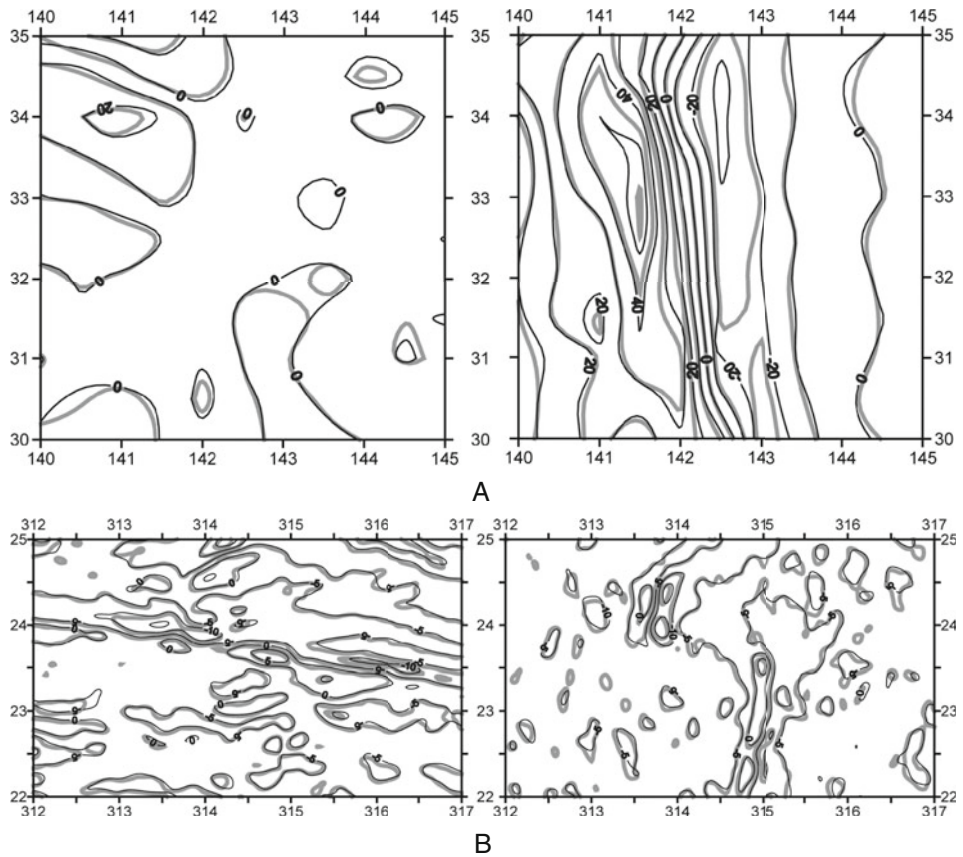


Fig. 55.1 TheVDCs: ξ (on the *left*) and η (on the *right*). The *thin line* is the field from Wenzel's GPM98A model; the *thick gray line* is the field computed by formula (2). (**a**) – Mariana trench; (**b**) – Kane fracture zone (contour intervals are $10''$ and $5''$, respectively)

$30' \times 30'$ in few regions. So there is a good reason to compute them for a more dense grid at the next studies. It is more difficult to modify correspondingly the software for meteorological modeling.

- Naturally, the uncertainty of the computed VDCs can be decreased with more adequate account of the far zones attraction, although it is small relative to the required accuracy. But again it is useful to increase the input grid density in the nearest zone.
- The main requirements to the information on VDCs ξ and η for modeling of AGCM and the short-term weather forecasting has been contemplated.

References

Crain, I.K. and B.K. Bhattacharyya (1967). Treatment of non-equispaced two-dimensional data with digital computer. *Geoexploration*, 5(4), 173–194.

Makosko, A.A. and B.D. Panin (2002). The atmosphere dynamics in non-uniform gravity field. St.Petersburg, p. 244 (in Russian: Макоско АА, Панин БД Динамика атмосферы в неоднородном поле силы тяжести).

Makosko, A.A., K.G. Rubinstein, V.M. Losev, and E.A. Boyarsky (2007). Mathematical modeling of the atmosphere in non-uniform gravity field. Nauka, Moscow, p. 58 (in Russian: Макоско АА, Рубинштейн КГ, Лосев ВМ, Боярский ЭА. Математическое моделирование атмосферы в неоднородном поле силы тяжести).

Parameters of the General Earth ellipsoid and the Earth gravity field. (1991). Moscow, VTU GS, 68 p (in Russian: Параметры общего земного шллипсоида и гравитационного поля Земли).

Sandwell, D.T. and W.H.F. Smith (1997). Marine gravity anomaly from Geosat and ERS 1 satellite altimetry. *J. Geophys. Res.*, 102, 10039–10054, 10 May.

Swain, C.J. (1976). A FORTRAN IV program for interpolating irregularly spaced data using the difference equations for minimum curvature. *Comput. Geosci.*, 1(4), 231–240.

Vening Meinesz, F.A. (1928). A formula expressing the deflection of the plumb-line in the gravity anomalies and some formulae for the gravity field and the gravity potential outside the geoid. *Verhandel-Koninkl. Ned. Akad. v. Wetenschap*, 31, 315–331.

Wenzel, H.G. (1998). Ultra high degree geopotential models GPM98A and GPM98B to degree 1800/Proceedings of joint meeting international gravity commission and international geoid commission, Budapest, 10–14 March, Rep 98:4, Finnish Geodetic Institute, Helsinki, pp. 71–80 or Wenzel, G. (1999). Ultra High Degree Geopotential Models GPM98A and GPM98B. *Bolletino di Geofisica Teorica ed Applicata*.

Chapter 56

On Finite Element and Finite Volume Methods and Their Application in Regional Gravity Field Modeling

Z. Fašková, R. Čunderlík, and K. Mikula

Abstract The article is focused on a solution to the geodetic boundary value problem (GBVP) by new numerical approaches, namely the finite element (FEM) and finite volume (FVM) methods. In spite of previous numerical approaches (like BEM or FFT), where the solution was sought on Earth's surface or its approximation, our numerical solution is computed in 3D computational domain above the Earth bounded by the chosen part of the Earth's surface – area of Slovakia, corresponding upper spherical artificial boundary and four other planar boundaries. On the upper spherical and planar boundaries the Dirichlet boundary condition (BC) are generated from EGM96 geopotential model. On the Earth's surface, discretized by series of triangles, we consider the surface gravity disturbances as the Neumann BC. They are obtained from discrete terrestrial gravimetric measurements. The disturbing potential as a direct numerical result is transformed to quasigeoidal heights.

56.1 Introduction

With the development of HPC (high-performance computing) facilities increases also an importance of numerical methods. With numerical methods we are able to get numerical solution of physical problems described by partial differential equations. The solution of the external GBVP is an important task in geodesy and needs in-depth tools and methods of applied mathematics. Numerical methods such as boundary element method (BEM) have been recently used by various groups in order to determine Earth's gravity field, see Klees (1992, 1995, 1998), Klees et al. (2001) and Čunderlík et al. (2000, 2004, 2008). In spite of previous approaches, where the solution is sought on a 2D hypersurface given by a sphere, ellipsoid or the Earth's surface, here we solve the geodetic BVP in 3D domains above the Earth surface. After discretization it leads to sparse linear systems which are comparable with full BEM matrices regarding the computational complexity. We get directly the Earth's potential solution in the whole 3D computational domain. In order to test ability of the new methods in solving real geodetic task we computed regional quasigeoid in Slovakia by FEM and FVM and made comparison with GPS/leveling test. We have observed qualitative and quantitative agreement.

56.2 Formulation of the Mixed GBVP

Originally, the GBVP deals with the infinite domain. In our approach using the FEM or FVM, we constructed an artificial boundary away from the approximate Earth surface, see Fig. 56.1, and due to giant size of the Earth, we restricted our computations only to a partial domain.

The bottom surface Γ_1 represents a part of the real Earth surface, discretized by triangles, covering e.g. a neighborhood of Slovakia, where the Neumann BC, see Čunderlík et al. (2000, 2004, 2008), in the form of gravity disturbance is given. The upper spherical part $\Gamma_2 = \{x;\ |x|=R\}$ of the domain represents the

Z. Fašková (✉)
Department of Mathematics and Descriptive Geometry, Faculty of Civil Engineering, The Slovak University of Technology, Bratislava 813 68, Slovakia
e-mail: faskova@math.sk

S.P. Mertikas (ed.), *Gravity, Geoid and Earth Observation*, International Association of Geodesy Symposia 135,
DOI 10.1007/978-3-642-10634-7_56, © Springer-Verlag Berlin Heidelberg 2010

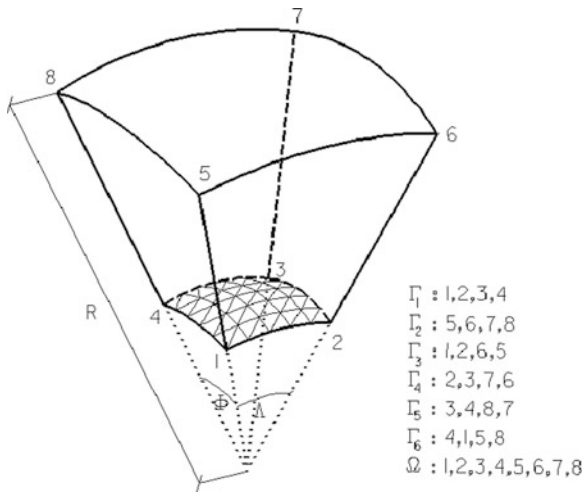


Fig. 56.1 Geometry of computational domain

artificial boundary where the Dirichlet BC is prescribed. On further artificial planar boundaries Γ_3, Γ_4, Γ_5, Γ_6 we use Dirichlet BC, too. Then our GBVP is defined as follows:

$$\Delta T(x) = 0, \quad x \in \Omega, \tag{1}$$

$$\frac{\partial T}{\partial n_{\Gamma_1}} = -\delta g^*(x) = -\delta g.\cos\mu, \quad on \quad \Gamma_1, \tag{2}$$

$$T(x) = T_{EGM-96}(x), \quad on \quad \Gamma_i, \tag{3}$$

where $i = 2, \ldots, 6$, $T_{EGM\text{-}96}$ represents the disturbing potential generated from global geopotential model EGM-96 and μ is angle between normal to equipotential surface U(P)=const and normal to Γ_1.

56.3 Solution of the Mixed GBVP by FEM

In accord with Reddy (1993), the first step is the division of the whole geometrically complex domain into a collection of geometrically simple subdomains called finite elements. Then one constructs the weak formulation of the differential equation on every element, namely

$$\int_{\Omega^e} \nabla w.\nabla T \, dx\, dy\, dz - \int_{\Gamma^e} w\, q_n \, d\sigma = 0, \tag{4}$$

where w is a weight function, Ω^e is a finite element, Γ^e is an element boundary and q_n denotes an inter-element fluxes. In each element the solution is approximated by a linear combination of basis functions in the form of linear polynomials $\Psi_j{}^e$ (which are harmonic), i.e., for $(x,y,z) \in \Omega^e$

$$T(x,y,z) \approx T^e(x,y,z) = \sum_{j=1}^{N} t_j^e \Psi_j^e(x,y,z) \tag{5}$$

Since the basis functions (see Fig. 56.2) are defined by

$$\Psi_j^e(x_i,y_i,z_i) = \begin{cases} \nearrow & 1, i = j \\ \searrow & 0, i \neq j \end{cases} \tag{6}$$

where (x_i,y_i,z_i), $i = 1,\ldots,N$ are nodes of the element, then $t_j{}^e$ $j = 1,\ldots,N$ represents the approximate values of solution T in element nodes. This is one of the main features of FEM. In order to obtain the element equation we consider $w = \Psi_i{}^e$, $i = 1,\ldots,N$ in (4) and for T we plug (5) into (4). By such approach we subsequently get

$$\int_{\Omega^e} \left(\frac{\partial \Psi_i^e}{\partial x} \frac{\partial \left(\sum_{j=1}^{N} t_j^e \Psi_j^e \right)}{\partial x} + \frac{\partial \Psi_i^e}{\partial y} \frac{\partial \left(\sum_{j=1}^{N} t_j^e \Psi_j^e \right)}{\partial y} + \right.$$

$$\left. + \frac{\partial \Psi_i^e}{\partial z} \frac{\partial \left(\sum_{j=1}^{N} t_j^e \Psi_j^e \right)}{\partial z} \right) dx\, dy\, dz - \int_{\Gamma_1^e} \Psi_i^e \, q_n \, d\sigma = 0$$

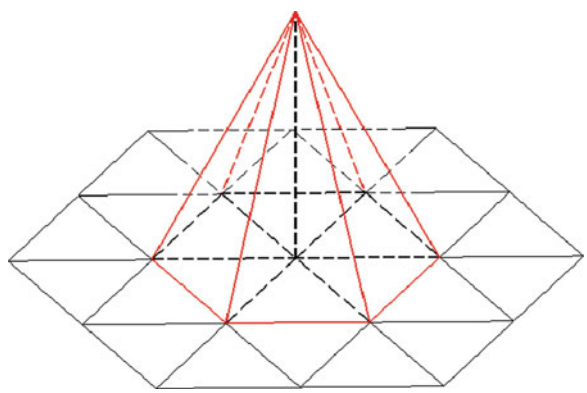


Fig. 56.2 Example of basis functions on triangular grid

for each element Ω^e. Using linearity of derivative and integration we get the linear system of the equations for each element

$$\sum_{j=1}^{N} t_j^e \int_{\Omega^e} \nabla\Psi_i^e \nabla\Psi_j^e \, dx\, dy\, dz - \int_{\Gamma_1^e} \Psi_i^e \, q_n \, d\sigma = 0, \quad (7)$$

where $i = 1,\ldots, N$, and it can be written in a matrix form

$$\begin{pmatrix} K_{11}^e & K_{12}^e & \cdots & K_{1N}^e \\ K_{21}^e & K_{22}^e & \cdots & K_{2N}^e \\ \cdots & \cdots & \cdots & \cdots \\ K_{N1}^e & K_{N2}^e & \cdots & K_{NN}^e \end{pmatrix} \begin{pmatrix} t_1^e \\ t_N^e \\ \cdots \\ t_N^e \end{pmatrix} = \begin{pmatrix} Q_1^e \\ Q_2^e \\ \cdots \\ Q_N^e \end{pmatrix}, \quad (8)$$

i.e., $\sum_{j=1}^{N} K_{ij}^e t_j^e - Q_i^e = 0$ where $\mathrm{K}=[\mathrm{K}^e{}_{\mathrm{ij}}]_{\mathrm{N}\times\mathrm{N}}$ is an element stiffness matrix and $\mathrm{Q}=[\mathrm{Q}^e{}_{\mathrm{i}}]_{\mathrm{N}}$ represents a vector of fluxes through element faces.

Finally, we assemble the element systems into the global finite element model. To that goal, we use the balance of the inter-element fluxes and continuity of numerical solution in nodes, cf. Fig. 56.3. Due to the balance, the fluxes (right hand sides of the element linear systems) are cancelled on inter-element boundaries and they remain on the boundary of the whole domain. Due to the Dirichlet resp. Neumann BC we eliminate either unknowns or fluxes on the boundary and we get the global system of equations which is uniquely solvable.

56.4 Numerical Experiments by FEM

All experiments presented in this section were performed by FEM software ANSYS.

Our computational domain has been the space above Slovakia, represented by a series of triangular areas with maximal diameter 10 km, up to the height 200 km. On one spherical and four planar boundaries of Ω we consider the disturbing potential generated from EGM-96, see Lemione et al. (1996), and on the bottom boundary the gravity disturbances computed from actual gravities, see Klobušiak and Pecár (2004), are used. The results, tested by 61 GPS/leveled points, with different size of approximating triangles can be seen in Table 56.1 and in Fig. 56.4.

Table 56.1 Statistics of regional quasigeoidal solutions with different sizes of approximating triangles, residuals are between 61 GPS/leveling test's points and FEM solution. All characteristics are in [m]

Element size	10 km	8 km	7 km	5 km
Min. residual	0.276	0.316	0.253	0.226
Mean residual	0.556	0.566	0.503	0.459
Max. residual	0.781	0.809	0.706	0.684
St. deviation	0.101	0.102	0.092	0.094
St. dev. after fitting	0.075	0.069	0.062	0.057

56.5 Solution of the Mixed GBVP by FVM

Let us have $(n_1 \times n_2 \times n_3)$ discrete points, n_1 is spherical longitude's, n_2 spherical latitude's and n_3 is radial dimension. We embed this structure into

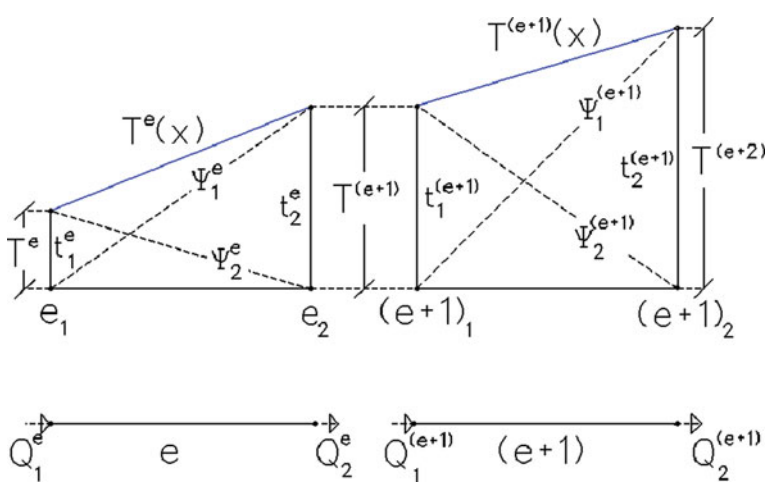


Fig. 56.3 Skeleton sketch of continuity of nodal values between two successive elements Ω^e and Ω^{e+1}, $t_2{}^e = t_1{}^{e+1}$ and balance of fluxes at their connecting nodes, $-Q_2{}^e = Q_1{}^{e+1}$

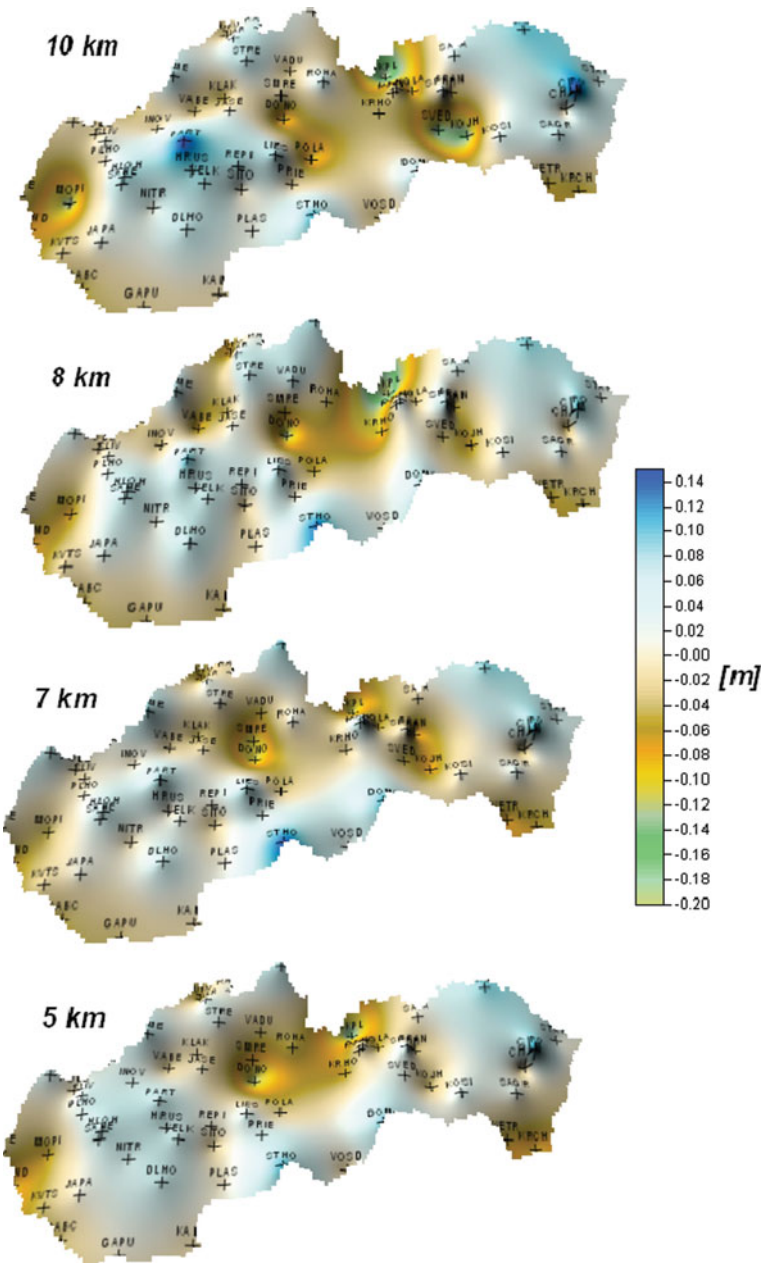


Fig. 56.4 GPS/leveling test, residuals after second order polynomial fitting

the finite volume mesh, where central point x_p of each volume is one of these discrete points, cf. Fig. 56.4. Then we denote common interface of two neighboring volumes p and q by e_{pq}. The measure of e_{pq} is labeled as $m(e_{pq})$ and the unit vector noral to e_{pq}, oriented from p to q is n_{pq}, and $d_{pq} = |x_p - x_q|$.

In order to derive discrete finite volume numerical scheme we apply Green theorem to the (1) to get local mass balance for every control volume p

$$-\int_p \Delta T \, dx\, dy\, dz = -\int_{\partial p} \nabla T \,.\, n \, d\sigma = -\int_{\partial p} \frac{\partial T}{\partial n} \, d\sigma, \tag{9}$$

and then we approximate numerically the normal derivative along the boundary of p. In such way we get from (9)

$$\sum_{q \in N_p} \frac{m(e_{pq})}{d_{pq}} (T_p - T_q) = 0, \tag{10}$$

where N_p is set of all neighbors q of p and $m(e_{pq})/d_{pq}$ is referred to as the transmissivity coefficient. More information about FVM can be found for instance in Eymard et al. (2003) and Mikula and Sgallari. (2003).

56.5.1 Numerical Scheme on Spherical Rectangular Grid

We restrict attention to specific situation depicted in Fig. 56.5 where we define indexes $i=1, \ldots, n_1$, $j=1, \ldots, n_2$ and $k=1, \ldots, n_3$ in the direction of the spherical longitude Λ, spherical latitude Φ and radial R, respectively. Then segments are: $h_1=(\Lambda_u-\Lambda_d)/n_1$, $h_2=(\Phi_u-\Phi_d)/n_2$ and $h_3=(R_u-R_d)/n_3$, where the index u denotes upper boundary and d the lower one in each direction with such notations. We can define the transmissivity coefficients $W_{i,j,k}$, $E_{i,j,k}$, $S_{i,j,k}$, $N_{i,j,k}$, $U_{i,j,k}$ and $D_{i,j,k}$ at the (west, east, south, north, upper and down) sides of the finite volume $p=(i, j, k)$

$$\begin{aligned} W_{i,j,k} &= E_{i,j,k} = \frac{h_2 h_3}{h_1}, \\ N_{i,j,k} &= S_{i,j,k} = \frac{h_1 h_3}{h_2}, \\ U_{i,j,k} &= \frac{h_1 h_2 (R_d + k h_3)^2}{h_3}, \\ D_{i,j,k} &= \frac{h_1 h_2 (R_d + (k-1) h_3)^2}{h_3}, \end{aligned} \tag{11}$$

as well as diagonal coefficients $P_{i,j,k}$,

$$P_{i,j,k} = W_{i,j,k} + E_{i,j,k} + N_{i,j,k} + S_{i,j,k} + U_{i,j,k} + D_{i,j,k}$$

Finally, with these definitions of the transmissivity coefficients we can write one row of the linear system in the form

$$\begin{aligned} &P_{i,j,k} u_{i,j,k} - W_{i,j,k} u_{i-1,j,k} - E_{i,j,k} u_{i+1,j,k} - S_{i,j,k} u_{i,j-1,k} - \\ &- N_{i,j,k} u_{i,j+1,k} - U_{i,j,k} u_{i,j,k+1} - D_{i,j,k} u_{i,j,k-1} = 0, \end{aligned} \tag{12}$$

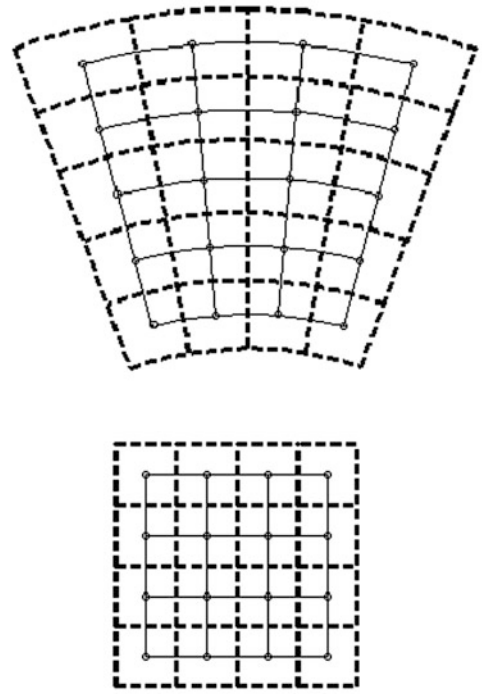


Fig. 56.5 Vertical and horizontal cut of the finite volume spherical rectangular grid ($n_1=4$, $n_2=4$, $n_3=5$)

Since matrix is sparse and diagonally dominant, the linear system can be solved by e.g. so-called SOR method.

56.6 Numerical Experiments by FVM

The experiment located in rectangle and bounded by spherical coordinates Φ: *(46.5, 50.5) degree* and Λ: *(15.5, 23.5) degree* included the Slovakia. Only spherical approximation of the Earth surface was used. The radius of lower boundary was chosen 6,371 [km] where actual gravities gained by detailed gravity mapping were applied. The radius of upper boundary was 7,300 [km].

Results can be seen in Table 56.2 and Fig. 56.6.

In comparison with FEM solution by means of ANSYS we have gained higher value of standard deviation, cf. Table 56.1, that can be caused by the spherical approximation of the Earth's surface.

Table 56.2 Statistics of quasigeoidal experiments in Slovak Republic using real gravity disturbances as Neumann BC

Element size [deg]	0.02×0.02
Min. res. [m]	0.212
Max. res. [m]	1.003
Mean res. [m]	0.613
St. deviation [m]	0.177
St. dev. after fitting [m]	0.080

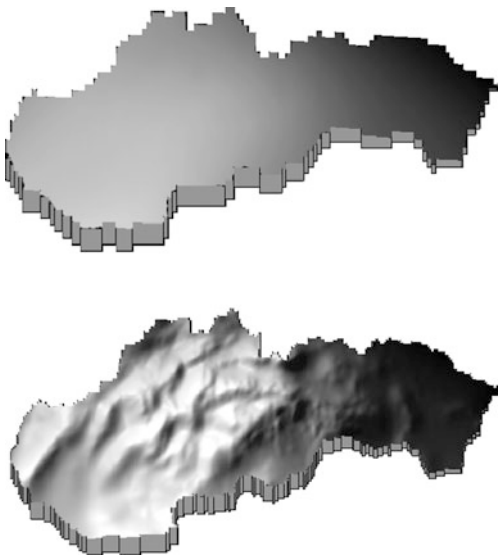


Fig. 56.6 Regional quasigeoidal model in area of Slovak Republic generated directly from EGM-96 and our solution using real gravity data and spherical rectangular grids with element's base $0.02° \times 0.02°$

56.7 Conclusions

The goal of this paper was to present new numerical methods to the solution of geodetic boundary value problems. We built the finite element and finite volume schemes that seek the numerical solution in 3D domains above Earth's surface, i.e., so we formulated GBVP in 3D domain and we have considered Neumann as well as Dirichlet BCs on different parts of the boundary. Consequently, full 3D solution was obtained directly. Our numerical methods were developed for spherical domains and in the case of FEM also for the part of boundary given by the real Earth's surface discretized by series of triangles. Our solutions were successfully verified by GPS/leveling test.

There are many new open questions and future tasks arising from this paper and probably the most important one is that our 3D FVM application deals only with spherical approximation of the Earth's surface. So, implementation including real Earth's surface discretization is a future challenge in order to improve the precision of the method.

Acknowledgement Authors gratefully thank to the financial support given by grant VEGA 1/3321/06, APVV-LPP-216-06 and APVV-0351-07.

References

ANSYS, online tutorial: www.ansys.com

Čunderlík, R., K. Mikula, and M. Mojzeš (2000). The boundary element method applied to the determination of the global quasigeoid. Proceedings of ALGORITMY 2000, pp. 301–308.

Čunderlík, R., K. Mikula, M. Mojzeš (2004). A comparison of the variational solution to the Neumann geodetic boundary value problem with the geopotential model EGM-96. *Contrib Geophys Geod* 34/3, 209–225.

Čunderlík, R., K. Mikula, and M. Mojzeš (2008). Numerical solution of the linearized fixed gravimetric boundary value problem. *J. Geod.,* 82(1), 15–29.

Eymard, R., T. Gallouet, and R. Herbin (2003). Finite volume methods. In: Handbook of Numerical Analysis, Elsevier 2000, pp. 713–1018.

Klees, R. (1992). Loesung des fixen geodaetischen Randwertprolems mit Hilfe der Randelementmethode. DGK. Reihe C., Nr. 382, Muenchen.

Klees, R. (1995). Boundary value problems and approximation of integral equations by finite elements. *Manuscripta Geodaetica*, 20, 345–361.

Klees, R. (1998). Topics on boundary element methods. Geodetic boundary value problems in view of the one centimeter geoid. Lecture Notes in Earth Sciences vol 65, Springer, Heidelberg, 482–531.

Klees, R., M. Van Gelderen, C. Lage, and C. Schwab (2001). Fast numerical solution of the linearized Molodensky prolem. *J. Geod.,* 75, 349–362.

Klobušiak, M. and J. Pecár (2004). Model and algorithm of effective processing of gravity measurements performed with a group of absolute and relative gravimeters. *GaKO*, 50/92(4–5), 99–110.

Lemione, F.G. et al. (1996). EGM-96 – The Development of the NASA GSFC and NIMA Joint Geopotetntial Model. http://cddis.gsfc.nasa.gov/926/egm96/egm96.html

Mikula, K. and F. Sgallari (2003). Semi-implicit finite volume scheme for image processing in 3D cylindrical geometry. *J. Comput Appl Math*, 161(1), 119–132.

Reddy, J.N. (1993). An introduction to the finite element method. 2nd ed. Mc Graw-Hill, Singapore.

Chapter 57

Quasi-Geoid of New Caledonia: Computation, Results and Analysis

P. Valty and H. Duquenne

Abstract The archipelago of New Caledonia is located in the Pacific Ocean, near the New Hebrides Trench. The gravity field is extremely rough in this area, free-air gravity anomalies varying from –230 to +200 mgal. Two vain attempts to compute a geoid model in 2000 and 2004 led the Territorial Government of New Caledonia to put IGN (French National Geographic Institute) in charge of a new calculation. Gravity data were provided by several institutions (Bureau Gravimétrique International, Institut de Recherches pour le Développement, Genavire, IGN) and were of various quality, so that data cleaning has been an important stage. Using the GRAVSOFT package, height anomalies have been computed by the residual terrain method combined with Stokes integration. By comparison of the quasi-geoid with levelled GPS points on the main island, accuracy has been estimated to be better than 9 cm, which shows a significant improvement with previous solutions. A grid to convert ellipsoidal heights into heights above mean sea level has been derived from the quasi-geoid and levelled GPS points. Its accuracy is about 4.5 cm. The shifts between vertical reference systems of principal islands of the archipelago have been determined. Differences between the geoid and the mean sea level at tide gauges, and their correlation with oceanic currents have also been studied and discussed in the paper.

P. Valty (✉)
IGN/LAREG, Champs sur Marne 77420, France
e-mail: pierre.valty@ign.fr

57.1 Introduction

The archipelago of New Caledonia is located in the Pacific Ocean, near the New Hebrides Trench. The gravity field is extremely rough in this area, due to these particularly huge oceanic trenches. Free-air gravity anomalies are for example varying from –230 to +200 mgal (Fig. 57.1).

The local organization DITTT (Direction des Infrastructures, de la Topographie et des Transports Territoriaux de la Nouvelle-Calédonie) charged first in 1999 the French ESGT (Ecole Supérieure des Géomètres et Topographes) to compute a first version of the quasi-geoid of New Caledonia. This computation (Duquenne, 2000) revealed gravimetric errors on the main island Grande-Terre. Through a new convention firmed in 2000 between the DITTT and the IGN (Institut Géographique National), it was decided to realize a new gravimetric campaign and a new version of the New-Caledonian quasi-geoid. The gravity measurements were entrusted to the IGN's SGN (Service de Géodésie et Nivellement) (IGN/SGN, 2003). During this time, the DITTT improved the quality of the GPS levelling points used for the determination of the grid of conversion between heights above the ellipsoid and altitudes.

Thus, a new version of the quasi-geoid of New-Caledonia has been computed in 2004 by the LAREG (Laboratoire de Recherche en Géodésie, Marne-la-Vallée, France) (Charpentier, 2004). The accuracy of results has been really improved since 2000, but several gravimetric data still remained

S.P. Mertikas (ed.), *Gravity, Geoid and Earth Observation*, International Association of Geodesy Symposia 135,
DOI 10.1007/978-3-642-10634-7_57, © Springer-Verlag Berlin Heidelberg 2010

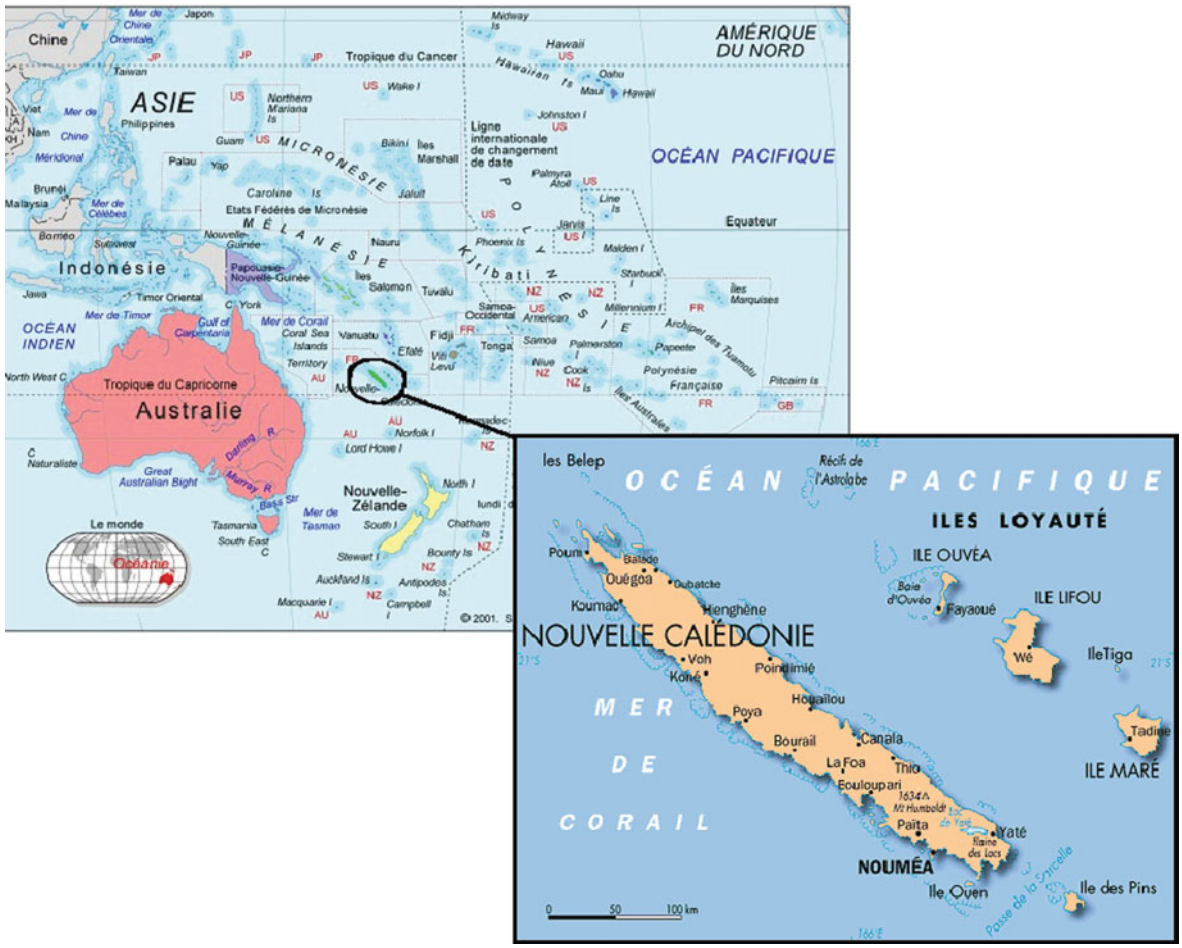


Fig. 57.1 Geographic situation of New Caledonia

problematic, specially in the Northern part of Grande-Terre.

At the hands of these difficulties, the DITTT charged the BGI (Bureau Gravimétrique International) to analyse the gravimetric data used for this computation (coming from measurements realized in the seventies and eighties). They concluded that gravimetric data should suffer from errors due to a default during the measurement processing. Thus, the BGI provided corrected gravimetric data for New-Caledonia (Sarrailh, 2006).

With these corrected data, the LAREG proceeded to the computation of a new quasi-geoid QGNC08 and of a grid to convert ellipsoidal heights into heights above mean sea level named RANC08.

57.2 Preparation and Validation of Gravity Data

57.2.1 Preparation of DTM (Digital Terrain Models)

DTM for New-Caledonia has been realized by merging the DTM from the IGN's "BD ALTI" with the DTM coming from "Shuttle Radar Topography Mission". Large step DTM and filtered DTM, used for computation, have been derived from the main DTM by using TCGRID (a module from Gravsoft package (Tscherning et al., 1992) used to make a low-scaled DTM from an accurate one).

57.2.2 Validation of Marine Gravity Data

As far as validation of gravity data is concerned, we can separate marine and terrestrial data.

The first ones come from the IRD (Institut de Recherche pour le Développement) and from the BGI. The gravity measurements of the IRD were conducted by the company GENAVIRE by means of four dedicated campaigns. On the other hand, BGI provided data from several campaigns.

The quality of marine data, coming from the IRD and from the BGI, is quite heterogeneous, so we had to be very careful for selecting the best gravity points. Two main strategies were used to clean them:

- comparison of free-air gravity anomalies in all cross-road points between each boat campaigns (by pairs). Any profile showing a difference of free-air anomalies greater than 10 mgal on three or more cross-road points was removed.
- comparison of free-air anomalies of each campaign with the interpolated free-air anomalies given by the Sandwell and Smith grid (Sandwell and Smith, 1997). We deleted any point far enough from the coast with a 60 mgal or more difference with the anomaly of the grid, and any profile with a standard deviation of the differences higher than 10 mgal (Fig. 57.2).

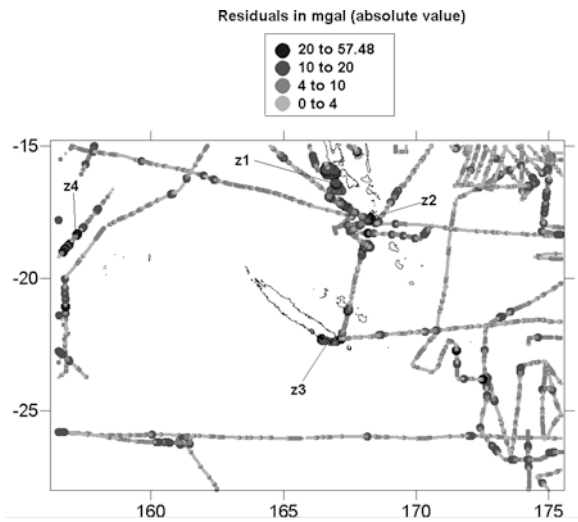


Fig. 57.2 Detection of raw gravity errors for all BGI campaigns (see legend above) Axes: latitude and longitude in degrees

For these procedures, we used two programs developed by Henri Duquenne (divcrois and ACDG).

Finally, between 5 and 20% of marine gravity data were deleted. Some gravity campaigns like IGN1 produced by GENAVIRE had 20% of removed gravity points.

57.2.3 Validation of Terrestrial Gravity Data

As far as the terrestrial gravimetric data are concerned, they come from three organizations:

- IRD (Institut de Recherche et Développement, France) with nearly 2,400 points
- BGI with 632 points
- IGN's SGN (Service de Géodésie et Nivellement): the gravity campaign was carried out in 2003 and provided 114 very high-quality gravity measurements. Thus, these new data should be taken as reference if any conflict with other campaign would appear, as we are sure of their accuracy.

The validation of terrestrial gravity data has been performed by comparison of gravity residual anomalies between the three main providers. To this end, we used some programs of Gravsoft package (such as CNVG, TC, GGM and GgridPlus). The main discrepancies came from the IRD points. Nearly 300 points from this gravity database had to be deleted (specially in the areas named z1 and z2 in Fig. 57.3). In contrast, BGI and SGN data were clearly consistent together.

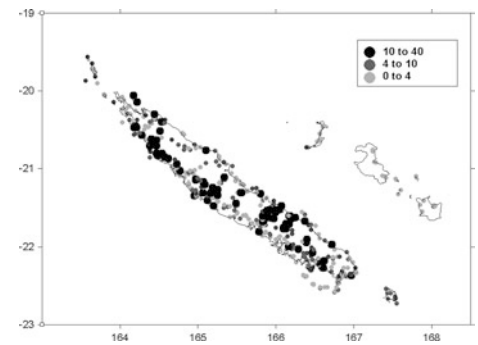


Fig. 57.3 Residuals obtained on the IRD gravimetric points, compared with the SGN and BGI data (unit: mgal): latitude and longitude in degrees

The validation of data is a step of great importance. As a matter of fact, we wanted to be sure that errors made during the two last computations would not be repeated. For example, most of the gravity data used for the computation performed in 2004 had been provided by IRD, and the quality of some of these points appears here as a bit suspicious.

57.3 Computation of Quasi-Geoid

57.3.1 Quick Explanation of the Computation

Computation of quasi-geoid has been performed using the remove-and-restore method, with the package Gravsoft (Tscherning et al., 1992) and some other programs developed by the LAREG. We used as a global field model EIGEN-GL04C. The final quasi-geoid grid has got the following characteristics:

- latitude: 24° South to 19° South
- longitude: 160° East to 172° East.
- sampling: 0.01° (in latitude and in longitude).

57.3.2 Test of FFT (Fast Fourier Transform) Strategy to Compute Stokes Integral

The computation of the quasi-geoid model gave us the opportunity to test the 1D spherical FFT method to compute Stokes' integral. Indeed, this method had been successfully tested under the area "Auvergne" (in France). We wanted to investigate whether the 1D-FFT integration would be able to replace the usual method (numerical integration) in the IGN's processus of geoid computation.

The residual geoid ondulation is calculated using Stokes' integral

$$\mathrm{N} = \frac{4}{4\pi\gamma}\int_{\sigma}\Delta g S(\psi)d\sigma$$

The integral is currently calculated through a numerical integration:

$$N(\varphi_1,\lambda) = \frac{R}{4\pi\gamma}\sum_{m=0}^{N-1} \times\left[\sum_{n=0}^{N-1}\Delta g(\varphi_m,\gamma_n)\cos(\varphi)S(\psi)\Delta\lambda\right]\Delta\varphi$$

Where

N is the residual height anomaly at point of latitude and longitude(φ_l,λ_k)
R is the geocentric distance of the computation point
γ is the value of the normal acceleration of gravity at the same point
Δg is the value of the residual free-air gravity anomaly at the integration point of latitude and longitude(φ_m,λ_n)
S(ψ) is Stokes' function given for the angle ψ

$$S(\psi) = \frac{1}{\sin(\psi/2)} - 6\sin(\psi/2) + 1 - 5\cos(\psi) - 3\cos(\psi)\ln(\sin(\psi/2) + \sin^2(\psi/2)$$

with ψ the angle between the computation point and the integration point

$$\psi = \arccos(\sin)(\varphi_1)\sin(\varphi_m) + \cos(\varphi_1)\cos(\varphi_m)\cos(\lambda_n - \lambda_k))$$

N can be also expressed using Fast Fourier Transform (Haagmans et al., 1993):

$$N(\varphi_1,\lambda_k) = \frac{R}{4\pi\gamma}F^{-1} \times\left[\sum_{m=0}^{N-1}F(\Delta g(\varphi_m,\gamma_k)\cos(\varphi_1)F(S\psi))\right]$$

where F is the FFT operator and F^{-1} the inverse FFT operator.

Using program SP1d from Gravsoft Package (Tscherning et al., 1992), we tested several options so as to get the best results for height anomalies. The main advantage of FFT is that computation time is much reduced. Since it is theoretically an exact method, the results given are exactly the same than the results obtained by the numerical method (Haagmans

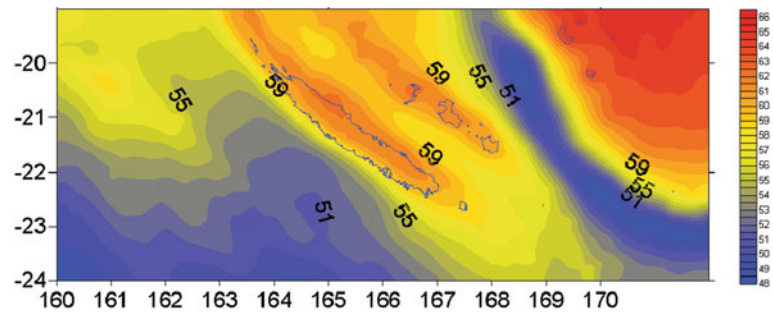


Fig. 57.4 Quasi-geoid QGNC08 (unit: m). Axes: latitude and longitude in degrees

et al., 1993). We just should be careful to use the good options (size of the kernel for example).

Results were successful: for the same area, the same residual anomalies can be determined with a computation time divided by nearly 100. Thus, this method was chosen to compute quasi-geoid (Fig. 57.4)

57.3.3 Evaluation of the Quality of Geoid Model and Computation of a Grid to Convert Ellipsoidal Heights into Altitudes

The last step in the computation consisted in realizing a grid to convert ellipsoidal heights (given by GPS) into altitudes. To obtain this grid from the computed quasi-geoid, we have to take into account the 2500 GPS levelling points recently corrected by the DITTT.

First, we have to determine the trend of the height anomaly of these GPS levelled points. One of the possible origins of this trend is the existence of a systematic error on the levelling network. For this purpose, we select about 2,200 of these 2,500 points. A first step consists in deleting some suspicious points (residuals of more than 15 cm). The standard deviation of these residuals is considered as the precision of the quasi-geoid: 11 cm on the archipelago and 9.7 cm on the main island "Grande-Terre" (Fig. 57.5).

The residuals can be separated into two parts: signal and noise (Figs. 57.6 and 57.7).

It is then possible to compute a grid of the signal on these GPS levelled points by means of kriging interpolation method. This grid is added to quasi-geoid grid (they must have exactly the same characteristics) to produce our conversion grid. The quality of

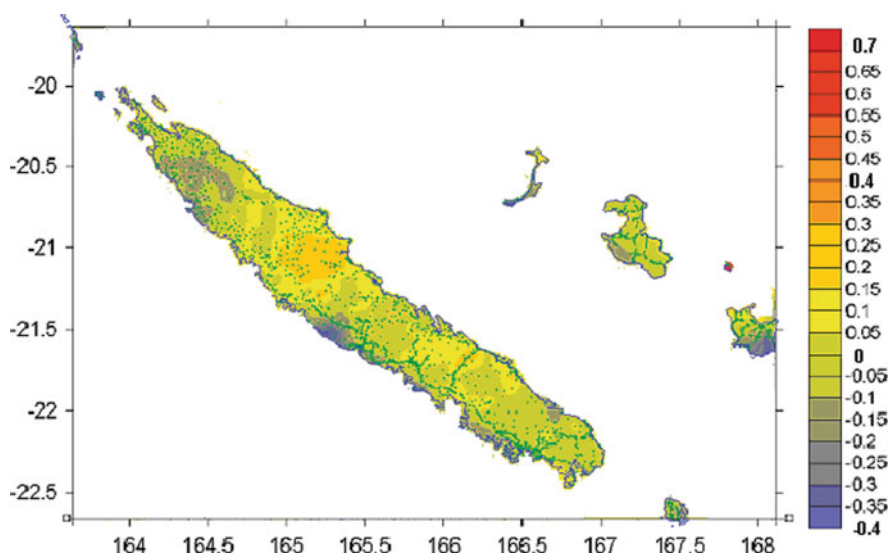


Fig. 57.5 Residuals obtained between GPS levelled points and quasi-geoid QGNC08, after having removed the main trend (unit: m). Axes: latitude and longitude in degrees

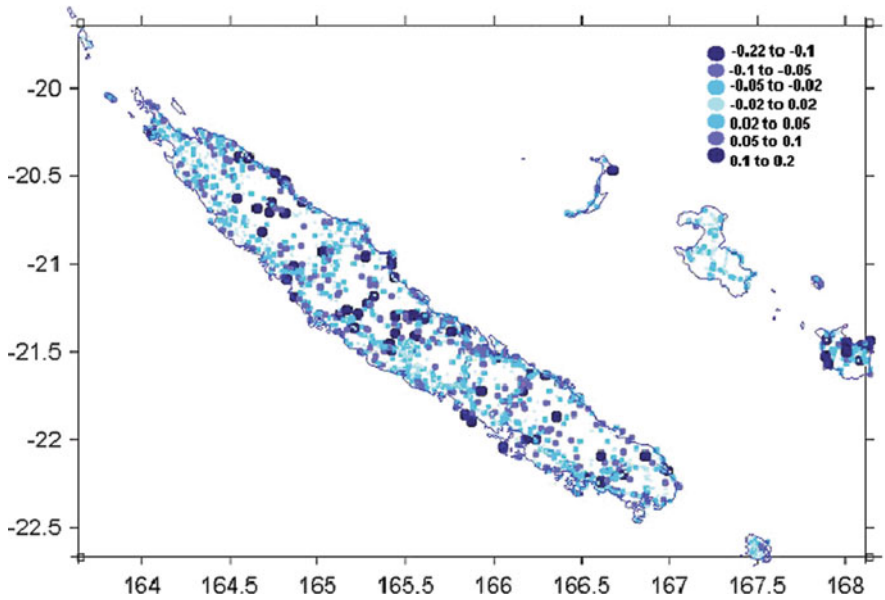


Fig. 57.6 Noise obtained on GPS levelled points (unit: m). Axes: latitude and longitude in degrees

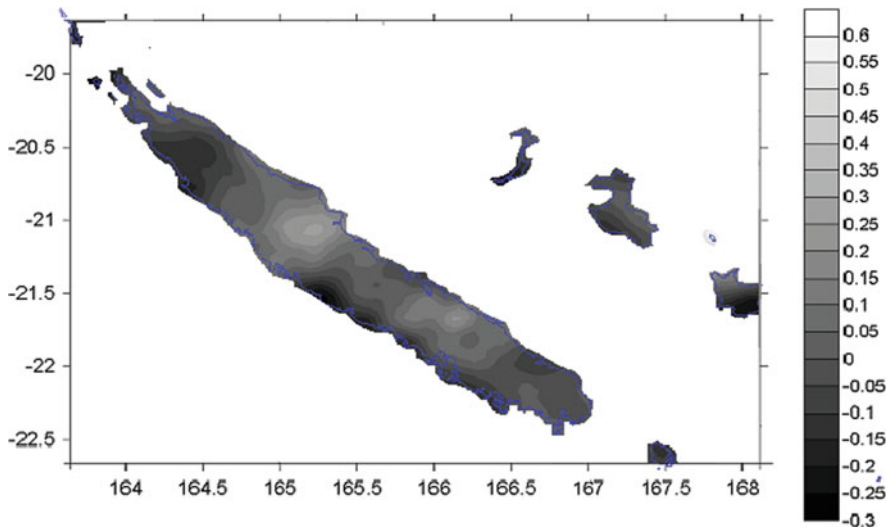


Fig. 57.7 Map of signal on GPS levelled points compared to QGNC08 (unit: m). Axes: latitude and longitude in degrees

this one can be evaluated by the comparison to the height anomaly obtained on the 311 other GPS levelled points (Fig. 57.8). The standard deviation of the residuals between the grid and these control points can be considered as the precision of the grid. Thus, the precision of the grid of conversion is of 4.5 cm. This is a main figure, because it will be this grid (and not specially the quasi-geoid) which will be applied by users.

57.3.4 Differences and Improvement Compared to Former Quasi-Geoid Determinations

To evaluate the quality of new quasi-geoid model, we analyzed the difference of heights between 2008's computation and 2000 and 2004's computations (Fig. 57.9).

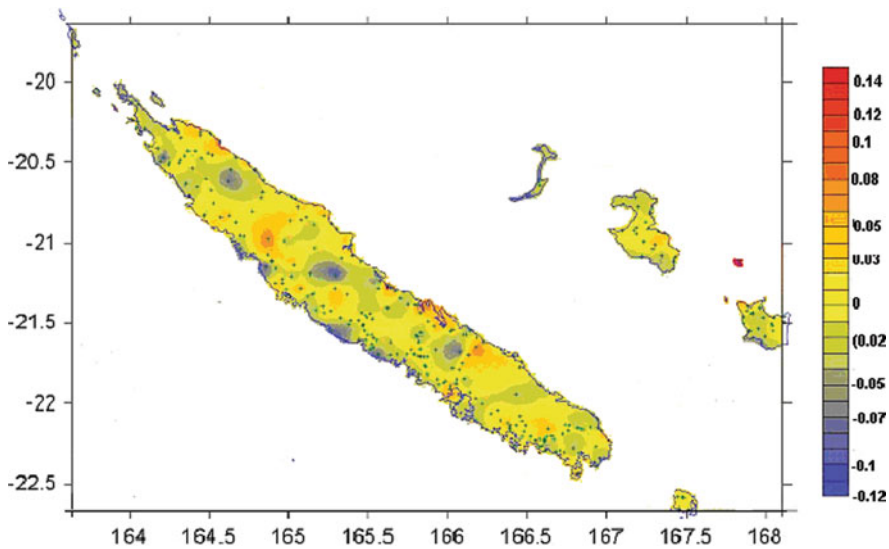


Fig. 57.8 Residuals obtained between GPS control points and grid RANC08 (unit: m). Axes: latitude and longitude in degrees

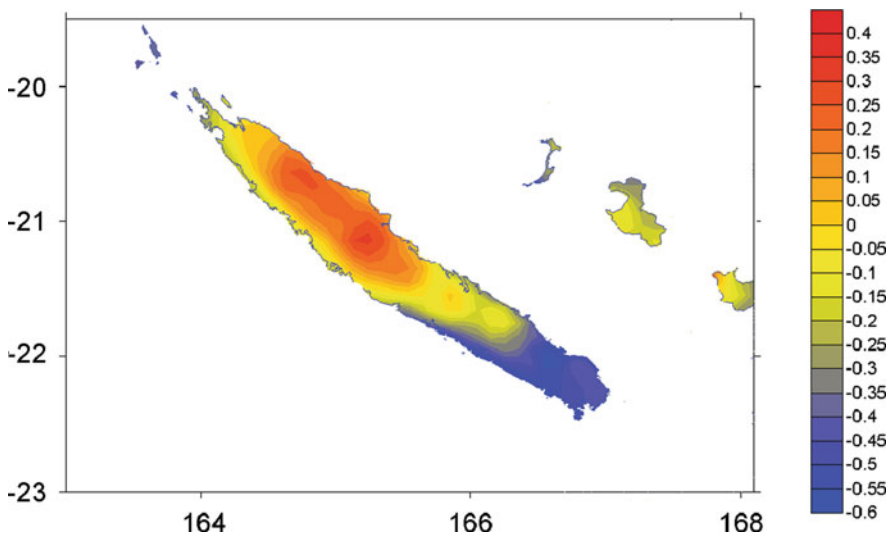


Fig. 57.9 Differences between QGNC08 and QGNC00 (unit: m). Axes: latitude and longitude in degrees

Table 57.1 Main statistics for geoid computations in 2000, 2004 and 2008

Year	Island	Precision of geoid(cm)	Precision of conversion grid(cm)	Bias
2008	Whole archipelago	11.1	4.1	1.114
	Grande-Terre	9.7	4.2	1.33
2004	Whole archipelago	14		0.664
	Grande-Terre	11.9		0.602
2000	Whole archipelago	14.5		0.833
	Grande-Terre	11.7		0.91

The analysis of these differences indicates that the amplitude of differences is of 80 cm between 2008 and 2004's computation and of around 1 m between 2008 and 2000's computations.

The data on Table 57.1 point out the improvement of accuracy of the geoid between 2000 and 2008. The precision of the reference grid was not computed in 2000 and 2004.

57.4 Analysing the Difference Between the Geoid and the Mean Sea Level Measured at Tide Gauges

57.4.1 Context and Main Issues

The SHOM (Service Hydrographique et Océanique de la Marine, France) published the height differences between the altitude system and the mean sea level measured at around fifteen tide gauges on the main island.

By definition, the geoid is the equipotential surface which would coincide with the mean ocean surface. In order to assess the quality of our quasi-geoid model, the difference of heights between the quasi-geoid and the mean sea level are computed.

The surface of quasi-geoid is not actually overlaid with the mean sea level, as shown on Fig. 57.10.

A possible method to interpret these differences (a 1 m bias was added to a 80 cm amplitude) can be to study the correlation between the height of quasi-geoid above the mean ocean level, the mean surface temperature of the ocean between 1993 and 2005 and the mean direction of oceanic surface streams (provided by the IRD of New Caledonia). The data (the mean temperature and the oceanic currents) are not available closer than 50 or 100 km from the coast.

57.4.2 Correlation with the Temperature

The first step consisted in an extrapolation of the mean surface oceanic temperature in a ring of about 10–20 km width around Grande-Terre. The correlation between the temperature and the height differences between quasi-geoid and mean sea level was computed inside this ring (Fig. 57.11).

The correlation coefficient was of 0.63. It means that when the ocean is colder, the quasi-geoid is much higher above the mean sea level. It is easy to notice that for example all around the North-Coast, the ocean is hotter but the mean sea level is higher compared to the quasi-geoid.

57.4.3 Possible Correlation with Oceanic Currents

It can be noticed that an important oceanic current is coming from the North-West of Grande-Terre. Its amplitude rises while it is running along the North coast.

Two main parameters should be considered in order to find an efficient method to evaluate the correlation between stream and mean sea level/geoid's height. Two main parameters should be taken into account: on one hand, the direction of the stream compared to

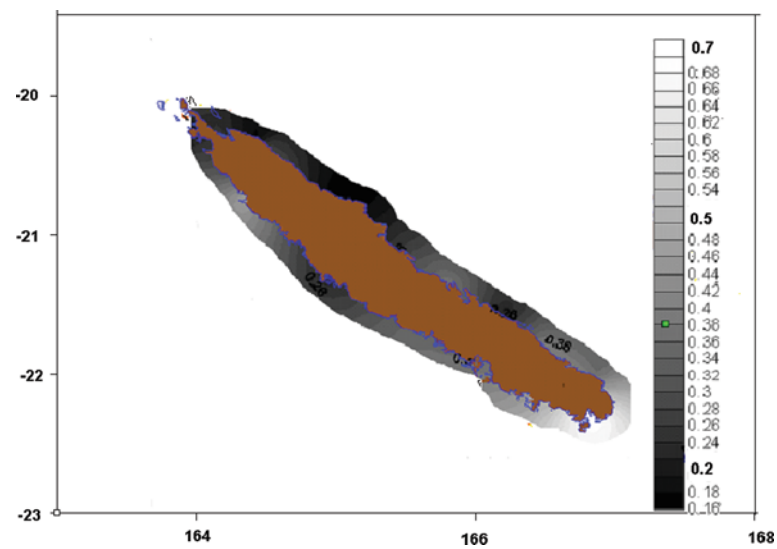


Fig. 57.10 Differences in meters at tide gauges between quasi-geoid QGNC08 and mean sea level (unit: m). Axes: latitude and longitude in degrees

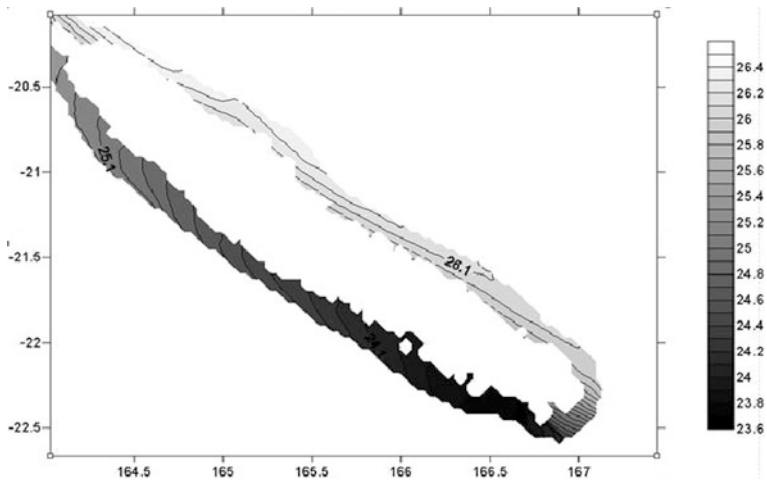


Fig. 57.11 Area of selection for the main water temperature and the quasi-geoid heights in order to compute the correlation with data of Fig. 57.11 (unit: m). Axes: latitude and longitude in degrees

the main orientation of Grande-Terre (North-West to South-East), on the other hand, the amplitude of the stream.

57.5 Conclusion

The computation of a new quasi-geoid (the third) permitted us to test several new methods, specially in order to improve geoid's computation procedure in expectation of the calculation of the new French quasi-geoid planned for 2009. For instance, computation of Stokes integral by using 1D FFT will be incorporated to the geoid computation procedure.

Improving the quality of the quasi-geoid of New Caledonia was rather tricky, due to the heterogeneity of gravity data. But thanks to a drastic data cleaning and to the work of the BGI we managed to get an improved quality for the new version of the quasi-geoid of New-Caledonia QGNC08.

Acknowledgements We are grateful to Jérôme Verdun for his careful reading of this paper.

References

Charpentier, L. (2004). Calcul du quasi-géoïde gravimétrique de Nouvelle-Calédonie. Rapport de stage, ESGT et IGN/LAREG.

Duquenne, H. (2000). Un modèle de quasi-géoïde et une grille de conversion altimétrique pour la Nouvelle-Calédonie. Technical report, Ecole Supérieure des Géomètres et Topographes, Le Mans, France.

Haagmans, R., E. de Min, and M. van Gelderen (1993). Fast evalutaion of convolution integrals on the sphere using 1D FFT, and a comparison with existing methods for Stokes' integral. *Manuscripta Geodaetica*, 18(5), 227.

IGN/SGN (2003). Campagne de mesures gravimétriques du territoire de Nouvelle Calédonie. Tech. report, Institut Géographique National.

Sandwell, D.T. and W.H.F. Smith (1997). Marine gravity anomaly from Geosat and ERS1 satellite altimetry. *J. Geophys. Res.*, 102(B5), 10039–10054.

Sarrailh, M. (2006). Validation des données gravimétriques de Nouvelle Calédonie. Rapport technique, Bureau Gravimétrique International.

Tscherning, C., R. Forsberg, and P. Knudsen (1992). The GRAVSOFT package for geoid determination. In: Proceeding of the First Continental Workshop on the Geoid in Europe, Research Institute of Geodesy, Topography and Cartography, Prague, Czech Republic

Chapter 58

Assessment of a Numerical Method for Computing the Spherical Harmonic Coefficients of the Gravitational Potential of a Constant Density Polyhedron

O. Jamet, J. Verdun, D. Tsoulis, and N. Gonindard

Abstract This study focuses on the assessment of a linear algorithm for computing the spherical harmonic coefficients of the gravitational potential of a constant density polyhedron. The ability to compute such an expansion would favor several applications, in particular in the field of the interpretation and assessment of GOCE gravitational models. The studied algorithm is the only known method that would achieve this computation at a computational cost depending linearly on the number of computed coefficients. We show that although this methods suffers from severe divergence issues, it could be applied to retrieve band-limited estimates of the potential generated by a constant density polyhedron.

58.1 Introduction

Constant density polyhedra provide a versatile representation of whole planetary bodies as well as density discontinuities inside a planet at any scale. This representation allows the exact computation of the gravitational potential of such features through well known analytical formulas (Barnett, 1976; Petrović, 1996; Pohánka, 1988). These formulas yield the potential value at any computation point, providing that their singularities are properly managed (Tsoulis and Petrović, 2001). Applications range from the accurate computation of the terrain effect (Tsoulis, 2001) to the modelling of the gravitational field of small planetary bodies (Simonelli et al., 1993; Werner and Scheeres, 1996). Such analytical computations show two major drawbacks. First, the computation is pointwise: one single computation yields the potential or its directional derivatives at a single computation point. The computation might become highly tedious as the number of computing locations increases. Secondly, in the context of some specific applications, one might seek for a band-limited estimate of the potential, which cannot be obtained through these analytical formulas.

In the context of the forthcoming GOCE satellite, we are here interested in numerical methods for computing the spherical harmonic expansion of the gravitational potential of a constant density polyhedron. A direct computation of such an expansion from the geometry of the polyhedron would provide on the one hand a band-limited estimate of the potential that would be directly comparable to GOCE derived potential models, and on the other hand a fast access to the value of this band-limited potential at a large number of locations. Such a tool would enhance the interpretation of GOCE data, allowing to remove the signal from known features (topography, local geological models, etc.) from GOCE derived gravitational models at chosen wavelengths. When the density of the body can be described as a function of the direct distance to its geometric center, the computation of the spherical harmonic expansion of its potential admits some numerical (Chao and Rubincam, 1989) or even analytical (Balmino, 1994; Martinec et al., 1989) solutions. In the case of the general polyhedron, no closed formulation is known. We are aware of two numerical methods, proposed by Werner (1997), and Jamet and Thomas (2004). Both rely on recursion relationships. The quadratic complexity of Werner's method

O. Jamet (✉)
Laboratoire de Recherche en Géodesie, IGN, Saint-Mandé 94160, France
e-mail: Olivier.Jamet@ign.fr

S.P. Mertikas (ed.), *Gravity, Geoid and Earth Observation*, International Association of Geodesy Symposia 135,
DOI 10.1007/978-3-642-10634-7_58, © Springer-Verlag Berlin Heidelberg 2010

makes it only applicable to very low degrees. The method by Jamet and Thomas is of linear complexity with respect to the number of computed coefficients and the number of edges of the polyhedron. It has never been numerically implemented yet. We focus here on the assessment of Jamet and Thomas's algorithm. The implementation was adapted in order to work with fully normalized spherical harmonics, as defined by Heiskanen and Moritz (1967, p. 31). In Sect. 58.2, we restrict ourselves to a brief presentation of the principles of the method. Then, in Sect. 58.3, we present some numerical experiments that underline the strenghts and weaknesses of the proposed method. Finally, in Sect. 58.4, we comment on the possible applications of this algorithm.

58.2 Algorithm

The spherical harmonic expansion of the gravitational potential of any finite body can be written as

$$V(r,\theta,\lambda) = \frac{GM}{r}\left\{1 + \sum_{n=1}^{+\infty}\sum_{m=0}^{n} V_{n,m}(r,\theta,\lambda)\right\}$$

with

$$V_{n,m}(r,\theta,\lambda) = c_{n,m}R_{n,m}(r,\theta,\lambda) + s_{n,m}S_{n,m}(r,\theta,\lambda) \quad (1)$$

where (r,θ,λ) are the spherical coordinates of the considered point (radius, co-latitude and longitude), G the gravitational constant, M the mass of the body, $R_{n,m}$ and $S_{n,m}$ are the irregular solid harmonics, defined here as

$$R_{n,m}(r,\theta,\lambda) = \left(\frac{a}{r}\right)^n P_{n,m}(\cos\theta)\cos(m\lambda)$$
$$S_{n,m}(r,\theta,\lambda) = \left(\frac{a}{r}\right)^n P_{n,m}(\cos\theta)\sin(m\lambda)$$

with a being an arbitrary length greater than the longest radius including the attracting sources. In this expression, $c_{n,m}$ and $s_{n,m}$ are the coefficients of the expansion to be computed. These coefficients, like their normalized counterparts, can be written as a volume integral defined over the whole body (Heiskanen and Moritz, 1967). When the body is of constant density, this volume integral writes

$$c_{n,m} = k_{n,m}^{(c)} \iiint_{Q\in body} h_{n,m}^{(c)}(Q)\,dv$$
$$s_{n,m} = k_{n,m}^{(s)} \iiint_{Q\in body} h_{n,m}^{(s)}(Q)\,dv$$

where dv is the volume element, $h_{n,m}^{(c)}$ and $h_{n,m}^{(s)}$ are the regular solid harmonics

$$h_{n,m}^{(c)}(r,\theta,\lambda) = \left(\frac{r}{a}\right)^n P_{n,m}(\cos\theta)\cos(m\lambda)$$
$$h_{n,m}^{(s)}(r,\theta,\lambda) = \left(\frac{r}{a}\right)^n P_{n,m}(\cos\theta)\sin(m\lambda)$$

while $k_{n,m}^{(c)}$ and $k_{n,m}^{(s)}$ are constants depending on the degree n, the order m and the density of the body. Jamet and Thomas's method relies on the following principles. Firstly, the polyhedron is decomposed into simplices originating at the origin of the coordinate system. The volume integral over each simplex is then converted into a surface integral over the corresponding planar face of the polyhedron by using the divergence theorem of Gauss. So far, this procedure is much similar to the methods for exhibiting analytical formulas of the potential, as the one used for instance by Petrović (1996). Applying the Stokes theorem to the surface integral yields then a recurrent relationship between the surface integrals of same order m and of consecutive degree n, from which one gets

$$c_{n,m} = \alpha_{n,m}c_{n-1,m} + \sum_{e\in edges} \beta_{n,m}^{e} \int_{Q\in e} h_{n,m}^{(c)}(Q)\,dl \quad (2)$$

$$s_{n,m} = \alpha_{n,m}s_{n-1,m} + \sum_{e\in edges} \beta_{n,m}^{e} \int_{Q\in e} h_{n,m}^{(s)}(Q)\,dl \quad (3)$$

where the line integrals are computed along each edge of this planar face, and where $\alpha_{n,m}$ and $\beta_{n,m}^{e}$ are constants depending on geometry of the handled planar face, its edges, and on degree n and order m. In particular Jamet and Thomas (2004) show that

$$\alpha_{n,m} = A(n,m)\,\frac{d}{\mathbf{u}_z.\mathbf{n}} \quad (4)$$

where $A(n,m)$ is a constant depending on degree and order, d is the distance from the origin of the frame to the plane of the face, $\mathbf{n}$ the unit vector normal to the face, and $\mathbf{u}_z$ the unit vector of the z axis of the frame. The line integrals themselves are expressed through a complex set of recurrent relationships that will not be exposed here. The complete set of relationships as well as their derivation can be found in Jamet and Thomas (2004). Similar relationships can be obtained for the

normalized spherical harmonic coefficients. The experiments presented in the following make use of the latter formulation.

$$\mathbf{G} = \begin{bmatrix} -2 & -1 & 1 \\ 1 & 0 & 1 \\ 0 & 1 & 1 \\ 0 & 0 & 0 \end{bmatrix}, \mathbf{H} = \begin{bmatrix} 1 & 2 & 3 \\ 1 & 4 & 2 \\ 3 & 4 & 1 \\ 2 & 4 & 3 \end{bmatrix}. \quad (5)$$

58.3 Assessment

In order to numerically evaluate the linear algorithm for the computation of polyhedral potential spherical harmonic coefficients, we set up a simple case study consisting of a single tetrahedron of constant density and compare the potential computed from its spherical harmonic expansion to the direct computation with closed analytical formulas (Petrović, 1996). This tetrahedron is the same test body as the one used by Werner (1997).

The geometry of the tetrahedron is shown in Fig. 58.1. Each of the four vertices is given by means of its coordinates relative to a local orthogonal reference frame. The origin of the reference frame has been arbitrarily chosen as one of the four vertices. Besides vertex coodinates, the implementation of the linear algorithm requires the knowledge of the vertex topology given as an extra topology matrix with the precondition that the normal vector to each corresponding face will point outside of the tetrahedron. Thus, the two matrices defining respectively the coordinates of the four vertices and their linkage are the following

Another important parameter in the numerical experiments is the location of the computation point. The expression of the potential in a spherical harmonic expansion implies that the numerical behavior of the series is essentially governed by the powers of the ratio of radii r_P/r_P where P corresponds to the observation point and Q is a point of the attracting source. It has been theoretically argued that when $r_P > r_Q$, the series converges for all points located outside a sphere enclosing all masses; for $r_P < r_Q$, the convergence area is again a sphere, such that the attracting masses are nowhere included or intersected (Tsoulis, 1999). The consequence for the numerical computation of the potential from its spherical harmonic expansion is that a higher degree of expansion using better precision spherical harmonic coefficients is needed for points located close to the attracting source. One should expect conversely that a small number of spherical harmonic coefficients would be sufficient for reaching the same agreement with the analytical value of the potential when the computation point is located at a large distance from the source. As a result, the best point for performing a numerically significant test of the linear algorithm has to be chosen within the convergence area

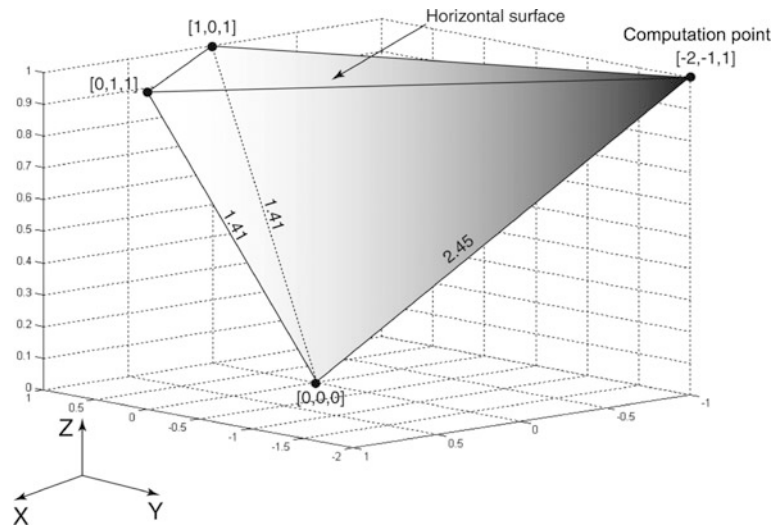


Fig. 58.1 Constant density tetrahedron (5.52 g/cm^3) taken as the attracting source in our numerical experiments. In this case, the *upper face* of the tetrahedon is *horizontal*. The farthest point from the origin has been taken as the computation point

as close as possible to the source. Thus, the computations in our numerical experiments took place at point [– 2, – 1,1] of the source tetrahedron where the convergence condition of spherical harmonic series is still satisfied.

Finally, like in Werner 1997, the constant density of the tetrahedral source was chosen equal to 5.52 g/cm^3, which corresponds to an average density value of the Earth's masses.

58.3.1 Case of Non Horizontal Faces

It should be noticed considering the geometry of the tetrahedron used in our experiments that the face formed by vertices numbered 1, 2, and 3 is horizontal, that is parallel to the *xy* plane of the reference frame. We wanted to investigate in detail whether such a geometry is too much specific and might hide some inherent numerical instabilities when used in the linear algorithm.

The first experiment we carried out for this reason consisted in calculating the potential values provided by the tetrahedra resulting from a rotation around the *x* axis of the above-mentioned tetrahedron. The potential values were compared to those obtained from a direct computation using closed analytical formulas and the results of the comparison are given in Fig. 58.2. It is clear from this figure that the convergence of the series is ensured when the face of the tetrahedron opposite to the origin is horizontal, which occurs for rotation angles equal respectively to 0° and 180°. Conversely, for small rotation angles (< 35° or > 135°) the convergence can be only observed at low degrees (< 25). For high rotation angles, the divergence immediately occurs except when the tetrahedron face is vertical. In this latter case, specific recursion formulas are used, that do not show the same instabilities.

It is likely that the numerical instabitity observed for a tetrahedron with a tilted face is due to the expression of the recursion fomulas used to calculate the coefficients (Eqs. 2 and 3). To put it more precisely, spherical harmonic coefficients of degree n are related to those of degree $n-1$ by the multiplicative factor $\alpha_{n,m}$ in inverse proportion to the cosine of the angle between the outer normal of the tetrahedron face $\mathbf{n}$ and the unit vector $\mathbf{u}_z$ of the z axis of the reference frame (Eq. 4). This factor increases appreciably when the tilt angle of the tetrahedron face increases, thus causing an exponential growth of the error propagated upon coefficients for increasing degrees. Other possible causes of instabilities that are not discussed here where identified in the recursion process for the computation of the line integrals (unpublished work). They are linked with the coordinates of the leading unit vector of the edges of the tetrahedron and might explain the dissymetry of Fig. 58.2 around the rotation angle 90°.

To cope with this instability, an alternative means for computing any tetrahedral source contribution would be to perform the computation in suitable reference frames where the faces involved in the recursion computation remain always horizontal. This method is theoretically justified by the fact that the potential value does not depend on the reference frame used to

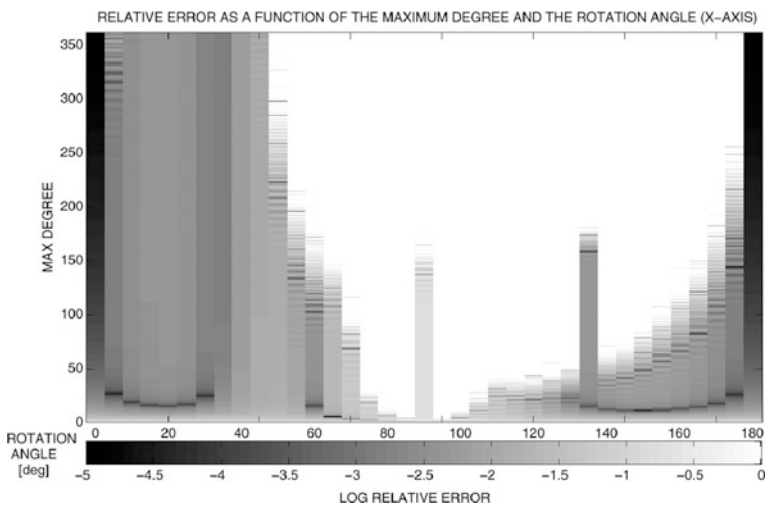


Fig. 58.2 Potential relative error as a function of both the rotation angle and the maximum degree of the spherical harmonic expansion. *White* indicates when the relative error is greater than 100%

locate the attracting source and the computation point. From now on, tetrahedral sources with one horizontal face will be only considered.

58.3.2 Precision in Coefficient Computation

For the purpose of estimating the precision in spherical harmonic coefficient computation by means of the linear algorithm, a computational method to determine the coefficient relative errors was devised and experimented with our case study. Figure 58.3 shows the relative errors affecting the coefficients, obtained by running the linear algorithm with a random perturbation of the last significant digit of all constant inputs at each step of the recursion and by comparing the results with a computation without perturbation. When using the linear algorithm, the coefficients are calculated vertically from the diagonal by increasing the degree at constant order. The figure indicates that the linear algorithm is stable when the degree increases except near the diagonal where degree and order are similar. The algorithm becomes stable again when the degree n and the order m satisfy $n > 1.8\,m$.

The maximum degree of the reachable spherical harmonic expansion by means of the linear algorithm can be increased by enlarging the range of the floating-point representation used in the computation. However, once the recursion formulas have become divergent, the coefficient values can no longer be recovered. This is the main limitation inherent to the linear algorithm, which means that some additional procedures should be needed to make the linear algorithm usable in practice at very high degrees.

58.3.3 Divergence Control

The last numerical experiment was intented to test the convergence of the linear algorithm for increasing spherical harmonic expansion degrees. Figure 58.4 shows the relative errors of the cumulated potential as a function of the maximum spherical harmonic degree. These errors have been calculated by comparing the values of the potential provided by the spherical harmonic series deduced from the linear algorithm and those calculated by means of close analytical formulas, thus giving the accuracy of the potential spherical harmonic series for each maximum degree of expansion. The same computation has been carried out with removal of all the coefficients that exhibit a formal relative error greater than 10^{-6} as calculated through the method described in Sect. 58.3.2. The potential spherical harmonic series has proven to actually converge up to degree 600. The divergence that occurs afterwards is outstanding, following a quasi-exponential growth of the error as the degree increases. The convergence which is obtained, on the other hand, after removing the less precise coefficients is nicely preserved up to degree 1,400 where the relative error of the potential determination is somewhat less than 10^{-5}.

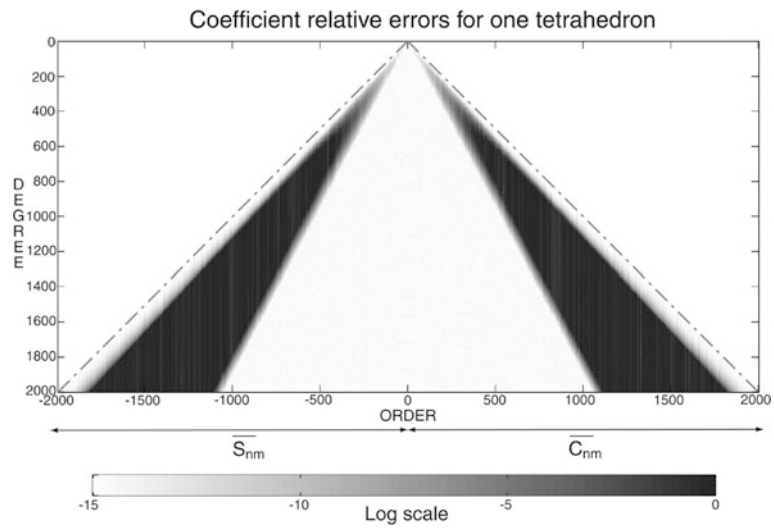


Fig. 58.3 Coefficient relative error as a function of both degree and order. *Black* indicates when the relative error is greater than 100%

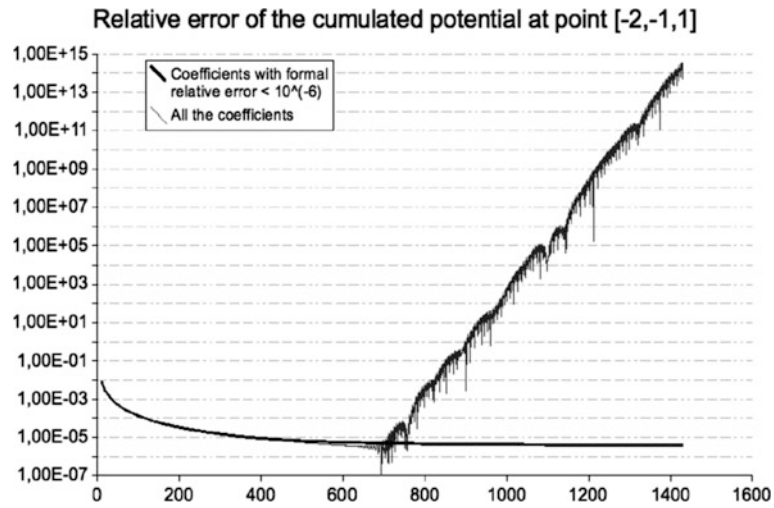


Fig. 58.4 Relative error of the cumulated potential as a function of the maximum degree of the spherical harmonic expansion computed with all the coefficients (*gray solid line*) and after removing coefficients with a formal error greater than 10^{-6} (*black thick solid line*)

Our findings suggest that the convergence of the potential spherical harmonic expansion resulting from this linear algorithm can be efficiently controlled to ensure the determination of the potential with a reasonable accuracy, which may be sufficient for many applications (terrain effect computation, interpretation of the gravitational signal through comparison of gravity maps, etc.).

58.4 Conclusions

A linear algorithm for computing potential spherical harmonic coefficients of constant density polyhedral sources has been implemented with a simple case study consisting of a single tetrahedron of constant density. The divergence of this algorithm when

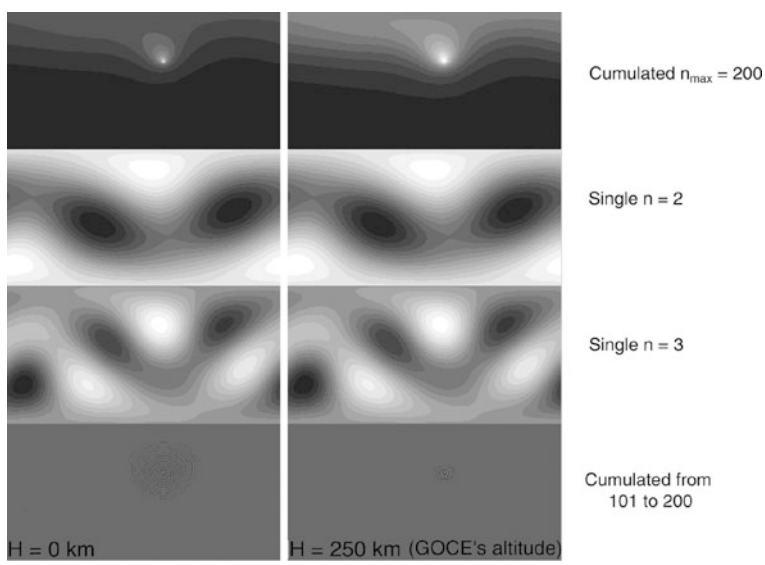


Fig. 58.5 These maps show the global variations of the T_{zz} component of the gravity tensor (latitude and longitude range from respectively -90° to +90° vertically and 0° − 360° horizontally) generated by the tetrahedral source of our case study, and computed on the Earth's surface and at GOCE's altitude (250 km). The *gray scale* does not correspond to absolute gravity gradient values, but shows only their relative amplitudes. As expected, the corner which is the closest to the Earth's surface can be revealed by the high degrees of the spherical harmonic expansion (*upper and lower maps*)

using a polyhedral source with a non horizontal face opposite to the origin of the frame has been demonstrated conclusively in our first numerical experiment. A change of reference frame which would link each tetrahedron to its horizontal configuration is essential before applying this linear algorithm, which can be readily performed using rotation matrices. The numerical estimation of the coefficient precision has provided the undisputed evidence that the linear algorithm exhibits inherent instabilities affecting the very first terms of the recursion formulas ($n \approx m$) at high degrees, which would have cast some doubt upon its efficiency. Fortunately, the effect of those numerical instabilities can be completely avoided by removing the coefficients of poor precision without significantly deteriorating the overall potential accuracy. Providing these precautions, the linear algorithm will be empowered to be used for many applications such as, and among others, gravity field and geoid modelling at desired resolution, exact filtering of terrain effects in the computation of residual terrain models or terrain corrections. Moreover, the computation of the potential coefficients generated by real terrestrial bodies will allow us to compare them directly to the coefficients retrieved by gravity exploring satellites such as GOCE. Figure 58.5 shows an illustration of the ability of the method to map the gravity field at desired resolution and at any location, thus allowing a forward modelling of the gravity sources detectable by GOCE.

References

Balmino, G. (1994). Gravitational potential harmonics from the shape of an homogeneous body. *Cel. Mech. Dyn. Astr.*, 60, 331–364.

Barnett, C.T. (1976). Theoretical modeling of the magnetic and gravitational fields of an arbitrary shaped three dimensional body. *Geophys.*, 41, 1353–1364.

Chao, B.F. and D.P. Rubincam (1989). The gravitational field of Phobos. *Geoph. Res. Let.*, 16, 859–862.

Heiskanen, W. and H. Moritz (1967). Physical Geodesy. WH Freeman and Company, San Fransisco.

Jamet, O. and E. Thomas (2004). A linear algorithm for computing the spherical harmonic coefficients of the gravitational potential from a constant density polyhedron. In *Proceedings of the Second International GOCE User Workshop, "GOCE, The Geoid and Oceanography"*, volume ESA SP-569, Frascati, Italy. ESA-ESRIN.

Martinec, Z., K. Pěč, and M. Burša, (1989). The Phobos gravitational field modeled on the basis of its topography. *Earth Moon Planet.*, 45, 219–235.

Petrović, S. (1996). Determination of the potential of homogeneous polyhedral bodies using line integrals. *J. Geod.*, 71, 44–52.

Pohánka, V. (1988). Optimum expression for computation of the gravity field of a homogeneous polyhedral body. *Geophys. Prosp.*, 36, 733–751.

Simonelli, D., P.C. Thomas, B.T. Carcich, and J. Vererka, (1993). The generation and use of numerical shape models for irregular solar system objects. *Icarus*, 103, 49–61.

Tsoulis, D. (1999). Multipole expressions for the gravitational field of some finite bodies. *Bollett. Geod. Sc. A.*, 58, 353–381.

Tsoulis, D. (2001). Terrain correction computations for a densely sampled dtm in the bavarian alps. *J. Geod.*, 75, 291–307.

Tsoulis, D. and S. Petrović (2001). On the singularities of the gravity field of a homogeneous polyhedral body. *Geophysics*, 66, 535–539.

Werner, R. (1997). Spherical harmonic coefficients for the potential of a constant-density polyhedron. *Comp. Geosc.*, 23, 1071–1077.

Werner, R.A. and D.J. Scheeres (1996). Exterior gravitation of a polyhedron derived and compared with harmonic and mascon gravitation representations of asteroid 4769 Castalia. *Cel. Mech. Dyn. Astr.*, 65, 313–344.

Chapter 59

Improving Gravity Field Modelling in the German-Danish Border Region by Combining Airborne, Satellite and Terrestrial Gravity Data

U. Schäfer, G. Liebsch, U. Schirmer, J. Ihde, A.V. Olesen, H. Skourup, R. Forsberg, and H. Pflug

Abstract In order to improve the gravity field and geoid modelling in the border area between Germany and Denmark including the Baltic Sea and North Sea, three airborne gravity surveys have been undertaken since 2006: BalGRACE-06, NorthGRACE-07, NorthGRACE-08 (*Bal*tic resp. *North* Sea *GR*avity *A*irborne *C*ampaign and *E*xamine). These endeavours were aiming to give a substantial contribution towards comparison, verification and improvement of the vertical reference in this area. During these campaigns more than 25,000 km of track data were gathered with three different models of LaCoste&Romberg gravimeters mounted in two different aircrafts.

Owing to the recent airborne gravity efforts we were able to cover most of the mentioned area yielding gravity anomalies with an accuracy better than 2 mgal according (i) to cross-over estimates and (ii) to comparison with non-airborne gravity data. Due to considerable turbulences on some flights not all of the airborne measurements could be successfully used. Data from turbulent flights were partly too noisy and did not meet the quality criteria. Attaining high-quality airborne gravity anomalies is still a demanding business.

In this study we present the data handling of the airborne gravity data from three campaigns carried out under quite different conditions. It is described how the airborne data have been checked, homogenized and used to fill-up various existing data gaps.

A first result of improved regional gravity field and geoid modelling is presented, using the newly obtained airborne gravity data in connection with existing terrestrial data and satellite observations.

U. Schäfer (✉)
Federal Agency for Cartography and Geodesy (BKG), Frankfurt am Main D-60598, Germany
e-mail: ufer@bkg.bund.de

59.1 Motivation

Before the BalGRACE and NorthGRACE campaigns the border region between Germany and Denmark and the adjacent Baltic and North Sea areas were characterized by a quite inhomogeneous spatial distribution of gravity points and of their measurement epochs. Compared to the land regions, the sea areas contain less observations with poorer data quality. In some areas, e.g. in the mud flats, lagoons, along coastlines, and around the numerous islands there were no observations at all (cf. to the previous existing gravity measurements, i.e. grey points in the background of Fig. 59.1).

By their inherent nature the different existing data (land gravity, marine gravity, and reliable satellite altimetry data) have practically no over-lapping zones in the near-coastal areas. Neither by terrestrial observations nor by ship-borne measurements only, is it possible to obtain an appropriate, homogeneous data coverage along and across the coastlines. In the last years airborne gravimetry has become a major tool for gravity data acquisition in such areas.

Acknowledging this, and recognizing that reliable gravity measurements carried out in a well-defined gravity reference system are a necessary precondition for advanced gravity field models on land as well as in the adjacent sea areas, the Federal Agency for Cartography and Geodesy (BKG) and the Danish National Space Center (DNSC) jointly carried out three airborne gravity campaigns in the

S.P. Mertikas (ed.), *Gravity, Geoid and Earth Observation*, International Association of Geodesy Symposia 135,
DOI 10.1007/978-3-642-10634-7_59, © Springer-Verlag Berlin Heidelberg 2010

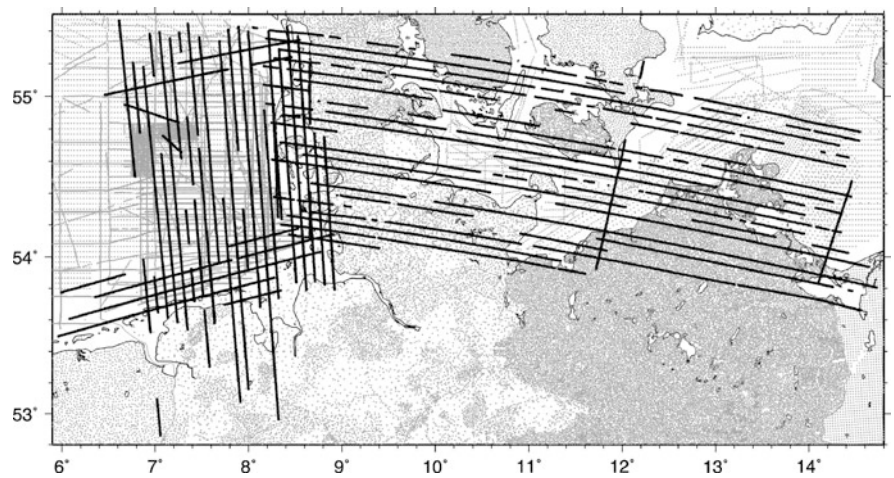


Fig. 59.1 Tracks of airborne campaigns in 2006–2008 with high-quality data (*grey points*: previous surface gravity data)

German-Danish border region between October 2006 and February 2008. During one campaign also the GFZ Potsdam joined the enterprise with its S124 LaCoste&Romberg gravimeter.

59.2 Survey Description

An overview information about the airborne surveys is given in Table 59.1. Besides the airborne gravimeter equipment four geodetic GPS receivers and an inertial navigation system (INS) were installed in the aircrafts. Temporarily GNSS stations were established in Esbjerg (2–3 receivers), in Roskilde (1 receiver) and Heringsdorf (1 receiver). Also the 1-sec-data from the German permanent net GREF have been recorded during these airborne surveys.

The base reading locations were connected to the Danish gravity network by relative gravimeters L&R G563 and G466. The gravity value at the apron reference point in Heringsdorf was determined by a transportable absolute gravimeter A10.

Unfortunately, the quality of measurements during the first two campaigns was particularly influenced by unfavourable weather conditions with partly considerable turbulences (autumnal windy conditions in October 2006 and thundery atmosphere in June 2007). Analysis of the airborne survey data indicates, that there was also a less optimal autopilot performance of the KingAir B200 aircraft in comparison to the Cessna 402C aircraft used during the latter campaign in February 2008. During the NorthGRACE-07 campaign there was identified an unusual propagation of aircraft vibration onto the S99 gravimeter sensor probably due to specific squeezed-up mounting of the S99 gravimeter together with the S124 airborne gravimeter. Very calm weather conditions prevailed during the last campaign.

59.3 Data Processing and Validation

The data processing reported here has been carried out along the lines described by Olesen (2003). Hence, free-air anomalies Δg at aircraft altitude are obtained from:

$$\Delta g = \mathrm{f}_z - \mathrm{f}_{z0} - h'' + \delta g_{\text{eötvös}} + \delta g_{\text{tilt}} + g_0 - \gamma_0 - \left(\frac{\partial \gamma}{\partial \mathrm{h}} (\mathrm{h} - N) + \frac{\partial^2 \gamma}{\partial \mathrm{h}^2} (h - N)^2 \right) \quad (1)$$

Table 59.1 Survey overview

Campaign	Time	Aircraft	LC&R Gravimeter No.	Flight altitudes [m]
BalGRACE 06	Oct 16–26, 2006	KingAir B200	S-38	300–1,500
NorthGRACE 07	Jun 04–16, 2007	KingAir B200	S-99, S124	300–1,000
NorthGRACE 08	Feb 03–10, 2008	Cessna 402 C	S-99	300–800

Table 59.2 Internal crossover analysis of airborne campaigns

Data set	Crossover points	RMS [mgal]	Max. deviation [mgal]
BalGRACE-06 little/no turbulence	26	1.79	2.77
BalGRACE-06 medium turbulence	34	2.13	4.62
NorthGRACE-07 intern	45	1.69	5.53
NorthGRACE-08 intern	13	1.97	3.61
NorthGRACE total	104	2.12	6.20

f_z – gravimeter observation; f_{z0} – gravity base reading at apron; h'' – vertical acceleration from GNSS; $\delta g_{eötvös}$ – Eötvös correction by formulas of Harlan (1968); δg_{tilt} – platform off-level correction; g_0 - gravity value at apron; γ_0 – normal gravity at the projection point of aircraft position onto the GRS80 ellipsoid; h – GNSS defined ellipsoidal height of the aircraft; N – geoid undulation (EGM96 is used throughout) at the projection point of aircraft position.

A first estimation of the data accuracy is given by analysis of crossover differences yielding RMS values around 2 mgal with maximal deviations of about 6 mgal (Table 59.2). These results were obtained, as usual without any a priori crossover adjustment.

The data of the different campaigns have been checked independently versus the previous existing surface data (e.g. terrestrial, shipborne, satellite altimetry data) in the area. These checks were performed by comparing the airborne data (i) with interpolated data using the GRAVSOFT routine "geogrid" and (ii) by using an analytical point mass model, that was derived with surface data only. Both approaches gave very similar results. The differences between newly obtained airborne data and the existing surface data are presented in Fig. 59.2, showing that most of the data lie within the assessed accuracy bounds of 2 mgal.

The NorthGRACE-07 data show a slightly larger bias and a larger asymmetry of the extrema towards positive values compared to NorthGRACE-08 (Table 59.3). The larger RMS of 2.1 mgal for NorthGRACE-08 is mainly due to the fact, that the amount of data gathered in areas with poor surface data coverage was considerably higher in the NorthGRACE-08 survey than in NorthGRACE-07. This yields to less reliable "ground-true" estimates and larger interpolation uncertainties by means of "geogrid" prediction.

The mean of all 46 crossover points of the NorthGRACE-07 data set is biased by +0.7 mgal against the mean of NorthGRACE-08 (cf. Table 59.4). The NorthGRACE-07 data are also biased by +0.4 mgal when compared to surface data.

Since the NorthGRACE-08 data were characterized as the most reliable ones by independent quality assessment, taking into account the flight conditions and the influence of turbulences on the gravimeter

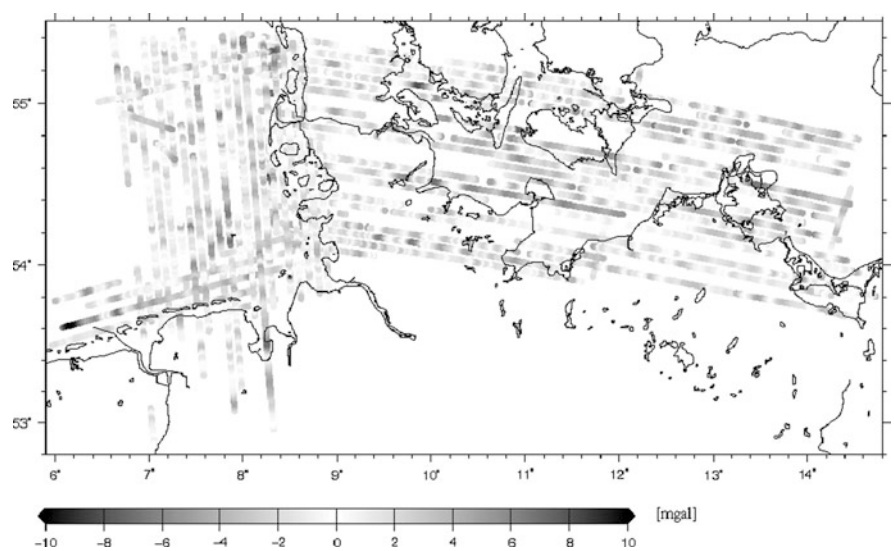


Fig. 59.2 Comparison of airborne and surface gravity data of airborne campaigns 2006–2008

Table 59.3 Comparison of airborne with surface gravity data (computed with "geogrid" using a correlation length of 20 km and an RMS value of 1 mgal)

Campaign	Evaluation points	Bias [mgal]	RMS [mgal]	Min [mgal]	Max [mgal]
BalGRACE-06	6,834	1.3	1.8	–4.7	+8.9
NorthGRACE-07	3,099	1.6	1.9	–4.7	+11.7
NorthGRACE-08	3,910	1.2	2.1	–6.4	+7.6

Table 59.4 Crossover analysis between NorthGRACE-07 and NorthGRACE-08 campaigns

Data set	crossover points	Bias [mgal]	RMS [mgal]	Max. deviation [mgal]
NorthGRACE-07 vs. 08 (before adjustment)	46	0.70	2.38	6.20
NorthGRACE-07 vs. 08 (after adjustment)	46	0.00	2.38	5.50

readings, the whole NorthGRACE-07 data set was adjusted to the NorthGRACE-08 data level by subtracting 0.7 mgal.

Data showing large vertical accelerations due to changes in flight altitude as well as data classified as heavy turbulent were discarded from the final data sets of the individual campaigns.

59.4 Results and Discussion

As indicated by the crossover assessments (cf. Table 59.2) the internal accuracy of the final data sets from the three campaigns varies between 1.7 and 2.1 mgal according to the RMS deviations. That implies a white noise along track error in the bounds between 1.2 and 1.5 mgal. This is in accordance with earlier DNSC airborne surveys in the central Baltic Sea (Forsberg et al., 2001), and is a very reasonable result for accuracies obtainable by means of current scalar airborne gravity campaigns using LaCoste&Romberg gravimeters. The overall accuracy level is confirmed (i) by a comparison of different campaigns (Table 59.2, last row; Table 59.4), yielding RMS deviations of maximal 2.4 mgal, implying a white noise along track error below 1.6 mgal, but also (ii) by comparison with surface gravity data (cf. Table 59.3).

The final gravity anomaly pattern of all three campaigns is given in Fig. 59.3. There are several areas with considerable benefit from the airborne gravity data. Figure 59.4 illustrates the gain obtained in two

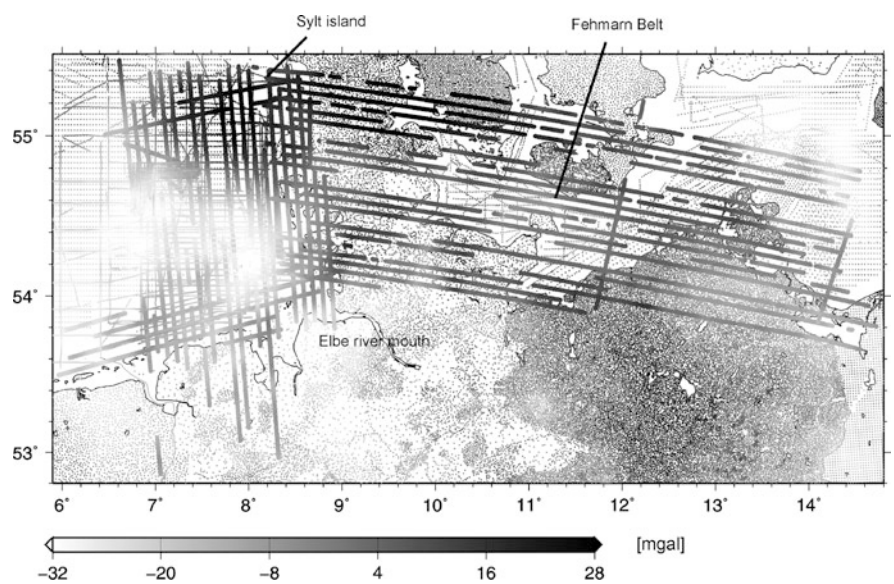


Fig. 59.3 Summary of the free air gravity anomalies obtained from all three campaigns (with underlayed surface gravity data)

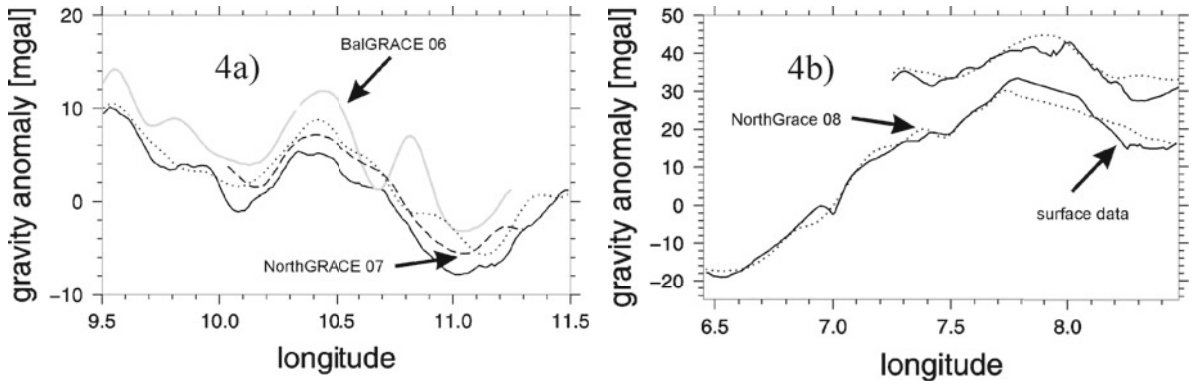


Fig. 59.4 Comparison of airborne and interpolated surface gravity data (using geogrid with a correlation length of 20 km)

areas where previously existed no data at all, or only a few older shipborne data. The first area (Fig. 59.4a) is located in the Baltic Sea (a track covering the Fehmarn Belt). This track had been flown independently by all three surveys with good results for both NorthGRACE campaigns (dotted and dashed lines).

The BalGRACE-06 track segment (Fig. 59.4a) was discarded (Skourup et al., 2008) due to the heavy turbulences that occurred during that flight. The black line represents the interpolated (sparse and not well distributed) surface data. Contrary to the BalGRACE-06 track segment, there is seen a quite good coincidence between the NorthGRACE-07 and NorthGRACE-08 data along this track in the Fehmarn Belt with RMS deviations of less than 1.2 mgal and maximal deviations below 2.8 mgal.

An even better coincidence is obtained in the Elbe river mouth in the North Sea where repeated track segments between both campaigns offer RMS deviation values of less than 0.8 mgal and maximal deviations that are less than 2.2 mgal.

The second area (Fig. 59.4b) is located in the North Sea (north of the Sylt island, east of 8 E). Since there were practically no previous data available at the eastern ends of both profiles the improvements in recording and determination of the gravity anomalies amount to several milligal thanks to the airborne data. The interpolated surface data in both plots should be interpreted with care due to the gaps in the surface data distribution.

In Fig. 59.5 an improved geoid model is presented, that incorporates the newly obtained airborne data. In total there have been used about 113,000 gravity disturbance values, including terrestrial and marine measurements, data derived from satellite altimetry, and, the new airborne data. Furthermore, the height

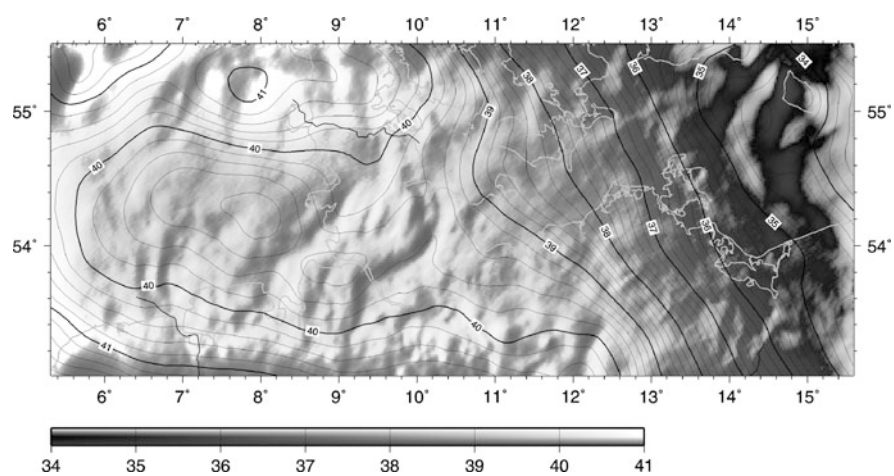


Fig. 59.5 Improved quasigeoid model incorporating the new airborne gravity data from the *airborne gravity campaigns* together with existing surface gravity and *GPS/levelling* data

anomalies or disturbing potential values received from the observations at 686 GPS/levelling points were incorporated. The final model is a combination of two solutions obtained within the remove-compute-restore approach from two different point mass approximations. The first solution is based on a point mass representation described by Liebsch et al. (2006). It uses more than 22,000 point masses located at depth levels of 5 , 30 , and 200 km.

The second solution uses (i) further 45,000 point masses with positions that are mirrored to observation point locations, and (ii) a special solver for the larger system of linear equations – the successive polynomial multiplication method (Strakhov et al., 1997). The RMS of the differences of quasigeoid heights between both solutions in 68,000 gridded control points is about 2 cm.

In comparison to previous models the changes of height anomalies due to the new quasigeoid model – a superposition of both mentioned solutions – reach up to 4 cm, particularly at the margins and in areas with former poor data coverage. These improvements underline the impact coming from the new airborne gravity data.

59.5 Conclusions

The employed intercomparison and validation of airborne data from different campaigns allow to create a homogeneous airborne gravity data set.

The new airborne gravity data obtained in the BalGRACE and NorthGRACE campaigns contribute:

- to better regional geoid modelling yielding improvements of the geoid up to ±4 cm in the Baltic and North Sea areas compared to previous geoid models
- to strengthen the control of the height reference systems used in Denmark and Germany.

These data are therefore of particular interest for practical geodetic applications – like the control of a planned fixed bridge connection between Germany and Denmark across the Fehmarn Belt but also within a more general scope – like a contribution to a pan-European height reference frame. In the border region between Germany and Denmark, where data sets of different quality and coverage coexists (good land data, moderate sea data, poor data in the transition zone) the combined examination of airborne and surface gravity anomalies leads not only to improved data acquisition but also to a deeper insight into the reliability and trustworthiness of both airborne and surface data.

References

Forsberg, R., A.V. Olesen, K. Keller, M. Møller, A. Gidskehaug, and D. Solheim (2001). Airborne Gravity and Geoid Surveys in the Arctic And Baltic Seas. In: Proceedings of International Symposium on Kinematic Systems in Geodesy, Geomatics and Navigation (KIS-2001), Banff, June 2001, pp. 586-593.

Harlan, R.B. (1968). Eötvös corrections for airborne gravimetry. *J. Geophys. Res.*, 73(14), 4675–4679.

Liebsch, G., U. Schirmer, J. Ihde, H. Denker, and J. Müller (2006). Quasigeoidbestimmung für Deutschland. *DVW-Schriftenreihe*, Band 49, S. 127–145.

Olesen, A.V. (2003). Improved airborne scalar gravimetry for regional gravity field mapping and geoid determination. Kort og Matrikelstyrelsen Technical Report no. 24, p. 55.

Skourup, H., R. Forsberg, S.L.S. Sørensen, C.J. Andersen, U. Schäfer, G. Liebsch, J. Ihde, and U. Schirmer (2008). Strengthening the vertical reference in the southern Baltic Sea by airborne gravimetry. XXIV IUGG General Assembly 2008, Perugia, Italy, July 2–13, 2008, Proceedings, Vol. 133, Part 2, 135–141, IAG Symposia, Springer Berlin Heidelberg.

Strakhov, V.N., U. Schäfer, A.V. Strakhov, and D.E. Teterin (1997). Ein neuer Ansatz zur Approximation des Gravitationsfeldes der Erde. INTAS-Report 93-1779, IfAG, Potsdam.

Chapter 60

An Inverse Gravimetric Problem with GOCE Data

M. Reguzzoni and D. Sampietro

Abstract Satellite missions dedicated to the estimation of the gravity field and its variation, like GRACE and GOCE, have drawn new attention on inverse gravimetric problems and, in particular, on the capability of these satellite data sets to describe nature and geographical location of the gravimetric signal.

In this paper a semi-analytical method to detect Earth's density anomalies, based on Fourier analysis and Wiener filter, has been developed. The method has been tested on simulated observations of the gravitational potential and its second radial derivatives with the aim of assessing the capability of the GOCE mission to detect the shape of the oceanic floor from satellite data only.

Despite the simplistic hypotheses involved in our example, positive results have been obtained, showing that the shape of the oceanic floor can be estimated with a reasonable accuracy at a resolution consistent with the expected GOCE performance.

60.1 The Problem and Proposed Solution

The determination of the structure of the Earth's interior, based on the inversion of Newton's gravitational potential (gravimetry problem), has been studied in various publications (see for example Ballani and Stromeyer, 1982, 1990; Hein et al., 1989; Vajda, 2006). Since the purpose of this paper is not to implement an inverse algorithm but rather to study the sensitivity of GOCE (ESA, 1999) data to local mass anomalies, we will work on such a problem, accepting very simplified hypotheses. So we try to detect and reconstruct a sea floor feature (mountain chain), orthogonally crossed by the GOCE orbits. First of all we neglect the Earth curvature; note that for some geophysical problems this is a frequently used approach (see Kirchner, 1997; Gangui, 1998; Lessel, 1998). Furthermore if the mountain chain is developing with homogeneous characteristics in the cross-track direction, the problem of reconstructing its shape can be considered essentially as a two dimensional problem and can be formulated and solved by a suitable application of the Fourier Transform. We basically suppose that the feature generating the gravity signal is a two-layer structure with one layer at 1 $\mathrm{g\,cm^{-3}}$ density (water) and the other at 2.67 $\mathrm{g\,cm^{-3}}$ (rocks), with a density contrast σ of 1.67 $\mathrm{g\,cm^{-3}}$. We assume that at the altitude of $h = 250$ km from the sea surface a GOCE-like satellite "observes" the anomalous potential T and its second radial derivatives T_{zz}. In this study the z axis has the origin at the satellite altitude and is downlooking (the geometry of the problem is represented in Fig. 60.1).

Since the ocean floor can be described by a function $D(x) = \overline{D} + \delta D(x)$ with $\overline{D} = \text{const}$ and $\delta D < 0$,, the deterministic model we have to invert is given by (Heiskanen and Moritz, 1967):

$$T(x) = \iint d\xi d\eta \int_{h}^{h+\overline{D}+\delta D(\xi)} \frac{G\sigma}{\sqrt{(x-\xi)^2+\eta^2+\zeta^2}} d\zeta \tag{1}$$

M. Reguzzoni (✉)
Italian National Institute of Oceanography and Applied Geophysics (OGS), c/o Politecnico di Milano, Polo Regionale di Como, Como 22100, Italy
e-mail: mirko@geomatica.como.polimi.it

S.P. Mertikas (ed.), *Gravity, Geoid and Earth Observation*, International Association of Geodesy Symposia 135,
DOI 10.1007/978-3-642-10634-7_60, © Springer-Verlag Berlin Heidelberg 2010

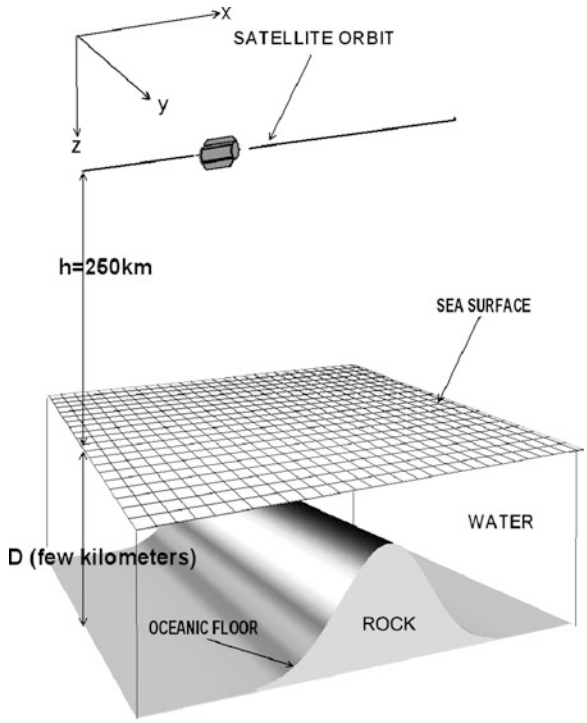


Fig. 60.1 Geometry of the problem

$$T_{zz}(x) = \frac{\partial^2}{\partial z^2}\iint d\xi d\eta \times \int_{h}^{h+\overline{D}+\delta D(\xi)} \frac{G\sigma}{\sqrt{(x-\xi)^2+\eta^2+(z-\zeta)^2}} d\zeta \Bigg|_{z=0} \quad (2)$$

where G is the gravitational constant and ξ, η, ζ are integration variables in the x, y, z directions, respectively. Note that in Eqs. (1) and (2) it is assumed that the satellite is flying along the x direction, with $y = z = 0$.

By linearizing such signals with respect to δD we get:

$$T(x) = \overline{T}(x) + \iint d\xi d\eta \frac{G\sigma}{\sqrt{(x-\xi)^2+\eta^2+(h+\overline{D})^2}} \delta D(\xi) \quad (3)$$

$$T_{zz}(x) = \overline{T}(x) + \frac{\partial^2}{\partial z^2}\iint d\xi d\eta \frac{G\sigma}{\sqrt{(x-\xi)^2+\eta^2+(z-h-\overline{D})^2}} \delta D(\xi)\Bigg|_{z=0} \quad (4)$$

where $\overline{T}(x)$ and $\overline{T}_{zz}(x)$ do not depend on δD and are subtracted from the satellite data.

In order to avoid divergiencies of the integrals, in reality we cannot let η span the whole real axis; so we have decided to perform the integral in η over the interval [-L, L], with L a fixed parameter. Among other things, this makes the example a little more realistic. With such a choice, Eqs. (3) and (4) become:

$$\delta T(x) = T(x) - \overline{T}(x) = \int_{-\infty}^{+\infty} k_T(x-\xi)\delta D(\xi) d\xi \quad (5)$$

$$\delta T_{zz}(x) = T_{zz}(x) - \overline{T}_{zz}(x) = \int_{-\infty}^{+\infty} k_{T_{zz}}(x-\xi)\delta D(\xi) d\xi \quad (6)$$

with:

$$k_T(x-\xi) = -G\sigma \log \frac{\left(\sqrt{(x-\xi)^2+(h+\overline{D})^2+L^2}+L\right)^2}{(x-\xi)^2+(h+\overline{D})^2} \quad (7)$$

$$k_{T_{zz}}(x-\xi) = \frac{2G\sigma L\left[(x-\xi)^4+(x-\xi)^2\left(L^2-\left(h+\overline{D}\right)^2\right)\right]}{\left((x-\xi)^2+\left(h+\overline{D}\right)^2\right)^2\left((x-\xi)^2+\left(h+\overline{D}\right)^2+L^2\right)^{\frac{3}{2}}} - \frac{2G\sigma L\left[\left(h+\overline{D}\right)^2\left(2\left(h+\overline{D}\right)^2+L^2\right)\right]}{\left((x-\xi)^2+\left(h+\overline{D}\right)^2\right)^2\left((x-\xi)^2+\left(h+\overline{D}\right)^2+L^2\right)^{\frac{3}{2}}}. \quad (8)$$

The form of Eqs. (5) and (6) has to be augmented with the noise of the observations performed by the GOCE instruments:

$$\delta T_0(x) = \int_{-\infty}^{+\infty} k_T(x-\xi)\delta D(\xi) d\xi + \upsilon \quad (9)$$

$$\delta T_{zz0}(x) = \int_{-\infty}^{+\infty} k_{T_{zz}}(x-\xi)\delta D(\xi) d\xi + \upsilon_{zz}. \quad (10)$$

In reality none of the two quantities is a direct observation. The potential T is derived from GPS tracking data, for example by applying the so called energy integral approach (Jekeli, 1999; Visser et al., 2003) and it

is known to have an almost white error with a standard deviation of the order of 0.3 $m^2\,s^{-2}$. The second radial derivatives T_{zz} are obtained by a preprocessing of the gradiometer observations, that in general are not exactly aligned with the radial direction (Cesare, 2002; Pail, 2005); however, the resulting data set has an error with spectral characteristics almost identical to the original observations (Migliaccio et al., 2004).

The idea is to get the best estimate of δD from Eqs. (9) and (10) and this can be done in an optimal way by the Wiener filter theory as applied to continuous data sets (Sansò and Sacerdote, 1996). Accordingly we can take the distributional Fourier trasform of Eqs. (9) and (10) to get the following expressions in the frequency domain:

$$\delta\hat{T}_0(f) = \hat{k}_T(f)\delta\hat{D}(f) + \hat{\upsilon}(f) \tag{11}$$

$$\delta\hat{T}_{zz0}(f) = \hat{k}_{T_{zz}}(f)\delta\hat{D}(f) + \hat{\upsilon}_{zz}(f) \tag{12}$$

where the covariances of $\hat{\upsilon}(f)$ and $\hat{\upsilon}_{zz}(f)$ are given by (Sansò and Sacerdote, 1996):

$$E\{\hat{\upsilon}(f)\hat{\upsilon}(f')\} = \delta(f - f')S_\upsilon(f) \tag{13}$$

$$E\{\hat{\upsilon}_{zz}(f)\hat{\upsilon}_{zz}(f')\} = \delta(f - f')S_{\upsilon_{zx}}(f). \tag{14}$$

In Eqs. (13) and (14), $S_\upsilon(f)$ and $S_{\upsilon_{zz}}(f)$ are the power spectra of the errors as determined in GOCE solution simulations (see for example Abrikosov and Schwintzer, 2004; Pail et al., 2005; Migliaccio et al., 2007).

The best solution is obviously to combine both equations producing the optimal Wiener estimator of $\delta\hat{D}(f)$. However, since each data type gives information mainly in different spectral intervals, we found it more clear and instructive to derive also separate estimators $\delta\hat{D}_T(f)$, $\delta\hat{D}_{Tzz}(f)$ from each equation and compare their error spectra with the spectrum of the signal δD.

We start from the estimator $\delta\hat{D}_T$ that can be derived from Eq. (11) if the spectrum $S_\upsilon(f)$ is known as well as the spectrum of δD, namely $S_{\delta D}(f)$. The latter is just computed as the square modulus of the Fourier transform $\delta\hat{D}(f)$. In this case the Wiener estimator is given by:

$$\delta\hat{D}_T(f) = \frac{S_{\delta D}(f)\,\hat{k}_T(f)}{S_{\delta D}(f)\,\hat{k}_T^2(f) + S_\upsilon(f)}\delta\hat{T}_0(f) \tag{15}$$

and the spectrum of the estimation error ϵ_T of $\delta\hat{D}_T$ is:

$$S_{\varepsilon_T}(f) = \frac{S_{\delta D}(f)S_\upsilon(f)}{S_{\delta D}(f)\hat{k}_T^2(f) + S_\upsilon(f)}. \tag{16}$$

Analogous formulae can be obtained for T_{zz}. We also derive the Wiener estimator combining both observables of Eqs. (11) and (12):

$$\delta\hat{D}_{T,\,T_{zz}}(f) = \lambda(f)\delta\hat{T}_0(f) + \gamma(f)\,\delta\hat{T}_{zz0}(f) \tag{17}$$

with:

$$\lambda = \frac{S_{\delta D}\,\hat{k}_T S_{\upsilon_{zz}}}{S_{\upsilon_{zz}}S_\upsilon + \hat{k}_{T_{zz}}^2 S_{\delta D}S_\upsilon + \hat{k}_T^2 S_{\delta D}S_{\upsilon_{zz}}}, \tag{18}$$

$$\gamma = \frac{S_{\delta D}\,\hat{k}_{T_{zz}}S_\upsilon}{S_{\upsilon_{zz}}S_\upsilon + \hat{k}_{T_{zz}}^2 S_{\delta D}S_\upsilon + \hat{k}_T^2 S_{\delta D}S_{\upsilon_{zz}}} \tag{19}$$

and its error spectrum:

$$S_{\varepsilon_{T,T_{zz}}} = \frac{S_{\delta D}S_{\upsilon zz}S_\upsilon}{S_{\upsilon_{zz}}S_\upsilon + \hat{k}_{T_{zz}}^2 S_{\delta D}S_\upsilon + \hat{k}_T^2 S_{\delta D}S_{\upsilon_{zz}}}. \tag{20}$$

For the sake of simplicity the dependence on the frequency f has been omitted in Eqs. (18), (19) and (20).

Finally we can say that $\delta\hat{D}$ is well estimated for those frequencies for which:

$$S_\varepsilon(f) \le \alpha S_{\delta D}(f), \tag{21}$$

where $S_\varepsilon(f)$ corresponds to $S_{\varepsilon_T}(f)$, $S_{\varepsilon_{T_{zz}}}(f)$ or $S_{\varepsilon_{T,T_{zz}}}(f)$ according to the data used in the Wiener estimator. In this study the threshold α is fixed at the value α=20%.

60.2 Results of Numerical Experiments

In our tests we consider a submarine mountain chain represented by the following gaussian model:

$$\delta D(x) = He^{-\frac{x^2}{2s^2}}, \tag{22}$$

where H is the maximum height and s is related to the width of the mountain chain. These two parameters have been changed in the different tests. The noise spectrum of the anomalous potential at satellite altitude has been taken as the spectrum of a pure white noise of magnitude 0.3 m^2s^{-2}, while the noise spectrum of T_{zz} is represented in Fig. 60.2 and has been derived

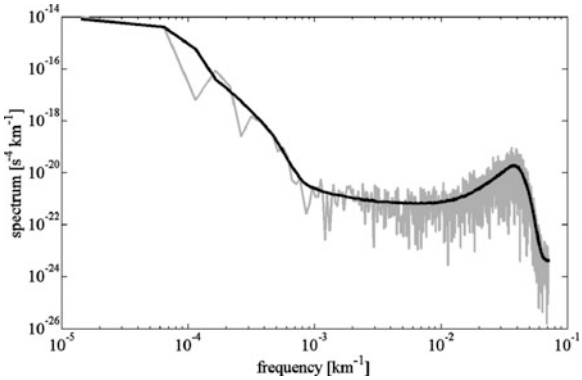


Fig. 60.2 Empirical (*grey*) and modeled (*black*) noise spectrum for T_{zz} GOCE observations

from realistic simulated data for the GOCE mission (Catastini et al., 2007).

To compare the performance of the method proposed in Sect. 60.1 for the two different types of observations, a first test assuming $\overline{D} = 2$ km, $L = 600$ km, $H = 1$ km and $s = 100$ km is made. Figure 60.3 illustrates the comparison between signal and error spectra for each different estimator, while in Table 60.1 the error root mean square (rms) between true and estimated signal is reported. It is easy to see from these results that low frequencies are well reconstructed using T observations, while T_{zz} gives information on higher frequencies. In particular T_{zz} has a significant contribution in the frequency range between 7.5×10^{-4} km^{-1} and 1.5×10^{-3} km^{-1}, according to the test defined in Eq. (21). Finally the multiple input approach is able to estimate both low and high frequencies, as expected.

Since the convolution kernels and the Wiener filters depend on the profile of δD, we perform a sensitivity analysis to investigate how the shape of the oceanic floor (defined by the parameters H and s) affects the estimation of the signal. The analysis is conducted only for the multiple input approach.

The result in Fig. 60.4 represents the error rms between true and estimated signal, divided by the signal rms: in this way a normalized index is computed. It can be seen that increasing the chain width, the relative error significantly decreases and the signal is nearly completely recovered. This happens because GOCE observations are collected at an altitude of about 250 km where the effect of density anomalies is inevitably smoothed; therefore lower resolution features are better detected and reconstructed. Increasing

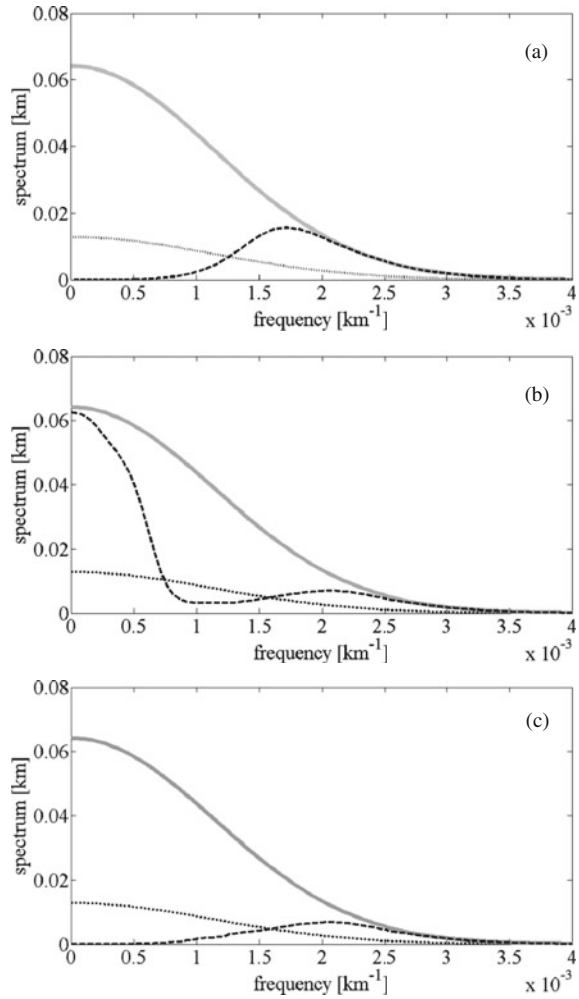


Fig. 60.3 Estimation error spectrum S_{ε} (*dashed line*) compared to the signal spectrum $S_{\delta D}$ (*solid line*) and to the threshold spectrum $0.2 \cdot S_{\delta D}$ (*dotted line*). Ocean surface with $H = 1$ km and $s = 100$ km. Wiener estimator based on T data (**a**), T_{zz} data (**b**), both T and T_{zz} data (**c**)

the height H has no effect when the chain is thin (small value of s), in the sense that it remains hardly detectable; on the other hand the effect is slightly negative in the case of large mountain chains. In fact, while low frequencies are still fully recovered, the remaining not detected high frequencies are now amplified, producing a small increase of the relative error.

An improvement in the signal reconstruction accuracy can be obtained if more than a single satellite track is processed. Considering n orbits, and assuming independent observations for each orbit, a rough computation allows to obtain the new observation noise

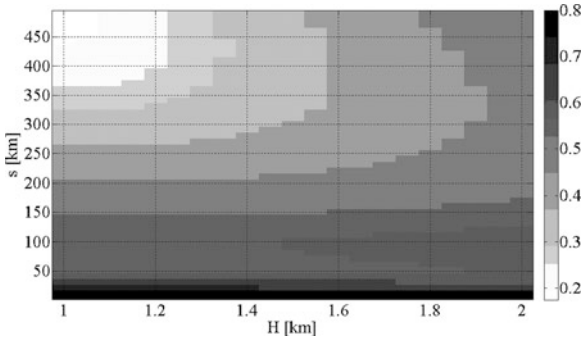


Fig. 60.4 Ratio between error and signal rms as a function of the oceanic floor parameters H and s

spectra as:

$$S_{\upsilon}^{(n)}(f) = \frac{S_{\upsilon}(f)}{n} \tag{23}$$

$$S_{\upsilon_{zz}}^{(n)}(f) = \frac{S_{\upsilon_{zz}}}{(f)} n. \tag{24}$$

The comparison between the estimation error spectra with $n = 1$ and $n = 10$ is shown in Fig. 60.5 for two different test scenarios, both based on the multiple input Wiener estimator. In the case of $H = 1$ km and $s = 100$ km, the signal is fully recovered when processing ten satellite tracks since the condition (21) is satisfied for all frequencies. Considering a thinner mountain chain, i.e. $H = 1$ km and $s = 50$ km, the improvement due to the higher number of observations is still quite significant, the signal is well recovered below 3.5×10^{-3} km^{-1} and the rms decreases from 0.045 to 0.037 km. However, the error of the highest frequencies (above 5×10^{-3} km^{-1} corresponding to a wavelength of 200 km) is not reduced at all and this happens because the signal at those frequencies is practically cancelled out at satellite altitude. This can be seen by looking at the kernel of the second radial derivatives, that is displayed in Fig. 60.6.

Table 60.1 rms of the differences between the estimated and the true signal using the three different Wiener predictors

T	T_{zz}	T, T_{zz}
0.25 km	0.056 km	0.054 km

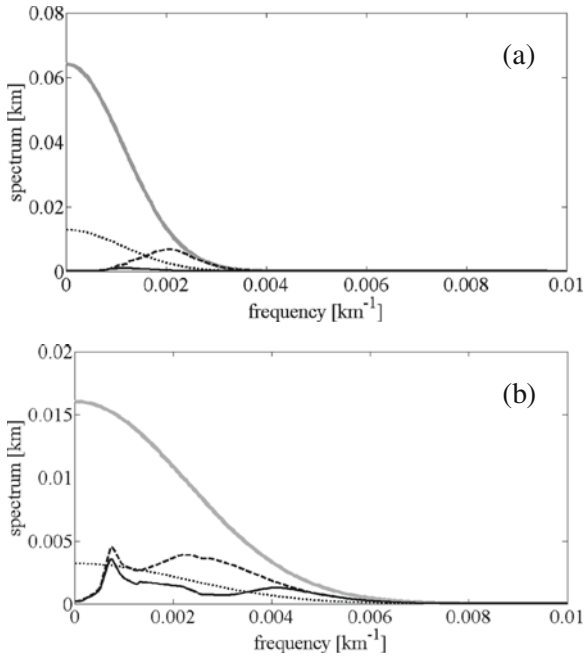


Fig. 60.5 Comparison between the estimation error spectra $S_{\varepsilon_{T,T_{zz}}}$ based on a single satellite orbit (*dashed line*) and ten satellite orbits (*black solid line*). Signal spectrum $S_{\delta D}$ (*grey solid line*) and threshold spectrum $0.2 \cdot S_{\delta D}$ (*dotted line*). $H = 1$ km and $s = 100$ km (**a**), $H = 1$ km $s = 50$ km (**b**)

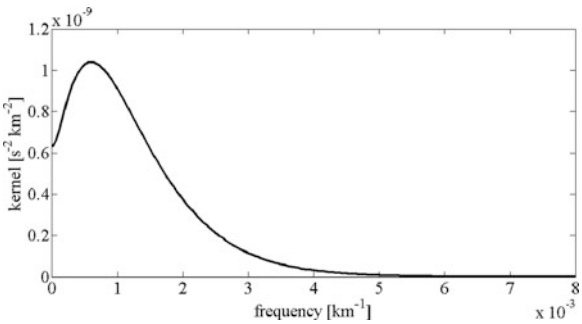


Fig. 60.6 Convolution kernel $\hat{k}_{T_{zz}}$ in the frequency domain for $\overline{D} = 2$ km, $L = 600$ km

60.3 Conclusions and Future Works

The inverse gravimetric problem of reconstructing the shape of the ocean floor using GOCE only observations has been studied. Despite the simplistic hypotheses (we neglected the effect of the Earth curvature and we assumed peculiar geometrical properties for the separation surface between water and rocks), positive

results have been obtained. In particular the shape of oceanic floor can be estimated using a single satellite track data with sufficient accuracy (rms <0.05 km) at a resolution of about 200 km (s = 50 km). A further improvement can be achieved by processing more than one satellite orbit: this reduces the noise spectra with the consequence of increasing the accuracy of the reconstructed model. Note that long wavelengths are well recovered thanks to the use of the gravitational potential, while higher resolution details come from gradiometric observations.

In our example, noise spectra of the GOCE observations are estimated from simulated data, while the signal spectrum of the oceanic floor has been computed from the true synthetic surface, which in reality is not available. Next step is to estimate this spectrum by making some statistical hypotheses for example on the altitude and the width of the oceanic mountain chain.

In addition, gridded data at satellite altitude can be used. Even if their covariance structure is not perfectly known (Reguzzoni and Tselfes, 2009), the higher accuracy of these data should improve the performance of the estimation procedure, while the better coverage of the area under study should allow for the detection of more general shapes of oceanic floor.

References

Abrikosov, O. and P. Schwintzer (2004). Recovery of the Earth's gravity field from GOCE satellite gravity gradiometry: a case study. In: Proceedings of the 2nd International GOCE User Workshop, 8–10 March 2004, Frascati, Italy.

Ballani, L. and D. Stromeyer (1982). The inverse gravimetric problem: a Hilbert space approach. In: Holota P. (ed), Proceedings of the International Symposium 'Figure of the Earth, the Moon, and other Planets', 20–25 September 1982, Prague, Czech Republic, pp. 359–373.

Ballani, L. and D. Stromeyer (1990). On the structure of uniqueness in linear inverse source problems. In: Vogel, A. et al. (eds), Theory and practice of geophysical data inversion, Proceedings of the 8th International Mathematical Geophysics Seminar on Model Optimization in Exploration Geophysics. Vieweg-Verlag, Braunschweig, Germany.

Catastini, G., S. Cesare, S. De Sanctis, M. Dumontel, M. Parisch, and G. Sechi (2007). Predictions of the GOCE in-flight performances with the End-to-End System Simulator. In: Proceedings of the 3rd International GOCE User Workshop, 6–8 November 2006, Frascati, Italy, pp. 9–16.

Cesare, S. (2002). Performance requirements and budgets for the gradiometric mission. *Technical Note*, GOC-TN-AI-0027, Alenia Spazio, Turin, Italy.

ESA (1999). Gravity Field and steady-state ocean circulation mission. *ESA SP-1233 (1)*, ESA Publication Division, c/o ESTEC, Noordwijk, The Netherlands.

Gangui, A.H. (1998). A combined structural interpretation based on seismic data and 3-D gravity modeling in the Northern Puna, Eastern Cordillera, Argentina. Dissertation FU Berlin, Berliner Geowissenschaftliche Abhandlungen, Reihe B, Band 27, Berlin, Germany.

Hein, G., F. Sansò, G. Strykowsky, and C.C. Tscherning (1989). On the Choice of Norm and Base Functions for the Solution of the Inverse Gravimetric Problem. Ricerche di Geodesia Topografia Fotogrammetria, Milano, Italy, CLUP, pp. 121–138.

Heiskanen, W.A. and H. Moritz (1967). Physical geodesy. Springer-Verlag, Wien, Austria.

Jekeli, C. (1999). The determination of gravitational potential differences from satellite-to-satellite tracking. *Celest. Mech. Dyn. Astr.*, 75, 85–101.

Kirchner, A. (1997). 3D-Dichtemodellierung zur Anpassung des Schwere- und des Schwerepotentialfeldes der zentralen Anden. Dissertation FU Berlin, Berliner Geowissenschaftliche Abhandlungen, Reihe B, Band 25, Berlin, Germany.

Lessel, K. (1998). Die Krustenstruktur der Zentralen Anden in Nordchile (21–24°S), abgeleitet aus 3D-Modellierungen refraktionsseismischer Daten. Dissertation FU Berlin, Berliner Geowissenschaftliche Abhandlungen, Reihe B, Band 31, Berlin, Germany.

Migliaccio, F., M. Reguzzoni, F. Sansò, N. Tselfes, C.C. Tscherning, and M. Veicherts (2007). The latest test of the space-wise approach for GOCE data analysis. In: Proceedings of the 3rd International GOCE User Workshop, 6–8 November 2006, Frascati, Italy, pp. 311–318.

Migliaccio, F., M. Reguzzoni, F. Sansò, and P. Zatelli (2004). GOCE: dealing with large attitude variations in the conceptual structure of the space-wise approach. In: Proceedings of the 2nd International GOCE User Workshop. 8–10 March 2004, Frascati, Italy.

Pail, R. (2005). A parametric study on the impact of satellite attitude errors on GOCE gravity field recovery. *J. Geod.*, 79(4–5), 231–241.

Pail, R., W.D. Schuh, and M. Wermuth (2005). GOCE Gravity Field Processing. In: Jekeli, C., L. Bastos, and J. Fernandes (eds), International Association of Geodesy Symposia, 'Gravity, geoid and space missions', vol. 129, Springer-Verlag, Berlin, Germany, pp. 36–41.

Reguzzoni, M. and N. Tselfes (2009). Optimal multi-step collocation: application to the space-wise approach for GOCE data analysis. *J. Geod.*, 83(1), 13–29.

Sansò, F. and F. Sacerdote (1996). Optimal linear estimation theory for continuous fields of observations. In: Lecture Notes in Earth Science: Inverse Methods, n. 63, Springer-Verlag, Wien, Austria.

Vajda, P. (2006). Inverse problem of gravimetry. In: Reiffers, M. (ed), Proceeding of the 15th Conference of Slovak Physicists, 11–14 September 2006, Stará Lesná, Slovak Republic, 37–41.

Visser, P.N.A.M., N. Sneeuw, and C. Gerlach (2003). Energy integral method for gravity field determination from satellite orbit coordinates. *J. Geod.*, 77(3–4), 207–216.

Part VI
Global Gravity Field Modeling and EGMO8

N. Pavlis and J. Huang

Chapter 61

Assessment of the EGM2008 Gravity Field in Algeria Using Gravity and GPS/Levelling Data

S.A. Benahmed Daho

Abstract The present work focuses on the evaluation of the EGM2008 geopotential model that was recently released by the NGA (*National Geospatial-Intelligence Agency*, *US*)/EGM-development team, in Algeria using the free air gravity anomalies supplied by BGI and GETECH, the precise GPS data collected from the international TYRGEONET (TYRhenian GEOdynamical NETwork) and ALGEONET (ALGerian GEOdynamical NETwork) projects and the last Algerian local gravimetric geoid model. Additional comparisons of the terrestrial point data with the corresponding values obtained from other geopotential models were made. Five global geopotential models were used in this comparison: the Preliminary Earth Gravitational Model PGM2007A, the combined CHAMP and GRACE model EIGEN-CG01C, the combined GRACE and LAGEOS model EIGEN-GL04C, OSU91A and EGM96.

The study shows that all tested models are an improvement over OSU91A geopotential model used in all previous Algerian geoid computations and that new released combined model (EGM2008) is relatively superior to other tested models in the Algerian region. According to our numerical results, the new EGM2008 model fits better the observed values used in this investigation. Its standard deviations fit with GPS/levelling data are 21.4 and 18.7 cm before and after fitting using four-parameters transformation model. We strongly recommend the use of this new model in the remove-restore technique for the computation of the improved geoid for Algeria.

S.A. Benahmed Daho (✉)
Geodetic Laboratory, National Centre of Space Techniques, Arzew 31200, Algeria
e-mail: d_benahmed@hotmaiI.com

61.1 Introduction

The choice of the best geopotential model to reduce geodetic data is one of the critical steps in the geoid computation. Over the last 40 years, continuing improvements and refinements to the basic theory have been paralleled by the availability of more accurate and complete data and by improvements in the computational resources available for numerical modelling studies. These advances have led to the development of a sequence of global geopotential models of increasing spherical harmonic degree and order, and hence resolution. The most recent models are released from satellite gravity missions CHAMP and GRACE. In 2008, a new and revolutionary Earth Gravitational Model EGM2008 was realised by NGA. EGM2008 combines satellite (GRACE), marine (satellite-altimetry-derived), and land gravity data to model the global gravity field with a geo-spatial resolution of 5 by 5 arcmin (Pavlis et al., 2008). It is complete to degree and order 2,159 and contains additional spherical harmonic coefficients up to degree 2,190. Its accuracy is largely dependent on the accuracy of GRACE, marine and land gravity data and their availability. The purpose of this work is to give a brief summary of the evaluation results for the EGM2008 Earth gravity model in Algeria using gravity and GPS/levelling data. In addition, the Preliminary Earth Gravity model PGM2007A, the Global Geopotential Models EIGEN-CG01C (Reigber et al., 2006) and EIGEN-GL04C (Förste et al., 2006) derived from the new satellite missions CHAMP, GRACE and LAGEOS, OSU91A and the recently most accurate high degree geopotential model EGM96, have been also compared with land gravity anomalies and GPS/levelling derived geoid

S.P. Mertikas (ed.), *Gravity, Geoid and Earth Observation*, International Association of Geodesy Symposia 135,
DOI 10.1007/978-3-642-10634-7_61, © Springer-Verlag Berlin Heidelberg 2010

heights in Algeria in order to find the GGM that best fits the local gravity field features over this region. The first one (PGM2007A) is developed to degree and order 2,160 with additional coefficients to degree 2,190 while the remaining tested GGM are complete to degree and order 360. So that the terrestrial point data are not "compatible" with the corresponding model values they require filtering before they can be compared to the GGM. This was done in order to ensure all data were within the same spectral bandwidth.

For this evaluation study, the validated land gravity anomalies supplied by the BGI, a pre-processed $5' \times 5'$ grid of the free air anomalies covering the area bounded by the limits $16° \leq \varphi \leq 40°$ and $-10° \leq \lambda \leq 14°$ provided by GETECH, some of the precise GPS data collected from the international TYRGEONET and ALGEONET projects covering the northern of Algerian territory and extending from $31° \leq \varphi \leq 37°$ in Latitude and $-2° \leq \lambda \leq 9°$ in Longitude with baseline length ranging from about 1–1,000 km and the last Algerian local gravimetric geoid model based on the OSU91A global geopotential model, were used. The statistical parameters considered in this work are the mean, the standard deviation of the differences between the geopotential models and tested data. The most informative of these statistics is the standard deviation because the mean of the differences is distorted by the exclusion of the zero-order term. Therefore, the best fitting GGM will have the lowest standard deviation between itself and the tested gravity field data.

61.2 Global Geopotential Model

The gravitational potential of the Earth can be represented outside the masses of the Earth by a set of spherical harmonic coefficients $\overline{C}_{nm}$ and $\overline{S}_{nm}$, called a geopotential model. These potential coefficients can be used to calculate various gravimetric quantities that depend on the Earth's gravitational potential. The foremost of the quantities are the geoid undulation and gravity anomalies. In spherical approximation, these quantities can be computed from a set of spherical harmonic coefficients by (Heiskanen and Moritz, 1967):

$$\Delta g = \frac{GM}{r^2} \sum_{n=2}^{N_{\max}} (n-1) \sum_{\mathrm{m}=0}^{\mathrm{n}} \left[\overline{\mathrm{C}}_{\mathrm{nm}} . \cos \mathrm{m}\lambda + \overline{S}_{nm} . \sin \mathrm{m}\lambda \right] \overline{P}_{nm}(\cos\theta) \tag{1}$$

$$N = \frac{GM}{r\gamma} \sum_{n=2}^{N_{\max}} \sum_{\mathrm{m}=0}^{\mathrm{n}} \left[\overline{C}_{\mathrm{nm}} . \cos \mathrm{m}\lambda + \overline{S}_{nm} . \sin \mathrm{m}\lambda \right] \overline{P}_{nm}(\cos\theta) \tag{2}$$

where θ, λ are the geocentric colatitude and longitude of the point where N will be determined, $\overline{C}_{nm}$,$\overline{S}_{nm}$ are the fully normalised spherical geopotential coefficients of the anomalous potential, $\overline{P}_{nm}$ are the fully normalised associated Legendre functions, $N_{\max}$ is the maximum degree of the geopotential model.

Several global geopotential coefficient models are available from the International Centre for Global Earth Models (ICGEM). In addition to a new released model EGM2008, five high degree geopotential models have been considered in this comparison: The preliminary Earth Gravity Model PGM2007A, the combined EIGEN-CG01C and EIGEN-GL04C derived LAGEOS, CHAMP and GRACE, models, OSU91A and EGM96. The fully normalised spherical harmonic coefficients ($\overline{C}_{nm}$and $\overline{S}_{nm}$) supplied for each of these geopotential models are used in Eqs. (1) and (2), together with the defining parameters of GRS80, to compute geoid heights and free-air gravity anomalies for this investigation.

61.3 Data Used

61.3.1 Gravity Data

Two data sets of free-air gravity anomalies were used for the comparison as control data:

– A set of 12472 terrestrial gravity anomalies covering the territory of Algeria, was supplied by the BGI. The accuracy of these measurements ranges from 0.1 to 0.2 mgal. The data set is referred to the IGSN71 gravity datum and reduced using the GRS80 gravity formula. All data have been checked and duplicate points removed in a consistent manner. Figure 61.1 shows the geographical distribution of the BGI gravity data.

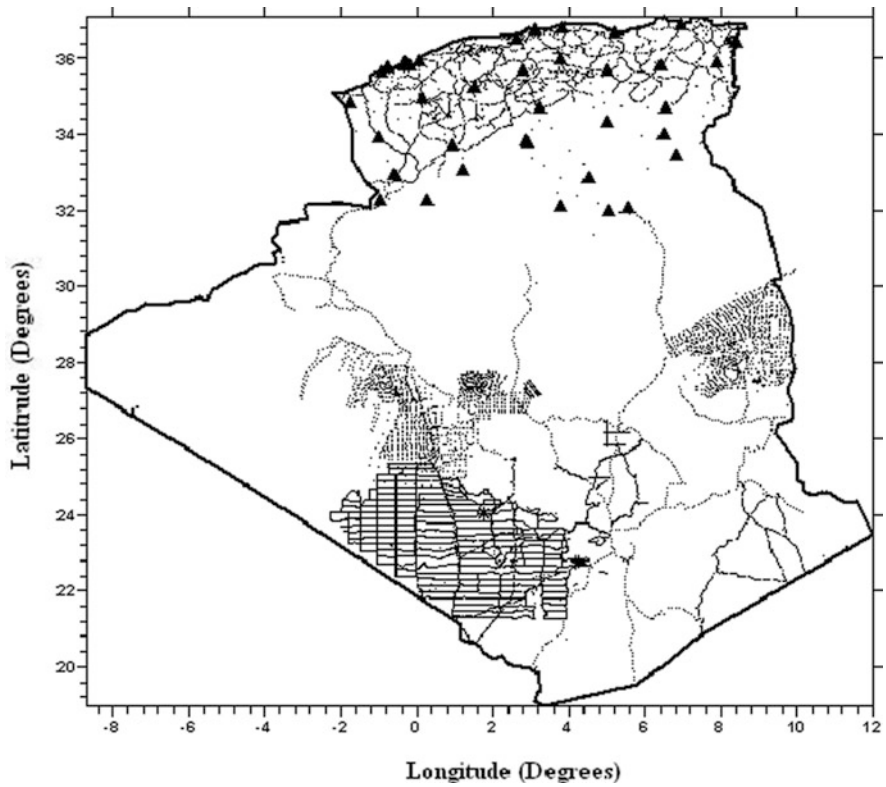


Fig. 61.1 Geographical distribution of BGI gravity measurements and GPS\levelling stations

– A pre-processed $5' \times 5'$ grid of the free air anomalies covering the area bounded by the limits $16° \leq \varphi \leq 40°$ and $-10° \leq \lambda \leq 14°$. This grid contains 289×289 points has been provided us by GETECH through the agreement between the National Centre of Space Techniques/Geodetic Laboratory and University of Leeds/GETECH without any information on the accuracy of different values. Figure 61.2 gives a graphical representation of the gravity data coverage in the computation area.

61.3.2 GPS/Levelling Data

There are several GPS/levelling points distributed over some regions of Algeria principally in the north part of the country. The distribution is fairly good but the total number of GPS stations is too small in relation to north part of Algerian's area. For this investigation, 45 precise GPS levelled points have been used of which 31 are benchmarks of the first order levelling network, and the others belong to the second order levelling network. All of these points are located in the north of Algeria territory between $31° \leq \varphi \leq 37°$ and $-2° \leq \lambda \leq 9°$ (see Fig. 61.1). The GPS observations were performed using ASHTECH Z-12 dual frequency receivers with an observation periods between 3 and 12 h and were processed with the Bernese GPS software version 4.2 (Beutler et al., 2001) using the precise ephemerides supplied by IGS. The computed ellipsoidal heights were referred to WGS84 system and their standard deviations do not exceed 3 cm. All GPS stations have been connected by traditional levelling to the national levelling network, which consists of orthometric heights.

61.3.3 Algerian Gravimetric Geoid Model

In view of the use of the GPS for the orthometric height computation, the National Centre of Space Techniques through the national projects of research, has recently focused a part of the current research on the precise geoid determination using different methods. The

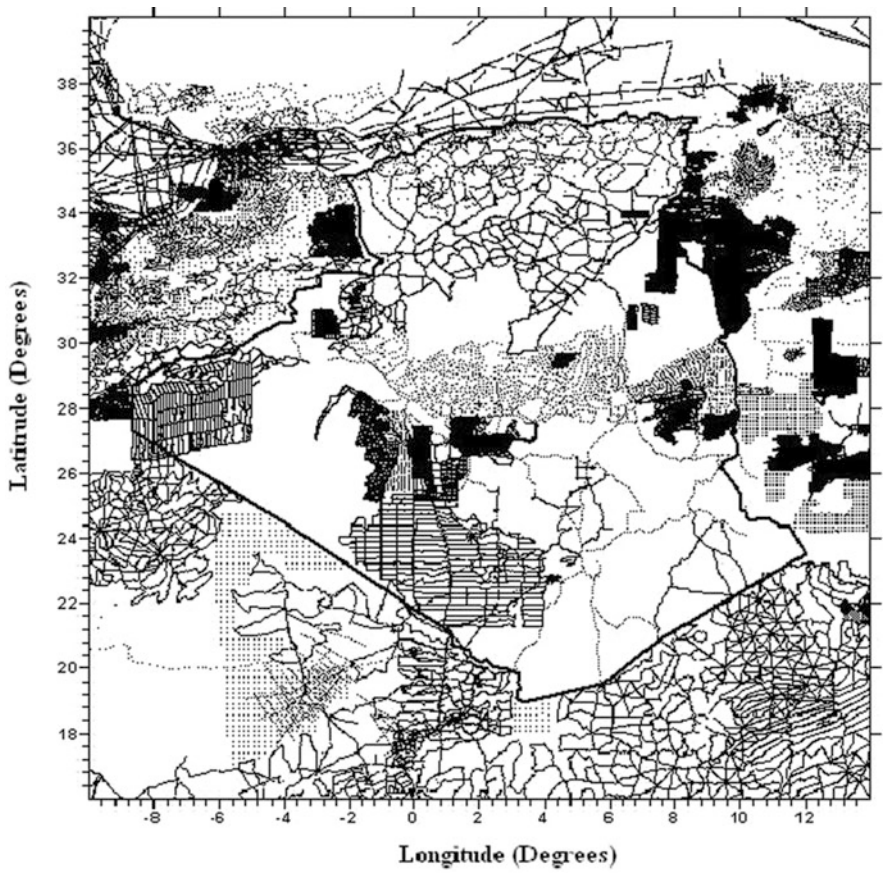


Fig. 61.2 Geographical distribution of GETECH gravity data

most recent solution of a preliminary geoid over the Algerian territory was done in 2002 using the spectral combination technique in connection with the remove-restore procedure (Forsberg and Sideris, 1993). For this computation, the pre-processed $5' \times 5'$ grid of the free air anomalies covering the area bounded by the limits $16° \leq \varphi \leq 40°$ and $-10° \leq \lambda \leq 14°$, derived by merging terrestrial gravity data and satellite altimetry data, have been used. This grid contains 289×289 points and has been provided us by GETECH. The computation of the effects of the topography according to the RTM reduction modelling method is based on the global topographic model GLOBE of $30'' \times 30''$. However, for the long wavelength gravity field information the spherical harmonic model OSU91A complete to degree and order 360 was employed. The final quasi-geoid was obtained by adding the geopotential model contribution and the residual terrain effect on the $5' \times 5'$ residual quasi-geoid grid. The major contributions to the final quasi-geoid were found to come from the OSU91A geopotential model. However, the Algerian height system is based on orthometric heights, so the gravimetrically determined quasi-geoid has been transformed to a geoid model and then compared to geoid undulations provided by GPS and levelling (Benahmed Daho and Fairhead, 2004).

61.4 Evaluation of the EGM2008

61.4.1 Comparison with Free Gravity Anomalies

The free air gravity anomalies from BGI and GETECH are compared with corresponding values computed from the EGM2008. The results, in mgal, for this comparison are summarised in Table 61.1. All the original data are referred to GRS80. The computations

Table 61.1 Free air gravity anomalies differences between the BGI and GETECH gravity data and EGM2008 geopotential model (Unit: [mgal])

	Min	Max	Mean	σ
BGI	–104.09	55.93	–0.61	6.12
GETECH	–271.94	110.91	–2.59	5.35

were carried out using the software program harmonic_synth_v02 developed by NGA and supplied to a new Joint Working Group established between IGFS and the IAG Commission2 for validation and quality assessment of GRACE-, CHAMP- and GOCE-based satellite-only and combined solutions for the Earth′s static gravity field. For most points, the differences are smaller than 10 mgal. There are very few stations where really large differences occur. The comparison with the BGI gravity data, indicates the EGM2008 model is able to recover gravity anomalies over 92.4% of the Algerian territory to within 10 mgal.

61.4.2 Comparison with GPS/Levelling Data

The global geopotential model EGM2008 was also compared with the previous GPS/Levelling data set available only in the northern part of Algeria. However, the EGM2008 coefficients in the tide-free system are used with reference to a mean Earth ellipsoid that differs from the WGS84 reference ellipsoidal. In order to reference the geoid to the WGS84 ellipsoid, an amount of –0.442 cm that corresponds to the zero-degree term for the EGM-based geoid heights, has been added to the output geoid heights obtained from the harmonic_synth software program. Table 61.2 summarises the statistics of the differences between the EGM2008 model and GPS/Levelling undulations in benchmarks. The standard deviation value of the absolute differences is ± 21.4 cm.

Table 61.2 Geoid heights differences, in meter, between the EGM2008 model and GPS/Levelling data (Unit: [ml])

	Min	Max	Mean	σ
EGM2008	–0.610	0.563	0.077	0.214

61.4.3 Comparison with Gravimetric Geoid Model

The difference between gravimetric geoid model for Algeria and geoid undulations computed by using EGM2008 model complete to degree 2,190 and order 2,159 range between –6.63 and 6.11 m with an average of 0.54 m and a standard deviation of about 1.29 m. The large discrepancies in Algeria, with the maximum (+6 m) occurring in the South and South-Western regions. No terrestrial data were available for these areas. The maximum negative difference occurs in Mediterranean Sea, outside the area of interest. These largest discrepancies are attributed, principally, to GETECH gridded gravity data quality used in the computation of the gravimetric geoid solution for Algeria (Benahmed Daho and Fairhead, 2004).

61.5 Comparisons Up to Degree 2,190 and Order 2,159

Additional comparisons of the terrestrial point data used in this study with the corresponding values obtained from some geopotential models, were made. In this comparison, we have used five global geopotential models: The preliminary Earth gravity model PGM2007A, the combined CHAMP and GRACE model EIGEN-CG01C, combined GRACE and LAGEOS model EIGEN-GL04C, OSU91A and EGM96. In order to make a fair comparison and taking into account the GGM omission error, all tested geopotential models were truncated to degree and order 360. Terrestrial point data used in this study are low-pass filtered using the high degree geopotential model EGM2008 from degree 361 to degree 2,190, i.e. free air gravity and geoid undulations information's in this spectral range are subtracted from the gravity data and the GPS/Levelling derived geoid heights data sets respectively before they are compared to the corresponding quantities obtained from the tested GGM. In addition, the geoid undulation derived from GPS/Levelling refers to the GRS80 ellipsoid and their corresponding values computed from GGM refer to a mean Earth ellipsoid that does not have the same dimensions as the WGS84 ellipsoid and hereby, it is necessary to take into account the effect of the

Table 61.3 Statistics of the reduced data between the BGI gravity data and the geopotential models (Unit: [mgal])

Models	Min	Max	Mean	σ
OSU91A	–97.28	87.34	1.55	7.75
EGM96	–101.21	63.62	–0.92	7.64
GL04C	–99.61	61.80	–0.68	7.81
CG01C	–99.21	61.51	–0.86	7.82
PGM2007A	–102.75	58.95	–0.58	**6.04**
EGM2008	–104.09	55.93	–0.61	**6.12**

Table 61.4 Statistical comparisons between global geopotential models and GETECH free-air gravity anomalies (Unit: [mgal])

Models	Min	Max	Mean	σ
OSU91A	–216.10	163.53	–2.26	18.65
EGM96	–225.06	155.37	–2.57	18.82
GL04C	–226.34	154.09	–2.61	18.79
CG01C	–225.15	154.17	–2.59	18.79
PGM2007A	–270.70	110.30	–2.60	**15.21**
EGM2008	–271.94	110.91	–2.59	**15.35**

different equatorial radius in the computation of the geoid undulation using the spherical harmonic expansion for each model. The results for these comparisons are summarised in Tables 61.3 and 61.4. All the original data are referred to GRS80. The computations were carried out using the FORTRAN program harmonic_synth_v02. We can see that the free air gravity anomalies computed from PGM2007A and EGM2008 have been significantly improved as compared to other tested geopotential models and that all models give almost the same results in terms of the standard deviation. This is because no new gravity data have been used in this region for the determination of the tested GGM models compared to OSU91A model.

Table 61.5 summarises the statistics of the differences in benchmarks between the tested geopotential models and GPS-based geoid heights. The standard deviations values of the differences show significant improvements with respect to OSU91A. All other models present very similar results. The best agreement (EGM2008) is at the ±21.4 cm level in terms of the standard deviation of the differences, before fitting. For the OSU91A, EGM96, EIGEN-GL04C, EIGEN-CG01C, and PGM2007A models, it is at the ±119.2, ±31.7, ±21.5, ±25.2 and ± 22.8 cm respectively.

To minimize the datum inconsistencies between the available height data, long-wavelength geoid errors and GPS and Levelling errors included in the ellipsoidal and orthometric heights, we have used a four-parameters transformation model. This model is the most commonly used in such adjustments and is given by the following formula (Heiskanen and Moritz, 1967):

$$N^{GPS}\text{-}\mathrm{N}^{\mathrm{GM}} = \mathrm{x}_0 + x_1 \cos(\varphi).\cos(\lambda) + x_2 \cos(\varphi).\sin(\lambda) + x_3 \sin(\varphi) + v_i \quad (3)$$

where (N^{GM}) is geoid undulation from GGM at a network of GPS benchmarks, ($\mathrm{N}^{\mathrm{GPS}}$) is the corresponding GPS/levelling-derived geoid height, x_0 is the shift parameter between the vertical datum implied by the GPS/levelling data and the gravimetric datum, and x_1, x_2 and x_3 are the three translation parameters in x, y, z axes between the coordinates system implied by the GPS data and the one implied by the gravimetric data.

All 45 GPS levelled stations are used as benchmarks in a least-squares adjustment. The statistics of the differences in benchmarks after fitting the systematic biases and tilts using a four-parameters model are summarised in Table 61.6. The fit improvement is almost up to 1.4 cm level for EIGEN-GL04C, 1.6 cm for EIGEN-CG01C, ±14.4 cm for EGM96, 58.9 cm for OSU91A, 3.3 cm for the preliminary

Table 61.5 Comparison of geoid undulations from geopotential models with GPS/Levelling derived geoid heights before fitting (Unit: [m])

Models	Min	Max	Mean	σ
OSU91A	–0.998	3.726	0.870	1.192
EGM96	–0.640	0.746	0.180	0.317
GL04C	–0.263	0.760	0.208	0.215
CG01C	–0.460	0.830	0.206	0.252
PGM2007A	–0.650	0.664	0.078	0.228
EGM2008	–0.610	0.563	0.077	**0.214**

Table 61.6 Comparison in benchmarks of geoid undulations from geopotential models with GPS-based geoid heights after fitting (Unit: [m])

Models	Min	Max	Mean	RMS
OSU91A	–1.276	1.245	0.000	0.603
EGM96	–0.522	0.334	0.000	**0.173**
GL04C	–0.528	0.466	0.000	0.201
CG01C	–0.596	0.617	0.000	0.236
PGM2007A	–0.494	0.386	0.000	0.195
EGM2008	–0.436	0.527	0.000	0.187

Table 61.7 Statistics of the differences in benchmarks between GPS-based and GGM geoid heights (Unit: [m])

Models	Min	Max	Mean	RMS
OSU91A	–1.047	3.706	0.777	1.279
(360)	**–0.422**	**1.399**	**0.000**	**0.585**
EGM96	–0.779	0.896	0.086	0.344
(360)	**–0.637**	**0.513**	**0.000**	**0.275**
GL04C	–0.559	0.740	0.112	0.334
(360)	**–0.555**	**0.506**	**0.000**	**0.300**
CG01C	–0.487	0.633	0.115	0.298
(360)	**–0.419**	**0.493**	**0.000**	**0.274**
PGM2007A	–0.650	0.664	0.077	0.228
(2190)	**–0.494**	**0.386**	**0.000**	**0.195**
EGM2008	–0.610	0.563	0.077	0.214
(2190)	**–0.436**	**0.527**	**0.000**	**0.187**

Earth gravity model PGM2007A, and 2.7 for the new released model EGM2008. These statistics show that optimal fit between the EGM96 and GPS/Levelling has been reached and that the four-parameters model absorbs the most of the inconsistencies between the available height data. In addition, we can see that the results from EGM96 after fitting remain very close to those given by the EGM2008 model in terms of the standard deviation.

In last step, no filtering has been applied to point-wise GPS-based geoid heights. The full spectral range of all GGM has been used. In this case, the computed differences between GPS-based and tested GGM geoid heights will thus contain not only the effect of the commission error of the underlying GGM, but the total effect of its omission error as well. Table 61.7 summarises the statistics in benchmarks of these differences. The statistics shown refer to the values of the original misclosures, whereas the statistics given in bold refer to the values of the residuals obtained after fitting using the previous parametric model. We can see that the EGM2008 geopotential model fits better the observed values before and after fitting using the four-parameters model. The geoid undulations computed from this model have been significantly improved as compared to other tested models.

61.6 Conclusion

This paper has described the comparisons of the GPS-based geoid heights and gravity anomalies in Algeria with those computed from the new released EGM2008. Additional comparisons of the terrestrial point data with the corresponding values obtained from the geopotential models PGM2007A, OSU91A, EGM96, and some GGM derived from the recent satellite missions CHAMP and GRACE complete to degree and order 360, were conducted. Based on the data sets used in the present work to evaluate the performances the new geopotential model EGM2008 within Algeria one has to note that in general the new models are an improvement over OSU91A geopotential model used in previous Algerian geoid computation. According to our numerical results, the EGM2008 fits best the observed values. The geoid undulations computed from this model have been significantly improved as compared to other tested models. The overall best agreement ($\pm$21.4 cm) before fitting is achieved when the global geopotential model EGM2008 was used. Unfortunately, the non-availability of GPS levelling data in the whole of the country with a homogeneous distribution and sufficient density does not allow a more reliable assessment at the national scale of the quality of the available global geopotential models tested in this study.

Acknowledgements The author wish to thank all Organisations and Persons who provided so kindly the many data that contributed to this work.

References

Benahmed Daho S.A. and J.D. Fairhead (2004). A new quasi-geoid computation from gravity and GPS data in Algeria. Newton's Bulletin No 2, A joint Bulletin of the Bureau Gravimétrique International and of the International Geoid Service – ISSN 1810-8547: pp 52–59.

Beutler G., H. Bock, E. Brockmann, R. Dach, P. Fridez, W. Gurtner, U. Hugentobler, D. Ineichen, J. Johnson, M. Meindl, L. Mervart, M. Rothacher, S. Schaer, T. Springer, and R. Weber (2001). Bernese GPS software version 4.2 manual, edited by U. Hugentobler, S. Schaer, and P. Fridez, Astron. Inst., University of Bern, Bern, p. 418.

Forsberg, R. and M.G. Sideris (1993). Geoid computation by multi-band spherical FFT approach, *Manuscrita Geodetica*, 18, 82–90.

Förste, C., F. Flechtner, R. Schmidt, R. König, U. Meyer, R. Stubenvoll, M. Rothacher, F. Barthelmes, K.H. Neumayer, R. Biancale, S. Bruinsma, and J.M. Lemoine (2006). A mean global gravity field model from the combination of satellite mission and altimetry/gravimetry surface gravity data. *Geophys. Res. Abstr.*, 8, 03462.

Heiskanen W.A. and H. Moritz (1967). Physical geodesy. Freeman & Co., San Francisco.

Pavlis, N.K., S.A. Holmes, S.C. Kenyon, and J.K. Factor (2008). An Earth Gravitational Model to Degree 2160: EGM2008, presented at the 2008 General Assembly of the European Geosciences Union, Vienna, Austria, April 13–18.

Reigber, C., P. Schwintzer, R. Stubenvoll, R. Schmidt, F. Flechtner, U. Meyer, R. König, H. Neumayer, C. Förste, F. Barthelmes, S.Y. Zhu, G. Balmino, R. Biancale, J.-M. Lemoine, H. Meixner, and J.C. Raimondo (2006). A High Resolution Global Gravity Field Model Combining CHAMP and GRACE Satellite Mission and Surface Data: EIGEN-CG01C. Scientific Technical Report STR06/07, GeoForschungsZentrum Potsdam.

Chapter 62

On High-Resolution Global Gravity Field Modelling by Direct BEM Using DNSC08

R. Čunderlík and K. Mikula

Abstract The paper deals with the global gravity field modelling using the boundary element method (BEM). The direct BEM formulation is applied to a solution to the fixed gravimetric boundary-value problem. We present a new model of geopotential at ocean obtained by BEM using the DNSC08 global marine gravity field. This model is compared with EGM-2008. High performance computations together with an elimination of the far zones' interactions allow a very refined integration over the all Earth's surface. Such approach results in a high-resolution global gravity field modelling.

62.1 Introduction

A precise determination of the geopotential in a global scale is mainly performed by spherical harmonics (SH). EGM-2008 up to degree 2,160 (Pavlis et al., 2008) represents *a quantum leap* in resolution and precision of geopotential models. Nevertheless, SH seams to be very efficient for the long wavelength part of the gravity field, while evaluation of the coefficients for the short wavelength part can be more complicated. Moreover, further increasing of degree of SH as well as reevaluation of coefficients for new available gravity data seams to be rather time consuming.

In contrary, efficient numerical methods like the boundary element method (BEM), finite element method (FEM) or finite volume mothod (FVM), have an advantage, that a successive refinement of the discretization is very straightforward and in general improves precision of numerical results. The price to be paid is large memory requirements. This drawback can be overcome using HPC (High-Performance Computing) facilities. Then the large-scale computations can be fast. From the geodetic applications of BEM to the gravity field modelling we mention (Klees et al., 2001; Čunderlík et al., 2008), and for FEM and FVM (Fašková et al., 2007).

In this paper we discuss a numerical solution to the fixed gravimetric boundary-value problem (FGBVP) by the direct BEM formulation. This approach is based on the collocation with linear basis functions (Čunderlík et al., 2008). The main limitation, enormous memory requirements, is partly reduced by parallel computing and partly by elimination of the far zones' interactions. In such a way, the Earth's surface can be discretized in a resolution comparable to SH up to degree 2,160.

The available DNSC08 global marine gravity field (Andersen et al., 2008) offers detail input data as boundary conditions (BC) at oceans. On lands, surface gravity disturbances are generated from EGM-2008. Due to adaptive refinements of a used grid, EGM-2008 data on lands does not influence significantly the results at oceans. Thus, geopotential obtained at oceans is achieved by a different numerical approach that geopotential obtained from EGM-2008.

R. Čunderlík (✉)
Department of Mathematics and Descriptive Geometry, Faculty of Civil Engineering, Slovak University of Technology, Bratislava 813 68, Slovakia
e-mail: cunderli@svf.stuba.sk

S.P. Mertikas (ed.), *Gravity, Geoid and Earth Observation*, International Association of Geodesy Symposia 135,
DOI 10.1007/978-3-642-10634-7_62, © Springer-Verlag Berlin Heidelberg 2010

62.2 Direct BEM for the Linearized FGBVP

The linearized FGBVP represents an exterior oblique derivative problem for the Laplace equation, cf. (Koch and Pope, 1972; Bjernhammar and Svensson, 1983) or (Grafarend, 1989)

$$\Delta T(x) = 0, \qquad x \in R^3\text{-}\,\Omega, \tag{1}$$

$$\langle \nabla T(x), s(x) \rangle = -\delta g(x), \quad x \in \Gamma_L, \tag{2}$$

$$T = \mathrm{O}(|\mathbf{x}|^{-1}) \quad \text{as} \quad \mathbf{x} \to \infty. \tag{3}$$

where T is the disturbing potential at any point $\boldsymbol{x}$, δg is the surface gravity disturbance, the domain Ω represents the body of the Earth with its boundary Γ (the Earth's surface), $\langle , \rangle$ is the inner product of two vectors and

$$\mathbf{s}(\mathbf{x}) = -\nabla U(\mathbf{x}) / \left| \nabla U(\mathbf{x}) \right|, \mathbf{x} \in \Gamma. \tag{4}$$

where U is the normal gravity potential. Equation (2) represents the oblique derivative BC as the normal to the Earth's surface Γdoes not coincide with the vector s defined by Eq. (4) (the surface deflection of the vertical is neglected). At oceans the obliqueness almost vanishes and the marine gravity disturbances practically represent the Neumann BC.

Let us apply the direct BEM formulation to the linear FGBVP in Eqs. (1), (2) and–(3). The main objective is to replace the Laplace equation (1) that governs the solution in the exterior domain $R^3 - \Omega$ by an equation that gives the solution on the boundary Γonly (see e.g. Brebbia et al., 1984 or Schatz et al., 1990). Such integral equations can be derived using Green's third identity, where a harmonic function T is represented as a superposition of the single-layer and double-layer potential. The same integral relation can be obtained through the method of weighted residual. A detailed derivation is discussed in (Čunderlík et al., 2008). Here we only present the final boundary integral equation (BIE),

$$\begin{aligned} \frac{1}{2}\, T(x) + \int_{\Gamma} T(y) \frac{\partial G}{\partial n_{\Gamma}}(x,y) d_y S = \\ = \int_{\Gamma} \frac{\partial T}{\partial n_{\Gamma}}(\mathbf{y}) \mathrm{G}(\mathbf{x},\mathbf{y}) d_y S, \quad \mathbf{x} \in \Gamma, \end{aligned} \tag{5}$$

where dS is the area element and the kernel function G is the fundamental solution of the Laplace equation,

$$\mathrm{G}(\mathbf{x},\mathbf{y}) = (4\pi |\mathbf{x}\text{–}\mathbf{y}|)^{-1}, \quad \mathbf{x},\mathbf{y} \in \mathrm{R}^3. \tag{6}$$

Later on, we use the same numerical technique as discussed in (Čunderlík et al., 2008), i.e. the collo-cation method with linear basis functions. In such a way we get a discrete form of BIE (5) that subsequently yields a linear system of equations. Then we input BC which leads to a dense nonsymmetric stiffness matrix. Since both the kernel functions in BIE (5) depend on direct distances only, components of the stiffness matrix are given only by the geometry of the fixed Earth's surface, i.e. they are invariant w.r.t. the input BC.

62.3 Numerical Experiment

Presented numerical experiment deals with a numerical solution of the linearized FGBVP. At first we model the fixed Earth's surface using the following datasets: (i) on lands we add the global topography model SRTM30_PLUS V1.0 (Becker and Sandwell, 2003) to EGM-96 (Lemoine et al., 1998) in order to get geocentric positions, (ii) at oceans/seas we use DNSC08-MSS (Andersen et al., 2008). Such Earth's topography is approximated by a triangulated surface (Čunderlík et al., 2008). Vertices of this triangulation represent collocation points were we need to insert input data as BC. At oceans/seas we transform available marine gravity anomalies from DNSC08-GRAV (Andersen et al., 2008) into the gravity disturbances. On lands we generate the surface gravity disturbances from EGM-2008 (Pavlis et al., 2008) using the GRAFIM software (Šprlák and Janák, 2006). The parameters of the normal gravity field are given by WGS-84 (NIMA, 2001).

A mesh size of the triangular elements is 0.2° in latitude. It represents 1,215,002 collocation points regularly distributed over the whole Earth's surface. The

corresponding dense stiffness matrix would require approximately 11 TB of the internal memory. In order to reduce such enormous memory requirements an elimination of the far zones' interactions is applied. Here we use approximate values of disturbing potential obtained from a coarse global numerical solution obtained by BEM. In such a way, the dense stiffness matrix is transformed into a sparse one (Čunderlík et al., 2008).

Final large-scale computations were accomplished on parallel computers with 128 GB of the distributed memory using standard MPI (Message Passing Interface) subroutines for the code parallelization (Aoyama and Nakano, 1999). As a linear solver we use the nonstationary iterative methods BiConjugate Gradient Stabilized (BiCGSTAB) method (Barrett et al., 1994), which is suitable for dense and nonsymetric matrices.

The obtained numerical solution of FGBVP is compared with EGM-2008, where the disturbing potential is transformed to height anomalies by the Brunce formula. Residuals are depicted in Fig. 62.1. Basic statistical characteristics of the residuals are presented in Table 62.1. The disturbing potential as a direct result is transformed into the geopotential. Figure 62.2 depicts the geopotential on DNSC08-MSS: (a) obtain by BEM, (b) evaluated from EGM-2008. Figure 62.3 shows details in different oceans.

62.4 Results and Discussion

The obtained numerical solution of the linearized FGBVP by the direct BEM shows a very good agreement with EGM-2008. The standard deviation of residuals between both models is 0.17 m. The residuals are higher on lands (Fig. 62.1, Table 62.1) despite the fact that here the surface gravity disturbances (BC) are generated from EGM-2008. It is due to the complicated Earth's surface where a level of the discretization is probably not sufficient, especially in mountainous areas with the highest residuals, e.g. in Himalayas and Andes (Fig. 62.1). Here we remind that the obtained disturbing potential is computed at collocation points directly on the Earth's surface.

At oceans, original input data are available from DNSC08. As we have observed, EGM-2008 data used as BC on lands does not significantly influ-ence results at oceans due to adaptive refinements of the triangulation. Thus, the numerical solution obtained by BEM at oceans can be considered as independent from EGM-2008. Then the standard deviation of residuals 0.12 m indicates high accuracy of the obtained numerical result. On the other hand, the mean values –0.37 m at oceans and –0.42 m on lands show an overall bias between solutions. This shift can be caused by the elimination of the far zones' interactions due

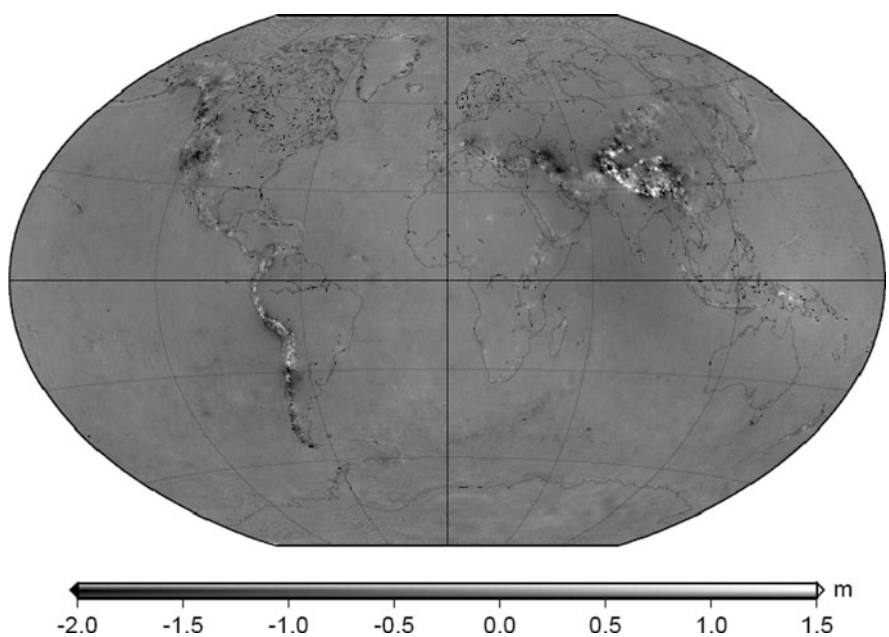


Fig. 62.1 Residuals between the numerical solution obtained by BEM and EGM-2008

Table 62.1 Statisitcal characteristics of residuals between the numerical solution by BEM and EGM-2008 for different regions

[m]	Total	Land	Ocean	N. Am.	S. Am.	Eur.	Afr.	Asia	Aus.	Ant.	Pac. Oc.	Atl. Oc.	Ind. Oc.	Arc.Oc.
Max	4.61	4.61	0.68	1.94	1.83	1.29	0.86	4.61	0.39	0.04	0.44	0.36	0.23	0.68
Min	−5.44	−5.44	−1.58	−2.66	−3.32	−2.39	−1.13	−5.45	−0.90	−0.88	−1.43	−1.58	−1.06	−1.00
Mean	−0.38	−0.42	−0.37	−0.43	−0.49	−0.46	−0.31	−0.51	−0.36	−0.41	−0.36	−0.35	−0.43	−0.33
St.D.	0.17	0.25	0.12	0.21	0.24	0.24	0.09	0.37	0.09	0.09	0.12	0.09	0.11	0.15

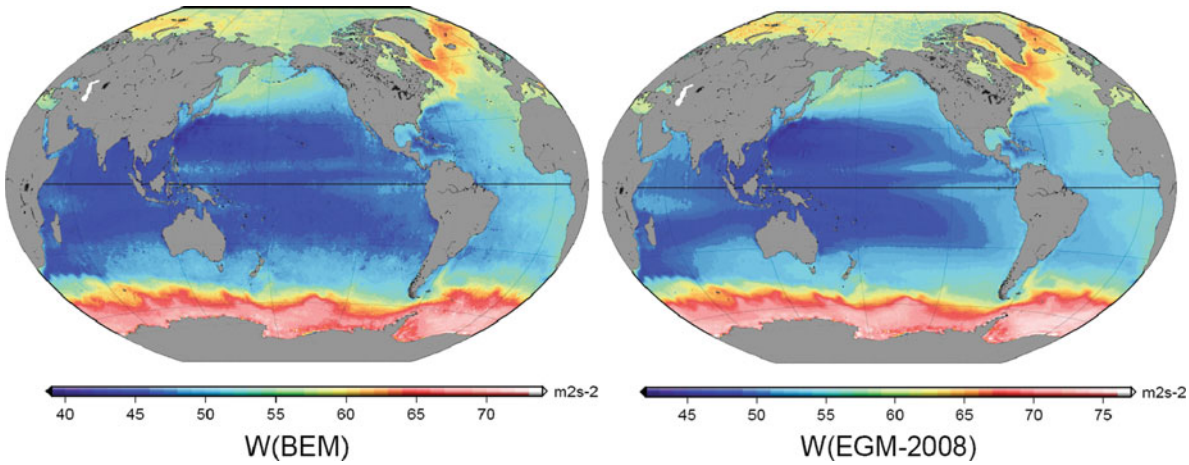


Fig. 62.2 The geopotential on the DNSC08 Mean Sea Surface (**a**) on the *left*: numerical solution by BEM, (**b**) on the *right*: EGM-2008

to biases in approximate values of disturbing potential obtained from coarse numerical solutions by BEM. Here an improvement can be expected by using the satellite geopotential models (e.g. from GRACE) for approximate values of the far zones.

The geopotential evaluated on the DNSC08-MSS for both models also show a good agreement. Global behaviour of the geopotential is very similar (Fig. 62.2). A positive sign is that the BEM solution separates the counter equatorial current slightly better. The differences can be seen mainly in details (Fig. 62.3). Here EGM-2008 is smoother with very slight striping due to SH. Our solution is not so smooth and reflects irregularities in input marine gravity data [e.g. in the Pacific Ocean (Fig. 62.3)]. It means that the obtained disturbing potential in small areas of abrupt gravity changes is not enough determined. This can be caused by the inaccurate transformation of the marine gravity anomalies of DNSC08-GRAV into gravity disturbances or by an insufficient discretization in these areas. In the second case an even fine discretization based on the adaptive refinement procedures can be challenging for further investigation.

Regarding a comparison between the presented new results and the previous results published in (Čunderlík et al., 2008), one can see an evident improvement. Considering standard deviations, new results are better even at oceans where altimetry derived gravity data from DNSC08 are used. Here we have to remind that in both cases we compare our numerical solution with the corresponding geopotential model from which we also simulate input data. Thus the statistical characteristics in both numerical experiments are not consistent. Despite this fact, better standard deviation of residuals with respect to more complex and realistic EGM-2008 emphasizes an improvement of the BEM solution. Higher maximal and minimal residuals appear only locally without any systematic tendencies, cf. Table 1 and Fig. 1 with Table 3 (the last column) and Fig. 4 in Čunderlík et al. (2008). It is probably due to the fact that input gravity data as BC interpolated from DNSC08_GRAV are more realistic than surface

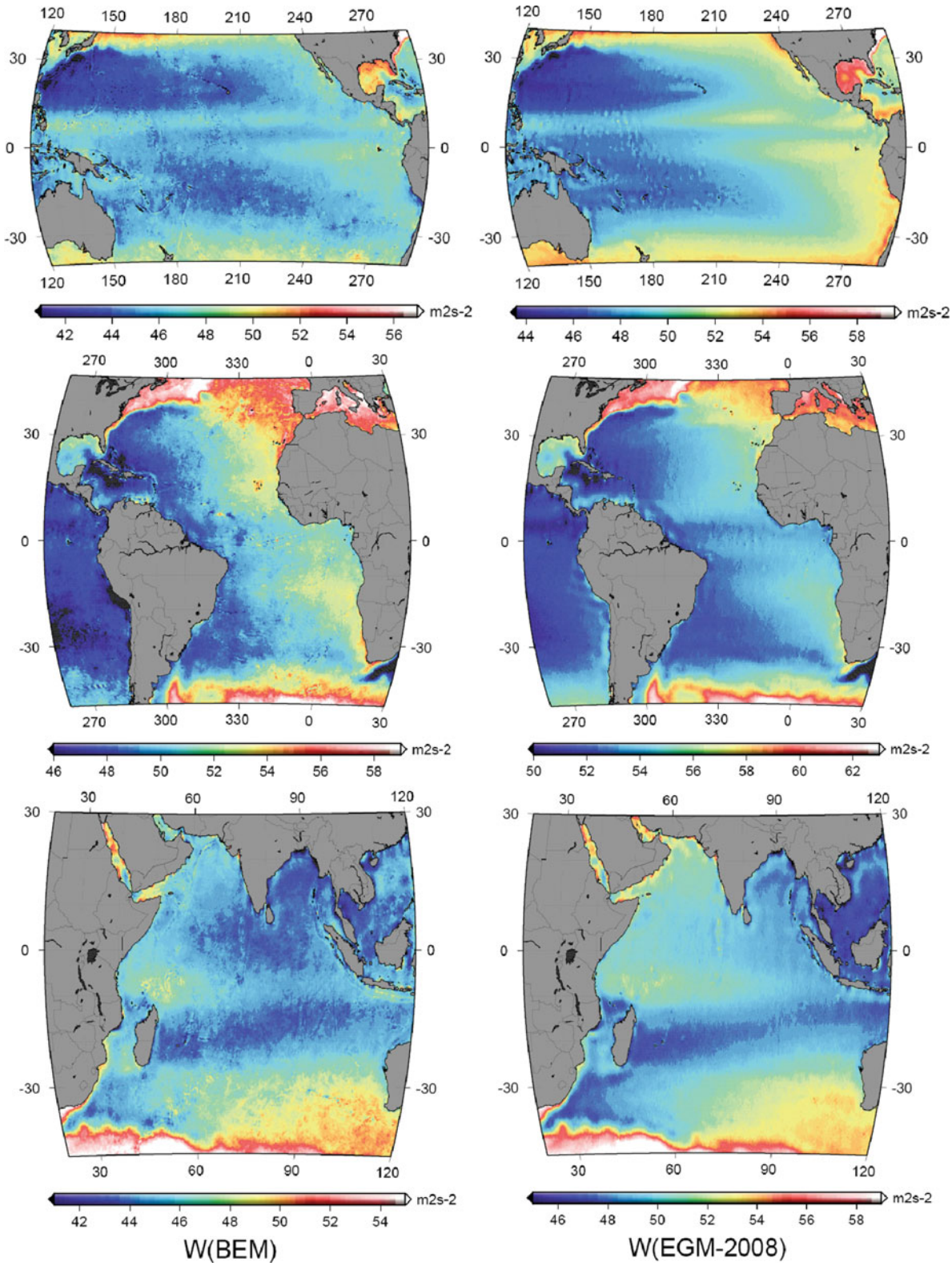


Fig. 62.3 The geopotential on the DNSC08 Mean Sea Surface – details in different oceans: (**a**) on the *left*: numerical solution by BEM, (**b**) on the *right*: EGM-2008

gravity disturbances simulated from EGM-96. To conclude, all these aspects demonstrate the potential of BEM as a feasible alternative to the spherical harmonic modelling.

Acknowledgements Authors gratefully thank to the financial support given by grants: VEGA 1/3321/06, APVV-LPP-216-06 and APVV-0351-07.

References

Andersen, O.B., P. Knudsen, and P. Berry (2008). The DNSC08 ocean wide altimetry derived gravity field. Presented at EGU-2008, Vienna, Austria, April.

Aoyama, Y. and J. Nakano (1999). RS/6000 SP: Practical MPI Programming. IBM, Poughkeepsie, New York.

Barrett, R., M. Berry, T.F. Chan, J. Demmel, J. Donato, J. Dongarra, V. Eijkhout, R. Pozo, C. Romine, and H. Van der Vorst (1994). Templates for the solution of linear systems: building blocks for iterative methods. http://www.netlib.org/templates/Templates.html

Becker, J. and D. Sandwell (2003). Accuracy and resolution of shuttle radar topography mission data. *Geophys. Res. Lett.*, 30(9), 1467.

Bjerhammar, A. and L. Svensson (1983). On the geodetic boundary-value problem for a fixed boundary surface – satellite approach. *Bull. Géod.*, 57, 382–393.

Brebbia, C.A., J.C.F. Telles, and L.C. Wrobel (1984). Boundary element techniques, theory and applications in engineering. Springer-Verlag, New York.

Čunderlík, R., K. Mikula, and M. Mojzeš (2008). Numerical solution of the linearized fixed gravimetric boundary-value problem. *J. Geod.,* 82, 15–29.

Fašková, Z., R. Čunderlík, J. Janák, K. Mikula, and M. Šprlák (2007). Gravimetric quasigeoid in Slovakia by the finite element method. *Kybernetika,* 43/6, 789–796.

Grafarend, E.W. (1989). The geoid and the gravimetric boundary-value problem. Rep 18 Dept Geod, The Royal Institute of Technology, Stockholm.

Klees, R., M. Van Gelderen, C. Lage, and C. Schwab (2001). Fast numerical solution of the linearized Molodensky problem. *J. Geod*., 75, 349–362.

Koch, K.R. and A.J. Pope (1972). Uniqueness and existence for the geodetic boundary value problem using the known surface of the earth. *Bull. Géod.*, 46, 467–476.

Lemoine, F.G., S.C. Kenyon, J.K. Factor, R.G. Trimmer, N.K. Pavlis, D.S. Chinn, C.M. Cox, S.M. Klosko, S.B. Luthcke, M.H. Torrence, Y.M. Wang, R.G. Williamson, E.C. Pavlis, R.H. Rapp, and T.R. Olson (1998). EGM-96 – The Development of the NASA GSFC and NIMA Joint Geopotential Model.

NASA Technical Report TP-1998-206861NIMA (2001) Department of Defense World Geodetic System 1984, Its Definition and Relationships With Local Geodetic Systems, 3rd Edition, National Geospatial-Intelligence Agency. Technical Report TR8350.2.

Pavlis, N.K., S.A. Holmes, S.C. Kenyon, and J.K. Factor (2008). An Earth Gravitational Model to Degree 2160: EGM2008, presented at the 2008 General Assembly of EGU, Vienna, Austria, April 13–18, 2008.

Schatz, A.H., V. Thomée, and W.L. Wendland (1990). Mathematical theory of finite and boundary element methods. Birkhäuser Verlag, Basel,.Boston,.Berlin.

Šprlák, M. and J. Janák (2006). Gravity field modeling. New program for gravity field modeling by spherical harmonic functions, *GaKO*, 1, 1–8.

Chapter 63

Is Australian Data Really Validating EGM2008, or Is EGM2008 Just in/Validating Australian Data?

S.J. Claessens, W.E. Featherstone, and I.M. Anjasmara

Abstract The tide-free release of the EGM2008 combined global geopotential model and its pre-release PGM2007A are compared with Australian land and marine gravity observations, co-located GPS-levelling on the [admittedly problematic] Australian Height Datum, astrogeodetic deflections of the vertical, and the AUSGeoid98 regional gravimetric quasi-geoid model. The results show that we cannot legitimately claim to truly validate EGM2008. Instead, EGM2008 confirms already-known problems with the Australian data, as well as revealing some previously unknown problems. If one wants to claim validation, then EGM2008 is validated because it can confirm the errors in our regional data. Simply, EGM2008 is a good model over Australia.

63.1 Introduction

Australia, as a significant landmass in the Southern Hemisphere with reasonable geodetic data coverage, has been used over the years for "ground truthing" global geopotential models (GGMs). Several studies have addressed this, mainly with a view to production of regional gravimetric geoid/quasigeoid models (e.g., Kirby et al., 1998). This paper continues this effort by comparing the tide-free version of EGM2008 and its pre-release PGM2007A, with Australian gravity-field-related data. This is part of the International Association of Geodesy's (IAG's) Inter-Commission Working Group 2 *Evaluation of Global Earth Gravity Models* (http://users.auth.gr/~kotsaki/IAG_JWG/IAG_JWG.html). In an attempt to provide a more complete and useful 'validation', we use some newer data not used before.

Our attempted "validation" has proven to be a two-way process, where PGM2007A and EGM2008 have confirmed problems that were already known (e.g., with AUSGeoid98 in the coastal zone), but it has identified some problems (e.g., with the Australian gravity data) that we were previously unaware of. This alone is testament to the quality of EGM2008, i.e., an implicit validation.

S.J. Claessens (✉)
The Institute for Geoscience Research, Western Australian Centre for Geodesy, Curtin University of Technology, Perth, WA 6845, Australia
e-mail: S.Claessens@curtin.edu.au

63.2 Description of Australian Data

63.2.1 Australian Gravity Data

The July 2007 release of the Australian national gravity database (cf. Murray, 1997), which contains 1,245,026 land and marine gravity observations, is used in this study. Second-order, atmospherically corrected, free-air gravity anomalies were recomputed from primary observations (i.e., the gravity values and their 3D coordinates).

The ship-track gravity data around Australia (Symonds and Willcox, 1976; Mather et al., 1976) is most problematic. In AUSGeoid98, these data were [incorrectly] assumed to have been crossover adjusted (Featherstone et al., 2001). However, they were not, as shown through comparison with multi-mission satellite altimetry data (Featherstone, 2003) or via point-mass modelling (Claessens et al., 2001). As such, the Australian ship-track data simply should not be

S.P. Mertikas (ed.), *Gravity, Geoid and Earth Observation*, International Association of Geodesy Symposia 135,
DOI 10.1007/978-3-642-10634-7_63, © Springer-Verlag Berlin Heidelberg 2010

used to try to "validate" EGM2008. Instead, EGM2008 invalidates these data.

63.2.2 Australian GPS-Levelling Data

A nation-wide GPS ellipsoidal height dataset (cf. Soltanpour et al., 2006), observed at 254 junction points of the Australian Height Datum (AHD) (Roelse et al., 1971), is used in this study. In addition, regional GPS-levelling datasets over the southwest seismic zone (SWSZ) in Western Australia (cf. Featherstone, 2004; Featherstone et al., 2004) and the South Australian Seismic Zone (SASZ) near Adelaide are used. These are probably the most reliable data sets available in Australia at the moment.

Of most concern in any GPS-levelling evaluation in Australia is the quality of the AHD. The AHD contains a predominantly north-south-oriented distortion of around 1–2 m (Featherstone, 2001, 2004, 2006). We believe that most of this distortion has been caused by the constraint of 32 tide gauges to mean sea level in the definition of the AHD. The mainly north-south-oriented sea-surface topography around Australia causes the adjustment to be north-south-tilted with respect to an equipotential surface.

63.2.3 Australian Vertical Deflection Data

Vertical deflections, being higher order derivatives of the Earth's disturbing potential, provide a better validation of high-degree GGMs (cf. Jekeli, 1999). During correspondence with the EGM2008 development team, we exchanged 1,080 Australian astro-geodetically observed vertical deflections/devi-ations. The main problem with the reliability of the Australian vertical deflections is that most, if not all, were observed over 40 years ago (cf. Kearsley, 1976). The accuracy is crudely estimated to be around one arc-second in each deflection component (Featherstone, 2006).

63.2.4 AUSGeoid98

AUSGeoid98 (Featherstone et al., 2001) remains the nationally recognised standard in Australia for the transformation of GPS-derived ellipsoidal heights to the AHD, despite being computed nearly a decade ago. It refers to the GRS80 ellipsoid. A new model is currently being computed based on EGM2008 (e.g., Featherstone et al., 2007). However, it is informative to compare EGM2008 with AUSGeoid98 to see if there are any spatial differences that warrant further investigation.

AUSGeoid98 was computed from EGM96 (Lemoine et al., 1998) to degree and order 360, the 1996 release of Geoscience Australia's gravity data (note the earlier comment on the quality of the Australian ship-track gravity data), marine gravity anomalies from Sandwell and Smith (1997; version 9.2), and terrain corrections from the version 1 Australian digital elevation model (DEM). Full details are in Featherstone et al. (2001).

63.3 Results

All gravity-field-related quantities computed from PGM2007A and EGM2008 in this Australian 'validation' used the HARMONIC_SYNTH.f FORTRAN software provided by the EGM2008 development team. All these computations were run to degree and order 2,160 with respect to the GRS80 ellipsoid.

63.3.1 Comparisons with Australian Gravity

First, due to the large number of gravity observations (~1.2 million) and the computer time required to evaluate EGM2008 up to degree and order 2,160 at all these points, the results presented below for the Australian land gravity anomalies have used pre-synthesis of EGM2008 on a 2 arc-minute grid, followed by bicubic interpolation to the gravity observations' locations.

The majority of the free-air gravity anomalies computed from PGM2007A over land show a good correspondence with the land free-air gravity anomalies, even in areas where there are large gravity anomaly gradients such as central Australia, and the correspondence of free-air gravity anomalies from EGM2008 is very similar (Table 63.1). The largest differences are in the mountainous regions, notably in Tasmania

Table 63.1 Fit of the geopotential models to Australian free-air gravity anomalies [units in mgal]

Model	# points	Degree	Max	Min	Mean	Std
Raw data	1,245,026	n/a	931.03	–229.85	4.292	26.565
PGM07A (land data)	1,095,065	2,160	68.74	–79.86	–0.296	4.954
EGM08 (land data)	1,095,065	2,160	68.73	–78.17	–0.296	4.924
PGM07A (marine data)	149,961	2,160	972.00	–171.69	–0.810	12.104
EGM08 (marine data)	149,961	2,160	970.96	–171.68	–0.748	12.034
EGM96 (all data)	1,245,026	360	988.67	–124.89	–0.424	12.611

and along the Great Dividing Range along the eastern Australian coastline.

The bulk of the free-air gravity anomalies computed from PGM2007A and EGM2008 correspond to the ship-track gravity anomalies to within ~5 mgal. However, several ship tracks show considerable biases of 50 mgal, or more, as was noted by Featherstone et al. (2001) who deleted most but not all of these (see later). This confirms that the Australian ship-track gravity database has not been crossover adjusted. We suspect that no ship-track data were used in PGM2007A and EGM2008, so these differences essentially reflect the difference between altimeter-derived gravity anomalies in PGM2007A/EGM2008 and the ship-tracks.

Unlike the comparison in Featherstone (2003), large differences are not seen near the coast, indicating that the altimeter data have been improved in these regions. This is from the use of re-tracked altimetry data. It should be noted that no outliers were removed in the computation of these statistics.

63.3.2 Comparisons with AUSGeoid98

Height anomalies (quasigeoid heights) were computed from PGM2007A and EGM2008 up to degree and order 2,160 on a $2' \times 2'$ grid and compared directly with the gravimetric-only AUSGeoid98 solution (Featherstone et al., 2001). This provides some of the most interesting results (Fig. 63.1 and Table 63.2).

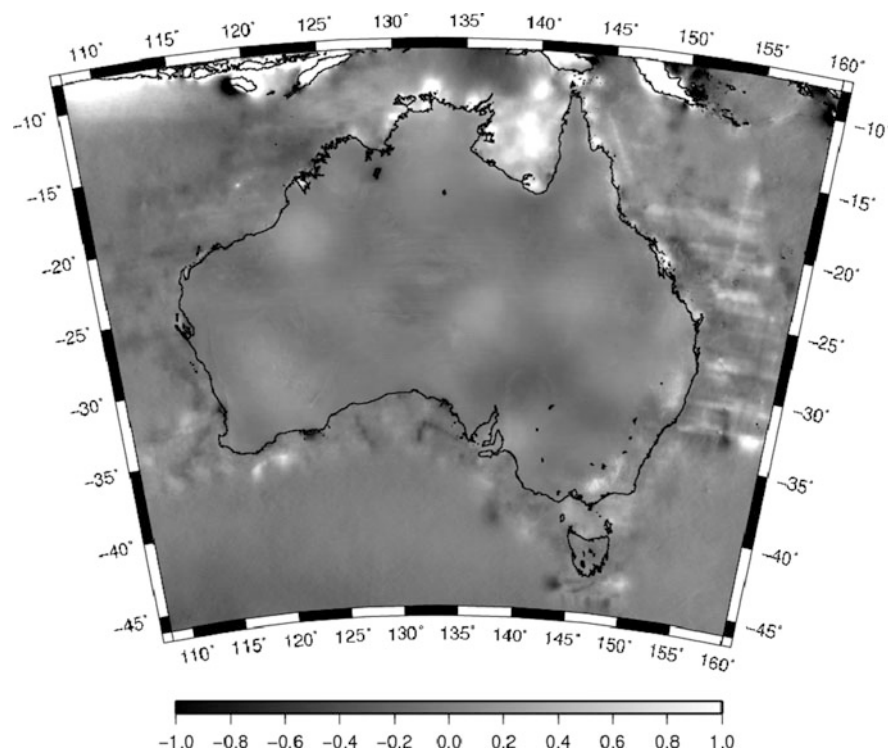


Fig. 63.1 Differences between height anomalies computed from EGM2008 and AUSGeoid98 [Lambert projection; units in m]

Table 63.2 Descriptive statistics of the absolute differences between quasigeoid heights computed from global models and AUSGeoid98 on a $2' \times 2'$ grid [units in m]

Model	Max	Min	Mean	Std
PGM2007A	13.062	–2.472	0.057	0.454
EGM2008	12.983	–2.476	0.064	0.458

The differences are mainly of a medium-wavelength nature over the Australian mainland (Fig. 63.1). From a comparison with the differences between EGM96 (used in AUSGeoid98) and GGM02C (Tapley et al., 2005), these differences seem to come mostly from the GRACE data used in EGM2008 (Mayer-Gürr). The largest medium-wavelength difference in Fig. 63.1 appears in the Gulf of Carpentaria (centred on 140°E, 12°S), where only a very limited number of ship-track gravity observations is available. An explanation for the differences may be that the altimeter-derived gravity anomalies were in error in this shallow sea. However, Tregoning et al. (2008) show that a weather-driven annual sea surface height variation of ~40 cm amplitude affects the GRACE solutions in this area. Therefore, the differences in this region may also be due to aliasing in the global geopotential models, though errors in the altimeter data cannot be ruled out. Clearly, this needs further attention.

The next most noticeable features in Fig. 63.1 are the stripes offshore (e.g., to the east of Queensland and northern New South Wales). These stripes are due to the unadjusted ship-track data used in AUSGeoid98 (discussed earlier). This can be seen more clearly in Fig. 63.2, which shows the differences of the ship-track gravity anomalies and EGM2008 gravity anomalies, overlaid on the differences in height anomalies between EGM2008 and AUSGeoid98 offshore Queensland. These differences are exacerbated by the

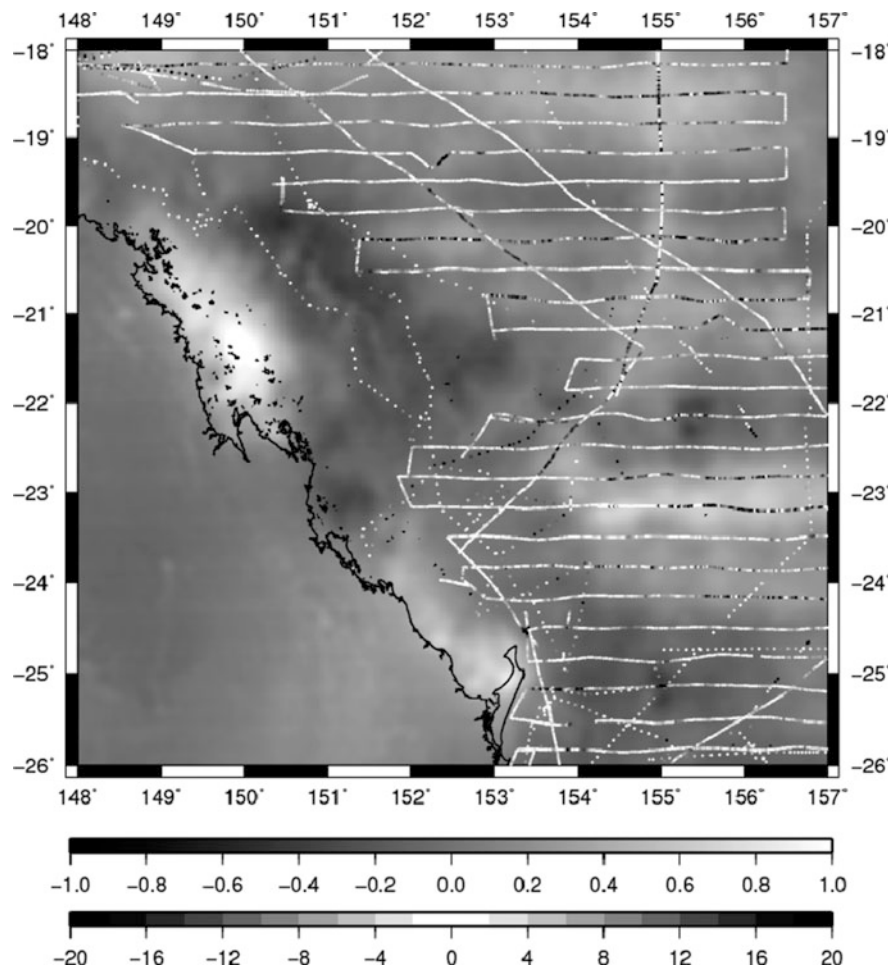


Fig. 63.2 Differences between height anomalies computed from EGM2008 and AUSGeoid98 off Queensland (*background surface*; *top scale bar*) and differences between free-air gravity anomalies from EGM2008 and from ship-track observations (*dotted points*; *bottom scale bar*) [Mercator projection; units in m and mgal]

presence of the Great Barrier Reef, which prevents dense ship-track surveys and complicates the tidal models in this region. In conclusion, EGM2008 clearly "invalidates" AUSGeoid98 in some marine areas.

63.3.3 Comparisons with GPS-Levelling

Table 63.3 indicates that PGM2007A and EGM2008 improve on many earlier gravity field solutions in terms of standard deviation (STD) of the differences with respect to 254 GPS-levelling points across Australia. It should, however, be recalled that the levelling data suffers from a north-south-oriented trend in the AHD (see earlier), which is clearly visible in Fig. 63.3. Therefore, statistics were also computed after removal of a bias and tilt. Both with and without removal of a bias and tilt (Table 63.3), EGM2008 shows the smallest STD of all quasigeoid models tested.

Comparisons were also made to the newer GPS-levelling data in the SWSZ and the SASZ (Tables 63.4 and 63.5). The STDs of AUSGeoid98, PGM2007A and EGM2008 are very similar for the regional GPS-levelling data sets in the SWSZ and SASZ,

Table 63.3 Descriptive statistics of the absolute differences between quasigeoid models and 254 nation-wide co-located GPS-AHD points [units in m]

		Bias/tilt not removed				Bias/tilt removed			
Model	Degree	Max	Min	Mean	Std	Max	Min	Mean	Std
EGM96	360	0.89	–0.96	0.009	0.334	–	–	–	–
GGM02C	200	0.95	–1.32	0.007	0.415	–	–	–	–
EIGEN-GL04C	360	0.79	–0.65	0.059	0.293	–	–	–	–
AUSGeoid98	~5,400	0.86	–0.72	0.077	0.284	0.52	–0.76	0.000	0.191
PGM2007A	2,160	0.66	–0.54	0.068	0.249	0.55	–0.77	0.000	0.179
EGM2008	2,160	0.65	–0.53	0.063	0.242	0.57	–0.70	0.000	0.173

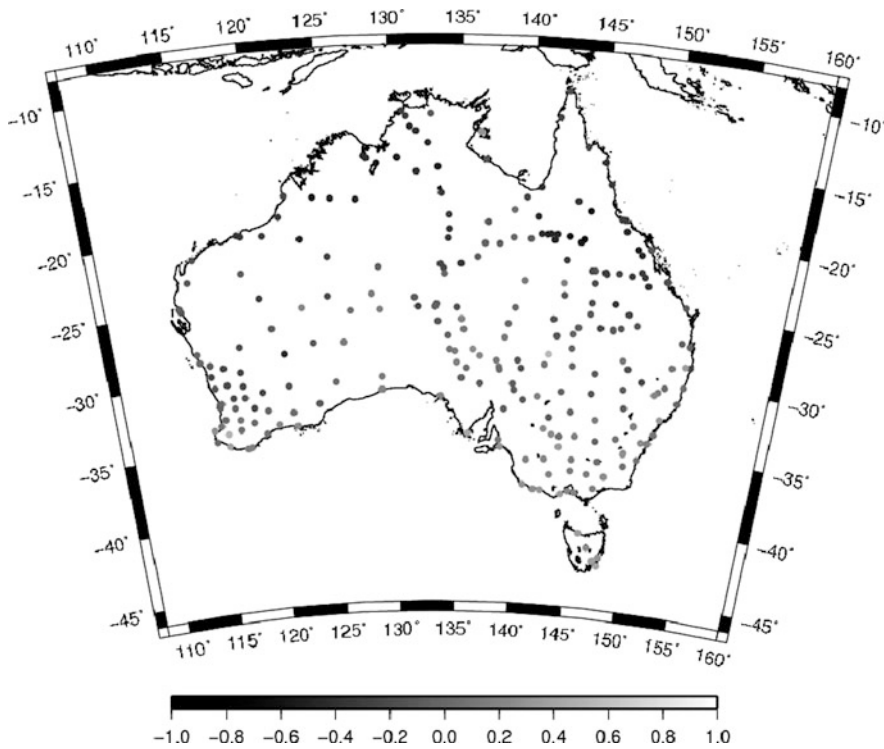


Fig. 63.3 Differences between height anomalies from 254 GPS-AHD points and EGM2008 [Lambert projection; units in m]

Table 63.4 Descriptive statistics of the absolute differences between quasigeoid models and 48 co-located GPS-AHD points in the SWSZ [units in m]

		Bias/tilt not removed				Bias/tilt removed			
Model	Degree	Max	Min	Mean	Std	Max	Min	Mean	Std
EGM96	360	1.174	–0.211	0.512	0.280	0.543	–0.606	0.000	0.244
AUSGeoid98	~5,400	0.196	–0.277	–0.010	0.128	0.097	–0.133	0.000	0.046
PGM2007A	2,160	0.160	–0.335	–0.002	0.120	0.092	–0.138	0.000	0.050
EGM2008	2,160	0.144	–0.305	–0.006	0.106	0.092	–0.130	0.000	0.046

Table 63.5 Descriptive statistics of the absolute differences between quasigeoid models and 45 co-located GPS-AHD points in the SASZ [units in m]

		Bias/tilt not removed				Bias/tilt removed			
Model	Degree	Max	Min	Mean	Std	Max	Min	Mean	Std
EGM96	360	1.637	–0.401	0.246	0.466	1.154	–0.732	0.000	0.396
AUSGeoid98	~5,400	0.313	–0.211	0.010	0.117	0.373	–0.210	0.000	0.105
PGM2007A	2,160	0.396	–0.322	–0.044	0.133	0.394	–0.196	0.000	0.102
EGM2008	2,160	0.402	–0.183	0.036	0.127	0.374	–0.183	0.000	0.100

whereas PGM2007A and EGM2008 agree significantly better with the nation-wide GPS-levelling data set (see Table 63.3). This is probably caused by the improved accuracy of the low degrees from GRACE in PGM2007A/EGM2008 compared to EGM96, which was used in AUSGeoid98.

Despite that AUSGeoid98, PGM2007A and EGM2008 all show a similar STD in the comparison in the SASZ (~10 cm after removal of bias and tilt, cf. Table 63.5), the direction of the estimated tilt is very different for AUSGeoid98. PGM2007A and EGM2008 reveal the expected north-south trend in the AHD (see earlier), whereas the direction of the trend is reversed for AUSGeoid98. Therefore, PGM2007A and EGM2008 are likely more accurate than AUSGeoid98. The reversed pattern in the comparison with AUSGeoid98 is due to an error in EGM96 in the SASZ, which has propagated into AUSGeoid98, albeit mitigated by local gravimetric data. PGM2007A and EGM2008 appear now to be free from this error, which is a positive validation for these models.

63.3.4 Comparisons with Vertical Deflections

The results of comparisons of vertical deflections computed from PGM2007A and EGM2008 to a set of 1,080 astrogeodetic vertical deflections over Australia are shown in Table 63.6. These results agree exactly with the statistics given by Pavlis et al. (2008). This validation is probably the strongest from the Australian data, even though the 40-year vintage of the Australian astrogeodetic observations is not ideal.

PGM2007A and EGM2008 seemingly slightly outperform AUSGeoid98 in Table 63.6, because for these models a Helmert deflection was computed directly at the surface of the Earth, which is more compatible with the astrogeodetic observations that yield Helmert deflections. On the other hand, AUSGeoid98 deflections are Pizzetti vertical deflections at the geoid because they were computed from the horizontal gradients of AUSGeoid98 (cf. Jekeli, 1999). As such, the curvature and torsion of the plumbline through

Table 63.6 Descriptive statistics of the absolute differences between quasigeoid models and 1,080 astrogeodetic observations of vertical deflections [units in arcsec]

		N–S deflection (ξ)				E–W deflection (η)			
Model	Degree	Max	Min	Mean	Std	Max	Min	Mean	Std
AUSGeoid98	~5,400	17.83	–7.76	–0.25	1.28	9.11	–12.65	–0.17	1.36
PGM07A	2,160	17.79	–6.95	–0.17	1.24	8.77	–11.35	–0.10	1.18
EGM08	2,160	17.69	–6.99	–0.17	1.18	8.70	–11.34	–0.098	1.28

the topography is neglected, which may account for part of the worse comparison for AUSGeoid98 (Table 63.6).

63.4 Conclusion

The tide-free PGM2007A and EGM2008 global models were compared with Australian land and marine gravity observations, co-located GPS-levelling on the [north-south-tilted] AHD, AUSGeoid98, and astro-geodetic deflections of the vertical. The results generally show that we cannot legitimately claim to truly validate EGM2008. Instead, EGM2008 confirms the already-known problems with the Australian data, as well as revealing some previously unknown problems. If one wants to claim validation, then EGM2008 is validated implicitly because it can confirm the errors in our regional data. Simply, EGM2008 is a good model over Australia.

Acknowledgements We acknowledge funding from the *Australian Research Council* via grant DP0663020. Naturally, the suppliers of data are thanked too.

References

Claessens, S.J., W.E. Featherstone, and F. Barthelmes (2001). Experiences with point-mass modelling in the Perth region, Western Australia. *Geomatics Res.Australasia 75*, 53–86.

Featherstone, W.E. (2001). Absolute and relative testing of gravimetric geoid models using Global Positioning System and orthometric height data. *Comput. Geosci.*, 27(7), 807–814, doi: 10.1016/S0098-3004(00)00169-2.

Featherstone, W.E. (2003). Improvement to long-wavelength Australian gravity anomalies expected from the GRACE, CHAMP and GOCE dedicated satellite gravimetry missions. *Explor. Geophys.,* 34(1–2), 69–76.

Featherstone, W.E. (2004). Evidence of a north-south trend between AUSGeoid98 and AHD in southwest Australia. *Surv. Rev.,* 37(291), 334–343.

Featherstone, W.E. (2006). Yet more evidence for a north-south slope in the AHD. *J. Spatial Sci.,* 51(2), 1–6; corrigendum in 52(1), 65–68.

Featherstone, W.E. et al. (2001). The AUSGeoid98 geoid model of Australia: data treatment, computations and comparisons with GPS/levelling data. *J. Geod.*, 75(5–6), 313–330, doi: 10.1007/s001900100177.

Featherstone, W.E. et al. (2004). GPS-geodetic monitoring of the southwest seismic zone of Western Australia: epoch-one. *J. Royal Soc. WA.,* 87(1), 1–9.

Featherstone, W.E. et al. (2007). Progress towards the new Australian geoid-type model as a replacement for AUSGeoid98, Proc SSC2007, Hobart, May [CD-ROM].

Jekeli, C. (1999). An analysis of vertical deflections derived from high-degree spherical harmonic models. *J. Geod.*, 73(1), 10–22, doi: 10.1007/s001900050213.

Kearsley, A.H.W. (1976). The computation of deflections of the vertical from gravity anomalies, UNISURV Rep S15, Univ of NSW, Sydney, p. 161.

Kirby, J.F., W.E. Featherstone, and A.H.W. Kearsley (1998). Tests of the DMA/GSFC geopotential models over Australia. *Int. Geod. Serv. Bull*., 7, 2–13.

Lemoine, F.G. et al. (1998). The development of the joint NASA, GSFC and the National Imagery and Mapping Agency (NIMA) geopotential model EGM96, NASA/TP-1998-206861, NASA, Greenbelt, p. 575.

Mather, R.S., C. Rizos, B. Hirsch, and B.C. Barlow (1976). An Australian gravity data bank for sea surface topography determinations (AUSGAD76), UNISURV G25, School of Surveying, Univ of NSW, Sydney, pp. 54–84.

Murray, A.S. (1997). The Australian national gravity database. *AGSO J. Aust. Geol. Geophys.*, 17, 145–155.

Pavlis, N.K., S.A. Holmes, S.C. Kenyon, and J.K. Factor (2008). An earth gravitational model degree 2160: EGM2008. Presented at the 2008 General Assembly of the European Geosciences Union, Vienna, Austria, April 13–18.

Roelse, A., H.W. Granger, and J.W. Graham (1971). The adjustment of the Australian levelling survey 1970-1971, Tech Rep 12, Div of National Mapping, Canberra, p. 81.

Sandwell, D.T. and W.H.F. Smith (1997). Marine gravity anomaly from Geosat and ERS-1 altimetry. *J. Geophys. Res*., 102(B5), 10039–10054.

Soltanpour, A., H. Nahavandchi, and W.E. Featherstone (2006). The use of second-generation wavelets to combine a gravimetric geoid model with GPS-levelling data. *J. Geod.,* 80(2), 82–93, doi: 10.1007/s00190-006-0033-0.

Symonds, P.A. and J.B. Willcox (1976). The gravity field offshore Australia. *BMR J. Aust. Geol. Geophys*., 1(1), 303–314.

Tapley, B. et al. (2005). GGM02 – An improved Earth gravity field model from GRACE. *J. Geod*., 79(8), 467–478, doi: 10.1007/s00190-005-0480-z.

Tregoning, P., K. Lambeck, and G. Ramillien (2008). GRACE estimates of sea surface height anomalies in the Gulf of Carpentaria, Australia. *Earth Planet. Sci. Lett*. 271(1–4), 241–244, doi: 10.1016/j.epsl.2008.04.018.

Chapter 64

Evaluation of EGM08 Using GPS and Leveling Heights in Greece

C. Kotsakis, K. Katsambalos, D. Ampatzidis, and M. Gianniou

Abstract This paper presents an overview of the evaluation results for the new Earth Gravitational Model (EGM08) that was recently released by the US National Geospatial- Intelligence Agency, using GPS and leveled orthometric heights in the area of Greece. Various comparisons of geoid undulations obtained from the EGM08 model and other combined geopotential models, in conjunction with GPS/leveling data, have been performed in both absolute (at individual points) and relative (for baselines of varying length) sense. The test network covers the entire part of the Greek mainland and it consists of more than 1,500 benchmarks that belong to the Hellenic national triangulation network, with direct leveling ties to the Hellenic vertical reference frame. The spatial positions of these benchmarks have been recently determined at cm-level accuracy (with respect to ITRF2000) through an extensive national GPS campaign that was organized in the frame of the HEPOS project. Our results suggest that EGM08 offers a major improvement (more than 50%) in the agreement level among geoidal, ellipsoidal and orthometric heights over the mainland part of Greece, compared to the performance of previous global geopotential models for the same area.

64.1 Introduction

The recent release of the new Earth Gravitational Model EGM08 by the US National Geospatial-Intelligence Agency (Pavlis et al., 2008) is undoubtedly a major breakthrough in global gravity field mapping. For the first time, a spherical harmonic (SH) model complete to degree and order 2,159, with additional SH coefficients extending up to degree 2,190 and order 2,159, is available for the Earth's external gravitational potential, leading to an unprecedented level of spatial sampling resolution (~9 km) for the recovery of gravity field functionals over the entire globe. Such a revolutionary step contributes in a most successful way to the continuing efforts of the geodetic community during the last years (and after the launch of the satellite missions CHAMP and GRACE) for a high-resolution and high-accuracy reference model of Earth's mean gravity field. Furthermore, it provides an indispensable tool to support new gravity field studies and other Earth monitoring projects, especially in view of the upcoming GOCE mission (scheduled for launch in February 2009) and the ongoing development of the Global Geodetic Observing System (GGOS).

Following the official release of the EGM08 model, there is an expected strong interest among geodesists to quantify its actual accuracy with several validation techniques and external data sets, independently of the estimation and error calibration procedures that were used for its development. In response to the above interest and as part of the related activities that have been coordinated by the IAG/IGFS Joint Working Group on the *Evaluation of Global Earth Gravity Models*, the objective of this paper is to present the results of the EGM08 validation tests that were performed in the area of Greece using GPS and leveled orthometric heights.

C. Kotsakis (✉)
Department of Geodesy and Surveying, School of Engineering, Aristotle University of Thessaloniki, Thessaloniki 541 24, Greece
e-mail: kotsaki@topo.auth.gr

S.P. Mertikas (ed.), *Gravity, Geoid and Earth Observation*, International Association of Geodesy Symposia 135,
DOI 10.1007/978-3-642-10634-7_64, © Springer-Verlag Berlin Heidelberg 2010

Our test network consists of 1,542 control points that belong to the Hellenic national triangulation network, and which are directly tied to the Hellenic national vertical reference frame through spirit (and in some cases trigonometric) leveling surveys. These control points were recently re-surveyed during a national GPS campaign in the frame of the HEPOS project (more details to be given in Sect. 64.2) and their spatial positions have been estimated anew at cm-level accuracy with respect to the ITRF2000 frame.

Key aspects of our study are the extensive national coverage and high spatial density of the underlying test network (see Fig. 64.1) which enabled us to identify the significant improvement that EGM08 yields, over other existing geopotential models, for the representation of gravity field features in certain mountainous areas around Greece (see Sect. 64.3). This is actually the first time that a detailed quality analysis for geopotential models is performed over the entire Hellenic mainland with the aid of precise GPS positioning. Hence, our study also provides a preliminary, yet reliable, assessment about the feasibility of EGM08 for determining orthometric height differences via GPS/geoid-based leveling techniques throughout Greece (see Sect. 64.4).

64.2 Data Sets

All our evaluation tests and related results that are presented in the next sections refer to the network of 1,542 GPS/leveling benchmarks shown in Fig. 64.1. The test network covers the entire mainland region of Greece with a relatively uniform spatial distribution. Note that control points with identified or suspected blunders (mainly in their orthometric heights that are provided by the Hellenic Military Geographic Service) have been removed from the following analysis and they are not included in this network.

Although a large number of additional GPS/leveling benchmarks were also available over the Greek islands, they have been deliberately excluded from our current tests to avoid misleading systematic effects in the evaluation results due to unknown vertical datum differences between the various islands and the mainland region.

64.2.1 Ellipsoidal Heights (HEPOS Project)

Due to current ongoing efforts for the enhancement of the spatial data infrastructure in Greece, a national GPS

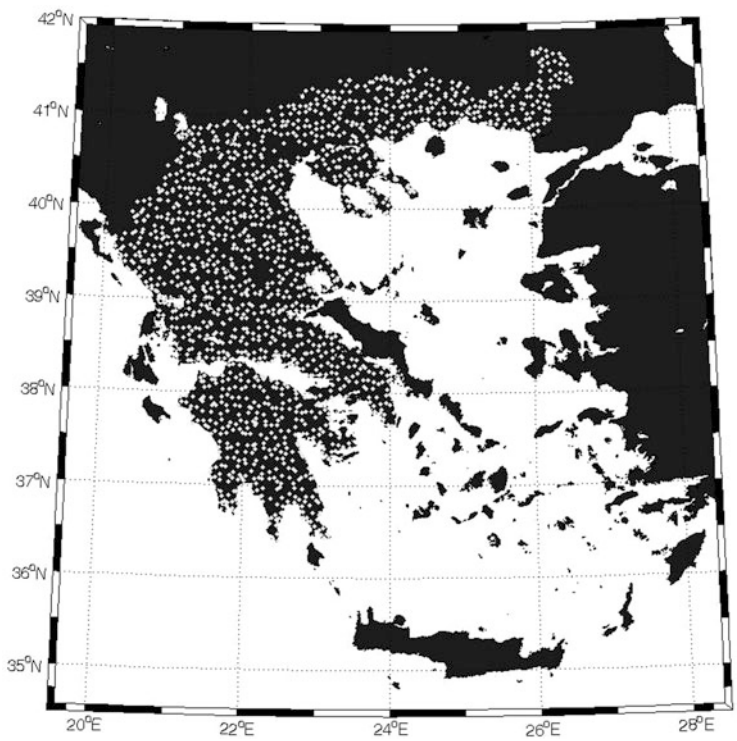


Fig. 64.1 Geographical distribution of the 1542 GPS/leveling benchmarks over the Greek mainland

campaign was performed in 2007 to obtain a sufficient number of control points with accurately known 3D spatial positions in an ITRF-type coordinate system. These activities have been initiated by the Ministry for the Environment, Planning and Public Works and the financial support of the EU and the Hellenic State, and they are part of the HEPOS (Hellenic Positioning System) project that will lead to the launch of a modern satellite-based positioning service for cadastral, mapping, geodetic and other types of geomatics applications in Greece. The entire project is coordinated by Ktimatologio S.A, a state-owned private sector firm that is responsible for the management of the Hellenic Cadastral system (see Gianniou, 2008).

The aforementioned GPS campaign involved more than 2,450 control stations within the existing national triangulation network (part of which are the 1,542 points shown in Fig. 64.1) that will provide the basis for determining a precise datum transformation model between the official Hellenic Geodetic Reference Frame of 1987 (HGRF87) and other ITRF/ETRF-type frames. The actual fieldwork was performed within a 6-month period (March to September 2007) using twelve dual-frequency Trimble 5700/5800 GPS receivers with Zephyr or R8 internal antennas. Thirty three of these points were used as base reference stations (with 24-h continuous GPS observations) to obtain baseline solutions with the rest of the network points (observation time for each rover station ranged between 1 and 3 h). In all cases, a 15-s sampling rate and a 15° elevation cut-off angle were used for the data collection. After the processing of the GPS observations using EUREF/EPN ties and IGS precise orbits, the geocentric Cartesian coordinates of all above stations were determined in ITRF2000 (epoch: 2007.236) and their geometric heights were subsequently derived with respect to the GRS80 reference ellipsoid. The accuracy of the ellipsoidal heights ranges between 2 and 5 cm, while the horizontal positioning accuracy is marginally better by 1–2 cm (1σ level).

64.2.2 Orthometric Heights

The orthometric heights for all points in our test network have been obtained through leveling survey ties to surrounding benchmarks of the national vertical reference frame. These local ties were performed in previous years from the Hellenic Military Geographic Service through spirit and trigonometric leveling techniques. Note that a large number of the 1,542 control points is located in highly mountainous areas (24% of the GPS/leveling benchmarks have orthometric heights H >800 m). The quality of the available orthometric heights in our test network is mainly affected by two factors: the internal accuracy and consistency of the Hellenic vertical datum (HVD), and the observation accuracy of the local leveling ties to the surrounding HVD benchmarks. Due to the absence of sufficient documentation, the actual accuracy of the orthometric heights at these points is largely unknown. Their values refer, in principle, to the Earth's equipotential surface that coincides with the mean sea level at the HVD's fundamental tide-gauge reference station located in Piraeus port (unknown W_o value).

64.2.3 GPS-Based Geoid Undulations

Based on the known ellipsoidal and orthometric heights, geoid undulations have been computed at the 1,542 GPS/leveling benchmarks of the test network according to the equation

$$N^{GPS} = h - H \tag{1}$$

The above values provide the external dataset upon which the EGM08 validation tests will be performed. Note that low-pass filtering has *not* been applied to the pointwise N^{GPS} heights. As a result, the effect of the *omission error* associated with all tested global geopotential models (GGMs) will be reflected in our evaluation results.

64.2.4 GGM-Based Geoid Undulations

Geoid undulations have also been computed at the 1,542 GPS/leveling benchmarks using several different GGMs. For the evaluation results presented herein we shall consider only the most recent "mixed" GGMs which incorporate the contribution from various types of satellite data (CHAMP, GRACE, SLR), terrestrial gravity data, and satellite altimetry data; see Table 64.1.

Table 64.1 GGMs used for the evaluation tests at the 1,542 GPS/leveling benchmarks

Models	n_{max}	Reference
EGM08	2190	Pavlis et al. (2008)
EIGEN-GL04C	360	Förste et al. (2006)
EIGEN-CG03C	360	Förste et al. (2005)
EIGEN-CG01C	360	Reigber et al. (2006)
GGM02C	200	Tapley et al. (2005)
EGM96	360	Lemoine et al. (1998)

The determination of GGM geoid undulations was carried out through the general formula (Rapp, 1997)

$$N = \zeta + \frac{\Delta g^{FA} - 0.1119H}{\bar{\gamma}} H + N_o \qquad (2)$$

where ζ and Δg^{FA} denote the height anomaly and free-air gravity anomaly, respectively, that are computed from the corresponding series expansions (up to n_{max}) based on the SH coefficients of each model and the GRS80 normal gravity field parameters. Only the gravitational potential coefficients with harmonic degree $n \geq 2$ were considered for these computations, thus excluding the contribution of the zero/first-degree harmonics. Note that EIGEN-CG01C and EIGEN-CG03C are the only models among the tested GGMs which are accompanied by non-zero first-degree SH coefficients (nevertheless their omission in the computation of the N values has a negligible effect in our evaluation results).

The term N_o represents the contribution of the zero-degree harmonic to the GGM-based geoid undulations with respect to the GRS80 reference ellipsoid. It is computed according to the well known formula (e.g. Heiskanen and Moritz, 1967)

$$N_o = \frac{GM - GM_o}{R\gamma} - \frac{W_o - U_o}{\gamma} \qquad (3)$$

where the parameters GM_o and U_o correspond to the Somigliana-Pizzeti normal gravity field generated by the GRS80 ellipsoid (Moritz, 1992)

$$GM_o = 398600.5000 \times 10^9 \, \mathrm{m^3 s^{-2}}$$

$$U_o = 62636860.85 \, \mathrm{m^2} s^{-2}$$

The Earth's geocentric gravitational constant (GM) and the constant gravity potential of the geoid (W_o) have been set to the following values

$$GM = 398600.4415 \times 10^9 \, \mathrm{m^3 s^{-2}}$$

$$W_o = 62636856.00 \, m^2 s^{-2} \quad (\textit{IERS Conventions} \, 2003)$$

while the mean Earth radius R and the mean normal gravity γ on the reference ellipsoid are taken equal to 6371008.771 m and 9.798 m s^{-2}, respectively (GRS80 values). Based on the above conventions, the zero-degree term from Eq. (3) yields the value $N_o = -0.442$ m, which has been added to the geoid undulations from all tested GGMs.

Note. The computation of the GGM geoid undulations from Eq. (2) was performed in the *zero-tide system* (with respect to a fixed reference ellipsoid – GRS80).

64.2.5 Height Statistics

The statistics of the individual height datasets that will be used in our evaluation tests are given in Table 64.2. Note that the statistics for the GGM geoid undulations refer to the values computed from Eq. (2) at the 1,542 GPS/leveling benchmarks using the *full spectral range* of each model.

Table 64.2 Statistics of the height datasets over the test network of 1,542 GPS/leveling benchmarks (units in m)

	Max	Min	Mean	σ
h	2562.753	24.950	545.676	442.418
H	2518.889	0.088	510.084	442.077
$N^{GPS} = h\text{-}H$	43.864	19.481	35.592	5.758
N (EGM08)	44.374	19.663	35.968	5.800
N (EGM08, n_{max}= *360*)	44.052	19.481	35.926	5.807
N (EIGEN-GL04C)	44.104	19.303	35.874	5.878
N (EIGEN-CG03C)	44.049	19.257	35.861	5.867
N (EIGEN-CG01C)	44.108	19.663	35.823	5.873
N (GGM02C)	44.034	19.771	35.905	5.780
N (EGM96)	44.007	19.687	36.037	5.753

From Table 64.2, it is evident the existence of a large discrepancy (>25 cm) between the zero reference surface of the Hellenic vertical datum (which is associated with an unknown W_o value) and the equipotential surface of the Earth's gravity field that is specified by $W_o = 62636856.00\ \mathrm{m^2 s^{-2}}$ and realized by the various geopotential models over the Greek mainland region.

It is interesting to observe the considerable offset of the full-resolution EGM08 geoid with respect to the geoid surface realized by the other geopotential models at the GPS/leveling benchmarks. This offset varies from 6 to 15 cm and it should be attributed to medium/long-wavelength systematic differences between EGM08 and the other GGMs over the Hellenic area.

64.3 Pointwise Tests

The statistics of the differences between N^{GPS} and the GGM geoid heights are shown in Table 64.3. In all cases, the values given in this table refer to the statistics after a simple (unweighted) least-squares *constant bias fit* was applied to the original misclosures *h-H-N* at the 1,542 GPS/leveling benchmarks. The significant variations in the estimated bias obtained from each tested model (see last column in Table 64.3) is an indication of large-scale systematic distortions among the GGM geoids, which are likely caused by medium/long-wavelength commission errors in their SH coefficients and additional omission errors in the pre-EGM08 models.

The new EGM08 model offers a remarkable improvement in the agreement among ellipsoidal, orthometric and geoid heights over Greece. Compared to all other GGMs, the standard deviation of the EGM08 residuals N^{GPS}-N decreases by a factor >3. The improvement is evident even with the 30′ limited-resolution version of the new model ($n_{max} = 360$), which matches the GPS geoid within ±37 cm in an average pointwise sense, while all previous GGMs of similar resolution do not perform better than ±42 cm. The major contribution, however, comes from the higher frequency band of EGM08 ($360 < n < 2{,}190$) which enhances the consistency between GGM and GPS geoid heights at ±14 cm (1σ level).

Table 64.3 Statistics of the differences N^{GPS}-N, after a least-squares bias fit, at the 1,542 GPS/leveling benchmarks (units in m)

	Max	Min	σ	Bias
EGM08 *(n_{max}= 2190)*	0.542	–0.437	0.142	–0.377
EGM08 *(n_{max}= 360)*	1.476	–1.287	0.370	–0.334
EIGEN-GL04C *(n_{max}= 360)*	1.773	–1.174	0.453	–0.283
EIGEN-CG03C *(n_{max}= 360)*	1.484	–1.173	0.453	–0.270
EIGEN-CG01C *(n_{max}= 360)*	1.571	–1.135	0.492	–0.231
GGM02C *(n_{max}= 200)*	2.112	–1.472	0.551	–0.313
EGM96 *(n_{max}= 360)*	1.577	–1.063	0.423	–0.446

The results of the pointwise evaluation reveal that EGM08 performs exceedingly better than the other models over the mountainous parts of the test network. This is indicated from the scatter plots of the residuals N^{GPS}-N (after the constant bias fit) with respect to the orthometric heights of the GPS/leveling benchmarks; see Fig. 64.2. These plots show a sizeable *height-dependent bias* between the GGM and the GPS geoid heights, which is considerably reduced in the case of EGM08. Apparently, the higher frequency content of the new model gives a better approximation for the terrain-dependent gravity field features over the Greek mainland, a fact that is clearly visible from the following plots.

Further manifestation of the strong correlation between the GGM/GPS geoid differences and the topographic height of the test points can be found in the color plots given in Kotsakis et al. (2008).

The spatial variations in the EGM08 residuals N^{GPS}-N over the test network did not show any particular systematic pattern (apart from their overall dependency on the topography). Both the latitude-dependent and longitude-dependent scatter plots of these residuals are free of any sizeable north/south or east/west tilts over the Greek mainland, as it can be seen in Fig. 64.3. In other GGMs, however, some strong localized tilts were identified in their undulation residuals with respect to the GPS geoid, mainly due to larger commission errors in their SH coefficients and significant aliasing errors resulting from their limited spatial resolution (see, e.g., the case of EGM96 shown in Fig. 64.3).

Overall, the EGM08 model outperforms all previous combined GGMs and it improves the statistical fit with the Hellenic GPS geoid by approximately 30 cm! It is interesting to note that about 54% of the 1,542 GPS/leveling benchmarks show an agreement between the EGM08 geoid and the GPS geoid that is better than 10 cm, while almost 75% of the same

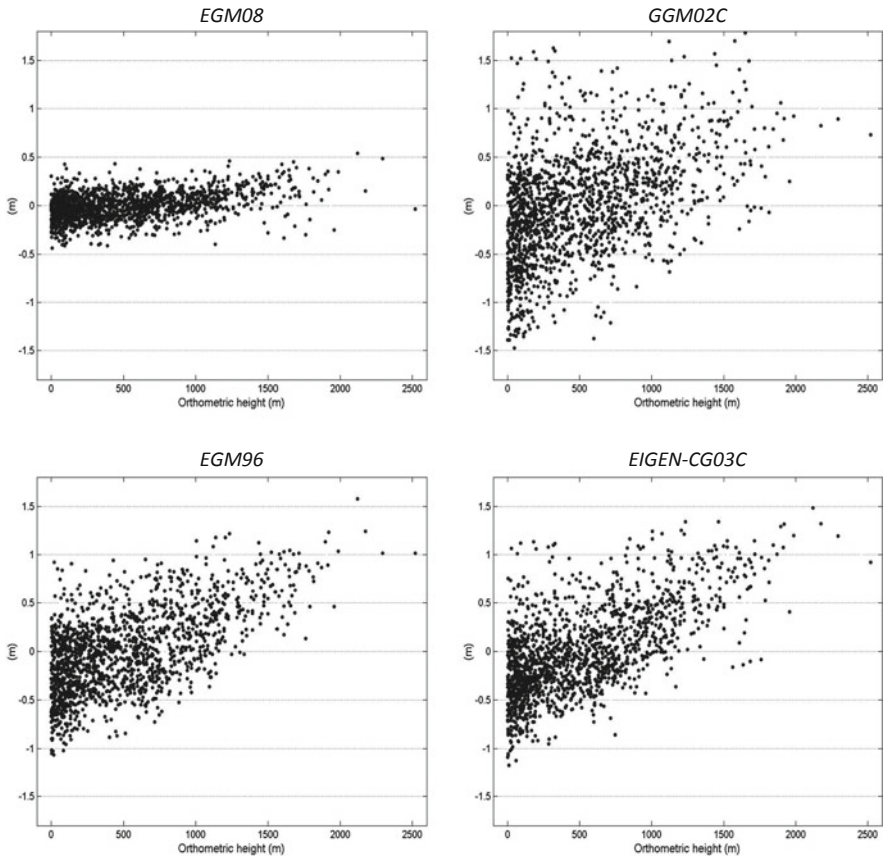


Fig. 64.2 Height-dependent variations of the differences N^{GPS}-N at the 1,542 GPS/leveling benchmarks

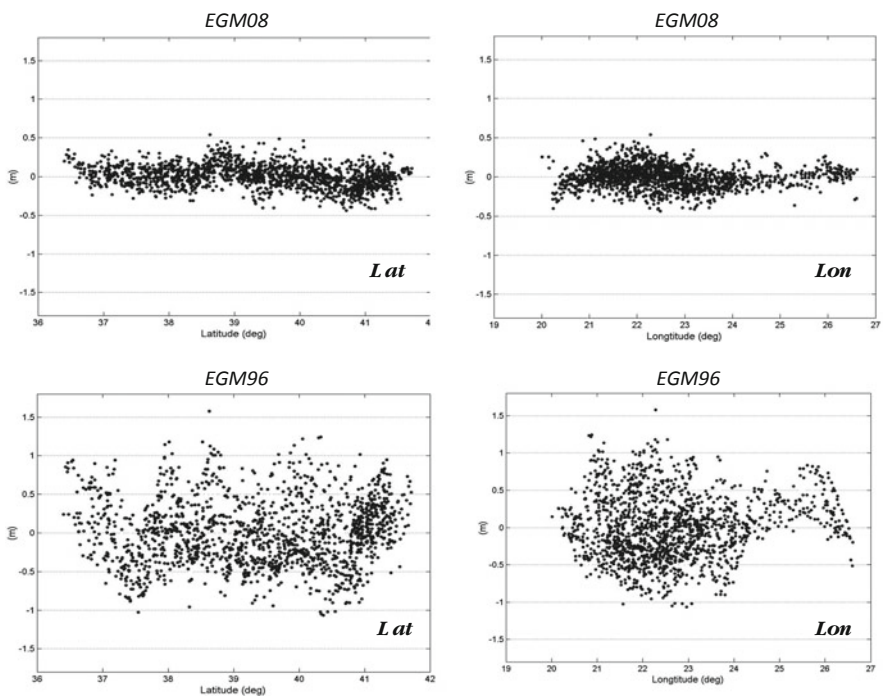


Fig. 64.3 Latitude-dependent and longitude-dependent variations of the differences N^{GPS}-N at the 1,542 GPS/leveling benchmarks

points exhibit a consistency between the two surfaces that is better than 15 cm. The corresponding percentages for the case of EGM96 decline to 18 and 28%, respectively.

64.4 Baseline Tests

In addition to the previous pointwise tests, another set of evaluation results was obtained through the comparison of GGM and GPS geoid-slope differences over the Hellenic network of 1,542 GPS/leveling benchmarks. For all baselines formed within this network, the following relative undulation differences were determined

$$\Delta N_{ij}^{GPS} - \Delta N_{ij} = (h_j - H_j - h_i + H_i) - (N_j - N_i) \quad (4)$$

after the implementation of a least-squares *bias/tilt fit* between the pointwise GGM and the GPS geoid heights.

Depending on the actual baseline length, the computed values from Eq. (4) were grouped into various spherical-distance classes and their statistics were then evaluated within each class. Given the actual coverage and spatial density of the GPS/leveling benchmarks in our test network, baselines with length from 2 km up to 600 km were considered for this evaluation scheme.

The statistics of the differences between the GGM-based and the GPS-based geoid slopes are given in Tables 64.4, 64.5 and 64.6 for three selected baseline classes. As seen from these tables, the full-resolution EGM08 model performs consistently better than all other combined GGMs over all classes. The improvement becomes more pronounced for increasing baseline length, since the resultant σ values are reduced by a factor of 1.4 for baselines <5 km, by a factor of 2 for baselines 5–10 km, and by a factor of 3.5 for baselines 10–50 km.

The overall behaviour of the σ values for the GGM/GPS geoid slope differences is shown in Fig. 64.4, over all baseline classes that were considered in our tests. The remarkable improvement in the relative undulation accuracy from the EGM08-based geoid is clearly visible, indicating a ΔN-consistency level with the external GPS/leveling data that varies from ± 6 to ± 19 cm (1σ level).

Table 64.4 Statistics of the relative GGM/GPS geoid height differences for baselines with length <5 km (number of baselines: 289, units in m)

	Max	Min	σ	Bias
EGM08 (n_{max}= *2,190*)	0.643	–0.474	0.111	0.006
EGM08 (n_{max}=*360*)	0.648	–0.534	0.154	0.003
EIGEN-GL04C (n_{max}= *360*)	0.649	–0.542	0.155	0.005
EIGEN-CG03C (n_{max}= *360*)	0.643	–0.540	0.155	0.005
EIGEN-CG01C (n_{max}= *360*)	0.640	–0.536	0.156	0.005
GGM02C (n_{max}= *200*)	0.685	–0.571	0.162	0.003
EGM96 (n_{max}= *360*)	0.643	–0.553	0.154	0.005

Table 64.5 Statistics of the relative GGM/GPS geoid height differences for baselines with length 5–10 km (number of baselines: 2,119, units in m)

	Max	Min	σ	Bias
EGM08 (n_{max}= *2,190*)	0.465	–0.629	0.125	0.001
EGM08 (n_{max}= *360*)	1.022	–1.044	0.248	–0.004
EIGEN-GL04C (n_{max}= *360*)	0.983	–0.988	0.251	–0.000
EIGEN-CG03C (n_{max}= *360*)	0.971	–1.026	0.251	–0.001
EIGEN-CG01C (n_{max}= *360*)	0.976	–1.039	0.252	–0.002
GGM02C (n_{max}= *200*)	0.967	–0.991	0.264	0.002
EGM96 (n_{max}= *360*)	0.963	–1.002	0.251	0.003

Table 64.6 Statistics of the relative GGM/GPS geoid height differences for baselines with length 10–50 km (number of baselines: 56,575, units in m)

	Max	Min	σ	Bias
EGM08 (n_{max}= *2,190*)	0.859	–0.781	0.164	–0.001
EGM08 (n_{max}= *360*)	2.778	–2.417	0.514	–0.012
EIGEN-GL04C (n_{max}= *360*)	2.480	–2.430	0.552	–0.019
EIGEN-CG03C (n_{max}= *360*)	2.335	–2.488	0.550	–0.021
EIGEN-CG01C (n_{max}= *360*)	2.335	–2.445	0.555	–0.021
GGM02C (n_{max}= *200*)	3.221	–2.760	0.627	–0.012
EGM96 (n_{max}= *360*)	2.532	–2.393	0.542	–0.013

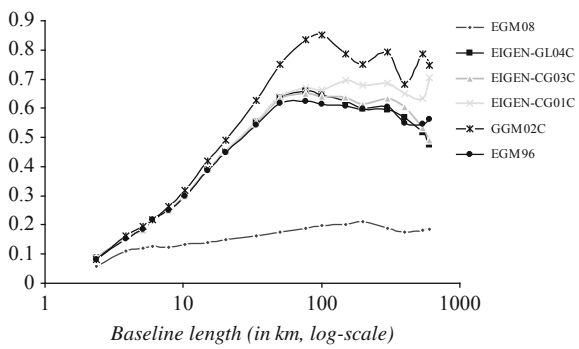


Fig. 64.4 Std of the differences $\Delta N_{ij}^{GPS} - \Delta N_{ij}$ in the network of 1,542 GPS/leveling benchmarks, as a function of the baseline length

Focusing on the ΔN evaluation results for short baselines (up to 30 km) can give us an indication for the expected accuracy in GPS/leveling projects when using an EGM08 reference geoid model over Greece. Our preliminary analysis in the test network showed that the agreement between the height differences ΔH_{ij} computed from: (a) the known orthometric heights and (b) the GPS/EGM08 ellipsoidal and geoid heights, can be approximated by the statistical error model $\sigma_{\Delta H} = \sigma_o L^{1/2}$ with σ_o ranging between 3 and 5 cm/km$^{1/2}$ (for baseline length L <30 km). Although such a performance cannot satisfy mm-level accuracy requirements for vertical positioning (which are achievable through spirit leveling techniques), it nevertheless provides a major step forward that can successfully accommodate a variety of engineering and surveying applications. Note that the corresponding performance of EGM96 in our test network is described by a relative accuracy factor of $\sigma_o \approx 9$ cm/km$^{1/2}$.

64.5 Conclusions

The results obtained from our evaluation study reveal the superiority of the EGM08 model over all existing combined GGMs for the Hellenic area, and they provide a promising testament for its future use in various geodetic applications in Greece.

Acknowledgements The GPS and leveling data used for this study were provided by Ktimatologio S.A under a research collaboration with the Department of Geodesy and Surveying (AUTh) in the frame of the HEPOS project.

References

Förste, C., F. Flechtner, R. Schmidt, R. König, U. Meyer, R. Stubenvoll, M. Rothacher, F. Barthelmes, K.H. Neumayer, R. Biancale, S. Bruinsma, and J-M. Lemoine (2006). A mean global gravity field model from the combination of satellite mission and altimetry/gravimetry surface gravity data. Poster presented at the EGU General Assembly, Vienna, Austria, April 2–7, 2006, Geophysical Research Abstracts, Vol. 8, 03462.

Förste, C., F. Flechtner, R. Schmidt, U. Meyer, R. Stubenvoll, F. Barthelmes, M. Rothacher, R. Biancale, S. Bruinsma, and J-M. Lemoine (2005). A new high resolution global gravity field model from the combination of GRACE satellite mission and altimetry/gravimetry surface gravity data. Poster presented at the EGU General Assembly, Vienna, Austria, April 24–29, Geophysical Research Abstracts, vol. 7, 04561.

Gianniou, M. (2008). HEPOS: Designing and implementing an RTK network. *Geoinformatics*, 11(1), 10–13.

Heiskanen, W. and H. Moritz (1967). Physical geodesy. WH Freeman, San Francisco.

Kotsakis, C., K. Katsambalos, D. Ampatzidis, and M. Gianniou (2008). Evaluation of EGM08 in Greece using GPS and leveling heights. Presented at the IAG International Symposium on Gravity, Geoid and Earth Observation, Chania, Greece, June 23–27, 2008 (colored slides available at http://users.auth.gr/~kotsaki/Crete2008.pdf).

Lemoine, F.G., S.C. Kenyon, J.K. Factor, R.G. Trimmer, N.K. Pavlis, D.S. Chinn, C.M. Cox, S.M. Klosko, S.B. Luthcke, M.H. Torrence, Y.M. Wang, R.G. Williamson, E.C. Pavlis, R.H. Rapp, and T.R. Olson (1998). The Development of the Joint NASA GSFC and the National Imagery and Mapping Agency (NIMA) Geopotential Model EGM96. NASA Technical Paper NASA/TP1998206 861, Goddard Space Flight Center, Greenbelt, Maryland.

Moritz, H. (1992). Geodetic Reference System 1980. *Bull. Geod.*, 62(2), 187–192.

Pavlis, N.K., S.A. Holmes, S.C. Kenyon, and J.K. Factor (2008). An Earth Gravitational Model to degree 2160: EGM2008. Presented at the 2008 General Assembly of the European Geosciences Union, Vienna, Austria, April 13–18.

Rapp, R.H. (1997). Use of potential coefficient models for geoid undulation determinations using a spherical harmonic representation of the height anomaly/geoid undulation difference. *J. Geod.*, 71, 282–289.

Reigber, C., P. Schwintzer, R. Stubenvoll, R. Schmidt, F. Flechtner, U. Meyer, R. König, H. Neumayer, C. Förste, F. Barthelmes, S.Y. Zhu, G. Balmino, R. Biancale, J-M. Lemoine, H. Meixner, and J.C. Raimondo (2006). A high resolution global gravity field model combining CHAMP and GRACE satellite mission and surface data: EIGEN-CG01C. Scientific Technical Report STR06/07, GeoForschungsZentrum (GFZ), Potsdam.

Tapley, B.D., J. Ries, S. Bettadpur, D. Chambers, M. Cheng, F. Condi, B. Gunter, Z. Kang, P. Nagel, R. Pastor, T. Pekker, S. Poole, and F. Wang (2005). GGM02 – An improved Earth gravity field from GRACE. *J. Geod.*, 79(8), 467–447.

Chapter 65

Validation of the New Earth Gravitational Model EGM08 Over the Baltic Countries

A. Ellmann

Abstract The Earth's geopotential models (EGM) in conjunction with regional terrestrial gravity data are often used in regional geoid determination. Thus, significant enhancements are expected due to the release of the new high resolution Earth Gravitational Model EGM08. Accordingly, this study validates the performance of the EGM08 model over the Baltic Sea region with an emphasis to Estonaia, Latvia and Lithuania. Three different sets of the "ground truth" are used in the comparisons. First, the EGM08-derived height anomalies are compared with an existing regional geoid model. The detected discrepancies range within ±0.3 m with a mean of –0.02 m, whereas the standard deviation (STD) of the discrepancies amounts to 0.08 m. The largest discrepancies are related to the areas where only a few data were available either for the regional geoid modeling or at the EGM08 compilation, or both. Second, the free-air gravity anomalies at the terrestrial data-points are compared with the EGM08 – derived anomalies. The STD of the anomaly discrepancies is 2.6 mgal. Finally, the EGM08 model is validated with respect to GPS-levelling data. The STD of detected discrepancies is 0.06 m, with a mean of 0.49 m. Thus, the EGM08 based quantities agree reasonably well with the tested datasets. Evidently, most of the available gravity data in the Baltic Sea region appear to be utilised at the EGM08 construction.

A. Ellmann (✉)
Department of Civil Engineering, Tallinn University of Technology, Tallinn, Estonia
e-mail: artu.ellmann@ttu.ee

65.1 Introduction

A new combined Earth gravitational model EGM08 (Pavlis et al., 2008) was released to the public in 2008. EGM08 takes advantage of recent satellite, terrestrial gravity, elevation and altimetry data. This activity is conducted by the National Geospatial-Intelligence Agency (NGA) of the USA. The resolution of the EGM08 is 5′ (corresponding to 9 km, i.e. to the spectral degree of ca 2,160), therefore also the global accuracy of the EGM08 is expected to be superior over earlier EGM's.

Regional improvements of global geoid models can be obtained by modifying Stokes's integral formula (Stokes, 1849). When solving the Stokes boundary value problem, strictly speaking, gravity anomalies over the entire Earth are required. In practice, however, the data availability is limited to some spatial domain ($\Omega_{\psi 0}$) around the computation point. Modified Stokes's formula (first proposed by Molodenskii et al., 1960) combines local terrestrial gravity anomalies and the EGM-derived long-wavelength component of the geoid. For instance a generalized Stokes scheme (cf. Vaníček and Sjöberg, 1991) can be used

$$N(\Omega) = \frac{R}{4\pi\gamma_0}\iint_{\Omega_{vo}} S^L(\psi) \times \left[\Delta g\,(R,\Omega) - \sum_{n=2}^{L}\Delta g_n(R,\Omega)\right] d\Omega' + \frac{R}{2\gamma_0}\sum_{n=2}^{L}\frac{2}{n-1}\Delta g_n(R,\Omega) \quad (1)$$

S.P. Mertikas (ed.), *Gravity, Geoid and Earth Observation*, International Association of Geodesy Symposia 135,
DOI 10.1007/978-3-642-10634-7_65, © Springer-Verlag Berlin Heidelberg 2010

where R is the mean radius of the Earth; ψ is the geocentric angle, the modified Stokes function $S^L(\psi)$, can be computed according to some algorithm (e.g. Wong and Gore, 1969; Vaníček and Kleusberg, 1987; Sjöberg, 1991, among others); γ_0 is the normal gravity at the reference ellipsoid, $\Delta g(R,\Omega)$ is gravity anomaly on the geoid level, Ω denotes a pair of geocentric coordinates (the spherical co-latitude θ and longitude λ), $d\Omega'$ is an infinitesimal surface element, ψ_0 is the radius of the integration cap, L is the modification degree.

Due to availability, quality, and type of data, the characteristics of a EGM vary regionally. Hence, the performance of any EGM needs to be validated in a regional scale by comparisons with other external data sets that depend on the same gravity field. Traditionally, the accuracy of the regional geoid modelling has been assessed by using GPS-levelling points. Apparently, the computations of new regional geoid models will also be based upon the global EGM08 model, the testing of which is necessary to assess its suitability for this task. In this contribution three different sets of the "ground truth" are used over the three Baltic countries – Estonia, Latvia and Lithuania. First, the EGM08-derived height anomaly is compared with an existing regional geoid model. Second, the free-air gravity anomalies at the terrestrial data-points are compared with the EGM08-derived anomalies. Finally, the EGM08 model is validated with respect to the GPS-levelling data. A brief summary concludes the paper.

65.2 Target Area

The EGM08 performance is examined within the following geographical boundaries: $53.83° < \phi < 60.06°$; $19.97° < \lambda < 28.52°$, see Fig. 65.1. Thus, in addition to Estonia, Latvia and Lithuania the target area includes partly also Russia, Belarus, Poland and Finland, together with a large portion of the Baltic Sea. The elevation extremes are 0 m at a shoreline and 318 m in southeast Estonia, whereas most of the target area comprises of sea and topography below 100 m. Therefore, no significant numerical differences (3 mm at most) between the geoid and height anomaly exists over the chosen target area.

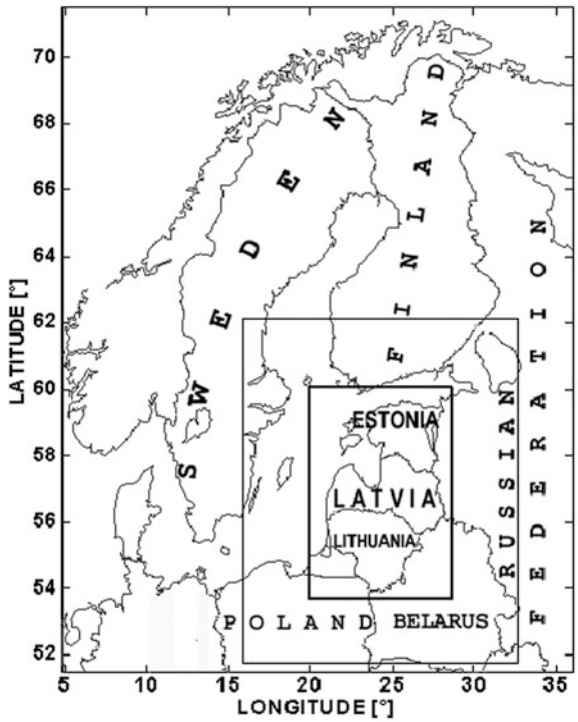


Fig. 65.1 Location of the target area (enclosed by the *bold rectangle*). *External rectangle* denotes the data area borders in the BALTgeoid-04 (Ellmann, 2005) computations

65.3 Comparisons with a Regional High-Resolution Geoid Model BALTgeoid-04

65.3.1 Regional BALTgeoid-04 Model

A recent Baltic geoid model was computed by Ellmann (2004, 2005). In his study the geoidal heights were estimated by the least squares modified Stokes's formula (cf. Sjöberg, 1991). The definition of the main computation criterias (such as the modification limit $L = 67$, the radius of the integration cap $\psi_0 = 2°$, etc) is explained in detail by (ibid.). An early GRACE-derived ("satellite-only") GGM01s model (Tapley et al., 2004) was used as the reference model. The resulting $1.5' \times 3'$ geoid model is depicted in Ellmann (2005, Fig. 2). The Baltic geoid model is mainly smooth (with a STD of the mean ~3 m), but it includes some local irregularities in the NW part of the target area. Their location is correlated with the local anomalies of the gravity field (cf. Ellmann, 2004,

Fig. 2.3). The quality of the BALTgeoid-04 model was assessed from the comparisons with the GPS and levelling datasets. The same sets of the control points will also be used for the evaluation of the EGM08-derived height anomalies, therefore more information on these data is given in Sect. 65.5. The GPS-levelling points form a surface, which is called here the "geometric geoid model" (N_{geom}= h–H). The following STD's of the discrepancies between the BALTgeoid-04 and N_{geom} were achieved: Baltic 5.8 cm, Estonia 4.0 cm, Latvia 6.0 cm and Lithuania 5.7 cm, respectively. It is also concluded that the accuracy of the BALTgeoid-04 model is at least of the same level as is the accuracy of the used control points (Ellmann, 2005).

65.3.2 Accounting for the Differences Between the EGM and GRS-80 Parameters

The BALTgeoid-04 geoidal heights are defined with respect to the GRS-80 (Geodetic Reference System; Moritz, 1992) ellipsoid. Also the physical constants of the GRS-80 are used for computing the normal gravity field in the Baltic countries. Furthermore, the GPS-derived geodetic heights are reckoned from the ETRS89 (European Terrestrial Reference System) oriented GRS-80 ellipsoid.

As is customary in geodesy, the mass of the reference ellipsoid is chosen to be equal to the mass of the Earth, and the origin of the reference ellipsoid is placed at Earth's gravity centre. However, in reality the EGM parameters may differ from the corresponding parameters of the adopted geodetic reference ellipsoid. Thus, the differences between the defining constants (the Earth's gravitational cons-tant GM, and the major semi-axis a of the ellipsoid versus reference radius for the spherical EGM) of the used EGM and adopted geodetic reference ellipsoid should be considered. The scaling can be introduced via zonal harmonics of the reference ellipsoid by an approach described in Vaníček and Kleusberg (1987, Sect. 65.5), see also Kirby and Featherstone (1997). In the discussion below the EGM-related values will be denoted by the subscript "*EGM*", whereas the subscript "*GRS*" denotes the geodetic reference ellipsoid related quantities.

It should be noted that the EGM08 geopotential model utilises GM_{EGM}= 398600.4415 $m^3 \cdot s^{-2}$, whereas GM_{GRS} = 398600.5 $m^3 \cdot s^{-2}$. The Earth's gravitational potential and its derivatives (such as the disturbing potential, gravity anomaly and geoidal heights) can be expressed in terms of an infinite series of spherical harmonics outside the attracting masses of the Earth. Since the EGM08 coefficients are referred to the bounding sphere with some radius a (the value a_{EGM} = 6378136.3 m is adopted at the compilation of the EGM08, whereas a_{GRS} = 6378137 m), then the EGM derived quantities, strictly speaking, ought be computed on the surface of the bounding sphere (or above it). However, the gravity field related quantities can be more or less safely computed inside of this sphere, as long as the evaluation point remains outside the topographic masses. Due to this, the EGM's are better suited for computing the ground related gravity quantities, such as the height anomaly (cf., Molodenskii et al., 1960), rather than the geoid. Note that over the continents the latter would require computations inside the topographic masses.

65.3.3 The EGM08-Derived Height Anomalies

The "tide-free" version of the EGM08 model (the file *EGM2008_to2190_TideFree.gz*, retrieved from URL:http://users.auth.gr/~kotsaki/IAG_JWG/EGM08_intro.html) contains fully-normalized, unitless spherical harmonic coefficients, complete to degree and order 2,159, plus additional coefficients extending to degree 2,190 and order 2,159. The EGM08-derived height anomalies ζ (at the topographic surface, with the geocentric radius of r_t= r_g+ H) were computed by the following formula:

$$\zeta_{EGM}(\Omega) = \frac{GM_{EGM} - GM_{GRS}}{r_t \gamma_T} + \frac{GM_{EGM}}{r_t \gamma_T} \sum_{n=2}^{2190} \left(\frac{a_{EGM}}{r_t} \right)^n \times \sum_{m=0}^{n} \{ \Delta \overline{C}_{nm} \cos m\lambda + \overline{S}_{nm} \sin m\lambda \} \overline{P}_{nm}(\cos\theta) \quad (2)$$

where the normal gravity γ_T is referred to the surface of the telluroid (with the geocentric radius of $r_T = r_{GRS} + H$); $\overline{C}_{nm}$ and $\overline{S}_{nm}$ are fully normalised spherical harmonic coefficients, of degree n and order m; $\overline{P}_{nm}(\cos\theta)$ are fully normalised associated *Legendre* functions. The first term on the right hand side of Eq. (2) represents the zero degree geoid scaling term, which is due to the difference between the *GM*-values of the EGM08 and that of the reference elliposoid (GRS-80). Using $R = 6{,}371$ km and $\gamma = 981$ Gal the zero degree geoid scaling term becomes –0.936 m. This value will be added to the EGM08-derived height anomalies. The (residual) zonal coeffcients $\Delta\overline{C}_{nm}$ account also for the differences between the reference radius of the EGM08 and semi-major axis of the GRS-80.

The above principles have also been realised in the *harmonic_synth_v02.f* code (by Holmes and Pavlis, version 05/01/2006, retrieved from the NGA webpage http://earth-info.nga.mil/GandG/wgs84/ gravitymod/new_egm/new_egm.html), which is used in the validation of the EGM08 geopotential model in the present study. However, the program does not account for the influence of the zero-degree term. Therefore, the EGM08-derived quantities are corrected for the missing zero-degree term.

The EGM08 height anomalies were computed at the grid nodes of the BALTgeoid-04 model. The conceptual differences between the geoid and height anomalies are well known, see e.g., Heiskanen and Moritz (1967, Chap. 8-3). Recall, however, that over the selected target area these differences are numerically insignificant. These differences are neglected in the following comparisons without affecting the objectives of the present study.

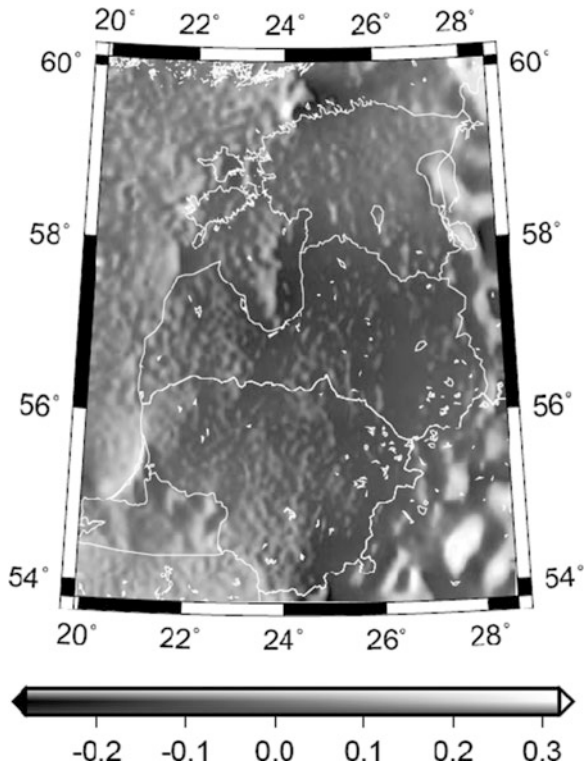


Fig. 65.2 Discrepancies between the BALTgeoid-04 model and EGM08 height anomalies ($n_{\max} = 2{,}190$) at the BALTgeoid-04 grid nodes (altogether 250 × 172 points). The discrepancies range from –0.289 to +0.338 m with a mean of –0.025 m. Generally, the EGM08 height anomalies appear to be higher than the BALTgeoid-04 model. Standard deviation of the detected discrepancies amounts to 0.077 m

65.3.4 The Results

The discrepancies between the BALTgeoid-04 model and EGM08 height anomalies (cf. Eq. (2)) at the BALTgeoid-04 grid nodes (altogether 250 × 172 points) are depicted in Fig. 65.2. Here we focus only on the general features of the discrepancies between the BALTgeoid-04 and EGM08 derived height anomalies. The range of the detected discrepancies varies within ±3 dm over the whole target area. The largest discrepancies are located outside the borders of Estonia, Latvia and Lithuania. Within the borders of the three countries the absolute range of the discrepancies remains smaller than 15 cm. Full statistics of the comparison can be found in Table 65.1.

The nature of the discrepancies between the two models appears to be quite complicated. Note that the discrepancies in the centre of the target area seem to possess a spectral content below degree 100.

It should be noted that the long wavelength component of the GGM01s (which was used as the BALTgeoid-04 reference model, with the degree $n_{\max} = 67$) and EGM08 model is very similar. The

Alternatively, the discrepancies could either be due to: (*i*) inadequate reproduction of the spectral content of the disturbing potential from the truncated Stokesian integration (cf. the first term on the right hand side

Table 65.1 The EGM08 validation results

		Statistics				
Type of the comparison	Unit	# of points	Min	Max	Mean	STD
BALTgeoid-04 minus ζ_{EGM}	[m]	250 × 172	–0.289	+0.338	–0.025	0.077
$\Delta g(r_t,\Omega) - \Delta g_{EGM}(r_t,\Omega)$	[mgal]	42,559	–19.283	17.962	–0.811	2.600
GPS-levelling (Kronstadt vertical datum)						
Baltic $N_{geom}-\zeta_{EGM}$	[m]	189	+0.346	+0.697	+0.493	0.060
Estonian $N_{geom}-\zeta_{EGM}$	[m]	26	+0.432	+0.642	+0.566	0.048
Latvian $N_{geom}-\zeta_{EGM}$	[m]	53	+0.346	+0.638	+0.481	0.063
Lithuanian $N_{geom}-\zeta_{EGM}$	[m]	110	+0.375	+0.697	+0.481	0.048

of Eq. (1)); (*ii*) deficiencies of the harmonic analysis when determining the EGM08 spherical harmonic coefficients; or (*iii*) both.

All in all, within the land masses of the three countries (Estonia, Latvia and Lithuania) the agreement between the BALTgeoid-04 and EGM08-derived height anomalies is reasonable, see Fig. 65.3. It should be noted that the terrestrial data coverage (used for the BALTgeoid-04 model, see Ellmann, 2005, Fig. 2) is satisfactory there.

Note that the discrepancies between the BALTgeoid-04 and EGM08-derived height anomaly possess shorter wavelength features over the eastern part (especially in the SE) of the target area, where only a few data were available for the BALTgeoid-04 computations. Hence, a more complete dataset was most likely available for the compilation of the EGM08 over the eastern part of the target area. The search for an explanation of the detected discrepancies over the Baltic Sea prompts us to have a closer look to the quality and coverage of the regional terrestrial data.

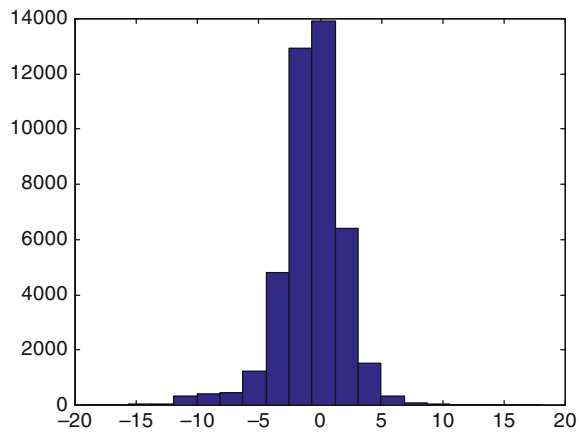


Fig. 65.3 Histogram of discrepancies between the terrestrial data and EGM08-derived free-air gravity anomalies. Unit is mgal. The total number of the points is 42,559

65.4 Comparisons with the Terrestrial Data

The gravity data (altogether 42,559 points) used in the current comparisons were obtained (in 2001) from the Danish National Survey and Cadastre, the authorized holder of the Nordic–Baltic gravity database. This international database is created and maintained within the frame of the activities of the Nordic Geodetic Commission. The national contact persons deliver the data to the database, whereas their responsibility is to ensure the quality and internal consistency of the national datasets. The co-verage of the terrestrial data points within the target area is more or less satisfactory, except the eastern part, where only a small number of Russian gravity points is available, see Ellmann (2005, Fig. 2).

The treatment of data, collected during several decades with different methods and equipment, and by different nations and specifications, requires careful study before geoid computation. It should be emphasised, however, that the gravity surveys of the three Baltic countries have historically been related to the same vertical system and gravity datum.

An extensive analysis of Nordic-Baltic gravity data is summarized in Ellmann (2001). The study revealed the presence of some (presuambly very small) systematic discrepancies between the used datasets. The systematic errors in Nordic-Baltic gravity datasets have also been noticed by other authors, see e.g., Omang

and Forsberg (2002). The elimination of these possible offsets is outside of the scope of the present study, since it requires a multilateral international involvement. Hence, any possible inherent systematic bias between the national datasets is simply ignored in earlier studies and in this comparision. This is supported by the circumstance, that many datasets of the Baltic Sea region most likely do not contain the atmospheric correction on the gravity measurements, which is recommended by the IAG (see Moritz, 1992, Sect. 65.5). Recall that at the sea level the IAG atmospheric correction on the gravity amounts to +0.87 mgal. In contrast, the attraction of the "beneath" atmospheric masses is naturally embedded in the spaceborne gravity results.

The EGM08 derived free-air anomalies Δg (at the topographic surface r_t) are computed at the locations of the observed terrestrial gravity points by the following formula (Heiskanen and Moritz, 1967, Eq. (2–151c.):

$$\Delta g_{EGM}(r_t,\Omega) = -\frac{GM_{EGM} - GM_{GRS}}{r_t^2} + \frac{GM_{EGM}}{r_t^2} \times \sum_{n=2}^{2190} (n-1) \cdot \left(\frac{a_{EGM}}{r_t}\right)^n \times \sum_{m=0}^{n} \{\Delta\overline{C}_{nm} \cos m\lambda + \overline{S}_{nm} \sin m\lambda\} \overline{P}_{nm}(\cos\theta) \tag{3}$$

Note that the first term on the right hand side is the zero degree scaling term of the gravity anomaly, which amounts to +0.144 mgal (to be added to the EGM08-derived anomalies).

The discrepancies between the measured and EGM08-derived gravity anomalies (terrestrial minus EGM08) vary from –19 to +18 mgal, with a mean of –0.81 mgal. Note the numerical value of the mean resembles the absolute range of the IAG atmospheric correction (which is presuambly missing in the Baltic datasets). This discrepancy should be studied and ultimately resolved in future geoid modellig works. Evidently, the atmospheric correction has correctly been accounted for at the EGM08 compilation. The obtained STD of the discrepancies is 2.60 mgal, the histogram of discrepancies is shown in Fig. 65.3.

In general, the EGM08-derived gravity anomalies agree reasonably well with the ground truth. However, there are some areas, where the discrepan-cies are much larger than the regional average. This may indicate that different (from the BALTgeoid-04 modelling) datasets were used (or no latest data were available) at the compilation of the EGM08.

65.5 Comparisons with GPS-Levelling Data

As is well known, inter-comparison of a geoid model, GPS-derived geodetic heights, and spirit-levelled (normal or orthometric) heights at discrete points gives a reasonable indication of the geoid model's accuracy. Thus the further validation of the EGM08 model relys on nationwide sets (one for each country) of high-precision geodetic points, for their locations see Fig. 65.4.

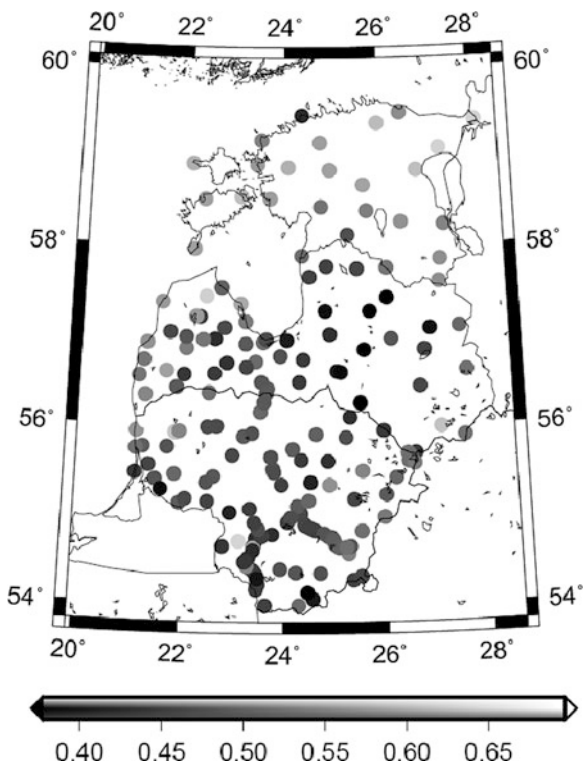


Fig. 65.4 Distribution of the Baltic GPS-levelling data (altogether 189 points) and their differences from the EGM08 height anomalies (developed up to degree 2,190). The discrepancies $[N_{geom} - \zeta_{EGM}]$ range from +0.346 to +0.697 m, with a mean of +0.493 m. The STD of the discrepancies amounts to 0.060 m. The colors of the data-points are proportional to the range of the detected discrepancies (cf. the colorbar). Unit is metre. The levellings are referred to the Kronstadt tide-gauge observations

First, the same constellation of the control points as used at the evaluation of the BALTgeoid-04 model will also be employed here. For all points the geodetic heights from GPS-measurements as well as levelling heights are available. The geodetic coordinates of the control points are related to the respective national realization of the new European Terrestrial Reference System ETRS-89. The spirit- levelled normal heights of all points refer to the Baltic Height System 1977 (Kronstadt tide-gauge).

The average distance among 26 evenly distributed Estonian control points is 50 km. The combined error of GPS-derived and spirit-levelled heights does not exceed 2–3 cm, most likely. Note that the geodetic heights are computed from the same GPS campaign and most of these points are directly connected to the high-precision levelling network. The Latvian and Lithuanian datasets (53 and 110 points, respectively) are denser. However, the accuracy of the used GPS-levelling points seems to be rather heterogeneous there.

The common Baltic geometric geoid is represented by the sum of the three national datasets (189 points). The numerical statistics of the detected differences are presented in Table 65.1. In particular, the mean of the differences reveals a positive offset (+0.49 m) of the Kronstadt vertical datum from the EGM08-derived global geoid. The resulting STD of differences 6.0 cm indicates almost the same level of accuracy, as it was achieved from the BALTgeoid-04 modelling (Ellmann, 2005). Note that the STD computations in Table 65.1 are based on the "raw" discrepancies, i.e. without applying any trend removal. Such comparisons are also produced on a country-by-country basis. The corresponding statistics can be found in Table 65.1. In particular, the STD of the discrepancies (after removing the mean) as of 0.048, 0.063 and 0.048 m were achieved for the Estonian, Latvian and Lithuanian GPS-levelling points, respectively. Very similar estimates were obtained also from the comparisons with the BALTgeoid-04 model (Ellmann, 2004, Table 2.3).

Note that the Estonian GPS-levelling geoid appears to be somewhat "higher" than the Latvian and Lithuanian geometrical geoid models, see the mean values (+0.56 m versus +0.48 m) in Table 65.1. It should be noted that for simplicity no temporal changes in the levelled heights were considered in this study. The Estonian territory is affected by the Fennoscandian post-glacial rebound. Conversely, the Latvian and Lithuanian points are located outside the land-uplift zone. Since the levellings have been performed over relatively long timespan then the Estonian solution may be contaminated with the land-uplift effect.

65.6 Summary and Conclusions

The performance of the EGM08 model was validated over the three Baltic countries – Estonia, Latvia and Lithuania. Three different sets of the "ground truth" were employed for this task.

First, the EGM08-derived height anomalies were compared with the high-resolution BALTgeoid-04 model. A reasonable agreement between the two models was detected. In particular, within the borders of Estonia, Latvia and Lithuania the absolute ranges of the discrepancies do not exceed 15 cm. Larger discrepancies (but not exceeding $\pm$ 3 dm) are related to the areas where only a few data were available for the BALTgeoid-04 modelling.

Second, the free-air gravity anomalies at the terrestrial data-points were compared with the EGM08-derived anomalies. This test yielded the STD of the discrepancies ~2.8 mgal, which is quite comparable with an average accuracy of the (historical) gravity surveys in the region of interest. Furthermore, the detected mean of the discrepancies, –0.82 mgal, may point out dissimilarities in the treatment of the atmospheric effects on gravity. This discrepancy should be studied and ultimately resolved for the sake of the consistency between the regional point-data and the spectral models of the Earth's gravity.

Finally, the quality of the EGM08 model was assessed with several sets of the GPS-levelling data. It is concluded, that the overall accuracy of the EGM08-derived height anomalies in the Baltic countries is almost of the same level as is the accuracy of the used control points, i.e. a few cm. Certainly, this conclusion cannot be extended automatically to other regions. Recall, that the Baltic Sea region is well studied gravimetrically, whereas most of the collected gravity data appear to be utilised at the EGM08 construction.

The EGM08 resolution and accuracy seem to be suitable for meaningful calculation of the offsets among different vertical datums. Clearly, the reliability and availability of the terrestrial gravity data (and their subsequent inclusion to the global gravity model)

over the region of interest are necessary preconditions for using the EGM08 global geoid (and its follow-ups) for defining offsets among different vertical datums worldwide.

Acknowledgements Dr. OCG Omang and Dr. C. Kotsakis are thanked for their constructive comments. This study is funded by the Estonian Science Foundation grant ETF7356 and the European Union Structural Funds, Project # 1.0101-0335. Dr. E. Parseliunas from the Vilnius Technical University, Lithuania and Mr. J. Kaminskis from the Latvian Geospatial Information Agency, are acknowledged for providing the GPS-levelling data.

References

Ellmann, A. (2001). Least squares modification of Stokes formula with applications to the Estonian geoid. Royal Institute of Technology, Division of Geodesy, Report No. 1056, Stockholm.

Ellmann, A. (2004). The geoid for the Baltic countries determined by the least squares modification of Stokes' formula. Royal Institute of Technology, Department of Infrastructure, Geodesy Report No. 1061, Stockholm.

Ellmann, A. (2005). Two deterministic and three stochastic modifications of Stokes's formula: a case study for the Baltic countries. *J. Geod.*, **79**, 11–23.

Heiskanen, W.A. and H. Moritz (1967). Physical geodesy. W.H. Freeman and Company. San Francisco.

Kirby, J.F. and W.E. Featherstone (1997). A study of zero- and first-degree terms in geopotential models over Australia. *Geomatics Res. Australasia*, 66, 93–108.

Molodenskii, M.S., V.F. Eremeev, and M.I. Yurkina (1960). *Methods for study of the external gravitational field and figure of the Earth*. (translated from Russian 1962). Israel program for scientific translations, Jerusalem.

Moritz H (1992) Geodetic Reference System 1980. *Bulletin Géodésique*, **66**, 187-192.

Omang, O.C.D. and R. Forsberg (2002). The northern European geoid: a case study on long-wavelenght geoid errors. *J. Geod.*, 76, 369–380.

Pavlis, N.K., S.A. Holmes, S.C. Kenyon, and J.K. Factor (2008). An Earth Gravitational Model to Degree 2160: EGM2008, presented at the 2008 General Assembly of the European Geosciences Union, Vienna, Austria, April 13–18.

Sjöberg, L.E. (1991). Refined least-squares modification of Stokes formula. *Manuscripta Geodetica*, 16, 367–375.

Stokes, G.G. (1849). On the variations of gravity on the surface of the Earth. *Trans. Cambridge Philos. Soc.*, 8, 672–695.

Tapley, B.D., S. Bettadpur, M.M. Watkins, and Ch. Reigber (2004). The gravity recovery and climate experiment: mission overview and early results. *Geophys. Res. Lett.*, 31, L09607, DOI:10.1029/2004GL019920.

Vaníček, P. and A. Kleusberg (1987). The Canadian geoid – Stokesian approach. Compilation of a precise regional geoid. *Manuscripta Geodaetica*, 12, 86–98.

Vaníček, P and L.E. Sjöberg (1991). Reformulation of Stokes's theory for higher than second-degree reference field and modification of integration kernels. *J. Geophy. Res.*, 96(B4), 6529–6339.

Wong, L. and R. Gore (1969). Accuracy of geoid heights from the modified Stokes kernels. *Geophys. J. Roy. Astron. Soc.*, 18, 81–91.

Chapter 66

Evaluation of EGM2008 by Comparison with Global and Local Gravity Solutions from CHAMP

M. Weigelt, N. Sneeuw, and W. Keller

Abstract New gravity field models incorporate GRACE data for the long wavelengths since it is one of the best available data sources. However, considering e.g. the degree difference RMS between EGM2008 and GGM02s, also discrepancies between these models occur which cannot solely be explained by numerical inaccuracies. Their validation is difficult since comparisons with existing GRACE models will always be biased. Maybe the best independent data set on a global scale is the CHAMP data. One the other hand, it is known that the accuracy of these solutions is approximately one order of magnitude worse than GRACE-only solutions. In this research, it has been investigated if CHAMP can serve as an indicator in the comparison of EGM2008 and GGM02s. The primary data source of CHAMP is its position and velocity measurements derived from GPS. They are based on purely kinematic orbits, which are independent of any a priori information and are provided by the Institute for Astronomical and Physical Geodesy at the Technical University Munich for the period of April 2002 to February 2004. The comparison is based on a global solution and a local refinement with Slepian functions in order to further improve the quality of the CHAMP solution. The latter is adopted because it can make better use of information in high-latitude areas where the data density is higher. However, the solutions are solely based on GPS measurements which have a poorer quality compared to the K-band ranging system of GRACE and thus prevents a real statement about the quality of the EGM2008.

M. Weigelt (✉)
Institute of Geodesy, Universität Stuttgart, Stuttgart 70174, Germany
e-mail: weigelt@gis.uni-stuttgart.de

66.1 Introduction

The evaluation of the gravity field model EGM2008 with CHAMP data will focus on the spectrum up to degree and order 70 due to the restricted spatial and spectral solvability of the CHAMP solution (Weigelt 2007). It is a comparison between a single satellite but independent solution and EGM2008, which contains GRACE, altimetric and terrestrial data. Three different data will be considered in the comparison: EGM2008 (Pavlis et al., 2008), the GGM02s GRACE-only solution (Tapley et al., 2005) and a 2 year CHAMP-only solution (Weigelt 2007).

Section 66.2 starts with a review of the data processing strategy for the CHAMP data. The primary measurements are positions, velocities and accelerations which need to be related to gravity field quantities. For this, the so-called energy balance approach is used to derive pseudo-potential observations along the orbit. A global spherical harmonic analysis is performed in order to derive the global satellite-only solution. Since the data is not equally distributed, a local refinement in areas with high data density can make better use of the available information (Garcia 2002). Here, the Slepian functions are employed (Simons et al., 2006) and a proof of concept is presented in Sect. 66.2.2.2. Subsequently, Sect. 66.3 presents the global and local validation results in an attempt to indicate whether the CHAMP data agrees better with EGM2008 or GGM02s.

S.P. Mertikas (ed.), *Gravity, Geoid and Earth Observation*, International Association of Geodesy Symposia 135,
DOI 10.1007/978-3-642-10634-7_66, © Springer-Verlag Berlin Heidelberg 2010

66.2 Data Processing

The section will overview gravity field recovery from CHAMP using the energy balance approach. More details about the data processing can be found in Weigelt (2007). The energy integral is used to derive pseudo-potential observations along the orbit (cf. Sect. 66.2.1), followed by a brute-force spherical harmonic analysis on the sphere. In Sect. 66.2.2 we justify why a local refinement could provide additional information in selected areas and introduce the framework of a Slepian analysis.

66.2.1 Global Gravity Field Recovery

The basic idea of this approach is to separate gravity field recovery and orbit determination into three steps. The first step is the derivation of the position data, which is done in a purely kinematic way. Data for the period April 2002 to February 2004 is provided by the Institute for Astronomical and Physical Geodesy (IAPG), Technical University Munich (Švehla and Rothacher 2005). The data is considered independent from a priori information since no dynamical model is used in the calculation. The kinematic derivation yields positions only, velocities have to be derived numerically by a fourth-order central difference Taylor differentiator (Khan and Ohba, 1999). Subsequently, pseudo-potential observations are calculated using the energy integral approach, which is based on the law of energy conservation (Jacobi, 1836, Jekeli, 1999, Gerlach et al., 2003). The basic formula is:

$$T = \frac{1}{2}\mathbf{v}^T\mathbf{v} - U - Z - \int \left(\mathbf{f} + \sum_i \mathbf{g}_i\right) d\mathbf{x} + c, \quad (1)$$

where T is the disturbing potential, U the normal potential and Z the centrifugal potential. The latter two can be calculated pointwise from the position data. The first term in equation Eq. (1) represents the kinetic energy and is derived from the velocity v of the satellite.

The integral contains the non-gravitational accelerations f as well as all known time-variable gravitational accelerations g_i. The former are measured using the accelerometer onboard CHAMP, the latter derived from models. The models for the time-variable gravitational accelerations g_i and corrections are summarised in Table 66.1. Transformations between the Earth-fixed and the inertial frame are done in accordance with the IERS Conventions 2003 (McCarthy, and Petit, 2003). Necessary calibration parameters of the accelerometer are determined together with the integration constant c using a comparison of the pseudo-observables with the disturbing potential along the orbit derived from a known a priori model (here EGM96).

Table 66.1 Utilised models for known corrections to CHAMP data

Source	Model
Astronomic tide	Sun/Moon (point masses) coordinates from DE405
Solid Earth tide	IERS Conv. 2003, Sect. 6.1
Solid Earth pole tide	IERS Conv. 2003, Sect. 6.2
Ocean tide	FES2004
Ocean pole tide	IERS Conv. 2003, Sect 6.3

The spherical harmonic analysis with its inherent downward continuation is done using a least-squares approach. The mathematical model connecting the pseudo-observable T with the spherical harmonic coefficients is the well-known formula for the spherical harmonics, e.g. Heiskanen and Moritz (1967). For the least squares adjustment the equation can be reorganised into matrix-vector form:

$$\mathbf{l} + \varepsilon = A\mathbf{x}, \quad (2)$$

where $\mathbf{l}$ is the observation vector and is filled with the observations T. It is a stochastic quantity, which is expressed by the model inconsistencies ε. The unknown vector $\mathbf{x}$ is formed by the spherical harmonic coefficients $\bar{K}_{lm}$. All other elements of the spherical harmonic expansion are part of the A-matrix, i.e. for one particular measurement k an element j of A reads:

$$a_{kj} = \frac{GM}{R}\left(\frac{R}{r}\right)^{n_j+1} P_{n_j,m_j}(\cos\theta_k) e^{im_j\lambda_k}. \quad (3)$$

The factor j denotes the column of the design matrix A and stands for a coefficient with one specific combination of degree l and order m. Here, the ordering is in accordance with Colombo (1983), which collects $\bar{C}_{lm}$- and $\bar{S}_{lm}$-coefficients for all degrees in blocks of ascending orders. As an example and considering a maximum degree of $L = 70$, the column $j = 3$ corresponds to $\bar{C}_{20}$, $j = 73$ to $\bar{C}_{21}$ and $j = 143$ to $\bar{S}_{21}$. The

solution is then achieved by a standard least-squares procedure.

66.2.2 Local Refinement with Slepian functions

The motivation for a local refinement comes from our investigations of the influence of the groundtrack pattern on the monthly global spherical harmonic solutions. It was shown by Seeuw et al., (2003), among others, that the data distribution and the groundtrack spacing influences the accuracy of the monthly CHAMP solutions. A similar effect for the GRACE-mission was discussed by Yamamoto et al. (2005) and Wagner et al. (2006).

It is also known that the orbits converge towards the poles, yielding a much higher data density in these areas. Fig. 66.1 shows the number of data points in 100km^2 patches versus the latitude. The increase of the data points per area is clearly visible. By utilising locally supported base functions, one can make better use of the information in the high-latitude areas.

66.2.2.1 An Empirical Localising Base Function

Consider a function f which is strictly contained within an arbitrarily shaped region ω on the sphere ω and will have no values outside this area, i.e. it is spacelimited. It can be described by an infinite spherical harmonic expansion, which cannot be implemented practically. Instead, the series will be truncated at a maximum degree L and thus the function is bandlimited. Strictly speaking, no spherical function can be spacelimited and bandlimited at the same time. However, a set of bandlimited functions can be found, which is optimally concentrated within the area ω, and vice versa a spacelimited function, which is optimally concentrated within an interval $0 \le l \le L$. Gilbert and Slepian (1977) showed that this leads to the same description as an algebraic eigenvalue problem. Albertella etal. (1999) considered the Slepian functions as a possible solution to the polar gap problem.

The idea is to maximise the ratio between the spacelimited and the unlimited norm and thus the spatial concentration of the bandlimited function. Using the bandlimited spherical harmonic synthesis formula and making use of the orthonormality relation of the normalised spherical surface harmonics, the relation reads

$$\xi = \frac{\sum_{l=0}^{L}\sum_{m=-l}^{l}\bar{f}_{lm}\sum_{n=0}^{L}\sum_{k=-n}^{n}D_{lmnk}\bar{f}_{nk}}{\sum_{l=0}^{L}\sum_{m=-l}^{l}\bar{f}_{lm}^2}, \qquad (4)$$

with

$$D_{lmnk} = \int_{\omega}\bar{Y}_{lm}\bar{Y}_{nk}\,d\Omega, \qquad (5)$$

where $\bar{f}_{lm}$ and $\bar{f}_{nk}$ are normalised spherical harmonic coefficients of degree l or n and order m or k. The elements D_{lmnk} can be arranged in a matrix $\mathbf{D}$ which is

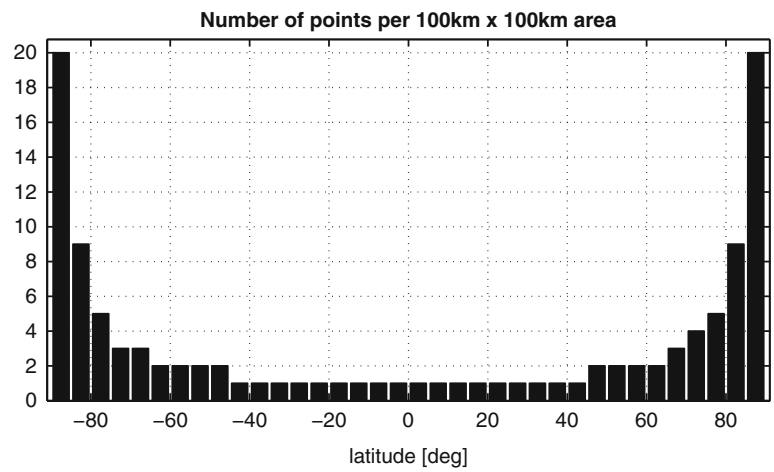


Fig. 66.1 Number of points per $100\,km^2$ area versus latitude

real, symmetric and positive definite. The solution of the spatial localization problem is found as the solution of an algebraic eigenvalue problem forming an orthogonal set of base functions (Simons et al., 2006):

$$\mathbf{D} = \mathbf{G}\,\boldsymbol{\Xi}\,\mathbf{G}^T, \tag{6}$$

where $\boldsymbol{\Xi}$ is a diagonal matrix which elements are the eigenvalues $\boldsymbol{\xi}$. These indicate the spatial concentration in the area $\boldsymbol{\omega}$. Using the associated Legendre functions for the calculation of D_{lmnk}, the eigenvalues will be normalised where 1 represents an optimal and 0 no concentration in the area of interest. Each column g^j of G represents an eigenvector and forms a base function $\bar{S}_j$ which can be reconstructed by:

$$\bar{S}_j(\lambda,\theta) = \sum_{l=0}^{L} \sum_{m=-l}^{l} g_{lm}^j \bar{Y}_{lm}(\lambda,\theta)\,. \tag{7}$$

The potential along the orbit can then be developed in Slepian base functions:

$$T(r,\theta,\lambda) = \frac{GM}{R} \sum_{j=1}^{(L+1)^2} \bar{\beta}_j \bar{S}_j(\lambda,\theta,r) \tag{8}$$

The unknown coefficients $\bar{\beta}_j$ are determined in a least-squares adjustment. Practically, not all $(L+1)^2$ Slepian coefficients are estimated when utilising local data. Here, only those with a concentration of 99% or higher will be estimated since only those are well supported by the data. Less concentrated base functions will either cause leakage errors or lead to a rank deficient design matrix.

66.2.2.2 Proof of Concept

Before the framework of a local refinement using Slepian functions is applied to the validation of EGM2008, the concept is proven in a test scenario with real CHAMP data from January 2003. Here, GGM02s will serve as a reference and the global spherical harmonic solution and the Slepian solution is compared to it. All solutions, the development of the kernel D_{lmnk} and the Slepian base functions are restricted to degree 70, since the maximum resolvable degree of the global CHAMP solution was found to be 70 (Weigelt 2007). The area of interest is a 23.5° spherical cap over Canada. Since only local data is to be used for the refinement, the long wavelength part cannot be estimated and needs to be reduced beforehand. For this, the monthly global spherical harmonic solution of January 2003 to degree and order 40 is used. Equation (8) can then be used to synthesise the data in the area of interest and compare the results in the spatial domain with GGM02s.

Figure 66.2 shows the comparison of the absolute values in terms of geoid height. The differences of the global spherical harmonic solution (top panel)

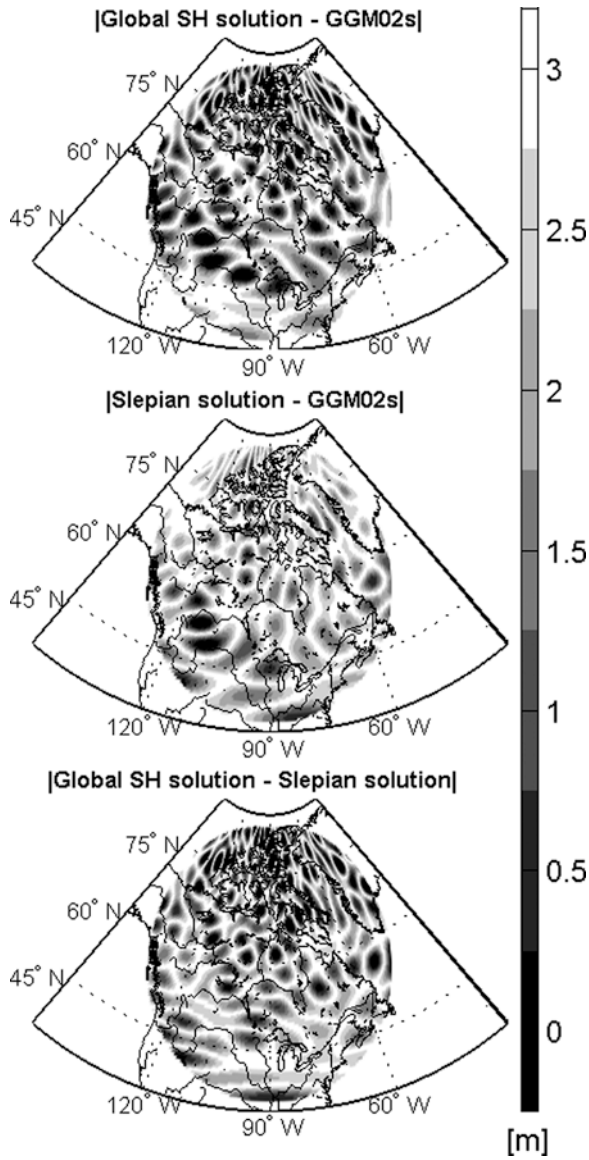


Fig. 66.2 Comparison of the absolute values in terms of geoid height: global solution versus GGM02s (*top*); Slepian versus GGM02s (*middle*); global solution versus Slepian (*bottom*)

Table 66.2 Statistics of the comparison in terms of geoid height

	Global SH (m)	Slepian (m)
Maximum	6.034	3.707
Minimum	−4.111	−3.277
RMS	1.350	0.972

grow with increasing latitude and are more pronounced than the Slepian solution (bottom panel). The pattern appears to be similar but in the latter case the absolute values are approximately half the size of the former. The difference of the global CHAMP solution and the Slepian solution shows an increased signal recovery with increasing latitude.

The statistics support this (Table 66.2). The maximum value is cut in half, the minimum value and the RMS is reduced by 25%. The results prove that the improvement is primarily due to better modelling of the short wavelength part of the spectrum, and it can be concluded that better use of the data can be made by a local refinement. In the case shown, the global spherical harmonic analysis is not able to take full advantage of the high data density in the high-latitude area.

66.3 Validation Results

Having outlined the data processing, this section will deal with the validation of EGM2008. Naturally, both EGM2008 and GGM02s will outperform the CHAMP solution due to the higher data quality. CHAMP models are solely based on GPS measurements which are approximately two order of magnitude worse than the K-band range rate observations of GRACE. The error propagates into the global spherical harmonic solutions which results in a by one order of magnitude poorer accuracy than GRACE (Tapley et al., 2005), i.e. a comparison in terms of absolute values does not make sense. Instead, the idea is to compare the differences of EGM2008 and GGM02s to CHAMP in the spectral and spatial domain and use the latter as an indicator.

66.3.1 Global Comparisons

The first comparison is done in the spectral domain. Fig. 66.3 shows error and difference degree RMS of the three solutions. The gray and black line with dot marks are the difference degree RMS between GGM02s and EGM2008 both w.r.t. CHAMP. Both curves are almost identical with the exception of degree 2. Here, the EGM2008 and the GGM02s solution disagree slightly, which might be related to the handling of the $\bar{C}_{21}$ and $\bar{S}_{21}$.

The bottom black solid line shows the difference degree RMS between EGM2008 and GGM02s. For all degrees, the difference between these two is smaller than the difference to CHAMP. Consequently, drawing a conclusion will be very difficult and it is a first indication that both fields will perform approximately

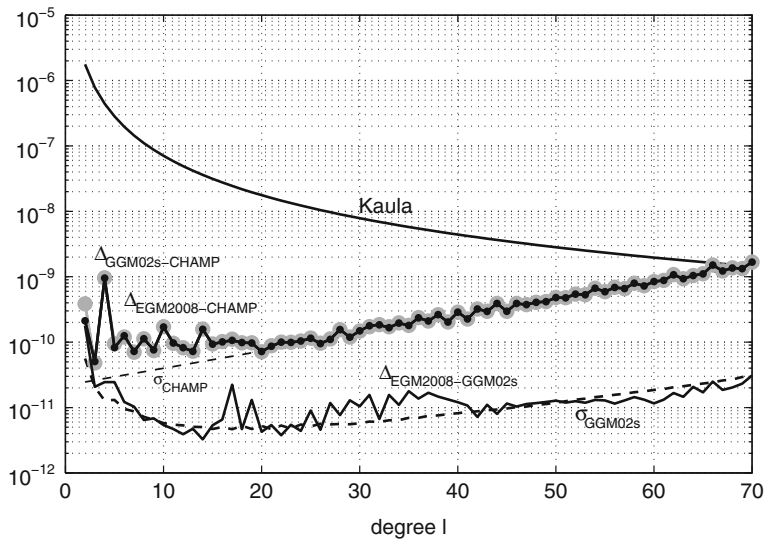


Fig. 66.3 Error and difference spectra of GGM02s, EGM2008 and the CHAMP-solution

equally in the comparison to the CHAMP data. The reason is simply the poorer quality of the latter. However, there is also a significant discrepancy between degree 15 and 20 and between 25 and 45 in the difference of EGM2008 and GGM02s and the error degree RMS of GGM02s. Note that the highest peak is at degree 16, which might be related to the orbit of GRACE since the satellites makes nearly 16 revolutions per day.

The comparison to the CHAMP data in the spatial domain and on a global scale is shown in Fig. 66.4 but it is inconclusive. Both solutions behave similarly and show no significantly different pattern. The maximum difference is 1.326 m for GGM02s and 1.342 m for EGM2008. The minimum is −1.338 m for GGM02s and −1.364 m for EGM2008 and they differ by 2.6 cm. However, the location is different and thus the comparison is invalid, especially taking the random nature of the differences in Fig. 66.4 into account. The RMS shows no significant difference and is 0.249 m for both. For comparison, the difference between EGM2008 and GGM02s is approximately two orders of magnitude smaller than in the comparisons to CHAMP.

Overall, it has to be concluded that the differences are not significant, and GGM02s and EGM2008 show the same behavior in the comparison to the global CHAMP solution.

66.3.2 Local Comparison

For the local refinement of the CHAMP solution, a latitude band from 60° *N* to 85° *N* is chosen and 141 base functions are used in the Slepian adjustment to

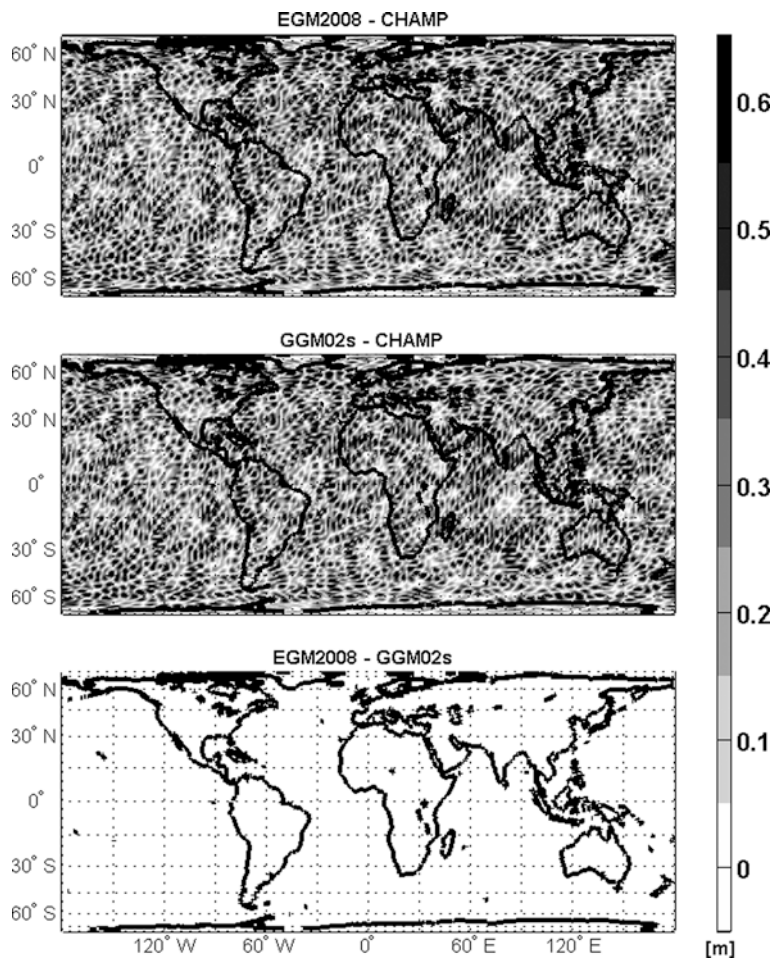


Fig. 66.4 Spatial comparison between GGM02s, EGM2008 and global CHAMP solution

improve the solution. In the remove step, the full global spherical harmonic solution from CHAMP to degree 70 is reduced. The recovered residual signal has a strength of $\delta N \approx 10\,cm$ which is added in the spatial domain to the spherical harmonic solution and hereafter called the Slepian solution. The comparison in the spatial domain between EGM2008, GGM02s and the Slepian solution is shown in Fig. 66.5 but again shows no significant differences. The top two panels, i.e. the comparison between EGM2008 and the Slepian solution and the comparison between GGM02s and the Slepian solution, are both dominated by the deficiencies in the CHAMP data (Table 66.3).

The difference between EGM2008 and the Slepian solution has a mean value which is by 4 mm higher.

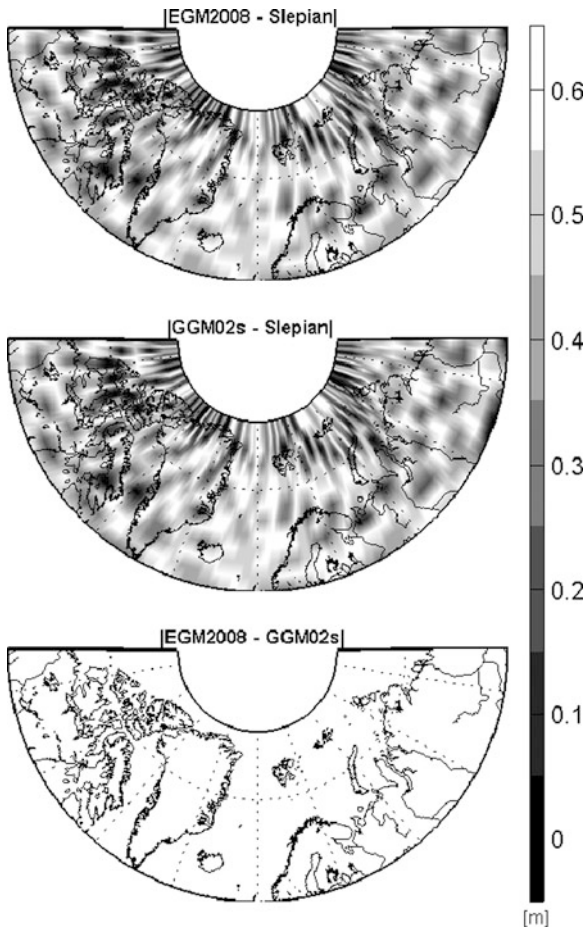


Fig. 66.5 Spatial comparison of the absolute values for a latitude band from 60° N to 85° N : EGM2008 versus Slepian solution (*top*); GGM02s versus Slepian solution (*middle*); EGM2008 versus GGM02s (*bottom*)

Table 66.3 Statistics of the comparison in terms of geoid height

	EGM2008-Slepian (m)	GGM02s-Slepian (m)	EGM2008-GGM02s (m)
Maximum	0.880	0.877	0.024
Minimum	−1.132	−1.122	−0.016
Mean	0.025	0.021	0.003
RMS	0.234	0.233	0.005

It is also reflected in the difference of EGM2008 and GGM02s. The maximum and minimum agree also slightly better for the comparison of GGM02s and CHAMP, i.e. there is very slight tendency of the CHAMP data towards the GRACE solution. Nevertheless, the differences are one order of magnitude higher than the comparison of EGM2008 and GGM02s thus the statistics cannot be considered significant.

66.4 Conclusions

In conclusion, the poorer quality of the CHAMP data prevents a real statement about the quality of the EGM2008. At best, one can say that the local CHAMP solution compares slightly better to the GRACE-only solution GGM02s than to the EGM2008. EGM2008 and GGM02s show differences from degree 15 to 45 which cannot be verified nor quantified in the comparison to the CHAMP data.

Acknowledgements We like to acknowledge Drazen Švehla from the Institute of Astronomical and Physical Geodesy, TU Munich for providing the kinematic position data for CHAMP and GFZ Potsdam for providing the acceleration data. We are also very thankful for the helpful comments of the two reviewers Dr. Will Featherstone and Dr. Thomas Gruber.

References

Albertella, A., F. Sansò, and N. Sneeuw (1999) Band-limited functions on a bounded spherical domain: the Slepian problem on the sphere. *J. Geod.*, 73, 436–447.

Colombo, O. (1983). Numerical methods for harmonic analysis on the sphere, *Tech. rep.*, Report No.310, Dept. Geod. Sci. and Surv., Ohio State Univ., Columbus, Ohio.

Garcia, R. (2002). Local geoid determination from GRACE, Ph.D. thesis, Ohio State University.

Gerlach, C., N. Sneeuw, P. Visser, and D. Švehla, (2003). CHAMP gravity field recovery using the energy balance approach. *Adv. Geosci.*, 1, 73–80.

Gilbert, E., and D. Slepian (1977). Doubly orthogonal concentrated polynomials. *SIAM J. Math. Anal.*, 8, 290–319.

Heiskanen, W. and H. Moritz (1967). Physical geodesy, W.H. Freeman and Company San Francisco.

Jacobi, C. (1836). Über ein neues Integral für den Fall der drei Körper, wenn die Bahn des störenden Planeten kreisförmig angenommen und die Masse des gestörten vernachlässigt wird., *Monthly reports of the Berlin Academy*.

Jekeli, C. (1999). The determination of gravitational potential differences from satellite-to-satellite tracking, *Celestial Mech. Dynamical/Astronomy*, *75*, 85–101, 1999.

Khan, I. and R. Ohba (1999). Closed-form expressions for the finite difference approximations of first and higher derivaties based on Taylor series. *J. Comput. Appl. Math.*, 107, 179–193.

McCarthy, D.D. and G. Petit (2003). IERS conventions 2003, *Tech. Rep. 32*, IERS, Frankfurt am Main, Verlag des Bundesamts für Kartographie und Geodäsie, updated version from 20th July 2006.

Pavlis, N.K., S.A. Holmes, S.C. Kenyon, and J.K. Factor (2008). An Earth Gravitational Model to Degree 2160: EGM2008, *presented at the 2008 General Assembly of the European Geosciences Union, Vienna, Austria, April 13–18*.

Simons, F., F. Dahlen, and M. Wieczorek (2006). Spatiospectral concentration on a sphere. *Siam Rev.*, 48(3), 504–536

Sneeuw, N., C. Gerlach, D. Švehla, and C. Gruber (2003). A first attempt at time-variable gravity field recovery from CHAMP using the energy balance approach. In: Gravity and Geoid 2002, Tziavos, I., (ed.), Proceedings of 3rd Meeting of the International Gravity and Geoid Commission, pp. 237–242, Editions ZITI, Thessaloniki, Greece.

Švehla, D. and M. Rothacher (2005). Kinematic precise orbit determination for gravity field determination. In: Sanso, f. (ed.) A window on the future of geodesy International Association of Geodesy Symposia, vol. 128, pp. 181–188, Springer, Berlina, Heidelberg 2005.

Tapley, B., J. Ries, S. Bettadpur, D. Chambers, M. Cheng, F. Condi, B. Gunter, Z. Kang, P. Nagel, R. Pastor, T. Pekker, S. Poole, and F. Wang. GGM02–An improved Earth gravity field model from GRACE. *J. Geod.*, 79, 467–478 (2006).

Wagner, C., D. McAdoo, J. Klokočník, and J. Kostelecký (2006). Degradation of geopotential recovery from short repeat-cycle orbits: application to GRACE monthly fields. *J. Geod.*, 80(2), 94–103.

Weigelt, M. (2007). Global and local gravity field recovery from satellite-to-satellite tracking, Ph.D. thesis, University of Calgary, http://www.geomatics.ucalgary.ca/graduatetheses .

Yamamoto, K., T. Otsubo, T. Kubo-oka, and Y. Fukuda (2005). A simulation study of effects of GRACE orbit decay on the gravity field recovery. *Earth Plane. Space*, 57, 291 – 295.

Chapter 67

Testing EGM2008 on Leveling Data from Scandinavia, Adjacent Baltic Areas, and Greenland

G. Strykowski and R. Forsberg

Abstract We tested EGM2008 on GPS/leveling data from Scandinavia and adjacent areas. EGM2008 performs at the same level as the best regional geoid model, NKG2004. However, the direct evaluation of EGM2008 is difficult in Greenland because no leveling data are available. Nevertheless, we show on 78 GPS-MSS data that EGM2008 also performs at the same level as the best regional geoid model GOCINA04.

67.1 Introduction

Prior to the official release of the new global geopotential model EGM2008 (Pavlis et al., 2008), complete to the degree and order 2,160, the authors contributed to the "EGM2007 Evaluation Project" by testing the preliminary model PGM2007A on leveling data from northern Europe (Scandinavia, the Baltic countries and the adjacent areas around the Baltic Sea) as well as from Greenland. The final report "PGM2007A evaluation on GPS-leveling data in Greenland and Scandinavia and adjacent areas" was submitted to the Joint IGFS/IAG Comission-2 Working Group and included as a "feed back"-contribution to improve the global model. The present work is a repetition of this exercise for the newly released EGM2008.

G. Strykowski (✉)
Department of Geodynamics, DTU Space, The Technical University of Denmark, Copenhagen Ø DK-2100, Denmark
e-mail: gs@space.dtu.dk

67.2 Scandinavia and Adjacent Areas

Scandinavia and adjacent Baltic areas is a sector covering Norway, Sweden, Finland, Denmark, Estonia, Latvia, Lithuania and a section of Poland. The sector is bounded by the following parallels and meridians: 53°N–73°N and 1°E–33°E.

The GPS/leveling data from Scandinavia and adjacent Baltic areas used for the evaluation of the PGM2007A model are the same as those used in the past for the evaluation of the regional Nordic geoid models. In fact, these formerly used GPS/leveling data sets were enhanced by the inclusion of additional leveling data from Norway, Sweden and Finland. Basically, the new data are more consistent (and recent) with respect to the epoch of the GPS campaigns and leveling. Because of the substantial land uplift in the area, this consistency is important.

The leveling data from the different countries consist usually of heights in their national height system, which can differ from country to country (orthometric heights, normal heights), but also in the way they are linked to the Mean Sea Level via a tide gauge (a vertical datum). In assessing the quality of the Nordic geoid model these national data sets are usually used separately (i.e. country wise). The main parameter for the "goodness-of-fit" in a given country is the standard deviation of the misfit between the gravimetric geoid/quasi-geoid model and the "geoid" derived from GPS and leveling measurements: $N = h - H$.

For the purpose of the regional comparison the GPS/leveling data from individual countries were corrected for relative vertical offset with respect to each other. The biases used were the assessed offset of each

S.P. Mertikas (ed.), *Gravity, Geoid and Earth Observation*, International Association of Geodesy Symposia 135,
DOI 10.1007/978-3-642-10634-7_67, © Springer-Verlag Berlin Heidelberg 2010

Table 67.1 The quasi-geoid models used in the comparison

Model	Comments
EGM96	Lemoine et al. (1998)
EGM96+GRACE2S	
NKG96	1996 regional geoid model for the Baltic and Nordic area
NKG2004	2004 regional geoid model for the Baltic and Nordic area
PGM2007A Zero Tide	Preliminary model released by NGA in 2007
EGM2008 Zero Tide	Pavlis et al. (2008)

countries height datum with respect to the common European Vertical Datum.

We compared the GPS/leveling data to the quasi-geoid models in Table 67.1:

The statistics of the comparison for the whole area are shown in Table 67.2.

From Table 67.2 and Fig. 67.1 we conclude, that EGM2008 model is excellent. It is at the same standard as the latest regional gravity model NKG2004. For the joint GPS/leveling data set (see above), this comparison is somehow misleading. On Fig. 67.1, the large misfit in Norway is most certainly caused by problems related to leveling. A problem is the inconsistency between the fixed epoch of the leveling and the fact that, in practice, the leveling was done over many years in the presence of a substantial land uplift caused by the post glacial rebound (Dr. Ove Omang, Norwegian Mapping Authority, personal communication). This leveling and height system problem for Norway is discussed in some details by Lysaker et al. (2007). One can notice that the large misfits to EGM2008 in Norway on Fig. 67.1 co-locate with the pattern on Fig. 4 in (Lysaker et al., 2007) showing the vertical land uplift velocities. This indicates, as stated, that the misfit in Norway is not a problem with the gravimetric model, but (most probably) with the GPS/leveling. The GPS/leveling data for Finland and Sweden were corrected for the land uplift to a common epoch.

A similar comparison for the individual countries (standard deviation) and for four of the models is shown in Table 67.3.

The conclusion from this comparison is that EGM2008 is an excellent model for Scandinavia and its adjacent areas. Its accuracy is similar to the current best regional geoid model (NKG2004).

From other reports, the new geopotential model EGM2008, performs also very well in other parts of the world when compared to GPS/leveling data. It renewed the discussion about the need for defining a global vertical datum. For this reason, it is of some interest to list the mean values of the deviation of the national geoid heights of the GPS/leveling data and the EGM2008 model. These values are listed in Table 67.4.

It should be emphasized, that the expression "the best available" GPS/leveling data does not mean "the best existing". The national mapping authorities in the involved countries have access to much better and denser GPS/leveling data, which also include a more

Table 67.2 Scandinavia and adjacent Baltic areas. Statistics of the comparison of GPS/leveling to different quasi-geoid models (Unit: m)

Model	Mean	Std. dev.	Rms	Min	Max
EGM96	0.38	0.26	0.46	−0.51	1.80
EGM96+GRACE2S	0.35	0.20	0.41	−0.66	1.18
NKG96	0.01	0.14	0.14	−0.61	0.51
NKG2004	0.03	0.11	0.11	−0.48	0.39
PGM2007A ZeroTide	−0.59	0.11	0.60	−0.96	−0.18
EGM2008 ZeroTide	−0.55	0.11	0.56	−0.91	−0.13

Table 67.3 Scandinavia and its adjacent areas. Standard deviation of the misfit between the best available national GPS/leveling data sets and different quasi-geoid models (Unit: m)

	N	EGM 96	NKG 2004	PGM 07A Zero Tide	EGM 2008 Zero Tide
Denmark	85	0.35	0.06	0.07	0.07
Estonia	31	0.25	0.07	0.06	0.07
Finland	154	0.14	0.04	0.07	0.07
Latvia	36	0.16	0.10	0.09	0.09
Lithuania	32	0.17	0.08	0.08	0.09
Norway	1,693	0.31	0.12	0.12	0.11
Poland	6	0.23	0.05	0.11	0.11
Sweden	910	0.15	0.04	0.03	0.03

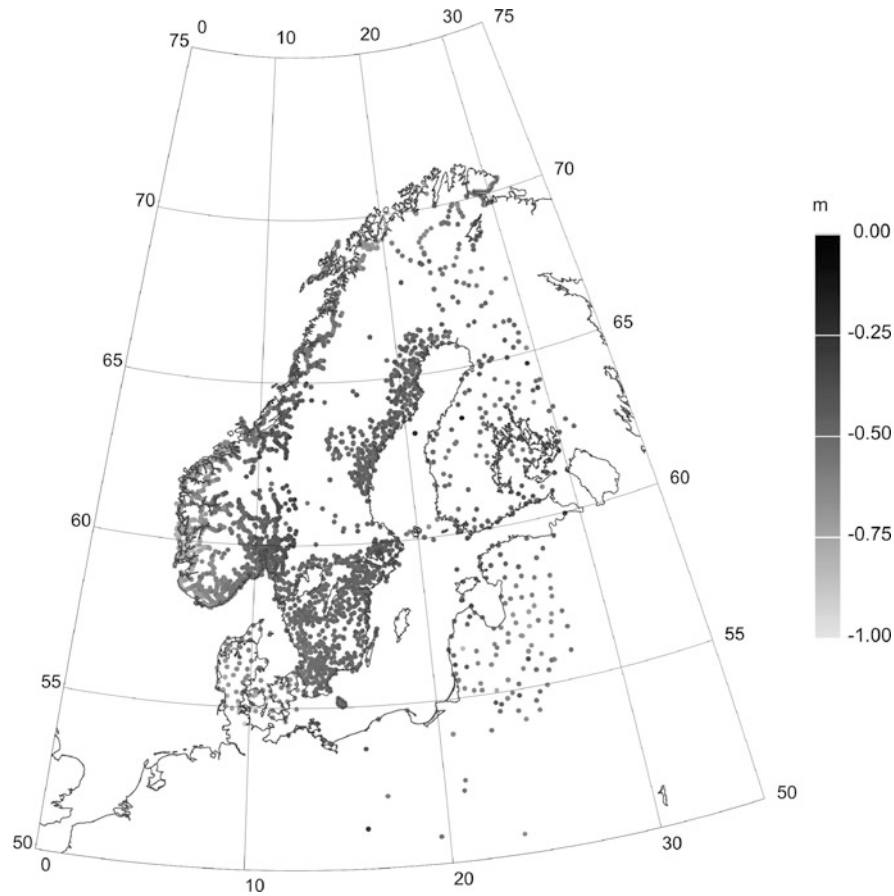


Fig. 67.1 $\varepsilon = (h\text{-}H^{lev})\text{-}N_{EGM2008}$ Comparison of the geoid heights from the joint GPS/leveling data set (3,144 points) for Scandinavia and adjacent Baltic areas to the EGM2008 model

thorough treatment of, especially, the regional land uplift, as well as a more consistent treatment of the difference in epochs between the GPS- and leveling campaigns. The GPS/leveling data used here are those used in the past under the auspices of the Nordic Geodetic Commission to model and to evaluate the regional geoid models (e.g. NKG96, NKG2004). In other words, there is much more to say about the quality of EGM2008 compared to the "best existing" national GPS/leveling data; especially in the neighboring countries like Poland, where the available data set is most probably not representative at all. In this context, the vertical offsets listed in Table 67.4 are only rough numbers and do not in any way claim to be an attempt to model the accurate vertical offsets between the national height systems and the global vertical datum.

Table 67.4 Mean deviation of the best available national GPS/leveling data from EGM2008 quasi-geoid

	$Mean(N_{lev} - N_{EGM2008})$ (m)
Denmark	–0.63
Estonia	–0.66
Finland	–0.51
Latvia	–0.60
Lithuania	–0.60
Norway	–0.57
Poland	–0.53
Sweden	–0.49

In this report we are only trying to assess: How does EGM2008 perform compared to the best regional geoid models? The answer to this question is that, for Scandinavia and adjacent Baltic areas, the fit of the new global model is at the same level as the best regional gravimetric geoid model (NKG2004).

67.3 Greenland

No leveling data exist between settlements in Greenland. A GPS-mean sea-level height data set is selected from recent GPS campaigns. GPS points are

all tied to ITRF, mainly through the REFGR Greenland fundamental GPS network. The height above mean sea level (MSL) of the GPS points are mostly based on older MSL determinations, usually from the 1960s, or more recent, often shorter-duration MSL and relative tide gauge campaigns. The GPS ellipsoidal heights and MSL-heights can be used for geoid validation through the following relation:

$$\mathrm{N}^{\mathrm{GPS}} = h^{GPS} - \mathrm{H}_{\mathrm{MSL}} - \mathrm{MDT}, \qquad (1)$$

where MDT is the mean dynamic topography.

We obtained the MDT from the OCCAM oceanographic model. This model does not include the local effects of fjords etc., so "GPS/leveling" data of this type might have significant errors due to local MDT effects, land uplift, and other errors. Figure 67.2 shows the locations of the GPS-MSS data.

For the evaluation of PGM2007A model the tide-free model was used. However, since the physical Earth is permanently deformed by tidal forces we are now using the zero tide model for the evaluation of EGM2008. Table 67.5 shows the effect of the MDT corrections for PGM2007A model. It is seen, that the mean value of the differences is reduced, whereas the standard deviation is only reduced slightly. This indicates that the used MDT model is not adequate for this local application.

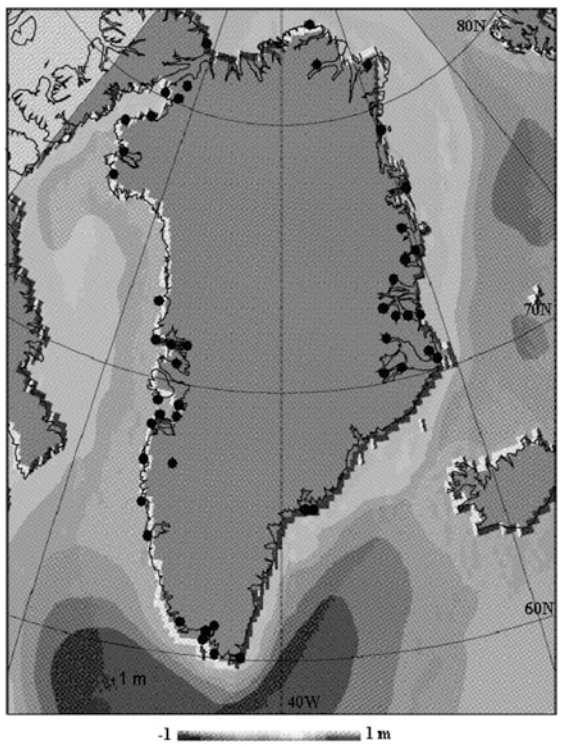


Fig. 67.2 Location of Greenland GPS stations (*dots*) and MDT from OCCAM model (contours)

Table 67.5 Comparison of EGM2008 and PGM2007A and other models to GPS-MSS data in Greenland (78 points)

Unit: m	Mean	Std. dev.	Min	Max
N = GPS-MSS-MDT	35.04	12.66	8.94	57.01
EGM2008, MDT	−0.19	0.40	−0.43	1.60
PGM2007A, no MDT	−0.63	0.45	−1.66	1.08
PGM2007A, MDT	−0.26	0.43	−1.20	1.45
EGM96, MDT	0.71	0.52	−0.52	2.62
GEOID96A, MDT	−1.09	0.83	−2.50	1.76
GOCINA04, MDT	−0.16	0.37	−0.98	1.44

MDT – corrected for mean dynamic topography; no MDT – not corrected for mean dynamic topography

Table 67.5 also shows the comparison of the GPS-MSS data (reduced for MDT) to other geoid models: EGM96, GEOID96A and GOCINA04. The latter two are local gravimetric geoid models, derived by somewhat different methods. GEOID96A uses EGM96 as reference, and utilizes least squares collocation to merge high-elevation airborne gravity data (Brozena et al., 1993) and surface data in the ice-free coastal regions; the GOCINA04 model uses a JPL GRACE model as reference, and uses only surface gravity data in the coastal region. Both models use ice thickness information and terrain reductions, and are based on spherical FFT methods.

Results in Table 67.5 indicate that PGM2007A and, especially, EGM2008 perform nearly at the same level as the "best" local geoid model – GOCINA04. The difference might be caused by the different weighting used for the high-altitude airborne gravity data, which might have long-wavelength errors not consistent with GRACE. However, other avenues for systematic errors are the use of terrain and ice reductions since large parts of the ice sheet do not have sufficiently accurate radar echo sounding depth data, especially near the margins of the ice sheet. It is also seen that the earlier geoid models have much larger errors, likely due to the absence of GRACE data. This is as expected.

67.4 Conclusions

For Scandinavia and adjacent Baltic areas the new global model EGM2008 is a net improvement over the latest global reference model EGM96 and almost as good as (and sometimes better than) the latest regional quasi-geoid model NKG2004. For Greenland, EGM2008 performs with an accuracy which is comparable to the best local geoid model GOCINA04.

Acknowledgements Dag Solheim and Ove Omang, The Norwegian Mapping Authority (Statens Kartverk), Norway, for discussing the problems with the GPS/leveling data in Norway. Prof. C. C. Tscherning, University of Copenhagen, Denmark, for providing software for computing EGM2008 in Windows and for help with the conference poster associated with this paper.

References

Brozena, J., M. Chalona, R. Forsberg, and G. Mader (1993). New Technology allows remote areas to be probed the Greenland Aerogeophysics Project. In: EOS Transactions American Geoph. Union, vol. 74(2), p. 18, January 1993.

Lemoine, F.G., S.C. Kenyon, J.K. Factor, R.G. Trimmer, N.K. Pavlis, D.S. Chinn, C.M. Cox, S.M. Klosko, S.B. Luthcke, M.H. Torrence, Y.M. Wang, R.G. Williamson, E.C. Pavlis, R.H. Rapp, and T.R. Olson (1998). The development of the Joint NASA GSFC and the National Imagery and Mapping Agency (NIMA) Geopotential Model EGM96. NASA/TP-1998-206861, Goddard Space Flight Center, July 1998. http://cddis.nasa.gov/926/egm96/egm96.html

Lysaker, D.I., O.C.D Omang, B.R. Pettersen, and D. Solheim (2007). Quasigeoid evaluation with improved height data for Norway. *J. Geod.*, 81, 617–627.

Pavlis, N.K., S. Holmes, S.C. Kenyon, and J.K. Factor (2008). An Earth Gravitational model to Degree 2160: EGM 2008. Presented EGU General Assembly, Vienna, April 2008.

Chapter 68

Least Squares, Galerkin and BVPs Applied to the Determination of Global Gravity Field Models

F. Sacerdote and F. Sansò

Abstract The determination of global gravity potential models is a central issue in Geodesy. In principle the existence of solutions, i.e. of harmonic potentials, given certain boundary conditions, depends on the solvability of certain boundary value problems (BVP) for the Laplace equation, an item that has recently received quite an impulse in terms of abstract theorems. Yet, the real problem is that of approximating such solutions. In general, least squares (l.s.) in Hilbert spaces can give an easy and converging solution to such a problem. Yet, l.s. is very demanding from the numerical point of view because of the notable variability of the boundary, be it the actual surface of the earth or the telluroid. Another, somewhat simpler, technique to approximate a BVP is the so called Galerkin method. The relation between the l.s. and Galerkin is analyzed and clarified. Finally, one has to recognize that in reality the true method used in geodesy to construct approximations is the use of the downward continuation followed by orthogonality relations. The paper shows that this geodetic approach can be seen as an approximation of the solution of Galerkin's system and, at the same time, as an accelerator of the so called change of boundary method.

68.1 Introduction

Earth gravity global models are in fact approximate solutions of BVPs, restricted to a finite-dimensional space of harmonic base functions. For historical reasons, for reasons of easy and fast computability and because after all the earth geoid is close to a sphere, the approximation space used by the majority of accurate and high resolution solutions is the one generated by spherical harmonics. The most recent model, EGM08 (N.K. Pavlis et al., same proceedings), is complete up to degree 2,160, corresponding to a $5' \times 5'$ resolution at ground level. This, as all the previous models, incorporates important information coming from satellite dynamics and, more recently, from spatial gravity observations; yet, such information has at most influence on harmonic degrees up to some maximum value between 100 and 200 (GRACE), with a prospect of reaching degree 250 with the next missions (GOCE, etc.). So, most of the coefficients $\{T_{nm}\}$ in the representation of the anomalous gravity potential

$$T(r,\sigma) = \sum_{n=2}^{N} T_{nm} S_{nm}(r,\sigma), \tag{1}$$

where: $\sigma = (\vartheta, \lambda), S_{nm}(r,\sigma) = \left(\frac{R}{r}\right)^{n+1} Y_{nm}(\sigma)$ are in fact derived from some approximation procedure of the solution of the linearized geodetic boundary-value problem, also known as the scalar Molodensky problem. Note should be taken that in (1) R is an arbitrary constant, because the sum in that formula is finite, although each specific solution method implies a natural choice for R as we shall see; moreover in (1), as in the sequel, we do not specify the limits of summation of the order index m, implying that this is added from $-n$ to n for each degree n.

The main ingredients of any approximation theory are:

F. Sacerdote (✉)
Dipartimento di Ingegneria Civile e Ambientale,
Università di Firenze, Firenze 50139, Italy

S.P. Mertikas (ed.), *Gravity, Geoid and Earth Observation*, International Association of Geodesy Symposia 135,
DOI 10.1007/978-3-642-10634-7_68, © Springer-Verlag Berlin Heidelberg 2010

- the fact that $\{S_{nm}\}$ be a complete sequence in the space to which T is assumed to belong; a fact long known in geodesy, as it can be derived, for any reasonable Hilbert space of solutions, as a corollary of the Runge-Krarup theorem;
- the fact that the boundary operator applied to $\{S_{nm}\}$ generates a complete sequence in the space to which data are assumed to belong.

Since we shall start our analysis, in Sect. 68.2, from the method of least squares, it is only natural to assume that our data, basically gravity anomalies, are square integrable on the boundary, i.e. the earth telluroid, S. That the Laplace equation has solutions with $L^2(S)$ boundary data is a theory that has been developed by Cimmino in the forties and fifties for the Dirichlet and the Neumann problem (Cimmino, 1940; Cimmino, 1952) and by Magenes for the oblique derivative problem (Magenes, 1955). Yet, it is only recently that useful conditions for the existence, uniqueness and stability of the solutions of Molodensky's problem with data in $L^2(S)$ have been derived (Sansò and Venuti, 2008). So now we have the two main tools allowing us to set up a Hilbertian l.s. theory. The advantage of such theory is that its solution is automatically known to converge to the true solution. The disadvantage is that its numerical solution has not been implemented in geodetic literature, despite the fact that l.s. is a method strongly bound to the geodetic tradition.

Of course there are in the literature proposals for the use of l.s. (see, for instance, Martinec, 1998), yet, to the knowledge of the authors, no attempt has been done for an extensive application to real data. However, one can see, as in Sect. 68.3, that the Galerkin projection method gives estimates of the coefficients T_{nm} quite close to that of l.s. By exploiting the convergence of the l.s. solution, the convergence of Galerkin's approach can be guessed too, although a rigorous proof is lacking. However, even the implementation of Galerkin's system is a hard numerical work, because high degree series of spherical harmonics have to be computed on a dense grid (e.g. $5' \times 5'$) of points on the earth telluroid. A research line along this idea is being pursued; starting already from the work of Klees (1997) and Lehmann (1997). Any way, up to now most geodetic solutions of the global approximation problem have tried to reduce the formulation of the problem itself down to a simple geometric surface, namely the ellipsoid or, ultimately, the sphere. On such surfaces in fact simple orthogonality relations of spherical harmonics hold true and can be used. Two methods of this kind have been applied in practice in geodetic literature: the so called change-of-boundary or pull-back method, and the downward continuation, which is in fact applied in EGM past and recent solutions. As for the first, some theoretical results guarantee the convergence of the method; the second, beyond the undisputable success from the numerical point of view, still needs theoretical analysis in order to be well understood. Yet, it is apparent that one way of viewing it is to consider it as an accelerator of the previous method through the downward continuation algorithm. This paper tries to create a bridge between theoretical results of the analysis of geodetic BVPs and numerical methods actually employed, in an attempt to clarify the state of the art and their natural relations.

68.2 LS Approach for Data at Ground Level and Satellite Coefficients

The coefficients T_{nm} of global models of the anomalous potential can be determined from a global coverage of gravity anomaly data at ground level. To this aim, gravity anomalies must be expressed as functionals of the anomalous potential:

$$\Delta g = -\mathbf{e}_\gamma \cdot \nabla T + \frac{\gamma'}{\gamma} T \equiv AT \tag{2}$$

where $\underline{\gamma}$ is the normal gravity vector, γ ts modulus, γ' its derivative in the direction of the ellipsoidal normal, and $\mathbf{e}_\gamma$ the unit vector in its direction.

In addition, it must be recalled that, if Δg is used as boundary data, the corresponding BVP for the anomalous potential is not well-posed, and it is necessary to modify the boundary condition, replacing Δg with $\Delta g + \sum_{j=1}^{3} a_j Z_j$, where Z_j are 3 suitable functions defined on the boundary surface and a_j are unknown coefficients to be determined, in order to obtain existence and uniqueness of the solution in the complement of the space generated by the external solid harmonics of degree 1.

More generally, it can be proved that, if a low-degree model is assumed to be known, say up to degree $L = 20$, it is possible to introduce a suitable

family of functions $\{Z_{rs}|r \le L,|s| \le r\}$ such that the BVP problem

$$\begin{cases} \Delta T = 0 & \text{in } \Omega \text{ (outside } S) \\ AT = \Delta g - \sum^{L} a_{rs} Z_{rs} & \text{on } S \\ T = 0(r^{-L-2}) & r \to \infty \end{cases} \tag{3}$$

is well-posed. Generally, S is assumed to be a star-shaped surface, described by the equation $r = R(\sigma)$, where the function $R(\sigma)$ has bounded first and second derivatives. The asymptotic condition in (3) implies that the expansion of T into external solid spherical harmonics starts from degree $L + 1$:

$$T = \sum_{n=L+1}^{\infty} T_{nm} S_{nm}, \text{ where } S_{nm} = \left(\frac{\overline{R}}{r}\right)^{n+1} Y_{nm}; \tag{4}$$

$\overline{R} > \sup R(\sigma)$ can be arbitrary, but in practice it is fixed as the radius of a sphere not far from the actual surface. The coefficients T_{nm} whose order is included in the interval between L and an upper level N depending on the density of the data, as well as a_{rs}, can be estimated by l.s., minimizing the squared norm

$$\left\| A\left(\sum_{n=L+1}^{N} T_{nm} S_{nm}\right) - \left(\Delta g - \sum_{r=0}^{L} a_{rs} Z_{rs}\right) \right\|^2_{L^2(S)} \tag{5}$$

with respect to T_{nm} and a_{rs}. The resulting normal system is

$$\begin{cases} \sum\limits_{L+1}^{N} (AS_{nm},AS_{jk}) T_{nm}^{(N)} + \sum^{L} (Z_{rs},AS_{jk}) a_{rs}^{(N)} = (\Delta g,AS_{jk}) \\ \sum\limits_{L+1}^{N} (AS_{nm},Z_{jk}) T_{nm}^{(N)} + \sum^{L} (Z_{rs},Z_{jk}) a_{rs}^{(N)} = (\Delta g,Z_{jk}) \end{cases} \tag{6}$$

where $(\cdot,\cdot)$ is the scalar product, the upper index (N) means that the solution actually depends on the maximum degree N. On the other hand, the family of functions $\{Z_{rs}|r \le L,|s| \le r\}$ can be chosen in such a way that their span is the orthogonal complement of $\{S_{jk}|j > L,|k| \le j\}$, and the operator A is one-to-one on the span of $\{S_{jk}|j > L,|k| \le j\}$. Hence, the set $\{Z_{rs},AS_{jk}|r \le L,j > L\}$ is a basis for $L^2(S)$. Therefore, the norm (5) can be made arbitrarily small for N sufficiently large and for a suitable choice of the coefficients, and the minimizing sequence $\{T_{nm}^{(N)},a_{rs}^{(N)}\}$ has a finite limit for $N \to \infty$. Consider now the function

$$T^{(N)}(r,\sigma) = \sum_{L+1}^{N} T_{nm}^{(N)} \left(\frac{\overline{R}}{r}\right)^{n+1} Y_{nm}(\sigma) \tag{7}$$

that is a finite sum of spherical harmonics. It is clear from the above reasoning that

$$AT^{(N)}|_S + \sum a_{rs}^{(N)} Z_{rs}|_S = \Delta g + \varepsilon^{(N)} \tag{8}$$

with $\lim\limits_{N\to\infty} \varepsilon^{(N)} = 0$ in $L^2(S)$; furthermore, if $\overline{S}$ is the spherical surface with radius $\overline{R}$, enclosing S,

$$T^{(N)}|_{\overline{S}} = \sum_{L+1}^{N} T_{nm}^{(N)} Y_{nm}. \tag{9}$$

On the other hand, given Δg, there exist $(T,\mathbf{a})$ satisfying (3), and it is possible to write

$$T|_{\overline{S}} = \sum_{L+1}^{\infty} T_{nm} Y_{nm}, \tag{10}$$

note that the choice $R = \overline{R}$ is precisely made in order to be able to write the exact relation (10) in terms of a $L^2(S)$-convergent series. Owing to the continuous dependence of T,T_{nm},a_{rs} on the boundary condition, by virtue of (8), $\lim\limits_{N\to\infty} T^{(N)} = T$, $\lim\limits_{N\to\infty} T_{nm}^{(N)} = T_{nm}$, $\lim\limits_{N\to\infty} a_{rs}^{(N)} = a_{rs}$. This result, however, does not imply that the series $\sum_{L+1}^{\infty} T_{nm} S_{nm}$ converges on S, as the ratio $\overline{R}/R(\sigma)$ is larger than 1, as it is known since long (Moritz, 1989). The coefficients T_{nm} can be directly computed from the integral relation

$$T_{nm} = \frac{1}{4\pi} \int T(\overline{R},\sigma) Y_{nm}(\sigma) d\sigma \tag{11}$$

suitably discretized, if some geodetic quantity related to the anomalous potential T can be determined, e.g. from satellite measurements, on the spherical surface $\overline{S}$, external to the earth's surface. In this case, the result is independent of the maximum degree N attained. It follows that, for fixed N, the coefficients $T_{nm}^{(N)}$ determined by l.s. from data at ground level are generally different from the coefficients T_{nm} obtained from satellite data, even though both of them are approaching the true T_{nm} for large N.

68.3 From Least Squares to Galerkin

In this section, as in the successive, we skip the part of the BVP which depends on the Z_{rs} functions that have been included in the rigorous formulation (3). We do that in order to concentrate the attention on the part depending on the harmonic coefficients T_{nm}. Reintroducing the terms $\sum a_{rs}Z_{rs}$ is straightforward. Formula (6) represents in some sense a projection into a finite-dimensional space and recalls the expression of a Galerkin system. Yet it is not easy to apply in numerical computations, owing to the structure of the operator A and to the scalar product in $L^2(S)$ which can be taken smooth, but otherwise irregular. A first simplification can be obtained by splitting the operator A: $A = A_0 + D$, where $A_0 = -e_{\mathbf{r}} \cdot \nabla - (2/r)$ (spherical approximation), and it can be proved that D is of the order of e^2. Hence, $AT = A_0T + DT$ can be approximated replacing DT with DT_{mod}, where T_{mod} is a known "reduction" model, and the boundary condition can be written as

$$A_0 T|_S = \Delta g - DT_{\text{mod}}|_S \equiv \Delta\tilde{g} \tag{12}$$

and the squared norm to be minimized by least squares is

$$\begin{aligned} &\left\| rA_0 \sum_{L+1}^{N} T_{nm} S_{nm} - r\Delta\tilde{g} \right\|^2_{L^2(S)} \\ &\quad = \left\| \sum_{L+1}^{N} (n-1) T_{nm} S_{nm} - r\Delta\tilde{g} \right\|^2_{L^2(S)} \end{aligned} \tag{13}$$

The corresponding minimizing equation is

$$\left(\left(\sum_{L+1}^{N} (n-1) T_{nm} S_{nm} - r\Delta\tilde{g} \right), (j-1) S_{jk} \right)_{L^2(S)} = 0 \tag{14}$$

from which one obtains

$$\sum_{L+1}^{N} (n-1) T_{nm} \left(S_{nm}, S_{jk}\right)_{L^2(S)} = \left(r\Delta\tilde{g}, S_{jk}\right)_{L^2(S)}. \tag{15}$$

Further simplifications from the numerical point of view may be accomplished by replacing the basis functions S_{jk} with Y_{jk} and using the scalar product in $L^2(\Sigma)$, where Σ is the unit sphere. This step may be justified by the fact that the relative variation of r on S is indeed very small, namely of the maximum order of magnitude of 10^{-3}. And in any case, the sequence $\{Y_{jk}\}$, which is orthonormal and complete in $L^2(\Sigma)$, is also a Riesz basis in $L^2(S)$ for every regular star-shaped S, so that we are allowed to use it in a Galerkin scheme. Hence, (15) is transformed into

$$\sum_{L+1}^{N} (n-1) T_{nm} \left(S_{nm}, Y_{jk}\right)_{L^2(\Sigma)} = \left(r\Delta\tilde{g}, Y_{jk}\right)_{L^2(\Sigma)}. \tag{15a}$$

i.e.

$$\begin{aligned} &\sum_{L+1}^{N} T_{nm} \frac{n-1}{4\pi} \int \left(\frac{\overline{R}}{R(\sigma)} \right)^{n+1} Y_{nm}(\sigma) Y_{jk}(\sigma) d\sigma = \\ &= \frac{1}{4\pi} \int R(\sigma) \Delta\tilde{g}(\sigma) Y_{jk}(\sigma) d\sigma, \end{aligned} \tag{16}$$

which can be written

$$\begin{aligned} &T_{jk}(j-1) + \sum_{L+1}^{N} T_{nm} \frac{n-1}{4\pi} \int \left[\left(\frac{\overline{R}}{R(\sigma)} \right)^{n+1} - 1 \right] \\ &\quad \times Y_{nm}(\sigma) Y_{jk}(\sigma) d\sigma \\ &= \frac{1}{4\pi} \int R(\sigma) \Delta\tilde{g}(\sigma) Y_{jk}(\sigma) d\sigma \end{aligned} \tag{17}$$

This expression is well suited for an iterative computation of the coefficients, starting from an approximate model.

Remark 3.1: Notice that in (15) we have reproduced the l.s. system assuming, as in Sect. 68.2, that the $L^2(S)$ norm was written as

$$\|f\|^2_{L^2(S)} = \frac{1}{4\pi} \int_S f^2(P) dS_P. \tag{18}$$

However, given that S is star-shaped, represented by the equation $r = R(\sigma)$, and that the inclination I of the normal to S with respect to $\mathbf{e}_r$ is always strictly smaller than $\pi/2$,one can write

$$dS_P = \frac{R^2(\sigma)}{\cos I(\sigma)} d\sigma. \tag{19}$$

Since $R^2/\cos I$ is bounded above and below by positive constants, the norm in (18) can also be taken as

$$\|f\|^2_{L^2(\Sigma)} = \frac{1}{4\pi}\int_{\Sigma} f^2(\sigma)d\sigma \tag{20}$$

exactly as we did in going from (15) to (16). An equivalent change of norm in a Hilbert space leaves its topological structure unchanged, because any sequence convergent in one norm is also convergent in the other one. So, by using this equivalent norm, we can write the l.s. and Galerkin system in the form

$$\sum_{L+1}^{N}(n-1)T^{(Q)}_{nm}\left(S_{nm},S_{jk}\right)_{L^2(\Sigma)} = \left(r\Delta\tilde{g},S_{jk}\right)_{L^2(\Sigma)} \tag{21}$$

$$\sum_{L+1}^{N}(n-1)T^{(G)}_{nm}\left(S_{nm},Y_{jk}\right)_{L^2(\Sigma)} = \left(r\Delta\tilde{g},Y_{jk}\right)_{L^2(\Sigma)}, \tag{22}$$

where the coefficients have been tagged with (Q) and (G) to distinguish from each other. Forming the difference between the two equations one finds

$$\sum_{L+1}^{N}(n-1)\left(T^{(G)}_{nm}-T^{(Q)}_{nm}\right)\left(S_{nm},Y_{jk}\right)_{L^2(\Sigma)} = \\ = \left(r\Delta\tilde{g}-\sum_{L+1}^{N}(n-1)T^{(Q)}_{nm}S_{nm},Y_{jk}-S_{jk}\right)_{L^2(\Sigma)}. \tag{23}$$

The interesting point in this equation is that, if we consider the right-hand side as the known term, we find that it is small for two reasons: first,

$$Y_{jk}(\sigma)-S_{jk}(\sigma) = \left[1-\left(\frac{\overline{R}}{R(\sigma)}\right)^{j+1}\right]Y_{jk}(\sigma) \tag{24}$$

is small because $\overline{R}$ and $R(\sigma)$ are close to each other, second as $r\Delta\tilde{g}-\sum_{L+1}^{N}(n-1)T^{(Q)}_{nm}S_{nm}$ is exactly the residual of l.s. approximation, which is known to tend to 0 in $L^2(S)$ and consequently in $L^2(\Sigma)$. This is not a proof that the difference $T^{(G)}_{nm}-T^{(Q)}_{nm}\to 0$, however it is a strong suggestion in this sense.

Remark 3.2: Up to now we have chosen to use coefficients that in some sense are referred to a sphere $\overline{S}$ with radius $\overline{R}$, because we wanted to compare the Galerkin coefficients, solution of the system (16), to the l.s. coefficients, as in the discussion of Remark 3.1. In turn, l.s. coefficients have been referred to the sphere $\overline{S}$ because we wanted to relate them, as we did in Sect. 68.2, to true coefficients of the anomalous potential, which can be referred only to an outer sphere. However, since in the next section we want to compare Galerkin's coefficients to those derived form the pull-back technique, we want to change the sphere $\overline{S}$ into another one, S_0, completely internal to the telluroid S. So we choose a radius $R_0 < \inf R(\sigma)$ and we recall that

$$T^{(R_0)}_{nm} = T^{(\overline{R})}_{nm}\left(\frac{\overline{R}}{R_0}\right)^{n+1} \tag{25}$$

so that (16) can be written for the $T^{(R_0)}_{nm}$ coefficients

$$\sum_{L+1}^{N}T^{(R_0)}_{nm}\frac{n-1}{4\pi}\int\left(\frac{R_0}{R(\sigma)}\right)^{n+1}Y_{nm}(\sigma)Y_{jk}(\sigma)d\sigma = \\ = \frac{1}{4\pi}\int R(\sigma)\Delta\tilde{g}(\sigma)Y_{jk}(\sigma)d\sigma. \tag{26}$$

Accordingly, (17) can be re-written as

$$T_{jk}(j-1)+\sum_{L+1}^{N}T_{nm}\frac{n-1}{4\pi}\int\left[\left(\frac{R_0}{R(\sigma)}\right)^{n+1}-1\right] \\ Y_{nm}(\sigma)Y_{jk}(\sigma)d\sigma \\ = \frac{1}{4\pi}\int R(\sigma)\Delta\tilde{g}(\sigma)Y_{jk}(\sigma)d\sigma. \tag{27}$$

Although not explicitly written, remember that (27) and (17) are different because in (17) the unkowns are $T^{(\overline{R})}_{nm}$, while in (27) they are $T^{(R_0)}_{nm}$.

68.4 Comparison with Pull-Back and Downward Continuation Procedures

A typical procedure that can be used to obtain an iterative solution of a BVP with a star-shaped, but otherwise irregular surface S is the so-called pull-back procedure. Given a boundary condition on S, expressed by a function f_0 of the variable σ, this function is used as boundary data on an internal spherical surface S_0

close to S. Given the easily determined solution T_0 of the corresponding BVP, that will be denoted as Gf_0, the boundary condition f_1 on S, which is different from f_0, can be computed; we shall put $f_1 = BT_0$. Then, a first correction to the solution can be determined using $\delta f_1 = f_0 - f_1$ as boundary condition on S_0, starting the iteration. The procedure may be integrated by applying to the boundary function a projection operator onto a finite-dimensional space generated by the spherical harmonics with degrees between $L+1$ and N:

$$\cdots \to \delta f_n = \delta f_{n-1} - f_n \to \delta f_n^{(LN)} \to \delta T_n = G\delta f_n^{(LN)} \to$$
$$\to f_{n+1} = B\delta T_n \to \delta f_{n+1} = \delta f_n - f_{n+1} \to \cdots$$

where, remember, G is the operator solving the BVP from the boundary condition on S_0 (it is assumed that the BVP is well-posed) and B is the boundary operator upon the surface S. From the iteration scheme it follows that $\sum_1^{N+1} f_i = B\left(T_0 + \sum_1^N \delta T_i\right)$. The convergence of the iterations is not proved for the present specific case. Yet, it must be remarked that a convergence result has been obtained for the Dirichlet problem in the Banach space of continuous functions endowed with the sup norm, with the application of the downward continuation for the change of boundary (Sansò and Sona, 1995). Anyway, assuming that convergence is fulfilled, δT_k must go to 0 for $k \to \infty$ and the same must be true for $\delta f_k^{(LN)}$, that is its boundary value on S_0. On the other hand, $\delta f_k^{(LN)} = f_0^{(LN)} - \sum_1^k f_i^{(LN)}$, whence $\sum_1^\infty f_i^{(LN)} = f_0^{(LN)}$, that means that the projections onto the space generated by the spherical harmonics with degrees between $L+1$ and $N$of the original boundary condition f_0 and of $\sum_1^\infty f_i$, i.e. the boundary value of $T_0 + \sum_1^\infty \delta T_i$, are identical. In order to write explicit formulas for the Molodensky problem, the starting point is (12): $A_0 T|_S = \Delta\tilde{g}_0(\sigma)$. Then, using $f_0 = R(\sigma)\Delta\tilde{g}_0(\sigma) = \sum g_{nm} Y_{nm}(\sigma)$, projected onto the harmonics with degrees between $L+1$ and N, as boundary condition on S_0, one obtains

$$T_0(r,\sigma) = Gf_0 = \sum_{L+1}^{N} \frac{g_{nm}}{n-1}\left(\frac{R_0}{r}\right)^{n+1} Y_{nm}(\sigma) \equiv$$
$$\equiv \sum_{L+1}^{N} T_{nm}^{(0)}\left(\frac{R_0}{r}\right)^{n+1} Y_{nm}(\sigma), \tag{28}$$

whose boundary value on S is

$$f_1(\sigma) = R(\sigma)\Delta\tilde{g}_1(\sigma) =$$
$$= \sum_{L+1}^{N} (n-1) T_{nm}^{(0)}\left(\frac{R_0}{R(\sigma)}\right)^{n+1} Y_{nm}(\sigma), \tag{29}$$

from which we compute

$$\delta f_1 = f_0 - f_1 = R(\sigma)\left(\Delta\tilde{g}_0(\sigma) - \Delta\tilde{g}_1(\sigma)\right) = f_0 - BT_0 =$$
$$= \sum_{L+1}^{N} (n-1) T_{nm}^{(0)}\left[1 - \left(\frac{R_0}{R(\sigma)}\right)^{n+1}\right] Y_{nm}(\sigma). \tag{30}$$

Let us write, for the sake of conciseness,

$$\frac{1}{4\pi}\int\left[\left(\frac{R_0}{R(\sigma)}\right)^{n+1} - 1\right] Y_{nm}(\sigma) Y_{jk}(\sigma) d\sigma = C_{nm,jk} \tag{31}$$

then from (30) we see that

$$\delta f_1^{(LN)}(\sigma) = -\sum_{j=L+1}^{N}\sum_{n=L+1}^{N} (n-1) T_{nm}^{(0)} C_{nm,jk} Y_{jk}(\sigma). \tag{32}$$

Now let us define $T_1 = T_0 + \delta T_1$, i.e. the first step in the series $T_0 + \sum_1^\infty \delta T_i$ which is supposed to be convergent to the true solution. Since, according to our scheme, $\delta T_1 = Gf_1^{(LN)}$, we can write

$$T_{jk}^{(1)} - \delta T_{jk}^{(1)} = T_{jk}^{(1)} + \frac{1}{j-1}\sum_{L+1}^{N} (n-1) T_{nm}^{(0)} C_{nm,jk} = T_{jk}^{(0)} =$$
$$= \frac{g_{jk}}{j-1} = \frac{1}{j-1}\frac{1}{4\pi}\int R(\sigma)\Delta\tilde{g}_0(\sigma) Y_{jk}(\sigma) d\sigma. \tag{33}$$

Multiplying (33) by $j-1$ we finally get

$$(j-1) T_{jk}^{(1)} +$$
$$+ \sum_{L+1}^{N} T_{nm}^{(0)} \frac{n-1}{4\pi}\int\left[\left(\frac{R_0}{R(\sigma)}\right)^{n+1} - 1\right] Y_{nm}(\sigma) Y_{jk}(\sigma) d\sigma =$$
$$= \frac{1}{4\pi}\int R(\sigma)\Delta\tilde{g}_0(\sigma) Y_{jk}(\sigma) d\sigma, \tag{34}$$

a quick look to (34) shows that this is just the first step of an iterative solution of (27). The same happens adding more δT_k. Therefore, we can conclude that the pull-back method with a fixed maximum degree n, when convergent, gives exactly the same solution as that of Galerkin's method. A final remark is that, instead of pull-backing the boundary values δf_{n+1} from

S to S_0, we could improve our procedure by observing that subsequently for $f_0, f_1, \cdots$ we can also compute, at least approximately, what we could improperly call $\partial f_0/\partial r, \partial f_1/\partial r, \cdots$; in fact, since $f_0, f_1, \cdots$ are values on S of functions that we can (approximately) harmonically continue down to S_0, they also possess radial derivatives that can be computed according to well-defined formulas. Therefore, before applying the solver G we could pull back f_0 to S_0 with formulas like (Sansò and Sona, 1995)

$$\tilde{f}_0 = f_0 - \frac{\partial f_0}{\partial r}\,(R(\sigma) - R_0)$$

In fact even higher order derivatives could be used. This is what is actually done for EGM models. This method, that we could call the downward continuation method, could therefore be seen basically as a numerical accelerator of the pull-back procedure.

68.5 Some Conclusions and Open Issues

In conclusion we could say that we have considered four types of approximate solutions of the BVP (3) or, in a simplified formulation, (12): l.s., Galerkin, pull-back and downward continuation.

The state of the art of these methods and their mutual relations can be summarized as follows:

1. l.s.: the method is not applied numerically, although it has clear convergence properties in $L^2(S)$;
2. Galerkin: the method leads to a numerical system quite close, but not identical, to that of l.s.; no convergence proof is available; a proof of quadratic convergence of $T_{nm}^{(G)}$ to $T_{nm}^{(Q)}$, as suggested in Remark 3.1, would be of great interest;
3. pull-back: the method is known to converge in simple cases with continuous data Δg; it has been applied numerically to produce the models GPM98 (Wenzel, 1998); its coefficients, when the maximum degree N is fixed, converge to Galerkin's coefficients;
4. downward continuation: the method can be viewed as an accelerator of pull-back; although no theoretical result is available for it, its numerical implementation gives excellent results.

As we can see, there is now a frame in which we can better view the methods used to produce global earth models, though the theoretical/numerical investigations on the subject are far from being accomplished.

Even more, the production of such high-degree global models continues to raise new questions, among which we would like to report at least two:

- since we densify the estimate of the field up to a resolution of $5' \times 5'$, can we improve our residual terrain correction procedure to make it unique worldwide and harmonize it with the global field estimation in the sense of defining a unified smooth reference surface for both estimation steps?
- Up to what degree is it sensible to push such procedures, i.e. is the maximum degree N bounded only by our computing capacity or should we limit it for practical reasons?

Indeed these, as the others, are interesting questions for future research.

References

Cimmino, G. (1940). Sul problema generalizzato di Dirichlet per l'equazione di Poisson. *Rend. Sem. Mat. Padova*, 11, 28–89.

Cimmino, G. (1952). Sulle equazioni differenziali alle derivate parziali di tipo ellittico, *Rend. Sem. Mat. Fis. Milano*, XIII, 183–203.

Klees, R. (1997). Topics on boundary element methods, Lecture Notes in Earth Sciences, Vol. 65, Springer, Berlin.

Lehmann, R. (1997). Solving geodetic boundary value problems with parallel computers, Lecture Notes in Earth Sciences, Vol. 65, 532–540.

Magenes, E. (1955). Sui problemi di derivata obliqua regolare per le equazioni lineari del 2. ordine di tipo ellittico. *Ann. Mat. Pura e Appl.*, 40, 143–160.

Martinec, Z. (1998). Boundary-Value Problems for the Gravimetric Determination of a Precise Geoid, Lecture Notes in Earth Sciences, Vol. 73, Springer, Berlin, pp. 482–427.

Moritz, H. (1989). Advanced physical geodesy. 2nd Edition, Wichmann, Karlsruhe.

Sansò, F. and G. Sona (1995). Gravity Reductions versus Approximate B.V.P.'s, In: Geodetic Theory Today, IAG Symposia 114, Springer.

Sansò, F. and G. Venuti (2008). On the explicit determination of stability constants for linearized geodetic boundary value problems. *J. Geod.*, 82, 909–916.

Wenzel, H.-G. (1998). Ultra-high degree geopotential models GPM98A, B and C to degree 1800, in Proceedings of the Joint Meeting of the International Gravity Commission and International Geoid Commission, Trieste, Bollettino di Geofisica Teorica ed Applicata.

Part VII
Temporal Gravity Changes and Geodynamics

N. Sneeuw and J. Kusche

Chapter 69

Terrestrial Water Storage from GRACE and Satellite Altimetry in the Okavango Delta (Botswana)

O.B. Andersen, P.E. Krogh, P. Bauer-Gottwein, S. Leiriao, R. Smith, and P. Berry

Abstract New technology can for the first time enable the accurate retrieval of the global and regional water budgets from space-borne and ground-based gravity surveys. Water is mankind's most critical natural resource, but it is being heavily used throughout the globe. The aim of this paper is to outline the HYDROGRAV project dealing with improving large scale hydrological model with time variable gravity observations. Also preliminary HYDROGRAV investigationsa of terrestrial water storage variations in the Okavango delta in Botswana are presented. Data from 4 years of satellite altimetry, GRACE derived TWS and GLDAS hydrological model all show a clear annual variation corresponding to the well known seasonality of the delta. However, they also all show an increasing trend in the amount of water storage in the region over the last 4 years.

69.1 Introduction

One of the fundamental connections between hydrology and geodesy stems from the fact that a 2.4 cm thick, infinitely extended layer of pure water located at any depth below a gravimeter generates an incremental gravitational acceleration of 1 μgal ($= 1 \times 10^{-8}$ m/s^2) (Knudsen and Andersen, 2002). Temporal change in terrestrial water storage (TWS) in the earth system is therefore proportional to the temporal change in the measured gravitational acceleration. The potential of time-lapse gravity surveys to monitor the status of water resources systems has been recognized since a long time and can benefit a number of disciplines (Crossley et al., 1999). Ground-based time-lapse gravity surveys were used successfully to determine alluvial aquifer storage and specific yield, which is a key parameter for the sustainable management of groundwater resources (Pool and Eychaner, 1995). Moreover, it has been demonstrated, that superconducting ground-based gravimeters reflect hydrological signals on the order of several microgals (Amalvict et al., 2004; Bower and Courtier, 1998; Neumeyer et al., 2006; Hinderer and Crossly, 2004).

The new generation of Scintrex portable gravimeters has enabled the possibility of local time-lapse surveys. The Scintrex instruments deliver local measurements with an accuracy of 4 μgal or 10 cm of water (Scintrex A-10, Scintrex CG-5) (www.scintrex.com).

With the launch of the GRACE satellites (Tapley et al., 2004) water storage estimates with an accuracy of 0.4 μgal or 1 cm of water are now achievable from space for spatial scales larger than 1,300 km (Andersen and Hinderer, 2005; Andersen et al., 2005). However these accuracies are constantly being improved with the longer timescale of data and improved GRACE data processing.

Recent investigations show that the inherent spatial and temporal resolution of GRACE data is around 300–400 km and 10 days (Rowlands et al., 2005). Such spatial and temporal resolution will enable the use of GRACE data for calibration of regional-scale hydrological models, and will deliver reliable observations of the regional part of the global hydrological cycle.

O.B. Andersen (✉)
DTU Space, Juliane Maries Vej, 2100 Copenhagen, Denmark
e-mail: oa@space.dtu.dk

S.P. Mertikas (ed.), *Gravity, Geoid and Earth Observation*, International Association of Geodesy Symposia 135,
DOI 10.1007/978-3-642-10634-7_69, © Springer-Verlag Berlin Heidelberg 2010

GRACE provides estimates of changes in total TWS including effects of surface water whereas hydrological model generally only provide soil moisture.

Satellite altimetry is a new way to obtain surface water storage or water stored in rivers, lakes and wetlands. Satellite altimetry was originally designed to retrieve heights in the open ocean where the return echoes generally correspond well to a mathematical model (Fu and Cazenave, 2001), which enables precise range to surface information. However, by allowing for a variety of return echos in the analysis of satellite altimeter data these can now be used to monitor water levels of large rivers, lakes and floodplains on time scales ranging from weeks to months.

69.2 The HYDROGRAV Project

Hydrological models have traditionally been calibrated using in situ water level (head data) using local gauges. However, this data reflects hydrological conditions at the local scale, whereas water resources management applications have to deal with much larger systems. Moreover, there is poor availability of reliable point observations of water level and discharge in many regions of the world and a number of drainage basins on the African continent are even ungauged, calling for other ways of calibrating hydrological models.

Figure 69.1 outlines the HYDROGRAV approach to use ground based and space borne gravity observations to constrain hydrological models. In the HYDROGRAV project the focus is placed on the following four focus tasks:

1. The hydrological forward problem
2. The geophysical forward problem
3. Data control/acquisition
4. Hydro-geophysical inverse problem

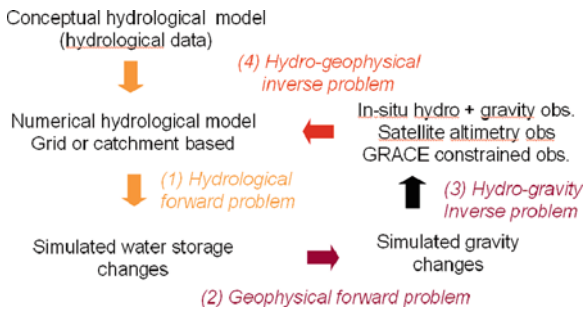


Fig. 69.1 The HYDROGRAV approach. The figure is read from the *upper left corner* and counter clockwise following the *arrows*. The *arrows* illustrate the focus tasks within the project

The hydrological forward problem concerns running a basin scale hydrological model for the region to simulate water storage changes.

The forward geophysical problem investigate methods for estimating accurate gravity field changes from local, and regional hydrological models both for in-situ and spaceborne measurement points.

The data acquisition step includes both ground-based and space-borne gravity observations and their processing as well as possible inclusion of satellite altimetry.

The hydro-geophysical inverse problem concerns using hydrological and gravity observations to constrain hydrological models. Data can also be satellite derived surface or TWS water storage from satellite altimetry and/or GRACE. More details can be found in Bauer-Gottwein et al. (2008) and Leiriao et al. (2009).

This way the prediction loop is closed and via the hydrological forward solution new and hopefully improved estimates of water storage changes can be made (and iterations be made if needed).

The Okavango delta in Botswana has been selected as the primary target area for the project.

Preliminary results are presented below. Here we have investigated available data for the last 5 years from GRACE and from satellite altimetry in the target region to obtain the annual and inter-annual signal during the period where GRACE temporal gravity variations and ENVISAT lake/river level satellite altimetry have been available simultaneously.

69.3 Preliminary Results for the Okavango Delta

The main wetland in the northern Botswana is the Okavango delta and it is a tropical wetland (about 30,000 km^2). Due to seasonal local rainfall and highly

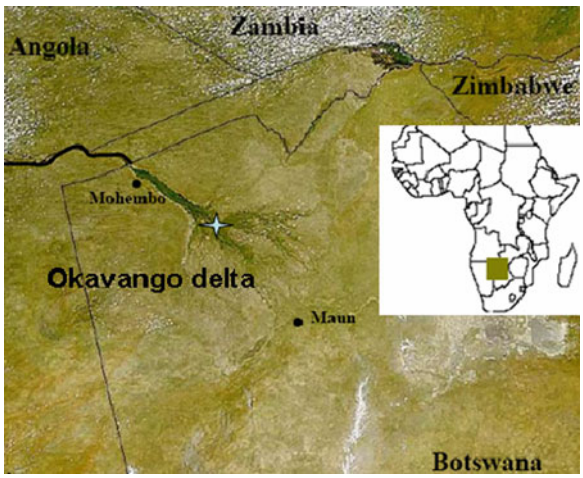


Fig. 69.2 Outline of the Okavango delta in northern Botswana. The *star* marks the location of the ENVISAT satellite altimeter data in the *center* of the Okavango delta. At Mohembo the only available river level gauge is found. The figure is courtesy of NASA global atlas

variable inflow from the catchments in mainly Angola located north of Botswana, large quantities of water are stored in the floodplains of the Okavango delta and are subsequently taken up by evapotranspiration (Bauer-Gottwein et al. 2006). The Okavango Delta is essential to prosperity of wildlife in the whole region and its location is outlined in Fig. 69.2.

The GRACE data used for this analysis are the level 1B data from January 2003 to July 2007. We apply a method for temporal gravity variation estimation using mass concentration blocks (mascon) developed by Rowlands et al., (2005). Using this method we can derive sub-monthly mass flux at 4° by 4° spatial resolution and at 10-day intervals over the Okavango region.

In order to investigate the change in TWS, GRACE data were corrected for other known contributions to gravity changes. These include contributions from solid Earth tides; ocean tides; atmosphere; pole tides and N-body perturbations using various models. The 10 days changes in gravity were then converted to changes in TWS using the infinite layer approximation (Knudsen and Andersen, 2002). One single mascon (16°S–20°S, and 20°–24°E) is used for this analysis.

The Global Land Data Assimilation System (GLDAS) data used here is output from the NOAH simulations with a hydrological model driven with observation-based forcing (Rodell et al., 2004). This model has previously been used to validate GRACE observations of terrestrial water storage change on inter-annual scales. (Andersen and Hinderer, 2005) The GLDAS 3-h temporal and 0.25° spatial resolution soil-moisture fields were integrated over each ten-days GRACE interval and four degree mascon in order to mimic the temporal and spatial resolution of the GRACE TWS data.

69.3.1 Annual TWS Variations

Results from GRACE derived TWS and the GLDAS NOAH hydrological model are shown in Fig. 69.3. GRACE represents temporal variations in TWS including surface and subsurface water, whereas GLDAS only accounts for soil moisture or subsurface water storage, over a region of nearly 400 by 400 km bounded by 16°S–20°S, and 20°–24°E. The Okavango delta only represent roughly 12–15% in terms of area so TWS in the overland zone surrounding the Okavango delta will also contribute to the total TWS change observed from GRACE and GLDAS.

Both the GRACE data and the GLDAS shows pronounced annual variations with maximum terrestrial water storage from the GRACE data peaking around

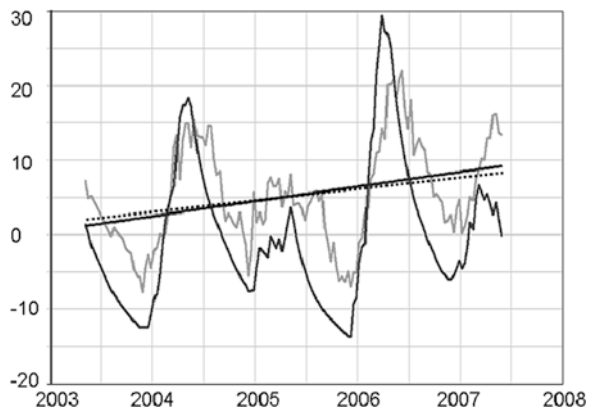


Fig. 69.3 GRACE estimated TWS (*grey*) and output from the GLDAS, NOAH simulation (*black*) of the terrestrial water storage variations in the Okavango delta (cm of water). The *solid and dotted black lines* represent the estimated linear trend over the 4-year period (June-2003 until June-2007) from GRACE and GLDAS, respectively

May-June and maximum terrestrial water storage from GLDAS peaking 1–2 month earlier. There is some question about the accuracy of annual and inter-annual signals from hydrological models (Steffen et al., 2008), and similarly, the annual signal also varies very much from year to year.

The terrestrial water storage from GLDAS model does not take into account surface water whereas GRACE measures the integrated water storage.

Satellite altimetry is a new way to obtain surface water storage or water stored in rivers, lakes and wetlands in poorly gauged rivers like the Okavango River and Wetland. Using the EAPRS rule-based expert system with ten retrackers configured for different terrain types, even complex echoes can be successfully retracked to yield heights over inland water (Berry et al., 1997). The footprint of the radar is typically several kilometers wide, but because water is far more reflective to microwave radiation at these frequencies than surrounding land, even very small targets a few tens of meters across can clearly be seen in the waveform shapes, which can be processed to yield height information (Garlick et al., 2005) Over the narrow open water surfaces in the Okavango delta only very few locations (mostly in the upstream part) could be identified where satellite altimetric time-series could be retrieved from retracking ENVISAT satellite data.

Variations in river level from the Okavango delta from satellite altimetry in Fig. 69.4 above also showed a pronounced temporal variation with an annual period. The satellite altimetry, however, only measures, at one point in space, the variation in surface water height and thus the amount of water stored on the land surface in the region. There is reasonable agreement in phase of the annual signal for all data sets (within 2 month). More detailed investigation into the amplitude and phase of the annual river level signal in the Okavango delta can be found in Christiansen et al. (2008).

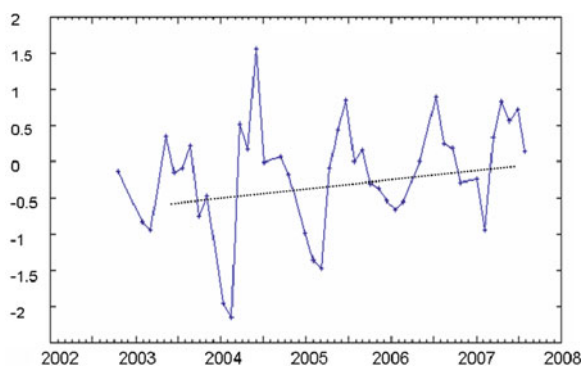


Fig. 69.4 Okavango river level height (m) from ENVISAT satellite altimeter retracked by the EAPRS expert system. The location of the data is shown with a star in Fig. 69.2 and is reasonably close to the center of the GRACE mascon solution. The linear trend over the 4-year period (June-2003 until June-2007) has been added as a *dotted line*

69.3.2 Inter-Annual TWS Variations

In both Figs. 69.3 and 69.4 inter-annual variations seen as increasing amount of water are evident as increasing linear trends over the period.

Linear trend for the GRACE water storage estimates have been added to Fig. 69.3 estimated over the 4 year period ranging between June 2003 and June 2007. For GRACE the linear increase correspond to roughly 2 cm of water per year (solid line) and GLDAS gives roughly 1.5 cm/year (dotted line). The similar estimate for the altimetric river level change is roughly 15 cm per year. In Fig. 69.4 a linear trend over the same 4 year period have been added to the figure as a dotted line. The two set of numbers are unfair to compare as they represent different (though related) quantities, but it is interesting to notice that they are of similar magnitude as the Okavango delta only takes up 10–15% of the total area in the mascon.

All three independent sources consistently show an increase in surface and total water storage for the whole period with a dominant increase around 2006 for GRACE and GLDAS but not for satellite altimetry. This fits well with hydrological estimates of the inter-annual pulse of the Okavango delta which already in 2004 predicted that the water storage would increase over the upcoming 2 years because of the 18 year cycle in precipitation in the region (Warne, 2004).

Investigations from the ENVISAT ASAR data (Bartsch et al., 2008) confirm that similar increase in soil moisture estimates can be seen from other remote sensing data. The in-situ gravity campaign carried out by DTU in 2008 also confirmed that numerous roads in and around the Okavango delta have been closed as the water level in the delta is currently considerably higher than in the early years of the decade.

69.4 Summary

In this paper the HYDROGRAV project was presented along with initial results focusing on the Okavango delta. HYDROGRAV aims at developing a complete modeling environment enabling the use of in situ and spaceborne data in calibration and validation of hydrological models. It will further provide a detailed evaluation of the utility of gravity data in different hydrological conditions.

The investigation of terrestrial water storage variation in the Okavango delta region from satellite altimetry, GRACE derived TWS and GLDAS hydrological model showed a clear annual variation corresponding to the well known pulse of the delta, and an increasing trend in the amount of water storage in the region over the last 4 years.

These preliminary results pave the way for further investigations of water storage variations from in-situ and spaceborne observations to constrain hydrological models for the Okavango delta in the HYDROGRAV project.

Acknowledgement The article is a contribution to the HYDROGRAV project funded by the Danish Agency of Science, Technology and Innovation under contract number 274-06-0341. The reviewers are acknowledged for great help in improving the manuscript.

References

Amalvict, M., J. Hinderer, J. Mäkinen, S. Rosat, and Y. Rogister (2004). Long-term and seasonal gravity changes at the Strasbourg station and their relation to crustal deformation and hydrology. *J. Geodynamics*, 38(3–5), 343–353.

Andersen, O.B. and J. Hinderer (2005). Global inter-annual gravity changes from GRACE: Early results. *Geop. Res. Lett.,* 32, L01402, doi:10.1029/2004GL020948.

Andersen, O.B., S.I. Seneviratne, J. Hinderer, and P. Viterbo (2005). GRACE-derived terrestrial water storage depletion associated with the 2003 European heat wave. *Geop. Res. Lett.*, 32, L18405, doi:10.1029/2005GL023574.

Bartsch, A.; Pathe, C; Sabel, D; Wagner, W; Doubkova, M. (2008) Soil Moisture Time Series from Active Radar in Support of Runoff Monitoring on Local, Catchment and Regional Scale, In *Proc. 2nd Space for hydrology symposium*, ESA SP., in press.

Bauer-Gottwein, P., T. Gumbricht, and W. Kinzelbach (2006). A regional coupled surface water/groundwater model of the Okavango Delta, Botswana. *Water Resources Res.,* 42(4), W04403, doi:10.1029/2005WR004234.

Bauer-Gottwein, P., S. Leiriao, X. He, and O. Andersen (2008). HYDROGRAV: improving hydrological model calibration with ground-based and space-borne timelapse gravity surveys. In Proceedings of 2nd Space for hydrology symposium*,* ESA-SP, in-press.

Berry, P.A.M., H. Bracke, and A. Jasper (1997). Retracking ERS-1 altimeter waveforms over land for topographic height determination: an expert systems approach. *ESA Pub. SP414,* 1, 403–408.

Bower, D.R. and N. Courtier (1998). Precipitation effects on gravity measurements at the Canadian Absolute Gravity Site. *Phys. Earth Planet. Inter.*, 106(3–4), 353–369.

Christiansen, L., P.E. Krogh, P. Bauer-Gottwein, O. Andersenm, B.S. Leirião, P. Binning, and D. Rosbjerg (2008). Local to Regional Hydrological Model Calibration for the Okavango River Basin from In-situ and Space Borne Gravity Observations. In Proceedings of 2nd Space for hydrology symp, ESA SP., in press.

Crossley, D., J. Hinderer, G. Casula, O. Francis, H.-T. Hsu, Y. Imanishi, G. Jentzsch, J. Kääriänen, J. Merriam, B. Meurers, J. Neumeyer, B. Richter, K. Shibuya, T. Sato, and T. van Dam (1999). Network of superconducting gravimeters benefits a number of disciplines. *EOS*, 80, 121–126.

Fu L-L. and A. Cazenave (2001). Satellite altimetry and Earth Sciences. In: Fu and Cazenave (eds), A handbook of techniques and applications. Int. Geophys series 69, Academic Press, p. 465.

Garlick, J.D., P.A.M. Berry, E.L. Mathers, and J. Benveniste (2005). The ENVISAT/ERS River and Lake Retracking System. In 2004 Envisat & ERS Symposium, ESA SP 572.

Hinderer, J. and D. Crossley (2004). Scientific achievements from the first phase (1997–2003) of the Global Geodynamics Project using a worldwide network of superconducting gravimeters. *J. Geodynamics,* 38, 237–262.

Knudsen P. and O. Andersen, O. (2002). Correcting GRACE gravity fields for ocean tide effects", *Geophys. Res. Lett.,* 29(8), 19-1, 1178, doi:10.1029/2001GL014005.

Leiriao, S., X. He, L. Christiansen, O.B Andersen, and P. Bauer-Gottwein (2009). Calculation of the temporal gravity variation from spatially varying water storage change in soils and aquifers. *J. Hydrol.*, 365(3–4), 302–309.

Neumeyer, J., F. Barthelmes, O. Dierks, F. Flechtner, M. Harnisch, G. Harnisch, J. Hinderer, Y. Imanishi, C. Kroner, B. Meurers, S. Petrovic, C. Reigber, R. Schmidt, P. Schwintzer, H. P Sun, and H. Virtanen (2006). Combination of temporal gravity variations resulting from superconducting gravimeter (SG) recordings, GRACE satellite observations and global hydrology models *J. Geod.,* 79(10–11), 573–585.

Pool, D.R. and J.H. Eychaner (1995). Measurements of Aquifer-storage change and specific yield using gravity surveys. *Ground Water*, 33(3), 425–432.

Rodell, M., P.R. Houser, U. Jambor, J. Gottschalck, K. Mitchell, C.-J. Meng, K. Arsenault, B. Cosgrove, J. Radakovich, M. Bosilovich, J.K. Entin, J.P. Walker, D. Lohmann, and D. Toll (2004). The global land data assimilation system. *Bull. Amer. Meteor. Soc.,* 85(3), 381–394.

Rowlands, D.D., S.B. Luthcke, S.M. Klosko, F.G.R. Lemoine, D.S. Chinn, J.J. McCarthy, C.M. Cox, and O.B. Anderson (2005). Resolving mass flux at high spatial and temporal

resolution using GRACE inter-satellite measurements. *Geop. Res. Lett.,* 32, L04310, doi:10.1029/2004GL021908.

Steffen, H., H. Denker, and J. Mueller (2008). Glacial isostatic adjustment in Fennoscandia from GRACE data and comparison with geodynamical models. *J. Geodynamics,* 46, 155–164.

Tapley, B.D., S. Bettadpur, M. Watkins, and C. Reigber (2004). The gravity recovery and climate experiment: mission overview and early results. *Geop. Res. Lett.,*31, L09607, doi:10.1029/2004GL019920.

Warne, K. (2004). Okavango – Africas miracle delta, *Natl. Geogr.*, 14, 42–67, December,

Chapter 70

Greenland Ice Sheet Mass Loss from GRACE Monthly Models

L. Sandberg Sørensen and R. Forsberg

Abstract The Greenland ice sheet is currently experiencing a net mass loss. There are however large discrepancies between the published qualitative mass loss estimates, based on different data sets and methods. There are even large differences between the results based on the same data sources, as is the case with those estimated from GRACE data.

In this chapter we have used a generalized inversion method to estimate the Greenland ice sheet mass change from the monthly global gravity solutions, provided by three different GRACE processing centers; CSR, JPL and GFZ.

In order to derive mass change from these monthly global gravity models, we first calculate the gravity trend from these. When isolating the gravity trend signal, which is caused by the ice mass change, we first subtract the signal produced by the postglacial rebound (PGR) in Greenland. This is done by a simple method based on the ice history model ICE-5G and on ground measurements made in Scandinavia. We find that the PGR signal corresponds to a mass change signal of approximately –4 Gt per year.

We conclude that there are large differences between these estimated mass change models. We find a total mass loss of 189, 146 and 67 Gt/year based on the CSR, GFZ and JPL solution respectively.

L.S. Sørensen (✉)
Department of Geodynamics, National Space Institute, DTU-Space, Copenhagen Ø DK-2100, Denmark
e-mail: slss@space.dtu.dk

70.1 Introduction

The Greenland ice sheet mass change is currently a hot topic. The IPCC report from 2007 stated that the response of the Greenland ice sheet to the observed climate changes is very poorly understood (Solomon et al., 2007). Much research has been done in order to improve our knowledge of the ice sheet, and in particular in estimating the mass loss of the ice sheet and hence the resulting sea level rise.

In recent years, many research groups have published Greenland ice sheet mass loss estimates, based on different data sets and methods (Chen et al., 2006; Rignot and Kanagaratnam, 2006; Veligcogna and Wahr, 2006; Luthcke et al., 2006).

It is clear though, that there is poor agreement between these estimates, which indicates that there are large differences in the way to handle the data. Even published results based on data solely from the Gravity Recovery and Climate Experiment (GRACE) are not all in agreement (Velicogna and Wahr, 2006; Luthcke et al., 2006; Wouters et al., 2008). Some of the published GRACE mass change estimates are listed in Table 70.1.

Table 70.1 Ice mass change estimates of the Greenland Ice Sheet by different authors, using different GRACE data time spans and methods

Authors	Time span	Mass change
Chen et al. (2006)	2002–2005	–219 ± 21 Gt/year
Luthcke et al. (2006)	2003–2005	–101 ± 16 Gt/year
Velicogna and Wahr (2006)	2002–2006	–227 ± 33 Gt/year
Wouters et al. (2008)	2003–2008	–179 ± 25 Gt/year

S.P. Mertikas (ed.), *Gravity, Geoid and Earth Observation*, International Association of Geodesy Symposia 135,
DOI 10.1007/978-3-642-10634-7_70, © Springer-Verlag Berlin Heidelberg 2010

This problem will be addressed in this paper, where we estimate the mass loss from monthly global gravity models derived from GRACE data using a new method.

The data used in this investigation are the monthly GRACE solutions provided by the three processing centers CSR, GFZ and JPL.

70.2 Data and Methods

The GRACE data consists of monthly spherical harmonic expansions of the Earth's gravity potential (GRACE Level-2 data). They are provided by the three processing centers CSR (Center for Space Research, University of Texas, USA), JPL (Jet Propulsion Laboratories, California, USA) and GFZ (now Helmholtz-Centre Potsdam GFZ, Germany). These solutions are represented by a set of Stokes harmonic coefficients up to a defined degree and order (Bettadpur, 2007).

We use the release 4 data sets (for JPL release 4.1), which are the latest public available data sets. The data sets are shortly described in Table 70.2. In this study we use the 68 epochs which are available from all three centers. Hence, the data time span is from 08-2002 to 08-2008, but with the months 09-2002, 12-2002, 01-2003, 06-2003, and 01-2004 missing. We have filtered the data by truncating all of the spherical harmonic expansions at degree and order 40, to limit the errors introduced to the GRACE data by the higher order coefficients.

With the new method, described in this paper, the gravity disturbance trends are stacked data, which strongly reduces noise. Hence it is not necessary to do any "de-striping" or filtering.

Table 70.2 Description of the available data sets. For all three data sets, the months June–July 2002 and June 2003 are missing due to missing accelerometer data. $(n,m)_{max}$ is the maximum degree and order of the spherical harmonic expansions as delivered by the processing centers

	CSR	GFZ	JPL
Release	04	04	04.1
Epochs	75	69	72
Start	04-2002	08-2002	04-2002
End	09-2008	09-2008	08-2008
$(n,m)_{max}$	60	120	120

70.2.1 Gravity Disturbance Trend

The ice mass change of the Greenland ice sheet, will be estimated from the gravity trend in the area. The first step is therefore to determine the change of the monthly gravity fields, δg, in time, which is done by a 4-parameter trend analysis of the gravity disturbances. A bias, trend and two seasonal terms are estimated in each grid cell of size 0.5° × 0.5° (1).

$$\delta g\,(t) = a + bt + c\,\cos\,(2\pi t) + d\,\sin\,(2\pi t)\,, \quad (1)$$

where t is given in decimal years. The resulting gravity trends at satellite altitude (500 km), based on the CSR, JPL and GFZ epochs respectively, are shown in Fig. 70.1.

There are clear differences between these gravity trends, but they do agree on a strong negative trend over southeast Greenland, indicating a mass loss in this region.

70.2.2 Post-Glacial Rebound

Postglacial rebound (PGR) is the viscoelastic response of the Earth as a result of the glacial unloading since the last glacial maximum. Some of the observed gravity trend originates from the PGR.

The gravity trend generated by the postglacial rebound must be subtracted from the observed gravity trend, in order to isolate the gravity trend signal from the ice mass change.

There is much debate on how to determine the PGR signal, and different approaches and models are used (Barletta et al., 2008; Velicogna et al., 2006). There are large uncertainties in both the Earth models and the ice history models used.

Due to the significant uncertainty in the Earth models, we choose to correct for the PGR gravity signal in a more empirical way. The uplift in Greenland, according to the ICE-5G model (Peltier, 2004), is shown in Fig. 70.2.

In order to convert the uplift model into a gravity trend, we assume a linear relationship (2) between height change, dh, and gravity change, dg, as found in Scandinavia 1965–2002 (Routsalainen, 2002)

$$dg = 0.23\left[\frac{\mu gal}{mm}\right] dh \quad (2)$$

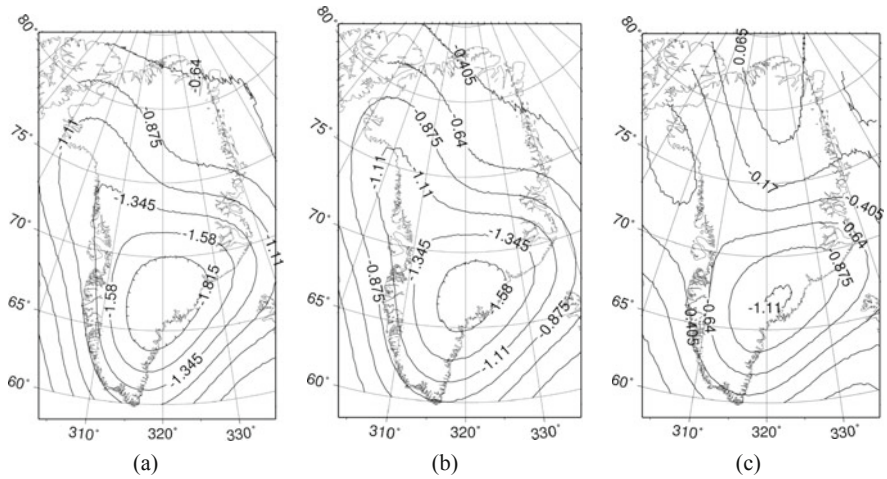


Fig. 70.1 Gravity trends at satellite altitude (500 km), given in μgal per year, based on (**a**) CSR-RL04, (**b**) GFZ-RL04 and (**c**) JPL-RL04.1 epochs. The large differences are apparent

The gravity change include the height change effect and the free air gradient is therefore subtracted.

The ICE-5G uplift is converted into a gravity signal at ground level, and upward continued to satellite altitude, where it is subtracted from the GRACE gravity disturbance trend.

The total PGR signal, found by this method, corresponds to a gravity trend generated by a mass loss of approximately 4 Gt per year, which agrees well with the PGR estimates from Velicogna and Wahr (2005).

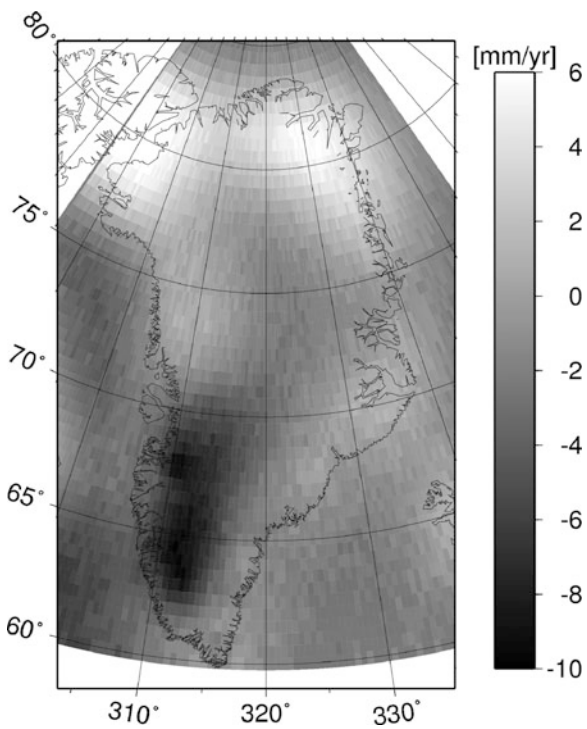


Fig. 70.2 Uplift in Greenland [mm/year] based on the ICE-5G ice history model

70.2.3 Inversion Method

We use a generalized inversion method to derive mass change estimates from gravity trends. This can be stated as a linear problem (3), with the response matrix **A**.

The observation vector, **y** (4) consists of the gravity trends at satellite altitude, defined in a grid covering the area in which the gravity trend is shown, see Fig. 70.1.

The model parameter vector, **x** (5) contains the point mass changes, and these will be solved for in a grid defined by the ice covered area of Greenland. This solution domain is shown in red in Fig. 70.3.

The relationship between the gravity trend and the mass points are given by (6) (Heiskanen and Moritz, 1967), where R is the Earth radius, r is the distance from the Earth center to the satellite and ψ is the spherical distance.

The problem is solved by using Tychonov generalized inversion with regularization λ (7).

$$\bar{y} = \underline{\underline{A}}\,\bar{x} \tag{3}$$

$$\bar{y} = \frac{\delta g_i}{\delta t}, \quad i = 1, \ldots, n \tag{4}$$

$$\bar{x} = \frac{\delta m_j}{\delta t}, \quad j = 1, \ldots, m \tag{5}$$

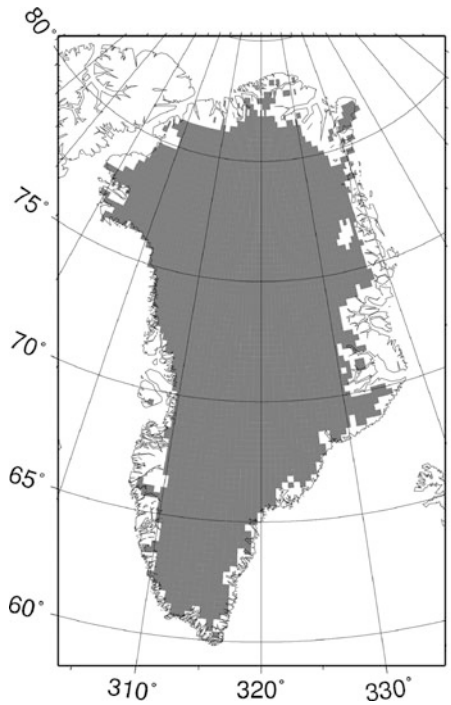


Fig. 70.3 The marked area is the solution domain for the inversion. In this grid, the point masses will be estimated

$$\delta g_i = \sum\nolimits_j \left\{ \frac{G\delta m_j \left(R^2 r - R^3 \cos\Psi_{ij}\right)}{\left(r^2 + R^2 - 2Rr\cos\Psi_{ij}\right)^{3/2}} \right\} \quad (6)$$

$$\bar{x} = \left[\underline{\underline{A}}^T \underline{\underline{A}} + \lambda \underline{\underline{I}}\right]^{-1} \underline{\underline{A}}^T y \quad (7)$$

The elastic uplift of the Earth, due to the present day unloading, generates a gravity change. This gravity change has not been taken into account in this study.

An estimate of the total mass change of the ice sheet is then found by summation of all the point mass changes, using point masses located only within the area of the ice sheet.

Because the inversion is an improperly posed problem, there is a strong correlation between the regularization parameter λ, and the resolution in parameter space. However, the total mass change remains nearly constant over a wide range of λ-values.

When deriving the mass change models, we use data of the observed gravity trend in an area that extend outside Greenland (the area is shown in Fig. 70.1). This means that our result can be biased by other mass change sources outside Greenland, such as for example the ice caps on Svalbard and Iceland, or changes in sea level. Such masses are easily included in the estimation scheme, and we found the aliasing effect of these small ice caps to be negligible for Greenland.

70.3 Mass Change Results

We derive three mass change models of the Greenland ice sheet, using the inversion method on the gravity trends (with PGR signal subtracted) over Greenland, as described above. These results are presented in Fig. 70.4, and are derived from CSR, JPL and GFZ gravity epochs respectively.

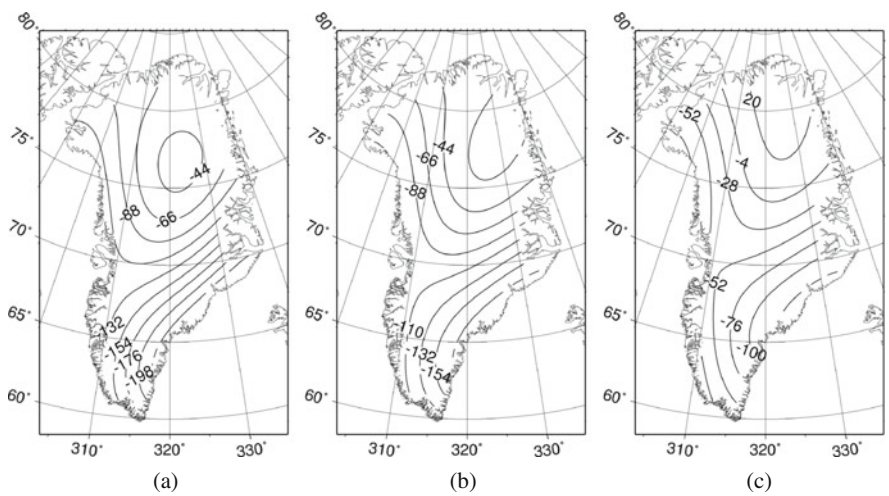


Fig. 70.4 Models of mass change in Greenland, given in mm equivalent water height per year, based on (**a**) CSR-RL04, (**b**) GFZ-RL04 and (**c**) JPL-RL04.1 epochs. We use here a regularization parameter which gives a relatively poor spatial resolution

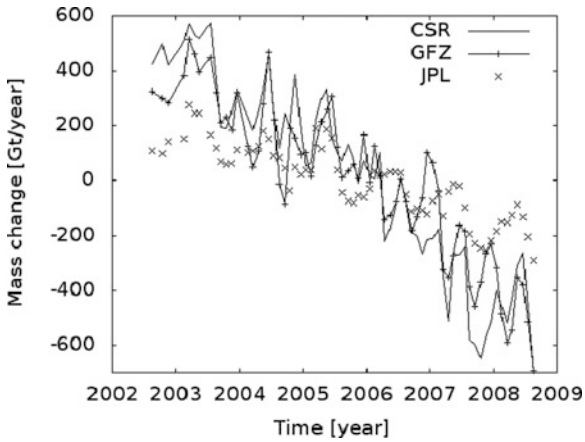


Fig. 70.5 Monthly mass change estimates for the Greenland Ice Sheet, given in Gt, from CSR-RL04, GFZ-RL04 and JPL-RL04.1 epochs

It is clear from Fig. 70.4, that the mass change models are significantly different in magnitude, but that the overall trend in the models are similar, represented by a mass loss near the ice edge and a mass gain in the central northern part of the ice sheet.

The total annual mass changes are found by summing up all of the mass points in the models, and they are found to be;

- 189 Gt/year based on CSR-RL04
- 146 Gt/year based on GFZ-RL04 and
- 67 Gt/year based on JPL-RL04.1 epochs.

The mass change derived from each monthly gravity field is shown in Fig. 70.5.

70.4 Conclusion

In this paper we show that significantly different mass loss results are obtained, when using GRACE epochs from the three different processing centers. We find mass change estimates of –189 Gt/year from CSR, –146 Gt/year from GFZ and –67 Gt/year from JPL data.

Even though the total mass loss estimates are very different, the same pattern is seen in the three mass change models (Fig. 70.4). There is a clear trend, that the mass loss is strongest near the ice edge, and the largest mass loss is found in southeast Greenland. This pattern is in good agreement with other observations (Rignot et al., 2004; Howat et al., 2007; Krabill et al., 2004).

As mentioned, we have neglected the gravity change due to present day elastic uplift in this study, which introduces an error in the mass change estimates. The choice is justified by the fact that the focus of this study is on the comparison between the 3 centers monthly solutions, rather than on the absolute mass change estimates. The elastic uplift signal will be implemented in future studies.

The large differences in mass change estimates, based on data sets from different processing centers, indicate that the GRACE data processing has not yet been fully exploited.

Acknowledgements The GRACE data were provided through the NASA-JPL PODAAC system.

We thank the two anonymous reviewers for their comments, which improved the manuscript.

References

Barletta, V.R., R. Sabadini, and A. Bordoni (2008). Isolating the PGR signal in the GRACE data: impact on mass balance estimates in Antarctica and Greenland. In:*Geophys. J. Int.,* doi:10.1111/j.1365-246X.2007.03630.x].

Bettadpur, S. (2007). Level-2 gravity field product user handbook (Rev 2.3), Center for Space Research, The University of Texas at Austin, February 20.

Chen, J.L., C.R. Wilson, and B.D. Tapley (2006). Satellite gravity measurements confirm accelerated melting of Greenland ice sheet. In: *Science,* doi: 10.1126/science.1129007.

Heiskanen, W.A. and H. Moritz (1967). Physical geodesy. Freeman and Co*,* San Francisco.

Howat, I.M., I. Joughin, and T.A. Scambos (2007). Rapid changes in ice discharge from Greenland Outlet Glaciers. In: *Science*, doi:10.1126/science.1138478.

Krabill, W., E. Hanna, P. Huybrechts, W. Abdalati, J. Cappelen, B. Csatho, E. Frederick, S. Manizade, C. Martin, J. Sonntag, R. Swift, R. Thomas, and J. Yungel (2004). Greenland Ice Sheet: Increased coastal thinning. In: *Geophys. Res. Lett.*, doi:10.1029/2004GL021533.

Luthcke, S.B., H.J. Zwally, W. Abdalati, D.D. Rowlands, R.D. Ray, R.S. Nerem, F.G. Lemoine, J.J. McCarthy, and D.S. Chinn (2006). Recent Greenland ice mass loss by drainage system from satellite gravity observations. In: *Science.* doi: 10.1126/science.1130776.

Peltier, W.R. (2004) Global glacial isostasy and the surface of the ice-age earth: the ice-5G (VM2) model and GRACE. In: *Annu. Rev. Earth Planet. Sci.* 32. 111–149.

Rignot, E., D. Braaten, S.P. Gogineni, W.B. Krabill, and J.R. McConnell (2004). Rapid ice discharge from southeast

Greenland glaciers, In: *Geophys. Res. Lett.*, doi:10.1029/2004GL019474.

Rignot, E. and P. Kanagaratnam (2006). Changes in the velocity structure of the Greenland ice sheet. In: *Science*, doi: 10.1126/science.1121381.

Ruotsalainen, H. (2002), The Fennoscandian land uplift gravity lines – a tool for the Nordic geodynamical studies. In: *Proceedings of 14th general meeting of the Nordic Geodetic Commission*, Espoo, Finland, 2002, pp. 107–110.

Solomon, S. D. Qin, M. Manning, Z. Chen, M. Marquis, K.B. Averyt, M. Tignor and H.L. Miller (2007). IPCC Summary for Policymakers. In: *Climate Change 2007: The Physical Science Basis*. Cambridge University Press, Cambridge, United Kingdom and New York, NY, USA.

Velicogna, I. and J. Wahr (2005). Greenland mass balance from GRACE. In: *Geophys. Res. Lett.*, doi: 10.1029/2005GL023955.

Veligcogna, I. and J. Wahr (2006). Acceleration of Greenland ice mass loss in spring 2004. In: *Nature*, doi:10.1038/nature05168.

Wouters, B., D. Chambers, and E.J.O. Schrama (2008). GRACE observes small-scale mass loss in Greenland. In: *Geoph. Res. Lett.*, doi: 10.1029/2008GL034816.

Chapter 71

Water Level Temporal Variation Analysis at Solimões and Amazonas Rivers

D. Blitzkow, A.C.O.C. Matos, I.O. Campos, E.S. Fonseca,
F.G.V. Almeida, and A.C.B. Barbosa

Abstract The Amazonas and Solimões rivers and their tributaries represent the largest river system in the world. It involves an extremely high water volume, discharging into the Atlantic Ocean approximately 20% of the total water volume of the whole world. The main factor which influences the water level is the intensive rainfall over those regions, consequence of the humid characteristic of the tropical climate. This paper is intended to show water level variation along both Solimões and Amazonas rivers as a direct consequence of three different kinds of ocean-atmosphere interactions: El-Niño, La-Niña and the inter-hemispheric Sea Surface Temperature – SST gradient into the Atlantic Ocean. For this study it has been used 13 limnimetric stations where geodetic heights were derived from GPS observations combined with GEOAMA (Amazon geoid model), developed at Laboratory of the Topography and Geodesy (LTG). The orthometric height of the water surface was derived. The variation of water level measurements from 1993 through 2006 has been analysed for the greatest flood and the lowest ebb periods, June and October respectively. This study allowed to calculate the river gradient in the mentioned period.

71.1 Introduction

An important part of rain in the Amazon is supplied by evapotranspiration of the ecosystems, with an annual average contribution of 55–60% from the total precipitation. Nevertheless, it doesn't mean that all evapotranspiration generated in the Amazon basin is totally converted into precipitation over the region. During the rainy season, the rainfall rate is usually greater than twice the evapotranspiration rate, which means that most of the humidity necessary to generate the rain is brought from outside the region.

The rain distribution from December through February shows a high precipitation region (exceeding 900 mm) located in the western and southern Amazon. The period from March through May is the rainy season in the central region of the Amazon near the equator. From June through August is the dry weather period for that region. In this way, the centre of maximum precipitation is shifted to the north, in Roraima and northern South America in the same epoch. During this period, the central part of the Amazon region is predominantly influenced by Hadley cell (atmospheric circulation cell with upward winds in the North Tropical Atlantic and downward winds in the Amazon region); thus this dry period remains until approximately September/October in the southern Amazon and a month later in central part.

Cutrim et al. (2000) showed that the north and east part of the Amazon basin is extremely affected by changes in the atmospheric circulation during El-Niño and La-Niña events. La-Niña is an oceanic-atmospheric phenomenon characterized by an anomalous cooling in the sea surface of Tropical Pacific Ocean. On the other hand, El-Niño is the anomalous warming in the Tropical Pacific.

El-Niño episodes in the Equatorial Pacific Eastern seem to reduce the total rainfall in the Amazon basin, while La-Niña events intensify the rain for the same region.

D. Blitzkow (✉)
Laboratory of Topography and Geodesy, Department of Transportation, University of São Paulo, EPUSP-PTR, São Paulo 61548, Brazil
e-mail: dblitzko@usp.br

S.P. Mertikas (ed.), *Gravity, Geoid and Earth Observation*, International Association of Geodesy Symposia 135,
DOI 10.1007/978-3-642-10634-7_71, © Springer-Verlag Berlin Heidelberg 2010

Many authors (Marengo, 1992, 2004; Uvo et al., 1998; Ronchail et al., 2002) emphasized that some of the drought periods at Amazon were due to:

1. The occurrence of intense El-Niño events;
2. The strong warming of sea surface of the tropical North Atlantic Ocean; or
3. Both of them (Marengo et al., 2008).

Anomalies of Sea Surface Temperature (ASST) in the tropical Pacific are responsible for less than 40% of the rainfall variability in the Amazon basin (Marengo, 1992; Uvo et al., 1998; Marengo et al., 2008). This fact suggests that other sources exist, such as the inter-hemispheric SST gradient pointing to the south of the Intertropical Atlantic Ocean, which affects mainly the north and central Amazon.

This activity allowed to get the river gradient throughout the years and to link it with three different ocean-atmosphere interactions: El-Niño, La-Niña and the inter-hemispheric SST gradient over Intertropical Atlantic Ocean.

71.2 Ocean-Atmosphere Interactions

The El-Niño/Southern Oscillation (ENSO) is a general phenomenon of circulation of the ocean-atmosphere interaction, associated with changes in the SST patterns and wind flux at the Equatorial Pacific, between the Peruvian Coast and west Australia.

The ENSO phenomenon can also be quantified by the Southern Oscillation Index (SOI). It represents the difference of the sea level pressures between the Central Pacific (Tahiti) and the western Pacific (Darwin/Australia). This index is related to changes in the air circulation in the low levels of the atmosphere, as a result of the heating/cooling of the sea surface in the region. Negative and positive values of SOI indicate the occurrence of El-Niño and La-Niña, respectively (Oliveira, 2001).

During ENSO events, anomalous warming of the ocean surface and weakness of the wind flux, changes in low and high levels of the atmosphere circulation are observed. Changes in wetness transport patterns and consequently variations in the distribution of rainfall in tropical regions at mid and high latitudes are also observed.

Table 71.1 El-Niño, La-Niña, SST gradient and river gradients (flood and ebb maximum months) by year (mm/km)

Year	El-Niño[a]	La Niña[a]	SST[b]	June	October
1993	S		V	21	*
1994	M		N	*	18
1995	M	W	N	19	17
1996		W	V	20	18
1997	S		P	20	*
1998	S	M	P	20	17
1999		M	N	21	17
2000		M	P	*	*
2001		M	P	20	17
2002	M		V	20	17
2003	M		V	20	18
2004	W		P	19	18
2005	W		P	19	17
2006	W		–	18	*

[a]CPTEC (2008): Strong (S); Moderate (M); Weak (W)
[b]Atlantic SST gradients (Marengo et al., 2008): Variable (V) ; Negative(N); Positive(P)
Insufficient data (*)

Souza et al. (2004) studied two different climate scenarios (as shown in Table 71.1):

1. Unfavourable rain period in the Amazon region is a consequence of: simultaneous occurrence of El-Niño in the Pacific Ocean and the inter-hemispheric SST gradient pointing to North Atlantic Ocean (index positive);
2. Favourable rain period in the Amazon region has another origin: simultaneous occurrence of La-Niña in the Pacific Ocean and the inter-hemispheric SST gradient pointing to South Atlantic Ocean (index negative).

These two scenarios contribute directly to the decrease or increase of rain periods in the Amazon region.

The second and third columns of the Table 71.1 show the last years that El-Niño and La-Niña events occurred and their estimated intensity. The information was obtained from the Center for Weather Forecasting and Climate Studies in Brazil (CPTEC – Centro de Previsão de Tempo e Estudos Climáticos, 2008).

Moura and Shukla (1981) were the first to examine the SST gradient over the Tropical Atlantic. The

positive gradient occurs when the water over the tropical North Atlantic basin is warmer than normal and over tropical South Atlantic is colder. In this case, there is a deficit of precipitation during Eastern Amazon and Northeast Brazil rainy season. The opposite case determines the negative gradient. In this case, the rainy season is anomalously wetter (Pezzi and Cavalcanti, 2001).

The Atlantic SST gradients for the period 1993–2005 were obtained in Marengo et al. (2008), as shown in Table 71.1.

71.3 Orthometric Height of the Water Surface

71.3.1 Data – GPS Data Over Bench Marks

In the framework of the Hydrology and Geochemistry of the Amazon Basin (HiBAm) international research program, there has been an attempt to determine the heights at various control points (zero of limnimeters scale) along the Amazon rivers, with reference to a consistent origin (geoid) (Campos, 2004). A total of 28 stations were selected to carry out GPS observations on Bench Marks (BM) established for this purpose as close as possible to the limnimeters. The GPS geodetic height has been connected to the control points by spirit levelling. This paper used 13 of these points over Solimões and Amazonas Rivers.

The GPS stations in the rivers are: Tabatinga (1); São Paulo de Olivença (2); Santo Antônio de Içа (3); Fonte Boa (4); C.Missões (5); Itapeuá (6); Manacapuru (7); P.Trapiche 15 (8); Parintins (9); Óbidos (10); Santarém (11); Porto de Moz (12); Porto de Santana (13).

71.3.2 Methodology

The geoidal height of limnimeters were obtained using the geoid model for the Brazilian Amazon region (Blitzkow et al., 2007), denominated GEOAMA, limited by 5ºN and 10ºS in latitude and 70ºW and 50ºW in longitude. GEOAMA was computed with Stokes-Helmert Geoid software (SHGEO), developed at the University of New Brunswick, Canada. The solution of the Stokes boundary value problem employs a modified Stokes's formula in conjunction with the low-degree contribution of the global geopotential model. The geoid model was derived by using the following data: digital terrain model SAM3s_v1 (Blitzkow et al., 2007); the global geopotential model EIGEN-GL04S1 (Förste et al., 2006), degree and order 150, derived from GRACE satellite; and terrestrial gravity data basically observed along the rivers. These data, used in this study, have been provided by Petrobras (Brazilian oil company) surveyed in 1960s, which consist of 98,176 points, basically along the rivers Amazon, Solimões, Madeira and the tributaries. The majority of data set was measured with LaCoste&Romberg gravitymeter with accuracy of 0.1 mgal.

Mean free air gravity anomalies in a 5′ grid were derived from point gravity data. The blocks without gravity information, EIGEN-GL04C geopotential model was used to fill in (Förste et al., 2006). Over the ocean, the satellite altimetry-derived gravity anomalies (Global Marine Gravity, 2 arc-minute) were used (KMS2002). This model was produced by the Geodetic Division of Kort og Matrikelstyrelsen, the National Survey and Cadastre of Denmark, processing Geosat and ERS-1 satellite altimetry data (Andersen and Knudsen, 1998).

The reduced Helmert gravity anomalies used EIGEN-GL04s1 up to the degree and order 60 as a reference spheroid (Blitzkow et al., 2007).

The orthometric heights H_{ZERO} (zero of the scale) for 13 GPS/levelling stations were computed according to the following equations:

$$H_{GPS-STA} \approx h - N_{GEOAMA} \tag{1}$$

$$H_{ZERO} = H_{GPS-STA} \pm dn \tag{2}$$

where N is the geoidal height; h the ellipsoidal height; and dn the spirit leveling height difference between GPS point and the control point.

The value of water levels (NA) at the specific date, added to H_{ZERO}, provides the orthometric height of the water surface,

$$z = H_{ZERO} + NA \tag{3}$$

71.4 Results and Discussion

El-Niño, La-Niña and the Tropical Atlantic Sea Surface Temperature anomalies are possible to study through the river longitudinal profile at highest (June, higher flooded period) and the lowest (October, lower ebb period) water level seasons. Figures 71.1 and 71.2 show the height of the water surface (z) versus estuary distance for the Solimões and Amazonas Rivers in El-Niño and La-Niña events, respectively. The vertical lines with a number on the top represent the position and the number of GPS stations described in Sect. 71.3.1.

In June, the difference of the highest water level season in the two figures is similar, except in 1999 (La-Niña) and 2005 (El-Niño). These differences are clearly visible at Solimões river, mainly in Tabatinga (1) near the border of Brazil with Peru and São Paulo de Olivença (2), because these stations have more influence of the Andes melting period (Almeida et al., 2007).

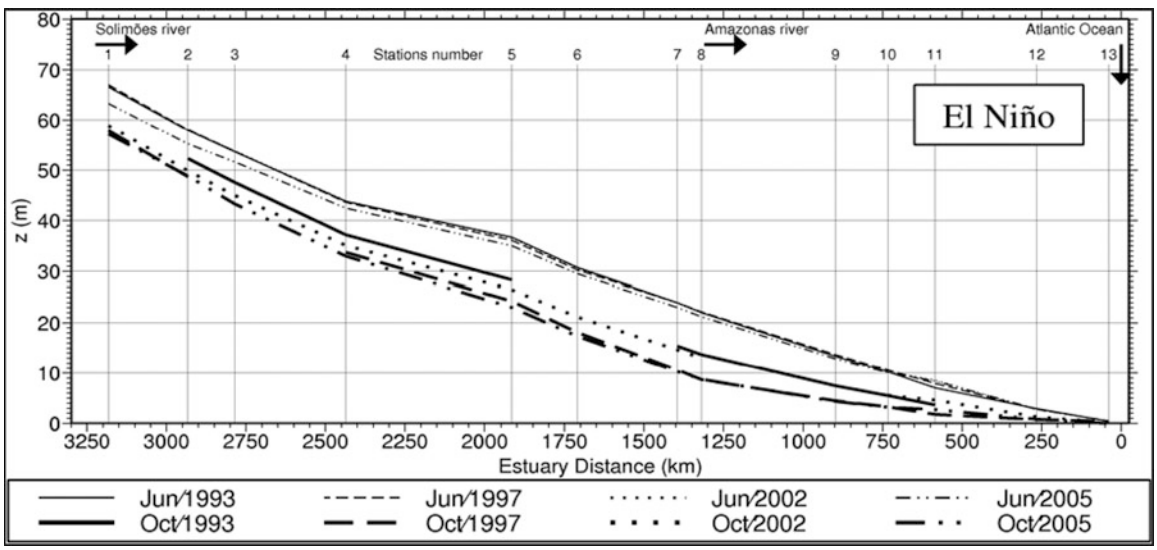


Fig. 71.1 Height of the water surface (z) versus estuary distance for the Solimões and Amazonas Rivers in El-Niño years

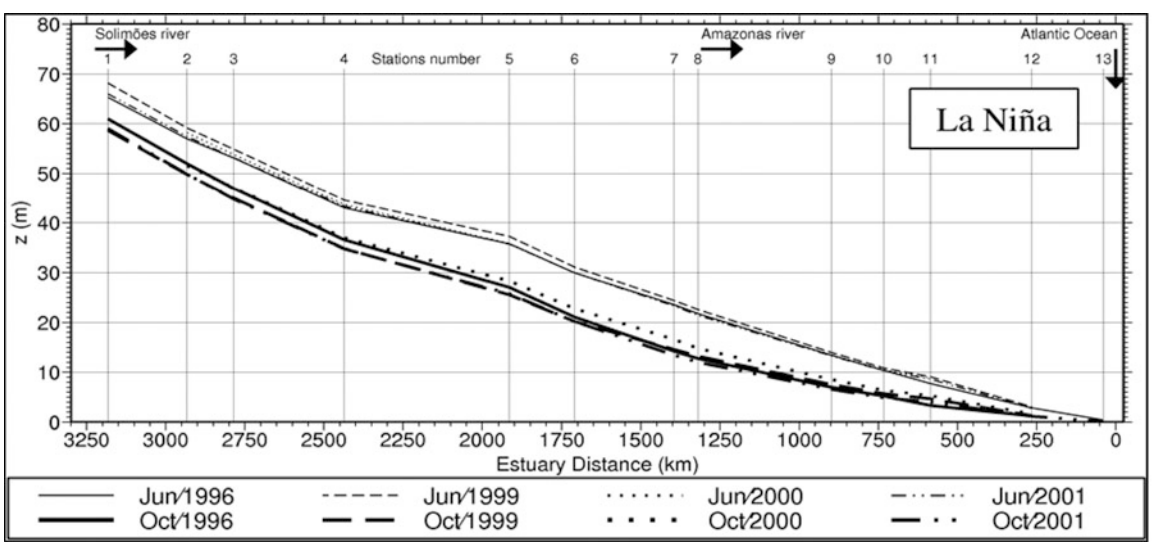


Fig. 71.2 Height of the water surface (z) versus estuary distance for the Solimões and Amazonas Rivers in La-Niña years

Table 71.2 Differences between orthometric heights of the water surface in June and October

Station number	Estuary distance (km)	Year Max. dif. (z June – z October) (m)													
		1993	1994	1995	1996	1997	1998	1999	2000	2001	2002	2003	2004	**2005**	2006
1	3182.7	–	–	6.3	4.3	9.2	8.1	**9.4**	–	7.0	7.7	6.9	4.0	**6.1**	3.6
2	2932.5	5.6	7.1	7.1	5.0	9.3	**9.5**	9.4	6.6	7.6	8.1	6.9	3.8	**6.4**	–
3	2785.0	6.1	7.1	7.6	6.1		**11.3**	9.9	6.7	8.4	8.8	7.4	4.4	**8.4**	–
4	2436.3	6.6	6.8	8.7	6.5	9.9	**11.3**	9.7	6.7	8.6	8.8	7.5	4.6	**9.5**	–
5	1915.6	8.4	–	–	8.7	11.9	**12.9**	11.7	7.5	9.9	10.0	9.0	5.3	**12.0**	–
6	1710.3	–	6.8	11.0	8.8	12.2	**12.6**	10.9	7.2	9.8	9.4	8.8	5.7	**12.2**	–
7	1395.9	8.6	7.1	11.79	9.4	**13.3**	11.6	9.8	6.8	9.8	9.3	8.4	6.6	**12.7**	–
8	1319.8	8.3	6.8	11.4	9.0	**13.5**	–	9.3	6.9	9.5	9.0	7.9	6.7	**12.5**	11.2
9	897.7	5.9	5.0	7.1	6.4	**9.2**	7.4	6.4	5.0	6.7	–	5.4	4.9	**8.5**	8.0
10	733.1	4.7	4.0	6.6	5.2	**7.3**	5.8	5.2	4.1	5.4	4.7	4.3	4.0	**6.9**	6.6
11	585.5	3.4		5.5	4.5	**6.2**	4.5	4.4	3.5	4.6	3.9	3.6	3.4	**5.7**	5.6
12	265.1	**2.9**	1.3	2.1	1.6	2.0	1.7	1.8	–	1.6	1.4	1.4	1.3	**2.0**	2.3
13	39.0	**–**	0.0	**0.4**	**0.4**	0.1	0.0	0.0	0.0	–	0.2	0.2	0.1	**0.0**	**0.4**

No information (–)

In the lowest ebb period the profile differences by year are visible at Solimões and Amazonas rivers. The year 1993, there was a strong El-Niño event but SST gradient was variable during the year and the profile isn't much different than La-Niña event in October. Nevertheless, in 1997 and 2005 occurred El-Niño and positive SST gradient. During these years, the water level of the Amazonas and Solimões rivers were lower than 1993.

The droughtf of 2005 was not related only to El-Niño. In this year, the temperature in the Tropical North Atlantic was the warmest recorded, the contrast between the tropical North and South Atlantic SST's was about 1.2°C, surpassed only by 1.8°C in 1958 (Marengo et al., 2008). The meteorological analysis showed a low pressure system over the ocean, that moved the wind to the tropics, resulting in lack of clouds and consequently absence of rain.

In general, the Amazon region is very flat and for this reason the river gradient (mean inclination of the river by kilometre), over Solimões and Amazonas rivers, is very small. The mean gradient from Tabatinga (1) up to Atlantic Ocean is around 20 mm/km (CPRM, 1999). Due to the study of the orthometric height of the water surface, it was possible to compute the river gradient in greatest flood and lowest ebb period year by year (two last columns of the Table 71.1). In a few years the gradient was impossible to be computed due to gaps in the data of ANA. Nevertheless, it is possible to see that the difference of the river gradients between June and October varies from 1 (2004) up to 4 mm/km (1999).

Table 71.2 shows the maximum differences for the orthometric heights of water surface between June and October and the respective year. In 1999, it showed highest difference in station 1. In 1998, it was since station 2 up to 6. In 1997, it was since 7 up to 11. It is possible to observe that the stations (5)–(8) present the highest differences, approximately 600 km of the Solimões river final, in the middle of the Amazonas basin, because the confluence of two important rivers in the main rivers (Solimões and Amazonas rivers): Madeira (near of the beginning of the Amazonas river) and Negro (end of Solimões river, in Manaus city). They contribute a great water volume, creating a natural hydraulic barrier and then it decreases the water flux. In particular, in 2005 it happened the lower ebb period of the last 50 years (Fig. 71.1), although this year doesn't show highest deference because since 2004 and 2005 (Fig. 71.1) the flood period showed lower values than the other years.

71.5 Conclusions

Due to the lack of roads and the forest density, it is impossible to carry out spirit levelling for establishing a vertical network in the region. An alternative is to use satellite geodesy associated with a geoid model.

Over the last 8 years, due to the involvement of LTG in the Amazon region, it was possible to determine the heights at various control points (zero of limnimeters scale) along the Amazon rivers and also to calculate a specific geoid model for this region (GEOAMA). Before the establishment of the vertical reference for the rivers, it was impossible to compute their gradient and to measure the height of the water surface since the riverhead in Tabatinga (Solimões River) up to estuary in Porto de Santana (Amazon River) at the different times of the year. Due to these efforts it is now possible to evaluate the monthly variation of the orthometric height of the water surface along these rivers (Figs. 71.1 and 71.2) and to relate with ocean-atmosphere interactions (Tables 71.1 and 71.2). Special attention was given to the year 2005 because two events occurred simultaneously: El-Niño event and the strong warming of sea surface of the tropical North Atlantic Ocean. For this year, the Amazon basin experienced the most drought of the last 50 years. This study is very important nowadays because recent climate models show the ocean warming as an effect of the increase of the greenhouse gases (Fearnside, 2008; Marengo et al., 2008). This fact has an important consequence for the environment and human life.

Acknowledgements The authors acknowledge Prof. Dr. Artur Ellmann (Tallinn University of Technology), Prof. Dr. Peter Vaníček and Prof Dr. Marcelo Carvalho dos Santos (University of New Brunswick), ANA agency for the hydrometric stations data. The Activity has been partially undertaken with the financial support of Government of Canada provided through the Canadian International Development Agency (CIDA).

References

Almeida, F.G.V., G. Ramillien, D. Blitzkow, S. Calmant, A. Cazenave, and I.O. Campos (2007). *Grace Satellite Data and In-situ Water Level Time-Variation Correlation Analysis in the Amazon Basin*, AGU2007 Fall Meeting: San Francisco, CA – 10–14 December.

Andersen, O.B. and P. Knudsen (1998). Global Marine Gravity Field from the ERS-1 and GEOSAT Geodetic Mission Altimetry. *J. Geophys. Res.,* 103(C4), 8129–8137.

Blitzkow, D., A.C.O.C Matos, I.O. Campos, A. Ellmann, P. Vaníček, and M.C. Santos (2007). An attempt for an Amazon geoid model using Helmert gravity anomaly. Earth: our changing planet, IAG General Assembly at IUGG XXIV 2007, Perugia Italia, July 2–13. Vol. 133, Part 2, 187–194, Springer Berlin Heidelberg.

Campos, I.O. (2004). Referencial altimétrico para a Bacia do Rio Amazonas. PhD thesis – Escola Politécnica, Universidade de São Paulo, São Paulo, p. 112.

CPRM – Companhia de Pesquisa de Recursos Minerais (1999). *Diagnóstico do Potencial Ecoturístico do Município de Monte Alegre*. Available online at: http://www.cprm.gov.br.

CPTEC – Centro de Previsão de Tempo e Estudos Climáticos (2008). *El-Niño e La-Niña.* Available online at: http://www.cptec.inpe.br/enos/.

Cutrim, E.M.C., D.W. Martin, D.G. Butzow, I.M. Silva, and E. Yulaeva (2000). Pilot analysis of hourly rainfall in Central and Eastern Amazonia. *J. Clim.,* 13(7), 1326–334.

Fearnside, P.M. (2008). Mudanças climáticas globais e a floresta amazônica. In: Buckeridge M. (ed), A Biologia e as Mudanças Climáticas Globais no Brasil. RiMa Editora, São Paulo, Brazil, 131–150. Available online at: http://philip.inpa.gov.br/publ_livres/Preprints/2008/USP% 20livro%20capitulo-port-7-clean.pdf.

Förste, Ch., F. Flechtner, R. Schmidt, R. König, U. Meyer, R. Stubenvoll, M. Rothacher, F. Barthelmes, H. Neumayer, R. Biancale, S. Bruinsma, J.M. Lemoine, and S. Loyer (2006). A mean global gravity field model from the combination of satellite mission and altimetry/gravimetry surface data – EIGEN-GL04C. *Geophy. Res. Abstr.,* 8, 03462.

Marengo, J.A. (1992). Interannual variability of surface climate in the Amazon basin. *Int. J. Climatol*., 12, 853–863.

Marengo, J. (2004). Interdecadal variability and trends of rainfall across the Amazon basin. *Theor. Appl Climatol.*, 78, 79–96.

Marengo, J.A., C.A. Nobre, J. tomasella, M.D. Oyama, G.S. Oliveira, R. Oliveira, H. Camargo, L.M. alves, and I.F. Brown (2008). The Drought of Amazonia in 2005. *J. Clim.,* 21, 495–516.

Moura A.D. and J. Shukla (1981). On the dynamics of droughts in northeast Brazil: observations, theory and numerical experiments with a general circulation model. *J. Atmos. Sci*., 38, 2653–2675.

Oliveira, G.S. (2001). O El-Niño e Você – o fenômeno climático. Editora Transtec, São José dos Campos, São Paulo.

Pezzi, L.P. and I.F.A. Cavalcanti (2001). The relative importance of ENSO and tropical Atlantic sea surface temperature anomalies for seasonal precipitation over South America: a numerical study. *Clim. Dyn.*, 17, 205–212.

Ronchail, J., G. Cochonneau, M. Molinier, J.-L. Guyot, A.G.M. Chaves, V. Guimarães, and E. Oliveira (2002). Interannual rainfall variability in the Amazon basin and sea-surface temperatures in the equatorial Pacific and the tropical Atlantic Oceans. *Int. J. Climatol*., 22, 1663–1686.

Souza, E.B., M.T. Kayano, and T. Ambrizzi (2004). The regional precipitation over the eastern Amazon northeast Brazil modulated by tropicall Pacific and Atlantic SST anomalies on weekly timescale. *Revista Brasileira de Meteorologia*, 19(2), 113–122.

Uvo, C.R.B., C.A Repelli, S.E. Zebiak, and Y. Kushinir (1998). The relationship between tropical Pacific and Atlantic SST and northeast Brazil monthly precipitation.*J. Clim.*, 11, 551–562.

Chapter 72

Spatiotemporal Analysis of the GRACE-Derived Mass Variations in North America by Means of Multi-Channel Singular Spectrum Analysis

E. Rangelova, W. van der Wal, M.G. Sideris, and P. Wu

Abstract We apply multi-channel singular spectrum analysis (MSSA) to infer the main spatiotemporal modes of mass variability in North America derived from GRACE monthly gravity field data. MSSA is a data-adaptive method for analyzing time lagged maps of variability on regional and global scales. The method proves useful in studying the annual and long-term continental water mass variations and the secular deformation signal associated with glacial isostatic adjustment (GIA) of the Earth.

We study the capabilities of the MSSA method using simulated spatiotemporal data series and address issues such as lag-window length, spectral mixing, and significance of the extracted modes. We investigate two cases using the GRACE RL-04 data. We analyze water mass variations derived from the GRACE data (corrected for GIA) and compare our results with the main modes extracted from the GLDAS/Noah and WGHM continental water storage models. Good agreement between the annual amplitudes exists in the Cordillera region, the WGHM model being closer to GRACE compared to GLDAS/Noah. Furthermore, we model the North American GIA signal using the GRACE data corrected for hydrology. Two peak signals are observed west (9–11 mm/year uplift rate) and southeast (11–13 mm/year) of Hudson Bay in agreement with the multi-dome geometry of the North American ice sheet in the ICE-5G model.

E. Rangelova (✉)
Department of Geomatics Engineering, Schulich School of Engineering, University of Calgary, Calgary, AB, Canada, T2N 1N4
e-mail: evrangel@ucalgary.ca

72.1 Introduction

The Gravity Recovery and Climate Experiment (GRACE) project (Tapley et al., 2004) delivers models of the Earth's gravity field every month to model continental water mass variations (e.g., Schmidt et al., 2006), deformation related to glacial isostatic adjustment (GIA) of the Earth (e.g., Tamisiea et al., 2007), and glacier/ice sheet mass changes (e.g., Luthcke et al., 2006), among others.

Chambers (2006), Schrama et al. (2007) and Rangelova et al. (2007) have shown that the statistically-based orthogonal bases of the method of principal component/empirical orthogonal functions (PC/EOF) analysis can be successfully applied to model the GRACE-derived mass variations at regional and global scales.

In this paper, we investigate the generalization of the PC/EOF analysis, i.e., the method of multi-channel singular spectrum analysis (MSSA) (e.g., Allen and Robertson, 1996), to analyze the mass variations in North America derived from GRACE monthly gravity field data. Working with maps of variability that are lagged in time, MSSA identifies coherent spatiotemporal patterns (empirical orthogonal functions) and principal components, in contrast to the conventional PC/EOF analysis, which identifies spatial patterns and their time evolutions. Similar to PC/EOF, MSSA allows for modelling inter-annual and long-term variations (in contrast with least-squares) because of the data-adaptive nature of the basis functions. Using a large number of time lags, however, MSSA is more successful in extracting a persistent oscillation (such as an annual cycle) from noise through identifying a pair of spatiotemporal patterns occurring sinusoidal in time and $\pi/2$ out of phase.

S.P. Mertikas (ed.), *Gravity, Geoid and Earth Observation*, International Association of Geodesy Symposia 135,
DOI 10.1007/978-3-642-10634-7_72, © Springer-Verlag Berlin Heidelberg 2010

72.2 Methodology

The main steps of the MSSA method are as follows:

1. Given a data set $\mathbf{d}(d_{tl:\,t=1,\,T;\,l=1,\,L})$ which consists of T fields (time epochs) each with L data points (spatial channels), and chosen M time lags (lag-window length), form a data trajectory matrix as follows (Allen and Robertson, 1996):

   1.1. Augment each channel with M lagged copies of itself:

$$\mathbf{D}_l \begin{pmatrix} d_{1,l} & d_{2,l} & \cdots & d_{M,l} \\ d_{2,l} & d_{3,l} & \cdots & d_{M+1,l} \\ \vdots & \vdots & \cdots & \vdots \\ d_{N,l} & d_{N+1,l} & \cdots & d_{T,l} \end{pmatrix}, \; 1 \le l \le L, \tag{1}$$

   where $N = T - M + 1$ is the number of overlapping views of the series for each point in a channel.

   1.2. Construct a $(N \times ML)$ trajectory matrix $\mathbf{D}$:

$$\mathbf{D} = \left(\mathbf{D}_1 \; \mathbf{D}_2 \cdots \mathbf{D}_L \right). \tag{2}$$

2. Apply singular value decomposition of $\mathbf{D}$:

$$\mathbf{D} = \eta \mathbf{P}_D \Lambda_D^{1/2} \mathbf{E}_D^T, \quad \eta = \max(N, LM), \tag{3}$$

   where η is a normalization factor. $\mathbf{P}_D$ contains N orthonormal vectors called spatiotemporal principal components (PCs) that are also eigen-vectors of the lag-covariance matrix $\mathbf{C}_D^{(P)} = (1/LM)\mathbf{D}\mathbf{D}^T$. The matrix $\mathbf{E}_D$ contains M orthonormal vectors called spatiotemporal empirical orthogonal functions (EOFs), also eigen-vectors of the lag-covariance matrix $\mathbf{C}_D^{(E)} = (1/N)\mathbf{D}^T\mathbf{D}z$. Finally, the diagonal elements of $\Lambda_D = \mathbf{P}_D^T \mathbf{C}_D^{(P)} \mathbf{P}_D = \mathbf{E}_D^T \mathbf{C}_D^{(E)} \mathbf{E}_D$ are proportional to the data variance in the PCs (EOFs).
3. Filter the trajectory matrix by suppressing the spatiotemporal EOFs of no interest:

$$\mathbf{D}' = \mathbf{D}\mathbf{E}_D(\mathbf{I} - \mathbf{K})\mathbf{E}_D^T, \tag{4}$$

   where $\mathbf{K}$ is a diagonal matrix with $K_{ii} = 0$ if the *ith* EOF is retained and $K_{ii} = 1$ otherwise. Note that $\mathbf{D}' = \left(\mathbf{D}'_1 \; \mathbf{D}'_2 \cdots \mathbf{D}'_L \right)$ contains the filtered augmented time series for the spatial channels.
4. Reconstruct the filtered series for the channels by averaging along the diagonals of $\mathbf{D}'_l, l = 1,L$ as shown by Golyandina et al. (2001, p. 17).

72.3 Description of Data Sets

72.3.1 GRACE Data

We use 62 RL-04 gravity field solutions from the Center for Space Research (CSR) from August 2002 to October 2007 excluding June 2003. To ensure continuous data in the time and space, we interpolate the missing solution using the estimates from a weighted least-squares fit of a trend and annual and semi-annual cycles to the time series of spherical harmonic coefficients. For each month, we replace the C_{20} coefficient with the value determined by satellite laser ranging. We also take care of the correlated errors (north-south stripes) in the GRACE-derived maps using the destriping filter developed by Swenson and Wahr (2006).

The GRACE-derived mass changes in equivalent water height are computed (Wahr et al., 1998):

$$\delta h(\varphi,\lambda,t) = \frac{R\rho_{ave}}{3\,\rho_w} \sum_{l=2}^{l_{\max}} \sum_{m=0}^{l} \frac{2\,l+1}{1+k_l} W_l P_{lm}(\sin\varphi) \cdot [\delta C_{lm}(t)\cos(m\lambda) + \delta S_{lm}(t)\sin(m\lambda)] \tag{5}$$

where $\delta C_{lm}(t)$ and $\delta S_{lm}(t)$ are the changes in the fully normalized cosine and sine spherical harmonic coefficients of degree l and order m at the time epoch t with respect to the mean values for the analyzed time period. $P_{lm}(\sin\varphi)$ is the fully normalized associated Legendre function of degree l and order m; R is the mean radius of the Earth, Φ and λ are the latitude and longitude of the computational point, and $l_{\max}$ (set to 50 in this paper) is the maximum spherical harmonic degree of the GRACE gravity field models. W_l are the degree-dependent coefficients of an isotropic Gaussian filter (a half-width of 400 km is chosen), which is applied to smooth the random errors in the GRACE spherical harmonic coefficients. Finally, ρ_w is the water density of 1,000 kg/m^3, ρ_{ave} is the average density of the solid

Earth, i.e., 5,517 kg/m^3, and k_l is the load Love number for degree l.

In addition to water mass changes, we analyze the GRACE-derived viscoelastic vertical crustal displacement signal in North America. This signal is computed by means of an approximate relationship (Wahr et al., 2000) between the geoid change and the viscoelastic vertical displacement of the crust for a viscoelastically deforming Earth.

72.3.2 Continental Water Storage Models

We use the Global Land Data Assimilation System (GLDAS) of Rodell et al. (2004). The model output (four layers of soil moisture, snow water equivalent, and canopy water storage) used in this study is based on the Noah land surface model (Chen et al., 1996). We compute water mass anomalies from the GLDAS/Noah monthly spatiotemporal maps for the time interval of the GRACE data by subtracting the mean. The second continental water storage model used is WaterGAP Global Hydrology Model (WGHM) of Döll et al. (2003) and Hunger and Döll (2008). In addition to soil, snow, canopy and groundwater storage, the model accounts for water stored in rivers, lakes, and reservoirs as well as for anthropogenic water use. The model outputs are averaged from the original 0.5° grids on 1° grids.

For the two models, we mask out the pixels that are within 0.7° of the centers of the glaciers with an area extent greater than 25 km^2 because glacier dynamics are not incorporated into the models. Also, Greenland is masked out entirely. To ensure the same spatial resolution as the GRACE-derived mass changes, we apply the de-striping and smoothing filters to the original continental water storage model outputs. In addition, we set the degree one spherical harmonic coefficients to zero because GRACE does not resolve those.

72.4 Analysis of Results

72.4.1 Analysis of Simulated Spatiotemporal Data

We simulate 63 epochs of monthly water mass variations in order to draw conclusions about the capabilities of the MSSA method to extract annual variations and trends from relatively short spatiotemporal series. To do this, we use the spatial annual amplitudes and phases of the GLDAS/Noah model in North America estimated by means of a least-squares fit to the grid points of the water mass anomalies. We also use the ICE-5G(VM2) model of Peltier (2004) to simulate the trend due to the ongoing GIA process in North America. Finally, we simulate noise using the residuals of the weighted least-squares fit to the GRACE-derived mass variations. The GRACE residuals are spatially correlated as a result of the integral GRACE measurements, the spatial averaging by the Gaussian filter and the geophysical signals not accounted for in the least-squares fit.

Figure 72.1 shows 32 spatiotemporal modes extracted from the simulated data using a lag-window length $M = 32$ months, which is the maximum possible lag-window for 63 time epochs. The top left plot shows that if the trend alone is present in the simulated data, one eigen-pair is generated and each component of the pair explains exactly 50% of the data variance. In the top right plot, the annual cycle alone generates an eigen-pair with components contributing unequally to the data variance. This is due to the small number of the overlapping views ($N = 32$), which controls the statistical significance of the extracted modes. For a fixed length time series, a trade-off exists between the information content (spectral resolution) ensured by the larger lag-window and the statistical significance. For the short GRACE series, the requirement for large lag-window length and a large number of overlapping views cannot be fulfilled, which forces the spatiotemporal modes of the annual cycle (the first eigen-pair) and trend (the second eigen-pair) in the bottom left plot of Fig. 72.1 to degenerate (spectral mixing). The variance associated with the trend spreads over the annual eigen-pair and the variance associated with the annual cycle spreads over the trend eigen-pair. Hence, the trend spatiotemporal PCs and EOFs show annual variations while the annual PCs and EOFs show trend behaviour.

If correlated noise is present in a short series with a large trend component (as in the simulated case in the bottom right plot of Fig. 72.1), artificial oscillations can be generated in the low frequency band of the eigen-spectrum due to orthogonality of the basis functions (Allen and Robertson, 1996). These artificial oscillations can degenerate with the trend and annual cycle or can be mistakenly identified as periodic variability. An ad hoc way to decrease this effect is to

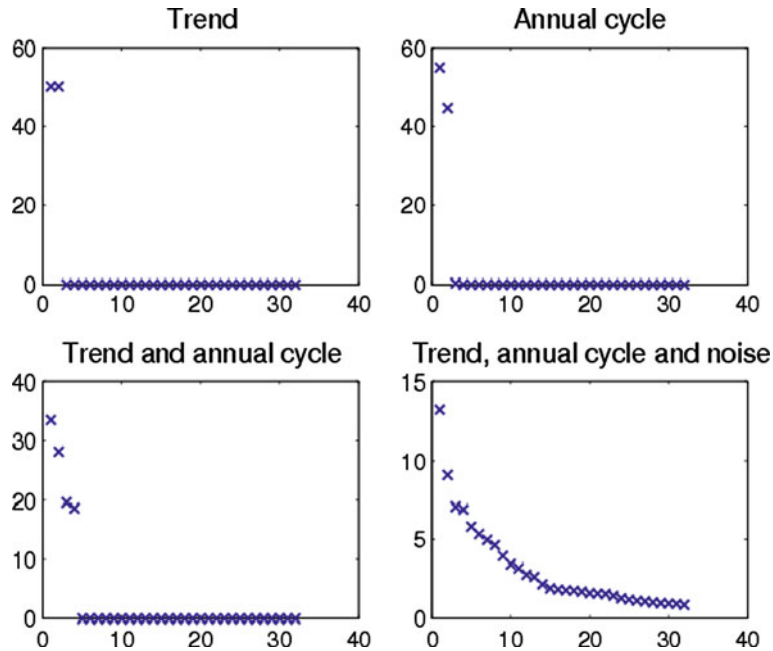


Fig. 72.1 Eigen-spectra (diagonal elements of Λ_D) of the simulated spatiotemporal series using a lag-window of 32 months. The *vertical axis* shows the percentage of data variance explained by each mode (*horizontal axis*)

remove the trend estimated by means of a least-squares fit, thus, suppressing the variance at the corresponding frequencies. When analyzing the GRACE-derived water mass variability, removal of the GIA signal reduces largely the variance of the long-term modes leaving the annual cycle as the dominant signal.

72.4.2 Analysis of Water Mass Variations

We now analyze water mass variations from real GRACE data, from which we remove the GIA signal. We subtract the spherical harmonic coefficients of the ICE-5G(VM2) model up to degree and order 50 from the GRACE spherical harmonic coefficients of the same maximum degree and order. The MSSA algorithm is applied with a lag-window of 24 months (a multiple of the annual period). This increases the statistical significance of the extracted annual signal.

Figure 72.2 shows the spatiotemporal modes from the GRACE series and the two continental water storage models. The first eigen-pair, which accounts for approximately 50% of the GRACE-derived data variance (Fig. 72.2a), corresponds to the annual water cycle. The third and fourth modes account for long-term changes that explain approximately 25% of the water mass variability. For the GLDAS/Noah model, the first eigen-pair (the annual cycle) explains approximately 50% of the data variance (Fig. 72.2b) as for GRACE. The long-term variations, however, comprise approximately 30% of the model data variability. Much higher variance of the water mass anomalies is explained by the annual cycle in the WGHM model (more than 60% in Fig. 72.2c), while the long-term variations comprise approximately 20% of the data variance. In the presence of correlated noise in the hydrology system, oscillations can be "indicated" by eigen-pairs as observed in the GLDAS/Noah spectrum (see the eigen-pair formed by the 5th and 6th modes). The statistical significance of such oscillations can be inferred through Monte Carlo MSSA.

The extracted annual variations represent mainly annual snow mass accumulation and melting in the Cordillera and the Québec-Labrador regions. Generally, very good agreement is observed between the GRACE-derived and the models' annual variability as shown in Fig. 72.3 by the reconstructed mass variations for 2006 using the first eigen-pairs in Fig. 72.2. In particular, the MSSA-extracted GRACE and GLDAS/Noah patterns of annual variability agree better than the PC/EOF-extracted patterns in Rangelova et al. (2007). GRACE observes the largest annual mass variations in the Cordillera region, where the annual amplitude is 10 cm water equivalent height

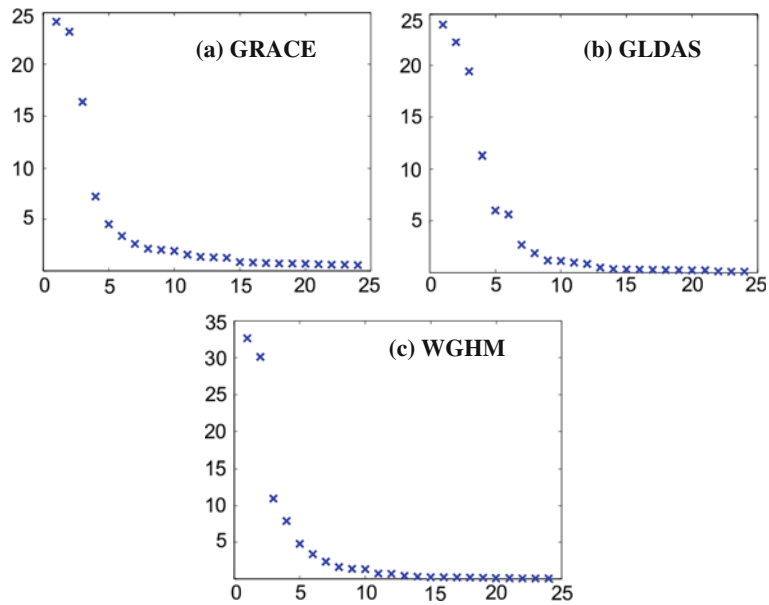


Fig. 72.2 Eigen-spectra of water mass variations for (**a**) GRACE, (**b**) GLDAS/Noah and (**c**) WGHM. *Vertical axis* shows the percentage of data variance explained by each mode (*horizontal axis*)

with a maximum (positive change with respect to the mean for the time interval) in April and a minimum (negative change) in September/October. The GLDAS/Noah (amplitude of 7 cm) and the WGHM (10 cm) annual changes in the Cordillera region reach a maximum in March and a minimum in September, i.e., a time shift of 1 month ahead of GRACE is observed in the hydrology models. Clearly, the WGHM amplitude is closer to the GRACE-derived amplitude than to the GLDAS one.

GRACE and the WGHM model have larger long-term variations (not plotted herein) compared to the GLDAS/Noah model. GRACE observes a mass increase over the western areas of North America and the Québec-Labrador region. An interesting observation is the mass deficiency developed in the Great Lakes area, which is also evident in the GLDAS/Noah and WGHM models but with a smaller magnitude. Opposite to GRACE,a mass decrease is observed in the Québec-Labrador region both for the GLDAS/Noah and WGHM models. This shows that the hydrology correction applied to the GRACE data to extract the GIA signal acts to increase the vertical crustal deformation in this region. The mass accumulation in the hydrology models southwest of Hudson Bay (Rangelova et al., 2007), which alters the geoid peak in that area associated with GIA, weakens towards the end of the time interval indicating that it might not be essential in the future epochs.

72.4.3 Analysis of GIA Deformation Signal

The GRACE-derived GIA deformation signal (in terms of rate of vertical displacement in mm/yr) is plotted in Fig. 72.4 for the two hydrology models removed from the GRACE data. The reconstruction step in Sect. 72.2 is performed using only the first eigen-pair in the spectra of the corrected GRACE fields. The deformation rate is computed by differencing the reconstructed fields of September 2007 and 2002. This is necessary in order to eliminate any effects from the degenerate annual signal (see the discussion in Sect. 72.4.1).

For both models in Fig. 72.4, two peak signals, are observed west and southeast of Hudson Bay (as first shown by Tamisiea et al., 2007), the latter being the larger one in magnitude. As the locations of the GIA peaks are relatively stable with increasing the length of the GRACE data series, the signal magnitude depends on the number of epochs available, the post-processing smoothing of the GRACE monthly data and the hydrology correction applied (e.g., van der Wal et al., 2008).

The GRACE/GLDAS deformation peaks are 9 and 11 mm/year, respectively, while the GRACE/WGHM peaks are larger being 11 and 13 mm/year. Locations of the peaks agree with the multi-dome structure of the North American ice sheet complex in the IGE-5G model of Peltier (2004). The predictions based on this ice model, however, show a larger peak signal west

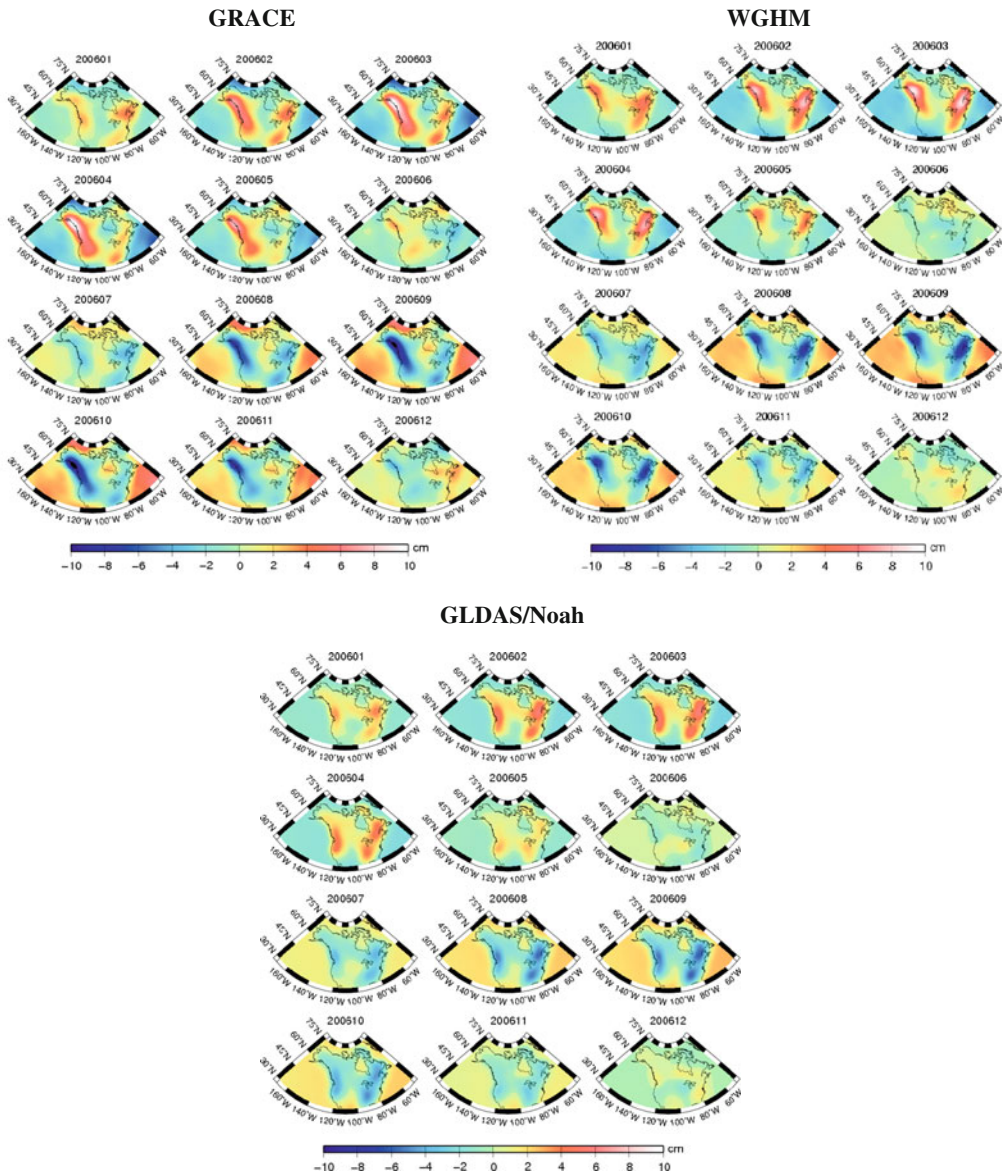


Fig. 72.3 Extracted annual mass variations for the year of 2006 using the first eigen-pairs from MSSA. All of the three models (GRACE-derived, GLDAS/Noah and WGHM) refer to the mean fields for the time interval August 2002 – October 2007

of Hudson Bay. It should be noted that the same rate estimated from MSSA is obtained by means of a least-squares fit to the time series of either the grid points of mass changes or spherical harmonic coefficients. This shows that the omitted modes in the MSSA procedure do not have an effect on the extracted GIA signal.

Finally, it should be noted that Fig. 72.4 also shows the climate ice mass loss signal in south-eastern Alaska as well as some residual long-term water mass variations over the Mississippi Drainage Basin/High Plains Aquifer area.

72.5 Conclusions

We have shown that the method of the multi-channel singular spectrum analysis (MSSA) can extract periodic and long-term water mass variations in North America from GRACE-derived series of mass changes. Similar to the PC/EOF analysis, MSSA has an advantage over the conventional least-squares fit of a trend and periodic variability because of the statistical data-adaptive basis functions. Thus, long-term and inter-annual mass variations can be studied.

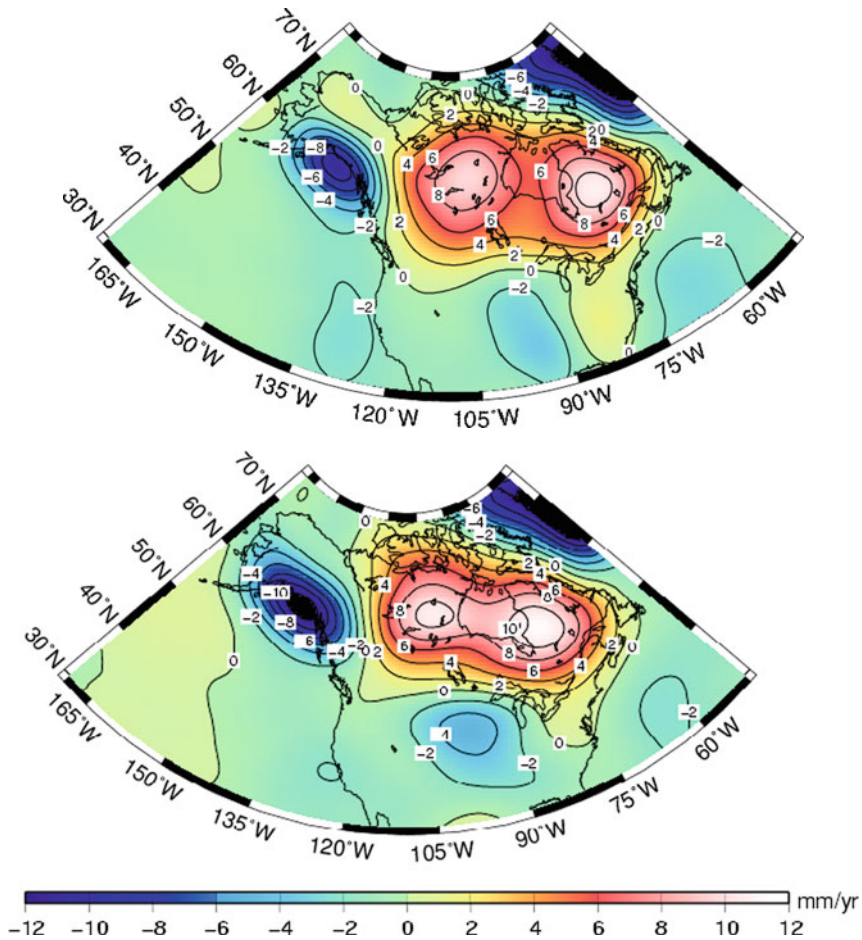


Fig. 72.4 The GRACE-derived GIA signal with the GLDAS/Noah (above) and the WGHM (below) corrections

The extracted by MSSA patterns of annual variability agree better than the ones extracted by PC/EOF. This has been observed for the GRACE-derived and GLDAS/Noah water mass variations. Having reduced noise, the MSSA results, however, still largely depend on the relatively short GRACE series, which is evident from the mixing of the trend and annual cycle as observed for the simulated data. This effect will decrease with the increase of the number of the available GRACE monthly gravity field solutions.

The annual water cycle derived from the GRACE data has a time lag of 1 month compared to the GLDAS/Noah and WGHM models in the Cordillera region and the same amplitude as the WGHM model. The GLDAS/Noah model has reduced amplitude.

Using MSSA, we have also modelled the secular GIA signal from the GRACE CSR RL-04 data. The derived deformation signal depends on the hydrology correction applied, and the signal peaks are larger when WGHM is used.

Acknowledgements The authors gratefully acknowledge R. Peltier for the GIA model, M. Rodell for the GLDAS model and P. Döll and Dr. Fiedler for the WGHM model. The two anonymous reviewers are acknowledged for their very helpful comments. Financial support is provided by GEOIDE NCE and NSERC, Canada.

References

Allen, M.R. and A.W. Robertson (1996). Distinguishing modulated oscillations from coloured noise in multivariate data sets. *Clim. Dyn.*, 12, 775–784.

Chambers, D.P. (2006). Observing seasonal steric sea level variations with GRACE and satellite altimetry. *J. Geophys. Res.*, 111, C03010, doi:10.1029/2005JG002914.

Chen, F. et al. (1996). Modeling of land surface evaporation by four schemes and comparison with FIFE observations. *J. Geophys. Res.*, 101(D3), 7251–7268.

Döll, P., F. Kaspar, and B. Lehner (2003). A global hydrological model for deriving water availability indicators: model tuning and validation. *J. Hydrol.*, 270 (1–2), 105–134.

Golyandina, N., V. Nekrutkin, and A. Zhigljavsky (2001). Analysis of time series structure – SSA and related techniques. Chapman & Hall/CRC, London, p. 305.

Hunger, M. and P. Döll (2008). Value of river discharge data for global-scale hydrological modeling. *Hydrol. Earth Syst. Sci.*, 12, 841–861.

Luthcke, S.B. et al. (2006). Recent greenland ice mass loss by drainage system from satellite gravity observations. Science, 314, 1286–1289.

Peltier, W.R. (2004). Global glacial isostasy and the surface of the ice-age earth: The ICE-5G (VM2) Model and GRACE. *Annu. Rev. Earth Planet. Sci.*, 32, 111–149.

Rangelova, E., W. van der Wal, A. Braun, M.G. Sideris, and P. Wu (2007). Analysis of GRACE time-variable mass redistribution signals over North America by means of principal component analysis. *J. Geophys. Res*., 112, F03002, doi: 10.1029/2006JF000615.

Rodell, M. et al. (2004). The global land data assimilation system. *Bull. Am. Meteorol. Soc*., 85(3), 381–394.

Schmidt, R. et al. (2006). GRACE observations of changes in continental water storage. *Global Planet. Change*, 50, 112–126.

Schrama, E.J.O., B. Wouters, and D.A. Lavallée (2007). Signal and noise in Gravity Recovery and Climate Experiment (GRACE) observed surface mass variations. *J. Geophys. Res*., 112, B08407, doi:10.1029/2006JB004882.

Swenson, S. and J. Wahr (2006). Post-processing removal of correlated errors in GRACE data. *Geophys. Res. Lett*., 33, doi:10.1029/2005GL025285.

Tamisiea, M.E., J.X. Mitrovica, and J.L. Davis (2007). GRACE Gravity data constrain ancient ice geometries and continental dynamics over Laurentia. Science, 316, doi: 10.1126/science.1137157.

Tapley, B.D., S. Bettadpur, M. Watkins, and C. Reigber (2004). The gravity recovery and climate experiment: Mission overview and early results. *Geophys. Res. Lett.*, 31, L09607, doi:10.1029/2004GL019920.

Van der W., P. Wu, M.G. Sideris, and C.K. Shum (2008). Use of GRACE determined secular gravity rates for glacial isostatic adjustment studies in North-America. *J. Geodyn.*, 46, 144–154.

Wahr, J., M. Molenaar, and F. Bryan (1998). Time variability of the Earth's gravity field: hydrology and oceanic effects and their possible detection using GRACE. *J. Geophys. Res.*, 103(B12), 30, 205–30, 229.

Wahr, J., D. Wingham, and C. Bentley (2000). A method of combining ICESat and GRACE satellite data to constrain Antarctic mass balance. *J. Geophys. Res*., 105(B7), 16, 279–16, 294.

Chapter 73

Analysing Five Years of GRACE Equivalent Water Height Variations Using the Principal Component Analysis

I.M. Anjasmara and M. Kuhn

Abstract In this study we use 59 monthly solutions (April 2002–May 2007) of the Earth's gravity field obtained from the Gravity Recovery and Climate Experiment (GRACE) satellite mission, expressed in equivalent water height (EWH). The GRACE-derived EWH values are analysed first in terms of the secular trend and RMS-variability before applying the statistically-based Principal Component Analysis (PCA), in order to obtain the most dominant spatial and temporal variations. On a global scale, we show that only 5 modes can express more than 80% of the total variability, including all major hydrological, cryospheric and post-glacial rebound signals. As expected, globally, the most dominant temporal variation is an annual signal followed by a secular trend. Apart from these well-known signals, we show that the PCA is able to reveal other periodic and a-periodic signals.

73.1 Introduction

Since its launch on 17 March 2002, the GRACE twin satellite mission provides valuable information on continental water storage variability (e.g., Ramillien et al., 2004; Tapley et al., 2004a). Today, GRACE time-variable gravity observations are routinely provided with a monthly temporal resolution and spatial resolutions of approximately 200–500 km (e.g., Wahr et al., 1998; Nerem et al., 2003; Ramillien et al., 2004; Tapley et al., 2004b), allowing mass changes on both regional and global scales to be inferred.

Up until today, many studies based on GRACE observations have studied the annual and secular mass variations producing the strongest time-variable signal in the Earth's gravity field (e.g., Ramilien et al., 2004; Wahr et al., 2004; Anderson and Hinderer, 2005; Rowlands et al., 2005; Hinderer et al., 2006; Schmidt et al., 2006). Most of these studies use analysing techniques that require some prior information on the signals to be studied, such as the assumption of a periodic signal (e.g., annual or semi-annual), thus do not allow for the detection of other a-periodic signals. Only few studies so far involving GRACE data have used the statistically-based Principal Component Analysis (PCA) (e.g., Preisendorfer, 1988; Jolliffe, 2002), also known as EOF analysis, that does not require any prior information. With an increased number of monthly solutions available (e.g., few years), the application of the PCA becomes an alternative analysing tool that is already well established in other areas, such as meteorology and oceanography.

De Viron et al. (2006) applied the PCA on GRACE data in order to detect inter-annual signals of the continental hydrology related to the El-Niño Southern Oscillation (ENSO) Index. Rangelova et al. (2007) have applied the PCA to GRACE data over North America in order to find correlations between Earth's gravity field changes and mass changes provided by different hydrological models. Schrama et al. (2007) and Wouters and Schrama (2007) benefited from properties of Empirical Orthogonal Functions (EOFs) to construct a low-pass filter that has been proven to reduce high-frequency errors in the GRACE data. This

I.M. Anjasmara (✉)
The Institute of Geoscience Research, Western Australian Centre for Geodesy, Curtin University of Technology, Perth, WA 6845, Australia
e-mail: ira@geodesy.its.ac.id

S.P. Mertikas (ed.), *Gravity, Geoid and Earth Observation*, International Association of Geodesy Symposia 135,
DOI 10.1007/978-3-642-10634-7_73, © Springer-Verlag Berlin Heidelberg 2010

was achieved through an approximation of the original GRACE gravity field signal by accounting only for the most dominant modes that represent most of the Earth's time-variable gravity signal.

In this study, we analyse the spatial and temporal variability of the Earth's surface mass changes by scrutinizing the secular trend and RMS variability. We apply the PCA and present the five dominant PCA modes and discuss their relations to geophysical origins. Unlike in other PCA studies (see above), we also show a possible long-periodic signal, a small increase of the annual signal's amplitude, an annual saw-tooth-like signal as well as signals associated with the 2004 Sumatra-Andaman earthquake.

73.2 Data and Methodology

73.2.1 GRACE Data Used

In this study, GRACE level-2 RL04 data generated at CSR University of Texas Austin were used. The monthly gravity field solutions cover a time-span of just over 5 years from April 2002 to May 2007, where June, July 2002 and June 2003 were excluded due to problems in the gravity recovery as a result of degradations of the GRACE satellite orbit (e.g., Wagner et al., 2006). However, these data gaps can be considered as non-critical to the PCA and therefore have been linearly interpolated, in order to construct a continuous spatial and temporal data set. The former consideration is based on the fact that our results do not show any anomalous behaviour around the data gaps (cf. the first PCA mode of the results).

The GRACE data, provided as monthly fully normalized spherical harmonic coefficients sets of the Earth's gravitational potential, have been converted into surface mass density changes according to Wahr et al. (1998) so to express EWH values on a 1° by 1° geographic grid. We also apply spatial smoothing through a Gaussian isotropic filter with a smoothing radius of 500 km, which is based on the study of Swenson et al. (2003) showing that minimum accumulative errors usually occur for smoothing radii between 200 and 600 km.

Applying the technique of Wahr et al. (1998), two considerations should be pointed out here: (i) it is assumed that mass changes are confined to a surface layer, which is not always the case such as for mass changes associated with glacial-isostatic adjustment; (ii) even though expressed as EWH values, GRACE-derived mass changes can be of any origin (cf. previous point), thus care has to be taken with the interpretation as hydrological signals.

For the PCA, the spatial-temporal information given by the 59 monthly EWH grids, reduced by the average over the same time period, have been combined in a $(p \times q)$ spatio-temporal matrix $\mathbf{H} = (h_{ij})$ with $i=1,\ldots,p$; $j=1,\ldots,q$. The q column vectors, $\mathbf{h}_j(\Omega)$, of $\mathbf{H}$ hold the EWH grid values at all locations, $\Omega = (\lambda,\varphi)$, with λ and ϕ are geographic longitude and latitude respectively. The temporal evolution of the EWH values at each grid location, Ω_i, is provided by the p row vectors, $\mathbf{h}_i(t)$.

73.2.2 The Principal Component Analysis

In this chapter, we briefly re-visit the two central relationships of the PCA and refer the mIore interested reader to standard text books (e.g., Preisendorfer, 1988; Jolliffe, 2002). The PCA decomposes the matrix $\mathbf{H}$ by a set of new basis functions $\mathbf{e}_j(\Omega)$, the empirical orthogonal functions (EOFs) depending on the location Ω and the corresponding expansion coefficients $\mathbf{a}_j$, the principal components (PCs) depending on the time of the monthly solutions t_j. The EOFs build the column vectors of the $(p \times q)$ matrix $\mathbf{E}$ and represent eigenvectors that are obtained through the eigenvalue decomposition $\mathbf{\Sigma e}_j = \lambda_j \mathbf{e}_j$ of the scatter matrix $\mathbf{\Sigma} = \mathbf{H}\mathbf{H}^T$ with λ_j being the jth eigenvalue. Once the set of EOFs has been derived, the expansion coefficients (or PCs) are obtained through the analysis formula

$$\mathbf{A} = \mathbf{H}^T\mathbf{E} = \sum_{i=1}^{p} \mathbf{h}_i^T(t)\mathbf{e}_i(t), \tag{1}$$

where the PCs, $\mathbf{a}_j$, form the column vectors of the matrix $\mathbf{A}$ and $\mathbf{e}_i(t)$ are the row vectors of the matrix $\mathbf{E}$. Based on Eq. (1) an alternative representation of H is then given by the synthesis formula

$$\mathbf{H} = \mathbf{E}\mathbf{A}^T = \sum_{j=1}^{q} \mathbf{e}_j(\Omega)\mathbf{a}_j^T, \tag{2}$$

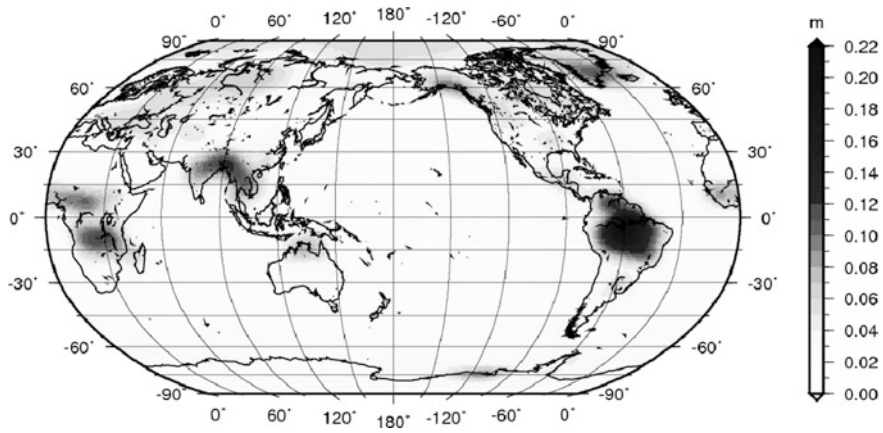


Fig. 73.1 Global distribution of EWH RMS values. Robinson projection

where **H** is expressed by q PCA modes formed by the individual EOFs and PCs.

While the above formalism can be applied to any signal **H**, the EOFs and PCs can be interpreted when dealing with a spatio-temporal matrix as in the case of GRACE data (see Sect. 73.2.1). In this particular case, the PCs represent a time series, which is associated with a geographical distribution given by the EOF providing the magnitude with which the PC has to be multiplied.

The magnitudes of the eigenvalues λ represent a measure for the relative contribution of the associated PCA mode to the overall variability of the signal. Therefore, if ordered with respect to decreasing magnitude, as will be done in the remainder of this article, the first few PCA modes represent the most dominant temporal and spatial patterns contained in **H**. Using only the first few modes in Eq. (2), usually most of the original variability is contained in the reconstructed signal, which demonstrates one important property of the PCA to be able to reduce the complexity of the original signal but keeping the most dominant temporal and spatial variability (e.g., Jolliffe, 2002).

73.3 Interpretation of the Results

73.3.1 RMS and Linear Trend

Before presenting the PCA results, we will have a look on the global distribution of RMS and secular trend values, which provide general information on the spatial distribution of short- and long-term variations of the Earth's surface mass changes. Figure 73.1 shows the global distribution of the RMS values build over the 5 year data period. Large variations are present over several hydrological basins as also found by several authors (e.g., Ramillien et al., 2004; Tapley et al., 2004a). The largest variations, related to hydrological signals, are found over South America, coinciding with the watersheds of the Amazon and Orinoco rivers. Other major variations can be found over the Ganges and Mekong watersheds in Asia and the Niger, Congo, Lake Victoria and Zambezi watersheds over Africa. In comparison to these rather strong signals, some weaker variation can be observed over the watersheds of Eastern Europe, the Mississippi and the Parana-Uruguay region as well as the tropical regions of Northern Australia and Central America.

Apart from hydrological signals, Fig. 73.1 also reveals considerable variations over various areas of the cryosphere, with the strongest variation over South-East Greenland. Further, cryospheric variations are detected over the Alaskan glaciers and along some coastal areas of Antarctica. Several more variations can be detected on a more regional scale, which however are not visible in Fig. 73.1 (e.g., Anjasmara, 2008).

It should be mentioned that the effects from the ocean and atmosphere have been removed from the GRACE data (e.g., Tapley et al., 2004b). This is why, no significant signals, except leakage signals from land, are visible over the oceans (cf. Fig. 73.1).

The linear EWH trends (cf. Fig. 73.2) for the same period have been obtained by a simultaneous least-squares fit of a trend and annual signal. Figure 73.2 shows many areas that either gradually gain (positive trend) or lose (negative trend) mass. As documented

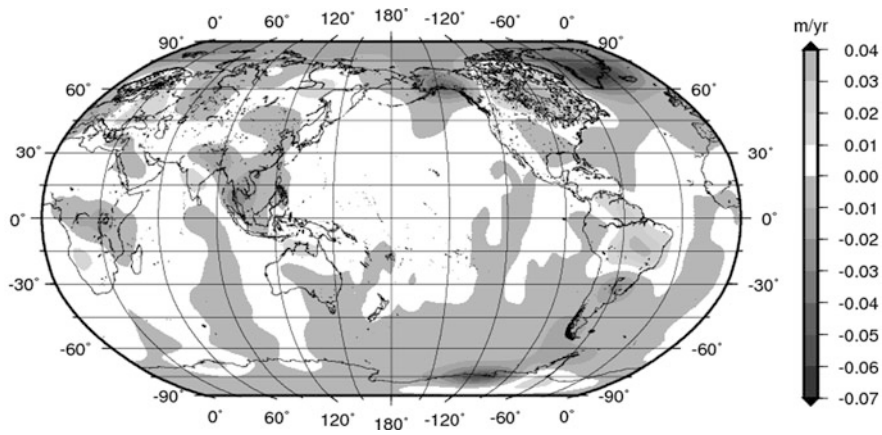


Fig. 73.2 Global distribution of EWH trends between April 2007 and May 2007. Robinson projection

by several authors, the most dominant (negative) trends are present over Greenland, Alaska and Antarctica, indicating large-scale mass loss over these areas (e.g., Velicogna and Wahr, 2005; Chen et al., 2006a, b, c; Luthcke et al., 2006; Ramillien et al., 2006). Other strong positive trends can be identified over the Canadian Shield and Fennoscandia being the result of a post-glacial rebound signal in these areas (e.g., Ekman and Makinen, 1996; Wu, 1998). Apart from the above areas, strong trends related to land hydrology signals are revealed over areas that also show large short-term variations (cf. RMS values in Fig. 73.1). Here, strong trends are visible over the Amazon, Orinoco and Parana-Uruguay watersheds over South America, the Ganges watersheds over Asia and Lake Victoria over Africa. Some weaker trends are also visible in South-West Africa, India, North Australia and the Lena and Mississippi watersheds.

73.3.2 PCA Results

While the global distribution of RMS values only provides an indication of regions with high variability, it does not provide information on the nature of the signals involved. The statistically-based PCA can provide the corresponding information without having the need to introduce prior information as has to be done with other techniques, such as the frequently used Harmonic Analysis (HA) technique (e.g., Kuhn et al., 2005).

We present and discuss the PCA results obtained from the 5-year of GRACE-derived EWH values (see Sect. 73.2.1). Hereby the PC's have been normalised to ± 1, thus the EOFs have been scaled by the PC's maximum magnitude so to correctly reconstruct the original signal. The five most dominant PCA modes are illustrated in Figs. 73.3, 73.4, 73.5, 73.6 and 73.7, which take up almost 82% of the overall variability (modes 1–5: 41.8, 21.0, 9.4, 6.5 and 3.0%). Please note the variable colour bars applied to the different figures. The PCs of the first four modes mostly show an annual and secular trend signal, thus indicating that most of the variability is taken up by these two signals.

Scrutinizing the EOF of the first PCA mode (cf. Fig. 73.3) reveals that the annual signal is mostly present over all land areas, thus correlated with the changing hydrology. In areas of the EOF with positive values, the annual signal is in phase with the PC and out of phase in areas with negative values (e.g., a half-year phase shift). Strong annual signals are present along the equatorial region, related to the same watersheds as identified by the RMS value. Only the tropical region over Northern Australia does show a weak RMS signal while it shows a stronger annual signal (cf. Fig. 73.1 vs. Fig. 73.3). The positive and negative magnitudes on the Northern and Southern hemispheres indicate a half-year phase shift, thus related to the seasons in the respective hemispheres. Apart from the strong signals along the equatorial regions, wide-spread annual signals can be identified over almost all land areas in the northern hemisphere, most likely related to changes in land-hydrology and/or snow cover.

Interestingly, both Greenland and Antarctica do not show any annual signal in PCA mode 1 (and PCA mode 4, see below), which we also confirmed by a HA.

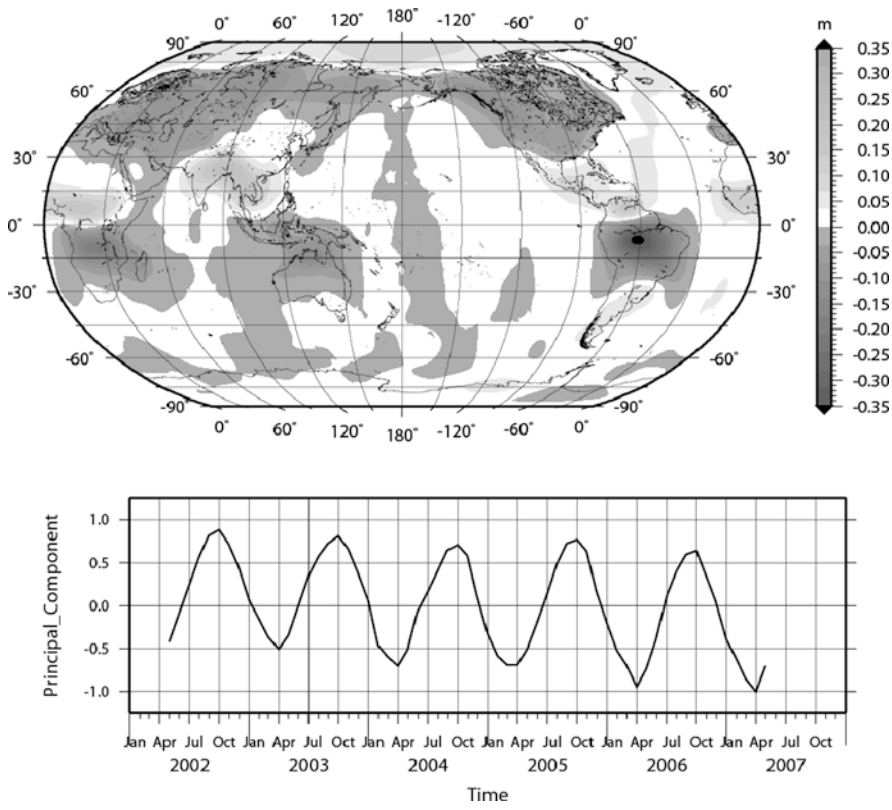


Fig. 73.3 First PCA mode (*top*: EOF, *bottom*: PC normalised to ± 1) covering 41.8% of the overall variability

Therefore, the RMS variability present in Fig. 73.1 has to be of different origin.

Figures 73.4 and 73.5 illustrate the second and third PCA modes, respectively. Both show a trend signal with further inter-annual signals superimposed on them. Both PCA modes combined, provide similar information as displayed and discussed with respect to the linear trend signal (cf. Fig. 73.2 and Sect. 73.3.1), thus the same discussion can be applied here. In addition we want to point out that the orthogonality constraints of the PCA may cause a mixing of the strong annual and trend signals (also visible in PCA mode 1, cf. Fig. 73.3).

The PCA mode 4 (cf. Fig. 73.6), again shows a clear annual signal. However, instead of having a sinusoidal shape like the PC in PCA mode 1 (cf. Fig. 73.3), here the PC has a saw-tooth like shape. Unlike for PCA mode 1, where the annual signal is present over many areas, the behaviour of PCA mode 4 is mostly present over the Amazon and Orinoco water sheds and the Lake Victoria. Furthermore, the respective PCs are about 3–4 months out of phase, where the PC of PCA mode 4 is preceding that of PCA mode 1. However, the reason for such behaviour is not clear.

A possible long-periodic signal is shown in the PC of PCA mode 5 (cf. Fig. 73.7). de Viron et al. (2006), for example, show that such signal could be related to the ENSO Index, which is correlated to land hydrology changes. However, due to the rather short time period and the low contribution of this mode to the overall variability (3%), it cannot be confirmed if this signal is real or only an artefact of the GRACE data processing.

A more detailed look on the PCs of PCA modes 1 and 4 demonstrates one of the great advantages of the PCA being able to identify signals that either gradually or abruptly changes over time. For example, the PC of PCA mode 1 shows an almost perfect annual signal with slightly increasing amplitude. As mentioned above, the annual signal visible in the PC of PCA mode 4 is more of a saw-tooth shape, which when modelled with sine- or cosine-waves will introduce an apparent semi-annual and shorter periodic signals

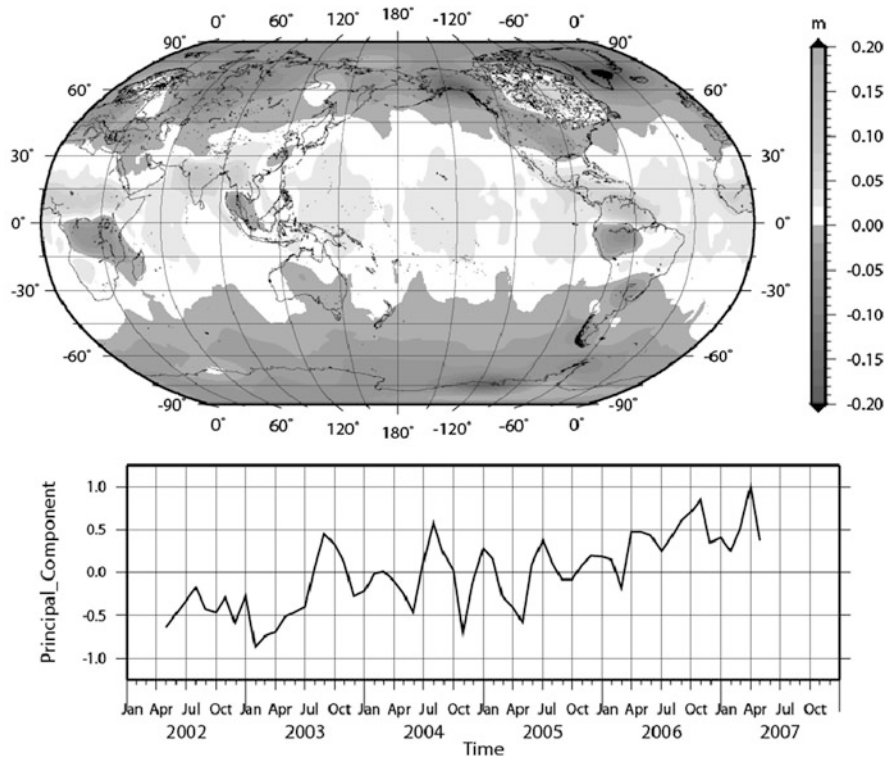


Fig. 73.4 Second PCA mode (*top*: EOF, *bottom*: PC normalised to ± 1) covering 21.0% of the overall variability

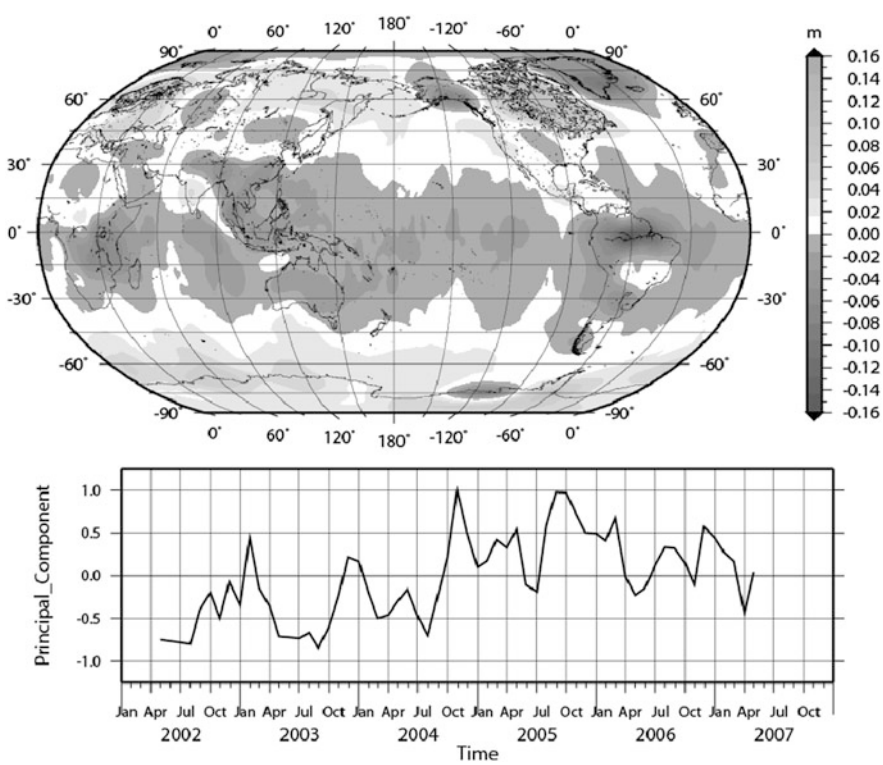


Fig. 73.5 Third PCA mode (*top*: EOF, *bottom*: PC normalised to ± 1) covering 9.4% of the overall variability

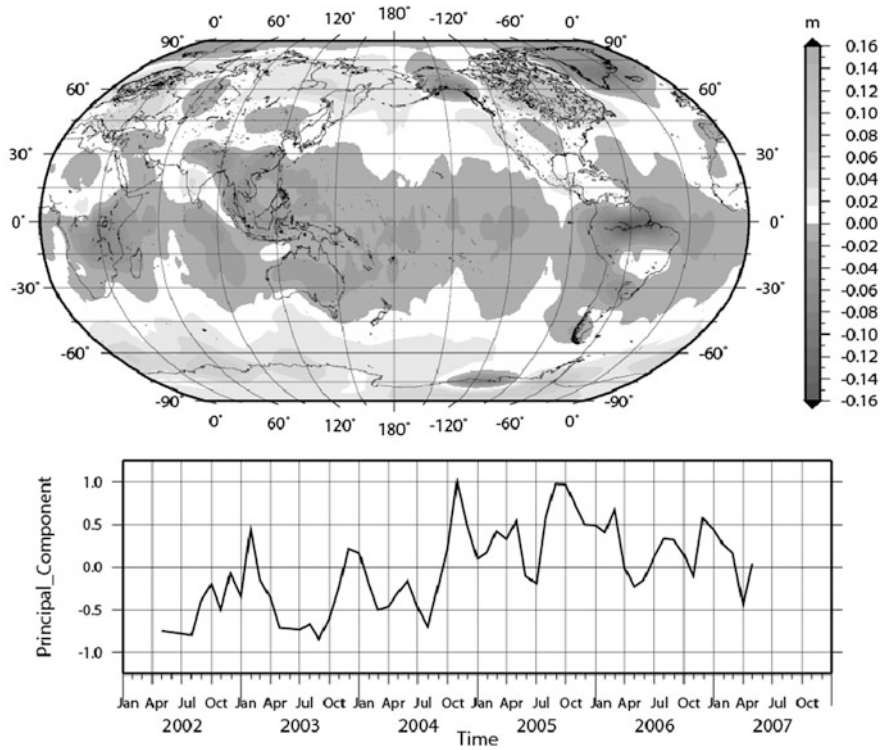


Fig. 73.6 Forth PCA mode (*top*: EOF, *bottom*: PC normalised to ±1) covering 6.5% of the overall variability

(e.g., Kuhn et al., 2005). Furthermore, the PCs of mode 2–4 are slightly disturbed around the time of the Sumatra-Andaman Earthquake in December 2004. This can be seen by a slight off-set of the corresponding PCs. While being rather small in PCA modes 2 and 4, this behaviour is much more pronounced if the PCA is applied to data over the corresponding region only (e.g., Anjasmara 2008). This is demonstrated in Fig. 73.8, showing the PC of PCA mode 1 obtained by analysing the GRACE-derived EWH changes over an approximately 1,500 km by 1,500 km area centred around the epicentre of the earthquake (e.g., Banerjee et al., 2005).

73.4 Conclusions

General information of the variability of the GRACE-derived EWHs was provided through the analysis of global EWH, RMS and trend values. The most significant areas of variability and secular changes have been discussed and further analysed through the results of the PCA. Regarding the PCA results, it has been shown that the PCA is able to reveal the major temporal variations of the Earth's gravity field, which have been documented elsewhere applying different modelling techniques.

As was expected from other studies, the PCA results showed that on a global scale, the most dominant spatial and temporal EHW variations are related to an annual signal followed by secular changes. Globally, these two signals account already for most of the variability, thus providing a good approximation of the spatio-temporal variation of the Earth's gravity field. On a more regional scale however, this behaviour can be much different (e.g., Anjasmara, 2008).

The PCA results of this study also show one important implication of the PCA being a statistically-based modelling technique. Instead of showing a smooth annual or trend signal, the PCA also detects variations to these signals (e.g., superimposed on them), as documented by slightly disturbed annual signals with changing amplitude and of saw-tooth shape and trends with superimposed inter-annual signals. Such information cannot be detected by applying modelling techniques that only look for a predefined signal, such as periodic sinusoidal signals through a HA or Fourier analysis.

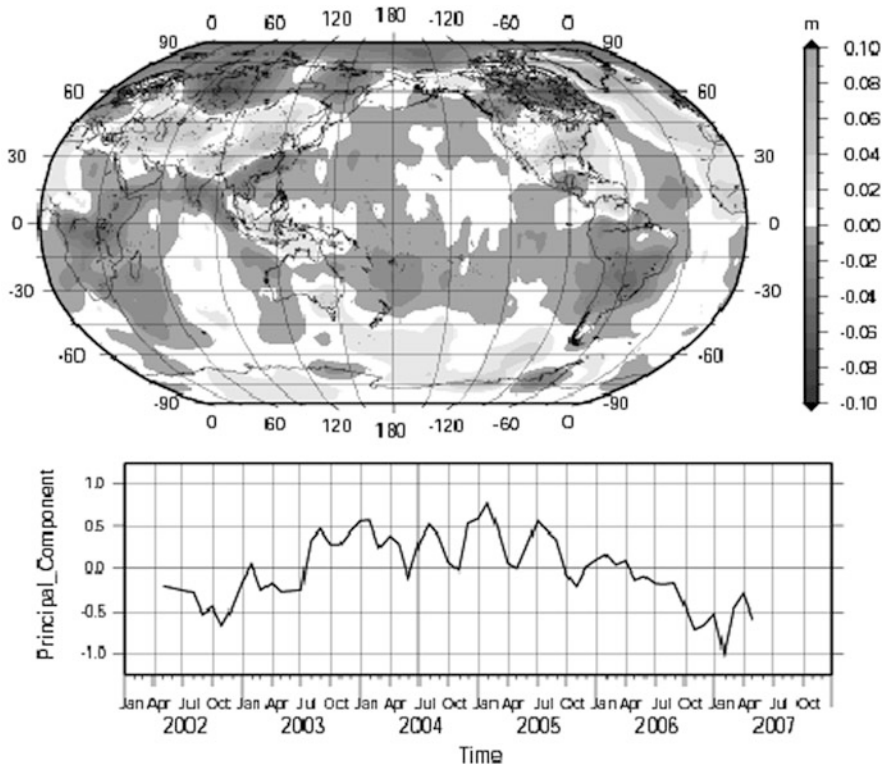


Fig. 73.7 Fifth PCA mode (*top*: EOF, *bottom*: PC normalised to ±1) covering 3.0% of the overall variability

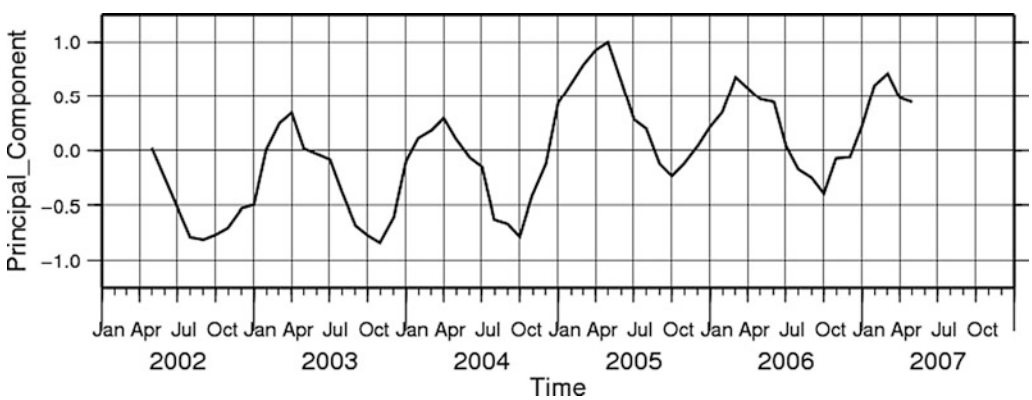


Fig. 73.8 PC of the first PCA mode (covering 72% of the overall variability) obtained by analysing GRACE-derived EWH changes around the epicentre of the Sumatra-Andaman earthquake. The PC is normalised to ±1

Finally, as GRACE-derived mass changes provide the integral information of all mass changes, the PCA like other techniques (e.g., HA) is not able to separate between different geophysical contributions without introducing additional information. Furthermore, the question remains open to what extent the PCA produces/ignores a realistic signal especially considering the higher modes.

Acknowledgements This study was funded by Australia Partnership Scholarship (APS-AusAid). We thank The Institute of Geoscience Research (TIGeR) for funds to present this work

at the IAG Symposium GGEO2008. We also thank Dr Oliver Baur from the Geodetic Institute of the University of Stuttgart, who kindly provided the GRACE mass estimates. Finally, we would like to thank two anonymous reviewers who helped to considerably improve the original manuscript. This is TIGeR publication 169.

References

Anderson, O.B. and J Hinderer (2005). Global inter-annual gravity changes from GRACE: early results. *Geophys. Res. Let.*, 32, L01402.

Anjasmara, I.M. (2008). Spatio-temporal analysis of GRACE gravity field variations using the Principal Component Analysis. Master Thesis, Curtin University of Technology, Perth, Australia.

Banerjee, P. et al. (2005). The size and duration of the Sumatra-Andaman Earthquake from far-field static offsets. *Science*, 308, 1769–1772.

Chen J.L. et al. (2006a). Alaskan mountain glacial melting observed by satellite gravimetry. *Earth Planet. Sci. Lett.,* 248, 368–378.

Chen J.L. et al. (2006b). Satellite gravity measurements confirm accelerated melting of Greenland ice sheet. *Science,* 313, 1958–1960.

Chen J.L. et al. (2006c). Antarctic mass rates from GRACE. *Geophys. Res. Lett.,* 33, L11502.

de Viron, O.D. et al. (2006). Extracting low frequency climate signal from GRACE data. *eEarth,* 1, 9–14.

Ekman, M. and J. Makinen (1996). Recent postglacial rebound, gravity change and mantle flow in Fennoscandia. *Geophys. J. Int.*, 126(1), 229–234.

Hinderer, J. et al. (2006). Seasonal changes in the European gravity field from GRACE: A comparison with superconducting gravimeters and hydrology model predictions. *J. Geodyn.*, 41(1–3), 59–68.

Jolliffe, I.T. (2002). Principal component analysis. Springer series in statistics, 2nd ed., Springer, New York.

Kuhn, M. et al. (2005). Low-frequency variations of the North Atlantic sea level measured by TOPEX/Poseidon altimetry. *Marine Geod* 28, 19–37.

Luthcke S.B. et al. (2006). Recent Greenland ice mass loss by drainage system from satellite gravity observations. *Science,* 314, 1286–1289.

Nerem, R.S. et al. (2003). Measuring the distribution of ocean mass using GRACE. *Space Sci. Rev.*, 108(1–2), 331–344.

Preisendorfer, R.W. (1988). Principal component analysis in meteorology and oceanography. Elsevier, New York.

Ramillien, G. et al. (2004). Global time variations of hydrological signals from GRACE satellite gravimetry. *Geophys. J. Int.*, 158, 813–826.

Ramillien G. et al. (2006). Interannual variations of the mass balance of the Antarctica and Greenland ice sheets from GRACE. *Global Planet. Change,* 53, 198–208.

Rangelova, E. et al. (2007). Analysis of Gravity Recovery and Climat Experiment time-variable mass redistribution signals over North America by means of principal component analysis. *J. Geophys. Res.,*112, F03002.

Rowlands, D.D. et al. (2005). Resolving mass flux at high spatial and temporal resolution using GRACE intersatellite measurements. *Geophys. Res. Lett.*, 32, L04310.

Schmidt, R. et al. (2006). GRACE observations of changes in continental water storage. *Global Planet. Change*, 50, 112–126.

Schrama, E.J.O. et al. (2007). Signal and noise in Gravity Recovery and Climate Experiment (GRACE) observed surface mass variations. *J. Geophys. Res.,*112, B0840.

Swenson, S. et al. (2003). Estimated accuracies of regional water storage variations inferred from the gravity recovery and climate experiment (GRACE). *Water Resour. Res.,* 39(8), 1223.

Tapley, B.D. et al. (2004a). GRACE measurements of mass variability in the Earth system. *Science,* 305, 503–505.

Tapley, B.D. et al. (2004b). The gravity recovery and climate experiment: mission overview and early results. *Geophys. Res. Lett.*, 31, L09607.

Velicogna I. and J. Wahr (2005). Greenland mass balance from GRACE. *Geophys. Res. Lett.,* 32, L18505.

Wahr, J. et al. (1998). Time-variability of the Earth's gravity field: Hydrological and oceanic effects and their possible detection using GRACE. *J. Geophys. Res.,* 103, 30205–30230.

Wahr, J. et al. (2004). Time-variable gravity from GRACE: First results. *Geophys. Res. Lett.*, 31, L11501.

Wagner, C.D. et al. (2006). Degradation of geopotential recovery from short repeat-cycle orbits: application to GRACE monthly fields. *J. Geod.,* 80, 94–103.

Wouters, B. and E.J.O. Schrama (2007). Improved accuracy of GRACE gravity solutions through empirical orthogonal function filtering of spherical harmonics. *Geophys. Res. Lett.*, 34, L23711.

Wu, P. (1998). Dynamics of the Ice Age earth: a modern perspective. Trans Tech Publications, Uetikon-Zuerich, Switzerland.

Chapter 74

Observed Gravity Change at Syowa Station Induced by Antarctic Ice Sheet Mass Change

K. Doi, K. Shibuya, Y. Aoyama, H. Ikeda, and Y. Fukuda

Abstract Continuous observations with superconducting gravimeters (SG) TT-70 #016 and CT#043 have been on-going since 1993 to monitor Earth tides and Earth's free oscillations at a gravity observation hut in Syowa Station, Antarctica. We obtained gravity residuals from the SG CT#043 data by subtracting Earth tides, effects of atmospheric pressure changes and polar motion, and instrumental drift from the original record. The smoothed gravity residuals obtained by taking a running mean of 33 days reveal variations from –5 to +5 μgal (10^{-8}m/s^2).

The Ice, Cloud, and Land Elevation Satellite (ICESat) was launched into high polar orbit in January 2003, and the Geoscience Laser Altimeter System (GLAS) the satellite is equipped with enables us to measure temporal volume changes across the Antarctic ice sheet. We evaluated ice sheet volume changes from changes in the topography observed by ICESat/GLAS and reduced them to mass changes by multiplying surface densities obtained by in situ measurements.

We calculated gravity changes induced by the ice sheet mass changes for 11 operation periods of ICESat/GLAS from the beginning of 2003 through the beginning of 2007. The expected gravity difference due to the ice sheet mass change is approximately 4.8 μgal in magnitude when we employ mass changes of all grid elements. The magnitude of observed gravity residuals is almost double that of the expected changes. The appearance of expected gravity changes, such as a trough pattern in 2003 is consistent with the observed changes.

K. Doi (✉)
National Institute of Polar Research, Tachikawa-shi 190-8518, Tokyo, Japan
e-mail: doi@nipr.ac.jp

74.1 Introduction

The monitoring of Antarctic ice sheet mass change is important estimating mass transport time variations of mass transport and may contribute to the prediction of future sea level changes. We have been observing temporal gravity change with SGs at Syowa Station (69°00′24.1274″ S, 39°35′08.0951″E), Antarctica since 1993. Gravity observation is one of the most effective methods to detect or monitor its mass redistribution over the Earth's surface in connection with movements of atmosphere, oceans, underground water and ice sheet as well as that of the Earth's interior. Syowa Station is located on an island close to the Antarctic continent, at a distance of about 5 km. Since a mass change in the continental ice sheet would have an effect on gravity observed at Syowa Station, we intend to detect signals associated with ice sheet mass changes in the SG record.

ICESat was launched into high polar orbit in January 2003 with orbital coverage from latitude 86°N–86°S (Zwally et al., 2003). GLAS the satellite is equipped with can measure Antarctic ice sheet topography with accuracy of ±10 cm. We can estimate ice sheet volume changes from changes in the topography observed by ICESat/GLAS. Volume change can be converted into mass change by multiplying some appropriate ice densities; thus, we can estimate gravity changes due to the changes in ice sheet mass attraction and loading.

In this study, we investigate the influences affecting Antarctic ice sheet mass changes on gravity by comparing gravity residuals observed at Syowa Station with estimated gravity change using ICESat/GLAS topography data over Antarctica.

S.P. Mertikas (ed.), *Gravity, Geoid and Earth Observation*, International Association of Geodesy Symposia 135,
DOI 10.1007/978-3-642-10634-7_74, © Springer-Verlag Berlin Heidelberg 2010

74.2 Estimation of Gravity Residuals

74.2.1 Observation

Continuous observation with a SG TT-70 #016 (hereinafter referred to as TT-70) began on March 22, 1993 (Sato et al., 1993) at a gravity observation hut (GOH) in Syowa Station. A new SG of CT type #043 with a 4-Kelvin cryocooler (hereinafter referred to as CT) was installed on a base for absolute gravity (AG) measurement in the GOH at April 18, 2003 (Ikeda et al., 2005). After parallel observation with the two SGs for about 6 months, TT-70 was replaced with CT at the end of 2003. AG measurements with two absolute gravimeters FG5 #210 and #203 were conducted for about 2 weeks in January 2004 in the AG basement by alternatively making use of the base to determine a scale factor of the CT as well as to monitor secular gravity change (Fukuda et al., 2005a; Hiraoka et al., 2005).

The records of SG CT contains a large instrumental drift, up to about 200 μgal/year, and the drift can be approached with an exponential first-order decaying function (Doi et al., 2008). Because of the large instrumental drift rate, position of the superconducting gravimeter sphere must be re-centered every year. The re-centering procedures have been conducted at the end or at the beginning of every year since 2004; therefore some jumps have yielded in the record of the SG CT relating to the re-centering procedures. Since it is not easy to estimate the size of jumps accurately, some extent of uncorrected jumps may remain in the corrected record.

74.2.2 Data Processing

We processed the data of SG TT-70 from January 1st through November 4, 2003, and that of SG CT from April 21, 2003 through January 31, 2007. The processing consisted of harmonic analysis and the estimation of effects of atmospheric pressure changes with BAYTAP-G (Tamura et al., 1991), the calculation of synthetic long period tides, the estimation of changes due to polar motion (Wahr, 1985), and the removal of instrumental drift of SG CT. Since the instrumental drift is not linear and the drift rate is gradually decreasing, we employed an exponential first-order decaying function as the fitting function. We the determined amplitude and diminishing factors of the exponential function and offset value by least squares fitting. Gravity residuals were obtained by subtracting tidal signals, atmospheric effects, polar motion effects and instrumental drift. In the calculation of long period tides, we employed tidal factors obtained by Iwano et al. (2005).

74.3 Estimation of Gravity Change Associated with Antarctic Ice Sheet Mass Change

74.3.1 Topography Change and Reduction to Mass Change

To estimate temporal change in ice sheet topography, we used ice elevation data (science data product GLA12) of 11 ICESat/GLAS observation periods from February 2003 through April 2007 (Zwally et al., 2003). We made 11 topographies for each GLAS observation period and estimated 11 topographic changes by subtracting a 500 m resolution Digital Elevation Model (DEM) for Antarctica (DiMarzio et al., 2007) from the 11 topographies. The 11 observation periods used here are indicated in Table 74.1. As an example, we show an obtained topographic change of an area surrounded by 20°E–60°E in longitude and 65°S–75°S in latitude for the acquisition period from February 17 to March 21, 2004 in Fig. 74.1. In the estimation of topographic changes, we also calculated root mean square difference for each

Table 74.1 ICESat/GLAS Acquisition periods

Period	Temporal coverage
1	2003-02-20 to 2003-03-21
2	2003-09-25 to 2003-11-18
3	2004-02-17 to 2004-03-21
4	2004-10-03 to 2004-11-08
5	2005-02-17 to 2005-03-24
6	2005-05-20 to 2005-06-23
7	2005-10-21 to 2005-11-24
8	2006-02-22 to 2006-03-27
9	2006-05-24 to 2006-06-26
10	2006-10-25 to 2006-11-27
11	2007-03-12 to 2007-04-14

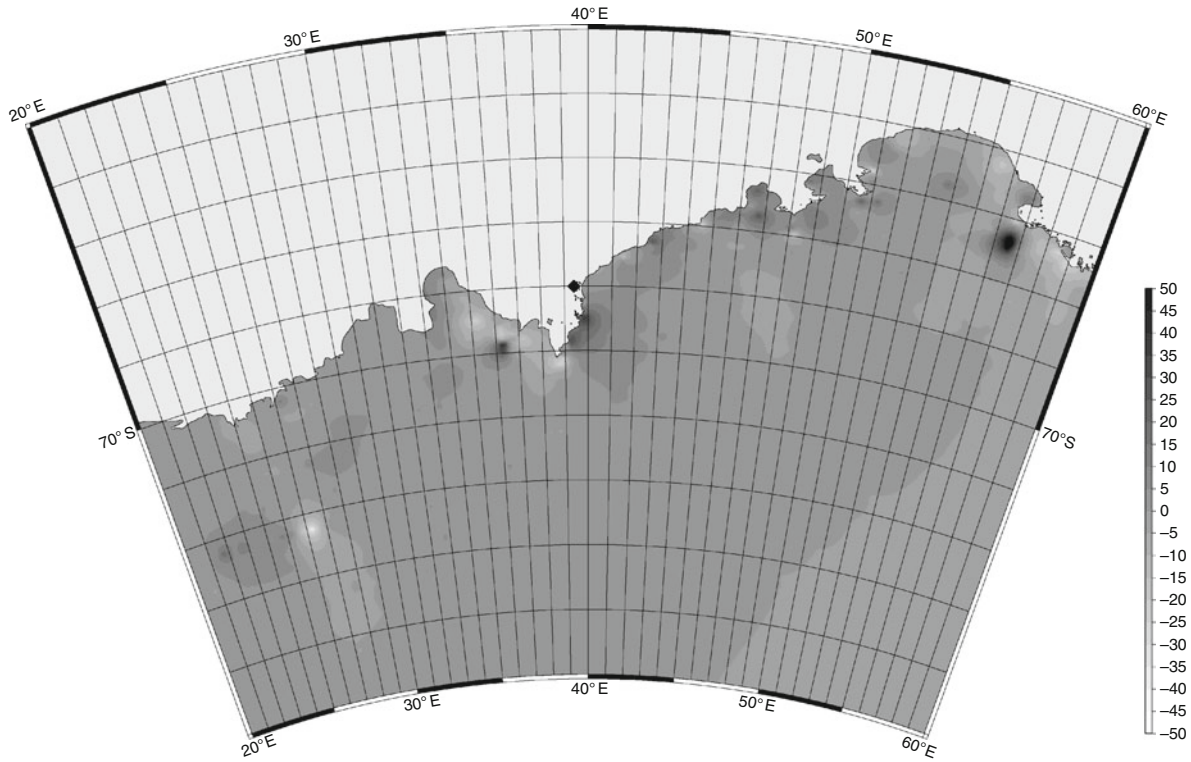


Fig. 74.1 Height Difference from ICESat/GLAS 500 m DEM of Antarctica for the Period from February 17 to March 21, 2004. The unit is m

grid element from the 11 topographic changes. The RMS values of grid elements around Syowa Station are mapped in Fig. 74.2.

Since the 11 obtained topographic changes of the entire Antarctic ice sheet are volume changes, we have to convert them into mass changes to estimate the effects on gravity. We applied the following formula to estimate accumulated snow densities ($kg \cdot m^{-3}$) at elevation h. The formulas were empirically obtained by Satow et al. (1999) based on accumulated snow densities measured during over-snow traverses in Dronning Maud Land, eastern Antarctica from 1968 to 1997.

$$\rho(h \leqq 2{,}000\,\mathrm{m}) = 0.03135h + 371.4,$$

$$\rho(2{,}000\,\mathrm{m} \leqq h \leqq 3{,}000\,\mathrm{m}) = -0.0330h + 500.0,$$

$$\rho(h \geqq 3{,}000\,\mathrm{m}) = -1.952 \times 10^{-4}h^2 + 1.221h - 1506.0.$$

The above densities were multiplied by the volume changes of the ice sheet, and mass changes in the ice sheet for the 11 periods were obtained.

74.3.2 Calculation of Expected Gravity Change

Mass changes around an observation site cause change in mass attraction, height change due to crustal deformation, and gravity potential change. These changes can be estimated in the same manner as ocean and atmospheric loading using a method proposed by Farrell (1972) that employs load Green's function. We calculated loading effects on gravity at Syowa Station using Farrell's method with loading Green's function for an Earth's structure model, PREM (Dziewonski and Anderson, 1981), given by Francis and Mazzega (1990). We made use of the position and size of each grid element used in a program for the computation of oceanic tidal loading effects, GOTIC2 (Matsumoto et al., 2001), because of the convenience in calculating loading effects and attractions of ice sheet mass.

To estimate the effects on gravity for the 11 observation periods, we performed calculations for three cases. In the first case, we estimated the effect using

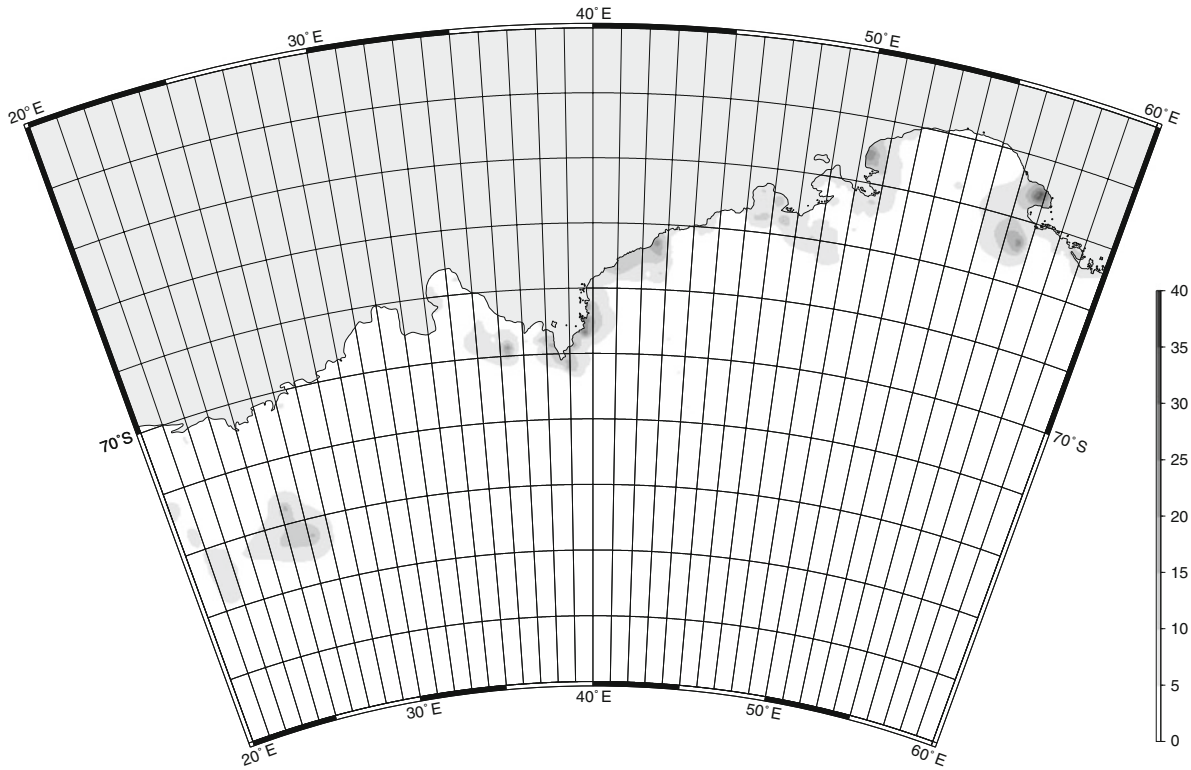


Fig. 74.2 RMS of Height Difference from ICESat/GLAS 500 m DEM of Antarctica. The unit is m

mass changes of all grid elements. In the other two cases, we used mass changes of grid elements whose RMS values are less than –30 and 15 m, and the height differences of the grid elements were replaced by averaged height difference over the entire continent of Antarctica for each ICESat observation period. The results for the three cases, as well as magnitudes of gravity variation and estimation errors, are shown in Table 74.2. The estimation errors were calculated from RMS values at each grid element. For the cases of RMS < 30 and RMS < 15 m, RMS values at the grid elements were replaced by RMS values of the averaged height differences. The expected gravity change is approximately 4.8 μgal in the period from February 2003 through April 2007, when mass changes of the all grid elements are used for the calculation.

Table 74.2 Expected gravity changes from ice sheet mass changes in μgal

Period	All	Rms < 30 m	Rms < 15 m
1	3.685	3.726	3.666
2	2.067	1.948	1.867
3	6.677	6.633	6.129
4	5.072	4.992	4.639
5	6.503	6.468	6.097
6	5.582	5.544	5.339
7	5.828	5.770	5.444
8	6.887	6.793	6.125
9	6.256	6.216	5.798
10	6.617	6.521	6.126
11	2.960	2.899	3.043
Δ g	4.820	4.845	4.262
Error	5.608	5.472	4.503

The amounts of expected gravity change for the three cases are almost equivalent and appearances of variations are also similar. (See also Fig. 74.3.) Positive expected gravity changes indicated in Table 74.2 basically correspond to ice sheet mass increase, although the magnitude of the effect at the observation site depends on the amount of mass change and the spatial distribution.

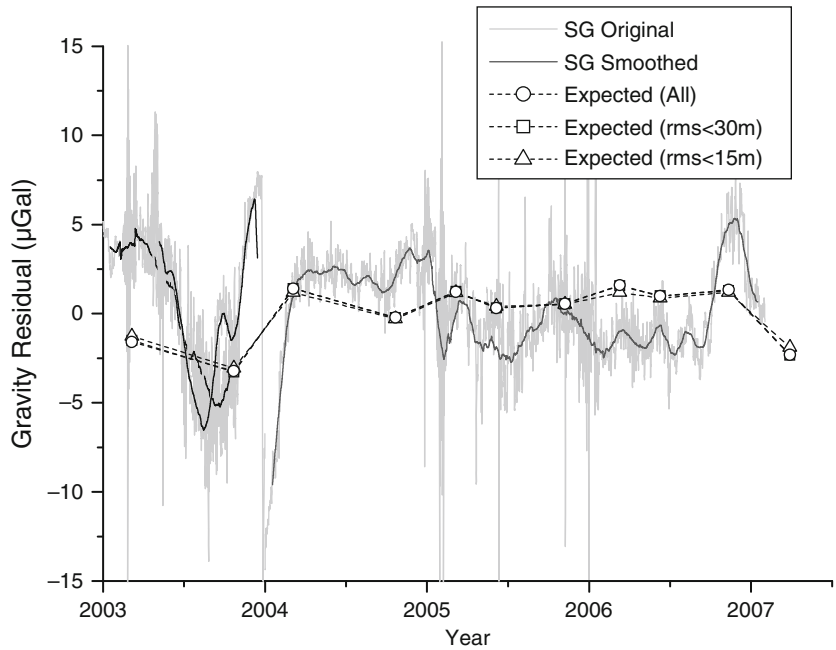


Fig. 74.3 Comparison of Observed Gravity Residuals with the Expected Gravity Changes

74.4 Comparisons of Observed Gravity Residuals with Expected Gravity Changes

Observed gravity residuals are plotted in Fig. 74.3, along with the expected gravity changes for the three cases. In Fig. 74.3, original gravity residuals for SG TT-70 and SG CT and smoothed curves are also indicated. The expected gravity changes are plotted after removing mean values. The smoothed curves were obtained by applying a 33-day running mean. The smoothed gravity residuals range from –5 to 5 μgal, while the magnitudes of expected gravity changes are almost half that of the observed ones when height differences of all grid elements are used for the calculation. We can see similar variation patterns such as the trough pattern in 2003, in both the observed gravity residuals and the expected gravity changes. The observed gravity changes in 2003 may have been induced by ice sheet mass changes. On the other hand, the observed gravity residuals from 2004 through mid-2006 reveal relatively small variations. The magnitude of the estimated gravity changes during the same period is also only 1.8 μgal.

Although we corrected for yearly jumps due to the annual re-centering in the SG CT record, incomplete jump correction may cause discrepancies in the appearance of variations.

Mass change due to non-tidal sea level changes may have an effect on gravity change at Syowa Station, although we have not corrected for the effect in the derivation of gravity residual data. Other than the influence of non-tidal sea level changes, local mass loading induced by snow drifts around the observation site may also cause gravity change. We plan to observe snow drift height change around the observation hut. We plan to investigate this local effect as well as the effect of non-tidal sea level changes in our future work. If these effects are corrected successfully, we could also discuss the influence induced by mass changes associated to runoff melt water under ice sheet.

Long-term gravity change, which is considered to be associated with Glacial Isostatic Adjustment, was observed to be –0.27 μgal/year using absolute gravity measurements at Syowa Station (Fukuda et al., 2005b). Upward displacements of 1.4–2.6 mm/year were also observed using GPS measurements at several observation sites around Syowa Station (Ozono et al., 2006). However detecting gravity changes using SG CT corresponding to these long term changes is difficult because of the large instrumental drift.

74.5 Summary

ICESat Laser altimetry data collected over the Antarctic continent enable us to estimate temporal mass changes in the Antarctic ice sheet. We estimated the temporal ice sheet mass changes using Antarctic ice sheet topographies of 11 ICESat/GLAS acquisition periods from February 2003 to April 2007 and 500 m resolution DEM of Antarctica derived from ICESat/GLAS. Gravity changes induced by the Antarctic ice sheet mass changes are estimated from obtained mass changes and the magnitude is approximately 4.8 μgal.

Gravity residuals observed by SG TT-70 and CT at Syowa Station after January 2003 were compared with the synthesized gravity changes. The observed gravity residual is almost twice the magnitude of the expected temporal gravity change. The appearance of the expected change in 2003 is consistent with the observed gravity changes, while its appearance in other periods was not as consistent. The discrepancy may be caused by mass change due to non-tidal sea level change, melt-water runoff under the ice sheet, and local snow drift around the observation site, as well as uncorrected jumps in SG records.

Acknowledgements We are grateful to all members from the Japanese Antarctic Research Expedition (JARE) 44 to JARE47 for their kind support while maintaining SG observation in Syowa Station, especially Dr. S. Sakanaka of JARE46 and Mr. K. Chida of JARE47, who made many efforts to obtain accurate gravity data in 2005 and 2006. This work was partially supported by a Grant-in-Aid for Scientific Research from the Ministry of Education, Culture, Sports, Science and Technology (No. 17540400).

References

DiMarzio, J., A. Brenner, R. Schutz, C.A. Shuman, and H.J. Zwally (2007). GLAS/ICESat 500 m laser altimetry digital elevation model of Antarctica. National Snow and Ice Data Center. Digital media, Boulder, Colorado USA.

Doi, K., K. Shibuya, H. Ikeda, and Y. Fukuda (2008). Continuous gravity observation with the superconducting gravimeter CT#043 at Syowa Station, Antarctica, Geodesy and geophysics observations in Antarctica, An overview in the IPY Perspective, A. Capra, R. Dietrich (eds.), Springer Berlin Heidelberg, pp. 237–247.

Dziewonski, A.M. and D.L. Anderson (1981). Preliminary reference Earth model (PREM). *Phys. Earth Planet. Inter.*, 25, 297–356.

Farrell, W.E. (1972). Deformation of the Earth by surface loads. *Rev. Geophys. Space Phys.*, 10, 761–797.

Francis, O. and P. Mazzega (1990). Global charts of ocean tide loading effects. *J. Geophys. Res.*, 95(C7), 11411–11424.

Fukuda, Y., S. Iwano, H. Ikeda, Y. Hiraoka, and K. Doi (2005a). Calibration of the superconducting gravimeter CT#043 with an absolute gravimeter FG5#210 at Syowa Station, Antarctica. *Polar Geosci.*, 18, 41–48.

Fukuda, Y., T. Higashi, S. Takemoto, S. Iwano, K. Doi, K. Shibuya, Y. Hiraoka, I. Kimura, H. McQueen, and R. Govind (2005b). Absolute gravity measurements in Australia and Syowa Station, Antarctica, GGSM2004, IAG International Symposium, Gravity, Geoid and Space Mission GGSM2004, C. Jekili, L. Bastos, J. Fernandes (eds.), IAG Symposia, 129, Springer, pp. 280–285.

Hiraoka, Y., I. Kimura, Y. Fukuda, K. Doi, and K. Shibuya (2005). Gravity measurements with the portable absolute gravimeter FG5 at Antarctica (III). *Bull. Geogr. Surv. Inst.*, 108, 21–27 (in Japanese).

Ikeda, H., K. Doi, Y. Fukuda, Y. Tamura, and K. Shibuya (2005). Installation of the superconducting gravimeter CT(#043) at Syowa Station, Antarctica. *Polar Geosci.*, 18, 49–57.

Iwano, S., Y. Fukuda, T. Sato, Y. Tamura, K. Matsumoto, and K. Shibuya (2005). Long-period tidal factors at Antarctica Syowa Station determined from 10 years of superconducting gravimeter data. *J. Geophys. Res.*, 110, B10403, doi:10.1029/2004JB03551.

Matsumoto, K., T. Sato, T. Takanezawa, and M. Ooe (2001). GOTIC2: A Program for computation of oceanic tidal loading effect. *J. Geod. Soc. Japan*, 47, 243–248.

Ozono, M., T. Tabei, K. Doi, K. Shibuya, and T. Sagiya (2006). Crustal movement of Antarctica and Syowa Station based on GPS measurements. *Earth Planet. Space*, 58, 795–804.

Sato, T., K. Shibuya, K. Okano, K. Kaminuma, and M. Ooe (1993). Observation of Earth tides and Earth's free oscillations with a superconducting gravimeter at Syowa Station (status report). Proc. NIPR Symp. Antarct. Geosci., 6, 17–25.

Satow K., O. Watanabe, H. Shoji, and H. Motoyama (1999). The relationship among accumulation rate, stable isotope ratio and surface temperature on the plateau of East Dronning Maud Land, Antarctica. *Polar Meteorol. Glaciol.*, 13, 43–52.

Tamura, Y., T. Sato, M. Ooe, and M. Ishiguro (1991). A procedure for tidal analysis with a Baysian information criterion. *Geophys. J. Int.*, 104, 507–516.

Wahr, J.M. (1985). Deformation induced by polar motion. *J. Geophys. Res.*, 90, 9363–9368.

Zwally H.J., R. Schutz, C. Bentley, J. Bufton, T. Herring, J. Minster, J. Spinhirne, and R. Thomas (2003). GLAS/ICESat L2 Antarctic and Greenland ice sheet altimetry data V001. National Snow and Ice Data Center, Boulder, CO.

Chapter 75

Evaluation of GRACE and ICESat Mass Change Estimates Over Antarctica

B.C. Gunter, R.E.M. Riva, T. Urban, R. Harpold, B. Schutz, P. Nagel, and M. Helsen

Abstract The goal of this study is to examine some of the many corrections and processing strategies that can have a significant influence on the ice mass change estimates computed from GRACE and ICESat mission data. These two missions, when combined, have the potential to generate new insights into the mass balance and geophysical processes of regions such as Antarctica, where such quantities are currently not well understood. Key to this combination is the identification of the major sources of uncertainty in the data processing. For the ICESat data, this includes an analysis into the calculation of the campaign biases, assumptions regarding the firn density, and a comparison between height rates derived from crossover and repeat track analysis. For the GRACE data, the focus will be on the impact of various GIA models and other a priori input values (i.e., C_{20}, geocenter motion, etc.). Comparisons with the latest data releases for both missions will be presented for the 4 year period spanning from October 2003 to October 2007. Recommendations for future work will also be discussed.

75.1 Introduction

The GRACE and ICESat missions have been collecting coincident data since 2003, providing valuable information into the mass and surface deformation changes of the Earth. The observations are particularly valuable for regions such as Antarctica, where the near-polar orbits of both satellites ensure a high density of measurements. For Antarctica, GRACE can directly observe mass changes at monthly time intervals, but the interpretation of the results is limited by the spatial resolution of the measurements (~500 km). The measurements from ICESat can also be converted to mass change estimates, with the advantage that the spatial resolution is much higher; however, as altimetry measurements, they are insensitive to subsurface mass changes. For example, a combination of accumulation and compaction can result in a zero net height change, even though a mass change may have occurred.

Other studies (Gunter et al., 2009) have shown that while the linear mass change trends computed from GRACE and ICESat data have high spatial correlations (i.e., features identified from either mission tend to be in the same geographical location and with the same sign), the actual mass change estimates were significantly different between the two missions. Much of the differences can be attributed to the various assumptions and input models used during processing. For example, GRACE by itself cannot separate the mass change due to ice loss/gain from that caused by glacial isostatic adjustment (GIA). As a result, models of the Earth's interior and of the long term global ice history must be used to remove the contribution of GIA from the total mass change signal observed from GRACE. These models are known to have large uncertainties, which will be discussed shortly.

ICESat must also rely on these same GIA models, but is less sensitive to its effects. Instead, the predominant sources of uncertainty for this data involve the computation of the campaign biases and the accurate

B.C. Gunter (✉)
Delft Institute of Earth Observation and Space Systems (DEOS), Delft University of Technology, Delft 2629HS, The Netherlands
e-mail: b.c.gunter@tudelft.nl

S.P. Mertikas (ed.), *Gravity, Geoid and Earth Observation*, International Association of Geodesy Symposia 135,
DOI 10.1007/978-3-642-10634-7_75, © Springer-Verlag Berlin Heidelberg 2010

estimation of the surface ice densities. Different processing strategies, such as using crossovers as opposed to repeat track analysis, can also impact the results.

In short, there are a number of items that must be considered for both missions. This paper will attempt to highlight some of these items, with the goal of identifying those elements that have the greatest impact on the final mass change estimates. This will be done by first discussing some of the major sources of uncertainty for each mission. Then, the results from a series of tests using mission data over a 4 year time span (October 2003 to October 2007) will be shown that will highlight how these variations can impact the mass change estimates, and potentially make the GRACE and ICESat results more consistent with each other.

75.2 GRACE

In this section, the uncertainties surrounding the mass change estimates from GRACE mission data will be discussed. This includes a treatment of the GIA models and the use of substituted coefficients for the oblateness and geocenter motion.

75.2.1 Glacial Isostatic Adjustment

For the results to be shown later, the effects of glacial isostatic adjustment (GIA) were accounted for in each GRACE solution using an incompressible self-gravitating normal modes model (Vermeersen and Sabadini, 1997) with combinations of different Earth and ice models. For comparison, two recent and widely used ice models were selected, one developed by Ivins and James (2005)(IJ05) and the other by Peltier (2004)(ICE-5G). For each ice model, the contribution of GIA was computed using a radially stratified Earth model with a viscosity jump between upper and lower mantle.

There are considerable differences between IJ05 and ICE-5G in terms of total ice load and melt history. In addition, the IJ05 model only describes ice loads over Antarctica, and does not provide information about the rest of the globe. The effect of ice loads on the Northern Hemisphere represents a significant portion of the total GIA signal observed in Antarctica. As a result, the contribution of the Northern Hemisphere was modeled separately using ICE-5G, with Earth model parameters fixed to those of VM2 (Peltier, 2004), providing surface mass changes of roughly 17 gigatons per year (Gt/year). In this way, the effect of different ice and Earth models has been limited to the GIA signal caused by Antarctic ice history. Note that future references to the IJ05 model in this paper will imply that this contribution from the Northern Hemisphere has been included.

There is a full range of Earth model parameters that can influence the final GIA contribution. To explore the impact of these choices, a range of mantle viscosities and lithospheric thicknesses were tested (again, only for loads over Antarctica). Upper mantle variations ranged from 1–10 $\times$ 10^{20} Pa·s, lower mantle variations from 1–100 $\times$ 10^{21} Pa·s, and lithospheric thicknesses from 65 to120 km. The total uncertainty introduced by these parameters, expressed in terms of Gt/year, is summarized in Fig. 75.1 for both the ICE-5G and IJ05 models. As the figure indicates, the choice of model, along with the variation of the mantle viscosities and lithospheric thicknesses, can alter the size of the GIA signal by up to 160 Gt/year (220 max – 60 min).

To limit the possibilities for the comparisons to be described in Sect. 75.4, a specific set of Earth model parameters were chosen for both the IJ05 and ICE-5G models. For ICE-5G, we used the recommended VM2 Earth model parameters. A recommended Earth model is not provided with IJ05, so the decision was made to use a slightly thinner lithosphere (100 km) and higher viscosity for the lower mantle (1 $\times$ 10^{22} Pa·s), in agreement with other previously published results (Mitrovica and Forte, 2004). In terms of mass change, the contribution of these two models over the whole continent was 172 Gt/year for ICE-5G and 123 Gt/year for IJ05. These two fixed parameter models are indicated by large grey symbols in Fig. 75.1.

75.2.2 The Influence of C_{20}

It is common practice to replace the Stokes coefficient related to the Earth's oblateness, i.e., the C_{20} spherical harmonic coefficient, with values obtained from satellite laser ranging (SLR) (Cheng and Tapley, 2008). This is because, for reasons that are currently not well understood, the current GRACE processing strategy

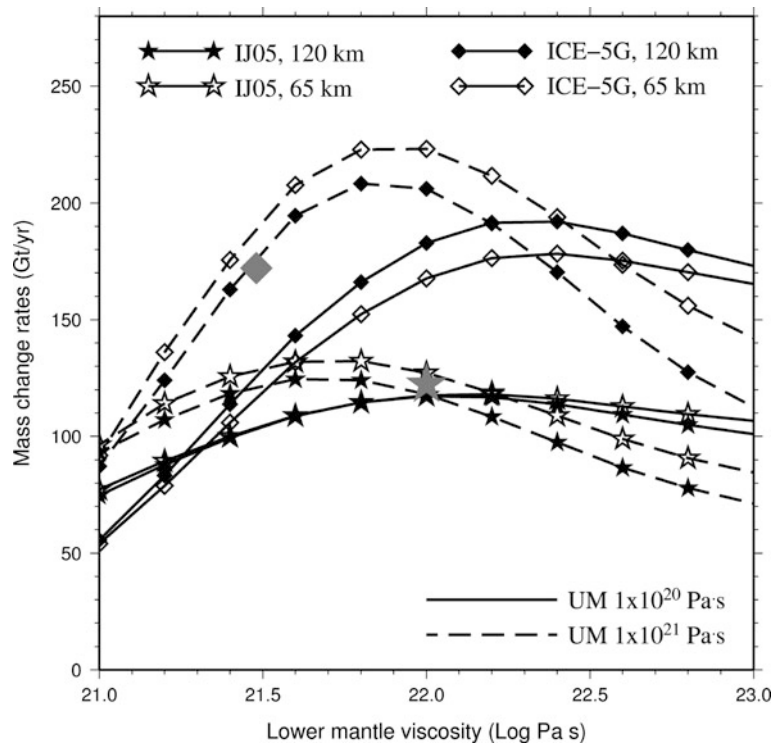


Fig. 75.1 Potential variations in the mass change contribution due to GIA for the ICE-5G and IJ05 ice models

generates C_{20} estimates that appear to be dominated by noise. For Antarctica, the C_{20} term is essentially a bias over the entire continent. The area of Antarctica is roughly 1.4×10^7 km^2, meaning that a bias error of only 1 mm of equivalent water height (or approximately 0.25 mm of geoid height, which is well below the current standard deviation for C_{20}) would translate into a mass change error of 14 Gt.

The RL04 processing standards (Bettadpur, 2007) also require that a secular rate be removed from the C_{20} term, and this rate is also derived from SLR (Cheng and Tapley, 2004). The cause of this secular rate is presumed to be a result of GIA; however, the predicted rate from roughly 20 years of SLR measurements (1.16×10^{-11}/year) is significantly less than the rate predicted from the GIA models mentioned in the previous section. For example, when using the standard VM2 Earth model parameters, the rate predicted from ICE-5G is 1.98×10^{-11}/year and from IJ05 it is 1.95×10^{-11}/year. Again, in terms of mass change, a rate change of 5×10^{-12}/year in C_{20} translates into approximately 17 Gt/year for Antarctica. This implies that the decision to use either modeled or observed C_{20} secular rates might introduce an error of up to ~30 Gt/year in the final mass change trend estimates.

75.2.3 Geocenter Motion

Another correction that should be considered when computing mass change estimates from GRACE is the influence of geocenter motion. Recent studies have shown (Davis et al., 2004; Wu et al., 2006) that excluding this correction can noticeably impact the results derived from GRACE. The correction itself is derived from the fact that the processing of the GRACE data is typically done within the context of a fixed reference frame, i.e., at a given epoch, typically J2000; however, the Earth's dynamics are in a constant state of flux, meaning that the center of mass of the Earth may change in time with respect to the center of figure of the Earth. It is this difference that can alter the mass change estimates if not taken into account.

The time series of geocenter motion (i.e., degree one spherical harmonic coefficients) used in this study were taken from Swenson et al. (2008), which are derived from comparisons with ocean models. Maximum annual variations of this time series are on the order of 1 cm equivalent water height, and a linear trend of -5 ± 21 Gt/year was estimated for

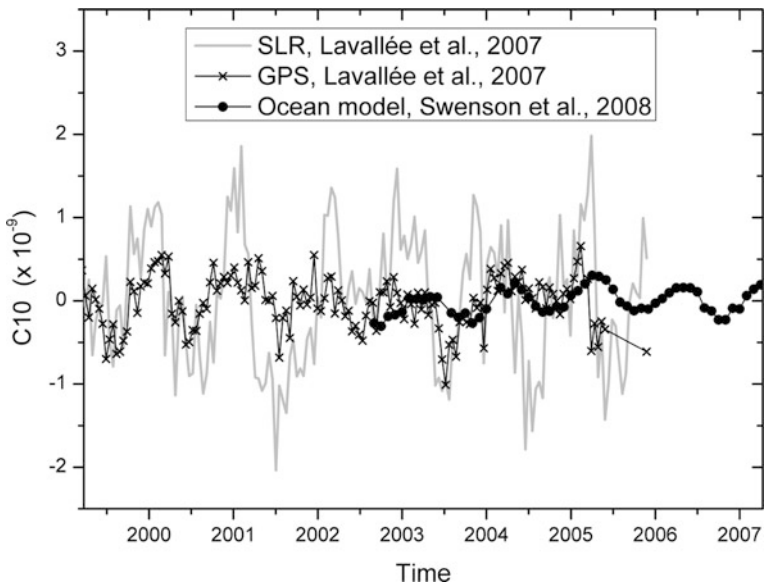


Fig. 75.2 A comparison of the C_{10} coefficient variations in times as computed through various techniques

Antarctica over the 4 year time span, demonstrating that the impact of the degree one terms is not neglible.

The reliability of any of the currently available degree one coefficients is difficult to assess with current technology. As a demonstration of this, Fig. 75.2 shows how the C_{10} coefficient time series derived from Swenson et al. compares against a similar time series derived from SLR and GPS data (Lavallée et al., 2007). The figure shows some similarities in certain time frames, in particular between the coefficients derived from GPS and ocean models, but other time frames show significant differences in both phase and magnitude. The point of this is to simply highlight that more investigations are necessary in order to come up with a reliable set of degree one coefficients. Until then, the uncertainty for these coefficients remains relatively high, which negatively impacts the mass trends computed for Antarctica.

75.3 ICESat

Having now reviewed some of the major sources of uncertainty of the GRACE data, the following discussion will now focus on those of the ICESat data. In particular, a discussion of the campaign biases, firn density models, and height rate computations. Though not covered here, one additional error source that could be important involves the irregular sampling rate of the ICESat campaigns, i.e., there are at most only three, 33-day campaigns per year. More research is needed to quantify this error, but some preliminary results can be found in Gunter et al. (2009).

75.3.1 Campaign Bias Correction

For reasons that are not currently well known, the standard processing of the ICESat heights contain a rate bias on the order of 2 cm/year. The determination of these campaign biases can be achieved through a comparison with a global mean sea surface model, as described by Urban et al. (2008). Unfortunately, this process can only examine the bias for latitudes less than 60, which is the coverage boundary of the sea surface models.

These biases represent a major source of uncertainty in the ICESat mass trend estimates, because it introduces a continent-wide height difference (much in the same way that the C_{20} coefficient biases the GRACE data). For example, a 1 cm/year rate bias translates into a ~100 Gt/year mass change trend, assuming an average density of 700 kg/m^3.

Because of the importance of accurately determining these biases, an alternate approach was devised to compute the biases in the region of Antarctica. The basic principle relies on the assumption that height changes in parts of East Antarctica are essentially

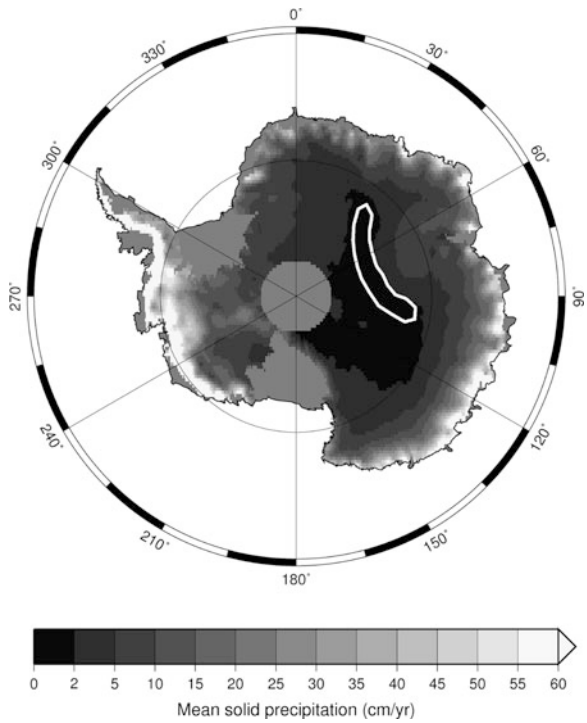


Fig. 75.3 Mean solid precipitation as derived from ECMWF operational data over the period Jan 2003 to Dec 2006. The *white outline* in East Antarctica represents the area used to compute the campaign biases

zero. This is supported by Fig. 75.3, which shows the mean solid precipitation over Antarctica based on ECMWF operational data over the period from January 2003 to December 2007. In the figure, the white outlined region in East represents the region that was used to compute the campaign biases, as this region has very little annual precipitation, i.e., it is assumed that this region undergoes zero height change. The bias computed from this region for the October 2003 to October 2007 timeframe is 2.1 cm/year for the crossover heights (see Sect. 75.3.3), which is relatively consistent with the value derived from the mean see surface models. For the repeat track data, this bias is larger at 4.7 cm/year. The potential causes for this will be discussed in Sect. 75.3.3.

75.3.2 Firn Density

The observations from ICESat can only be used to estimate volume changes over time, and can not be used directly to compute mass changes. To do this, assumptions need to be made about the density of the observed volume changes. Direct observations of these densities do not exist over the whole continent, so these quantities must be modeled using other, indirect data sources. The physical processes that determine these densities are complex and require knowledge about the accumulation and climate over the continent. Hence, the models that estimate the surface density, as well as the firn compaction, have large uncertainties. Regional changes in these density models can alter the estimated mass change trends by tens of Gt/year, and using a constant density value introduces even more error, as the total mass change depends heavily on localized density variations. It is expected that these models will improve in the future, and recent studies have been encouraging (Helsen et al., 2008). For this particular study, a modified version of the density model described by Kaspers et al. (2004) was used to ensure that the recent ice loss in the Amundsen Sea sector was accounted for (see Gunter et al., 2009 for details).

75.3.3 Repeat Track Versus Crossover

How the actual individual ICESat height measurements are processed is another important factor. The two primary options available include crossover analysis and repeat track analysis.

Crossovers tend to be more reliable, since a minimum of two interpolated measurements are used to compute each measurement point. The downside to this is that the acceptance criteria is higher, i.e., two cloud-free measurements must be available at each crossover point, reducing the total number of height measurements available. As the number of crossover points drops off rapidly as distance from the poles increases, this is an issue for the coastal regions of Antarctica, where most of the mass flux occurs.

Repeat track analysis retains more observations in the coastal areas, but suffers from larger standard deviations in the measurements. In repeat track analysis, different repeats of the same track are fit to a model, which includes parameters such as elevation change rate. The tracks from these different campaigns can be several hundreds of meters apart from each other, however, reducing the accuracy of the computed

parameters. In addition, the model chosen may not represent the region being observed very well.

While further investigation into the differences between repeat track and crossover analysis is still pending, Harpold et al. (2007) have shown that results for both techniques are comparable. Visually, the repeat track analysis tends to show greater contrast in the coastal areas, which may be due to the increased number of observations for these areas. As already mentioned, these coastal areas are where much of the ice flow takes place, so in this respect the repeat track results may hold an advantage when investigating mass change trends.

75.4 Mass Change Estimates

Using the corrections that were discussed in the previous section, mass trend estimates were computed from the GRACE and ICESat data sets over the October 2003 to October 2007 time span. This study made use of the latest release of data for each mission, i.e., RL04 for GRACE (48 months) and RL428 for ICESat (11 campaigns), both available from the Center for Space Research (CSR). For the details surrounding the processing of this data (i.e., spatial filtering, editing, etc.), see Gunter et al. (2009) and Urban et al. (2008). The results are summarized below in Table 75.1.

For the GRACE results, the primary variant was the GIA model. Other corrections were fixed to the values discussed earlier, i.e., the C_{20} values were taken from SLR, modeled rates were used for the the secular rates for C_{20} (and several other low degree coefficients), and degree 1 coefficients were included using values generated by Swenson et al. (2008). For ICESat, a modified version of Kaspers et al. (2004) density model was used, in addition to the removal of the campaign bias computed from the East Antarctica "zero" precipitation zone. Only mass changes over the grounded ice sheets were evaluated, using boundaries described by Vaughan et al. (1999).

Table 75.1 Comparison of GRACE and ICESat mass change estimates over the entire Antarctic continent for the time spanning from October 2003 to October 2007

	ICE-5G	IJ05
ICESat – RT	–97.1 Gt/year	–94.7 Gt/year
ICESat – CX	–60.2 Gt/year	–57.8 Gt/year
GRACE	–107.0 Gt/year	–75.2 Gt/year

A comparison of the values in Table 75.1 shows that the ICESat data is relatively insensitive to the GIA model used, but the values change substantially depending on whether repeat track or crossovers are used. For GRACE, it is clear the choice of GIA model is important, as there is a near 30 Gt/year difference between the two models. Depending on the choice of GIA model and ICESat processing used (i.e., crossover or repeat track), the total mass loss computed by ICESat can be larger or smaller than that predicted by GRACE. It is also interesting to note that the values derived from the repeat track analysis are much closer to the GRACE value (using ICE-5G) than the crossover results. This may be a consequence of the significantly larger bias computed for the repeat track data, or it may indicate that the repeat track data is more accurately observing the changes in the coastal regions. In either case, more rigorous investigations need to be made before any definite conclusions can be reached.

75.5 Summary

A number of corrections need to be applied when computing ice mass change trends using either GRACE or ICESat mission data. The items discussed in this paper represent some of the larger sources of uncertainty in the current data processing strategies for each mission. Some of these corrections rely on modeled quantities, such as the influence of GIA and the surface ice densities, while others can be derived from ancillary data, such as the campaign biases and C_{20} values.

In short, for each data type, there are several corrections that could each potentially alter the final computed mass trend by well over 20 Gt/year. This, of course, makes the interpretation of their combined results difficult; however, it is clear from other studies (Gunter et al., 2009) that there exists a high degree of spatial correlation between the GRACE and ICESat data sets. In this study, using variations in some of the corrections mentioned above, it was shown that the GRACE and ICESat results can indeed overlap. This implies that while the absolute trend values may not be reliable, there might exist some combination of corrections that produce consistent results for both missions. The efforts of future work will be to find this

combination of corrections that are believed to be correct and that yield these consistent results. The process of doing so may provide valuable insights into the mass balance and geophysical processes of Antarctica.

Acknowledgements Parts of this study were funded by NASA grants NAS5-99005 and NAS5-97213, as well as a grant from the Delft Earth foundation.

References

Bettadpur, S. (2007). CSR Level-2 Processing Standards Document for Product Release 04, GRACE 327-742, Center for Space Research, 3.1 ed.

Cheng, M. and B.D. Tapley (2004). Variations in the earth's oblateness during the past 28 years. *J. Geophys. Res.*, 109(B9), B09402.

Davis, J., P. Elósegui, J. Mitrovica, and M. Tamisiea (2004). Climate-driven deformation of the solid earth from GRACE and GPS. *Geophys. Res. Lett.*, 31, L24605.

Gunter, B.C., T. Urban, R. Riva, M. Helsen, R. Harpold, S. Poole, P. Nagel, B. Schutz, and B. Tapley (2009). A comparison of coincident GRACE and ICESat data over Antarctica. *J. Geod.*, doi: 10.1007/s00190-009-0323-4.

Harpold, R, T. Urban, C. Webb, and B. Schutz (2007). Assessment of ICESat repeat track estimation techniques for polar elevation change detection. *Eos Trans. AGU,*88(52), Fall Meet. Suppl., Abstract C23A-0943.

Helsen, M., M. van den Broeke, R. van de Wal, W. van de Berg, E van Meijgaard, C. Davis, Y. Li, and I. Goodwin (2008). Elevation changes in Antarctica mainly determined by accumulation variability. *Science,* 320(5883), 1626–1629.

Ivins, E.R. and T.S. James (2005). Antarctic glacial isostatic adjustment: a new assessment. *Antarct. Sci.*, 17(4), 541–553.

Kaspers, K., R. van de Wal, M. van den Broeke, J. Schwander, N. van Lipzig, and C. Brenninkmeijer (2004). Model calculations of the age of firn air across the Antarctic continent. *Atmos. Chem. Phys.*, 4, 1365–1380.

Lavallée, D., P. Moore, P.J. Clarke, Q. Zhang, and C. Hancock (2007). Low degree variation in the surface mass load from GPS and SLR. IUGG2007, Perugia, Italy.

Mitrovica J and A. Forte (2004). A new inference of mantle viscosity based upon joint inversion of convection and glacial isostatic adjustment data. *Earth Planet. Sci. Lett.,* 225, 177–189.

Peltier, W. (2004). Global glacial isostasy and the surface of the ice-age earth: The ICE-5G (VM2) model and GRACE. *Annu. Rev. Earth Planet. Sci.*, 32, 111–149.

Swenson, S., D. Chambers, and J. Wahr (2008). Estimating geocenter variations from a combination of GRACE and ocean model output. *J. Geophys. Res.*, doi:10.1029/2007JB005338.

Urban, T., R. Gutierrez, and B. Schutz (2008). Analysis of ICESat laser altimetry elevations over ocean surfaces: sea state and cloud effects, 3645, IEEE Int. Geosci. and Rem. Sens. Symp., Boston, MA, July 7–11.

Vaughan, D., J. Bamber, M. Giovinetto, J. Russel, and A. Cooper (1999). Reassessment of net surface mass balance in Antarctica. *J. Clim.,* 12(4), 933–946.

Vermeersen, L. and R. Sabadini (1997). A new class of stratified viscoelastic models by analytical techniques. *Geophys. J. Int.*, 129, 531–570.

Wu, X., M. Heflin, E. Ivins, and I. Fukumori (2006). Seasonal and interannual global surface mass variations from multisatellite geodetic data. *J. Geophys. Res.*, 111, B09401, doi:10.1029/2005JB004100.

Chapter 76

Baltic Sea Mass Variations from GRACE: Comparison with In Situ and Modelled Sea Level Heights

J. Virtanen, J. Mäkinen, M. Bilker-Koivula, H. Virtanen, M. Nordman, A. Kangas, M. Johansson, C.K. Shum, H. Lee, L. Wang, and M. Thomas

Abstract The monthly variation in the water mass of the semi-enclosed Baltic Sea is about 60 Gt RMS over an area of 390,000km^2. The Baltic has a dense network of tide gauges (TGs), and several high-resolution regional hydrodynamic models, making it one of the best-monitored seas for mass variations of this size in the world. We investigate the performance of different GRACE gravity field solutions to recover this oceanic mass variation using in situ measurements of sea-level heights. For GRACE, we use both the standard monthly solutions as well as regional solutions to estimate the total water storage in the Baltic Sea.

For the "ground truth", we use sea-level measurements in the network of tide gauges around the Baltic Sea. For comparison, we have access to data from two hydrodynamic models. The water mass estimated from the constructed sea surfaces is then compared with different GRACE estimates. At present, we ignore the steric anomalies, as they are small in the Baltic Sea. We also discuss the "leakage" between land hydrology and the Baltic Sea in the GRACE estimates of water storage.

76.1 Introduction

The sea-level variations in semi-enclosed Baltic Sea have been monitored in several complementary ways for more than a century (Novotny et al., 2006). The Baltic has a dense network of tide gauges (TGs), and several altimetry missions (like TOPEX/Poseidon, ERS-1/2, ENVISAT) have provided observations over the region. Moreover, several high-resolution oceanographic models have been developed for forecasting purposes as well as for studying different physical and biological phenemena. Covering an area of some 390,000km^2, the Baltic can be considered to be one of the best-monitored seas for mass variations of this size in the world. Now the satellite gravity mission GRACE (Tapley et al., 2004) provides a method to directly measure the total water mass variability in the Baltic.

The GRACE mission has provided global solutions for Earth gravity field since mid-2002. The standard data products are monthly spherical harmonics (SH) coefficients that can be used to make global estimates of mass variations. GRACE has been used to study ocean mass variation from global (Chambers et al., 2004) to regional scales, e.g., by Kuo et al. (2008) in the Southern Ocean. Fenoglio-Marc et al. (2006) analyse the mass variation in the Mediterranean Sea, a semi-enclosed basin with an area of 2.5 million km^2, while Swenson and Wahr (2007) carry out a similar study for the smaller Caspian Sea (areal extent of 436,000km^2, comparable to the Baltic). Both use satellite altimetry as independent in situ measurements and find good agreements between the two data products.

We investigate the capability of GRACE to recover the mass variation in the Baltic on monthly scale. We make use of two different regional solutions based on the GRACE K-band microwave ranging (KBR) measurements alongside the standard monthly gravity fields. As in situ measurements, we use tide gauge recordings of sea-level variations. In addition we make use of two hydrodynamic models of the Baltic Sea for

J. Virtanen (✉)
Finnish Geodetic Institute, Masala FI-02431, Finland
e-mail: jenni.virtanen@fgi.fi

S.P. Mertikas (ed.), *Gravity, Geoid and Earth Observation*, International Association of Geodesy Symposia 135,
DOI 10.1007/978-3-642-10634-7_76, © Springer-Verlag Berlin Heidelberg 2010

verification and optional patching of the TG data as well as for estimating the contribution of steric effects to observed sea-level variations.

The paper is organized as follows. In Sect. 76.2, we describe the different data sets used and the processings steps needed. In Sect. 76.3, we present the results while Sect. 76.4 is left for discussion.

76.2 Data and Processing

76.2.1 GRACE Mass Variation

We use three GRACE gravity field solutions to estimate water storage changes. First, we use the standard level-2 Release-4 monthly solutions from the Center for Space Research at the University of Texas (CSR). Second, we use two regional solutions, one from Ohio State University (OSU) and another from NASA's Goddard Space Flight Center (GSFC).

The CSR gravity field solutions consist of monthly sets of SH coefficients. The coeffiecients can be converted to equivalent water thickness as described in Swenson and Wahr (2002). We use the gravity solutions to degree and order 60 and apply Gaussian filtering to reduce the effect of errors in high-degree coefficients. We use an averaging kernel for the Baltic Sea constructed by convolving a 400 km half-width Gaussian function with the mask of the Baltic Sea area (Fig. 76.1).

In the pre-processing of the GRACE level-2 data, the non-tidal oceanic and atmospheric effects have been removed using the AOD1B de-aliasing product (Flechtner, 2007). In Release 4, the product includes a contribution for the Baltic Sea, which needs to be restored for this study. We use the output from the GRACE ocean dealiasing model OMCT, Ocean Model for Circulation and Tides (Thomas and Dobslaw, 2004), which is the oceanic part of AOD1B product. After removing the effect of the atmosphere (i.e., surface pressure), we convert the monthly-averaged ocean bottom pressure (OBP) fields over the Baltic Sea to SH coefficients, which are added back to the GRACE coefficients.

For comparison, we include two regional GRACE solutions to this study. The OSU solutions are based on in situ disturbance potential measurements derived

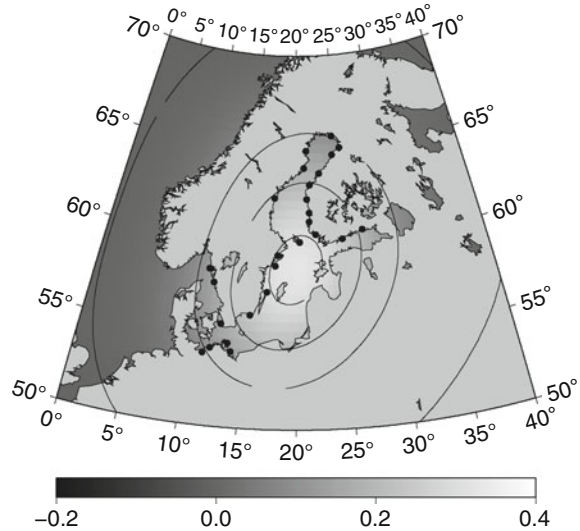


Fig. 76.1 The Baltic area and the Gaussian averaging kernel used for basin averages of water mass variations. Locations of the PSMSL TG stations from which data is used are marked with *black dots*

directly from GRACE KBR data via the energy conservation method (Han et al., 2005). The spatial resolution of the monthly solutions is 220 km. The AOD1B de-alising product has been applied when processing the KBR data, so we make use of the SH coefficients computed from the OMCT grids to restore the removed signal, see Sect. 76.3. NASA has made available the mass concentration (mascon) solutions described by Rowlands et al. (2005). Their 10-day solutions are based on defining differential SH coefficients in small blocks of 4 by 4°(see http://grace.sg-inc.com). The mascon solutions contain an inverse barometer (IB) correction for the Baltic Sea (Luthcke personal comm 2008 unication), which has been restored using the air pressure grids from HIRLAM (High Resolution Limited Area Model). Finally, monthly averages have been computed to be consistent with the other GRACE data sets.

76.2.2 Baltic Sea Variation

The mass variation in the Baltic Sea is due to both internal redistribution of the water mass and due to changes in the so-called fill level caused by water

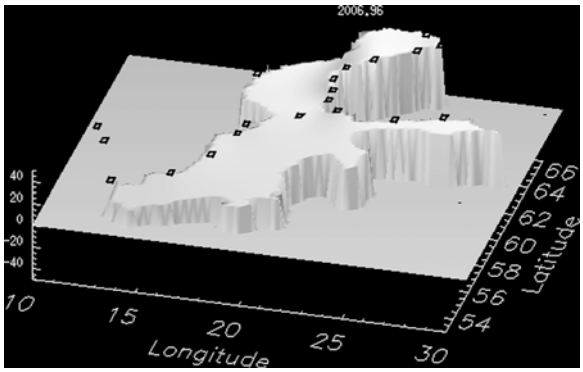


Fig. 76.2 Smooth sea surfaces are created by fitting the monthly PSMSL sea-level data, here December 2006 (showing the stations used).

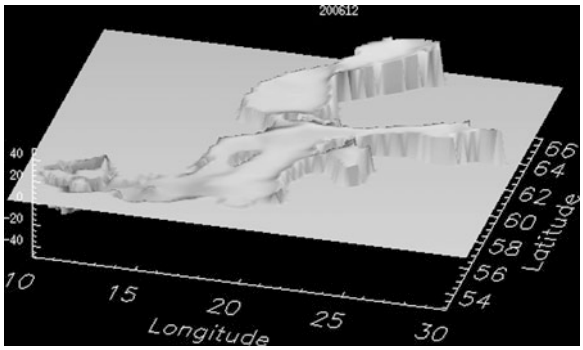


Fig. 76.3 Sea surface obtained by averaging from hourly sea-level predictions of the Baltic model "Wetehinen", December 2006

exchange with the North Sea through the Danish Straits. Both changes are driven mainly by atmospheric pressure and wind (Myrberg et al. 2006). Monthly variation in the fill level can be up to 0.8 m with an rms of 0.15 m. As the total area of the Baltic is 390,000km^2, these sea-level variations correspond to approximately 300 and 60 km^3 in total water volume, respectively.

We estimate sea-level anomalies using monthly TG data from the Permanent Service for Mean Sea Level (PSMSL; Woodworth and Player, 2003) as ground truth. During the analysed time span from 2003 to 2006, the number of TG stations for which data was available varied from 22 to 26 depending on the month (see Fig. 76.1; data is available with a delay of several months, here as of March 2008). Monthly series of sea surfaces are created by fitting minimum-curvature-surface splines to the PSMSL sea level heights at TGs (for an example, see Fig. 76.2). Before this, a reference value for each TG is subtracted. The reference value is the intercept (at the epoch 2000.0) of the regression line through the whole length of the TG record. The sea surface relative to these reference values can always be described by a very smooth function, which minimizes the influence of missing data points.

In addition we make use of two hydrodynamic models, the global OMCT model and the Baltic model "Wetehinen". OMCT was described in the previous section, while Wetehinen is a high-resolution water-level forecasting model from the Finnish Meteorological Institute (Kangas, 2007). The TG interpolation scheme might suffer from coastal effects and give biased heights at the open sea. Using Wetehinen we could check that while this may be true at hourly-daily timescales, for monthly data the effects are negligible (Fig. 76.3). Wetehinen might also be used to patch the TG surfaces over areas which have little or no data. However, on monthly scales we found that no patching was necessary.

The PSMSL data give us variation in volume while GRACE detects the variation in mass. Thus, we need to estimate the steric contribution to the sea level variation in order to compare the two. OMCT model provides 3-dimensional fields of temperature and salinity, so we esimate steric anomalies by computing the difference between the OMCT sea level and reduced OBP fields (effect of atmosphere removed). As shown

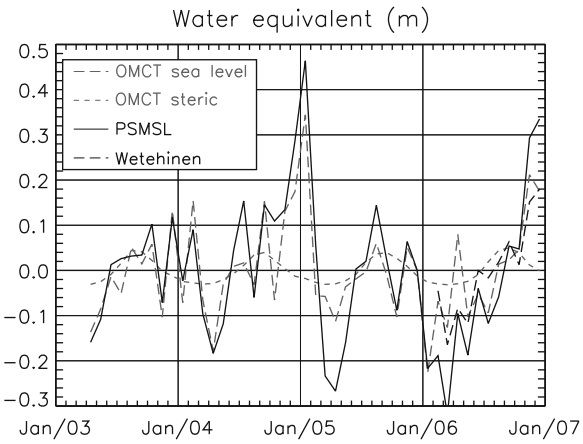


Fig. 76.4 Total water storage estimates for the Baltic. The effect of steric anomalies is estimated from OMCT model as a difference between sea level and ocean *bottom pressure* grids, and is found to be small. No steric correction is thus applied at present

in Fig. 76.4, the basin average of the OMCT steric contribution has an annual peak-to-peak amplitude of $\sim 8\,cm$. The value is comparable to 5 cm estimated in Myrberg et al. (2006) for the Baltic Sea, and globally the annual steric amplitude is also generally below 10 cm (Dobslaw, personal communication, 2009). But since the amplitude is only $\sim 10\%$ of the peak-to-peak amplitude of the total sea-level variation, the thermosteric sea level or correction is omitted in the present study as a small effect (also C.Y. Kuo, personal communiation, 2008).

76.2.3 Continental Hydrology

When GRACE data is used to study specific regions, the SH series representation combined with spatial averaging causes the mass estimates to be contaminated by signals outside the region.

In our earlier GRACE studies (Virtanen et al., 2007, Bilker-Koivula et al., 2007) we have seen that Baltic Sea is a major source of mass variation in the area. The amplitude of monthly variability for the Baltic Sea is $\sim$ 80 cm peak-to-peak (see Fig.76.2) while that of the total water storage variation over Finland, a similar-sized area, is $\sim$ 12 cm (Bilker-Koivula et al., 2007). When the extent of the region is close to the smoothing radius, as is the case for the Baltic, the signal leakage between regions (from land to sea, or vice versa) can be a major problem. This is particularly true for the leakage of the Baltic signal to terrestrial hydrology estimates, and in the future, we will study the performance of the GRACE background models in removing this leakage.

To remove the signal leakage from land to the Baltic Sea, we derive estimates of the surrounding mass variability by using different hydrological models:

- GLDAS - Global Land Data Assimilation System (Rodell et al., 2004)
- CPC - Climate Prediction Center (Fan and van den Dool, 2004)
- WSFS - Watershed Simulation and Forecasting System (Vehviläinen et al., 2005).

The WSFS model contains all components of terrestrial water storage (e.g. soil moisture, groundwater, surface water, snow) and covers the land area of Finland including cross-boundary watersheds. Also the GLDAS data contains snow and has shown good agreement when compared with the WSFS model over Finland. The CPC is a soil-moisture model only, but its thick "leaky bucket" layer is capable of accounting partly for snow and groundwater as well. For futher improvement, the CPC subgrids over Finland have been patched with the high-resolution WSFS model.

76.3 Results

To estimate water storage variations in the Baltic Sea, we use the different data sets to compute time series of basin averages from April 2003 (start date for GSFC data) to December 2006. Spatial averaging is carried out as described by, e.g., Swenson and Wahr (2002). For the gridded data sets (GSFC and OSU solutions, as well as PSMSL data), we apply an exact kernel to the water mass grids: value of 1 in the Baltic, 0 elsewhere. Both GRACE solutions are first interpolated to denser grids to gain better accuracy. For GRACE CSR solutions, the approximate kernel shown in Fig. 76.1 (Gaussian 400 km filter) is applied. As described in Sect. 76.2.1, we have first restored the oceanic variation for the Baltic Sea to all three GRACE solutions. For OSU solutions, the derived SH coefficients for the OMCT data were processed to basin averages using the same approach than for the GRACE CSR data above (assuming perhaps conservatively a smoothing radius of 400 km), and the two time series were added up.

Since the filtering needed for the GRACE solutions causes part of the true signal to leak outside the area of interest, the computed timeseries are not directly comparable. We have derived a scaling factor of 0.25 for the CSR solution by applying the same approximate kernel to a uniform layer of water in the Baltic Sea. Although the regional GRACE solutions should better describe the signal solely from the area of interest, they also are not completely free of signal leakage. Thus, we have defined a scaling factor of 0.5 for the GSFC and OSU solutions experimentally by comparing the time series to the PSMSL data. In Fig. 76.5, the GRACE time series have been upscaled by the scaling factors (i.e. multiplied by 1/0.25 or 1/0.5) to match the observed PSMSL variation. In addition, each GRACE time series is detrended using regression

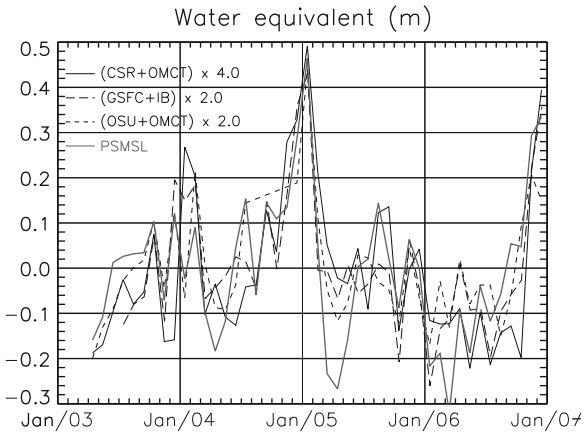


Fig. 76.5 Total Baltic water storage, estimates based on different GRACE solutions. The timeseries for regional solutions, OSU and GSFC, agree best with ground truth (here PSMSL). Note that all GRACE solutions suffer from signal contamination from land hydrology to some extent

to remove long-term variability (such as post-glacial rebound).

For the CSR solutions, we can estimate the contribution of hydrological signal from surrounding land due to filtering. The gridded land hydrology data is converted to spectral domain, filtered and computed back to equivalent water through basin averaging. Fig. 76.6 illustrates the reduction step by step: (1) the Baltic signal removed during pre-processing is restored to the original data using the OMCT model ("CSR+OMCT"), (2) leakage from surrounding land areas is corrected for by removing water mass

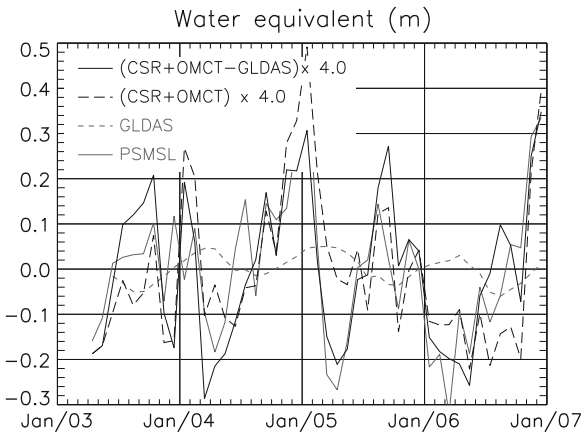


Fig. 76.6 Basin averages of water mass anomalies in the Baltic Sea computed from GRACE CSR gravity field solutions. Leakage from land is corrected by the GLDAS hydrology model, reduction of the GRACE solutions is described in the text.

Table 76.1 Cross-correlation coefficient in Column 2 describes the phase correlation between the different GRACE solutions in Column 1 and the ground truth (PSMSL TG estimate). Column 3 gauges the goodness of the prediction of monthly variation in Baltic mass by the GRACE estimates. The number given is the fraction of the variance of the PSMSL TG estimate they explain. Column 4 gives the rms residual of the PSMSL TG estimate as a water column after subtracting the prediction. For comparison, the rms of the PSMSL signal is 0.16 m.

GRACE estimate	Cross-corr.	Explained variance	Rms (m)*
CSR+OMCT	0.70	0.53	0.137
OSU+OMCT	0.83	0.68	0.118
GSFC+IB	0.79	0.70	0.115
CSR+OMCT-GLDAS	0.79	0.57	0.133
CSR+OMCT-CPC	0.81	0.55	0.135

*Multiply the water column in metres by 390 to get the mass in gigatons.

estimates computed from the land hydrology models (here, "CSR+OMCT-GLDAS", similar result was obtained using CPC).

To compare the agreement between the different GRACE solutions and our in situ ground truth (Figs. 76.5 and 76.6), we compute some statistical measures which are given in Table 76.1. First, we compute the root-mean-square (rms) values for the residual time series ("ground truth minus GRACE"). The smaller the number, the better the prediction. For comparison, we give the rms of the ground truth, i.e., the PSMSL signal (0.16 m). Next, we estimate the ability of the different GRACE solutions to predict the monthly variation in Baltic mass. First, we compute linear cross-correlation coefficients between the GRACE and PSMSL time series. But as the correlation is indifferent to the scale of the GRACE estimate, we also estimate the fraction of the variance of the ground truth explained by the GRACE predictions ("explained variance"). This is given by: $r^2 = 1 - \mathrm{var(PSMSL\text{-}GRACE)/var(PSMSL)}$, where *var* is the variance. The higher the number, the better the prediction.

76.4 Discussion

All our GRACE solutions recover the water mass variation in the Baltic Sea to some extent, while the time series of the regional estimates, OSU and GSFC, agree

most closely with the observed sea-level variations. Their residual rms values are close to 11 cm as compared to 14 cm for the CSR solution, and some 70 % of the observed variance of PSMSL is explained. For the CSR, the comparison is somewhat worse but agreement in phase improves considerably after correcting for the signal leakage using hydrological models, as can be seen from the cross-correlation values of 0.70 and 0.79, respectively (for GLDAS; see Table 76.1). The poor agreement in amplitudes manifested by the relatively large rms values for all GRACE solutions are most likely due to the small areal extent and complex shape of the studied geographical region, showing that the Baltic Sea is probably close to the limit of detection for GRACE. Another factor that may complicate the recovery of the Baltic variation is the surrounding hydrological signal, which is partly out of phase with the Baltic signal (Fig. 6, see also the discussion in Klees et al. (2008)). The plausibility of these explanations is the subject to further studies.

The OSU and GSFC solutions (OSU+OMCT, GSFC+IB) are at present comparable with the CSR without the leakage correction (CSR+OMCT), but a similar correction can be applied for them too. Preliminary results (not shown here) indicate that improvement can be achieved in agreement for both phases and amplitudes. Leakage correction for the regional solutions will be studied in more detail in the future.

As for the ground truth data, we find that mass variations on monthly scales can be well described by surfaces fitted to tide gauge measurements alone. We found the contribution of steric anomalies to be small for the present study, but yet not negligible. The steric effects will be studied further, as they are needed also for satellite altimetry which we plan to include in the analysis in the future.

We will also address the leakage of the Baltic signal to GRACE estimates for land water due to the averaging process required for the standard gravity field solutions. As seen from Fig. 76.4, there are discrepancies between OMCT model and in situ data. We will test the different Baltic data to find the best way to correct for this leakage.

Acknowledgements Funded by the Academy of Finland (decision numbers 117094 and 116426). The OSU research is partially supported by NASA and the Ohio State University Climate, Water and Carbon program. The authors would like to thank the Finnish Environment Institute (Dr. B. Vehviläinen) for providing the WSFS models and Finnish Meteorological Institute (Dr. M. Kangas) for the HIRLAM data. The GRACE Level 2 data products are provided by UT/CSR, and the mascon solutions by NASA/GSFC.

References

Bilker-Koivula, M., J. Virtanen, H. Virtanen, J. Mäkinen, and M. Tervo (2007). Analysis of GRACE monthly gravity field models using water storage time series. In: *Proceedings of XXIII Geophysics Days*, Oulu, Finland, May 23–24, p.6.

Chambers, D.P., J. Wahr, and R.S. Nerem (2004). Preliminary observations of global ocean mass variations with GRACE. *Geophys. Res. Lett.* 31, 13310.

Fan, Y. and H. van den Dool (2004). The Climate Prediction Center global monthly soil moisture data set at 0.5° resolution for 1948 - present. *J. Geophys. Res.* 109, D10102, doi:1029/2003JD004345.

Fenoglio-Marc, L., J. Kusche and J. Becker (2006). Mass variation in the Mediterranean Sea from GRACE and its validation by altimetry, steric and hydrologic fields. *Geophys. Res. Lett.*, 33, L19606, doi:10.1029/2006GL026851.

Flechtner, F. (2007). GRACE 327-750 (GR-GFZ-AOD-0001) Gravity Recovery and Climate Experiment. AOD1B product description document for product releases 01 to 04 (Rev. 3.1, April 13).

Han, S.C., C.K. Shum, C. Jekeli, and D. Alsdorf (2005). Improved estimation of terrestrial water storage changes from GRACE. *Geophys. Res. Letters*, 32, L07302.

Kangas, A. (2007). Itämeren vedenkorkeuden mallinnus kaksiulotteisella hydrodynaamisella mallilla (in Finnish). In: *Proceedings of XXIII Geophysics Days*, Oulu, Finland, May 23–24, p.6.

Klees, R., E.A. Revtova, B.C. Gunter, P. Ditmar, E. Oudman, H.C. Winsemius, and H.H.G Savenije (2008). The design of an optimal filter for monthly GRACE gravity models. *Geophys. J. Int.,* 175, 417–432.

Kuo, C., C. Shum, J. Guo, Y. Yi, A. Braun, I. Fukumori, K. Matsumoto, T. Sato, and K. Shibuya (2008). Southern Ocean Mass Variation Studies Using GRACE and Satellite Altimetry, *Earth Planet. Space*, 60, 1–9.

Myrberg, K., M. Leppäranta, and H. Kuosa (2006). Itämeren fysiikka, tila and tulevaisuus (in Finnish). Yliopistopaino, Helsinki, p.202.

Novotny, K., G. Liebsch, A. Lehmann and R. Dietrich (2006). Variability of sea surface heights in the Baltic sea: an intercomparison of observations and model simulations. Mar Geod. 29, 113–134.

Rodell, M., P.R. Houser, U. Jambor, J. Gottschalck, K. Mitchell, C.-J. Meng, K. Arsenault, B. Cosgrove, J. Radakovich, M. Bosilovich, J.K. Entin, J.P. Walker, D. Lohmann, and D. Toll (2004). The global land data assimilation system. *Bull. Amer. Meteor. Soc.* 85(3), 381–394.

Rowlands D.D, S.B. Luthcke, S.M. Klosko, F.G.R. Lemoine, D.S. Chinn, J.J. McCarthy, C.M. Cox, and O.B. Andersen (2005). Resolving mass flux at high spatial and temporal resolution using GRACE intersatellite measurements. *Geophys. Res. Lett.* 32, L04310.

Swenson, S. and J. Wahr (2002). Methods of inferring regional surface-mass anomalies from Gravity Recovery and Climate Experiment (GRACE) measurements of time-variable gravity. *J. Geophys Res.,* 107, 2193, doi: 10.129/2001JB000576.

Swenson, S. and J. Wahr (2007). Multi-sensor analysis of water storage variations of the Caspian Sea. *Geophys. Res. Lett.* 34, L16401.

Tapley, B.D., S. Bettadpur, M. Watkins, and C. Reigber (2004). The gravity recovery and climate experiment: Mission overview and early results. *Geophys, Res. Lett.,* 31, L09607, doi: 10.1029/2004GL019920.

Thomas, M. and H. Dobslaw (2004). On the impact of baroclinic ocean dynamics on the Earth's gravity field . In: *Proceedings of Joint CHAMP/GRACE Science Team Meeting 2004*, p.6.

Vehviläinen, B., M. Huttunen, and I. Huttunen (2005). Hydrological forcasting and real time monitoring in Finland: The Watershed Simulation and Forcasting System (WSFS). In: *Intern. confer. on innovation advances and mplementation of flood forecasting technology*, Tromso, Norway, 10p.

Virtanen J., J. Mäkinen, M. Bilker-Koivula, and H. Virtanen (2007). Itämeren korkeuden vaihtelun vaikutus GRACE-painovoima-aikasarjaan (in Finnish). In: *Proceedings of XXIII Geophysics Days*, Oulu, Finland, May 23–24, p6

Woodworth, P. and R. Player (2003). The Permanent service for mean seal level: an update to the 21st century. *J. Coas. Res.*, 19(2), 287–295.

Chapter 77

Water Storage in Africa from the Optimised GRACE Monthly Models: Iterative Approach

E. Revtova, R. Klees, P. Ditmar, X. Liu, H.C. Winsemius, and H.H.G. Savenije

Abstract Water storage variability in southern Africa and particularly in the Zambezi river basin is evaluated using optimally smoothed GRACE gravity field models recently developed at Delft University of Technology. Poor availability and low quality of hydrological in situ data make independent GRACE estimates valuable for hydrological modeling.The output of available hydrological models in the target areas is therefore used for the quantification of the sample correlation and the main discrepancy between the water storage estimates from GRACE and hydrology. Moreover, an attempt to identify the main sources of the discrepancy is made.The results of the study show the maximum sample correlation between optimal water storage estimates from GRACE and from the Lumped Elementary Watershed (LEW) regional hydrological model in the North and North-East of the Zambezi river basin. The maximum discrepancy of about 0.025 m between the mean water storage variations over the Zambezi river basin from LEW and GRACE has been observed in spring, when the water storage is the largest.The estimated signal leakage (bias) caused by the optimal filtering is practically negligible when compared with the GRACE estimates produced by other research centers, though it is considerable for hydrological applications and would require a bias correction for areas smaller then $0.5 \cdot 10^6 km^2$.A large discrepancy between LEW regional hydrological models of release 2008 (LEW-R2008) and 2006 (LEW-R2006) has been unexpectedly observed, especially in fall 2004 and spring 2005. This finding is presumably related to the use of the suspected higher quality of TRMM rainfall data with respect to FEWS rainfall data, respectively.It is finally concluded that the optimal GRACE estimates can be beneficially used to constrain regional hydrological models for their further improvement.

E. Revtova (✉)
Department of Earth Observations and Space Systems, Delft University of Technology, Delft, The Netherlands
e-mail: e.Revtova@tudelft.nl

77.1 Introduction

Launched in 2002, the Gravity Recovery and Climate Experiment (GRACE) satellite mission designed to collect gravimetric observations is considered as an extremely valuable tool to monitor mass transport within the Earth's system. Already for 6 years different research centers have been processing GRACE data to obtain highly accurate monthly gravity field models.

Processing and analysis of GRACE data have been complicated by the presence of various sources of noise distorting the results (particularly, at high spatial frequencies). To get a reasonable mass transport estimate one typically applies a simple isotropic low-pass filter. Unfortunately such an approach introduces an additional error (under- or overestimation of mass transport signals by $\sim 50 - 70\%$, Klees et al., 2007). With the new time series of GRACE monthly models and their normal matrices obtained at DEOS (Delft institute of Earth Observations and Space Systems, Liu, 2008) it became possible to develop and apply procedures for global and regional optimal filtering (Klees et al., 2008).

The filter is constructed iteratively from GRACE data itself. Such a filtering can be applied in two ways: (i) as a regularization in the least square adjustment of the GRACE level-1 data or (ii) as a post-processing

S.P. Mertikas (ed.), *Gravity, Geoid and Earth Observation*, International Association of Geodesy Symposia 135,
DOI 10.1007/978-3-642-10634-7_77, © Springer-Verlag Berlin Heidelberg 2010

of the GRACE Level-2 data. In practice, the second approach is preferred as it is easy to implement and does not require a multiple re-processing of the Level-1 GRACE data. Full signal and noise variance-covariance matrices are used in the post-processing.

The purpose of this paper is to estimate the water storage variations in Africa using the new optimally filtered monthly GRACE DEOS models and compare them with the available regional and global hydrological models. Particularly, it is important to assess discrepancies among the models and analyse the possible sources of the discrepancies using the following approaches: (1) sample correlation analysis among the models; (2) comparisons with rainfall data; (3) estimating the bias (signal leakage) caused by the filtering.

77.2 Methodology on the Optimal Filter Design

The optimal filter designed in the study seeks to minimize a clearly-defined objective function. Suppose that f is the mass change function (expressed in units of equivalent water height) and f_w is the filtered mass change unction; furthermore, $\hat{f}$ and $\hat{f}_w$ are the corresponding quantities as inferred from GRACE data. We assume that all these functions are defined on the surface of the mean Earth sphere σ_R with radius R. Consequently, f is related to f_w in the following way:

$$f_w(x) = \frac{1}{4\pi R^2} \int_{\sigma_R} f(y) W(x,y) \mathrm{d}\sigma_R(y); \qquad (1)$$

where $W(x,y)$ is the filter function, and x and y denote points on the sphere. The same relation exists between the estimates $\hat{f}_w$ and $\hat{f}$. The most general filter function is a two-point function, which can be represented in terms of surface spherical harmonics as follows:

$$W(x,y) = \sum_{l,m} \sum_{p,q} W_{lm,pq} \bar{Y}_{l,m}(x) \bar{Y}_{p,q}(y); \qquad (2)$$

where l and p stand for a spherical harmonic degree; m and q denote a spherical harmonic order, $\bar{Y}_{l,m}$ and $\bar{Y}_{p,q}$ are the 4π-normalized surface spherical harmonics, and $W_{lm,pq}$ are the spherical harmonic coefficients of the filter. The filter function $W(x,y)$ is (i) anisotropic as it depends on both degree and order, and (ii) non-symmetric with respect to the points x and y.

To determine the filter coefficients, a wide range of objective functions can be used. The filter we design minimizes the global mean of the mean-square error (MSE):

$$\mathrm{MSE}_{\mathrm{ave}} = \frac{1}{4\pi R^2} \int_{\sigma_R} E(f - \hat{f}_w)^2 \mathrm{d}\sigma_R, \qquad (3)$$

where E is the statistical expectation operator. In other words, we minimize the difference between the actual (unfiltered) mass change f and the filtered estimation of mass change $\hat{f}_w$. Thereafter, we call this filter the optimal Anisotropic Non-Symmetric (ANS) filter. One can show that the minimizer of $\mathrm{MSE}_{\mathrm{ave}}$ is

$$W = D(C + D)^{-1} \qquad (4)$$

where W is the matrix composed of the filter coefficients in such a way that each pair of indices (l,m) corresponds to a particular row of W; C is the full noise variance-covariance matrix of the spherical harmonic coefficients of the estimated mass change function $\hat{f}$; and D is the signal variance-covariance matrix associated with the spherical harmonic coefficients of the mass change function f.

77.3 Procedure

According to the methodology presented above, monthly optimal filters can only be designed if both the error and signal covariance matrices are available. We derive both matrices from GRACE data itself. In general, the filtering procedure can be outlined as follows:

As input, we use the GRACE monthly models and their normal matrices obtained at DEOS (Liu, 2008) for the period February 2003 - February 2006 ($N_m =$ 36 months, except June 2003) taking the degrees and orders from $lmin = 2$ to $lmax = 70$ (except: January, June, July and September 2004 and December 2005, for which $lmax = 50$; and June 2006 for which $lmax = 60$).

First, we iteratively filter GRACE monthly gravity solutions with a simultaneous estimation of signal covariance matrix:

1. The signal variance-covariance matrix D is built in the spatial domain as a diagonal matrix (the signal is assumed to be uncorrelated in the spatial domain). At the initialization phase, we assume that the signal variance in the continents L^2 and in the oceans O^2 is constant, and defined as $L = 5$cm and $O = 0.75$cm, respectively. Then, the signal variances are propagated into the domain of spherical harmonics and a proper degree-dependent scaling is applied (refer to Klees et al, 2008 for more details).
2. The monthly ANS filters $W_{lm,pq}$ are designed with Eq. (4), the full error covariance matrix C being obtained by the inversion and a proper re-scaling of the normal matrix of the given month.
3. The ANS filters obtained under (2) are used to smooth the DEOS GRACE monthly models which are then stored in terms of Stokes coefficients.
4. The sets of filtered Stokes coefficients are interpreted as monthly signals and used in the next iteration to re-define the signal covariance matrix D as described under (1). Notice that only one signal covariance matrix D is built from n_m monthly solutions.

   The procedure is repeated until the rms difference between the filtered solutions at two successive iterations reaches the level 0.0035m (being 10% of the standard deviation of the GRACE solutions) in terms of water storage.

Finally, we use the optimally filtered GRACE models to reconstruct the regional water storage variations in the target areas (southern Africa and the Zambezi river basin, cf. Fig. 77.1).

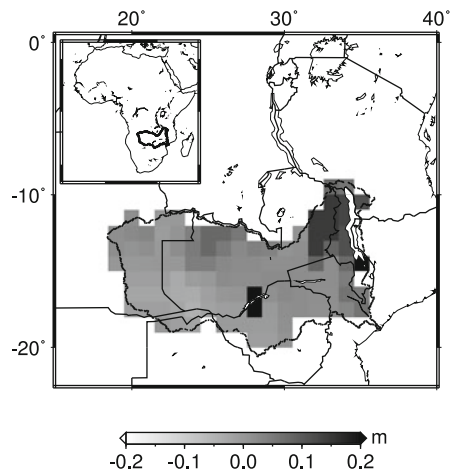


Fig. 77.1 LEW-R2008 model output in terms of water storage variaions in April 2005 in the Zambezi river basin (southern Africa)

77.4 Hydrological Modeling

There are two types of hydrological models used in the study: Global Land Data Assimilation System (GLDAS), which is a global hydrological model (Rodell et al., 2004) and regional LEW (Winsemius et al., 2006). Both models are of resolution $0.5° \times 0.5°$.

The output of GLDAS global hydrological model is used for the estimation of water storage variation in the target areas and sample correlation analysis, while the regional hydrological model LEW was additionally used for the bias computation.

The variant of the LEW model used in this study is release LEW-R2008, which covers the Zambezi river basin (area $\sim 1.3 \times 10^6 \text{km}^2$). It is an updated version of the LEW-R2006 model covering the territory of southern Africa by Winsemius et al., 2006a. The LEW-R2008 model has been forced with the rainfall product TRMM (Simpson et al., 1996), while the FEWS RFE 2.0 (Famine Early Warning System) rainfall product has been used to force the LEW-R2006 model (Winsemius et al., 2006b).

The LEW approach has some advantages with respect to global hydrological models since it enables the implicit incorporation of redistribution of surface runoff in downstream located model units, called LEWs, that represent e.g. a wetland, lake or man-made reservoir.

77.5 Results

Water storage variations in Africa have been computed from DEOS GRACE optimally filtered solutions (DEOS-ANS) for the period February 2003 – February 2006 (cf. top left plot in Fig. 77.2 for April 2005). For a comparison, the estimates produced from the destriped and smoothed with simple isotropic 400-km Gaussian filter DEOS GRACE solutions (DEOS-DSG400), LEW-R2006 regional and GLDAS global hydrological models are also given in the Figure. A 400-km Gaussian filter is chosen as the water storage

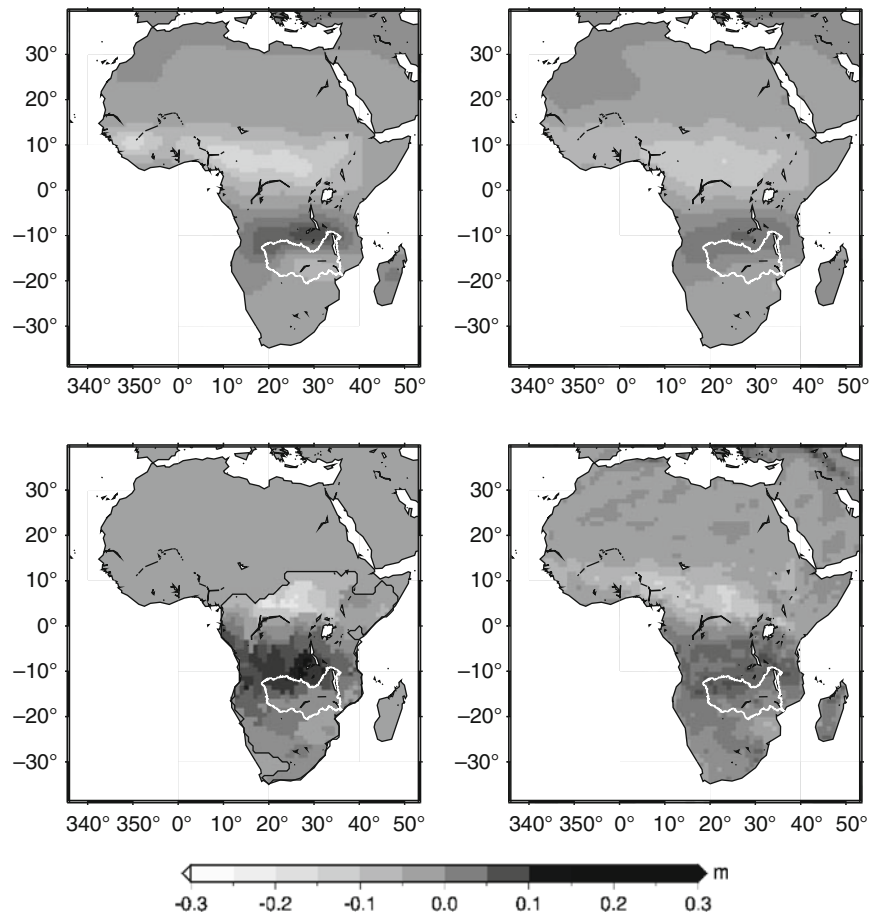


Fig. 77.2. Water storage variations for April 2005 in Africa from: (i) Top: (left) "GRACE, DEOS-ANS", (right) "GRACE, DEOS-DSG400"; (ii) Bottom: (left) "LEW-R2006, Africa", (right) "GLDAS, global"

estimates from GRACE smoothed with such a filter fit best to those from the LEW-R2006 model and from the optimally filtered GRACE.

The areas with large water storage variations are present in all the plots of Fig. 77.2, though a difference in the amplitudes and spatial distribution is observed. The amplitude from GRACE DEOS-ANS is the closest to one from LEW-R2006. GLDAS and DEOS-DSG400 estimates have lower spatial resolution and much lower amplitudes, which has been observed for all the monthly estimates.

In general the DEOS-ANS global solution shows a significantly stronger signal, especially in the areas where the intertropical convergence zone moves over Africa (along the equator).

A qualitative indication of whether this signal is in fact a physically present phenomenon, can be obtained when 1 month of accumulated rainfall data from TRMM in the intertropical convergence zone in Africa is compared to the difference between 2 consecutive monthly GRACE solutions. An example for the period between March 16th, 2005 and April 15th, 2005 is given in Fig. 77.3. Accumulated rainfall data suggests a strong mass change signal along the equator, particularly around Lake Victoria and north of the Zambezi river basin, which is indeed clearly visible in the global DEOS-ANS solution, however, local rainfall is likely to cause an increase in the local storage which will not always be present in GRACE monthly mean water storage variation estimate.

The time series of the mean water storage variations from GRACE, GLDAS and LEW-R2008 over the Zambezi river basin for the same time period are given in Fig. 77.4. For a better comparison, the yearly sine functions have been fit through the time series of each model. The amplitudes of the yearly sine functions (A) differ among the models, but clearly the DEOS-ANS estimates with $A = 0.093$m/year are

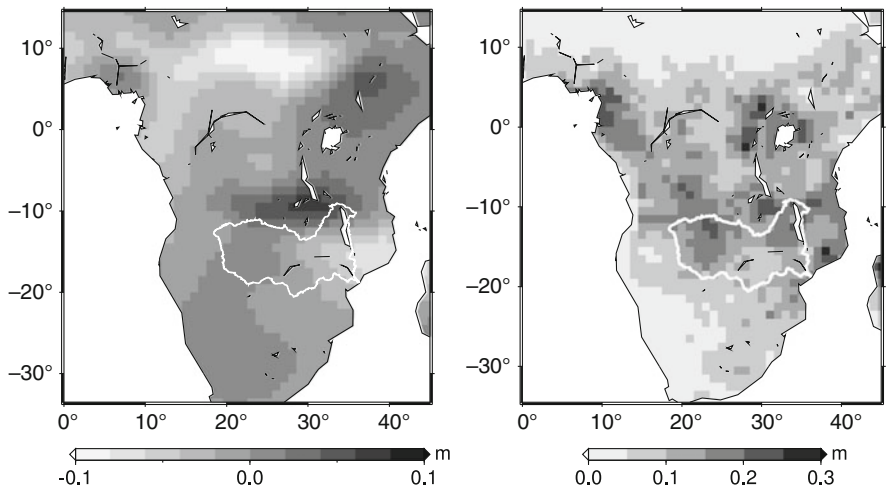


Fig. 77.3 Water storage change estimates from GRACE DEOS-ANS solution (left) and TRMM accumulated rainfall data (right) between March and April 2005.

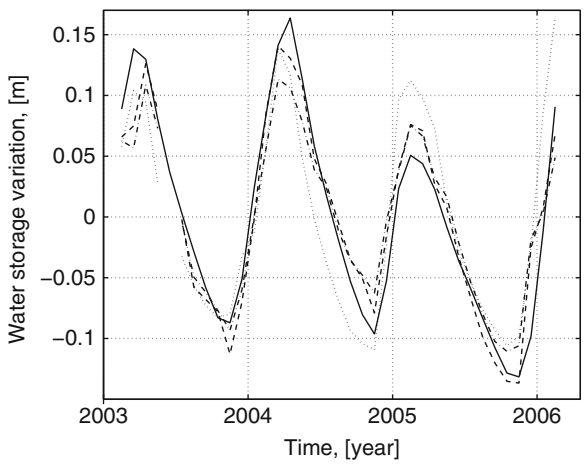


Fig. 77.4 The monthly mean water storage variations in the Zambezi river basin from:(*solid*) LEW-R2008; (*dotted*) GLDAS; (*dashdot*) DEOS-DSG400; (*dashed*) DEOS-ANS

Table 77.1 Standard deviations of the differences between the water storage estimates from LEW and GLDAS, LEW and GRACE DEOS-DSG400, and LEW and GRACE DEOS-ANS in [m]

Model	LEW-R2006	LEW-R2008
GLDAS	0.026	0.043
DEOS-DSG400	0.040	0.030
DEOS-ANS	0.036	0.024

closer to LEW-R2008 ($A = 0.095 rmm/year$) than to GLDAS with $A = 0.103 rmm/year$. At the same time GLDAS has the largest amplitude while DEOS-DSG400's amplitude $A = 0.079 rmm/year$ is the smallest.

We have also estimated the standard deviation of the differences between the time series of both LEW-R2006 and LEW-R2008, and the models DEOS-ANS, DEOS-DSG400 and GLDAS. It is worth mentioning that the best fit to LEW-R2006 is given by the GLDAS model with $std = 0.026$m while to LEW-R2008 by the DEOS-ANS solution with $std = 0.024$m. The standard deviations for all the models are given in the Table 77.1. To assess the ANS filter performance we have also smoothed the LEW-R2008 with the ANS filter, and estimated the mean water storage variations in the Zambezi river basin and the bias caused by this filtering procedure (refer to Klees et al., 2008). For a comparison, we have also destriped and smoothed LEW-R2008 with 400-km Gaussian filter (DSG400),

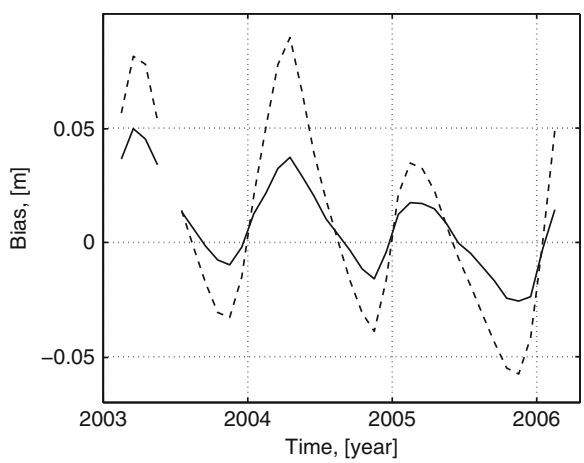


Fig. 77.5 The bias estimates caused by different filtering techniques applied to LEW-R2008 in the Zambezi river basin: (*dashed*) Destriping + Gaussian 400 km; (*solid*) ANS filtering

and then estimated the mean water storage variation and the bias caused by these procedures.

ANS filtering causes much smaller bias (~ 2 times) in the obtained estimates than DSG400, which is clearly seen from Figure 77.5. Moreover, it is found that the bias strongly depends on the size of the area: the smaller the area, the larger the bias, thus for the areas less then $0.5 \times 10^6 \text{km}^2$ it is advised to apply a bias correction.

To validate and compare the models, the time series of spatially distributed water storage variations obtained from GRACE, LEW and GLDAS have been used to make the correlation analysis. To this end, the "sample correlation coefficients" $R(i)$ per each grid point (i) between LEW and GRACE, as well as between LEW and GLDAS, have been estimated, both in the Zambezi river basin and in southern Africa. In doing so, we used the following expression:

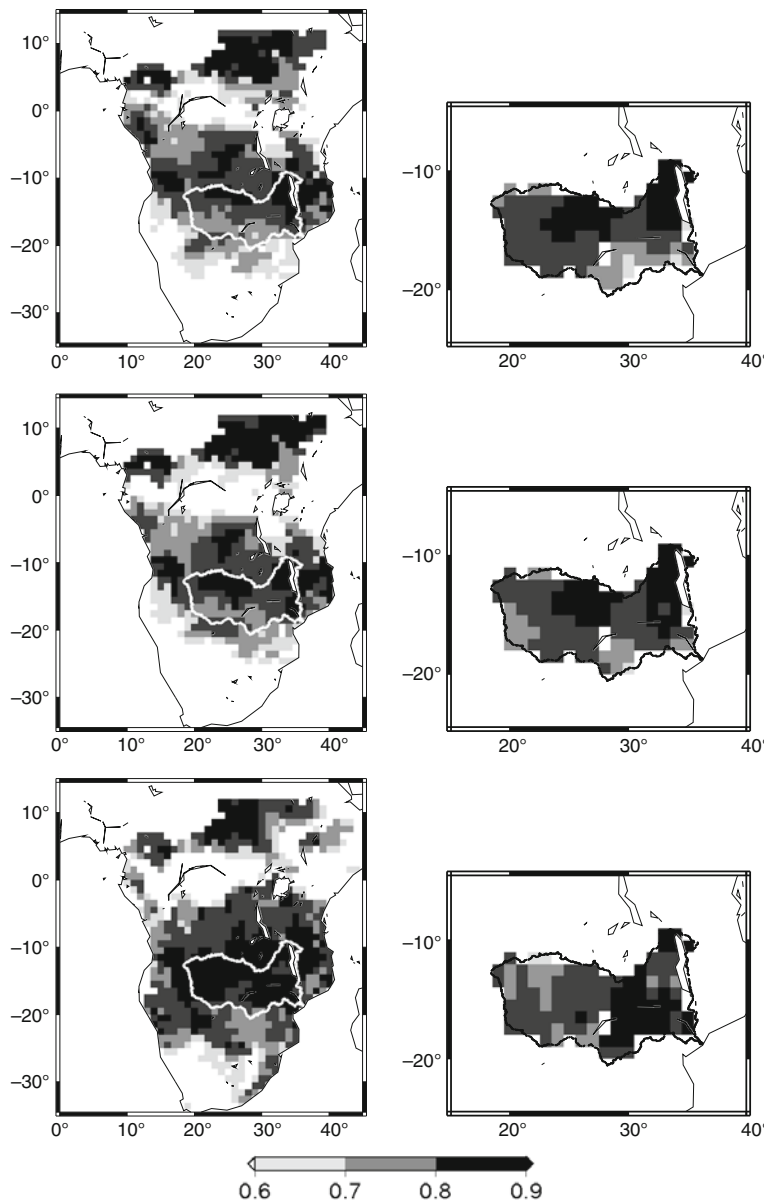


Fig. 77.6 The "sample correlation coefficients" in southern Africa and the Zambezi river basin between regional hydrological model LEW-R2006 (left column)/ LEW-R2008 (right column) and: (top) "GRACE, DEOS-ANS"; (middle) "GRACE, DEOS-DSG400" (bottom) "GLDAS, original";

$$R^i = \frac{\sum_{t=1}^{T} (S1_t^i - \bar{S1}^i)(S2_t^i - \bar{S2}^i)}{\sqrt{\sum_{t=1}^{T} (S1_t^i - \bar{S1}^i)^2 \sum_{t=1}^{T} (S2_t^i - \bar{S2}^i)^2}} \quad (5)$$

where $S1_t^i$ and $S2_t^i$ are the time series $t = \{1{:}T\}$ of water storage variations from the considered models, and $\bar{S1}^i$ and $\bar{S2}^i$ are their means, respectively.

The results of the correlation analysis are shown in Fig. 77.6. Note that for the correlation analysis in southern Africa the LEW-R2006 hydrological model is used, while for the Zambezi river basin - LEW-R2008.

The close consideration of the correlation fields shows that:

(i) in the Zambezi river basin the high correlation coefficients between 0.8 and 1.0 are observed mostly in the North, while lower 0.65 – 0.8 in the South. This effect can be explained by the limited discharge data available for the LEW model calibration. Moreover, some grid points have very low correlation (e.g. in Fig. 77.6, right column, at 17°S, 28°E) caused by the high storage anomaly in the man-made lake Kariba when compared to the natural surroundings.
(ii) there is a large discrepancy between LEW-R2006 and LEW-R2008 in the Zambezi basin (also seen in correlations between LEW and GLDAS). Such a result could be explained by the different rainfall data used as input to force the LEW models of different releases (see Sect. 77.4).
(iii) very low correlations are observed on the border between the positive and negative water storage variation.
(iv) in Africa large correlations are observed in the areas with high rainfall.

Items (iii) and (iv) can be clarified by the presence of local rainfall events visible in LEW but not reflected in the GRACE monthly mean estimates, and hardly visible in the output of the GLDAS global hydrological model.

77.6 Conclusions

The optimal filter is a powerful tool to extract maximum information from monthly GRACE solutions. The filter is designed iteratively from GRACE data itself, without the use of any a priori information. Consequently, the water storage estimates are obtained completely independently of hydrological models.

The optimally filtered GRACE DEOS models (DEOS-ANS) show a remarkable improvement when compared to traditional models (e.g. destriping + Gaussian filter 400 km) in terms of both annual amplitudes and preservation of spatial resolution.

The bias caused by the optimal ANS filtering is significantly smaller than in the case of the traditional model post-processing, which reduces the need for a bias correction, though it is advised to apply a bias correction for both the target areas smaller then $0.5 \times 10^6 \text{km}^2$ and hydrological applications.

The highest correlation between GRACE and hydrology in the Zambezi river basin is observed in the north of the area. Overall in southern Africa higher correlation is observed in the areas with large water storage variation and rainfall events, which is related to the particular rainfall data used to force the model.

The areas with more pronounced water storage variations, observed in GRACE, are also visible in TRMM rainfall data as the areas with localized high rainfall amounts. This gives confidence in the quality of the optimally filtered GRACE estimates.

Lower correlation in the south of the Zambezi can be explained by the limited discharge data available for the calibration of the LEW model.

A large discrepancy is observed between LEW-R2006 and LEW-R2008 in the Zambezi, especially in spring of 2005. Most probably, this is caused by uncertainties in the rainfall data used to force the models.

In the future, GRACE-based water storage estimates can be used to constrain hydrological models, which will probably reduce the influence of such uncertainties.

Acknowledgements The support of the project by the Dutch Organization for Scientific Research (NWO) and the Water Research Center Delft (WRCD) is greatly acknowledged

References

Klees, R., E.A. Revtova, B.C. Gunter, P. Ditmar, E. Oudman, H.C. Winsemius, and H.H.G. Savenije, (2008). The design of an optimal filter for monthly GRACE gravity models. *Geophys. J. Int.*, 175(2),417– 432.

Klees, R., E.A. Zapreeva, H.C. Winsemius, and H.H.G. Savenije, (2007). The bias in GRACE estimates of continental water storage variations. *Hydrol. Earth Syst. Sci.*, 11, 1227–1241. http://www.hydrol-earth-syst-sci.net/11/1227/2007/hess-11-1227-2007.html.

Liu, X. (2008). Global gravity field recovery from satellite-to-satellite tracking data with the acceleration approach. *PhD thesis, Delft University of Technology*.

Rodell, M., P.R. Houser, U. Jambor, J. Gottschalck, K. Mitchell, C.J. Meng, K. Arsenault, B. Cosgrove, J. Radakovich, M. Bosilovich, J.K. Entin, J.P. Walker, D. Lohmann, and D. Toll, (2004). The Global Land Data Assimilation System. *Bull. Am. Meteorol. Soc.*, 85,381–394.

Simpson, J., C. Kummerow, W.K. Tao, and R.F. Adler, (1996). On the tropical rainfall measuring mission (TRMM). *Meteorol. Atm. Phy.*, 60,278–295.

H.C. Winsemius, H.H.G. Savenije, A.M.J. Gerrits, E.A. Zapreeva, and R. Klees, (2006a). Comparison of two model approaches in the Zambezi river basin with regard to model confidence and identifiability. *Hydrol. Earth Syst. Sci.*, 10,339–352.

Winsemius, H.C., H. H.G. Savenije, N. van de Giessen, B. van de Hurk, E.A. Zapreeva, and R. Klees, (2006b). Assessment of Gravity Recovery and Climate Experiment (GRACE) temporal signature over the upper Zambezi. *Water Resour Res*, 42,W12201.

Chapter 78

Estimating Sub-Monthly Global Mass Transport Signals Using GRACE, GPS and OBP Data Sets

M.J.F. Jansen, B.C. Gunter, R. Rietbroek, C. Dahle, J. Kusche, F. Flechtner, S.-E. Brunnabend, and J. Schröter

Abstract In an effort to learn more about the sub-monthly variations in the global mass transport processes of the Earth, a study has been performed in which the feasibility of using weekly GRACE gravity solutions, in combination with GPS displacement data and ocean bottom pressure (OBP) models, is examined. A sensitivity study was conducted in which a range of solutions using different combinations of these three data sets were compared to each other, and with the time span of each combination ranging from 1 to 4 weeks. Data sets included weekly GFZ RL04 GRACE covariance matrices, as well as IGS GPS solutions and a new FESOM global OBP model, developed at AWI. The results showed that the temporal resolution of the solutions could be increased, while still maintaining reasonable levels of accuracy, if either GPS or OBP data were included in the combination. In particular, a 2-week triple combination of GRACE, GPS and OBP data was found to have approximately the same accuracy over land as a standard monthly GRACE solution, up to degree and order 30. These results provide encouraging support for future work involving real-data combinations.

78.1 Introduction

For over 5 years now, GRACE (Gravity Recovery and Climate Experiment) has been providing the scientific community with highly accurate gravity field models. These models can be used to learn more about temporal variations in the gravity field and related mass transport on and within the Earth. The GRACE gravity fields are given in spherical harmonic coefficients from degree 2 to degree 60 or higher. In addition, these solutions are typically released at monthly intervals, as this time frame is needed for the ground track coverage to become sufficiently dense enough to generate high quality solutions, i.e., mass changes with uncertainties of 2 cm or less in terms of equivalent water height (EWH), at spatial scales of approximately 400 km Schmidt et al., 2008. Unfortunately, for most end users, this limits the observation of mass transport variations to those that occur at time scales greater than 1 month. If signals less than 1 month are desired, one option is to simply create GRACE solutions at sub-monthly intervals; however, this usually comes at the price of reduced accuracy and spatial resolution. One partial solution to this, which is explored in this study, is the potential benefit of combining sub-monthly GRACE solutions with other data sets in an effort to maintain the solution accuracy at these higher temporal resolutions.

In an effort to learn more about the sub-monthly variations in the global mass transport processes of the Earth, a sensitivity study has been performed in which weekly GRACE gravity solutions from August and December 2006 are combined with solutions derived from GPS displacement data and modelled ocean bottom pressure (OBP) data. Because the GPS and OBP data sets represent a series of fixed points on the Earth's surface, their spatial coverage does not change with time like the GRACE ground tracks. As a result, the combination of these data sets with GRACE is not expected to significantly improve the spatial resolution of the solution; however, their inclusion should,

M.J.F. Jansen (✉)
Delft Institute of Earth Observation and Space Systems, Delft, TU, The Netherlands
e-mail: M.J.F.Jansen@tudelft.nl

S.P. Mertikas (ed.), *Gravity, Geoid and Earth Observation*, International Association of Geodesy Symposia 135,
DOI 10.1007/978-3-642-10634-7_78, © Springer-Verlag Berlin Heidelberg 2010

at a minimum, improve the temporal resolution and accuracy of the low degree signals.

This article will first explain the different data sets involved and how they can be used to estimate the mass transport at the Earth's surface. In the following section, the methods that were used to examine the different combinations will be explained. Thereafter, the results coming from these different methods will be shown. Finally the article will close with the conclusions and a discussion about future work.

78.2 Data Sets

To perform the combination, the three data sets are transformed into spherical harmonics representing the total surface load.

$$\Delta\sigma(p) = a\rho_{\mathrm{w}} \sum_{l=0}^{L} \sum_{m=0}^{l} C^{\sigma}_{lm} Y^{\mathrm{C}}_{lm}(p) + S^{\sigma}_{lm} Y^{\mathrm{S}}_{lm}(p)$$

where Y_{lm} are the fully normalized spherical harmonics and the superscripts $^{\mathrm{C,S}}$ stands for cosine or sine. The indices l,m represent the degree and order of the spherical harmonics, with the maximum degree of the solution given by L. The argument p represents a point on the Earth surface. The variables C^{σ}_{lm},S^{σ}_{lm} are the spherical harmonic coefficients for surface mass loading, given in dimensionless quantities. The mean radius of the Earth is represented by a, and ρ_{w} is the density of water (1,025kg/m^3 in this study). Throughout this article, the surface loading is expressed in terms of EWH by dividing $\Delta\sigma$ with ρ_{w}. Here, EWH stands for a layer of water with variable thickness that will give the same pressure on the Earth surface as the loading it represents. In this section, it is explained how the data sets are used and inverted into spherical harmonics.

78.2.1 GRACE Weekly Data

For the covariance study presented here, the GRACE data products selected consisted of a pair of 4 sequential weekly normal equation matrices provided by the GeoforschungsZentrum (GFZ). The first 4 weeks came from August 2006, which was a month that was known to perform well compared to other solutions (i.e., based on a comparison of calibrated errors from the various monthly solutions). The second four weeks were taken from December 2006, and included 1 week in which measurement errors or data availability were worse than usual. With respect to the other weeks, this bad week has a cumulative degree error at degree 30 which is twice as large as normal (6.4 cm versus 13.3 cm). These normal equation systems were generated according to the same release level 04 (RL04) processing standards as the standard monthly solutions (Schmidt et al., 2008); however, their solution space was shortened from degree 150 to degree 60 by fixing the gravity parameters from degree 61 to 150. As these covariance matrices represent formal error propagation, using these matrices directly in our study would have resulted in an overly optimistic contribution of GRACE to the combination. To overcome this problem, the matrices were scaled using the calibrated standard deviations given with the monthly solutions. First, the four weekly normal matrices were combined and inverted into a covariance matrix, corresponding to one monthly combination. The factors between the diagonal elements of this covariance matrix, and their corresponding calibrated standard deviations coming from the GFZ monthly solution, were calculated. These factors were used to scale the weekly normal matrices to a more reasonable value. Finally, the geoid coefficients had to be transformed into loading using the following relation, given in Wahr et al. (1998),

$$C^{\mathrm{g}}_{lm} = \frac{3\rho_{\mathrm{w}}}{\rho_{\mathrm{e}}} \frac{(1+k'_l)}{2l+1} C^{\sigma}_{lm}$$

where the k'_l are the elastic loading Love numbers which give the ratio between the loading potential and the resulting gravitational potential caused by the elastic response of the Earth, and ρ_{e} is the average density of the Earth. The two top plots in Fig. 78.1 show the projection of the two calibrated monthly covariance matrices on the Earth surface.

78.2.2 GPS Station Positions

For the GPS contribution, weekly solutions of the station coordinates were used from the publicly available International GNSS Service (IGS) products. Stations which had suspicious time steps were removed or when stations did not have a continuous operating

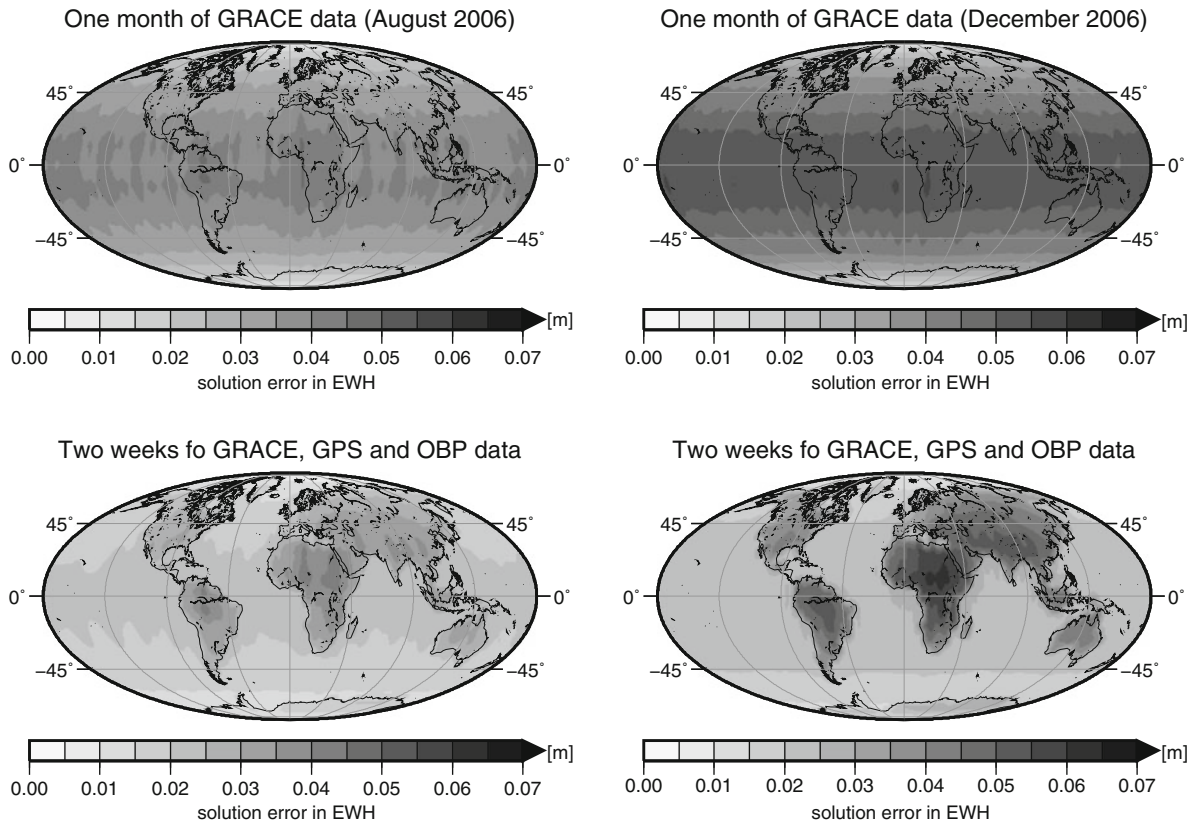


Fig. 1 Error in EWH for solutions computed from data having both good (August 2006, *left column*) and bad (December 2006, *right column*) error characteristics. The *top plots* show a GRACE-only solution using 1 month of data. The *bottom plots* show a combination of GRACE with OBP and GPS using 2 weeks of data. For all solutions, the spherical harmonic from degree 2 to 30 were included

period greater than 1 year, resulting in about 180 reliable sites. Data snooping was also performed using a 3-sigma rule, by generating a global solution up to degree 7 and then identifying outliers with respect to the formal errors. To generate a global solution up to degree 7, the regularisation scheme from Kusche and Schrama (2005) was used to limit the signal over the oceans. From the full SINEX files, the covariance of the respective stations were extracted and transformed into a local frame with the use of the station's position. The IGS point displacements were related to the loading by an elastic Earth model represented by elastic loading Love numbers. For this inversion, the functional model explained in Kusche and Schrama 2005 was used, resulting in ten additional parameters besides the spherical harmonics. These additional parameters (7 Helmert parameters, 3 geocenter motion parameters) were treated as local parameters for the IGS data sets. In the global and local scheme used in this paper, the global parameters are estimated by all of the data sets used in the combination, while the local parameters are estimated using only one data set.

78.2.3 Ocean Bottom Pressure Estimations

For the OBP data set, the Alfred-Wegener-Institut (AWI) provided a set of weekly solutions coming from their preliminary Finite Element Sea-Ice Ocean Model (FESOM) model Timmermann et al, 2009. The OBP output of this ocean circulation model are given on a grid of 1.5×1.5 deg cells. The grid cells were block averaged over 5×5 degree grid cells, and those grid cells which had their centre on land were removed.

It is generally difficult to assess the accuracy of these OBP grids; however, here we have assumed that these OBP grid cells are corrupted by an uncorrelated noise of 500 Pa (5 cm in EWH). This assumed noise is larger than the one suggested by Wu et al. (2006), who corrupted the ECCO model by an uncorrelated noise of 3 cm, for an average of 10 days. During the inversion from grid cells to spherical harmonics, the geocenter motion was also estimated and treated as local parameters. In addition, a spatially uniform layer was co-estimated at each epoch to correct for the unknown total ocean mass change.

78.3 Analysis Method

The combinations of the different data sets on different time spans were performed on the normal equations level. The time span varied from 1 to 4 weeks of data, where the latter essentially represents a monthly solution. For the combinations of GRACE with IGS or FESOM, all parameters other than spherical harmonics were interpreted as local parameters. Those cases where both the IGS and FESOM data sets were used, their mutual local parameters (i.e., geocenter motion) were handled as global parameters. For more information about the local and global parameter scheme, see Jansen et al. (2009). The estimation of the spherical harmonics, for all cases, were computed from degree 2 until 30.

Comparisons between the various solutions were done primarily by examining quantities computed from the formal errors. Calculation of the (square-root) error degree variances, as well as geographic plots of the errors, served to provide both a quantitative and visual evaluation of the results.

While most of these evaluations are done on a global scale, assessing the improvement of regional averages due to the combined solutions can also be very valuable, especially for hydrological applications. To compute this, we first start with the expression for the improvement of a single coefficient,

$$r_i = \frac{\hat{\sigma}_i^{(\mathrm{ref})} - \hat{\sigma}_i^{(\mathrm{new})}}{\hat{\sigma}_i^{(\mathrm{ref})}}, \qquad (1)$$

where $\hat{\sigma}_i$ is the standard deviation of the estimated parameter i, derived from the covariance matrix. For a region average, the standard deviation can be calculated by

$$\hat{\sigma}^2_{(\mathrm{region})} = \mathbf{s}^T_{(\mathrm{region})} \bar{\mathbf{N}}^{-1} \mathbf{s}_{(\mathrm{region})},$$

where $\mathbf{s}_{(\mathrm{region})}$ is the vector that holds the normalized spherical harmonic coefficients of a region function Wahr et al., 1998. The $\hat{\sigma}_{(\mathrm{region})}$ can be used in eq. (1) to calculate the improvement of a particular region, such as an ocean or continental river basin.

78.4 Results

The results given in this section are based primarily on the month of August 2006, although some additional comparisons are made with another month, December 2006. When looking at the calibrated errors published for the various monthly solutions, August 2006 has better than average solution quality, while December 2006 is on the lower end of the spectrum. By comparing these 2 months, the impact of additional data sets can be seen for both a "good" and "bad" GRACE solution.

78.4.1 Formal Error Propagation

The transition of the 1-week GRACE-only solution to the 4-week GRACE-GPS-OBP combination, though not shown here in its entirety, nicely illustrates the point at which the sub-monthly combined solutions approach the accuracy of the standard monthly GRACE solution. Figure 78.1 shows four global error maps that indicate the point where, over the continents, the sub-monthly combination approaches that of the monthly GRACE solution. The 2 months mentioned previously, August (left) and December (right) 2006, were used to highlight the improvement of the combination for GRACE solutions of different quality. The top plots represents the monthly GRACE-only solutions and the bottom plots are the triple combination solutions for 2 weeks of data for each month. When only the errors over the continents are taken into consideration, the two different solutions again

look quite similar. Over the oceans the triple combination appears much stronger due to the inclusion of the FESOM model. Though not shown here, the 1 week triple combination shows, on average, the same total error as the monthly GRACE solution, but has a smaller error over the oceans and a larger error over the continents.

The (square-root) degree error variances for August 2006, in units of EWH, are shown in Fig. 78.2 for the different combinations for 4 weeks of data and 2 weeks of data. In general, the OBP data has the largest overall contribution, due mainly to its lower formal errors; however, the GPS data does help in the determination of the degree 1 and 2 coefficients, even in the triple combination. Comparing the 4 week GRACE solution and the 2 week triple combination shows that, per degree, the formal errors of the triple combination are lower than the GRACE-only ones. As before with the geographical plots, for the 1 week triple combination (not shown), the degree errors curves also appear to be very close to the monthly GRACE solution. Based on these results, the point at which the accuracy of the combined solutions surpasses that of the standard monthly solution is estimated to be around the 2 week time frame.

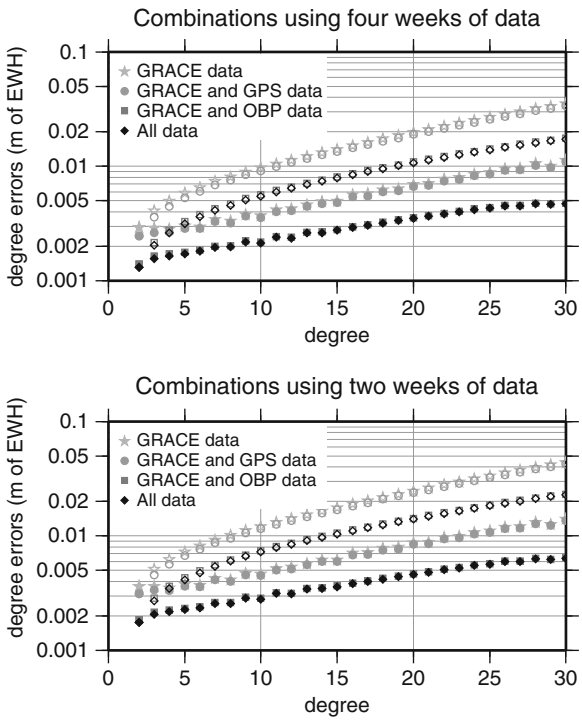


Fig.78.2 The (square-root) degree error variances in EWH for the different combinations and time frames for the month of August 2006. The *top plot* shows the results when using 4 weeks of data and the *bottom plot* when using only 2 weeks of data. The open symbols give the cumulative degree error

78.4.2 Regional Averages

To further validate the claim of the previous subsection, the regional analysis shown in Table 78.1 was performed. Here, the standard deviation of the mean for a range of major ocean and continental river basins were computed and used in Eq. (1), with the reference standard deviation coming from the monthly GRACE solution. This way, the values represent the percent improvement (positive or negative) of the combined solutions over the standard monthly field. Note that for these comparisons, the solutions were first smoothed with a 500 km Gaussian filter to reduce the Gibbs effect along the edges of the basin functions. The results again show that the combined solutions, in particular the triple combination of GRACE, GPS and OBP, show a significant improvement at the 2-week time frame over the standard monthly GRACE solutions. It is important to note that those regions which are close to the poles (Antarctica, Southern Ocean and Arctic Ocean) are largely influenced by the improvement of the $C_{2,0}$ coefficient. Based on these results, the point at which the accuracy of the combined solutions surpasses that of the standard monthly solution is again around the 2 week time frame.

78.4.3 Degree 1 and the $C_{2,0}$ Coefficient

The geocenter motion, which can be expressed in degree 1 coefficients for surface loading, can be estimated when the IGS and/or FESOM data is included in the combination, i.e., GRACE is not sensitive to the degree 1 coefficients and therefore cannot be used to directly estimate their value. Shown in the top plot of Fig. 78.3 are the errors for the degree 1 coefficients for various solutions.

The different combinations with GRACE are referenced against a 4 week combination of FESOM with IGS, estimated to a maximum degree of 15 and 30. The maximum degree of 30 is at the limit of solution

Table 78.1 This table shows the improvement of different regional mean with respect to a monthly GRACE solution in terms of 1 sigma reduction percentage. The combinations were performed to degree and order 30. To calculate the region mean, a Gaussian filter with a radius of 500 was applied to smooth the regional function

	GRACE+GPS				GRACE+OBP				GRACE+OBP+GPS			
Region	1week	2week	3week	4week	1week	2week	3week	4week	1week	2week	3week	4week
Artic Ocean[a]	–48.6	−0.2	17.7	21.7	27.7	49.3	58.6	61.7	30.4	51.2	60.1	63.3
North Atlantic	–66.6	−14.9	6.2	9.6	−27.3	12.1	28.7	32.3	−19.9	17.0	32.5	36.5
South Atlantic	–70.6	−17.1	4.5	7.3	−10.2	22.6	36.8	41.4	−5.2	26.0	39.5	44.3
Indian Ocean	–64.9	−13.7	7.5	9.8	−5.8	25.9	39.7	43.7	−0.7	29.4	42.6	45.8
North Pacific	–59.2	−10.3	9.4	12.5	−8.4	23.6	37.5	41.1	−3.4	27.1	40.3	44.4
South Pacific	–69.3	−19.8	4.8	6.8	−0.0	29.8	42.6	47.0	3.4	32.0	44.5	49.1
Southern Ocean[a]	–48.4	−1.1	17.2	21.3	30.2	50.8	59.8	63.2	32.7	52.5	61.2	64.6
All Oceans	–62.9	−13.6	7.5	9.9	−13.2	20.5	36.3	39.2	−8.8	23.5	37.7	41.8
Greenland	–67.1	−14.0	7.1	10.4	−3.0	28.2	41.8	45.7	−1.4	29.3	42.6	46.6
Ob basin	–68.6	−16.9	4.8	7.8	−31.0	8.2	25.1	28.6	−27.3	10.7	27.1	30.8
Mississippi basin	–73.5	−20.1	1.4	5.4	−45.7	−1.6	16.8	20.6	−41.7	1.0	18.9	23.0
Congo basin	–72.3	−18.8	2.6	6.0	−23.4	13.3	29.2	33.2	−20.2	15.4	30.8	35.0
Amazon basin	–68.0	−16.5	4.1	7.0	−13.8	19.7	33.8	37.9	−11.4	21.3	35.2	39.3
Australia	–68.9	−17.8	3.8	6.3	−13.6	19.8	34.2	38.8	−9.6	22.4	36.4	41.1
Antarctica[a]	–48.0	−1.5	16.9	20.8	21.3	44.4	54.5	57.2	23.6	46.0	55.9	58.6

[a]Values are dominated by the improvement of $C_{2,0}$

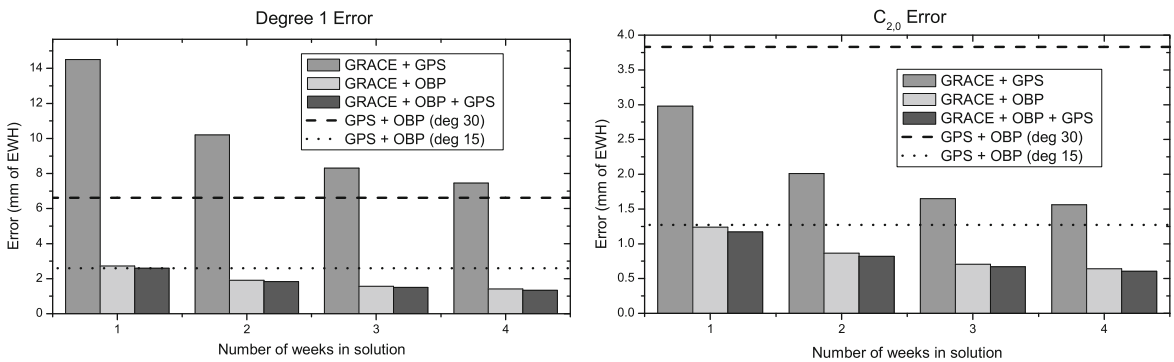


Fig. 78.3 Two bar plots showing the estimated errors of the degree 1 and $C_{2,0}$ in millimeters of EWH. The combinations were done up to degree and order 30. The reference error comes from a GPS+OBP combination for 4 weeks estimated up to degree and order 30 and 15

convergence for a FESOM IGS combination, resulting in large errors, but for the maximum degree of 15, the error of the solution is around 10 cm. These results show that GRACE does help in estimating the degree 1 coefficients in the triple combination and, again, the 2 week triple combination drops below the monthly FESOM/IGS combination. Since GRACE is not directly able to observe geocenter motion, the improvements seen in degree 1 for the combination solutions are due to the reduction of errors in the higher degrees in combination with the correlation between the higher degrees and degree 1. The bottom plot of Fig. 78.3 shows the same results for $C_{2,0}$. It is interesting to note that, for this particular coefficient, even the 1-week triple combination is able to determine this value with the same level of accuracy as the monthly GRACE solution.

78.5 Conclusions

Based on the evaluation of the calibrated error covariance matrices of the weekly solutions, it appears possible to estimate sub-monthly values of the low degree harmonics when multiple data sets are combined. In particular, the triple combination of GRACE, GPS and

OBP data shows that coefficients below degree 30 can be estimated at 2-week intervals with an equal or better level of accuracy as the monthly GRACE solutions. These results indicate that the temporal resolution of large scale mass transport processes might be improved through the combination of GRACE with GPS and OBP data. Future work will attempt to validate the results of this sensitivity study using a complete time series of real data.

One has to keep in mind that when combining three different data set there will be inconsistencies between them. For instance, the atmospheric loading signal is already present in the OBP and GPS data sets, but for the GRACE solution it is removed as part of the de-aliasing process. Thus, for the GRACE solutions, the de-aliasing products have to be added back into the solution before combining it with OBP or GPS data, as the total signal of the surface loading is desired. Also, the trend inside the surface loading signal is not the same for all of the data sets. In the GPS preprocessing, a trend from the station positions has to be removed so that the signal contains loading displacements. This means that a trend has to be removed from the other two data sets before combining these data sets with GPS.

Further complications arise from technique-specific errors. E. g., one has to keep in mind that incorrect tropospheric zenith delay modeling causes errors that map into height change signals. Residual transformation parameters of the individual reference frame realizations are co-estimated in our approach (cf. Kusche and Schrama 2005; Wu et al. 2006) and serve for validation purposes. Munekane (2007) observed that residual variations of the network scale, expected from not modelled second-order ionospheric delay in GPS analysis, are significantly smaller as compared to scale variations estimated jointly with geocenter motion from a global GPS loading inversion.

Acknowledgements Support for this study was provided in part by the Nederlandse Organisatie voor Wetenschappelijk Onderzoek (NWO), Aard- en Levenswetenschappen (ALW) division, grant number ALW1PJ/07011, and the German Research Foundation (DFG), under grant KU 1207/6-1, within the Special Priority Program SPP 1257 Mass Transport and Mass Distribution in the System Earth.

References

Jansen, M., B. Gunter, and J. Kusche, (2009). The impact of GRACE, GPS, and OBP data on estimates of global mass redistribution. *Geophys. J. Int.,* doi:10.1111/j.1365-246X.2008.04031.x.

Kusche, J. and E.J.O. Schrama, (2005). Surface mass redistribution inversion from global GPS deformation and GRACE gravity data. *J. Geophys. Res.*, 110(B9),. doi:10.1029/2004JB003556.

Munekane, H. (2007). Ocean mass variations from GRACE and tsunami gauges. *J. Geophys. Res.*, 112, B07403. doi:10.1029/2006JB004618.

Schmidt, R., F. Flechtner, O. Meyer, K.H. Neumayer, C., Dahle, R. König, and J. Kusche, (2008). Hydrological signals observed by the GRACE satellites. *Surv. Geophys.*, doi:10.1007/s10712-008-9033-3.

Timmermann, R. S. Danilov, J. Schröter, C., Böning, D. Sidorenko, and K. Rollenhagen, (2009). Ocean circulation and sea ice distribution in a finite element global sea ice-ocean model. *Ocean Model*, 27,114–129. doi:10.1016/j.ocemod.2008.10.009.

Wahr, J, Molenaar, M, and Bryan, F (1998). Time variablility of the earth's gravity field: Hydrological and oceanic effects and their possible detection using GRACE. *J. Geophys. Res.*, 103(B12),30,205–30 229.

Wu, X. M. Heflin, E. Ivins, and I. Fukumori, (2006). Seasonal and interannual global surface mass variations from multi-satellite geodetic data. *J. Geophys. Res. Solid Earth.*, 111, doi:10.1029/2005JB004100.

Chapter 79

Regular Gravity Field Variations and Mass Transport in the Earth System from DEOS Models Based on GRACE Satellite Data

P. Ditmar, X. Liu, R. Klees, E. Revtova, B. Vermeersen, R. Riva, C. Siemes, and Q. Zhao

Abstract Regular mass variations in the Earth system are analyzed using a new time series of gravity field models produced at DEOS. The subjects of special attention are secular trends as well as seasonal (annual and semi-annual) variations. It is found, in particular, that (i) the largest negative trends, which are associated with shrinking ice sheets in polar areas, reach 18–20 cm in terms of water height per year; (ii) the largest positive trends, which are presumably related to the post-glacial rebound, reach 7–9 cm/year; (iii) the largest peak-to-peak seasonal variations, which are mostly observed in large river basins, reach 50–100 cm/year. Furthermore, the confidence of secular trends is computed per point in order to isolate persistent trends. The set of locations where relatively small but persistent trends are observed includes Svalbard archipelago, Pamir mountains, Congo watershed, and Enderby Land in Antarctica.

79.1 Introduction

Direct observation of the global mass re-distribution in the Earth system became possible after the launch of the Gravity Recovery and Climate Experiment (GRACE) satellite mission, which was brought into orbit in 2002 (Tapley, 1997;Tapley et al., 2004; Wahr et al., 2004). The accuracy of GRACE measurements is so high that temporal variations of the Earth's gravity field are clearly observed even at a regional scale. These variations can be directly linked to the mass re-distribution in the Earth system.

A new time series of models of global gravity field variations has been recently produced at DEOS (Liu, 2008). The time series spans the interval from 2003 to Feb. 2006 with a temporal resolution of 1 month. In total, the time series consists of 35 models. Two months (Jun. 2003 and Dec. 2005) are skipped because of a lack of data. The models are represented in terms of spherical harmonics. Most of them are completed to degree 70 (in a few cases, the maximum degree is set equal to 50 or 60). All the models were subject to a post-processing with a statistically optimal full-matrix Wiener filter (Klees et al., 2008). Thanks to that, common artefacts of GRACE models, e.g along-track stripes, are totally removed, whereas the spatial resolution of the models remains high.

The subject of this article is the analysis and quantification of regular gravity field variations on the basis of the produced models. The regular variations at a given grid node are represented in terms of equivalent water layer thickness H, which is derived from the set of spherical harmonic coefficients as follows: (Wahr amd Molenaar, 1998):

$$H(\phi,\lambda,t) = \frac{R}{3}\frac{\rho_{av}}{\rho_w}\sum_{l=2}^{L_{\max}}\frac{2l+1}{1+k_l'} \times \sum_{m=-l}^{l}\bar{C}_{lm}(t)\,\bar{Y}_{lm}(\phi,\lambda), \quad (1)$$

where $L_{\max}$ is the maximal degree in the spherical harmonic expansion, R is the equatorial Earth's radius (6378136.3 m), ρ_{av} is the average Earth's density (5,517kg/m^3), ρ_w is the water density (1,000kg/m^3), k_l' is the load Love number of order l, $\bar{Y}_{lm}$ is the 4π-normalized surface spherical harmonic of degree l and

P. Ditmar (✉)
Delft Institute of Earth Observation and Space Systems (DEOS), Delft University of Technology, HS Delft 2629, The Netherlands
e-mail: P.G.Ditmar@tudelft.nl

S.P. Mertikas (ed.), *Gravity, Geoid and Earth Observation*, International Association of Geodesy Symposia 135,
DOI 10.1007/978-3-642-10634-7_79, © Springer-Verlag Berlin Heidelberg 2010

order m (positive and negative orders correspond to harmonics with a cosinusoidal and sinusoidal dependence on longitude, respectively), and $\bar{C}_{lm}(t)$ are the spherical harmonic coefficients. The values are computed at the nodes of an equiangular grid with a step of $1° \times 1°$.

At each grid node, the time series of water layer thicknesses is parameterized as a combination of annual and semi-annual signals supplemented by a linear trend:

$$H(t) = A + Bt + C\sin(\omega t) + D\cos(\omega t) + E\sin(2\omega t) + F\cos(2\omega t), \quad (2)$$

where $\omega = 2\pi/T$ with $T = 1$ year.

Table 79.1 Strongest negative trends (in cm of equivalent water layer thickness per year)

Location	Latitude	Longitude	Trend
Gulf of Alaska	61°	–144°	–20
Getz ice shelf (Antarctica)	–76°	–115°	–19
South-East Greenland	66°	–38°	–18

Table 79.2 Strongest positive trends (in cm of equivalent water layer thickness per year)

Location	Latitude	Longitude	Trend
Manitoba (Hudson Bay)	54°	–101°	9
Fennoscandia	64°	16°	8
Orinoco river basin	–5°	–63°	8
Palmer Land (Antarctica)	–76°	–68°	7

79.2 Secular Trends

The obtained secular trends are shown in Fig. 79.1. A few points where the secular trends attain extreme values are listed in the Tables 79.1 and 79.2.

Obviously, the strongest negative trends are associated with ice loss in polar areas. Interpretation of the positive trends is, however, not so straightforward. A comparison with modeled post-glacial rebound (PGR) signals (Fig. 79.2) leads to the conclusion that the PGR is probably responsible, at least partly, for the observed trends in Fennoscandia and Palmer Land. At the same time, it is worth noticing that the PGR model as well as other GRACE-based solutions show a significantly smaller trend in Fennoscandia (Steffen et al., 2008) than the DEOS models. Most probably, this discrepancy can be explained by an additional contribution of the hydrological signal in 2003–2005. Furthermore, the trends observed near the Hudson Bay show a different pattern than other solutions: two spots to the West from the Hudson bay can be clearly observed, whereas both the PGR model and alternative GRACE-based models show only one spot there (Tamisiea, 2007; van der Wal, 2008). The most probable explanation of the differences between the GRACE-based models is a higher resolution of the DEOS models achieved thanks to the usage of the optimal filter. As far as the difference form the PGR model is concerned, presence of two spots instead of one can be explained by a limited accuracy of the PGR model or by the presence

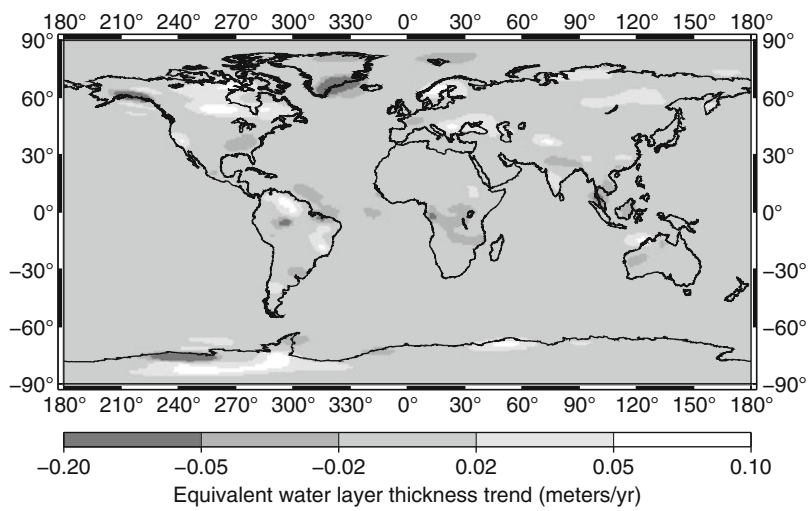


Fig. 79.1 Secular trends derived from the DEOS GRACE models

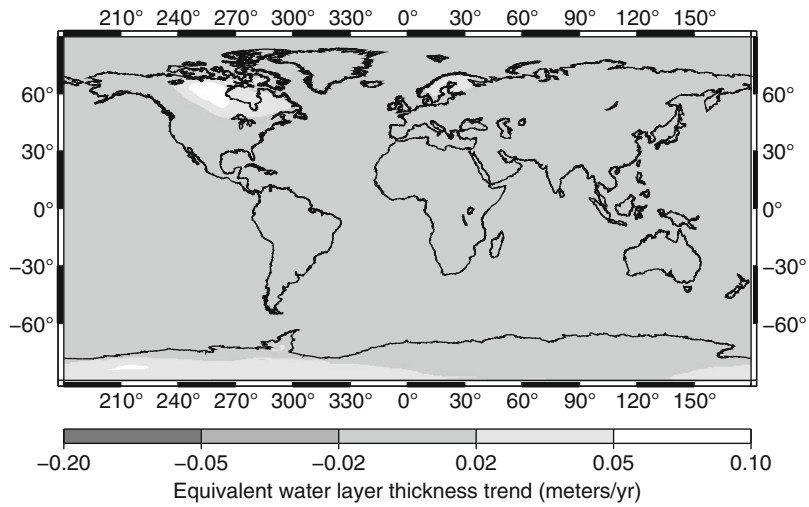


Fig. 79.2 Expected secular trends due to the post-glacial rebound. The trends are modeled on the basis of the ice model ICE-5G and the Earth's viscosity model VM2 of Peltier (2004)

of signals of other origin (e.g. hydrology) in GRACE data. The observed trend in Orinoco river basin is definitely unrelated to PGR and, most probably, can be associated with hydrology (i.e. water stock variations).

We have also made an attempt to distinguish persistent trends and those caused by inter-seasonal variations (e.g. of the hydrological origin). It goes without saying that the term "persistent trends" must be understood as "trends persistently observed in the time interval under consideration'. Analysis of a relatively short time series does allow any conclusions to be drawn about the persistency of the observed trends in the long term.

To identify persistent trends, the confidence c of the observed trends is computed at each grid node as follows (Sackett, 2001):

$$c = B\frac{\sqrt{N}}{\delta B}, \tag{3}$$

where B is the trend, δB is the trend standard deviation derived from trend values estimated on the yearly basis, and $N = 3$ years. Unfortunately, a straightforward application of Eq. (3) may result in a high confidence also at the locations where the estimated standard deviation δB is small just by chance: a set of three numbers (yearly trends) results in an underestimation of the actual standard deviation if these numbers happen to be nearly coincident. To reduce the influence of this effect, we compare each point-wise standard deviation of the trend with the average value on the globe. If the point-wise standard deviation is less than the average one, the latter is used in Eq. (3). The map of estimated confidences (Fig. 79.3) allows persistent trends to be identified. Remarkably, most of the locations with a high confidence are associated with geographical objects where large mass variations can be easily explained by hydrological or climatological processes (e.g. Svalbard archipelago, Pamir mountains, Congo watershed). Explanation of mass variations at some other locations (e.g. in the Enderby Land in Antarctica) requires further studies. The high-confidence spots in the ocean near Alaska's and Antarctica's coasts are, most probably, artefacts due to the Gibbs phenomenon. These features will probably vanish after increasing the maximal spherical harmonic degree in monthly models.

79.3 Seasonal Variations

The seasonal variations represented by the function $C\sin(\omega t)+D\cos(\omega t)+E\sin(2\omega t)+F\cos(2\omega t)$ have been synthesized per grid node for a further analysis.

Firstly, the peak-to-peak amplitude of seasonal variations was derived at each grid node as the difference between the maximal and minimal value of the equivalent water layer thickness (Fig. 79.4). With no doubt, most of the variations are caused by hydrological processes. This can be seen, in particular, from a comparison with a similar map derived from the GLDAS hydrological model (Rodell et al., 2004) for the same collection of months as are covered by the DEOS GRACE models (Fig. 79.5). The differences between

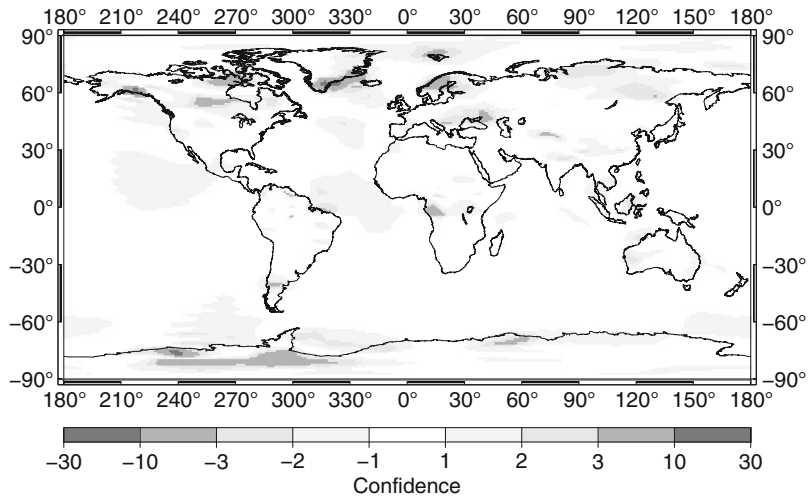


Fig. 79.3 Confidence of secular trends derived from the DEOS GRACE models

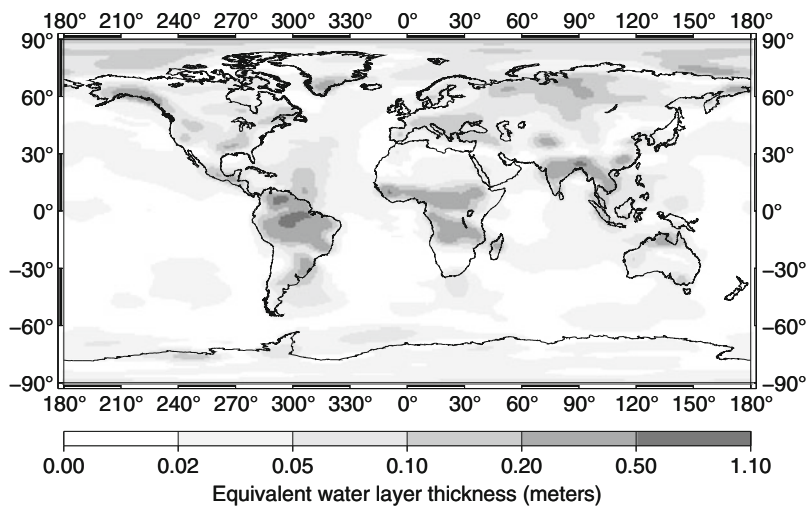


Fig. 79.4 Peak-to-peak amplitudes of seasonal mass variations derived from the DEOS GRACE models

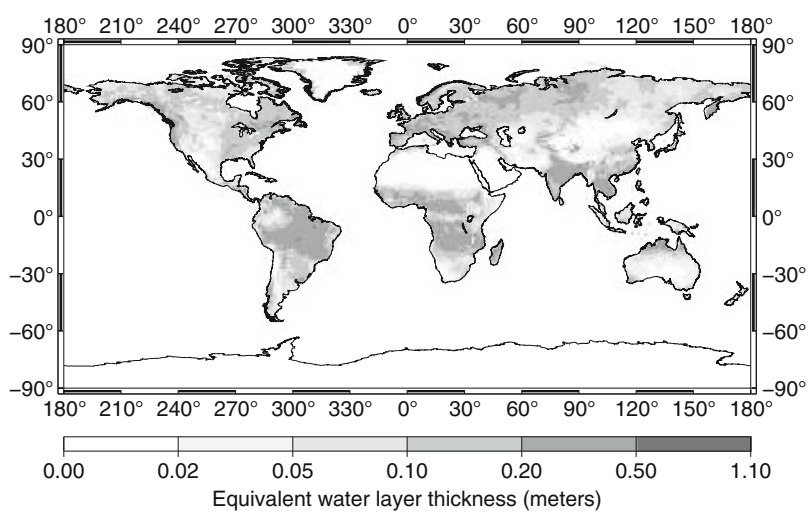


Fig. 79.5 Peak-to-peak amplitudes of seasonal mass variations derived from the GLDAS hydrological model

Table 79.3 Largest peak-to-peak amplitudes of seasonal mass variations (in cm of equivalent water layer thickness per year)

Location	Latitude	Longitude	Trend
Amazon river basin	–4°	–61°	104
Orinoco river basin	6°	–68°	77
Brahmaputra river basin	25°	90°	62
Niger river basin	11°	–10°	51
Gulf of Alaska	61°	–143°	47

the hydrological model and the GRACE-based models can be mostly explained by the fact that GLDAS does not describe some of the hydrological processes (e.g. variations of ground water stocks). Remarkably, the sites of the largest mass loss (cf. Fig.79.1) also show large seasonal variations. The points with the largest peak-to-peak amplitudes are listed in Table 79.3.

Secondly, the time of the maximum and minimum mass storage at each point has been found (Figs. 79.6 and 79.7). As expected, the observed pattern reflects mass re-distribution driven by the change of seasons. For example, the seasonal maximum in Canada and Siberia is reached in March or April, which is the time of the largest snow accumulation. The maxima in Amazon river basin and the South part of Africa, which are observed at the same time, correspond to the peak of the rain season. On the other hand, the peak of the rain season in the tropical areas of the northern hemisphere takes place in late summer or autumn, and this is reflected in the time of the maximal mass storage in Orinoco river basin, equatorial Africa (to the North from the equator) and South-East Asia. Notice that the interval between the maximum and minimum may deviate from 6 months due to the presence of semi-annual variations.

Thirdly, the total amplitude of semi-annual variations

$$\sqrt{E^2 + F^2} \tag{4}$$

and their contribution

$$\frac{\sqrt{E^2 + F^2}}{\sqrt{C^2 + D^2 + E^2 + F^2}} \tag{5}$$

to the seasonal cycle have been calculated (Figs. 79.8 and 79.9). Originally, it was expected that the contribution of semi-annual variations would reflect minor deviations of the seasonal cycle from sinusoidal behavior or, in the absence of these variations, just random noise. Consequently, the range between 0 and 0.5 was foreseen. The only exception areas we have expected are the vicinity of the equator and some other tropical areas (Fig. 79.10), where relatively strong semi-annual variations can be explained by a peculiar precipitation pattern. In practice, however, the contribution of semi-annual variations is dominant also in some non-tropical areas (e.g. around the Baltic sea, near the Hudson bay, and in Antarctica). Explanation of this phenomenon requires further studies.

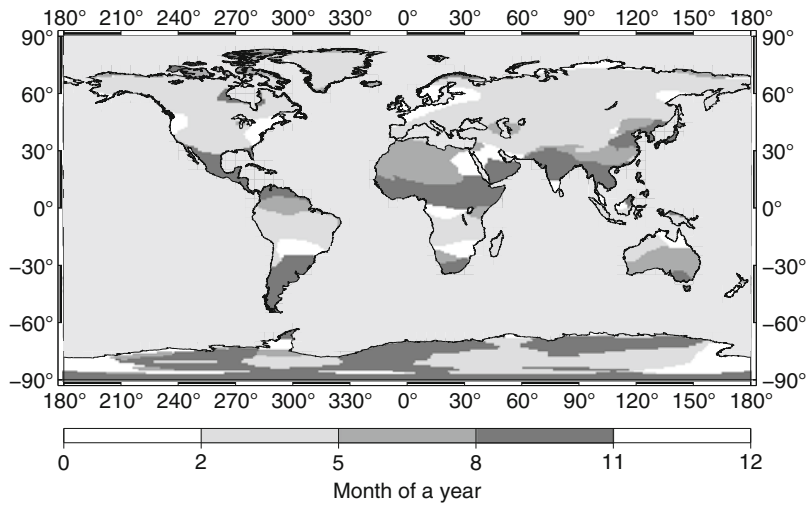


Fig. 79.6 Time of the maximum mass storage derived from the DEOS GRACE models

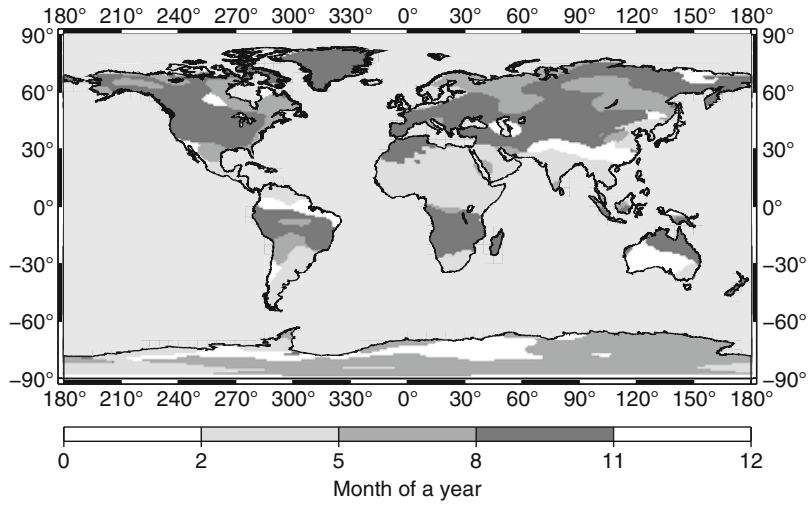


Fig. 79.7 Time of the minimum mass storage derived from the DEOS GRACE models

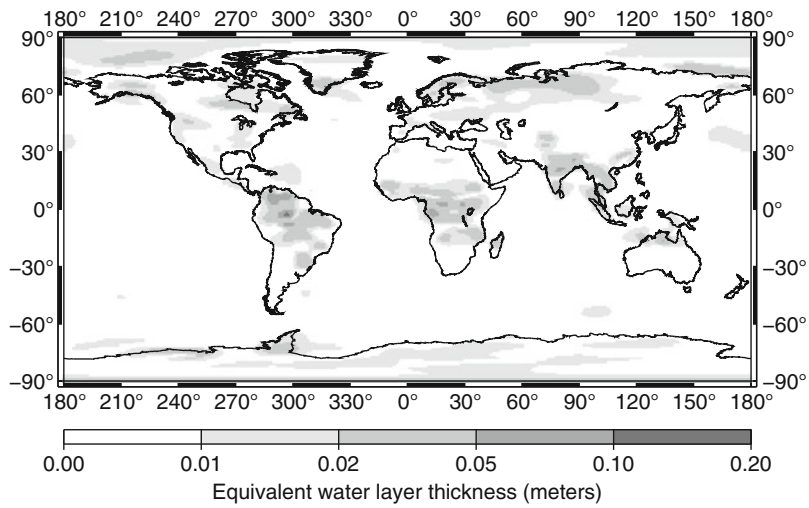


Fig. 79.8 The total amplitude of semi-annual variations derived from the DEOS GRACE models

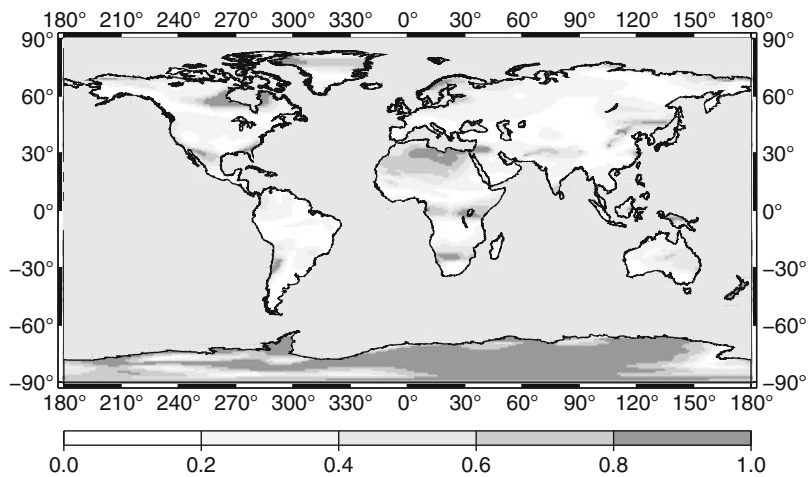


Fig. 79.9 Contribution of semi-annual variations to the seasonal cycle derived from the DEOS GRACE model

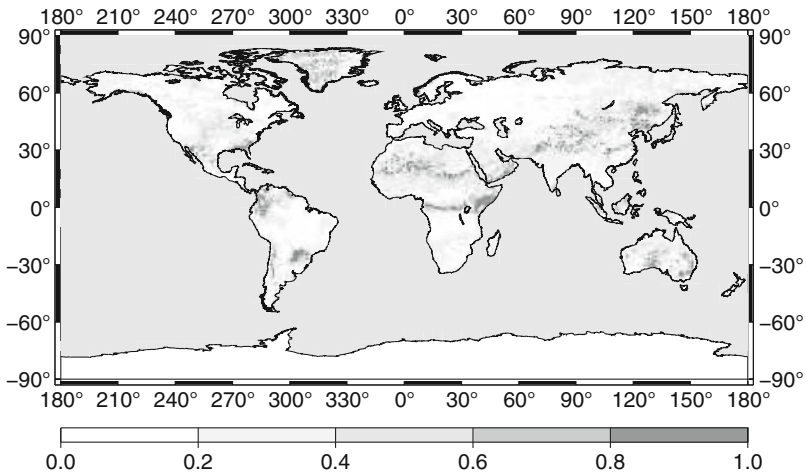


Fig. 79.10 Contribution of semi-annual variations to the seasonal cycle derived from the GLDAS hydrological model.

79.4 Selected Time Series

To provide more insight into the observed mass variations, time series for a number of selected locations are shown (Figs. 79.11, 79.12, 79.13 and 79.14). Secular trends at the locations with a high confidence (cf. Sect. 79.2) can be observed with a naked eye. Furthermore, semi-annual variations in Antarctica can be observed.

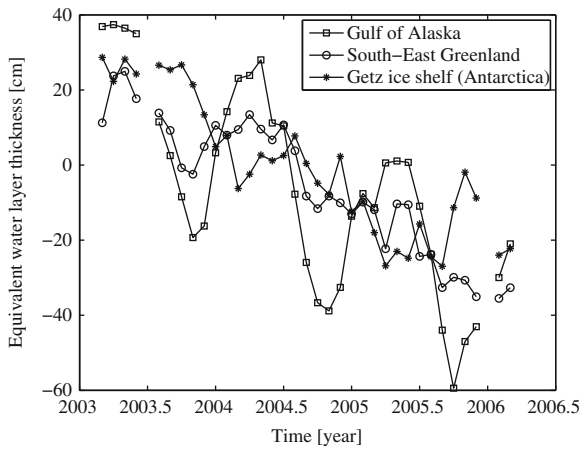


Fig. 79.11 Temporal mass variations at the locations with the largest mass loss

79.5 Conclusions

On the basis of the conducted analysis, the following conclusions can be drawn:

- The fastest mass losses on Earth are caused by shrinking ice glaciers. These losses reach the level of at least 18–20 cm (in terms of water heights) per year.
- The fastest persistent mass gains are probably caused by PGR and reach 7–9 cm (in terms of water heights) per year.
- The observed positive trends are not fully consistent with the considered PGR model and can probably be used to improve the latter one.
- Relatively small persistent secular trends (both positive and negative) are observed at a number of other locations (e.g. Svalbard archipelago, Pamir mountains, Congo watershed, Enderby Land in Antarctica). Further analysis of these trends is advisable.

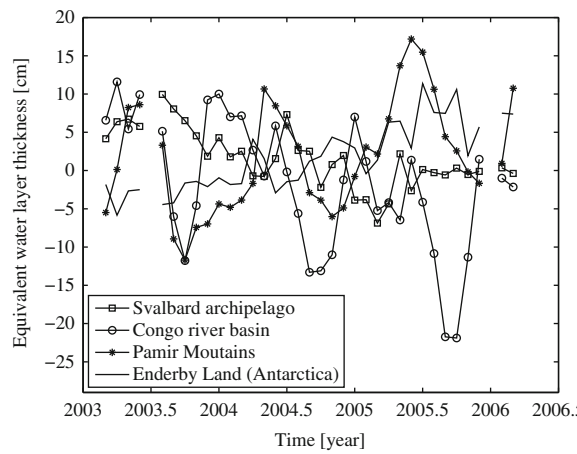


Fig. 79.12 Temporal mass variations at some other locations with persistent secular trends (cf. Fig. 79.3).

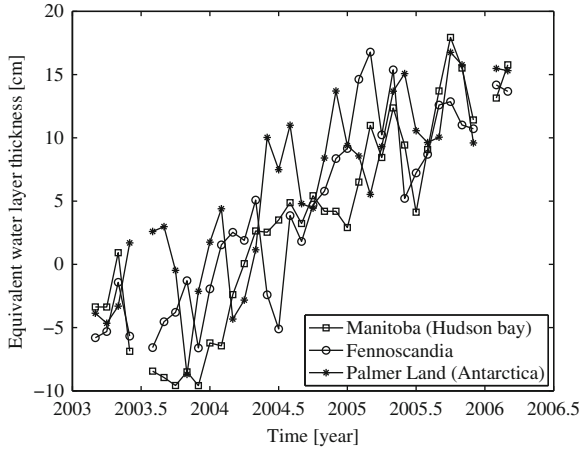


Fig. 79.13 Temporal mass variations at the locations with the largest mass gain

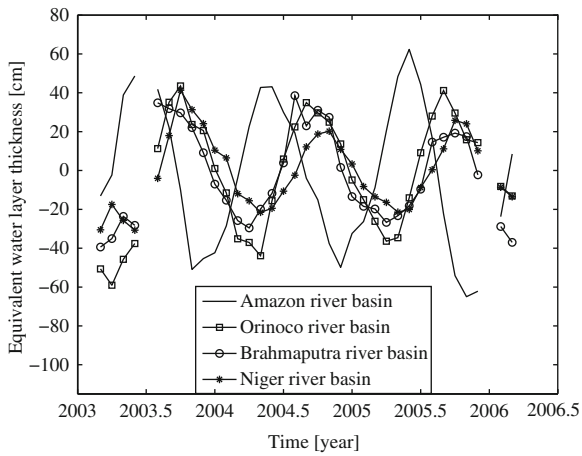


Fig. 79.14 Temporal mass variations at the locations with the largest peak-to-peak amplitudes of seasonal changes

- The largest peak-to-peak amplitude of seasonal mass variations is observed in the Amazon river basin and exceeds 1 m (in terms of water layer thickness). At a number of other locations, the seasonal variations are above 0.5 m. The major causes of seasonal mass variations are accumulation and ablation of continental stocks of water, snow, and ice.

Acknowledgements The computations were partly done on super-computers in the framework of the grant SG-027, which was provided by Stichting Nationale Computerfaciliteiten (NCF). The support of NCF is gratefully acknowledged.

References

Klees, R, E.A. Revtova, B. Gunter, P. Ditmar, E. Oudman, H.C. Winsemius, and H.H. Savenije (2008). The design of an optimal filter for monthly GRACE gravity field models. *Geophys. J. Int.*, 175, 417-432.

Liu, X. (2008). it Global gravity field recovery from satellite-to-satellite tracking data with the acceleration approach (Ph. D. Thesis), Nederland Geodetic Commission, Publications on Geodesy, Vol. 68, Delft, The Netherlands.

Peltier, W.R. (2004). Global glacial isostasy and the surface of the ice-age Earth: The ICE-5G (VM2) Model and GRACE. *Ann. Rev. Earth Planet., Sci.*, 32, 111–149.

Rodell, M., P.R. Houser, U. Jambor, J. Gottschalck, K. Mitchell, C.-J. Meng, K. Arsenault, B. Cosgrove, J. Radakovich, M. Bosilovich, J.K. Entin, J.P. Walker, D. Lohmann, and D. Toll (2004). The Global land data assimilation system. *Bull. Amer. Meteor. Soc.*, 85(3), 381–394.

Sackett, D.L. (2001). Why randomized controlled trials fail but needn't: 2. Failure to employ physiological statistics, or the only formula a clinician-trialist is ever likely to need (or understand!). *CMAJ*, 165 (9), 1226–1337 (available on-line as http://www.cmaj.ca/cgi/content/full/165/9/1226).

Steffen, H., H. Denker, and J. Müller (2008). Glacial isostatic adjustment in Fennoscandia from GRACE data and comparison with geodynamical models. *J. Geodyn*, 46, 155–164.

Tamisiea, M.E., J.X. Mitrovica, and J.L. Davis (2007). GRACE gravity data constrain ancient ice geometries and continental dynamics over Laurentia. *Science*, 316, 881–883.

Tapley, B.D. (1997). The gravity recovery and climate experiment GRACE. *Suppl. EOS Trans. the Am. Geophys. Union*, 78, (46) 163.

Tapley, B.D., S. Bettadpur, J.C. Ries, P.F. Thompson, and M. M. Watkins (2004). GRACE measurements of mass variability in the Earth system. *Science*, 294, 2342–2345.

Wahr, J. and M. Molenaar (1998). Time variability of the Earth's gravity field: Hydrological and oceanic effects and their possible detection using GRACE. *Geophys. Res.*, 103, (B12) 30, 205-30, 229.

Wahr, J., S. Swenson, V. Zlotnicki, and I. Velicogna (2004). Time-variable gravity from GRACE: First results. *Geophys. Res. Lett.*, 31, L11501, doi: 10.1029/2004GL019779.

van der Wal, W., P. Wu, M.G.Sideris, and C.K. Shum (2008). Use of GRACE determined secular gravity rates for glacial isostatic adjustment studies in North-America. *J. Geodyn.*, 46, 144–154.

Chapter 80

Estimating GRACE Monthly Water Storage Change Consistent with Hydrology by Assimilating Hydrological Information

B. Devaraju, N. Sneeuw, H. Kindt, and J. Riegger

Abstract A sequential estimation approach is used for constraining GRACE monthly estimates of mass changes with observed hydrological data, which is available for 20% of the land area, in order to improve the overall quality of the GRACE dataset. It is expected that the hydrological data constrains GRACE by utilising the correlations within the spherical harmonic coefficients, which is described by a simulated covariance matrix. Due to the dependancy of the approach on the stochastic information of GRACE, the influence of different structures of the GRACE covariance matrix were also tested. Initial results show that the hydrology constraints replace GRACE completely in the constrained areas, and contribute only meagrely outside the constrained areas. This hints at better parametrization of the model. The tests with different structures of the GRACE covariance matrix indicate that the block-diagonal structure approximates the full covariance matrix very well.

80.1 Hydrology and GRACE

GRACE gravity measurements provide a direct measure of water storage changes over continents. As such it enables, for the first time, to close the water balance (1) at continental/regional scales.

$$P - R - ET_{\mathrm{a}} = \frac{\partial S}{\partial t}, \tag{1}$$

where P is precipitation, R is run-off, ET_{a} is actual evapotranspiration, and $\frac{\partial S}{\partial t}$ is the total water storage change, all expressed in $(\frac{\mathrm{mm}}{\mathrm{month}})$.

Initially, it was thought that the water storage change estimates from GRACE could be used for calibrating hydrological models. However, GRACE has not met the expected level of accuracy (Schmidt et al., 2008). This inaccuracy is contributed by the large errors in the higher harmonic degrees of the GRACE solutions. Various filtering techniques tailor-made for GRACE data have been developed to counteract the errors. Filtering dampens signal amplitude in addition to reducing noise, which is an undesired artefact. Hence, the filtered datasets have to be validated with other reliable hydrological datasets prior to their usage (Swenson et al., 2006).

The validation of GRACE hydrological mass estimates on a global scale has been mainly confined to hydrology models instead of observed (measured) hydrology datasets, because measurement of evapotranspiration in (1) is difficult and hence, only information from models is available. However, for particular catchments evapotranspiration is negligible due to their geographical setting and climatic regime: catchments in the *Arctic regions*, where the winters are extremely cold (e.g. Yukon in Fig. 80.1); and catchments in dry regions like deserts where the precipitation is very meagre that evapotranspiration can be completely neglected (e.g. Western Sahara in Fig. 80.1). This reduces (1) for such catchments to,

$$P - R \approx \frac{\partial S}{\partial t}, \tag{2}$$

which, for dischargeless catchments, is further reduced to $P \approx \frac{\partial S}{\partial t}$.

B. Devaraju (✉)
Institute of Geodesy, Universität Stuttgart, Stuttgart, Germany
e-mail: devaraju@gis.uni-stuttgart.de

S.P. Mertikas (ed.), *Gravity, Geoid and Earth Observation*, International Association of Geodesy Symposia 135,
DOI 10.1007/978-3-642-10634-7_80, © Springer-Verlag Berlin Heidelberg 2010

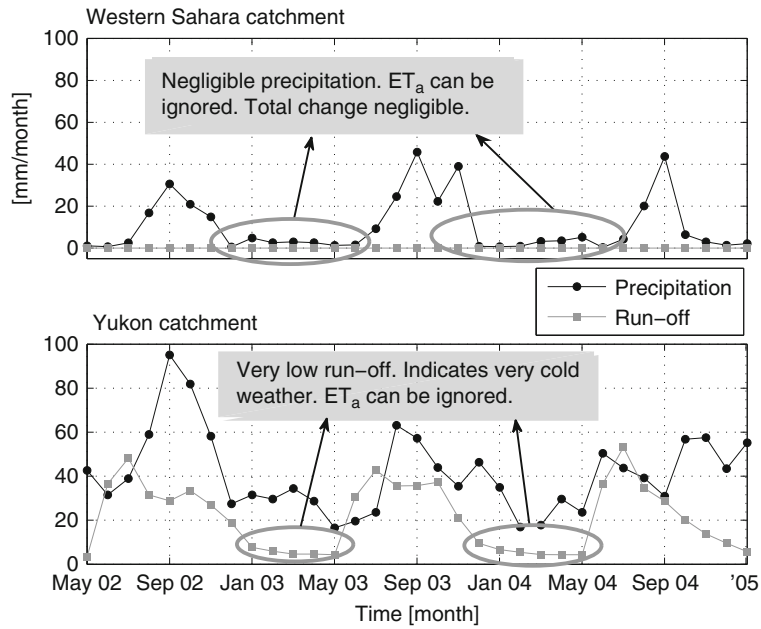


Fig. 80.1 *Circled regions* in Sahara show the dry periods, and in Yukon, run-off in the *circled periods* stay constant even if precipitation fluctuates indicating frozen conditions

The water storage change calculated from measured hydrological data using (2) can now be directly compared with GRACE water storage change estimates. Such measurement-based data is available for only about 20% of the land mass, which is used in this contribution for constraining the unfiltered GRACE monthly solutions in order to improve their overall quality. The idea is to use the correlations present between the GRACE spherical harmonic coefficients, described by its error covariance matrix, to spread the constraints globally.

The constraining problem can be treated as a sequential estimation problem (Bjöerck, 1996), and thereby re-estimate the monthly spherical harmonic coefficients by assimilating GRACE and hydrology. This technique is illustrated for the month of January 2003 with GRACE CSR release 4 dataset. Data assimilation has been performed before, for e.g., using continuous GPS observations Kusche and Schrama, 2005, but not with observed hydrological data.

80.2 Data and Methodology

80.2.1 Data

GRACE: The sequential estimation scheme was applied to GRACE level-2 data, which is provided as a set of spherical harmonic coefficients along with their variances. This data is provided as monthly sets from which the time-variable mass changes are calculated. Following Wahr et al. (1998), these mass changes are expressed in terms of rate of change of water equivalent height as follows:

$$\dot{h}_{\mathrm{w}}(\theta,\lambda;i) = \sum_{l=0}^{L=60} \Lambda_l \sum_{m=-l}^{l} \overline{Y}_{lm}(\theta,\lambda)\dot{\overline{K}}_{lm}(i), \qquad (3a)$$

$$\dot{h}_{\mathrm{w}} = \overline{Y}\Lambda\dot{\overline{K}} \qquad \text{matrix-vector form}, \qquad (3b)$$

$$\dot{\overline{K}}_{lm}(i) = \left(\frac{\overline{K}_{lm}(i+1) - \overline{K}_{lm}(i-1)}{t_{i+1} - t_{i-1}}\right), \qquad (3c)$$

$$\Lambda_l = \frac{a\rho_{\mathrm{ave}}}{3\rho_{\mathrm{w}}}\frac{2l+1}{1+k_l} \quad . \qquad (3d)$$

where $\dot{h}_{\mathrm{w}}$ is the water equivalent height in $(mm/month)$ at (θ,λ) for the time point i and $\dot{h}_{\mathrm{w}} = \frac{\partial S}{\partial t}$ for catchments, $\overline{Y}_{lm}(\theta,\lambda)$ are the normalized surface spherical harmonics, $\dot{\overline{K}}_{lm}$ are the normalized form of rate of change in spherical harmonic coefficients calculated using the three-point mid-point numerical differentiator (3c), Λ_l are the isotropic transfer coefficients that convert geoid changes to equivalent water height $(mm/month)$ changes, L is maximum degree of spherical harmonic expansion ($L = 60$), l is the degree, m is the order, k_l is the load Love number for degree l, a is the semi-major axis of the reference ellipsoid, ρ_{ave} is the average density of Earth, and ρ_{w} is the density of sea-water.

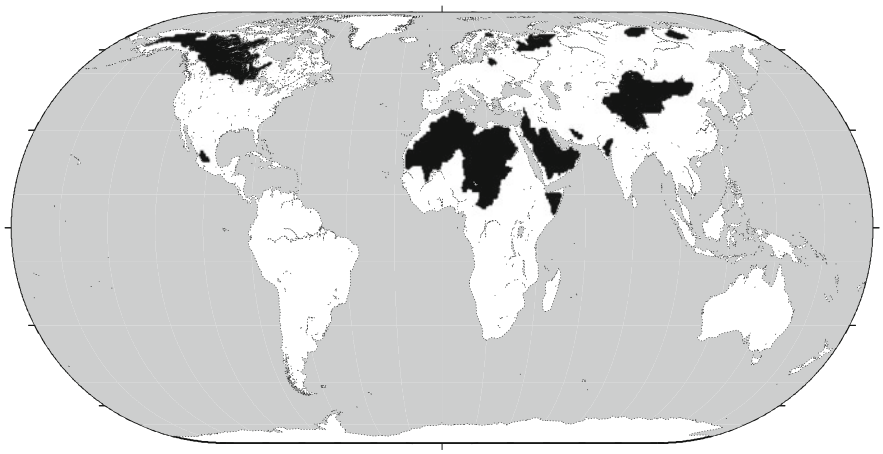


Fig. 80.2 Catchments that served as hydrological mass constraints

Hydrology: For the case of hydrology, only precipitation and discharge data are required due to (2). Precipitation data was obtained from the Global Precipitation Climatology Centre (GPCC) and discharge data from the Global Runoff Data Centre (GRDC) and the national hydrological services. The discharge of the catchments were then converted into run-off quantities. Then catchments whose evapotranspiration can be neglected are chosen based on the principles explained in Sect. 80.1, which are discussed in detail in (Kind et al. 2008). In the end there were 60 catchments that could be used, but only 28 of them (Fig 80.2) were usable due to data gaps. The storage changes obtained from these catchments are modelled in terms of spherical harmonics using (3a).

80.2.2 Sequential Estimation and Data Assimilation

Sequential estimation is performed in cases where there is a constant inflow of new data to estimate a set of unchanging parameters. This type of estimation is very common in navigation and estimation of geodetic co-ordinates of the national networks. The observation data inflow need not only be in the temporal sense, but also from different sources, which is then data assimilation via sequential estimation.

$$E\left\{\begin{bmatrix}\dot{\hat{\overline{K}}}_{\mathrm{G}}\\ \dot{h}_{\mathrm{w}}\end{bmatrix}\right\} = \begin{bmatrix} I \\ \overline{Y}\Lambda\end{bmatrix}\dot{\overline{K}}; \tag{4a}$$

$$D\left\{\begin{bmatrix}\dot{\hat{\overline{K}}}_{\mathrm{G}}\\ \dot{h}_{\mathrm{w}}\end{bmatrix}\right\} = \begin{bmatrix} Q_{\mathrm{G}} & 0 \\ 0 & Q_{\mathrm{H}}\end{bmatrix} \tag{4b}$$

$$\dot{\hat{\overline{K}}} = \left(\Lambda^{\top}\overline{Y}^{\top}Q_{\mathrm{H}}^{-1}\overline{Y}\Lambda + Q_{\mathrm{G}}^{-1}\right)^{-1} \left(\Lambda^{\top}\overline{Y}^{\top}Q_{\mathrm{H}}^{-1}\dot{h}_{\mathrm{w}} + Q_{\mathrm{G}}^{-1}\dot{\hat{\overline{K}}}_{\mathrm{G}}\right) \tag{4c}$$

$$Q_K = \left(\Lambda^{\top}\overline{Y}^{\top}Q_{\mathrm{H}}^{-1}\overline{Y}\Lambda + Q_{\mathrm{G}}^{-1}\right)^{-1} \tag{4d}$$

where $E\{\cdot\}$ is the expectation operator; $D\{\cdot\}$ is the dispersion operator; $\dot{\hat{\overline{K}}}_{\mathrm{G}}$ is derived from (3b) using GRACE CSR release 4 dataset; $\dot{h}_{\mathrm{w}}$ is the estimate from (2) for all the constraining catchments; Q_{G} and Q_{H} are the respective covariance matrices of GRACE and hydrology datasets; and $\dot{\hat{\overline{K}}}$ is the new sequential estimate after constraining GRACE with hydrology, with Q_K describing its covariance.

The advantage of using sequential estimation for data assimilation is that the individual datasets need not all be processed together, and they can be *sequentially* assimilated into the system. Thus we do not have to process the GRACE level-1B data (orbit, K-band range rates, and dealiasing data) and the hydrology data together.

80.3 Stochastics of the Data

GRACE: The spherical harmonic coefficients distributed as GRACE level-2 data along with their variances. The full covariance matrices are usually not provided by the data centres. However, a full

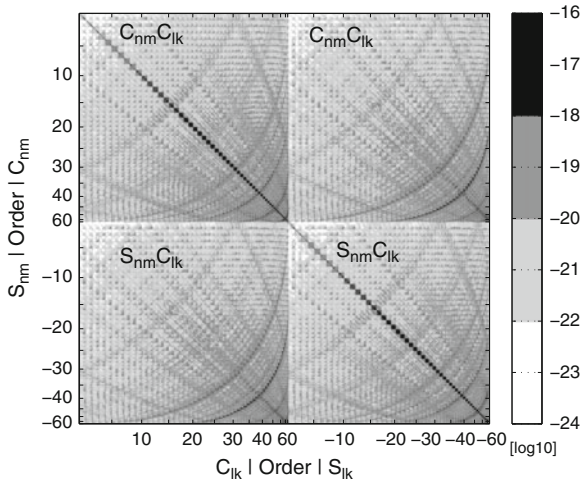


Fig. 80.3 Simulated variance-covariance matrix

covariance matrix would be required for the method to succeed as the correlations between the spherical harmonic coefficients would be needed to spread the hydrological constraints globally. Hence, we simulate a full covariance matrix based on the method applied by Kusche and Schrama (2005).

An example of a simulated covariance matrix is shown in Fig. 80.3. The coefficients in the matrix are arranged in order-leading form, and it can be seen that there is a heavy block-diagonal structure to the covariances. This suggests that the degrees within an order are more correlated than the orders within a degree, an observation already made by Swenson and Wahr (2006). Also, Han (2003) showed that for GRACE type of orbits block-diagonality can be safely assumed. Hence full and block-diagonal GRACE covariance matrices were used to analyse their impact on the outcome. If a full covariance matrix can be replaced by a block-diagonal covariance matrix, then the computation time will decrease considerably. In addition, a case when no correlations between the coefficients are considered (diagonal covariance matrix) is also analysed.

Hydrology: The stochastic information for the hydrological data was taken from hydrology literature. In general, precipitation data can be considered accurate to 5–40% of the estimates Fuchs et al., 2007 and the discharge data is accurate to 30% (Shiklomanov et al., 2006) in the Arctic regions. For the analysis, the upper limit error of discharge data (30% of the estimates) was chosen as the uncertainty of the precipitation and discharge data, uniformly for all the catchments.

$$\sigma_P(j) = 0.3P(j);\ \sigma_R(j) = 0.3R(j) \tag{5a}$$

$$\sigma_h^2(j) = \sigma_P^2(j) + \sigma_R^2(j),\ j = 1,2,\ldots,28 \tag{5b}$$

where, σ are the measurement errors, and j represents the catchments. The measurement errors between the catchments are assumed to be uncorrelated, and so Q_{H} in (4b) is a diagonal covariance matrix. In (5) the accuracy of the hydrological data can be chosen to be any percentage of the estimates, but it will not affect the results as the unfiltered GRACE mass change estimates are highly erroneous.

80.4 Results and Discussion

80.4.1 Hydrology-Constrained Solutions

The method outlined in the set of Eq. 4 were applied to the GRACE and hydrology data to re-estimate the rates of change in spherical harmonic coefficients. Three different covariance matrix structures of GRACE were used in order to assess the optimal covariance structure. The results are shown in Figs. 80.4 and 80.6.

Spatial domain The mass estimates that were used for constraining the GRACE solutions have all been recovered completely (cf. Fig. 80.5), and also the adjacent regions have been smoothed heavily. This smoothing of the adjacent area is conspicuous around north-eastern Africa, parts of the Indian subcontinent, Mongolia, Tibet and China. Though the difference between unconstrained and constrained solutions is significant with an RMS of 415 mm/month, the stripes have not vanished. As a consequence the signal amplitudes of the constrained solution are unrealistic outside the constrained regions.

Spectral domain The signal degree variances of degrees $l > 22$ in both the constrained and unconstrained solutions, shown in Fig. 80.6, are most likely dominated by errors as the variances increase with degree instead of decreasing, beyond degree 22. The signal degree variances of the constrained coefficients closely follow those of the unconstrained coefficients, while the error degree variances of the constrained coefficients are slightly lower than that of the unconstrained coefficients. This behaviour is due to (4d), where the covariance is the inverse of the weights,

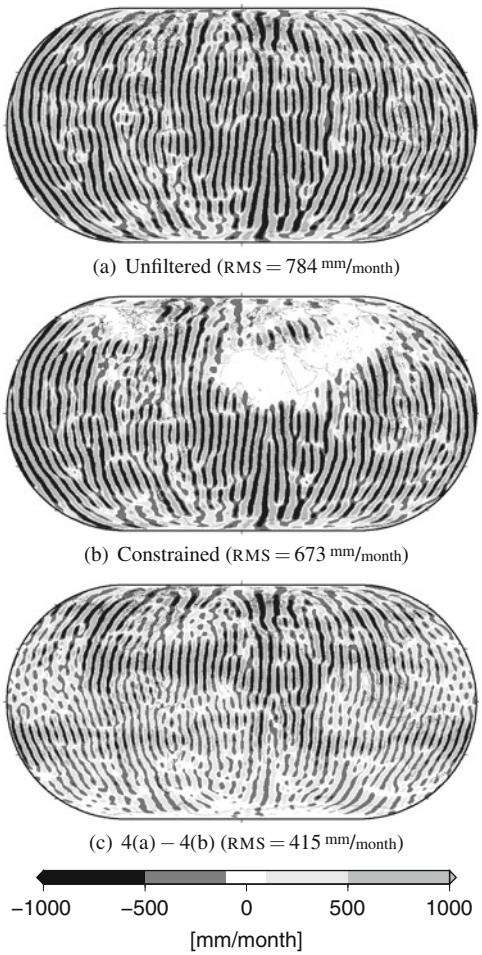


Fig. 80.4 Maps of the unfiltered and constrained mass estimates, and also their differences. The constrained mass estimates mapped here were computed using a full covariance matrix

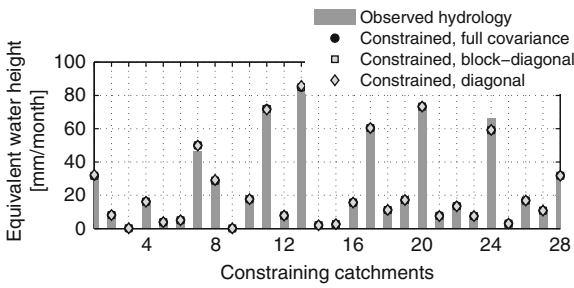


Fig. 80.5 Difference between the constrained and observed hydrological mass estimates in the constraining catchments

and since weights always add up the covariance keeps reducing. Further, a marked difference is seen in the error variances of degree two, where the error exceeds the signal in the unfiltered case and those errors have been suppressed in the constrained solutions. The

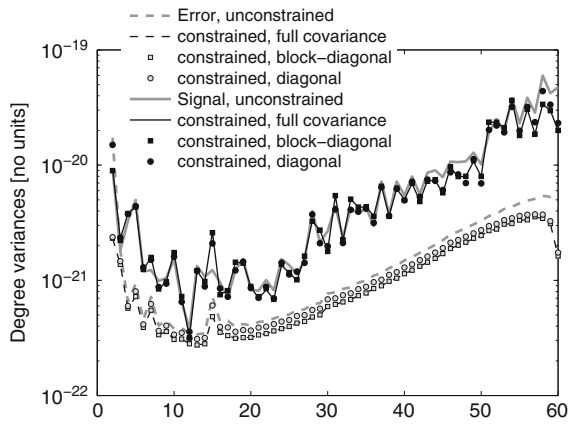


Fig. 80.6 Comparison of the signal and error degree variances of the constrained solutions obtained using various covariance structures with those of the unconstrained solution

signal variance of degree 15 shows significant increase after constraining, and similarly, there is also noticeable decrease in the signal variances beyond degree 45.

80.4.2 Contribution of Hydrological Constraints

In order to assess the contribution of hydrology, the redundancy numbers of the spherical harmonic coefficients and the mass changes were investigated. Redundancy numbers, shown in (6), provide the percentage contribution to the whole sequential estimate from each of the input datasets (Bouman, 2000).

$$R_{\mathrm{H}} = Q_K \left(\Lambda^{\top} \overline{Y}^{\top} Q_{\mathrm{H}}^{-1} \overline{Y} \Lambda \right); R_{\mathrm{G}} = Q_K Q_{\mathrm{G}}^{-1} \qquad (6a)$$

$$R_{\mathrm{G}}(\mathrm{GRACE}) + R_{\mathrm{H}}\,(\mathrm{Hydrology}) = I \qquad (6b)$$

Spectral domain Redundancy numbers of the spherical harmonic coefficients are shown in Fig. 80.7 for all the three cases that were computed. The contribution of hydrology in the spectral domain has been predominantly in the higher degrees, mostly after degree 22. Also, there is a substantial contribution from hydrology to the $C_{2,0}$ and $C_{15,15}$ terms. This is also reflected in the degree variances of the constrained solutions shown in Fig. 80.6. It is also seen that hydrology contributes significantly to the poorly-determined sectorial/near-sectorial coefficients, and meagrely to the tesseral and zonal coefficients of the lower degrees ($l \leq 22$).

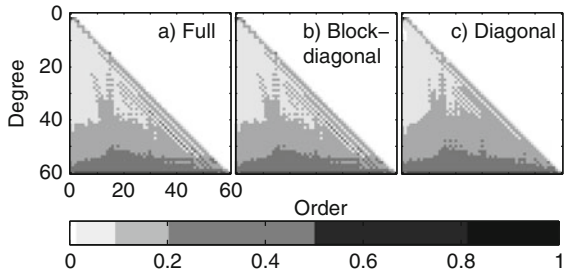


Fig. 80.7 Contribution of the hydrological mass constraints

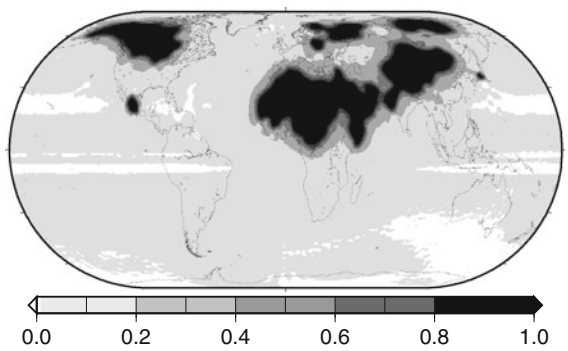


Fig. 80.8 Contribution of hydrology visualized in the spatial domain when constrained with a full covariance matrix

Spatial domain Figure 80.8 illustrates the contribution of hydrology (R_H) to every pixel in the spatial domain. It is at once evident that hydrology replaces GRACE completely in the constrained regions, while it contributes meagrely outside the constrained regions. The significant difference between the constrained and unconstrained solutions is explained by the global contribution of hydrology, while the stripy nature of the unconstrained regions in the constrained solution is explained by the magnitude of that global contribution (1–5%). It should also be noted that the magnitude of contribution drops rapidly from the constrained regions to the unconstrained regions.

80.4.3 Impact of Covariance Matrix Structure

The influence of the covariance structure in the estimation is shown in Fig. 80.7 and 80.9. The difference between the full and block-diagonal covariances (Fig. 80.9a) is less significant than the difference between full and diagonal covariances (Fig. 80.9b). The reason behind these differences are clearly indicated by Fig. 80.7, where the contribution from hydrology is very similar when full/block-diagonal covariances are used as opposed to diagonal covariances. The main difference lies in the near-sectorial terms beyond degree 30. Even with more contribution in the near-sectorial terms in the diagonal covariance case, the amplitude of the stripes are more compared to the other two cases. In Fig. 80.6 the signal variance of degree 2 increases with the use of diagonal covariances, while there is no change with the use of full/block-diagonal covariances. Further, the error degree variances of the diagonal covariance case is slightly higher than the other two cases.

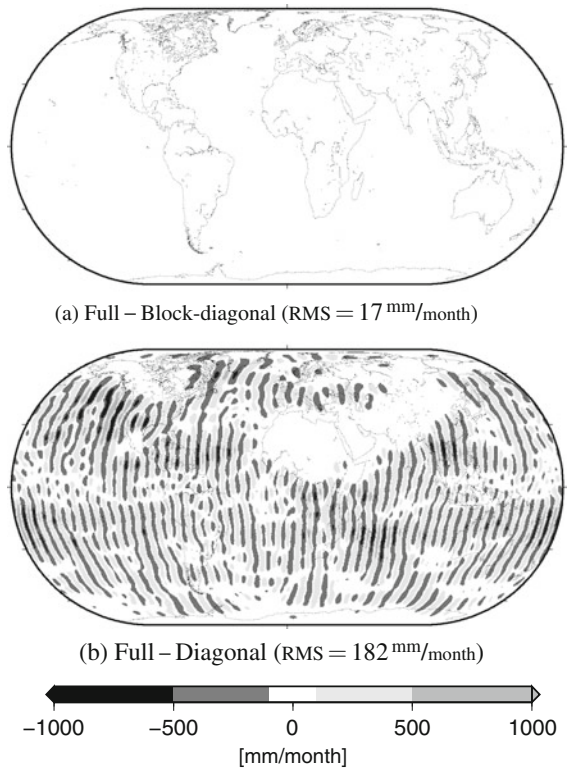


Fig. 80.9 Differences between the mass estimates obtained using different covariance matrix structures

80.4.4 Discussion

It is clear from the results that the hydrological constraints were not successful in constraining the regions

outside the constrained catchments, and only contribute meagrely to those regions even after using the full covariance matrix of GRACE. The reasons could be the ignoring of signal covariances between the catchments; the simulated nature of the GRACE covariance matrices; and/or improper parameterization of the hydrological constraints. The simulated nature of the GRACE covariances can be omitted as it has been proven to be effective in a similar case of data assimilation by Kusche and Schrama (2005). The main reason could be the parameterization of hydrological constraints as they cannot contain information about all the coefficients upto degree and order 60 due to their sparsity and non-global coverage. And, it also remains to be seen after re-parameterization if the signal covariances between the catchments are needed on top of the GRACE covariances to constrain the mass changes.

Hydrology replaces GRACE mass estimates completely in the constrained catchments after constraining, which is a reaffirmation of the fact that hydrology is relatively more accurate than GRACE. The least squares estimator has to replace erroneous GRACE with relatively accurate hydrology to get least squares of the residuals. An impact of least squares estimator is also seen in the way the hydrological constraints were distributed among the coefficients. The constraints were spread to the poorly-determined degree 2 and sectorial/near-sectorial coefficients, and to highly noisy coefficients of degrees $l > 22$. A meagre amount is also smudged into the tesseral and zonal coefficients of degrees $l \leq 22$, which could imply that these coefficients are more accurate. However, this needs to be verified after re-parameterization of the hydrology constraints.

Finally, the tests with GRACE covariance structures yielded the expected results that block-diagonal covariance structure is a very good approximation of the full covariance. Therefore, in future computations the full covariance structure will be replaced by a block-diagonal, which will immensely speed up the calculations. However, in this contribution the issue of proper weightage of the stochastics of the contributing datasets via variance components was not touched upon. Here, both GRACE and hydrology are assumed to have equal weightage, which is not true, and so, variance components of the datasets have to be estimated.

80.5 Summary and Outlook

A sequential estimation method was used to constrain GRACE monthly mass change estimates with reliable hydrological data available for 20% of the land mass, in order to improve the overall quality of the GRACE dataset. This method was demonstrated with three different GRACE covariance structures for January 2003. The results show that the method was not able to constrain the regions outside the constraining catchments utilising the correlations within the GRACE coefficients, which could be mainly due to the improper parameterization of the hydrological constraints. The test of different covariance structures of GRACE indicated that block-diagonal covariance approximates the full covariance very well and hence can be used in place of the full covariance matrix for future computations.

In order to improve this method further, proper parameterization of the hydrological constraints must be carried out along with the estimation of variance components of the contributing datasets. This will reveal if the signal covariances between the catchments will be required on top of the GRACE covariances for constrained mass estimation.

Acknowledgements This work was carried out as part of the *Direct Water Balance* project funded by the Deutsche Forschungsgemeinschaft (DFG) sponsored Special Priority Programme, *Mass transport and mass distribution in the Earth System* (SPP 1257).

The authors thank two anonymous reviewers, whose comments helped improve the content of the manuscript considerably. The authors extend their thanks to GPCC, GRDC, and PO.DAAC (Physical Oceanography Distributed Active Archive Center) projects for providing precipitation, discharge, and CSR release 4 GRACE data, respectively.

References

Björck, Å. (1996). Numerical methods for least squares problems. SIAM.

Bouman, J. (2000). *Quality assessment of satellite-based global gravity field models*. Tech. Rep. 48, Publications on Geodesy, Netherlands Geodetic Commission.

Fuchs, T. U. Schneider B. Rudolf (2007). Global precipitation analysis of the GPCC. Product handbook, Global Precipitation Climatology Centre (GPCC), Deutscher Wetterdienst, Offenbach a. M., Germany.

Han, S.C. (2003). *Efficient global gravity determination from satellite-to-satellite tracking*. Tech. Rep. 467, Department of Civil and Environmental Engineering and Geodetic Science.

Kindt, H., J. Riegger et al. (2008). Evaluation of GRACE measurements with hydrologic data. In: *Geophys. Res. Abstr.*, 10, EGU2008–A–05 980.

Kusche, J. E.J.O. Schrama (2005). Surface mass redistribution inversion from global GPS deformation and Gravity Recovery and Climate Experiment (GRACE) gravity data. *J. Geophys. Res.* 110:B09 409.

Schmidt, R., F. Flechtner, U. Meyer et al. (2008). Hydrological signals observed by GRACE satellites. *Surv. Geophys.*, DOI:10.1007/s10712-008-9033-3.

Shiklomanov, A.I., T.I. Yalovleva, R.B. Lammers et al. (2006). Cold region river discharge uncertainty–estimates from large russian rivers. *J. Hydrol.* 326, 231–256.

Swenson S., J. Wahr (2006). Post-processing removal of correlated, errors in GRACE data. *Geophy. Res. Let.* 33, L08 402.

Swenson S., P.J.F. Yeh, J. Wahr, J. Famiglietti (2006). A comparison of terrestrial water storage variations from GRACE with in situ measurements from Illinois. *Geophys. Res. Let.* 33, L16 401.

Wahr, J., M. Molenaar, F. Bryan (1998). Time variability of the Earth's gravity field: Hydrological and oceanic effects and their possible detection using GRACE. *J. Geophys. Res.* 103(B12), 30,205–30,229.

Chapter 81

Secular Geoid Rate from GRACE for Vertical Datum Modernization

W. van der Wal, E. Rangelova, M.G. Sideris, and P. Wu

Abstract GRACE-derived geoid rates are studied for North-America, where the adjustment of the Earth to ancient ice sheets causes a secular geoid increase up to 1.3 mm/year. These significant geoid changes are of particular interest for establishing a new geoid-based vertical datum in Canada and other high accuracy applications. To quantify the uncertainty of the derived rate of change of the geoid, several methods for GRACE error approximation are studied using: (i) calibrated standard deviations, (ii) a full covariance matrix, and (iii) residuals of least-squares fit of a trend and periodic variations to the time series of spectral coefficients. It is found that the residuals give the largest error estimates, probably because correlated errors are captured better. Furthermore, through maximizing the signal-to-noise ratio, it is found that the Swenson and Wahr (2006) filter of correlated GRACE errors should be applied to coefficients above degree 22 and order 4. Measurement errors are largely longitude independent, with magnitude around 0.06 mm/year. The largest geoid rate uncertainty is estimated in the area of present-day ice melt in Alaska and south of the Great Lakes and south-west of Hudson Bay (over 0.3 mm/year) due to uncertainty in continental water storage. For the creation of a geoid rate model based on GRACE data it is important that efforts are focused on reducing uncertainty in these areas, rather than improving post-processing.

W. Van derWal (✉)
Department of Geomatics Engineering, University of Calgary, Calgary, AB, T2N 1N4, Canada
e-mail: wouter_van_der_wal@hotmail.com

81.1 Introduction

The static geoid has reached an accuracy level where time-dependent effects on the geoid become significant. For applications where high geoid accuracy is needed, such as precise georeferencing, oceanography, hazard assessment and monitoring, a static geoid model that is provided by the national survey agency can be accompanied by a model of the secular changes of the geoid (or "dynamical vertical datum"). The GRACE satellite mission provides monthly gravity field solutions from which a secular geoid rate can be estimated. A dynamical vertical datum can be constructed by combining terrestrial and satellite data (Rangelova, 2007). However, in this paper we investigate measurement and systematic errors in the geoid rate from GRACE data alone. It should be mentioned that recently the Swedish national survey agency has incorporated a hybrid of terrestrial data and geophysical model for Glacial Isostatic Adjustment (GIA) to homogenize leveling observations (Ågren and Svensson, 2007) for readjustment of the leveling network.

The study area is North America, where the dominant source of long-term geoid change is GIA. This process is an ongoing response to melting of ice sheets that covered a large part of North America roughly 20,000 years ago. The rebound of the crust is accompanied by mass inflow in the Earth's mantle, which causes an increase in gravity and a geoid rise at a fixed location. Present-day glacier melting in Alaska and Greenland contributes significantly to the obtained secular geoid rate. It has to be decided whether a geoid rate model provided to users includes a secular component due to long-term glacier melting. Because

S.P. Mertikas (ed.), *Gravity, Geoid and Earth Observation*, International Association of Geodesy Symposia 135,
DOI 10.1007/978-3-642-10634-7_81, © Springer-Verlag Berlin Heidelberg 2010

glacier melting can have large interannual variations (e.g., Witze, 2008), we regard it as noise here and try to remove it from the geoid rate obtained from GRACE. The goals of this paper are:

1. To present a filtering procedure which is tailored for the long-term geoid rate in North America.
2. To present an error estimate for the GRACE derived geoid rate in North America which accounts for systematic and random errors in non-GIA processes that affect the secular geoid rate.

New in this paper compared to previous works that analyze the GRACE derived secular geoid or gravity rate signal over North America or Fennoscandia (Rangelova, 2007; Tamisiea et al., 2007; Rangelova and Sideris, 2008; Van der Wal et al., 2008; Steffen et al., 2008) are the following:

- Three different methods are compared for approximating measurement errors after filtering the monthly gravity fields.
- The destriping filter is tailored to give maximum synthesized signal to noise ratio for the geoid rate.

81.2 Methodology

We use CSR release 4 GRACE data (August 2002–July 2007, June 2003 missing). Trend, annual and semi-annual signals are estimated by least-squares estimation. Degree 1 coefficients are not provided due to the choice of reference system for GRACE data processing and we do not attempt to model them here as that requires the use of geophysical models (e.g., Swenson et al., 2008). C_{20} error estimates from GRACE are still noisier than those obtained from Satellite Laser Ranging (SLR) measurements (Bettadpur, 2008), and the standard deviations for degree 2 are such that they would dominate other errors in an investigation of measurement errors. Moreover, C_{20} in particular is plagued by aliasing of signal at the K1 and K2 tidal frequency which is as of yet impossible to separate from a secular trend (Ries, pers. comm., 2008). Therefore, we omit degree 2 terms in a comparison of measurement errors in Fig. 81.1 and use SLR determined values for C_{20} for all other results and standard deviations.

The geoid rate is filtered by the destriping filter of Swenson and Wahr (2006) which fits a spline polynomial to consecutive odd or even degree coefficients for a particular order. The artificial correlation between coefficients is represented by this polynomial fit and removed from each coefficient. In addition to this filter, we use a Gaussian filter halfwidth of 400 km, which is close to values used in other studies, and show its effect on cumulative degree variances.

Continental water storage variations are removed by subtracting the total vertical water output from the WaterGAP Global Hydrology Model (WGHM) (Döll et al., 2003; Hunger and Döll, 2008) which provides good agreement with GRACE on interannual timescales (Rangelova et al., 2008). Glaciers are simulated by melting of a block of ice located in areas of melting in Alaska and Greenland, as in Van der Wal et al. (2008). Ice is assumed to melt uniformly, accounting for elastic displacement of the crust, but not for self-consistent distribution of melt water. Simulation of detailed melt geometry is not necessary as only the long wavelengths leak into the GIA area. The value for ice melt for Greenland (183 Gt/year) is obtained by averaging two recent estimates from Velicogna (211 Gt/year) and Luthcke (154 Gt/year) that are reported in Witze (2008). For Alaska, we use the recent estimate of Luthcke et al. (2008), 84 Gt/year).

We assume that all error sources are uncorrelated and hence their contribution can be combined in a vector sum as follows:

$$\sigma_{\dot{N}} = \sqrt{\left(\dot{N}_{LaD,i} - \dot{N}_{WGHM,i}\right)^2 + \left(\sigma_{\dot{N}_{GRACE},i}\right)^2 + \left(\sigma_{\dot{N}_{glaciers},i}\right)^2} \quad (1)$$

where $\dot{N}_{LaD,i}$ is the secular geoid rate for grid point i from the LaD hydrology model (Milly and Shmakin, 2002) and $\dot{N}_{WGHM,i}$ is the geoid rate from the WGHM model. The difference between the two models is a crude approximation for the uncertainty in each of the models. $\sigma_{\dot{N}_{glaciers},i}$ is the error in geoid rate resulting from using the difference between the Velicogna and the Luthcke estimate (27 Gt/year) and the difference between two esimtimates based on different epochs, reported in Luthcke et al. (2008) (18 Gt/year) in the glacier simulation. $\sigma_{\dot{N}_{GRACE},i}$ is the random error present in the GRACE data. We use the following three different methods to approximate those.

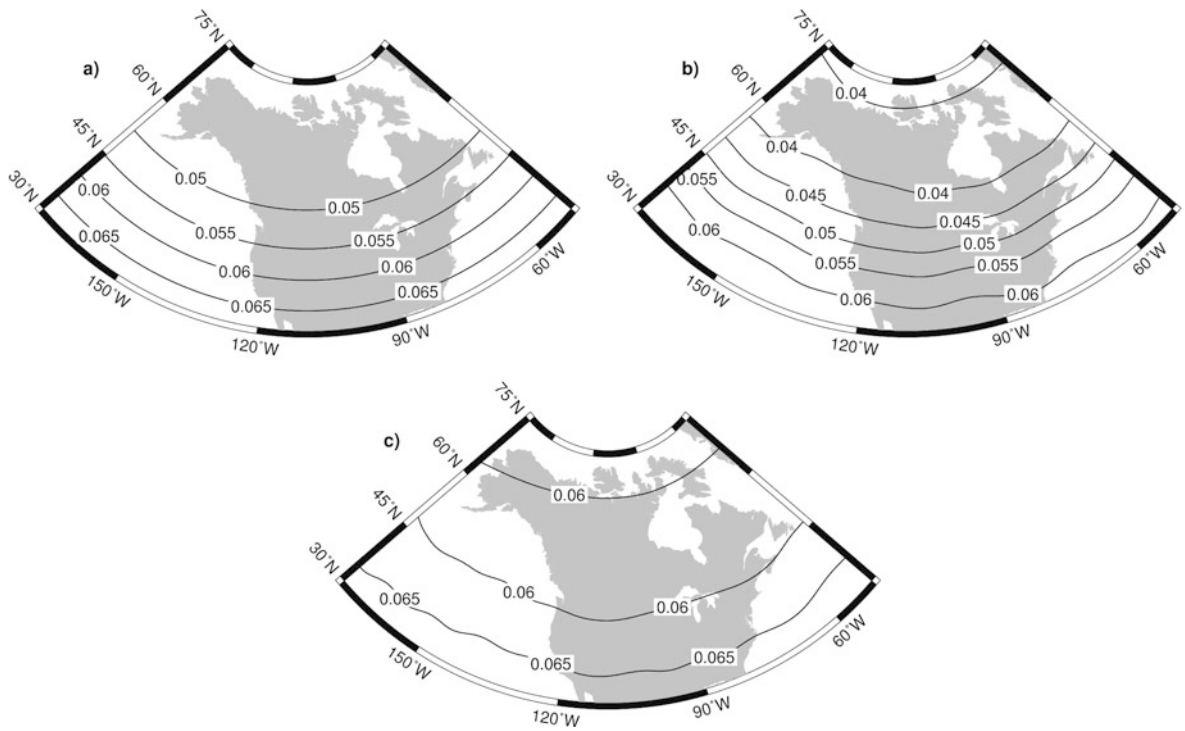


Fig. 81.1 Spatial pattern of GRACE derived geoid rate [mm/year] errors by different methods after destriping filtering, see description in next section. (**a**): Calibrated standard deviations for all months. (**b**): full VC matrix (Dec. 2006). (**c**): residuals

1. *Calibrated standard deviations.* A variance covariance (VC) matrix C is used with the squared calibrated standard deviations (provided by CSR) on the diagonal and zeros outside. The VC matrix is propagated through the destriping filter according to:

$$\mathrm{C}' = \mathrm{MCM}^T \tag{2}$$

where M represents the destriping filter (see Swenson and Wahr, 2006, on how to compute the matrix elements). The error in the geoid rate estimated for a particular degree and order coefficient is obtained from:

$$\sigma_{\dot{N}_{lm}} = \left(\mathrm{A}^{\mathrm{T}}\mathrm{PA}\right)^{-1} \tag{3}$$

in which the weight matrix P contains the monthly standard deviations for that coefficient, and A is the normal matrix for estimating a trend, annual and semi-annual cycle in that coefficient.

2. *Full covariance matrix*. From the 12 months in 2006 for which covariance matrices were made available, December 2006 gives the largest error and hence is used in the comparison. The error in the geoid rate is computed from the individual standard deviations by (Velicogna and Wahr, 2002):

$$\sigma_{\dot{N}_{GRACE,i}} = 12\sqrt{\frac{12}{(n-1)\,n\,(n+1)}}\sigma_{N_{GRACE,i}} \tag{4}$$

in which $n = 59$ months and i is a grid point.

The VC matrix does not describe well the systematic errors that cause the striping pattern in GRACE data, because the cause for the stripes does not lie solely in the measurement geometry and measurement noise (Bettadpur, pers. comm., 2008). Therefore method 1 and 2 will underestimate these errors and we introduce residuals (Wahr et al., 2004) as third method.

3. *Residuals.* It is assumed that the least-squares estimated secular, annual and semi-annual signal in each grid point represent a physical process and the residuals are used to approximate the errors (as in Wahr et al., 2004). The residuals have the disadvantage that the secular, annual and semi-annual signals are considered errorless while in reality they can contain stripes as well. On the other hand, non-periodic or non-secular

signal can be part of the residuals, mainly for low degrees (Wahr et al., 2004).

Geoid rate errors computed by methods 1, 2 and 3 are presented in Fig. 81.1. Comparing Fig. 81.1a, b, c it can be seen that using a full VC matrix results in an error estimate which is slightly different from using calibrated standard deviations for each individual month. Comparing Fig. 81.1c to the other error estimates, it appears that the use of residuals leads to a slightly larger and hence more conservative error estimate over the GIA area. This is likely because correlated errors are better represented by this error estimation method. Standard deviations obtained after propagating the error information through the destriping filter can be scaled to fit the magnitude of the residuals (Wahr et al., 2006), but this is not pursued here.

81.3 Tailoring the Filter

The filter of Swenson and Wahr (2006) can be tuned by changing the window length, the order of the polynomial and the coefficients that are to be filtered. Here we study the latter by investigating the effect on a synthesized signal-to-noise ratio that is constructed as:

$$SNR = \frac{1}{N}\sum_{i=1}^{N} \frac{\dot{N}_{GIA,i}}{\sqrt{\left(\dot{N}_{LaD,i} - \dot{N}_{WGHM,i}\right)^2 + \left(\sigma_{\dot{N}_{GRACE,i}}\right)^2 + \left(\sigma_{\dot{N}_{glaciers},i}\right)^2}} \quad (5)$$

where N is the number of grid points used (we use 554 grid points in an area around Hudson Bay; see Van der Wal et al. (2008). $\dot{N}_{GIA,i}$is the geoid rate from a GIA model with the ICE-3G loading history (Tushingham and Peltier, 1991), upper mantle viscosity of 4×10^{20} Pas and lower mantle viscosity of 6×10^{21} Pas.

These particular values were selected because this model fits the GRACE data reasonably well, out of a selection of models investigated in Van der Wal et al. (2008). A model with ICE-5G changes the signal-to-noise ratio only slightly (not shown).

Since errors determined by method 3 depend on the signal, they appear less suitable when used to find optimal filter parameters. For comparison, we determine measurement errors in equation 5 by method 1 and method 3. Figure 81.2 shows that both methods give the same cut-off degree (23) and order (5) for maximum signal to noise ratio and these parameters are used for Fig. 81.1. Using the GLDAS hydrology model (Rodell et al., 2004) instead of LaD gives cut-off parameters of degree 25 and order 6. It should be noted that for the geoid rate the signal-to-noise ratio depends less on the filter parameters than gravity rate (van der Wal et al., 2008) so tailoring the filter is less critical for the secular geoid rate.

To show the effect of smoothing, cumulative degree variances are plotted in Fig. 81.3. The GIA model is well above the total uncertainty for all degrees. Smoothing with a 400 km filter halfwidth can be seen to decrease the degree variance of the total uncertainty (especially above degree 40), while the degree variance of the GIA model smoothed with the same filter is only slightly reduced.

A definitive conclusion on the Gaussian filter halfwidth can not be made, because the amount of smoothing that should be applied to the estimated geoid rate depends on the spatial accuracy that is desired. However, it seems sensible to apply some smoothing because the sum of all errors might still be underestimated. In the following, a 400 km halfwidth will be used.

Cumulative degree variances are summed over all orders and therefore do not describe the errors specifically for North America, thus the final results are presented in the spatial domain. The parameters determined in Fig. 81.2 are used to produce the geoid rate depicted in Fig. 81.4a. The uncertainty in Fig. 81.4b is computed with Eq. 1 and shows large values centered on Alaska, which are the result of the uncertainty in present day ice melt and the difference in (mis-) modeling between the WGHM and LaD global hydrology models in areas of permanent snow. Outside Alaska and the Great Lakes area, the uncertainty is up to 0.33 mm/year.

With the present-day knowledge of global hydrology models, correcting GRACE data for the purpose of deriving secular GIA trends might introduce larger (and not well known) errors than neglecting such corrections. However, any secular geoid rate derived from GRACE will depend to some extent on knowledge of continental water storage and present-day ice melting and any error estimate should reflect that.

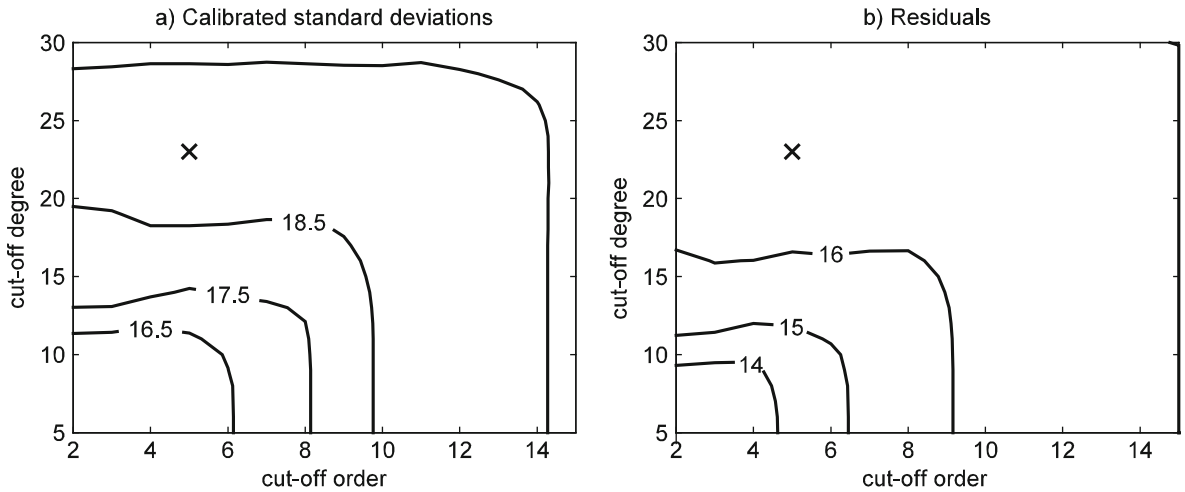


Fig. 81.2 Contours of signal to noise ratio (see description in text) for the minimum spherical harmonic degree and order that is used in the destriping filter. (**a**): calibrated standard deviations used to compute random errors, (**b**) residuals used to compute random errors

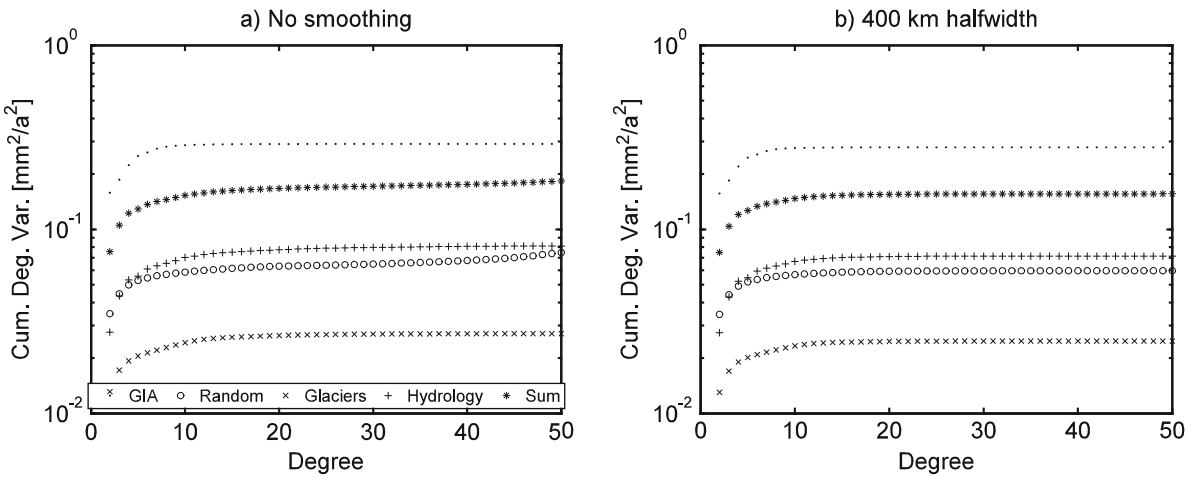


Fig. 81.3 Cumulative error degree variances for GIA model, glacier melting uncertainty, hydrology model uncertainty, random errors and sum of all uncertainty. (**a**): no Gaussian smoothing, (**b**): 400 km Gaussian filter halfwidth

81.4 Discussion

We have extracted a secular geoid rate from GRACE data using a tailored destriping filter of Swenson and Wahr (2006) and included error estimates accounting for uncertainty in present day ice melt and continental water storage variations. Variations in present-day ice melt are regarded as noise, since it is not known if they persist over the timescale at which the secular geoid rate model should be valid.

By computing GRACE measurement errors in several ways, it is shown that using one covariance matrix gives similar results as error propagation using the calibrated standard deviations for all months. Therefore, a covariance matrix does not give much extra error information and likely does not capture the correlated errors well as can be expected. The use of residuals after estimation of trend, annual and semi-annual components (Wahr et al., 2004) gives larger error estimates in North America and is the preferred method for esti-

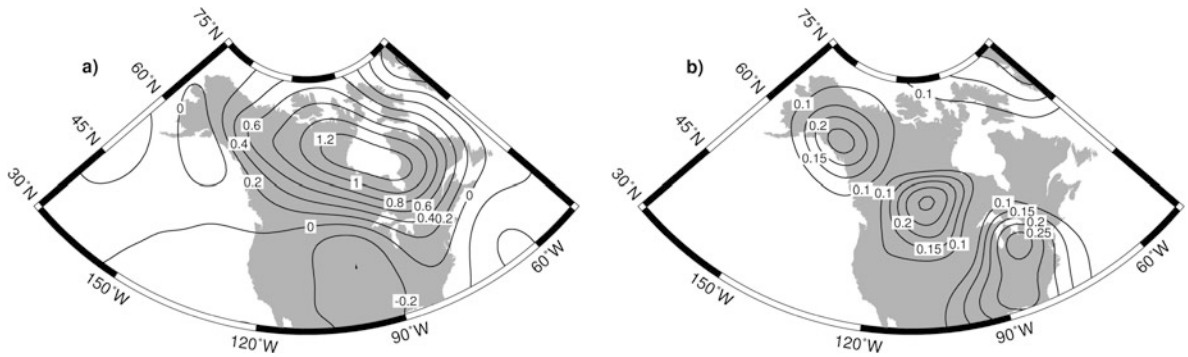


Fig. 81.4 (**a**): Geoid rate computed from GRACE with WGHM and Alaska and Greenland glaciers subtracted, after the destriping filter (applied to coefficients with degree greater than 22 and order greater than 4) and Gaussian smoothing with a 400 km halfwidth. The maximum is 1.33 mm/year. (**b**): uncertainty of the geoid rate computed by Eq. 1 with random errors computed with method 3. The maximum is 0.33 mm/year

mating the error in the secular geoid rate in this paper. When designing a filter for GIA, residuals and calibrated standard deviations yield the same parameters, therefore both can be used.

The replacement of C_{20} by its SLR-observed value does not affect the spatial pattern much but increases the maximum geoid rate by 0.33 mm/year. It remains to be seen if other harmonics are affected by similar aliasing as C_{20}.

Acknowledgements We thank the two anynomous reviewers for their comments, John Ries and Srinivas Bettadpur of CSR Texas for providing sample covariance matrices and for discussion, John Wahr, Holger Steffen and Balaji Devaraju for discussion and advice for GRACE data analysis, Kristina Fiedler and Petra Döll for providing the WGHM model output, Chris Milly for making available the LaD model output and Matt Rodell for making available the GLDAS model output. Financial support has been provided by NSERC and GEOIDE NCE grants to Drs. Sideris and Wu.

References

Ågren, J. and R. Svensson (2007). System definition and postglacial land uplift model for the new Swedish height system RH 2000. Lantmäteriet, Rapportserie: Geodesi och Geografiska informationssystem, 2006:X (in print), Gävle.

Bettadpur, S. (2008). GRACE: Progress towards product improvement, and prospects for synergy with GOCE, 2008. Oral presentation, GGEO 2008 Symposium, June 23–27, Chania, Crete, Greece.

Döll, P., F. Kaspar, and B., Lehner (2003). A global hydrological model for deriving water availability indicators: model tuning and validation. *J. Hydrol.*, 270, 105–134.

Hunger, M. and P. Döll (2008). Value of river discharge data for global-scale hydrological modeling. *Hydrol. Earth Syst. Sci.*, 12, 841–861.

Luthcke, S., A. Arendt, D. Rowlands, J. McCarthy, and C. Larsen (2008). Recent glacier mass changes in the Gulf of Alaska region from GRACE mascon solutions. J. Glaciol., 54(188), 767–777.

Milly, P.C.D. and A.B. Shmakin (2002). Global modeling of land water and energy balances, part I: The land dynamics (LaD) model. *J. Hydrometeorol.*, 3(3), 283–299.

Rangelova, E. (2007). A dynamic vertical datum for Canada. PhD thesis, Dept. of Geomatics Engineering, University of Calgary.

Rangelova, E. and M.G. Sideris (2008). Contributions of terrestrial and GRACE data to the study of the secular geoid changes in North America. *J. Geodyn.*, 46, 131–143, doi:10.1016/j.jog.2008.03.006.

Rangelova, E., W. van der Wal, M.G. Sideris, and P. Wu (2008). Spatiotemporal analysis of the GRACE-derived mass variations in North America by means of multi-channel singular spectrum analysis, GGEO 2008 Symposium, June 23–27, accepted for proceedings.

Rodell, M., P.R. Houser, U. Jambor, J. Gottschalck, K. Mitchell, C.-J. Meng, K. Arsenault, B. Cosgrove, J. Radakovich, M. Bosilovich, J.K. Entin, J.P. Walker, D. Lohmann, and D. Toll (2004). The global land data assimilation system. *Bull. Am. Meteorol. Soc.*, 85(3), 381–394.

Steffen, H., H. Denker, and J. Müller (2008). Glacial isostatic adjustment in Fennoscandia from GRACE data and comparison with geodynamical models. *J. Geodyn*., 46, 155–164.

Swenson, S., D. Chambers, and J. Wahr (2008). Estimating geocenter variations from a combination of GRACE and ocean model output. *J. Geophys. Res.*, 113, doi:10.1029/2007JB005338.

Swenson, S. and J. Wahr (2006). Post-processing removal of correlated errors in GRACE data. *Geophys. Res. Lett*., 33, L08402, doi:10.1029/2005GL025285.

Tamisiea, M.E., J.X. Mitrovica, and J.L. Davis (2007). GRACE Gravity data constrain ancient ice geometries and continental dynamics over Laurentia. *Science*, 316, 881–883.

Tushingham, A.M. and W.R. Peltier (1991). ICE-3G: A new global model of late Pleistocene deglacation based upon

geophysical predictions of post-glacial relative sea level change. *J. Geophys. Res.*, 96(B3), 4497–4523.

Van der Wal, W., P. Wu, M.G. Sideris, and C.K. Shum (2008). Use of GRACE determined secular gravity rates for glacial isostatic adjustment studies in North-America. *J. Geodyn.*, 46, 144–155, doi:10.1016/j.jog.2008.03.007.

Velicogna, I. and J. Wahr (2002). Postglacial rebound and Earth's viscosity structure from GRACE. *J. Geophys. Res.*, 107(B12), doi: 10.1029/2001JB001735.

Wahr, J., S. Swenson, and I. Velicogna (2006). Accuracy of GRACE mass estimates. *Geophys. Res. Lett*., 33, doi: 10.1029/2005GL025305.

Wahr, J., S. Swenson, V. Zlotnicki, and I. Velicogna (2004). Time-variable gravity from GRACE: First results. *Geophys. Res. Lett.*, 31, L11501, doi:10.1029/2004GL019779.

Witze, A. (2008). Climate change: losing Greenland. *Nature*, 452, 798–802, doi:10.1038/452798a.

Chapter 82

Ten-Day Gravity Field Solutions Inferred from GRACE Data

J.M. Lemoine, S.L. Bruinsma, and R. Biancale

Abstract The GRACE mission is designed to monitor temporal variations in the fluid mass at the surface of the Earth. 177 satellite-only geopotential solutions to degree and order 50 were computed every 10 days for the period 29 July 2002 through 30 September 2007. These solutions were obtained using a processing strategy, background model and solution stabilization in particular, which are different from the ones used by the GRACE project. A temporal and spatial resolution of 10 days and approximately 666 km (spherical harmonics up to degree 30) is achieved without significant streaking effects in the maps and good continuity across the solutions. The EIGEN-GL04C gravity field model, which is constructed exclusively with GRACE and LAGEOS data to degree and order 70, is used as the mean field to which all 10-day solutions are compared in order to infer temporal variations. After conversion to equivalent water height, the maps can be used to evaluate seasonal and linear variations in water mass storage. The uncertainty in the new solutions is estimated at 20–30 mm equivalent water height, or about 10% of the amplitude of the water mass variation of the Amazone basin.

82.1 Introduction

The objective of the GRACE (Gravity Recovery and Climate Experiment; Tapley et al., 2004) twin-satellite mission is to map the global gravity field of the Earth every 30 days. The temporal variability due to mass redistribution of the surface fluid envelopes can be inferred from changes in the GRACE monthly gravity field solutions. The satellites, jointly managed by NASA (National Aeronautics and Space Administration) and DLR (Deutsches Zentrum für Luft- und Raumfahrt), were launched on 17 March 2002 in a near-circular orbit at about 500 km altitude. They are separated from each other by approximately 220 km along-track, which distance is measured using a very precise K-band microwave ranging system. Furthermore, the science payload of each satellite consists of a Global Positioning System (GPS) receiver, laser retro-reflector, star sensors, and high precision accelerometers.

In this study, new 10-day solutions are computed by means of dynamic least-squares orbit adjustment and subsequent parameter recovery through the estimation of corrections to a background gravity model. We present results obtained using the same numerical approach as the GRACE project, i.e., GFZ Potsdam (GeoForschungsZentrum Potsdam, Germany) and CSR (Center for Space Research, Austin, USA), but with a different processing strategy. In particular, a different background gravity model is applied and a different parameterization, as well as a constraint in the inversion. Artefacts, such as north-south streaking patterns, thanks to the constraint, much less affect the solutions. Instead of using the K-band range-rates (KBRR) that are provided in the level-1B data files, these were derived in-house from the biased K-band ranges. A total of 177 (out of 185) satellite-only gravity field solutions expressed in normalized spherical harmonic coefficients to degree and order 50, given every 10 days, were computed, covering 29 July 2002 through 30 September 2007. These truly 10-day solutions are compared to our

J.M. Lemoine (✉)
CNES/GRGS, Toulouse Cedex 31401, France
e-mail: jean-michel.lemoine@cnes.fr

S.P. Mertikas (ed.), *Gravity, Geoid and Earth Observation*, International Association of Geodesy Symposia 135,
DOI 10.1007/978-3-642-10634-7_82, © Springer-Verlag Berlin Heidelberg 2010

published 30-day solutions (Lemoine et al., 2007), which are available on-line on the server of the Bureau Gravimétrique International (http://bgi.cnes.fr:8110/geoidvariations/README.html.). The temporal gravity field solutions, after conversion to equivalent water heights, can be used to infer variations in water mass storage; detailed interpretation of these variations, however, is out of scope of this paper.

The next section reviews the processing strategy, i.e., background model, the data (pre) processing, the parameterization of the computation, and the solution strategy using a specific constraint. Section 82.3 presents the gravity field solutions, and the hydrological mass anomaly signals that can be inferred from the sequence of 30- and 10-day solutions over several river basins are presented. The conclusions are presented in Sect. 82.4.

82.2 Processing Strategy

82.2.1 GRACE: Background Models and Parameterization

The CNES/GRGS (Centre National d'Etudes Spatiales/Groupe de Recherches de géodésie spatiale) precise orbit determination software, GINS, is used for (inter-)satellite tracking data reduction and the generation of normal matrices. The gravitational background force model is identical to the one listed in Table 1 of Lemoine et al. (2007) except for the a-priori gravity field model: presently EIGEN-GLO4C (Foerste et al., 2007) to degree and order (d/o) 180 is used. A notable difference with other groups is the use of the barotropic MOG2D ocean model (Carrère and Lyard, 2003), which is applied after removal of a 2 year mean, i.e., it is mass preserving. This model differs significantly from the ocean mass variation model AOD1B (Flechtner, 2003) used by the GRACE project, in particular in the southern Arctic Ocean (the circumpolar current). The water mass storage (soil moisture, snow cover, glaciers, oceans, etc.) is not modelled; therefore, differences between the static and the time-variable gravity field solutions will be due to these not modelled effects mainly, whereas a small part is due to background model errors, the baroclinic response of the ocean, and post-glacial rebound too. The geocenter motion is not modelled since it is not part of the IERS 2003 conventions (McCarthy and Petit, 2004).

The effect of the surface forces acting on the satellites is removed using calibrated accelerometer measurements in combination with the attitude quaternions. Bias and scale factor corrections are estimated per 24-h arc in all three directions.

The parameterization of the K-band range-rate tracking data (KBRR) was not modified with respect to Lemoine et al. (2007): bias, bias-rate, 1-, 2-, 3-CPR terms *per revolution*.

82.2.2 LAGEOS

The harmonics of very-low degree, in particular degree 2, cannot be estimated accurately with GRACE data only. Therefore, LAGEOS-1 and -2 orbits are computed followed by normal equation generation over the same time period as GRACE in order to stabilize the gravity field solutions. Due to their altitude of almost 6,000 km, the sensitivity of the orbit with respect to the gravity field is limited to degrees 2 through about 10, but it is particularly sensitive to J_2. The orbit processing standards were identical to those applied for GRACE, but the SLR (Satellite Laser Ranging; International Laser Ranging Service, Pearlman et al., 2002) data were reduced in 10-day arcs that exactly cover the time intervals of the gravity field solutions.

82.2.3 Ten-Day Gravity Field Solutions

The published (reference) 30-day temporal gravity field solutions are constructed by accumulating three consecutive GRACE and LAGEOS 10-day normal matrices in which the central 10-day matrix is given double weight (Lemoine et al., 2007). They are computed every 10 days in order to have a higher temporal resolution; nevertheless they are not truly 10-day solutions because 30 days of data were actually used. The solve-for parameters are the harmonic coefficients of degrees 2 through 50. The degree 1 geopotential coefficients are not estimated in our solutions (i.e., fixed to zero), even though this is possible thanks to LAGEOS. The new solutions are obtained by solving the same coefficients, but per 10 days.

Both the reference and the 10-day solutions can only be computed accurately to about degree 30 due to a combination of insufficient ground track coverage, and measurement, processing, and background modelling errors; estimating to higher degrees results in geoid height difference plots that show the typical north-south streaking and degraded accuracy at all degrees. However, spectral leakage affects the solutions if the degrees greater 30 are not estimated. To avoid the above-cited problems, the coefficients of degrees 31 through 50 are gradually constrained to those of a mean solution, for which we have selected EIGEN-GL04C (Foerste et al., 2007); the degrees 51 through 160 are substituted by the EIGEN-GL04C coefficients. This is admittedly not an unbiased constraint, and as a result using our solutions (10- and 30-day) leads to *underestimation* of amplitudes and slopes by about 10–15%. However, any filtering method brings this kind of problem (i.e., the signal is altered after filtering). We are presently attempting to solve this problem by means of constraining to a gravity field model that contains mean, slope, and annual coefficients up to some degree.

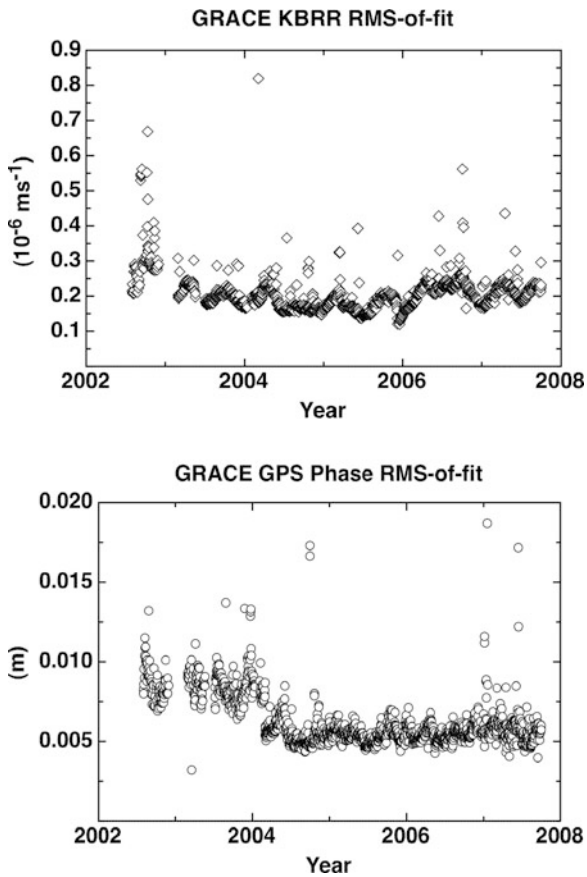


Fig. 82.1 The RMS-of-fit of the GRACE GPS phase and KBRR residuals for all arcs retained in the 10-day solutions

82.3 Results

Hundred and seventy seven time-variable gravity field solutions expressed in normalized spherical harmonic coefficients up to degree and order 50 were computed, covering 29 July 2002 through 30 September 2007. Due to instrumental problems (GPS, accelerometer, or K-band system) and the resulting data gaps, 8 solutions are missing. The RMS'-of-fit of the GPS phase and the KBRR residuals are presented in Fig. 82.1. The average RMS-of-fit taking all GRACE

arcs into account is 6.2 mm and 29.2 cm for the GPS phase and range, respectively, and 0.205 μm/s for the KBRR residuals. The figure shows that the quality of the data is improving with time, and that solutions for the years 2002 in particular and 2003 to a lesser degree are likely to be significantly less accurate than after that date. In fact, the authors recommend that 2002 solutions be used with caution, or not at all. The dominantly annual signal that is visible in the KBRR residuals is due to the hydrology cycle (i.e., the signal we are trying to determine).

The 10-day solutions are evaluated by means of comparison to the reference 30-day solutions (impact of the less-dense ground-track coverage), by computing the RMS of the geoid variation over the oceans and the Sahara (regions of little to very little variation), and by inspecting the continuity of the consecutive solutions for specific large river basins.

Figure 82.2 shows the recovered basin-averaged equivalent water height (EWH) estimates of two large river basins, the Amazone (top) and the Yangtze (bottom), obtained using the 10-day and the reference solutions, respectively. The absolute difference between the 10-day and reference solutions is up to 45 mm, and 10 mm on average. In case of the Amazone, the continuity (i.e., the presence of isolated large values and outliers) is good and similar to the reference solutions, except for a peak in the beginning of 2003. The continuity of the recovered water heights per 10-days for the

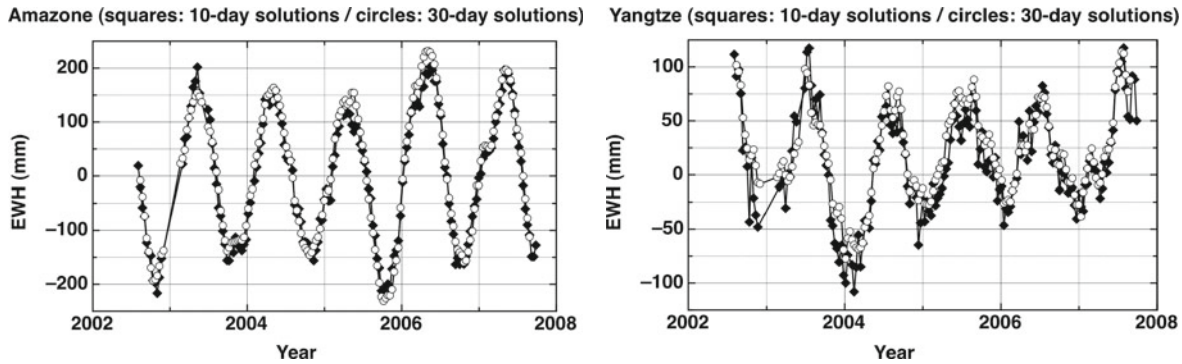


Fig. 82.2 The recovered basin-averaged equivalent water heights of the Amazone (*top*) and Yangtze (*bottom*) rivers

Yangtze appears to be worse than for the Amazone, bur this is in fact a visual effect due to scale: the amplitudes are more than twice smaller.

Figure 82.3 shows the average geoid variation expressed in equivalent water height over the oceans. The mean ocean mass variations presented in Fig. 82.3 agree at the few mm level with the results obtained by Chambers et al. (2004), which were obtained using the CSR monthly GRACE solutions.

The GRACE solutions, when averaged over very large surfaces, have an uncertainty at the few mm level, but much larger for river basins. The uncertainty is estimated by means of computing the variations, expressed in EWH, over the Sahara desert, which has a very weak hydrological signal. The recovered time series is shown in Fig. 82.4. The average absolute difference between the 10- and 30-day solutions is again about 10 mm after 2004; for 2002 and 2003, the differences are 20 mm on average. Based on Fig. 82.4, and the RMS over the oceans and the Sahara (about 40 mm; this includes signal as well), we estimate the uncertainty of the 10-day solutions to be 20–30 mm.

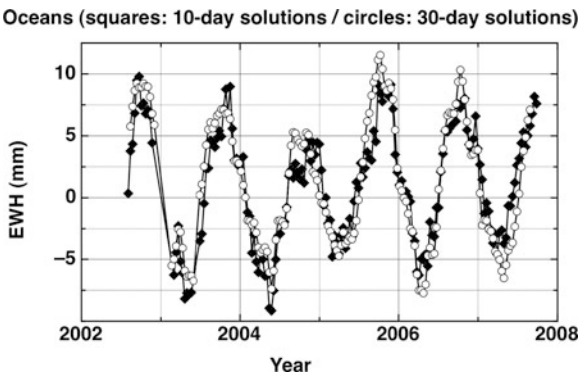


Fig. 82.3 The recovered equivalent water heights averaged over all ocean surfaces

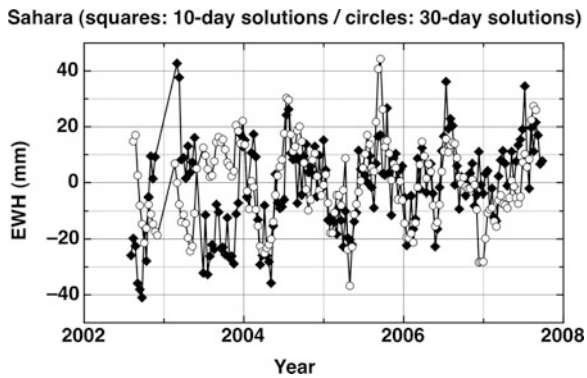


Fig. 82.4 The recovered equivalent water heights averaged over the Sahara desert

82.4 Conclusions

The 177 CNES/GRGS 10-day geopotential solutions available, covering July 2002 through September 2007, are a good alternative to the GRACE project solutions because of their accuracy and resolution. The resolution of approximately 666 km on the globe per 10 days is comparable to what is achieved with the 30-day (reference) solutions. Higher resolution could not be reached at present. Using the solutions, water mass storage signals over large drainage basins are estimated with good continuity, although slightly less than with 30-day solutions because of (a larger sensitivity to) outliers.

The average absolute difference between the 10-day and reference 30-day solutions is about 10 mm. The uncertainty of the solutions is estimated at approximately 20–30 mm.

Acknowledgments The authors thank ISDC for the GRACE data distribution. P. Gegout (IPG Strasbourg) provided the grids used in the 3D-atmosphere model. H. Bock (University of Bern) provided the GPS clock corrections.

References

Carrère, L. and F. Lyard (2003). Modeling the barotropic response of the global ocean to atmospheric wind and pressure forcing – comparisons with observations. *Geophys. Res. Lett*., 30, doi:10.1029/2002GL016473.

Chambers, D.P., J. Wahr, and R.S. Nerem (2004) Preliminary observations of global ocean mass variations with GRACE. *Geophys. Res. Lett.,* 31, L13310, doi:10.1029/2004GL020461.

Flechtner, F. (2003). AOD1B product description document. GRACE 327-750, Center for Space Research, University of Texas at Austin, Austin.

Foerste, C. et al. (2007). The GFZ Potsdam/GRGS satellite-only and combined gravity field models: EIGEN-GL04S1 and EIGEN-GL04C. *J. Geod*., doi: 10.1007/s00190-007-0183-8.

Lemoine, J.M., S. Bruinsma, S. Loyer, R. Biancale, J.C. Marty, F. Perosanz, and G. Balmino (2007). Temporal gravity field models inferred from GRACE data. *Adv. Space Res.,* 39, 1620–1629.

McCarthy, D.D. and G. Petit (Eds). (2004). IERS Conventions (2003). IERS Technical Note 32, Frankfurt am Main: Verlag des Bundesamts für Kartographie und Geodäsie.

Pearlman, M.R., J.J. Degnan, J.M. Bosworth (2002). The International Laser Ranging service. *Adv. Space Res.,* 30(2), 135–143.

Tapley, B.D., S. Bettadpur, M. Watkins et al. (2004). The gravity recovery and climate experiment: Mission overview and early results. *Geophys. Res. Lett.,* 31, L09607, doi:10.1029/2004GL019920.

Part VIII
Earth Observation and the Global Geodetic Observing System (GGOS)

R. Gross and Hans-Peter Plag

Chapter 83

GGP (Global Geodynamics Project): An International Network of Superconducting Gravimeters to Study Time-Variable Gravity

D. Crossley and J. Hinderer

Abstract The Global Geodynamics Project (GGP) is an international network of superconducting gravimeters (SG) first established in 1997 and further extended in 2003. It was decided during the last IUGG assembly in 2007 to move to a permanent network hosted by IAG and become part of GGOS. Several new locations are being planned to extend the network to about 30 stations in 2008/2009. One of the present tasks within GGP is to prepare raw GGP data (at sampling times of 1–5 s) for inclusion into the IRIS data set for the seismologists to include in normal mode studies of the Earth. Of continuing interest within GGP is the issue of combining measurements from absolute gravimeters and permanent GPS at the SG stations for a variety of long-term studies of the gravity field such as tectonic uplift, subduction zone slip, post-glacial rebound and present-day ice melting. One of the most interesting new ideas within GGOS is the determination of the geocenter using a combination of satellite and ground-based gravimetry. The GGP network can provide a unique contribution in this respect through continuous data at the stations where absolute gravimeters (AG) will be deployed. The continuous monitoring of time-variable gravity is a tool to investigate many aspects of global Earth dynamics and to contribute to other sciences such as seismology, oceanography, earth rotation, hydrology, volcanology, and tectonics. Another promising application is the use of SG sub-networks in Europe and Asia to validate time-varying satellite gravity observations (GRACE, GOCE) due to continental hydrology and large-scale seismic deformation.

D. Crossley (✉)
Department of Earth and Atmospheric Sciences, Saint Louis University, St. Louis, MO 63108, USA
e-mail: crossleydj@gmail.com

83.1 GGP Stations

This paper is in part a review of the GGP superconducting gravimeter (SG) network, for the benefit of those who may not be familiar with ground-based time-variable gravity observations. Later, we emphasize the connection between GGP and some of the goals of the GGOS program. We begin, as usual, with a map of stations (Fig. 83.1) that shows the distribution of the 25 or so currently recording SG stations, together with the locations of some older stations and others planned for the near future. Note that the original designation Dehradun (India) has been changed to the actual site, Ghuttu.

The SG is a complex instrument requiring specific site properties, and, in common with other comparable technologies, there is a cluster of sites in Europe and Asia, and elsewhere the distribution is more widely scattered. It is noteworthy that scientists in Germany and Japan have made efforts to locate instruments in some of the more remote sites. For example Syowa (Antarctic), Ny-Alesund (Norway), Canberra (Australia), and Bandung (Indonesia) were established by the Japanese, and Sutherland (S. Africa), Concepcion (Chile), and Manaus (Brazil) by the Germans. The French are planning stations in Djougou (Benin Republic) and Tahiti, the latter being the new location for ICET (International Center of Earth Tides). ICET is hosted at the University of French Polynesia, under its new director J.-P. Barriot, and ICET (in partnership with GFZ Potsdam) runs the GGP database. Recently new installations have been realized in S. Korea, Taiwan, Czech Republic, and India, funded by the countries themselves. The paucity of sites in N. America is perhaps unusual as the

S.P. Mertikas (ed.), *Gravity, Geoid and Earth Observation*, International Association of Geodesy Symposia 135,
DOI 10.1007/978-3-642-10634-7_83, © Springer-Verlag Berlin Heidelberg 2010

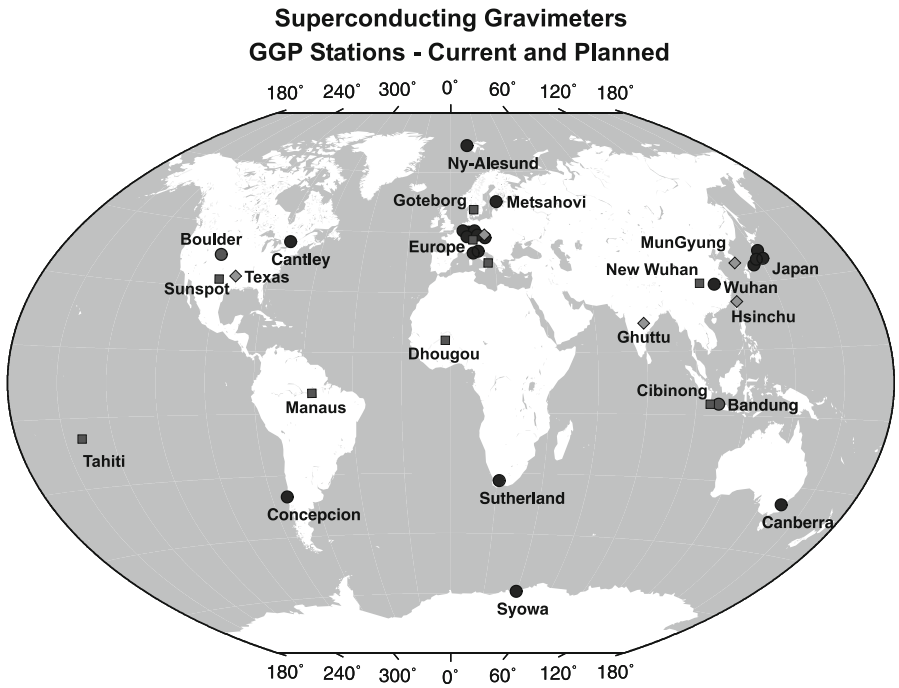


Fig. 83.1 Distribution of SG stations: *light circles* are operational, *dark circles* are stopped, diamonds are new installations, and *squares* are planned

instrument is manufactured in San Diego (GWR Instruments); but Boulder will be refurbished, and a new site is being established in Texas. The use of gravity observations for geodetic purposes in the US and Canada has languished behind that in Europe (compared for example to the equal use of GPS), not just due to the cost difference for an SG.

83.2 A Typical GGP Site

A typical GGP site needs additional instrumentation to record secular gravity changes and environmental variables that are so intimately associated with the time variation of gravity. Figure 83.2 shows a collection of such instruments for station J9 in Strasbourg (except for 2(b) that is at St. Croix-aux-Mines in the Vosges). Not shown is a vertical well for monitoring groundwater level. This particular instrument (SG) is located in an underground bunker beneath the soil moisture layer, but above groundwater level (Fig. 83.3).

In the case of J9, the monitoring of the local soil conditions has been extended to measurements such as a penetrometer (to measure lithology), soil compaction, electrical DC resistivity, and detailed topography. Other well-instrumented sites include Bad Homburg, Moxa, Wettzell, Membach and Medicina, Standard at all sites is accurate timekeeping and continuous GPS. In the early days of SG recording, the two primary concerns were the gravity signal itself and the barometric pressure, with an accurate clock for sampling. The additional instruments cited above are invaluable in assessing the role played by local environmental conditions (driven primarily by rainfall), in the time domain gravity residual over times between hours and years.

83.3 Performance of the SG

It is somewhat remarkable that the SG, in operation for about 40 years, has maintained a more or less constant precision and accuracy level over that whole time span. The first "commercial" operating machines were installed in Bad Homburg, Brussels, Strasbourg, and Wuhan in the mid 1980s. Of great interest was Richter's (1987) first comparison between two slightly different models (TT40 and TT60), in which the gravity residual signal (after subtraction

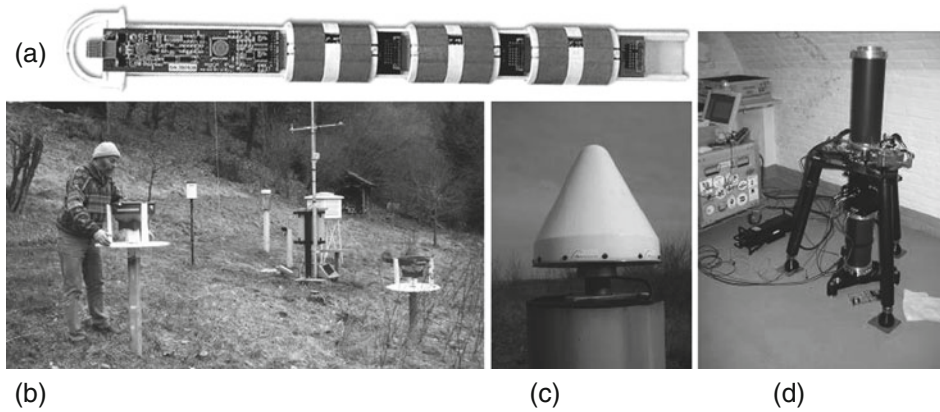


Fig. 83.2 Auxiliary instruments for an SG site (**a**) Sentek soil moisture meter (**b**) a met station (barometer, temperature, wind, humidity) with several pluviometers, (**c**) continuous GPS, and (**d**) FG5 absolute gravimeter

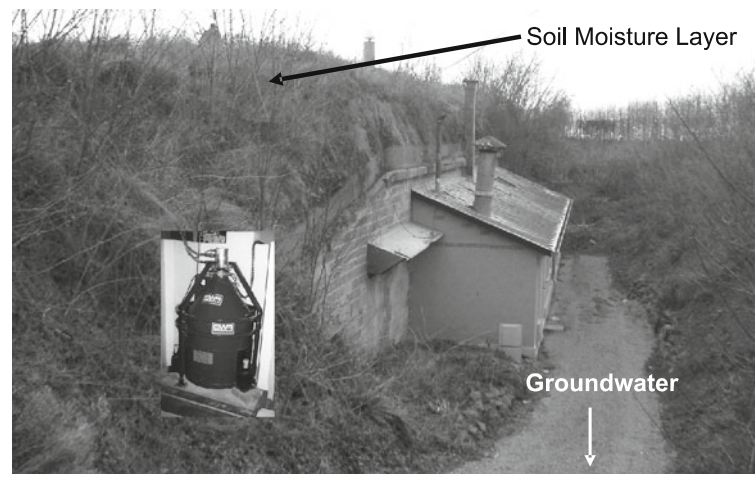


Fig. 83.3 Composite of the Strasbourg SG, model CO26, in a bunker below the soil moisture level

of tides and the atmospheric pressure effect) showed agreement in variations at about 0.1 μgal (1 μgal = 10^{-8} ms^{-2}). This type of comparison has been repeated several times since (e.g. Kroner et al., 2005), with similar conclusions, thus reinforcing the frequent claim that ground deformation can be reliably measured to at least 0.1 μgal by the SG.

As discussed frequently (e.g. Hinderer et al., 2007), the specifications of the SG are: sampling =1–5 s (higher rates have been achieved for specialized purposes), precision (least significant bit) = 0.1 ngal (1 ngal = 10^{-11} m s^{-2}), frequency domain accuracy (observation of small non-linear tidal waves) = 0.1 ngal, time domain accuracy 0.1 μgal (as above).

Two important characteristics of SGs are their calibration stability, which is probably better than 0.01% (Amalvict and Hinderer, 2007), and their small drift rate (0–5 μgal yr^{-1}). Stability is ensured by the superconducting currents that support the 2.54 cm niobium sphere. Early SG models had a noticeably exponential instrument drift that decayed over periods of several years after initial installation. It is still the case that the drift of a particular instrument is a difficult variable to predict, but a significant reduction in drift has followed improving technology and manufacturing. Most recent instruments, such as the SG currently in Hsinchu (Taiwan, Fig. 83.4), typically have very low initial drift and eventual drift rates that sometimes barely exceed the accuracy of the absolute gravimeters (AGs) that are used to calibrate the SGs. AGs have a typical precision of 1 μgal and an accuracy of 1–3 μgal.

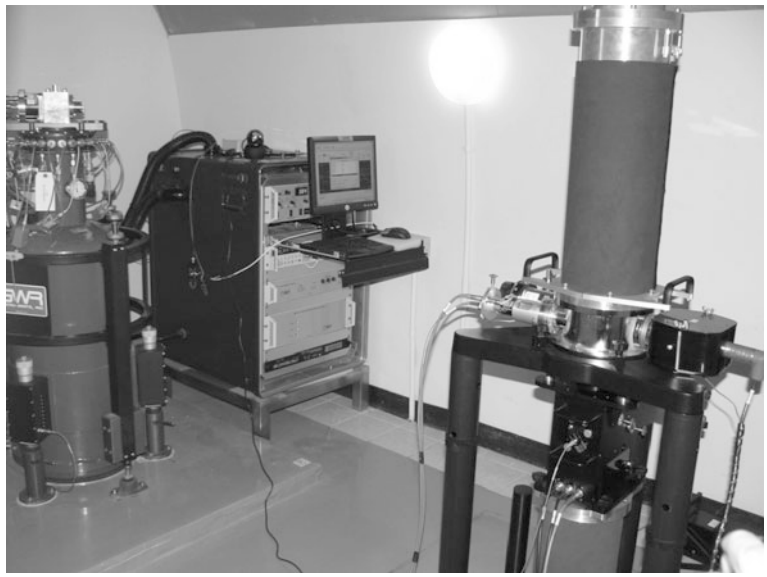


Fig. 83.4 GWR model SGT48 operating in Hsinchu, Taiwan. The dewar sits on the ground, and can maintain liquid helium indefinitely; it is shown with a standard electronics and data acquisition package, and also an AG

83.4 How GGP Functions

GGP began as a project of the IUGG interdisciplinary group SEDI (Study of the Earth's Deep Interior), in 1990, largely through the efforts of several Canadian geophysicists (Crossley et al., 1999). The idea was to set up a global network of SGs to detect possible core modes, or internal gravity waves in the Earth's liquid core, a project spurred by initial optimism that such waves would be detectable in the gravity spectrum at periods between 6 and 24 h. The goals of the project rapidly expanded to observing the complete spectrum of gravity variations, from seconds to years. Coherent global signals obviously exist at a number of frequencies (e.g. seismic normal modes, tides, atmospheric pressure waves, and polar motion), and for such signals the stacking of records from the global GGP data set is necessary. On the other hand, many gravity signals are generated by more local effects such as earthquake displacement fields, hydrological variations, weather systems, and secular tectonics. Thus GGP became a widely-based project that puts the full range of the SG to use for both geophysical and geodetic purposes.

GGP began recording collectively on 1 July 1997 and ICET was the organization for archiving the data because of the strong historical connection between tidal gravity variations, SGs, and ICET. From the beginning, GGP data quickly overwhelmed in volume the traditional tidal data from a variety of spring gravimeters, tiltmeters and strainmeters, and ICET devoted additional manpower to processing and checking the data. The database servers were not at ICET, but through mutual agreement accessed through the International System and Data Center (ISDC) at GFZ Potsdam. The new interface for GGP data is http://isdc.gfz-potsdam.de/

All GGP groups use the data format originating with Wenzel (1996), known as PRETERNA, in which every value (predominantly gravity and pressure), are time tagged in the original units (volt). The only processing is a decimation filter from the original samples to 1-min values, but no other corrections are done. The full signal is saved with a precision of 7.5+ digits, ensuring that the tides are adequately recorded as well as the smallest tidal waves (see above). Users should realize that gaps, spikes and offsets still have to be treated if a clean continuous time series is required, or otherwise avoided if the series is processed as non-contiguous blocks. ICET provides corrected minute data on their website, but this treatment is designed for tidal analysis and may not be suitable for all purposes, especially long period studies. A full discussion of data treatment is given in Hinderer et al. (2007).

GGP groups upload 1 month files to ICET within 6 months of data collection. They are then available to other groups who have provided data for a "restricted circulation" of a further 6 months. After 1 year of collection, the GGP data is freely available.

With some exceptions, (mainly due to instrument or data acquisition problems), most groups follow this timetable voluntarily, which is one of the key points of the success of GGP. The other feature of GGP is a strict adherence to the quality of site, data acquisition parameters, and data formatting.

GGP was incorporated into the IAG as Inter-Commission Project #3.1 in 2003; it is a joint project between Commission 3 (Earth Rotation and Geodynamics) and Commission 2 (The Gravity Field). GGP has a Chair and Secretary elected every 4 years at the IUGG meeting, and has a mailing list of 120 members. Reviews are given by Crossley et al. (1999) and Crossley (2004); further details can be found at http://www.eas.slu.edu/GGP/ggphome.html

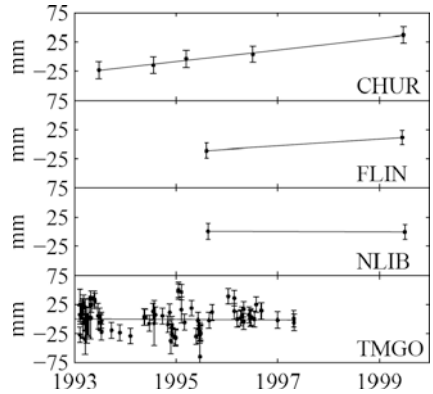


Fig. 83.5 Vertical motion at several sites in N. America, showing PGR over a 6-year time period. AG gravity measurements are scaled by the factor –6.5 mm/μgal, as reported in the original paper (Fig. 83.3); *tick marks* on the *right axis* are spaced every 7.7 μgal

83.5 GGP and GGOS

We now turn to the main issue in this paper, which is the relationship between GGP and GGOS (Global Geodetic Observing System). As outlined by Plag (2008), GGOS is the primary program of the IAG to coordinate the recording and dissemination of all geodetic data for Earth monitoring, designed to be a fully functioning system by 2010. GGP plays a small but important role in GGOS, namely the recording of the gravity field and especially its time variations. A recent review of this topic was given by Crossley and Hinderer (2008).

83.5.1 AG and SG Observations

We begin by going back to a paper by Larson and van Dam (2000) on the measurement of post glacial rebound (PGR) using absolute gravity measurements. Figure 83.5 shows 5 measurements at CHUR (Churchill), 2 each at FLIN (Flin Flon) and NLIB (North Liberty), and a cluster of measurements at TMGO (Table Mountain Gravity Observatory). The AG error bars show a typical formal standard deviation of about 2 μgal. CHUR shows a clear positive trend that is much weaker at the other sites. Many more recent studies have since provided better data on PGR at Canadian sites, but we are using this earlier paper to make an important point about the effect of hydrology on AG measurements.

When frequent AG measurements are available, they often show a scatter such as for TMGO, as noted by Larson and van Dam. In this case, what is the cause? We show in Fig. 83.6 an SG time series with AG data (several meters) for 2 years beginning in April 1995. Both data sets confirm a gravity decrease between days 50 and 150 of the record. The SG recording was without noticeable problems over the whole time span, so we are fairly sure there are no hidden offsets in the data. Tides, atmospheric pressure and polar motion are subtracted, and for the SG an exponential drift was removed (but this was not fitted to the AG data). Figure 83.6 thus confirms the inference in Fig. 83.5 that there is no AG gravity trend between 1993 and 1999 at TMGO. But Fig. 83.6 shows while some of the AG scatter is confirmed by the more detailed SG residuals, other values may be biased by instrumental effects.

The conclusion from this one example is that where there is the possibility of combining AG and SG observations, it will be much easier to assess the quality of the AG data, even when long time periods are of interest. The only caveat in using SG series as a reference is that offsets must be removed with care, and instrumental drift be appropriately modeled. The most detailed comparison of SG and AG data to date is the work of Wziontek et al. (2006). They show that AG steps can be estimated, and corrected if desired, using SG observations.

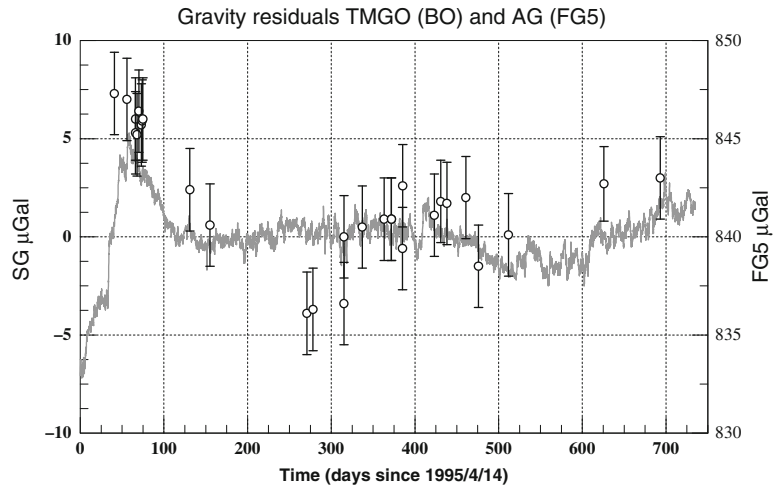


Fig. 83.6 A comparison of SG and AG measurements at TMGO from April 1995 (Crossley et al., 1998)

It goes without saying that any intercomparison of AG instruments should actively use a collocated SG to monitor the short term temporal variations of gravity, probably with a significant reduction in bias between AG determinations.

83.5.2 SG Drift

There are a very large number of studies where SG and AG measurements have been compared and combined to assess the drift rate of the SG and its calibration. It is sometimes argued that the SG is unsuitable for long-term gravity variations because it does have a drift, but in practice this is not a critical limitation. Almost all SG studies have concluded that the SG instrument drift is a simple mathematical function that could be due to leakage of trapped magnetic flux when the instrument is initialized (i.e. the sphere is levitated). This leakage can be expressed either as a decaying exponential, or a linear, function of time; the two are indistinguishable after the instrument has been operating for some time. It is virtually impossible to separate SG drift from actual secular gravity changes except by comparison with AG data, save for the initial installation of the SG when a clear exponential behavior may be seen.

Thus we conclude that at any important geodetic site where gravity is to be monitored, the combined use of AG and SG data is highly recommended. The complementary and independent nature of the technologies ensures that data from one of the instruments will in all cases significantly benefit the interpretation of data from the other. Such reasoning applies to the plan to use AG and GPS measurements to determine the offset of the Earth's center of mass from the origin of the Terrestrial Reference System (Plag et al., 2007).

83.5.3 Hydrology Effects on Gravity

Returning to the data from TMGO, Crossley et al. (1998) modeled the effect of hydrology by converting the observed rainfall to variations in the thickness of the groundwater layer below the instrument, and fitting a 2-time-constant model to the observed gravity (Fig. 83.7). This was done because groundwater was

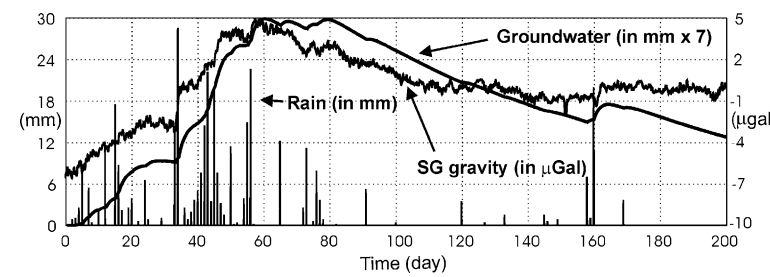


Fig. 83.7 Rainfall converted to groundwater level and compared to SG residuals at TMGO

not measured on site. The water layer was treated as a Bouguer slab attraction, but no loading was included. A good agreement was found for a recharge time constant of 4 h (time for rainfall to enter the water layer) and a discharge time constant of 91 day (time for groundwater to drain). Similar values were obtained using this model at Bad Homburg by Harnisch et al. (2006).

Figure 83.7 demonstrates that gravity residuals up to 5 μgal or more can be dominated by hydrological effects at a station. Where there is rainfall (and there are no SGs yet located in desert regions), the effects can occur within minutes of rainfall and last several months. It is unlikely that the effects of the atmosphere and hydrology can be fully separated due to the limitations of modeling in the local area around a gravimeter. Moreover, the regional and global attraction and loading that occurs for both the atmosphere and hydrosphere is data intensive and requires considerable numerical computations, particularly at a time sampling of 3 h or less.

Nevertheless progress in modeling the gravity effects of hydrology has been considerable in the past 10 years, due primarily to availability of high quality data from SGs, and the increasing use of hydrological instrumentation at a station (as described in Sect. 83.2). Of the many SG sites where hydrology has been observed and modeled, we select a few to show the range of current results.

The above-ground SG station Medicina, on the Po Plain in northern Italy, is close to Bologna. Zerbini et al. (2007) have made an effort to model all possible effects on gravity by including soil moisture and compaction, non-tidal ocean flow, 3-D mass effects in the atmosphere, and the vertical deformation observed by GPS, and of course AG data (Fig. 83.8). Overall the model is a good fit to the SG and AG data, and a clear seasonal signal is seen in most variables at about the ±2 μgal level. Unlike TMGO, the AG values within their error bars coincide with the SG series. Note also the hydrology follows gravity because the SG is on the surface.

Next we show the much more complex hydrological situation at Moxa, Germany (Kroner and Jahr, 2006). At this site the SG is located underground, beneath a layer of soil and vegetation that is above the instrument. In the surrounding area there is a small valley floor with a creek and steep sides with dense forest. Figure 83.9 shows two samples (at different time periods) of precipitation and groundwater level and the observed SG residuals. Note the expected relation between precipitation and groundwater recharge and discharge (cf. Fig. 83.7); the gravity response in the upper panel (Fig. 83.9a) is quite complex, but simpler in the lower series, Figs 83.9b, d. In both cases, gravity decreases due to increased soil moisture above the instrument. Much additional work has been done at Moxa, especially on experiments to inject water at various locations and measure the gravity effect. Recently all the vegetation immediately above the SG was removed to simplify the gravity response. The site has also been surveyed repeatedly with portable gravimeters to assess the spatial gravity variations (Naujoks et al., 2007).

A similar situation occurs at station J9 in Strasbourg where the soil moisture layer (Fig. 83.3) retains moisture and gravity decreases, despite the addition of groundwater. The time constants for recharge and

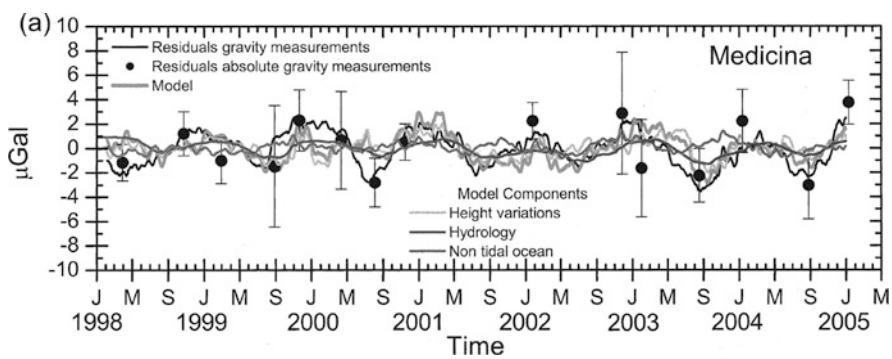


Fig. 83.8 Integrated model for gravity effects from height variations, hydrology and ocean effects, compared to observed SG and AG data

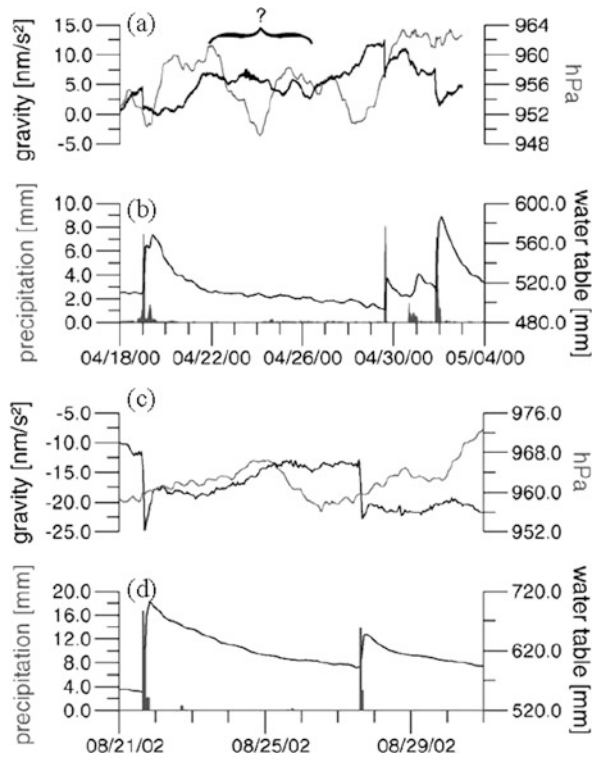


Fig. 83.9 (**a**) and (**c**) SG residuals and pressure, with (**b**) and (**d**), rain and groundwater levels, for two time periods at Moxa (from Kroner and Jahr, 2006). The ? indicates unknown pressure effects

discharge (this time of the soil layer itself), are a few hour and 1–2 months respectively. The hydrology has been instrumented and analyzed in detail by Longuevergne et al. (2007). Similar work has been reported for stations Matsushiro, Metsahovi, and Membach.

Conceptually the easiest way to model hydrology variations in gravity is the empirical approach, involving rainfall as input to various reservoirs, connected by variable fluxes (e.g. with exponential time dependency). The good agreement in predicting observed flow with such models gives hope that the models can be extended to treat the variation of gravity at an SG installation. Additional hydrological data would help to constrain some of the fluxes and reservoir volumes. This approach is easier than a full physical flow model. Site selection is very important for both SGs and AGs, and the best way to avoid complex modeling is to assess the potential hydrology at stations, avoiding those that may be highly variable.

83.5.4 GGP and GRACE

We turn briefly to another topic of considerable relevance to GGOS, which is the gravity field as from the GRACE satellites. Ground validation of GRACE must inevitably be done with point measurements, and some means must be found to spatially average these over distances of 500–100 km for comparison with GRACE. Our approach is to use the European sub-array, as reported elsewhere, and use the empirical orthogonal function decomposition of a gridded version of the ground field at 0.25º cells. We find (Crossley et al., 2007) that the more recent CNES/GRGS 10-day version of the GRACE fields shows details that for some time intervals is similar to the GGP 10-day filtered field. The first principle component for the GRGS solution has higher amplitude than GGP field, but the higher time sampling (compared to the 1-month CSR and GFZ solutions) reveals short term fluctuations in the middle of 2006 that correlate better with GGP. New stations in Europe, Pecny, Walferdange, and Goteborg (Sweden) will add weight to this comparison, and permit other GRACE solutions and to be tested against GGP data.

83.6 Other GGP Projects

Many projects within GGP extend to areas other than hydrology. At the short periods of the Earth's normal modes (1–54 min), GGP data has been successfully used to observe the amplitudes of the long period modes, particularly ${}_0S_0$, at frequencies less than 1 mHz (Xu et al., 2008; Rosat et al., 2007). SG's compare very favorably to seismometers in this period range. One goal of GGP is to permit SG data to be sent directly to IRIS for inclusion in future normal mode studies. The delay in implementing this has been due to the problem of characterizing the SG instrument response in the form required by seismologists.

Lambert et al. (2006) showed AG data in the Cascadia subduction zone that corresponds with a well-defined sawtooth displacement whose onset defines a slip event is identified with seismic tremors. The gravity offset is a few μgal that can easily be seen on an SG, and should correlate with frequent AG data. It has already been established that SGs can detect the static offset associated with large earthquakes

(Imanishi et al., 2004), but the poor global coverage is insufficient to be able to easily observe events from large subduction zones (such as Sumatra).

83.7 Conclusions

1. the GGP network is attaining a more uniform global coverage as new stations in Asia, Africa and the Southern Hemisphere are installed. New SGs in Europe will help GRACE validation and other stations are being installed for specific purposes such as aquifer studies.
2. GGP can benefit GGOS if the concept of collocated AG and SG sites is embraced by the AG community, and
3. GGP supports the new Agrav database initiative to add AG data at GGP sites; we will soon be able to transfer high-rate SG data to IRIS for seismology.

Acknowledgments This research is supported by an NSF EAR Grant No. 0409381 (USA), and the CNRS (France).

References

Amalvict, M. and J. Hinderer (2007). Is the calibration factor stable in time? *Proceedings of the First Asian Workshop on SGs*, Taiwan, http://space.cv.nctu.edu.tw/SG/Amalvict_CalibrationSG.pdf.

Crossley, D. (2004). Preface to the global geodynamics project. *J. Geodyn*., 38, 225–236.

Crossley D., C. de Linage, J. Hinderer, and J.-P. Boy (2007). GRACE Solutions for the gravity field over Central Europe compared to the surface field as recorded by the GGP network. *Eos Trans. AGU,* 88(52), Fall Meet. Suppl., Abstract U21C-0625.

Crossley, D. and J. Hinderer (2008). The contribution of GGP superconducting gravimeters to GGOS. In: Sideris M.G. (ed.), Observing our changing Earth, IAG Symposia, Vol. 133, pp. 841–852, Springer Verlag, Berlin.

Crossley D., J. Hinderer, G. Casula, O. Francis, H.-T. Hsu, Y. Imanishi, G. Jentsch, J. Kaarianen, J. Merriam, B. Meurers, J. Neumeyer, B. Richter, K. Shibuya, T. Sato, and T. van Dam (1999). Network of superconducting gravimeters benefits a number of disciplines. *EOS, Trans. Am. Geophys. U*., 80, 121–126.

Crossley, D., H. Xu, and T. Van Dam (1998). Comprehensive analysis of 2 years of data from Table Mountain, Colorado. *Proceedings of the 13th Int. Symp. Earth Tides*, Ducarme, B., and Paquet, P. (eds), pp. 659–668. Royal Observatory of Brussels.

Harnisch G., M. Harnisch, and R. Falk (2006). Hydrological influences on the gravity variations recorded at Bad Homburg. *Bull. d'Inf. Marees Terr*., 142, 11331–11342.

Hinderer, J., D. Crossley, and R. Warburton (2007). Superconducting gravimetry. In: Herring, T. and G. Schubert (eds.), Treatise on geophysics, Vol 3, Elsevier.

Imanishi, Y., T. Sato, T. Higashi, W. Sun, and S. Okubo (2004). A network of superconducting gravimeters detects submicrogal coseismic gravity changes. *Science*, 306, 476–478.

Kroner, C., O. Dierks, J. Neumeyer, and H. Wilmes (2005). Analysis of observations with dual sensor superconducting gravimeters. *Phys. Earth Planet. Int*., 153(4), 210–219.

Kroner, C. and T. Jahr (2006). Hydrological experiments around the superconducting gravimeter at Moxa Observatory. *J. Geodyn*., 41, 268–275.

Lambert, A., N. Courtier, N., and T. S. James (2006). Long-term monitoring by absolute gravimetry: tides to postglacial rebound. *J. Geodynamics*, 41, 307–317.

Larson, K. and T. van Dam (2000). Measuring postglacial rebound with GPS and absolute gravity. *GRL*, 27, 3925–3928.

Longuevergne, L., G. Ferhat, P. Ulrich, J.-P. Boy, N. Florsch, and J. Hinderer (2007). Towards physical modeling of local-scale hydrological contribution of soils for precise gravimetric corrections in Strasbourg. *Proceedings of the First Asian Workshop on SGs*, http://space.cv.nctu.edu.tw/SG/longuevergne_taiwan_2007.pdf, Taiwan.

Naujoks, M., C. Kroner, T. Jahr, P. Krause, and A. Weise (2007). Gravimetric 3D modeling and observation of time-dependent gravity variations to improve small-scale hydrological modeling, *poster, session HW2004,* IUGG XXIV General Assembly, Perugia, Italy.

Plag, H.-P. (2008). The Global Geodetic Observing System (GGOS): A Key Component in the Global Earth Observation System of Systems, IAG Symposium Gravity, Geoid, and Earth Obseration, Chania, Crete, 23–27 June.

Plag, H.-P., C. Kreemer, and W. Hammond (2007). Combination of GPS-observed vertical motion with absolute gravity changes constrain the tie between reference frame origin and Earth center of mass, in: *Report of the Seventh SNARF Workshop*, held in Monterrey, California, 28 March, 2007.

Richter, B. (1987). Das supraleitende Gravimeter, Deutsche Geodät. Komm., Reihe C, 329, Frankfurt am Main, p. 124.

Rosat, S., W. Sun, and T. Sato (2007). Geographical variations of the ${}_0S_0$ normal mode amplitude: predictions and observations after the Sumatra-Andaman earthquake. *Earth Planet. Space*, 59, 307–311.

Wenzel, H.-G. (1996). The nanogal software: Earth tide processing package ETERNA 3.30. *Bull. Inf. Mar. Terr*., 124, 9425–9439.

Wziontek, H., R. Falk, H. Wilmes, and P. Wolf (2006). Rigorous combination of superconducting and absolute gravity measurements with respect to instrumental properties. *Bull. d'Inf. Marees Terr*., 142, 11417–11422.

Xu, Y., D. Crossley, and R. Herrmann (2008). Amplitude and Q of ${}_0S_0$ from the Sumatra earthquake as recorded on superconducting gravimeters and seismometers. *Seis. Res. Lett.*, 79(6), 797–805.

Zerbini, S., B. Richter, F. Rocca, T. van Dam, and F. Matonti (2007). A combination of space and terrestrial geodetic techniques to monitor land subsidence: case study, the southeastern Po Plain, Italy. *J. Geophys. Res*., 112, B05401, doi: 10.1029/2006JB004338.

Chapter 84

Surface Mass Loading Estimates from GRACE and GPS

E.J.O. Schrama and B. Wouters

Abstract In this paper we discuss the properties of an Empirical Orthogonal Filter approach applied to monthly GRACE gravity solutions which are used to estimate surface mass thickness maps. The vertical loading effect caused by this surface mass is also visible in IGS data acquired within the GRACE observation window. The comparison of GRACE to GPS allows us to constrain the Empirical Orthogonal Filter compression level to 3 and a smoothing radius to 4 or 5° whereby the discrepancy between both datasets for vertical loading signals is around 1.9 mm for 59 IGS stations. The comparison assumes that temporal gravity field changes occur on frequencies shorter than about 3 years because of the way we preprocess the GPS data and GRACE surface mass estimates. We notice that EOF filter residuals do exhibit the presence of systematic geophysical effects which are not represented in the first few EOF modes. The EOF filter residuals contain for instance S_2 ocean tide errors that show up at a period of 161 days, also we observe a semi-annual hydrology signal which is coherent with GLDAS model predictions. New is the presence of an unexplained inter-annual signal in the GRACE derived surface mass estimates at EOF mode 4 and onward. Possible explanations for this residual signal are discussed.

E.J.O. Schrama (✉)
Faculty of Aerospace Engineering Astrodynamics and Satellite Systems, Delft University of Technology, HS Delft 2629, The Netherlands
e-mail: e.j.o.schrama@tudelft.nl

84.1 Introduction

The GRACE (Gravity Recovery and Climate Experiment) mission is designed to map the Earth's gravity field at monthly intervals with a spatial resolution of about 500 km. The solutions provided by the GRACE science team demonstrate that a wide variety of surface mass signals can be observed. For this paper we used the RL04 solution developed by the Center of Space Research (CSR) at the University of Texas. We use all available monthly gravity solutions up to the beginning of 2008 and represent the temporal signal as a surface mass layer under the assumption of a thin elastic lithosphere. We selected 67 monthly coefficient sets collected since the start of the mission and concluded that solutions 1 and 2 in 2002 should be removed because they are significantly affected by track noise. In order to separate signal and noise by means of Empirical Orthogonal Functions (hereafter: EOFs) we use the method described in Schrama et al. (2007). New in this paper is that additional monthly solutions affect the tuning of the EOF filter method. Furthermore the EOF residuals do exhibit a new inter-annual feature previously unseen in the GRACE RL04 data.

In Sect. 84.2 we discuss the problem that there is no unique algorithm to separate signal and noise in the GRACE data. This means that the choice for selecting a specific number of EOF modes or a Gaussian smoothing radius remains an arbitrary choice. Our suggestion to optimize the filter parameters is to compare the surface mass loading signal observed by GRACE to vertical deformations observed at all IGS stations that show a sufficient data record length and that coincide with the GRACE observation window. In Sect. 84.3 we

S.P. Mertikas (ed.), *Gravity, Geoid and Earth Observation*, International Association of Geodesy Symposia 135,
DOI 10.1007/978-3-642-10634-7_84, © Springer-Verlag Berlin Heidelberg 2010

show that the choice of the new EOF filter parameters differs with respect to our earlier results presented in Schrama et al. (2007). In this section we will also discuss characteristics of signal and noise retrieved by the EOF filter. Section 84.4 summarizes our conclusions and recommendations.

84.2 Method

As explained in the introduction we use the fourth release of the GRACE monthly gravity field solutions as provided by the CSR to the geodetic community. After pre-selection we have 65 spherical harmonic coefficient sets complete to spherical harmonic degree and order 60. With the present release of the GRACE data it is necessary to further suppress the noise in the data. The method discussed in this paper is based upon an EOF technique that it applied to Gaussian smoothed surface mass data. The method assumes an EOF compression level and a smoothing radius which are calibration parameters of the filter. Section 84.2.1 discusses all necessary steps to derive Gaussian smoothed monthly surface mass thickness fields. Section 84.2.2 explains the relation between singular value decomposition and the eigenvectors and eigenvalues of temporal and spatial covariance matrices.

84.2.1 Smoothed equivalent water height grids

For this study we are interested in the potential coefficient differences of individual monthly solutions relative to a mean. For the latter we have chosen the average of 65 monthly GRACE potential coefficient sets. Removing biases from the spherical harmonic coefficient sets is a necessary condition for the here assumed EOF method which is related to an eigenvector analysis of covariance matrices. During the generation of the monthly surface mass thickness maps we have also ignored the contribution of the oblateness term of the Earth's gravity field (C_{20}) which is known to be contaminated in the GRACE products, for a discussion see also Cheng and Tapley (2004).

After de-trending the coefficient sets and removing the oblateness term the remaining spherical harmonic coefficient differences are converted into equivalent water height thickness grids. For this we use a convolution algorithm described in Schrama et al. (2007), the method requires a half amplitude averaging radius τ which determines the spatial smoothing in the surface mass grids. Essentially the spherical convolution procedure is based on two independent steps which are the result of the elastic loading theory of Farrell (1972) and the Gaussian spherical convolution described by Jekeli (1981). The Green function that implements the smoothing method is completely determined by the choice of τ, but, the Green function that follows from the paper of Farrell (1972) relies on the definition of a layered Earth model whereby the material properties by layer follow from seismologic data. This study ignores variations in load Love numbers so that all computations are based on the values provided byFarrell (1972). Alternative load Love number sets such as developed by Pagiatakis (1990) could be considered, but the choice between either should not lead to a significant differences in equivalent water height estimates.

84.2.2 Singular Value Decomposition

We have chosen to apply the EOF method to smoothed surface mass thickness grids as described in Sect. 84.2.1. In the current implementation all nodes in the spherical grids are equally weighted, yet this choice is somewhat arbitrary and different applications exist. In Wouters and Schrama (2007) the EOF algorithm is applied to spherical harmonic coefficients grouped by order m, yet their method is different because the input data and the leading EOF detection methods follow a different implementation than in the current manuscript. The Gaussian smoothed grids are stored column-wise in data matrix D which is input to a singular value decomposition algortihm. An arbitrary row of D contains a realization of equivalent water heights at a selected node in a spherical grid, while an arbitrary column of the D matrix displays a realization of the full surface mass field at a given time step.

The singular value decomposition algorithm decomposes the data matrix into the product $D = ULV'$ where L contains singular values and where U and V are orthogonal matrices that contain eigenvectors of the spatial and temporal covariance matrices DD'

and $D'D$ respectively. The "spatial" covariance matrix describes the variance of surface mass values at grid nodes on the main diagonal while correlations between grid node values can be obtained from off-diagonal values. The "time" covariance matrix returns the total variance of a surface mass grid at a given time step on the main diagonal of the $D'D$ matrix while correlations between time steps can be derived from off-diagonal values in the $D'D$ matrix. One can show that eigenvectors of DD' are stored as columns in the U matrix and that the diagonal of L contains square root of the eigenvalues λ of DD'. For the $D'D$ covariance matrix the eigenvectors are stored in the V matrix while the eigenvalues λ are identical for DD' and $D'D$. The geometric multiplicity of the eigenvalue space is the same: $G_\lambda(D'D) = G_\lambda(DD')$.

Compression of the D matrix results in an approximation referred to as $D^\#$. This technique replaces zeros at singular values L which are below a selected threshold. In other words, L becomes $L^\#$ so that $D^\# = UL^\#V'$. The signal is now contained in $D^\#$ and noise can be estimated from $D - D^\#$. In Schrama et al. (2007) spectral properties of $D - D^\#$ are extensively compared to formal co- variances contained in the GGM02C gravity model and simulated background model errors. The consequence of compressing D is that we approximate the signal by the most energetic modes in the EOF analysis. EOF mode i is a combination of columns U_i and V_i and the singular value L_i. The latter is indicative for the contribution of EOF mode i to the total variance contained in D. An EOF analysis as described above to the GRACE equivalent water height data shows that there are at least three dominant modes. Yet the outcome of this problem depends on the radius τ as introduced during spherical convolution, see Sect. 84.2.1.

84.3 Results

The conclusion of section 2 is that we identified two control parameters in the EOF filter method which are the Gaussian smoothing radius τ and the number of EOF modes that form $D^\#$, also referred to as the compression level of the EOF method. For the given situation it is necessary to optimize as well τ as the compression level. In Sect. 84.3.1 we discuss known features in $D^\#$ that are unlikely to change by extending the length of the GRACE data set. In Sect. 84.3.2 we compare $D^\#$ to external IGS data. In Sect. 84.3.3 we discuss EOF filter residuals contained in $D - D^\#$.

84.3.1 EOF Modes

Characteristic modes that appear as the most energetic EOFs are related to the annual cycle and the secular trends in the GRACE EQWHs. The spring-autumn cycle shows a characteristic variance of 33% at 4° Gaussian smoothing. A second EOF is the Winter-Summer annual cycle that appears to contribute 6.9% to the total signal variance. According to Tapley et al. (2004) this signal is mostly caused by variations in the continental hydrology. The spatial patterns of EOF 1 and 2 show almost the same characteristics compared to Schrama et al. (2007) when we include additional monthly GRACE gravity solutions. Yet the evolution in time of the selected EOF does allow more variations.

A third EOF which contains 13.5% of the total variance at 4 degree smoothing shows the Glacial Isostatic Adjustment signal in the Hudson bay region where we clearly see evidence for two Pleistocene ice domes, cf. Tamisiea et.al. 2007. This EOF also shows secular signals in the Fennoscandian region,the exterior of Antarctica, Greenland, Alaska. Furthermore this mode shows long term climate signals such as the drought in Africa and remnants of the 26 December 2004 Sumatra Earthquake signal whereby the western mass anomaly directly follows the Sumatra trench. By adding additional months of GRACE data more details can be distinguished in the first three EOFs, furthermore it is easier to reduce the smoothing radius from 6.75° degree used inSchrama et al. (2007) to 4 or 5° in this paper.

The variance contained by EOF mode depends on the selected smoothing radius and the compression level used in the algorithm. Variance percentages contained in the solutions as a function of the EOF compression level and the smoothing radius are shown in Table 84.1. The conclusion from the cumulative variance test is that a short Gaussian smoothing radius requires a high EOF compression level and visa versa. Yet it is difficult to draw definite conclusions from such an analysis, i.e. there is no unique distinction between signal and noise modes based on their contribution to the total variance.

Table 84.1 Cumulative variance percentages obtained by the EOF method, the left column is the EOF compression level, the top row is the Gaussian smoothing radius. The remaining table entries contain cumulative variance percentages

	4.00	5.00	6.25	7.50	8.75	10.00
1	33.01	41.49	47.43	51.04	53.30	54.65
2	46.50	56.32	62.63	66.07	68.03	69.14
3	53.43	63.91	70.53	74.03	75.94	76.96
4	57.53	68.15	75.04	78.69	80.72	81.84
5	61.09	70.80	77.15	80.77	82.86	84.07
6	64.18	72.84	78.91	82.47	84.62	85.93
7	66.61	74.68	80.60	84.08	86.20	87.53
8	68.68	76.39	82.12	85.43	87.41	88.66
9	70.39	77.98	83.38	86.54	88.43	89.66
10	71.94	79.44	84.51	87.60	89.43	90.63

Table 84.2 Number of IGS stations that satisfy the condition $rms \leq 3.5$ mm and $r \geq 0.5$ for GPS vertical loading compared to GRACE vertical elastic loading estimates. *Top row*: smoothing radius in degrees. *Left column*: EOF compression level (number of EOFs in solution)

	4.00	5.00	6.25	7.50	8.75	10.0
2	53	54	55	56	57	58
3	68	67	66	63	61	61
4	63	62	61	58	58	55
5	63	61	60	59	56	53
6	57	61	60	57	55	51
7	58	61	61	60	57	57

84.3.2 Comparison to IGS Data

In order to refine the optimum EOF compression level and the smoothing radius Schrama et al. (2007) compared GRACE surface mass loading estimates to vertical deformations observed at IGS sites. Since this paper more GRACE and IGS data have become available in the time frame 2002–2008. Table 84.2 shows the number of stations out of the original set of 205 IGS stations that show a rms difference less than 3.5 mm rms and a correlation greater than 0.5 compared to the vertical loading derived from the GRACE data. We used the veritical deformation data obtained from Remi Ferland, air pressure loading deformation was removed from the GPS data whereby use was made of NCEP reanalysis sea level pressure data.

Table 84.2 suggests that a compression level of 3 and 4° Gaussian smoothing are preferred, which is an improvement compared to the results shown in Schrama et al. (2007) who found an optimum at 5 or 6.25° smoothing with 43 months of GRACE data.

84.3.3 EOF Filter Residuals

At 4° smoothing EOF mode 4 is already affected by track patterns which disappear when we maintain a stricter intake policy of monthly potential coefficient sets. At 5° smoothing the EOF modes 1–3 closely resemble the EOF modes at 4° smoothing. The exception is EOF mode 4 which is mostly free from track noise at 5° smoothing. The spatial representation of EOF 4 at 5° smoothing is shown in Fig. 84.1. The

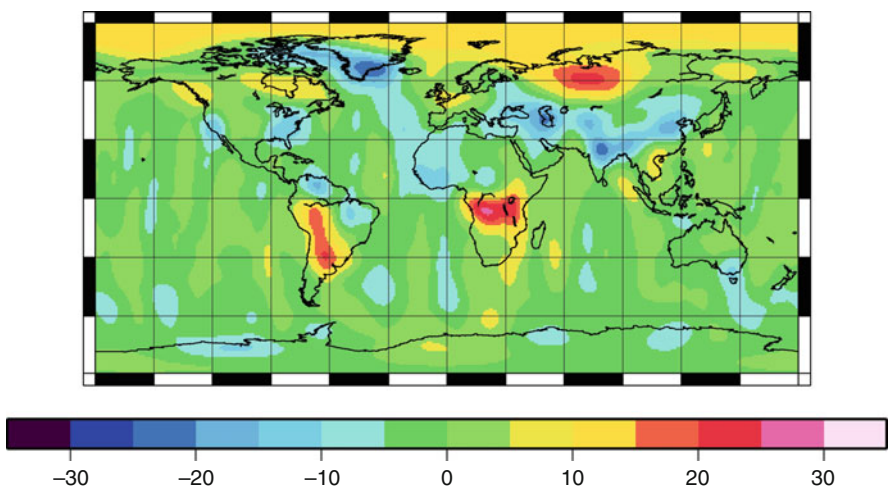


Fig. 84.1 Spatial pattern belonging to the EOF mode 4 derived from equivalent water height data computeed with a 5° smoothing radius. The contribution of this EOF to the total variance is 4.2%

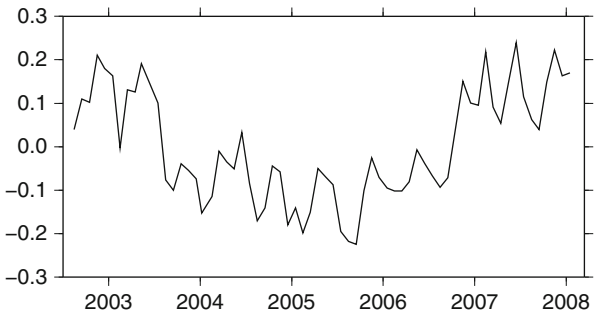


Fig. 84.2 The time function that applies to mode 4 shown in Fig. 84.1. Known features are the 180 day hydrology signal and the 161 day S_2 tidal aliasing. The interannual signal is not well understood. (Note: in order to reconstruct the original signal values Fig. 84.1 and 84.2 should be multiplied to obtain the equivalent water height signal in cm)

evalution in time of this signal is shown in Fig. 84.2. A part of the signal in mode 4 is known to display a semi-annual hydrology signal since it closely resembles the corresponding feature shown in the GLDAS model, see also Schrama et al. (2007). The semi-annual signal is clearly seen in Fig. 84.2, futhermore we know with the present release of the GRACE GSM coefficients that there exists a S_2 tidal aliasing signal at a period of 161 days, cf. Ray et al. (2003), which is apparently not captured by the FES2004 background model used by the GRACE science team.

Figure 84.2 does also display a new feature in the form of a long periodic signal resembling an inter-annual feature. A possible candidate could be a tidal alias with a periodicity that matches approximately the full length of the used GRACE dataset. If we look for the corresponding tidal frequency then K_1 might be the right candidate, since this component aliases to a period of 7.48 year in the GRACE dataset as is suggested by Ray et al. 2003.

Another possibility could be that the long periodic signal in Fig. 84.2 is somehow related to the presence of an ENSO which would result in an a-typical patterns of precipitation and evaporation which are in- and output for continental hydrology. The strongest event would have been the ENSO cycle that started in the winter of 2006/2007 which resulted in the La Nina of 2007. The evolution in time displayed in Fig. 84.2 shows a correlation coefficient of approximately 0.5 to the NINO3.4 index derived from altimetry, cf. DEOS (2008). Whether this is a relevant fact requires futher investigation.

84.4 Conclusions

In this paper we describe the consequence of including additional monthly gravity solutions to the EOF filter method described inSchrama et al. (2007). An extension of the GRACE input dataset allows us to shorten the Gaussian smoothing radius. to 4° smoothing, although the solutions at 5° smoothing is somewhat more free of track noise. An independent set of 205 IGS stations is used for tuning our EOF. filter method. Residual signals at EOF mode 4 at 5° smoothing appear to be contaminated by a long periodic feature that is not well understood. The correlation factor of the time evolution of mode 4 is about 0.5 relative to the NINO3.4 index which might indicate that GRACE is catching a signal related to the ENSO. Mode 4 is mostly a continental pattern which is unlikely to correspond to known tidal aliasing periods such at K1 or K2.

Acknowledgments We thank Remi Ferland for making available daily global IGS deformation vectors to the community, we also thank two anonymous referees for valuable comments that have improved our paper.

References

Cheng, M. and B.D. Tapley (2004). Variations in the Earth's oblateness during the past 28 years, *it JGR*, 109, B09402, doi:10.1029/2004JB003028.

Cox C.M. and Chao B.F. (2002) Detection of a large-scale mass redistribution in the terrestrial system since 1998, Science Volume 297, Issue 5582, 2 August 2002, Pages 831–833, doi:10.1126/science.1072188

DEOS (2008). El Niño observed by ERS/Envisat altimetry, http://rads.tudelft.nl/enso/, last visited 20-June.

Dickey, J.O., Marcus, S.L. and Willis, J.K. (2008) Ocean cooling: Constraints from changes in Earth's dynamic oblateness (J_2) and altimetry, Geophysical Research Letters, Vol 35 Pages 18608–doi:10.1029/2008GL035115

Dickey J.O. Marcus S.L. De Viron, O, Fukumori I (2002) Recent earth oblateness variations: Unraveling climate and postglacial rebound effects, Science Volume 298, Issue 5600, 6 December 2002, Pages 1975–1977, doi:10.1126/ science.1077777

Farrell, W.E. (1972). Deformation of the Earth by surface loads. *Rev.Geoph. Space Phys.*, 10,761–797.

Jekeli, C. (1981). Alternative methods to smooth the Earth's gravity field, Report 327 Department of Geodetic Science and Surveying, Ohio State University, Columbus OH.

Pagiatakis, S. (1990). The response of a realistic earth to ocean tide loading. *Geophy. J. Int.*, 103, 541–560.

Ray, R.D., Rowlands, D.D., and G.D Egbert (2003). Tidal models in a new era of satellite gravimetry. *Space Sci Rev.* 108, 271–282.

Schrama E.J.O., B. Wouters, D.A. Lavallee (2007). Signal and noise in GRACE observed surface mass variations. *J. Geophys. Res.*, 112 B08407, doi:10.1029/2006JB004882.

Schmidt R. Petrovic S., Güntner, Barthemes F, Wünsch C., Kusche J. (2008) Periodic components of water storage changes from GRACE and global hydrology models Journal of Geophysical Research B: Solid Earth 113 (8), art. no. B08419

Tapley B.D., S. Bettadpur, J.C. Ries, P.F. Thompson, and M.M. Watkins (2004). GRACE measurements of mass variability in the Earth system, Science, 305, 5683, doi:10.1126/science.1099192.

Tamisiea, M.E.,; Mitrovica, J.X., and Davis, J.L., (2007). GRACE gravity data constrain ancient ice geometries and continental dynamics over Laurentia. *Sci.* 316, 881–883

Wahr J.M., Molenaar and M, Bryan F. (1998) Time variability of the Earth's gravity field: Hydrological and oceanic effects and their possible detection using GRACE, Journal of Geophysical Research B: Solid Earth 103 (B12), pp. 30205–30229.

Wouters B. and E.J.O. Schrama (2007). Improved accuracy of GRACE gravity solutions through empirical orthogonal function filtering of spherical harmonics. Geophys. Res. Lett., 34, L23711, doi:10.1029/2007GL032098.

Chapter 85

A Unified Approach to Modeling the Effects of Earthquakes on the Three Pillars of Geodesy

R.S. Gross and B.F. Chao

Abstract Besides generating seismic waves that eventually dissipate an earthquake also generates a static displacement field everywhere within the Earth, causing the geometrical shape of both the Earth's outer surface and of internal boundaries such as the core-mantle boundary to change. By rearranging the Earth's mass earthquakes also cause the Earth's rotation and gravitational field to change. Earthquakes therefore affect all three pillars of geodesy, namely, the Earth's geometrical shape, rotation, and gravity. These effects of earthquakes are usually modeled separately, with flat Earth models typically being used to compute changes in site positions and spherical Earth models being used to compute changes in the Earth's rotation and global gravitational field. Here, a unified approach to computing changes in the three pillars of geodesy is described. As an example of this approach it is applied to the 2004 Sumatran earthquake. A preliminary comparison of predicted and SLR-observed degree-2 zonal gravitational field coefficients does not reveal the expected step-like change at the epoch of the earthquake.

85.1 Introduction

The Earth is a dynamic system with a fluid, mobile atmosphere and oceans, a continually changing global distribution of ice, snow, and water, a fluid core that is undergoing hydromagnetic motion, a mantle both thermally convecting and rebounding from the glacial loading of the last ice age, and mobile tectonic plates. In addition, external forces due to the gravitational attraction of the Sun, Moon, and planets also act upon the Earth. These internal dynamical processes and external gravitational forces exert torques on the Earth or displace its mass, thereby causing its shape, rotation, and gravity to change. These three fundamental properties of the Earth – its shape, rotation, and gravity – are the three pillars of geodesy.

But these three pillars of geodesy do not stand alone. They are interconnected by both common observing systems and by common excitation mechanisms. For example, the space-geodetic measurement technique of satellite laser ranging (SLR) can be used to determine changes in the positions of the laser ranging stations and hence changes in the shape of the Earth, can be used to determine changes in the orientation of the network of laser ranging stations with respect to the orbiting satellites and hence changes in the Earth's rotation, and can be used to determine changes in the orbits of the satellites and hence changes in the Earth's gravitational field. Global navigation satellite systems can also be used to determine changes in all three pillars of geodesy, while very long baseline interferometry can be used to determine changes in shape and rotation but not in gravity.

The three pillars of geodesy are also connected by common excitation mechanisms. For example, changes in the distribution of mass within the atmosphere and oceans change the Earth's gravitational field, change the Earth's shape by changing the load acting on the solid but not rigid surface of the Earth, and change the Earth's rotation by changing the inertia tensor of the Earth.

R.S. Gross (✉)
Jet Propulsion Laboratory, California Institute of Technology, Pasadena, CA 91109-8099, USA
e-mail: Richard.Gross@jpl.nasa.gov

S.P. Mertikas (ed.), *Gravity, Geoid and Earth Observation*, International Association of Geodesy Symposia 135,
DOI 10.1007/978-3-642-10634-7_85, © Springer-Verlag Berlin Heidelberg 2010

This interconnectedness of the three pillars of geodesy allows them to be jointly used to study common sources of excitation, thereby allowing greater understanding of the excitation mechanisms to be gained than would be possible if they were studied separately. But jointly using shape, rotation, and gravity measurements to study some common excitation mechanism means that a consistent model for the effect of that mechanism on all three pillars of geodesy must be used. Unfortunately, this is not always the case. For example, the effects of earthquakes on site positions is usually modeled using a flat Earth model, their effects on Earth rotation is by necessity modeled using a spherical Earth model, and their effects on gravity is sometimes modeled using a flat Earth model and sometimes modeled using a spherical Earth model. Here, a unified approach to modeling the effects of earthquakes on all three pillars of geodesy is presented. As an example of this approach it is applied to the 2004 Sumatran earthquake.

85.2 A Unified Approach

The unified approach presented here is based upon using normal mode eigenfunctions of realistic spherically symmetric Earth models as basis functions of the displacement field generated by an earthquake. The modeled 3D displacement field is then used to compute changes in the Earth's shape, rotation, and gravity. This approach has been given in detail by Chao and Gross (1987) and has been recently summarized by Gross and Chao (2006). It is therefore only briefly described here.

85.2.1 Earthquake Displacement Field

The 3D time-dependent displacement field $\mathbf{u}(\mathbf{r}, t)$ generated by an earthquake is obtained by solving the equation of motion (e.g., Lapwood and Usami, 1981; Dahlen and Tromp, 1998):

$$\nabla \cdot \boldsymbol{\tau} + \mathbf{f_g} + \mathbf{f_s}(\mathbf{r}, t) = \rho(\mathbf{r}) \frac{\partial^2 \mathbf{u}(\mathbf{r}, t)}{\partial t^2} \qquad (1)$$

where $\boldsymbol{\tau}$ is the stress tensor, $\mathbf{f_g}$ is the body force per unit volume due to self-gravitation, $\mathbf{f_s}(\mathbf{r},t)$ is the body force per unit volume due to the earthquake source, and $\rho(\mathbf{r})$ is the mass density. Since the normal mode eigenfunctions $\mathbf{u_k}(\mathbf{r})$ form a complete set spanning displacement space they can be used as basis functions for the displacement field:

$$\mathbf{u}(\mathbf{r}, t) = \sum_k a_k(t) \mathbf{u}_\mathbf{k}^*(\mathbf{r}) \qquad (2)$$

where the asterisk denotes complex conjugation.

In general, a spherically symmetric, non-rotating, elastic, isotropic (SNREI) Earth model has both poloidal (spheroidal) and toroidal (torsional) normal modes. The eigenfunctions $({}_n\sigma_l^m(\mathbf{r}),\ {}_n\tau_l^m(\mathbf{r}))$ of the (poloidal, toroidal) normal modes can be written in terms of scalar functions of radius ${}_nU_l(r)$, ${}_nV_l(r)$, and ${}_nW_l(r)$ as (e.g., Gilbert and Dziewonski, 1975):

$${}_n\sigma_l^m(\mathbf{r}) = {}_nU_l(r) Y_{lm}(\theta, \phi)\hat{\mathbf{r}} + {}_nV_l(r) \nabla_\mathbf{h} Y_{lm}(\theta, \phi) \qquad (3)$$

$${}_n\tau_l^m(\mathbf{r}) = -{}_nW_l(r) \hat{\mathbf{r}} \times \nabla_\mathbf{h} Y_{lm}(\theta, \phi) \qquad (4)$$

where the hat denotes a vector of unit length, θ is colatitude, ϕ is East longitude, the $Y_{lm}(\theta, \phi)$ are the fully normalized surface spherical harmonic functions of degree l and order m, n is the radial overtone number, and $\nabla_\mathbf{h}$ is the horizontal gradient operator. For spherically symmetric Earth models the scalar eigenfunctions ${}_nU_l(r), {}_nV_l(r)$, and ${}_nW_l(r)$ do not depend on order m.

Both poloidal and toroidal normal modes have horizontal components and they are therefore both needed when modeling earthquake-induced changes in the horizontal positions of sites. But because toroidal modes have no component in the radial direction they are not needed when modeling changes in the vertical positions of sites or when modeling changes in the Earth's rotation or gravity.

The permanent coseismic displacement field generated by an earthquake is recovered by letting time t go to infinity in Eq. (2). In this static limit the normal mode expansion coefficients $a_k(\infty)$ can be shown to be (e.g., Gilbert, 1970):

$$a_k(\infty) = \frac{1}{\Omega_k^2} \mathbf{M} \colon \boldsymbol{\varepsilon}_\mathbf{k}(\mathbf{r_s}) \qquad (5)$$

where ω_k is the eigenfrequency of the k'th normal mode, $\mathbf{M}$ is the seismic moment tensor (e.g., Aki and Richards, 1980, p. 351), the "**:**" denotes the double dot

product of two tensors, and $\boldsymbol{\varepsilon}_{\mathbf{k}}(\mathbf{r}_s)$ is the strain tensor of the k'th normal mode eigenfunction evaluated at the centroid of the earthquake source:

$$\boldsymbol{\varepsilon}_{\mathbf{k}}(\mathbf{r}_s) = \frac{1}{2}\left[\nabla \mathbf{u}_{\mathbf{k}}(\mathbf{r}_s) + (\nabla \mathbf{u}_{\mathbf{k}}(\mathbf{r}_s))^{\mathbf{T}}\right] \tag{6}$$

In deriving Eq. (5) for the normal mode expansion coefficients in the static limit it has been assumed that the earthquake source can be represented by a point source with a step function time history. This model of the earthquake source is valid for spatial dimensions much larger than the dimensions of the earthquake's source and for time spans much longer than the earthquake's duration. More complicated earthquake source functions can be modeled by superimposing point sources appropriately distributed in space and time.

85.2.2 Change in Shape

Equation (2) gives the modeled displacement field generated by an earthquake given the normal mode eigenfunctions and eigenvalues of an Earth model and the moment tensor representation of the earthquake's source. In the static limit ($t \to \infty$) and by setting the radius r to be the radius a of the outer surface of the Earth this equation can be used to model the coseismic change in the shape of the Earth caused by an earthquake. By setting the radius to be the radius of some internal boundary such as the core-mantle boundary it can be used to model the coseismic change in the shape of that boundary.

Cannelli et al. (2007) modeled the change in the shape of the core-mantle boundary caused by the 2004 Sumatran earthquake. The spherically symmetric, self-gravitating, incompressible Earth model that they used was a volume-averaged version of the Preliminary Reference Earth Model (PREM; Dziewonski and Anderson, 1981). The model of Tsai et al. (2005), consisting of 5 point sources to represent a propagating slip pulse, was used to model the source of the earthquake. In the coseismic case they found that the core-mantle boundary should have been depressed by about 4 mm beneath the earthquake source and that it should have been vertically displaced by about 0.5 mm at distances greater than 50° from the source. The horizontal coseismic displacements of the core-mantle boundary were found to be about the same size as the radial displacements.

85.2.3 Change in Rotation

Under the principle of the conservation of angular momentum and in the absence of external torques the rotation of the solid Earth will change as the mass distribution of the solid Earth changes and as angular momentum is exchanged between the solid and fluid regions of the Earth. To first order, polar motion $\mathbf{p}(t) = p_x(t) - i\,p_y(t)$ and length-of-day $\Delta\Lambda(t)$ are related to their respective excitation functions $\boldsymbol{\chi}(t) = \chi_x(t) + i\,\chi_y(t)$ and $\chi_z(t)$ by (e.g., Gross, 2007):

$$\mathbf{p}(t) + \frac{i}{\sigma_o}\frac{d\mathbf{p}(t)}{dt} = \boldsymbol{\chi}(t) \tag{7}$$

$$\frac{\Delta\Lambda(t)}{\Lambda_o} = \chi_z(t) \tag{8}$$

where σ_o is the complex-valued frequency of the Chandler wobble and Λ_o is the nominal length-of-day of 86,400 s. Note that by convention the y-component of polar motion is positive towards 90°W longitude whereas the y-component of the excitation function is positive towards 90°E longitude. The excitation functions $\chi_i(t)$, which depend on relative angular momenta $h_i(t)$ and on mass redistribution through the inertia tensor $\Delta I_{ij}(t)$, are given by (Gross, 2007):

$$\chi_x(t) = \frac{h_x(t) + \Omega[1 + (k'_2 + \Delta k'_{an})]\Delta I_{xz}(t)}{[C - A' + A'_m + \varepsilon_c A_c]\sigma_0} \tag{9}$$

$$\chi_y(t) = \frac{h_y(t) + \Omega[1 + (k'_2 + \Delta k'_{an})]\Delta I_{yz}(t)}{[C - A' + A'_m + \varepsilon_c A_c]\sigma_0} \tag{10}$$

$$\chi_z(t) = k_r \frac{h_z(t) + \Omega[1 + \alpha_3(k'_2 + \Delta k'_{an})]\Delta I_{zz}(t)}{C_m \Omega} \tag{11}$$

where Ω is the mean angular velocity of the Earth, $\Delta k'_{an}$ accounts for the effects of mantle anelasticity on the degree-2 load Love number k'_2, C is the greatest principal moment of inertia of the whole Earth, C_m is that of the crust and mantle, A' is the average of the least and intermediate principal moments of inertia of the whole Earth, A'_m is that of the crust and mantle, A_c is the least principal moment of inertia of the core, ε_c

is the ellipticity of the surface of the core, α_3 is a factor modifying the degree-2 load Love number because of core decoupling, and k_r is a factor having a value near unity that accounts for the effects of rotational deformation on the length-of-day.

Earthquakes do not load the solid Earth and if they are assumed to occur instantaneously then they generate no relative angular momentum. So for earthquakes the excitation functions become:

$$\chi_x(t) = \frac{\Omega}{\left[C - A' + A'_m + \varepsilon_c A_c\right]\sigma_o} \Delta I_{xz}(t) \qquad (12)$$

$$\chi_y(t) = \frac{\Omega}{\left[C - A' + A'_m + \varepsilon_c A_c\right]\sigma_o} \Delta I_{yz}(t) \qquad (13)$$

$$\chi_z(t) = \frac{\Delta\Lambda(t)}{\Lambda_o} = \frac{k_r}{C_m} \Delta I_{zz}(t) \qquad (14)$$

Computing the effects of earthquakes on polar motion excitation and length-of-day therefore requires computing the change to the Earth's inertia tensor that is caused by the earthquake.

The inertia tensor $\mathbf{I}$ is defined by:

$$\mathbf{I} = \int_{V_o} (r^2\,\mathbf{I} - \mathbf{r}\,\mathbf{r})\rho(\mathbf{r})\,dV \qquad (15)$$

where $\mathbf{I}$ is the identity tensor. The change in the inertia tensor caused by an earthquake can be computed by using the Lagrangian approach of following a mass element $dM = \rho(\mathbf{r})\,dV$ as it is displaced from its initial position $\mathbf{r}$ to its perturbed position $\mathbf{r}+\mathbf{u}$. Assuming that the displacements $\mathbf{u}$ caused by the earthquake are small, then the integrand in Eq. (15) can be expanded in a Taylor series. Keeping terms to first order yields:

$$\boldsymbol{\Delta}\mathbf{I} = \int_{V_o} [2(\mathbf{r}\cdot\mathbf{u})\mathbf{I} - (\mathbf{u}\mathbf{r} + \mathbf{r}\mathbf{u})]\,\rho(\mathbf{r})dV \qquad (16)$$

where the integral extends over the initial, undeformed volume V_o of the Earth model and $\mathbf{u}$ is the coseismic displacement field given by equation (2) in the static limit ($t\to\infty$).

Gross and Chao (2006) used this approach to model the effect of the 2004 Sumatran earthquake on the Earth's rotation. The SNREI Earth model that they used was the transversely isotropic version of PREM. Its eigenvalues and eigenfunctions were computed using the MINOS computer code. The 5 sub-event model of Tsai et al. (2005) was used to model the earthquake source. The resulting coseismic displacement field was used in Eq. (16) to compute the change to the Earth's inertia tensor; Eqs. (12), (13) and (14) were then used to compute the change to the polar motion excitation functions and to the length-of-day. They found that the 2004 Sumatran earthquake should have changed the (x, y) components of the excitation function by (–1.4, 1.8) milliarcseconds (mas) and the length-of-day by –6.8 microseconds (μs). These predicted changes are less than the current measurement uncertainty of about 5 mas for polar motion excitation and about 10 μs for length-of-day. And in fact Gross and Chao (2006) found no evidence of an earthquake-induced change when they examined observations of polar motion excitation and length-of-day. Similar results for the predicted coseismic change in polar motion excitation caused by the 2004 Sumatran earthquake have been given by Sabadini et al. (2007).

85.2.4 Change in Gravity

The gravitational potential $U(\mathbf{r_0})$ of the Earth evaluated at some external field point $\mathbf{r_0}(r_o,\theta_o,\phi_o)$ can be expressed as (e.g., Kaula, 1966):

$$U(\mathbf{r_0}) = \frac{GM}{r_o}\sum_{l=0}^{\infty}\sum_{m=0}^{l}\left(\frac{a}{r_o}\right)^l (C_{lm}\cos m\phi_o + S_{lm}\sin m\phi_o)\tilde{P}_{lm}(\cos\theta_o) \qquad (17)$$

where G is the gravitational constant, M is the mass of the Earth, a is the radius of the Earth, and the $\tilde{P}_{lm}$ are the 4π-normalized associated Legendre functions of degree l and order m. The dimensionless expansion coefficients C_{lm} and S_{lm} are known as Stokes coefficients and are the normalized multipole moments of the Earth's density field $\rho(\mathbf{r})$:

$$C_{lm} + i\,S_{lm} = \frac{N_{lm}}{Ma^l}\int_{V_o} r^l\,Y_{lm}(\theta,\phi)\rho(\mathbf{r})dV \qquad (18)$$

where the N_{lm} are normalization factors:

$$N_{lm} = (-1)^m\frac{2}{2l+1}\sqrt{(2-\delta_{m0})\pi} \qquad (19)$$

The static displacement field generated by an earthquake perturbs the Earth's density field which by Eq. (18) causes the Stokes coefficients and hence the Earth's gravitational field to change. Like the change in the inertia tensor, the change in the Stokes coefficients caused by an earthquake can be computed using the Lagrangian approach of following a mass element dM as it is displaced from its initial position $\mathbf{r}$ to its perturbed position $\mathbf{r}+\mathbf{u}$. Expanding the integrand in Eq. (18) in a Taylor series and keeping terms to first order yields:

$$\Delta C_{lm} + i\,\Delta S_{lm} = \frac{N_{lm}}{Ma^l}\int_{V_o} r^{l-1}\,\mathbf{u}\cdot(\hat{\mathbf{r}}l + \nabla_{\mathbf{h}}) \times Y_{lm}(\theta,\phi)\rho(\mathbf{r})dV \tag{20}$$

where the integral extends over the initial, undeformed volume V_o of the Earth model.

Gross and Chao (2006) used Eq. (20) to model the effect of the 2004 Sumatran earthquake on selected low-degree coefficients of the Earth's gravitational field using the same Earth model and earthquake source properties that they used when modeling its effect on the Earth's rotation. They found that it should have changed the degree-2 zonal coefficient of the Earth's gravitational field ΔC_{20} by about 1.06×10^{-11} or by about twice the approximate uncertainty in SLR measurements of this coefficient. The predicted change in the degree-3, degree-4, and degree-5 zonal coefficients were all found to be much smaller than their respective SLR measurement uncertainties. Similar results for the predicted coseismic change in the degree-2 zonal gravitational field coefficient have been given by Cannelli et al. (2007).

Since the predicted change in the degree-2 zonal coefficient was found by Gross and Chao (2006) to be greater than the SLR measurement uncertainty, a preliminary examination of SLR measurements was conducted here in order to search for a change that could possibly be caused by the 2004 Sumatran earthquake. The particular SLR series used in this search was the so-called GRACE replacement series that is produced by the GRACE project as a replacement for the degree-2 zonal GRACE-determined coefficients (Cheng and Ries, 2007). This series is given at monthly intervals and is the same series that Gross et al. (2009) found to be in best agreement with gravity changes caused by modeled variations in atmospheric surface pressure, ocean-bottom pressure, and water stored on land.

In order to recover the full SLR-determined signal the atmosphere/ocean dealiasing product was first added back to the SLR series. Then the effects of the ocean pole tide were removed using the self-consistent equilibrium ocean pole tide model of Desai (2002); the effects of atmospheric surface pressure variations were removed using the pressure fields of the National Centers for Environmental Prediction/National Center for Atmospheric Research reanalysis project (Kalnay et al., 1996) assuming that the oceans respond as an inverted barometer; the effects of ocean-bottom pressure variations were removed using the bottom pressure fields of a data assimilating oceanic general circulation model, designated kf049f, that was run at the Jet Propulsion Laboratory as part of their participation in the Estimating the Circulation and Climate of the Ocean consortium (Stammer et al., 2002); the effects of variations in water stored on land were removed using the Euphrates version of the Land Dynamics (LaD) model of Milly and Shmakin (2002); and the effects of imposing global mass conservation on the surface geophysical fluids were also removed (see Gross et al., 2009 for further details). Finally, residual seasonal variations in the SLR series were removed by least-squares fitting and removing a mean, a trend, and periodic terms at the annual, semiannual, and terannual frequencies.

The grey curve in Fig. 85.1 shows the resulting residual degree-2 zonal SLR measurements; the black curve shows the predicted change caused by the 2004

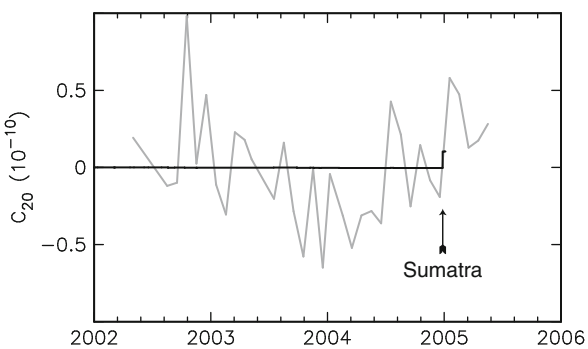


Fig. 85.1 Observed and modeled degree-2 zonal spherical harmonic coefficients of the Earth's gravitational field. The observed coefficients are from SLR (*grey curve*). The effects of atmospheric surface pressure, ocean-bottom pressure, land hydrology, and a global mass-conserving ocean layer have been removed from the observed coefficients as have a mean, a trend, and periodic terms at the annual, semiannual, and terannual frequencies. The *black curve* shows the change caused by the 2004 Sumatran earthquake as predicted by Gross and Chao (2006). The *arrow* indicates the epoch of the earthquake

Sumatran earthquake. As can be seen, there is little evidence of a step-like change in the residual SLR gravitational field measurements at the epoch of the 2004 Sumatran earthquake.

85.3 Discussion and Summary

A unified approach to modeling the effects of earthquakes on the three pillars of geodesy has been presented here. This approach is based on using normal mode eigenfunctions of realistic spherically symmetric Earth models as basis functions of the 3D displacement field generated by the earthquake. With this approach the effects of sphericity, layering, and self-gravitation are automatically taken into account, effects that are generally not included when using flat Earth models but that can be important when modeling the effects of great earthquakes like the 2004 Sumatran event. For example, Banerjee et al. (2007, online material) compared site displacements computed using a homogeneous halfspace model to those computed using the realistic spherically symmetric PREM Earth model, finding differences of as much as a factor of 2–3 in the modeled site displacements.

While spherically symmetric Earth models have been used to separately study the effects of the 2004 Sumatran earthquake on site positions (e.g., Banerjee et al., 2007), Earth rotation (e.g., Sabadini et al., 2007), and global gravity (e.g., Panet et al., 2007), the effects have not yet been studied jointly. The full power of the global geodetic observing system will be unleashed only when joint studies of the three pillars of geodesy are undertaken.

Acknowledgements The MINOS computer code was supplied to us by G. Masters whom we thank. The work of one of the authors (RSG) described in this paper was performed at the Jet Propulsion Laboratory, California Institute of Technology, under contract with the National Aeronautics and Space Administration. Support for this work was provided by the Earth Surface and Interior Focus Area of NASA's Science Mission Directorate.

References

Aki, K. and P.G. Richards (1980). Quantitative seismology. Freeman, New York.

Banerjee, P., F. Pollitz, B. Nagarajan, and R. Bürgmann (2007). Coseismic slip distribution of the 26 December 2004 Sumatra-Andaman and 28 March 2005 Nias earthquakes from GPS static offsets. *Bull. Seism. Soc. Am.*, 97(1A), S86–S102, doi:10.1785/0120050609.

Cannelli, V., D. Melini, P. De Michelis, A. Piersanti, and F. Florindo (2007). Core-mantle boundary deformations and J_2 variations resulting from the 2004 Sumatra earthquake. *Geophys. J. Int.*, 170, 718–724.

Chao, B.F. and R.S. Gross (1987). Changes in the Earth's rotation and low-degree gravitational field induced by earthquakes. *Geophys. J. R. astr. Soc.*, 91, 569–596.

Cheng, M.K. and J. Ries (2007). Monthly estimates of C20 from 5 SLR satellites. GRACE Technical Note 05, p. 2, Center for Space Research, Univ. Texas, Austin.

Dahlen, F.A. and J. Tromp (1998). Theoretical global seismology. Princeton University Press, Princeton, NJ.

Desai, S.D. (2002). Observing the pole tide with satellite altimetry. *J. Geophys. Res.*, 107(C11), 3186, doi:10.1029/2001JC001224.

Dziewonski, A.M. and D.L. Anderson (1981). Preliminary reference Earth model. *Phys. Earth Planet. Inter.,*25*,* 297–356.

Gilbert, F. (1970). Excitation of the normal modes of the Earth by earthquake sources. *Geophys. J. R. astr. Soc.*, 22, 223–226.

Gilbert, F. and A.M. Dziewonski (1975). An application of normal mode theory to the retrieval of structural parameters and source mechanisms from seismic spectra. *Phil. Trans. R. Soc. London,*A278, 187–269.

Gross, R.S. (2007). Earth rotation variations – long period. In: Herring, T.A. (ed), Physical geodesy, Treatise on Geophysics vol. 3, pp. 239–294, Elsevier, Oxford.

Gross, R.S. and B.F. Chao (2006). The rotational and gravitational signature of the December 26, 2004 Sumatran earthquake. *Surv. Geophs.*, 27, 615–632.

Gross, R.S., D.A. Lavallée, G. Blewitt, and P.J. Clarke (2009). Consistency of Earth rotation, gravity, and shape measurements. In: Sideris, M.G. (ed), Observing our changing Earth, IAG Symposia vol. 133, pp. 463–472, Springer-Verlag, New York.

Kalnay, E., M. Kanamitsu, R. Kistler, W. Collins, D. Deaven, L. Gandin, M. Iredell, S. Saha, G. White, J. Woollen, Y. Zhu, M. Chelliah, W. Ebisuzaki, W. Higgins, J. Janowiak, K.C. Mo, C. Ropelewski, J. Wang, A. Leetmaa, R. Reynolds, R. Jenne, and D. Joseph (1996). The NCEP/NCAR 40-year reanalysis project. *Bull. Amer. Met. Soc.*, 77, 437–471.

Kaula, W.M. (1966). Theory of satellite geodesy. Blaisdell, Waltham, Mass.

Lapwood, E.R. and T. Usami (1981). Free oscillations of the Earth. Cambridge University Press, Cambridge.

Milly, P.C.D. and A.B. Shmakin (2002). Global modeling of land water and energy balances. Part I: The Land Dynamics (LaD) model. *J. Hydrometeor.*, 3(3), 283–299.

Panet, I., V. Mikhailov, M. Diament, F. Pollitz, G. King, O. de Viron, M. Holschneider, R. Biancale, and J.-M. Lemoine (2007). Coseismic and post-seismic signatures of the Sumatra 2004 December and 2005 March earthquakes in GRACE satellite gravity. *Geophys. J. Int.*, 171, 177–190.

Sabadini, R., R.E.M. Riva, and G. Dalla Via (2007). Coseismic rotation changes from the 2004 Sumatra earthquake: The effects of Earth's compressibility versus earthquake induced topography. *Geophys. J. Int.*, 171, 231–243.

Stammer, D., C. Wunsch, I. Fukumori, and J. Marshall (2002). State estimation improves prospects for ocean research. *Eos Trans. Amer. Geophys. Union*, 83(27), 289–295.

Tsai, V.C., M. Nettles, G. Ekström, and A.M. Dziewonski (2005). Multiple CMT source analysis of the 2004 Sumatra earthquake. *Geophys. Res. Lett.*, 32, L17304, doi:10.1029/2005GL023813.

Chapter 86

Modeling and Observation of Loading Contribution to Time-Variable GPS Sites Positions

P. Gegout, J.-P. Boy, J. Hinderer, and G. Ferhat

Abstract We investigate loading consequences on the time-variable GPS station positions of one hundred stations around the world during the 2001–2006 time period. We model the three dimensional site displacements using a Love number formalism to describe the elastic deformation of a spherical Earth model submitted to atmospheric, oceanic and hydrological loadings.

We produce site position time series using the GPS analysis software GAMIT/GLOBK with or without inserting a combination of loading models and study their impact on 3D site positions. First of all, we compare the variability of modeled and observed site positions without integrating loading. We secondly study the variability reduction in the GPS site positions provided by the loading when integrating it in the GAMIT Software as an a priori contribution to the station motion model.

We conclude that the seasonal variability of site vertical displacement is quite well explained by our model at several locations, mainly located at mid-latitudes in the northern hemisphere, while it is much less understood near coastal areas.

86.1 Introduction

For 15 years, loading models have been enhanced continuously: from atmospheric loading with crude spatial resolution (Gegout and Cazenave, 1991) to high resolution three dimensional atmo-spheric loading and time-variable gravity field modeling (Biancale et al, 2000), from crude oceanic inverted barometer response to dynamical response of the oceans to the barometric forcing using hydro-dynamical models like MOG2D (Carrère and Lyard, 2003), from crude low resolution bucket models to high resolution data assimilation hydrological models like GLDAS (Rodell et al., 2004). We have modeled various loading contribution to each one of the three pillars of geodesy: surface and satellite gravity, rotation and surface deformation.

Despite the recent substantial advances of satellite gravimetry, the temporal resolution of satellite gravity is at best 10 days (Biancale et al., 2005). In Earth rotation problems, the loading processes are marginal with respect to wind transport in angular momentum budgets (Gross et al., 2004). For investigating high frequency consequences of loading, for periods ranging from 1 day to 1 year, time-variable surface gravity (Boy et al., 2002) and time-variable Earth's shape (Petrov and Boy, 2004) are up to now best suited.

We therefore decided to study observations of the time-varying Earth's shape to confront our loading models. As we need a dense spatial coverage of the Earth surface, we therefore decided to use GPS positioning techniques to sample the Earth's shape using simultaneously one hundred GPS stations.

The GPS technique has known multiple enhancements during the last 10 years: vertical residuals have decreased from tens of centimeters to a few centimeters. Are these residuals connected to Earth deformation due to loading?

In this study, we model and observe loading contribution to time-variable GPS Sites positions, keeping in mind the two following questions: are we able to detect and identify loading contribution to GPS position with

P. Gegout (✉)
Institut de Physique du Globe de Strasbourg, Strasbourg 67084, France
e-mail: Pascal.Gegout@eost.u-strasbg.fr

S.P. Mertikas (ed.), *Gravity, Geoid and Earth Observation*, International Association of Geodesy Symposia 135,
DOI 10.1007/978-3-642-10634-7_86, © Springer-Verlag Berlin Heidelberg 2010

nowadays precision? Does the integration of loading models into the GPS processing improve vertical positioning?

Our goal is not to seek for a precise agreement, since involved physical phenomena and accuracies may significantly vary from one site to another. GPS positions have a formal accuracy of several millimeters, the size of the loading consequences we are looking for. We wish to conduct a plausibity test between the physical processes we account for, model and estimate from global data assimilation systems and observe through the Global Positioning System. We therefore use simple Fourier transforms techniques to reach this last goal.

86.2 Modeling Loading Contributions

The solid Earth has the property to deform under the pressure and gravitational forces exerted by surface loads. All surface loads may be expressed in terms of equivalent pressure (Pa) or equivalent water height (mm of water) but will be handled in term of millimeter of displacement. The properties of Earth deformation are described by the Load Love Numbers we estimate from a spherical Earth model. A comparison of our Love numbers with others can be found in (van Dam et al., 2003).

Figures 86.1 and 86.2 are computed for the whole Earth using the spherical harmonics formalism but accurate three dimensional site displacements time series are evaluated using refined Green's functions (Boy et al., 2002; Boy and Hinderer, 2006).

86.2.1 Atmospheric and Oceanic Loading

The state of the Atmosphere and the load it induces on the solid Earth and Oceans is known through the ECMWF operational data assimilation system: the spatial resolution is given by a spherical harmonics truncation at degree T512 which is equivalent to an N256 Gaussian grid. The time sampling is 6 h.

The barotropic response of the oceans forced by the ECMWF pressure and winds is provided by MOG2D (Carrère and Lyard, 2003) and added to the atmospheric term in order to provide pressure and gravitational forcing at the solid Earth surface (Boy and Lyard, 2008). Baroclinic effects are not modeled.

Time-variable horizontal and vertical positions are estimated, at each time step, for all sites, for the period beginning of 2001 to the end of 2006, for modeling purposes and before integration in the GAMIT positioning software.

A basic statistical analysis, the estimation of the standard (RMS) deviation at each grid point over the year 2002, provides a quick overview of the regions of interest where the vertical displacement induced by loading is significant (Fig. 86.1).

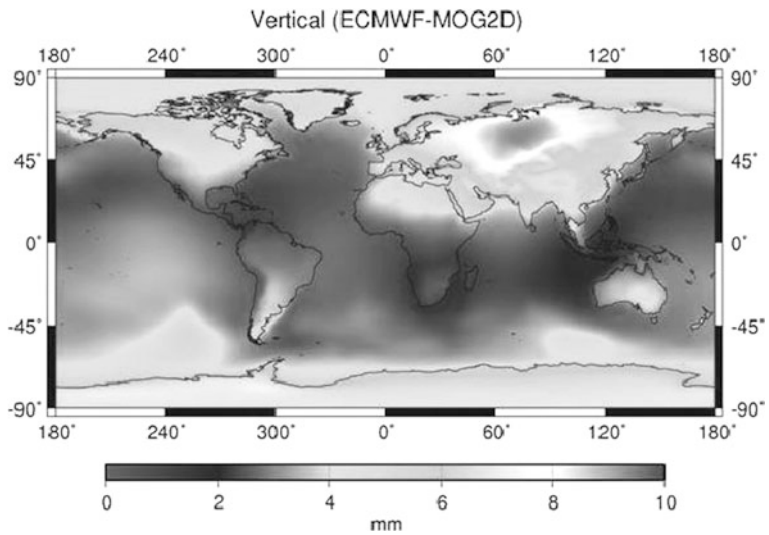


Fig. 86.1 Variability of the vertical displacement (RMS) due to atmospheric and oceanic loading in 2002

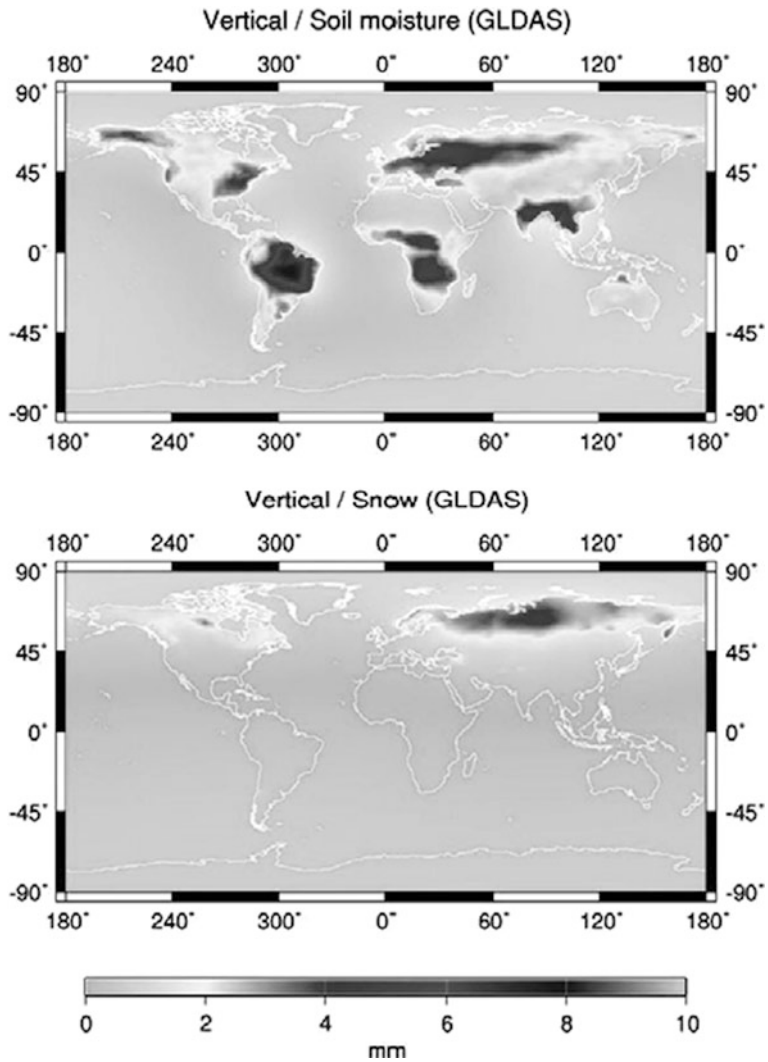


Fig. 86.2 Variability of the vertical displacement (RMS) induced respectively by soil moisture and snow in 2002

The annual variability dominates this picture since variability at other timescales has less power. We notice that annual variabilities with RMS deviation greater than 5 mm are found over large continental areas: Eurasia, North America and Antarctica. A special mention is made for Siberia where annual vertical displacement can reach up to 10 mm. These large continental areas are submitted to mid-latitude climate which is characterized by the succession of anticyclones and depressions at synoptic timescales with a strong annual variability. There is no similar continental domain at mid-latitudes in the southern hemisphere.

Central and South America, Africa and Australia, are submitted to other meteorological regimes and are surrounded by large oceanic areas. The dynamic response of the oceans provides a significant departure from the inverted barometer response but atmospheric effects on the vertical component are compensated by oceanic effects. This mechanical coupling explains the relatively small modeled vertical displacement of 2–3 mm.

The accuracy of this modeled displacement is evaluated by the departure of NCEP from ECMWF model which shows differences lower than 1 mm over all continents except Antarctica (2 mm).

The comparison between a static IB model and a dynamic ocean shows that MOG2D modify by 1.5 mm the annual variability except near some specific resonant basins (not shown).

86.2.2 Hydrological Loading

Hydrological loading is made of soil moisture and snow height. These loading are estimated from the GLDAS/NOAH (Rodell et al., 2004). Groundwater is not included. GLDAS assimilate various data sources to describe global water storage with a quarter degree spatial resolution and three hourly time sampling, but omits Greenland and Antarctica.

The variabilities (RMS) in 2002 of the vertical displacement induced by soil moisture and snow are shown on Fig. 86.2a, b respectively. We point out some coarse features from Fig. 86.2, even if some more precise insight is required at each site. The vertical displacement annual variability due to hydrological loading is large (greater than 5 mm)

Over Eurasia and Alaska, the hydrological loading, made of soil moisture and snow loads, reach coarsely the same amplitude as the atmospheric/oceanic loading and is lagged by three months. The sum of all loads effects exhibit large annual and semi-annual vertical displacements in these regions.

In South America and Africa, the hydrological loading is much more significant (6–8 mm) than the atmospheric/oceanic loading (2 mm). In Asia the soil moisture associated to monsoons induce a vertical displacement of 5 mm.

The comparison between hydrological loading derived from GLDAS and ECMWF assimilation scheme provide an idea of the uncertainties. Over Eurasia and North America, the differences of the annual variability due to the snow reach 2–4 mm. The differences relative to soil moisture reach an average of 2 mm over all continents.

We define our reference model, labeled AOH, which contains Atmospheric (ECMWF), Oceanic (MOG2D) and Hydrological (GLDAS) Loadings.

86.3 Observations of GPS Sites Positions

The displacement of GPS sites is determined for one hundred sites equally distributed around the world and selected among the best sites by a statistical analysis on IGS solutions.

We solve for all these sites in one single GAMIT processing (King and Bock, 2008) in double differences mode, solving for narrow and wide lanes ambiguities. Our main strategy is to form as many as possible double differences between sites to tighten the network, enhance ambiguity resolutions and realization of the reference frame.

We use an elevation cutoff of 10°. We modified the NAO99 tide model (11 components) to take into account the degree one deformation.

We adjust a priori coordinates and IGS precise orbits in two iterations, zenithal delays every 2 h and use a priori Vienna Mapping Functions (Boehm et al., 2006). The daily repeatability solutions presented hereafter are derived from GLOBK (Herring, 2008).

We process twice the 6-y series, once without the load (GPS), secondly integrating the AOH load (GPS&AOH) by "applying the ATM load" (Tregoning and van Dam, 2005). Solving for one hundred sites is heavily CPU time consuming. Months of CPU time of our cluster were required.

86.3.1 Detection of the Loading Contribution to the Time-Variable GPS Position at Potsdam

Are we able to detect loading contribution inside GPS vertical position with nowadays precision?

We present the case study of Potsdam which significantly reveals features which are common to most northern hemisphere's sites. Substituting the inverted barometer by a dynamic response does not change substantially the model at this site located inside the European continent (Fig. 86.3 and 86.4).

We notice that both spectrums coincide very well in the 10–100 days interval. This part of the time-variable vertical displacement is well resolved by the atmospheric loading and corresponds to the regime of anticyclones and depressions at mid-latitudes. This was also reported from comparison with gravimetric measurements (Boy and Lyard 2008). The 2–10 days interval shows a decrease of modeled displacement when the observed one stagnate around an amplitude of 0.5 mm.

The modeled variability in the 100–1,000 days, weaker than the observed one (Fig. 86.4), is enhanced by the addition of hydrological loading (Fig. 86.5), especially at annual and semi-annual periods.

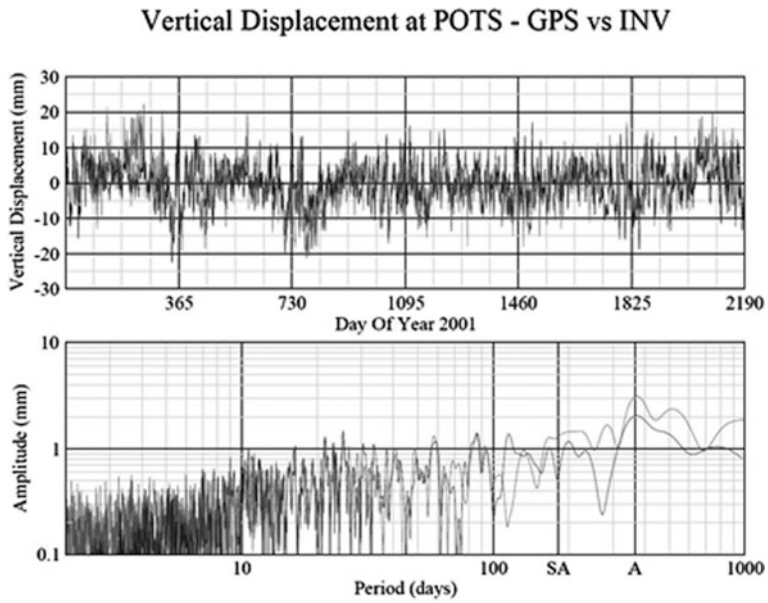


Fig. 86.3 Vertical displacement and periodogram observed at Potsdam in 2001–2006 (GPS in *grey*) and modeled under the inverted barometer assumption (ECMWF & IB in *black*)

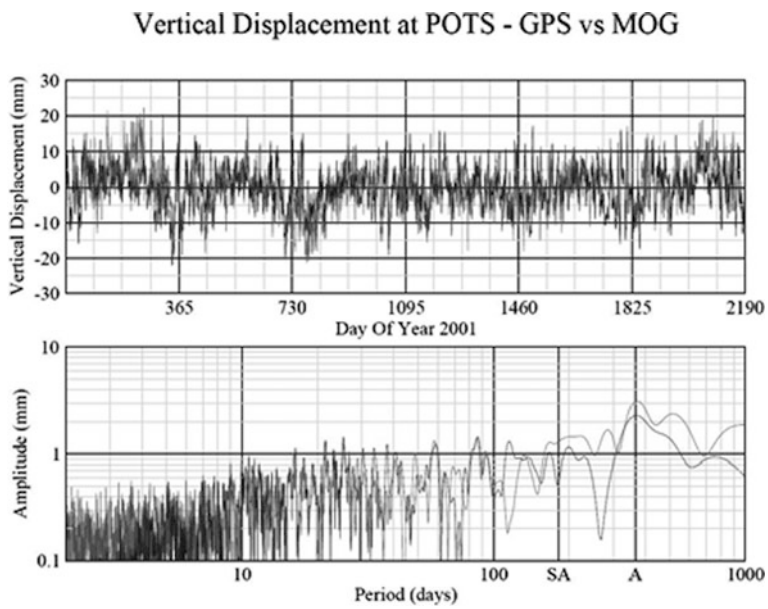


Fig. 86.4 Vertical displacement and periodogram observed (GPS in *grey*) and modeled (ECMWF & MOG2D in *black*)

86.3.2 Integration of the AOH Model Inside the GPS Analysis Software GAMIT at Potsdam

First of all, we have to underline that solved ambiguities are quite different from one run to the other which integrates the predicted AOH sites displacements. This demonstrate the sensitivity of the solution to the a priori stations position but also the impact of integrating simultaneously the AOH load as an a priori at all one hundred sites.

Figure 86.6 shows that the residual GPS&AOH signal (black) is weaker than the GPS one (grey). Throughout the spectrum, its spectral content is below the GPS one. Biases and errors are therefore corrected

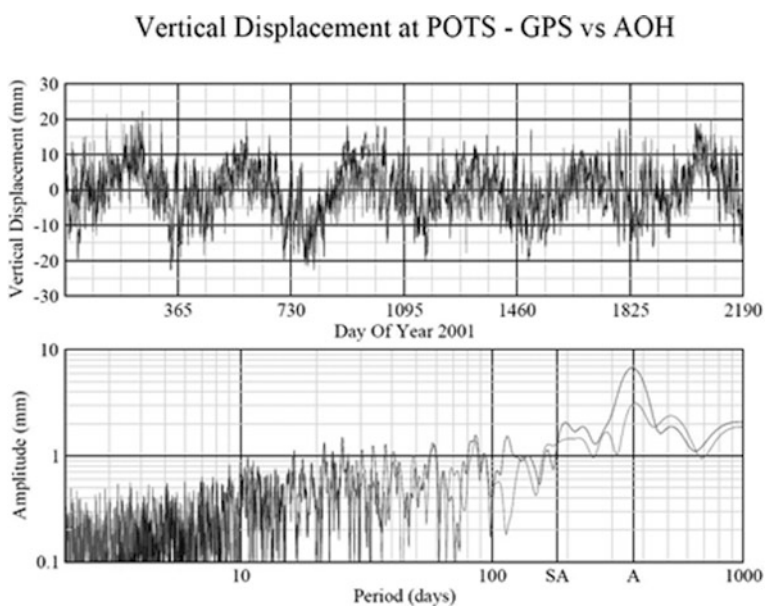


Fig. 86.5 Vertical displacement and periodogram observed at Potsdam (GPS in *grey*) and modeled (AOH in *black*)

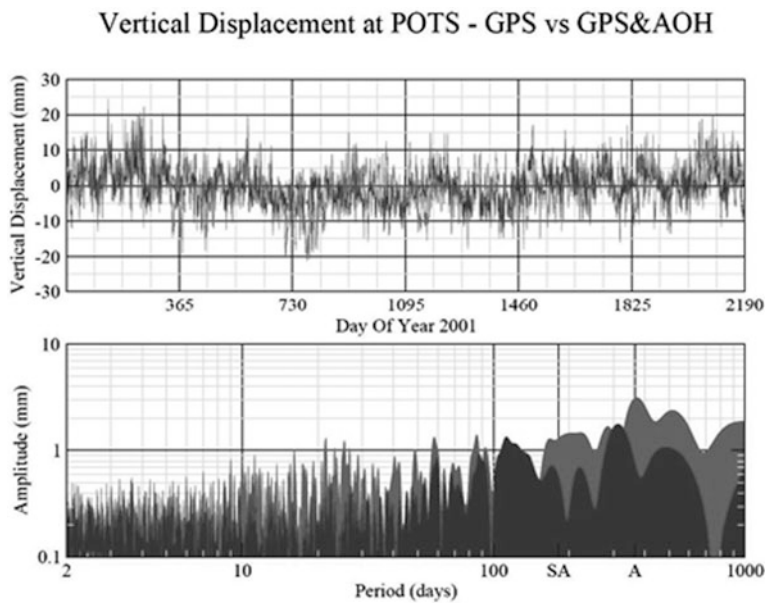


Fig. 86.6 Vertical displacement and periodogram observed at Potsdam (GPS in *grey*) and observed with integration of the modeled AOH loading (GPS&AOH in *black*)

with better initial conditions. Since the adjustment process is not linear, the AOH loading provides a better fit than the expected one from the comparison GPS versus AOH alone (Fig. 86.5).

In the 2–10 days interval, a few tenths of millimeter are gained at some specific periods. In the 10–100 days interval, amplitudes of vertical displacement residuals decrease from 1 to 0.5 mm. The annual variability decreases from 3 to 0.8 mm and the semi-annual one from 1 to 0.2 mm. Significant improvements are noticeable at seasonal and inter-annual time scales.

From another point of view, some spectral peaks may present some anomalies and could not been explained only by loading consequences. These anomalous peaks, at 350 days and harmonics, may come from specific orbital effects as reported by (Ray et al., 2008). We notice poor reduction near 90 and 120 days for Potsdam as well as for other sites.

86.4 Integration of the AOH Loading Model: Comparison of Two GPS Solutions

Does the integration of loading models inside the GPS processing improve sites vertical positioning?

Since most of the variability is carried at seasonal frequencies and especially at the annual frequency, amplitude reduction of the vertical displacement residuals throughout the network provides a fair indication of the performance of the AOH model.

86.4.1 Annual Variability Reduction in the Northern Hemisphere

Although the reduction of residual amplitude is less significant than the presented case study of Potsdam, the same qualitative conclusions can be drawn at most sites of the northern hemisphere above 40°N (Fig. 86.7). This result coincide with the previous comments on loading variabilities which stand that atmospheric, oceanic and hydrological loadings largest variabilities are observed in the northern hemisphere. Observation of these variabilities through GPS sites displacement comforts us to think that these variabilities are realistic even if their uncertainty remains large.

In the northern hemisphere, the oceans/continents distribution allows to equally distribute sites which pair to build double difference and solve efficiently ambiguities. We report significant improvements between previous run based on GAMIT 10.21 and the present one based on version 10.33 which include an enhanced ambiguity resolution scheme. Covering the southern hemisphere the same way is unfortunately not possible and it may lead to less positioning accuracy.

Although time-variable horizontal displacements are also introduced at the observation level, we don't

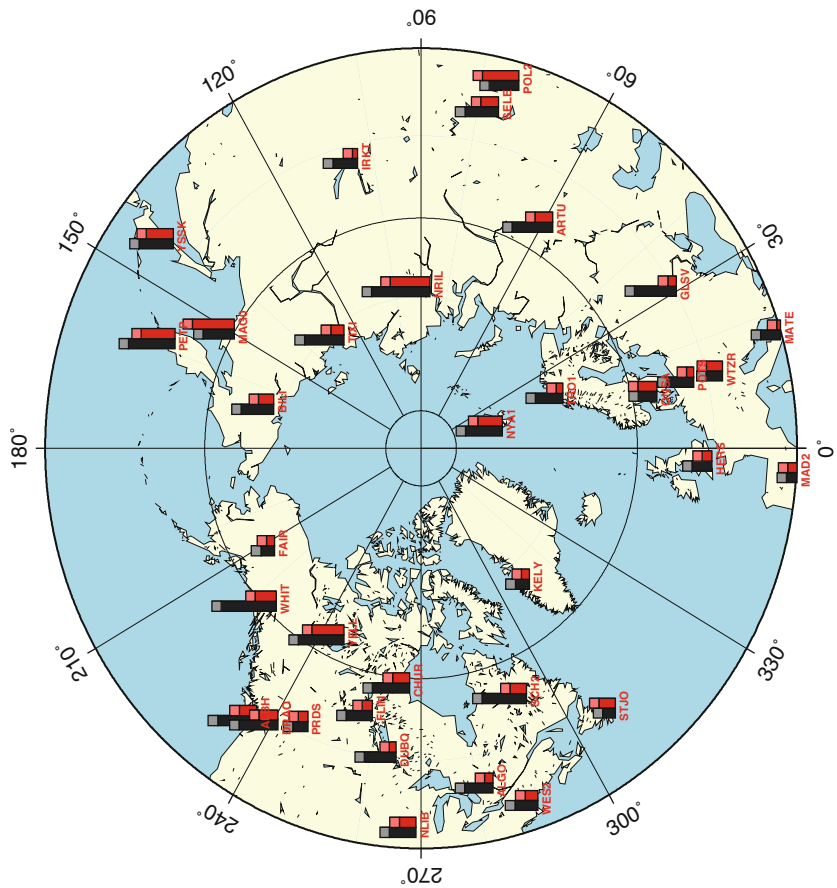


Fig. 86.7 Annual variability of the vertical displacement in the northern hemisphere: comparison of annual amplitudes of GPS and GPS&AOH solutions. At Potsdam the annual resi-dual amplitude decreases from 3 (GPS, *left bar*) to 0.8 mm (GPS&AOH, *right bar*). *Top* of 3d-bars are *light shaded*

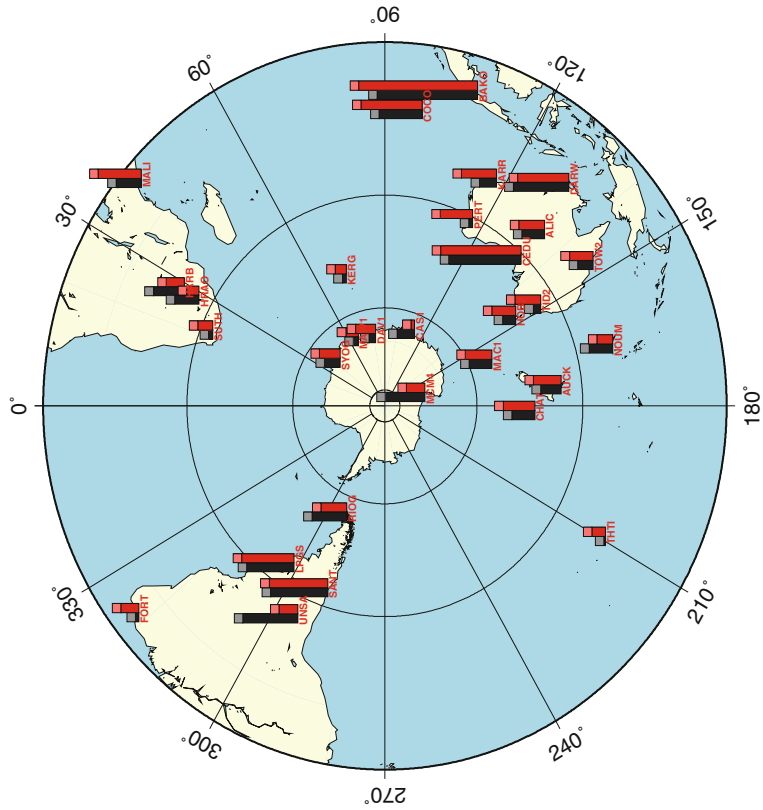


Fig. 86.8 Annual variability of the vertical displacement in the southern hemisphere: comparison of annual amplitudes of GPS and GPS&AOH solutions. At HRAO the annual residual amplitude decreases from 3.2 (GPS, *left black* 3d-bar) to 1.6 mm (GPS&AOH, *right grey* 3d-bar)

have any improvements. The mean amplitude of these horizontal displacements is 0.4 mm and horizontal seasonal displacements reach 0.8 mm.

There is no significant positioning improvement as some sites like St-John STJO, Ny-Alesund NYA1, Petropavlovsk PETP. For these coastal sites or islands, the modeled vertical displacement is much smaller (0.5 mm) than the observed one (3 mm).

86.4.2 Variability in the Southern Hemisphere

The same conclusions can be drawn in the southern hemisphere: most sites among the 30 sites of this hemisphere are coastal sites (Fig. 86.8). The modeled vertical displacement is much weaker than the observed one and we do not explain the large annual variations which are nevertheless observed. In most cases, the integration of the loading model increases the residuals. We notice improvements at a few sites: UNSA, HRAO, HARB, CAS1, MCM4.

86.5 Conclusion

Integrating the AOH (Atmospheric, Oceanic and Hydrological) loading for all GPS sites as an a priori of the GAMIT processing and solving for 100 sites simultaneously allow solving for vertical site positions at the millimeter level at mid and high latitudes of the northern hemisphere which is quite regularly sampled by 60 stations. Spectral and coherence analyses of some sites show statistically significant common spectral peaks but also specific anomalous peaks in GPS observations.

In the southern hemisphere, the GPS&AOH solution which integrates AOH loading does not improve the residual vertical position. The southern hemisphere is poorly sampled and most of the 30 sites are located nearby oceans.

Uncertainties in AOH loading were estimated by comparing different models and may contribute to a discrepancy of 2–3 mm. It is likely that unmodeled or mismodeled local oceanic effects and specific tropospheric propagation effects cause the GPS time series to be much more noisy and inaccurate near oceans.

We have to tune our GPS processing methods, enhance loading models and test several loading realizations to better understand the remaining disagreements between modeling and observation.

Acknowledgments The authors thank Matthew Rodell and Florent Lyard for providing their insights and datasets. We thank IGS, ECMWF, NCEP for providing data and products, and GAMITeers, T. Herring, R. King and P. Tregoning, for continuously improving and implementing new methods inside GAMIT/GLOBK.

References

Biancale, R., G. Balmino, J.-M. Lemoine, J.-C. Marty, B. Moynot, F. Barlier., P. Exertier, O. Laurain, P. Gegout, P. Schwintzer, Ch. Reigber, A. Bode, Th. Gruber, R. König, F.-H. Massmann, J.C. Raimondo, R. Schmidt, and S.Y. Zhu. (2000). A new global Earth′s gravity field model from satellite orbit perturbations: GRIM5-S1**.** *Geophys. Res. Lett.*, 27, 3611–3614.

Biancale R., J.-M. Lemoine, G. Balmino, S. Loyer, S. Bruinsma, F. Perosanz, J.-C. Marty, and P. Gegout (2005). 3 years of decadal geoid variations from GRACE and LAGEOS data, CNES/GRGS product, December.

Boehm J., B. Werl, and H. Schuh (2006). Troposphere mapping func-tions for GPS and very long baseline interferometry from European Centre for Medium-range Weather Forecasts operational analysis data. *J. Geophys. Res.*, 111, B02406, doi:10.1029/2005JB003629.

Boy, J.-P., P. Gegout, and J. Hinderer (2002). Reduction of surface gravity data from global atmospheric pressure loading. *Geophys. J. Int.*, 149, 534–545.

Boy, J.-P. and J. Hinderer (2006). Study of the seasonal gravity signal in superconducting gravimeter data. *J. Geodyn*, 41, 227–233.

Boy, J.-P. and F. Lyard (2008). High-Frequency non-tidal ocean loading effects on surface gravity measurements. *Geophys. J. Int.*, 175, 35–45.

Carrère, L. and F. Lyard (2003). Modeling the barotropic response of the global ocean to atmospheric wind and pressure forcing – comparisons with observations. *Geophys. Res. Lett.*, 30(6), 1275, doi: 10.1029/2002GL016473.

Gegout P. and Cazenave A. (1991). Geodynamics parameters derived from 7 years of laser data on Lageos. *Geophys. Res. Lett.*, 18, 1739–1742.

Gross, R.S., I. Fukumori, D. Menemenlis, and P. Gegout (2004). Atmospheric and oceanic excitation of length-of-day variations during 1980–2000. *J. Geophys. Res.*, 109, B01406, doi: 10.1029/2003JB002432.

Herring, T.A. (2008). GLOBK: Global Kalman filter VLBI and GPS Analysis Program version 10.33. Massachusetts Institute of Technology (MIT), Cambridge.

King, R. W. and Bock, Y. (2008). Documentation for the GAMIT analysis software, release 10.33. Massachusetts Institute of Technology (MIT), Cambridge.

Petrov, L. and Boy, J.-P. (2004). Study of the atmospheric pressure loading signal in VLBI observations. *J. Geophys. Res.*, 109, B03405, doi: 10.1029/2003JB002500.

Ray J., Z. Altamimi, X. Collilieux, T. van Dam (2008). Anomalous harmonics in the spectra of GPS position estimates. *GPS Solut*. 12, 55–64, DOI 10.1007/s10291-007-0067-7.

Rodell, M., P.R. Houser, U. Jambor, J. Gottschalck, K. Mitchell, C.-J. Meng, K. Arsenault, B. Cosgrove, J. Radakovich, M. Bosilovich, J.K. Entin, J.P. Walker, D. Lohmann, and D. Toll (2004). The global land data assimilation system. *Bull. Amer. Meteor. Soc.*, 85(3), 381–394.

Tregoning, P. and T.M. van Dam (2005). Atmospheric pressure loading corrections applied to GPS data at the observation level. *Geophys. Res. Lett.*, 32, L22310, doi:10.1029/2005GL024104.

van Dam, T., H.-P. Plag, O. Francis, and P. Gegout. (2003). GGFC Special Bureau for Loading: Current status and Plans, in Proceedings of the IERS Workshop on Combination Research and Global Geophysical Fluids, Bavarian Academy of Sciences, Munich, Germany, 18–21 November 2002, IERS Tech. Note 30, edited by B. Richter, W. Schwegmann, and W. R. Dick, pp. 180–198, Int. Earth Rotation Serv., Paris.

Chapter 87

Investigating the Effects of Earthquakes Using HEPOS

M. Gianniou

Abstract KTIMATOLOGIO S.A. developed the HEllenic POsitioning System (HEPOS) for facilitating the establishment of the National Cadastre in Greece. HEPOS is a modern RTK-network consisting of 98 permanent GPS reference stations distributed throughout Greece. Like in any other RTK-network, the coordinates of the reference stations must be estimated with high accuracy, on the order of 1 cm. This requirement is a great challenge for HEPOS, due to the strong geodynamic effects taking place in Greece. Besides the slow displacements caused by the individual velocities of the different tectonic plates, abrupt displacements may occur as a result of strong earthquakes.

During the first months of the operation of HEPOS, several strong earthquakes (ML >6.0) with different characteristics took place in certain areas of Greece. By post-processing and analyzing GPS observations of the reference stations of HEPOS, it was proved that some earthquakes have detectable effects on the positions of the reference stations. The paper describes the methodology that has been used for revealing these effects as well as the results that have been obtained.

87.1 Introduction

During the last 2 decades, geodynamics has been taking advantage of space-based positioning techniques for determining crustal movements. At the beginning, VLBI and SLR techniques were used (see e.g. Drewes, 1992). These techniques required equipment that was expensive and very difficult to transport. The development of satellite positioning systems and particularly GPS, gave the opportunity for extended measurement campaigns. But this method was still demanding and costly mainly due to the long observation time which is required for achieving the needed accuracy and the necessity for periodically repeating the measurement for studying the dynamic behaviour of the movements.

In the last decade the use of permanent GNSS reference stations (RS) offers a perfect opportunity to monitor the geodynamic effects on a permanent base and at low cost. An example of a network of permanent stations that is established for geodynamic research and monitoring is the Bay Area Regional Deformation (BARD) network in northern California (Murray and Segall, 2001). Smaller networks are established in certain regions of Greece by the Centre for the Observation and Modelling of Earthquakes and Tectonics (COMET) and the National Technical University of Athens (Floyd et. al., 2005).

The reference stations of HEPOS are distributed over the whole country and are continuously operating, offering good possibilities for geodynamic research. HEPOS is designed and built primarily for daily RTK-surveying. The locations of the stations have been selected in order to optimize the coverage and the RTK-performance. Furthermore, they had to be installed in protected sites having the needed infrastructure (Gianniou, 2008). For these reasons the stations are installed on buildings and not on bedrock, which would be optimal from geodynamic point of view. However, HEPOS can well contribute to the geodynamic research, as will be shown in this work.

M. Gianniou (✉)
Geodetic Department, KTIMATOLOGIO S.A.,
Hellenic Cadastre, Athens 15231, Greece
e-mail: mgianniu@ktimatologio.gr

S.P. Mertikas (ed.), *Gravity, Geoid and Earth Observation*, International Association of Geodesy Symposia 135,
DOI 10.1007/978-3-642-10634-7_87, © Springer-Verlag Berlin Heidelberg 2010

It is well known that earthquakes have several effects. One of these is permanent displacements that sometimes take place in the area around the epicentre. The effects of each earthquake depend on its characteristics, with the magnitude and the focal depths playing important roles (Konstantinou et. al., 2006). In this work four strong earthquakes with different magnitudes and focal depths will be investigated in order to find out if they caused measurable displacements and the magnitude and direction of these movements.

87.2 Methodology Followed

87.2.1 Earthquakes Investigated

The four earthquakes investigated in this paper took place during the first half of 2008 in four different places in Greece. Table 87.1 gives the basic data about each earthquake (EQ), namely the date and time (GMT) of the event, the geographic latitude and longitude of the epicentre, the depth and the local magnitude. These data are taken from the web site of the Geodynamic Institute of the National Observatory of Athens. Figure 87.1 shows the positions of the reference stations of HEPOS (gray levels denote prefectures) and the epicentres of the earthquakes. The epicentres of earthquakes IIIa and IIIb are close to each other. For simplicity, only the epicentre of the strongest earthquake is displayed. The connection lines between the RSs denote the area where network solutions (VRS: Virtual Reference Station, FKP: Flächen Korrekturparameter, MAC: Master Auxiliary Concept) are supported, whereas the circles denote the coverage of Single Reference Stations. More details can be found in Gianniou (2008).

Table 87.1 Earthquakes investigated

EQ	Date	Time (GMT)	Lat (N)	Long (E)	Depth (Km)	Ml
I	6/1/08	05:14	37.11	22.78	86	6.1
II	4/2/08	22:15	38.09	21.94	25	5.0
III a	14/2/08	10:09	36.50	21.78	41	6.2
III b	14/2/08	12:08	36.22	21.75	38	6.1
IV	8/6/08	12:25	37.93	21.41	21	6.5

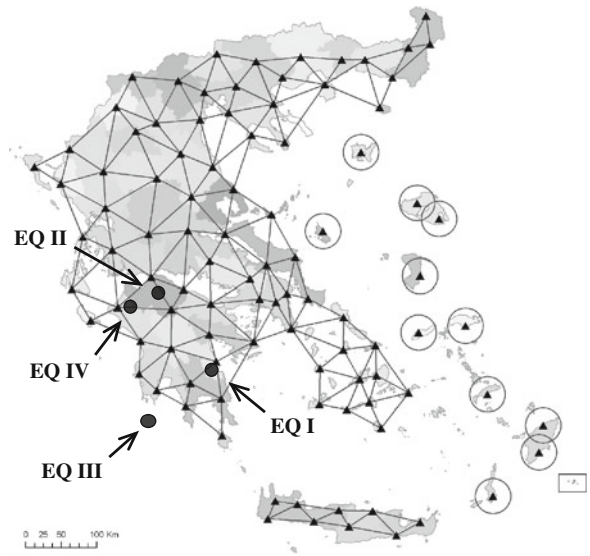


Fig. 87.1 The 98 reference stations of HEPOS and the epicentres of the earthquakes

87.2.2 Selection of Reference Stations

Having the location of each epicentre, a critical question had to be answered, namely "which reference stations should be used in order to search for possible displacements caused by the earthquake". For selecting these RSs several parameters are considered. Firstly, both stations that could have been displaced (suspected RSs) and stations that are expected to be uninfluenced (unsuspected RSs) should be used. This approach offers a validation of the results of the GPS data processing. Among the unsuspected RSs one is selected as the Master RS, as will be explained in Sect. 87.2.3. Figures 87.2, 87.3, 87.4 and 87.5 show the RSs used for investigating the EQ I–IV, respectively.

For considering a RS as suspicious or unsuspicious, one should take into account different parameters, like the distance between the RS and the epicentre, the geotectonic zone of each RS, known faults in the area etc. The RSs used in this work belong to the four different geotectonic zones in the area, namely the Ionian, Gavrovo, Pindos and Paxos zones (Kahle et al., 1992). In the case of EQ I (Fig. 87.2) the RS 004A is the most likely to be displaced, the RSs 002A, 003A, 010A, 055A and 056A should be investigated and are treated

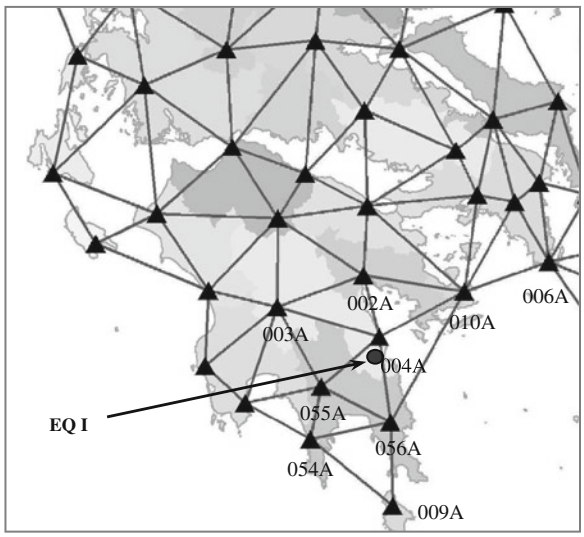


Fig. 87.2 Reference Stations used for EQ I: (Master RS: 006A)

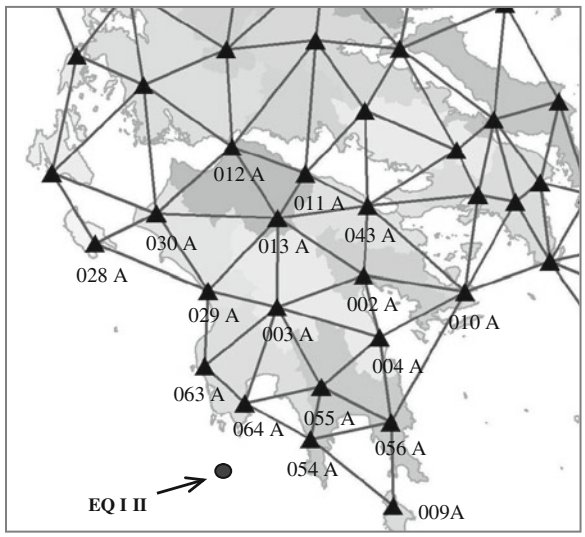


Fig. 87.4 Reference Stations used for EQ IIIa,b: (Master RS: 013A)

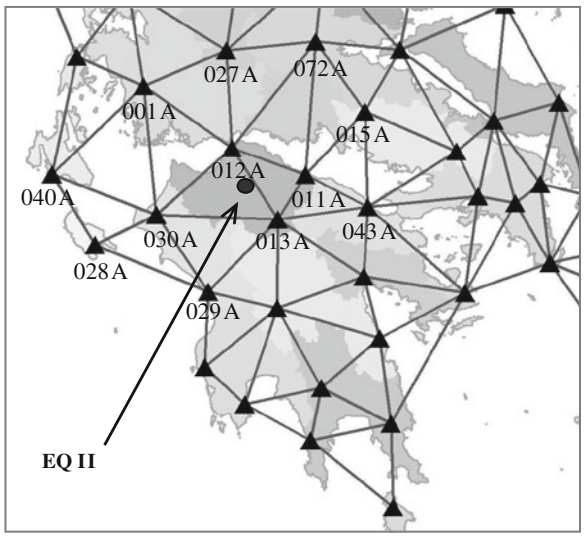


Fig. 87.3 Reference Stations used for EQ II: (Master RS: 015A)

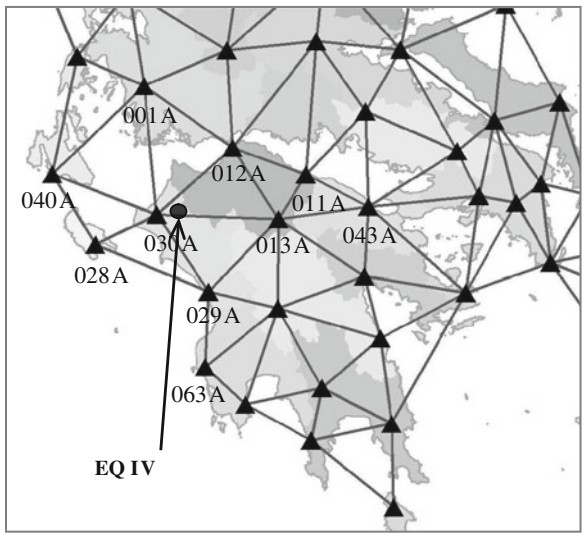


Fig. 87.5 Reference Stations used for EQ IV: (Master RS: 043A)

also as suspected, whereas RSs 006A, 009A and 054A are expected to be uninfluenced.

Looking at Figs. 87.2, 87.3, 87.4 and 87.5, one sees that in case of EQ III more stations than in any other case are used. The reason for that is that EQ III has been used as a pilot study within this work. The large number of unsuspected RSs is used in order to have a good assessment of the achieved precision in the day-by-day solutions.

87.2.3 Processing of GPS Data

Having decided which reference stations should be used for each EQ, the question of how to process the data had to be answered. Two strategies are tested: Strategy A′: solving the baselines from one RS to all others; and strategy B′: creating a network of baselines between neighbor stations followed by a minimally constrained least-squares adjustment.

In both strategies a Master RS is used. Following strategy A′, the Master RS is the one from which the baselines to the other RSs are formed. In order to ensure high precision in the baseline computation, the Master RS should be relative close the others. Following strategy B′, the Master station is the one used for minimally constraining the network adjustment.

As mentioned above, the data used in this study are GPS observations, collected at the Reference Stations of HEPOS. All RSs are equipped with Trimble NetRS receivers and Trimble Zephyr Geodetic Antennas with Radomes (IGS code: "TRM41249.00 TZGD"). The typical logging interval for static baselines used for geodynamic applications is 60 s. However, HEPOS is a surveying-oriented network and only 1 and 15 s data are permanently archived. In this work the 15 s data are used. These data are stored in daily files (0-24 GMT). Data from several days before and after each earthquake are processed in order to assess the normal repeatability of the solution that can be achieved using the above mentioned strategies.

Regardless of strategy, the baseline processing is always done with exceptional care, in order to achieve high precision. External error sources like electromagnetic interferences or ionospheric disturbances had to be detected in order to avoid biased estimations (Gianniou, 1996). These biases cause variations that could be misinterpreted as changes in the position of the station.

Generally, for geodynamic applications, scientific software packages are used for exploiting the highest accuracy that GNSS measurements can give. These packages model parameters like nutation/precesion, tidal and atmospheric loading, solid earth tides, etc. However, for investigating sudden changes in the coordinates, simpler software packages can also be used. In this work all computations are made using Trimble Total Control ver. 2.73. The baseline processing is done with the following parameters: 13° elevation cut-off mask, iono-free linear combination of phase double-differences as observable, fixed phase ambiguities, IGS final precise orbits, NGS antenna phase-centre model, Goad and Goodman tropospheric model. The only exceptions to the above were made for EQ IV. This earthquake took place at the time of writing. In this case IGS rapid orbits are used and fewer days after the event are processed.

In order to distinguish between the horizontal and vertical positions of the RSs, the ECEF coordinates of the RSs are projected using the 3-parameter datum transformation between WGS'84 and the Greek Datum and the Transverse Mercator projection.

87.3 Data Analysis

87.3.1 Comparing Processing Strategies

In order to compare the effectiveness of strategies A and B, the data from EQ II are processed using both strategies. Following strategy A′, 11 baselines connecting the Master RS (015a) to each one of the other RSs, i.e. the stations annotated with their codes in Fig. 87.3 are solved for each day. Following strategy B′, the 24 baselines shown in Fig. 87.3 are processed and then the baseline vectors are adjusted with minimal constraints to produce the daily solution. Each strategy is used to process the same dataset consisting of 24 days in sequence. In order to compare the two strategies, the standard deviation of E, N and h over the 24 days is computed. Figures 87.6 and 87.7 give the standard deviations of the N and h, respectively, for both strategies. As can be seen in Fig. 87.6, the results of strategy B′ are slightly better than the results of strategy A′. The standard deviations of E (not shown here) are practically equivalent. Regarding the standard deviation of h, strategy A′ is generally slightly better, something that will be further investigated. From Figs. 87.6 and 87.7 it can be concluded that for the purposes of this work (search for horizontal displacements only) both strategies can be used. This conclusion will be confirmed by the data analysis in Sect. 87.3.2.

87.3.2 Investigation of Displacements

This section contains diagrams showing the daily variation of Easting and Northing at different RSs

For each earthquake, a period of 2–3 weeks before and after the event is used in order to obtain reliable results. The y-axis of all diagrams is scaled to the same extent (4.5 cm), so that comparisons between all cases can be made directly. Diagrams are made for E, N and h for all stations for all earthquakes. In the following the most representative ones are given.

Figure 87.8 gives the variation of Northing for RS 004A. The variations are less than 1 cm throughout the whole period. There is no obvious permanent change in the coordinate after the day of EQ I.

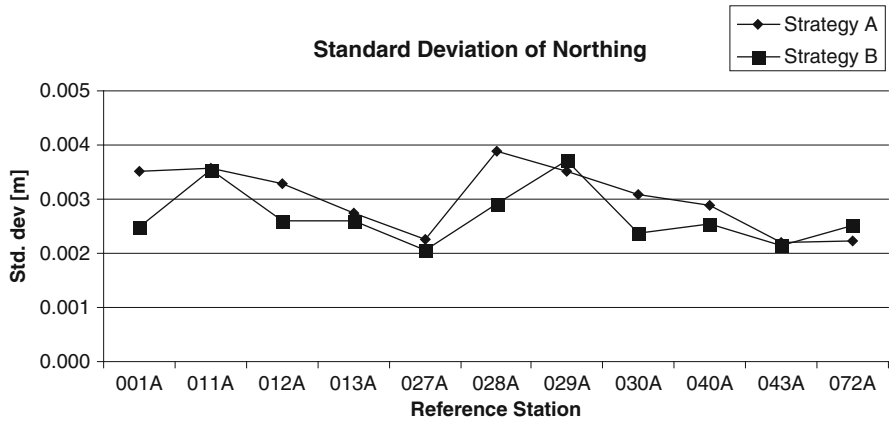


Fig. 87.6 Comparison of strategies A′ and B′: Estimation of N

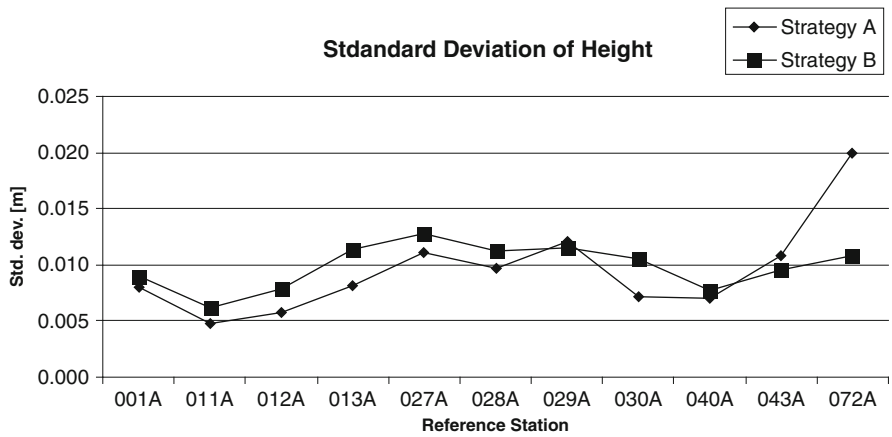


Fig. 87.7 Comparison of strategies A′ and B′: Estimation of h

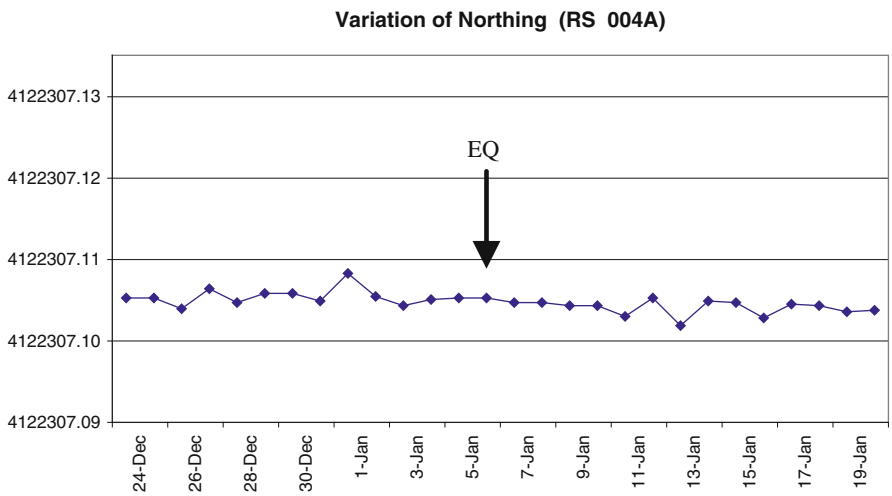


Fig. 87.8 EQ I: Variation of Northing for RS 004A

Figure 87.9 gives the variation of Easting for RS 012A. The variations are a little higher than in Fig. 87.8, but still under 1 cm throughout the whole period. Also in this case, there is no obvious permanent change in the coordinate after the earthquake II.

In Fig. 87.10 there is a sudden change (of about 2 cm) in Northing of RS 064A, taking place at the day of the EQ III. There is also an indication of a falling trend. However, this trend is within the 1 cm noise level. So, no safe results can be concluded about this falling trend. A very similar behaviour can be seen in Fig. 87.11 for RS 063A. However, the magnitude of the sudden change is quite smaller; about 8 mm. Similar behaviour results also for also RS 054A and 055A with changes about 1 cm and 6 mm, respectively. The variations of Easting are generally slightly less.

Within the 17 RSs used for EQ III (see Fig. 87.4) there where detectable changes at four of them; i.e. 064A, 054A, 055A and 063A. The estimated displacement vectors are shown in Fig. 87.12. Clearly, there is a correlation between the magnitude of displacements and the distance between RS and epicentre.

For the EQ IV there were detectable movements for the stations 029A and 030A, with maximum amplitude in the order of 1 cm. An example is given in Fig. 87.13, which gives the variation of Easting for RS 030A.

Regarding the height, there were no detectable vertical displacements in any of the cases EQI-EQIV. This

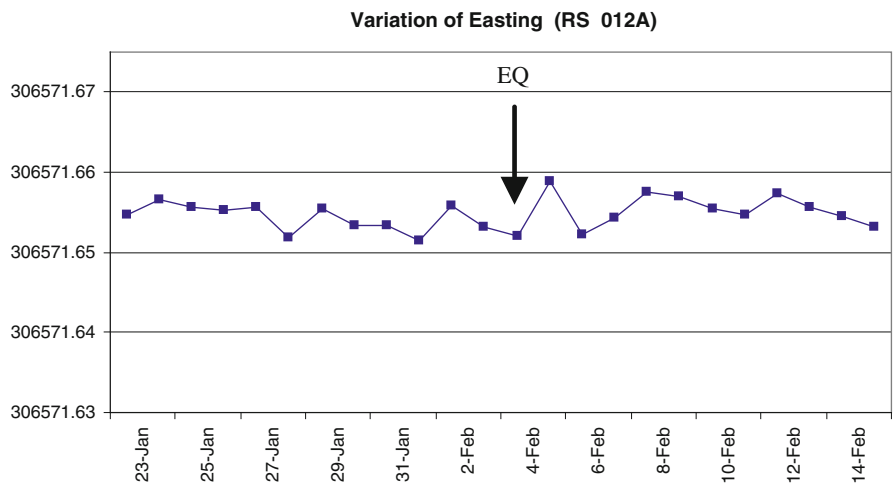


Fig. 87.9 EQ II: Variation of Easting for RS 012A

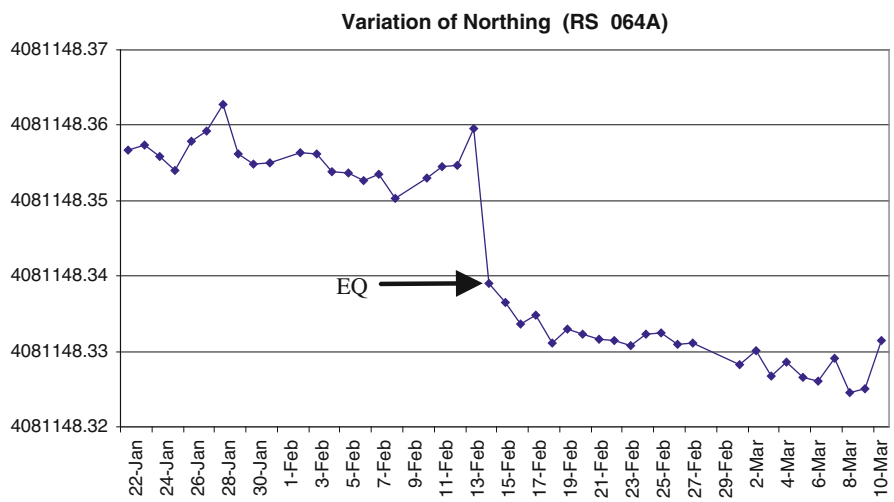


Fig. 87.10 EQ III: Variation of Northing for RS 064A

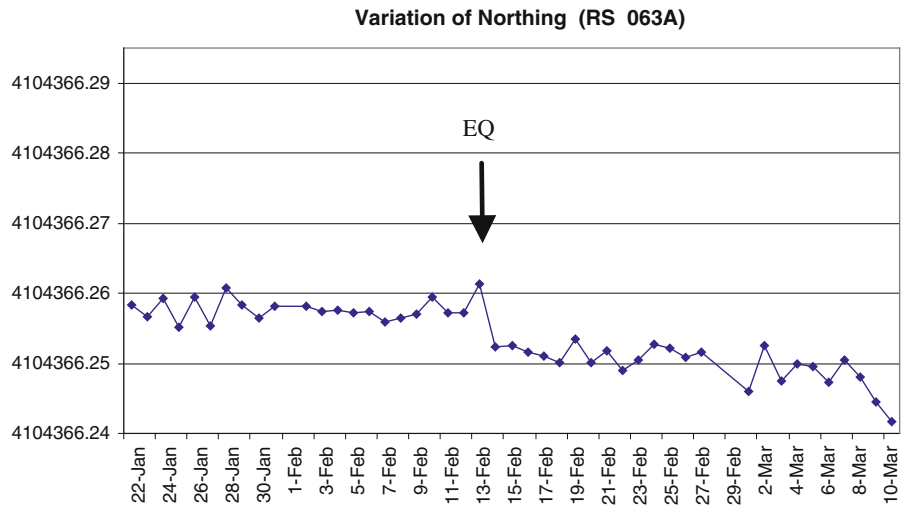


Fig. 87.11 EQ III: Variation of Northing for RS 063A

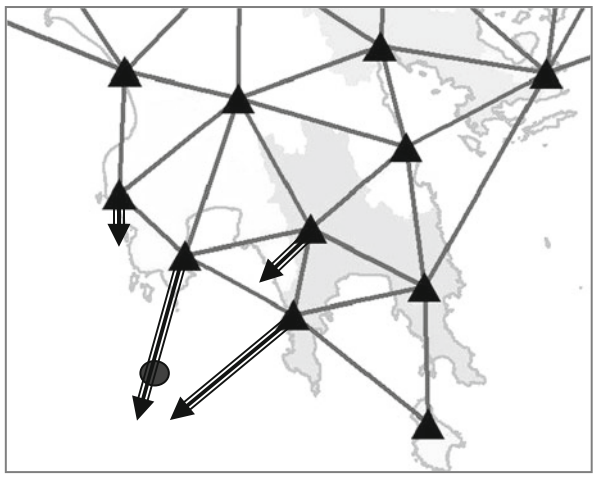


Fig. 87.12 EQ III: Approximate displacements of the reference stations (longest arrow corresponds to 2.1 cm)

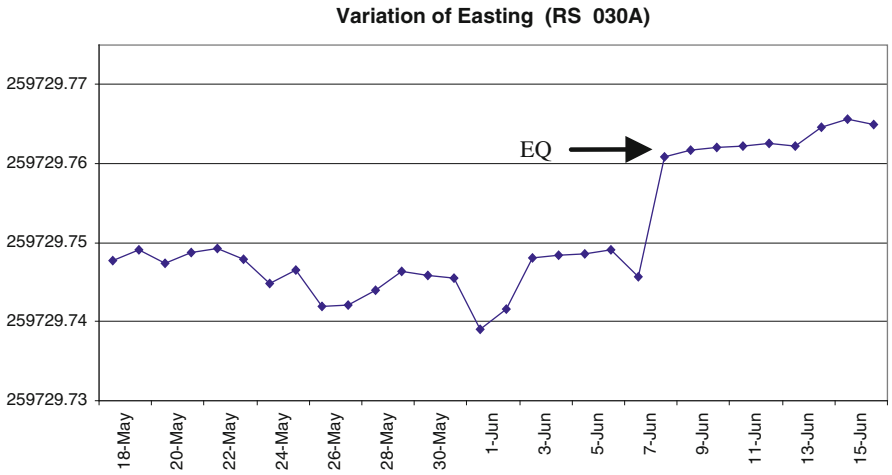


Fig. 87.13 EQ IV: Variation of Easting for RS 030A

was actually expected, mainly due to the high noise level in the estimation of height by means of standard GNSS techniques.

87.4 Conclusions – Further Research

The data analysis in the previous chapter showed that strong earthquakes can cause permanent displacements that can be estimated by means of the GPS data collected at the reference stations of HEPOS. The examination of the magnitudes and directions of these displacements in connection with the focal mechanism of each earthquake could be important for seismological research. The future analysis of the effects of a large number of different earthquakes can lead to useful conclusions.

Some analysis has been done using an epoch-wise solution. In some cases the exact time of the earthquake could be recognized by the change in the coordinates. However, the coordinates of any epoch-wise solution have much higher noise than a daily solution, something that has to be considered carefully when interpreting the results.

Acknowledgments Useful discussions with Professor George Katsiaris, Managing Director of KTIMATOLOGIO S.A., are warmly acknowledged. Miss Ifigenia Stavropoulou, KTIMATOLOGIO S.A. – Geodetic Department, assisted the numerous GPS data processing. The HEPOS project is part of the Operational Program "Information Society" and is co-funded by the EU.

References

Drewes, H. (1992). Comparison of Global SLR and VLBI Solutions for Plate Kinematic and Crustal Deformations Research, In: *Proceedings of the International Workshop on Global Positioning Systems n Geosciences.*, Chania, Greece, June 8–10, pp. 154–166.

Floyd, M.A., J.-M. Nocquet, DH. Billiris, D. Paradisis, P. England, and B. Parsons (2005). Preliminary results from the COMET CGPS network. *Geophys. Res. Abstr.*, 7, 07607.

Gianniou, M. (1996). Genauigkeitssteigerung bei kurzzeitstatischen und kinematischen Satellitenmessungen bis hin zur Echtzeitanwendung, *Deutsche Geodätische Kommission*, Reice C, Dissertationen, Heft Nr. 458, München.

Gianniou, M. (2008). HEPOS:.Designing and Implementing an RTK Network. Geoinformatics Magazine for Surveying, Mapping & GIS Professionals, Jan/Feb 2008 Vol. 11, pp. 10–13.

Kahle, H.-G., M.V. Müller, S. Müller, H. Drewes, Kaniuth, K. Stuber, H. Tremel, S. Zerbini, G. Corrado, G. Veis, H. Billiris, and D. Paradisis (1992). Crustal Deformation Monitoring in the Alpine System and the Central Mediterranean Sea using GPS. In: *Proceedings of the International Workshop on Global Positioning Systems n Geosciences.*, Chania, Greece, June 8–10, pp. 167–182.

Konstantinou, K., S. Kalogeras, N. Melis, M. Kourouzidis, and G. Stavrakakis (2006). The 8 January 2006 Earthquake (Mw 6.7) Offshore Kithira Island, Southern Greece: seismological, strong-motion, and macroseismic observations of an intermediate-depth event. *Seismol. Res. Lett.,* 77(5), 544–553, September/October.

Murray, M.H. and Segall, P. (2001) Modeling broadscale deformation in Northern California and Nevada from plate motions and elastic strain accumulation. *Geophys. Res. Lett.*, 28, 4315–4318.

Chapter 88

Assessment of Degree-2 Zonal Gravitational Changes from GRACE, Earth Rotation, Climate Models, and Satellite Laser Ranging

J.L. Chen and C.R. Wilson

Abstract Four independent time series of degree-2 zonal gravitational variations ΔC_{20} are compared for the period April 2002 to February 2008. We examine estimates from the Gravity Recovery and Climate Experiment (GRACE), Earth rotation variations, climate models (AOW), and satellite laser ranging (SLR). At the annual period, all ΔC_{20} estimates agree remarkably well, and good correlation is found among these time series at nonseasonal time scales as well. SLR and AOW ΔC_{20} time series show the best agreement in a broad band of frequencies with the maximum cross-correlation coefficient of 0.86 at nonseasonal time scales. GRACE monthly ΔC_{20} estimates are subject to significant aliasing effects due to errors in high-frequency tide models, especially the S_2 and K_2 tides. Correctly removing winds and ocean currents and other motion related excitations from length-of-day (LOD) observations plays a key role in estimating ΔC_{20} from LOD, especially at interannual or longer time scales.

88.1 Introduction

The Earth gravitational change is caused by mass redistribution within the Earth system, including the atmosphere, ocean, hydrosphere, and cryosphere. The degree-2 zonal spherical harmonics ΔC_{20} represent one of the longest wavelengths' gravitational variations, commonly referring to the "oblateness" of the Earth. Air and water contributions dominate at periods less than a few years (Chen et al., 2000), while mass redistribution within the solid Earth due to tectonics and postglacial rebound (PGR) is the primary contributor at decadal and longer time scales (Mitrovica and Peltier, 1993). Satellite laser ranging (SLR) has been an effective technique for measuring low degree gravitational changes, with time series extending over more than 2 decades. SLR is especially useful in measuring the lowest degree even zonal harmonics (especially ΔC_{20}, also called -J2 in the literature) (Yoder et al., 1983). SLR estimates of ΔC_{20} show variations over a broad frequency band, with seasonal variability most prominent (Chen et al., 2000). A linear trend ($\sim$0.116 $\times$ 10^{-10} per year) in ΔC_{20} is well determined from SLR (Yoder et al., 1983), and widely accepted as PGR effect following the last glacial maximum (Mitrovica and Peltier, 1993). Advancements in processing methods, and tracking of multiple satellites have improved SLR estimates, especially of individual low-degree zonal terms (Cheng and Tapley, 2004).

Advanced climate models of the atmosphere, ocean, and land hydrology provide independent estimates of Earth's gravity changes. Models give time variations in global gridded fields of atmospheric surface pressure, ocean bottom pressure, and terrestrial water storage, which can be used to estimate gravity change. Model estimates are generally consistent with geodetic observations, especially for even zonal harmonics, including ΔC_{20} (Chen et al., 2000).

Estimates of degree-2 gravitational changes may also be obtained from measured Earth Orientation Parameters (EOP), including polar motion (X, Y) and length-of-day (LOD). At periods less than a few years, EOP variations mainly arise from two sources: surface mass load variations (atmospheric surface pressure,

J.L. Chen (✉)
Center for Space Research, University of Texas, Austin, TX 78712, USA
e-mail: chen@csr.utexas.edu

S.P. Mertikas (ed.), *Gravity, Geoid and Earth Observation*, International Association of Geodesy Symposia 135,
DOI 10.1007/978-3-642-10634-7_88, © Springer-Verlag Berlin Heidelberg 2010

ocean bottom pressure, and terrestrial water storage); and mass motion (winds and ocean currents). Excitation of LOD due to surface mass load variations are proportional to changes in ΔC_{20} (Eubanks, 1993). Thus estimates of ΔC_{20} from measured LOD changes are possible, provided that wind and ocean current contributions can be estimated using numerical ocean and atmospheric models. Previous studies (e.g., Chen et al., 2000; Gross et al., 2004) indicate that this can be done, and that EOP estimates of ΔC_{20} agree well with geophysical model predictions and SLR estimates.

Launched March 2002, the Gravity Recovery and Climate Experiment (GRACE) satellite gravity mission measures Earth gravity with unprecedented accuracy. GRACE provides Earth gravity as sets of spherical harmonics coefficients at intervals of approximately 30 days. Time variations in GRACE gravity fields have been shown to measure mass redistribution within the Earth system associated with a variety of climate processes. In early GRACE solutions, such as release 1 (RL01) degree-2 spherical harmonics, especially the non-zonal harmonics ΔC_{21} and ΔS_{21}, are significantly affected by the lack of ocean pole tide (OPT) and appropriate solid earth pole tide (SEPT) corrections. if these pole tide corrections were appropriately applied, GRACE-observed degree-2 gravity changes agree reasonably well with other measurements (Chen et al., 2004).

A recent study (Chen and Wilson, 2008) compares GRACE-observed ΔC_{21}, ΔS_{21}, and ΔC_{20} variations from the new release 4 (RL04) solutions (with OPT and an updated SEPT corrections applied), with estimates from Earth rotation, climate models, and SLR, and show significantly improved agreement among these independent estimates. However, GRACE RL04 ΔC_{20} show some strong interannual variability (since 2006) that is not consistent with SLR and climate model estimates. Interestingly, LOD-derived ΔC_{20} appear to follow GRACE ΔC_{20} time series (for the interannual variability after 2006) for unquantified reasons (Chen and Wilson, 2008). GRACE RL04 ΔC_{20} time series show a significant 161-day aliasing signal from the S2 tides errors (Knudsen, 2003).

Here we extend the study of Chen and Wilson (2008) to examine a longer record of GRACE time series and SLR and LOD observations, and focus only on the degree-2 zonal spherical harmonics ΔC_{20}. The main purposes are to better understand the variability and tidal alias errors in GRACE ΔC_{20} time series, and to better understand what may affect LOD-derived ΔC_{20} estimates. Because of the particular spatial mode of ΔC_{20} harmonics, GRACE ΔC_{20} estimates could be particularly sensitive to expected large (atmospheric and oceanic) tidal errors in high latitudes, due to the lack of satellite altimetry and in situ meteorological data to constrain the tide models. With a longer GRACE time series, we can examine some tidal alias errors that have much longer aliasing periods, such as the 3.73 years from the K2 tide errors (Luthcke et al., 2006).

88.2 Data Processing

88.2.1 GRACE Solutions

GRACE RL04 solutions includes 67 approximately monthly average gravity fields, covering the period April 2002 to February 2008, provided by the Center for Space Research (CSR), University of Texas at Austin. RL04 is based upon a new background gravity model – a combination of GGM02C and EGM96 (Bettadpur, 2007); a new semi-diurnal and diurnal ocean tide model FES2004 (Lyard et al., 2006); and an updated SEPT model following IERS2003 (McCarthy and Petit, 2003). OPT effects are modeled using a self-consistent equilibrium model SCEQ from satellite altimeter data (Desai, 2002).

Non-tidal atmospheric and oceanic contributions are removed in the level-2 de-aliasing process, which employs data-assimilating numerical models of atmosphere and oceans. Each monthly field includes a separate file (GAC) with monthly average numerical model values of atmospheric and oceanic contributions (removed in de-aliasing). To compare GRACE with EOP, SLR, and climate models' estimates, GAC atmospheric and oceanic effects must be added to GRACE fields. A linear drift ($\sim 0.116 \times 10^{-10}$ per year) of ΔC_{20} (based on SLR measurements) is removed during GRACE data processing (Bettadpur, 2007).

RL04 fields (from August 2002 to December 2007) from the GeoForschungsZentrum (GFZ) (Flechtner, 2007) are also included for comparison, which are based on the same (or very similar) background geophysical models (as used in CSR RL04), but different processing techniques.

88.2.2 Δ C_{20} from LOD Observations

Fully normalized ΔC_{20} variations can be derived from LOD excitations after ocean current and wind effects are removed as (Chen et al., 2004),

$$\Delta C_{20} = -(1 + k_2') \cdot \frac{3}{2\sqrt{5}} \cdot \frac{C_m}{0.753 R^2 M} \cdot x_3^{mass} \quad (1)$$

Here M and R are mass and mean radius of the Earth, and Cm (7.1236×10^{37} kg m^2) he principal inertia moment of Earth's mantle (Eubanks, 1993). k'_2 is the degree-2 load Love number (–0.301), accounting for elastic deformational effects on gravitational change. x_3^{mass} can be computed from, $x_3^{mass} = x_3^{obs} - x_3^{motion}$ where, x_3^{obs} are excitations from observed LOD time series, and x_3^{motion} are wind and ocean current effects estimated from atmospheric and oceanic numerical models.

We follow the same procedures and use the same data sources as in Chen and Wilson (2008) to compute observed LOD excitations and wind and ocean current contributions, and extend the computations to cover a longer time period (up to December 2007). All time series (LOD, wind, and ocean current excitations) are interpolated into uniform daily intervals. Then daily ΔC_{20} variations from Eq. (1) were smoothed by a 30-day sliding window, and resampled in time to match the GRACE RL04 time series.

Observed LOD variations (thin curves in Fig. 88.1) show evident strong long-term variability with time scales of several years or longer, which is believed to be related to the Earth core-mantle coupling (Hide, 1989) and other long-term geophysical processes (such as tectonics and PGR). We first remove these long-term variability by a Butterworth low-pass filter with a specified cut-off period. The 3 thick curves in Fig. 88.1 show the low-pass results from a 3, 4, and 5 years' cut-off period, respectively.

Figure 88.2 show LOD (or EOP as labeled in this and other figures) derived ΔC_{20} variations in 3 cases, when long-term LOD variability is removed using a low-pass filter with 3, 4, and 5 years' cut-off period (shown in Fig. 88.1) and atmospheric wind and ocean current contributions are removed using climate model estimates (Chen and Wilson, 2008). In all 3 cases, LOD ΔC_{20} time series appear to show an evident interannual variability since 2006. This may be simply caused by the end-effect of the low-pass filtering or, to some extent, may reflect real gravity change (see more discussions later).

88.2.3 Δ C_{20} from Climate Models

ΔC_{20} variations can be computed from model-estimated mass load changes of the atmosphere, ocean, and land water storage (AOW). We combine atmospheric and oceanic contributions from GRACE GAC files (representing ocean and atmosphere mass effects) (Bettadpur, 2007) with hydrological estimates from the global land data assimilation system (GLDAS)

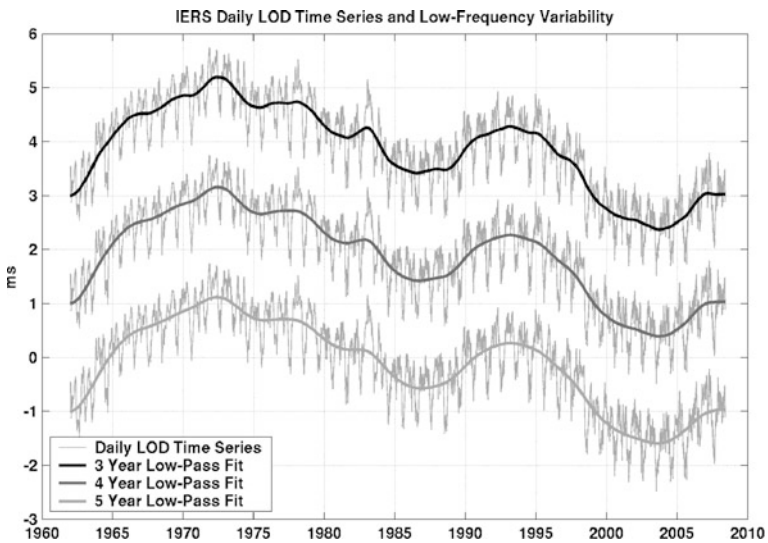


Fig. 88.1 Observed daily LOD time series (*thin curves*) from IERS C04 05, superimposed by low frequency variability from a low-pass filter with 3, 4, and 5 years cut-off periods. The 3 pairs are offset purposely for clarity

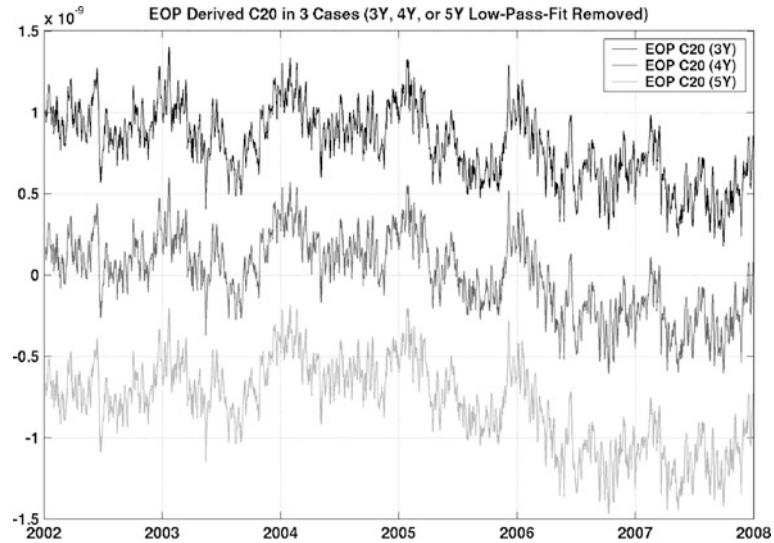


Fig. 88.2 LOD (or EOP as labeled in plot) derived ΔC_{20} time series in 3 cases, when long-term variability in LOD is removed using a Butterworth low-pass filter with a 3, 4, and 5 years cut-off period, respectively

(Rodell et al., 2004). For details of computations of AOW ΔC_{20} variations see Chen and Wilson (2008).

88.2.4 SLR ΔC_{20} Estimates

SLR estimates of monthly ΔC_{20} variations from April 2002 to February 2008 are derived from laser tracking of multiple satellites, including Starlette, Ajisai, Stella, and LAGEOS 1 and 2 (Cheng and Ries, 2008). These satellites are spherical, allowing surface forces to be modeled with great precision (Cheng and Tapley, 2004). Models and other constants employed in SLR analysis follow GRACE RL04 standards (Cheng and Ries, 2008). SLR estimates were provided by the GRACE project in which they are used to validate GRACE estimates. SLR ΔC_{20} estimates are consistent with GRACE RL04 standards (i.e., based on same background geophysical models).

88.3 Comparisons of ΔC_{20} Estimates

Figure 88.3 shows monthly time series of ΔC_{20} from GRACE (labeled in the figure as CSR RL04), LOD, climate models (labeled AOW), and SLR. All time series have had mean values removed. All four estimates of ΔC_{20} agree well with each other, especially at seasonal time scales, though EOP shows more interannual variability. This may be residual variations remaining after low-cut filtering of the LOD series. SLR and AOW estimates agree remarkably well during the entire 6 years period.

Amplitudes and phases of annual and semiannual variations are estimated from each series using unweighted least squares, with results in Table 88.1. Annual variations of 4 independent ΔC_{20} time series from GRC, EOP, AOW, and SLR agree very well in both amplitude and phase. GFZ RL04 ΔC_{20} estimates are also included for comparison. It should be noticed that EOP result is not completely independent from SLR estimates, as it incorporates SLR data in the combination.

GRACE ΔC_{20} series appears to show increased interannual variability since 2006, and the last few solutions (in early 2008) start returning to the mean territory. Interestingly, LOD-derived ΔC_{20} series seems to follow GRACE results nicely in the last 2 years. However, both SLR and AOW estimates do not show such an evident variability. To better understand GRACE ΔC_{20} estimates, we compare CSR RL04 and GFZ RL04 ΔC_{20} time series in Fig. 88.5a. GFZ ΔC_{20} series show significantly smaller interannual variability than CSR ΔC_{20} series. Figure 88.5b shows the power spectrum density (PSD) of CSR RL04 and GFZ RL04 ΔC_{20} time series. The periods of S_2 and K_2 tidal

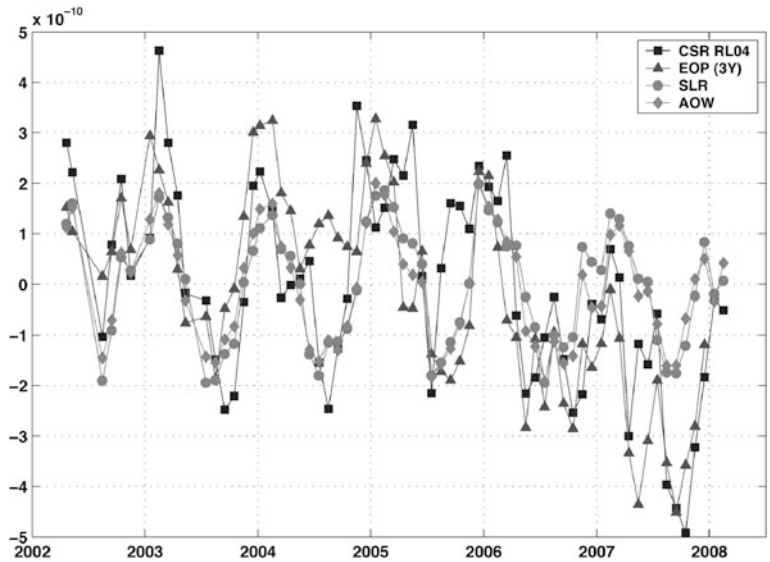


Fig. 88.3 Comparison of monthly ΔC_{20} time series from GRACE (CSR RL04), LOD (EOP), SLR, and climate models (AOW) during the period April 2002 to February 2008

Table 88.1 Amplitude and phase of annual and semiannual ΔC_{20} variations estimated from GRACE (GRC) CSR and GFZ RL04 solutions, Earth rotation (EOP), geophysical modes (AOW), and SLR. The phase is defined as ϕ in $\sin(2\pi(t - t_0) + \phi)$, where t_0 refers to h^0 on January 1

Gravity change	Annual		Semiannual	
	Amplitude ($\times 10^{-10}$)	Phase (degree)	Amplitude ($\times 10^{-10}$)	Phase (degree)
ΔC_{20} (GRC-CSR)	1.48	44	0.12	138
ΔC_{20} (GRC-GFZ)	1.68	61	0.74	114
ΔC_{20} (EOP)	1.41	66	0.80	57
ΔC_{20} (AOW)	1.37	50	0.10	163
ΔC_{20} (SLR)	1.44	45	0.24	180

alias errors (with periods of 161-day and 3.73-year) are marked by dashed lines (Fig. 88.5b).

The 161-day and 3.73-year S_2 and K_2 tidal alias errors are evident in GRACE ΔC_{20} time series, and the CSR RL04 estimates are subject to significantly larger S_2 and K_2 tidal alias errors. The large interannual variability in CSR RL04 ΔC_{20} time series partly reflects the 3.73-year K_2 alias errors. When the S_2 and K_2 tidal alias errors are removed from CSR RL04 ΔC_{20} series, using unweighted least squares fit (annual and semiannual sinusoids and a linear trend are also fitted at the same time, but not removed), the "suspicious" interannual variability in CSR RL04 ΔC_{20} series is significantly reduced (see Fig. 88.4), although some other long-term variability still exists. Please note that a linear trend ($\sim 0.116 \times 10^{-10}$ per year) in ΔC_{20} determined from SLR has been removed from both GRACE RL04 (Bettadpur, 2007) and SLR ΔC_{20} series (Cheng and Ries, 2008).

88.4 Conclusions

We examine four separate estimates of ΔC_{20} variations from GRACE, Earth rotation (EOP), climate modes (AOW) and SLR, for the period April 2002 to February 2008. At seasonal time scales, these four ΔC_{20} time series agree remarkably well in both amplitude and phase, and good correlation is found among these time series at nonseasonal time scales as well. SLR and AOW ΔC_{20} time series show the best agreement in a broad band of frequencies with the maximum cross-correlation coefficient of 0.86 at nonseasonal time scales (well over the 99% significance level at $\sim$0.31). The large semiannual variability in LOD-derived ΔC_{20} time series is likely introduced by errors in the upper atmospheric winds (Chen, 2005) or ocean current fields.

The large interannual variability (becoming more evident since 2006) in GRACE (CSR) ΔC_{20} time series is largely attributed to K_2 tide alias errors (with a period of 3.73-year). The 161-day S_2 tide alias

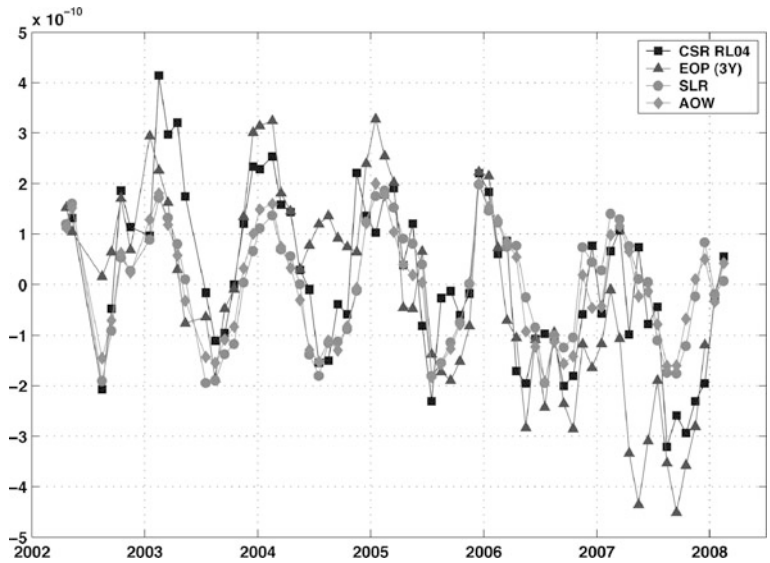


Fig. 88.4 Same as in Fig. 88.3, but the S_2 and K_2 alias errors (with periods of 161-day and 3.73-year) in CSR RL04 ΔC_{20} time series have been removed using unweighted least squares fits (annual and semiannual sinusoids and a linear trend are fitted at the same time)

errors are also evident in GRACE ΔC_{20} estimates. For unquantified reasons, CSR RL04 C_{20} estimates appear more sensitive to tidal alias errors. Although appearing less affected by the S_2 and K_2 alias errors (see Fig. 88.5b), GFZ RL04 ΔC_{20} estimates show significantly larger annual and semiannual variability than CSR RL04 and three other separate estimates (i.e., LOD, AOW, and SLR) (see Table 88.1).

88.5 Discussion

Accurately determined low-degree gravity changes are important in monitoring large-scale mass variations in the atmosphere, ocean, hydrosphere, and cryosphere at a variety of time scales. Independent estimates of low-degree gravity changes (e.g., ΔC_{20}) from Earth rotation, climate models, and SLR are useful to validate GRACE measurements. Inter-comparison of ΔC_{20} estimates from different techniques are useful in identifying and quantifying errors associated with each technique. As examples, this study confirms that GRACE ΔC_{20} estimates are subject to significant tidal alias errors, especially from S_2 and K_2 tide errors. After the S_2 and K_2 tide errors are removed, CSR RL04 ΔC_{20} time series become more consistent with other estimates. The remaining long-term variability in CSR RL04 ΔC_{20} series (after the S_2 and K_2 tide errors are removed) is likely from other artifacts, e.g., other longer period alias errors (such as the 7.46-year alias errors from K_1 tides) (Knudsen, 2003). Aside from showing large S_2 and K_2 tide alias errors, CSR RL04 ΔC_{20} estimates show better agreement with SLR, AOW, and LOD estimates at seasonal time scales than GFZ RL04 series.

Estimates of variations in low-degree gravity changes from EOP are sensitive to errors in numerical model wind and ocean current fields. This is especially true for ΔC_{20} because winds cause over 90% of LOD variations at time scales of a few years and less. Winds from pressure levels above 10 millibars are not included in the NCEP reanalysis model used in the computation (Chen and Wilson, 2008). Zonal winds at this level and above may be significant contributors to LOD (Chen, 2005), suggesting that their inclusion may improve EOP ΔC_{20} estimates. How to appropriately remove the long-term variability in LOD time series also plays a critical role in estimating ΔC_{20} from LOD. Although all three LOD-derived ΔC_{20} time series appear to show similar interannual variability as CSR RL04 solutions (since 2006), which may be due to end-effect of the low-pass filtering. A longer LOD time series can help to improve LOD-derived ΔC_{20} estimates, especially at interannual time scales.

GRACE ΔC_{20} estimates could be particularly sensitive to tidal alias errors, as large tidal errors are expected in high latitudes due to the lack of satellite altimetry data or meteorological data to constrain

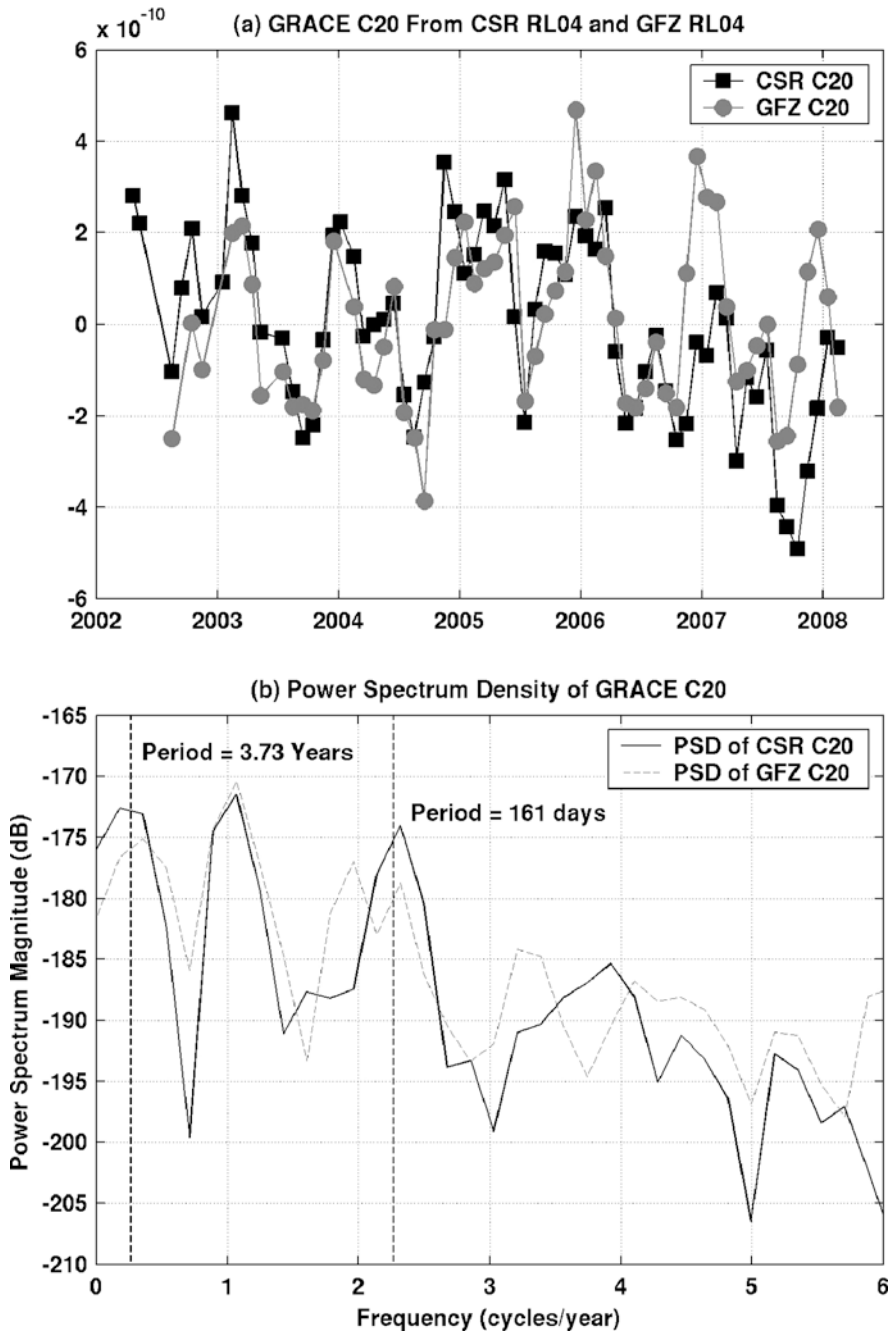


Fig. 88.5 (**a**) ΔC_{20} time series from CSR RL04 and GFZ RL04. (**b**) Power spectrum density of CSR RL04 and GFZ RL04 ΔC_{20} time series

ocean and atmospheric tides (in high latitudes). This will translate into large impact on GRACE ΔC_{20} estimates due to the special spatial mode of ΔC_{20} harmonics. However, it's interesting to notice that the GFZ RL04 solutions, based on same (or very similar) background geophysical models, show significantly smaller alias errors (as compared to CSR RL04 solutions). Therefore, alias errors in GRACE solutions are apparently related to both tide models' errors and data processing techniques (used in deriving GRACE solutions). Schrama et al. (2007) suggest that the present-day errors in the GRACE (CSR RL04)) data are significantly larger than those forecasted by tide models differences. Further studies are needed in

order to understand the sensitivity of alias errors of GRACE ΔC_{20} and other harmonics to (atmosphere and ocean) tide modes errors.

Acknowledgments The authors would like to thank the two anonymous reviewers for their insightful comments. This research was supported by a NASA PECASE Award (NNG04G060G) and NSF IPY Program (ANT-0632195).

References

Bettadpur, S. (2007). CSR Level-2 Processing Standards Document for Product Release 04, GRACE 327-742, Revision 3.1, The GRACE Project, Center for Space Research, University of Texas at Austin.

Chen, J.L. (2005). Global mass balance and the length-of-day variation. *J. Geophys. Res.*, 110, B08404, 10.1029/2004JB003474.

Chen, J.L., C.R. Wilson, R.J. Eanes, and B.D. Tapley (2000). A new assessment of long wavelength gravitational variations. *J. Geophys. Res*., 105(B7), 16271–16278.

Chen, J.L., C.R. Wilson, B.D. Tapley, and J. Ries (2004). Low degree gravitational changes from GRACE: validation and interpretation. *Geophys. Res. Lett.*, 31(22), L22607, 10.1029/2004GL021670.

Chen, J.L. and C.R. Wilson (2008). Low degree gravitational changes from GRACE, Earth rotation, geophysical models, and satellite laser ranging. *J. Geophys. Res.*, 113, B06402, 10.1029/2007JB005397.

Cheng, M. and B.D. Tapley (2004). Variations in the Earth′s oblateness during the past 28 years. *J. Geophys. Res. (Solid Earth)*, 109(B18), B09402, doi:10.1029/2004JB003028.

Cheng, M.K. and J. Ries (2008). Monthly estimates of C20 from 5 SLR satellites, GRACE Technical Note #05, The GRACE Project, Center for Space Research, University of Texas at Austin.

Desai, S. (2002), Observing the pole tide with satellite altimetry. *J. Geophys. Res.*, 107, C11, 3186, doi:10.1029/2001JC001224.

Eubanks, T.M. (1993). Variations in the orientation of the earth, in Contributions of pace Geodesy to Geodynamic: Earth Dynamics, Geodyn. Ser., vol. 24, edited by D. Smith and D. Turcotte, pp. 1–54, AGU, Washington,D.C.

Flechtner, F. (2007). GFZ level-2 processing standards document for level-2 product release 0004, p. 17, GeoForschungsZentrum Potsdam, Potsdam, Germany.

Gross, R.S., G. Blewitt, P.J. Clarke, and D. Lavallée (2004). Degree-2 harmonics of the Earth's mass load estimated from GPS and Earth rotation data. *Geophys. Res. Lett.*, 31, L07601, doi:10.1029/2004GL019589.

Hide, R. (1989). Fluctuations in the Earth's rotation and the topography of the core-mantle interface. *Phil. Trans. R. Soc. Lond. Ser. A,* 328, 351–363.

Knudsen, P. (2003). Ocean tides in GRACE monthly averaged gravity fields. *Space Sci. Rev.,* 108, 261–270.

Luthcke, S.B., H.J. Zwally, W. Abdalati, D.D. Rowlands, R.D. Ray, R.S. Nerem, F.G. Lemoine, J.J. McCarthy, and D.S. Chinn (2006), Recent greenland ice mass loss by drainage system from satellite gravity observations. *Science*, 314, 1286–1289, doi:10.1126/science.1130776.

Lyard, F., F. Lefevre, T. Letellier, and O. Francis (2006). Modelling the global ocean tides: Insights from FES2004. *Ocean Dyn.*, 56, 394–415.

McCarthy, D.D. and G. Petit (eds.) (2003). IERS Conventions, IERS Tech. Note 32, Int. Earth Rotation and Ref. Syst. Serv., Paris.

Mitrovica, J.X. and W.R. Peltier (1993). Present-day secular variations in the zonal harmonics of Earth's geopotential. *J. Geophys. Res*., 98, 44509–44526.

Rodell, M., P.R. Houser, U. Jambor, J. Gottschalck, K. Mitchell, C.-J. Meng, K. Arsenault, B. Cosgrove, J. Radakovich, M. Bosilovich, J.K. Entin, J.P. Walker, D. Lohmann, and D. Toll (2004). The global land data assimilation system. *Bull. Amer. Meteor. Soc.*, 85(3), 381–394.

Schrama, E.J.O., B. Wouters, and D.A. Lavallée (2007). Signal and Noise in Gravity Recovery and Climate Experiment (GRACE) observed surface mass variations, Vol. 112, B08407, doi:10.1029/2006JB004882.

Yoder, C.F., J.G. Williams, J.O. Dickey, B.E. Schutz, R.J. Eanes, and B.D. Tapley (1983). Secular variation of Earth's gravitational harmonic J coefficient from Lageos and non-tidal acceleration of Earth rotation. Nature, 303, 757–762.

Part IX
Geodetic Monitoring of Natural Hazards and a Changing Environment

A. Braun and R. Forsberg

Chapter 89

PALSAR InSAR Observation and Modeling of Crustal Deformation Due to the 2007 Chuetsu-Oki Earthquake in Niigata, Japan

M. Furuya, Y. Takada, and Y. Aoki

Abstract On June 16 2007 (AM 10:13 in Japan Standard Time), an earthquake of magnitude 6.8 took place about 10 km offshore of Chuetsu area in Niigata, Japan.

Using L-band PALSAR InSAR (Interferometric Synthetic Aperture Radar) data, we could detect not only coseismic broad deformation but also significant aseismic deformation nearly 15 km away from the epicenter along an anticline axis. They mostly turned out to terminate within 3 days after the earthquake. The aseismic slip was modeled by a combination of west-dipping fault and east-dipping fault, which appear to be detachment faults on the western and eastern flank of the anticline. The moment magnitude released by the aseismic slip is estimated to be M_w 5.98. This observation demonstrates that a fault-related fold grows aseismically, and therefore seismic hazard is actually low for this particular fold. Although there is a dense GPS network in Japan, we should note that the aseismic signal was only detectable by InSAR data.

89.1 Introduction

PALSAR is an L-band SAR sensor onboard ALOS (Advanced Land Observation Satellite), which was launched in January 2006 by Japan Aerospace Exploration Agency (JAXA). In contrast to other satellite SAR sensors, PALSAR uses a longer wavelength microwave, which is known to achieve good coherence even in densely vegetated areas (Rosen et al., 1996). Meanwhile, there are more than 1,200 GPS stations in Japan now. They were established with a goal of predicting earthquake and volcanic eruptions, and have been generating many interesting science results. Some people were in doubt about whether InSAR would be useful in understanding physics of earthquakes and volcanoes. In this paper, we show crustal deformation signals that could not be detected if PALSAR was unavailable. It was associated with an earthquake last year in Niigata, Japan. We call it Chuetsu-Oki earthquake; "Oki" stands for offshore in Japanese.

The Niigata basin is located at a diffuse plate boundary between Eurasian (EU) plate and North American (NA) plate (Fig. 89.1). Although there are no clear plate boundaries, GPS data indicate that a broad area from Niigata to Kobe is undergoing significant strain concentrations (Sagiya et al., 2000). Over the past 50 years, there have been a couple of large inland earthquakes (Fig. 89.1), and the 2007 Chuetsu-Oki earthquake is one of such events. Geologically, this area is known for active folding and thick sedimentary layer (Ikeda, 2002; Sato and Kato, 2005; Okamura et al., 2007). Our PALSAR InSAR data turned out to have important implications for active folding processes.

89.2 Data and Processing

We used four ascending and three descending PALSAR images, which cover the earthquake on July 16. The beam mode is fine beam single polarization (FBS), and the off-nadir angle is 34.3°.

We have processed from level-1.0 PALSAR data, using Gamma software (Wegmüller and Werner,

M. Furuya (✉)
Department of Natural History Sciences, Hokkaido University, Sapporo 060-0810, Japan
e-mail: furuya@mail.sci.hokudai.ac.jp

S.P. Mertikas (ed.), *Gravity, Geoid and Earth Observation*, International Association of Geodesy Symposia 135,
DOI 10.1007/978-3-642-10634-7_89, © Springer-Verlag Berlin Heidelberg 2010

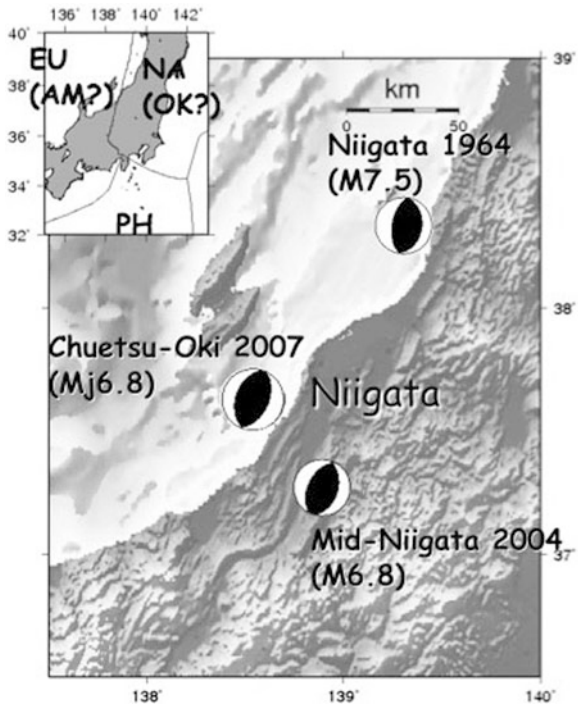


Fig. 89.1 Niigata area and three recent largest earthquakes. Inset shows the studies area and major tectonic plates around Japan: Eurasian (EU), North American (NA) and Philippine Sea (PH). EU and NA are possibly Amur (AM) and Okhotsk (OK) plate, respectively, and their boundaries denoted as *dashed line* are not clear. Kobe city is ∼500 km SW of Niigata

1997). To eliminate topographic fringes, we tried both 50-m resolution digital elevation model
(DEM) by Geographical Survey Institute, Japan, and 15-m resolution DEM generated from Advanced Spaceborne Thermal Emission and Reflection Radiometer (ASTER). For image registration prior to generating interferograms, we applied a so-called elevation dependent co-registration technique. While the phase-unwrapped results shown below are derived by minimum-cost-flow technique (Constantini, 1998), we confirmed that same results were obtained by branch-cut technique as well.

89.3 Observation Results

Figure 89.2 shows results from descending track. The left two columns are covering the earthquake, and the right column is the result of post-seismic pair. We see that there was no significant post-seismic deformation. The difference of two rows is which digital elevation model was used to take out topographic fringes. Because ASTER DEM has finer spatial resolution, it could reveal more detailed signals. We should also note that the earliest post-earthquake image was acquired on July 19, which is 3 days after the event.

Figure 89.3a shows a stack of descending interferograms; black dots indicate aftershocks.

These broad signals near the coast are obviously due to the earthquake. Besides, we should note that there is a clear phase offset extending about 30 km.

Interestingly, the location of the phase offset closely matches a ridge called Nishiyama hill (Fig. 89.3b), which is thought to be an anticline axis. Also, despite the significant deformation, there are very few aftershocks. In other words, we have found that active folding occurs aseismically.

Figure 89.4 show ascending interferograms. Now, the deformation signal near the anticline axis became much clearer. Unlike GPS, InSAR measures range changes in radar line of sight, and there is one caution in the interpretation of these InSAR data. For ascending track in this particular case, the GPS horizontal displacements are nearly perpendicular to the radar line of sight, and thus the ascending data is insensitive to horizontal motion. Thus, the range change amplitude is about a half of that in descending data. Figure 89.5 is a stack of ascending interferograms. We can again observe broad signals along the coast and clear localized signals near the fold axis. Again, it should be noted that there are virtually no aftershocks near the anticline axis. These localized signals thus represent aseismic deformation. Also, the small blob to the east is actually not an artifact by atmosphere in view of another adjacent ascending track to the east (Fig. 89.6). The signal pattern and the sense of deformation are consistent with the previous ascending images.

89.4 Modeling Results and Discussion

How do we interpret the observation? Our idea is that a main shock under the sea generates broad deformation signals near the epicenter, and that aseismic faults around the anticline axis caused localized signals. We infer these fault location, geometry and slip distribution, using the dislocation Green function by Okada (1992). Following a similar approach by Jónsson et al. (2002), we first fix the location and

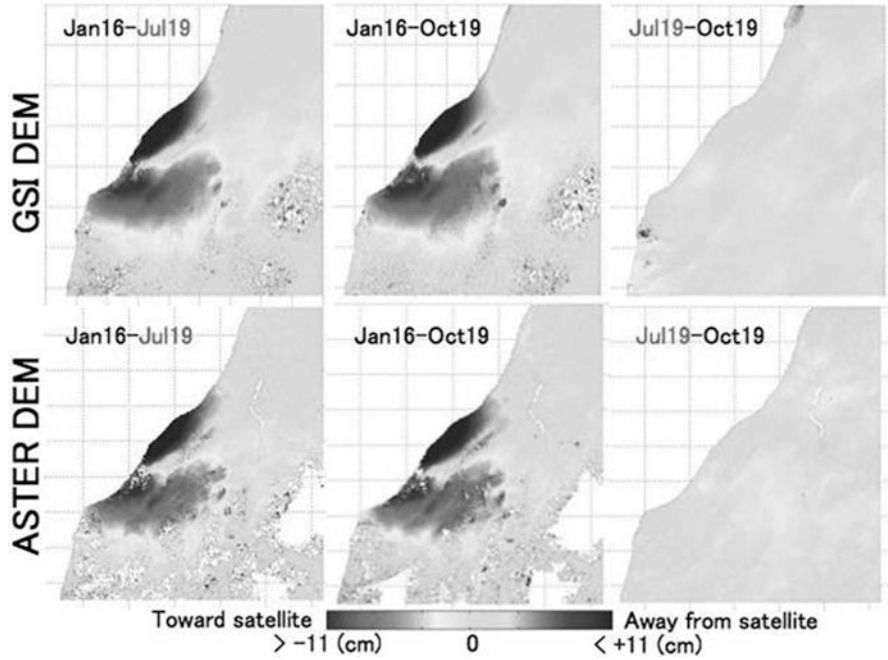


Fig. 89.2 PALSAR InSAR observation results for descending track, Path 60 and Frame 2860–2870. GSI DEM and ASTER DEM were used to eliminate topographic effects in the *top row* and *bottom row*, respectively. Of the two lobes, the northern (southern) lobe decreases (increases) 10 cm or more. No significant displacements greater than ~5 cm were detected after July 19, 2007, 3 days after the earthquake

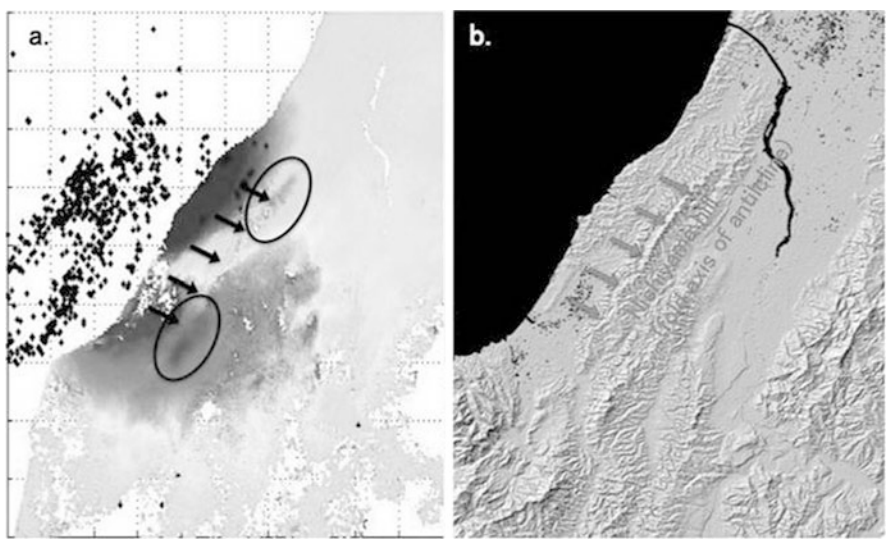


Fig. 89.3 (**a**) Stacked result of two descending images. Color scale is the same as in Fig. 89.2. *Dots* in the sea represent aftershocks. Phase jumps indicated by *arrows* and *circles* are associated with folding. (**b**) Shaded relief map. *Arrows* are located at the same points as in (**a**), and indicate Nishiyama hill, a fold axis of anticline

geometry of the faults, and then solve a linear least squares problem on the slip distribution with a smoothness constraint. Regarding the main shock fault, we assume a simple southeast dipping fault for the main shock, whose location and geometry are well constrained by aftershock data. For the aseismic fault, we must carefully set source faults. In Figs. 89.7 and 89.8, we show the actual contribution of aseismic deformation for both descending and ascending data. In order to understand what signals are expected

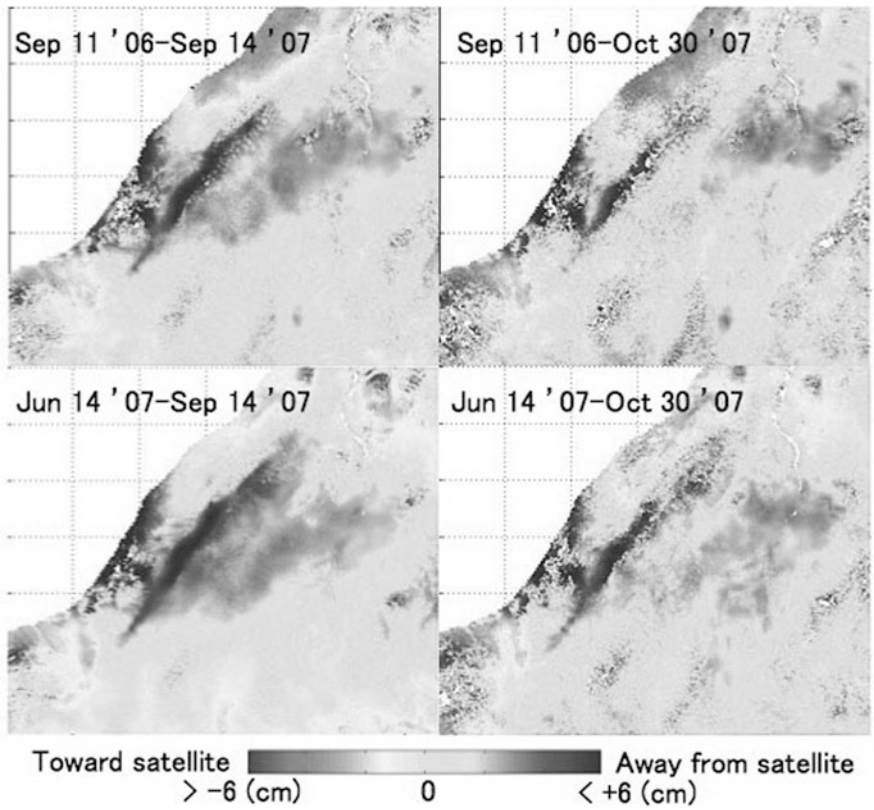


Fig. 89.4 PALSAR InSAR observation results for ascending track. Path 407 and Frame 730–740

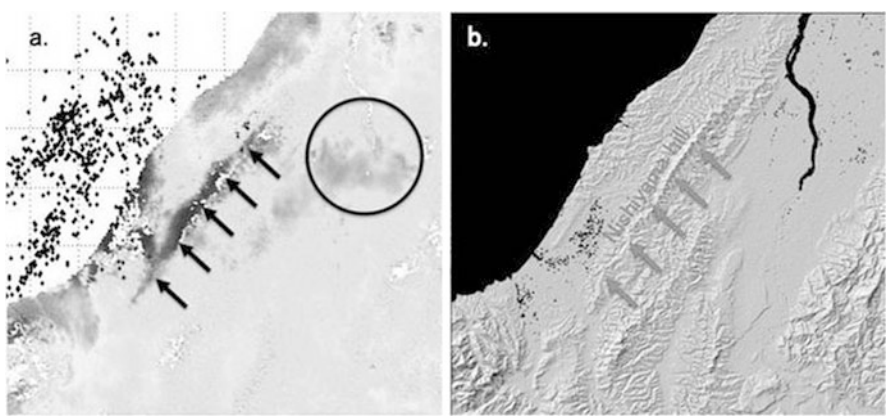


Fig. 89.5 (**a**) Stacked result of two ascending images. Color scale is the same as in Fig. 89.4. The *circled area* also underwent deformation in view of the adjacent track data in Fig. 89.6 below. (**b**) Shaded relief map. *Arrows* indicate Nishiyama hill

depending on dip angles and to reproduce these aseismic signals, we carried out a simple forward modeling, and repeated numerous trials and errors. It turns out that the actual aseismic deformation is so complicated that we could not explain the observation by a single fault. We thus propose a combination of both west dipping and east dipping faults in our modeling.

Figure 89.7 is a modeling result for descending data. In the upper left, we show a map view of fault sources and aftershocks. The main-shock fault is offshore, and the two inland faults are our preferred aseismic faults. One is northwest dipping and the other is southeast dipping. In the calculated interferogram, we see that not only the broad signal but also localized signals

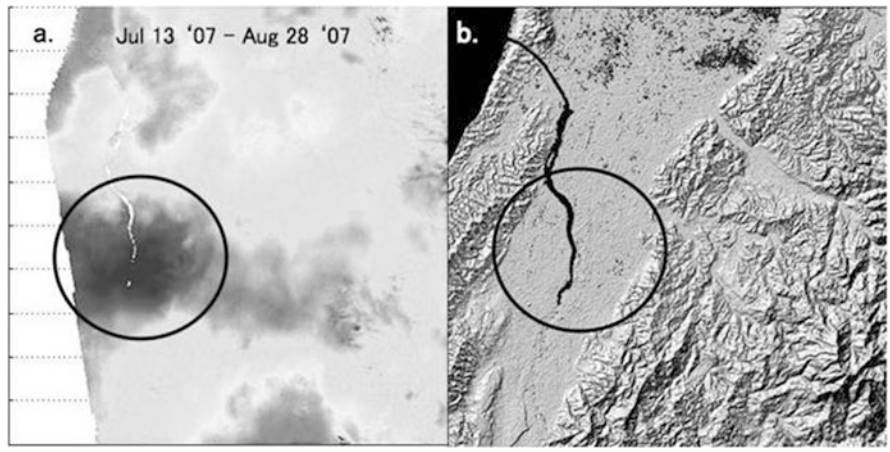


Fig. 89.6 (**a**) Another ascending image to the east. Color scale is the same as in Fig. 89.4. The *circled area* is the same as that in Fig. 89.5(**a**) above. (**b**) Shaded relief map of the area

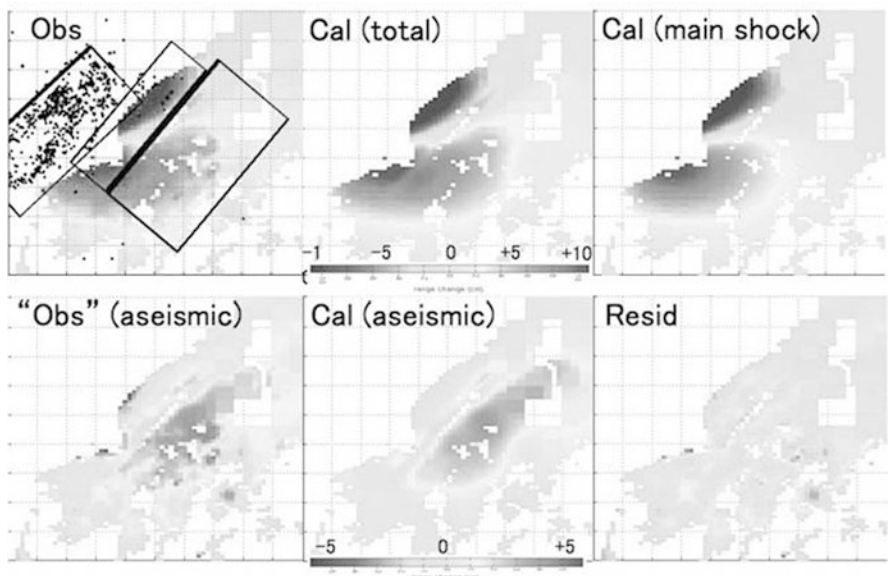


Fig. 89.7 Comparison of observed and modeled descending interfergram. The Obs in the *upper left* represents observation data, and location of three fault models and aftershocks are also shown. The three Cal is computed range changes, and contributions from all three faults are shown in Cal (total). Cal (main shock) and Cal (aseismic) are contributions from the main shock and aseismic faults, respectively. Residuals are differences between Obs and Cal(total), and are mostly less than 2 cm. See Fig. 89.9 for fault geometry

near the fold axis are well reproduced. Contributions by the main shock and aseismic faults are also shown in Fig. 89.7. Unless we introduce these two aseismic faults, we cannot reproduce this observation. The residuals are mostly less than 2 cm, and the agreement is quite good.

Figure 89.8 is a modeling result for ascending data. The observed and calculated data look similar to each other. In case of ascending data, both main shock and aseismic faults are generating similar order of signal amplitude but reverse in their sign. The residuals between observation and calculation are again mostly less than 2 cm.

Figure 89.9 shows location and geometry of our fault model. The bottom depth of the main shock fault is 13 km, and the top depth is 0.8 km where there are

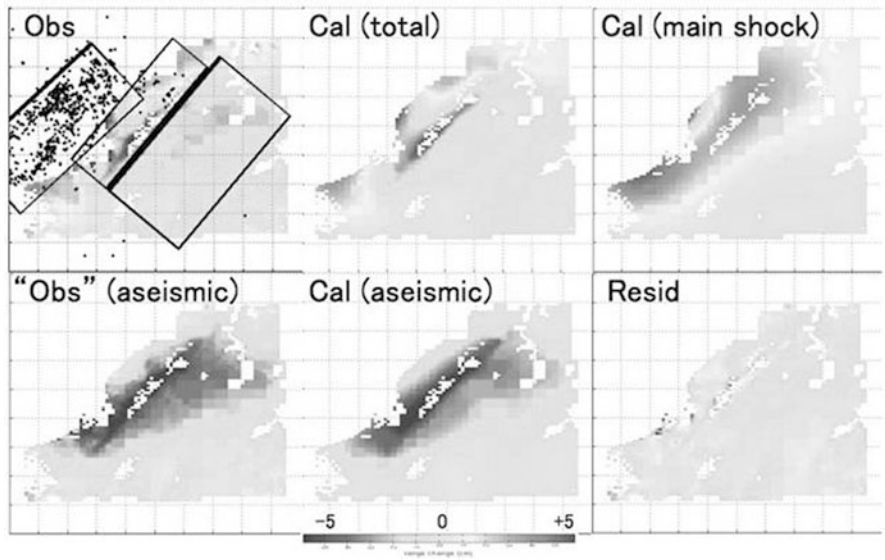


Fig. 89.8 Comparison of observed and modeled ascending interfergram. Obs and Cal are similarly defined as those in Fig. 89.7. Residuals are differences between Obs and Cal (total), and are mostly less than 2 cm

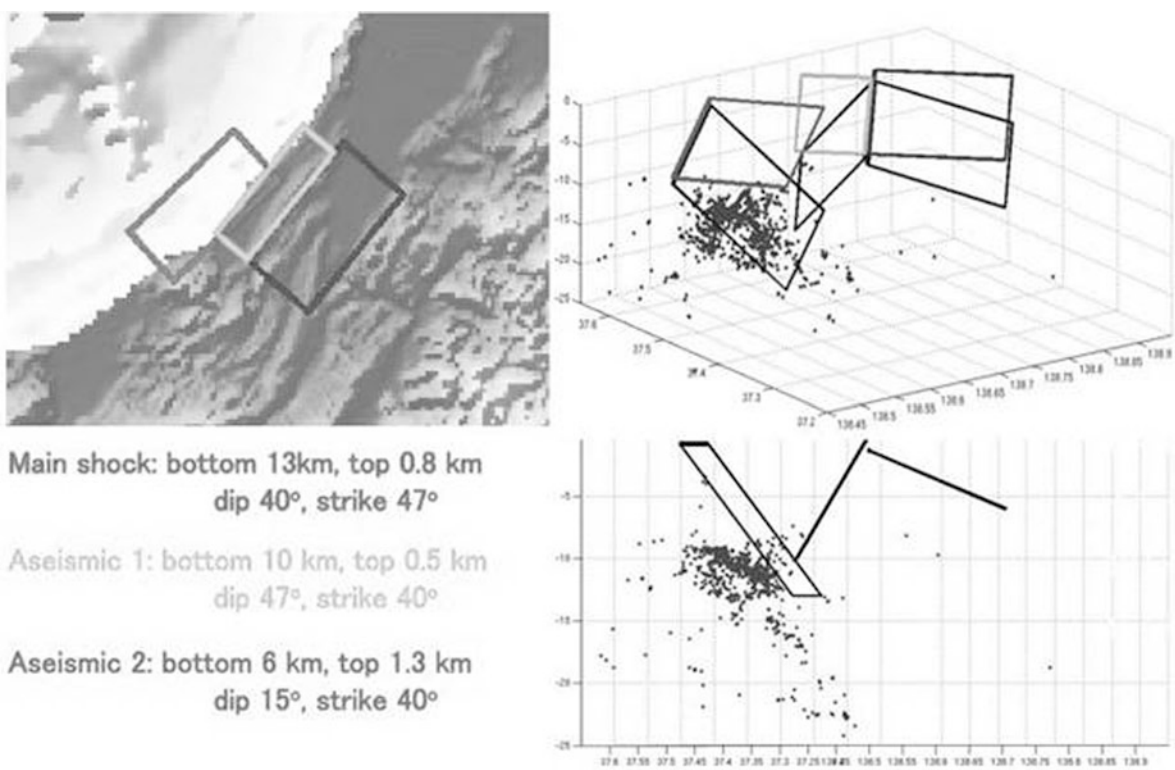


Fig. 89.9 Location and geometry of main shock fault (east-dipping) and two aseismic faults to the east

few aftershocks. The two aseismic faults are shallower, and have lower dip angle.

Figure 89.10 shows slip distributions for the main shock (Fig. 89.10a) and aseismic slip (Fig. 89.10b). The inferred moment magnitude for the main shock is M_w 6.62 with rigidity of 30 GPa. This value itself is quite consistent with a number of seismological estimates (Aoi et al., 2007; Hikima and Koketsu, 2007; Yamanaka, 2007; Yagi, 2007). Figure 89.10b shows slip distribution for aseismic faults, and the estimated moment magnitude is M_w 5.96 and 5.98 for northwest and southeast dipping aseismic fault. According to the geometry, they appear to be detachment faults, connecting to the anticline axis. In view of the inferred slip distribution, there are some dip slip components in the deeper part. However, at the shallowest part, strike slip components are dominating, and the slip direction is similar in both northwest and southeast dipping fault. Our estimate of aseismic slip demonstrates that folds are caused not only by pure dip slip but also by strike slip motion.

Recently, using almost the same PALSAR InSAR data, Nishimura et al. (2008) estimated that the moment release due to the aseismic slip was M_w 4.2,

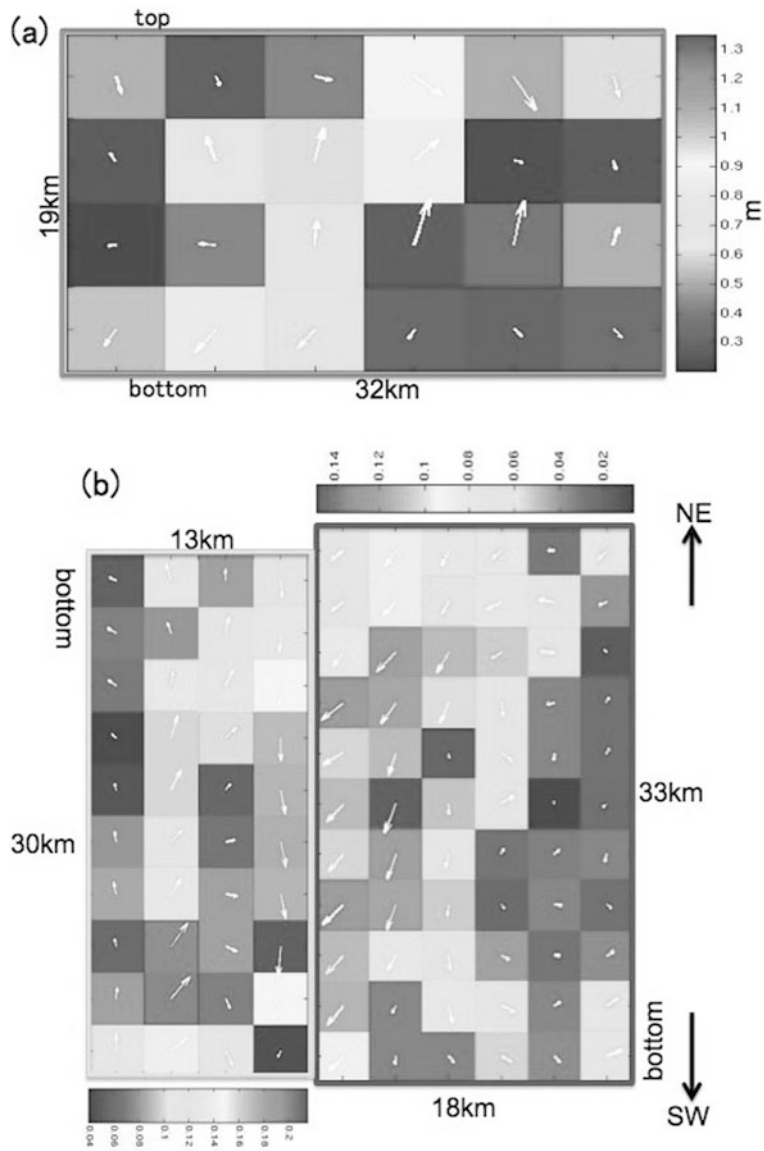


Fig. 89.10 Slip distribution on fault sources. (**a**) Main shock fault, (**b**) Two aseismic faults. See Fig. 89.9 for their location and geometry. Unit of slip is in meter

which is overwhelmingly smaller than our estimate. Although the original SAR data is the same as ours, we notice that the Fig. 89.2 in Nishimura et al is significantly different from our corresponding data in Figs. 89.7 and 89.8. In particular, while our aseismic "observed" range changes are broadly distributed (see lower-left in Fig. 89.8), Nishimura et al's data are localized only around the anticline axis. We think that probably due to this difference in deformed area in the ascending image, the big difference in the estimated moment release did come out. In other words, the fault model for the main shock must be different from ours, but Nishimura et al. (2008) did not show their main shock model. The main shock fault would significantly change the signals in ascending data.

Actually, our study is not the first detection of aseismic deformation of a fold-and-thrust belt. Fielding et al. (2004) reported such a signal associated an earthquake of magnitude 6.9. However, the post earthquake SAR image in their study was acquired 6 months after the event. Thus, it remained uncertain when the aseismic slip took place.

To answer this question, please recall that the earliest post-earthquake image was acquired 3 days after the event. We also examined daily GPS coordinates from the permanent GPS network. We found that the crustal deformation associated with this earthquake terminated mostly within 3 days. Therefore, it turns out that aseismic slip associated with fault-related folding is not as slow as a so-called slow earthquake that would take months or more (e.g., Ide et al. 2007; Furuya and Satyabala, 2008), but not as fast as generating short-period elastic waves. This might be a good news for local residents near fold belt, since seismic hazard potential should have been lowered.

Acknowledgement The ownership of PALSAR data belongs to JAXA/METI. PALSAR level 1.0 data are shared among PALSAR Interferometry Consortium to Study our Evolving Land (PIXEL), and provided from JAXA under a cooperative research contract with ERI, Univ. Tokyo. Hypocenter data was provided from Dr. Aitaro Kato. ASTER DEM is based on ASTER data beta processed by the AIST GEO Grid from ASTER data owned by METI. MF and YT are supported from the grant-in-aid for scientific research, JSPS (19340123). Two anonymous referees are acknowledged for their comments and suggestions.

References

Aoi, S., H. Sekiguchi, N. Morikawa,, T. Kunugi, and M. Shirasaka (2007). Source Process of the 2007 Niigata-ken Chuetsu-oki Earthquake Derived from Near-fault Strong Motion Data, http://www.k-net.bosai.go.jp/k-net/topics/chuetsuoki20070716/inversion/ksw_ver070816_NIED_Inv_eng.pdf.

Constantini, M. (1998). A novel phase unwrapping method based on network programming. *IEEE Trans. Geosci. Remote Sens.*, 36, 813–821.

Fielding, E.J., T.J. Wright, J. Muller, B.E. Parsons, and R. Walker (2004). Aseismic deformation of a fold-and-thrust belt imaged by synthetic aperture radar interferometry near Shahdad, southeast Iran. *Geology*, 32(7), 577–580.

Furuya M. and S.P. Satyabala (2008). Slow earthquake in Afghanistan detected by InSAR. *Geophys. Res. Lett*., 35, L06309, doi:10.1029/2007GL033049.

Hikima, K. and K. Koketsu (2007). Source Process of the 2007 Niigata-ken Chuetsu-oki Earthquake (in Japanese) http://taro.eri.u-tokyo.ac.jp/saigai/chuetsuoki/source/index.html.

Ide, S., G.C. Beroza, D.R. Shelly, and T. Uchide (2007). A scaling law for slow earthquakes. *Nature*, 447, doi:10.1038/nature05780.

Ikeda, Y. (2002). The Origin and mechanism of active folding in Japan. *Active Fault Res*., 22, 67–70 (in Japanese with English abstract).

Jónsson, S., H. Zebker, P. Segall, and F. Amelung (2002). Fault slip distribution of the 1999 *M*w 7.1 hector mine, California, earthquake, estimated from satellite radar and GPS measurementsinternal deformation due to the shear and tensile faults in a half-space. *Bull. Seismo. Soc. Am.*, 92, 1377–1389.

Nishimura T., M. Tobita, H. Yarai, T. Amagai, M. Fujiwara, H. Une, and M. Koarai (2008). Episodic growth of fault-related fold in northern Japan observed by SAR interferometry. *Geophys. Res. Lett.,* 35, L13301, doi: 10.1029/2008GL034337.

Okada, Y. (1992). Internal deformation due to the shear and tensile faults in a half-space. *Bull. Seismo. Soc. Am.*, 82, 1018–1042.

Okamura Y., T. Ishiyama, and Y. Yanagisawa (2007). Fault-related folds above the source fault of the 2004 mid-Niigata Prefecture earthquake, in a fold-and-thrust belt caused by basin inversion along the eastern margin of the Japan Sea. *J. Geophys. Res*., 112, B03S08, doi: 10.1029/2006JB004320.

Rosen, P., S. Hensley, H. Zebker, F. Webb, and E. Fielding (1996). Surface deformation and coherence measurements of Kilauea Volcano, Hawaii, from SIR-C radar interferometry.*J. Geophys. Res.,* 101(E10), 23109–23125.

Sagiya, T., S. Miyazaki, and T. Tada (2000). Continuous GPS array and present-day crustal deformation of Japan. *PAGEOPH*, 157, 2303–2322.

Sato, H. and N. Kato (2005). Relationship between geologic structure and the source fault of the 2004 Mid-Niigata Prefecture EarthquakeT, central Japan. *Earth Planet. Space*, 57, 453–457.

Wegmüler, U. and C. Werner (1997). Gamma SAR processor and interferometry software, In *Proceedings of the 3rd ERS Symposium*, ESA SP-414, 1686–1692.

Yagi, Y. (2007). Source Process of the 2007 Niigata-ken Chuetsu-oki Earthquake, www.geol.tsukuba.ac.jp/~yagi-y/EQ/2007niigata/index.html.

Yamanaka, Y. (2007). Source Process of the 2007 Niigata-ken Chuetsu-oki Earthquake (in Japanese), www.seis.nagoya-u.ac.jp/sanchu/Seismo_Note/2007/NGY2a.html.

Chapter 90

On the Accuracy of LiDAR Derived Digital Surface Models

M. Al-Durgham, G. Fotopoulos, and C. Glennie

Abstract The use of LiDAR data for developing high resolution topographic models of urban and rural areas has been widespread for more than a decade. In particular, the derived high resolution digital surface models (DSMs) are commonly used as input (among other models and parameters) for predicting the coverage of flooded regions. The accuracy of such digital surface models varies depending on a number of factors, from system components (including positioning technology, e.g., GPS/INS, laser scanner and boresighting parameters), data processing (point clouds, interpolation) and signal-target/surface interaction (i.e., backscatter signal strength, laser incidence angle/geometry). The main objective of this paper is to quantify the absolute and relative accuracy of the derived digital surface models. LiDAR data collected over an urban area in Canada from an airborne platform is used for the analysis and compared to precise DGPS survey data. In addition to inter-comparative first order statistical measures, the iterative closest point matching of point clouds method is employed for a consistent analysis. Results provide an indication of the contributing factors to the total error budget for vertical heights in this region which is found to be at the 3 cm level (1 sigma).

90.1 Introduction

The use of LiDAR data for a myriad of applications involving digital surface models at local and regional scales such as forestry (Benoît et al., 2001), flood modeling (Cobby et al., 2001), and 3D GIS models (Zhou et al., 2004) is now common practice. This is due to a number of advantages offered by LiDAR which include, but are not limited to, (i) significant spatial coverage over a short period of time, (ii) accessibility to otherwise non-surveyed areas (i.e., harsh terrain and environmental conditions), (iii) achievable resolution at the few centimetres to decimetre level, and (iv) efficiency in producing a digital surface model (2.5D), see Kraus and Pfeifer (2001) and Shan and Sampath (2005) for detailed examples.

Numerous studies have been conducted on the accuracy (both absolute and relative) assessment of LiDAR data. The American Society for Photogrammetry and Remote Sensing (ASPRS) vertical accuracy standards for generating 0.5 m contour interval maps requires LiDAR's vertical accuracy to be within 4.6 cm Root Mean Square Error (RMSE). Other studies have demonstrated that LiDAR technology is capable of $\pm$8.6 cm (Glennie, 2007) using Terrapoint's airborne laser terrain mapper (ALTM) system flown at an altitude of 1,000 m and $\pm$18.9 cm (Hodgson and Bresnahan, 2004) using the Optech ALTM flown at an altitude of 1,207 m over solid horizontal terrain.

The errors associated with LiDAR derived digital surface models originate from system components, namely a global positioning (GPS) unit that provides 3D positioning information, an inertial measurement unit (IMU) that measures the attitude of the airborne platform, and a laser unit that emits pulses (~1,500 nm in our case) to obtain range information for the ground features. The integration of the sensor information is achieved through a calibration process that yields boresighting parameters referring all data to a common reference system (Toth, 2002).

M. Al-Durgham (✉)
Department of Civil Engineering, University of Toronto, Toronto, ON M5S 1A4, Canada
e-mail: mohannad.al.durgham@utoronto.ca

S.P. Mertikas (ed.), *Gravity, Geoid and Earth Observation*, International Association of Geodesy Symposia 135,
DOI 10.1007/978-3-642-10634-7_90, © Springer-Verlag Berlin Heidelberg 2010

The derived ground coordinates will inherit any systematic and random errors that exist in the LiDAR system (i.e., integrated GNSS/IMU, boresighting, and laser rotating mirror errors), see Katzenbeisser (2003), Morin and El-Sheimy (2002), Glennie et al. (2006), and Glennie (2007) for more details. The error budget is also dependent on the surface characteristics of the target(s) and more specifically the type of target (forest, grass, rock, etc.), the slope of the surface, signal penetration and scattering (Schaer et al., 2007; Hodgson and Bresnahan, 2004).

The focus of this paper is to quantify the total error budget associated with LiDAR derived DSMs (DSMs in this urban case include terrain and buildings) in a manner that has been achieved for other precise geodetic technologies (i.e., GPS, precise levelling). The first phase in this analysis involves processing the data to remove any outliers (i.e., LiDAR points that belong to trees, bushes, and light poles) and to ensure that LiDAR point clouds are describing similar physical features. The latter is achieved through the use of the iterative closest point (ICP) method (Zhang, 1994). The second phase in the assessment procedure involves a detailed investigation into the type of interpolation scheme and refinements that are made in areas with occlusions (a typical feature in any LiDAR data set, Priestnall et al., 2000).



Fig. 90.1 Distribution of GPS control points in the study area

90.2 Description of Data

A LiDAR dataset that consists of 22 strips covering a 6 km^2 area over the city of Ottawa, Canada is used in this study. Since this data set is a full waveform LiDAR which provides detailed information about ground features, all returns were used for the quality assessment of LiDAR data as opposed to using only a single return. The average point spacing is approximately 30 cm and the orthometric heights (H) accuracy $\sigma = \pm 5$ cm according to Terrapoint USA Inc. The dataset was collected during a leafs-on season which introduced numerous non-ground points requiring filtering before conducting the accuracy assessment.

In addition to the LiDAR data, two ground control point datasets collected using RTK-GPS are used. The first control set contains 45 points (referenced to as GPS-45) primarily situated along roadways with an average vertical (height) accuracy of ± 2 cm. The second control set consists of 1,592 points (referenced to as GPS-1592) with a ± 4 cm vertical accuracy. It should be noted that the height assessment conducted herein is with respect to orthometric heights (based on the Canadian regional geoid model, CGG2000). A visual representation of the GPS data is provided in Fig. 90.1.

90.2.1 Removal of Non-planar Points

Before the evaluation process can be conducted, the LiDAR data must be filtered to remove any outliers. In order to address this issue, a fast and automatic planar patches segmentation technique based on the region growing algorithm is employed. Using this approach 33% of the LiDAR points were detected as outliers in an 80 $\times$ 80 m area for the case depicted in Fig. 90.2.

Using the planar patch segmentation method to remove non-ground points is relevant in this case because (i) all of the control points were collected from street surfaces, and (ii) other filtering techniques might fail to filter out all outliers (known as commission error, Keqi et al., 2003). In this study, the estimated vertical accuracy of the LiDAR data of ± 5 cm is used as a strict threshold for planar patch extraction which provided correct classification verified through visual inspection of random samples.

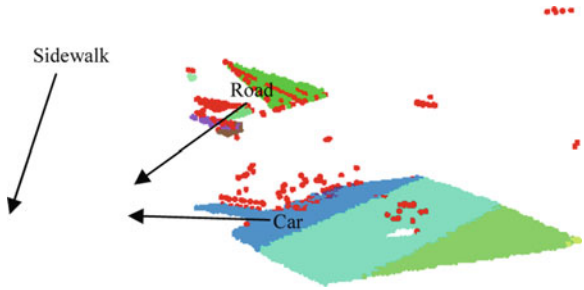


Fig. 90.2 Region growing segmentation results. The red color corresponds to points classified as non-planar

90.2.2 Interpolation of LiDAR Points

In order to compare and analyze the irregularly distributed LiDAR points with the GPS control points, the LiDAR points are interpolated at the GPS locations. In this case, the triangle based interpolation method is used which is based on the following formulation (Watson and Philip, 1984):

$$\mathrm{H}(\mathrm{x},\mathrm{y}) = \sum_{i}^{n} w_i \mathrm{f}(\mathrm{x}_i,\mathrm{y}_i) \tag{1}$$

where H is the unknown height of the computational point, x, and y are the horizontal coordinates of the computational point, x_i, and y_i are the coordinates of the i^{th} neighbouring point used in the interpolation, n is the total number of neighbouring points, and w_i is the weight given to every neighbouring point based on a 2D linear distance from the computation point.

The most straightforward implementation of Eq. (1) is a linear form where 3 neighbouring points are used that form the perimeter of the triangle encompassing the computation point (x, y) (also known as Delaunay triangulation, Sambridge et al., 1995). Therefore, the linear form of Eq. (1) can be rewritten in terms of a plane equation as follows:

$$\mathrm{H} = a\mathrm{x} + b\mathrm{y} + c \tag{2}$$

where a, b, and c are the plane parameters to be estimated. In the case of higher order triangular based interpolation, more parameters are estimated and therefore, more neighbouring nodes are used. In this case, the definition of neighbours is expanded to the nodes sharing sides of the Voronoi cells (Watson and Philip, 1984; Sambridge et al., 1995).

Differences between the interpolated heights and the control points using three interpolation techniques were performed, namely the nearest neighbour, triangle based linear interpolation, and the triangle based cubic interpolation. Since all of the control points were collected over road surfaces, which are considered planer over a short range, the three techniques yield very similar results and therefore, only the linear interpolation results are presented.

90.3 Assessment of Absolute Vertical Accuracy of LiDAR Data

Figure 90.3 shows the mean height difference $\mu_{\Delta \mathrm{H}}$ computed by

$$\mu_{\Delta \mathrm{H}} = \frac{\sum_{i}^{k} \left(\mathrm{H}^{i}_{\mathrm{GPS}} - \mathrm{H}^{i}_{\mathrm{LiDAR}}\right)}{k} \tag{3}$$

where $\mathrm{H}^{i}_{\mathrm{GPS}}$ is the orthometric height of control point i, $\mathrm{H}^{i}_{\mathrm{LiDAR}}$ is the orthometric height of the interpolated LiDAR height at the location of point i, and k is the total number of control points used in the mean height difference calculation. Note that results are shown for 17 strips only since the control set GPS-1592 appears only in those strips, and a representing sample of the standard deviations is shown as well. A comparison between the results for each data set (GPS-45 and GPS-1592) reveals an offset averaging 7.9 cm with

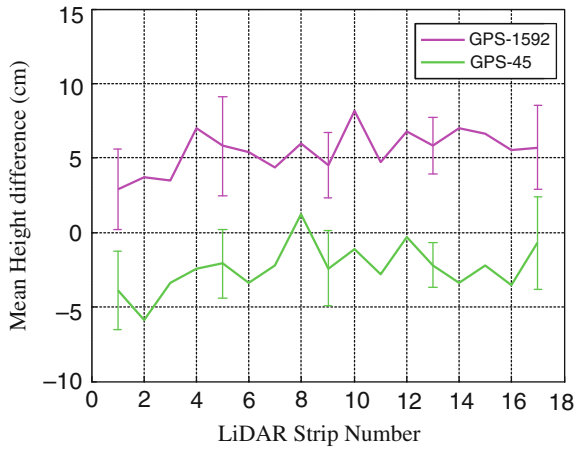


Fig. 90.3 Mean height difference and standard deviation between LiDAR points and GPS control points

a maximum of 10 cm. This inconsistency may be attributed, in part, to the different accuracy and means by which the control points were measured (GPS-1592 was collected from a moving vehicle and is on average 2 cm less accurate than the GPS-45 data set). When the average bias was removed from GPS-1592 to coincide with GPS-45 and then the absolute accuracy reassessed using the adjusted GPS-1592, it was found that the two control surfaces residuals agree at 1.5 cm RMS.

This independent assessment of the accuracy of the LiDAR derived orthometric heights is comparable to the expected accuracy of ±5 cm from other studies, see e.g., Glennie et al. (2006), Glennie (2007), Hodgson and Bresnahan (2004), and Ahokas et al. (2003).

90.4 Assessment of Relative Vertical Accuracy of LiDAR Data

The inherent consistency of the LiDAR data is assessed by comparing overlapping LiDAR data strips. In this particular case, the overlapping strips ranges from 50 to 100% which allows for a thorough assessment. Although the strips overlap, the points comprising the various strips are not routinely co-located and therefore the iterative closest point method (Zhang, 1994; Rusinkiewicz and Levoy, 2001) is implemented to remove systematic inconsistencies between LiDAR strips, thus achieving a homogeneous framework for comparison. Figure 90.4 outlines the key steps for implementing the ICP method which is based on the Euclidean distance as described by Besl and McKay (1992) formulation of the ICP.

Cloud A and *Cloud B* are the overlapping input point clouds, *Kd-Tree* (k-dimensional binary search tree) is an indexing algorithm that is efficient for identifying data point matches between two point clouds (Bentley, 1990) resulting in a new *Cloud C* (e.g., a subset of *Cloud A* or *B*). An iterative six-parameter conformal transformation is applied to create *Cloud D* and is used to optimally align the initial point cloud data sets as follows:

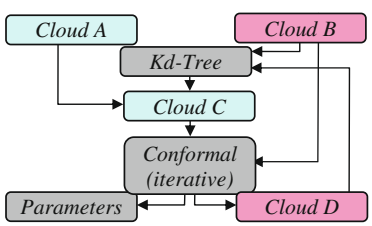


Fig. 90.4 Key steps of the ICP method

$$\begin{bmatrix} x_B \\ y_B \\ z_B \end{bmatrix} = \begin{bmatrix} t_X \\ t_Y \\ t_Z \end{bmatrix} + \mathbf{R} \begin{bmatrix} x_A \\ y_A \\ z_A \end{bmatrix} \tag{4}$$

where, x_A, y_A, z_A, x_B, y_B, and z_B are the 3D coordinates of the points in clouds **A** and **B** respectively, t_X, t_Y, and $t_Z$are the shifts to be estimated along the x, y, and z axes of a right handed system, respectively and **R** is a 3 × 3 rotation matrix given by

$$\mathbf{R} = \mathbf{R}_\omega \mathbf{R}_\varphi \mathbf{R}_k \tag{5}$$

where, $\mathbf{R}_\omega$, $\mathbf{R}_\phi$, and $\mathbf{R}_k$ are the rotation matrices around the x, y, and z axes respectively (Hotine, 1969). The 6 unknown parameters (t_X, t_Y, t_Z, ω, ϕ, k) are solved using a minimum of 3 points via an unweighted iterative least-squares adjustment. The stopping criteria for the iteration are user-defined thresholds. In this case, it was noticed that the estimation of the rotation angles requires more iterations and therefore, the stopping criteria was based on the significance of changes in the estimated rotations (0.1 s). Most of solutions were achieved between 80 and 120 iterations. Alternatively, Horn's method (1987) could be used instead to provide a closed form solution for the transformation parameters. The corresponding standard deviation of the conformal transformation solution is given by

$$\sigma = \sqrt{\frac{(y - A\hat{x})}{(3m - 6)}} \approx \sqrt{\frac{(y - A\hat{x})}{3m}} \tag{6}$$

where, $\hat{x}$ is a vector that contains the updates for the initial estimates (set to zero in this case) of the unknown parameters, **A** is a the design matrix relating the measurements/data points to the unknown parameters, **y** is a vector that contains the difference between first point cloud coordinates and the transformed second point cloud coordinates, and *m* is the number of points. It is worth mentioning that both point clouds must be shifted into a local coordinate system with an origin defined at the centroid of point *Cloud B* in order to avoid a numerically unstable system (see, Al-Durgham, 2007, for examples).

Table 1 Computed RMS height differences before ICP transformation

Reference strip		Model strip		RMS before adjustment (cm)	RMS after adjustment (cm)
A	NE	B	SW	6.7	3.4
A	NE	C	SE	6.7	3.5
A	NE	D	NW	6.4	4.8

This relative accuracy assessment yielded many results for each pair of strips. A representative sample, consisting of 317 points in 10 overlapping areas is used to compute the RMS for the mean height differences ($\mu\Delta H_{LiDAR1-LiDAR2}$) and the results are provided in Table 90.1. In this table, the model strips are examined for consistency with respect to strip A (Reference).

After the transformation, the computed RMS values reduce from ~6.7 cm before the adjustment to 3.5 cm for 66% of the cases. This indicates a systematic bias in the LiDAR strips and it was found that this bias is acting mainly along the flying direction with a magnitude of 8 cm introducing a vertical component of roughly 3 cm at surfaces with a 20° slope (e.g., a building roof). This along track bias could be caused by various LiDAR components such as the estimated borsighting parameters and the non-orthogonality of the laser scanner beam along the flight direction (Al-Durgham, 2007).

90.5 Improving the Interpolation Performance in Areas with Occlusions

As mentioned previously, point clouds resulting from LiDAR measurements are irregularly distributed with a point spacing that is dependent on a combination of system parameters such as, the airborne platform speed, rotating mirror angle, as well as the variable target surface heights. Moreover, the LiDAR data contains gaps (occlusions) resulting from significant changes in the ground target heights as depicted in color in Fig. 90.5. The objective of this section is to improve the interpolation performance in areas with occlusions occurring in urban LiDAR data.

Common techniques for dealing with occlusions involve manual or semi-automatic digitization of breaklines (Zhou et al., 2004). However, this approach can be cumbersome and prone to errors based on user-skill. As an alternative, an artificial-point scheme has been implemented in this study to alleviate the interpolation error in occluded areas. Figure 90.6 demonstrates this approach.

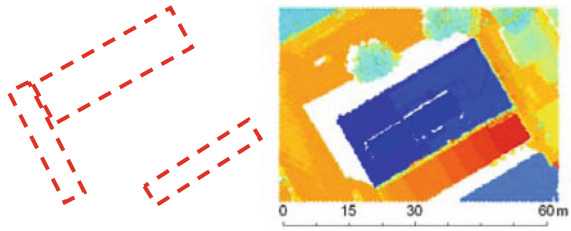


Fig. 90.5 Color coded LiDAR points showing data gaps (*white*)

An artificial point (B_i) is included to the LiDAR point cloud before interpolation. The coordinates of the artificial point could (x_i, y_i, z_{i+1}) are computed from the two neighbouring points (neighbourhood is based on the sequence at which points are stored in the original LiDAR data). However, it is known that no duplicate points should exist in a Delaunay based interpolation (Shewchuk, 1996); therefore, the artificial point must be shifted about 1 mm towards point P_1. This method is made possible because the temporal sequence of the data collection is known to the user and therefore sudden variations in the horizontal and vertical can be identified.

Figure 90.6 depicts the interpolated digital surface model before and after the artificial point inclusion. An improvement of 5:1 was achieved in the building edge when compared to Fig. 90.7a. One limitation of the proposed method is that it assumes that the terrain in the occluded area does not vary (and is free

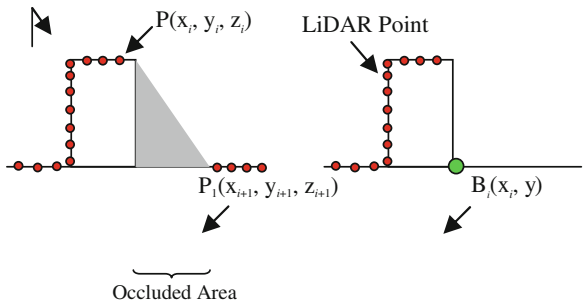


Fig. 90.6 Adding artificial points to LiDAR data

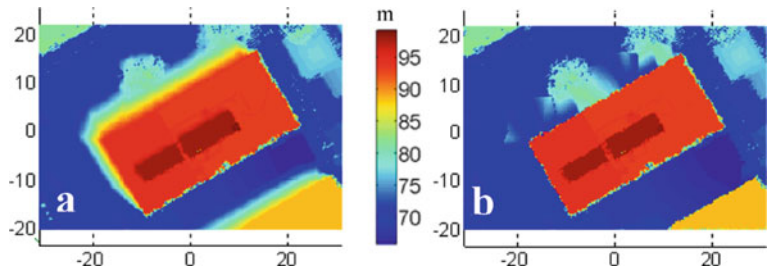


Fig. 90.7 Generating DSM before (**a**) and after (**b**) adding artificial points and removing trees

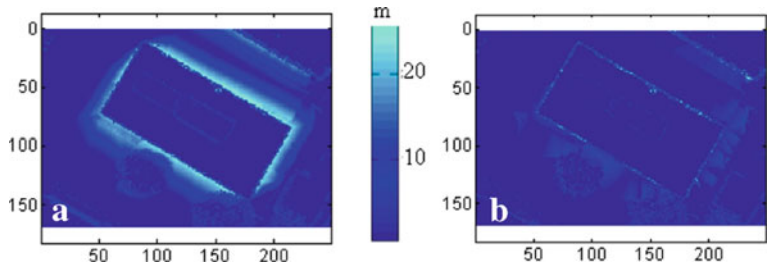


Fig. 90.8 Subtracting DSMs before (**a**) and after (**b**) adding artificial points and removing trees

of features such as trees), which is a valid assumption for urban areas in most cases. If this assumption does not represent reality, then an incorrect recovery of heights may be obtained, which should be resolved using point classification (Kraus and Pfeifer, 2001) before the interpolation process.

To further assess the performance of this procedure, the same area shown in Fig. 90.7 is extracted from a different set of LiDAR strips with an opposite look angle. The resulting digital surface model difference derived from the opposing strips is shown in Fig. 90.8. The mean height difference in this 25 m high building is ~4 m (Fig. 90.8a) with an improvement down to ~0.8 m after artificial points are included in Fig. 90.8b.

This process of adding artificial points before interpolating LiDAR data improves the quality of the resulting DSM and provides a time efficient solution to gaps rather than using breaklines.

90.6 Conclusions

The need to quantify the total error budget associated with LiDAR in a manner that has been achieved for other precise geodetic technologies has increased as the implementation/application of DSMs (not to mention DTMs) becomes more widespread. This paper investigated the absolute and relative vertical accuracy of LiDAR derived DSMs in a typical urban environment. Results showed an absolute agreement of ~2 and 6 cm when compared to GPS control data, namely GPS- 45 and GPS-1542, respectively. Other studies report approximately 5–10 cm achievable accuracies for a 1 km airborne platform altitude. In terms of relative accuracy a overall average value of 3.5 cm RMS was found (after adjustment). Furthermore, an improvement in interpolation performance for this urban region (with 25 m average building heights) of 5:1 was demonstrated by introducing artificial points in occluded areas (a common issue in urban LiDAR data sets). Future work will focus on the type of target and associated achievable accuracy levels.

References

Ahokas, E., H. Kaarttinen, J. Hyyppä (2003). A quality assessment of airborne laser scanner data. Proceedings of the ISPRS Working Group III/3 Workshop "3-D Reconstruction from Airborne Laserscanner and InSAR Data". Dresden, Germany, October 8–10, vol. 34, Part 3/W13, pp. 1–7.

Al-Durgham, M. (2007). Alternative Methodologies for the Quality Control of LiDAR Systems, M.Sc. thesis (UCGE Report No. 20259), University of Calgary.

Benoît, A., B. St-Onge, and N. Achaichia (2001). Measuring forest canopy height using a combination of LiDAR and aerial photography data. *Int. Arch. Photogramm. Remote Sensing Spat. Inf. Sci.*, 34(Part 3/W4), 131–137.

Bentley, J. (1990). K-d Trees for Semidynamic Point Sets. SCG '90: Proceedings 6th Annual Symposium on Computational Geometry, pp. 187–197.

Besl, P.J. and H.D. McKay (1992). A method for registration of 3-D shapes. *IEEE Trans. Pattern Anal. Mach. Intell.*, 14(2), 239–256.

Cobby, D.M., D.C. Mason, and I.J. Davenport (2001). Image processing of airborne scanning laser altimetry data for improved river flood modelling. *ISPRS J. Photogramm. Remote Sensing*, 56(2), 121–138.

Glennie, C., K. Kusevic, and P. Mrstik (2006). Performance analysis of a kinematic terrestrial LIDAR scanning system. Proceedings of MAPPS/ASPRS Fall Conference, Measuring the Earth (Part II). San Antonio, Texas, Nov. 6–10. CD Procs.

Glennie, C. (2007). Rigorous 3D error analysis of kinematic scanning LiDAR systems. *J. Appl. Geod.*, 1(3),147–157.

Hodgson, M.E. and P. Bresnahan (2004). Accuracy of airborne LiDAR-derived elevation: empirical assessment and error budget. *Photogramm. Eng. Remote Sensing*, 70(3),331–339.

Horn, B.K.P. (1987). Closed-form solution of absolute orientation using unit quaternions. *J. Opt. Soc. Am.*, 4(4),629–642.

Hotine, M. (1969). Mathematical geodesy. ESSA Monogr No 2, US Department of Commerce, Washington, DC.

Katzenbeisser, R. (2003). About the calibration of LiDAR sensors. *Int. Arch. Photogramm. Remote Sensing Spat. Inf. Sci.*, 34(Part 3/W13),59–64.

Keqi, Z., C. Shu-Ching, D. Whitman, S. Mei-Ling, J. Yan, C. Zhang (2003). A progressive morphological filter for removing non-ground measurements from airborne LIDAR data. *IEEE Transactions on Geoscience and Remote Sensing.* 41, No. 4, 872–882.

Kraus, K. and N. Pfeifer (2001). Advanced DTM generation from LIDAR data. *Int. Arch. Photogramm. Remote Sensing*, 34(3/W4), Annapolis, MD, USA, 23–30.

Morin, K. and N. El-Sheimy (2002). Post-mission adjustment methods of airborne laser scanning data. Proceedings of FIG XXII International Congress. Washington, USA, April 19–26, CD Procs.

Priestnall, G, J. Jaafar, and A. Duncan (2000). Extracting urban features from LiDAR digital surface models. *Comput. Environ. Urban Syst.*, 24(2), 65–78.

Rusinkiewicz, S. and M. Levoy. (2001). Efficient variants of the ICP algorithm. Proceedings of the International Conference on 3D Digital Imaging and Modeling, pp. 145–152.

Sambridge, M., J. Braun, and H. McQueen (1995). Geophysical parameterization and interpolation of irregular data using natural neighbours. *Geophys. J. Int.*, 122(3), 837–857.

Schaer, P., J. Skaloud, S. Landtwing, and K. Legat (2007). Accuracy estimation for laser point cloud including scanning geometry. 5th International Symposium on Mobile Mapping Technology (MMT2007), Padua, Italy, May 29–31, CD Procs.

Shan, J. and A. Sampath (2005). Urban DEM generation from raw Lidar data: a labelling algorithm and its performance. *Photogramm. Eng. Remote Sensing*, 71(2), 217–226.

Shewchuk, J. (1996). Triangle: engineering a 2D quality mesh generator and delaunay triangulator. The Workshop on Applied Computational Geometry, Towards Geometric Engineering, Philadelphia, USA, May 27–28, pp. 203–222.

Toth, K. (2002). Calibrating airborne LIDAR systems. Proceedings of ISPRS Commission II Symposium, Xi'an, China, August 20–23, pp. 475–480.

Watson, F. and M. Philip (1984). Triangle based interpolation. *Math. Geol.*, 16(8), 779–795.

Zhang, Z. (1994). Iterative point matching for registration of free-form curves and surfaces. *Int. J. Comput. Vis.*, 13(2), 119–152.

Zhou, G., C. Song, J. Simmers, and Cheng, P. (2004). Urban 3D GIS from LiDAR and digital aerial images. *Comput. Geosci.*, 30(4), 345–353.

Chapter 91

Multiscale Segmentation of Polarimetric SAR Data Using Pauli Analysis Images

M. Dabboor, A. Braun, and V. Karathanassi

Abstract Image segmentation is a crucial process that affects the output of any segment-based classification method and governs the interpretation process. There are many approaches for segmentation of polarimetric SAR data, such as region growing and split-merge to name a few, that have been proposed recently. This paper presents the development of a new segmentation approach based on the dominant scattering mechanisms that contribute to the backscattering process, using Pauli analysis images as input data. After accomplishing the segmentation based on the scattering mechanism, further segmentation is performed by the calculation and segmentation of histograms into homogeneous regions. State-of-art ALOS polarimetric SAR data are used in the study area which is located in the southern United Kingdom and includes the city of Minehead.

91.1 Introduction

Different methods have been proposed to analyse polarimetric SAR data such as the (a) Pauli analysis method which produces the surface, double bounce and 45° tilted double bounce, Papathanassiou (1999), (b) Cloude–Pottier analysis method which produces the entropy, a-angle and anisotropy images and other derivatives, Pottier and Lee (1999), (c) Freeman–Durdan analysis method which produces the double bounce, surface and volume images, Freeman and Durdanet al. (1998), (d) analysis to sphere, diplane and helix, Hellmann (1999), (e) analysis based on the Huynen parameters, Titin-Schnaider (1999), (f) decomposition based on different combinations of entropy and anisotropy, Pottier and Durdan (1999).

In a previous study, it was indicated that information provided by Cloude–Pottier analysis and the images produced by different combinations of entropy and anisotropy were crucial for the determination of the number of the scattering mechanisms which participated in a knowledge-based classification procedure, Dabboor and Karathanassi (2005). Various other segmentation approaches of polarimetric SAR data have been proposed in the literature, see for example Beaulieu and Touzi (2004), Lee et al. (2001), Grandi et al.(2001). Especially, Lee et al. (2001) in their work have proposed a segmentation approach based on 3D histograms, calculated from the Pauli analysis images.

In this paper, the Pauli analysis method is investigated through the development and evaluation of a new segmentation methodology applied to Pauli analysis images. The proposed segmentation methodology focuses on the hierarchicalization of the scattering mechanisms provided by the Pauli analysis method.

91.2 Segmentation Approach

91.2.1 Pauli Analysis Method

The proposed method is based on the analysis images calculated from the Pauli decomposition.

Pauli analysis is one of the basic SAR polarimetric data analysis methods, Papathanassiou (1999). In this

M. Dabboor (✉)
Department of Geomatics Engineering, Schulich School of Engineering, University of Calgary, Calgary, AB T2N 1N4, Canada
e-mail: mddabboo@ucalgary.ca

S.P. Mertikas (ed.), *Gravity, Geoid and Earth Observation*, International Association of Geodesy Symposia 135,
DOI 10.1007/978-3-642-10634-7_91, © Springer-Verlag Berlin Heidelberg 2010

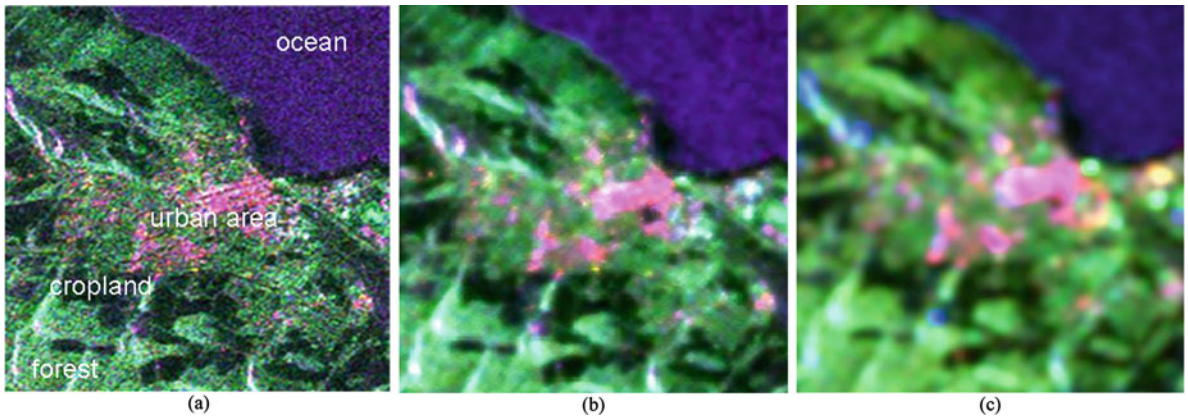


Fig. 91.1 (**a**) Original polarimetric SAR image: *Red* = S_{HH}, *Green* = S_{HV}, *Blue* = S_{VV}, (**b**) Data after removing speckle with a Lee-filter, (**c**) Pauli analysis images: *Red* = double bounce, *Green* = 45° double bounce, *Blue* = surface

method, the 3 by 3 coherency matrix T is decomposed into three independent matrices, whereby each matrix represents a single scattering process. These matrices constitute the Pauli base Ψ_P which is related to the physics of wave scattering, Papathanassiou (1999):

$$\Psi_P = \left\{ \frac{1}{\sqrt{2}} \begin{bmatrix} 1 & 0 \\ 0 & 1 \end{bmatrix}, \frac{1}{\sqrt{2}} \begin{bmatrix} 1 & 0 \\ 0 & -1 \end{bmatrix}, \frac{1}{\sqrt{2}} \begin{bmatrix} 0 & 1 \\ 1 & 0 \end{bmatrix} \right\} \quad (1)$$

The corresponding scattering vector is then:

$$\vec{k} = \frac{1}{\sqrt{2}} \left(S_{HH} + S_{VV} \; S_{HH} - S_{VV} \; 2S_{HV} \right)^T \quad (2)$$

where S_{ij} are the scattering amplitudes and H and V indicating the horizontal and vertical polarization, respectively.

This method interprets the surface, double bounce and 45° tilted double bounce scattering mechanisms. The Pauli components are computed as follows:

$$\begin{aligned} &\text{Pauli1 (double bounce)} = S_{HH} - S_{VV} \\ &\text{Pauli2 (45° tilted double bounce)} = 2S_{HV} \\ &\text{Pauli3 (surface)} = S_{HH} + S_{VV} \end{aligned} \quad (3)$$

91.2.2 Speckle Removing

The complexity of polarimetric SAR data segmentation is related to the presence of coherent speckle. Thus, removing the speckle is a required fundamental step before further processing polarimetric SAR data. In SAR images of less than 500 by 500 pixels, the repetitive application of the Lee filter (applied three times in the study area) can effectively remove the noise speckle and discriminate between the different types of scatterers, Lee et al. (2001). Figure 91.1a shows the polarimetric SAR image of the study area in the Southern UK (300 by 300 pixels, center coordinate: Latitude 51° 12′ 17.77″, Longitude 3° 28′ 39.81″). The main surface types in the study area are ocean, urban area, forest and cropland. Figure 91.1b shows the data after applying the Lee filter three times to remove the speckle.

91.2.3 New Segmentation Method

The proposed method is based on the analysis images calculated from the Pauli decomposition. Removing the speckle from the available polarimetric SAR data, the Pauli decomposition is applied in order to calculate the surface, double bounce and 45° tilted double bounce analysis images, Fig. 91.1c.

In the first segmentation level, the data are segmented based on the scattering behaviour that appears in each pixel. Thus, the resulting segmentation contains: (1) areas where the surface scattering mechanism is dominant, e.g. ocean and urban areas; (2) areas where the 45° tilted double bounce scattering mechanism is dominant, e.g. forest and vegetation; and (3) areas where the double bounce scattering mechanism is dominant, e.g. urban regions and rough terrain.

Because the dominant scattering mechanism is not sufficient for the complete description of the scattering behaviour of the targets, the second in amplitude scattering mechanism is taken into consideration in the second processing step. Thus, in the second segmentation level, the areas where one distinct scattering mechanism is dominant are segmented into three sub-areas, according to their second dominant scattering mechanism.

Since the segmentation based on the hierarchicalization of the scattering mechanisms is accomplished, a third step segmentation is proposed in order to exploit inherent variations within each scattering mechanism. Thus, in the third segmentation level sub-areas are further segmented based on their histograms. A non parametric histogram segmentation algorithm, based on the binomial probability, is applied to the calculated histograms, Delon et al. (2007). The segmentation procedure is summarized in Fig. 91.2.

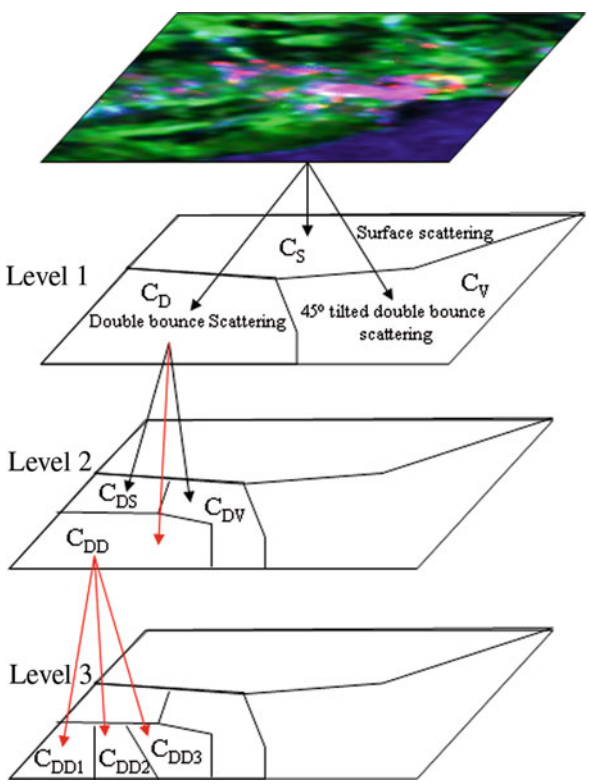


Fig. 91.2 The 3-level segmentation procedure. *Red arrows* indicate an area with double bounce scattering mechanism only

91.2.3.1 First Segmentation Level

The Pauli images are used as input data in the segmentation process. The first segmentation level is performed based on the dominant scattering mechanism that appears in each pixel. The areas' dominant scattering mechanisms are shown in Fig. 91.3a. It is observed that several surface types, for example parts of the urban area and forest/cropland exhibit the same dominant scattering mechanism (45° tilted double bounce) shown in green in Fig. 91.3a

91.2.3.2 Second Segmentation Level

In the second segmentation level, the second most significant value is taken into consideration. For example, an area labelled as C_D is further segmented into three sub-areas C_{DD}, C_{DV} and C_{DS}, using the following relations:

$$k \in \begin{cases} C_{DD} & if \frac{P_D}{P_S+P_V+P_D} \geq 0.5 \\ C_{DV} & if \frac{P_D}{P_S+P_V+P_D} < 0.5, p_V \geq P_S \\ C_{DS} & if \frac{P_D}{P_S+P_V+P_D} < 0.5, p_S > P_V \end{cases} \quad (4)$$

k is a pixel which belongs to area C_D, P_D is the amplitude of the first dominant scattering mechanism, P_V and P_S are the amplitudes of the remaining mechanisms. After applying the second level segmentation, Fig. 91.3b demonstrates that surface types have been properly segmented into sub-areas. For example, the forest/cropland area is further segmented into sub-areas without being confused with other surface types. In addition, the shallow water near the coastline is separated from the deep water.

91.2.3.3 Third Segmentation Level

More detailed segmentation of the sub-areas is performed by calculating and segmenting their histograms, using a histogram-based segmentation algorithm. Each histogram is divided into homogeneous regions. Figure 91.3c shows the results of the third segmentation level.

As appears in Fig. 91.3c, the sub-area where the 45° tilted double bounce scattering mechanism is the only dominant mechanism is now split up into four regions

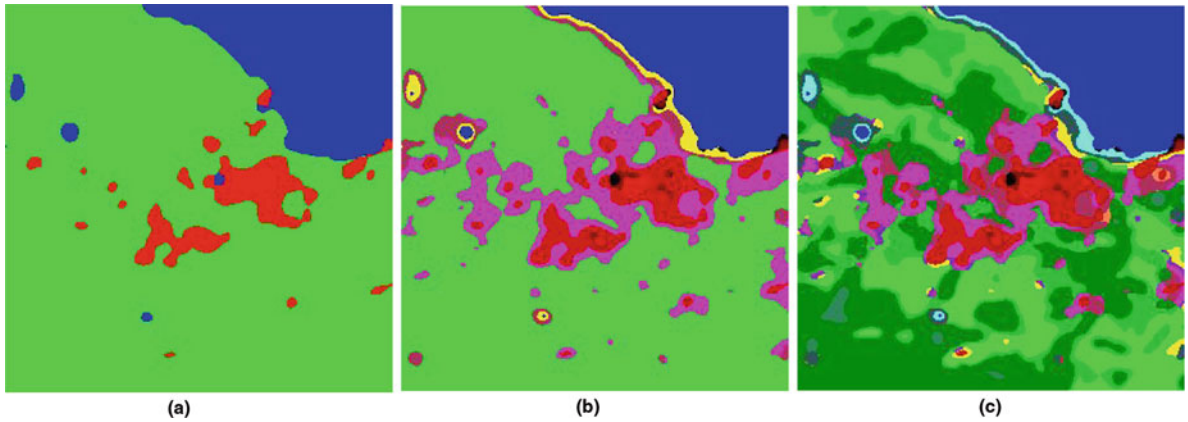


Fig. 91.3 (**a**) First segmentation level: *Red* = double bounce, *Green* = 45° double bounce, *Blue* = surface, (**b**) Second segmentation level: C_{SS} = *blue*, C_{SV} = *yellow*, C_{SD} = *black*, C_{DD} = open *red*, C_{DV} = *red*, C_{DS} = *dark red*, C_{VV} = *green*, C_{VD} = *magenta*, C_{VS} = *maroon*, (**c**) Third segmentation level: C_{VV1} = open *green*, C_{VV2} = *green*, C_{VV3} = *dark green*, C_{VV4} = *sea green*, C_{VD1} = *yellow*, C_{VD2} = *purple*, C_{VD3} = *magenta*, C_{VD4}= *maroon*, C_{VD5} = coral

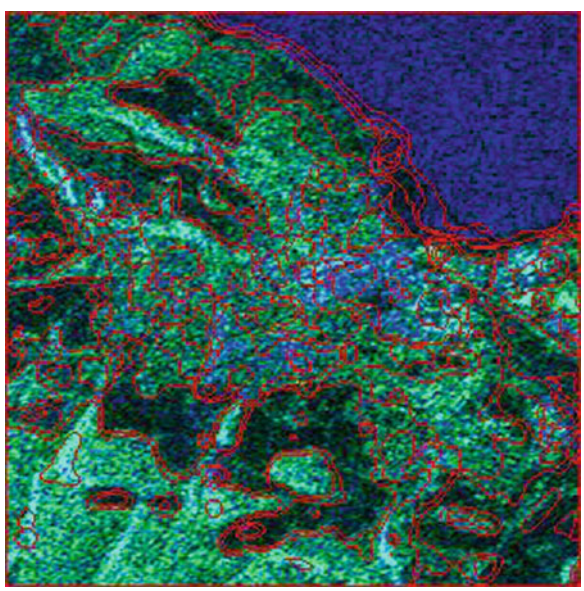


Fig. 91.4 The edges of the resulting segments over the initial polarimetric SAR data (*Red* = edges, *Green* = S_{HV}, *Blue* = S_{VV})

C_{VV1}, C_{VV2}, C_{VV3}, and C_{VV4}. Thus, forest is separated from the cropland. The sub-area where the 45° tilted double scattering mechanism is dominant and the double bounce scattering mechanism is also significant is segmented into five regions C_{VD1}, C_{VD2}, C_{VD3}, C_{VD4}, and C_{VD5}. Thus, more detailed segmentation of the urban area can be achieved. In addition, the forested areas are separated from croplands. Figure 91.4 shows the edges of the segments over the initial polarimetric SAR data. Comparison of the segmentation results with the available electo-optical image (ALOS AVNIR) validated the proposed approach for SAR image segmentation.

91.3 Conclusions

In this paper, a methodology for the multiscale segmentation of polarimetric SAR data using Pauli analysis images is described. The proposed method exploits completely the scattering information that was obtained by the Pauli decomposition in the segmentation process and thus goes beyond traditional segmentation methods. A non parametric histogram segmentation algorithm based on the binomial probability was used for further segmentation of the data which improved the classification. The comparison of the resulted segmentation with an electro-optical image (ALOS AVNIR) of the study area shows its effectiveness after validation. Once more ALOS data becomes available, the new segmentation method will be further applied to different surface types (e.g. ice, snow, bare rocks, wetlands) in order to investigate the robustness of the method.

Acknowledgement The authors would like to thank the Japan Aerospace Exploration Agency (JAXA) for providing the ALOS PALSAR image. The authors are grateful for valuable discussions with Dr. Julie Delon.

References

Beaulieu, J. and R. Touzi (2004). Segmentation of Textured Polarimetric SAR Scenes by Likelihood Approximation. *IEEE Trans. Geosci. Remote Sens.*, 42(10), 2063–2072.

Dabboor, M. and V. Karathanassi (2005). A knowledge–based Classification Method for Polarimetric SAR Data. *SPIE Europe International Symposium, Remote Sensing*, Belgium.

Delon, J., A. Desolneux, J. Lisani, and A. Petro (2007). A non parametric approach for histogram segmentation. *IEEE Trans. Image Process.*, 16, 253–261.

Freeman, A. and S. Durdan (1998). A Three-Component Scattering Model for Polarimetric SAR Data. *IEEE Trans. Geosci. Remote Sens.,* 36(3), 963–973.

Grandi, D.F., J.S. Lee, P. Siqueira, A. Baraldi, and M. Simard (2001). Segmentation and Labeling of Polarimetric SAR Data: Can Wavelets Help? *Proceedings of the International Geoscience and Remote Sensing Symposium*, Sydney.

Hellmann, M. (1999). Classification of Full Polarimetric SAR Data for Cartographic Application. PhD thesis, Oberpfaffenhofen, Germany.

Lee, J.S., M.R. Grunes, E. Pottier, and L. Ferro-Famil (2001). Segmentation of Polarimetric SAR Images. *Proceedings of the International Geoscience and Remote Sensing Symposium*, Sydney.

Papathanassiou, K.P. (1999). Polarimetric SAR Interferometry. PhD Thesis, University of Graz, Austria.

Pottier, E. and J.S. Lee (1999). Application of the H/A/α Polarimetric Decomposition Theorem for Unsupervised Classification of Fully Polarimetric SAR Data Based on the Wishart Distribution. *Proceedings of the CEOS'99*, Toulouse, France.

Titin-Schnaider, C. (1999). Radar Polarimetry for Vegetation Observation. *Proceedings of the CEOS-SAR Workshop*, Toulouse, France.